ADVANCED IMAGING METHODS IN NEUROSCIENCE

EDITED BY: João O. Malva, Jorge Valero, Miguel Castelo-Branco and Alard Roebroeck

PUBLISHED IN: Frontiers in Neuroscience

frontiers Research Topics

frontiers

Frontiers eBook Copyright Statement

The copyright in the text of individual articles in this eBook is the property of their respective authors or their respective institutions or funders. The copyright in graphics and images within each article may be subject to copyright of other parties. In both cases this is subject to a license granted to Frontiers.

The compilation of articles constituting this eBook is the property of Frontiers.

Each article within this eBook, and the eBook itself, are published under the most recent version of the Creative Commons CC-BY licence. The version current at the date of publication of this eBook is CC-BY 4.0. If the CC-BY licence is updated, the licence granted by Frontiers is automatically updated to the new version.

When exercising any right under the CC-BY licence, Frontiers must be attributed as the original publisher of the article or eBook, as applicable.

Authors have the responsibility of ensuring that any graphics or other materials which are the property of others may be included in the CC-BY licence, but this should be checked before relying on the CC-BY licence to reproduce those materials. Any copyright notices relating to those materials must be complied with.

Copyright and source acknowledgement notices may not be removed and must be displayed in any copy, derivative work or partial copy which includes the elements in question.

All copyright, and all rights therein, are protected by national and international copyright laws. The above represents a summary only. For further information please read Frontiers' Conditions for Website Use and Copyright Statement, and the applicable CC-BY licence.

ISSN 1664-8714
ISBN 978-2-88971-725-5
DOI 10.3389/978-2-88971-725-5

About Frontiers

Frontiers is more than just an open-access publisher of scholarly articles: it is a pioneering approach to the world of academia, radically improving the way scholarly research is managed. The grand vision of Frontiers is a world where all people have an equal opportunity to seek, share and generate knowledge. Frontiers provides immediate and permanent online open access to all its publications, but this alone is not enough to realize our grand goals.

Frontiers Journal Series

The Frontiers Journal Series is a multi-tier and interdisciplinary set of open-access, online journals, promising a paradigm shift from the current review, selection and dissemination processes in academic publishing. All Frontiers journals are driven by researchers for researchers; therefore, they constitute a service to the scholarly community. At the same time, the Frontiers Journal Series operates on a revolutionary invention, the tiered publishing system, initially addressing specific communities of scholars, and gradually climbing up to broader public understanding, thus serving the interests of the lay society, too.

Dedication to Quality

Each Frontiers article is a landmark of the highest quality, thanks to genuinely collaborative interactions between authors and review editors, who include some of the world's best academicians. Research must be certified by peers before entering a stream of knowledge that may eventually reach the public - and shape society; therefore, Frontiers only applies the most rigorous and unbiased reviews.
Frontiers revolutionizes research publishing by freely delivering the most outstanding research, evaluated with no bias from both the academic and social point of view. By applying the most advanced information technologies, Frontiers is catapulting scholarly publishing into a new generation.

What are Frontiers Research Topics?

Frontiers Research Topics are very popular trademarks of the Frontiers Journals Series: they are collections of at least ten articles, all centered on a particular subject. With their unique mix of varied contributions from Original Research to Review Articles, Frontiers Research Topics unify the most influential researchers, the latest key findings and historical advances in a hot research area! Find out more on how to host your own Frontiers Research Topic or contribute to one as an author by contacting the Frontiers Editorial Office: frontiersin.org/about/contact

ADVANCED IMAGING METHODS IN NEUROSCIENCE

Topic Editors:
João O. Malva, University of Coimbra, Portugal
Jorge Valero, University of Salamanca, Spain
Miguel Castelo-Branco, Coimbra Institute for Biomedical Imaging and Translational Research (CIBIT), Portugal
Alard Roebroeck, Maastricht University, Netherlands

Citation: Malva, J. O., Valero, J., Castelo-Branco, M., Roebroeck, A., eds. (2021). Advanced Imaging Methods in Neuroscience. Lausanne: Frontiers Media SA. doi: 10.3389/978-2-88971-725-5

Table of Contents

07 ***A Novel Method for Assessing Cerebral Edema, Infarcted Zone and Blood-Brain Barrier Breakdown in a Single Post-stroke Rodent Brain***
Ruslan Kuts, Dmitry Frank, Benjamin F. Gruenbaum, Julia Grinshpun, Israel Melamed, Boris Knyazer, Oleg Tarabrin, Vladislav Zvenigorodsky, Ilan Shelef, Alexander Zlotnik and Matthew Boyko

20 ***ACOEC-FD: Ant Colony Optimization for Learning Brain Effective Connectivity Networks From Functional MRI and Diffusion Tensor Imaging***
Junzhong Ji, Jinduo Liu, Aixiao Zou and Aidong Zhang

35 ***Examination of Structural Variations of the Circle of Willis by 3D Time-of-Flight Magnetic Resonance Angiography***
Jing Li, Jue Wang, Xiao-er Wei, Yu-wu Zhao, Feng Wang and Yue-hua Li

41 ***Amide Proton Transfer Imaging in Predicting Isocitrate Dehydrogenase 1 Mutation Status of Grade II/III Gliomas Based on Support Vector Machine***
Yu Han, Wen Wang, Yang Yang, Ying-Zhi Sun, Gang Xiao, Qiang Tian, Jin Zhang, Guang-Bin Cui and Lin-Feng Yan

52 ***Pushing the Limits of EEG: Estimation of Large-Scale Functional Brain Networks and Their Dynamics Validated by Simultaneous fMRI***
Rodolfo Abreu, Marco Simões and Miguel Castelo-Branco

69 ***Activatable Fluorescence Imaging of Macrophages in Cerebral Aneurysms Using Iron Oxide Nanoparticles Conjugated With Indocyanine Green***
Hiroyuki Ikeda, Akira Ishii, Kohei Sano, Hideo Chihara, Daisuke Arai, Yu Abekura, Hidehisa Nishi, Masahiro Ono, Hideo Saji and Susumu Miyamoto

79 ***Harmonization of Brain Diffusion MRI: Concepts and Methods***
Maíra Siqueira Pinto, Roberto Paolella, Thibo Billiet, Pieter Van Dyck, Pieter-Jan Guns, Ben Jeurissen, Annemie Ribbens, Arnold J. den Dekker and Jan Sijbers

96 **In vivo** ***MRI Successfully Reveals the Malformation of Cortical Development in Infant Rats***
Minyoung Lee, Eun-Jin Kim, Dong-Cheol Woo, Woo-Hyun Shim and Mi-Sun Yum

107 ***Object-Based Analyses in FIJI/ImageJ to Measure Local RNA Translation Sites in Neurites in Response to Aβ1-42 Oligomers***
María Gamarra, Maite Blanco-Urrejola, Andreia F. R. Batista, Josune Imaz and Jimena Baleriola

125 ***Corrigendum: Object-Based Analyses in FIJI/ImageJ to Measure Local RNA Translation Sites in Neurites in Response to Aβ1-42 Oligomers***
María Gamarra, Maite Blanco-Urrejola, Andreia F. R. Batista, Josune Imaz and Jimena Baleriola

127 ***Histological Correlates of Diffusion-Weighted Magnetic Resonance Microscopy in a Mouse Model of Mesial Temporal Lobe Epilepsy***
Katharina Göbel-Guéniot, Johannes Gerlach, Robert Kamberger, Jochen Leupold, Dominik von Elverfeldt, Jürgen Hennig, Jan G. Korvink, Carola A. Haas and Pierre LeVan

143 ***Improved Visualization of Focal Cortical Dysplasia With Surface-Based Multiparametric Quantitative MRI***
Michelle Maiworm, Ulrike Nöth, Elke Hattingen, Helmuth Steinmetz, Susanne Knake, Felix Rosenow, Ralf Deichmann, Marlies Wagner and René-Maxime Gracien

151 ***A Fully Automated Method for Segmenting Arteries and Quantifying Vessel Radii on Magnetic Resonance Angiography Images of Varying Projection Thickness***
Sivakami Avadiappan, Seyedmehdi Payabvash, Melanie A. Morrison, Angela Jakary, Christopher P. Hess and Janine M. Lupo

165 ***NOSA, an Analytical Toolbox for Multicellular Optical Electrophysiology***
Sebastian Oltmanns, Frauke Sophie Abben, Anatoli Ender, Sophie Aimon, Richard Kovacs, Stephan J. Sigrist, Douglas A. Storace, Jörg R. P. Geiger and Davide Raccuglia

179 ***Glutamate Chemical Exchange Saturation Transfer (GluCEST) Magnetic Resonance Imaging in Pre-clinical and Clinical Applications for Encephalitis***
Yanlong Jia, Yanzi Chen, Kuan Geng, Yan Cheng, Yan Li, Jinming Qiu, Huaidong Huang, Runrun Wang, Yunping Zhang and Renhua Wu

190 ***Investigating the Reliability of Population Receptive Field Size Estimates Using fMRI***
Agustin Lage-Castellanos, Giancarlo Valente, Mario Senden and Federico De Martino

207 **In vivo** ***PET Imaging of Gliogenesis After Cerebral Ischemia in Rats***
María Ardaya, Ana Joya, Daniel Padro, Sandra Plaza-García, Vanessa Gómez-Vallejo, Mercedes Sánchez, Maider Garbizu, Unai Cossío, Carlos Matute, Fabio Cavaliere, Jordi Llop and Abraham Martín

217 ***Deciphering Brain Function by Miniaturized Fluorescence Microscopy in Freely Behaving Animals***
Sarah Malvaut, Vlad-Stefan Constantinescu, Harold Dehez, Sead Doric and Armen Saghatelyan

230 ***Pyneal: Open Source Real-Time fMRI Software***
Jeff J. MacInnes, R. Alison Adcock, Andrea Stocco, Chantel S. Prat, Rajesh P. N. Rao and Kathryn C. Dickerson

246 ***Initial Experience of Challenge-Free MRI-Based Oxygen Extraction Fraction Mapping of Ischemic Stroke at Various Stages: Comparison With Perfusion and Diffusion Mapping***
Shun Zhang, Junghun Cho, Thanh D. Nguyen, Pascal Spincemaille, Ajay Gupta, Wenzhen Zhu and Yi Wang

257 ***Snowball ICA: A Model Order Free Independent Component Analysis Strategy for Functional Magnetic Resonance Imaging Data***
Guoqiang Hu, Abigail B. Waters, Serdar Aslan, Blaise Frederick, Fengyu Cong and Lisa D. Nickerson

272 ***Imaging the Neuroimmune Dynamics Across Space and Time***
Micaël Carrier, Marie-Ève Robert, Fernando González Ibáñez, Michèle Desjardins and Marie-Ève Tremblay

285 ***Rapidly (and Successfully) Translating Novel Brain Radiotracers From Animal Research Into Clinical Use***
Robert C. Shaw, Gilles D. Tamagnan and Adriana Alexandre S. Tavares

303 *Cell Calcium Imaging as a Reliable Method to Study Neuron–Glial Circuits*
Ricardo Augusto de Melo Reis, Hércules Rezende Freitas and Fernando Garcia de Mello

317 *Tissue Clearing and Expansion Methods for Imaging Brain Pathology in Neurodegeneration: From Circuits to Synapses and Beyond*
Arnaldo Parra-Damas and Carlos A. Saura

329 *Current Techniques for Investigating the Brain Extracellular Space*
Federico N. Soria, Cristina Miguelez, Olga Peñagarikano and Jan Tønnesen

344 *The Application of MR Spectroscopy and MR Perfusion in Cerebral Syphilitic Gumma: A Case Report*
Linyang Cui, Jie Liu, Wenjun Zhang, Zushan Xu and Hongjun Hou

349 *Dissecting Neuronal Activation on a Brain-Wide Scale With Immediate Early Genes*
Alessandra Franceschini, Irene Costantini, Francesco S. Pavone and Ludovico Silvestri

366 *Alterations in Sub-Axonal Architecture Between Normal Aging and Parkinson's Diseased Human Brains Using Label-Free Cryogenic X-ray Nanotomography*
Hung Tri Tran, Esther H. R. Tsai, Amanda J. Lewis, Tim Moors, J. G. J. M. Bol, Iman Rostami, Ana Diaz, Allert J. Jonker, Manuel Guizar-Sicairos, Joerg Raabe, Henning Stahlberg, Wilma D. J. van de Berg, Mirko Holler and Sarah H. Shahmoradian

388 *Zero Echo Time MRAC on FDG-PET/MR Maintains Diagnostic Accuracy for Alzheimer's Disease; A Simulation Study Combining ADNI-Data*
Takahiro Ando, Bradley Kemp, Geoffrey Warnock, Tetsuro Sekine, Sandeep Kaushik, Florian Wiesinger and Gaspar Delso for the Alzheimer's Disease Neuroimaging Initiative

397 *Functional Segregation of Human Brain Networks Across the Lifespan: An Exploratory Analysis of Static and Dynamic Resting-State Functional Connectivity*
Benjamin M. Rosenberg, Eva Mennigen, Martin M. Monti and Roselinde H. Kaiser

409 *Preliminary Study of Subclinical Brain Alterations in Patients With Asymptomatic Carotid Vulnerable Plaques Using Intravoxel Incoherent Motion Imaging by Voxelwise Comparison: A Study of Whole-Brain Imaging Measures*
Jiuqing Guo, Lirong OuYang, Xiaoyi Wang, Weihua Liao, Qing Huang, Wei He, Gaofeng Zhou and Shuai Yang

422 *Unraveling the Nanoscopic Organization and Function of Central Mammalian Presynapses With Super-Resolution Microscopy*
Lia G. Carvalhais, Vera C. Martinho, Elisabete Ferreiro and Paulo S. Pinheiro

437 *Clear and Consistent Imaging of Hippocampal Internal Architecture With High Resolution Multiple Image Co-registration and Averaging (HR-MICRA)*
Lawrence Ver Hoef, Hrishikesh Deshpande, Joel Cure, Goutham Selladurai, Julia Beattie, Richard E. Kennedy, Robert C. Knowlton and Jerzy P. Szaflarski

449 ***Correcting for Non-stationarity in BOLD-fMRI Connectivity Analyses***
Catherine E. Davey, David B. Grayden and Leigh A. Johnston

465 ***Contextual MEG and EEG Source Estimates Using Spatiotemporal LSTM Networks***
Christoph Dinh, John G. Samuelsson, Alexander Hunold, Matti S. Hämäläinen and Sheraz Khan

480 ***ConvDip: A Convolutional Neural Network for Better EEG Source Imaging***
Lukas Hecker, Rebekka Rupprecht, Ludger Tebartz Van Elst and Jürgen Kornmeier

frontiers in Neuroscience

METHODS
published: 16 October 2019
doi: 10.3389/fnins.2019.01105

A Novel Method for Assessing Cerebral Edema, Infarcted Zone and Blood-Brain Barrier Breakdown in a Single Post-stroke Rodent Brain

Ruslan Kuts[1†], Dmitry Frank[1†], Benjamin F. Gruenbaum[2], Julia Grinshpun[1], Israel Melamed[3], Boris Knyazer[4], Oleg Tarabrin[5], Vladislav Zvenigorodsky[6], Ilan Shelef[6], Alexander Zlotnik[1] and Matthew Boyko[1*]*

[1] Division of Anesthesiology and Critical Care, Soroka University Medical Center and the Faculty of Health Sciences, Ben-Gurion University of the Negev, Beersheba, Israel, [2] Department of Anesthesiology, Yale University School of Medicine, New Haven, CT, United States, [3] Department of Neurosurgery, Soroka University Medical Center and the Faculty of Health Sciences, Ben-Gurion University of the Negev, Beersheba, Israel, [4] Department of Ophthalmology, Soroka University Medical Center and the Faculty of Health Sciences, Ben-Gurion University of the Negev, Beersheba, Israel, [5] Department of Anesthesiology and Intensive Care with Postgraduate Education, Odessa National Medical University, Odessa, Ukraine, [6] Department of Radiology, Soroka University Medical Center and the Faculty of Health Sciences, Ben-Gurion University of the Negev, Beersheba, Israel

OPEN ACCESS

Edited by:
Miguel Castelo-Branco,
Coimbra Institute for Biomedical Imaging and Translational Research (CIBIT), Portugal

Reviewed by:
Gaurav Kumar,
Indian Institute of Technology (BHU), India
Joao Miguel Castelhano,
University of Coimbra, Portugal

***Correspondence:**
Benjamin F. Gruenbaum
benjamin.gruenbaum@yale.edu
Matthew Boyko
matthewboykoresearch@gmail.com

[†] These authors have contributed equally to this work

Specialty section:
This article was submitted to Brain Imaging Methods, a section of the journal Frontiers in Neuroscience

Received: 20 June 2019
Accepted: 01 October 2019
Published: 16 October 2019

Citation:
Kuts R, Frank D, Gruenbaum BF, Grinshpun J, Melamed I, Knyazer B, Tarabrin O, Zvenigorodsky V, Shelef I, Zlotnik A and Boyko M (2019) A Novel Method for Assessing Cerebral Edema, Infarcted Zone and Blood-Brain Barrier Breakdown in a Single Post-stroke Rodent Brain. Front. Neurosci. 13:1105. doi: 10.3389/fnins.2019.01105

Stroke is a major cause of global morbidity and mortality. Middle cerebral artery occlusion (MCAO) has historically been the most common animal model of simulating ischemic stroke. The extent of neurological injury after MCAO is typically measured by cerebral edema, infarct zone, and blood-brain barrier (BBB) permeability. A significant limitation of these methods is that separate sets of brains must be used for each measurement. Here we examine an alternative method of measuring cerebral edema, infarct zone and BBB permeability following MCAO in the same set of brain samples. Ninety-six rats were randomly divided into three experimental groups. Group 1 (n = 27) was used for the evaluation of infarct zone and brain edema in rats post-MCAO (n = 17) vs. sham-operated controls (n = 10). Group 2 (n = 27) was used for the evaluation of BBB breakdown in rats post-MCAO (n = 15) vs. sham-operated controls (n = 10). In Group 3 (n = 42), all three parameters were measured in the same set of brain slices in rats post-MCAO (n = 26) vs. sham-operated controls (n = 16). The effect of Evans blue on the accuracy of measuring infarct zone by 2,3,5-triphenyltetrazolium chloride (TTC) staining was determined by measuring infarct zone with and without an applied blue filter. The effects of various concentrations of TTC (0, 0.05, 0.35, 0.5, 1, and 2%) on the accuracy of measuring BBB permeability was also assessed. There was an increase in infarct volume ($p < 0.01$), brain edema ($p < 0.01$) and BBB breakdown ($p < 0.01$) in rats following MCAO compared to sham-operated controls, whether measured separately or together in the same set of brain samples. Evans blue had an effect on measuring infarct volume that was minimized by the application of a blue filter on scanned brain

slices. There was no difference in the Evans blue extravasation index for the brain tissue samples without TTC compared to brain tissue samples incubated in TTC. Our results demonstrate that measuring cerebral edema, infarct zone and BBB permeability following MCAO can accurately be measured in the same set of brain samples.

Keywords: stroke, middle cerebral artery occlusion, rodent, model, methods

INTRODUCTION

Stroke is a leading cause of death and disability (Warlow, 1998; Lloyd-Jones et al., 2009; Feigin et al., 2016, 2017). Over 16 million people worldwide suffer from stroke each year with approximately one-third resulting in death and another third developing permanent disability (Bejot et al., 2016; Thrift et al., 2017). Stroke is also a source of substantial economic burden, with an estimated annual cost in the United States and European Union of $34 billion (Benjamin et al., 2017) and €45 billion (Wilkins et al., 2017), respectively. Animal models are necessary to better understand the pathophysiology of stroke and to advance the development of new therapies targeted at reducing and repairing neurological damage.

Ischemic stroke accounts for over 80% of all strokes and results from an occlusion of a major cerebral artery, most often the middle cerebral artery or one of its branches (Lloyd-Jones et al., 2009). Consequently, middle cerebral artery occlusion (MCAO) has historically been the most common animal model of simulating ischemic stroke (Waltz et al., 1966; Hudgins and Garcia, 1970; Albanese et al., 1980; Tamura et al., 1981; Shigeno et al., 1985; Aspey et al., 1998). When determining the extent of neurological injury in the MCAO model, measured outcomes include cerebral edema (O'Brien et al., 1974; Chen et al., 2006; Durukan and Tatlisumak, 2007), infarct zone (Wang-Fischer, 2008; Liu et al., 2009) and blood-brain barrier (BBB) permeability (Belayev et al., 1996; Sifat et al., 2017; Jiang et al., 2018). Following MCAO, the most popular techniques for measuring brain edema are drying (Chen et al., 2006) or calculating hemispheric volumes (Boyko et al., 2010, 2019b). The infarct zone is mostly determined by a 2,3,5-triphenyltetrazolium chloride (TTC) staining method (Liu et al., 2009) that differentiates between infarcted and viable tissue (Joshi et al., 2004). To measure the BBB breakdown, a spectrometry technique using Evans blue staining is most commonly used (Belayev et al., 1996).

A significant limitation of these methods to assess neurological injury after MCAO is that separate sets of brains must be used for each measurement. Thus, in order to obtain accurate and statistically reliable results, researchers tend to use large number of brain samples resulting in a large number of euthanized animals. Therefore, there is a significant ethical and economical benefit if all three of these parameters could be measured post-MCAO in a single set of rodent brains.

There is evidence in the literature that several parameters can be used on the same brain sample. For example, a combination of TTC staining and immunofluorescent staining methods (Li et al., 2018) as well as other molecular and biochemical analyses after TTC staining (Kramer et al., 2010) have been described. Calculating brain hemisphere volumes to assess brain edema has been performed in our laboratory together with TTC staining to calculate infarct zone using the same brain set (Boyko et al., 2019b). However, measuring BBB permeability in the same set of brain samples remains a challenge and has yet to be described in the literature. This is likely due to the possible influence of one staining technique on the accuracy of a subsequent staining method (Evans blue and TTC, for example). The purpose of the present study was to examine an alternative method of measuring all three parameters following MCAO in the same set of brain samples: cerebral edema, infarct zone and BBB permeability.

For this purpose, we combined the following protocols in a single set of rat brains: TTC staining for measuring infarct zone, calculating hemispheric volumes to measure cerebral edema, and a spectrometry technique using Evans blue staining for evaluating BBB breakdown. We evaluated the effects of TTC staining on the accuracy of BBB permeability measurements, as well as the effects of Evans blue staining on the accuracy of infarct zone measurements. We further compared histologic techniques of assessing neurological injury post-MCAO to Magnetic Resonance Imaging (MRI) techniques. This new approach may serve as an effective, economical, and ethically favorable model for measuring neurological injury after MCAO.

MATERIALS AND METHODS

The experiments were conducted in accordance with the recommendations of the Declarations of Helsinki and Tokyo and the Guidelines for the Use of Experimental Animals of the European Community. The experiments were approved by the Animal Care Committee of Ben-Gurion University of the Negev, Israel.

Animals

The experiments were carried out on a total of 96 Sprague-Dawley rats (Harlan Laboratories, Israel) with no overt pathology, weighing between 300 and 400 g each. Purina Chow and water were available *ad libitum*. Rats were maintained in a 12:12 h light–dark cycle and at constant temperature (22°C ± 1°C).

Experimental Design

Ninety-six rats were randomly divided into three experimental groups. Group 1 (n = 27) was used for the evaluation of infarct zone and brain edema using original techniques previously described in the literature (Kaplan et al., 1991; Joshi et al., 2004; Boyko et al., 2011a, 2013). These rats were subjected to either MCAO (n = 17, of which 11 remained after exclusion criteria) or used as a sham-operated control group without MCAO (n = 10).

TTC staining was used 24 h after MCAO to measure infarct zone and cerebral edema was measured by calculating hemispheric volumes. Group 2 (n = 27) was used for the evaluation of BBB breakdown using the original technique previously described (Boyko et al., 2012). These rats were subjected to either MCAO (n = 17, of which 12 remained after exclusion criteria) or used as a sham-operated control group without MCAO (n = 10). BBB disruption was determined 24 h after MCAO by a spectrometry technique using an intravenous injection of 2% Evans blue in saline (4 ml/kg). Group 3 (n = 42) was used to assess the feasibility of a new technique measuring all three parameters in the same set of brain slices: infarct zone by TTC staining, cerebral edema by calculating hemispheric volumes, and BBB breakdown by Evans blue staining. These rats were subjected to either MCAO (n = 26, of which 19 remained after exclusion criteria) or used as a sham-operated control group without MCAO (n = 16). The new technique for measuring all three parameters is described below. All rats underwent evaluation of neurological deficit 24 h after the operation.

Surgery for MCAO Model of Stroke

The MCAO procedure was performed according to the method described by Zea Longa (Longa et al., 1989), modified by an internal carotid artery (ICA) approach (Boyko et al., 2010). This approach was chosen because it has been shown to produce lower variability in the infarct volume, better weight gain after surgery and reduced mortality (Boyko et al., 2010).

The operation was performed under aseptic conditions in accordance with accepted principles in animal surgeries. Rats were anesthetized with a mixture of isoflurane (4% for induction, 2% for surgery, 1.3% for maintenance) in 24% oxygen (2 l/min) without tracheotomy, and were allowed to breathe spontaneously. Core body temperature was maintained at 37°C throughout the procedure with a rectal temperature-regulated heating pad. Body temperature was kept constant between rats to minimize any effect of hypothermia or hyperthermia on neurological outcome and neurological injury. Physiological parameters, including mean arterial pressure, heart rate and O2 saturation of arterial blood, were monitored.

The right common carotid artery (CCA) was exposed through a midline neck incision and was carefully dissected from surrounding tissues, from its bifurcation to the base of the skull. The catheter was then inserted via the ICA to achieve MCAO. The thread was then fixed by tying a silk filament over the ICA immediately above the CCA bifurcation and proximal to filament insertion point. The purpose of this proximal ligation was to occlude the ICA while the additional distal ligation was used to reduce the bleeding around the filament and to secure it in place. The suture was left in place permanently and the incision was closed using surgical sutures. After this procedure, the anesthesia was discontinued, and rats returned to their cages for recovery. The duration of the entire surgery was approximately 25–30 min. There were no differences in the time allotted for anesthesia between groups in order to control the effects of isoflurane, pO2, or pCO2. Rats that died within 24 h of the MCAO procedure were excluded from this study.

Measurement of Neurological Deficit

An observer, who was blinded to the surgical procedure, tested the animals for neurological deficits 24 h after MCAO (Menzies et al., 1992). This scoring method was used as an exclusion criterion to identify and exclude rats that did not develop neurological deficits following MCAO. This exclusion criterion was to control for anatomic variations in rats' middle cerebral artery branches (Rubino and Young, 1988; Fox et al., 1993; Zhao et al., 2008). Motor deficits were graded on a cumulative scale from 0 to 4. A score of 0 was given for no visible neurological deficits; a score of 1 was given for forelimb flexion; a score of 2 was given for contralateral weak forelimb grip (the operator places the animal on an absorbent pad and gently pulls the tail); a score of 3 was given for circling to the paretic side only when pulled by the tail (the animal was allowed to move about freely on the absorbent pad); and a score of 4 was given for spontaneous circling (Boyko et al., 2011a).

Measurement of Brain Infarct Volume (Original Technique)

In order to measure the extent of brain edema in group 1, the TTC staining method was performed 24 h after the operation, as previously described (Kuts et al., 2019). The rats from each experiment subgroup were euthanized by inspiration of high CO2 and were decapitated. Their brains were quickly isolated and sectioned into 6 coronal slices, each 2 mm of thickness. The set of slices from each brain was incubated for 30 min at 37°C in 0.05% TTC. Following staining, the slices were scanned with an optical scanner (Canon Cano Scan 4200F; resolution 1600 × 1600 dpi). The unstained areas of the fixed brain slices were defined as infarcted, as described in the literature (Kuts et al., 2019). The size of brain injury was measured by the National Institutes of Health ImageJ software 1.37v, calculated in arbitrary units (pixels) and expressed as a percentage of the normal areas in the contralateral unaffected hemisphere. The total size of infarction was obtained by numeric integration of the area of marked pallor, measured in six consecutive 2 mm coronal sections (Boyko et al., 2011b). In order to correct for the tissue swelling factor, the following formula was utilized: corrected infarct size = infarct size × contralateral hemisphere size/ipsilateral hemisphere size. Infarcted volume was expressed as a percentage of the total brain (Boyko et al., 2011c).

Measurement of Brain Edema (Original Technique)

The extent of right cerebral hemisphere edema was measured 24 h after the operation in Group 1. The volumes of both hemispheres were calculated in the arbitrary units (pixels) from the summation of coronal slice areas using the National Institutes of Health ImageJ software 1.37v, after they were scanned with an optical scanner (Canon Cano Scan 4200F; resolution 1600 × 1600 dpi). Brain edema was expressed as a percentage of the normal areas in the contralateral unaffected hemisphere. The extent of swelling was calculated using the Kaplan method: extent of edema = (the volume of right hemisphere – the volume of left hemisphere)/the volume of left hemisphere (Boyko et al., 2019a).

Measurement of BBB Disruption (Original Technique)

In order to measure the extent of BBB disruption in Group 2, a spectrometry technique using Evans blue staining was performed 24 h after the operation. Two percent Evans blue in saline (4 ml/kg) was administered intravenously through a cannulated tail vein as a blood-brain permeability tracer and was allowed to circulate for 60 min. To remove the intravascularly localized dye, the rats' chests were opened, and the animals were perfused with cooled saline through the left ventricle at a pressure of 110 mm Hg until colorless perfusion fluid was obtained from the right atrium. Their brains were quickly isolated and sliced rostro caudally into serial 2-mm thick slices. Then the brain slices were divided into the left and right hemisphere and measurements of vascular permeability were made by comparing their weight with pre-weighed loci in the six slices. Each brain area was weighted and homogenized in 1 ml of 50% trichloroacetic acid (weight/volume) and was centrifuged at 10,000 × *g* for 20 min and the supernatant was diluted 1:3 with 96% ethanol. A fluorescence detector (model Infinite 200 PRO multimode reader; Tecan, Männedorf Switzerland) was used at an excitation wavelength of 620 nm (bandwidth 10 nm) and an emission wavelength of 680 nm (bandwidth 10 nm). Calculations were based on external standards in the solvent (10 ± 500 ng/ml). Data were expressed as mean ± SD (in ng/g of protein) of extravasated Evans blue dye per gram of brain tissue (Boyko et al., 2012).

New Technique for Measuring BBB Breakdown, Brain Infarct Volume and Brain Edema

For the rats in Group 3, 2% Evans blue in saline (4 ml/kg) was injected through the cannulated tail vein as a blood-brain permeability tracer and was allowed to circulate for 60 min. The rats' chests were opened and the animals were perfused with cooled saline through the left ventricle. Their brains were quickly isolated and sectioned into 6 coronal slices, each 2 mm of thickness. The set of slices from each brain was then scanned (this scan was needed to later assess the effects of Evans blue staining on the accuracy of measuring infarct zone and is not required in the final protocol) and incubated for 30 min at 37°C in 0.05% TTC. The slices were again scanned with an optical scanner. Infarct zone and brain edema was measured with the National Institutes of Health ImageJ software 1.37v (Boyko et al., 2011c, 2019a). For these measurements, the computer program converts the scan into a black and white image and then uses a threshold function to mask and calculate the pixels that are either black or white (see **Figure 1**). In order to remove the effects of the Evans dye on this process, we added a blue filter using the Channel Mixer function (Image > Adjustments > Channel Mixer) from the Adobe Photoshop CS2 software program prior to calculating brain infarct zone and brain edema. After scanned, the following was performed in order to measure BBB disruption. The brain slice samples were divided into the left and right hemisphere and measurements of vascular permeability were made by comparing their weight with pre-weighed loci in the six slices. Each brain area was weighted and homogenized in 1 ml of 50% trichloroacetic acid (weight/volume) and was centrifuged at 10,000 × *g* for 20 min and the supernatant was diluted 1:3 with 96% ethanol. A fluorescence detector was used at an excitation wavelength of 620 nm (bandwidth 10 nm) and an emission wavelength of 680 nm (bandwidth 10 nm).

Measurement of BBB Disruption by Brain Image Scanning

BBB disruption was also determined by a brain image scanning technique that has been described in the literature (Boyko et al., 2013) (see **Figures 2A–D**). Using the National Institutes of Health ImageJ software V1.63, the area of dye extravasation was measured using the previously described formula (Kumai et al., 2007): BBB disruption (as a percent): [left hemisphere – (right hemisphere – area stained blue)]/left hemisphere × 100. This was compared to the method of determining BBB disruption by spectrometry.

Evaluating the Effect of Evans Blue Staining on the Accuracy of Measuring Infarct Zone

In order to evaluate the effects of Evans blue staining on the accuracy of measuring infarct zone, and the efficacy of the blue filter on scanned images to minimize this effect, the following procedure was performed. The six brain slices from Group 2 were scanned prior to being homogenized in 1 ml of 50% trichloroacetic acid during the measurement of BBB disruption via the original technique described above (**Figure 1**). The Evans blue extravasation index was then evaluated in these brain samples after the blue filter was applied.

Evaluating the Effect of TTC Staining on the Accuracy of Measuring BBB Permeability

In order to assess the effect of TCC on the accuracy of measuring BBB permeability, samples not incubated in TTC were compared to brain tissue samples incubated in TTC solutions of various concentrations (0.05, 0.35, 0.5, 1, and 2%). Initially, it was a solution with 0% TTC concentrations on a standard 96-well plate, which was tested on a spectrograph. Then, TTC was added to each well based on the calculation of how much TTC is contained in brain samples when stained with solutions TTC of various concentrations. After each test, we increased the concentration until we reached 2%. BBB disruption was determined by spectrometry as described above.

Comparison to MRI Techniques

In order to compare the original histologic to MRI imaging techniques, we analyzed data obtained from our previous work (Boyko et al., 2019b; Frank et al., 2019). The experimental procedure was carried out on a 3T MRI clinical scanner (Ingenia, Philips Medical Systems, Best, Netherlands), fitted out with a gradient system of 45 mT/m at 225 μs ramp time, using a commercial eight-channel receive-only wrist coil. MRI was performed 24 h after surgery for 17 post-MCAO and 19 sham-operated rats.

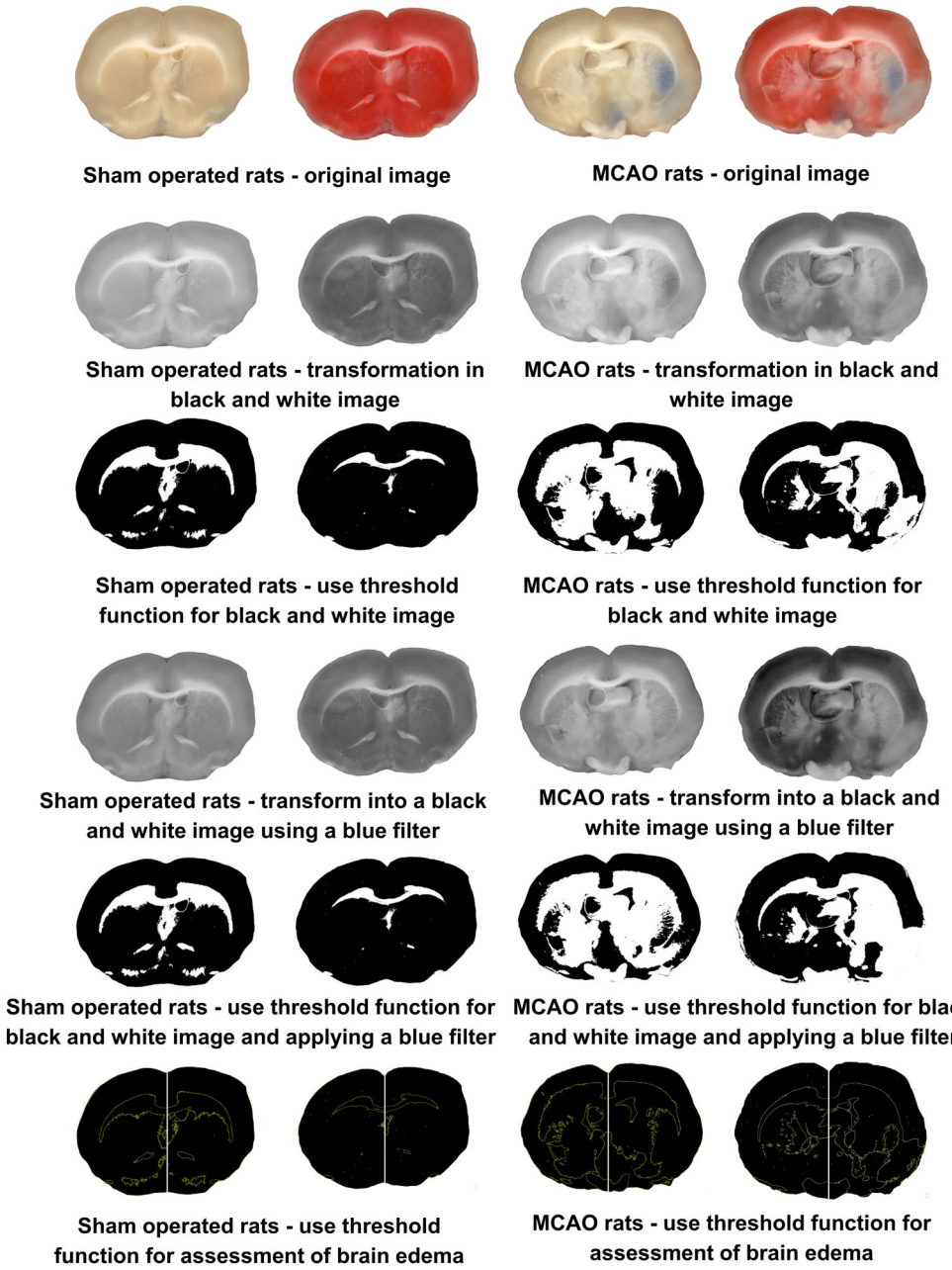

FIGURE 1 | Histological brain scans from sham-operated rats and rats post-MCAO. Column one is a sham-operated brain slice without staining. Column two is a sham-operated brain slice with TTC staining. Column three is a post-MCAO brain slice with Evans blue staining. Column four is a post-MCAO brain slice with Evans blue and TTC staining.

Preceding examination, a body restrainer was used to fix the rats for MRI. Animals, after horizontal placement into plastic holders, were given 4% isoflurane via inhalation from the anesthesia system, with 2% isoflurane mixed in 28% oxygen and 72% room air used for maintenance. A heating reel, filled with water and controlled thermostatically, was used to keep the body temperature of animals at 36.5–37.0°C. We measured pO2, pCO2, pH, arterial blood pressure, and the body core temperature before MRI and cannulated the tail artery and tail vein of rats.

T1 permeability studies were performed using a segmented 3D T1w-FFE sequence with 50 dynamics for a total scan time of 25:52 min. The scan parameters were TR/TE = 16/4.9 ms, turbo factor = 48, SENSE factor 1.5, resolution (freq × phase × slice) = 0.30 × 0.37 × 2.0 mm, tip angle = 80 and two signal averages for a scan time of 31 s/dynamic. Three calibration scans with identical resolution preceded the dynamic sequence with tip angles 50, 100, and 150. The contrast agent was injected after the 5th dynamic

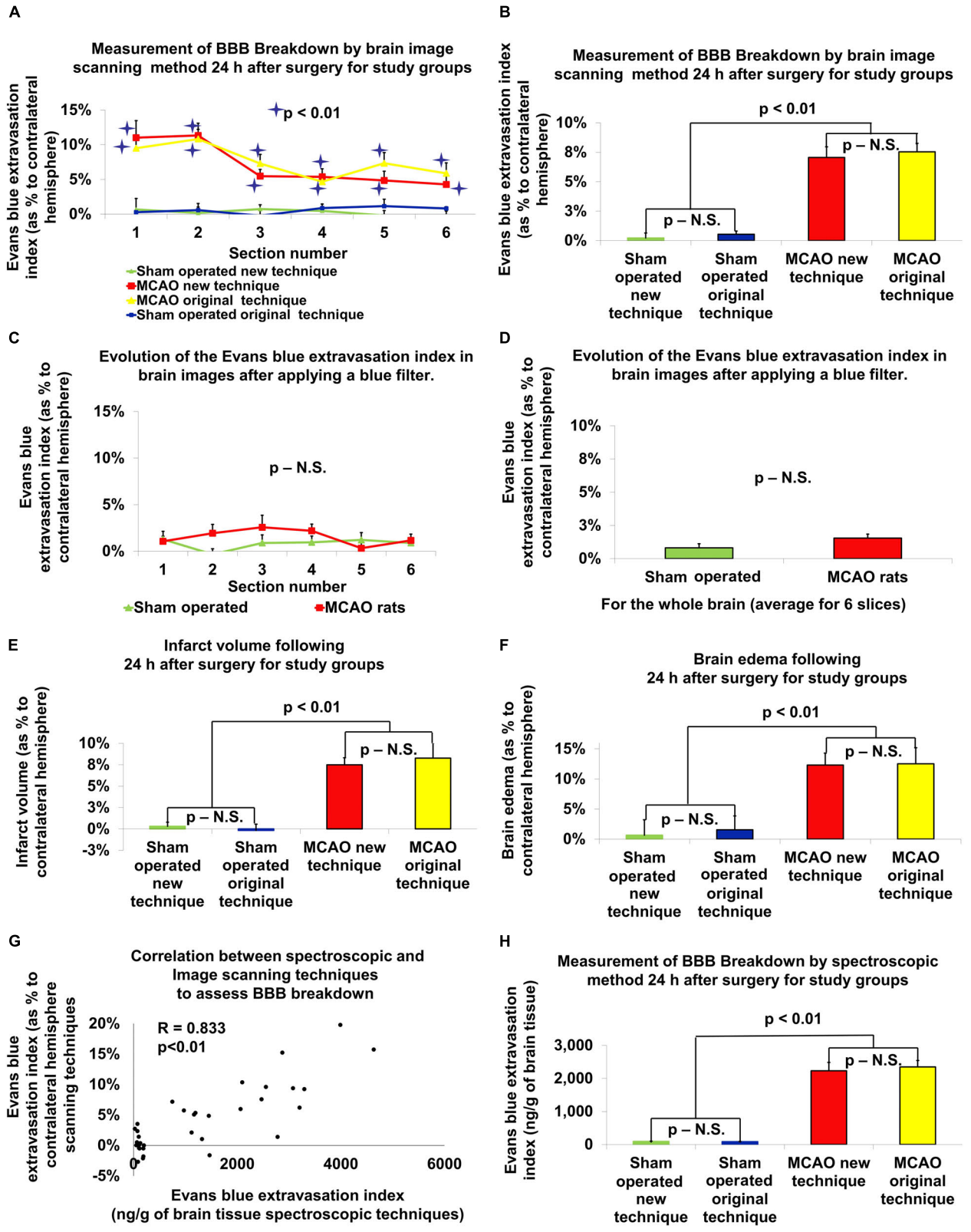

FIGURE 2 | The new vs. original technique in evaluating cerebral edema, infarct zone and BBB permeability after MCAO. There was a significant difference in BBB breakdown measured by the brain image scanning method in all six brain slices in rats post-MCAO compared to sham-operated rats ($p < 0.01$; **A**; a significance

(Continued)

FIGURE 2 | Continued
asterisk indicates the difference between post-MCAO and sham-operated rats). The BBB breakdown, measured by the evaluation of the scanned brain slices, was significantly increased after MCAO compared to the sham-operated rats in both techniques ($p < 0.01$; **B**). After the application of the blue filter, there was no significant difference found between rats that underwent MCAO compared to sham-operated rats **(C,D)**. Both the new and old technique showed an increase in infarct volume ($p < 0.01$; **E**), brain edema ($p < 0.01$; **F**) and BBB breakdown ($p < 0.01$; **H**), following MCAO compared to sham-operated rats. There was no difference found between the old and new techniques. There was no difference found between the old and new techniques. There was a high correlation between the Evans blue extravasation index in brain tissue measured by the spectroscopic method and by the evaluation of scanned brain slices ($r = 0.833$, $p < 0.01$; **G**). The data is expressed as a mean percentage of the contralateral hemisphere ± SEM, or mean Evans blue extravasation index in ng/g of brain tissue ± SEM.

scan. The K-trans were calculated using the original Philips software package.

We used two MRI sequences: a T2-weighted (T2W) sequence for anatomical imaging and the validation of brain edema 24 h post-MCAO, and diffusion-weighted imaging (DWI) for measurements of regional apparent diffusion coefficient (ADC) vales during MCAO calculation of ischemic lesion volumes. All two MRI sequences were run to cover the entire brain, in 2-mm thick consecutive coronal slices, with an in-plane field of-view. Other MRI parameters in play were as follows: T2-weighted. Repetition time (TR)/echo time (TE) = 3000/80 ms was used to acquire the T2W turbo spin echo (TSE) sequence. The turbo factor was 14. The in-plane resolution was 0.37 × 0.31 mm, matrix size 192 × 182, with a slice width of 2.0 mm. We acquired 14 slices in the axial plane with zero gaps and four averages after scan completion at 5:18 min.

The diffusion tensor imaging (DTI) sequence served as a multi-shot, stimulated echo acquisition mode (STEAM) planar imaging (EPI) sequence to reduce susceptibility artifacts. The repetition time/mixing-time/echo time (TR/TM/TE) was 1355/15/143 ms. The SENSE parallel imaging factor was 1.3, and the epi (turbo) factor was 19. The *b*-value for obtaining six diffusion gradient encoding directions was 1000 s/mm2. The in-plane resolution used to create seven contiguous 2.0 mm thick slices in the axial plane was 0.50 × 0.51 mm, with matrix size 100 × 82. We were able to obtain six averages from scanning in 8:40 min.

An expert blinded to the experimental procedure carried out image analysis using a Philips software package and an ImageJ software, performed calculations, and analyzed results. The Philips software package (Ingenia, Philips Medical Systems, Best, Netherlands) was used to individual ROI's for assessment BBB breakdown and to produce a map for the brain images generate quantitative ADC maps, in mm^2/s, which were subsequently analyzed using the Image J software 1.50i version[1], described previously (Boyko et al., 2019b; Frank et al., 2019). The viability thresholds used for the identification of every pixel showing irregular ADC features on the slide were $0.53 \times 10^{-3} mm^2/s$ for ADC (Bardutzky et al., 2005).

Calculation of infarcted zone was performed by the Ratios of Ipsilateral and Contralateral Cerebral Hemispheres (RICH) method. The calculation of the lesion volume with the correction for tissue swelling by the RICH technique was done using the following formula (Boyko et al., 2013, 2019b): Corrected infarct size = infarct size × contralateral hemisphere size/ipsilateral hemisphere size. The infarcted brain volume was measured as a percentage of the total brain (Boyko et al., 2013, 2019b).

Calculation of brain edema was performed by the RICH method. The calculation of brain edema by the RICH technique was done by comparing the contralateral and ipsilateral hemispheres, and performed using the following formula: Brain edema = (the volume of right hemisphere – the volume of left hemisphere)/the volume of left hemisphere (Boyko et al., 2019a).

Statistical Analysis

Statistical analysis was performed with the SPSS 22 package (SPSS Inc., Chicago, IL, United States). The Kolmogorov–Smirnov test was used, considering the number of rats in each group for deciding the appropriate test for the comparisons between the different parameters. For non-parametric data, we used the appropriate tests suitable for non-parametric data. The neurological severity scores are expressed as the median and 25–75 percentile range, and were compared by the Mann–Whitney *U* test. Infarct volume, brain edema and BBB breakdown are expressed as a mean percentage of the contralateral hemisphere ± SEM, or mean Evans blue extravasation index in ng/g of brain tissue ± SEM. and compared by the Mann–Whitney *U* test or *t*-test according to Kolmogorov–Smirnov test and group size. We calculated the correlation between (1) infarct zone (2) brain edema and (3) BBB breakdown assessment by MRI and histological methods. A correlation was also calculated for analyzing the standard curve for measurements of Evans blue extravasation index. Correlations were calculated using the Spearman's test for non-parametric data or Pearson's test for parametric data. Criteria for parametric data were (1) normal distribution (The Kolmogorov–Smirnov test was used) (2) $n > 30$ and (3) the data correspond to an interval scale. The various concentration of TTC in brain samples were compared to brain samples with 0% TTC concertation using the Wilcoxon Signed Ranks Test. Results were considered statistically significant when $P < 0.05$, and highly significant when $P < 0.01$.

RESULTS

Mortality

The mortality rate in this study was 20.0% for the 60 total rats that underwent MCAO (48 survived). There was a 0% mortality rate in the 36 sham-operated rats.

Neurological Deficit

Of the 48 rats who survived the MCAO procedure, 6 rats that that did not develop neurologic deficits at 24 h post-MCAO

[1]http://rsb.info.nih.gov/ij/

were excluded. The remaining rats who underwent MCAO had significantly impaired neurologic performance, i.e., a higher neurological severity score, compared to controls ($p < 0.001$). The median neurological severity score was significantly higher in these 42 post-MCAO rats compared to the 36 sham-operated rats (3, range 2–4 vs. 0, range 0–0, $p < 0.001$) according to a Mann–Whitney test. The data are measured as a count and expressed as median and 25–75 percentile range.

Brain Infarct Volume

The infarct zone, measured 24 h after stroke induction, was significantly increased for the 11 rats that underwent MCAO compared to the 10 sham-operated rats using the original technique (8.27% ± 1.78 vs. -0.18% ± 0.75, $U = 1$, $p < 0.01$, $r = 0.69$, according Mann–Whitney test). Using the new technique, there was a significant increase in the brain infarct volume after 24 h in the 19 rats that underwent MCAO compared to the 16 sham-operated rats [7.49% ± 0.82 vs. 0.31% ± 0.48, $t(28.49) = 7.56$, $p < 0.01$, according to independent-samples t-test]. There was no significant difference between the original and new technique in measuring infarct volume (**Figure 2E**). The data is expressed as a mean percentage of the contralateral hemisphere ± SEM.

Brain Edema

The extent of brain edema, measured 24 h after stroke induction, was significantly increased for the 11 rats that underwent MCAO compared to the 10 sham-operated rats using the original technique (12.53% ± 2.65 vs. 1.54% ± 2.31, $U = 22$, $p < 0.05$, $r = 0.562$, according Mann–Whitney test). Using the new technique, there was a significant increase in the extent of brain edema after 24 h in the 19 rats that underwent MCAO compared to the 16 sham-operated rats [12.31% ± 1.97 vs. 0.64% ± 2.57, $t(29.37) = 3.61$, $p = 0.01$, $d = 1.23$, according to independent-samples t-test]. There was no significant difference between the original and new technique in measuring brain edema (**Figure 2F**). The data is expressed as a mean percentage of the contralateral hemisphere ± SEM.

BBB Breakdown

The analysis of BBB breakdown (presented in **Figures 2G,H**), measured by the spectroscopic method 24 h after stroke induction, was significantly increased for the 12 rats that underwent MCAO compared to the 10 sham-operated rats using the original technique (2352 ng/g ± 194 vs. 85 ng/g ± 8, $U = 0$, $p < 0.01$, $r = 0.92$, according Mann–Whitney test). Using the new technique, there was a significant increase in the extent of BBB breakdown after 24 h in the 19 rats that underwent MCAO compared to the 16 sham-operated rats [2235 ng/g ± 253 vs. 94 ng/g ± 9, $t(18.05) = 8.47$ $p < 0.01$, $d = 2.7$, according to independent-samples t-test]. There was no significant difference between the original and new technique in measuring brain edema (**Figure 2H**). The data are measured in ng/g of brain tissue and presented as mean ± SEM.

The BBB breakdown, measured by the evaluation of the scanned brain slices 24 h after stroke induction, was significantly increased for the 12 rats that underwent MCAO compared to the 10 sham-operated rats using the original technique (7.54% ± 0.72 vs. 0.53% ± 0.27, $U = 0$, $p < 0.01$, $r = 0.88$, according Mann–Whitney test; **Figure 2B**). More specifically, there was a significant difference in BBB breakdown measured by the brain image scanning method in all 6 brain slices in rats post-MCAO compared to the 6 brain slices from the sham-operated rats (**Figure 2A**). Using the new technique, there was a significant increase in the extent of BBB breakdown after 24 h in the 19 rats that underwent MCAO compared to the 16 sham-operated rats [7.06% ± 0.9 vs. 0.22% ± 0.42, $t(25.78) = 6.85$, $p < 0.01$, $d = 2.26$, according to independent-samples t-test]. There was no significant difference between measuring BBB breakdown by spectroscopy compared to the brain image scanning method. The data is expressed as a mean percentage of the contralateral hemisphere ± SEM. Analysis of the Evans blue extravasation index in brain tissue measured by the spectroscopic method and by the evaluation of scanned brain slices showed a high and significant correlation ($r = 0.833$, $p < 0.01$; **Figure 2G**).

Evans Blue on the Accuracy of Measuring Infarct Zone

In order to evaluate the effect of Evans blue on the accuracy of measuring infarct zone, we compared the Evans blue extravasation index in scanned brain slices after applying the blue filter. These brain slices were scanned before being homogenized in 1 ml of 50% trichloroacetic acid during the measurement of BBB disruption via the original technique. After the application of the blue filter, there was no significant difference found between rats that underwent MCAO compared to sham-operated rats (**Figures 2C,D**). The data is expressed as a mean percentage of the contralateral hemisphere ± SEM.

TTC on the Accuracy of Measuring BBB Permeability

Since the new technique of measuring BBB permeability used brain slices that were preincubated in TTC, we studied the effects of various concentrations of TTC (0, 0.05, 0.35, 0.5, 1, and 2%) on the accuracy of measuring BBB permeability. The Evans blue extravasation index for the brain tissue samples without TTC were not significantly different than the brain tissue samples incubated in TTC at concentrations of 0.05–2% compared to 0% (**Figure 3A** and **Table 1**). Creating standard curves for Evans blue with concentrations ranging from 0 to 2000 ng in 200 μL DDW, we found no significant difference between brain samples without TTC and brain samples incubated in TTC at concentrations of 0.05–2% (**Figure 3B** and **Table 2**). Furthermore, we found a high correlation in the Evans blue standard curve at each of the incubated TTC concentrations tested (**Figures 3C–H**).

Comparison to MRI Techniques

MRI techniques for assessing neurologic injury post-MCAO was compared to histological techniques. There was a high correlation between the TTC staining, %RICH lesion volume calculation with edema correction assessment, and the ADC-applied MRI assessment of the lesion volume [$rs(36) = 0.739$, $p < 0.01$], 24 h after ischemia onset. There was a moderate

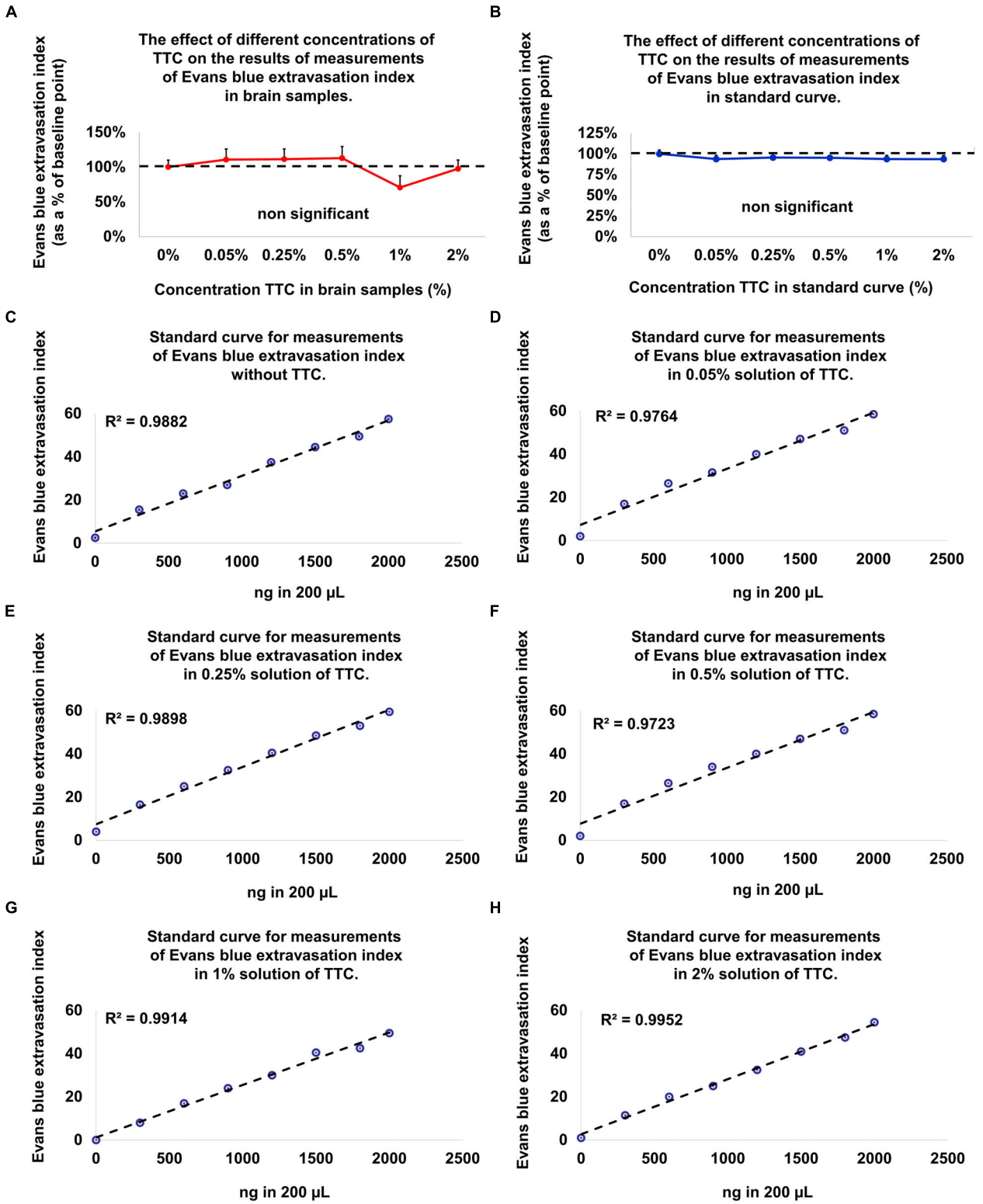

FIGURE 3 | Evolution of the Evans blue standard curve and in brain samples at different TTC concentrations compared to baseline (without TTC). **(A)** There is no difference in the Evans blue extravasation index for the standard curve without TTC compared to brain tissue samples incubated in TTC. Data is presented as a percentage of baseline ± SEM. **(B)** There is no difference in the Evans blue extravasation index for the brain tissue samples without TTC compared to brain tissue samples incubated in TTC. Data is presented as a percentage of baseline ± SEM. **(C–H)** An Evans blue standard curve with concentrations ranging from 0 to 2000 ng in 200 µL DDW and amount of TTC solution (0–2%), equivalent to the content in the brain tissue.

TABLE 1 | Evolution of the Evans blue extravasation index in brain samples at different TTC concentrations compared to baseline (brain samples without TTC).

Groups	*n* = 96		
	Mean and SEM%	**Variability %**	***P*-value**
Measurements of Evans blue extravasation index in brain samples without TTC.	100 ± 10	97	
Measurements of Evans blue extravasation index in brain samples amount 0.05% solution of TTC, equivalent to the content in the brain tissue.	110.6 ± 15.3	135	Non-significant compare to baseline
Measurements of Evans blue extravasation index in brain samples amount 0.25% solution of TTC, equivalent to the content in the brain tissue.	111.3 ± 14.7	129	Non-significant compare to baseline
Measurements of Evans blue extravasation index in brain samples amount 0.5% solution of TTC, equivalent to the content in the brain tissue.	112.9 ± 16.5	144	Non-significant compare to baseline
Measurements of Evans blue extravasation index in brain samples amount 1% solution of TTC, equivalent to the content in the brain tissue.	70.6 ± 16.9	235	Non-significant compare to baseline
Measurements of Evans blue extravasation index in brain samples amount 2% solution of TTC, equivalent to the content in the brain tissue.	97.6 ± 12.5	125	Non-significant compare to baseline

TABLE 2 | Evolution of the Evans blue standard curve at different TTC concentrations compared to baseline (Evans blue standard curve without TTC).

Groups	*n* = 96			
	Mean and SEM%	**Variability %**	R^2	***p*-value**
An Evans blue standard curve was established with concentrations ranging from 0 to 2000 ng in 200 μL DDW	100 ± 4.6	46	R^2 = 0.9988	
An Evans blue standard curve was established with concentrations ranging from 0 to 2000 ng in 200 μL DDW and amount of 0.05% TTC solution, equivalent to the content in the brain tissue.	93.6 ± 4.5	47	R^2 = 0.9764	Non-significant compare to baseline
An Evans blue standard curve was established with concentrations ranging from 0 to 2000 ng in 200 μL DDW and amount of 0.25% TTC solution, equivalent to the content in the brain tissue.	95.4 ± 2.9	29	R^2 = 0.9898	Non-significant compare to baseline
An Evans blue standard curve was established with concentrations ranging from 0 to 2000 ng in 200 μL DDW and amount of 0.5% TTC solution, equivalent to the content in the brain tissue.	95.2 ± 2.2	23	R^2 = 0.9723	Non-significant compare to baseline
An Evans blue standard curve was established with concentrations ranging from 0 to 2000 ng in 200 μL DDW and amount of 1% TTC solution, equivalent to the content in the brain tissue.	93.6 ± 4.5	47	R^2 = 0.9914	Non-significant compare to baseline
An Evans blue standard curve was established with concentrations ranging from 0 to 2000 ng in 200 μL DDW and amount of 2% TTC solution, equivalent to the content in the brain tissue.	93.5 ± 4.5	48	R^2 = 0.9952	Non-significant compare to baseline

correlations between the T2% RICH -MRI assessment of brain edema and %RICH assessment of brain edema in histological methods [$rs(36) = 0.633$, $p < 0.01$], 24 h after ischemia onset. There was a low correlation between the Ktrans -MRI assessment and the Evans blue extravasation index performed by the histological method [$rs(36) = 0.46$, $p < 0.01$], 24 h after ischemia onset (**Table 3**).

DISCUSSION

In this study, we describe a novel method of measuring cerebral edema, infarct zone and BBB permeability following MCAO in the same set of brain samples. Our results demonstrate that these parameters of neurological injury following MCAO can accurately be measured in the same set of brain samples.

We compared the original techniques of measuring post-MCAO infarct zone, cerebral edema and BBB breakdown individually on different brain samples, to a new technique of measuring all of these parameters together in a single set of brain samples. For this purpose, we used three groups of rats. Infarct zone and brain edema was measured in group one using the original technique previously described (Kaplan et al., 1991; Joshi et al., 2004; Boyko et al., 2011a, 2013), BBB disruption was measured in the second group using the original technique previously described (Boyko et al., 2012), and all 3 parameters were measured in the third group on a single set of brain samples using a new technique. Both the original and new techniques were able to correctly identify neurological injury following MCAO in all three groups compared to sham-operated controls. Furthermore, there were no significant differences found between the new and old techniques.

We further wanted to evaluate the effect of Evans blue on the accuracy of infarct zone measurements. For these measurements, the ImageJ computer program converts the scan into a black and white image and then uses a threshold function to mask and calculate the pixels that are either black or white. Brain areas dyed with Evans blue, prior to incubation in TTC solution, were found to be categorized as normal (black) tissue. As a result, no

TABLE 3 | Comparing histological and MRI techniques on assessment of neurologic injury.

	MRI techniques		
	Brain Edema from T2	**K^{trans} extravasation index**	**ADC**
Histological method			
Brain Edema	*R*s = 0.633; *n* = 36		
Evans blue extravasation index		*R*s = 0.46; *n* = 36	
Infarct zone			*R*s = 0.739; *n* = 36

There was a high correlation between the TTC staining, %RICH lesion volume calculation with edema correction assessment, and the ADC-applied MRI assessment of the lesion volume [rs(36) = 0.739, p < 0.01], 24 h after ischemia onset. There was a moderate correlations between the T2% RICH - MRI assessment of brain edema and %RICH assessment of brain edema in histological methods [rs(36) = 0.633, p < 0.01], 24 h after ischemia onset. There was a low correlation between the Ktrans -MRI assessment and the Evans blue extravasation index performed by the histological method [rs(36) = 0.46, p < 0.01], 24 h after ischemia onset. MRI, Magnetic Resonance Imaging; TTC, 2,3,5-triphenyltetrazolium chloride; RICH, the Ratios of Ipsilateral and Contralateral Cerebral Hemispheres.

difference could be found in the infarct zone between rats that underwent MCAO compared to control sham-operated rats. This feature actually allows a method of evaluating the area of BBB breakdown by scanned images, as previously described (Boyko et al., 2013). Our results suggest a high correlation between measuring BBB via this brain image scanning method compared to a traditional spectrometric method. Adding a blue filer on scanned brain slices to remove the effects of Evans dye allowed the infarct zone to be measured.

Since the new technique of measuring BBB permeability used brain slices that were preincubated in TTC, we studied the effects of various concentrations of TTC (0, 0.05, 0.35, 0.5, 1, and 2%) on the accuracy of measuring BBB permeability. Our protocol requires TTC concentrations of 0.05%; however, the literature describes protocols with concentrations of TTC up to 2% (Popp et al., 2009). Our results suggest that there was no difference in the Evans blue extravasation index between the brain tissue samples without TTC and brain tissue samples incubated in TTC at concentrations of 0.05–2%.

The goal of this study was to evaluate an alternative method of measuring three parameters of neurological injury following MCAO (cerebral edema, infarct zone and BBB permeability) via histologic examination in the same set of brain samples. It's important to note that this is also possible to do with MRI technology. MRI also avoids euthanasia, which is ethically preferred. MRI is further useful for behavioral studies in post-stroke rats, and we have used this technique in our own laboratory in the past for these experiments (Frank et al., 2019). However, in practice histological methods are much more commonly used and remain the gold standard for assessing brain injury after stroke (Liu et al., 2009). This is likely due to the economic burden and limited access and availability of MRI equipment in most laboratories. The resolution using histological methods are also currently superior to MRI technology, even with high tesla magnets. Here, we compared histological and MRI techniques on assessment of neurologic injury. Due to the fact that the correlation between BBB rupture and cerebral edema, which we obtained by comparing MRI and histological methods, did not reach high levels, we considered that comparing the data obtained using the same methodology (i.e., histological) would be methodologically more accurate. However, a limitation to this study is that the new histological technique was not directly compared to known *in vivo* techniques of assessing neurologic injury, such as MRI.

CONCLUSION

This study describes the efficacy of a new technique to evaluate cerebral edema, infarct zone and BBB permeability after MCAO in the same set of brain samples. Our results suggest no difference in histological outcomes using this new method compared to the original method of using different brain samples for each measurement. Statistical analysis did not show an effect of TTC on BBB permeability measurements using spectrometry. Furthermore, the results suggest that the use of a blue filter completely removes the blue color from the scanned brain images and makes it possible to measure the infarct zone and brain edema effectively. We believe that this novel approach is a practical, accurate, cost-efficient, and ethically favorable model for measuring neurological injury after MCAO, and may promote future studies to help better understand and treat stroke.

DATA AVAILABILITY STATEMENT

The datasets generated for this study are available on request to the corresponding author.

ETHICS STATEMENT

The animal study was reviewed and approved by the Animal Care Committee of Ben-Gurion University of the Negev, Israel and conducted in accordance with the recommendations of the Declaration of Helsinki and Tokyo and the Guidelines for the Use of Experimental Animals of the European Community.

AUTHOR CONTRIBUTIONS

RK, DF, BG, and MB: study conception, data collection and analysis, and manuscript writing/editing and final approval. JG, IM, BK, OT, VZ, IS, and AZ: data collection and analysis, and manuscript editing and final approval.

ACKNOWLEDGMENTS

The authors gratefully acknowledge Dr. Yotam Zata and Dr. Evgeni Brotfain at Soroka Medical Center for their contribution in data analysis. This research was partly supported by the Israel Science Foundation (Grant No. 1490/15) awarded to MB and AZ.

REFERENCES

Albanese, V., Tommasino, C., Spadaro, A., and Tomasello, F. (1980). A transbasisphenoidal approach for selective occlusion of the middle cerebral artery in rats. *Experientia* 36, 1302–1304. doi: 10.1007/bf01969602

Aspey, B. S., Cohen, S., Patel, Y., Terruli, M., and Harrison, M. J. (1998). Middle cerebral artery occlusion in the rat: consistent protocol for a model of stroke. *Neuropathol. Appl. Neurobiol.* 24, 487–497. doi: 10.1046/j.1365-2990.1998.00146.x

Bardutzky, J., Shen, Q., Henninger, N., Bouley, J., Duong, T. Q., and Fisher, M. (2005). Differences in ischemic lesion evolution in different rat strains using diffusion and perfusion imaging. *Stroke* 36, 2000–2005. doi: 10.1161/01.str.0000177486.85508.4d

Bejot, Y., Daubail, B., and Giroud, M. (2016). Epidemiology of stroke and transient ischemic attacks: current knowledge and perspectives. *Rev. Neurol.* 172, 59–68. doi: 10.1016/j.neurol.2015.07.013

Belayev, L., Busto, R., Zhao, W., and Ginsberg, M. D. (1996). Quantitative evaluation of blood-brain barrier permeability following middle cerebral artery occlusion in rats. *Brain Res.* 739, 88–96. doi: 10.1016/s0006-8993(96)00815-3

Benjamin, E. J., Blaha, M. J., Chiuve, S. E., Cushman, M., Das, S. R., Deo, R., et al. (2017). Heart disease and stroke statistics-2017 update: a report from the American Heart Association. *Circulation* 135, e146–e603.

Boyko, M., Kuts, R., Gruenbaum, B. F., Tsenter, P., Grinshpun, J., Frank, D., et al. (2019a). An alternative model of laser-induced stroke in the motor cortex of rats. *Biol. Proced. Online* 21:9. doi: 10.1186/s12575-019-0097-x

Boyko, M., Zvenigorodsky, V., Grinshpun, J., Shiyntum, H. N., Melamed, I., Kutz, R., et al. (2019b). Establishment of novel technical methods for evaluating brain edema and lesion volume in stroked rats: a standardization of measurement procedures. *Brain Res.* 1718, 12–21. doi: 10.1016/j.brainres.2019.04.022

Boyko, M., Kutz, R., Gruenbaum, B. F., Cohen, H., Kozlovsky, N., Gruenbaum, S. E., et al. (2013). The influence of aging on poststroke depression using a rat model via middle cerebral artery occlusion. *Cogn. Affect Behav. Neurosci.* 13, 847–859. doi: 10.3758/s13415-013-0177-3

Boyko, M., Melamed, I., Gruenbaum, B. F., Gruenbaum, S. E., Ohayon, S., Leibowitz, A., et al. (2012). The effect of blood glutamate scavengers oxaloacetate and pyruvate on neurological outcome in a rat model of subarachnoid hemorrhage. *Neurotherapeutics* 9, 649–657. doi: 10.1007/s13311-012-0129-6

Boyko, M., Ohayon, S., Goldsmith, T., Douvdevani, A., Gruenbaum, B. F., Melamed, I., et al. (2011a). Cell-free DNA–a marker to predict ischemic brain damage in a rat stroke experimental model. *J. Neurosurg Anesthesiol* 23, 222–228. doi: 10.1097/ANA.0b013e31821b536a

Boyko, M., Ohayon, S., Goldsmith, T., Novack, L., Novack, V., Perry, Z. H., et al. (2011b). Morphological and neuro-behavioral parallels in the rat model of stroke. *Behav. Brain Res.* 223, 17–23. doi: 10.1016/j.bbr.2011.03.019

Boyko, M., Zlotnik, A., Gruenbaum, B. F., Gruenbaum, S. E., Ohayon, S., Kuts, R., et al. (2011c). Pyruvate's blood glutamate scavenging activity contributes to the spectrum of its neuroprotective mechanisms in a rat model of stroke. *Eur. J. Neurosci.* 34, 1432–1441. doi: 10.1111/j.1460-9568.2011.07864.x

Boyko, M., Zlotnik, A., Gruenbaum, B. F., Gruenbaum, S. E., Ohayon, S., Goldsmith, T., et al. (2010). An experimental model of focal ischemia using an internal carotid artery approach. *J. Neurosci. Methods* 193, 246–253. doi: 10.1016/j.jneumeth.2010.08.026

Chen, C. H., Toung, T. J., Sapirstein, A., and Bhardwaj, A. (2006). Effect of duration of osmotherapy on blood-brain barrier disruption and regional cerebral edema after experimental stroke. *J. Cereb. Blood Flow Metab.* 26, 951–958. doi: 10.1038/sj.jcbfm.9600248

Durukan, A., and Tatlisumak, T. (2007). Acute ischemic stroke: overview of major experimental rodent models, pathophysiology, and therapy of focal cerebral ischemia. *Pharmacol. Biochem. Behav.* 87, 179–197. doi: 10.1016/j.pbb.2007.04.015

Feigin, V. L., Norrving, B., and Mensah, G. A. (2017). Global burden of stroke. *Circ. Res.* 120, 439–448. doi: 10.1161/CIRCRESAHA.116.308413

Feigin, V. L., Roth, G. A., Naghavi, M., Parmar, P., Krishnamurthi, R., Chugh, S., et al. (2016). Global burden of stroke and risk factors in 188 countries, during 1990-2013: a systematic analysis for the global burden of disease study 2013. *Lancet Neurol.* 15, 913–924. doi: 10.1016/S1474-4422(16)30073-4

Fox, G., Gallacher, D., Shevde, S., Loftus, J., and Swayne, G. (1993). Anatomic variation of the middle cerebral artery in the sprague-dawley rat. *Stroke* 24, 2087–2092. doi: 10.1161/01.str.24.12.2087

Frank, D., Kuts, R., Tsenter, P., Gruenbaum, B. F., Grinshpun, Y., Zvenigorodsky, V., et al. (2019). The effect of pyruvate on the development and progression of post-stroke depression: a new therapeutic approach. *Neuropharmacology* 155, 173–184. doi: 10.1016/j.neuropharm.2019.05.035

Hudgins, W. R., and Garcia, J. H. (1970). Transorbital approach to the middle cerebral artery of the squirrel monkey: a technique for experimental cerebral infarction applicable to ultrastructural studies. *Stroke* 1, 107–111. doi: 10.1161/01.str.1.2.107

Jiang, X., Andjelkovic, A. V., Zhu, L., Yang, T., Bennett, M. V. L., Chen, J., et al. (2018). Blood-brain barrier dysfunction and recovery after ischemic stroke. *Prog. Neurobiol.* 16, 144–171. doi: 10.1016/j.pneurobio.2017.10.001

Joshi, C. N., Jain, S. K., and Murthy, P. S. (2004). An optimized triphenyltetrazolium chloride method for identification of cerebral infarcts. *Brain Res. Brain Res. Protoc.* 13, 11–17. doi: 10.1016/j.brainresprot.2003.12.001

Kaplan, B., Brint, S., Tanabe, J., Jacewicz, M., Wang, X. J., and Pulsinelli, W. (1991). Temporal thresholds for neocortical infarction in rats subjected to reversible focal cerebral ischemia. *Stroke* 22, 1032–1039. doi: 10.1161/01.str.22.8.1032

Kramer, M., Dang, J., Baertling, F., Denecke, B., Clarner, T., Kirsch, C., et al. (2010). TTC staining of damaged brain areas after MCA occlusion in the rat does not constrict quantitative gene and protein analyses. *J. Neurosci. Methods* 187, 84–89. doi: 10.1016/j.jneumeth.2009.12.020

Kumai, Y., Ooboshi, H., Ibayashi, S., Ishikawa, E., Sugimori, H., Kamouchi, M., et al. (2007). Postischemic gene transfer of soluble Flt-1 protects against brain ischemia with marked attenuation of blood-brain barrier permeability. *J. Cereb. Blood Flow Metab.* 27, 1152–1160. doi: 10.1038/sj.jcbfm.9600420

Kuts, R., Melamed, I., Shiyntum, H. N., Frank, D., Grinshpun, J., Zlotnik, A., et al. (2019). A middle cerebral artery occlusion technique for inducing post-stroke depression in rats. *J. Vis. Exp.* 22. doi: 10.3791/58875

Li, L., Yu, Q., and Liang, W. (2018). Use of 2,3,5-triphenyltetrazolium chloride-stained brain tissues for immunofluorescence analyses after focal cerebral ischemia in rats. *Pathol. Res. Pract.* 214, 174–179. doi: 10.1016/j.prp.2017.11.016

Liu, S., Zhen, G., Meloni, B. P., Campbell, K., and Winn, H. R. (2009). Rodent stroke model guidelines for preclinical stroke trials (1st edition). *J. Exp. Stroke Transl. Med.* 2, 2–27. doi: 10.6030/1939-067x-2.2.2

Lloyd-Jones, D., Adams, R., Carnethon, M., De Simone, G., Ferguson, T. B., Flegal, K., et al. (2009). Heart disease and stroke statistics–2009 update: a report from the American Heart Association Statistics committee and stroke statistics subcommittee. *Circulation* 119, 480–486.

Longa, E. Z., Weinstein, P. R., Carlson, S., and Cummins, R. (1989). Reversible middle cerebral artery occlusion without craniectomy in rats. *Stroke* 20, 84–91. doi: 10.1161/01.str.20.1.84

Menzies, S. A., Hoff, J. T., and Betz, A. L. (1992). Middle cerebral artery occlusion in rats: a neurological and pathological evaluation of a reproducible model. *Neurosurgery* 31, 100–106.

O'Brien, M. D., Jordan, M. M., and Waltz, A. G. (1974). Ischemic cerebral edema and the blood-brain barrier. distributions of pertechnetate, albumin, sodium, and antipyrine in brains of cats after occlusion of the middle cerebral artery. *Arch. Neurol.* 30, 461–465.

Popp, A., Jaenisch, N., Witte, O. W., and Frahm, C. (2009). Identification of ischemic regions in a rat model of stroke. *PLoS One* 4:e4764. doi: 10.1371/journal.pone.0004764

Rubino, G. J., and Young, W. (1988). Ischemic cortical lesions after permanent occlusion of individual middle cerebral artery branches in rats. *Stroke* 19, 870–877. doi: 10.1161/01.str.19.7.870

Shigeno, T., Mcculloch, J., Graham, D. I., Mendelow, A. D., and Teasdale, G. M. (1985). Pure cortical ischemia versus striatal ischemia. Circulatory, metabolic, and neuropathologic consequences. *Surg. Neurol.* 24, 47–51. doi: 10.1016/0090-3019(85)90063-1

Sifat, A. E., Vaidya, B., and Abbruscato, T. J. (2017). Blood-brain barrier protection as a therapeutic strategy for acute ischemic stroke. *AAPS J.* 19, 957–972. doi: 10.1208/s12248-017-0091-7

Tamura, A., Graham, D. I., Mcculloch, J., and Teasdale, G. M. (1981). Focal cerebral ischaemia in the rat: 1. Description of technique and early neuropathological consequences following middle cerebral artery occlusion. *J. Cereb. Blood Flow Metab.* 1, 53–60. doi: 10.1038/jcbfm.1981.6

Thrift, A. G., Thayabaranathan, T., Howard, G., Howard, V. J., Rothwell, P. M., Feigin, V. L., et al. (2017). Global stroke statistics. *Int. J. Stroke* 12, 13–32. doi: 10.1177/1747493016676285

Waltz, A. G., Sundt, T. M. Jr., and Owen, C. A. Jr. (1966). Effect of middle cerebral artery occlusion on cortical blood flow in animals. *Neurology* 16, 1185–1190.

Wang-Fischer, Y. (2008). *Manual of Stroke Models in Rats*. Boca Raton, FA: CRC press.

Warlow, C. P. (1998). Epidemiology of stroke. *Lancet* 352(Suppl. 3), SIII1–SIII4.

Wilkins, E., Wilson, L., Wickramasinghe, K., Bhatnagar, P., Leal, J., Luengo-Fernandez, R., et al. (2017). *European Cardiovascular Disease Statistics 2017*. Brussels: European Heart Network.

Zhao, H., Mayhan, W. G., and Sun, H. (2008). A modified suture technique produces consistent cerebral infarction in rats. *Brain Res.* 1246, 158–166. doi: 10.1016/j.brainres.2008.08.096

Conflict of Interest: The authors declare that the research was conducted in the absence of any commercial or financial relationships that could be construed as a potential conflict of interest.

Copyright © 2019 Kuts, Frank, Gruenbaum, Grinshpun, Melamed, Knyazer, Tarabrin, Zvenigorodsky, Shelef, Zlotnik and Boyko. This is an open-access article distributed under the terms of the Creative Commons Attribution License (CC BY). The use, distribution or reproduction in other forums is permitted, provided the original author(s) and the copyright owner(s) are credited and that the original publication in this journal is cited, in accordance with accepted academic practice. No use, distribution or reproduction is permitted which does not comply with these terms.

frontiers in Neuroscience

ORIGINAL RESEARCH
published: 12 December 2019
doi: 10.3389/fnins.2019.01290

ACOEC-FD: Ant Colony Optimization for Learning Brain Effective Connectivity Networks From Functional MRI and Diffusion Tensor Imaging

Junzhong Ji[1]*, *Jinduo Liu*[1], *Aixiao Zou*[1] and *Aidong Zhang*[2]

[1] Beijing Key Laboratory of Multimedia and Intelligent Software Technology, Beijing Artificial Intelligence Institute, Faculty of Information Technology, Beijing University of Technology, Beijing, China, [2] Department of Computer Science, University of Virginia, Charlottesville, VA, United States

Identifying brain effective connectivity (EC) networks from neuroimaging data has become an effective tool that can evaluate normal brain functions and the injuries associated with neurodegenerative diseases. So far, there are many methods used to identify EC networks. However, most of the research currently focus on learning EC networks from single modal imaging data such as functional magnetic resonance imaging (fMRI) data. This paper proposes a new method, called ACOEC-FD, to learn EC networks from fMRI and diffusion tensor imaging (DTI) using ant colony optimization (ACO). First, ACOEC-FD uses DTI data to acquire some positively correlated relations among regions of interest (ROI), and takes them as anatomical constraint information to effectively restrict the search space of candidate arcs in an EC network. ACOEC-FD then achieves multi-modal imaging data integration by incorporating anatomical constraint information into the heuristic function of probabilistic transition rules to effectively encourage ants more likely to search for connections between structurally connected regions. Through simulation studies on generated datasets and real fMRI-DTI datasets, we demonstrate that the proposed approach results in improved inference results on EC compared to some methods that only used fMRI data.

Keywords: functional magnetic resonance imaging, diffusion tensor imaging, brain effective connectivity networks, anatomical constraint information, ant colony optimization

OPEN ACCESS

Edited by:
Alard Roebroeck,
Maastricht University, Netherlands

Reviewed by:
Hyunjin Park,
Sungkyunkwan University, South Korea
Ruogu Fang,
University of Florida, United States

***Correspondence:**
Junzhong Ji
jjz01@bjut.edu.cn

Specialty section:
This article was submitted to Brain Imaging Methods, a section of the journal Frontiers in Neuroscience

Received: *30 May 2019*
Accepted: *14 November 2019*
Published: *12 December 2019*

Citation:
Ji J, Liu J, Zou A and Zhang A (2019) ACOEC-FD: Ant Colony Optimization for Learning Brain Effective Connectivity Networks From Functional MRI and Diffusion Tensor Imaging. Front. Neurosci. 13:1290. doi: 10.3389/fnins.2019.01290

1. INTRODUCTION

As an important method in brain science, brain imaging reveals the anatomic structure and function of a brain through images and imaging techniques such as functional MRI (fMRI), electroencephalography, magnetoencephalography, structural MRI and diffusion tensor imaging (DTI), and provides a powerful technical tool to understand the working mechanisms of the brain. Recently, the imaging data is often used to study connectivity in the human brain, that is, how brain regions interact with each other within networks to understand brain functioning and to handle cognitive processes (Friston, 2011). In particular, the resting-state fMRI data has been used to learn brain effective connectivity (EC) networks, which has aroused great interests among researchers. Different from the functional connectivity (FC) network, which is an undirected

graph, an EC network is a directed graph where a node represents a brain region and a directed edge characterizes a causal effect of interval neural activity in the brain. By identifying and distinguishing brain EC differences between normal and abnormal subjects, people can understand the roles that connectivity patterns and their disruption play in mental health disorders and brain diseases, and can evaluate each abnormal brain EC and its relationship with injuries of neurodegenerative diseases, such as epilepsy, Alzheimer's disease (AD), schizophrenia, and autism, etc. Therefore, learning the brain EC from fMRI data can help elucidate the pathogenesis of cerebral diseases, which plays an important role in performing an early diagnosis of brain diseases and pathological studies.

Within the past decade, many computational methods and mathematical models have been proposed to identify EC involved in the human brain (Patel et al., 2006; Shimizu et al., 2006; Rykhlevskaia et al., 2008; Stephan et al., 2009; Dauwels et al., 2010; Ramsey et al., 2010; Seth, 2011; Smith et al., 2011; Sui et al., 2012; Wu et al., 2013; Zhu et al., 2013; Ide et al., 2014; Mumford and Ramsey, 2014; Zhou et al., 2015; Ji et al., 2016; Liu et al., 2016; Dang et al., 2017; Havlicek et al., 2017; Xu et al., 2017; Lennartz et al., 2018; Karwowski et al., 2019). These studies can be roughly divided into two categories, one is the model-driven approach while the other is the data-driven approach. The model-driven approaches usually require the prior models or hypothesis to conduct a valid connectivity analysis, which does not perform well for those situations where prior knowledge is insufficient (Wu et al., 2013). The data-driven approaches can directly extract causal interactions from fMRI data without any prior knowledge, and gradually become the mainstream method in identifying EC (Patel et al., 2006; Shimizu et al., 2006; Dauwels et al., 2010; Ramsey et al., 2010; Seth, 2011; Xu et al., 2017). Common methods belonging to the second category include: the Linear non-Gaussian acyclic model (LiNGAM) algorithm (Shimizu et al., 2006), The Granger causality (GC) algorithm (Seth, 2011), the Generalized synchronization (GS) algorithm (Dauwels et al., 2010), Patel's condition dependence measurement (Patel) algorithm (Patel et al., 2006), the Greedy equivalence search (GES) algorithm (Ramsey et al., 2010), and the Prediction Correlation (P-corr) (Xu et al., 2017) algorithm, etc. Though these methods have their own advantages in some ways, they have a common limitation on the direction estimation of EC. Recently, a data-driven approach based on Bayesian networks (BNs) has been greatly developed and has become an emerging approach for learning the brain EC (Ide et al., 2014; Mumford and Ramsey, 2014; Zhou et al., 2015). The main reason is that BN methods can accurately infer the functional connectivity between brain regions (Smith et al., 2011). However, they do not perform well on inferring causal directions. To overcome this problem, Ji et al. successively developed two swarm intelligent algorithms called AIAEC (Sui et al., 2012) and ACOEC (Liu et al., 2016) in 2016, which respectively use an artificial immune algorithm and an ant colony algorithm to infer EC between different brain regions. By means of two randomly global searching mechanisms in the candidate solution space, both AIAEC and ACOEC obtain higher accuracy on identifying the directions of EC compared with other methods. In particular, ACOEC not only has the same excellent identification ability on connections and directions of EC networks as that of AIAEC, but can also get the strengths of these connections, thus it is a more promising method of studying EC.

In recent years, multimodal analysis from multiple imaging data provides new insights for the progress of learning EC studies. This is because many studies have produced evidence, that FC based on fMRI is positively correlated with structural connectivity (SC) between brain regions based on DTI in the brain network (Rykhlevskaia et al., 2008; Sui et al., 2012; Zhu et al., 2013). Obviously, a multimodal analysis could provide a more reliable basis than a single modality analysis to differentiate brain patterns under various conditions such as normal, diseased, or aging (Dang et al., 2017). Up to now, there are some fusion methodologies for combining DTI and fMRI data (Zhu et al., 2013), for instance, a few studies have fused FC with axonal connectivity (AC). However, there are only two tentative studies (Stephan et al., 2009; Dang et al., 2017) that fuse EC with AC. Enno et al. used diffusion weighted imaging and probabilistic tractography to specify anatomically informed priors for dynamic causal models (DCMs) of fMRI data. More specially, the anatomical likelihood of a given connection was used to inform the prior variance of the corresponding coupling parameter in the DCM (Stephan et al., 2009). Dang et al. proposed a unified probabilistic framework that combines information from both DTI and fMRI data to learn EC using dynamic Bayesian networks, where a novel anatomically-informed score that simultaneously evaluates the fitness of a given connectivity structure to both sources was given (Dang et al., 2017). This type of research focuses on DCM-based methods using DTI and fMRI data. Therefore, how to further explore other novel fusing methods to identify EC from fMRI and DTI data is still an open and challenging research topic.

In this paper, a new method employing Ant Colony Optimization to learn EC from fMRI and DTI data is presented, named ACOEC-FD. First, ACOEC-FD uses DTI data to acquire some positively correlated relations among regions of interest (ROIs), and takes them as anatomical constraint information to effectively restrict the scope of available candidate arcs, reduce the space of candidate solutions, and induce ants to avoid many unnecessary searches. Then, by combining the global score increase of a solution with the local anatomical constraint information between two corresponding ROIs, a new heuristic function with a better search ability is given to induct the process of ant stochastic searches. We then develop a new heuristic function with a better search ability to induct the process of ant stochastic searches. The experimental results on generated data and real fMRI-DTI datasets show that the new algorithm is more effective and efficient in identifying EC, and greatly enhances the convergence speed and learning quality compared to ACOEC and some other methods that only use single modality data.

2. RELATED WORKS

2.1. Ant Colony Optimization (ACO)

Ant colony optimization (ACO) is a meta-heuristic search algorithm inspired by the ant foraging theory. Ants use

pheromones to communicate with each other in their feeding process. The more pheromones released on a route, the greater the probability is of ants selecting that route, which means that the more pheromones deposited on the shorter path over equal periods of time is, the greater the number of ants selecting the shorter path becomes. Thus, when one ant finds a very short path, other ants are more likely to follow this path. Such information feedback eventually leads all ants to select and follow the shortest path. In detail, each ant finds a solution starting from a start node and moving to feasible neighbor nodes step-by-step to construct a new solution. In the meantime, pheromones also evaporate over time during the process. For infrequently traveled paths, pheromone trails become weaker, and vice versa.

2.2. ACO for Learning Brain Effective Connectivity (ACOEC)

ACOEC (Liu et al., 2016) employs ACO to search for the best EC network, and takes each EC network as a directed acyclic graph (DAG) just like other methods based on BNs. It views each ant in ACO as an available solution (an EC network), employs a K2 scoring metric to evaluate each ant in a population, and guides ants to construct and search for the global maximum with the best K2 score in a feasible solution space.

In ACOEC, each ant k starts from an empty graph $G(0)$ including all nodes (ROIs) and no arc, and proceeds by adding an arc at a time, and this process will be repeatedly performed until there is no way to make the score of the candidate solution higher by adding an arc. At time t, the probabilistic transition rule that an ant k selects a directed arc a_{ij} between two ROIs X_i and X_j from the current set of candidate arcs is defined as:

$$a_{i,j} = \begin{cases} arg\ max_{i,j \in DA_k(t)}\{[\tau_{ij}(t)] \cdot [\eta_{ij}(t)]^{\beta}\}, & if\ q \leq q_0, \\ a_{I,J}, & otherwise, \end{cases} \quad (1)$$

where $\tau_{ij}(t)$ is the pheromone concentration, $\eta_{ij}(t)$ represent the heuristic information of a_{ij}, and β is the weighted coefficient which controls $\eta_{ij}(t)$ to influence the selection of arcs. $DA_k(t)$ $(i, j \in DA_k(t))$ is the set of all candidate arcs whose heuristic information is larger than zero; q_0 $(0 \leq q_0 < 1)$ is an initial parameter that determines the relative importance of exploration vs. exploitation; q is a random number uniformly sampled in [0,1]; and I and J are a pair of ROIs randomly selected according to the probability in the following way:

$$p_{ij}^{k}(t) = \begin{cases} \dfrac{[\tau_{ij}(t)]^{\alpha} \cdot [\eta_{ij}(t)]^{\beta}}{\sum_{r,l \in DA_k(t)} [\tau_{rl}(t)]^{\alpha} \cdot [\eta_{rl}(t)]^{\beta}}, & if\ i, j \in DA_k(t), \\ 0, & otherwise, \end{cases} \quad (2)$$

where α denotes the relative importance of $\tau_{ij}(t)$ left by ants. The heuristic function η_{ij} is defined as follows:

$$\eta_{ij}(t) = \omega \cdot (f(X_i, Pa(X_i) \cup X_j) - f(X_i, Pa(X_i))), \quad (3)$$

where $f(X_i, Pa(X_i))$ is the K2 score of the initial structure while $f(X_i, Pa(X_i) \cup X_j)$ is the K2 score of new structure by adding an arc $X_j \rightarrow X_i$, $\omega = 1 + Inf(X_i, X_j)$ is a weighted factor associated with the arc connecting intensity, and $Inf(X_i, X_j)$ represents the mutual information between X_i and X_j.

For $\tau_{ij}(t)$, ACOEC respectively carries out two pheromone updating processes. Moreover, once the iterations of ant colony searching end, the algorithm gets the optimal solution G^+, i.e., EC network with the highest k2 score, and calculates the connection strength for every arc in G^+.

3. THE ACOEC-FD ALGORITHM

To enhance the performance of ACOEC, we employ two new strategies to learn the EC network from fMRI and DTI data.

3.1. Main Idea

As mentioned in some studies, the functional dynamics of a brain region is closely related to the pattern of its anatomical connections (Honey et al., 2007; van den Heuvel et al., 2009), and the anatomical fiber properties contribute to dynamic connectivity among homologous brain regions (Honey et al., 2009). Higher values of functional coherence in particular are linked to stronger AC (Xue et al., 2015). Motivated by such prior research, ACOEC-FD first uses DTI data to acquire anatomical constraint information, and then applies it to reduce the search space of the ant colony, which makes a candidate complete connection diagram become a limited connection diagram with smaller connections. Second, ACOEC-FD re-uses the obtained information to revise the heuristic function and to induct ants searching in the reduced space fast. The main process of ACOEC-FD is shown in **Figure 1**.

3.2. Acquiring Anatomical Constraint Information

First, we use FMRIB Software Library (FSL) to perform DTI data processing of multiple subjects, employ automated anatomical labeling (AAL) to partition the brain into N ROIs, and obtain the mean fractional anisotropy (FA) value of each ROI for every subject. We then calculate the Pearson correlation coefficient for each pair of ROIs X_i and X_j as follows:

$$r(X_i, X_j) = \frac{1}{n-1} \sum_{l=1}^{n} \left(\frac{X_i^l - \overline{X_i}}{\delta_{X_i}}\right)\left(\frac{X_j^l - \overline{X_j}}{\delta_{X_j}}\right), \quad (4)$$

where n is the number of DTI samples, $\overline{X_i}$ and δ_{X_i} are respectively the FA mean and standard deviation of X_i. $r(X_i, X_j)$ describes the intensity of linear correlation between two ROIs, and its range is $[-1, 1]$ where $r(X_i, X_j) > 0$ show that X_i and X_j are positively correlated by means of FA values. The greater the value of $r(X_i, X_j)$, the stronger the anatomical connection strength between X_i and X_j. Based on all positively correlated relations, we build the adjacency matrix of the network of brain structures, and take it as anatomical constraint information to carry out two following processes in ACOEC-FD.

3.3. Reducing Search Space by Using Anatomical Constraint Information

The ACOEC algorithm is an iterative optimization algorithm, which stochastically searches for the optimal solution from all

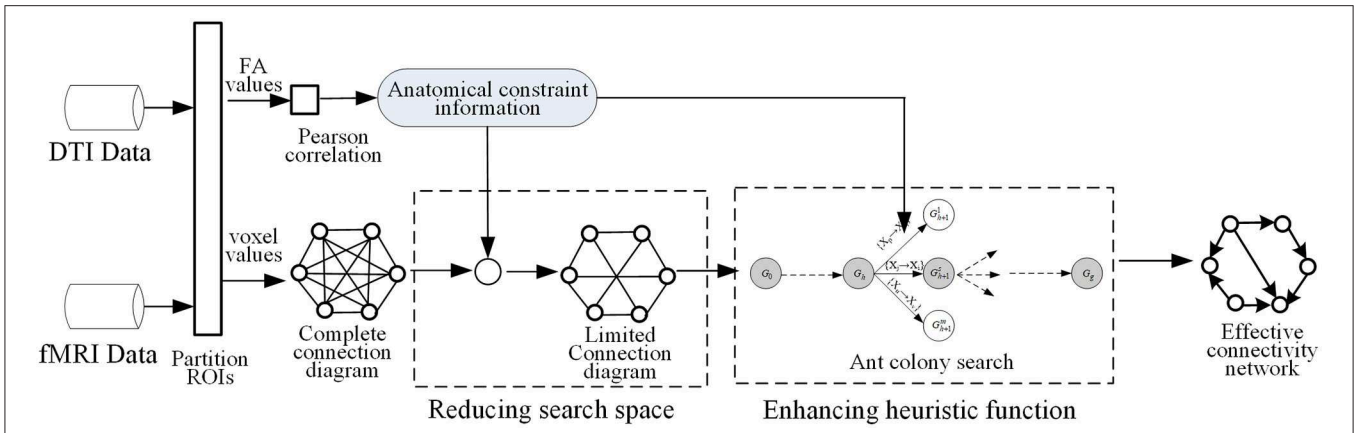

FIGURE 1 | The main process of learning an effective connectivity network by ACOEC-FD.

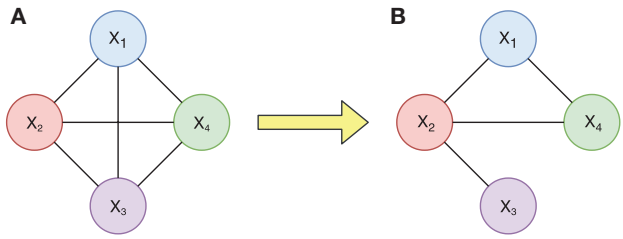

FIGURE 2 | Changes of a connection diagram with 4 nodes. **(A)** Candidate connection diagram with four nodes. **(B)** Limited connection diagram with only four corresponding connections.

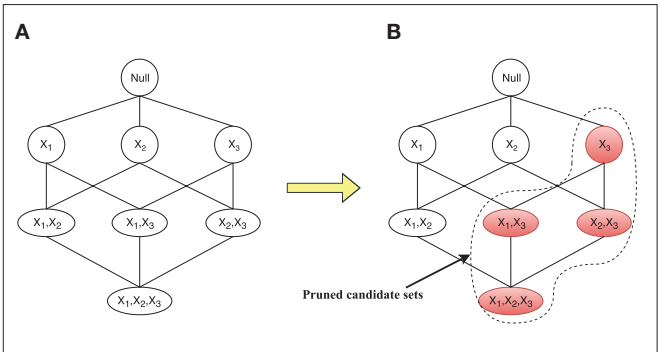

FIGURE 3 | Corresponding changes of the search space for the candidate parent node set for X_4. **(A)** Search space equal to the whole state space. **(B)** Search space is reduced to four candidate parent node sets.

feasible solutions. In ACOEC, each ant selects a satisfied arc from a candidate connection diagram at each step in an iteration, thus the complexity of the candidate connection diagram determines the complexity of ACOEC to a large extent. Furthermore, if some useful strategies are developed to simplify the candidate connection diagram, then the search space of solutions will be greatly reduced. In light of the idea of that AC is necessary for EC, ACOEC-FD first uses anatomical constraint information obtained to reduce the search space before ants search. More specifically, we remove some redundant connections that do not satisfy the anatomical constraints based on DTI data from the initial connection diagram, and change the complete connection diagram to a limited connection diagram.

For example, we consider the changes of a candidate connection diagram with four nodes in **Figure 2**. **Figure 2A** is a complete connection diagram built on four ROIs, which has all six connections. If we use DTI data to acquire the anatomical constraint information $r(X_1, X_2) > 0$, $r(X_2, X_4) > 0$, $r(X_2, X_3) > 0$, and $r(X_1, X_4) > 0$, then we will obtain a limited connection diagram with only four corresponding connections, shown in **Figure 2B**.

The different initial connection diagrams will directly determine the size of search spaces of some nodes at different iterations. Corresponding to the connection diagrams in **Figure 2**, the changes in search spaces for the parent set of X_4 are given in **Figure 3**. **Figure 3A** shows the search space equal to the whole state space when there are connections between all X_4 and other nodes, and **Figure 3B** depicts that the search space is greatly reduced to four candidate parent node sets {}, $\{X_1\}$, $\{X_2\}$, and $\{X_1, X_2\}$. Since the connection between X_1 and X_4 fails to satisfy the anatomical constraint, those candidate parent node sets for X_4, shaded in **Figure 3B**, could be pruned.

Using this strategy, the connections that failed to satisfy the anatomical constraints, will be prevented from being constructed by ants, thus the search spaces for many nodes would be greatly reduced, which would reduce the computational time required for ACO to learn EC.

3.4. Revising Heuristic Function by Reusing Anatomical Constraint Information

In ACOEC, the heuristic function is defined as the product of the connecting intensity of an arc and the score increase introduced by adding an arc, which integrates the global information (score increase) with the local information (arc connecting intensity) and guides an ant to select arcs. However, the definition has a drawback, in that it only provides the heuristic information of arcs from the view of FC, and overlooks other relevant and available information. That makes the heuristic information unilateral and might influence the searching ability of the heuristic function. Considering that some study results show that

stronger levels of EC (derived from fMRI data) are associated with stronger levels of AC (derived from DTI data), the new heuristic function of a directed arc is defined as:

$$\eta_{ij}(t) = \omega \cdot \omega' \cdot (f(X_i, Pa(X_i) \cup X_j) - f(X_i, Pa(X_i))), \quad (5)$$

where a new weighted factor $\omega' = 1 + r(X_i, X_j)$ is concerned with the anatomical connecting intensity of the corresponding arc, and $r(X_i, X_j) > 0$ represents the arc a_{ij} to be positively correlated. $r(X_i, X_j) > 0$ reflects whether the two nodes are correlated and how much that correlation is; thus, it can also be used as heuristic information to induce ant selecting arcs. A new heuristic function employs the local correlation information of arcs from DTI to participate in selecting an arc. Obviously, when two connecting intensities of an arc from both fMRI and DTI data are strong, and the score increase by adding the arc is large, the heuristic function value is great, and vice versa. That is, such arcs, which not only have significant function connecting intensities on fMRI but also have strong anatomical connecting evidence on DTI, are more likely to be explored. Because the revision of the heuristic function can cause ACO to avoid some unnecessary explorations for some structures that lack anatomical connectivity evidence, this would also reduce the computational time required for ACO to learn EC.

3.5. Algorithm Description

In summary, ACOEC-FD employs two strategies, combining fMRI with DTI, to improve ACOEC. First, the Pearson correlation coefficient computing is introduced so that anatomical constraint information from DTI is exploited to restrict the search space, thus avoiding some unnecessary searches. Second, the anatomical constraint information from DTI is re-used in the new heuristic function, enhancing the purpose of construction solutions during ant random searching (i.e., heuristic ability). In other words, ACOEC-FD not only makes use of anatomical constraint information to reduce the search space, but also takes it as other heuristic information to induce random searching. In contrast to ACOEC, there are two main differences: (1) using Pearson correlation coefficient computing to obtain a limited connection graph so that the search space is greatly reduced; (2) combining anatomical constraint information base on DTI with the functional connectivity information (mutual information and score increase) based on fMRI to propose a more powerful heuristic function. In fact, effective connectivity can exist without underlying anatomical connections. However, some important connections may be ignored as the search space is restricted to the regions that possess anatomical connections. To overcome this issue, we perform local optimization when all ants finish their searching. The local optimization operation can get the effective connectivity under the situation when there is no anatomical connection between two brain regions. In detail, if an arc is important and has a higher K2 score, the arc will be added even if there is no anatomical connection. Finally, the termination condition of the ACOEC-FD is that once the algorithm obtains the same optimal solution for 10 successive generations, the search phase will end.

Algorithm 1 provides the main processes of ACOEC-FD.

Algorithm 1: ACOEC-FD

Input: Functional MRI Data, Diffusion tensor imaging Data.
Output: Brain EC network.
Initialization:
Set some parameters;
Reducing search space:
for *every pair of brain regions a and b* **do**
  Calculate the mutual information ;
  Calculate the Pearson correlation coefficient using Equation (4);
end
Reduce search space by anatomical constraint information;
Searching for effective connectivity network:
Set $G^+ = G(0)$;
repeat
  for *k = 1 to m* **do**
    Ant *k* construct Graph using Equation (1) and Equation (2);
    Locally update pheromone τ_{ij};
    Calculate heuristic information η_{ij} using Equation (5);
    Obtain the best solution G^+ at the time.
    Globally update pheromone τ_{ij};
  end
  Perform local optimization and update G^+;
until *termination condition is satisfied*;
Calculation of connection strength;
Return: Effective connectivity network (G^+).

3.6. Algorithm Analysis

The main cost of the ACO algorithm is the computation of statistic factors. Let L be the number of iterations, m be the number of ant colony, and N be the number of ROIs, the complexity of ACOEC can be simply summarized as $O(N^2) + O(L \cdot m \cdot N^2) + O(N^2) + O(1) \approx O((L \cdot m + 2) \cdot N^2)$ according to its processes. In contrast to ACOEC, ACOEC-FD performs two changes in the first two processes, thus the complexity level is the same as ACOEC though the complexity of the initialization process slightly increases from $O(N^2)$ to $O(3 \cdot N^2)$. Notably, ACOEC-FD first employs anatomical constraint information to reduce the search space, which will greatly decrease candidate connections (N^2), and then merges anatomical constraint information into the heuristic function to induct the process of stochastic searches, which may effectively decrease the number of iterations (L).

4. EXPERIMENTAL RESULTS

To assess the performance of ACOEC-FD, we first use a common evaluation method, which is to test the algorithm and its new strategies on a set of simulated fMRI and DTI data, generated from known ground-truth networks. Then, to illustrate the application potential of ACOEC-FD, we apply it to real AD datasets to discriminate EC differences between four subject

groups. The experimental platform is a PC with Intel (R) Core (TM) i7-4770, 3.40GHz CPU, 16 GB RAM, and Windows 7. Codes are available at https://github.com/teddyduo/teddyduo.

4.1. Datasets

4.1.1. Simulation Datasets

The generation model of simulations is referenced in the methods of Smith et al. (2011), which used the dynamic causal modeling (DCM) to generate the neural timeseries. The neural network model is shown as:

$$\dot{z} = \sigma Az + Cu, \tag{6}$$

where z is the neural timeseries, $\dot{z}$ is its rate of change, u is the external inputs (gaussian noises), C is the external input matrix where only diagonal elements are 1 and others are 0, and the matric A determines the network connections between nodes which indicate the ground-truth. The sizes of the matrix C and A are $N \times N$, and σ controls the neural lag between ROIs.

The BOLD fMRI timeseries are obtained from the neural timeseries after convolution with a hemodynamic response function (HRF). We set the session duration to 10 min, and the BOLD fMRI timeseries are sampled with a TR of 3 s, so the number of timepoints is 200. Based on different ROIs, we generate four simulated fMRI datasets, namely Sim1, Sim2, Sim3, and Sim4, whose number of ROIs are 12, 48, 96, and 116, respectively. Each simulation comprises 50 separate subjects, and all of these subjects use the same simulation parameters. Additionally, we also generated a set of anatomical connections corresponding to the effective connections in the four simulations. Synthetic anatomical connections corresponding to no dynamic influence are randomly given zero probability, or one, because the presence of anatomical connections does not determine effective connectivity, which is dynamic in nature (Dang et al., 2017). The ground-truth of the four simulations are shown in **Figure 4**, where each connection matrix corresponding to an effective connectivity network is shown. In detail, a value of 1 means there is a directed connection between these two nodes.

4.1.2. Real Alzheimer's Disease Datasets

Real data used in this article was obtained from the ADNI database (adni.loni.usc.edu). For details, please see http://www.adni-info.org.

In this study, we used 35 subjects from the ADNI database presenting concurrently volumetric $T1$-weighted (T1-w), DTI and fMRI data. These subjects belong to four groups according to ADNI baseline diagnosis: healthy controls (HC), and early MCI (EMCI), late MCI (LMCI), and AD patients. The subject selection criteria are as follows: The session duration and time points of each subject's fMRI data are the same, furthermore, for each subject, the MRI (contains T1-w and fMRI data) and DTI data were obtained at the same time. The characteristics of the subjects are shown in **Table 1**.

Neuroimaging MRI data including high-resolution fMRI data and DTI data was acquired using a 3T MRI scanner (Siemens) and an 8-channel receive only head coil. fMRI sequence parameters include: Slices = 48; volumes = 140; TR/TE = 3,000/30 ms; FA = 90°; Matrix = 64×64. DTI sequence (spin echo with echo planar readout): axial plane; Slices = 80; gradient directions = 54.0; TR/TE = 7,200/56 ms; FA = 90°; Slice thickness=2.0 mm, Reconstruction matrix = 256×256; b = 1,000 s/mm^2. For more data acquisition information, please see http://www.adni-info.org.

fMRI data preprocessing was performed using the Data Processing Assistant for Resting-State fMRI (DPARSF, http://www.restfmri.net), which is based on Statistical Parametric Mapping (SPM8, http://www.fil.ion.ucl.ac.uk/spm) and Resting-State fMRI Data Analysis Toolkit (REST). The steps used for preprocessing are as follows: (1) Arrange the DICOM files and discard the first 10 time points of each session; (2) Set parameters, DPARSF will then give all the preprocessed (slice timing, realign, normalize, smooth) data; (3) Define ROIs and get fMRI time series data. In this paper, we employed two methods of dividing ROIs: (1) Use a brain template to parcellate the whole cortex into multiple brain regions, and treat each brain as a ROI, e.g., we utilize the AAL template to achieve 116 ROIs; (2) Decompose several independent brain networks from fMRI data, and define these specific networks as ROIs, e.g., we define some ROIs from the Default Mode Network (DMN) and the Executive Control Network (ECN) based on the literature.

DTI data were preprocessed using the FSL toolbox (https://fsl.fmrib.ox.ac.uk/fsl/fslwiki/FSL). The steps are as follows: (1) Transform raw DICOM images into NIFTI format using dcm2nii; (2) Create a mask using brain extraction which segments the brain from the skull and other extracranial structures; (3) Correct the head motion and eddy current distortion of images; (4) Utilize the brain template (same with the fMRI data) to define ROIs, and get the FA value for every ROI by computing the averaging FA of all fibers inside each region.

After fMRI data preprocessing, the preprocessed fMRI data also requires discrete processing. The reason is that ACOEC-FD employs the K2 metric, which requires data discretization. According to the number of time points, the discretized instance data are obtained for the whole brain, where each instance includes the discretized values of all brain regions (nodes) at the corresponding time point. For each node's timeseries of a subject, the range of voxel values is divided into several equal parts, thus each part contains the same number of voxel values. Then the voxel value of each node is quantized at every instance into a discrete value. For instance, a node's timeseries is quantized into five parts, including very low (set value = 0), low (set value = 1), medium (set value = 2), high (set value = 3), and very high (set value = 4), with each of the five parts containing 20% of the data points.

4.2. Evaluation Metrics

We compared the learned results to the ground-truths on four common graph metrics (Ji et al., 2016; Liu et al., 2016; Zheng et al., 2018): (1) Precision (PRE), (2) Recall (REC), (3) F1-measure (F1), (4) Structural Hamming distance (SHD). In detail, SHD is the total number of edge additions, deletions, and reversals needed to convert the learned effective connectivity network into the ground-truth network. Let L_{net} denote the

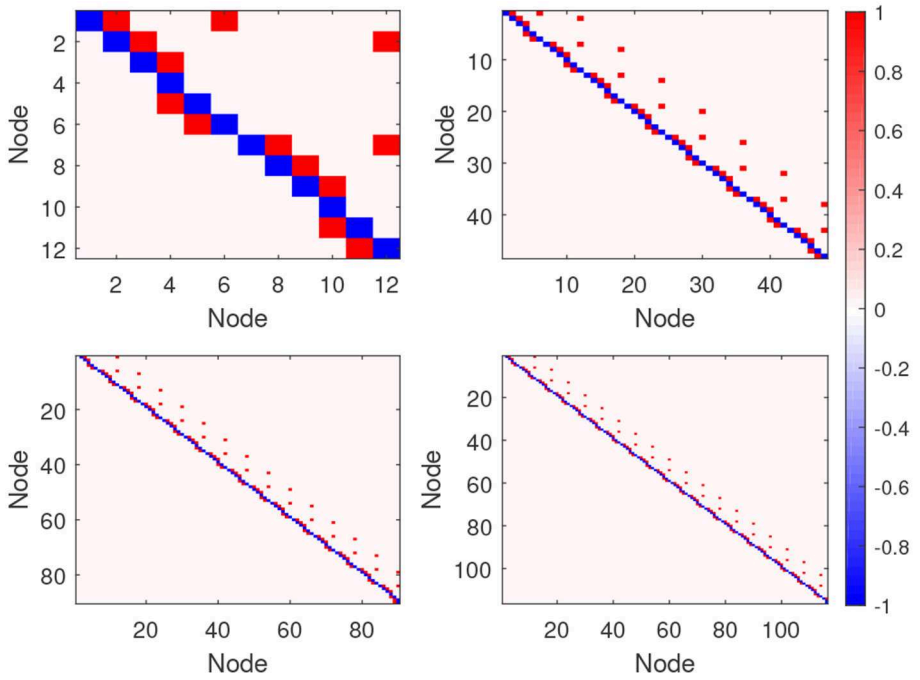

FIGURE 4 | The connection matrix of the four ground-truths on the four simulation datasets: The upper left is Sim1, upper right is Sim2, lower left is Sim3, and lower right is Sim4. For each network graph the corresponding connection matrix is shown, where an element in the upper diagonal of the matrix (red gird) implies a directed connection from a lower-numbered node to a higher-numbered one, and an element in the lower diagonal of the matrix (red gird) implies a directed connection from a higher-numbered node to a lower-numbered one.

learned network and G_{net} express the ground-truth network. The four evaluation metrics are then given by:

$$PRE = \frac{SD}{TD_{L_{net}}}, \tag{7}$$

$$REC = \frac{SD}{TD_{G_{net}}}, \tag{8}$$

$$F1 = \frac{2 * PRE * REC}{PRE + REC}, \tag{9}$$

$$SHD = RD + FD + MD, \tag{10}$$

where SD represents the number of same directed arcs (arcs are both in L_{net} and G_{net}), RD represents the number of reversed directed arcs (arcs have different directions between G_{net} and L_{net}), FD represents the number of false arcs (arcs are not in G_{net} but in L_{net}), MD represents the number of missing arcs (arcs are not in L_{net} but in G_{net}), $TD_{L_{net}}$, and $TD_{G_{net}}$, respectively denote the total number of directed arcs in L_{net} and G_{net}.

4.3. Contributions of Two New Strategies

First, to quantitatively examine the effectiveness and efficiency of two new strategies, we employed four algorithms to learn EC structures from simulated data sets with different node scales. The four algorithms are respectively the original ACOEC, an improved ACOEC-1 (only add reducing search space with anatomical constraint information), another improved ACOEC-2 (only add revising the heuristic function with anatomical constraint information), and ACOEC-FD with two new strategies. The experimental results on four datasets are shown in **Figure 5**, where the performance of the algorithms is evaluated using four measures: Precision (PRE), Recall (REC), F1-measure (F1), and Structural Hamming distance (SHD).

TABLE 1 | The characteristics of the HC, EMCI, LMCI, and AD.

	HC	EMCI	LMCI	AD
Num.[a]	10	10	10	5
Gender[b]	8F/2M	3F/7M	4F/6M	3F/2M
Mean Age[c]	75.3 ± 7.7	78.7 ± 5.0	80.0 ± 9.0	74.1 ± 12.0
Age Range[d]	[65–87]	[70–86]	[68–96]	[56–89]

[a] *Number of subjects.*
[b] *F, Female; M, Male.*
[c] *The mean age ± standard deviation.*
[d] *The age range (years old).*

In the following section, we analyze how the two new strategies contribute to ACOEC algorithm on different simulations. From **Figure 5**, we can see that the two strategies can slightly increase the PRE, REC, and F1 values of the ACOEC algorithm, and the improving rate is about 1 to 6%. More specifically, ACOEC-1 employs anatomical constraint information to effectively reduce the search space, which increases the possibility that ants obtain a better solution. ACOEC-2 uses the new heuristic function with anatomical constraint information to enhance the ant random search ability

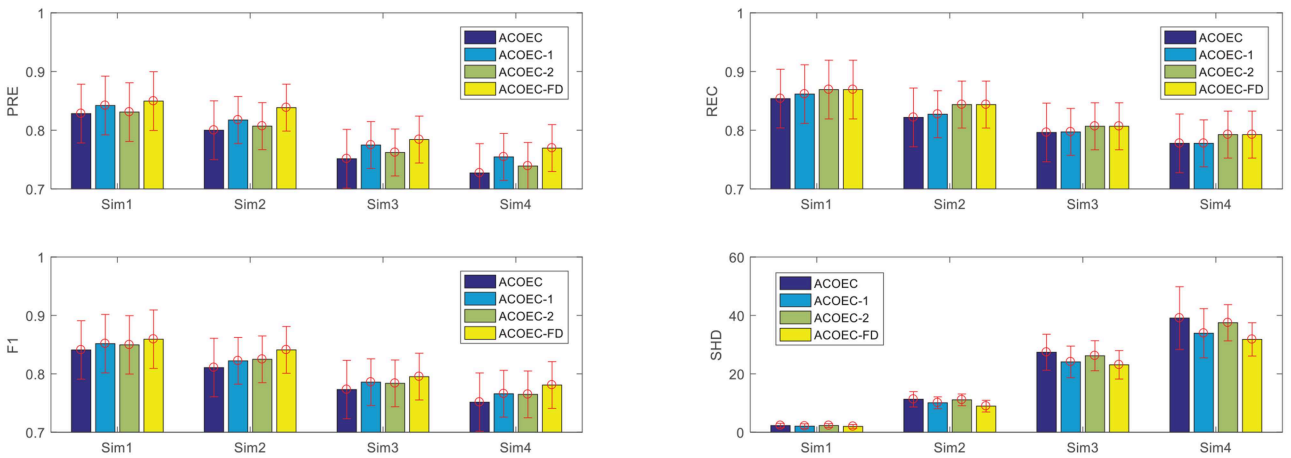

FIGURE 5 | Contributions of two new strategies for ACOEC. Horizontal axis corresponds to the four simulation data sets, vertical axis corresponds to the four measurements on each simulation. Error bars represent standard deviation for the given metric over 10 runs.

TABLE 2 | Contributions of two new strategies on time performance.

Data (nodes)	Algorithms	Times (s)
Sim1 (12)	ACOEC	3.92 ± 0.25
	ACOEC-1	2.97 ± 0.18
	ACOEC-2	3.66 ± 0.21
	ACOEC-FD	3.38 ± 0.19
Sim2 (48)	ACOEC	270.36 ± 9.20
	ACOEC-1	149.49 ± 4.18
	ACOEC-2	256.71 ± 8.20
	ACOEC-FD	123.04 ± 3.13
Sim3 (90)	ACOEC	1411.62 ± 144.96
	ACOEC-1	639.76 ± 16.87
	ACOEC-2	1091.15 ± 90.42
	ACOEC-FD	577.34 ± 87.63
Sim4 (116)	ACOEC	3342.85 ± 115.52
	ACOEC-1	968.67 ± 70.41
	ACOEC-2	1931.10 ± 87.45
	ACOEC-FD	796.57 ± 27.19

to some extent. The lower SHD values for three improved algorithms show that both of the two strategies can make the ACOEC algorithm have fewer incorrect arcs. Specifically, effectively reducing the search space may decrease the likelihood of an unexpected arc addition, while the new heuristic function with anatomical constraint information plays a better role in determining the directions of arcs. This result indicates that two strategies can improve the SHD performance of the ACOEC algorithm from two different point of view.

Furthermore, we compared the time performance of the four algorithms, focusing on the running time to learn a brain EC network. The reported results are summarized in **Table 2**, where the $\mu \pm \sigma$ indicates the mean μ and the standard deviation σ over 10 executions independently carried out by the corresponding algorithm. It is important to note that the two strategies can significantly improve the convergence performance. By reducing the search space, ACOEC-1 greatly decreases the running time compared to ACOEC. In particular, when the node number is larger, e.g., 48, 90, and 116, the strategy becomes more efficient. The reduced time is 120, 771, and 2,372 s, and the improving ratios are about 54, 59, and 94%, respectively. Moreover, the new heuristic function also improves the convergence performance while maintaining a better solution quality. The reduced time is 0.26, 14, 320 and 1,411 s for four cases, respectively. The main reason is that anatomical constraint information is integrated into the heuristic function to make the arc selection more reasonable, which reduces the number of iterations.

The results in **Figure 5** and **Table 2** show that based on anatomical constraint information, ACOEC-FD integrates two strategies of reducing the search space and revising heuristic function into ACOEC, which can not only greatly accelerate the process of learning EC networks but can also effectively improve the learning results in all cases.

4.4. Comparing ACOEC-FD With Other Algorithms

To illustrate ACOEC-FD's ability to accurately infer EC, we compare it with another 10 algorithms only using fMRI data. These algorithms are the LiNGAM, ParceLiNGAM (Tashiro et al., 2014), pairwise LiNGAM (PWLiNGAM) (Hyvärinen and Smith, 2013), GC, GS, Patel, GES, P-corr, AIAEC, and the ACOEC algorithm, respectively. They are classic methods used to identify brain EC networks, some of them perform well on Smith's simulated dataset, and some of them are state-of-the-art methods. The parameters of the algorithms under comparison are based on existing literature (Ji et al., 2016; Liu et al., 2016). The default parameter configurations of the corresponding methods are as follows. LiNGAM uses the parameters where *Prune Factor* = 1.0. ParceLiNGAM runs with *Alpha* = 0.05. PWLiNGAM is performed with *method* = 1. GC is set as *max_lag* $\in [1, 30]$, *Alpha* = 0.05. GS is performed with *tau* =

TABLE 3 | Comparisons of 11 algorithms on the four simulations.

Sim	Metrics	Algorithms										
		LiNGAM	ParceLiNGAM	PWLiNGAM	GC	GS	Patel	GES	P-corr	AIAEC	ACOEC	ACOEC-FD
Sim1	PRE	0.57	0.77	0.85	0.61	0.62	0.85	0.69	0.85	0.84 ± 0.06	0.83 ± 0.07	0.85 ± 0.06
	REC	0.62	0.77	0.85	0.85	0.62	0.85	0.69	0.85	0.85 ± 0.06	0.85 ± 0.06	0.87 ± 0.06
	F1	0.59	0.77	0.85	0.71	0.62	0.85	0.69	0.85	0.84 ± 0.06	0.84 ± 0.06	0.86 ± 0.06
	SHD	6	3	2	7	5	2	4	2	2.2 ± 0.72	2.3 ± 0.74	1.8 ± 0.67
Sim2	PRE	0.54	0.69	0.76	0.52	0.58	0.73	0.59	0.54	0.80 ± 0.08	0.80 ± 0.08	0.83 ± 0.07
	REC	0.64	0.73	0.80	0.76	0.65	0.82	0.64	0.56	0.81 ± 0.08	0.82 ± 0.08	0.84 ± 0.07
	F1	0.58	0.71	0.78	0.62	0.62	0.77	0.61	0.55	0.81 ± 0.08	0.81 ± 0.08	0.84 ± 0.07
	SHD	30	18	14	39	26	17	24	26	11.6 ± 4.62	11.3 ± 4.55	8.9 ± 4.02
Sim3	PRE	0.51	0.66	0.71	0.47	0.53	0.69	0.59	0.56	0.76 ± 0.08	0.75 ± 0.08	0.78 ± 0.07
	REC	0.61	0.71	0.76	0.75	0.63	0.78	0.63	0.58	0.80 ± 0.08	0.80 ± 0.07	0.81 ± 0.07
	F1	0.55	0.69	0.73	0.58	0.58	0.73	0.61	0.57	0.78 ± 0.08	0.77 ± 0.07	0.80 ± 0.07
	SHD	61	38	33	88	57	37	45	48	26.4 ± 8.05	26.8 ± 8.08	23.1 ± 6.88
Sim4	PRE	0.50	0.62	0.69	0.48	0.52	0.67	0.56	0.54	0.74 ± 0.08	0.73 ± 0.09	0.77 ± 0.08
	REC	0.59	0.69	0.76	0.67	0.60	0.75	0.60	0.56	0.78 ± 0.08	0.78 ± 0.08	0.79 ± 0.08
	F1	0.54	0.65	0.72	0.56	0.56	0.71	0.58	0.55	0.75 ± 0.08	0.75 ± 0.08	0.78 ± 0.08
	SHD	80	56	46	96	75	50	64	64	39.1 ± 10.16	39.3 ± 10.42	31.8 ± 7.29

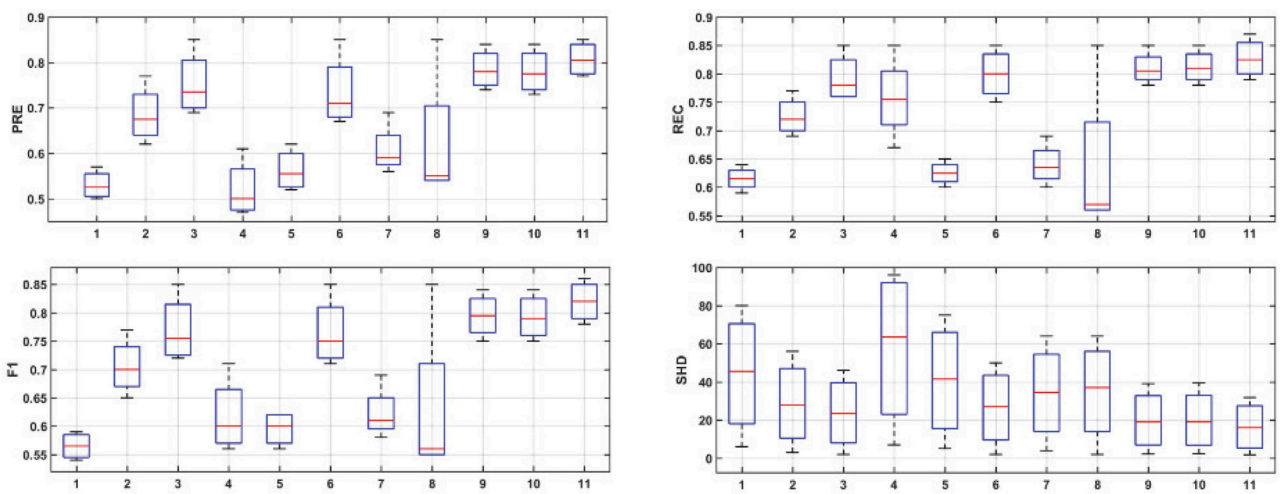

FIGURE 6 | Results for simulation experiments of 11 algorithms. The horizontal axis corresponds to the eleven algorithms, which are LiNGAM (1), ParceLiNGAM (2), PWLiNGAM (3), GC (4), GS (5), Patel (6), GES (7), P-corr (8), AIAEC (9), ACOEC (10), and ACOEC-FD (11), respectively. The vertical axis corresponds to the four measurements.

2, $m = 10$, $nn = 10$, *and theiler* $= 50$. Patel runs with $bin = 0.75$. The parameters of GES is set as $PenaltyDiscount = 1.0$, and $NumPatternstoSave = 1$. P-corr runs with $BOLDMaxlength = 15$, $TR = 3$. The AIAEC is set as $P_s = 0.5$, $P_c = 0.6$, $P_m = 0.4$, $T = 150$, $N = 80$, and $M = 70$. ACOEC and ACOEC-FD use the parameters where $\alpha = 1$, $\beta = 2$, $\rho = 0.2$, $q_0 = 0.8$, $a = 10$, $NC = 100$, $l_{step} = 10$.. AIAEC, ACOEC, and ACOEC-FD are random optimization methods, whose results are not always same during each run, so we show the mean μ and the standard deviation σ results over 10 random runs. If the standard deviation is zero, we only show the mean value.

In our experiments, we compared 11 different algorithms, to illustrate which one is the best one. We ran them on four simulation datasets, and the detailed results are shown in **Table 3**. From Sim1 to Sim4 in **Table 3**, the number of nodes increased from 12, to 48, 90, and 116. Following the chain of Sim1-Sim2-Sim3-Sim4, we can see that most of the algorithms including ACOEC-FD decrease very little on four evaluated metrics. However, three swarm intelligence-based algorithms (AIAEC, ACOEC, and ACOEC-FD) obtained prominent results compared to those of another eight algorithms. Compared to AIAEC and ACOEC, ACOEC-FD has a better and more reliable performance when the number of nodes increases. In Sim4, the ACOEC-FD's PRE, REC, and F1 value retain better values (0.77, 0.79, and 0.78) which are higher than those of the other 10 algorithms, while SHD mean value is

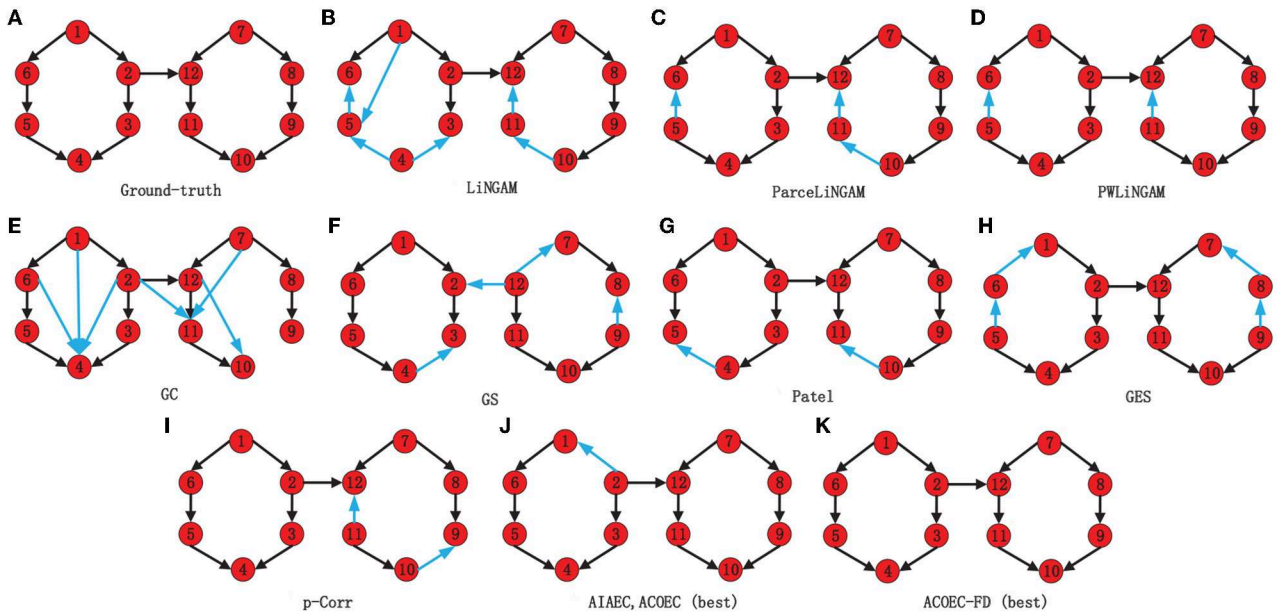

FIGURE 7 | Comparison of G_{net} and L_{net} by 11 different algorithms on Sim1. The eleven algorithms, which are the Ground-truth **(A)**, LiNGAM **(B)**, ParceLiNGAM **(C)**, PWLiNGAM **(D)**, GC **(E)**, GS **(F)**, Patel **(G)**, GES **(H)**, P-corr **(I)**, AIAEC and ACOEC **(J)**, and ACOEC-FD **(K)**, respectively. In each graph, black lines mean that the connections and directions in this graph are consistent with the G_{net}, while the blue lines are not.

31.8, which is the smallest value among all 11 algorithms. Therefore, most of the algorithms do not perform well when the number of nodes is large, however, ACOEC-FD using fMRI and DTI data can still achieve good performance and have fewer mistakes.

Figure 6 provides the box plots of PRE, REC, F1, and SHD comparisons for the 11 algorithms on four simulations. It is clear that ACOEC-FD achieved the best performance whether on PRE, REC, F1, or SHD compared to the other algorithms. As shown in **Figure 6**, we also found that GC performed worse on PRE and SHD but performed better on REC. This is mainly because GC always has a lot of extra adding arcs, which influences the PRE and SHD metrics. P-corr performed badly on PRE, REC and F1 metrics, but its SHD value was not too high. This is because P-corr has extremely few adding and missing arcs though it has a lot of reverse arcs from the comparison between the L_net and G_net. This result shows that different metrics can evaluate the performance of algorithms from different angles. However, in all evaluated metrics, ACOEC-FD performed the best, and the mean of each metric is significantly better than the other algorithms.

In order to present the results more clearly and intuitively, we provide the network structure diagram learned by various algorithms on Sim1 as an instance. **Figure 7** shows a comparison of G_{net} and L_{net} by 11 algorithms, where (a) is G_{net}, (b)-(k) are L_{net} by 11 algorithms, and the blue arcs in L_{net} are the error arcs identified. Obviously, the EC network identified by ACOEC-FD is completely consistent with G_{net} while there is at least one error arc in other L_{net} learned by other algorithms. This instance also verifies that ACOEC-FD can more accurately infer EC using multimodal Data.

TABLE 4 | The Friedman test results of 11 algorithms on four metrics.

	p-value	Chi-squared	Degrees of freedom (df)
PRE	1.2744×10^{-4}	34.95	10
REC	1.2370×10^{-4}	35.02	10
F1	2.0531×10^{-4}	33.73	10
SHD	7.2612×10^{-5}	36.37	10

Finally, we use the Friedman test and the *post-hoc* test to attest the efficiency of the corresponding algorithms. If the *p*-value obtained from the test is less than 0.05, we consider that a significant difference exists in the corresponding experimental results. The result of the Friedman test (*p*-value, chi-squared and degrees of freedom) is shown in **Table 4**, which indicates that there is a significant difference between the 11 compared algorithms on the four evaluate metrics. Therefore, we employ *post-hoc* test to find out which pairs of algorithms are significantly different from each other. The *post-hoc* test results on the PRE, REC, F1, and SHD are shown in **Tables 5**–**8**, respectively. Bold type signifies statistically significant results (p-value < 0.05).

From **Table 5**, we can find that AIAEC and ACOEC-FD are significantly better (p-value<0.05) than GC, and the p-values are 0.0353 and 0.0027, respectively. Besides, only the ACOEC-FD algorithm is significantly better than LiNGAM (p-values = 0.0078 < 0.05). This result indicates that the ACOEC-FD algorithm has more outstanding results on the PRE metric compared with other algorithms.

Table 6 shows that only the ACOEC-FD algorithm is significantly better than LiNGAM, GS, GES, and P-corr, and the

TABLE 5 | The *post-hoc* test results of *p*-values on PRE value.

	ParceLiNGAM	PWLiNGAM	GC	GS	Patel	GES	P-corr	AIAEC	ACOEC	ACOEC-FD
LiNGAM	0.8537	0.1613	1.0000	1.0000	0.3221	0.9786	0.9613	0.0795	0.1410	**0.0078**
ParceLiNGAM		0.9892	0.6955	0.9926	0.9993	1.0000	1.0000	0.9496	0.9845	0.5816
PWLiNGAM			0.0795	0.5036	1.0000	0.9003	0.9358	1.0000	1.0000	0.9969
GC				0.9988	0.1819	0.9193	0.8781	**0.0353**	0.0685	**0.0027**
GS					0.7315	1.0000	1.0000	0.3221	0.4657	0.0578
Patel						0.9786	0.9892	1.0000	1.0000	0.9709
GES							1.0000	0.7644	0.8781	0.2911
P-corr								0.8265	0.9192	0.3557
AIAEC									1.0000	0.9998
ACOEC										0.9980

TABLE 6 | The *post-hoc* test results of *p*-values on REC value.

	ParceLiNGAM	PWLiNGAM	GC	GS	Patel	GES	P-corr	AIAEC	ACOEC	ACOEC-FD
LiNGAM	0.9673	0.4003	0.7789	1.0000	0.2366	1.0000	1.0000	0.1244	0.0804	**0.0038**
ParceLiNGAM		0.9944	1.0000	0.9992	0.9673	0.9992	0.9944	0.8894	0.8106	0.2366
PWLiNGAM			1.0000	0.7455	1.0000	0.7455	0.5956	1.0000	0.9998	0.8894
GC				0.9673	0.9992	0.9673	0.9102	0.9915	0.9758	0.5551
GS					0.5551	1.0000	1.0000	0.3644	0.2661	**0.0242**
Patel						0.5551	0.4003	1.0000	1.0000	0.9673
GES							1.0000	0.3644	0.2661	**0.0242**
P-corr								0.2366	0.1642	**0.0117**
AIAEC									1.0000	0.9943
ACOEC										0.9986

TABLE 7 | The *post-hoc* test results of *p*-values on F1 value.

	ParceLiNGAM	PWLiNGAM	GC	GS	Patel	GES	P-corr	AIAEC	ACOEC	ACOEC-FD
LiNGAM	0.6969	0.1076	0.9892	0.9981	0.1845	0.9847	0.9969	0.0422	0.0587	**0.0014**
ParceLiNGAM		0.9951	0.9993	0.9951	0.9993	0.9996	0.9969	0.9617	0.9788	0.4661
PWLiNGAM			0.7663	0.6223	1.0000	0.7979	0.6598	1.0000	1.0000	0.9788
GC				1.0000	0.8790	1.0000	1.0000	0.5446	0.6223	0.0801
GS					0.7663	1.0000	1.0000	0.3926	0.4661	**0.0422**
Patel						0.9006	0.7979	1.0000	1.0000	0.9360
GES							1.0000	0.5830	0.6598	0.0935
P-corr								0.4285	0.5050	0.0505
AIAEC									1.0000	0.9981
ACOEC										0.9951

p-values are 0.0038, 0.0242, 0.0242, and 0.0117, respectively. The results indicate that the ACOEC-FD algorithm perform well on the REC metric.

From **Table 7**, we can see that the ACOEC-FD algorithm is significantly better than LiNGAM and GS. However, there is no significant difference between other algorithms. These results indicate that the ACOEC-FD algorithm has a better performance on the F1 metric.

The results in **Table 8** clearly show that the AIAEC and ACOEC-FD algorithms are significantly better than GC, with *P*-values of 0.0256 and 0.0010, respectively. Additionally, only the ACOEC-FD algorithm is significantly better than LiNGAM and GS. From these experimental results, we can draw the conclusion that ACOEC-FD is superior to the other 10 algorithms on the four evaluate metrics and has a significant difference in some performances when compared to some algorithms.

4.5. Application of ACOEC-FD on Alzheimer's Disease

In this section, we present an application example that we use ACOEC-FD on, in four real Alzheimer's Disease datasets to discriminate EMCI, LMCI, and AD from HC. The EC networks

TABLE 8 | The *post-hoc* test results of *p*-values on SHD value.

	ParceLiNGAM	PWLiNGAM	GC	GS	Patel	GES	P-corr	AIAEC	ACOEC	ACOEC-FD
LiNGAM	0.8811	0.2109	1.000	1.000	0.3965	0.9895	0.9510	0.0948	0.1654	**0.0056**
ParceLiNGAM		0.9928	0.6265	0.9895	0.9997	1.000	1.000	0.9510	0.9850	0.4719
PWLiNGAM			0.0795	0.5036	1.0000	0.9003	0.9358	1.0000	1.0000	0.9969
GC				0.9981	0.1655	0.9023	0.7695	**0.0256**	0.0519	**0.0010**
GS					0.7359	1.0000	0.9981	0.2958	0.4335	**0.0312**
Patel						0.9792	0.9970	1.0000	1.0000	0.9211
GES							1.0000	0.7359	0.8568	0.1879
P-corr								0.8811	0.9510	0.3290
AIAEC									1.0000	0.9989
ACOEC										0.9928

learned for four different groups are graphically rendered in a circular diagram format in **Figure 8**. For each circular diagram, the outermost rings denote the brain regions and the lines in the center express the EC. The labels are achieved by the AAL template, which consists of 116 ROIs. Each brain regions is represented by a circle with differentiated colors (some may be the same), and the arrow colors are consistent with their parent nodes.

Following the chain of HC-EMCI-LMCI-AD in **Figure 8**, the EC number in each group is 356, 251, 205, and 191, respectively. That is, as the disease worsens, the EC number will be less and less. In detail, the number of reduced directions and the number of reversed directions between the HC and AD group are 165 and 58, respectively. In particular, there are significant decreases of EC in the Precuneus, Occipital, Precentral, Insula, and Hippocampus brain regions etc. These findings once again verify previous studies implicating that there are changes in these regions related to MCI and AD, which can help explain and predict the progression and evolution of AD disease (He et al., 2008; Ribeiro et al., 2015). From **Figure 8** we find that the brain EC in the hippocampus has a significant reduction from the ECMI group to the LMCI group and to the AD group, and there are very few ECs in the AD group. The reason may be that the center of memory function is mainly located in the temporal lobe, especially in the hippocampus. Therefore, the reduction of the EC in the hippocampus directly leads to brain memory function degradation, causing people to have mild cognitive impairment. As the disease continues to worsen, the brain EC of the hippocampal region becomes less and less. In fact, structural decline usually occurs earlier than functional decline, so ACOEC-FD utilizes the probabilities of structural connections between regions as supplemental criteria for establishing these effective connectivity networks, whose constructed networks are more in line with the physiological structure of the human brain. Moreover, we find that some regions of the cerebellum in AD patients also show decreased EC compared to those of HC subjects, which is different from many results under single modal data (Wang et al., 2007; Qi et al., 2010). This phenomenon may be related to compensatory processes for MCI and AD patients, however, the implicative mechanism behind the phenomenon remains unclear, and it needs to be further discussed and studied.

TABLE 9 | The ROIs of DMN and ECN.

Net	ROI	Detailed description	Location
DMN	(1)PCC	Posterior Cingulate Cortex	–9, –54, 24
	(2)LHIP	Left Hippocampus	–26, –20, –10
	(3)RHIP	Right Hippocampus	28, –19, –10
	(4)MPFC	Medial Prefrontal Cortex	48, –57, 24
ECN	(5)LDLPFC	Left Dorsolateral Prefrontal Cortex	–48, 27, 21
	(6)RDLPFC	Right Dorsolateral Prefrontal Cortex	54, 33, 24
	(7)LPPC	Left Posterior Parietal Cortex	–30, –69, 39
	(8)RPPC	Right Posterior Parietal Cortex	36, –66, 48
	(9)APFC	Anterior Prefrontal Cortex	–6, 33, 45

Neuroimaging studies have shown that there are abnormalities in brain function and structural networks in AD and patients with a pre-existing condition, especially in the Default Mode Network (DMN) and the Executive Control Network (ECN) (Dennis and Thompson, 2014; Zhu et al., 2016; Badhwar et al., 2017; Liu et al., 2018). We therefore used ACOEC-FD on the two networks to further explore the difference between AD patients and HC subjects. We chose nine regions of interest (ROIs) from the two networks based on the literature (Power et al., 2011). Detailed information is provided in **Table 9**.

Figure 9 summarizes the brain effective connectivity networks learned by ACOEC-FD. Compared with the HC subjects' EC network (**Figure 9B**), the AD patients' EC network (**Figure 9A**) has fewer connections. We also find that there are some opposing directions in AD patients between the left and right brain compared to HC subjects. This finding seems interesting as the neural influence and information transfer between the left and right brain may differ between HC and AD groups. In the current study, the reduction of EC has been confirmed to be closely related to AD disease, while the situation of reverse connection is rarely reported. However, the reverse of the brain EC may also be a cause of illness, which cannot be confirmed through common brain connectivity network research. Therefore, the ACOEC-FD algorithm can provide a new perspective for the diagnosis and analysis of AD disease.

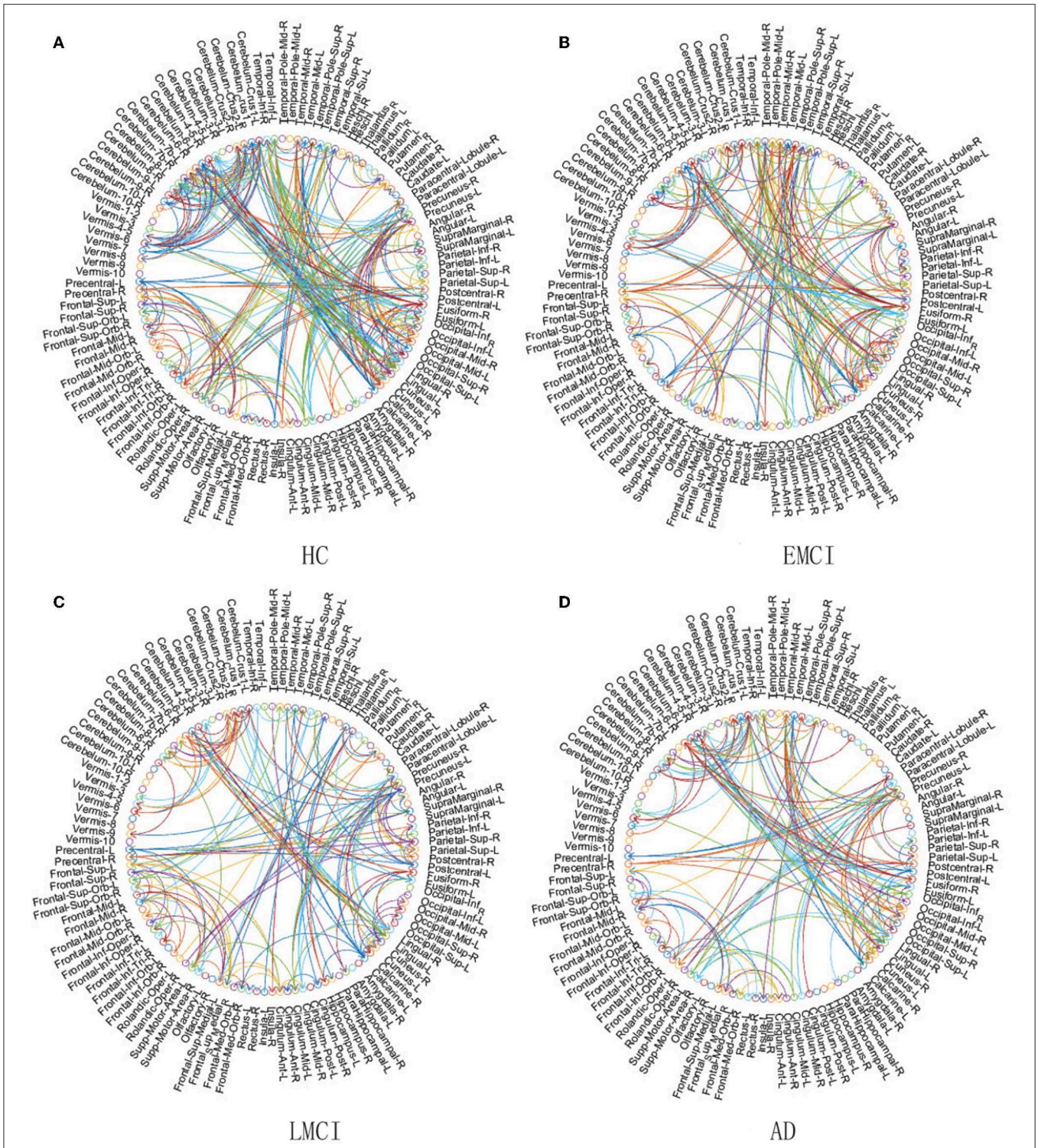

FIGURE 8 | Comparison of four EC networks for HC **(A)**, EMCI **(B)**, LMCI **(C)**, and AD **(D)** groups on real fMRI data.

In this study, our research was focused on AD patients, but actually the new method can also be applied to other brain diseases, i.e., epilepsy, schizophrenia, and autism, etc. Our future work will aim at applying the proposed methodology to other brain diseases.

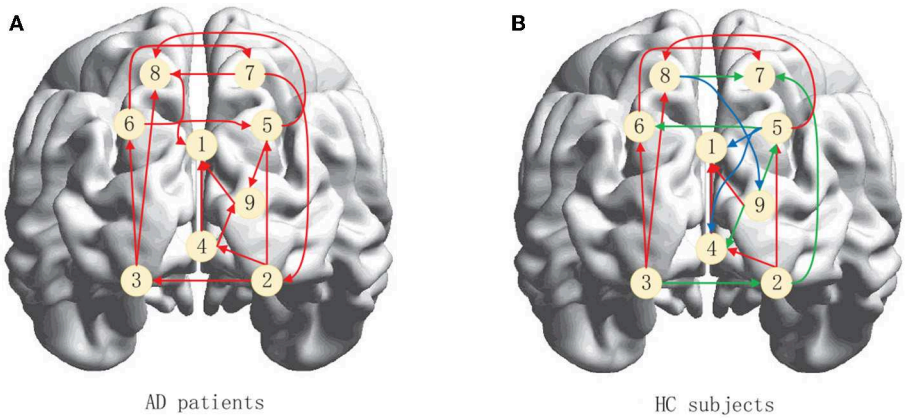

FIGURE 9 | Brain effective connectivity networks learned by ACOEC-FD. **(A,B)** are graphical illustrations of the brain effective connectivity networks for AD patients and HC subjects, respectively. The red arrows in **(B)** indicate that the effective connectivity is the same as **(A)**, whereas blue arrows show additional connections, while green arrows show reversed connections.

5. CONCLUSIONS

By allowing stronger structural connectivity to lead to a greater probability of non-zero functional or effective connectivity, structural information has been incorporated into some studies to identify FC and EC. This paper proposes a new method, called ACOEC-FD, to learn EC from fMRI and DTI data. It uses DTI data to acquire anatomical constraint information, and constrains the search space of EC estimations. Then, by merging anatomical constraint information into the heuristic function, ACOEC-FD can select those ideal structures with stronger AC evidence. We used the generated data and real fMRI-DTI datasets to test our new algorithm in this study, and our experiments show some promising results and interesting observations. In general, our work contributes a novel EC learning framework of ACO merged DTI and fMRI data, which may have significant application potentials in cognitive neuroscience in the future.

DATA AVAILABILITY STATEMENT

Publicly available datasets were analyzed in this study. This data can be found here: https://ida.loni.usc.edu/login.jsp?project=ADNI&page=HOME.

ETHICS STATEMENT

The studies involving human participants were reviewed and approved by ADNI. Written informed consent for participation was not required for this study in accordance with the national legislation and the institutional requirements.

AUTHOR CONTRIBUTIONS

JJ conceived the work. JL and AZo performed the experimental analysis. JJ and JL prepared the manuscript with revisions by AZh. All authors read and approved the final manuscript.

FUNDING

This work was partly supported by the National Natural Science Foundation of China (NSFC) under Grant Nos. 61672065, 61906010, and 61906007.

ACKNOWLEDGMENTS

We thank the reviewers for their insightful comments. In part data collection and sharing of this article were obtained from the Alzheimer's Disease Neuroimaging Initiative (ADNI) database (adni.loni.usc.edu). As such, the investigators within the ADNI contributed to the design and implementation of ADNI and/or provided data but did not participate in analysis or writing of this paper.

REFERENCES

Badhwar, A., Tam, A., Dansereau, C., Orban, P., Hoffstaedter, F., and Bellec, P. (2017). Resting-state network dysfunction in Alzheimer's disease: a systematic review and meta-analysis. *Alzheimers Dement. Diagn. Assess. Dis. Monit.* 8, 73–85. doi: 10.1016/j.dadm.2017.03.007

Dang, S., Chaudhury, S., Lall, B., and Roy, P. K. (2017). Tractography-based score for learning effective connectivity from multimodal imaging data using dynamic bayesian networks. *IEEE Trans. Biomed. Eng.* 99, 1. doi: 10.1109/TBME.2017.2738035

Dauwels, J., Vialatte, F., Musha, T., and Cichocki, A. (2010). A comparative study of synchrony measures for the early diagnosis of Alzheimers disease based on EEG. *J. Neurosci. Methods* 49, 668–693. doi: 10.1016/j.neuroimage.2009.06.056

Dennis, E. L., and Thompson, P. M. (2014). Functional brain connectivity using fMRI in aging and Alzheimer's disease. *Neuropsychol. Rev.* 24, 49–62. doi: 10.1007/s11065-014-9249-6

Friston, K. J. (2011). Functional and effective connectivity: a review. *Brain Connect.* 1, 13–36. doi: 10.1089/brain.2011.0008

Havlicek, M., Roebroeck, A., Friston, K. J., Gardumi, A., Ivanov, D., and Uludag, K. (2017). On the importance of modeling fMRI transients when estimating effective connectivity: a dynamic causal modeling study using ASL data. *Neuroimage* 155, 217–233. doi: 10.1016/j.neuroimage.2017.03.017

He, Y., Chen, Z., and Evans, A. (2008). Structural insights into aberrant topological patterns of large-scale cortical networks in Alzheimer's disease. *J. Neurosci.* 4, 4756–4766. doi: 10.1523/JNEUROSCI.0141-08.2008

Honey, C. J., Kotter, R., Breakspear, M., and Sporns, O. (2007). Network structure of cerebral cortex shapes functional connectivity on multiple time scales. *Proc. Natl. Acad. Sci. U.S.A.* 104, 10240–10245. doi: 10.1073/pnas.0701519104

Honey, C. J., Sporns, O., Cammoun, L., Gigandet, X., Thiran, J. P., and Meuli, R. (2009). Predicting human resting-state functional connectivity from structural connectivity. *Proc. Natl. Acad. Sci. U.S.A.* 106, 2035–2040. doi: 10.1073/pnas.0811168106

Hyvärinen, A., and Smith, S. M. (2013). Pairwise likelihood ratios for estimation of non-Gaussian structural equation models. *J. Mach. Learn. Res.* 14, 111–152. Available online at: https://dl.acm.org/citation.cfm?id=2567709.2502585

Ide, J. S., Zhang, S., and Chiang-shan, R. L. (2014). Bayesian network models in brain functional connectivity analysis. *Int. J. Approximate Reason.* 55, 22–35. doi: 10.1016/j.ijar.2013.03.013

Ji, J., Liu, J., Liang, P., and Zhang, A. (2016). Learning effective connectivity network structure from fMRI data based on artificial immune algorithm. *PLoS ONE* 11:e0152600. doi: 10.1371/journal.pone.0152600

Karwowski, W., Vasheghani Farahani, F., and Lighthall, N. (2019). Application of graph theory for identifying connectivity patterns in human brain networks: a systematic review. *Front. Neurosci.* 13:585. doi: 10.3389/fnins.2019.00585

Lennartz, C., Schiefer, J., Rotter, S., Hennig, J., and LeVan, P. (2018). Sparse estimation of resting-state effective connectivity from fMRI cross-spectra. *Front. Neurosci.* 12:287. doi: 10.3389/fnins.2018.00287

Liu, J., Ji. J., Zhang, A., and Liang. P. (2016). "An ant colony optimization algorithm for learning brain effective connectivity network from fMRI data," in *IEEE International Conference on Bioinformatics and Biomedicine* (IEEE: Shenzhen), 360–367. doi: 10.1109/BIBM.2016.7822546

Liu, X., Chen, X., Zheng, W., Xia, M., Han, Y., Song, H., et al. (2018). Altered functional connectivity of insular subregions in Alzheimer's disease. *Front. Aging Neurosci.* 10:107. doi: 10.3389/fnagi.2018.00107

Mumford, J. A., and Ramsey, J. D. (2014). Bayesian networks for fMRI: a primer. *Neuroimage* 86, 573–582. doi: 10.1016/j.neuroimage.2013.10.020

Patel, R. S., Bowman, F. D. B., and Rilling, J. K. (2006). A Bayesian approach to determining connectivity of the human brain. *Hum. Brain Mapp.* 27, 267–276. doi: 10.1002/hbm.20182

Power, J. D., Cohen, A. L., Nelson, S. M., Wig, G. S., Barnes, K. A., Church, J. A., et al. (2011). Functional network organization of the human brain. *Neuron* 72, 665–678. doi: 10.1016/j.neuron.2011.09.006

Qi, Z., Wu, X., Wang, Z., Zhang, N., Dong, H., and Yao, L. (2010). Impairment and compensation coexist in amnestic mci default mode network. *Neuroimage* 50, 48–55. doi: 10.1016/j.neuroimage.2009.12.025

Ramsey, J. D., Hanson, S. J., Hanson, C., Halchenko, Y. O., Poldrack, R. A., and Glymour, C. (2010). Six problems for causal inference from fMRI. *Neuroimage* 49, 1545–1558. doi: 10.1016/j.neuroimage.2009.08.065

Ribeiro, A. S., Lacerda, L. M., Silva, N. A. D., and Ferreira, H. A. (2015). Multimodal imaging of brain connectivity using the mibca toolbox: preliminary application to Alzheimer disease. *IEEE Trans. Nucl. Sci.* 6, 604–611. doi: 10.1109/TNS.2015.2417764

Rykhlevskaia, E., Gratton, G., and Fabiani, M. (2008). Combining structural and functional neuroimaging data for studying brain connectivity: a review. *Psychophysiology* 45, 173–187. doi: 10.1111/j.1469-8986.2007.00621.x

Seth, A. K. (2011). A MATLAB toolbox for Granger causal connectivity analysis. *J. Neurosci. Methods* 186, 262–273. doi: 10.1016/j.jneumeth.2009.11.020

Shimizu, S., Hoyer, P. O., Hyvainen, A., and Kerminen, A. (2006). A linear non-Gaussian acyclic model for causal discovery. *J. Mach. Learn. Res.* 7, 2003–2030. Available online at: https://dl.acm.org/citation.cfm?id=1248619

Smith, S. M., Miller, K. L., Salimi-Khorshidi, G., Webster, M., Beckmann, C. F., Nichols, T. E., et al. (2011). Network modelling methods for fMRI. *Neuroimage* 54, 875–891. doi: 10.1016/j.neuroimage.2010.08.063

Stephan, K. E., Tittgemeyer, M., Knsche, T. R., Moran, R. J., and Friston, K. J. (2009). Tractography-based priors for dynamic causal models. *Neuroimage* 47, 1628. doi: 10.1016/j.neuroimage.2009.05.096

Sui, J., Adali, T., Yu, Q., Chen, J., and Calhoun, V. D. (2012). A review of multivariate methods for multimodal fusion of brain imaging data. *J. Neurosci. Methods* 204, 68–81. doi: 10.1016/j.jneumeth.2011.10.031

Tashiro, T., Shimizu, S., Hyvärinen, A., and Washio, T. (2014). ParceLiNGAM: a causal ordering method robust against latent confounders. *Neural Comput.* 26, 57–83. doi: 10.1162/NECO_a_00533

van den Heuvel, M. P., Mandl, R. C. W., Kahn, R. S., and Hulshoff Pol, H. E. (2009). Functionally linked resting-state networks reflect the underlying structural connectivity architecture of the human brain. *Hum. Brain Mapp.* 30, 3127–3141. doi: 10.1002/hbm.20737

Wang, K., Liang, M., Wang, L., Tian, L., Zhang, X., and Li, K. (2007). Altered functional connectivity in early Alzheimer's disease: a resting-state fMRI study. *Hum. Brain Mapp.* 28, 967–978. doi: 10.1002/hbm.20324

Wu, G., Liao, W., Stramaglia, S., Ding, J., Chen, H., and Marinazzo, D. (2013). A blind deconvolution approach to recover effective connectivity brain networks from resting state fMRI data. *Med. Image Anal.* 17, 365–374. doi: 10.1016/j.media.2013.01.003

Xu, N., Spreng, R. N., and Doerschuk, P. C. (2017). Initial validation for the estimation of resting-state fMRI effective connectivity by a generalization of the correlation approach. *Front. Neurosci.* 11:271. doi: 10.3389/fnins.2017.00271

Xue, W., Bowman, D. B., Pileggi, A. V., and Mayer, A. R. (2015). A multimodal approach for determining brain networks by jointly modeling functional and structural connectivity. *Front. Comput. Neurosci.* 9:22. doi: 10.3389/fncom.2015.00022

Zheng X, Aragam B, Ravikumar P, and Xing, E. P. (2018). DAGs with NO TEARS: smooth optimization for structure learning. *arXiv preprint* arXiv:1803.01422.

Zhou, L., Wang, L., Liu, L., Ogunbonam, P., and Shen, D. (2015). Learning discriminative bayesian networks from high-dimensional continuous neuroimaging data. *IEEE Trans. Pattern Anal. Mach. Intell.* 38, 2269–2283. doi: 10.1109/TPAMI.2015.2511754

Zhu, D., Zhang, T., Jiang, X., Hu, X., Chen, H., Yang, N., et al. (2013). Fusing DTI and fMRI data: a survey of methods and applications. *Neuroimage* 102, 184–191. doi: 10.1016/j.neuroimage.2013.09.071

Zhu, H., Zhou, P., Alcauter, S., Chen, Y., Cao, H., Tian, M., et al. (2016). Changes of intranetwork and internetwork functional connectivity in Alzheimer's disease and mild cognitive impairment. *J. Neural Eng.* 13:046008. doi: 10.1088/1741-2560/13/4/046008

Conflict of Interest: The authors declare that the research was conducted in the absence of any commercial or financial relationships that could be construed as a potential conflict of interest.

Copyright © 2019 Ji, Liu, Zou and Zhang. This is an open-access article distributed under the terms of the Creative Commons Attribution License (CC BY). The use, distribution or reproduction in other forums is permitted, provided the original author(s) and the copyright owner(s) are credited and that the original publication in this journal is cited, in accordance with accepted academic practice. No use, distribution or reproduction is permitted which does not comply with these terms.

frontiers in Neuroscience

ORIGINAL RESEARCH
published: 11 February 2020
doi: 10.3389/fnins.2020.00071

Examination of Structural Variations of the Circle of Willis by 3D Time-of-Flight Magnetic Resonance Angiography

Jing Li[1†], *Jue Wang*[2†], *Xiao-er Wei*[1], *Yu-wu Zhao*[1], *Feng Wang*[1] *and Yue-hua Li*[1*]

[1] *Shanghai Jiao Tong University Affiliated Sixth People's Hospital, Shanghai, China,* [2] *Shanghai Tenth People's Hospital, Tongji University, Shanghai, China*

Objectives: To explore structural variations of the circle of Willis using three-dimensional time-of-flight magnetic resonance angiography (3D-TOF-MRA), and to compare this modality with digital subtraction angiography (DSA).

Methods: A total of 819 consecutive patients suspected of having cerebral vascular diseases underwent 3D-TOF-MRA, followed by DSA within 2 weeks. We report accuracy, sensitivity, specificity, positive predictive value (PPV), and negative predictive value (NPV) of 3D-TOF-MRA compared with DSA.

Results: The sensitivity and specificity of combined analyses were 90–100 and 98–100%, respectively. The sensitivity and NPV of 3D-TOF-MRA images for A-, C-, D-, and H-types of circle of Willis anomalies were 100%. The specificity, accuracy and sensitivity were all 100% for detecting absence of the anterior communicating artery (ACOA). Sensitivity, specificity, PPV, and NPV were all 100% for detecting F-type. The sensitivity and PPV of volume rendered (VR) images for the B-, E-, and G-types were relatively low (85.0, 86.2, and 73.8%, respectively). Maximum intensity projection (MIP) was somewhat better (88.3, 89.2, and 81.8%, respectively). Combined analyses were better still (95.8, 96.1, and 99.0%, respectively). Specificity and NPVs were high (99.3–100%).

Conclusions: 3D-TOF-MRA compares well to DSA for evaluation of the structure of the circle of Willis. As 3D-TOF-MRA is a non-invasive modality, it may be preferred as a means to evaluate structural variations of the circle of Willis.

Keywords: magnetic resonance angiography, digital substraction angiography, brain vascular malformation, circle of Willis, 3D-TOF-MRA

OPEN ACCESS

Edited by:
Miguel Castelo-Branco, Coimbra Institute for Biomedical Imaging and Translational Research (CIBIT), Portugal

Reviewed by:
Danny J. J. Wang, University of Southern California, United States
Roberto Viviani, University of Innsbruck, Austria

***Correspondence:**
Yue-hua Li
liyuehua0529@163.com

[†]*These authors share first authorship*

Specialty section:
This article was submitted to Brain Imaging Methods, a section of the journal Frontiers in Neuroscience

Received: *22 September 2019*
Accepted: *20 January 2020*
Published: *11 February 2020*

Citation:
Li J, Wang J, Wei X-E, Zhao Y-W, Wang F and Li Y-H (2020) Examination of Structural Variations of the Circle of Willis by 3D Time-of-Flight Magnetic Resonance Angiography. Front. Neurosci. 14:71. doi: 10.3389/fnins.2020.00071

INTRODUCTION

The circle of Willis is the most important intracranial pathway for collateral circulation. It plays critical roles in maintenance of stable intracranial blood flow and perfusion pressure. Developmental type, variation, and degree of opening of the structure all affect its function as a source of compensatory flow. Some studies suggest that aneurysm, stroke, and other cerebrovascular diseases are associated with structural variations of the circle of Willis (Alpers et al., 1959; Kayembe et al., 1984; Schomer et al., 1994). Therefore, it is important to conduct a large-scale epidemiological investigation so as to understand these variations, to explore the mechanism of cerebral vascular diseases, and to improve the accuracy of diagnosis and safety of treatment.

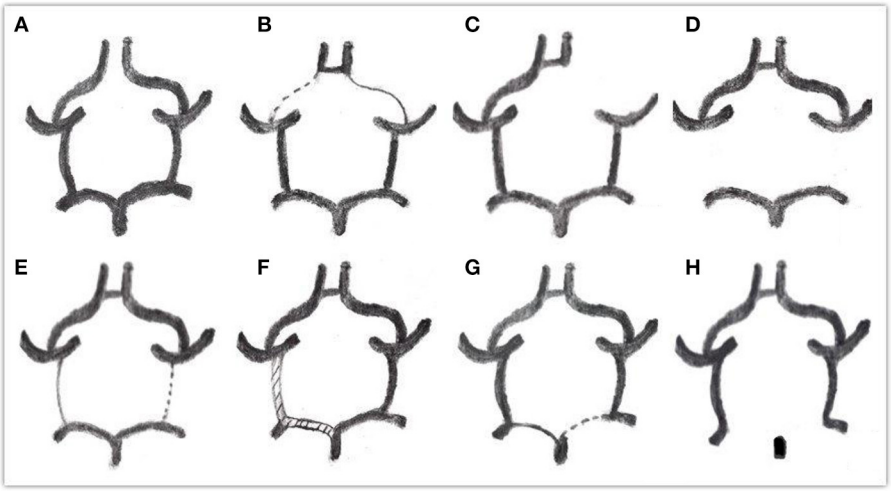

FIGURE 1 | Classification of the circle of wills. **(A–H)** types.

Current imaging methods include the transcranial Doppler (TCD), digital subtraction angiography (DSA), computed tomography angiography (CTA) and magnetic resonance angiography (MRA), of which DSA is the gold standard (Grolimund et al., 1987; Alberico et al., 1995; Katz et al., 1995). However, DSA is an invasive modality, with a number of drawbacks, such as radiation exposure, and requirement for contrast agent, and so forth. CTA is an excellent diagnostic modality, however, it also requires injection of contrast agent and exposure to radiation, with attendant effects on bone and calcification. Time-of-flight magnetic resonance angiography (3D-TOF-MRA), by contrast, is non-invasive, relatively inexpensive and efficient. There is no exposure to radiation or contrast agent. It can be applied to a wide number of indications (Krabbehartkamp et al., 1998). 3D-TOF-MRA has already been widely applied in diagnosis of cerebral vascular disease (Yano et al., 1997), however there is no large study comparing 3D-TOF-MRA with DSA, the gold standard for diagnosis. With the development of high-field-strength MR imaging, it is now possible to precisely and non-invasively visualize the microvasculature of the human brain, *in vivo*, using 3D-TOF-MRA (Hendrikse et al., 2008b; Vuillier et al., 2008; Chen et al., 2011).

The purpose of this study was to explore the structure of the circle of Willis using MR Angiography, and to compare the results to those of DSA as the standard.

MATERIALS AND METHODS

Study Subjects

Between June 2007 and June 2016, 819 consecutive patients who were suspected cerebral vascular diseases detected by MRA were retrospectively collected. Before each patient was admitted to the hospital for an examination, an informed consent was signed, which agreed that all examination information will be used by the hospital in the research. They underwent DSA examinations within 2 weeks after MRA. We regarded the results of volume rendering (VR) DSA as the gold standard. To identify the components of the circle of Willis, we defined the A1 segment of the anterior cerebral artery (A1), the anterior communicating artery (ACOA), the P1 segment of the posterior cerebral artery (P1), and the posterior communicating artery (PCOA) from the results of DSA imaging.

Through observation and measurement of the ACOA, A1, PCOA, and P1 segment, the specific classification of types was as follows (Alpers et al., 1959; Riggs and Rupp, 1963) (**Figure 1**).

A: ACoA absent

B: One or both A1 arteries diameters below 1 mm

C: One or both A1 arteries absent

D: One or both PCOA arteries absent

E: One or both PCOA arteries diameters below 1 mm

F: One or both PCOA arteries diameters equal to P1's, all above 1 mm

G: One or both P1 arteries diameters below 1 mm, far less than PCOA

H: One or both P1 arteries absent.

Image Acquisition

We perfomed all MRA examinations on a 3.0 T system (Achieva X-Series, Philips Medical Systems) with a Sense-Head-8 receiver head coil. 3D-TOF MRA was obtained using 3D T1-weighted fast field sequences with the following settings: field of view (FOV), 250 × 190 × 108 mm; voxel size, 0.342 × 0.7 × 0.6 mm; repetition time/echo time, 35/7 msec; four slabs (180 slices), slice thickness, 0.8 mm; flip angle, 20°; matrix, 732 × 1,024; acquisition time of 8 min and 56 s. Several techniques were used to ensure perfect image quality for visualizing small cerebral arteries, including SENSE (SENSitivity Encoding), MOTSA (multiple over-lapping thin-slab acquisitio), TONE (tilted optimized non-saturating excitation), and SLINKY (Sliding interleaved KY). Then we transferred the acquired image data sets to a workstation (EWS, Philips Medical). The 3D image reconstruction was performed

by MIP (maximum intensity projection) and VR (Volume Rendering) with a specialized software package for 3D volume inspection with a 1,024 × 1,024 matrix (Philips Medical).

DSA

An interventional neuroradiologist performed DSA within 14 days of MRA (median, 10.3 days; range, 1 h−14 days). We perfomed conventional 2D-DSA on a monoplanar unit (Axiom Artis VB22N, Siemens) with a 17–20 cm field of view (FOV) and a 1,024 × 1,024 matrix. We performed rotational angiography with 200° rotational run, an 8-s, injecting 3–4 mL contrast medium per second, and acquiring 200 images. We reconstructed the 3D images by VR on a workstation (SyngoXWP VA70B; Siemens) with a 1,283 × 5,123 matrix. Two observers (M.H.L. And W.W., with 22 and 15 years of experience, respectively, in neurointerventional radiology), who were blinded to previous imaging results and all clinical, identified the morphology of vessels in this study.

Review of MRA Images

Two observers (Y. H. L., and X. E. W., with 18 and 15 years of experience, respectively, in neurointerventional radiology) were blinded to VR-DSA results and all clinical. They independently analyzed the 3D-TOF-MRA data sets on an offline-workstation with the use of the single artery highlighting approach from multiple on-screen viewing angles. In order to locate small vessels, the source images and MIPs were presented on-screen, thus allowing for adjusting the appropriate threshold of window width and level. The measurement of vascular diameter had a very important relationship with window width and window level. The W/L setting value of VR is constant, which is 450 ± 50/1,000 ± 50. The value of MIP is 1,300 ± 50/700 ± 50, and the value of original axial images is 1,000 ± 50/450 ± 50. With such parameters the vascular wall margin is very clear and the contrast is the highest.

We sought the starting point and end point of every vessel in the circle of Willis from the original images by slice tracking to estimate the continuity of vessels. Finally, three types of image were combined to the make an assessment. If a vessel in a VR and MIP image was not detected, or start/stop bits were not checked on the original images, a determination of absence of blood vessels was made. Discrepant conclusions were resolved by a third reviewer (M.H.L, with 20 years of experience in neurointerventional radiology). The diagnosis of the two observers was subjected to Kappa consistency assessment.

Statistical Analyses

SPSS (version 13.0, SPSS Inc., Chicago, IL) was used for statistical analyses. DSA was regarded as the standard for analyzing differences in specificity, sensitivity, positive predictive value (PPV), negative predictive value (NPV), and accuracy between the original images, VR images, MIP images, and combined analyses.

RESULTS

The consistency of each circle of Willis diagnosis by two diagnostic physicians is displayed in **Table 1**. With DSA results as the standard, specificity, sensitivity, PPV, NPV and accuracy between VR, MIP, the original images, and the combined analyses are displayed in **Table 2**. Comparison of MRA and DSA for each circle of Willis type is shown in **Figure 2**.

The Kappa values of different types of Willis rings were observed in the range of 0.8–1 by different methods, suggesting a high degree of consistency between the the two observers.

Compared with VR and MIP, the sensitivity, specificity, PPV, NPV, and accuracy of combined analyses of each image was substantially better. The results agree well with DSA results.

Sensitivity and NPV of MRA images for A-, C-, D-, and H-types were all 100%, suggesting that MRA images are sensitive to the absence of blood vessels. Specificity, accuracy and sensitivity of the combined analyses for absence of ACOA were all 100%, consistent with DSA results.

Sensitivity, specificity, PPV, NPV and accuracy of MRA revealing F-type were all 100%, suggesting that MRA is sensitive and accurate for vessels with diameter ≥ 1 mm.

Sensitivity and PPV of VR images for the B-, E-, and G-types were relatively low (85.0, 86.2, and 73.8%, respectively). MIP was somewhat better (88.3, 89.2, and 81.8%, respectively). Combined analysis was better still (95.8, 96.1, and 99.0%, respectively). However, specificity and NPV were high (99.3–100%), suggesting that specificity of MRA revealing slim blood vessels was higher.

DISCUSSION

We demonstrated that high-resolution 3D-TOF-MRA compares well to DSA in evaluation of the structure of the circle of Willis. 3D-TOF-MRA is a non-invasive imaging method, which employs no contrast agent, no radiation, and does not require intubation of the patient. The method is convenient, cost-effective, and reproducible. 3D-TOF-MRA directly images vascular structures at multiple angles. These advantages suggest that the modality can serve as the preferred means of evaluating structural variations of the circle of Willis.

We used 3D-TOF-MRA with high resolution. We used a phased array coil and short TEs to increase the quality of MRA images. It was perfomed by using strong gradients and long acquisition times (Dagirmanjian et al., 1995). SENSE used parallel imaging to significantly shorten scan times and reduce artifacts while still maintaining good image quality. We used TONE to improve the display of outflow from a 3D volume. To

TABLE 1 | Consistency of the various circle of Willis types diagnosed by two observers (Kappa).

	VR	MIP	Combined
A	1	0.95	0.84
B	0.98	0.83	0.91
C	1	0.96	0.97
D	1	0.98	0.98
E	0.97	0.89	0.95
F	1	1	1
G	0.93	0.80	0.97
H	1	0.88	0.92

TABLE 2 | Specificity, sensitivity, PPV, NPV, and accuracy between VR, MIP, the original images and the combined analysis of the various types the circle of Willis.

	Sensitivity (%)	Specificity (%)	PPV(%)	NPV (%)	Accuracy(%)
VR					
A	100	97.8	84.0	100	98.0
B	85.0	99.3	97.8	94.9	95.6
C	100	98.4	96.7	100	98.9
D	100	94.1	94.4	100	97.1
E	86.2	99.3	98.0	99.3	96.5
F	100	100	100	100	100
G	73.8	100	100	98.3	98.4
H	100	93.8	87.4	100	95.7
MIP					
A	100	98.3	87.5	100	98.5
B	88.3	99.6	98.7	96.2	96.8
C	100	98.7	97.2	100	99.1
D	100	96.1	96.2	100	98.0
E	89.2	99.6	98.8	96.1	96.8
F	100	100	100	100	100
G	81.8	100	100	99.0	99.0
H	100	95.5	90.5	100	96.9
Com					
A	100	100	100	100	100
B	95.8	99.7	99.1	98.7	98.8
C	100	100	100	100	100
D	100	98.0	98.0	100	99.0
E	96.1	99.9	99.6	98.7	98.9
F	100	100	100	100	100
G	90.0	100	100	99.5	99.5
H	100	98.3	95.9	100	98.7

smooth the uneven background suppression, which might be the main disadvantage of TONE, we simultaneously applied MOTSA and SLINKY (Liu and Rutt, 1998; Kirchhof et al., 2002). MOTSA useed TONE RF excitation to compensate for the saturation of the flow signal at the edge of the slab. Furthermore, SLINKY improved the display of vessels with slow blood flow, allowing visualization of complex vascular lesions.

This study demonstrates that original images consisting of VR and MIP were more sensitive and accurate than the single means for evaluating the structure of the circle of Willis. Because some loss of image information may occur during the process of reconstruction, the original images might provide more details, and the missed diagnosis rate might be reduced (Urchuk and Plewes, 1992). The original image can reveal not only thinner vessels, but also improved the accuracy of diagnosis by layer. In this study, the sensitivity, accuracy and specificity of the diagnosis were further improved by the combination of the original image and the reconstructed image. Because VR and MIP images can be observed by rotation, the overlapping of blood vessels can be greatly reduced. The diagnostic efficacy of the combination of the three approaches was close to that of DSA.

We did not perform the neck compression test with DSA, therefore the determination of A-type (ACOA absent) may be a certain deviation. In order to observe the opening of the ACOA, the contralateral carotid artery angiography was done by oppressing of the ipsilateral carotid artery. But the neck compression test will increase the duration and radiation dose, so it was not applicable to all patients. In the specific analysis of A-type in the DSA and MRA results, we found MRA positive rates as high as 85% of those diagnosed by DSA, while the other 15% may be related to the absence of the neck compression test. This suggests that the false negative rate of ACOA seen on MRA may be falsely elevated.

Sensitivity, specificity, PPV, NPV, and accuracy of F-type diagnosis by MRA were 100%, suggesting that MRA is sensitive and accurate for vessels with diameter $\geq$1 mm. The diagnostic performance was equivalent to DSA. In addition, we showed that sensitivity and PPV of VR images for the B-, E-, and G-type were relatively low, MIP was somewhat better, and combined analyses were better still. However, the specificity and NPV of the three methods were high, suggesting that MRA is not sensitive enough to demonstrate slim blood vessels, but is nevertheless highly accurate.

Previous studies have shown that the overall sensitivity of MRA is >80%, proving the presence or absence of arterial segments of the circle of Willis (Fürst et al., 1993; Patrux et al., 1994; Stock et al., 1996; Hendrikse et al., 2008a). Specificity of MRA (63–100%) varied depending on the MRA technology and analysis methods. Stock et al. (1996) performed MRA on a 1.5T system. They found that MIP images had a sensitivity of 87% and a specificity of 88%. The MRA source images depicted a vascular segment with a sensitivity of 89% and a specificity of 63%. The PPV of an arterial segment with a diameter of at least 1 mm was 99%. Hendrikse et al. (2008a) compared 3D-TOF-MRA with 2D phase contrast images with DSA. They found that the sensitivity and specificity of collateral blood flow measurements at the anterior portion of the Willis ring were 83 and 77%, respectively. However, the sensitivity of MRA to PCOA is low (33%). In this study, VR showed PCOA sensitivity of 86.2%, MIP of 89.2%, with combined analysis sensitivity increasing to 96.1%. Our study not only had a larger sample size than the earlier published articles, but also the MRA examinations were performed on a 3T system whose images return higher resolution. The sensitivity, specificity and sensitivity were substantially improved, especially combined analysis: 90–100, 98–100%, respectively. PPV for arterial segments at least 1 mm in diameter was 100%.

A CTA study of the circle of Willis reported sensitivity and specificity >90%. However, the description of structural dysplasia had certain limitations. Sensitivity was 52.6%, specificity was 98.3% (Han et al., 2011). But there are well-known disadvantages, such as radiation exposure, renal toxicity due to contrast agent, and adverse effects on bone ossification and calcification. All this points to the superiority of MRA.

The use of 3D-TOF-MRA technology provides the means to perform large-scale epidemiological surveys, and to establish a morphological quantitative imaging database of the circle of Willis and the basilar artery branches. There the modality could contribute to understanding the pathogenesis, diagnosis, and treatment of cerebrovascular disease.

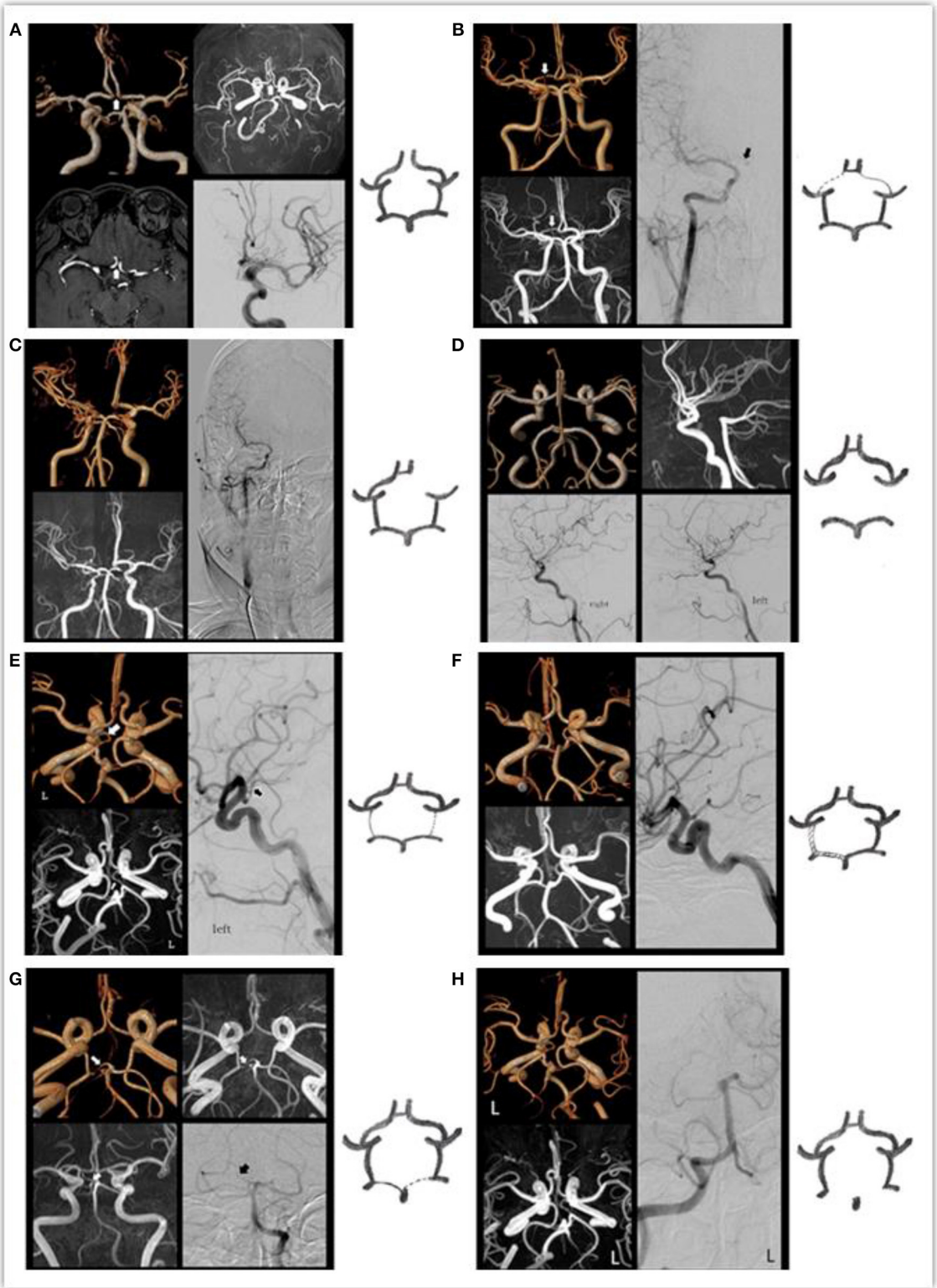

FIGURE 2 | The MRA and DSA of the various types of the circle of Willis: **(A)** arrow indicates absent ACOA. **(B)** Arrow indicates right slim A1. **(C)** Absent right A1. **(D)** Absent bilateral PCOAs. **(E)** Arrow indicates left slim PCOA. **(F)** Bilateral PCOAs = P1 > 1 mm. **(G)** Arrow indicates he right slim P1. **(H)** Absent right P1.

DATA AVAILABILITY STATEMENT

All datasets generated for this study are included in the article/supplementary material.

ETHICS STATEMENT

The studies involving human participants were reviewed and approved by Ethics committee of the Shanghai sixth people's hospital affiliated to Shanghai Jiao Tong university. The patients/participants provided their written informed consent to participate in this study.

AUTHOR CONTRIBUTIONS

Y-HL and Y-WZ contributed conception and design of the study. X-EW organized the database. FW performed the statistical analysis. JL wrote the first draft of the manuscript. JW wrote sections of the manuscript. All authors contributed to manuscript revision, read, and approved the submitted version.

FUNDING

This research was supported by National Natural Science Foundation of China No. 81471656, Shanghai Talent Development Fund No. 201555, Shanghai Municipal Education Commission-Gaofeng Clinical Medicine Grant Support No. 2016427, Clinical Science and Technology Innovation Project of Shanghai Shen Kang Hospital Development Center No. SHDC22015038, Shanghai Municipal Science and Technology Commission Medical Guide Project No. 16411968900, and Shanghai Key Discipline of Medical Imaging (No. 2017ZZ02005).

REFERENCES

Alberico, R. A., Patel, M., Casey, S., Jacobs, B., Maguire, W., and Decker, R. (1995). Evaluation of the circle of Willis with three-dimensional CT angiography in patients with suspected intracranial aneurysms. *Am. J. Neuroradiol.* 16, 1579–1580.

Alpers, B. J., Berry, R. G., and Paddison, R. M. (1959). Anatomical studies of the circle of willis in normal brain. *Arch. Neurol. Psychiatry* 81:409. doi: 10.1001/archneurpsyc.1959.02340160007002

Chen, Y. C., Li, M. H., Li, Y. H., and Qiao, R. H. (2011). Analysis of correlation between the number of lenticulostriate arteries and hypertension based on high-resolution MR angiography findings. *Am. J. Neuroradiol.* 32, 1899–1903. doi: 10.3174/ajnr.A2667

Dagirmanjian, A., Ross, J. S., Obuchowski, N., Lewin, J. S., Tkach, J. A., Ruggieri, P. M., et al. (1995). High resolution, magnetization transfer saturation, variable flip angle, time-of-flight MRA in the detection of intracranial vascular stenoses. *J. Comp. Assist. Tomogr.* 19:700.doi: 10.1097/00004728-199509000-00003

Fürst, G., Steinmetz, H., Fischer, H., Skutta, B., Sitzer, M., Aulich, A., et al. (1993). Selective MR angiography and intracranial collateral blood flow. *J. Comput. Assist. Tomogr.* 17, 178–183. doi: 10.1097/00004728-199303000-00004

Grolimund, P., Seiler, R. W., Aaslid, R., Huber, P., and Zurbruegg, H. (1987). Evaluation of cerebrovascular disease by combined extracranial and transcranial Doppler sonography. Experience in 1,039 patients. *Stroke* 18, 1018–1024. doi: 10.1161/01.STR.18.6.1018

Han, A., Yoon, D. Y., Chang, S. K., Lim, K. J., Cho, B. M., Shin, Y. C., et al. (2011). Accuracy of CT angiography in the assessment of the circle of Willis: comparison of volume-rendered images and digital subtraction angiography. *Acta Radiol.* 52, 889–893. doi: 10.1258/ar.2011.110223

Hendrikse, J., Klijn, C. J., van Huffelen, A. C., Kappelle, L. J., and van der Grond, J. (2008a). Diagnosing cerebral collateral flow patterns: accuracy of non-invasive testing. *Cerebrovasc. Dis.* 25, 430–437. doi: 10.1159/000121344

Hendrikse, J., Zwanenburg, J. J., Visser, F., Takahara, T., and Luijten, P. (2008b). Noninvasive depiction of the lenticulostriate arteries with time-of-flight MR angiography at 7.0T. *Cerebrovasc. Dis.* 26, 624–629. doi: 10.1159/000166838

Katz, D. A., Marks, M. P., Napel, S. A., Bracci, P. M., and Roberts, S. L. (1995). Circle of Willis: evaluation with spiral CT angiography, MR angiography, and conventional angiography. *Radiology* 195, 445–449. doi: 10.1148/radiology.195.2.7724764

Kayembe, K. N., Sasahara, M., and Hazama, F. (1984). Cerebral aneurysms and variations in the circle of Willis. *Stroke* 15, 846–850. doi: 10.1161/01.STR.15.5.846

Kirchhof, K., Welzel, T., Jansen, O., and Sartor, K. (2002). More reliable noninvasive visualization of the cerebral veins and dural sinuses: comparison of three MR angiographic techniques. *Radiology*. 224, 804–810. doi: 10.1148/radiol.2243011019

Krabbehartkamp, M. J., van der Grond, J., de Leeuw, F. E., de Groot, J. C., Algra, A., Hillen, B., et al. (1998). Circle of Willis: morphologic variation on three-dimensional time-of-flight MR angiograms. *Radiology* 207, 103–111. doi: 10.1148/radiology.207.1.9530305

Liu, K., and Rutt, B. K. (1998). Sliding interleaved kY (SLINKY) acquisition: a novel 3D MRA technique with suppressed slab boundary artifact. *J. Magn. Reson. Imaging* 8, 903–911. doi: 10.1002/jmri.1880080421

Patrux, B., Laissy, J. P., Jouini, S., Kawiecki, W., Coty, P., Thiébot, J., et al. (1994). Magnetic resonance angiography (MRA) of the circle of Willis: a prospective comparison with conventional angiography in 54 subjects. *Neuroradiology* 36, 193–197. doi: 10.1007/BF00588129

Riggs, H. E., and Rupp, C. (1963). Variation in form of circle of willis. the relation of the variations to collateral circulation: anatomic analysis. *Arch. Neurol.* 8, 8–14. doi: 10.1001/archneur.1963.00460010024002

Schomer, D. F., Marks, M. P., Steinberg, G. K., Johnstone, I. M., Boothroyd, D. B., Ross, M. R., et al. (1994). The anatomy of the posterior communicating artery as a risk factor for ischemic cerebral infarction. *N. Engl. J. Med.* 330, 1565–1570. doi: 10.1056/NEJM199406023302204

Stock, K. W., Wetzel, S., Kirsch, E., Bongartz, G., Steinbrich, W., and Radue, E. W. (1996). Anatomic evaluation of the circle of Willis: MR angiography versus intraarterial digital subtraction angiography. *Am. J. Neuroradiol.* 17, 1495–1499.

Urchuk, S. N., and Plewes D. B. (1992). Mechanisms of flow-induced signal loss in MR angiography. *J. Magn. Reson. Imaging.* 2, 453–462. doi: 10.1002/jmri.1880020415

Vuillier, F., Medeiros, E., Moulin, T., Cattin, F., Bonneville, J. F., and Tatu, L. (2008). Main anatomical features of the M1 segment of the middle cerebral artery: a 3D time-of-fight magnetic resonance angiography at 3T study. *Surg. Radiol. Anat.* 30, 509–514. doi: 10.1007/s00276-008-0360-3

Yano, T., Kodama, T., Suzuki, Y., and Watanabe, K. (1997). Gadolinium-enhanced 3D time-of-flight MR angiography. *Exp. Clin. Eval.* 38, 47–54. doi: 10.1080/02841859709171241

Conflict of Interest: The authors declare that the research was conducted in the absence of any commercial or financial relationships that could be construed as a potential conflict of interest.

Copyright © 2020 Li, Wang, Wei, Zhao, Wang and Li. This is an open-access article distributed under the terms of the Creative Commons Attribution License (CC BY). The use, distribution or reproduction in other forums is permitted, provided the original author(s) and the copyright owner(s) are credited and that the original publication in this journal is cited, in accordance with accepted academic practice. No use, distribution or reproduction is permitted which does not comply with these terms.

frontiers in Neuroscience

ORIGINAL RESEARCH
published: 21 February 2020
doi: 10.3389/fnins.2020.00144

Amide Proton Transfer Imaging in Predicting Isocitrate Dehydrogenase 1 Mutation Status of Grade II/III Gliomas Based on Support Vector Machine

Yu Han†, Wen Wang†, Yang Yang, Ying-Zhi Sun, Gang Xiao, Qiang Tian, Jin Zhang, Guang-Bin Cui and Lin-Feng Yan**

Department of Radiology & Functional and Molecular Imaging Key Lab of Shaanxi Province, Tangdu Hospital, Fourth Military Medical University, Xi'an, China

OPEN ACCESS

Edited by:
Miguel Castelo-Branco, Coimbra Institute for Biomedical Imaging and Translational Research (CIBIT), Portugal

Reviewed by:
Dong-Hoon Lee, The University of Sydney, Australia
Bing Zhang, Nanjing Drum Tower Hospital, China

***Correspondence:**
Guang-Bin Cui
cuigbtd@fmmu.edu.cn; cgbtd@126.com
Lin-Feng Yan
yanlinfeng@fmmu.edu.cn

†These authors have contributed equally to this work

Specialty section:
This article was submitted to Brain Imaging Methods, a section of the journal Frontiers in Neuroscience

Received: *07 November 2019*
Accepted: *05 February 2020*
Published: *21 February 2020*

Citation:
Han Y, Wang W, Yang Y, Sun Y-Z, Xiao G, Tian Q, Zhang J, Cui G-B and Yan L-F (2020) Amide Proton Transfer Imaging in Predicting Isocitrate Dehydrogenase 1 Mutation Status of Grade II/III Gliomas Based on Support Vector Machine. Front. Neurosci. 14:144. doi: 10.3389/fnins.2020.00144

Background: To compare the efficacies of univariate and radiomics analyses of amide proton transfer weighted (APT_W) imaging in predicting isocitrate dehydrogenase 1 (*IDH1*) mutation of grade II/III gliomas.

Methods: Fifty-nine grade II/III glioma patients with known *IDH1* mutation status were prospectively included (*IDH1* wild type, 16; *IDH1* mutation, 43). A total of 1044 quantitative radiomics features were extracted from APT_W images. The efficacies of univariate and radiomics analyses in predicting *IDH1* mutation were compared. Feature values were compared between two groups with independent *t*-test and receiver operating characteristic (ROC) analysis was applied to evaluate the predicting efficacy of each feature. Cases were randomly assigned to either the training (n = 49) or test cohort (n = 10) for the radiomics analysis. Support vector machine with recursive feature elimination (SVM-RFE) was adopted to select the optimal feature subset. The adverse impact of the imbalance dataset in the training cohort was solved by synthetic minority oversampling technique (SMOTE). Subsequently, the performance of SVM model was assessed on both training and test cohort.

Results: As for univariate analysis, 18 features were significantly different between *IDH1* wild-type and mutant groups ($P < 0.05$). Among these parameters, *High Gray Level Run Emphasis All Direction offset 8 SD* achieved the biggest area under the curve (AUC) (0.769) with the accuracy of 0.799. As for radiomics analysis, SVM model was established using 19 features selected with SVM-RFE. The AUC and accuracy for *IDH1* mutation on training set were 0.892 and 0.952, while on the testing set were 0.7 and 0.84, respectively.

Conclusion: Radiomics strategy based on APT image features is potentially useful for preoperative estimating *IDH1* mutation status.

Keywords: glioma, radiomics, isocitrate dehydrogenase 1 mutation, support vector machine, magnetic resonance imaging

INTRODUCTION

World Health Organization (WHO) grade II/III gliomas include a heterogeneous group of infiltrative neoplasms with astrocytic and oligodendroglia morphology (Louis et al., 2016). Much interest has been focused on histologic class over the past several decades (Daumas-Duport et al., 1988; Fuller and Scheithauer, 2007). However, highly variable clinical behaviors are not adequately predicted based on the histologic phenotype (van den Bent, 2010; Reuss et al., 2015). Therefore, revealing the specific molecular hallmarks has the potential to reduce bias and improve diagnosis as well as prognosis. Notably, in the 2016 WHO classification of central nervous system (CNS) tumors, grade II/III astrocytomas are molecularly divided into *IDH* mutant, *IDH* wild-type, and not otherwise specified categories, emphasizing the diagnostic and prognostic value of *IDH* mutation status in glioma (Louis et al., 2016).

*IDH*s are critical enzymes that catalyze the oxidative decarboxylation of isocitrate to α-ketoglutarate (α-KG) (Yan et al., 2009). *IDH* mutations occur in up to 75% of WHO grade II/III gliomas, but are rarely found in primary glioblastomas (Hartmann et al., 2009; Yang et al., 2012). Patients with *IDH* mutation were more sensitive to chemoradiation therapy and survived longer than *IDH* wild-type ones (Sanson et al., 2009; van den Bent et al., 2010). Moreover, *IDH* mutation would help stratify grade II/III gliomas into subgroups with distinct prognostic characteristics, therapeutic response, and clinical management (Rohle et al., 2013; Olar et al., 2015; Reuss et al., 2015; Jiang T. et al., 2016).

Currently, *IDH* mutation is determined by immunohistochemical staining and DNA sequencing, both are invasive methods with major limitations associated with inherent sampling bias or inability to predict the patient prognosis before surgical resection (Agarwal et al., 2013). As a non-invasive diagnostic tool, magnetic resonance imaging (MRI) technique plays an important role in determining *IDH* mutation. Although promising, the results of most previous experimental studies are conflicting (Arita et al., 2018; Suh et al., 2018), which has hampered consistent clinical application. Notably, identification of 2-hydroxyglutarate (2HG), the metabolite of mutated *IDH*, with MR spectroscopy (MRS) is suggested to be an optimal strategy in identifying *IDH* mutation (Andronesi et al., 2012; Choi et al., 2012; Pope et al., 2012). However, this technique requires a large tumor volume (de la Fuente et al., 2016) and is time-consuming, which limits its application. In addition, partial volume effects between different tumor regions may obscure the identification of 2-HG in smaller regions.

Because widespread disturbances of cellular metabolism occur after *IDH* mutation, including alteration of amino acid concentrations and enzymatic activity (Reitman et al., 2011), and global downregulation of protein expression (Doll et al., 2017). Therefore, more specific imaging modalities are urgently needed to identify *IDH* mutation. Amide proton transfer weighted (APT_W) imaging is a promising molecular MR imaging technique developed to non-invasively quantify endogenous proteins and peptides (Zhou et al., 2003). For gliomas, APT_W imaging was consistently demonstrating potential for grading (Togao et al., 2014), differential diagnosis (Jiang S. et al., 2016; Yu et al., 2017), and treatment response assessment (Sagiyama et al., 2014). Although APT_W imaging has been used in a study (Jiang et al., 2017) to predict *IDH* mutation and encouraging results has been obtained, only univariate analysis was focused on histogram and conventional parameters such as the mean, minimal, or maximal values extracted from manually drawn region of interest (ROI). Higher-dimensional quantitative features from APT_W images were not fully utilized.

Recently, radiomics analysis has drawn attention (Gillies et al., 2016; Kotrotsou et al., 2016). A large amount of quantitative high-dimensional features can be extracted, processed and analyzed to discover their associations with underlying pathology and genomics. Currently, radiomics approach based on other advanced MRI techniques are promising in predicting glioma genotype (Li et al., 2018; Shofty et al., 2018) and patient survival (Prasanna et al., 2017). However, radiomics analysis based on APT_W images in predicting *IDH* mutation has not been reported yet.

Based on these observations, the purpose of this study was to explore whether radiomics analysis of APT_W images could acquire a higher efficacy than commonly used univariate analysis in predicting *IDH* mutation of grade II/III gliomas.

MATERIALS AND METHODS

Patient Population

This prospective single institution study has been approved by the Ethics Committee of Tangdu Hospital (TDLL-20151013) and was also registered to ClinicalTrials.gov (NCT03102112).[1] From June 2016 to October 2017, a total of 429 consecutive patients with suspected gliomas underwent the MRI scanning.

Inclusion criteria were: (1) receiving no corticosteroid, surgery or any conservative treatment before MRI scan; (2) pathologically confirmed grade II/III gliomas based on the 2016 WHO classification; (3) underwent near total or gross total resection. Eighty-one patients were enrolled in this study. Among them, 22 patients were excluded for the following reasons: (1) without APT_W image (n = 8); (2) the image quality was unsatisfying with susceptibility or motion artifacts (n = 10); (3) without *IDH* information (n = 4). Finally, 59 patients were enrolled. The process flow diagram is shown in **Figure 1**.

Imaging Data Acquisition

The whole brain MRI examinations were performed on a 3T MRI system (Discovery MR750, General Electric Medical System, Milwaukee, WI, United States) with an eight-channel head coil (GE Medical System). Conventional MRI, contrast-enhanced MRI, and APT_W imaging were implemented during the examination.

Conventional MRI scanning included four sequences. (1) axial T_1-weighted spin-echo image (T_1WI): repetition time/echo time (TR/TE), 1750 ms/24 ms; matrix size, 256 × 256; field of view (FOV), 24 cm × 24 cm; number of excitation, 1; slice

[1] https://www.clinicaltrials.gov/

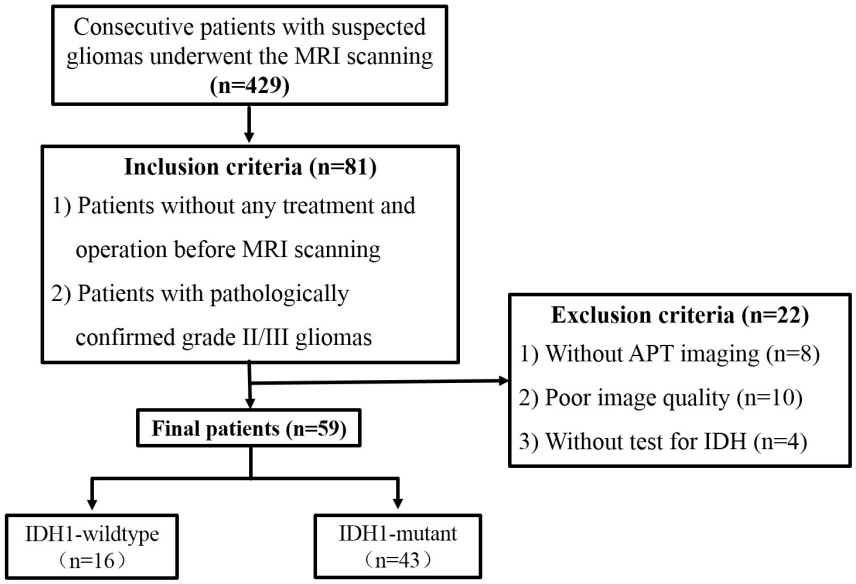

FIGURE 1 | Flow diagram for patient selection.

thickness, 5 mm; gap, 1.5 mm. (2) T_2-weighted spin-echo image (T_2WI): TR/TE, 4247 ms/93 ms; matrix size, 512 × 512; FOV, 24 cm × 24 cm; number of excitation, 1; slice thickness, 5 mm; gap, 1.5 mm. (3) sagittal T_2WI: TR/TE, 4338 ms/96 ms; matrix size, 384 × 384; FOV, 24 cm × 24 cm; number of excitation, 2; slice thickness, 5 mm; gap, 1.0 mm. (4) axial fluid-attenuated inversion recovery (FLAIR): TR/TE, 8000 ms/165 ms; matrix size, 256 × 256; FOV, 24 cm × 24 cm; number of excitation, 1; slice thickness, 5 mm; gap, 1.5 mm.

Amide proton transfer weighted imaging was performed prior to the injection of contrast agents. Single-section transverse APT_W image at the maximum area of the tumor was obtained with a single-shot echo planar imaging (EPI) sequence using the following parameters: TR/TE, 3000 ms/22.6 ms; matrix size, 128 × 128; FOV, 24 cm × 24 cm; section thickness, 8 mm. Saturation scheme included a total of 4 saturation pulses placed before the EPI readout. The parameters for saturation scheme were as the follows: Fermi-shape saturation pulse width is 500 ms, pulse amplitude 2.0 μT, saturation frequencies include 49 frequency points as well as 3 S_0 (without saturation pulses). The frequency points were 0, ±25, ±50, ±75, ±100, ±125, ±150, ±175, ±200, ±225, ±250, ±275, ±300, ±325, ±350, ±375, ±400, ±425, ±450, ±475, ±500, ±525, ±550, ±575, ±600 Hz. B_0 filed map demonstrating the local field shift in Hz was generated from APTw images at the frequency between 275 and −275 Hz.

Finally, contrast-enhanced T_1WI sequence was acquired in the transverse, sagittal, and coronal planes after intravenous administration of 0.1 mmol/kg gadodiamide (Omniscan; GE Healthcare, Co., Cork, Ireland).

After MRI acquisition, all raw data of APT_W images were transferred to the workstation (Advantage Workstation 4.6; GE Medical Systems) to generate the B_0 map and B_0 corrected magnetization transfer ratio asymmetry (MTR_{asym}) at 3.5 ppm parametric maps (Part 1 of **Figure 2**). The APT effect was quantified using MTR_{asym} at 3.5 ppm with respect to the water resonance using the following formula:

$$MTR_{asym} = [S(-3.5\ ppm) - S(+3.5\ ppm)] / S \text{ with pixel-by-pixel } B_0 \text{ correction}$$

Tumor Segmentation

All images were anonymized and stored in DICOM format. Two experienced neuroradiologists (L-FY and GX who have 7 and 5 years of experience, respectively, in neuro-oncology imaging) reviewed the conventional plain and contrast-enhanced MR images carefully to determine the margin of tumor. The APT raw data were imported into the ITK-SNAP software (version 3.6.0)[2] and the S_0 map of APT raw data were identified. The contour line of the ROI was drawn manually based on S_0 map while attempting to maintain an approximate distance of 2–3 mm from the tumor margin to minimize the partial volume effect. As shown in **Figure 3**, two-dimensional ROI including tumor, possible edema, cystic degeneration and necrosis was acquired for each patient.

Feature Extraction and Robustness Analysis

As depicted in Part 2 of **Figure 2**, using a non-commercial Analysis-Kit software (GE Healthcare, China), the method of quantitative feature extraction was conducted on MTR_{asym} (3.5 ppm) parametric maps. Forty-two first-order histogram, 983 s-order texture [432 gray level co-occurrence matrix (GLCM), 540 gray level run length matrix (GLRLM), and

[2]http://itk-snap.org

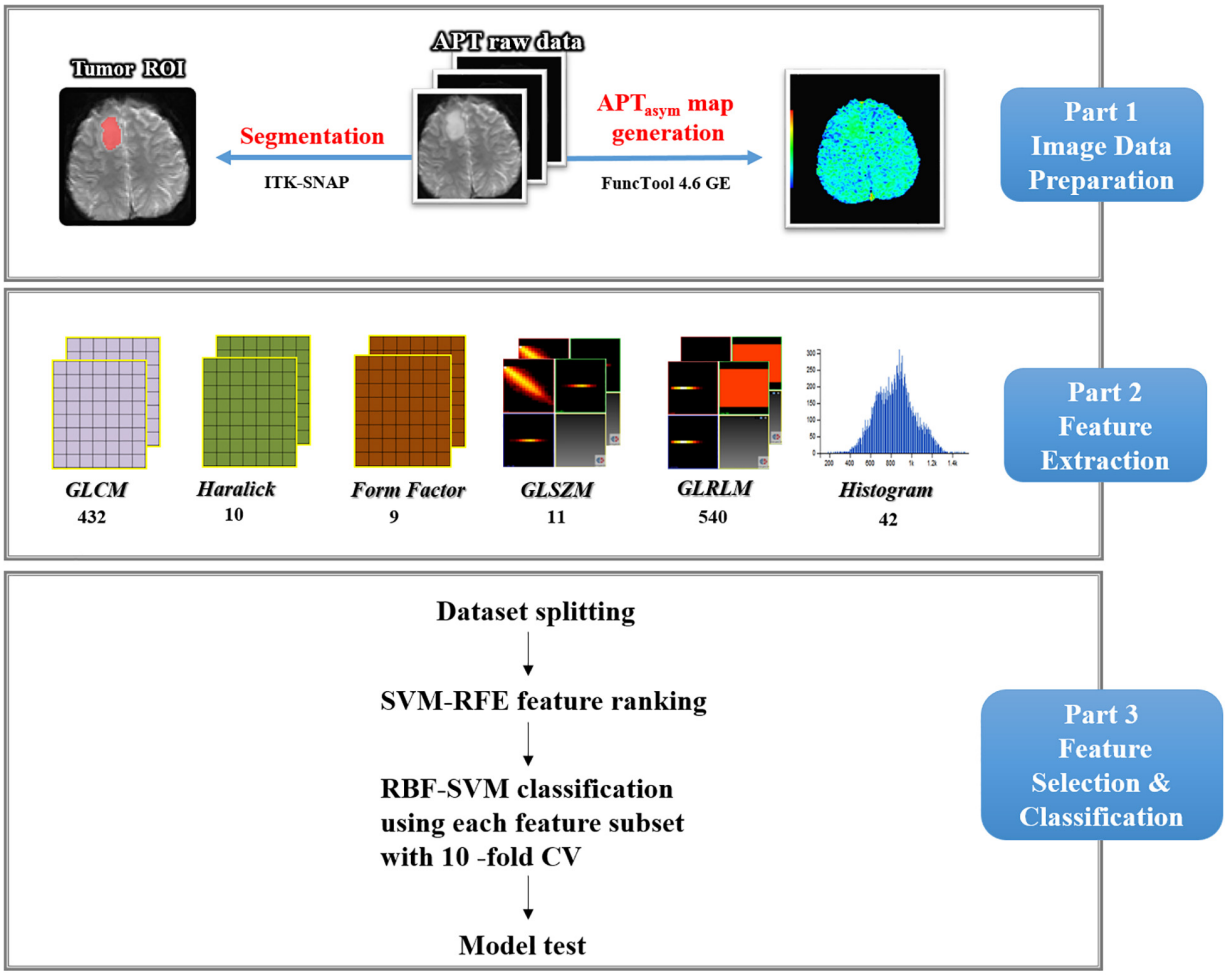

FIGURE 2 | Study flow chart. First, APT$_{asym}$ map was generated from APT raw data and ROI segmentation was done. Second, six types of texture features within ROIs were extracted by using Analysis-Kinetics software, including the histogram, form, GLCM, GLRLM, GLSZM, and Haralick features. At last, automatic glioma *IDH1* mutation classification using RBF-SVM combined with SVM-RFE feature selection and 10-fold cross-validation were carried out. Finally, model was tested by the pre-reserved test data.

11 gray level size zone matrix (GLSZM)], 9 form and 10 Haralick features were extracted from MTR$_{asym}$ (3.5 ppm) parametric maps. Thus, a total of 1044 quantitative features were obtained from the original images. Details regarding the quantitative features extracted in this study are presented in **Supplementary Appendix S1**.

As all the extracted data depend on the ROIs delineated by radiologists, the robustness of all the features was evaluated by both test-retest analysis and inter-rater analysis. For test-retest analysis, ROIs for each patient were segmented twice by one rater based on 20 randomly selected patients. Another 20 randomly selected patients were independently segmented by two raters for interrater analysis. The features extracted from these ROIs were assessed using the intraclass correlation coefficient (ICC).

Machine Learning Classification

As shown in Part 3 of **Figure 2**, the classification procedure included data grouping, data augmentation, feature selection, model building and model testing. First, the majority of patients' data from each group were randomly selected to train the model, i.e., 11 *IDH1* wild type and 38 *IDH1* mutation. To solve the potential impact of the imbalance dataset in the training cohort, a synthetic minority oversampling technique (SMOTE) was applied to solve this issue and its merit has also been confirmed in our previous study (Zhang et al., 2017). In this study, the number of *IDH1* wild-type patients in training data were augmented to that of *IDH1* mutation, i.e., 0.38. The synthetic cases would have features with values similar to the existing cases and were not merely replications, thus improving the representation of the minority group in the dataset. The data of five patients in each group were left out for testing without applying SMOTE.

Highly correlated or less effective features may lead to the overfitting issue as well as increase the computing burden. Thus, SVM-based recursive feature elimination (SVM-RFE) algorithm was applied to select the most effective features in the training set to prevent overfitting and improve model generalization. It is

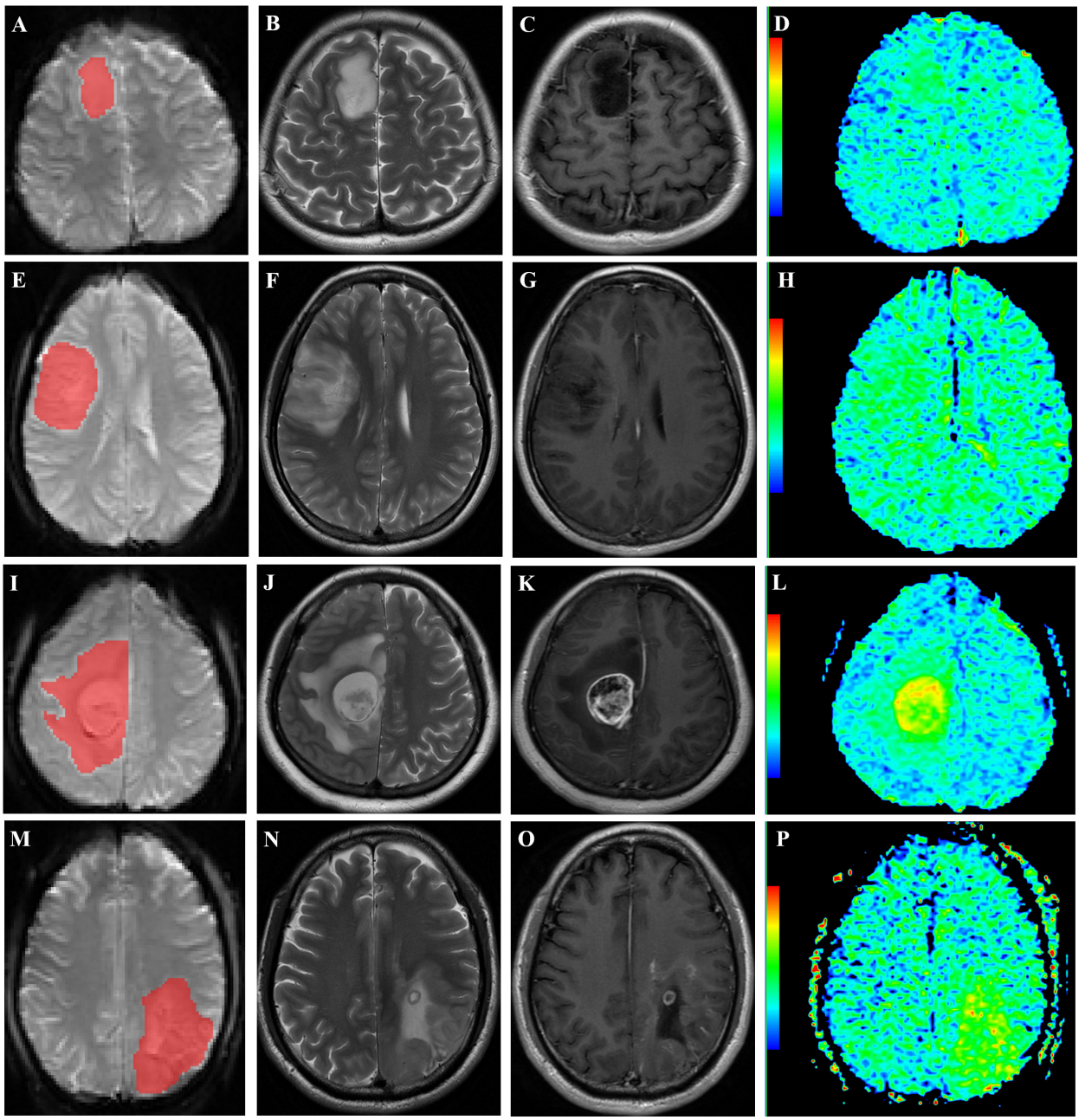

FIGURE 3 | Representative cases. **(A–D)**: a 36-year-old woman with WHO grade II diffuse astrocytoma with *IDH1* mutation in the right frontal lobe. ROI selection is based on S_0 map of APT raw data **(A)**. The lesion shows hyperintensity on axial T_2WI **(B)** and no enhancement on postcontrast T_1WI **(C)**. The APT_W image **(D)** exhibits increased signal intensity in the lesion. **E–H**: a 31-year-old woman with WHO grade II diffuse astrocytoma with *IDH1* wild type in the right frontal lobe. ROI selection is based on S_0 map of APT raw data **(E)**. The lesion shows heterogeneous hyperintensity on axial T_2WI **(F)** and no enhancement on postcontrast T_1WI **(G)**. The APT_W image **(H)** exhibits increased signal intensity in the lesion. **I–L**: a 31-year-old woman with anaplastic astrocytoma with *IDH1* mutation in the right frontal lobe. ROI selection is based on S_0 map of APT raw data **(I)**. The tumor and peritumoral edema shows hyperintensity on axial T_2WI **(J)** and heterogeneous enhancement of tumor on postcontrast T_1WI **(K)**. The APTw image **(L)** exhibits increased signal intensity in the tumor and peritumoral edema. **(M–P)**: a 45-year-old man with anaplastic oligodendroglioma with *IDH1* wild type in the left parietal lobe. ROI selection is based on S_0 map of APT raw data **(M)**. The tumor shows heterogeneous hyperintensity on axial T_2WI **(N)** and ring-like and strip-like enhancement within tumor on postcontrast T1WI **(O)**. The APTw image **(P)** exhibits increased signal intensity in the tumor.

able to rank the features according to their weight during N times iterations (N is the total number of extracted features). At each iteration, the feature with the minimal weight was eliminated, leading the feature ranking from the most to the least important one. Then, N feature subsets were established by selecting the first n features from the ranked sequence ($1 \leq n \leq N$). To compare the

performance of different feature subsets, each subset was input into SVM with radial basis function (RBF) kernel and tested with 10-fold cross-validation.

All the classifications were performed using Waikato Environment for Knowledge Analysis (WEKA, version 3.8.2). SVM constructs a hyperplane that provides the optimal separation boundary to maximize the separation of the objects in a high-dimensional space, and this approach is widely used because of its stability and favorable performance. In this feature space, a decision surface is created with different subspaces. Each subspace corresponds to one class of training data. Once the training is completed, the test data are mapped to the feature space. A class is then assigned to those data depending on which subspace they are mapped to. Before that, each feature was normalized into the range from 0 to 1. A RBF kernel maps the original data with the kernel function as $K(x) = \exp(gx - t^2)$, where x and t are two feature vectors, and gamma (g) controls the shape of the decision hyperplane. Loss function assesses the degree of inconsistency between the predicted and real values. The parameter g in the kernel function and epsilon in loss function were set to 1/3 (default value, 1/max_index) and 0.1, respectively. Probability estimation and shrinking heuristics were applied. The optimal feature subset would be got according to the classification performance. Then, the test data were put into the model built by using the optimal feature subset to test the performance of the final model.

The classification accuracy and AUC were measured in both training and test cohorts to evaluate the predictive efficiency of the radiomics model.

Histopathological Evaluation

Resected tumor tissues were processed using standard clinical techniques. *IDH1* R132H analysis was confirmed by immunohistochemistry and DNA sequencing as previously described (Yip et al., 2012; Agarwal et al., 2013). Paraffin sections of the intracranial tumor specimens were stained with *IDH1* R132H mutation-specific antibodies (1:50; H09 clone, Dianova). The *IDH* forward primer (5′-ACC AAA TGG CAC CAT ACG A-3′) and reverse primer (5′-GCA AAATCA CAT TAT TGC CAA C-3′) were designed to amplify exon 4 (codon R132) of the *IDH* gene.

Statistical Analysis

All statistical analyses were performed by using SPSS 20.0 software (IBM Corp, Chicago, IL, United States), WEKA software (WEKA version 3.8.2), and R software (version 3.3.2). All the extracted features in our study were assessed using ICC for both test-retest and inter-rater analyses. According to a previous study (Gevaert et al., 2014), features with ICC $\geq$ 0.6 were considered as robust against intra- and inter-rater uncertainties. The normal distribution of data was investigated with Kolmogorov-Smirnov (K-S) test. The between-group comparisons of quantitative data (age and quantitative features), categorical data (gender, cortical involvement, midline cross and location) were analyzed using independent sample *t*-test and chi-square test. Receiver operating characteristic (ROC) curve analysis was performed to determine the performance of single feature or radiomics model, and accuracy and area under the curve (AUC) were obtained. $P < 0.05$ indicated a significant difference.

RESULTS

Patients Characteristics and Feature Robustness

Among 59 patients enrolled in this study, 16 were *IDH1* wild-type (male, 11; female, 5; age range, 3–76 years), and the remained 43 were *IDH1* mutant (male, 25; female, 18; age range, 17–67 years). Age and radiomics features were normally distributed. Statistical results were summarized in **Table 1**. There were no significant differences in age, gender, midline cross and multi-lobe involvement between the two groups ($P > 0.05$), whereas *IDH1* mutant gliomas were mostly located in the frontal lobe and involving the cortex ($P < 0.05$).

Among 1044 radiomics features, the ICCs of 1038 features for both test-retest analysis (0.823-1) and interrater analysis (0.712-1) were greater than 0.6, thus were robust for further analysis.

Univariate Analyses for IDH1 Mutation Prediction

Significant differences were observed in 18 out of 1038 extracted quantitative features between the *IDH1* wild-type and mutant groups, including 8 first-order histograms, 6 GLCM and 4 GLRLM. The accuracies and AUC of these features were shown in **Table 2**. Among 18 features, *High Gray Level Run Emphasis All Direction offset 8 SD* achieved the highest AUC [0.769, 95% confidence interval (CI) 0.641–0.869] with the accuracy of 0.799.

TABLE 1 | Baseline demographics and clinical characteristics of patients.

	***IDH*-mutant**	***IDH* wild-type**	***P*-value**
Patients (*N*/%)	72.9% (43/59)	27.1% (16/59)	NA
Age (mean ± SD)	44.32 ± 10.68	40.18 ± 19.17	0.298
Gender (*N*/%)			0.333
Male	58.1% (25/43)	68.8% (11/16)	
Female	41.9% (18/43)	31.2% (5/16)	
Cortical involvement (*N*/%)	93.0% (40/43)	56.2% (9/16)	0.002
Cross the midline (*N*/%)	16.3% (7/43)	0 (0/16)	0.173
More than two lobes involved (*N*/%)	37.2% (16/43)	56.2% (9/16)	0.241
Location (*N*/%)			
Frontal lobe	76.7% (33/43)	43.8% (7/16)	0.027
Parietal lobe	4.7% (2/43)	12.5% (2/16)	0.295
Temporal lobe	9.3% (4/43)	18.7% (3/16)	0.375
Other locations	9.3% (4/43)	25% (4/16)	0.194
Histologic subtype (*N*/%)	Diffuse astrocytoma	Anaplastic astrocytoma	
	54% (20/37)	63.6% (14/22)	
	Oligodendroglioma	Anaplastic oligodendroglioma	NA
	46% (17/37)	36.4% (8/22)	

TABLE 2 | Diagnostic performance of univariate analyses in predicting *IDH1* mutation.

Parameter	Accuracy (%)	Sensitivity (%)	Specificity (%)	AUC (95% CI)	*P*-value
Histogram					
H1	74.5	76.7	68.7	0.702 (0.569–0.814)	0.015
H2	74.6	76.8	68.8	0.702 (0.586–0.827)	0.019
H3	74.6	74.4	75.0	0.734 (0.603–0.841)	0.003
H4	74.6	76.7	68.8	0.719 (0.587–0.829)	0.007
H5	74.6	72.1	81.2	0.734 (0.603–0.841)	0.004
H6	76.2	76.7	75.0	0.725 (0.594–0.833)	0.006
H7	74.5	76.7	68.7	0.711 (0.578–0.821)	0.011
H8	71.2	69.8	75.0	0.695 (0.561–0.808)	0.003
GLCM					
G1	59.3	51.2	81.3	0.696 (0.563–0.809)	0.012
G2	62.7	55.8	81.3	0.664 (0.529–0.782)	0.034
G3	69.1	69.1	68.8	0.710 (0.576–0.822)	0.006
G4	77.6	90.2	43.8	0.691 (0.555–0.807)	0.018
G5	71.3	72.5	54.6	0.687 (0.567–0.789)	0.043
G6	69.0	69.1	68.8	0.710 (0.576–0.822)	0.006
GLRLM					
R1	66.1	60.5	81.2	0.670 (0.535–0.787)	0.033
R2	66.1	65.1	68.7	0.667 (0.532–0.784)	0.033
R3	67.8	67.4	68.7	0.712 (0.580–0.823)	0.005
R4	79.9	88.7	56.3	0.769 (0.641–0.869)	<0.001

H1, RMS; H2, percentile 70; H3, percentile 75; H4, percentile 80; H5, percentile 85; H6, percentile 90; H7, percentile 95; H8, quantile 0.975; G1, correlation all direction offset 2 SD; G2, correlation angle 45 offset 4; G3, cluster shade angle 45 offset 7; G4, cluster prominence angle 45 offset 7; G5, cluster shade all direction offset 8 SD; G6, inverse difference moment angle 135 offset 6; R1, long run high gray level emphasis angle 135 offset 1; R2, short run emphasis all direction offset6; R3, long run emphasis all direction offset 6; R4, high gray level run emphasis all direction offset 8 SD.

Machine-Learning for Predicting IDH1 Mutation

Based on the *IDH1* mutation status, 1038 robust features extracted from APT_W images were employed to construct the machine-learning model. Nineteen features were selected to be the optimal feature subset for *IDH1* mutation prediction using SVM-RFE. **Figure 4** illustrates the feature selection process. With the participation of new twenty ranked features sequentially, the overall tendencies of classification accuracy first declined and gradually increased. The peak of curve was achieved by using the top-20 feature subset. For the top-20 features, classification accuracy was evaluated again with inclusion of each ranked feature one by one. The best performance was achieved by using the top-19 feature subset, which was determined as the optimal feature subset.

Afterward, the independent test data were used to test the final solution in order to confirm the actual classification power. The test accuracy and AUC of the model were 0.70 and 0.84, respectively.

Optimal Feature Subset Analysis

As described above, 19 out of the 1038 features were selected to be the optimal feature subset to establish *IDH1* mutation prediction model. It can be observed that GLCM features ($n = 13$) accounted for a high proportion, and the rest ($n = 6$) were GLRLM features. Detailed descriptions of the 19 features are listed in **Table 3**. The ROC and the heat maps of feature correlations before and after feature selection were shown in **Figure 5**. The machine-learning model achieved better discriminative ability to predict *IDH1* mutation, with the ACC and AUC of 0.892 and 0.952, respectively (**Figure 5A**). As further demonstrated in **Figure 5B**, before feature selection, there was mass redundant information among the 1038 features, which appeared as the high correlation coefficients ranging from −1 (blue) to 1 (red). After feature selection, 19 optimal features had a relatively low correlation and high effectiveness, as shown in **Figure 5C**.

The contributing weight and correlation coefficient between each feature and the classification class of the optimal feature subset were shown in **Figure 6**. It is obvious that the corresponding trend of the blue and orange bars of each feature does not match, which indicates that the performance of an individual feature does not determine its contribution to the optimal feature subset. That is to say the feature subset does not necessarily require that each feature to be very powerful, but the complementarity between features can help the subset achieve the best results. Therefore, to simply combine several individual parameters with higher classification performance may not achieve enough good results.

DISCUSSION

In this study, the histogram and high-order features were extracted from APT_W images. Both univariate and radiomics analyses were performed to compare the efficacies in predicting *IDH1* mutation. Our SVM model achieved an AUC of 0.952 and 0.84 in the training set and test set, respectively. Notably, the efficacy achieved by SVM model was superior to that of univariate analysis.

Jiang et al. (2017) first confirmed the ability of APT_W images in identifying the *IDH1* mutation status. Based on their study, *IDH* wild-type gliomas were associated with relatively high APT_W signal intensities as compared with *IDH*-mutant ones. Similarly, our univariate analysis revealed that 8 out of 18 determinant variables were histogram features. Among these histogram features, the higher AUCs (0.734) were achieved by using the 75th and 85th percentile APT_W values. However, different from their study, the best diagnostic performance was achieved by using *High Gray Level Run Emphasis All Direction offset 8 SD* with AUC of 0.769. Furthermore, the highest AUC of 0.952 was achieved by using radiomics model. The following factors may contribute to the differences: (1) different study population; only WHO grade II gliomas with relatively small sample size were enrolled in their study. In light of the 2016 WHO classification, the anaplasia and mitotic activity in WHO grade II from III gliomas may result in inter-observer variability. Furthermore, clinical outcome differences of grade II/III gliomas rely far more on molecular subtypes than on grading, suggesting that molecular parameters may in fact be a better tool in identifying subgroups with distinct prognosis. Consequently, in

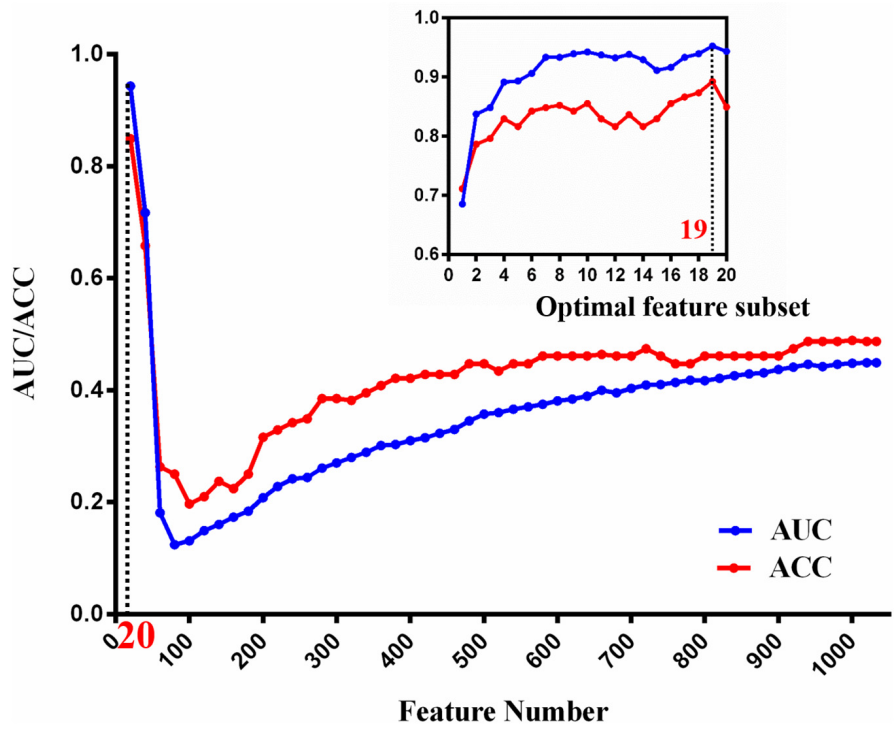

FIGURE 4 | The tendency of classification AUC and ACC value during optimal attribute determination of machine-learning model. The horizontal axis is the attribute number and the vertical axis is the AUC/ACC value. The local classification performance at peak point is magnified to view on the top right corner.

accordance with cancer genome archive (TCGA), we merged WHO grade II/III gliomas as "lower grade glioma"; (2) different ROI strategy; in their study, both whole tumor histogram-based and multi-ROI-based analyses were adopted. The best AUC of 0.89 was achieved by multi-ROI-based maximal APTw value. Though suitable for application in clinical practice, the hot-spot ROI analysis might limit the reproducibility of the results. (3) different order feature and statistical methodology; conventional univariate analysis based on first-order features (maximum, minimum and other histogram features) were used in their study. In our study, apart from histogram features, higher order features were extracted. Moreover, radiomics analyses were performed for feature selection and classifier modeling.

Our study expands the current scarce but promising evidence on the diagnostic ability of APT_W images to predict *IDH1* mutation. Both univariate and radiomics analyses were performed. The efficacy achieved by radiomics analysis was superior to that with univariate analysis. The promising results may be partially attributed to two reasons: (1) Compared to first-order texture features based on histograms of the original image, higher order features provided spatial information among pixels and may better reflect the tumor heterogeneity (Hu et al., 2015); (2) Machine learning method enabled the integration of quantitative textural image features to build a model to predict *IDH1* mutation. Especially, the SVM classifier is considered to be a robust and effective machine-learning approach that has been predominately used in the fields of neuroimaging and molecular biology.

TABLE 3 | The optimal radiomic features selected by the SVM-RFE method.

Gray level co-occurrence matrix (GLCM) (*n* = 13)	Gray level run-length matrix (GLRLM) (*n* = 6)
Correlation all direction offset4 SD; GLCM Entropy angle45 offset2; Inertia all direction offset3; Haralick Correlation angle45 offset1; Inverse difference moment angle0 offset5; Inertia angle0 offset2; Cluster prominence all direction offset1 SD; Inverse difference moment angle135 offset1; GLCM Energy angle135 offset3; Correlation angle0 offset1; Inverse difference moment angle135 offset9; Inverse difference moment all direction offset7 SD; Correlation angle135 offset5; Cluster prominence angle135 offset2	Run length non-uniformity angle0 offset1; Low gray level run emphasis angle90 offset3; Long run low gray level emphasis angle45 offset6; Long run low gray level emphasis all direction offset5; Run length non-uniformity all direction offset5; High gray level run emphasis angle0 offset8

In addition, the promising prediction performance partly benefited from the feature selection procedure (to decrease the redundancy between features and the risk of model overfitting) by identifying a set of the most contributing features. Here, in the optimal feature subset for *IDH1* mutation prediction, most of the selected features were GLCM and GLRLM, which partly benefited from their high proportion in raw feature sets. However, it is worth noting that selected GLCM and GLRLM represent voxel-based change of grayscale and could reflect the complexity and heterogeneity of the

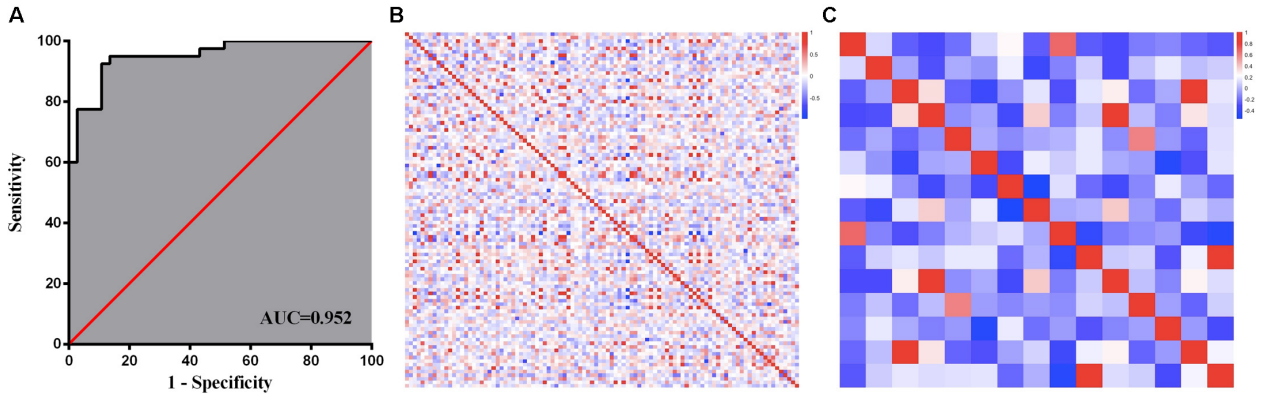

FIGURE 5 | Feature selection and analysis. ROC curve of machine-learning model **(A)**; Heat maps of feature correlation analysis before **(B)** and after **(C)** feature selection.

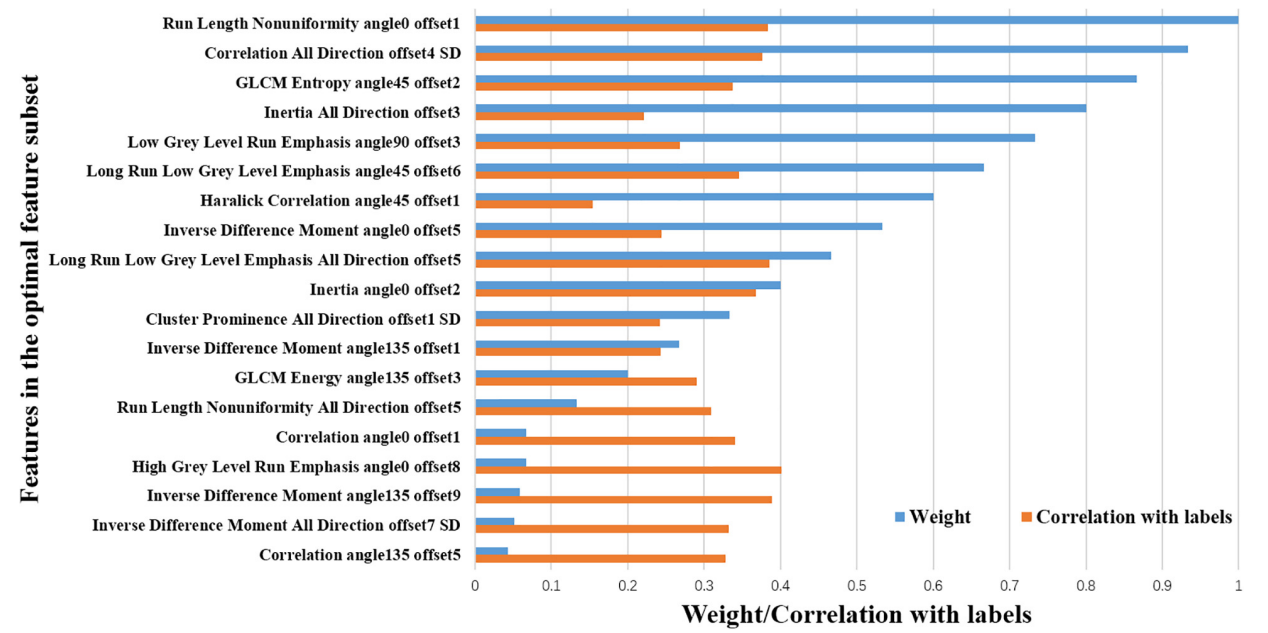

FIGURE 6 | Analysis of the optimal feature subset of machine-learning model. The blue bars represent the contribution weights of the optimal feature subset of machine-learning model. The orange bars represent the correlation coefficient for features and the classification class.

tumor. Although the underlying biological mechanism for how these features relate to *IDH1* mutation status is presently unclear, our findings is in accordance with previous studies (Choi et al., 2016; Liu et al., 2018; Zhang et al., 2018). Besides, the results suggested that the feature subset does not necessarily require that each feature be very powerful, but the complementarity between features can help the subset achieve the best results.

There are several limitations in this study. First, our sample size was relatively small, especially for the *IDH1* wild-type group due to the inherent *IDH1* mutation distribution ratio in the general population. The results presented here require confirmation in a larger study. Second, only two-dimensional ROIs at each representative slice were delineated for feature extraction. Third, we did not thoroughly reveal the biological process behind the selected texture feature. Lastly, multi-model MRI data should be integrated into our model to improve efficiency of *IDH1* mutation prediction.

CONCLUSION

In conclusion, the current study revealed that radiomic features derived from APT_W images are associated with *IDH1* mutation status in grade II/III gliomas. Using texture analysis and SVM, a machine learning model was established and the *IDH1* mutation status was predicted effectively. Our findings indicate that quantitative radiomics analysis based on APT_W images can

potentially provide a non-invasive methodology for mutation status detection.

DATA AVAILABILITY STATEMENT

The datasets generated for this study are available on request to the corresponding author.

ETHICS STATEMENT

The studies involving human participants were reviewed and approved by the Ethics Committee of Tangdu Hospital. Written informed consent to participate in this study was provided by the participants' legal guardian/next of kin.

AUTHOR CONTRIBUTIONS

G-BC, L-FY, YH, and WW contributed to the conception and design of the study and drafting the work. YY, GX, Y-ZS, QT, and JZ contributed to the acquisition, analysis and interpretation of the data, and drafting and revision the work. All authors gave the final approval and agreement to all the aspects of the work.

FUNDING

This study received financial support from the National Key Research and Development Program of China (No. 2016YFC0107105) to G-BC, the Young Talent Foundation of Tangdu Hospital to WW, the Key Industrial Chain Projects in the Field of Social Development of Shaanxi Province (No. 2019ZDLSF02-07) to G-BC, and the General Projects in the Field of Social Development of Shaanxi Province (No. 2019SF-002) to L-FY.

ACKNOWLEDGMENTS

We would like to thank Dr. Xiao-Cheng Wei from GE Healthcare for providing technical support regarding the appropriate amide proton transfer weighted imaging and data analysis.

SUPPLEMENTARY MATERIAL

The Supplementary Material for this article can be found online at: https://www.frontiersin.org/articles/10.3389/fnins.2020.00144/full#supplementary-material

REFERENCES

Agarwal, S., Sharma, M. C., Jha, P., Pathak, P., Suri, V., Sarkar, C., et al. (2013). Comparative study of IDH1 mutations in gliomas by immunohistochemistry and DNA sequencing. *Neurol. Oncol.* 15, 718–726. doi: 10.1093/neuonc/not015

Andronesi, O. C., Kim, G. S., Gerstner, E., Batchelor, T., Tzika, A. A., Fantin, V. R., et al. (2012). Detection of 2-hydroxyglutarate in IDH-mutated glioma patients by in vivo spectral-editing and 2D correlation magnetic resonance spectroscopy. *Sci. Transl. Med.* 4:116ra114. doi: 10.1126/scitranslmed.3002693

Arita, H., Kinoshita, M., Kawaguchi, A., Takahashi, M., Narita, Y., Terakawa, Y., et al. (2018). Lesion location implemented magnetic resonance imaging radiomics for predicting IDH and TERT promoter mutations in grade II/III gliomas. *Sci. Rep.* 8:11773. doi: 10.1038/s41598-018-30273-4

Choi, C., Ganji, S. K., DeBerardinis, R. J., Hatanpaa, K. J., Rakheja, D., Kovacs, Z., et al. (2012). 2-hydroxyglutarate detection by magnetic resonance spectroscopy in IDH-mutated patients with gliomas. *Nat. Med.* 18, 624–629. doi: 10.1038/nm.2682

Choi, E. R., Lee, H. Y., Jeong, J. Y., Choi, Y. L., Kim, J., Bae, J., et al. (2016). Quantitative image variables reflect the intratumoral pathologic heterogeneity of lung adenocarcinoma. *Oncotarget* 7, 67302–67313. doi: 10.18632/oncotarget.11693

Daumas-Duport, C., Scheithauer, B., O'Fallon, J., and Kelly, P. (1988). Grading of astrocytomas. A simple and reproducible method. *Cancer* 62, 2152–2165. doi: 10.1002/1097-0142(19881115)62:10<2152::aid-cncr2820621015>3.0.co;2-t

de la Fuente, M. I., Young, R. J., Rubel, J., Rosenblum, M., Tisnado, J., Briggs, S., et al. (2016). Integration of 2-hydroxyglutarate-proton magnetic resonance spectroscopy into clinical practice for disease monitoring in isocitrate dehydrogenase-mutant glioma. *Neurol. Oncol.* 18, 283–290. doi: 10.1093/neuonc/nov307

Doll, S., Urisman, A., Oses-Prieto, J. A., Arnott, D., and Burlingame, A. L. (2017). Quantitative proteomics reveals fundamental regulatory differences in oncogenic HRAS and isocitrate dehydrogenase (IDH1) driven astrocytoma. *Mol. Cell Proteom.* 16, 39–56. doi: 10.1074/mcp.M116.063883

Fuller, G. N., and Scheithauer, B. W. (2007). The 2007 revised world health organization (WHO) classification of tumours of the central nervous system: newly codified entities. *Brain Pathol.* 17, 304–307. doi: 10.1111/j.1750-3639.2007.00084.x

Gevaert, O., Mitchell, L. A., Achrol, A. S., Xu, J., Echegaray, S., Steinberg, G. K., et al. (2014). Glioblastoma multiforme: exploratory radiogenomic analysis by using quantitative image features. *Radiology* 273, 168–174. doi: 10.1148/radiol.14131731

Gillies, R. J., Kinahan, P. E., and Hricak, H. (2016). Radiomics: images are more than pictures. They are data. *Radiology* 278, 563–577. doi: 10.1148/radiol.2015151169

Hartmann, C., Meyer, J., Balss, J., Capper, D., Mueller, W., Christians, A., et al. (2009). Type and frequency of IDH1 and IDH2 mutations are related to astrocytic and oligodendroglial differentiation and age: a study of 1,010 diffuse gliomas. *Acta Neuropathol.* 118, 469–474. doi: 10.1007/s00401-009-0561-9

Hu, L. S., Ning, S., Eschbacher, J. M., Gaw, N., Dueck, A. C., Smith, K. A., et al. (2015). Multi-parametric MRI and texture analysis to visualize spatial histologic heterogeneity and tumor extent in glioblastoma. *PLoS One* 10:e0141506. doi: 10.1371/journal.pone.0141506

Jiang, S., Yu, H., Wang, X., Lu, S., Li, Y., Feng, L., et al. (2016). Molecular MRI differentiation between primary central nervous system lymphomas and high-grade gliomas using endogenous protein-based amide proton transfer MR imaging at 3 Tesla. *Eur. Radiol.* 26, 64–71. doi: 10.1007/s00330-015-3805-1

Jiang, S., Zou, T., Eberhart, C. G., Villalobos, M. A. V., Heo, H. Y., Zhang, Y., et al. (2017). Predicting *IDH* mutation status in grade II gliomas using amide proton transfer-weighted (APTw) MRI. *Magn. Reson. Med.* 78, 1100–1109. doi: 10.1002/mrm.26820

Jiang, T., Mao, Y., Ma, W., Mao, Q., You, Y., Yang, X., et al. (2016). CGCG clinical practice guidelines for the management of adult diffuse gliomas. *Cancer Lett.* 375, 263–273. doi: 10.1016/j.canlet.2016.01.024

Kotrotsou, A., Zinn, P. O., and Colen, R. R. (2016). Radiomics in brain tumors: an emerging technique for characterization of tumor environment. *Magn. Reson. Imaging Clin. N. Am.* 24, 719–729. doi: 10.1016/j.mric.2016.06.006

Li, Y., Liu, X., Qian, Z., Sun, Z., Xu, K., Wang, K., et al. (2018). Genotype prediction of ATRX mutation in lower-grade gliomas using an MRI radiomics signature. *Eur. Radiol.* 28, 2960–2968. doi: 10.1007/s00330-017-5267-0

Liu, S., Zheng, H., Zhang, Y., Chen, L., Guan, W., Guan, Y., et al. (2018). Whole-volume apparent diffusion coefficient-based entropy parameters for assessment

of gastric cancer aggressiveness. *J. Magn. Reson. Imaging* 47, 168–175. doi: 10.1002/jmri.25752

Louis, D. N., Perry, A., Reifenberger, G., von Deimling, A., Figarella-Branger, D., Cavenee, W. K., et al. (2016). The 2016 world health organization classification of tumors of the central nervous system: a summary. *Acta Neuropathol.* 131, 803–820. doi: 10.1007/s00401-016-1545-1

Olar, A., Wani, K. M., Alfaro-Munoz, K. D., Heathcock, L. E., van Thuijl, H. F., Gilbert, M. R., et al. (2015). IDH mutation status and role of WHO grade and mitotic index in overall survival in grade II-III diffuse gliomas. *Acta Neuropathol.* 129, 585–596. doi: 10.1007/s00401-015-1398-z

Pope, W. B., Prins, R. M., Albert Thomas, M., Nagarajan, R., Yen, K. E., Bittinger, M. A., et al. (2012). Non-invasive detection of 2-hydroxyglutarate and other metabolites in IDH1 mutant glioma patients using magnetic resonance spectroscopy. *J. Neurooncol.* 107, 197–205. doi: 10.1007/s11060-011-0737-8

Prasanna, P., Patel, J., Partovi, S., Madabhushi, A., and Tiwari, P. (2017). Radiomic features from the peritumoral brain parenchyma on treatment-naive multi-parametric MR imaging predict long versus short-term survival in glioblastoma multiforme: preliminary findings. *Eur. Radiol.* 27, 4188–4197. doi: 10.1007/s00330-016-4637-3

Reitman, Z. J., Jin, G., Karoly, E. D., Spasojevic, I., Yang, J., Kinzler, K. W., et al. (2011). Profiling the effects of isocitrate dehydrogenase 1 and 2 mutations on the cellular metabolome. *Proc. Natl. Acad. Sci. U.S.A.* 108, 3270–3275. doi: 10.1073/pnas.1019393108

Reuss, D. E., Mamatjan, Y., Schrimpf, D., Capper, D., Hovestadt, V., Kratz, A., et al. (2015). IDH mutant diffuse and anaplastic astrocytomas have similar age at presentation and little difference in survival: a grading problem for WHO. *Acta Neuropathol.* 129, 867–873. doi: 10.1007/s00401-015-1438-8

Rohle, D., Popovici-Muller, J., Palaskas, N., Turcan, S., Grommes, C., Campos, C., et al. (2013). An inhibitor of mutant IDH1 delays growth and promotes differentiation of glioma cells. *Science* 340, 626–630. doi: 10.1126/science.1236062

Sagiyama, K., Mashimo, T., Togao, O., Vemireddy, V., Hatanpaa, K. J., Maher, E. A., et al. (2014). In vivo chemical exchange saturation transfer imaging allows early detection of a therapeutic response in glioblastoma. *Proc. Natl. Acad. Sci. U.S.A.* 111, 4542–4547. doi: 10.1073/pnas.1323855111

Sanson, M., Marie, Y., Paris, S., Idbaih, A., Laffaire, J., Ducray, F., et al. (2009). Isocitrate dehydrogenase 1 codon 132 mutation is an important prognostic biomarker in gliomas. *J. Clin. Oncol.* 27, 4150–4154. doi: 10.1200/JCO.2009.21.9832

Shofty, B., Artzi, M., Ben Bashat, D., Liberman, G., Haim, O., Kashanian, A., et al. (2018). MRI radiomics analysis of molecular alterations in low-grade gliomas. *Int. J. Comput. Assist. Radiol. Surg.* 13, 563–571. doi: 10.1007/s11548-017-1691-5

Suh, C. H., Kim, H. S., Jung, S. C., Choi, C. G., and Kim, S. J. (2018). Imaging prediction of isocitrate dehydrogenase (IDH) mutation in patients with glioma: a systemic review and meta-analysis. *Eur. Radiol.* 20, 1573–1583. doi: 10.1007/s00330-018-5608-7

Togao, O., Yoshiura, T., Keupp, J., Hiwatashi, A., Yamashita, K., Kikuchi, K., et al. (2014). Amide proton transfer imaging of adult diffuse gliomas: correlation with histopathological grades. *Neurol. Oncol.* 16, 441–448. doi: 10.1093/neuonc/not158

van den Bent, M. J. (2010). Interobserver variation of the histopathological diagnosis in clinical trials on glioma: a clinician's perspective. *Acta Neuropathol.* 120, 297–304. doi: 10.1007/s00401-010-0725-7

van den Bent, M. J., Dubbink, H. J., Marie, Y., Brandes, A. A., Taphoorn, M. J., Wesseling, P., et al. (2010). IDH1 and IDH2 mutations are prognostic but not predictive for outcome in anaplastic oligodendroglial tumors: a report of the european organization for research and treatment of cancer brain tumor group. *Clin. Cancer Res.* 16, 1597–1604. doi: 10.1158/1078-0432.CCR-09-2902

Yan, H., Parsons, D. W., Jin, G., McLendon, R., Rasheed, B. A., Yuan, W., et al. (2009). IDH1 and IDH2 mutations in gliomas. *N. Engl. J. Med.* 360, 765–773. doi: 10.1056/NEJMoa0808710

Yang, H., Ye, D., Guan, K. L., and Xiong, Y. (2012). IDH1 and IDH2 mutations in tumorigenesis: mechanistic insights and clinical perspectives. *Clin. Cancer Res.* 18, 5562–5571. doi: 10.1158/1078-0432.CCR-12-1773

Yip, S., Butterfield, Y. S., Morozova, O., Chittaranjan, S., Blough, M. D., An, J., et al. (2012). Concurrent CIC mutations, IDH mutations, and 1p/19q loss distinguish oligodendrogliomas from other cancers. *J. Pathol.* 226, 7–16. doi: 10.1002/path.2995

Yu, H., Lou, H., Zou, T., Wang, X., Jiang, S., Huang, Z., et al. (2017). Applying protein-based amide proton transfer MR imaging to distinguish solitary brain metastases from glioblastoma. *Eur. Radiol.* 27, 4516–4524. doi: 10.1007/s00330-017-4867-z

Zhang, X., Tian, Q., Wang, L., Liu, Y., Li, B., Liang, Z., et al. (2018). Radiomics strategy for molecular subtype stratification of lower-grade glioma: detecting IDH and TP53 mutations based on multimodal MRI. *J. Magn. Reson. Imaging.* 48, 916–926. doi: 10.1002/jmri.25960

Zhang, X., Yan, L. F., Hu, Y. C., Li, G., Yang, Y., Han, Y., et al. (2017). Optimizing a machine learning based glioma grading system using multi-parametric MRI histogram and texture features. *Oncotarget* 8, 47816–47830. doi: 10.18632/oncotarget.18001

Zhou, J., Lal, B., Wilson, D. A., Laterra, J., and van Zijl, P. C. (2003). Amide proton transfer (APT) contrast for imaging of brain tumors. *Magn. Reson. Med.* 50, 1120–1126. doi: 10.1002/mrm.10651

Conflict of Interest: The authors declare that the research was conducted in the absence of any commercial or financial relationships that could be construed as a potential conflict of interest.

Copyright © 2020 Han, Wang, Yang, Sun, Xiao, Tian, Zhang, Cui and Yan. This is an open-access article distributed under the terms of the Creative Commons Attribution License (CC BY). The use, distribution or reproduction in other forums is permitted, provided the original author(s) and the copyright owner(s) are credited and that the original publication in this journal is cited, in accordance with accepted academic practice. No use, distribution or reproduction is permitted which does not comply with these terms.

frontiers in Neuroscience

ORIGINAL RESEARCH
published: 16 April 2020
doi: 10.3389/fnins.2020.00323

Pushing the Limits of EEG: Estimation of Large-Scale Functional Brain Networks and Their Dynamics Validated by Simultaneous fMRI

*Rodolfo Abreu[1], Marco Simões[1,2] and Miguel Castelo-Branco[1]**

[1] Faculty of Medicine, Coimbra Institute for Biomedical Imaging and Translational Research (CIBIT), Institute for Nuclear Sciences Applied to Health (ICNAS), University of Coimbra, Coimbra, Portugal, [2] Center for Informatics and Systems (CISUC), University of Coimbra, Coimbra, Portugal

OPEN ACCESS

Edited by:
Pedro Antonio Valdes-Sosa, Clinical Hospital of Chengdu Brain Science Institute, China

Reviewed by:
Sepideh Sadaghiani, University of Illinois at Urbana–Champaign, United States
Andrew P. Bagshaw, University of Birmingham, United Kingdom

***Correspondence:**
Miguel Castelo-Branco
mcbranco@fmed.uc.pt

Specialty section:
This article was submitted to Brain Imaging Methods, a section of the journal Frontiers in Neuroscience

Received: *19 November 2019*
Accepted: *19 March 2020*
Published: *16 April 2020*

Citation:
Abreu R, Simões M and Castelo-Branco M (2020) Pushing the Limits of EEG: Estimation of Large-Scale Functional Brain Networks and Their Dynamics Validated by Simultaneous fMRI. Front. Neurosci. 14:323. doi: 10.3389/fnins.2020.00323

Functional magnetic resonance imaging (fMRI) is the technique of choice for detecting large-scale functional brain networks and to investigate their dynamics. Because fMRI measures brain activity indirectly, electroencephalography (EEG) has been recently considered a feasible tool for detecting such networks, particularly the resting-state networks (RSNs). However, a truly unbiased validation of such claims is still missing, which can only be accomplished by using simultaneously acquired EEG and fMRI data, due to the spontaneous nature of the activity underlying the RSNs. Additionally, EEG is still poorly explored for the purpose of mapping task-specific networks, and no studies so far have been focused on investigating networks' dynamic functional connectivity (dFC) with EEG. Here, we started by validating RSNs derived from the continuous reconstruction of EEG sources by directly comparing them with those derived from simultaneous fMRI data of 10 healthy participants, and obtaining an average overlap (quantified by the Dice coefficient) of 0.4. We also showed the ability of EEG to map the facial expressions processing network (FEPN), highlighting regions near the posterior superior temporal sulcus, where the FEPN is anchored. Then, we measured the dFC using EEG for the first time in this context, estimated dFC brain states using dictionary learning, and compared such states with those obtained from the fMRI. We found a statistically significant match between fMRI and EEG dFC states, and determined the existence of two matched dFC states which contribution over time was associated with the brain activity at the FEPN, showing that the dynamics of FEPN can be captured by both fMRI and EEG. Our results push the limits of EEG toward being used as a brain imaging tool, while supporting the growing literature on EEG correlates of (dynamic) functional connectivity measured with fMRI, and providing novel insights into the coupling mechanisms underlying the two imaging techniques.

Keywords: simultaneous EEG-fMRI, large-scale functional brain networks, dynamic functional connectivity (dFNC), electrical source imaging (ESI), task-based fMRI, resting-state functional network connectivity (rs-FNC)

INTRODUCTION

A large-scale functional brain network is defined as a subset of interconnected, possibly distant, brain regions that interact with each other in order to perform a plethora of tasks of different levels of complexity (Bressler and Menon, 2010). The identification of such networks led to pivotal findings regarding brain function in healthy humans (van den Heuvel and Hulshoff Pol, 2010), and by discriminating changes in some properties of those networks due to disease, a better understanding of their pathophysiology was possible (Du et al., 2018). Because of its remarkable spatial resolution and whole-brain coverage, functional magnetic resonance imaging (fMRI) is currently the imaging technique of choice to measure the connectivity strength (or functional connectivity, FC) between brain regions, and consequently reconstruct such functional networks with a few millimeter resolution, despite its modest temporal resolution in the order of seconds (van den Heuvel and Hulshoff Pol, 2010; Lee et al., 2013). While task-based fMRI studies have allowed to map the brain regions that specifically respond to the task of interest (Barch et al., 2013), several large-scale functional networks can be found in the normal brain during rest – the so-called resting-state networks (RSNs) – which exhibit temporally correlated spontaneous fluctuations in the blood-oxygen-level-dependent (BOLD) signal (Biswal et al., 1995; Smith et al., 2009). RSNs are typically identified by decomposing the fMRI data using spatial independent component analysis (sICA), under the hypothesis that the resulting independent components (including the RSNs) are statistically independent in space (Beckmann et al., 2005).

Importantly, RSNs are also identified under the assumption that their functional connectivity is static; however, current literature suggests that brain networks in general continuously reorganize in response to both internal and external stimuli at multiple time-scales, resulting in temporal fluctuations of their FC – the so-called dynamic functional connectivity (dFC) (Hutchison et al., 2013; Calhoun et al., 2014; Preti et al., 2017). Specifically, it has been shown that dFC correlates with brain state (stimulation/task, eyes closure vs. eyes open, vigilance, sleep, anesthesia, and drug manipulation) as well as with age, gender and disease [for a review, please refer to Thompson (2018)]. dFC correlates of disease are believed to be particularly relevant for its characterization, and recent studies have demonstrated that dFC discriminates healthy from patient populations better than static FC (Du et al., 2018). Under the assumption that brain function dynamics can be described by a limited number of states (Preti et al., 2017), a significant number of studies have dedicated to the identification of such brain states from the dFC, by applying pattern recognition techniques, particularly clustering (Allen et al., 2014), principal component analysis (Leonardi et al., 2013), and dictionary learning (Leonardi et al., 2014; Abreu et al., 2019).

Despite the undoubted insights that the study of brain networks' (dynamic) functional connectivity with fMRI has provided so far, this imaging technique is only capable of indirectly measuring brain activity/connectivity, delayed by the hemodynamic response (Logothetis et al., 2001). In contrast, magnetoencephalography (MEG) and electroencephalography (EEG) measure the activity of large populations of neurons directly, and because of their high temporal resolution at the sub-millisecond scale, they represent in principle ideal approaches to study brain functional connectivity (Niedermeyer and Lopes Da Silva, 2005). Whole-brain FC studies using MEG or EEG, however, require the challenging procedure of reconstructing the sources responsible for generating the signals measured at the scalp (Mantini et al., 2011; Michel and Murray, 2012). Due to continuous technological advances, a reliable reconstruction of MEG and EEG is now possible, opening the pathway for the study of large-scale FC with high temporal resolution. In fact, RSNs typically identified with fMRI were first replicated on MEG (Brookes et al., 2011; Mantini et al., 2011), and more recently on EEG (Liu et al., 2017, 2018), by first performing continuous electrical source imaging (cESI), which reconstructs their underlying sources over time (Vulliemoz et al., 2010a; Michel and Murray, 2012), and then applying sICA to the resulting dataset. This suggests that temporally coherent fluctuations across distant brain regions can also be captured with MEG and EEG. Motivated by its portability, low cost and ease of use (Niedermeyer and Lopes Da Silva, 2005), and more importantly, the possibility of combining it with other imaging modalities, particularly fMRI (Abreu et al., 2018), EEG is frequently preferred over MEG.

Because reconstructing EEG sources involves a complex pipeline (Michel et al., 2004; Michel and Murray, 2012), a recent study has systematically investigated the impact of the several processing steps on the accurate identification of RSNs with EEG during rest (Liu et al., 2018). However, the ground truth considered was based on RSNs derived from separately acquired fMRI data; additionally, the feasibility of using EEG data to map task-specific brain networks has been poorly explored, and the estimation of dFC and the associated brain states with EEG is yet to be investigated. Because RSNs have been shown to be also present in task-based fMRI studies (Di et al., 2013; Cole et al., 2016), in this paper we start by validating in a truly unbiased manner the results from Liu et al. (2017, 2018) by identifying RSNs on fMRI and EEG data acquired simultaneously from 10 healthy participants performing a neurofeedback (NF) task. Next, we mapped the target region of the NF (the facial expressions processing network, FEPN) with fMRI and EEG, and compared the resulting networks. Finally, we estimated dFC brain states also from fMRI and EEG, and determined into which extent these techniques match.

MATERIALS AND METHODS

Participants

Ten healthy participants (mean age: 26 ± 3 years; 9 males) performed a simultaneous EEG-fMRI NF session. All participants had normal or corrected-to-normal vision, and no history of neurological disorders. The study was approved by the Ethics Commission of the Faculty of Medicine of the University of Coimbra and was conducted in accordance with the declaration of Helsinki. All subjects provided written informed consent to participate in the study.

Experimental Protocol

The session was performed at the Portuguese Brain Imaging Network (Coimbra, Portugal) and consisted of four simultaneous EEG-fMRI runs: first, a functional localizer specifically developed to identify the FEPN (anchored on the posterior Superior Temporal Sulcus region; pSTS), followed by three NF runs (of alternated up and down regulation). The first two NF runs used either visual or auditory feedback (random order) and the third had no feedback presented to the participant. The participants were given a mental strategy to follow during the NF runs, but were instructed to adapt it to maximize the modulation outcomes presented by the feedback.

For the localizer run, 8 s blocks of dynamic facial expressions (happy, sad or alternated between happy and sad expressions) morphed into the face of a realistic human virtual character are contrasted with 8 s blocks consisting of the same face with a static neutral expression, or motion blocks of moving dots. This rigorous contrast is able to identify regions that respond to the dynamic aspects of the facial expressions but not to the face itself or the movement aspects of the stimuli (Direito et al., 2019). The NF runs consist of 24 s blocks of alternated up and down regulation of the activity extracted in real-time from the pSTS region identified in the localizer run. For the first two NF runs, the participants were presented with visual feedback (materialized in the intensity level of the facial expression displayed by the virtual avatar) or auditory feedback (consisting of high and low pitch beep sounds, corresponding to increasing or decreasing the amplitude of the BOLD signal in the pSTS region, respectively). A detailed description of the protocol can be found in the **Supplementary Material**, and in our previous paper (Direito et al., 2019), where we assessed the neuroscientific aspects of the fMRI NF sessions.

EEG-fMRI Data Acquisition

Imaging was performed on a 3T Siemens Magnetom Trio MRI scanner (Siemens, Erlangen) using a 12-channel RF receive coil. The functional images were acquired using a 2D multi-slice gradient-echo echo-planar imaging (GE-EPI) sequence, with the following parameters: TR/TE = 2000/30 ms, voxel size = 4.0 mm × 4.0 mm × 3.0 mm, 33 axial slices, FOV = 256 mm × 256 mm, FA = 90°, yielding a total coverage of the occipital and posterior temporal lobe. The start of each trial was synchronized with the acquisition of the functional images. A T_1-weighted, magnetization-prepared rapid acquisition gradient-echo (MPRAGE) sequence was used for the acquisition of structural data (1 mm isotropic, 176 slices, TR/TE = 2530/3.42 ms), allowing for the subsequent co-registration of the functional data. For each participant, 160 fMRI volumes were acquired during the localizer run, yielding approximately 5.33 min of duration; the remaining three functional (NF) runs consisted of 300 volumes (10 min).

The EEG signal was recorded using the MR-compatible 64-channel NeuroScan SynAmps2 system and the Maglink software, with a cap containing 64 Ag/AgCl non-magnetic electrodes positioned according to the 10/10 coordinate system, a dedicated electrode for referencing placed close to the Cz position, and two electrodes placed on the chest for electrocardiogram (EKG) recording. EEG, EKG, and fMRI data were acquired simultaneously in a continuous way, and synchronized by means of a Syncbox (NordicNeuroLab, United States) device. EEG and EKG signals were recorded at a sampling rate of 10 kHz. No filters were applied during the recordings. The helium cooling system was not turned off, as it may carry the associated risk of helium boil-off in certain systems (Mullinger et al., 2008), and thus is not permitted in some clinical sites as the one used in this study.

Outside the MR scanner and prior to the beginning of the experiment, each subject was submitted to an EEG-only acquisition while performing the localizer stimulation experiment. These data were used to check the quality of the EEG recorded inside the MR scanner, after the removal of gradient switching and pulse artifacts.

All the procedures described next were coded in MATLAB, and are available together with all data upon request.

Data Pre-processing

Electroencephalography (EEG)

Removal of EEG artifacts

EEG data underwent gradient artifact correction on a volume-wise basis using a standard artifact template subtraction (AAS) approach (Allen et al., 2000). Then, bad epochs of 2 s (corresponding to one TR) were manually identified and removed from the EEG signal; these were selected based on EEG segments of abnormally high amplitude and/or frequency, or whenever the gradient artifact correction algorithm failed to remove the artifact, typically in the beginning and ending of the recordings. Bad channels were visually inspected and interpolated. For the removal of the pulse artifact, the method presented in Abreu et al. (2016) was employed, whereby the EEG data are first decomposed using independent component analysis (ICA), followed by AAS to remove the artifact occurrences from the independent components (ICs) associated with the artifact. The corrected EEG data are then obtained by reconstructing the signal using the artifact-corrected ICs together with the original non-artifact-related ICs. Finally, the EEG data were down-sampled to 250 Hz and band-pass filtered to 1–45 Hz. For the purpose of removing the pulse artifact from the EEG, and the physiological noise from the fMRI (described below), the Pan-Tompkins algorithm (Pan and Tompkins, 1985) was optimized and used for the detection of R peaks on the EKG data (Abreu et al., 2017).

Continuous EEG source imaging

The pre-processed EEG data were then submitted to an EEG source imaging (ESI) procedure. Specifically, the so-called continuous ESI was performed, with the purpose of estimating the temporal variations of the EEG sources responsible for generating the electrical potential distributions measured at the scalp with a high temporal resolution. A realistic head model was built by first segmenting each subject's structural image into 12 tissue classes (skin, eyes, muscle, fat, spongy bone, compact bone, cortical gray matter, cerebellar gray matter, cortical white matter, cerebellar white matter, cerebrospinal fluid, and brain stem), each with a specific electrical conductivity [depicted in

Supplementary Table S1; from Liu et al. (2017)]. Because this is not feasible using the currently available tools (which allow segmentation up to six tissues), a state-of-the-art brain tissue model was used (MIDA, available online; Iacono et al., 2015), and co-registered into the structural image using FSL's tool FNIRT (Jenkinson and Smith, 2001; Jenkinson et al., 2002). The transformed MIDA model onto the structural image of each participant was then visually inspected for assessing the quality of the registration step. The electrode positions were co-registered to the skin compartment by first considering their standard positions, and then manually adjusting them to match the distortions clearly observed on the structural images. Finally, the SimBio finite element model (FEM; Wolters et al., 2004) algorithm implemented in FieldTrip (Oostenveld et al., 2011) was then used for numerically approximating the volume conduction model (the number of FEM elements in each tissue compartment is depicted in **Supplementary Table S1**). The source dipoles were placed on a 4-mm 3D grid only spanning the cortical gray matter, followed by the estimation of the leadfield matrix, which maps each possible dipole configuration onto a scalp potential distribution (the forward problem). The inverse problem was solved through a distributed inversion solution approach using the exact low resolution brain electromagnetic tomography (eLORETA; Pascual-Marqui et al., 2011) algorithm, which estimates the strength j of each dipole on the source grid at the x (j_x), y (j_y), and z (j_z) directions. For each EEG time sample t, the overall strength of a dipole was computed as:

$$p(t) = \sqrt{j_x^2(t) + j_y^2(t) + j_z^2(t)} \quad (1)$$

This was computed for all dipoles and time samples, yielding a 4D (3D $\times$ t) dataset (EEG-ESI). The time-series of dipole strength was then downsampled to 1 Hz. These processing steps were selected based on previous studies that comprehensively investigated their impact on detecting RSNs from EEG-ESI data, concluding that this was the optimal processing pipeline (Liu et al., 2017, 2018).

Functional Magnetic Resonance Imaging (fMRI)

The first 10 s of data were discarded to allow the BOLD-fMRI signal to reach steady-state, and non-brain tissue was removed using FSL's tool BET (Smith, 2002). Subsequently, slice timing and motion correction were performed using FSL's tool MCFLIRT (Jenkinson et al., 2002). Then, a high-pass temporal filtering with a cut-off period of 100 s was applied, and spatial smoothing using a Gaussian kernel with full width at half-maximum (FWHM) of 5 mm was performed. Physiological noise was removed by linear regression using the following regressors (Abreu et al., 2017): (1) quasi-periodic BOLD fluctuations related to cardiac cycles were modeled by a fourth order Fourier series using RETROICOR (Glover et al., 2000); (2) aperiodic BOLD fluctuations associated with changes in the heart rate were modeled by convolution with the respective impulse response function [as described in Chang et al. (2009)]; (3) the average BOLD fluctuations in white matter (WM) and cerebrospinal fluid (CSF); (4) the six motion parameters estimated by MCFLIRT; and (5) scan nulling regressors (motion scrubbing) associated with volumes acquired during periods of large head motion (12 $\pm$ 7 scrubbed volumes, averaged across runs and subjects); these were determined using the FSL's utility *fsl_motion_outliers*, whereby the DVARS metric proposed in Power et al. (2012) is first computed, and then thresholded at the 75th percentile plus 1.5 times the inter-quartile range. Because the respiratory traces were not recorded, the associated physiological fluctuations in the BOLD signal were not removed. Finally, volumes corresponding to bad epochs identified on the EEG were removed.

For each participant, WM and CSF masks were obtained from the respective T_1-weighted structural image by segmentation into gray matter, WM and CSF using FSL's tool FAST (Zhang et al., 2001). The functional images were co-registered with the respective T_1-weighted structural images using FSL's tool FLIRT, and subsequently with the Montreal Neurological Institute (MNI) (Collins et al., 1994) template, using FSL's tool FNIRT (Jenkinson and Smith, 2001; Jenkinson et al., 2002). Both WM and CSF masks were transformed into functional space and were then eroded using a 3 mm spherical kernel in order to minimize partial volume effects (Jo et al., 2010). Additionally, the eroded CSF mask was intersected with a mask of the large ventricles from the MNI space, following the rationale described in Chang and Glover (2009).

Data Analysis

In this section, the several data analyses performed on both fMRI and EEG-ESI for the identification of RSNs, the FEPN and the dFC brain states are described. Except when stated otherwise, the same procedures were applied to the fMRI and EEG-ESI data.

Identification of Resting-State Networks (RSNs)

ICA decomposition

Following the approach described in Liu et al. (2017, 2018), the pre-processed fMRI and EEG-ESI data were submitted to a group-level probabilistic spatial ICA (sICA) decomposition using the FSL's tool MELODIC (Beckmann and Smith, 2004), whereby the data of all participants for each run are temporally concatenated prior to the sICA step, as recommended in the MELODIC's guide for the identification of RSNs[1]. The optimal number of independent components (ICs) was automatically estimated for the fMRI data based on the eigenspectrum of its covariance matrix (Beckmann and Smith, 2004), with an average of approximately 40 ICs across runs. Because the dimensionality estimation algorithm in MELODIC is tailored for fMRI data, and for consistency purposes, the EEG-ESI data were also decomposed into 40 ICs. Nonetheless, when applying this algorithm to the EEG-ESI data, a similar number of ICs was estimated, differing no more than five ICs across runs with relation to those estimated from the fMRI data.

Automatic identification of RSNs

An automatic procedure for the identification of well-known RSNs was then applied, in which the spatial maps of the ICs (thresholded at Z = 3.0) were compared with those of the 10 RSN templates described in Smith et al. (2009), in terms of

[1]https://fsl.fmrib.ox.ac.uk/fsl/fslwiki/MELODIC

spatial overlap computed as the Dice coefficient (Dice, 1945). For each template, the IC map yielding the highest Dice coefficient was determined as the corresponding RSN. In the cases of non-mutually exclusive assignments, the optimal assignment was determined by randomizing the order of the RSN templates (up to a maximum of 10,000 possible combinations were considered, for computational purposes), and then sequentially, and mutually exclusively, assigning them to the IC maps based on their Dice coefficient. The assignment with the highest average Dice coefficient across all RSN templates was then deemed optimal, yielding the final set of RSNs: three visual networks (RSN 1–3), the default mode network (DMN and RSN4), a cerebellum network (RSN5), a motor network (RSN6), an auditory network (RSN7), the salience network (RSN8), a right language network (RSN9), and a left language network (RSN10). Although the RSN templates serve as an independent validation of the RSNs, the Dice coefficient between fMRI and EEG-ESI RSNs was also computed, thus allowing to directly compare our results with the current literature (Liu et al., 2017, 2018).

Statistical validation

In order to statistically validate the abovementioned spatial overlaps, a null model based on the concept of commonly used permutation tests was defined. Specifically, since it was hypothesized that 10 RSNs could be unequivocally identified among the 40 fMRI and EEG-ESI ICs (based on their substantially higher overlap with RSN templates when compared with other ICs unrelated with RSNs), the null model was obtained from the Dice coefficients computed for all the possible combinations of RSN templates and fMRI/EEG-ESI ICs (a total of 40 [ICs] × 10 [RSNs] = 400 values). In this way, for each run, null distributions of Dice coefficients were defined for: (1) the overlap between RSN templates and fMRI ICs; (2) the overlap between RSN templates and EEG-ESI ICs; and (3) the overlap between fMRI and EEG-ESI ICs. By computing their associated 95th percentile, a statistical threshold was then determined for each analysis, against which the average Dice coefficients across RSNs were tested (values in **Table 1**).

Mapping of the Facial Expressions Processing Network

For the purpose of mapping the regions in the FEPN, a general linear model (GLM) framework was used on both fMRI and EEG-ESI data. Although uncommon, the rationale of also using a GLM to analyze EEG data followed that of previous studies (Custo et al., 2014; Gonçalves et al., 2014), including the LIMO EEG toolbox which was specifically designed under this framework (Pernet et al., 2011). For the localizer run of each participant, a GLM comprising five regressors was built (one for each condition; described in section "Experimental Protocol"), based on unit boxcar functions with ones during the respective condition to be modeled, and zeros elsewhere. While this GLM was used directly to model the activity of the FEPN on the EEG-ESI data since no hemodynamic delay is expected, for the fMRI data, the regressors were convolved with a canonical, double-gamma hemodynamic response function (HRF) to account for such delay (Friston et al., 1995). The respective GLMs were then fitted to the pre-processed fMRI and the EEG-ESI data using the FSL's improved linear model (FILM) (Woolrich et al., 2001), and voxels exhibiting significant signal changes when contrasting the facial expression conditions with the neutral and motion conditions (balanced) were identified by cluster thresholding (voxel $Z > 2.7$, cluster $p < 0.05$). Group activation maps were then obtained using the FSL's Local Analysis of Mixed Effects (FLAME) (Beckmann et al., 2003).

Dynamic Functional Connectivity Analysis

Estimation of dFC

For each run, the dFC was estimated between $R = 90$ non-overlapping regions of interest (ROIs) of the cerebrum according to the automated anatomical labeling (AAL) atlas (Tzourio-Mazoyer et al., 2002). These ROIs were co-registered from the MNI space into the participant's functional space, and the EEG-ESI and the pre-processed fMRI data were then averaged within each ROI. Regarding the latter, the resulting BOLD signals were low-pass filtered with a cutoff frequency of 0.1 Hz, because synchronized BOLD fluctuations of neuronal origin mainly occur within this frequency range (Biswal et al., 1995; Cordes et al., 2001). No filtering was applied to the parcel-averaged EEG-ESI signals.

The dFC was estimated by means of a sliding window correlation approach using a window length of 42 s (21 TRs) with a step of 6 s (3 TRs) for the fMRI data, and a window length of 40 s (40 time points) with a step of 5 s (5 time points) for the EEG-ESI data. Such window lengths were selected based on a recent meta-analysis revealing that physiologically meaningful, and statistically validated dFC fluctuations can be detected on the fMRI when using a window length between 30 and 60 s (Preti et al., 2017). Additionally, our previous study focused on the detection of epileptic dFC states from simultaneous EEG-fMRI data also showed the ability to detect epileptic dFC states irrespective of the window length within the abovementioned interval (Abreu et al., 2019). With this combination of parameters, comparable properties are expected to be captured on fMRI and EEG-ESI dFC data, while guaranteeing that all points at the end of the dFC data are considered when building the respective last sliding windows. The pairwise Pearson correlation coefficient was computed for all pairs of ROI-averaged BOLD-fMRI and EEG-ESI signals for each sliding window. The final dFC matrix was obtained by extracting the upper triangular part of each correlation matrix, vectorising it and subtracting the static FC for each participant (average across all participant-specific windows), yielding a matrix $\mathbf{C}_\mathrm{p} = [\mathbf{c}_1, \ldots, \mathbf{c}_\mathrm{T}] \in \mathbb{R}^{\mathrm{M}\times\mathrm{T}}$, where $M = (R^2 - R)/2$ with R denoting the number of ROIs and T the number of windows. The group matrix $\mathbf{C}$ was obtained by concatenating in time the vectorised, static FC-subtracted $\mathbf{C}_\mathrm{p}$ matrices of each participant.

Identification of dFC brain states

In our previous study, we comprehensively compared the performance of several methods (including the most commonly used k-means clustering and principal component analysis) with distinct degrees of sparsity in time, at identifying dFC states associated with epilepsy (Abreu et al., 2019). We found that an l_1-norm regularized dictionary learning (DL) approach yielded the best results. The proposed approach can be formulated as the

TABLE 1 | Dice coefficients between the fMRI and EEG RSNs and RSN templates from Smith et al. (2009), and between the RSNs derived from fMRI and EEG-ESI data, for each run separately.

Functional runs	fMRI RSNs vs. RSN templates		EEG RSNs vs. RSN templates		fMRI RSNs vs. EEG RSNs	
	d_{max}	$\bar{d}$	d_{max}	$\bar{d}$	d_{max}	$\bar{d}$
Auditory feedback	0.7	0.5	0.6	0.4	0.5	0.4
Visual feedback	0.7	0.5	0.6	0.4	0.5	0.3
Transfer run	0.7	0.5	0.6	0.4	0.5	0.4
Localizer	0.6	0.5	0.5	0.4	0.7	0.4

matrix factorization problem $\mathbf{C}= \mathbf{DA}$, where $\mathbf{D} = [\mathbf{d}_1, \ldots, \mathbf{d}_k] \in \mathbb{R}^{M\times k}$, and $\mathbf{A} = [\mathbf{a}_1, \ldots, \mathbf{a}_T] \in \mathbb{R}^{k\times T}$ represent the correlation matrices and associated weight time-courses of each dFC state, respectively; and k is the number of dFC states. These are estimated by solving the optimization problem given by:

$$\arg\min_{\mathbf{D},\mathbf{A}} \|\mathbf{C} - \mathbf{DA}\|_F \quad (2)$$

so that the reconstruction error of $\mathbf{C}$, $E = \|\mathbf{C} - \mathbf{DA}\|_F^2$, is minimized; $\|\cdot\|_F$ denotes the Frobenius norm of a matrix. The estimation of $\mathbf{D}$ and $\mathbf{A}$ was performed using the algorithms implemented in the MATLAB toolbox SPArse Modeling Software (SPAMS, Mairal et al., 2010). The sparsity of the solutions was controlled by a non-negative parameter λ on an l_1-norm regularization framework. The optimal k and λ were determined using a 5–5-fold nested cross-validation (Meir-Hasson et al., 2014), whereby the external 5-fold cross-validation divided the data into train and test sets. For each train set (or external fold), an additional inner 5-fold cross-validation was used, from which a set of optimal k and λ was determined for each external fold by minimizing the Bayesian information criterion (BIC); this metric penalizes model complexity, thus favoring a more parsimonious estimation of dFC states. The most recurrent set of optimal k and λ across the external folds was then identified, characterizing the final dictionary learning model. k was varied between 5 and 10, in steps of one; and λ was varied across ten values from 1 to 0.1259, in decreasing exponential steps.

Matching of EEG-ESI and fMRI dFC brain states

In contrast with the identification of RSNs, whereby templates derived from previous fMRI studies of large populations are available, dFC state templates are yet to be discovered, as this is still a fairly recent research topic (Preti et al., 2017; Thompson, 2018). Thus, the dFC states estimated from the EEG-ESI data can only be cross, rather than independently, validated by the dFC states estimated from the fMRI data. Because the optimal number of dFC states was $k = 10$ for all runs and for both fMRI and EEG-ESI data (although varying the optimal regularization parameter: $\lambda = 1$ for the fMRI, the sparsest solution, and $\lambda = 0.25$ for the EEG-ESI, corresponding to a solution of intermediate sparsity), a one-to-one match between the dFC states from both datasets was determined by computing the pairwise spatial correlation between the associated correlation matrices $\mathbf{D}$, and identifying the dFC state pairs with the highest, and statistically significant correlation ($p < 0.05$, corrected for multiple comparisons using the Bonferroni correction). Similarly to the assignment procedure of RSNs, in cases of non-mutually exclusive pairs of dFC states, the optimal match was determined by randomizing the order of the fMRI dFC states, and then sequentially, and mutually exclusively, matching them to the EEG-ESI dFC states based on their spatial correlation. The match with the highest average spatial correlation across all ten dFC states was then deemed optimal.

Since dFC states are also characterized by weight time-courses $\mathbf{A}$ representing their contribution to the overall dFC over time, the Pearson correlation between each dFC state time-course and the contrast defined for mapping the FEPN was computed (for the localizer run), in order to verify which, if any, of the fMRI or EEG-ESI dFC states were associated with the expected brain activity at the FEPN.

Validation analyses

Because of the lack of an independent validation as the one available for the RSN analyses by the template maps, additional statistical tests were then performed here. First, the statistical significance of the dFC states estimated from both fMRI and EEG-ESI data recorded on each run was assessed by building a data-driven null distribution, following the work described in Leonardi et al. (2013) and Abreu et al. (2019). Specifically, for each run, the fMRI and EEG-ESI $\mathbf{C}$ matrices were first FFT transformed and, for each connectivity pair, a random, uniformly distributed, phase was added; the inverse FFT was then applied to transform the data back to the time domain. The null distribution consisted of estimating $\mathbf{D}$ from the phase-randomized $\mathbf{C}$ matrices using the optimal parameters k and λ, computing the reconstruction error $E(i)=\|\mathbf{C}\text{-}\mathbf{d}_i\mathbf{a}_i\|_F^2$ of each dictionary $\mathbf{d}_i$ with weight $\mathbf{a}_i$ ($i = 1, \ldots, k$), and repeating this procedure 10,000 times. dFC states estimated from the true data with a reconstruction error (calculated as above) below the fifth percentile of the null distribution in E were deemed meaningful.

Next, in order to validate the matching of fMRI and EEG-ESI dFC states, the dFC states estimated from the phase-randomized fMRI data were spatially correlated with the dFC states estimated from the true EEG-ESI data, and their statistical significance investigated.

Finally, in order to assess the impact of the window length, we repeated the procedures described above (estimation of dFC brain states and their matching across modalities, and the respective statistical validation) with three different values of the window length within the adequate interval suggested in Preti et al. (2017): 30, 50, and 60 s, corresponding to 15/30, 25/50, and 30/60 time points for the fMRI and EEG-ESI data, respectively.

RESULTS

Identification of RSNs

We started by validating the results from Liu et al. (2017, 2018) in a truly unbiased manner by identifying RSNs on the fMRI and EEG data recorded simultaneously using spatial ICA, and comparing them with the respective templates from Smith et al. (2009); these results are shown in **Figure 1** (for the auditory and visual feedback runs, and the transfer run) and **Figure 2** (for the localizer run). The selected ICs and the RSN templates show a substantial overlap for all RSNs and imaging techniques, although slightly higher when considering the RSNs identified on the fMRI data, as expected and quantified by the Dice coefficient (values shown in **Figure 3**, for all possible combinations of fMRI/EEG-ESI ICs and RSN templates, and for all runs). The maximum ($d_{\max}$) and average ($\bar{d}$) Dice coefficients between fMRI and EEG-ESI RSNs and the RSN templates are depicted in **Table 1**. Despite the comparable Dice coefficients between the two imaging techniques, with an average of 0.5 and 0.4 for the fMRI and EEG-ESI data across all runs, respectively, it should be noted that RSNs 3 (visual), 6 (motor), and 7 (auditory) were only partially represented on the respective EEG-ESI ICs on all runs, typically including only one of the hemispheres. Additionally, it was not possible to recover RSN 5 (cerebellum) with either fMRI or EEG-ESI data likely because of the limited spatial coverage of this brain region. Noteworthy, however, is the remarkable overall consistency of the RSNs identified on both fMRI and EEG-ESI data across the four runs. The Dice coefficient between the fMRI and EEG-ESI RSNs is also shown in **Table 1**, with the average values across runs ranging from 0.3 to 0.4, and the maximum values ranging from 0.5 to 0.7. All these values were statistically significant, as they were above the 95th percentile of their respective null distribution.

Mapping of the FEPN

Next, we mapped the FEPN using a GLM framework on both the fMRI and EEG-ESI data; the group activation maps of all participants is also shown in **Figure 2** (bottom). Similarly to what was observed on RSNs 3, 6, and 7, a unilateral (right hemisphere) activation was observed when analyzing the EEG-ESI data, in contrast with the bilateral activation found on the fMRI data. Nonetheless, both maps notably overlap in the left pre-central gyrus. At the posterior superior temporal sulcus (pSTS, visible in the sagittal slices), activations on both fMRI and EEG-ESI were observed, although the latter were found to be located more posteriorly in pSTS, as expected, relatively to the former. Although only present in the EEG-ESI data, frontal activations were also observed.

Estimation of dFC Brain States

Finally, we estimated dFC states from both fMRI and EEG-ESI data using an l_1-norm regularized dictionary learning approach, and identified the optimal match between them. Importantly, all fMRI and EEG-ESI dFC states from all runs survived the statistical validation with phase-randomized data, supporting their physiological meaning. The fMRI dFC states and their matched EEG-ESI dFC states are shown in **Figure 4**, for all runs. Although it may not be visually clear, a match was obtained between fMRI and EEG-ESI dFC states, quantified by the spatial correlation across the matched dFC states (values shown in **Figure 5**, for all possible combinations of fMRI and EEG-ESI dFC states, and for all runs). Specifically, the maximum and average spatial correlations ($s_{\max}$ and $\bar{s}$, respectively) between matched dFC states were $s_{\max} = 0.4$, $\bar{s} = 0.2$ for both the localizer and transfer runs, and $s_{\max} = 0.5$, $\bar{s} = 0.3$ and $s_{\max} = 0.6$, $\bar{s} = 0.3$ for the auditory and visual feedback runs, respectively. This match was validated by statistically assessing the spatial correlation between dFC states estimated from phase-randomized fMRI data, and dFC states estimated from true EEG-ESI data. For all runs, we observed that dFC states did not match in any of the 10,000 randomizations performed, as no statistically significant spatial correlations ($p > 0.05$, corrected for multiple comparisons using the Bonferroni correction) were found between any possible pairs of states, and thus supporting the statistical validity of our findings. Importantly, the spatial correlation values were not substantially affected by the window length, despite a small decrease for larger (>50 s) window lengths; these are shown in **Supplementary Table S2**. For the additional window lengths and all runs, the estimated dFC states and their match between the fMRI and EEG-ESI also survived the respective statistical tests.

When analyzing the correlation between the weight time-courses of all dFC states and the contrast defined for mapping the FEPN on the localizer run, two fMRI and two EEG-ESI dFC states were found to exhibit a significant ($p < 0.05$, corrected for multiple comparisons using the Bonferroni correction) correlation r: states #2 ($r = 0.22$) and #7 ($r = 0.17$) for the fMRI data, and states #4 ($r = 0.14$) and #9 ($r = 0.19$) for the EEG-ESI data; the results are shown in **Figure 5**, at the bottom. Interestingly, fMRI state #2 is also matched with EEG-ESI state #9 in terms of their spatial correlation, highlighting the consistency of this finding for the localizer run.

DISCUSSION

Here we comprehensively investigated the extent at which EEG can be used as a tool to identify large-scale functional networks, which are typically detected on fMRI. Importantly, this is the first study to do so in a truly unbiased manner, by comparing the results obtained from fMRI and EEG data acquired simultaneously. Moreover, we investigated for the first time the feasibility of mapping task-specific brain networks, and of estimating the dFC and associated dFC states, with EEG in such conditions.

EEG and Resting-State Networks

Although the detection of RSNs with EEG was not reported until recently, EEG signatures of RSNs derived from simultaneously acquired fMRI data have already been reported, namely the EEG spectral power averaged across the five well-known EEG rhythms (Goldman et al., 2002; Moosmann et al., 2003; Laufs et al., 2006; Scheeringa et al., 2008). By including the associated time-courses in a regression analysis of BOLD signals representative

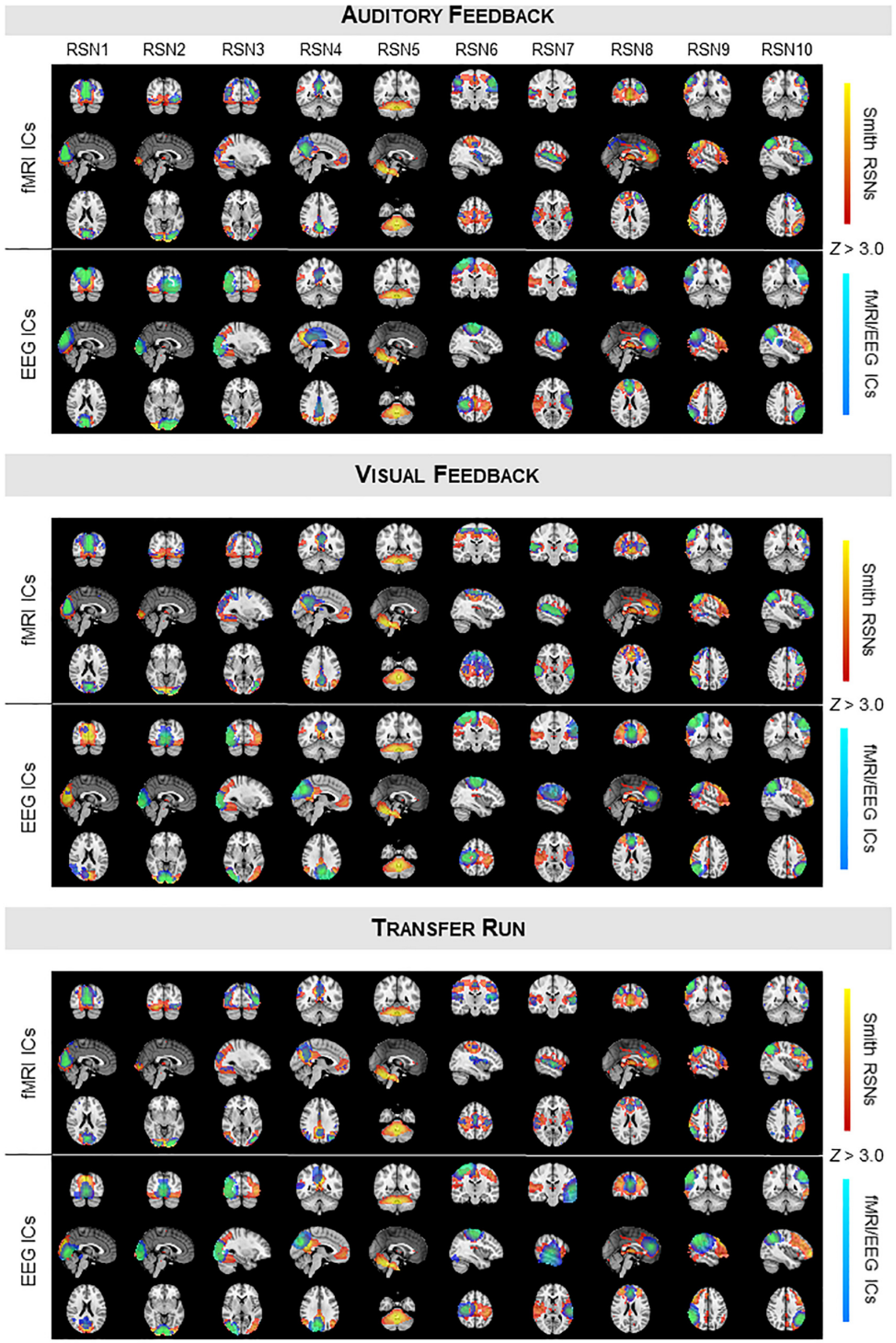

FIGURE 1 | Group RSNs identified on fMRI and EEG-ESI data for the auditory feedback **(top)**, visual feedback **(middle)**, and transfer runs **(bottom)**. For each run, the RSN templates (in red–yellow) from Smith et al. (2009) are superimposed with the fMRI **(top)** and EEG **(middle)** ICs (in blue–light blue) selected for each RSN template, according to their Dice coefficient.

of the RSNs, the contribution of each EEG rhythm, and its interaction with the remaining rhythms, was found to be specific for each RSN (Mantini et al., 2007; de Munck et al., 2009). Because resting-state EEG is also known to exhibit spontaneous fluctuations that can be described by a limited number of scalp topographies of electrical potentials that remain stable for

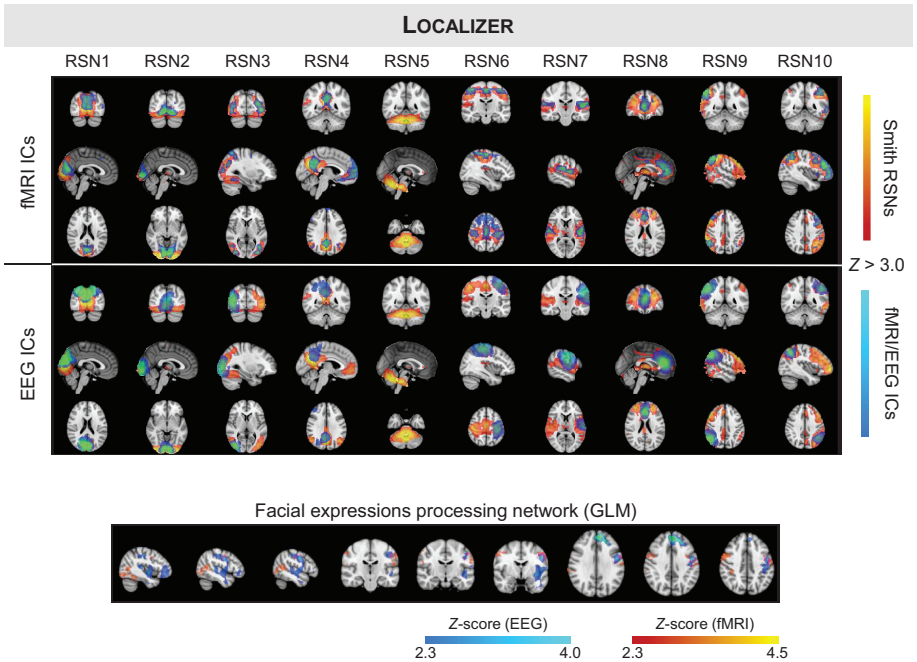

FIGURE 2 | Same as in **Figure 1**, but showing the group RSNs identified on fMRI and EEG-ESI data for the localizer run. The group activation maps of the task-specific facial expressions processing network using fMRI (in red–yellow) and EEG (in blue–light blue) are also shown at the bottom, with the overlapping regions highlighted in pink.

short (∼100 ms) periods of time (EEG microstates; Michel and Koenig, 2018), it was hypothesized that RSNs were reflected on both EEG and fMRI. Despite their methodological differences, a few studies have confirmed such hypothesis (Britz et al., 2010; Musso et al., 2010; Yuan et al., 2012; Bréchet et al., 2019; Hunyadi et al., 2019), with one study even establishing a one-to-one relationship between EEG microstates and fMRI RSNs (Britz et al., 2010), which, however, has been widely debated (Michel and Koenig, 2018).

Based on these findings, it is therefore expected that RSNs are also explicitly reflected on the EEG. This was first suggested by previous studies showing the ability of functional connectomes (covariance matrices of signals averaged across gray matter parceled according to an atlas) extracted from source-reconstructed EEG data across each EEG rhythm, to predict functional connectomes derived from simultaneously acquired fMRI data (Deligianni et al., 2014), and more recently to predict anatomical connectomes derived from diffusion MRI data as well (Wirsich et al., 2017). Contradictory results, however, have been reported regarding the relative importance of each EEG rhythm for predicting the fMRI functional connectomes. Moreover, these studies were focused on functional connectomes and their derived RSNs, rather than the RSNs more conventionally defined as in Smith et al. (2009).

Such RSNs were first detected on EEG recordings by decomposing, with spatial ICA and at the subject level, the temporally concatenated power of the source-reconstructed EEG data across each rhythm, followed by a clustering step on the resulting ICs from all subjects to identify group-level RSNs (Sockeel et al., 2016). These were then compared with RSNs derived from the fMRI data, with only a sub-set of RSNs presenting a clear overlap between imaging techniques. Considering instead the broadband, rather than band-specific, power of the EEG sources (Liu et al., 2017) also suggested the identification of RSNs on the EEG. Although these findings were validated by RSNs derived from fMRI data, the ground truth considered was not ideal as the two signals were not acquired simultaneously, and therefore do not account for the well-known inter-subject and inter-session variability of the recordings (Smith et al., 2005; Corsi-Cabrera et al., 2007). More importantly, because RSNs result from the temporal coherency of spontaneous activity, cross-validating results from two imaging techniques requires their concurrent acquisition (Abreu et al., 2018). Besides comparing the RSNs obtained from fMRI and EEG data acquired simultaneously, here we considered as ground truth the RSN templates from Smith et al. (2009), which are commonly used in the literature to inform the identification of RSNs. In this way, an independent validation could be performed; one limitation, however, relates with the nature of such templates, as they were derived from fMRI data recorded from a large population of healthy subjects, and therefore may positively bias the amount of overlap (here quantified by the Dice coefficient) between the fMRI RSNs and their templates, relatively to the RSNs derived from the EEG. Our results are in line with this observation, as the maximum and average Dice coefficient across RSNs were systematically higher for the fMRI than those for the EEG, in all four runs. Nonetheless, comparable Dice coefficients were observed between the two

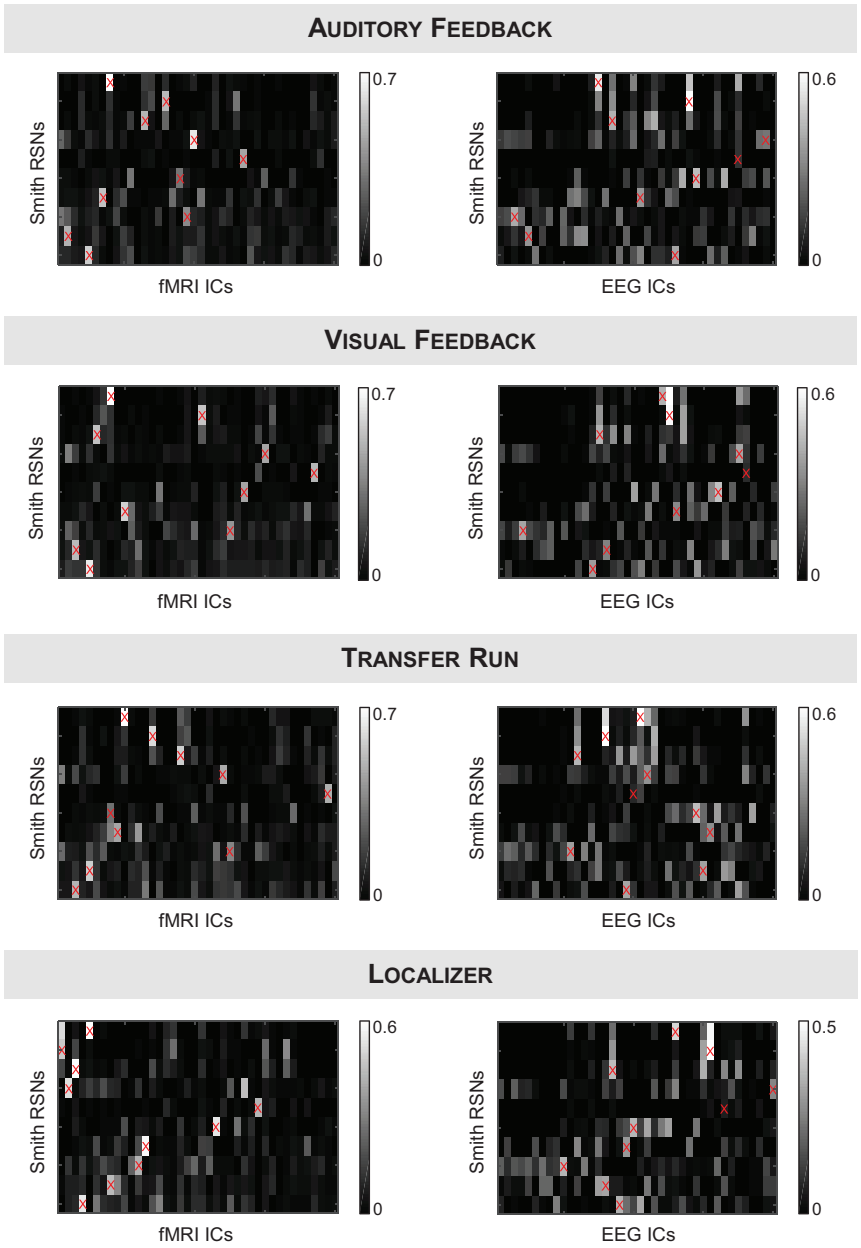

FIGURE 3 | Dice coefficients between all possible combinations of **(left)** fMRI ICs or **(right)** EEG-ESI ICs (*x*-axis) and the RSN templates (*y*-axis) from Smith et al. (2009), for the (from top to bottom) auditory feedback, visual feedback, transfer, and localizer runs. fMRI/EEG-ESI ICs assigned to RSN templates are marked by a red cross.

imaging techniques; it should be noted, however, that fMRI ICs typically exhibited a notable overlap with a single RSN template, rather than having multiple ICs competing for the RSN template, as observed with some EEG ICs. Such apparent higher specificity of the fMRI data may again be partially explained by the RSN templates being derived from fMRI data. Because the RSNs were obtained from simultaneous EEG-fMRI data, our results further support the existence of EEG correlates of RSNs. Similarly to the fMRI-derived RSN templates, by applying the methodology here proposed to a larger set of EEG-fMRI recordings, EEG-based RSN templates could in principle be obtained, and potentially be used to investigate differences from the fMRI-derived RSN templates.

Continuous Source Imaging of EEG Acquired Simultaneously With fMRI

In the study of Liu et al. (2017), continuous EEG source imaging (cESI) was performed under optimal conditions, from high-density (256 channels) recordings outside the MR scanner.

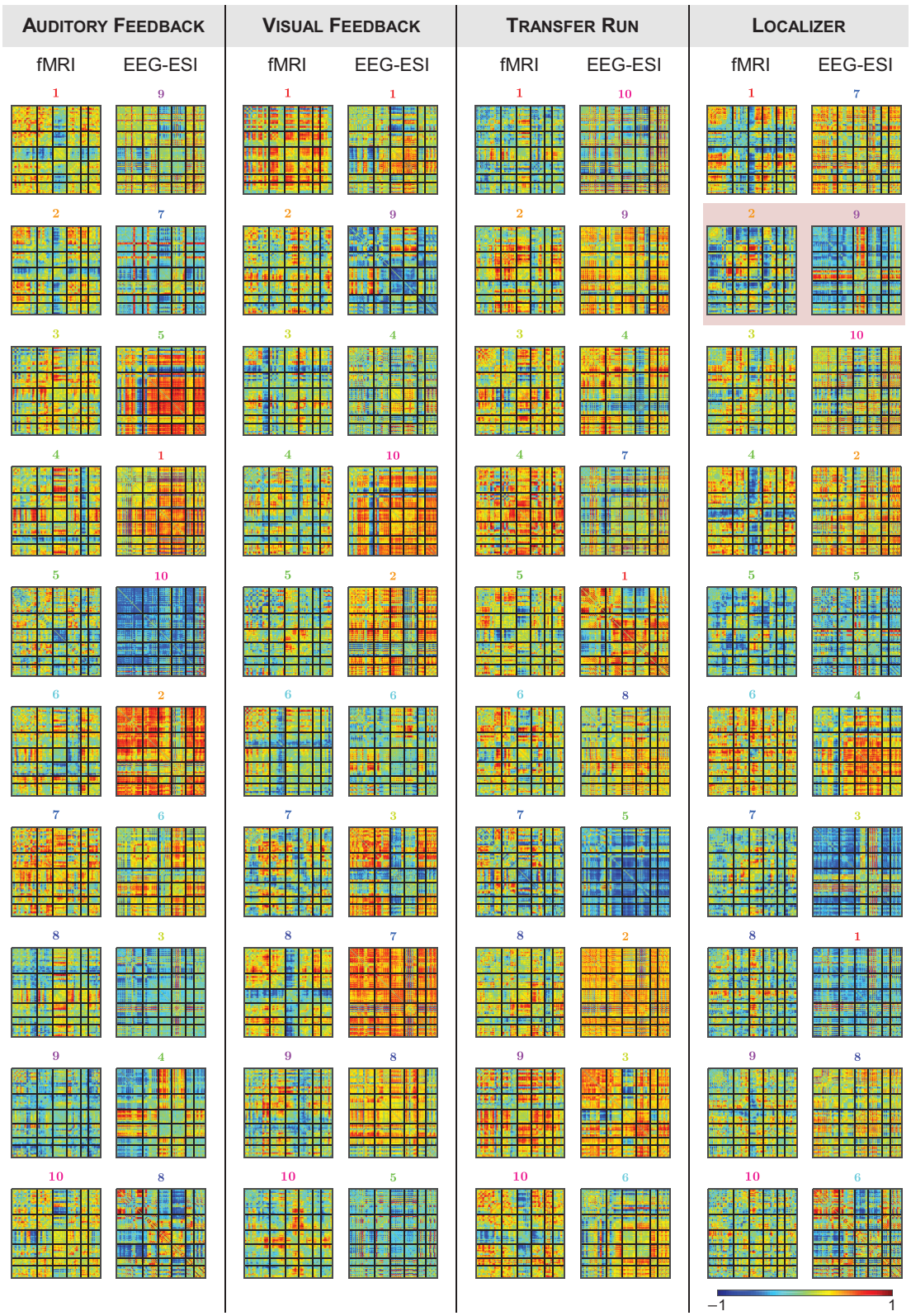

FIGURE 4 | Group dFC states estimated from fMRI and EEG-ESI data for the (from left to right) auditory feedback, visual feedback, transfer, and localizer runs. For each run, the correlation matrices (normalized between –1 and 1, for visualization purposes) of the dFC states estimated from the fMRI data **(left)** and the matched EEG-ESI dFC states **(right)** are shown. For the localizer run, fMRI state #2 and EEG-ESI state #9 are highlighted by the red square, as these two matched dFC states were associated with the activity at the FEPN.

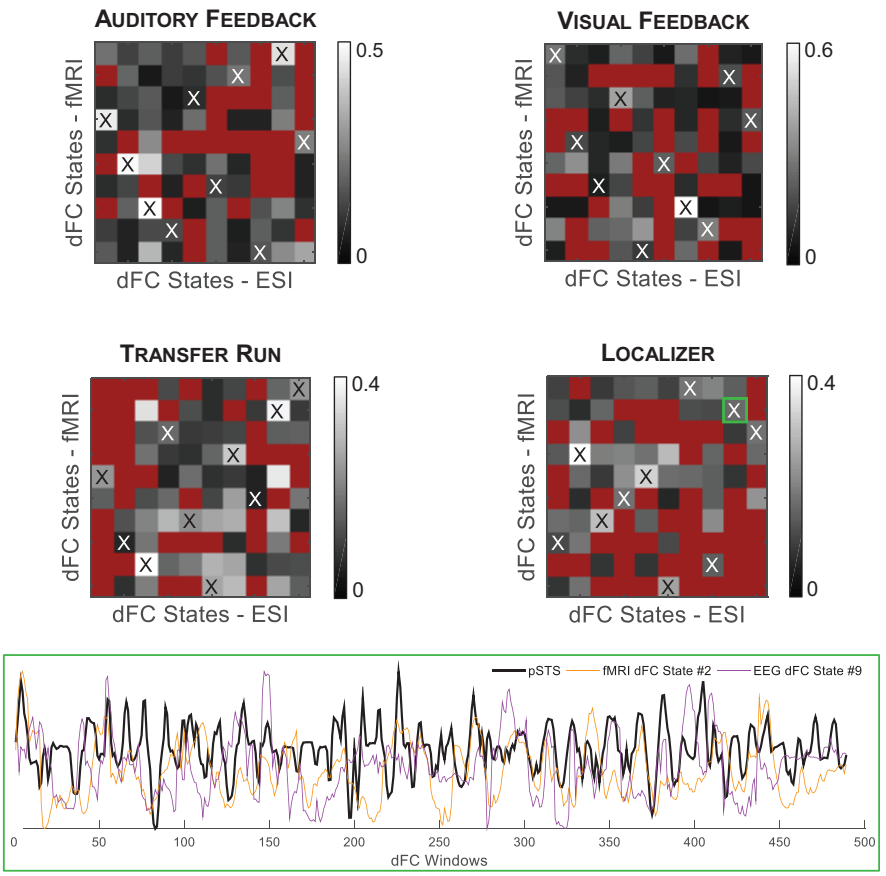

FIGURE 5 | (Top) Spatial correlation between all possible combinations of fMRI (*y*-axis) and EEG-ESI (*x*-axis) dFC state correlation matrices, for the auditory feedback, visual feedback, transfer, and localizer runs. Red squares denote non-statistically significant ($p > 0.05$) spatial correlation values. Matched fMRI and EEG-ESI dFC states are marked by the black or white cross. **(Bottom)** For the localizer run, the contribution over time of the matched fMRI state #2 and EEG-ESI state #9 (further highlighted by the green square) is shown (orange and purple traces, respectively), superimposed with the contrast of interest used to map the FEPN (black trace).

Despite the potential loss in data quality, the feasibility of performing cESI on EEG data acquired simultaneously with fMRI has already been demonstrated (Groening et al., 2009; Vulliemoz et al., 2009, 2010a,b; Siniatchkin et al., 2010), particularly using EEG caps with a conventional spatial coverage (32 or 64 channels). In fact, simulation studies showed that an almost perfect source reconstruction can be obtained with only 68 channels, reaching a plateau at 100 channels (Michel et al., 2004). Since several processing steps are carried out when performing cESI, their impact on the detection of RSNs with EEG was systematically investigated by Liu et al. (2018), with the electrode density being the most relevant factor, followed by the head model and source localization algorithm chosen. Using the recommended setup and processing pipeline, Liu et al. (2018) reported an average correlation between fMRI and EEG RSNs of 0.6. Here, we used the same processing pipeline, but applied to 64-channel EEG data acquired simultaneously with fMRI, with a maximum/average Dice coefficient of 0.5/0.4 (averaged across runs). These slightly poorer results may partially be explained by the potential loss in data quality due to the presence of MR-induced artifact residuals; nonetheless, our results demonstrate the feasibility of using cESI applied to low-density EEG data acquired simultaneously with fMRI, for detecting RSNs.

Mapping of Task-Specific Brain Networks With EEG

We used EEG for mapping a task-specific brain network: specifically, we attempted to map the FEPN from the fMRI and EEG recordings of the localizer run using a GLM framework. Although uncommon, such framework has been previously applied to source-reconstructed M/EEG data: the first studies were focused on quantifying the contribution of event-related (Brookes et al., 2004) or band-limited frequency power (Trujillo-Barreto et al., 2008) waveforms associated with a specific activity of interest. By adopting this model-based analysis of the EEG, the generators underlying such activity of interest can in principle be isolated from the remaining ones. Similarly to our study, previous reports have also used GLM to analyze broadband EEG data, for

better characterizing the impulse response function associated with different types of visual stimuli (Gonçalves et al., 2014), or for more accurately localizing the generators of EEG microstates (Custo et al., 2014). These studies and their promising results motivated our chosen approach to model EEG-ESI data with the task-specific expected response function, with the additional benefit of providing an activation map directly comparable with that from the conventional GLM analysis of the fMRI data.

Despite the small overall overlap (Dice coefficient of 0.1), the group activation maps of each imaging technique overlapped at the left pre-central gyrus, which is known to be involved in the processing of face expressions (Fox et al., 2009; Radua et al., 2010). Although non-overlapping, relevant fMRI and EEG-ESI activations were found at the postcentral sulcus and the posterior superior temporal sulcus (pSTS), the latter being the anchor of the FEPN (Srinivasan et al., 2016; Wang et al., 2016). The concordant activations at (or close to) pSTS are in agreement with our previous work (Direito et al., 2019), and also with a study specifically focused on the functional segmentation of the STS (Deen et al., 2015). The latter showed that among several social perception and cognition tasks, the participants consistently responded to the perception of faces mainly at pSTS, highlighting the relevance of these activated brain regions. Interestingly, the EEG-ESI data also exhibited frontal activations, which have been shown to play a role in this cognitive task (Kesler-West et al., 2001); however, this result cannot be truly validated as such activations were not present in the fMRI data.

In contrast with the bilateral fMRI activation map, which is consistent with the results from Deen et al. (2015) and Direito et al. (2019), an unexpected lateralization of the FEPN was observed when derived from the EEG data. Such lateralization was also observed on some of the RSNs, where bilateral RSN templates only partially overlapped with unilateral EEG RSNs. Importantly, this does not result from a systematic limitation of cESI, as other bilateral RSN templates were fully recovered by the EEG. Nonetheless, several limitations of ESI have been acknowledged, particularly the non-uniqueness of the inverse problem. This challenge is only partially overcome by making assumptions about the neuronal sources in order to constrain the solution space, which would otherwise be infinite. Furthermore, ESI solutions are strongly biased toward cortical (and focal) sources of electrical activity, because of the lack of sensitivity of reconstruction algorithms with respect to deep gray matter sources, invariably tending to shift solutions to the cortical surface (Michel et al., 2004; Michel and Murray, 2012). Notwithstanding these limitations, we verified consistently overlapping maps for most of the RSNs and the task-specific FEPN, enforcing the feasibility of this approach.

Dynamic Functional Connectivity and Brain States

Although unreported so far, the match between dFC states derived from fMRI and EEG data found in the present study was somewhat expected, considering that a number of studies have already found EEG correlates of dFC fluctuations and brain states measured with simultaneous fMRI (Tagliazucchi and Laufs, 2015), motivated by the yet unclear physiological underpinnings of dFC (Thompson, 2018). These studies were mainly focused on healthy subjects (Chang and Glover, 2010; Allen et al., 2017) and epilepsy patients (Laufs et al., 2014; Lopes et al., 2014; Preti et al., 2014; Omidvarnia et al., 2017; Abreu et al., 2019). Interestingly, when comparing the contrast of interest for mapping the FEPN with the contribution over time of each fMRI and EEG dFC state, we found that the contribution of two matched dFC states based on their spatial correlation were significantly correlated with the FEPN contrast. The identification of fMRI dFC states specifically associated with a given activity of interest extracted from the EEG had already been suggested (Abreu et al., 2019). While this study shows the potential of fMRI to capture dFC fluctuations associated with specific brain activities, our finding extends it, and specifically suggests that fluctuations in the functional connectivity of the FEPN can be captured by both fMRI and EEG, thus supporting the physiological meaning of the also statistically validated match found between fMRI and EEG dFC states. Our results thus further evidence the existence of EEG correlates of dFC, and open new lines of research where dFC fluctuations of large-scale functional networks can be investigated with EEG, a technique that more directly measures brain activity when compared with fMRI.

Limitations

In this multimodal study, a small sample size was considered, which inevitably hinders our conclusions to be generalized to future studies applying the proposed methodology. Nonetheless, given the consistency of our results regarding the detection of RSNs, the mapping of the task-related FEPN, and the identification of matched dFC states across modalities, particularly those associated with the FEPN, we believe that this study provides a strong proof-of-concept on the use of EEG as a brain imaging tool.

Another important aspect of our study is that the participants were performing a neurofeedback (NF) task. This relates to our additional goal of testing the transfer of an already validated fMRI NF intervention to an EEG setup, with the purpose of generalizing and disseminating such intervention. This motivates this study's investigation on the possibility of mapping a task network of interest (the face expressions processing network, FEPN) with EEG. Despite some reported differences between co-activation networks and RSNs (Di et al., 2013), it has been shown that RSNs can also be accurately identified on fMRI data collected from participants performing tasks in general (Cole et al., 2016). This has thus motivated our study to address both the intrinsic and task-related connectivity aspects from a static and dynamic point of view. NF tasks, however, are known to modulate the strength of intra- and inter-network connections, which may influence the functional organization of RSNs (Sitaram et al., 2017). Importantly, the NF task used in this study was tailored to modulate the percent signal change of the BOLD signal measured at a limited and well-defined brain region in pSTS, rather than the connectivity strength of specific RSNs (Direito et al., 2019). Moreover, assuming that this NF task is nonetheless modulating the RSNs, it has also been shown that NF is able to induce the

desired changes on both EEG and fMRI when performing real-time simultaneous EEG-fMRI NF (Zich et al., 2015; Zotev et al., 2016). It is then expected that potential modulations on the RSNs and/or dFC states will be reflected on both EEG and fMRI data, and thus in principle not confounding our results. Naturally, this could only be confirmed in future studies applying the proposed methodologies to resting-state data.

CONCLUSION

In this study, we validated in a truly unbiased manner the existence of RSNs reflected on both fMRI and EEG data, while also supporting the feasibility of continuous electrical source imaging to low-density EEG data acquired simultaneously with fMRI. We also showed that EEG can be used for mapping task-specific networks (particularly the facial expression processing network, FEPN), as well as to study the dynamics of functional networks, and extract their representative dFC states. Importantly, we also determined that fluctuations in the functional connectivity of the FEPN can be captured on both fMRI and EEG. Additionally, our results support the emerging literature on EEG correlates of (dynamic) functional connectivity measured with fMRI, and therefore provide novel insights into the coupling mechanisms underlying the two imaging techniques. Our analyses push the limits of EEG toward being used as a brain imaging tool, allowing researchers and clinics to more efficiently leverage the high temporal resolution, low cost, portability and ease of use that characterize the EEG.

DATA AVAILABILITY STATEMENT

The datasets generated for this study are available on request to the corresponding author.

ETHICS STATEMENT

The studies involving human participants were reviewed and approved by Ethics Commission of the Faculty of Medicine of the University of Coimbra. The patients/participants provided their written informed consent to participate in this study.

AUTHOR CONTRIBUTIONS

RA was responsible for performing all the data analyses and writing the manuscript. MS acquired all the data, and was responsible for designing and coding the experimental protocol, and reviewed the manuscript. MC-B supervised this study, and reviewed the manuscript.

FUNDING

This work was supported by Grants Funded by Fundação para a Ciência e Tecnologia, PAC –286 MEDPERSYST, POCI-01-0145-FEDER-016428, BIGDATIMAGE, CENTRO-01-0145-FEDER-000016 financed by Centro 2020 FEDER, COMPETE, FCT UID/4539/2013 – COMPETE, POCI-01-0145-FEDER-007440, and CONNECT.BCI POCI-01-0145-FEDER-30852.

SUPPLEMENTARY MATERIAL

The Supplementary Material for this article can be found online at: https://www.frontiersin.org/articles/10.3389/fnins.2020.00323/full#supplementary-material

REFERENCES

Abreu, R., Leal, A., and Figueiredo, P. (2018). EEG-Informed fMRI: a review of data analysis methods. *Front. Hum. Neurosci.* 12:29. doi: 10.3389/fnhum.2018.00029

Abreu, R., Leal, A., and Figueiredo, P. (2019). Identification of epileptic brain states by dynamic functional connectivity analysis of simultaneous EEG-fMRI: a dictionary learning approach. *Sci. Rep.* 9:638. doi: 10.1038/s41598-018-36976-y

Abreu, R., Leite, M., Jorge, J., Grouiller, F., van der Zwaag, W., Leal, A., et al. (2016). Ballistocardiogram artifact correction taking into account physiological signal preservation in simultaneous EEG-fMRI. *Neuroimage* 135, 45–63. doi: 10.1016/j.neuroimage.2016.03.034

Abreu, R., Nunes, S., Leal, A., and Figueiredo, P. (2017). Physiological noise correction using ECG-derived respiratory signals for enhanced mapping of spontaneous neuronal activity with simultaneous EEG-fMRI. *Neuroimage* 154, 115–127. doi: 10.1016/J.NEUROIMAGE.2016.08.008

Allen, E. A., Damaraju, E., Eichele, T., Wu, L., and Calhoun, V. D. (2017). EEG signatures of dynamic functional network connectivity states. *Brain Topogr* 31, 101–116. doi: 10.1007/s10548-017-0546-2

Allen, E. A., Damaraju, E., Plis, S. M., Erhardt, E. B., Eichele, T., and Calhoun, V. D. (2014). Tracking whole-brain connectivity dynamics in the resting state. *Cereb. Cortex* 24, 663–676. doi: 10.1093/cercor/bhs352

Allen, P. J., Josephs, O., and Turner, R. (2000). A method for removing imaging artifact from continuous EEG recorded during functional MRI. *Neuroimage* 12, 230–239. doi: 10.1006/nimg.2000.0599

Barch, D. M., Burgess, G. C., Harms, M. P., Petersen, S. E., Schlaggar, B. L., Corbetta, M., et al. (2013). Function in the human connectome: task-fMRI and individual differences in behavior. *Neuroimage* 80, 169–189. doi: 10.1016/J.NEUROIMAGE.2013.05.033

Beckmann, C. F., DeLuca, M., Devlin, J. T., and Smith, S. M. (2005). Investigations into resting-state connectivity using independent component analysis. *Philos. Trans. R. Soc. B Biol. Sci.* 360, 1001–1013. doi: 10.1098/rstb.2005.1634

Beckmann, C. F., Jenkinson, M., and Smith, S. M. (2003). General multilevel linear modeling for group analysis in FMRI. *Neuroimage* 20, 1052–1063. doi: 10.1016/S1053-8119(03)00435-X

Beckmann, C. F., and Smith, S. M. (2004). Probabilistic independent component analysis for functional magnetic resonance imaging. *IEEE Trans. Med. Imaging* 23, 137–152. doi: 10.1109/TMI.2003.822821

Biswal, B., Zerrin Yetkin, F., Haughton, V. M., and Hyde, J. S. (1995). Functional connectivity in the motor cortex of resting human brain using echo-planar mri. *Magn. Reson. Med.* 34, 537–541. doi: 10.1002/mrm.1910340409

Bréchet, L., Brunet, D., Birot, G., Gruetter, R., Michel, C. M., and Jorge, J. (2019). Capturing the spatiotemporal dynamics of self-generated, task-initiated thoughts with EEG and fMRI. *Neuroimage* 194, 82–92. doi: 10.1016/J.NEUROIMAGE.2019.03.029

Bressler, S. L., and Menon, V. (2010). Large-scale brain networks in cognition: emerging methods and principles. *Trends Cogn. Sci.* 14, 277–290. doi: 10.1016/J.TICS.2010.04.004

Britz, J., Van De Ville, D., and Michel, C. M. (2010). BOLD correlates of EEG topography reveal rapid resting-state network

dynamics. *Neuroimage* 52, 1162–1170. doi: 10.1016/j.neuroimage.2010.02.052

Brookes, M. J., Gibson, A. M., Hall, S. D., Furlong, P. L., Barnes, G. R., Hillebrand, A., et al. (2004). A general linear model for MEG beamformer imaging. *Neuroimage* 23, 936–946. doi: 10.1016/j.neuroimage.2004.06.031

Brookes, M. J., Woolrich, M., Luckhoo, H., Price, D., Hale, J. R., Stephenson, M. C., et al. (2011). Investigating the electrophysiological basis of resting state networks using magnetoencephalography. *Proc. Natl. Acad. Sci. U.S.A* 4, 16783–16788. doi: 10.1073/pnas.1112685108

Calhoun, V. D., Miller, R., Pearlson, G., and Adalı, T. (2014). The chronnectome: time-varying connectivity networks as the next frontier in fMRI data discovery. *Neuron* 84, 262–274. doi: 10.1016/j.neuron.2014.10.015

Chang, C., Cunningham, J. P., and Glover, G. H. (2009). Influence of heart rate on the BOLD signal: the cardiac response function. *Neuroimage* 44, 857–869. doi: 10.1016/j.neuroimage.2008.09.029

Chang, C., and Glover, G. H. (2009). Effects of model-based physiological noise correction on default mode network anti-correlations and correlations. *Neuroimage* 47, 1448–1459. doi: 10.1016/j.neuroimage.2009.05.012

Chang, C., and Glover, G. H. (2010). Time-frequency dynamics of resting-state brain connectivity measured with fMRI. *Neuroimage* 50, 81–98. doi: 10.1016/j.neuroimage.2009.12.011

Cole, M. W., Ito, T., Bassett, D. S., and Schultz, D. H. (2016). Activity flow over resting-state networks shapes cognitive task activations. *Nat. Neurosci.* 19, 1718–1726. doi: 10.1038/nn.4406

Collins, D. L., Neelin, P., Peters, T. M., and Evans, A. C. (1994). Automatic 3D intersubject registration of MR volumetric data in standardized Talairach space. *J. Comput. Assist. Tomogr.* 18, 192–205. doi: 10.1097/00004728-199403000-00005

Cordes, D., Haughton, V. M., Arfanakis, K., Carew, J. D., Turski, P. A., Moritz, C. H., et al. (2001). Frequencies contributing to functional connectivity in the cerebral cortex in "Resting-state" data. *AJNR Am. J. Neuroradiol.* 22, 1326–1333.

Corsi-Cabrera, M., Galindo-Vilchis, L., del-Río-Portilla, Y., Arce, C., and Ramos-Loyo, J. (2007). Within-subject reliability and inter-session stability of EEG power and coherent activity in women evaluated monthly over nine months. *Clin. Neurophysiol.* 118, 9–21. doi: 10.1016/J.CLINPH.2006.08.013

Custo, A., Vulliemoz, S., Grouiller, F., Van De Ville, D., and Michel, C. (2014). EEG source imaging of brain states using spatiotemporal regression. *Neuroimage* 96, 106–116. doi: 10.1016/j.neuroimage.2014.04.002

de Munck, J. C., Gonçalves, S. I., Mammoliti, R., Heethaar, R. M., Lopes, and da Silva, F. H. (2009). Interactions between different EEG frequency bands and their effect on alpha-fMRI correlations. *Neuroimage* 47, 69–76. doi: 10.1016/j.neuroimage.2009.04.029

Deen, B., Koldewyn, K., Kanwisher, N., and Saxe, R. (2015). Functional organization of social perception and cognition in the superior temporal sulcus. *Cereb. Cortex* 25, 4596–4609. doi: 10.1093/cercor/bhv111

Deligianni, F., Centeno, M., Carmichael, D. W., and Clayden, J. D. (2014). Relating resting-state fMRI and EEG whole-brain connectomes across frequency bands. *Front. Neurosci.* 8:258. doi: 10.3389/fnins.2014.00258

Di, X., Gohel, S., Kim, E. H., and Biswal, B. B. (2013). Task vs. rest—different network configurations between the coactivation and the resting-state brain networks. *Front. Hum. Neurosci.* 7:493. doi: 10.3389/fnhum.2013.00493

Dice, L. R. (1945). Measures of the amount of ecologic association between species. *Ecology* 26, 297–302. doi: 10.2307/1932409

Direito, B., Lima, J., Simões, M., Sayal, A., Sousa, T., Luehrs, M., et al. (2019). Targeting dynamic facial processing mechanisms in superior temporal sulcus using a novel fMRI neurofeedback target. *Neuroscience* 406, 97–108. doi: 10.1016/j.neuroscience.2019.02.024

Du, Y., Fu, Z., and Calhoun, V. D. (2018). Classification and prediction of brain disorders using functional connectivity: promising but challenging. *Front. Neurosci.* 12:525. doi: 10.3389/fnins.2018.00525

Fox, C. J., Iaria, G., and Barton, J. J. S. S. (2009). Defining the face processing network: optimization of the functional localizer in fMRI. *Hum. Brain Mapp.* 30, 1637–1651. doi: 10.1002/hbm.20630

Friston, K. J., Holmes, A. P., Poline, J.-B., Grasby, P. J., Williams, S. C., Frackowiak, R. S., et al. (1995). Analysis of fMRI time-series revisited. *Neuroimage* 2, 45–53. doi: 10.1006/nimg.1995.1007

Glover, G. H., Li, T. Q., and Ress, D. (2000). Image-based method for retrospective correction of physiological motion effects in fMRI: RETROICOR. *Magn. Reson. Med.* 44, 162–167. doi: 10.1002/1522-2594(200007)44:1<162::AID-MRM23>3.0.CO;2-E

Goldman, R. I., Stern, J. M., Engel, J., and Cohen, M. S. (2002). Simultaneous EEG and fMRI of the alpha rhythm. *Neuroreport* 13, 2487–2492. doi: 10.1097/00001756-200212200-00022

Gonçalves, N. R., Whelan, R., Foxe, J. J., and Lalor, E. C. (2014). Towards obtaining spatiotemporally precise responses to continuous sensory stimuli in humans: a general linear modeling approach to EEG. *Neuroimage* 97, 196–205. doi: 10.1016/j.neuroimage.2014.04.012

Groening, K., Brodbeck, V., Moeller, F., Wolff, S., van Baalen, A., Michel, C. M., et al. (2009). Combination of EEG–fMRI and EEG source analysis improves interpretation of spike-associated activation networks in paediatric pharmacoresistant focal epilepsies. *Neuroimage* 46, 827–833. doi: 10.1016/j.neuroimage.2009.02.026

Hunyadi, B., Woolrich, M. W., Quinn, A. J., Vidaurre, D., and De Vos, M. (2019). A dynamic system of brain networks revealed by fast transient EEG fluctuations and their fMRI correlates. *Neuroimage* 185, 72–82. doi: 10.1016/j.neuroimage.2018.09.082

Hutchison, R. M., Womelsdorf, T., Allen, E. A., Bandettini, P. A., Calhoun, V. D., Corbetta, M., et al. (2013). Dynamic functional connectivity: promise, issues, and interpretations. *Neuroimage* 80, 360–378. doi: 10.1016/j.neuroimage.2013.05.079

Iacono, M. I., Neufeld, E., Akinnagbe, E., Bower, K., Wolf, J., Vogiatzis Oikonomidis, I., et al. (2015). MIDA: a multimodal imaging-based detailed anatomical model of the human head and neck. *PLoS One* 10:e0124126. doi: 10.1371/journal.pone.0124126

Jenkinson, M., Bannister, P., Brady, M., and Smith, S. (2002). Improved optimization for the robust and accurate linear registration and motion correction of brain images. *Neuroimage* 17, 825–841. doi: 10.1006/nimg.2002.1132

Jenkinson, M., and Smith, S. (2001). A global optimisation method for robust affine registration of brain images. *Med. Image Anal.* 5, 143–156. doi: 10.1016/S1361-8415(01)00036-6

Jo, H. J., Saad, Z. S., Simmons, W. K., Milbury, L. A., and Cox, R. W. (2010). Mapping sources of correlation in resting state FMRI, with artifact detection and removal. *Neuroimage* 52, 571–582. doi: 10.1016/j.neuroimage.2010.04.246

Kesler-West, M. L., Andersen, A. H., Smith, C. D., Avison, M. J., Davis, C. E., Kryscio, R. J., et al. (2001). Neural substrates of facial emotion processing using fMRI. *Cogn. Brain Res.* 11, 213–226. doi: 10.1016/S0926-6410(00)00073-2

Laufs, H., Holt, J. L., Elfont, R., Krams, M., Paul, J. S., Krakow, K., et al. (2006). Where the BOLD signal goes when alpha EEG leaves. *Neuroimage* 31, 1408–1418. doi: 10.1016/j.neuroimage.2006.02.002

Laufs, H., Rodionov, R., Thornton, R., Duncan, J. S., Lemieux, L., and Tagliazucchi, E. (2014). Altered fMRI connectivity dynamics in temporal lobe epilepsy might explain seizure semiology. *Front. Neurol.* 5:175. doi: 10.3389/fneur.2014.00175

Lee, M. H., Smyser, C. D., and Shimony, J. S. (2013). Resting-state fMRI: a review of methods and clinical applications. *AJNR. Am. J. Neuroradiol.* 34, 1866–1872. doi: 10.3174/ajnr.A3263

Leonardi, N., Richiardi, J., Gschwind, M., Simioni, S., Annoni, J. M., Schluep, M., et al. (2013). Principal components of functional connectivity: a new approach to study dynamic brain connectivity during rest. *Neuroimage* 83, 937–950. doi: 10.1016/j.neuroimage.2013.07.019

Leonardi, N., Shirer, W. R., Greicius, M. D., and Van De Ville, D. (2014). Disentangling dynamic networks: separated and joint expressions of functional connectivity patterns in time. *Hum. Brain Mapp.* 35, 5984–5995. doi: 10.1002/hbm.22599

Liu, Q., Farahibozorg, S., Porcaro, C., Wenderoth, N., and Mantini, D. (2017). Detecting large-scale networks in the human brain using high-density electroencephalography. *Hum. Brain Mapp.* 38, 4631–4643. doi: 10.1002/hbm.23688

Liu, Q., Ganzetti, M., Wenderoth, N., and Mantini, D. (2018). Detecting large-scale brain networks using EEG: impact of electrode density, head modeling and source localization. *Front. Neuroinform.* 12:14. doi: 10.3389/fninf.2018.00004

Logothetis, N. K., Pauls, J., Augath, M., Trinath, T., and Oeltermann, A. (2001). Neurophysiological investigation of the basis of the fMRI signal. *Nature* 412, 150–157. doi: 10.1038/35084005

Lopes, R., Moeller, F., Besson, P., Ogez, F., Szurhaj, W., Leclerc, X., et al. (2014). Study on the relationships between intrinsic functional connectivity of the default mode network and transient epileptic activity. *Front. Neurol.* 5:201. doi: 10.3389/fneur.2014.00201

Mairal, J., Bach, F., Ponce, J., and Sapiro, G. (2010). Online learning for matrix factorization and sparse coding. *J. Mach. Learn. Res.* 11, 19–60. doi: 10.1016/j.neunet.2012.05.003

Mantini, D., Penna, S., Della, Marzetti, L., de Pasquale, F., Pizzella, V., et al. (2011). A signal-processing pipeline for magnetoencephalography resting-state networks. *Brain Connect.* 1, 49–59. doi: 10.1089/brain.2011.0001

Mantini, D., Perrucci, M. G., Del Gratta, C., Romani, G. L., and Corbetta, M. (2007). Electrophysiological signatures of resting state networks in the human brain. *Proc. Natl. Acad. Sci. U.S.A.* 104, 13170–13175. doi: 10.1073/pnas.0700668104

Meir-Hasson, Y., Kinreich, S., Podlipsky, I., Hendler, T., and Intrator, N. (2014). An EEG finger-print of fMRI deep regional activation. *Neuroimage* 102, 128–141. doi: 10.1016/j.neuroimage.2013.11.004

Michel, C. M., and Koenig, T. (2018). EEG microstates as a tool for studying the temporal dynamics of whole-brain neuronal networks: a review. *Neuroimage* 180, 577–593. doi: 10.1016/j.neuroimage.2017.11.062

Michel, C. M., and Murray, M. M. (2012). Towards the utilization of EEG as a brain imaging tool. *Neuroimage* 61, 371–385. doi: 10.1016/j.neuroimage.2011.12.039

Michel, C. M., Murray, M. M., Lantz, G., Gonzalez, S., Spinelli, L., Grave, et al. (2004). EEG source imaging. *Clin. Neurophysiol.* 115, 2195–2222. doi: 10.1016/j.clinph.2004.06.001

Moosmann, M., Ritter, P., Krastel, I., Brink, A., Thees, S., Blankenburg, F., et al. (2003). Correlates of alpha rhythm in functional magnetic resonance imaging and near infrared spectroscopy. *Neuroimage* 20, 145–158. doi: 10.1016/S1053-8119(03)00344-6

Mullinger, K., Brookes, M., Stevenson, C., Morgan, P., and Bowtell, R. (2008). Exploring the feasibility of simultaneous electroencephalography/functional magnetic resonance imaging at 7 T. *Magn. Reson. Imaging* 26, 968–977. doi: 10.1016/j.mri.2008.02.014

Musso, F., Brinkmeyer, J., Mobascher, A., Warbrick, T., and Winterer, G. (2010). Spontaneous brain activity and EEG microstates. A novel EEG/fMRI analysis approach to explore resting-state networks. *Neuroimage* 52, 1149–1161. doi: 10.1016/j.neuroimage.2010.01.093

Niedermeyer, E., and Lopes Da Silva, F. H. (2005). *Electroencephalography: Basic Principles, Clinical Applications, and Related Fields*, 6th Edn. Wolters Kluwer Health. Available online at: https://books.google.com/books?hl=pt-PT&lr=&id=tndqYGPHQdEC&pgis=1 (accessed May 22, 2015).

Omidvarnia, A., Pedersen, M., Vaughan, D. N., Walz, J. M., Abbott, D. F., Zalesky, A., et al. (2017). Dynamic coupling between fMRI local connectivity and interictal EEG in focal epilepsy: a wavelet analysis approach. *Hum. Brain Mapp.* 38, 5356–5374. doi: 10.1002/hbm.23723

Oostenveld, R., Fries, P., Maris, E., and Schoffelen, J.-M. (2011). FieldTrip: open source software for advanced analysis of MEG, EEG, and invasive electrophysiological data. *Comput. Intell. Neurosci.* 2011, 1–9. doi: 10.1155/2011/156869

Pan, J., and Tompkins, W. J. (1985). A real-time QRS detection algorithm. *IEEE Trans. Biomed. Eng.* 32, 230–236. doi: 10.1109/TBME.1985.325532

Pascual-Marqui, R. D., Lehmann, D., Koukkou, M., Kochi, K., Anderer, P., Saletu, B., et al. (2011). Assessing interactions in the brain with exact low-resolution electromagnetic tomography. *Philos. Trans. R. Soc. A Math. Phys. Eng. Sci.* 369, 3768–3784. doi: 10.1098/rsta.2011.0081

Pernet, C. R., Chauveau, N., Gaspar, C., and Rousselet, G. A. (2011). LIMO EEG: a toolbox for hierarchical linear modeling of electroencephalographic data. *Comput. Intell. Neurosci.* 2011:831409. doi: 10.1155/2011/831409

Power, J. D., Barnes, K. A., Snyder, A. Z., Schlaggar, B. L., and Petersen, S. E. (2012). Spurious but systematic correlations in functional connectivity MRI networks arise from subject motion. *Neuroimage* 59, 2142–2154. doi: 10.1016/j.neuroimage.2011.10.018

Preti, M. G., Bolton, T. A., and Van De Ville, D. (2017). The dynamic functional connectome: state-of-the-art and perspectives. *Neuroimage* 160, 41–54. doi: 10.1016/J.NEUROIMAGE.2016.12.061

Preti, M. G., Leonardi, N., Karahanoglu, F. I., Grouiller, F., Genetti, M., Seeck, M., et al. (2014). "Epileptic network activity revealed by dynamic functional connectivity in simultaneous EEG-fMRI," in *Proceedings of the 2014 IEEE 11th International Symposium on Biomedical Imaging (ISBI) (IEEE)* (Beijing: IEEE), 9–12. doi: 10.1109/ISBI.2014.6867796

Radua, J., Phillips, M. L., Russell, T., Lawrence, N., Marshall, N., Kalidindi, S., et al. (2010). Neural response to specific components of fearful faces in healthy and schizophrenic adults. *Neuroimage* 49, 939–946. doi: 10.1016/j.neuroimage.2009.08.030

Scheeringa, R., Bastiaansen, M. C. M., Petersson, K. M., Oostenveld, R., Norris, D. G., and Hagoort, P. (2008). Frontal theta EEG activity correlates negatively with the default mode network in resting state. *Int. J. Psychophysiol.* 67, 242–251. doi: 10.1016/j.ijpsycho.2007.05.017

Siniatchkin, M., Groening, K., Moehring, J., Moeller, F., Boor, R., Brodbeck, V., et al. (2010). Neuronal networks in children with continuous spikes and waves during slow sleep. *Brain* 133, 2798–2813. doi: 10.1093/brain/awq183

Sitaram, R., Ros, T., Stoeckel, L., Haller, S., Scharnowski, F., Lewis-Peacock, J., et al. (2017). Closed-loop brain training: the science of neurofeedback. *Nat. Rev. Neurosci.* 18, 86–100. doi: 10.1038/nrn.2016.164

Smith, S. M. (2002). Fast robust automated brain extraction. *Hum. Brain Mapp.* 17, 143–155. doi: 10.1002/hbm.10062

Smith, S. M., Beckmann, C. F., Ramnani, N., Woolrich, M. W., Bannister, P. R., Jenkinson, M., et al. (2005). Variability in fMRI: a re-examination of inter-session differences. *Hum. Brain Mapp.* 24, 248–257. doi: 10.1002/hbm.20080

Smith, S. M., Fox, P. T., Miller, K. L., Glahn, D. C., Fox, P. M., Mackay, C. E., et al. (2009). Correspondence of the brain's functional architecture during activation and rest. *Proc. Natl. Acad. Sci. U.S.A.* 106, 13040–13045. doi: 10.1073/pnas.0905267106

Sockeel, S., Schwartz, D., Pélégrini-Issac, M., and Benali, H. (2016). Large-scale functional networks identified from resting-state EEG using spatial ICA. *PLoS One* 11:e0146845. doi: 10.1371/journal.pone.0146845

Srinivasan, R., Golomb, J. D., and Martinez, A. M. (2016). A neural basis of facial action recognition in humans. *J. Neurosci.* 36, 4434–4442. doi: 10.1523/JNEUROSCI.1704-15.2016

Tagliazucchi, E., and Laufs, H. (2015). Multimodal imaging of dynamic functional connectivity. *Front. Neurol.* 6:10. doi: 10.3389/fneur.2015.00010

Thompson, G. J. (2018). Neural and metabolic basis of dynamic resting state fMRI. *Neuroimage* 180, 448–462. doi: 10.1016/J.NEUROIMAGE.2017.09.010

Trujillo-Barreto, N. J., Aubert-Vázquez, E., and Penny, W. D. (2008). Bayesian M/EEG source reconstruction with spatio-temporal priors. *Neuroimage* 39, 318–335. doi: 10.1016/j.neuroimage.2007.07.062

Tzourio-Mazoyer, N., Landeau, B., Papathanassiou, D., Crivello, F., Etard, O., Delcroix, N., et al. (2002). Automated anatomical labeling of activations in SPM using a macroscopic anatomical parcellation of the mni mri single-subject brain. *Neuroimage* 15, 273–289. doi: 10.1006/nimg.2001.0978

van den Heuvel, M. P., and Hulshoff Pol, H. E. (2010). Exploring the brain network: a review on resting-state fMRI functional connectivity. *Eur. Neuropsychopharmacol.* 20, 519–534. doi: 10.1016/J.EURONEURO.2010.03.008

Vulliemoz, S., Lemieux, L., Daunizeau, J., Michel, C. M., and Duncan, J. S. (2010a). The combination of EEG source imaging and EEG-correlated functional MRI to map epileptic networks. *Epilepsia* 51, 491–505. doi: 10.1111/j.1528-1167.2009.02342.x

Vulliemoz, S., Rodionov, R., Carmichael, D. W., Thornton, R., Guye, M., Lhatoo, S. D., et al. (2010b). Continuous EEG source imaging enhances analysis of EEG-fMRI in focal epilepsy. *Neuroimage* 49, 3219–3229. doi: 10.1016/j.neuroimage.2009.11.055

Vulliemoz, S., Thornton, R., Rodionov, R., Carmichael, D. W., Guye, M., Lhatoo, S., et al. (2009). The spatio-temporal mapping of epileptic networks: Combination of EEG–fMRI and EEG source imaging. *Neuroimage* 46, 834–843. doi: 10.1016/j.neuroimage.2009.01.070

Wang, X., Song, Y., Zhen, Z., and Liu, J. (2016). Functional integration of the posterior superior temporal sulcus correlates with facial expression recognition. *Hum. Brain Mapp.* 37, 1930–1940. doi: 10.1002/hbm.23145

Wirsich, J., Ridley, B., Besson, P., Jirsa, V., Bénar, C., Ranjeva, J. P., et al. (2017). Complementary contributions of concurrent EEG and fMRI connectivity for predicting structural connectivity. *Neuroimage* 161, 251–260. doi: 10.1016/j.neuroimage.2017.08.055

Wolters, C. H., Grasedyck, L., and Hackbusch, W. (2004). Efficient computation of lead field bases and influence matrix for the FEM-based EEG and MEG inverse problem. *Inverse Probl.* 20, 1099–1116. doi: 10.1088/0266-5611/20/4/007

Woolrich, M. W., Ripley, B. D., Brady, M., and Smith, S. M. (2001). Temporal autocorrelation in univariate linear modeling of FMRI data. *Neuroimage* 14, 1370–1386. doi: 10.1006/nimg.2001.0931

Yuan, H., Zotev, V., Phillips, R., Drevets, W. C., and Bodurka, J. (2012). Spatiotemporal dynamics of the brain at rest - Exploring EEG microstates as electrophysiological signatures of BOLD resting state networks. *Neuroimage* 60, 2062–2072. doi: 10.1016/j.neuroimage.2012.02.031

Zhang, Y., Brady, M., and Smith, S. (2001). Segmentation of brain MR images through a hidden Markov random field model and the expectation-maximization algorithm. *IEEE Trans. Med. Imaging* 20, 45–57. doi: 10.1109/42.906424

Zich, C., Debener, S., Kranczioch, C., Bleichner, M. G., Gutberlet, I., and De Vos, M. (2015). Real-time EEG feedback during simultaneous EEG-fMRI identifies the cortical signature of motor imagery. *Neuroimage* 114, 438–447. doi: 10.1016/j.neuroimage.2015.04.020

Zotev, V., Yuan, H., Misaki, M., Phillips, R., Young, K. D., Feldner, M. T., et al. (2016). Correlation between amygdala BOLD activity and frontal EEG asymmetry during real-time fMRI neurofeedback training in patients with depression. *Neuroimage Clin.* 11, 224–238. doi: 10.1016/J.NICL.2016.02.003

Conflict of Interest: The authors declare that the research was conducted in the absence of any commercial or financial relationships that could be construed as a potential conflict of interest.

Copyright © 2020 Abreu, Simões and Castelo-Branco. This is an open-access article distributed under the terms of the Creative Commons Attribution License (CC BY). The use, distribution or reproduction in other forums is permitted, provided the original author(s) and the copyright owner(s) are credited and that the original publication in this journal is cited, in accordance with accepted academic practice. No use, distribution or reproduction is permitted which does not comply with these terms.

frontiers in Neuroscience

ORIGINAL RESEARCH
published: 22 April 2020
doi: 10.3389/fnins.2020.00370

Activatable Fluorescence Imaging of Macrophages in Cerebral Aneurysms Using Iron Oxide Nanoparticles Conjugated With Indocyanine Green

Hiroyuki Ikeda[1,2], Akira Ishii[1], Kohei Sano[2,3]*, Hideo Chihara[1], Daisuke Arai[1], Yu Abekura[1], Hidehisa Nishi[1], Masahiro Ono[2], Hideo Saji[2] and Susumu Miyamoto[1]*

[1] Department of Neurosurgery, Kyoto University Graduate School of Medicine, Kyoto, Japan, [2] Department of Patho-Functional Bioanalysis, Graduate School of Pharmaceutical Sciences, Kyoto University, Kyoto, Japan, [3] Laboratory of Biophysical Chemistry, Kobe Pharmaceutical University, Kobe, Japan

Background and Purpose: Chronic inflammation is involved in the formation and enlargement of cerebral aneurysms (CAs), with macrophages playing a key role in the process. The present study evaluated visualization of macrophages present in CAs using an activatable fluorescent probe (IONP-ICG) comprising an iron oxide nanoparticles (IONPs) conjugated with indocyanine green (ICG).

Methods: IONP-ICG was intravenously administered to 15-week-old CA model rats (n = 8), and *ex vivo* near-infrared fluorescence (NIRF) imaging and histological assessment of exposed CAs and cerebral arteries were performed 48 h later. Similar evaluations were performed in the control group, which included CA model rats given IONPs or ICG (n = 8 each).

Results: ICG-derived NIRF signals were detected in three IONP-ICG group rats but not in IONP or ICG control groups. Among the three rats that exhibited signals, NIRF signal accumulation was observed in the CA of two rats and at the site of hemodynamic stress in the left posterior cerebral artery in one rat. Histologically, NIRF signals correlated strongly with macrophage localization. A total of 13 CAs formed in the IONP-ICG group. The number of macrophages in the CA wall was significantly greater in the two CAs that exhibited NIRF signals compared to the remaining 11 CAs that did not (P = 0.037). Moreover, all 11 CAs that did not exhibit NIRF signals were iron-negative, while the two CAs that exhibited NIRF signals were both iron-positive (P = 0.013).

Conclusion: NIRF imaging using an activatable IONP-ICG probe is feasible for detecting the macrophage-rich regions in CAs and the cerebral artery wall, which is considered an early lesion in the process of CA formation.

Keywords: macrophage, inflammation, cerebral aneurysm, iron oxide nanoparticles, fluorescent imaging, indocyanine green

OPEN ACCESS

Edited by:
Jorge Valero, Achucarro Basque Center for Neuroscience, Spain

Reviewed by:
Ashwin B. Parthasarathy, University of South Florida, United States
João O. Malva, University of Coimbra, Portugal

****Correspondence:***
Hiroyuki Ikeda
rocky@kuhp.kyoto-u.ac.jp
Kohei Sano
ksano@kobepharma-u.ac.jp

Specialty section:
This article was submitted to Brain Imaging Methods, a section of the journal Frontiers in Neuroscience

Received: *24 September 2019*
Accepted: *26 March 2020*
Published: *22 April 2020*

Citation:
Ikeda H, Ishii A, Sano K, Chihara H, Arai D, Abekura Y, Nishi H, Ono M, Saji H and Miyamoto S (2020) Activatable Fluorescence Imaging of Macrophages in Cerebral Aneurysms Using Iron Oxide Nanoparticles Conjugated With Indocyanine Green. Front. Neurosci. 14:370. doi: 10.3389/fnins.2020.00370

INTRODUCTION

Chronic inflammation is involved in the formation and enlargement of cerebral aneurysms (CAs), and macrophages, which are the primary inflammatory cells that accumulate in the aneurysm wall, play an essential role in these processes (Aoki et al., 2007a,b, 2017a; Kanematsu et al., 2011; Kataoka, 2015). Moreover, a greater number of macrophages are known to be present in the aneurysm wall

of ruptured CAs compared to unruptured, suggesting an association between macrophages and CA rupture (Frosen et al., 2004). For this reason, macrophage imaging may enable identification of early lesions in the CA formation process as well as prediction of enlargement and rupture. As a molecular imaging method that detects chronic inflammation, near-infrared fluorescence (NIRF) has been gaining attention. Specifically, NIRF probes are highly sensitive, offer relatively good tissue permeability, present minimal effects from autofluorescence, and exhibit quantifiable fluorescence intensity (Deguchi et al., 2006; Kaijzel et al., 2010). However, effective preclinical NIRF probes have yet to be reported in the CA field.

Iron oxide nanoparticles (IONPs) have been widely utilized *in vivo* due to their high biocompatibility and low toxicity (Arami et al., 2015), and the ultrasmall superparamagnetic IONP ferumoxytol (AMAG Pharmaceuticals, Lexington, MA, United States) gained approval from the United States Food and Drug Administration in 2009 (Lu et al., 2010). Since intravenously administered ferumoxytol is non-specifically taken up by macrophages, IONPs accumulate at inflammatory sites where macrophages are present, thereby changing the local magnetic field (Hasan et al., 2012; Aoki et al., 2017b). This property suggests its potential for use in magnetic resonance imaging, enabling non-invasive imaging of macrophages accumulating in the CA of humans. On the other hand, indocyanine green (ICG), another biocompatible and minimally toxic substance (Cherrick et al., 1960), is the only NIRF dye approved by the United States Food and Drug Administration to be used for clinical purposes. For these reasons, a probe incorporating IONPs and ICG may offer a highly biocompatible NIRF probe that targets macrophages accumulating in CAs.

When multiple fluorescent molecules are in proximity to each other, their interaction leads to fluorescence self-quenching (Hama et al., 2007). Moreover, interactions between ICG and carrier molecules can lead to auto-quenching (Ogawa et al., 2009). Considering these properties, it is possible that ICG-conjugated carrier molecules could be used as target cell-specific activatable probes with high background signal ratios. Since CAs are relatively small targets, detection of chronic inflammation using a target cell-activatable probe would be diagnostically useful. We previously synthesized a NIRF probe (IONP-ICG) comprising IONPs conjugated with ICG and demonstrated its potential as an activatable probe which targets macrophages (Ikeda et al., 2018). In particular, we confirmed macrophage uptake of quenched IONP-ICG *in vitro* and intracellular activation of NIRF. Furthermore, IONP-ICG synthesized by mixing with a molecular ratio of 1:20 IONP:ICG enabled NIRF imaging of macrophages in atherosclerotic plaques with the greatest background ratio. Therefore, we postulated that NIRF imaging using an IONP-ICG probe might enable targeted visualization of CA macrophages, facilitating prediction of the formation, enlargement, and rupture of CAs. The present study evaluated whether macrophages localized to CAs can be specifically detected using our activatable IONP-ICG NIRF probe.

MATERIALS AND METHODS

Materials

IONPs coated with dextran (nanomag®-D-spio; diameter, 20 nm; mean molecular weight, 3500 kDa; amino groups on particle surface) were purchased from Corefront Co. (Tokyo, Japan). ICG-EG4-Sulfo-OSu was purchased from Dojindo Molecular Technologies (Kumamoto, Japan). Methoxypolyethylene glycol (PEG) succinate *N*-hydroxysuccinimide (NHS) (PEG-NHS-ester; molecular weight, 2 kDa; SUNBRIGHT® ME-020CS) was purchased from NOF America Co. (White Plains, NY, United States). ICG was purchased from Tokyo Chemical Industry Co., Ltd. (Tokyo, Japan).

Synthesis of IONP-ICG and IONPs Conjugated With PEG (IONP-PEG)

Synthesis of IONP-ICG was performed according to our previous report (Ikeda et al., 2018). Briefly, IONP-ICG was synthesized by mixing the IONP nanomag®-D-spio (2.4 mg Fe, 1.43 nmol) and ICG-EG4-Sulfo-OSu (8.5 mmol/L in dimethyl sulfoxide) in a 1:20 IONP:ICG molecular ratio (ICG-EG4-Sulfo-OSu, 28.6 nmol). The concentration of IONPs and ICG in synthesized IONP-ICG was determined by measuring the absorption at 535 and 768 nm using a Shimadzu UV-Vis NIR system (UV-1800; Kyoto, Japan) to determine the number of ICG molecules conjugated to each IONP. As a control probe, IONP-PEG was synthesized by mixing the IONP nanomag®-D-spio (2.4 mg Fe, 1.43 nmol) and PEG-NHS-ester (1.43 mg, 715 nmol) to quench the amino groups of the particles.

Animal Models

All animal experiments were conducted following institutional guidelines and were approved by the Kyoto University Animal Care Committee. CA model rats were prepared as described previously (Hashimoto et al., 1980), with some modifications. CAs were formed by inducing hemodynamic stress through ligation of the left renal artery and left common carotid artery in 7-week-old male Sprague Dawley rats (Japan SLC, Shizuoka, Japan). These surgeries were conducted under general anesthesia with intraperitoneal injection of 50 mg/kg pentobarbital. Rats were fed chow containing 8% NaCl and 0.12% 3-aminopropionitrile (Tokyo Chemical), an inhibitor of lysyl oxidase that catalyzes the cross-linking of collagen and elastin, for 8 weeks. Furthermore, 3-aminopropionitrile fumarate (1000 mg/kg; Tokyo Chemical) was injected intraperitoneally four times at weekly intervals immediately after surgery to promote enlargement of CAs. At 15 weeks, IONP-ICG group rats (n = 8) were intravenously injected with IONP-ICG (27.9 mg Fe/kg, 0.5 mmol Fe/kg, 16.6 nmol IONP-ICG/kg) via the tail vein. The mean number of ICG molecules conjugated to each IONP in IONP-ICG was 7.5 ± 0.6 in the present study. Control group rats were injected with either IONP-PEG (27.9 mg Fe/kg, 0.5 mmol Fe/kg, 16.6 nmol IONP-PEG/kg; n = 8) or ICG (96.6 μg ICG/kg, 125 nmol ICG/kg; n = 8). In total, 24 rats were used in the present study (n = 8 per group).

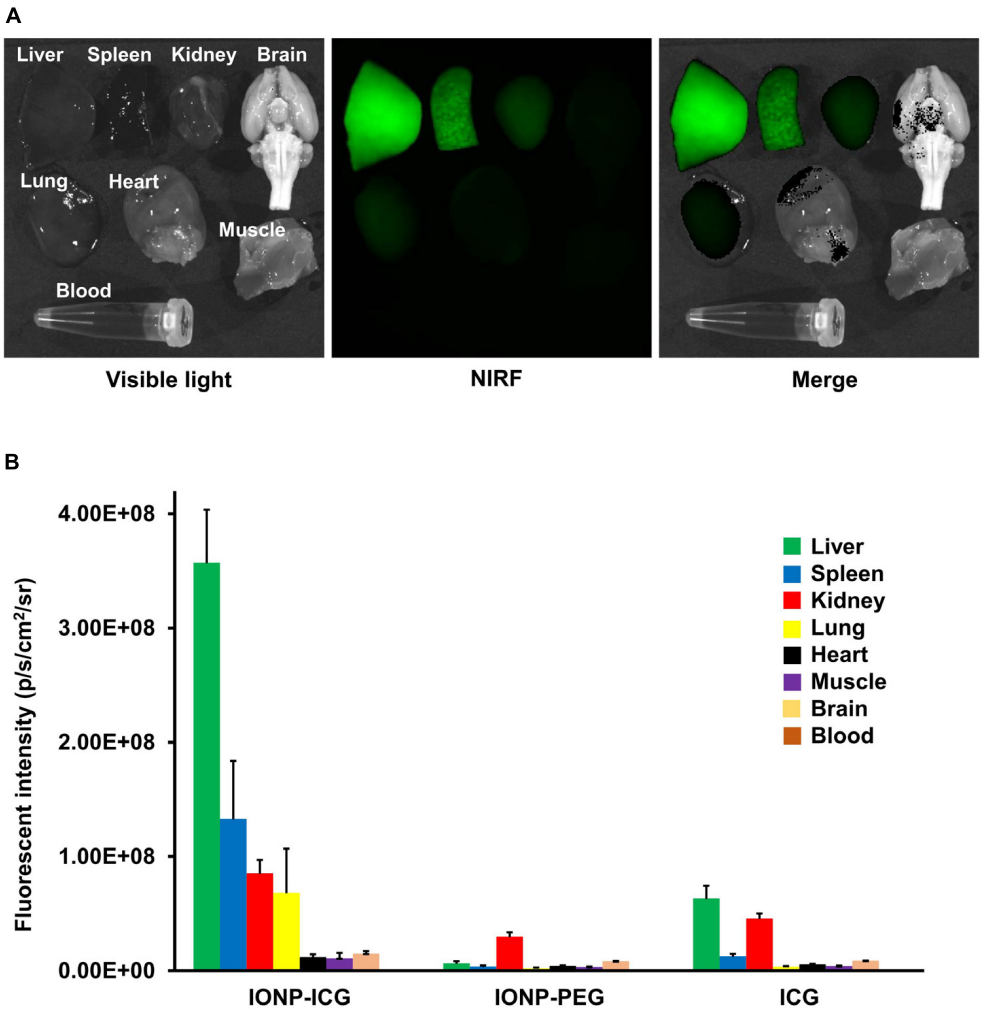

FIGURE 1 | Representative images after IONP-ICG administration and biodistribution of NIRF signals 48 h after administration of probes. **(A)** Representative images of visible light, NIRF, and merged imaging of the liver, spleen, kidney, lung, heart, muscle, brain, and blood after IONP-ICG administration. **(B)** Graphical representation of NIRF signal intensity in each organ after administration of IONP-ICG, IONP-PEG, and ICG (n = 8 each). All values are expressed as the mean ± standard deviation.

Biodistribution Study

48 h after probe administration, rats were deeply anesthetized with an intraperitoneal injection of 50 mg/kg pentobarbital and perfused transcardially with 4% paraformaldehyde after 500 μL of blood was collected from the heart to measure the fluorescence intensity. After euthanasia by cervical dislocation and decapitation, the brain along with cerebral arteries, liver, spleen, kidneys, lungs, heart, and muscles were dissected. Cerebral arteries were stripped from the brain after the microscopic observation described below. Fluorescence images of tissues were acquired using an IVIS Imaging System 200 (excitation/emission, 745/820 nm; exposure time, 1 s; PerkinElmer, Waltham, MA, United States) to determine the distribution of ICG. Similar-sized regions of interest were circled within respective tissues, and the mean fluorescence intensity (p/s/cm^2/sr) of each region of interest after subtraction of background fluorescence was measured.

NIRF Imaging

Excised brains were washed with 0.04% bromophenol blue solution to facilitate visualization of cerebral arteries by visible light imaging then immediately washed with phosphate-buffered saline. After, brains were imaged *ex vivo* using a Nuance EX multispectral imaging camera (PerkinElmer) mounted on an MVX10 macro zoom fluorescence stereomicroscope (Olympus, Tokyo, Japan) equipped with a Cy7 filter set (excitation/emission, 670–745/776 nm long-pass). NIRF images of the brain were acquired by multispectral imaging at 10-nm wavelength increments from 770 to 950 nm with an exposure time of 5 s. Nuance version 3.0.2 software (PerkinElmer) was used to examine the fluorescence signals derived from ICG by measuring the fluorescence spectra, unmixing the autofluorescence spectra of the tissues, and eliminating background noise. Visible light and NIRF imaging were performed from the ventral side of the

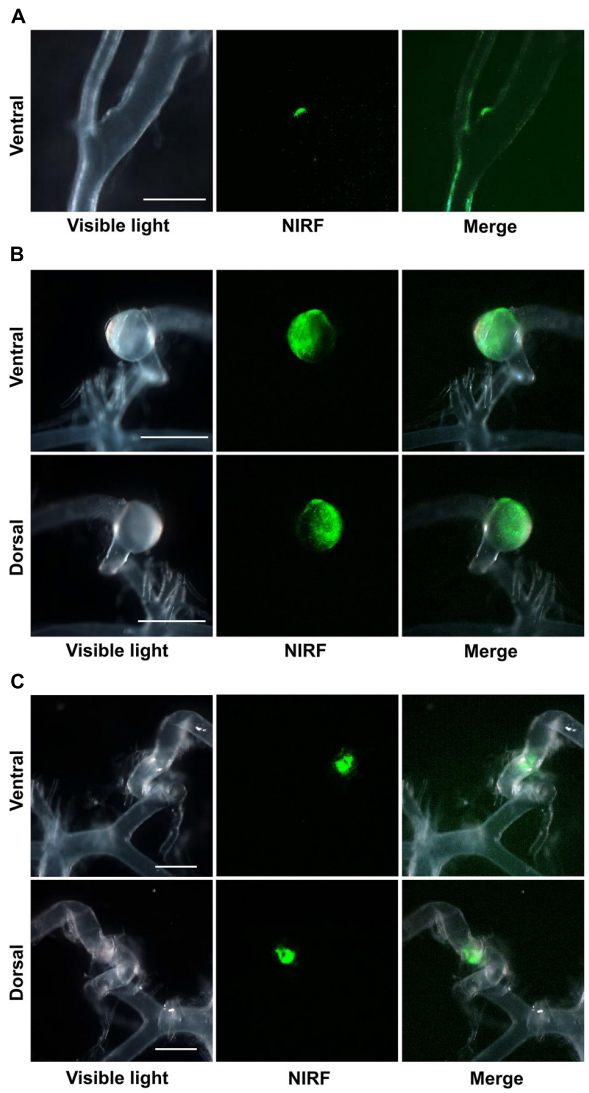

FIGURE 2 | NIRF imaging of excised CAs and cerebral arteries. **(A)** Visible light, NIRF, and merged NIRF and visible light images from the ventral side of NIRF-case 1. NIRF signals were observed at the bulging CA that formed along the right anterior cerebral artery at a site distal to the bifurcation of the right anterior cerebral and olfactory arteries. Scale bar, 500 μm; original magnification, 25×. **(B)** Visible light, NIRF, and merged NIRF and visible light images from both ventral and dorsal sides of NIRF-case 2. NIRF signals were observed in the saccular CA that formed at the bent portion of the left posterior cerebral artery. An abundance of spotted NIRF signals was observed at the aneurysm wall on the larger curvature side of the CA, while NIRF signal was hardly detected at the CA wall on the smaller curvature side. Scale bars, 1 mm; original magnification, 25×. **(C)** Visible light, NIRF, and merged NIRF and visible light images from both ventral and dorsal sides of NIRF-case 3. NIRF signals were localized to the bent portion of the left posterior cerebral artery, and a CA had not formed at this site. Scale bars, 500 μm; original magnification, 25×.

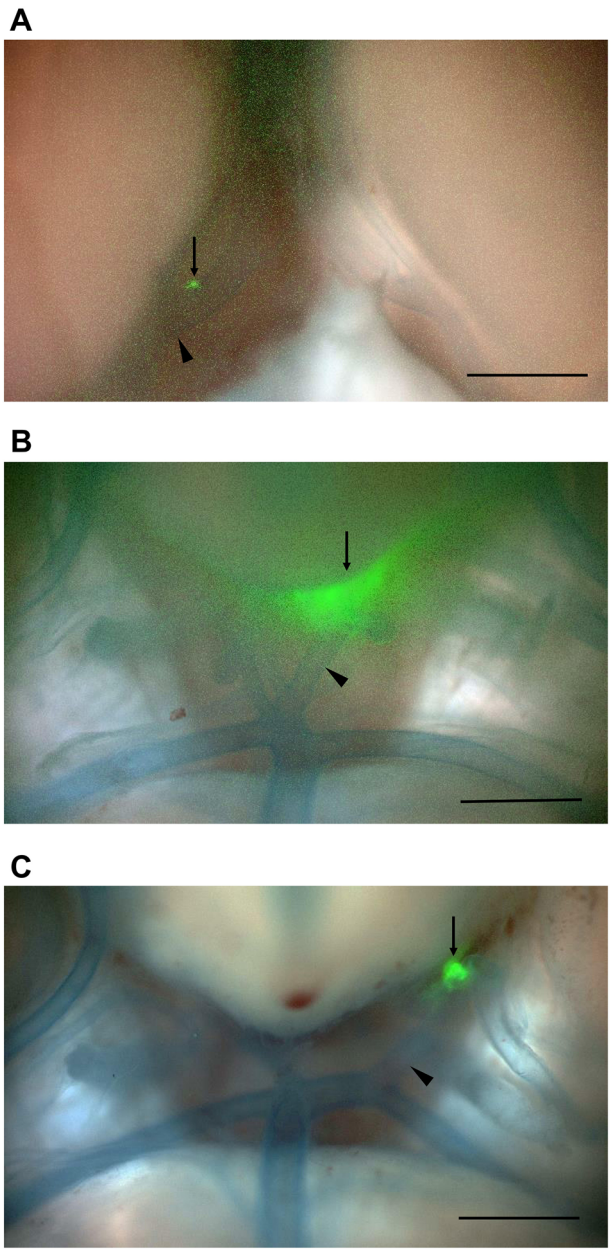

FIGURE 3 | NIRF imaging of CAs and cerebral arteries with the brain in the background. Merged NIRF and visible light images from the ventral side. **(A)** NIRF signals in the bulging CA (arrow) that formed along the right anterior cerebral artery at a site distal to the bifurcation (arrowhead) of the right anterior cerebral and olfactory arteries in NIRF-case 1 were detected. **(B)** NIRF signals in the saccular CA (arrow) that formed at the bent portion of the left posterior cerebral artery (arrowhead) in NIRF-case 2 were detected. **(C)** Localized NIRF signals at the bent portion (arrow) of the left posterior cerebral artery (arrowhead) in NIRF-case 3 were clearly detected. Scale bars, 1 mm; original magnification, 25×.

brain. Cerebral arteries as well as whole circle of Willis arterial rings stripped from the brain underwent visible light and NIRF imaging.

Histology and Fluorescence Microscopy

Cerebral aneurysm was defined as bulging or saccular shape of the cerebral artery wall with disruption of the internal elastic

lamina. CAs were searched by stereomicroscopy from the ventral side of the brain and from both ventral and dorsal sides of cerebral arteries stripped from the brain. Bifurcations of the right anterior cerebral and olfactory arteries, including the CAs, as well as stereomicroscopy-detected CAs in the area around the circle of Willis arterial rings were carefully excised. Two or more CAs arising side-by-side at the same location were evaluated separately. In addition, if CAs could not be detected by stereomicroscopy, arteries showing NIRF signals derived from ICG were still excised. Cryosections (thickness, 10 μm) were obtained from freshly frozen samples. ICG NIRF signals were observed using a BZ-X710 fluorescence microscope (KEYENCE, Osaka, Japan) equipped with a filter for ICG (excitation/emission, 775–825/845–900 nm). Immunohistological staining was then performed using an anti-mouse ionized calcium binding adapter molecule 1 (Iba1) antibody (Wako Pure Chemical Industries, Osaka, Japan) for localization of macrophages. Iron staining was performed using a Berlin blue staining set (Wako Pure Chemical Industries). Elastica van Gieson (EVG) staining was performed to assess disruption of the internal elastic lamina. Light microscopy was performed using an FSX100 microscope (Olympus).

Morphological evaluation of CAs was performed as described previously (Ikedo et al., 2017), with some modifications. CA size was defined as the mean maximum height and width including the aneurysm wall. Aneurysm wall thickness was measured at the tip of the CA. Cell counting was performed as described previously (Aoki et al., 2009), with some modifications. Macrophages within the aneurysm wall were manually counted under 40 × magnification in a selected circular field (diameter, 100 μm) at the tip of the CA. The same lower threshold value was set for obtained images using cellSens Dimension software (Olympus) to determine whether cells were immunostain-positive or not; detected cells were defined as positive. For iron staining, blue spots within the CA wall corresponding to iron deposition were defined as iron-positive.

Statistical Analysis

Statistical analyses were performed using JMP version 11 software (SAS Institute, Cary, NC, United States). Quantitative data were expressed as the mean ± standard deviation. Fisher's exact test between two groups and Pearson's Chi-square test between three groups were used to examine categorical variables. The Mann-Whitney *U*-test between two groups and Kruskal-Wallis test followed by the Steel-Dwass test between three groups or more were used for continuous variables. A $P < 0.05$ was considered statistically significant.

RESULTS

Biodistribution Study

The results of biodistribution studies 48 h after probe administration are summarized in **Figure 1**. In the IONP-ICG group, the greatest accumulation of NIRF signal was in the liver, followed by the spleen, kidney, and lung. NIRF signal intensity was significantly lower in the heart, muscle, brain, and blood ($P < 0.05$). In the IONP-PEG group, the NIRF signal was highest in the kidney, with barely any detected in other organs. In the ICG group, the NIRF signal was most intense in the liver followed by the kidney; accumulation was negligible in other organs. Comparison of each organ between the three groups revealed significantly greater NIRF signal accumulation in the IONP-ICG compared to IONP-PEG and ICG groups for all organs except the blood ($P < 0.001$). NIRF signal intensities in the blood were extremely low in all three groups and did not differ significantly between them ($P = 0.11$).

NIRF Imaging

ICG-derived NIRF signals were detected in the CA or cerebral artery of three IONP-ICG rats by NIRF imaging. In contrast, ICG-derived NIRF signals were not detected in IONP-PEG or ICG groups. **Figures 2**, **3** show stereomicroscopic findings from the three rats that exhibited NIRF signals ("NIRF-cases 1–3"). In NIRF-case 1, NIRF signal was observed at a bulging CA that formed along the right anterior cerebral artery distal to the bifurcation of the right anterior cerebral and olfactory arteries (**Figure 2A**). NIRF signal could be detected when this CA was examined with the brain in the background (**Figure 3A**). In NIRF-case 2, NIRF signal was observed at a saccular CA formed at the bent portion of the left posterior cerebral artery. NIRF signals accumulated abundantly in a spotted manner at the aneurysm wall of the larger curvature of the CA, with negligible detection on the aneurysm wall of the smaller curvature of the CA (**Figure 2B**). NIRF signal could be detected when this CA was examined with the brain in the background (**Figure 3B**). In NIRF-case 3, NIRF signal was localized at a bent portion of the left posterior cerebral artery, and no CA had formed at this site according to stereomicroscopic examination (**Figure 2C**). When this cerebral artery was examined with the brain in the background, the NIRF signal in the cerebral artery was clearly detectable (**Figure 3C**).

Morphological and Histological Findings of CAs

Microscopic and histological findings detected CAs in all 24 rats included in the study, amounting to 38 total CAs. Of them, 13 were in the IONP-ICG group, 13 in the IONP-PEG, and 12 in the ICG group. **Table 1** shows the details of morphological and histological findings of all CAs within each group. Of the 38 CAs, 33 formed at the bifurcation of the right anterior cerebral and olfactory arteries, four at the left posterior cerebral artery, and one at the anterior communicating artery. All saccular CAs formed at the left posterior cerebral artery, with one in the IONP-ICG group, and three in the IONP-PEG; saccular CAs did not form in the ICG group.

Mean CA size was 150 ± 190 μm (range, 41–1028 μm) overall, with 130 ± 176 μm (range, 41–710 μm) in the IONP-ICG group, 208 ± 257 μm (range, 48–1028 μm) in the IONP-PEG group, and 101 ± 60 μm (range, 43–247 μm) in the ICG group. The mean size of the four saccular CAs at the left posterior cerebral artery was 573 ± 366 μm (range, 268–1028 μm), which was significantly greater than that of bulging CAs (97 ± 48 μm; range, 41–247 μm; $P = 0.0013$). Mean CA wall thickness was 17.2 ± 22.7 μm (range,

TABLE 1 | Morphological and histological evaluations of cerebral aneurysms.

	Total (*n* = 24)	IONP-ICG (*n* = 8)	IONP-PEG (*n* = 8)	ICG (*n* = 8)
Aneurysm	38	13	13	12
Saccular aneurysm	4	1	3	0
Mean aneurysm size (μm)	150 ± 190	130 ± 176	208 ± 257	101 ± 60
Mean aneurysm wall thickness (μm)	17.2 ± 22.7 (*n* = 37)	16.8 ± 5.6	22.5 ± 33.8 (*n* = 12)	11.5 ± 3.5
Mean number of macrophages	6.6 ± 7.5	5.8 ± 6.3	10.0 ± 2.8	3.8 ± 2.0
Iron positivity	5 (13%)	2 (15%)	3 (23%)	0 (0%)

In IONP-ICG, IONP-PEG, and ICG groups, the numbers of cerebral aneurysms found were 13, 13, and 12, respectively. Saccular aneurysms were observed in IONP-ICG and IONP-PEG groups. The aneurysm size, aneurysm wall thickness, and number of macrophages in cerebral aneurysms were measured. These values are shown as the mean ± standard deviation. Numbers in parentheses (iron positivity) correspond to percentages of the total number of cerebral aneurysms in that group. None of the items listed in this Table differed significantly between individual groups. IONP-ICG, iron oxide nanoparticles (IONPs) conjugated with indocyanine green (ICG); IONP-PEG, IONPs conjugated with methoxypolyethylene glycol (PEG).

6–118 μm) overall, with 16.8 ± 5.6 μm (range, 7–83 μm) in the IONP-ICG group, 22.5 ± 33.8 μm (range, 6–118 μm) in the IONP-PEG group, and 11.5 ± 3.5 μm (range, 6–18 μm) in the ICG group. One saccular CA in the left posterior cerebral artery in the IONP-PEG group did not have a lumen, preventing measurement of CA wall thickness. Therefore, this CA was excluded from the calculation of overall mean CA wall thickness. The mean wall thickness of three saccular CAs of the left posterior cerebral artery was 88.7 ± 30.0 μm (range, 65–118 μm), which is significantly thicker than that of bulging CAs (10.9 ± 3.4 μm; range, 6.0–18.0 μm; $P = 0.0047$).

The mean number of macrophages was 6.6 ± 7.5 (range, 0–36) overall, with 5.8 ± 6.3 (range, 0–20) in the IONP-ICG group, 10.0 ± 2.8 (range, 1–36) in the IONP-PEG group, and 3.8 ± 2.0 (range, 1–7) in the ICG group. The mean number of macrophages in the four saccular CAs of the left posterior cerebral artery was 24.3 ± 8.0 (range, 18–36), which was significantly greater than that of bulging CAs (4.5 ± 3.6; range, 0–20; $P = 0.0014$). An iron-positive wall was observed in five CAs (13%) overall, with two (15%) in the IONP-ICG group, three (23%) in the IONP-PEG, and 0 (0%) in the ICG group. All four saccular CAs of the left posterior cerebral artery were iron-positive. None of the items listed in **Table 1** differed significantly between individual groups (number of CAs, $P = 0.99$; number of saccular CAs, $P = 0.16$; CA size, $P = 0.15$; CA wall thickness, $P = 0.98$; number of macrophages, $P = 0.13$; iron positivity, $P = 0.22$).

Histological Findings of Lesions With NIRF Signals

Figure 4 shows histological findings for the three rats with NIRF signals in a CA or cerebral artery. In NIRF-case 1, a very small CA formed at the bifurcation of the right anterior cerebral and olfactory arteries, and a bulging CA formed along the right anterior cerebral artery distal to the very small CA. Fluorescence microscopic examination of an unstained section detected NIRF signal at the wall of the distal CA with the strongest intensity at its tip. This NIRF signal in the CA wall correlated strongly with the localization of Iba1-positive macrophages. Iron staining showed blue areas in the CA wall with high NIRF signal. EVG staining revealed continuous disruption of the internal elastic lamina from the bifurcation of the right anterior cerebral and olfactory arteries to the distal side of the distal CA (**Figure 4A**). In NIRF-case 2, the wall on the larger curvature side of the saccular CA was thicker than the artery wall, but the CA wall on the smaller curvature side had not thickened. Fluorescence microscopy of the unstained section showed an abundance of spotted NIRF signals at the thickened CA wall, but negligible signals at the CA wall that had not thickened. The NIRF signal in the CA wall correlated strongly with Iba1-positive macrophage localization, and iron staining showed very small blue areas scattered within the thickened CA wall (**Figure 4B**). In NIRF-case 3, fluorescence microscopy of the unstained section showed NIRF signals localized to the adventitia of the artery wall. Iba1-positive macrophages accumulated along the entire circumference of the artery wall adventitia. The NIRF signal of the artery wall correlated strongly with Iba1-positive macrophage localization, and iron staining showed a few very small blue areas distributed at the artery wall adventitia. EVG staining did not detect disruptions of the internal elastic lamina of the artery wall (**Figure 4C**).

To determine the type of CAs that exhibited NIRF signals, the two CAs in the IONP-ICG group with NIRF signals were compared with the 11 CAs of this group without signals (**Table 2**). Although the mean size of CAs with NIRF signals (399 μm; actual size, 89, 710 μm) was obviously larger than those without (81 ± 29 μm; range, 41–120 μm), the difference was no significant ($P = 0.28$). The mean wall thickness of CAs with and without NIRF signals was 49.0 μm (actual thickness, 15, 83 μm) and 10.9 ± 3.9 μm (range, 7–18 μm), respectively; this difference was not significant ($P = 0.092$). On the other hand, the mean number of macrophages in CAs with NIRF signals (19.0; actual numbers, 18, 20) was significantly different from those without signals (3.4 ± 2.3; range, 0–7; $P = 0.037$). Furthermore, both CAs with NIRF signals showed iron-positive staining, while all 11 CAs without signals were iron-negative, indicating that CAs with NIRF signals were significantly more likely to be iron-positive ($P = 0.013$).

DISCUSSION

Using an activatable IONP-ICG NIRF probe, the present study successfully detected localized macrophage-rich CA-associated chronic inflammation in rats. Specifically, histological findings showed a strong correlation between NIRF signals in the

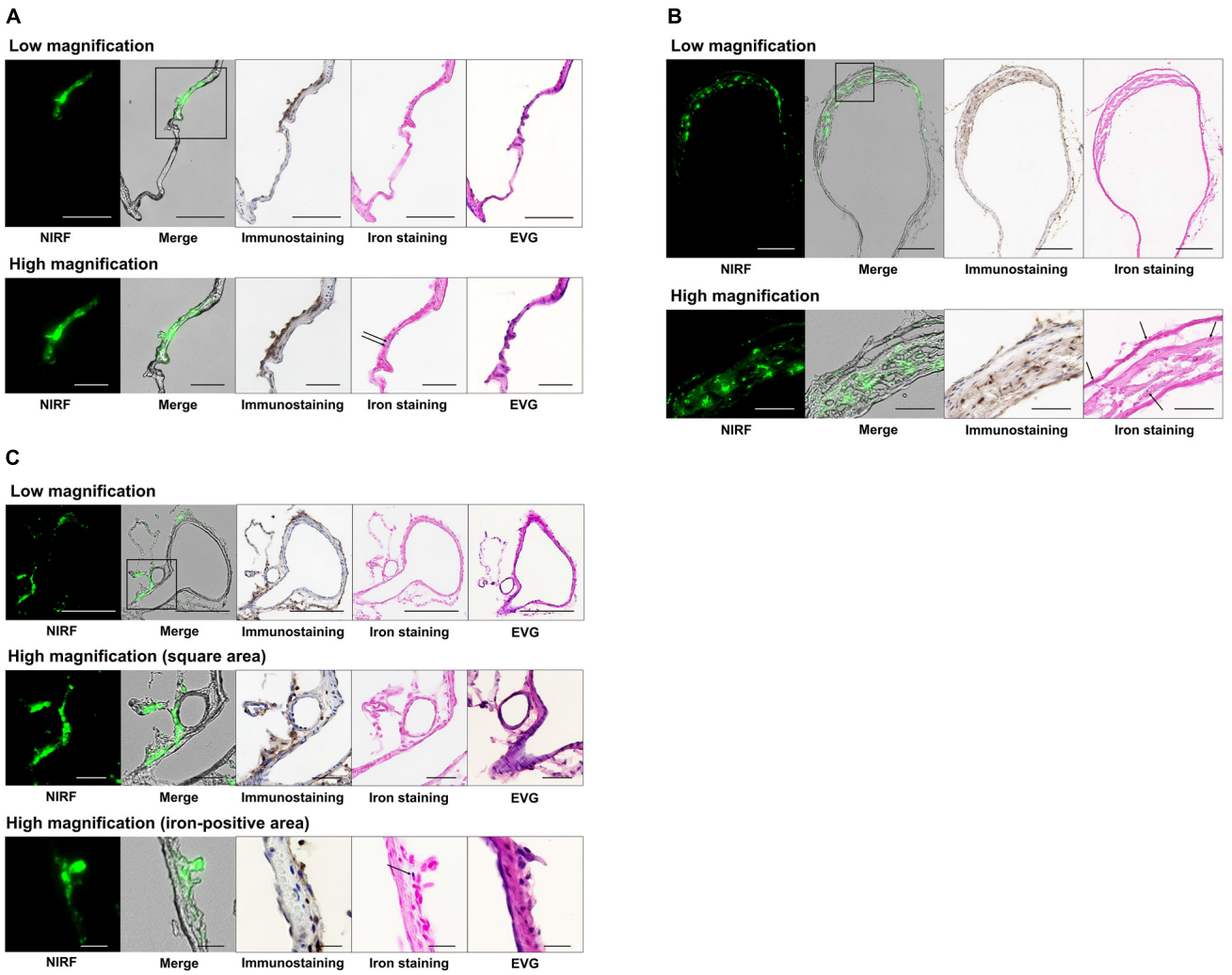

FIGURE 4 | Histology and fluorescence microscopy of CAs and cerebral arteries with NIRF signals. NIRF, merged NIRF and bright-field images, Iba1 immunostaining, iron staining, and EVG staining were performed. High magnification images other than the iron-positive area of **(C)** depict the square region within the low magnification images. **(A)** CA in NIRF-case 1. NIRF signals correlated very well with the presence of macrophage infiltration (Iba1 immunostaining) in the CA. Iron staining showed blue areas (arrows) at the CA wall with a high NIRF signal. EVG staining showed continuous disruption of the internal elastic lamina from the bifurcation of the right anterior cerebral and olfactory arteries to the distal side of the distal CA wall. Scale bars: low magnification, 100 μm; high magnification, 50 μm. **(B)** CA in NIRF-case 2. NIRF signals correlated very well with the presence of macrophage infiltration in the CA. Iron staining showed very small blue areas (arrows) scattered within the thickened CA wall. Scale bars: low magnification, 200 μm; high magnification, 50 μm. **(C)** Left posterior cerebral artery in NIRF-case 3. NIRF signals correlated very well with the presence of macrophage infiltration in the adventitia of the cerebral artery. Iron staining shows a small number of very small blue areas (arrow) at the adventitia. EVG staining did not detect any disruption of the internal elastic lamina of the artery wall. Scale bars: low magnification, 200 μm; high magnification (square area), 50 μm; high magnification (iron-positive area), 20 μm.

CA wall and macrophages-rich regions. Furthermore, iron positivity in the same area indicates that NIRF signals were derived from the IONP-ICG administered to live rats. In other words, intravenously administered IONP-ICG was taken up by macrophages accumulating in the CA wall, leading to activation of quenched IONP-ICG fluorescence. Thus, we concluded that macrophage localization can be determined in CAs through NIRF imaging.

The quenching of fluorescence probably occurred via the interaction between ICG and IONP (energy transfer) (Ogawa et al., 2009; Sano et al., 2013). Although the detailed mechanism on fluorescence activation was not clarified in this study and our previous report (Ikeda et al., 2018), we speculated the fluorescence could be activated when the distance between ICG molecule and IONP was increased after being processed in the lysosomes. INOPs are taken by macrophages and retained in lysosomes (Muller et al., 2007).Therefore, we speculated that IONP-ICG was activated in lysosomes and emitted fluorescence like the previously reported target cell-activatable probe (Ogawa et al., 2009; Urano et al., 2009).

As mentioned above, IONPs decrease magnetic resonance imaging signals in the aneurysm wall when taken up by

TABLE 2 | Relationship between cerebral aneurysms with and without near-infrared fluorescence (NIRF) signals after administration of IONP-ICG.

	Total aneurysm (*n* = 13)	NIRF (+) (*n* = 2)	NIRF (–) (*n* = 11)	*P*-value
Saccular aneurysm	1 (8%)	1 (50%)	0 (0%)	0.15
Mean aneurysm size (μm)	130 ± 176	399 [89, 710]	81 ± 29	0.28
Mean aneurysm wall thickness (μm)	16.8 ± 5.6	49.0 [15, 83]	10.9 ± 3.9	0.092
Mean number of macrophages	5.8 ± 6.3	19.0 [18, 20]	3.4 ± 2.3	0.037
Iron positivity	2 (15%)	2 (100%)	0 (0%)	0.013

Among cerebral aneurysms (n = 13) found in IONP-ICG group, there were two cerebral aneurysms with NIRF signals. The aneurysm size, aneurysm wall thickness, and number of macrophages in cerebral aneurysms were measured. These values are shown as the mean ± standard deviation except for NIRF (+) group. In NIRF (+) group, actual values measured are described in brackets. Numbers in parentheses (saccular aneurysm and iron positivity) correspond to percentages of the total number of cerebral aneurysms in that group. P-values were calculated by Mann-Whitney U test, except for iron positivity (Fisher's exact test). IONP-ICG was accumulated in the cerebral aneurysms with large number of macrophages. IONP-ICG, iron oxide nanoparticles (IONPs) conjugated with indocyanine green (ICG).

macrophages (Hasan et al., 2012; Aoki et al., 2017b). A previous report showed that acetylsalicylic acid was able to inhibit IONP-induced decreases in magnetic resonance signal intensity by reducing the content of macrophages in the aneurysm wall (Hasan et al., 2013). Thus, quantitative evaluation of NIRF signals in the CA not only facilitates identification of macrophage localization sites, but also provides an index of macrophage content therein. In the present study, signals were only detected in two CAs in the IONP-ICG group, suggesting that IONP-ICG NIRF detection is associated with a greater accumulation of macrophages in the CA wall. On the other hand, the number of macrophages was significantly smaller in CAs in which signals were too low to detect by NIRF imaging.

In general, macrophages are categorized into two subsets: classically activated M1 macrophages that demonstrate pro-inflammatory effects and alternatively activated M2 macrophages that exhibit anti-inflammatory effects. Development of CAs is characterized by heightened polarization of M1 macrophages (Shao et al., 2017). Based on a previous *in vitro* experiment demonstrating that divergent differentiation of macrophages into M1 or M2 subsets does not affect uptake of IONPs (Aoki et al., 2017b), NIRF localization in the present study appears to reflect macrophage localization in general, with no predilection for different subsets. However, a mixture of macrophages with and without NIRF signal was evident within the same cryosection of NIRF-cases 1–3 (**Figure 4**), indicating that the IONP-ICG uptake capacity of macrophages may differ partially depending on the macrophage subset, extent of activation, or extent of accumulation.

The left posterior cerebral artery of NIRF-case 3 in the current study did not exhibit CAs or disruptions of the internal elastic lamina. However, NIRF signal was detected at the bent portion of the left posterior cerebral artery, with macrophage accumulation in the artery wall adventitia, indicating the accumulation of macrophages with a high IONP-ICG uptake capacity. In our CA rat models, the left common carotid artery was ligated which caused hemodynamic stress in the left posterior cerebral artery, representing collateral circulation for areas perfused by the left common carotid artery. The four saccular CAs at the left posterior cerebral artery that experienced hemodynamic stress were significantly larger and showed thicker walls compared to bulging CAs. This is attributable to the presence of numerous iron-positive macrophages, which could contribute to CA enlargement. Therefore, in NIRF-case 3, IONP-ICG was taken up by macrophages which could induce inflammatory responses in the left posterior cerebral artery, suggesting that early detection of a pathological stage prior to disruption of the internal elastic lamina that ultimately transforms into a CA.

Macrophages play a major role in chronic inflammation of CAs and are thought to be associated with their formation, enlargement, and rupture. Anatomical factors such as aneurysm size, shape, and site of occurrence are important for evaluating the rupture risk of unruptured CAs and determining whether surgical procedures should be performed (Morita et al., 2012). Moreover, while size is a primary risk factor for rupture, small CAs can enlarge over time, potentially resulting in rupture and subarachnoid hemorrhage. Macrophage-based imaging may enable visualization of clinically crucial aspects, namely the formation and enlargement of CAs, as well as the localization of lesions that may rupture. CAs treated with radical surgery under craniotomy occasionally lead to re-enlargement and subarachnoid hemorrhage (Tsutsumi et al., 2001; Hokari et al., 2016). By visualizing the inflammatory response in CAs (i.e., macrophage localization), intraoperative detection of artery walls that require treatment may be possible in real-time, which would improve the provision of surgical support and curability of CAs. Furthermore, macrophage-based imaging of CAs would enable three-dimensional visualization of the spread of CA inflammation. Hemodynamic stress on the endothelial cells of the cerebral artery triggers excessive inflammation in the artery wall, becoming a factor contributing to the induction of CAs (Kataoka, 2015). Inflammatory response as well as hemodynamic stress at the aneurysm wall has been suggested to be involved in the development, enlargement, and rupture of CAs, although no studies thus far have evaluated these factors in the same CA. NIRF imaging of the inflammatory response at the aneurysm wall and simultaneous quantitative evaluation of the hemodynamic stress using three-dimensional simulation through computational fluid dynamics (Sforza et al., 2009) may enable evaluation of the association between inflammatory response and hemodynamic stress. This in turn could lead to further elucidation of the pathology of CA development, enlargement, and rupture.

In the present study, NIRF signals were localized to macrophage-rich regions; however, iron staining was mostly

negative at the CAs or the bent portion of the left posterior cerebral artery where ICG fluorescent signals were detected. This result was similar to that in atherosclerotic plaques shown in our previous study (Ikeda et al., 2018). It is possible that the sensitivity of iron staining might be insufficient due to relatively fewer infiltrating macrophages in these regions. Moreover, since iron staining is unable to detect IONPs prior to their degradation (Levy et al., 2011), it is possible that waiting more than 48 h after IONP-ICG injection before animal sacrifice and sample analysis would produce different results.

Several limitations to this study must be considered. First, CAs were examined *ex vivo* because it was rather difficult to expose and image CAs while *in vivo*. Because NIRF signals of CAs could be detected even with the brain in the background (**Figure 3**) and the NIRF signal intensity of blood was extremely low (**Figure 1B**), NIRF signals can likely be detected in the CA under *in vivo* conditions. However, the effects of the pulse in the CA and cerebral artery under actual *in vivo* conditions need to be taken into account. Second, since NIRF imaging in animal CA models is not entirely the same as that in humans, further examinations are needed to clarify whether the present results are applicable to human CAs. The dose of IONPs per body weight needed to visualize CA macrophages is considered to differ significantly between animals (50 mg ferumoxytol/kg) and humans (2.5–5 mg ferumoxytol/kg) (Hasan et al., 2012; Aoki et al., 2017b). Furthermore, since the conjugation of fluorescent molecules to IONP may affect the *in vivo* kinetics (Arami et al., 2015), determination of the appropriate dose and *in vivo* kinetics of IONP-ICG for visualizing CA macrophages in humans is needed. Third, the IONP-ICG group in this study was small (eight rats with 13 CAs), indicating the necessity for caution when interpreting statistical results.

In the present study, we demonstrated the potential of an activatable IONP-ICG NIRF probe for imaging of macrophages that accumulate in CAs. The individual reagents used (IONPs, ICG, PEG) are highly biocompatible and approved for clinical use by the United States Food and Drug Administration (Fruijtier-Polloth, 2005) indicating that the synthesized IONP-ICG not approved by the United States Food and Drug Administration would also have good biocompatibility. Although studies to confirm the safety of IONP-ICG are necessary before use in humans can be considered, the possibility of its clinical application in NIRF imaging for CA macrophages in humans is anticipated.

CONCLUSION

Using activatable IONP-ICG NIRF imaging, we for the first time succeeded in detecting the macrophage-rich regions in CAs and/or the cerebral artery wall, which is considered an early lesion in the process of CA development.

DATA AVAILABILITY STATEMENT

The datasets analyzed in this manuscript are not publicly available. Requests to access the datasets should be directed to rocky@kuhp.kyoto-u.ac.jp.

ETHICS STATEMENT

The animal study was reviewed and approved by Kyoto University Animal Care Committee.

AUTHOR CONTRIBUTIONS

HI, AI, and KS conceived and designed the study. HI and KS performed the experiments and wrote the manuscript. HI analyzed the data. All authors read, reviewed, edited and approved the manuscript.

FUNDING

This work was supported in part by the Japan Society for the Promotion of Science KAKENHI Grant (No. 18K08992) to AI. Co-author KS received a research fund from the Suzuken Memorial Foundation. Co-author AI received a research fund from Sanofi and Otsuka Pharmaceutical. Neither the first author nor any other co-author has any conflicts of interest.

ACKNOWLEDGMENTS

The authors thank the laboratory staff of the Department of Patho-Functional Bioanalysis in the Graduate School of Pharmaceutical Sciences at Kyoto University for their valuable technical assistance. The authors would like to thank Enago (www.enago.jp) for the English language review.

REFERENCES

Aoki, T., Frosen, J., Fukuda, M., Bando, K., Shioi, G., Tsuji, K., et al. (2017a). Prostaglandin E2-EP2-NF-κB signaling in macrophages as a potential therapeutic target for intracranial aneurysms. *Sci. Signal.* 10:eaah6037. doi: 10.1126/scisignal.aah6037

Aoki, T., Saito, M., Koseki, H., Tsuji, K., Tsuji, A., Murata, K., et al. (2017b). Macrophage imaging of cerebral aneurysms with ferumoxytol: an exploratory study in an animal model and in patients. *J. Stroke Cerebrovasc. Dis.* 26, 2055–2064. doi: 10.1016/j.jstrokecerebrovasdis.2016.10.026

Aoki, T., Kataoka, H., Ishibashi, R., Nakagami, H., Nozaki, K., Morishita, R., et al. (2009). Pitavastatin suppresses formation and progression of cerebral aneurysms through inhibition of the nuclear factor kappaB pathway. *Neurosurgery* 64, 357–365.

Aoki, T., Kataoka, H., Morimoto, M., Nozaki, K., and Hashimoto, N. (2007a). Macrophage-derived matrix metalloproteinase-2 and -9 promote the progression of cerebral aneurysms in rats. *Stroke* 38, 162–169. doi: 10.1161/01.str.0000252129.18605.c8

Aoki, T., Kataoka, H., Shimamura, M., Nakagami, H., Wakayama, K., Moriwaki, T., et al. (2007b). NF-kappaB is a key mediator of cerebral aneurysm formation. *Circulation* 116, 2830–2840. doi: 10.1161/circulationaha.107.728303

Arami, H., Khandhar, A., Liggitt, D., and Krishnan, K. M. (2015). In vivo delivery, pharmacokinetics, biodistribution and toxicity of iron oxide nanoparticles. *Chem. Soc. Rev.* 44, 8576–8607. doi: 10.1039/c5cs00541h

Cherrick, G. R., Stein, S. W., Leevy, C. M., and Davidson, C. S. (1960). Indocyanine green: observations on its physical properties, plasma decay, and hepatic extraction. *J. Clin. Invest.* 39, 592–600. doi: 10.1172/jci104072

Deguchi, J. O., Aikawa, M., Tung, C. H., Aikawa, E., Kim, D. E., Ntziachristos, V., et al. (2006). Inflammation in atherosclerosis: visualizing matrix metalloproteinase action in macrophages in vivo. *Circulation* 114, 55–62. doi: 10.1161/circulationaha.106.619056

Frosen, J., Piippo, A., Paetau, A., Kangasniemi, M., Niemela, M., Hernesniemi, J., et al. (2004). Remodeling of saccular cerebral artery aneurysm wall is associated with rupture: histological analysis of 24 unruptured and 42 ruptured cases. *Stroke* 35, 2287–2293. doi: 10.1161/01.str.0000140636.30204.da

Fruijtier-Polloth, C. (2005). Safety assessment on polyethylene glycols (PEGs) and their derivatives as used in cosmetic products. *Toxicology* 214, 1–38. doi: 10.1016/j.tox.2005.06.001

Hama, Y., Urano, Y., Koyama, Y., Kamiya, M., Bernardo, M., Paik, R. S., et al. (2007). A target cell-specific activatable fluorescence probe for in vivo molecular imaging of cancer based on a self-quenched avidin-rhodamine conjugate. *Cancer Res.* 67, 2791–2799. doi: 10.1158/0008-5472.can-06-3315

Hasan, D. M., Chalouhi, N., Jabbour, P., Dumont, A. S., Kung, D. K., Magnotta, V. A., et al. (2013). Evidence that acetylsalicylic acid attenuates inflammation in the walls of human cerebral aneurysms: preliminary results. *J. Am. Heart Assoc.* 2:e000019.

Hasan, D. M., Mahaney, K. B., Magnotta, V. A., Kung, D. K., Lawton, M. T., Hashimoto, T., et al. (2012). Macrophage imaging within human cerebral aneurysms wall using ferumoxytol-enhanced MRI: a pilot study. *Arterioscler. Thromb. Vasc. Biol.* 32, 1032–1038. doi: 10.1161/atvbaha.111.239871

Hashimoto, N., Handa, H., Nagata, I., and Hazama, F. (1980). Experimentally induced cerebral aneurysms in rats: part v. Relation of hemodynamics in the circle of willis to formation of aneurysms. *Surg. Neurol.* 13, 41–45.

Hokari, M., Kazumara, K., Nakayama, N., Ushikoshi, S., Sugiyama, T., Asaoka, K., et al. (2016). Treatment of recurrent intracranial aneurysms after clipping: a report of 23 cases and a review of the literature. *World Neurosurg.* 92, 434–444. doi: 10.1016/j.wneu.2016.05.053

Ikeda, H., Ishii, A., Sano, K., Chihara, H., Arai, D., Abekura, Y., et al. (2018). Activatable fluorescence imaging of macrophages in atherosclerotic plaques using iron oxide nanoparticles conjugated with indocyanine green. *Atherosclerosis* 275, 1–10. doi: 10.1016/j.atherosclerosis.2018.05.028

Ikedo, T., Minami, M., Kataoka, H., Hayashi, K., Nagata, M., Fujikawa, R., et al. (2017). Dipeptidyl peptidase-4 inhibitor anagliptin prevents intracranial aneurysm growth by suppressing macrophage infiltration and activation. *J. Am. Heart Assoc.* 6:e004777.

Kaijzel, E. L., van Heijningen, P. M., Wielopolski, P. A., Vermeij, M., Koning, G. A., van Cappellen, W. A., et al. (2010). Multimodality imaging reveals a gradual increase in matrix metalloproteinase activity at aneurysmal lesions in live fibulin-4 mice. *Circ. Cardiovasc. Imaging* 3, 567–577. doi: 10.1161/circimaging.109.933093

Kanematsu, Y., Kanematsu, M., Kurihara, C., Tada, Y., Tsou, T. L., van Rooijen, N., et al. (2011). Critical roles of macrophages in the formation of intracranial aneurysm. *Stroke* 42, 173–178. doi: 10.1161/strokeaha.110.590976

Kataoka, H. (2015). Molecular mechanisms of the formation and progression of intracranial aneurysms. *Neuro Med. Chir.* 55, 214–229. doi: 10.2176/nmc.ra.2014-0337

Levy, M., Luciani, N., Alloyeau, D., Elgrabli, D., Deveaux, V., Pechoux, C., et al. (2011). Long term in vivo biotransformation of iron oxide nanoparticles. *Biomaterials* 32, 3988–3999. doi: 10.1016/j.biomaterials.2011.02.031

Lu, M., Cohen, M. H., Rieves, D., and Pazdur, R. (2010). FDA report: ferumoxytol for intravenous iron therapy in adult patients with chronic kidney disease. *Am. J. Hematol.* 85, 315–319.

Morita, A., Kirino, T., Hashi, K., Aoki, N., Fukuhara, S., Hashimoto, N., et al. (2012). The natural course of unruptured cerebral aneurysms in a japanese cohort. *N. Engl. J. Med.* 366, 2474–2482. doi: 10.1056/nejmoa1113260

Muller, K., Skepper, J. N., Posfai, M., Trivedi, R., Howarth, S., Corot, C., et al. (2007). Effect of ultrasmall superparamagnetic iron oxide nanoparticles (Ferumoxtran-10) on human monocyte-macrophages in vitro. *Biomaterials* 28, 1629–1642. doi: 10.1016/j.biomaterials.2006.12.003

Ogawa, M., Kosaka, N., Choyke, P. L., and Kobayashi, H. (2009). In vivo molecular imaging of cancer with a quenching near-infrared fluorescent probe using conjugates of monoclonal antibodies and indocyanine green. *Cancer Res.* 69, 1268–1272. doi: 10.1158/0008-5472.can-08-3116

Sano, K., Nakajima, T., Miyazaki, K., Ohuchi, Y., Ikegami, T., Choyke, P. L., et al. (2013). Short PEG-linkers improve the performance of targeted, activatable monoclonal antibody-indocyanine green optical imaging probes. *Bioconjug Chem.* 24, 811–816. doi: 10.1021/bc400050k

Sforza, D. M., Putman, C. M., and Cebral, J. R. (2009). Hemodynamics of cerebral aneurysms. *Annu. Rev. Fluid Mech.* 41, 91–107.

Shao, L., Qin, X., Liu, J., Jian, Z., Xiong, X., and Liu, R. (2017). Macrophage polarization in cerebral aneurysm: perspectives and potential targets. *J. Immunol. Res.* 2017:8160589.

Tsutsumi, K., Ueki, K., Morita, A., Usui, M., and Kirino, T. (2001). Risk of aneurysm recurrence in patients with clipped cerebral aneurysms: results of long-term follow-up angiography. *Stroke* 32, 1191–1194. doi: 10.1161/01.str.32.5.1191

Urano, Y., Asanuma, D., Hama, Y., Koyama, Y., Barrett, T., Kamiya, M., et al. (2009). Selective molecular imaging of viable cancer cells with pH-activatable fluorescence probes. *Nat. Med.* 15, 104–109. doi: 10.1038/nm.1854

Conflict of Interest: The authors declare that the research was conducted in the absence of any commercial or financial relationships that could be construed as a potential conflict of interest.

Copyright © 2020 Ikeda, Ishii, Sano, Chihara, Arai, Abekura, Nishi, Ono, Saji and Miyamoto. This is an open-access article distributed under the terms of the Creative Commons Attribution License (CC BY). The use, distribution or reproduction in other forums is permitted, provided the original author(s) and the copyright owner(s) are credited and that the original publication in this journal is cited, in accordance with accepted academic practice. No use, distribution or reproduction is permitted which does not comply with these terms.

frontiers in Neuroscience

REVIEW
published: 06 May 2020
doi: 10.3389/fnins.2020.00396

Harmonization of Brain Diffusion MRI: Concepts and Methods

Maíra Siqueira Pinto[1,2†], Roberto Paolella[2,3†], Thibo Billiet[3], Pieter Van Dyck[1], Pieter-Jan Guns[4], Ben Jeurissen[2], Annemie Ribbens[3], Arnold J. den Dekker[2] and Jan Sijbers[2]*

[1] Department of Radiology, Antwerp University Hospital, University of Antwerp, Antwerp, Belgium, [2] imec–Vision Lab, University of Antwerp, Antwerp, Belgium, [3] Icometrix, Leuven, Belgium, [4] Physiopharmacology, University of Antwerp, Antwerp, Belgium

MRI diffusion data suffers from significant inter- and intra-site variability, which hinders multi-site and/or longitudinal diffusion studies. This variability may arise from a range of factors, such as hardware, reconstruction algorithms and acquisition settings. To allow a reliable comparison and joint analysis of diffusion data across sites and over time, there is a clear need for robust data harmonization methods. This review article provides a comprehensive overview of diffusion data harmonization concepts and methods, and their limitations. Overall, the methods for the harmonization of multi-site diffusion images can be categorized in two main groups: diffusion parametric map harmonization (DPMH) and diffusion weighted image harmonization (DWIH). Whereas DPMH harmonizes the diffusion parametric maps (e.g., FA, MD, and MK), DWIH harmonizes the diffusion-weighted images. Defining a gold standard harmonization technique for dMRI data is still an ongoing challenge. Nevertheless, in this paper we provide two classification tools, namely a feature table and a flowchart, which aim to guide the readers in selecting an appropriate harmonization method for their study.

Keywords: harmonization, normalization, diffusion MRI, multi-site, inter-scanner, review

OPEN ACCESS

Edited by:
Alard Roebroeck, Maastricht University, Netherlands

Reviewed by:
Daniel Güllmar, Friedrich-Schiller University of Jena, Germany
Suyash P. Awate, Indian Institute of Technology Bombay, India

****Correspondence:***
Maíra Siqueira Pinto
mairaspinto@gmail.com

† These authors have contributed equally to this work

Specialty section:
This article was submitted to Brain Imaging Methods, a section of the journal Frontiers in Neuroscience

Received: *18 July 2019*
Accepted: *30 March 2020*
Published: *06 May 2020*

Citation:
Pinto MS, Paolella R, Billiet T, Van Dyck P, Guns P-J, Jeurissen B, Ribbens A, den Dekker AJ and Sijbers J (2020) Harmonization of Brain Diffusion MRI: Concepts and Methods. Front. Neurosci. 14:396. doi: 10.3389/fnins.2020.00396

INTRODUCTION

Diffusion-weighted magnetic resonance imaging (dMRI) is an MRI technique in which the image contrast is related to the diffusion of water molecules inside tissues. dMRI has brought great innovation to neuroimaging analysis, since it enables non-invasive probing of brain microstructure. Nevertheless, many studies using diffusion data rely on small sample sizes, leading to poor reproducibility of results. Fortunately, research is evolving toward large multicenter studies with the aim of increasing statistical power. However, the success of a joint analysis is highly dependent on the comparability of the multi-site data.

Diffusion data of the same subject obtained at different sites and/or acquired at different time points can be different due to local and/or temporal scanner characteristics resulting in a high inter- and intra-scanner variability (Vollmar et al., 2010; Grech-Sollars et al., 2015; Nencka et al., 2017). These variabilities may arise from a range of factors, such as hardware (scanner manufacturer, field strength, transmitter/receiver coils, magnetic field inhomogeneities, etc.), reconstruction algorithms (SENSE, GRAPPA, etc.), acquisition parameters (voxel size, number of gradient directions, echo time, repetition time, etc.), and image quality [signal to noise ratio (SNR), etc.] (Alexander et al., 2006; Ni et al., 2006; Jones, 2010; Vollmar et al., 2010). All these factors affect

the final diffusion signal intensity and consequently the diffusion metrics, preventing reliable multi-site and/or longitudinal diffusion studies (Pfefferbaum et al., 2003; Vollmar et al., 2010; Mirzaalian et al., 2018).

In literature, many conflicting inferences have been reported between studies, in which findings based on small distinct cohorts are used to generalize conclusions for an entire population, without considering intra- and inter-site differences (Button et al., 2013; Kelly et al., 2018; Smith and Nichols, 2018). To determine the site effects on diffusion data, a number of studies examined diffusion phantom data to detect scanner related variabilities (Teipel et al., 2011; Zhu et al., 2011; Walker et al., 2013; Pullens et al., 2017; Timmermans et al., 2019). Up to 7% of inter-site variability in diffusion metrics was demonstrated in phantoms (Teipel et al., 2011; Palacios et al., 2017). However, using parameters obtained from phantom data to correct human data is not advised due to the structural complexity of human biological tissue (Karayumak et al., 2019).

Previous research has established that inter-site variability is non-uniform across the white matter of the human brain, with a variability up to 5% in diffusion metrics of major brain tracts (Vollmar et al., 2010; Grech-Sollars et al., 2015; Nencka et al., 2017). Recently, investigators have examined the reproducibility of multi-shell diffusion images in a multi-site study involving traveling subjects (Tong et al., 2019). A 7.7% median inter-center coefficient of variation was estimated for the track density maps in whole white matter among the subjects. These inter-site variabilities in diffusion metrics are similar to the changes due to pathologies. For example, in the work of Kumar et al. (2009), it was shown that the variability in diffusion metrics in the corpus callosum between controls, mild Traumatic Brain Injury (TBI) and moderate TBI patients, are of the same order as intra-scanner changes. Furthermore, a quantitative study by Mahoney et al. reported longitudinal changes in diffusion metrics in dementia patients compared to controls in the same order of the site variabilities (Mahoney et al., 2015). From these findings, we can infer that it is crucial to reduce the variability across multi-center diffusion data.

Inter-site variability can be reduced by acquiring data with scanners from the same manufacturer at each site and using similar acquisition parameters (Vollmar et al., 2010; Fox et al., 2012; Cannon et al., 2014). However, diffusion parameters of subjects scanned using the same acquisition protocol may still differ significantly across sites (Nyholm et al., 2013; Jovicich et al., 2014; Mirzaalian et al., 2015). These differences may come from several sources, such as sensitivity of head coils, imaging gradient non-linearities, magnetic field inhomogeneities and other scanner related factors. Hence, there is a substantial need for robust harmonization techniques (Jenkins et al., 2016; Jovicich et al., 2019). The overall concept of harmonization methods is to apply statistical or mathematical concepts to reduce unwanted site variability while maintaining the biological content. In the last decade a multitude of harmonization methods have been developed.

For this review, we have categorized the brain dMRI methods in two main groups depending on the data-format used as input for harmonization. The first category uses calculated diffusion (para)metric maps, such as Fractional Anisotropy (FA), Mean, Axial and Radial Diffusivity (MD, AD, and RD, respectively), Kurtosis Anisotropy (KA), Mean, Axial, and Radial Kurtosis (MK, AK, and RK, respectively), as input (i.e., diffusion parametric map harmonization; DPMH). While the second category uses diffusion weighted images (DWI) as input (i.e., diffusion weighted image harmonization; DWIH).

To the authors' knowledge, no previous study has provided an extensive report of diffusion harmonization methods. In this review paper, a comprehensive overview of those methods is presented, including an investigative analysis of their strengths and weaknesses. DPMH and DWIH methods reported since 2009 are described. This paper is organized as follows. Section "Literature Search" describes the search mechanism used for selecting the literature on brain diffusion data harmonization. In Section "Requirements for Harmonization," the requirements for harmonization are specified. Sections "Diffusion Parametric Map Harmonization Methods" and "Diffusion Weighted Image Harmonization Methods" depict the DPMH and DWIH harmonization methods reported in the literature. Section "Discussion" then presents an overview of the main characteristics of the methods and a guideline that helps the user to select an adequate harmonization method for her/his data. Finally, in Section "Conclusion" conclusions are drawn.

LITERATURE SEARCH

Two authors (MSP and RP) independently performed a literature search across two databases (PubMed and Google Scholar) using combinations of the following search terms: "harmonization," "harmonisation," "normalization," "normalisation," "multi-site," "multi-center," "inter-site," "intra-scanner," "diffusion," "MRI," "DTI," "meta-analysis," "covariates," "spherical harmonics," "deep learning." Besides the usual search engines, additional important papers were selected by checking the reference lists of identified relevant publications on data harmonization. After removing the duplicates, all identified articles were screened by title and abstract. Studies were included if they described diffusion harmonization methods and concepts.

REQUIREMENTS FOR HARMONIZATION

For the majority of dMRI harmonization procedures, co-registration is of crucial importance. Co-registration of diffusion images aims to find spatial transformations to map different images to a common reference space, allowing direct comparison of various image properties. Prior to harmonization, a voxel-by-voxel correspondence between multiple diffusion volumes is needed, in order to minimize errors in subsequent calculations. In particular, voxel-wise DPMH and DWIH approaches require all subjects to be in the same space in order to extract common features that are

site-related rather than anatomically specific. The common space can be a study-specific template or a standard brain atlas template, as for example, the ICBM152 template of the Montreal Neurological Institute (MNI) space[1]. Many tools are available for registering diffusion images, such as Advanced Normalization Tools (ANTs; Avants et al., 2011), FMRIB Software Library (FSL; Jenkinson et al., 2012), and elastix (Klein et al., 2010; Shamonin et al., 2014).

Additionally, a dataset with a balanced number of subjects per site is advised for robust harmonization. Many DPMH and DWIH methods use these subjects to efficiently learn a set of so-called mapping parameters used to characterize the differences between the images across scanners. Additionally, an important requirement, especially for DWIH methods, is the availability of training data, i.e., matched subjects across sites for obtaining the mapping parameters between sites. Age, gender, handedness, and socio-economic status need to be matched among the subjects to remove the statistical differences at group level. Moreover, for some machine learning techniques, there is a need for DWI data of individual subjects that are scanned at different sites, within a small interval of time, to train a network to recognize site-related underlying inter-scanner/inter-site differences in the characteristics of the images to harmonize.

Overall, for all the methods, it is highly recommended to use a balanced dataset and to co-register the diffusion images or maps to a common template. The recommendations are to assure that statistical differences are only due to hardware, software and protocol differences, and ensure spatial compatibility intra- and inter-subjects during the harmonization procedure. Furthermore, each method has its own specifications and limitations that are described in the following sections.

DIFFUSION PARAMETRIC MAP HARMONIZATION METHODS

Diffusion parametric map harmonization methods perform particular transformations on the diffusion parametric maps that enable data pooling and reduction of unwanted intra- and inter-site variability. For a joint analysis of multi-site diffusion metric maps that have been estimated using a given diffusion model [e.g., diffusion tensor imaging (DTI), diffusion kurtosis imaging (DKI), neurite orientation dispersion and density imaging (NODDI), etc.], statistical or mathematical DPMH methods can be applied. The purpose of these methods is to perform joint statistical analysis on multi-site data. It can be performed in two ways: (1) without modifying the original diffusion parametric maps (see Subsection "Modeling Inter-Site Variability Within the Statistical Analysis"); (2) by modifying the parametric maps with *a posteriori* analysis (see Subsection "Harmonizing the Parametric Maps Based on Regression of Covariates"). DPMH methods allow to pool DWI parametric maps obtained from different diffusion acquisition schemes (diffusion directions, *b*-values, repetition time, echo time, etc.). The DPMH methods described below are meta-analysis, mega-analysis, and regression of covariates.

[1]http://www.bic.mni.mcgill.ca/ServicesAtlases/ICBM152NLin2009

Modeling Inter-Site Variability Within the Statistical Analysis

Meta-Analysis

Meta-analysis is a popular statistical analysis technique in biomedical research that combines results of independent multi-site and/or longitudinal studies. The general concept is to perform a group-wise statistical analysis separately for each site, followed by a weighted combination of effect size over the different studies to strengthen conclusions about the research question (Zhu et al., 2019). Meta-analysis is useful to pool retrospective data with sample sizes that are too small to draw valid conclusions independently (Petitti, 1994).

Figure 1 presents an example of meta-analysis in which statistical inferences are obtained independently per site from the FA maps of different groups of subjects. As a first step, an intra-site statistical analysis is performed. The resulting statistical scores (e.g., *z*-score) of the metric of interest (e.g., FA) can then be weighted by each site's sample size or with respect to an estimate of precision, such as effect size (Salimi-Khorshidi et al., 2009), to obtain the final statistical score. In contrast to this approach, the overall statistical score can also be obtained by modeling site as a random effect (Worsley, 2002; Beckmann et al., 2003; Woolrich et al., 2004). For example, in the work of Teipel et al. (2012), meta-analysis was used to investigate FA and MD differences between dementia patients and controls in a multi-site study, taking scanner effects into account. Voxel-based *t*-statistics were converted to *z*-scores after which a variance component analysis was applied, effectively reducing effects of site (random effect), age and gender (fixed effects).

One of the main advantages of meta-analysis is the possibility to pool data from small/underpowered studies to derive robust conclusions. It is also the only way to pool studies for which only aggregated data are reported (e.g., group difference statistics or the mean FA per region of interest) and for which the whole brain images are not available. However, one drawback is that if the statistics performed in the individual studies are biased by study size, the population estimate will be also affected. Another disadvantage is that the statistical analysis should first be performed separately for each diffusion metric of interest.

Mega-Analysis

In contrast to meta-analysis, mega-analysis refers to a technique of summarizing the statistics from the individual subjects of all sites to jointly evaluate population group differences (Jahanshad et al., 2013; Zhu et al., 2019). As depicted in **Figure 1**, in mega-analysis group-difference statistics are not calculated for each site separately. Instead, group differences are identified by a site-weighted combination of the statistical scores from all individuals jointly.

When the individual diffusion data (e.g., FA) is available per subject, the measures can be pooled to calculate the effect size across the entire group in a mega-analysis. To take into account the variability due to site differences, the site effect can be modeled using a mixed linear model statistical approach (or another statistical method to analyze the dataset), just as in meta-analysis.

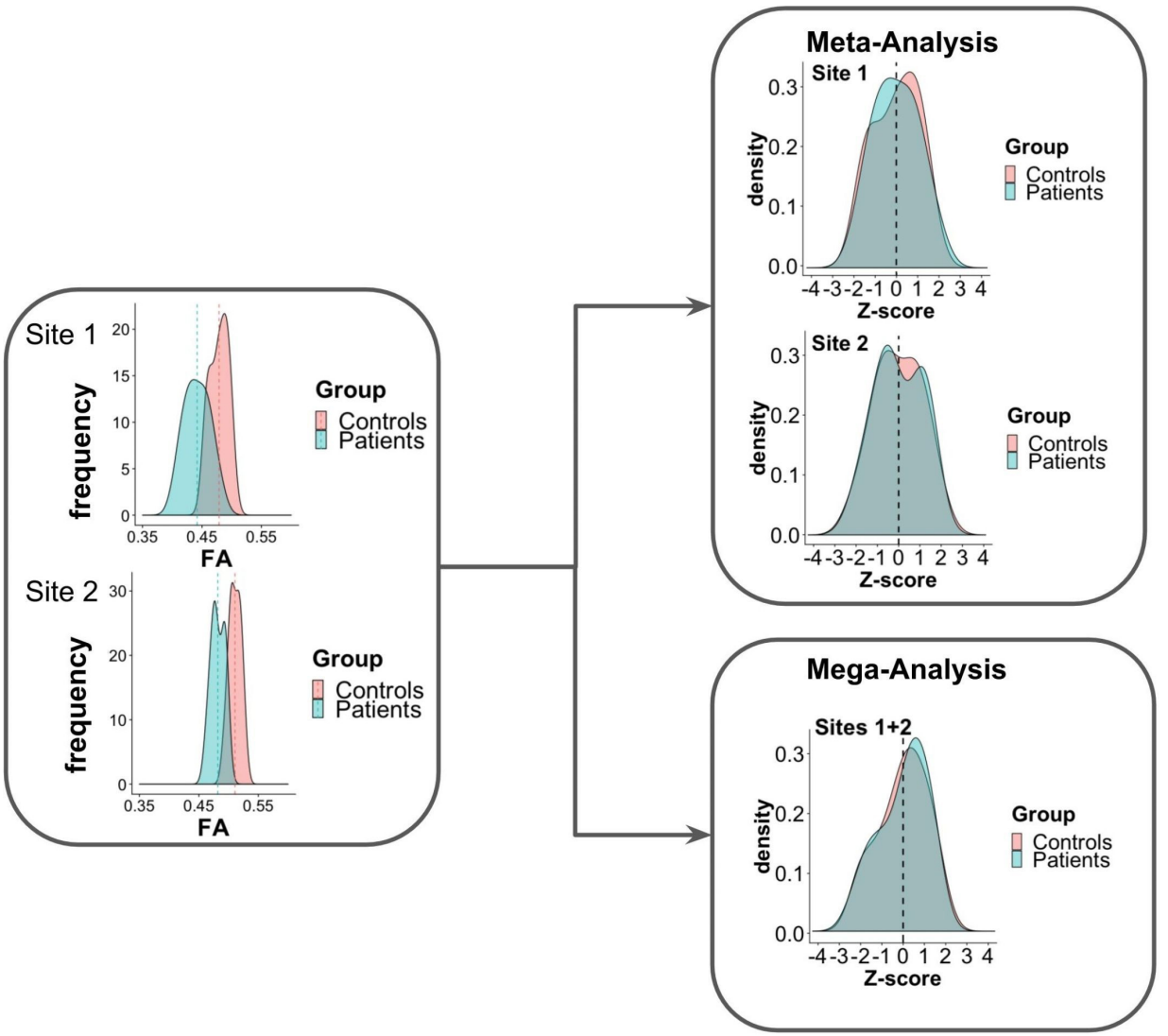

FIGURE 1 | Scheme of meta- and mega-analysis. FA measures from sites 1 and 2, for two groups of subjects: controls and patients. The FA frequency for each group is estimated for each of the sites. Meta-analysis performs the statistical evaluation between groups for each site separately, followed by a weighted combination of its statistical results, while in mega-analysis a weighted statistical evaluation is performed for all sites jointly.

While not directly harmonizing the imaging data itself, mega-analysis allows a joint analysis of two (or more) datasets to evaluate a common characteristic in the population (Jahanshad et al., 2013; Kochunov et al., 2014; Zhu et al., 2019). Some limitations in this approach are that the size of the cohort may not be sufficient to capture the variance of the entire population, pre-processing steps could be very different for each site (if the FA maps are computed independently), and the statistical analysis has to be performed separately for each variable (e.g., FA, MD, AD, and RD).

Meta-and mega-analysis have successfully been adopted in the field of neuroimaging by the Enhancing NeuroImaging Genetics through Meta-Analysis (ENIGMA) consortium (Jahanshad et al., 2013; Kochunov et al., 2014). The general concept of the harmonization method proposed by the ENIGMA-DTI group is that each site preprocesses the diffusion metric maps (e.g., FA) separately. The statistical scores are harmonized using meta- or mega-analysis, to improve data comparability and robustness. Findings of the ENIGMA-DTI group indicate that results obtained by meta- and mega-analysis may differ, in favor of the latter. In multi-center studies with a moderate amount of variation between cohorts, a mega-analysis statistical framework appears to be the better approach to investigate structural neuroimaging data, showing greater stability and higher power for jointly analyzing the data (Kochunov et al., 2014). Nonetheless, when the individual diffusion metric maps are not available, meta-analysis could serve as a valuable alternative. However, meta-analysis should be performed carefully and one should take into account cohort trends (Kochunov et al., 2014).

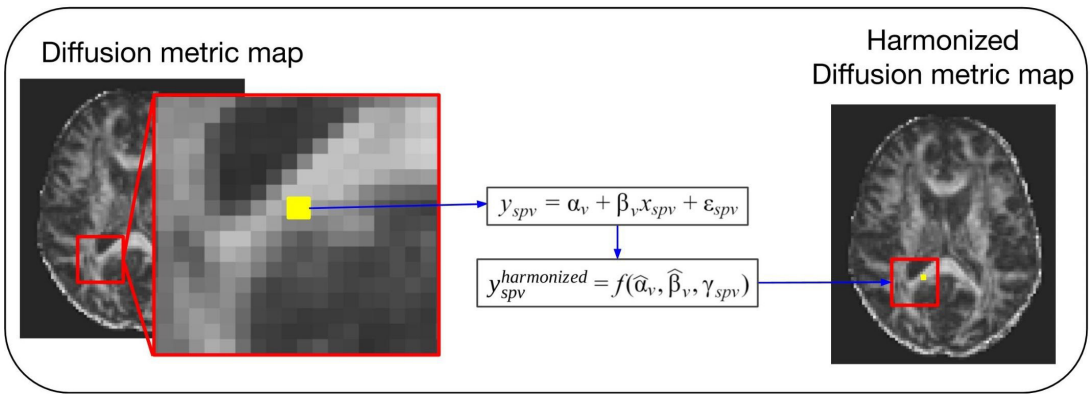

FIGURE 2 | General scheme of a voxel-wise regression of covariates harmonization approach. For these methods the voxel intensity of the diffusion metric maps (y_{spv}, the intensity for a specific site *s*, subject *p* and voxel *v*) is modeled as a combination of a voxel-wise intercept (α_v), a voxel-wise slope (β_v) multiplied by a model-specific dependent variable (x_{spv}), and an error component (ε_{spv}). Each of the regression of covariates approaches will have a different model and dependent variable to describe the biological and site-related effects on the diffusion metric intensities. Next, the estimated coefficients are used to compute the new harmonized diffusion intensity values ($y_{spv}^{harmonized}$).

Harmonizing the Parametric Maps Based on Regression of Covariates

Covariates, also known as explanatory variables, are variables that may affect the estimate of the diffusion metric under study. These covariates can be variables of clinical interest or unwanted confounding variables, such as MR hardware (e.g., scanner manufacturer, field strength, and coils), software, acquisition parameters (e.g., echo time, repetition time, *b*-value, and gradient directions) or image quality. One way to handle unwanted variability due to confounding factors is the use of regression models (Pourhoseingholi et al., 2012). This approach is illustrated in **Figure 2**. After fitting a regression model to the diffusion values, adjusted values can be derived that no longer contain the effect of the covariates. The use of the regression of covariates harmonization approach to correct for variability in software and hardware has been reported extensively in the literature (Forsyth et al., 2014; Venkatraman et al., 2015; Fortin et al., 2016, 2017; Pohl et al., 2016; Timmermans et al., 2019). Regression of covariates methods can be divided into two categories: global harmonization methods and voxel-wise harmonization methods. Both classes are described below.

The methods present different options for harmonizing diffusion metric maps (e.g., FA and MD maps). For briefness, we use the notation y_{spv}^{method} to denote the diffusion metric measure *y* harmonized by a specific *method*, at site *s*, for subject *p* and voxel *v*.

Global Harmonization

Human-phantom based harmonization (HuP)

A straightforward approach for data harmonization is to apply scanner-specific correction factors derived from human phantom data (i.e., a group of individuals scanned at multiple scanners/sites within a short period of time) (Pohl et al., 2016). One scanner type is defined as the reference (*R*) and the other as the target (*T*). The goal is to correct the diffusion metric maps of the target site. For this purpose, a correction factor (*F*) is calculated as the ratio of the mean value (across the human phantoms) of the diffusion metric in the reference and target, respectively: $F = \frac{\sum_p \bar{y}_p^R / N}{\sum_p \bar{y}_p^T / N}$, where $\bar{y}_p^R$ and $\bar{y}_p^T$ are the mean metric value across the white matter voxels for human phantom *p* at the reference and target site, respectively, and *N* is the number of human phantoms. Successively, once the scanner-specific correction factors are determined, metric maps *y* for subject *p* and voxel *v* scanned in the target scanner (y_{spv}) are scaled by the appropriate correction factor in order to obtain the HuP-harmonized diffusion metric maps: $y_{spv}^{HuP} = y_{spv} F$.

The main advantages of the correction factor are its simple derivation and the fact that it has been demonstrated to correct for differences that are likely attributable to the MR system manufacturer (Pohl et al., 2016). However, human phantom datasets from multiple sites are required. Moreover, a unique correction factor per scanner type only partially reduces the harmonization problem due to its intrinsic non-linearity, i.e., scanner type differences are not uniform but vary in a highly non-linear fashion across the brain (Karayumak et al., 2019).

Hardware-phantom based harmonization (HaP)

Timmermans et al. (2019) presented global multi-site harmonization models, using phantom data acquired at multiple centers in a longitudinal study. For this study, dedicated diffusion single-strand phantoms were developed by HQ Imaging (Heidelberg, Germany). The study aimed to build a comprehensive model for the variability of FA. Protocol-specific and site-specific effects were included in the models, considering hardware (scanner vendor and head coil), software, acquisition parameters (bandwidth, TE, and TR), image quality (signal-to-noise ratio and mean residual), as fixed predictor variables, and site as random predictor variable, taking into account that

fixed predictors relate to effects that are constant across all individuals, and random predictors relate to effects that vary across individuals.

Different models were proposed to describe the diffusion metric values y_p of the phantoms p considering the differences between acquisitions and were evaluated via the combination of the fixed and random predictors (x_p and z_p, respectively): $y_p^{HaP} = \beta_0 + \beta_n x_p + b_{0p} + b_{np} z_p + \varepsilon_p$, where β_0 is the fixed intercept, β_n the fixed effects slope, b_{0p} the random intercept per phantom, b_{np} the random slope per phantom, and ε_p the error. In order to find the most comprehensive model for the diffusion metric data, many linear mixed effects models were evaluated by the Akaike information criterion (AIC). The selection of model parameters was based on three model categories: protocol-specific intercept, protocol-specific intercept with quality effects, and protocol-specific intercept with protocol-specific quality effects. Each model was further divided into submodels depending on the included variables. AIC is used to select which model best describes the variations in the metric intensities. The results showed that scanner manufacturer, SNR, head coil, bandwidth and TE are the covariates that best describe the sources of variability in the inter-site phantom data, and should be used to harmonize the diffusion metric maps of multi-center studies.

The use of hardware phantoms for harmonization has several advantages. Hardware phantoms can be scanned multiple times, for a longer time, and their images do not suffer from motion artifacts. The phantom content is controllable and remains stable over time. Duplicated phantoms can be easily obtained by several sites, obviating transport. The main drawback of hardware phantom based harmonization is that such phantoms do not fully represent the complexity of the human brain, and therefore have different, intra- and inter-scanner variabilities. Obviously, voxel-wise harmonization (cf., Section "Voxel-Wise Harmonization") of brain dMRI is not possible using phantom data.

Global scaling (GS)

In the global scaling method presented by Fortin et al., 2017, a linear model is used to correct the site effect on the diffusion metric maps (Fortin et al., 2017). The estimated location ($\theta_{s,location}$) and scale ($\theta_{s,scale}$) model parameters, per site s, encapsule the variabilities in the diffusion metric maps due to site effects. They are estimated by fitting a linear regression model: $\bar{Y}_s = \theta_{s,location} + \theta_{s,scale}\,\bar{Y} + \varepsilon_s$, where $\bar{Y}_s$ is an $n_v \times 1$ vector containing the average diffusion metric intensity per voxel for the number of voxels n_v computed over all subjects of site s, $\bar{Y}$is an n_v x1 vector containing the average diffusion metric intensity per voxel for the number of voxels n_v computed over all subjects of all sites together (considered a reference), and ε_s is the residual error. From the estimated parameters, the harmonized diffusion metric maps are calculated as: $y_{spv}^{GS} = \frac{y_{spv} - \hat{\theta}_{s,location}}{\hat{\theta}_{s,scale}}$.

The main advantage of global scaling is that it takes into account information from all sites. Some disadvantages are that the removal of site effects can also remove biological variability, and that it does not account for spatial heterogeneity of the site effects in the brain.

Voxel-Wise Harmonization

Removal of Artificial Voxel Effect by Linear regression (RAVEL)

The Removal of Artificial Voxel Effect by Linear regression (RAVEL) method (Fortin et al., 2016) uses voxels in the cerebrospinal fluid (CSF) voxels as control region. The CSF-voxels are used for harmonization because their diffusion metric intensities are unassociated with disease or other clinical factors and are theoretically only influenced by site-related variabilities. In this method, the voxel-wise intensity of the diffusion metric maps (y_{spv}) is described as a combination of four components: the average intensity in the sample ($\alpha 1^t$), the known clinical covariates of interest (βX^t), the unknown site-related factors (γZ^t) and a residual (R): $y_{spv} = \alpha 1^t + \beta X^t + \gamma Z^t + R$. Where the symbol t indicates the transpose operation, y_{spv} is the $v \times p$ matrix containing the registered and normalized voxel intensities for v voxels and p subjects, $\alpha 1^t$ is a $v \times 1$ vector containing the average voxel intensity per site, X is a $p \times k$ matrix containing for each subject p the correspondent biological covariates k, β is the coefficient matrix associated with X, Z is a $p \times m$ matrix containing for each subject p the associated m unwanted coefficient factors and γ is the coefficient matrix associated with Z.

The CSF voxels are used to estimate the unknown/unwanted factors (Z^t) by assuming that α and β are null for the CSF since there is no association between control voxels and clinical features. Thus, the CSF diffusion intensities (y_{spv}^{CSF}) are described as: $y_{spv}^{CSF} = \gamma_{CSF} Z^t + R_{CSF}$. Singular value decomposition is used to obtain the first latent factors (w_{1sp}) from the CSF voxels, representing the site-related variability common to all voxels. Next, the voxel-wise RAVEL coefficients (ψ_v) are estimated fitting the linear regression model to the voxel-wise diffusion intensities (y_{spv}) and the first latent factors (w_{1sp}): $y_{spv} = \alpha_v + \psi_v w_{1sp} + \varepsilon_{spv}$, where ε_{spv} is the residual error. Lastly, the RAVEL-harmonized diffusion metric map intensities are computed: $y_{spv}^{RAVEL} = y_{spv} - \hat{\psi}_v w_{1sp}$.

An advantage of the RAVEL method is that it is a voxel-wise harmonization method that uses intra-subject information that is not affected by disease (CSF control region) for improving comparability between subjects. However, if these control regions do not carry the information about the inter-site variability and/or are related to the parameter of interest, then the correction may remove relevant biological information, becoming a disadvantage to use this method in such cases.

Surrogate Variable Analysis (SVA)

Surrogate Variable Analysis (SVA) identifies and estimates unknown, unmodeled or unwanted sources of variation from the data (Leek et al., 2012; Fortin et al., 2017). The so-called batch effects can be defined as measurements of unwanted variability that have qualitatively different behavior across conditions and are unrelated to the biological or scientific variables in a study (Leek et al., 2010). In the context of multi-site harmonization, SVA is particularly useful when it is not known which datasets belong to which site. Through singular value decomposition, the data is decomposed into a set of m surrogate variables (z_1, ..., z_m). Variables with the largest variance, and which are not covarying

with *a priori* defined factors of interest such as age, gender or diagnosis, are then regressed out of the data. The voxel-wise SVA coefficients (Φ_{mv}) are estimated by fitting the surrogate variables (z_{msv}, for surrogate variable m, site s and voxel v) and the original diffusion metric intensities (y_{spv}, for site s, subject p and voxel v) to the linear regression model: $y_{spv} = \alpha_v + \sum_{n=1}^{m} \Phi_{nv} z_{nsp} + \varepsilon_{spv}$, where α_v is the voxel-wise overall measure of the diffusion metric and ε_{spv} is the residual error. Next, the SVA-harmonized diffusion metric map intensities (y_{spv}^{SVA}) are computed as: $y_{spv}^{SVA} = y_{spv} - \sum_{n=1}^{m} \hat{\Phi}_{nv} z_{nsp}$.

Surrogate variable analysis is implemented in the SVA package for R, and is applicable voxel-wise (Leek et al., 2012). A strong point is that it estimates all common sources of latent variation, without needing to know their exact origin (e.g., site). Nonetheless, if this inherent variation is related to biological variability (e.g., patients in site A, controls in site B) then SVA is not appropriate.

Combined association test (ComBat)

The combined association test (ComBat) uses regression of covariates for data harmonization (Fortin et al., 2017). It started as a batch effect correction tool (similar to SVA) used in genomics, in which the batch effect is known (Johnson et al., 2007). It is a powerful and fast alternative for SVA in cases where site is an *a priori* known factor.

ComBat describes the non-harmonized diffusion metric in each voxel (y_{spv}, for site s, subjects p and voxel v) by an adjustment model that consists of the following terms: an overall measure of the diffusion metric (α_v), the product of a design matrix (X_{sp}) containing the covariates of interest (e.g., gender and age) and the vector of corresponding regression coefficients (β_v), a term representing the so-called additive site effects (γ_{sv}) and, finally, the product of a normally distributed error term (ε_{spv}) and a factor representing the so-called multiplicative site effects (δ_{sv}): $y_{spv} = \alpha_v + X_{sp}\beta_v + \gamma_{sv} + \delta_{sv}\varepsilon_{spv}$. The site-specific parameters of the adjustment model are assumed to have parametric prior distributions, being a normal distribution for the additive factor (γ_{sv}) and an inverse gamma distribution for the multiplicative factor (δ_{sv}). The parametric distributions are estimated from the data, using an empirical Bayes framework to decrease the variance of the site effects. It assumes that all voxels share a common distribution, and are used to infer the properties of the site-effects. Subsequently, ComBat-harmonized diffusion parameter maps are created based on the estimated additive and multiplicative factors (γ_{sv}^{*} and δ_{sv}^{*}, respectively): $y_{spv}^{ComBat} = \frac{y_{spv} - \hat{\alpha}_v - X_{sp}\hat{\beta}_v - \gamma_{sv}^{*}}{\delta_{sv}^{*}} + \hat{\alpha}_v + X_{sp}\hat{\beta}_v$.

It was reported that the ComBat harmonization method preserves between-subject biological information (Fortin et al., 2017). However, a limitation of this method is that the optimization procedure assumes the site effect parameters to follow a particular parametric prior distribution (Gaussian and Inverse-gamma), which might not generalize to all scenarios or measures. Moreover, it is not clear how non-linearities in the signal due to site effects propagate through the preprocessing techniques, as well as model fitting procedures.

DIFFUSION WEIGHTED IMAGE HARMONIZATION METHODS

Diffusion parametric map harmonization methods for data pooling and joint analysis, meta- and mega-analysis and regression of covariates, have been reported extensively in the literature. Nonetheless, the harmonization of diffusion metric maps has several drawbacks, as described in section 4 for each of the methods. Recall that one of the main drawbacks is the lack of knowledge on how the scanner-specific non-linearities propagate in the diffusion model fit, possibly affecting the harmonization procedure of the diffusion metric maps. Recently, the use of the dMRI intensity signal has been proposed to perform model-free harmonization approaches. These methods are categorized as DWIH (Mirzaalian et al., 2015; Koppers et al., 2018; Huynh et al., 2019; Karayumak et al., 2019; Tax et al., 2019). DWIH methods rely on mapping the DWI images to a reference space. An overview of these DWIH approaches is given below. The methods described are the rotation invariant spherical harmonics method, machine learning algorithms, and the method of moments.

Rotation Invariant Spherical Harmonics (RISH)

The use of rotation invariant spherical harmonics (RISH) for dMRI signal harmonization has been first proposed by Mirzaalian et al. (2015) and several improvements to this method have been presented since then (Mirzaalian et al., 2016, 2018; Karayumak et al., 2019).

The core idea of the RISH method is to map the diffusion weighted imaging (DWI) data from a target (T) site to a reference (R) site. The voxel-wise DWI signal intensity $S = [s_1, \ldots, s_g]^t$, along g unique directions, can be compactly represented in a spherical harmonics (SH) basis: $S \approx \sum_i \sum_j C_{ij} Y_{ij}$, composed by SH basis functions (Y_{ij}) and their corresponding coefficients (C_{ij}) of order i and degree j, with j = 1,2,...,2i + 1. The RISH features, per harmonic order, are extracted from the estimated SH coefficients as: $RISH_i = ||C_i^2|| = \sum_{j=1}^{2i+1} (C_{ij}^2)$.

The harmonization procedure, which is illustrated in **Figure 3**, consists of two parts: (1) learning scale maps between sites from training data and (2) applying the learned scale maps to harmonize all DWI of the target site. The learning part is performed using training data that is a subset of subjects that are matched by age and gender for both sites. From the DWI, the RISH features are calculated and used to create a multivariate template, per b-value shell. In template space, the voxel-wise expected value per site s and per harmonic order i [$E_i^s(v)$] of RISH features is calculated as the sample mean over the number of training subjects (N_s): $E_i^s(v) \approx \sum_{p=1}^{N_s} RISH_i^s(v,p)/N_s$, where s represents the site, v the voxel location in template space and p the training subject. Then, voxel-wise scale maps (Φ_i) are computed for each harmonic order i: $\Phi_i(v,R,T) = \sqrt{\frac{E_i^R(v)}{E_i^T(v)+\varepsilon}}$. Next, in the application part, the scale maps are used to calculate the harmonized SH coefficients of the target data per harmonic

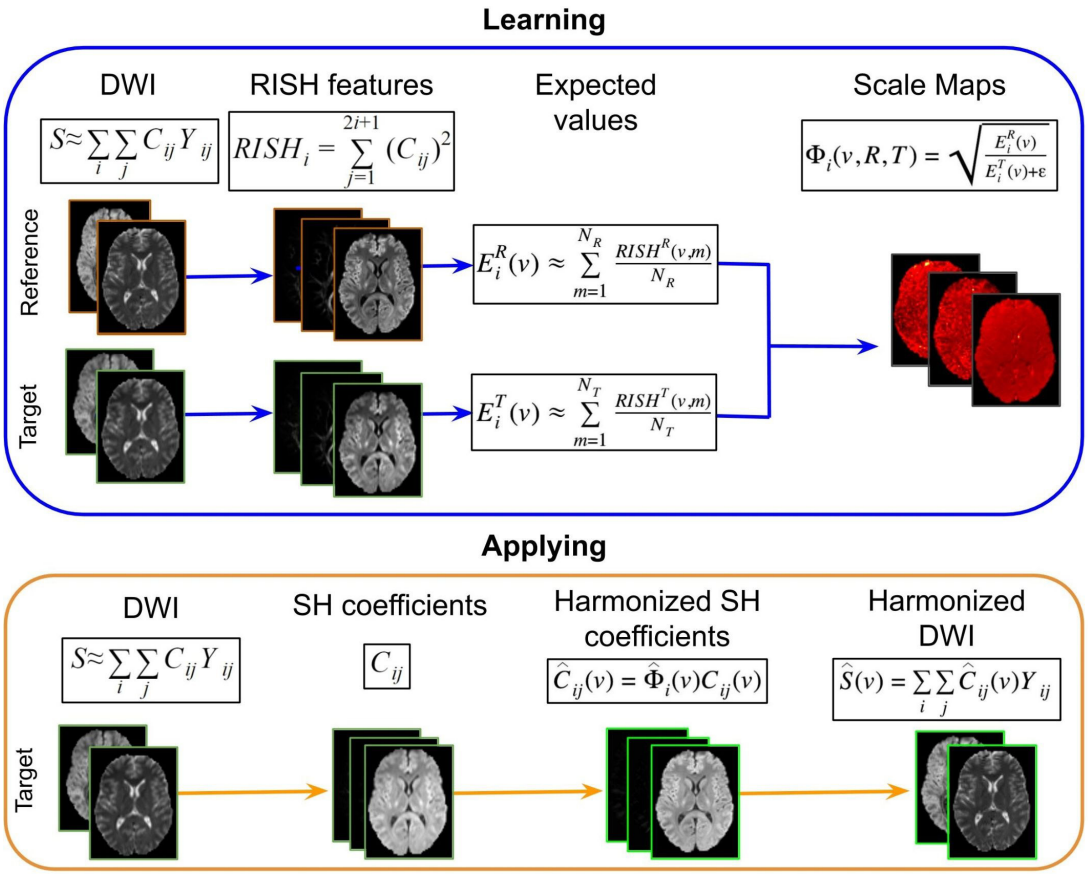

FIGURE 3 | Representation of the RISH harmonization approach. Consider the purpose of modifying the DWI acquired in a target site, to correspond to the DWI acquired in the reference site. In the learning part using matched subjects, the RISH features are computed in native space from the DWI for the two data sets separately: reference (*R*) and target (*T*) sites. Then RISH features are transformed to a common space, the expected values are calculated per site *s* and per harmonic order *i* (E_i^s), after which the scale maps are calculated (Φ_i). The scale maps, which are computed for each harmonic order *i*, represent the transformation of the RISH features from target to reference site. Next, in the application step, the SH coefficients from the target site are calculated, the scale maps are warped into native space and applied to the SH coefficients, creating harmonized SH coefficients in native space. Those are transformed back to the signal intensity domain, obtaining the harmonized DWI. Thus, harmonized DWI from the target site can be jointly analyzed with the ones from the reference site.

order: $\hat{C}_{ij}(v) = \hat{\Phi}_i(v)C_{ij}(v)$. Next, the image is transformed from SH domain back to the intensity signal domain $[\hat{S}(v)]$ using the harmonized SH coefficients: $\hat{S}(v) = \sum_i \sum_j \hat{C}_{ij}(v)Y_{ij}$.

Rotation invariant spherical harmonics has many advantages, the most important one being that it harmonizes the raw dMRI signal in a model-independent manner. The mapping captures only site-related differences, preserving the between-subject biological variation and fiber orientation (Karayumak et al., 2019). However, a limitation is that it requires dMRI data with similar acquisition parameters across sites. It also requires the same number of matched controls that are scanned in both reference and target sites to obtain the scale maps.

Machine Learning

In the past decade, several diffusion data harmonization methods have been developed employing a machine learning approach, such as sparse dictionary learning (SDL) and deep learning (DL).

Sparse Dictionary Learning (SDL)

Sparse dictionary learning is a representation learning method aiming at representing the input data as a linear combination of elements (the sparse dictionary), thus reducing the complexity of the harmonization problem (Mairal et al., 2010). The dictionary elements are small patches of spatial and angular image features (e.g., 3 × 3 × 3 × 5 voxels) that are learnt from the data itself. From a large set of random features, SDL extracts the common features with which full images can be reconstructed. The idea behind applying SDL for harmonization is that when a sparse dictionary can be constructed from data originating from multiple sites, the learnt imaging features will not include features of inter-site variability, as those are not common across the input data. Reconstructing dMRI data with a sparse dictionary, would then effectively harmonize the data (St-Jean et al., 2016; St-Jean et al., 2017).

An advantage of this method is that modeling a signal with such a sparse decomposition (sparse coding) is very effective in detecting salient regions that are related to the more informative

areas. However, a disadvantage is that, depending on the interest points and the type/resolution of the image, sometimes only a few regions are detected.

Deep Learning (DL)

The DL approach, which is illustrated in **Figure 4**, consists of two steps: (1) Training: the learning stage in which the network parameters are optimized using the DWI from the same subjects acquired in two sites (target and reference) and (2) Inference: the trained network is applied to harmonize all subjects of the target site.

The current deep learning algorithms for diffusion data harmonization are mainly based on spherical harmonic features. The aim is to bring all the images in the same SH domain, by modifying the SH coefficients of the target data creating harmonized DWIs of the target site that are comparable to the DWIs from reference site. To achieve this, the network is trained to generate the harmonized image starting from the image acquired at a target site, using the image acquired in the reference site as ground truth, as illustrated in **Figure 4**. Hence, diffusion data from subjects that were acquired in both reference and target sites are used for training the network. Once it is trained, the inference can be done for other subjects from the target site, to create harmonized images.

Tax et al. (2019) presented a summary of four deep learning algorithms and one sparse dictionary learning harmonization algorithm used to evaluate two harmonization tasks in diffusion MRI: scanner-to-scanner mapping and angular- and spatial-resolution enhancement, i.e., mapping between standard and state-of-the-art acquisitions. Each of the algorithms was built with different net architectures and strategies. The deep learning algorithms that were evaluated by Tax et al. (2019) are: spherical harmonic network (SHNet), spherical harmonic residual network (SHResNet), spherical network (SphericalNet), and fully convolutional shuffling network (FCSNet). The used SH coefficients, on which the net is based, are obtained starting from the diffusion signal of the same subjects scanned in different scanners and with different acquisition schemes. Here we summarize some of these methods. A more extensive benchmark can be found in Tax et al. (2019).

Spherical Harmonic Network (SHNet)

Spherical Harmonic Network is based on a classical Fully Connected Network (FCN) architecture, composed of a cascade of three fully connected layers, in which the rectified linear unity (ReLU) function is used as the activation function (Golkov et al., 2016; Koppers et al., 2017). Next, a batch normalization layer is used to stabilize. The different weights of the neural network layers are tuned by using paired images from different sites. The net is trained by matching data between the target site and the reference site to obtain the harmonized image. Once the network is trained, it can be used to harmonize unseen datasets from the target site. The main advantage of this network is that it is a simple FCN approach to tackle the harmonization problem. However, it might not be sufficiently sensitive to learn all the complex features of an accurate harmonization procedure.

Spherical Harmonic Residual Network (SHResNet)

A Convolutional Neural Network (CNN) approach has been presented by Koppers et al. (2018). In this case, the network algorithm is based on the novel concept of residual structure by He et al. (2016). This approach is based on the difference between the input and the ground truth (target signal). The main building blocks of SHResNet are so-called functional units consisting of three convolutional layers, where each functional unit predicts the coefficients of a single SH order (Koppers et al., 2017). The main advantage of using a residual network structure consists in the robustness against the degradation problem (decrease of accuracy due to the increased network depth) and hence enabling the use of a deeper network (more convolutional layers). Nonetheless, the harmonization is done per harmonic order of the SH signal, thus, the signal from both target and reference should have the same SH orders.

Spherical Network (SphericalNet)

SphericalNet is a novel deep learning approach based on spherical surface convolutions (Koppers and Merhof, 2018). It transforms the signal from SH space into spherical surface space, and performs three spherical surface convolutions. After each of these convolutions, a sigmoid activation function is applied in order to limit the signal's range between 0 and 1 (Tax et al., 2019). The signal is converted back to SH space, followed by three 3-D convolutional layers with parametric ReLU as activation. Spatial information is combined in the last convolutional layer to project neighborhood info into one voxel. The advantage of this algorithm is that it uses spherical information during spatial convolution to improve accuracy in the harmonization procedure. However, for this algorithm the intensity signal has to be transformed twice (for SH domain and then to spherical surface domain), which could introduce additional complexity to the harmonization problem.

Fully Convolutional Shuffling Network (FCSNet)

Fully convolutional network is a patch-based deep learning harmonization algorithm inspired by Tanno et al. (2017). The architecture of this network contains four hidden convolutional layers with ReLU activation. Large patches are used as input, overlayed to cover the entire brain, and smaller patches are obtained as output. The last layer contains a "shuffle" operation and is composed of "skip" connections to increase the prediction accuracy. The cost function for this algorithm has two parts: channel-wise loss and loss on the function-value. The algorithm uses the patched-based fully convolutional network for diffusion data harmonization and resolution enhancement. One advantage of this approach is the use of large patches that inform about the local neighborhood and are beneficial for the harmonization procedure. On the other hand, neighborhood data could be biased and end up corrupting the harmonization algorithm.

Deep learning algorithms demonstrated the robust capability of solving non-linear problems such as data harmonization. However, some limitations are: (1) overfitting, i.e., when the model is more accurate in fitting known data but less accurate in predicting unseen data, (2) the need for a large amount of matched subjects scanned at different sites with similar

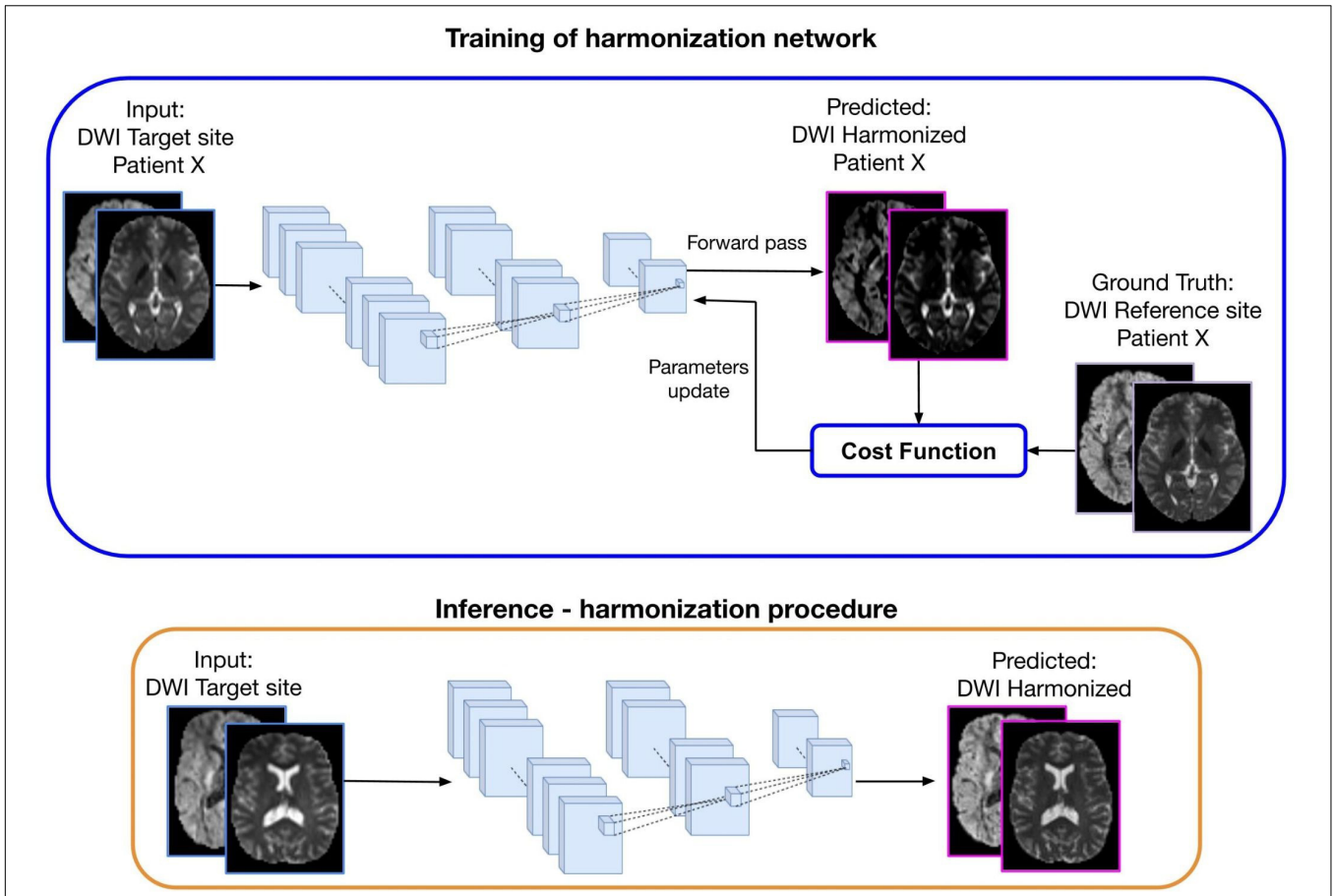

FIGURE 4 | Representation of a deep learning approach for diffusion data harmonization. The purpose of the method is to modify the DWI acquired at the target site, to correspond to the DWI of the same subject acquired at the reference site. In the training part, DWI from the target site is used as input and DWI from the reference site as ground truth, for patient *X*. Matched subjects are used to tune the weights of the harmonization network. During the forward phase, the network produces the predicted harmonized DWI that is compared with the corresponding expected DWI from the reference site. The difference between the predicted and the ground-truth (cost function) is back propagated into the network to update the weights in such a way that the loss decreases and the predicted harmonized DWI is closer to the ground truth. In the inference step, the trained network is used to generate the predicted harmonized DWI from unseen DWI data of the target site, which then become comparable to the DWI from the reference site.

acquisition sequences per site for training and (3) possible distortion of pathological information, if the net is trained with healthy subjects and then applied to patients.

Method of Moments (MoM)

Method of Moments is a statistical harmonization approach that uses spherical moments to map DWI images from target to reference sites (Huynh et al., 2019). The first moment (M_1) corresponds to the spherical mean and the second central moment (C_2) corresponds to the spherical variance. The core idea is to match the spherical mean and spherical variance in order to correct for unwanted variability. Each voxel-wise n-th spherical moment (M_n) is defined as the diffusion signal at constant b-value (S_b) raised to the power of n integrated over all directions g: $M_\mathrm{n}[S_\mathrm{b}] = \int S_\mathrm{b}^\mathrm{n}(g)dg$. MoM matches M_1 and C_2 per b-shell b using the mapping function (f_θ): $M_1[R_\mathrm{b}] = M_1[f_\theta(T_\mathrm{b})]$ and $C_2[R_\mathrm{b}] = C_2[f_\theta(T_\mathrm{b})]$, where R_b is the diffusion signal acquired at the reference site, and T_b the signal at the target site. Considering the mapping function as $f_{\theta=\{\alpha,\beta\}}(S) = \alpha S + \beta$, α and β are the mapping coefficients calculated as $\alpha_b = \sqrt{\frac{C_2[R_\mathrm{b}]}{C_2[T_\mathrm{b}]}}$ and $\beta_\mathrm{b} = M_1[R_\mathrm{b}] - \alpha_\mathrm{b} M_1[T_\mathrm{b}]$. The MoM parameters are calculated in template space and then warped back to native space of the target subjects and applied to the DWI images. The MoM-harmonized DWI signal is $S_\mathrm{b}^\mathrm{MoM} = \alpha_\mathrm{b} S_\mathrm{b} + \beta_\mathrm{b}$.

The MoM approach is illustrated in **Figure 5**. In this method, M_1 and C_2 are computed in native space from the DWIs acquired in the reference and target sites. Next, the moment images are warped into a common space that is defined by the target data at the population level. Population moment median images across subjects are calculated for each of the moments for each of the sites. The mapping parameters (α and β) for the target site are obtained by matching the population median moments using the linear mapping function f_θ. These parameters are warped to native space for each of the subjects of the target site and the mapping function is applied voxel-wise. Lastly, the harmonized DWI of the target data is obtained.

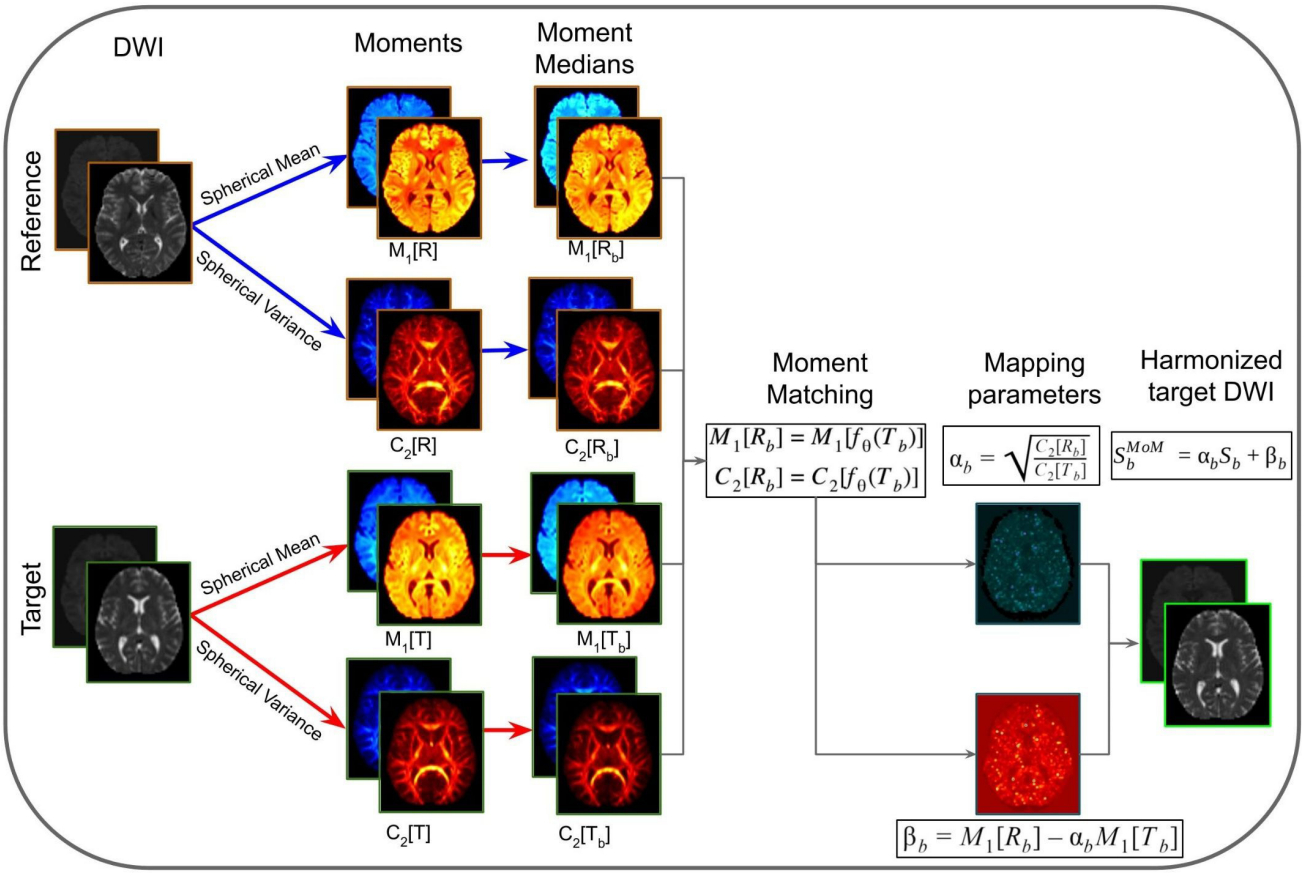

FIGURE 5 | Representation of the method of moments harmonization pipeline. The purpose of the method is to modify the DWI of the target site, to correspond to the DWI acquired in the reference site. Initially, the diffusion signal in the reference (*R*) and target (*T*) are used to compute spherical means ($M_1[R]$ and $M_1[T]$) and spherical variances ($C_2[R]$ and $C_2[T]$) in native space for each b-shells (*b*). The spherical moments are warped to a common space, based on the target population. Then the moment medians are calculated across subjects ($M_1[R_b]$, $C_2[R_b]$, $M_1[T_b]$, and $C_2[T_b]$). Afterward, the mapping parameters (α_b and β_b) are calculated per b-shell, by matching the population moments. The mapping parameters are warped to native space and applied voxel-wise to the DWI images of target site subjects, obtaining the harmonized DWI.

Advantages of the MoM are that it (1) allows direct harmonization of DWI images, without the need to represent them in any other space domain (e.g., SH space); (2) preserves directional information of the signal; (3) does not require that reference and target data have the same number of gradient directions; (4) does not require training data or matched populations with controls/patients, and (5) allows the harmonization of either a subject or a population of subjects. However, MoM as described in Huynh et al. (2019) does not harmonize multi-site data with different spatial resolution or different *b*-values. Possible solutions to cope with different spatial resolutions and different *b*-values would be to resample the reference data to the resolution of the target data, and rescale the signal, respectively, both prior to harmonization.

DISCUSSION

Multi-center and/or longitudinal studies using diffusion MRI data are significantly affected by inter- and intra-site variability. Sources of variability include, but are not limited to, hardware, acquisition settings, reconstruction algorithms, incompatible data formats and data quality. To cope with this variability, regulations and strategies are needed to facilitate harmonization of multi-center diffusion MRI data. In that respect, MR scanner vendors and researchers have a responsibility regarding the access and storage of DWI data, and transparency on reconstruction algorithms, acquisition protocols and applied pre- and post-processing steps. Ideally, worldwide governments should ally to enforce regulations regarding calibration procedures to MR scanner vendors. The use of the same quantitative calibration phantom and a standard procedure would decrease inter-scanner variability (Keenan et al., 2017; Prohl et al., 2019).

The need for harmonization has increased with the availability of large diffusion MRI multi-center datasets. Examples of these are the Human Connectome Project (HCP[2]), the Alzheimer's

[2]https://www.humanconnectome.org/

Disease Neuroimaging Initiative (ADNI[3]), CENTER-TBI[4], and the Cross-scanner and cross-protocol diffusion MRI data harmonization (Tax et al., 2019). For performing joint analysis of data that have been acquired with multiple acquisition settings, several statistical and mathematical harmonization approaches have been developed to reduce unwanted site variability while preserving the biological variability.

To overcome the challenges with respect to joint analysis of multi-center diffusion data, the scientific community has gathered to participate in challenges on data harmonization. The Diffusion MRI Data Harmonization[5] 2017 and the Multi-shell Diffusion MRI Harmonization Challenge 2018 (MUSHAC[6]) were proposed with the aim to evaluate the performance of algorithms that enable the harmonization of DWI data. From the last challenge, Ning et al. (2019) presented a summary of results comparing the effects of DWIH methods on diffusion parametric maps. Different DWIH methods were used to harmonize the multi-shell DWI data. The algorithms range over three approaches: interpolation-based, regression-based and CNN algorithms. Diffusion parametric maps were calculated before and after the harmonization procedure, such as FA, MD, and MK. The results demonstrated that the harmonization algorithms are significantly effective in reducing the variability and maintaining the biological information.

In this paper, we have reviewed a variety of harmonization methods proposed in the literature. The decision as to which method to use depends on several aspects, such as the study design, the research question and the available data. In **Table 1**, we have categorized the reviewed methods in terms of their intrinsic properties. This categorization may help to select a harmonization method, given a certain diffusion MRI dataset and a specific research question. Additionally, **Figure 6** shows a flowchart that could provide guidance for selecting the most appropriate harmonization strategy.

For example, the flowchart can be applied to the study of Zavaliangos-Petropulu et al. (2019), who assessed the relation between diffusion MRI indices and cognitive impairment in brain aging using the ADNI3 dataset. In this study, new harmonized metrics maps (FA, MD, AD, and RD) were created using the ComBat method to remove any site-effects from the results. Following the flowchart presented in **Figure 6**, first, the research was related to the harmonization of diffusion metric maps, thus, the right segment of the chart is suggested to be followed. Next, the researchers aimed to create new harmonized maps, in this case the choice of a regression of covariates method was logical and appropriate. Along these lines, the suggested harmonization approach by our flowchart is in agreement with the decision from the authors.

In general, it is an ongoing challenge to define a gold standard for dMRI harmonization. A possible explanation for this might come from the complexity of removing the unwanted variability. The sources of unwanted variability may stem from differences in number of subjects acquired per site, MRI hardware, acquisition protocol (voxel size, repetition time, echo time, number of diffusion directions, number of b-shells, etc.), pre-processing steps and co-registration effects. In these circumstances, the preservation of expected biological variability is a useful criterion for evaluating the efficacy of harmonization methods, but this is only possible when the same subjects are scanned at different sites. When traveling human phantoms are included in the study design this provides a ground truth and allows for carefully evaluating the newly computed features and their accuracy and precision (Tax et al., 2019). However, traveling human phantoms datasets are mostly absent from a scenario of multi-center studies, where distinct subjects are scanned at different sites. Additionally, a note of caution in both cases is due here since anatomical differences or co-registration deformations (to a common space) may cause significant errors in the harmonization.

Although DPMH approaches have demonstrated their ability to harmonize diffusion metric measures for joint analysis in multi-center studies, there are some drawbacks, which can be avoided by using DWIH methods. First, DPMH methods require different transforms to harmonize each of the diffusion metrics of interest. This may have implications for multivariate analyses, as it is not guaranteed that subject-specific patterns (e.g., high FA in combination with low MD) are preserved after both metrics are harmonized separately. Second, DWIH methods do not rely on a specific diffusion model, hence unwanted variation is not propagated (and as a result made more complex) through model fitting. Moreover, any diffusion metric estimated from DWIH harmonized DWIs will automatically be harmonized as well. In this regard, DWIH approaches are more promising for reliable harmonization.

In a recent study by Cetin-Karayumak et al. (2019), DWIH was applied to harmonize diffusion MRI multi-site data prior to detection of white matter abnormalities in schizophrenia patients. RISH was retrospectively applied to DWIs of 13 different sites to remove the site-related differences. For this, a reference site was chosen and the DWI data from the other 12 sites were harmonized accordingly. The harmonization performance was evaluated in a group of matched controls, using their FA maps before and after harmonization. It was shown that the statistical differences between sites were removed and the inter-subject biological differences were preserved.

Nonetheless, many challenges remain for diffusion data harmonization in multi-center studies. Ideally, novel harmonization methods should not require training data of subjects scanned in multiple centers, and be applicable to data acquired with different spatial resolution, number of b shells, or number of diffusion gradient directions. Moreover, the availability of easily implementable methods and open-source platforms are important assets to encourage researchers to perform diffusion data harmonization in multi-center and longitudinal studies.

Furthermore, harmonization methods should be generalizable to clinical cases. Up to now, serious challenges that limit voxel-wise harmonization of DWI data of clinical patients are the co-registration requirement, since disease-related anatomical alterations may severely complicate co-registration,

[3]http://adni.loni.usc.edu/

[4]https://www.center-tbi.eu/

[5]https://projects.iq.harvard.edu/cdmri2017/challenge

[6]https://projects.iq.harvard.edu/cdmri2018/challenge

TABLE 1 | Overview of the harmonization methods presented in this review.

Category	Method		References	Statistical harmonization	Creates new harmonized images	Individual measures required	Same subjects acquired in multiple centers required	Training data required	Similar acquisition protocols required	Inter subject co-registration of DWI required	Mapping parameters on template space
DPMH		Meta-analysis	Salimi-Khorshidi et al., 2009; Teipel et al., 2012; Jahanshad et al., 2013; Kochunov et al., 2014; Zhu et al., 2019	X							
		Mega-analysis		X		X					
	Regression of covariates	Human-phantom based harmonization (HuP)	Pohl et al., 2016	X	X	X			X		
		Hardware-phantom based harmonization (HaP)	Timmermans et al., 2019	X		X			X		
		Global Scaling (GS)	Fortin et al., 2017	X	X	X				X	
		Removal of Artificial Voxel Effect by Linear Regression (RAVEL)	Fortin et al., 2016	X	X	X				X	X
		Surrogate Variable Analysis (SVA)	Leek et al., 2012; Fortin et al., 2017	X	X	X				X	X
		Combined association test (ComBat)	Fortin et al., 2017	X	X	X				X	X
DWIH	Rotation Invariant Spherical Harmonics (RISH)		Mirzaalian et al., 2015, 2016, 2018; Karayumak et al., 2019		X	X		X	X	X	X
	Machine learning	Sparse Dictionary Learning (SDL)	St-Jean et al., 2016, 2017; Tax et al., 2019		X	X	X			X	
		Deep Learning (DL)	Golkov et al., 2016; Koppers et al., 2017, 2018; Tanno et al., 2017; Koppers and Merhof, 2018; Tax et al., 2019		X	X	X			X	
	Method of Moments (MoM)		Huynh et al., 2019	X	X	X				X	X

Comparison between the methods related to: implementation of statistical harmonization, creation of new harmonized images, requirement of individual measures, requirement of images from the same subjects acquired in multiple centers, requirement of training data (i.e., matched subjects across sites are needed for obtaining the mapping between sites), requirement of similar acquisition protocols (i.e., diffusion directions, b-values, spatial resolution, TR, TE, SNR, etc.), requirement of inter subject co-registration, and implementation of mapping between sites through mapping parameters on template space. The X denotes if the method requires or performs the specific condition described in the column.

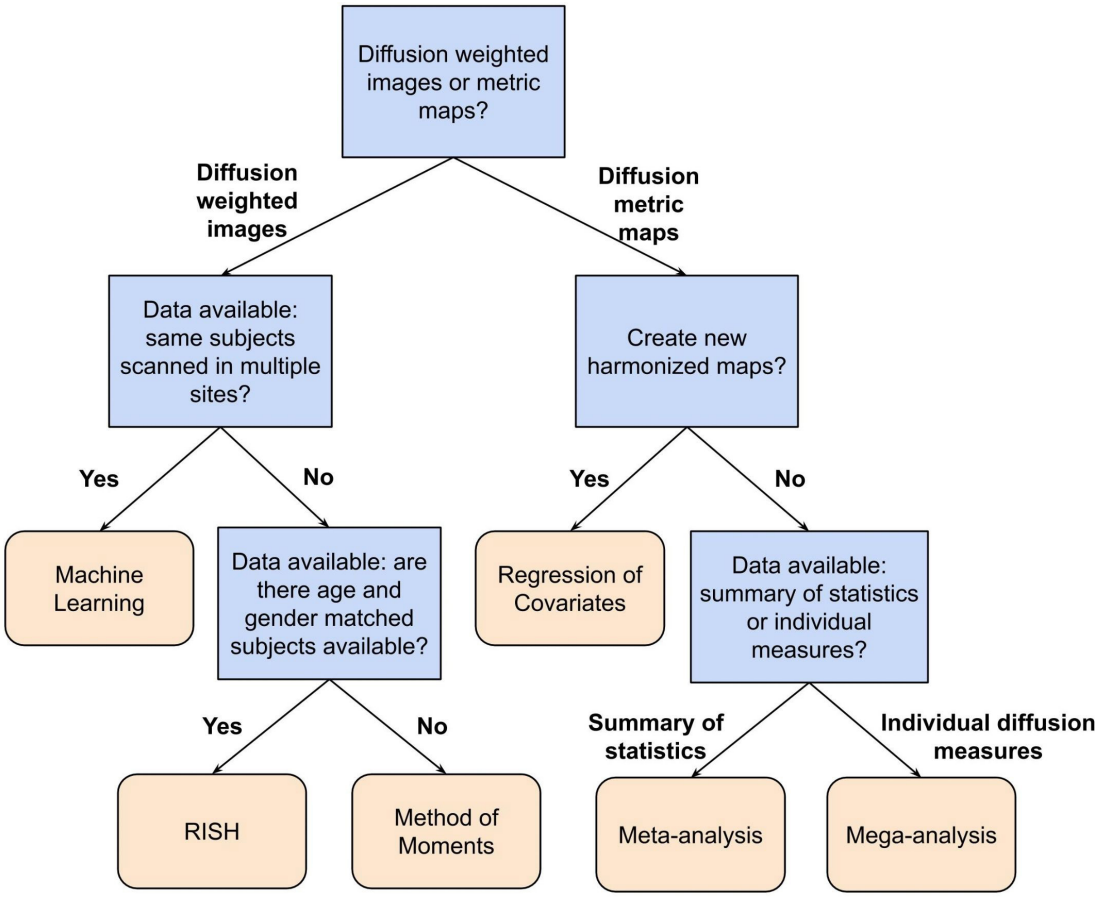

FIGURE 6 | Flowchart describing a possible way to select a suitable harmonization method depending on the available data and research question at hand. In this flowchart, the first question to be answered is: Do you want to harmonize the DWI or the diffusion metric maps? For harmonization of the diffusion metric maps (right segment of the flowchart), the following question is: Do you want to create new harmonized metric maps? If so, the suggested harmonization approach would be one of the regression of covariates methods. In case of a negative answer, the next question is: Do you have individual measures available or a summary of statistics? If the user has a summary of statistics, the suggestion is to use a meta-analysis approach, otherwise, if one has individual diffusion measures, the suggestion is to harmonize the data using a mega-analysis approach. On the other hand, for harmonization of DWIs (left segment of the flowchart), the next question is: Do you have DWIs of the same subjects acquired in multiple sites? In case of an affirmative answer, the suggested approach is machine learning, which comprehends deep learning and sparse dictionary learning methods. In case of a negative answer, the following question is: Do you have DWIs of a cohort of subjects that is age- and gender-matched between the sites? If the user has matched data, the RISH method is suggested. Otherwise, the method of moments is the suggested approach.

and the condition that the pathological content (e.g., diffusion properties of lesions) should be harmonized while the expected biological variability should not be affected. To overcome these limitations, the use of clinical data during the training of DWIH harmonization approaches would be valuable.

CONCLUSION

While dMRI is routinely used in clinical workflows, comparing the signal intensity of dMRI scans across sites and over time is challenging. Harmonization methods aim to overcome this by recalibrating/recalculating either the DWI signal intensities or the resulting diffusion metrics. In this article an overview of harmonization methods in the literature was presented, covering meta- and mega-analysis, regression of covariates, rotation invariant spherical harmonics, machine learning algorithms and the method of moments. The proposed feature table and flowchart present the main characteristics of the methods, assisting in the decision of which method to use depending on the study design and the available data. Future developments of diffusion harmonization methods may benefit from focusing on DWIH approaches, avoiding unwanted variation propagates through diffusion model fitting.

AUTHOR CONTRIBUTIONS

MP and RP wrote the manuscript with comments from TB, PVD, P-JG, BJ, AR, AdD, and JS. MP and RP contributed equally to this manuscript. All authors read and approved the final manuscript.

FUNDING

This project has received funding from the European Union's Horizon 2020 research and innovation programme under the Marie Skłodowska-Curie grant agreement No 764513. PVD and BJ are supported by the Research Foundation (FWO) Flanders, Belgium. This work was also supported by the European Space Agency (ESA) and BELSPO Prodex and the Flemish Government under the Research program Artificial Intelligence (AI) Flanders. The diffusion data used for **Figures 3**, **4**, and **5** were acquired at the United Kingdom National Facility for *In Vivo* MR Imaging of Human Tissue Microstructure located in CUBRIC funded by the EPSRC (grant EP/M029778/1), and The Wolfson Foundation. Acquisition and processing of the data was supported by a Rubicon grant from the NWO (680-50-1527), a Wellcome Trust Investigator Award (096646/Z/11/Z), and a Wellcome Trust Strategic Award (104943/Z/14/Z). This database was initiated by the 2017 and 2018 MICCAI Computational Diffusion MRI committees (Chantal Tax, Francesco Grussu, Enrico Kaden, Lipeng Ning, Jelle Veraart, Elisenda Bonet-Carne, and Farshid Sepehrband) and CUBRIC, Cardiff University (Chantal Tax, Derek Jones, Umesh Rudrapatna, John Evans, Greg Parker, Slawomir Kusmia, Cyril Charron, and David Linden).

REFERENCES

Alexander, A. L., Lee, J. E., Wu, Y. C., and Field, A. S. (2006). Comparison of diffusion tensor imaging measurements at 3.0 *T versus* 1.5 T with and without parallel imaging. *Neuroimag. Clin. N. Am.* 16, 299–309. doi: 10.1016/j.nic.2006.02.006

Avants, B. B., Tustison, N. J., Song, G., Cook, P. A., Klein, A., and Gee, J. C. (2011). A reproducible evaluation of ants similarity metric performance in brain image registration. *Neuroimage* 54, 2033–2044.

Beckmann, C. F., Jenkinson, M., and Smith, S. M. (2003). General multilevel linear modeling for group analysis in FMRI. *Neuroimage* 20, 1052–1063. doi: 10.1016/S1053-8119(03)00435-X

Button, K. S., Ioannidis, J. P. A., Mokrysz, C., Nosek, B. A., Flint, J., Robinson, E. S. J., et al. (2013). "Power failure: why small sample size undermines the reliability of neuroscience": Erratum. *Nat. Rev. Neurosci.* 14:442.

Cannon, T. D., Sun, F., McEwen, S. J., Papademetris, X., He, G., van Erp, T. G. M., et al. (2014). Reliability of neuroanatomical measurements in a multisite longitudinal study of youth at risk for psychosis. *Hum. Brain Mapp.* 35, 2424–2434. doi: 10.1002/hbm.22338

Cetin-Karayumak, S., Di Biase, M. A., Chunga, N., Reid, B., Somes, N., Lyall, A. E., et al. (2019). White matter abnormalities across the lifespan of schizophrenia: a harmonized multi-site diffusion MRI study. *Mol. Psychiatry* doi: 10.1038/s41380-019-0509-y [Epub ahead of print]

Forsyth, J. K., McEwen, S. C., Gee, D. G., Bearden, C. E., Addington, J., Goodyear, B., et al. (2014). Reliability of functional magnetic resonance imaging activation during working memory in a multi-site study: analysis from the North American prodrome longitudinal study. *Neuroimage* 97, 41–52. doi: 10.1016/j.neuroimage.2014.04.027

Fortin, J. P., Parker, D., Tunç, B., Watanabe, T., Elliott, M. A., Ruparel, K., et al. (2017). Harmonization of multi-site diffusion tensor imaging data. *Neuroimage* 161, 149–170. doi: 10.1016/j.neuroimage.2017.08.047

Fortin, J. P., Sweeney, E. M., Muschelli, J., Crainiceanu, C. M., and Shinohara, R. T. (2016). Removing inter-subject technical variability in magnetic resonance imaging studies. *Neuroimage* 132, 198–212. doi: 10.1016/j.neuroimage.2016.02.036

Fox, R. J., Sakaie, K., Lee, J.-C., Debbins, J. P., Liu, Y., Arnold, D. L., et al. (2012). A validation study of multicenter diffusion tensor imaging: reliability of fractional anisotropy and diffusivity values. *Am. J. Neuroradiol.* 33, 695–700. doi: 10.3174/ajnr.A2844

Golkov, V., Dosovitskiy, A., Sperl, J. I., Menzel, M. I., Czisch, M., Samann, P., et al. (2016). Q-space deep learning: twelve-fold shorter and model-free diffusion MRI scans. *IEEE Trans. Med. Imaging* 35, 1344–1351. doi: 10.1109/tmi.2016.2551324

Grech-Sollars, M., Hales, P. W., Miyazaki, K., Raschke, F., Rodriguez, D., Wilson, M., et al. (2015). Multi-centre reproducibility of diffusion MRI parameters for clinical sequences in the brain. *NMR Biomed.* 28, 468–485. doi: 10.1002/nbm.3269

He, K., Zhang, X., Ren, S., and Sun, J. (2016). "Deep residual learning for image recognition," in *Proceedings of the IEEE Computer Society Conference on Computer Vision and Pattern Recognition*, San Juan, 770–778. doi: 10.1109/CVPR.2016.90

Huynh, K. M., Chen, G., Wu, Y., Shen, D., and Yap, P. (2019). Multi-site harmonization of diffusion MRI data via method of moments. *IEEE Trans. Med. Imaging* 38, 1599–1609. doi: 10.1109/tmi.2019.2895020

Jahanshad, N., Kochunov, P. V., Sprooten, E., Mandl, R. C., Nichols, T. E., Almasy, L., et al. (2013). Multi-site genetic analysis of diffusion images and voxelwise heritability analysis: a pilot project of the ENIGMA–DTI working group. *Neuroimage* 81, 455–469. doi: 10.1016/j.neuroimage.2013.04.061

Jenkins, J., Chang, L. C., Hutchinson, E., Irfanoglu, M. O., and Pierpaoli, C. (2016). "Harmonization of methods to facilitate reproducibility in medical data processing: applications to diffusion tensor magnetic resonance imaging," in *Proceedings–2016 IEEE International Conference on Big Data, Big Data 2016*, Washington, DC, 3992–3994. doi: 10.1109/BigData.2016.7841086

Jenkinson, M., Beckmann, C. F., Behrens, T. E. J., Woolrich, M. W., and Smith, S. M. (2012). FSL. *Neuroimage* 62, 782–790. doi: 10.1016/J.NEUROIMAGE.2011.09.015

Johnson, W. E., Li, C., and Rabinovic, A. (2007). Adjusting batch effects in microarray expression data using empirical Bayes methods. *Biostatistics* 8, 118–127. doi: 10.1093/biostatistics/kxj037

Jones, D. K. (2010). Precision and accuracy in diffusion tensor magnetic resonance imaging. *Topics Magn. Reson. Imaging* 21, 87–99. doi: 10.1097/RMR.0b013e31821e56ac

Jovicich, J., Barkhof, F., Babiloni, C., Herholz, K., Mulert, C., van Berckel, B. N. M., et al. (2019). Harmonization of neuroimaging biomarkers for neurodegenerative diseases: a survey in the imaging community of perceived barriers and suggested actions. *Alzheimer's Dementia* 11, 69–73. doi: 10.1016/j.dadm.2018.11.005

Jovicich, J., Marizzoni, M., Bosch, B., Bartrés-Faz, D., Arnold, J., Benninghoff, J., et al. (2014). Multisite longitudinal reliability of tract-based spatial statistics in diffusion tensor imaging of healthy elderly subjects. *Neuroimage* 101, 390–403. doi: 10.1016/j.neuroimage.2014.06.075

Karayumak, S. C., Bouix, S., Ning, L., James, A., Crow, T., Shenton, M., et al. (2019). Retrospective harmonization of multi-site diffusion MRI data acquired with different acquisition parameters. *Neuroimage* 184, 180–200. doi: 10.1016/j.neuroimage.2018.08.073

Keenan, K. E., Ainslie, M., Barker, A. J., Boss, M. A., Cecil, K. M., Charles, C., et al. (2017). Quantitative magnetic resonance imaging phantoms: a review and the need for a system phantom. *Magn. Reson. Med.* 79, 48–61. doi: 10.1002/mrm.26982

Kelly, S., Jahanshad, N., Zalesky, A., Kochunov, P., Agartz, I., Alloza, C., et al. (2018). Widespread white matter microstructural differences in schizophrenia across 4322 individuals: results from the ENIGMA Schizophrenia DTI working group. *Mol. Psychiatry* 23, 1261–1269. doi: 10.1038/mp.2017.170

Klein, S., Staring, M., Murphy, K., Viergever, M. A., and Pluim, J. (2010). elastix: a toolbox for intensity- based medical image registration. *IEEE Trans. Med. Imaging* 29, 196–205. doi: 10.1109/TMI.2009.2035616

Kochunov, P., Jahanshad, N., Sprooten, E., Nichols, T. E., Mandl, R. C., Almasy, L., et al. (2014). Multi-site study of additive genetic effects on fractional anisotropy of cerebral white matter: comparing meta and megaanalytical approaches for data pooling. *Neuroimage* 95, 136–150. doi: 10.1016/j.neuroimage.2014.03.033

Koppers, S., Bloy, L., Berman, J. I., Tax, C. M. W., Edgar, J. C., and Merhof, D. (2018). "Spherical harmonic residual network for diffusion signal harmonization," in *Computational Diffusion MRI*, eds E. Bonet-Carne, F. Grussu, L. Ning, F. Sepehrband, C. M. W. Tax (Berlin: Springer).

Koppers, S., Haarburger, C., and Merhof, D. (2017). "Diffusion MRI signal augmentation: from single shell to multi shell with deep learning," in *Proceedings of the Computational Diffusion MRI: MICCAI Workshop*, Athens, 61–70. doi: 10.1007/978-3-319-54130-3_5

Koppers, S., and Merhof, D. (2018). *DELIMIT PyTorch - An extension for Deep Learning in Diffusion Imaging*. Available online at: http://arxiv.org/abs/1808.01517 (accessed June 20, 2019).

Kumar, R., Gupta, R. K., Husain, M., Chaudhry, C., Srivastava, A., Saksena, S., et al. (2009). Comparative evaluation of corpus callosum DTI metrics in acute mild and moderate traumatic brain injury: its correlation with neuropsychometric test. *Brain Injury* 23, 675–685. doi: 10.1080/02699050903014915

Leek, J. T., Johnson, W. E., Parker, H. S., Jaffe, A. E., and Storey, J. D. (2012). The SVA package for removing batch effects and other unwanted variation in high-throughput experiments. *Bioinformatics* 28, 882–883. doi: 10.1093/bioinformatics/bts034

Leek, J. T., Scharpf, R. B., Bravo, H. C., Simcha, D., Langmead, B., Johnson, W. E., et al. (2010). Tackling the widespread and critical impact of batch effects in high-throughput data. *Nat. Rev. Genet.* 11, 733–739. doi: 10.1038/nrg2825

Mahoney, C. J., Simpson, I. J. A., Nicholas, J. M., Fletcher, P. D., Downey, L. E., Golden, H. L., et al. (2015). Longitudinal diffusion tensor imaging in frontotemporal dementia. *Ann. Neurol.* 77, 33–46. doi: 10.1002/ana.24296

Mairal, J., Bach, F., Ponce, J., and Sapiro, G. (2010). Online learning for matrix factorization and sparse coding. *J. Mach. Learn. Res.* 11, 19–60. doi: 10.1145/1756006.1756008

Mirzaalian, H., de Pierrefeu, A., Savadjiev, P., Pasternak, O., Bouix, S., Kubicki, M., Rathi, Y. (2015). Harmonizing Diffusion MRI Data Across Multiple Sites and Scanners. in *Medical Image Computing and Computer-Assisted Intervention – MICCAI 2015*, eds N. Navab, J. Hornegger, W. M. Wells, & A. Frangi (Cham: Springer International Publishing), doi: 10.1007/978-3-319-24553-9_2

Mirzaalian, H., Ning, L., Savadjiev, P., Pasternak, O., Bouix, S., Michailovich, O., et al. (2016). Inter-site and inter-scanner diffusion MRI data harmonization. *Neuroimage* 135, 311–323. doi: 10.1016/j.neuroimage.2016.04.041

Mirzaalian, H., Ning, L., Savadjiev, P., Pasternak, O., Bouix, S., Michailovich, O., et al. (2018). Multi-site harmonization of diffusion MRI data in a registration framework. *Brain Imaging Behav.* 12, 284–295. doi: 10.1007/s11682-016-9670-y

Nencka, A. S., Meier, T. B., Wang, Y., Muftuler, L. T., Wu, Y.-C., Saykin, A. J., et al. (2017). Stability of MRI metrics in the advanced research core of the NCAA-DoD concussion assessment, research and education (CARE) consortium. *Brain Imaging Behav.* 12, 1121–1140. doi: 10.1007/s11682-017-9775-y

Ni, H., Kavcic, V., Zhu, T., Ekholm, S., and Zhong, J. (2006). Effects of number of diffusion gradient directions on derived diffusion tensor imaging indices in human brain. *Am. J. Neuroradiol.* 27, 1776–1781.

Ning, L., Bonet-Carne, E., Grussu, F., Sepehrband, F., Kaden, E., Veraart, J., et al. (2019). "Muti-shell diffusion MRI harmonisation and enhancement challenge (MUSHAC): progress and results," in *Proceedings of the Computational Diffusion MRI: International MICCAI Workshop*, eds L. Ning, C. M. W. Tax, F. Grussu, E. Bonet-Carne, & F. Sepehrband (Cham: Springer), 217–224. doi: 10.1007/978-3-030-05831-9_18

Nyholm, T., Jonsson, J., Söderström, K., Bergström, P., Carlberg, A., Frykholm, G., et al. (2013). Variability in prostate and seminal vesicle delineations defined on magnetic resonance images, a multi-observer, -center and -sequence study. *Radiat. Oncol.* 8:126. doi: 10.1186/1748-717X-8-126

Palacios, E. M., Martin, A. J., Boss, M. A., Ezekiel, F., Chang, Y. S., Yuh, E. L., et al. (2017). Toward precision and reproducibility of diffusion tensor imaging: a multicenter diffusion phantom and traveling volunteer study. *Am. J. Neuroradiol.* 38, 537–545. doi: 10.3174/ajnr.A5025

Petitti, D. B. (1994). *Meta-Analysis, Decision Analysis, and Cost-Effectiveness Analysis: Methods for Quantitative Synthesis in Medicine*. New York, NY: Oxford University Press.

Pfefferbaum, A., Adalsteinsson, E., and Sullivan, E. V. (2003). Replicability of diffusion tensor imaging measurements of fractional anisotropy and trace in brain. *J. Magn. Reson. Imaging* 18, 427–433. doi: 10.1002/jmri.10377

Pohl, K. M., Sullivan, E. V., Rohlfing, T., Chu, W., Kwon, D., Nichols, B. N., et al. (2016). Harmonizing DTI measurements across scanners to examine the development of white matter microstructure in 803 adolescents of the NCANDA study. *Neuroimage* 130, 194–213. doi: 10.1016/j.neuroimage.2016.01.061

Pourhoseingholi, M. A., Baghestani, A. R., and Vahedi, M. (2012). How to control confounding effects by statistical analysis. *Gastroenterol. Hepatol.* 5, 79–83. doi: 10.22037/ghfbb.v5i2.246

Prohl, A. K., Scherrer, B., Tomas-Fernandez, X., Filip-Dhima, R., Kapur, K., Velasco-Annis, C., et al. (2019). Reproducibility of structural and diffusion tensor imaging in the TACERN multi-center study. *Front. Integr. Neurosci.* 13:24. doi: 10.3389/fnint.2019.00024

Pullens, P., Bladt, P., Sijbers, J., Maas, A. I. R., and Parizel, P. M. (2017). Technical Note: a safe, cheap, and easy-to-use isotropic diffusion MRI phantom for clinical and multicenter studies. *Med. Phys.* 44, 1063–1070. doi: 10.1002/mp.12101

Salimi-Khorshidi, G., Smith, S. M., Keltner, J. R., Wager, T. D., and Nichols, T. E. (2009). Meta-analysis of neuroimaging data: a comparison of image-based and coordinate-based pooling of studies. *Neuroimage* 45, 810–823. doi: 10.1016/j.neuroimage.2008.12.039

Shamonin, D. P., Bron, E. E., Lelieveldt, B. P., Smits, M., Klein, S., Staring, M., et al. (2014). Fast parallel image registration on CPU and GPU for diagnostic classification of Alzheimer's disease. *Front. Neuroinform.* 7:50. doi: 10.3389/fninf.2013.00050

Smith, S. M., and Nichols, T. E. (2018). Statistical Challenges in "Big Data". *Hum. Neuroimag. Neuron* 97, 263–268. doi: 10.1016/j.neuron.2017.12.018

St-Jean, S., Coupé, P., and Descoteaux, M. (2016). Non local spatial and angular matching: enabling higher spatial resolution diffusion MRI datasets through adaptive denoising. *Med. Image Anal.* 32, 115–130. doi: 10.1016/j.media.2016.02.010

St-Jean, S., Viergever, M., and Leemans, A. (2017). "A unified framework for upsampling and denoising of diffusion MRI data," in *Proceedings of the 25th Annual Meeting of ISMRM*, Honolulu, HI, 3533.

Tanno, R., Worrall, D. E., Ghosh, A., Kaden, E., Sotiropoulos, S. N., Criminisi, A., et al. (2017). "Bayesian image quality transfer with CNNs: exploring uncertainty in dMRI super-resolution," *Medical Image Computing and Computer Assisted Intervention - MICCAI 2017. MICCAI 2017. Lecture Notes in Computer Science*, eds M. Descoteaux, L. Maier-Hein, A. Franz, P. Jannin, D. Collins, S. Duchesne (Cham: Springer), Vol 10433, 611–619. doi: 10.1007/978-3-319-66182-7_70

Tax, C. M., Grussu, F., Kaden, E., Ning, L., Rudrapatna, U., John Evans, C., et al. (2019). Cross-scanner and cross-protocol diffusion MRI data harmonisation: a benchmark database and evaluation of algorithms. *Neuroimage* 195, 285–299. doi: 10.1016/j.neuroimage.2019.01.077

Teipel, S. J., Reuter, S., Stieltjes, B., Acosta-Cabronero, J., Ernemann, U., Fellgiebel, A., et al. (2011). Multicenter stability of diffusion tensor imaging measures: a European clinical and physical phantom study. *Psychiatry Res. Neuroimaging* 194, 363–371. doi: 10.1016/j.pscychresns.2011.05.012

Teipel, S. J., Wegrzyn, M., Meindl, T., Frisoni, G., Bokde, A. L. W., Fellgiebel, A., et al. (2012). Anatomical MRI and DTI in the diagnosis of Alzheimer's disease: a european multicenter study. *J. Alzheimer's Dis.* 31, S33–S47. doi: 10.3233/jad-2012-112118

Timmermans, C., Smeets, D., Verheyden, J., Terzopoulos, V., Anania, V., Parizel, P. M., et al. (2019). Potential of a statistical approach for the standardization of multicenter diffusion tensor data: a phantom study. *J. Magn. Reson. Imaging* 49, 955–965. doi: 10.1002/jmri.26333

Tong, Q., He, H., Gong, T., Li, C., Liang, P., Qian, T., et al. (2019). Reproducibility of multi-shell diffusion tractography on traveling subjects: a multicenter study prospective. *Magn. Reson. Imaging* 59, 1–9. doi: 10.1016/j.mri.2019.02.011

Venkatraman, V., Dimoka, A., Pavlou, P. A., Vo, K., Hampton, W., Bollinger, B., et al. (2015). Predicting advertising success beyond traditional measures: new insights from neurophysiological methods and market response modeling. *J. Mark. Res.* 52, 436–452. doi: 10.1509/jmr.13.0593

Vollmar, C., O'Muircheartaigh, J., Barker, G. J., Symms, M. R., Thompson, P., Kumari, V., et al. (2010). Identical, but not the same: intra-site and inter-site reproducibility of fractional anisotropy measures on two 3.0T scanners. *Neuroimage* 51, 1384–1394. doi: 10.1016/j.neuroimage.2010.03.046

Walker, L., Curry, M., Nayak, A., Lange, N., and Pierpaoli, C. (2013). A framework for the analysis of phantom data in multicenter diffusion tensor imaging studies. *Hum. Brain Mapp.* 34, 2439–2454. doi: 10.1002/hbm.22081

Woolrich, M. W., Behrens, T. E. J., Beckmann, C. F., Jenkinson, M., and Smith, S. M. (2004). Multilevel linear modelling for FMRI group analysis using Bayesian inference. *Neuroimage* 21, 1732–1747. doi: 10.1016/j.neuroimage.2003.12.023

Worsley, A. (2002). Nutrition knowledge and food consumption: can nutrition knowledge change food behaviour? *Asia Pacific J. Clin. Nutr.* 11, S579–S585. doi: 10.1046/j.1440-6047.11.supp3.7.x

Zavaliangos-Petropulu, A., Nir, T. M., Thomopoulos, S. I., Reid, R. I., Bernstein, M. A., Borowski, B., et al. (2019). Diffusion MRI indices and their relation to cognitive impairment in brain aging: the updated multi-protocol approach in ADNI3. *Front. Neuroinform.* 13:2. doi: 10.3389/fninf.2019.00002

Zhu, A. H., Moyer, D. C., Nir, T. M., Thompson, P. M., and Jahanshad, N. (2019). *Challenges and Opportunities in dMRI Data Harmonization. In Computational Diffusion MRI*. Berlin: Springer International Publishing, 157–172. doi: 10.1007/978-3-030-05831-9_13

Zhu, T., Hu, R., Qiu, X., Taylor, M., Tso, Y., Yiannoutsos, C., et al. (2011). Measurements?: a diffusion phantom and human brain study. *Neuroimage* 56, 1398–1411. doi: 10.1016/j.neuroimage.2011.02.010.Quantification

Conflict of Interest: The authors declare that the research was conducted in the absence of any commercial or financial relationships that could be construed as a potential conflict of interest.

Copyright © 2020 Pinto, Paolella, Billiet, Van Dyck, Guns, Jeurissen, Ribbens, den Dekker and Sijbers. This is an open-access article distributed under the terms of the Creative Commons Attribution License (CC BY). The use, distribution or reproduction in other forums is permitted, provided the original author(s) and the copyright owner(s) are credited and that the original publication in this journal is cited, in accordance with accepted academic practice. No use, distribution or reproduction is permitted which does not comply with these terms.

frontiers in Neuroscience

ORIGINAL RESEARCH
published: 20 May 2020
doi: 10.3389/fnins.2020.00510

In vivo MRI Successfully Reveals the Malformation of Cortical Development in Infant Rats

*Minyoung Lee[1,2], Eun-Jin Kim[2], Dong-Cheol Woo[2], Woo-Hyun Shim[2,3] and Mi-Sun Yum[1,2]**

[1] Department of Pediatrics, Asan Medical Center, Asan Medical Institute of Convergence Science and Technology, University of Ulsan College of Medicine, Seoul, South Korea, [2] Asan Institute for Life Sciences, Asan Medical Center, Seoul, South Korea, [3] Department of Radiology, Asan Medical Center Children's Hospital, University of Ulsan College of Medicine, Ulsan, South Korea

OPEN ACCESS

Edited by:
Miguel Castelo-Branco, Coimbra Institute for Biomedical Imaging and Translational Research (CIBIT), Portugal

Reviewed by:
Julien Flament, Commissariat à l'Energie Atomique et aux Energies Alternatives (CEA), France
Francesca Colciaghi, Carlo Besta Neurological Institute (IRCCS), Italy

***Correspondence:**
Mi-Sun Yum
misun.yum@gmail.com

Specialty section:
This article was submitted to Brain Imaging Methods, a section of the journal Frontiers in Neuroscience

Received: 20 January 2020
Accepted: 24 April 2020
Published: 20 May 2020

Citation:
Lee M, Kim E-J, Woo D-C, Shim W-H and Yum M-S (2020) In vivo MRI Successfully Reveals the Malformation of Cortical Development in Infant Rats. Front. Neurosci. 14:510. doi: 10.3389/fnins.2020.00510

Objective: Malformations of cortical development (MCDs) are major causes of intractable epilepsies. To characterize the early neuroimaging findings of MCDs, we tried to identify the MRI features consistent with pathological findings in an infant rat MCD model, prenatally exposed to methylazoxymethanol (MAM), by using newly developed MRI techniques.

Methods: At gestational day 15, two doses of MAM (15 mg/kg intraperitoneally) or normal saline were injected into pregnant rats. The offspring underwent *in vivo* MRI, including glutamate chemical exchange saturation transfer (GluCEST), ^{1}H-MR spectroscopy, and diffusion tensor imaging, at postnatal day (P) 15 using a 7T small-animal imaging system. Another set of prenatally MAM-exposed rats were sacrificed for histological staining.

Results: At P15, the retrosplenial cortex (RSC) of rats with MCDs showed decreased neuronal nuclei, parvalbumin, and reelin expressions. Moreover, dendritic arborization of pyramidal cells in the RSC significantly decreased in infant rats with MCDs. *In vivo* MRI showed significantly decreased GluCEST (%) in the RSC of rats with MCDs (p = 0.000) and a significant correlation between GluCEST (%) and RSC thickness (r = 0.685, p = 0.003). The rats with MCDs showed reduced glutamate (p = 0.002), *N*-acetylaspartate (p = 0.002), and macromolecule and lipid levels (p = 0.027) and significantly reduced fractional anisotropy values in the RSC.

Conclusion: *In vivo* MRI revealed reduced neuronal population and dendritic arborization in the RSC of infant rats with MCDs during the early postnatal period. These pathological changes of the cortex could serve as clinical imaging biomarkers of MCDs in infants.

Keywords: malformations of cortical development (MCD), methylazoxymethanol (MAM), animal model, GABAergic neurons, GluCEST, *in vivo* MRI, infant rats

INTRODUCTION

The cerebral cortex is composed of six layers of glutamatergic and inhibitory interneurons (Kwan et al., 2012). The migration of these neurons into the proper layer of the cerebral cortex is an essential process during early cortical development, and its disruption causes malformations of cortical development (MCDs). MCDs are a broad spectrum of diseases caused by genetic or environmental insults (Colciaghi et al., 2011; Guerrini and Dobyns, 2014) and are associated with many neurological diseases, including developmental delay and intractable epilepsies (Kelsom and Lu, 2013; Wamsley and Fishell, 2017).

In particular, MCDs are the most common cause of pediatric intractable epilepsy (Barkovich et al., 2015; Iffland and Crino, 2017; Kim et al., 2017), and epilepsy surgery is the only curative treatment option because of the poor response to anticonvulsant drugs (Colciaghi et al., 2011; Barkovich et al., 2015). However, in clinical settings, localization of MCDs for epilepsy surgery is not always possible with current imaging techniques, especially in infants or in individuals with small focal cortical dysplasia (FCD). In addition, many patients with FCD type I are diagnosed only after the surgical excision of epileptic foci, and some of them experience surgical failures due to incomplete resection (Choi et al., 2018; Chen et al., 2019). Thus, non-invasive imaging diagnosis of FCD is important to offer the right therapeutic option to patients with intractable focal epilepsies (Jayalakshmi et al., 2019).

Various animal models of MCDs have been used for translational research (Kuzniecky, 2015; Luhmann, 2016), and the methylazoxymethanol (MAM) model is one of them. The offspring of MAM-treated rats are affected by developmental brain abnormalities similar to those observed in patients with MCDs (Chevassus-Au-Louis et al., 1999; Colacitti et al., 1999; Luhmann, 2016; Kim et al., 2017). Previously, our group reported *in vivo* anatomical disruption as well as increased spasm susceptibility, cognitive impairment, and abnormal cortical electrical activities in this MAM-induced MCD rat model (Kim et al., 2017).

Using this MAM-induced MCD rat model, we first tried to analyze the pathological characteristics of MCDs during infancy, and then to determine whether the MCD cortex can be distinguished from normal tissue by using newly developed brain MRI techniques.

MATERIALS AND METHODS

Animals

The experiments were approved by the Institutional Animal Care and Use Committee of the Ulsan University College of Medicine and conformed to the Revised Guide for the Care and Use of Laboratory Animals (8th Edition, 2011). Timed-pregnant Sprague-Dawley rats were purchased (Orient Bio Inc., Seoul, Korea) at gestational day 14 (G14) and housed individually in the animal facility. On G15, two doses of MAM (15 mg/kg intraperitoneally; MRIGlobal, Kansas City, MO, United states) were injected into pregnant rats, and normal saline was injected into controls at 830 and 1,830 h. Delivery occurred consistently on G21, which was considered postnatal day (P) 0 for the offspring. The overall experimental schedule is described in **Figure 1**.

Measurement of Cortical Neurons, Morphological Analysis, and Immunoflorescence

The MAM-exposed rats and corresponding controls were transcardially perfused with 4% paraformaldehyde on P15 under deep anesthesia, and their brains were removed and cryoprotected. Serial coronal sections (20 μM thickness) were cut using a cryocut microtome and stored at −80°C for staining procedures.

For cresyl violet staining, the sections were fixed in 4% paraformaldehyde solution for 15 min and defatted in 70% ethanol solution containing 0.5% acetic acid for 5 min and washed. Thereafter, these sections were dipped in 0.3% cresyl violet solution for 3 min and washed.

A modified Golgi-Cox impregnation technique was performed using FD Rapid GolgiStain kit (FD NeuroTechnologies, Ellicott City, MD, United States) according to the manufacturer's instructions. The brains of P15 rats were rinsed with distilled water to remove blood and trimmed to ∼1 cm thickness. The tissue was immersed in an impregnation solution for 2 weeks, transferred to solution C for 3 to 4 days, and cut into 120 μM-thick sections using a cryostat. The sections were mounted on silane-coated slides and stained with solutions D and E and dehydrated.

For immunofluorescence, six to eight sections were reacted per each rat and **Supplementary Table S1** indicates the number of animals used in these experiments. The slides were

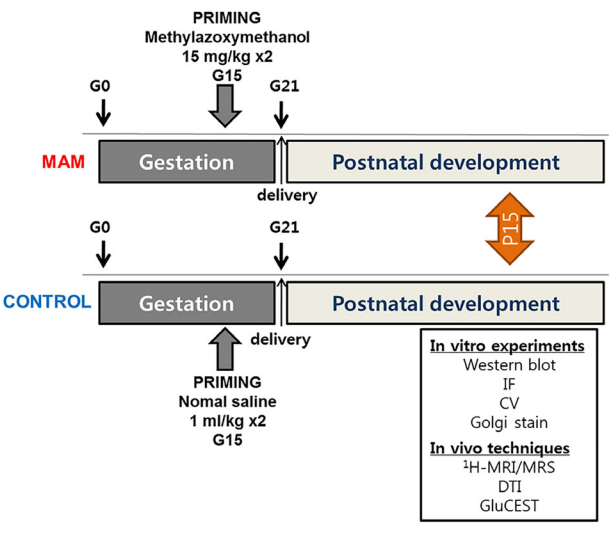

FIGURE 1 | The timeline of experimental procedures. MRS, MR spectroscopy; DTI, diffusion tensor imaging; GluCEST, glutamate chemical exchange saturation transfer; MAM, methylazoxymethanol; IF, immunofluorescence staining; CV, cresyl violet staining.

washed and incubated in a blocking solution (containing 5% normal host serum and 0.1% BSA/0.3% Triton X-100) for 1 h after antigen retrieval (heating the slides on a hot plate at 50°C for 20 min). Primary antibodies [anti-MBP, a marker for myelinatin, 1: 500; anti-TBR1, for layer VI neurons; 1: 250, and anti-parvalbumin, for GABAergic neurons, 1: 500; Abcam, Cambridge, United Kingdom; anti-MAP2, for neuronal dendrites, 1: 1,000; anti-neuronal nuclei (NeuN), for neurons, 1: 500, and anti-reelin, for neuronal migration, 1: 1,000; EMD Millipore, MA, United States] with blocking solution were applied for 24 h at 4°C, and fluorescein-labeled secondary antibodies [fluorescein anti-mouse immunoglobulin G (IgG), fluorescein anti-rabbit IgG, and Cy®3 anti-rabbit IgG, Vector Laboratories; Alexa Fluor 594 anti-rat IgG, Thermo Fisher Scientific] were serially applied for 1 h at room temperature. DAPI (VECTASHIELD, Vector Laboratories, Inc., United States) counterstaining has performed.

All the images were acquired under a microscope (Olympus BX-53, Olympus corporation, Tokyo, Japan) with a digital camera (Olympus microscope digital camera, 5M CCD, Olympus corporation, Tokyo, Japan) and analyzed using Olympus cellSens standard 1.13 (Olympus corporation, Tokyo, Japan) and ImageJ software (NIH, Bethesda, MD, United States). The Golgi-impregnated staining was analyzed for a section per each animal at 100x and 200X magnification using Olympus CellSens standard 1.13 and ImageJ software. After taking picture for each focus at each magnification of the microscope, neurons were 3D-reconstructed by the Stack function of the ImageJ program. Stereological cell counting was done in selected area of the retrosplenial cortex (RSC) and the length of apical dendrites and the number of second branches of basal dendrites of the layer V pyramidal neurons were evaluated for two neurons per each animal. We analyzed apical dendrite length using Simple Neurite Tracer among Plugins of ImageJ, and basal dendrites were counted while looking directly with a microscope at a magnification of 400X. The pyramidal neurons were selected according to the following criteria: (1) triangular soma, (2) one apical dendrite, and (3) presence of basal dendrites; non-pyramidal neurons were counted as interneurons.

Western Blot Analysis

For western blot analysis, bilateral cortical tissues from the bregma to posterior hippocampal area without the hippocampus (anteroposterior, 0 to −5 mM) were obtained from the control and MAM-exposed rats at P15. Isolated tissues from each rat were homogenized using PRO-PREP (iNtRON Biotechnology, Inc., Gyeonggi-do, Korea) at −4°C in an ice bath, and the protein samples were quantified using BSA. The acquired proteins were separated using SDS-PAGE and transferred to PVDF membranes. The membranes were blocked with 10% skim milk in tris-buffered saline with Tween-20 (TBST solution) for 1 h at room temperature. Thereafter, the membranes were incubated overnight at 4°C with the following primary antibodies: anti-NeuN (EMD Millipore, 1: 5,000), anti-GAD65 (EMD Millipore, 1: 5,000), and anti-parvalbumin (Abcam, 1: 2,000); anti-β-actin (Santa Cruz Biotechnology, Inc., Texas, United States, 1: 20,000) was used as a loading control (**Supplementary Table S2**). The membranes were then incubated in anti-rabbit IgG, HRP-linked antibody (Cell Signaling, Technology, Inc., MA, United States, 1: 10,000), or anti-mouse IgG, HRP antibody (Enzo Life Science, Inc., NY, United States, 1: 20,000) for 90 min at room temperature. The membranes were further rinsed with TBST and developed using an ECL solution (Clarity Western ECL substrate, Bio-Rad, CA, United States) on Fusion Solo S (Vilber Lourmat SAS, France). Normalization was performed by developing parallel western blots probed with β-actin antibody and analyzed via densitometry using Evolution-Capt (Fusion Software, Vilber Lourmat SAS).

In vivo MRI Studies

Animals were maintained under anesthesia with 1% isoflurane in a 1:2 mixture of O_2:N_2O while monitoring their respiratory rate, electrocardiogram, and rectal temperature. MR images were acquired using a 7T/160 mM bore animal MRI system (PharmaScan, Bruker, Ettlingen, Germany) with the Paravision 6.0.1. software in a configuration comprising a 72 mM transmit volume coil and a mouse brain surface receiver coil.

Diffusion tensor imaging (DTI) was performed using a four-shot DT-echo planar imaging sequence (TR = 3.7s; TE = 20 ms; B0 = 1,000 s/mM^2) with a 10 ms interval between the application of diffusion gradient pulses, a 4 ms diffusion gradient duration, a gradient amplitude of 46.52 mT/m, and Jones' 30 gradient scheme. The fractional anisotropy (FA) maps of rats were calculated by using the Diffusion Toolkit software.[1] For group comparison, we co-registered all FA images to the rat brain atlas using AFNI (the rat brain atlas in AFNI software, named mgh_wh_templete). The group FA-maps were obtained by averaging across subjects, and the group difference between MAM-exposed rats and control rats was calculated using unpaired, two-tailed *t*-test. The resulting difference t-maps were then thresholded at the FDR-corrected $p < 0.01$. All data analyses were processed using AFNI.

Glutamate chemical exchange saturation transfer (GluCEST) images were acquired and analyzed as previously reported in our group (Lee et al., 2018). GluCEST images were acquired using T_2-weighted imaging (rapid acquisition with relaxation enhancement [RARE]) with a frequency selective saturation preparation pulse comprised a Gaussian pulse and a total duration of 1,000 ms (irradiation offset of 500.0 Hz and interpulse delay of 10 μs) at a B_1 peak of 5.6 μT. Z-spectra were obtained from –5.0 ppm to +5.0 ppm with intervals of 0.33 ppm (total, 31 images). The sequence parameters were as follows: repetition time/echo time (TR/TE) = 4,200/36.4 ms, field of view = 30 × 30 mM^2, slice thickness = 1 mM, matrix size = 96 × 96, RARE factor = 16, echo spacing = 6.066 ms, and average = 1. To measure the GluCEST (%), the regions of interest, manually drawn on the RSC in T_2-weighted anatomical MR images, were overlaid on the GluCEST maps. GluCEST contrast is measured as the asymmetry between an image obtained with saturation at the resonant frequency of exchangeable amine protons (+3 ppm downfield from water for glutamate) and an image with saturation

[1] http://trackvis.org/

equidistant upfield from water (–3 ppm), according to the following equation:

$$\text{GluCEST}(\%) = \frac{S_{-3.0ppm} - S_{+3.0ppm}}{S_{-3.0ppm}} * 100$$

where $S_{-3.0\text{ppm}}$ and $S_{+3.0\text{ppm}}$ are the magnetizations obtained with saturation at a specified offset from the water resonance of 4.7 ppm. The B0/B1 maps on the same slices were acquired for B_0 and B_1 correction. The B_0 map was calculated by linearly fitting the accumulated phase per pixel following phase unwrapping against the echo time differences from gradient echo (GRE) images collected at TEs of = 1.9 and 2.6 ms. B_1 maps were calculated by using the double-angle method (flip angles 30° and 60°) and the linear correction for B_1 was calculated as the ratio of the actual B_1 to the expected value.

^{1}H-MRS was performed at P15 in MAM-exposed rat (n = 10) and control (n = 10). The MR spectra were acquired through a signal voxel (from bregma to –3.0 mM in a coronal section, 1.2 × 1.3 × 3 mM^3; **Figure 2A**) in the RSC using a point-resolved spectroscopy (PRESS) sequence for 128 acquisitions with TR/TE = 5,000/13.4 ms. For quantification, unsuppressed water signals were also acquired from the same voxel (average = 8). The water-suppressed time domain data were analyzed between 0.2 and 4.0 ppm, without further T1 or T2 correction. For quantification, all the MR spectra were processed with the linear combination analysis method (LC Model ver. 6.0, Los Angeles, CA, United States) and absolute metabolite concentrations (mmol/kg wet weight) were calculated using the unsuppressed water signal as an internal reference (assuming 80% brain water content; Terpstra et al., 2010; Lee et al., 2018). The *in vivo* proton spectra were judged to have an acceptable value if the standard deviation of the fit for the metabolite was less than 20%.

Statistical Analysis

Statistical analyses were performed using IBM SPSS Statistics for Windows, Version 22.0 (IBM Corp., Armonk, NY, United States). The level of significance was preset to $p < 0.05$. Two-group comparisons of the concentrations of metabolites and cortical neuron analysis were performed using the Mann-Whitney U-test. Student's t-test was used for protein expression data following normal distribution in two-group comparisons. Spearman's correlation analysis was used to analyze the correlation between GluCEST (%) and cortical length or several neurometabolites. To control the group differences, partial correlation analysis was used to determine the associations among neurometabolites in control and MAM-exposed rats. We planned studies of a continuous response variable from independent control and experimental subjects with 1 control(s) per experimental subject. In previous experiments, the responses within each subject group was normally distributed for these experiments. Using preliminary data means with standard deviations, we extracted the number of animals we needed to be able to reject the null hypothesis that the population means of the experimental and control groups are equal with probability (power) 0.95. The Type I error probability associated with this test of this null hypothesis is 0.05. The number of animals in each group were 4 or more for MRS and GluCEST imaging, 9 for Golgi staining, 14 for WB and IF staining.

RESULTS

Cortical Neuronal Paucity and Dendritic Arborization Failure in the RSC of the Infant Rat Model of MCDs

Cresyl violet staining showed collapsed cortical structures in infant rats prenatally exposed to MAM (**Figure 3A**). Immunofluorescence staining of the RSC were qualitatively evaluated and MBP, MAP2 immunoreactivity and NeuN-, parvalbumin-, GAD65- positive neuronal populations were sparser in MAM-exposed infant rats than in controls (**Figures 3B,C**). There were relatively scantier reelin immunoreactivity in RSC of MAM-exposed animals and TBR1 (+) neurons dispersed more widely and the layer VI was obliterated in MAM-exposed rats compared to those in controls (**Figure 3C**). The protein expressions of NeuN, parvalbumin, and GAD65 were also significantly decreased in rats with MCDs (NeuN, p = 0.000; parvalbumin, p = 0.000; GAD65, p = 0.003; **Figure 3D**).

Golgi staining also showed a significantly smaller number of cortical neurons in infant rats with MCDs (n = 5) than in controls (n = 5, p = 0.009; **Figure 4C**). The pyramidal neurons of rats with MCDs exhibited shorter apical dendrites as well as a smaller number of basal dendrites than did controls (n = 10; apical dendrites, p = 0.001; basal dendrites, p = 0.000; **Figures 4D,E**).

In vivo MR Structural and GluCEST Imaging in Rats With MCDs During Infancy

In vivo MRI at P15 also showed the anatomical changes caused by prenatal MAM exposure, which were comparable to the pathological changes. The dorsal-to-ventral whole-brain length and RSC length were significantly lesser in infant rats with MCDs (n = 23, p = 0.000; **Figures 5A–C**) than in controls (n = 24).

The RSC of MAM-exposed rats (n = 8) showed significantly lower GluCEST (%) than that of controls at P15 (n = 8, p = 0.000; **Figures 5D,E** and **Supplementary Figure S1**). A significant positive correlation was also observed between whole-brain length, cortical length, cortical brain length ratio, and GluCEST (%) when the rats prenatally exposed to MAM and controls were combined (**Figure 5F**: r = 0.785, p = 0.000; **G**: r = 0.685, p = 0.003; **H**: r = 0.688, p = 0.003).

In vivo Neurometabolic/DTI Changes in the RSC of the Infant Rat Model of MCDs

Infant rats with MCDs showed microstructural and neurometabolic changes corresponding to the pathological data. MRS analysis focusing on the RSC showed a significant reduction in neurometabolite levels, including those of glutamate (p = 0.002), glutamate-plus-glutamine (p = 0.017), NAA (p = 0.002), total NAA (p = 0.004), macromolecule 09 (p = 0.024),

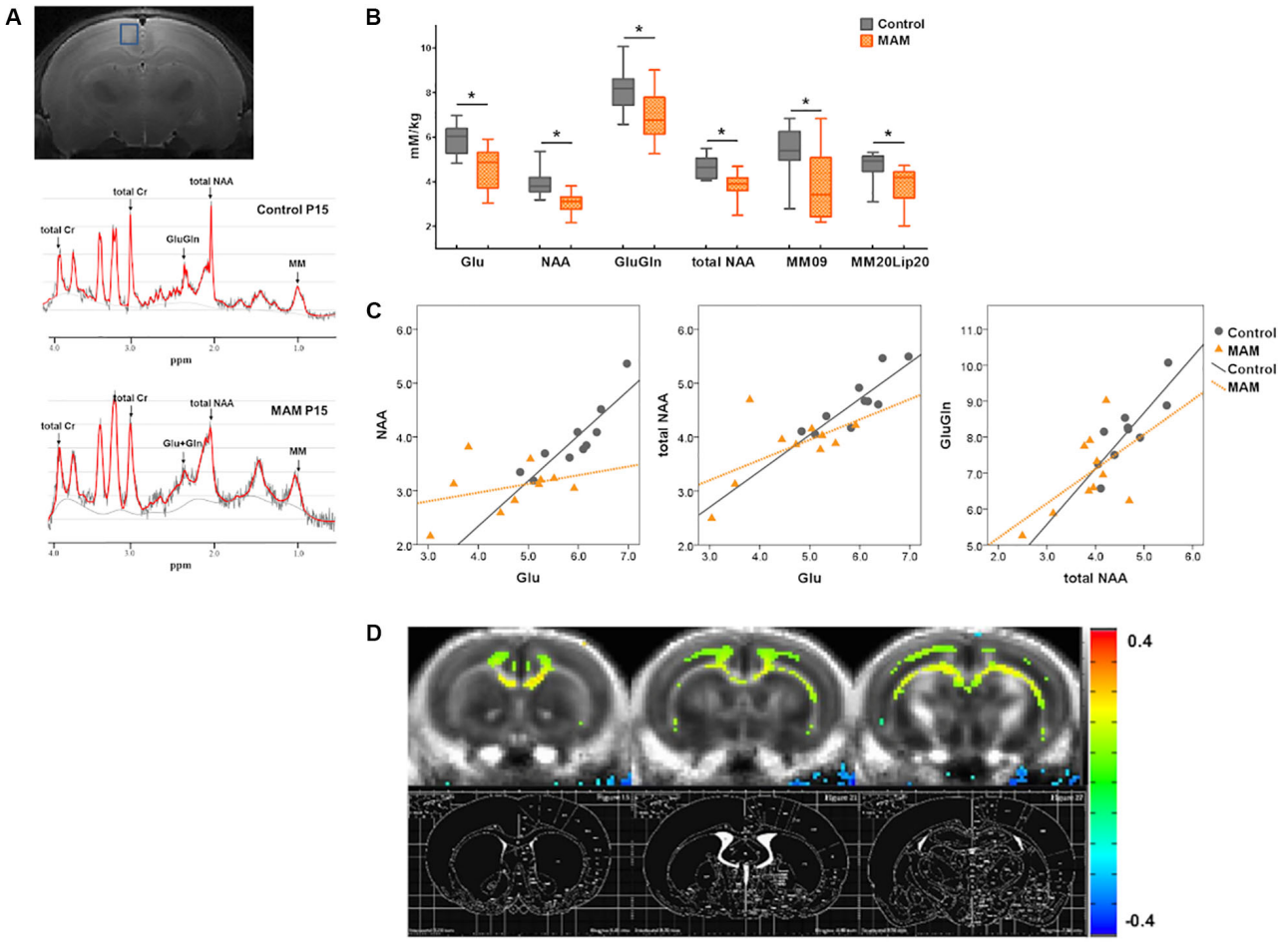

FIGURE 2 | *In vivo* neuroimaging changes in rats with malformations of cortical development (MCDs) during infancy. **(A)** At postnatal day 15 (P15), regions of interest for MR spectroscopy data acquisition are depicted in the coronal planes in the retrosplenial cortex (RSC) (upper); an example of an MR spectrum is also shown (lower). **(B)** In infant rats with MCDs, glutamate (Glu), glutamate-plus-glutamine (GluGln), *N*-acetylaspartate (NAA), total NAA, macromolecule (MM), and lipid (Lip) levels are significantly lower (n = 10, Glu mean = 4.645, SD = 0.933, GluGln mean = 6.941, SD = 1.097, NAA mean = 3.069, SD = 0.472, total NAA mean = 3.819, SD = 0.61, MM09 mean = 3.829, SD = 1.561, MM20Lip20 mean = 3.82, SD = 0.9 $p < 0.05$) than those in controls (n = 10, Glu mean = 5.912, SD = 0.656, GluGln mean = 8.144, SD = 0.952, NAA mean = 3.952, SD = 0.625, total NAA mean = 4.654, SD = 0.516, MM09 mean = 5.364, SD = 1.118, MM20Lip20 mean = 4.71, SD = 0.652). **(C)** A significant positive correlation is observed between Glu and NAA, Glu and total NAA, and total NAA and GluGln when the partial correlation analysis is performed by controlling group differences (Glu and NAA levels: r = 0.563, p = 0.012, df = 17; Glu and tNAA levels: r = 0.676, p = 0.001, df = 17; total NAA and GluGln levels: r = 0.664, p = 0.002, df = 17). When the correlation analysis was done in each group, controls showed significant positive correlation of glutamate and NAA levels (r = 0.903, p = 0.000), glutamate and total NAA levels (r = 0.855, p = 0.002), and total NAA and GluGln levels (r = 0.794, p = 0.006) but there is no significant correlation of these neurometabolites in MCD rats (glutamate and NAA levels: r = 0.248; p = 0.489; glutamate and total NAA levels: r = 0.442; p = 0.200; total NAA and GluGln levels: r = 0.418; p = 0.229). **(D)** Subtraction FA-maps (control rats minus MAM-exposed rats) are shown over control-group-averaged FA-map (threshold FDR-corrected $p < 0.01$). The rat brain atlas defined by Paxinos and Watson (2014) was also shown for the references. The MAM-exposed rats showed significant reduction of FA values in the cingulate cortex, corpus callosum, cingulum, and deep white matter including external capsule (control; n = 16, MAM; n = 15). *Statistically significant, $p < 0.05$.

and macromolecule 20-plus-lipid 20 (p = 0.027), in infant rats with MCDs (n = 10) than in controls (n = 10; **Figure 2B**). A significant positive correlation was also observed between glutamate and NAA, glutamate and total NAA, as well as total NAA and glutamate-plus-glutamine when the partial correlation analysis was performed by controlling group differences (glutamate and NAA levels: r = 0.563, p = 0.012, df = 17; glutamate and total NAA levels: r = 0.676, p = 0.001, df = 17; total NAA and glutamate-plus-glutamine levels: r = 0.664, p = 0.002, df = 17, **Figure 2C**). When the correlation analysis was done in each group, control group showed significant positive correlation of these glutamate and NAA (r = 0.903, p = 0.000), glutamate and total NAA (r = 0.855, p = 0.002), and total NAA and glutamate-plus-glutamine levels (r = 0.794, p = 0.006) but MCD rats did not show correlation of these metabolites (glutamate and NAA: r = 0.248, p = 0.489; glutamate and total NAA: r = 0.442, p = 0.200; total NAA and glutamate-plus-glutamine: r = 0.418, p = 0.229).

Microstructural analysis also revealed decreased FA values in the cingulate cortex, corpus callosum, cingulum, and deep white

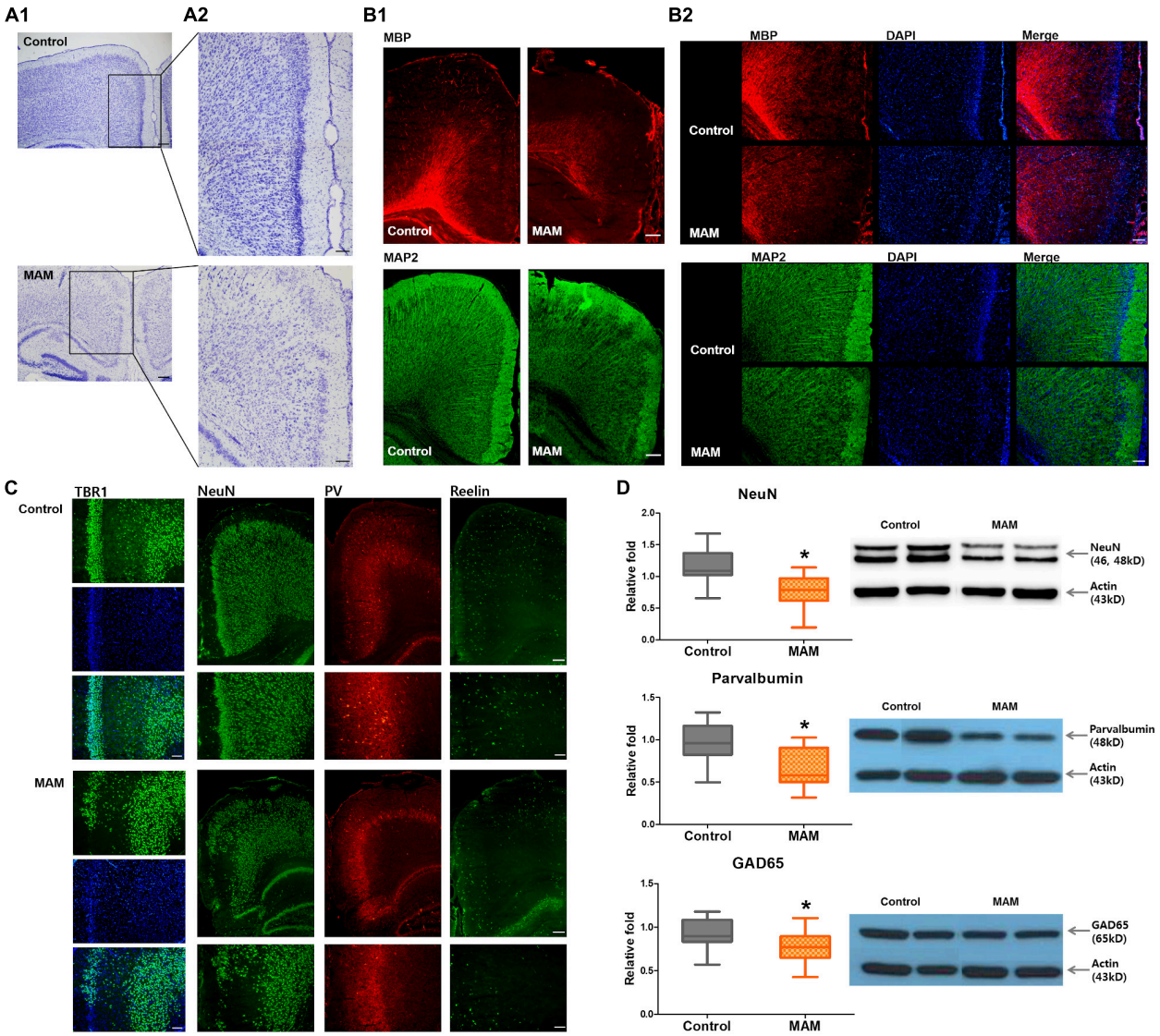

FIGURE 3 | Microstructural changes in the retrosplenial cortex (RSC) and deficiency of cortical interneurons in infant rats with malformations of cortical development (MCDs). **(A)** Pathological alteration of the cortical structure is shown by cresyl violet staining. Scale bars: **(A1)** 200 μM; **(A2)** 100 μM. **(B)** Immunofluorescence studies show sparser MBP staining and collapsed microstructures with MAP2. Scale bars: **(B1)** 200 μM; **(B2)** 100 μM. **(C)** In infant rats with MCDs, TBR1, neuronal nuclei (NeuN), parvalbumin (PV), and reelin expressions in the RSC are scantier than those in controls. Scale bars: lower, 200 μM; upper, 100 μM. **(D)** Western blot analysis shows significant reductions of NeuN (control; $n = 32$, mean = 1.174, $SD = 0.232$, MAM; $n = 24$, mean = 0.769, $SD = 0.247$, $p = 0.000$), PV (control; $n = 23$, mean = 0.979, $SD = 0.231$, MAM; $n = 19$, mean = 0.65, $SD = 0.217$, $p = 0.000$), and GAD65 (control; $n = 30$, mean = 0.928, $SD = 0.171$, MAM; $n = 22$, mean = 0.77, $SD = 0.186$, $p = 0.003$) in the cortex of rats with MCDs. MAM, methylazoxymethanol. *Statistically significant, $p < 0.05$.

matter including external capsule in MAM-exposed rats at P15 (MAM-exposed rats, $n = 15$; controls, $n = 16$; **Figure 2D**).

DISCUSSION

MCDs, which show the disrupted developmental process of the brain, are closely related to intractable epilepsy and developmental delay (Barkovich et al., 2012; Kuzniecky, 2015; Becker and Beck, 2018). Many studies have shown that MAM-induced MCD rats have structural abnormalities similar to those observed in patients with MCDs, but most studies have focused on adult rats and pathologic changes (Moore et al., 2006; Lodge and Grace, 2009; Chin et al., 2011). As epilepsy associated with MCDs often occurs during infancy and is frequently refractory to current treatments (Tassi et al., 2002; Kang et al., 2013), we tried to explore the early developmental changes of MCDs during infancy.

Although neocortical structures in the early developmental period have not been extensively investigated in this rat model, the altered firing properties of their neuronal subpopulations at 3–7 weeks of age and abnormal neocortical electrical activities

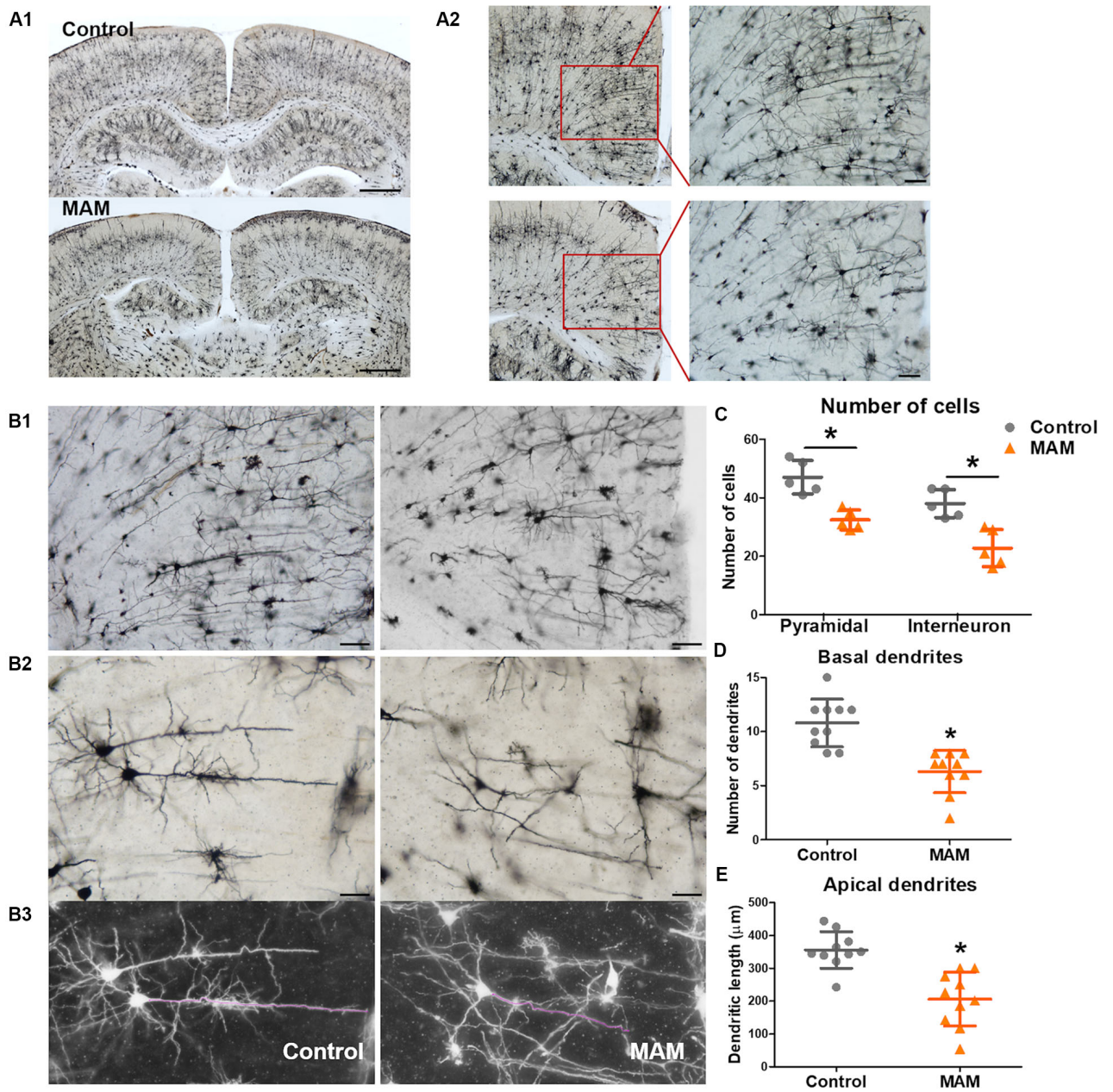

FIGURE 4 | Dendritic arborization of retrosplenial cortex (RSC) pyramidal cells in an infant rat model of malformations of cortical development (MCDs). **(A)** Golgi staining reveals cortical neuronal deficits in infant rats with MCDs (control; $n = 5$, MAM; $n = 5$). **(B,C)** In the RSC, the numbers of pyramidal cells and interneurons are significantly reduced (control; $n = 5$, mean = 47.0, $SD = 5.701$, mean = 38.0, $SD = 4.796$, MAM; $n = 5$, mean = 32.4, $SD = 3.435$, mean = 22.8, $SD = 6.380$, $p = 0.009$). **(D,E)** The number of basal dendrites of pyramidal cells and the length of apical dendrites are significantly reduced (control; $n = 10$, mean = 10.8, $SD = 2.201$, mean = 356.066, $SD = 55.919$, MAM; $n = 10$, mean = 6.3, $SD = 1.947$, mean = 206.131, $SD = 81.888$). Scale bars: **(A1)** 1 mM; **(A2)** 100 μM; **(B1)** 100 μM; **(B2)** 50 μM. MAM, methylazoxymethanol. *Statistically significant, $p < 0.05$.

at P15 have been reported (Chevassus-Au-Louis et al., 1998; Kim et al., 2017). To demonstrate the abnormal neocortical neuronal migration at early stages, we selected the RSC for pathological investigation in this study. In imaging studies, including MRS, on small animals using regions of interest, the RSC is relatively more easily recognizable and accessible than are other neocortical structures. The RSC is known to be associated with the default mode network and cognitive functions such as navigation, learning, and memory (Sugar et al., 2011).

In young rats prenatally exposed to MAM, we could show the histopathologic features of MCDs (Garbossa and Vercelli, 2003; Pang et al., 2008; Barkovich et al., 2012; Kuzniecky, 2015), such as the collapse of the cortex layer, alteration of cortical structures, hypomyelination, and abnormalities of microtubule

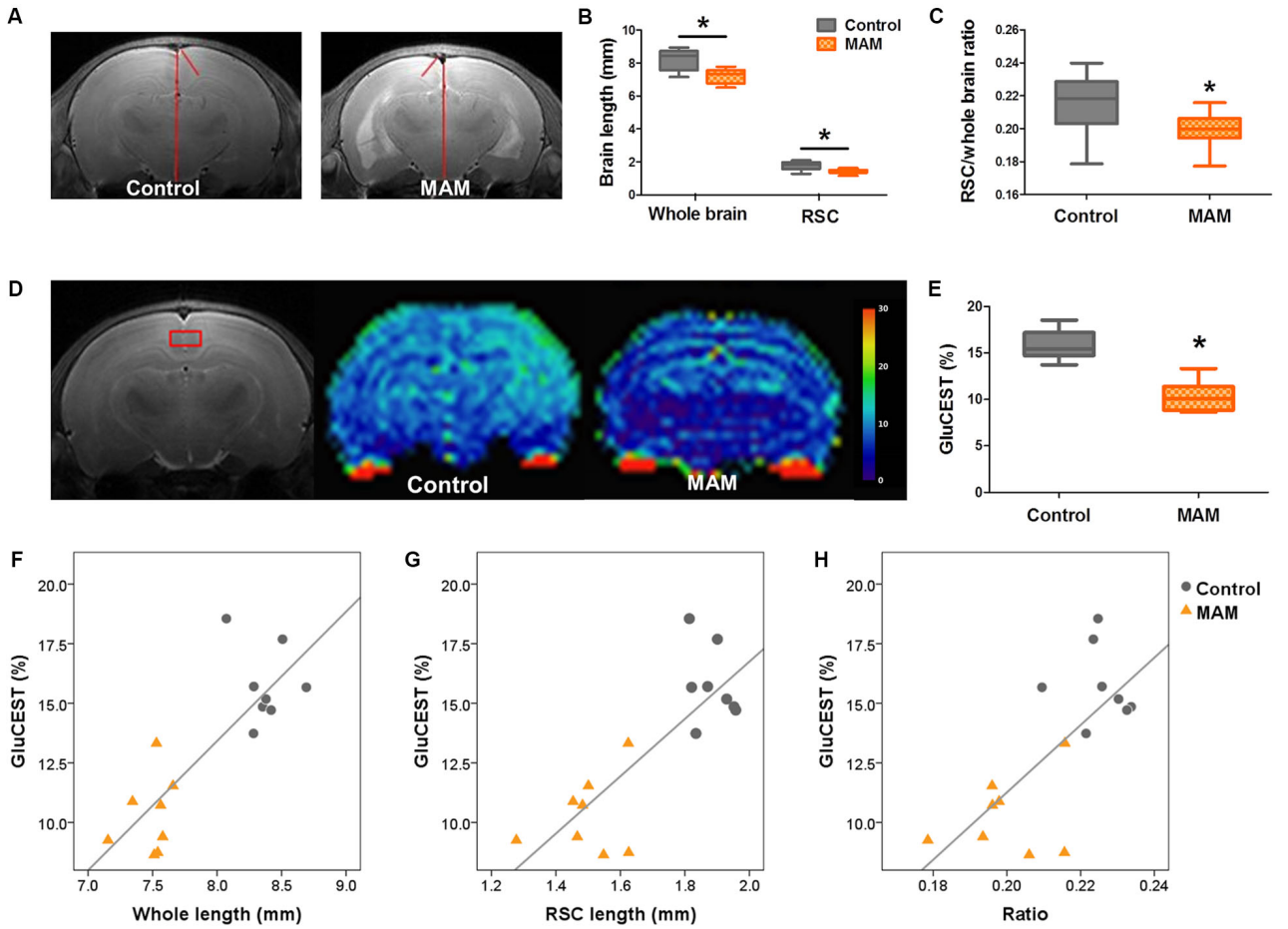

FIGURE 5 | *In vivo* MR structural and GluCEST imaging in rats with MCDs during infancy. **(A)** In representative T2-weighted MR images, the length of the whole brain and retrosplenial cortex (RSC) are measured (red lines) at 3 mM posterior to the bregma. **(B)** In infant rats with malformations of cortical development (MCDs), the length of the whole brain and RSC, and **(C)** the ratio of the RSC to cortex are significantly decreased (methylazoxymethanol [MAM], $n = 23$, mean = 7.194, $SD = 0.435$, mean = 1.433, $SD = 0.132$, mean = 0.199, $SD = 0.011$; Control, $n = 24$, mean = 8.215, $SD = 0.562$, mean = 1.783, $SD = 0.235$, mean = 0.216, $SD = 0.016$; $p = 0.000$). **(D,E)** Glutamate chemical exchange saturation transfer (GluCEST) level (%) measured from the RSC (red box) is more significantly reduced in rats with MCDs ($n = 8$, mean = 10.309, $SD = 1.616$) than in controls ($n = 8$, mean = 15.761, $SD = 1.599$, $p = 0.000$). **(F–H)** A significant positive correlation is observed between GluCEST (%) and cortical length when the two groups are combined (**F:** $r = 0.785$, $p = 0.000$; **G:** $r = 0.685$, $p = 0.003$; **H:** $r = 0.688$, $p = 0.003$). *Statistically significant, $p < 0.05$.

formation (**Figure 3**). Golgi staining of the RSC also showed reduced numbers of cortical neurons and dendritic arborization of pyramidal cells in infant rats with MCDs (**Figure 4**). This result is consistent with that of a previous study on MAM-induced pathological changes in the brains of Wistar albino rats at P12 and adulthood (Garbossa and Vercelli, 2003). In addition, a significant reduction in parvalbumin-positive cells was identified in the RSC (**Figures 3C,D**). Although inhibitory interneurons account for a relatively small proportion of cortical cells, inhibitory cortical neuronal dysfunction is known to cause various neurological diseases, including epilepsy and autism, since these neurons play an important role in the cortical network (Kelsom and Lu, 2013; Wamsley and Fishell, 2017). Previous studies have reported that other MAM-induced MCD models showed distorted functional connection of hippocampal-neocortical neurons (Chevassus-Au-Louis et al., 1998) and alteration of interneuron migration due to aberrant $GABA_A$ activity in the neocortex (Abbah and Juliano, 2014). In this study, prenatally MAM-exposed rats also showed decreased GAD65 expression in the RSC, which may be consistent with altered GABAergic activity in the neocortex (Ji et al., 1999; Stork et al., 2000; Silva et al., 2002; Wieronska et al., 2010). Furthermore, abnormal TBR1 immunoreactivity and significant reduction of reelin, which regulates neuronal migration processes by controlling cell-cell interactions (Niu et al., 2008; Wieronska et al., 2010; Lee and D'Arcangelo, 2016; Wasser and Herz, 2017), were observed in this model at P15. These overall failures of cortical migration and dendritic arborization of pyramidal cells, as well as insufficient numbers of inhibitory interneurons, may result in the seizure susceptibility of this model during infancy. However, no dysmorphic neurons or balloon cells are observed in these young rats with MCDs, and these pathologic findings

are consistent with the International League Against Epilepsy classification of FCD type I (Blumcke et al., 2011), which is rarely delineated using current imaging techniques.

On the basis of these pathological findings, we also tested whether the MCDs in infancy can be diagnosed through *in vivo* imaging techniques in clinical settings. We observed a quantifiable reduction in RSC length and whole-brain length, as previously shown in this model (Kim et al., 2017), which are potential biomarkers of FCD in clinical settings (**Figures 5A–C**). A new imaging technique involving glutamate measurement, GluCEST imaging, also revealed significantly decreased glutamate in the RSC, and 1H-MRS analysis supported this finding by showing a significant reduction in glutamate and glutamate-plus-glutamine in the RSC (**Figures 2B**, **5D,E**). A significant correlation was also observed between GluCEST (%) and RSC length/whole-brain length, suggesting GluCEST (%) was a potential biomarker of FCD (**Figures 5F–H**). GluCEST imaging is emerging molecular MRI technique with higher spatial resolution than MRS, potentially allowing for more precise visualization of the excitatory network of high glutamate concentrations (Davis et al., 2015). In addition to its crucial function in cognition (Pepin et al., 2016), glutamate is a major excitatory neurotransmitter in the central nervous system that is closely associated with epilepsy (Eid et al., 2016) and glutamate also has key roles in the radial migration of pyramidal neurons as well as tangential migration (Luhmann et al., 2015). Thus, this neurometabolic profile found in the present study can be indirectly associated with the abnormal cortical migration observed in the MAM-induced MCD rats at P15 and can be a useful marker of epileptic foci (Davis et al., 2015). However, there are several confounding factors in interpreting GluCEST results including the signal contributions from amines in proteins and nuclear Overhouser effects (NOE) (Cui and Zu, 2020). Thus, the changes in GluCEST in these rats with MCD can be caused by the changes in content or conformation of proteins in these pathological tissues as well as glutamate. Abnormal neuronal development in malformed cortex as well as the dendritic arborization failures in this study (Andreae and Burrone, 2015) can be associated with these *in vivo* imaging changes of GluCEST and decrease of cortical thickness.

Moreover, *in vivo* ^{1}H-MRS also showed findings comparable with the pathological changes of the MCD cortex. Reduced NAA, macromolecules and lipid levels were observed in the RSC of rats prenatally exposed to MAM (**Figure 2B**), which was consistent with the pathological reduction in cortical neurons as well as decreased dendritic arborizations identified in this study (**Figures 3**, **4**) and previous human studies (Woermann et al., 2001; Mueller et al., 2005; Blüml and Panigrahy, 2013). Additional analysis showed a clear positive correlation between glutamate and NAA, glutamate and total NAA, as well as total NAA and glutamate-plus-glutamine in the RSC of control rats at P15. However, these correlations were obscured in rats prenatally exposed to MAM, thus suggesting the disrupted neuronal development of the RSC in these rats.

A significant reduction in FA was observed in the cingulate cortex, corpus callosum, cingulum, and deep white matter including external capsule of the rats prenatally exposed to MAM in this study; this finding is also observed in patients with FCD (Lee et al., 2004; Donkels et al., 2017). The measure of anisotropy reflects changes in myelination, dendritic architecture of the cortical neuron, and fiber connection (Huppi and Dubois, 2006). FA is considered to be an indirect indicator of myelination and is generally increases with advancing age (Semple et al., 2013). In this early developmental period P15, the corpus callosum, cingulum, external capsule is in rapid myelinating process (Downes and Mullins, 2014) and impaired developmental process in MAM-exposed rats may attribute the significant reduction of FA in these areas. Therefore, FA reduction in the RSC, cingulum and corpus callosum of this MCD model, reflecting the malformed brain with white matter paucity and abnormal dendritic arborization, can be a biomarker of white matter deterioration. Overall, these unconventional *in vivo* imaging data obtained in this study could reflect the pathological changes in MCDs and can be used in clinics to improve the diagnosis of focal cortical abnormalities in patients with intractable epilepsy.

This study showed deficits of cortical interneurons and dendritic arborization failures in the cortex of rats prenatally exposed to MAM at P15 and corresponding *in vivo* MRI characteristics by using new imaging techniques. These MRI characteristics should be further validated as diagnostic biomarkers of MCD.

DATA AVAILABILITY STATEMENT

All datasets generated for this study are included in the article/**Supplementary Material**.

ETHICS STATEMENT

The animal study was reviewed and approved by the Institutional Animal Care and Use Committee of the Ulsan University College of Medicine and conformed to the Revised Guide for the Care and Use of Laboratory Animals (8th Edition, 2011).

AUTHOR CONTRIBUTIONS

ML and M-SY contributed to the conception, design of the study, and drafting the manuscript and figures. ML and E-JK contributed to the acquisition of data. ML, E-JK, D-CW, W-HS, and M-SY contributed to the analysis of data.

FUNDING

This work was supported by the Basic Science Research Program through the National Research Foundation of Korea (NRF) funded by the Ministry of Education (NRF-2018R1D1A1A02085427) and a grant (2020-551) from Asan Institute for Life Sciences, Seoul, Korea. ML was supported by

Basic Science Research Program through the NRF funded by the Ministry of Education (NRF-2019R1A6A3A01090600).

ACKNOWLEDGMENTS

We thank the core facilities of the Magnetic Resonance Core at the ConveRgence mEDIcine research center (CREDIT), Asan Medical Center for the use of their shared equipment, services and expertise. We also would like to thank Editage (www.editage.co.kr) for English language editing.

SUPPLEMENTARY MATERIAL

The Supplementary Material for this article can be found online at: https://www.frontiersin.org/articles/10.3389/fnins.2020.00510/full#supplementary-material

REFERENCES

Abbah, J., and Juliano, S. L. (2014). Altered migratory behavior of interneurons in a model of cortical dysplasia: the influence of elevated GABAA activity. *Cereb. Cortex* 24, 2297–2308. doi: 10.1093/cercor/bht073

Andreae, L. C., and Burrone, J. (2015). Spontaneous neurotransmitter release shapes dendritic arbors via long-range activation of NMDA receptors. *Cell Rep.* 10, 873–882. doi: 10.1016/j.celrep.2015.01.032

Barkovich, A. J., Dobyns, W. B., and Guerrini, R. (2015). Malformations of cortical development and epilepsy. *Cold Spring Harb. Perspect Med.* 5:a022392. doi: 10.1101/cshperspect.a022392

Barkovich, A. J., Guerrini, R., Kuzniecky, R. I., Jackson, G. D., and Dobyns, W. B. (2012). A developmental and genetic classification for malformations of cortical development: update 2012. *Brain* 135, 1348–1369. doi: 10.1093/brain/aws019

Becker, A. J., and Beck, H. (2018). New developments in understanding focal cortical malformations. *Curr. Opin. Neurol.* 31, 151–155. doi: 10.1097/WCO.0000000000000531

Blumcke, I., Thom, M., Aronica, E., Armstrong, D. D., Vinters, H. V., Palmini, A., et al. (2011). The clinicopathologic spectrum of focal cortical dysplasias: a consensus classification proposed by an ad hoc Task Force of the ILAE Diagnostic Methods Commission. *Epilepsia* 52, 158–174. doi: 10.1111/j.1528-1167.2010.02777.x

Blüml, S., and Panigrahy, A. (2013). *MR Spectroscopy Of Pediatric Brain Disorders*. New York, NY: Springer.

Chen, J., Huang, Z., Li, L., Ren, L., and Wang, Y. (2019). Histological type of focal cortical dysplasia is associated with the risk of postsurgical seizure in children and adolescents. *Ther. Clin. Risk Manag.* 15, 877–884. doi: 10.2147/TCRM.S203039

Chevassus-Au-Louis, N., Baraban, S. C., Gaiarsa, J. L., and Ben-Ari, Y. (1999). Cortical malformations and epilepsy: new insights from animal models. *Epilepsia* 40, 811–821. doi: 10.1111/j.1528-1157.1999.tb00786.x

Chevassus-Au-Louis, N., Congar, P., Represa, A., Ben-Ari, Y., and Gaiarsa, J. L. (1998). Neuronal migration disorders: heterotopic neocortical neurons in CA1 provide a bridge between the hippocampus and the neocortex. *Proc. Natl. Acad. Sci. U.S.A.* 95, 10263–10268. doi: 10.1073/pnas.95.17.10263

Chin, C. L., Curzon, P., Schwartz, A. J., O'connor, E. M., Rueter, L. E., Fox, G. B., et al. (2011). Structural abnormalities revealed by magnetic resonance imaging in rats prenatally exposed to methylazoxymethanol acetate parallel cerebral pathology in schizophrenia. *Synapse* 65, 393–403. doi: 10.1002/syn.20857

Choi, S. A., Kim, S. Y., Kim, H., Kim, W. J., Kim, H., Hwang, H., et al. (2018). Surgical outcome and predictive factors of epilepsy surgery in pediatric isolated focal cortical dysplasia. *Epilepsy Res.* 139, 54–59. doi: 10.1016/j.eplepsyres.2017.11.012

Colacitti, C., Sancini, G., Debiasi, S., Franceschetti, S., Caputi, A., Frassoni, C., et al. (1999). Prenatal methylazoxymethanol treatment in rats produces brain abnormalities with morphological similarities to human developmental brain dysgeneses. *J. Neuropathol. Exp. Neurol.* 58, 92–106. doi: 10.1097/00005072-199901000-00010

Colciaghi, F., Finardi, A., Frasca, A., Balosso, S., Nobili, P., Carriero, G., et al. (2011). Status epilepticus-induced pathologic plasticity in a rat model of focal cortical dysplasia. *Brain* 134, 2828–2843. doi: 10.1093/brain/awr045

Cui, J., and Zu, Z. (2020). Towards the molecular origin of glutamate CEST (GluCEST) imaging in rat brain. *Magn. Reson. Med.* 83, 1405–1417. doi: 10.1002/mrm.28021

Davis, K. A., Nanga, R. P., Das, S., Chen, S. H., Hadar, P. N., Pollard, J. R., et al. (2015). Glutamate imaging (GluCEST) lateralizes epileptic foci in nonlesional temporal lobe epilepsy. *Sci. Transl. Med.* 7:309ra161. doi: 10.1126/scitranslmed.aaa7095

Donkels, C., Pfeifer, D., Janz, P., Huber, S., Nakagawa, J., Prinz, M., et al. (2017). Whole transcriptome screening reveals myelination deficits in dysplastic human temporal neocortex. *Cereb. Cortex* 27, 1558–1572. doi: 10.1093/cercor/bhv346

Downes, N., and Mullins, P. (2014). The development of myelin in the brain of the juvenile rat. *Toxicol. Pathol.* 42, 913–922. doi: 10.1177/0192623313503518

Eid, T., Gruenbaum, S. E., Dhaher, R., Lee, T. W., Zhou, Y., and Danbolt, N. C. (2016). The glutamate-glutamine cycle in epilepsy. *Adv. Neurobiol.* 13, 351–400.

Garbossa, D., and Vercelli, A. (2003). Experimentally-induced microencephaly: effects on cortical neurons. *Brain Res. Bull.* 60, 329–338. doi: 10.1016/s0361-9230(03)00053-4

Guerrini, R., and Dobyns, W. B. (2014). Malformations of cortical development: clinical features and genetic causes. *Lancet Neurol.* 13, 710–726. doi: 10.1016/S1474-4422(14)70040-7

Huppi, P. S., and Dubois, J. (2006). Diffusion tensor imaging of brain development. *Semin. Fetal. Neonatal. Med.* 11, 489–497.

Iffland, P. H. II, and Crino, P. B. (2017). Focal cortical dysplasia: gene mutations, cell signaling, and therapeutic implications. *Annu. Rev. Pathol.* 12, 547–571. doi: 10.1146/annurev-pathol-052016-100138

Jayalakshmi, S., Nanda, S. K., Vooturi, S., Vadapalli, R., Sudhakar, P., Madigubba, S., et al. (2019). Focal cortical dysplasia and refractory epilepsy: role of multimodality imaging and outcome of surgery. *AJNR Am. J. Neuroradiol.* 40, 892–898. doi: 10.3174/ajnr.A6041

Ji, F., Kanbara, N., and Obata, K. (1999). GABA and histogenesis in fetal and neonatal mouse brain lacking both the isoforms of glutamic acid decarboxylase. *Neurosci. Res.* 33, 187–194. doi: 10.1016/s0168-0102(99)00011-5

Kang, J. W., Rhie, S. K., Yu, R., Eom, S., Hong, W., Kim, S. H., et al. (2013). Seizure outcome of infantile spasms with focal cortical dysplasia. *Brain Dev.* 35, 816–820. doi: 10.1016/j.braindev.2013.06.013

Kelsom, C., and Lu, W. (2013). Development and specification of GABAergic cortical interneurons. *Cell Biosci.* 3:19. doi: 10.1186/2045-3701-3-19

Kim, E. H., Yum, M. S., Lee, M., Kim, E. J., Shim, W. H., and Ko, T. S. (2017). A New rat model of epileptic spasms based on methylazoxymethanol-induced malformations of cortical development. *Front. Neurol.* 8:271. doi: 10.3389/fneur.2017.00271

Kuzniecky, R. (2015). Epilepsy and malformations of cortical development: new developments. *Curr. Opin. Neurol.* 28, 151–157. doi: 10.1097/WCO.0000000000000175

Kwan, K. Y., Sestan, N., and Anton, E. S. (2012). Transcriptional co-regulation of neuronal migration and laminar identity in the neocortex. *Development* 139, 1535–1546. doi: 10.1242/dev.069963

Lee, G. H., and D'Arcangelo, G. (2016). New insights into reelin-mediated signaling pathways. *Front. Cell Neurosci.* 10:122. doi: 10.3389/fncel.2016.00122

Lee, M., Yum, M. S., Woo, D. C., Shim, W. H., Ko, T. S., and Velisek, L. (2018). In vivo multimodal magnetic resonance imaging changes After N-Methyl-d-Aspartate-triggered spasms in infant rats. *Front. Neurol.* 9:248. doi: 10.3389/fneur.2018.00248

Lee, S. K., Kim, D. I., Mori, S., Kim, J., Kim, H. D., Heo, K., et al. (2004). Diffusion tensor MRI visualizes decreased subcortical fiber connectivity in focal cortical dysplasia. *Neuroimage* 22, 1826–1829. doi: 10.1016/j.neuroimage.2004.04.028

Lodge, D. J., and Grace, A. A. (2009). Gestational methylazoxymethanol acetate administration: a developmental disruption model of schizophrenia. *Behav. Brain Res.* 204, 306–312. doi: 10.1016/j.bbr.2009.01.031

Luhmann, H. J. (2016). Models of cortical malformation–Chemical and physical. *J. Neurosci. Methods* 260, 62–72. doi: 10.1016/j.jneumeth.2015.03.034

Luhmann, H. J., Fukuda, A., and Kilb, W. (2015). Control of cortical neuronal migration by glutamate and GABA. *Front. Cell Neurosci.* 9:4. doi: 10.3389/fncel.2015.00004

Moore, H., Jentsch, J. D., Ghajarnia, M., Geyer, M. A., and Grace, A. A. (2006). A neurobehavioral systems analysis of adult rats exposed to methylazoxymethanol acetate on E17: implications for the neuropathology of schizophrenia. *Biol. Psychiatry* 60, 253–264. doi: 10.1016/j.biopsych.2006.01.003

Mueller, S. G., Laxer, K. D., Barakos, J. A., Cashdollar, N., Flenniken, D. L., Vermathen, P., et al. (2005). Metabolic characteristics of cortical malformations causing epilepsy. *J. Neurol.* 252, 1082–1092. doi: 10.1007/s00415-005-0819-7

Niu, S., Yabut, O., and D'arcangelo, G. (2008). The Reelin signaling pathway promotes dendritic spine development in hippocampal neurons. *J. Neurosci.* 28, 10339–10348. doi: 10.1523/JNEUROSCI.1917-08.2008

Pang, T., Atefy, R., and Sheen, V. (2008). Malformations of cortical development. *Neurologist* 14, 181–191. doi: 10.1097/NRL.0b013e31816606b9

Paxinos, G., and Watson, C. (2014). *Paxino's and Watson's the Rat Brain in Stereotaxic Coordinates*. Amsterdam, Boston: Elsevier/AP, Academic Press is an imprint of Elsevier.

Pepin, J., Francelle, L., Carrillo-De Sauvage, M. A., De Longprez, L., Gipchtein, P., Cambon, K., et al. (2016). In vivo imaging of brain glutamate defects in a knock-in mouse model of Huntington's disease. *Neuroimage* 139, 53–64. doi: 10.1016/j.neuroimage.2016.06.023

Semple, B. D., Blomgren, K., Gimlin, K., Ferriero, D. M., and Noble-Haeusslein, L. J. (2013). Brain development in rodents and humans: identifying benchmarks of maturation and vulnerability to injury across species. *Progr. Neurobiol.* 106-107, 1–16. doi: 10.1016/j.pneurobio.2013.04.001

Silva, A. V., Sanabria, E. R., Cavalheiro, E. A., and Spreafico, R. (2002). Alterations of the neocortical GABAergic system in the pilocarpine model of temporal lobe epilepsy: neuronal damage and immunocytochemical changes in chronic epileptic rats. *Brain Res. Bull.* 58, 417–421. doi: 10.1016/s0361-9230(02)00811-0

Stork, O., Ji, F. Y., Kaneko, K., Stork, S., Yoshinobu, Y., Moriya, T., et al. (2000). Postnatal development of a GABA deficit and disturbance of neural functions in mice lacking GAD65. *Brain Res.* 865, 45–58. doi: 10.1016/s0006-8993(00)02206-x

Sugar, J., Witter, M. P., Van Strien, N. M., and Cappaert, N. L. (2011). The retrosplenial cortex: intrinsic connectivity and connections with the (para)hippocampal region in the rat. An interactive connectome. *Front. Neuroinform.* 5:7. doi: 10.3389/fninf.2011.00007

Tassi, L., Colombo, N., Garbelli, R., Francione, S., Lo Russo, G., Mai, R., et al. (2002). Focal cortical dysplasia: neuropathological subtypes, EEG, neuroimaging and surgical outcome. *Brain* 125, 1719–1732. doi: 10.1093/brain/awf175

Terpstra, M., Rao, R., and Tkac, I. (2010). Region-specific changes in ascorbate concentration during rat brain development quantified by in vivo (1)H NMR spectroscopy. *NMR Biomed.* 23, 1038–1043. doi: 10.1002/nbm.1528

Wamsley, B., and Fishell, G. (2017). Genetic and activity-dependent mechanisms underlying interneuron diversity. *Nat. Rev. Neurosci.* 18, 299–309. doi: 10.1038/nrn.2017.30

Wasser, C. R., and Herz, J. (2017). Reelin: neurodevelopmental architect and homeostatic regulator of excitatory synapses. *J. Biol. Chem.* 292, 1330–1338. doi: 10.1074/jbc.R116.766782

Wieronska, J. M., Branski, P., Siwek, A., Dybala, M., Nowak, G., and Pilc, A. (2010). GABAergic dysfunction in mGlu7 receptor-deficient mice as reflected by decreased levels of glutamic acid decarboxylase 65 and 67kDa and increased reelin proteins in the hippocampus. *Brain Res.* 1334, 12–24. doi: 10.1016/j.brainres.2010.03.078

Woermann, F. G., Mclean, M. A., Bartlett, P. A., Barker, G. J., and Duncan, J. S. (2001). Quantitative short echo time proton magnetic resonance spectroscopic imaging study of malformations of cortical development causing epilepsy. *Brain* 124, 427–436. doi: 10.1093/brain/124.2.427

Conflict of Interest: The authors declare that the research was conducted in the absence of any commercial or financial relationships that could be construed as a potential conflict of interest.

Copyright © 2020 Lee, Kim, Woo, Shim and Yum. This is an open-access article distributed under the terms of the Creative Commons Attribution License (CC BY). The use, distribution or reproduction in other forums is permitted, provided the original author(s) and the copyright owner(s) are credited and that the original publication in this journal is cited, in accordance with accepted academic practice. No use, distribution or reproduction is permitted which does not comply with these terms.

frontiers in Neuroscience

ORIGINAL RESEARCH
published: 03 June 2020
doi: 10.3389/fnins.2020.00547

Object-Based Analyses in FIJI/ImageJ to Measure Local RNA Translation Sites in Neurites in Response to Aβ1-42 Oligomers

*María Gamarra[1,2], Maite Blanco-Urrejola[1,2,3], Andreia F. R. Batista[1,4,5], Josune Imaz[2] and Jimena Baleriola[1,3,6]**

[1] Achucarro Basque Center for Neuroscience, Leioa, Spain, [2] Department of Neurosciences, Faculty of Medicine and Nursing, University of the Basque Country, Bilbao, Spain, [3] Department of Cell Biology and Histology, Faculty of Medicine and Nursing, University of the Basque Country, Leioa, Spain, [4] Life and Health Sciences Research Institute, School of Medicine, University of Minho, Braga, Portugal, [5] ICVS/3B's, PT Associate Laboratory, Universidade do Minho, Guimarães, Portugal, [6] IKERBASQUE Basque Foundation for Science, Bilbao, Spain

Subcellular protein delivery is especially important in signal transduction and cell behavior, and is typically achieved by localization signals within the protein. However, protein delivery can also rely on localization of mRNAs that are translated at target sites. Although once considered heretical, RNA localization has proven to be highly conserved in eukaryotes. RNA localization and localized translation are especially relevant in polarized cells like neurons where neurites extend dozens to hundreds of centimeters away from the soma. Local translation confers dendrites and axons the capacity to respond to their environment in an acute manner without fully relying on somatic signals. The relevance of local protein synthesis in neuron development, maintenance and disease has not been fully acknowledged until recent years, partly due to the limited amount of locally produced proteins. For instance, in hippocampal neurons levels of newly synthesized somatic proteins can be more than 20–30 times greater than translation levels of neuritic proteins. Thus local translation events can be easily overlooked under the microscope. Here we describe an object-based analysis used to visualize and quantify local RNA translation sites in neurites. Newly synthesized proteins are tagged with puromycin and endogenous RNAs labeled with SYTO. After imaging, signals corresponding to neuritic RNAs and proteins are filtered with a Laplacian operator to enhance the edges. Resulting pixels are converted into objects and selected by automatic masking followed by signal smoothing. Objects corresponding to RNA or protein and colocalized objects (RNA and protein) are quantified along individual neurites. Colocalization between RNA and protein in neurites correspond to newly synthesized proteins arising from localized RNAs and represent localized translation sites. To test the validity of our analyses we have compared control neurons to $A\beta_{1-42}$-treated neurons. Aβ is involved in the pathology of Alzheimer's disease and was previously reported to induce local translation in axons and dendrites which in

OPEN ACCESS

Edited by:
João O. Malva, University of Coimbra, Portugal

Reviewed by:
Luisa Cortes, University of Coimbra, Portugal
Ramiro Almeida, University of Aveiro, Portugal

***Correspondence:**
Jimena Baleriola
jimena.baleriola@achucarro.org

Specialty section:
This article was submitted to Brain Imaging Methods, a section of the journal Frontiers in Neuroscience

Received: *19 December 2019*
Accepted: *04 May 2020*
Published: *03 June 2020*

Citation:
Gamarra M, Blanco-Urrejola M, Batista AFR, Imaz J and Baleriola J (2020) Object-Based Analyses in FIJI/ImageJ to Measure Local RNA Translation Sites in Neurites in Response to Aβ1-42 Oligomers. Front. Neurosci. 14:547. doi: 10.3389/fnins.2020.00547

turn contributes to the disease. We have observed that Aβ increases the synthesis of neuritic proteins as well as the fraction of translating RNAs in distal sites of the neurite, suggesting an induction of local protein synthesis. Our results thus confirm previous reports and validate our quantification method.

Keywords: local protein synthesis, RNA localization, neurites, fluorescence microscopy, FIJI/ImageJ analyses, colocalization analyses

INTRODUCTION

Among all cell types, neurons are the most morphologically complex. The nucleus is contained in a cell body or soma, from where several neurites emerge. Neuronal dendrites measure around ten millimeters and axons can reach one meter of length in vertebrates (Bannister and Larkman, 1995b). This extremely polarized morphology reflects the also polarized function of neurons. Whereas dendrites receive signals, the cell body processes them and axons are responsible for transmitting information to adjacent neurons. To maintain a proper function, each neuronal compartment needs to react temporally and spatially in an acute manner in order to rapidly adapt to changes in the environment. These implies that compartmentalized signaling events are required and therefore neuronal proteins must be asymmetrically distributed.

The origin of neuritic proteins (both dendritic and axonal) has been discussed for years. It was classically thought that proteins that support dendritic and axonal functions are synthesized in the soma and then transported to the target compartment at peripheral sites of the neuron. However, in the 19th century, the possibility of neurites, especially axons, producing their own proteins locally was already hypothesized (review in Bolton, 1901). This unconventional view of protein distribution to different neuronal compartments has been finally accepted by the scientific community. In order to synthesize proteins locally, messenger RNAs (mRNAs) and components of translational machinery must be transported to neurites. mRNAs are localized to dendrites and axons as part of ribonucleoprotein (RNPs) complexes in a translationally repressed state. Exogenous stimulus sensed by neurites influence the local translation machinery and mRNAs are released from RNPs complexes. Once associated to localized ribosomes, mRNAs are translated and proteins are synthesized independently from the soma and thus the endoplasmic reticulum (ER) (Jung et al., 2012).

The requirement of local intra-dendritic translation for nervous system plasticity has been extensively studied. Local translation in axons is involved in growth cone behavior, axonal pathfinding and maintenance, as well as in retrograde signaling (reviewed in Jung et al., 2014; Holt et al., 2019). More recently, it has been reported that adult axons are also able to respond to pathological insults by changing their local translatome. In particular, after a nerve injury, mRNAs are locally translated and newly synthesized proteins contribute to axonal regeneration (Terenzio et al., 2018). Similarly, in the central nervous system (CNS) intra-axonal protein synthesis induced by $A\beta_{1-42}$ oligomers, whose accumulation is central to Alzheimer's disease (AD), contributes to neurodegeneration (Baleriola et al., 2014; Walker et al., 2018). Interestingly some authors have linked intra-dendritic translation and Tau mislocalization and hyperphosphorylation (Kobayashi et al., 2017; Li and Gotz, 2017). Thus, dysregulation of local protein synthesis might play a more relevant role in nervous system dysfunction than previously acknowledged.

AD is characterized by synaptic dysfunction during early stages (Palop and Mucke, 2010). Understanding dynamic early changes in the local proteome is in our view crucial to understand basic pathological mechanisms underlying AD and likely other neurological diseases. An accurate quantification of local translation foci, which is the aim of this study, might therefore give important clues to the extent to which changes in the local translatome contribute to the disease. Currently the most frequently used techniques to detect local translation in neurons are FUNCAT (FlUorescent Non–Canonical Amino acid Tagging) and SUnSET (SUrface SEnsing of Translation). The first utilizes modified amino acids, such azidohomoalanine, that get incorporated into the nascent polypeptide chain. The non-canonical amino acids are then tagged with a fluorophore in a cycloaddition reaction (Dieterich et al., 2010). SUnSET is based in the use of the antibiotic puromycin, which mimics an aminoacyl-transfer RNA (tRNA). Puromycin binds to the acceptor site of the ribosome during translation elongation leading to translation termination. The truncated puromycilated polypeptide can be detected by immunofluorescence using an anti-puromycin antibody (Schmidt et al., 2009). The fluorescence signal measured by both approaches is used as a readout of protein synthesis. Nevertheless, the low amount of locally produced proteins entails a limitation in the study of this phenomenon. For instance, our own results indicate that levels of newly synthesized neuritic proteins can be 20 to 30 times lower than somatic protein levels in unstimulated conditions. Thus, local translation sites in neurites can be easily overlooked when analyzing *de novo* synthesis by fluorescence microscopy. To overcome this situation, we have developed a simple method that helps visualize and quantify puromycin-positive sites in neurites by filtering and binarizing imaged cells using FIJI/ImageJ. Moreover, we have used a combination of RNA and protein staining techniques followed by object-based colocalization to detect sites of local RNA translation in neurons.

MATERIALS AND METHODS

Animals

All animal protocols followed the European directive 2010/63/EU and were approved by the UPV/EHU ethics committee.

Sprague-Dawley rats were bred in local facilities and embryonic brains were obtained from CO_2 euthanized pregnant rats.

Neuronal Cultures

Hippocampal neurons were prepared from embryonic day 18 rat embryos (E18) as described (Banker and Goslin, 1998). Briefly, hippocampi were dissected from embryonic brains and dissociated in TrypLE Express (Gibco, Thermo Fisher Scientific, Waltham MA, United States) for 10 min at 37°C. Cells were washed twice with Hank's balanced salt solution (HBSS, Gibco) and resuspended in plating medium containing 10% fetal bovine serum, 2 mM L-glutamine and 50 $U.ml^{-1}$ penicillin-streptomycin in Neurobasal (all from Gibco). Cells were homogenized with a pasteur pipette and centrifuged for 5 min at 800 rpm. Cells were resuspended in plating medium. Hippocampal neurons were cultured on poly-D-lysine-coated coverslips in 24-well plates at low density (35.000 cells/cm^2), similar to previous reports in which newly synthesized proteins along individual neurites were visualized (Dieterich et al., 2010; Graber et al., 2013; Hafner et al., 2019). Cultures were maintained at 37°C in a 5% CO_2 humidified incubator. After 1 day *in vitro* (1 DIV) the medium was replaced with growth medium (1× B27, 2 mM glutamine, and 50 $U.ml^{-1}$ penicillin-streptomycin in Neurobasal). To avoid the growth of glia, half of the medium was replaced with fresh medium containing 20 μM of 5-fluorodeoxyuridine and uridine (Sigma Aldrich, Merck, Darmstadt, Germany) every 3 days. Treatments were performed at 9–10 DIV.

Oligomeric Aβ Preparation and Treatments

Soluble oligomeric amyloid-β ($A\beta_{1-42}$) was prepared as previously described (Quintela-Lopez et al., 2019). Synthetic $A\beta_{1-42}$ (Bachem, Bubendorf, Switzerland) was dissolved in hexafluoroisopropanol (HFIP, Sigma Aldrich) to 1 mM, aliquoted and dried. For oligomer formation, the peptides were resuspended in dry dimethylsulfoxide (DMSO; 5 mM, Sigma Aldrich) and Hams F-12 (PromoCell Labclinics, Barcelona, Spain) was added to adjust the final concentration to 100 μM. Peptides were incubated overnight at 4°C. Oligomerized Aβ was added to neurons at 9 DIV at a 3 μM concentration and incubated for 24 h. DMSO was used as vehicle control.

Puromycylation Assay

Puromicyn is a tRNA analog, which is incorporated into the nascent polypeptide chain in a ribosome-catalyzed reaction. This technique allows the *in situ* detection of protein synthesis with an anti-puromicyn antibody. At 10 DIV, DMSO- and Aβ-treated neurons were exposed to 2 μM puromycin (Sigma Aldrich) for 5–30 min as indicated. Control conditions with no puromicyn received only fresh growth medium (vehicle). To verify that puromycin labels newly synthesized proteins, 40 μM of the translation inhibitor anisomycin (Sigma Aldrich) was co-incubated with puromycin. Cells were washed with cold PBS with 3 $\mu g.ml^{-1}$ digitonin (Sigma Aldrich) and fixed in 4% paraformaldehyde (PFA), 4% sucrose in PBS.

Immunocytochemistry

Neurons were fixed for 20 min at room temperature in 4% PFA, 4% sucrose in PBS. Cells were washed three times with PBS, permeabilized and blocked for 30 min in 3% BSA, 100 mM glycine and 0.25% Triton X-100. Next, samples were incubated overnight at 4°C with primary antibodies including mouse anti-puromycin (1:500, MABE343, Merck Millipore), rabbit and chicken anti-βIII tubulin (1:500, ab18207 and ab107216, respectively, Abcam, Cambridge, United Kingdom), rabbit anti-Tau (1:1000, ab32057, Abcam) and rabbit anti-calreticulin (1:500, ab92516, Abcam). After three PBS washes, cells were incubated for 1 hr at room temperature with fluorophore-conjugated secondary antibodies: anti-mouse Alexa Fluor 594 (1:200, A-11005, Invitrogen, Thermo Fisher Scientific), anti-rabbit Alexa Fluor 488 (1:200, A-21206, Invitrogen), anti-chicken DyLight 350 (1:200, SA5-10069, Invitrogen), anti-rabbit Alexa Fluor 647 (1:200, A-31573, Invitrogen) and anti-rabbit DyLight 405 (1:200, 611-146-002, Rockland Immunochemicals, Pottstown, PA, United States). Samples were washed three times with PBS and mounted with ProLong Gold antifade reagent (P-36930, Invitrogen). Whenever stated, a no-primary-antibody negative control was used.

To label endogenous RNAs neurons were washed once with cold PBS with 3 $\mu g.ml^{-1}$ digitonin (Sigma Aldrich), once with 50% methanol in PBS and fixed in cold 100% methanol for 5 min. Samples were rehydrated by washing them in 50% methanol in PBS once and in PBS three times. Following the standard immunocytochemistry procedure, cells were incubated for 20 min at room temperature with SYTO RNASelect green fluorescent dye in PBS (500 nM, S-32703, Invitrogen). Samples were washed with PBS and mounted with ProLong Gold antifade reagent. Some fixed neurons were incubated with 50 μg/ml DNAse or RNAse (Sigma) for 10 min at room temperature to assess the selectivity of the SYTO labeling.

Image Acquisition and Processing

Images were acquired using an objective EC Plan-Neofluar 40×/1,30 Oil DIC M27 on an Axio-Observer Z1 microscope equipped with AxioCam MRm Rev. 3 (Zeiss, Oberkochen, Germany) and Hamamatsu EM-CCD ImagEM (Hamamatsu Photonics, Hamamatsu, Japan) digital cameras. Settings for image acquisition where determined in a random field of a DMSO-treated sample ensuring pixel intensities were within the linear range and avoiding pixel saturation. Images were acquired with ZEN 2 (blue edition) version 2.0.0.0. software (Zeiss). Settings were kept identical for all sampled cells in any given experiment. Whenever possible, five random fields per coverslip and two coverslips per experimental condition were imaged. Most images were acquired with AxioCam, however if cells were imaged in the far red spectrum, the Hamamatsu camera was used.

For figure preparation, the staining of interest (puromycin, calreticulin, SYTO) was converted from grayscale to RGB or to a colorimetric scale (heatmaps) in non-binarized images. Binarized images used for assisted quantification of translation sites were obtained as will be specified below. In all cases

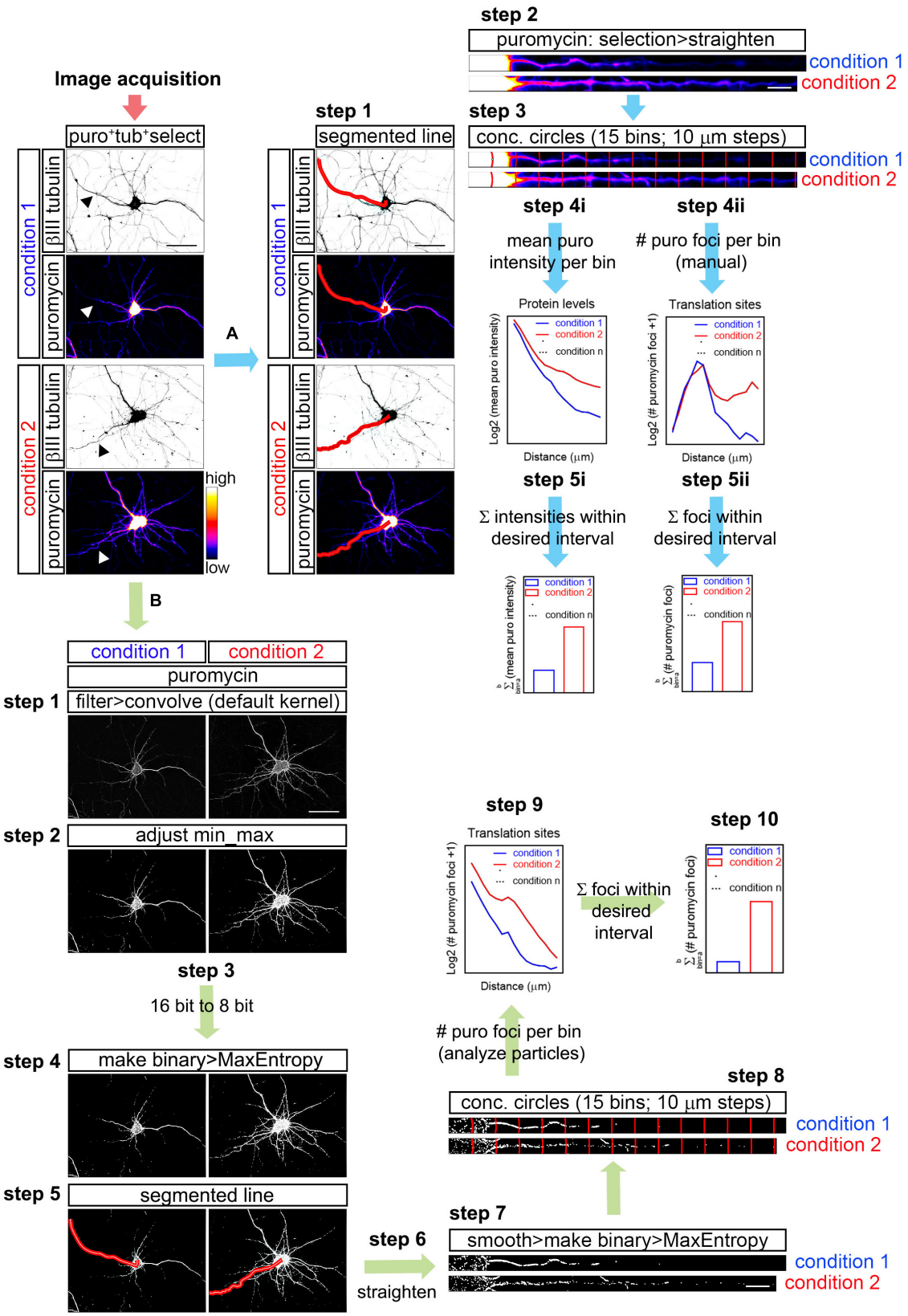

FIGURE 1 | Continued

FIGURE 1 | Workflow for puromycin quantification in unprocessed and processed images. **(A)** Workflow A shows puromycin intensity analyses (**path i**) and visual inspection of puromycin translation sites in raw images (**path ii**). After image acquisition, the longest puromycin- and βIII-positive neurite (arrowheads in the first panel) was selected with a segmented line, straighten and divided into 10 μm bins with the concentric_circles plugin (**steps 2** and **3**). Mean puromycin intensity per bin, corresponding to protein levels, was measured and represented as the Log2 (mean puro intensity) vs. distance (**step 4i**). The total fluorescent intensity of the puromycin within the desired interval (soma, neurites, etc. . .) disregarding the bin position is shown as Σ (mean puro intensity; **step 5i**). For visual inspection of puromycin foci, path ii was followed. Number of puromycin foci per bin, corresponding to translation sites, was quantified (Log2 (# puromycin foci + 1) vs. distance; **step 4ii**). The total number of puromycin foci within the desired interval (soma, meurites, etc. . .) disregarding the bin position is plotted as Σ (# puromycin foci; **step 5ii**). **(B)** The assisted analyses of puromycin-positive foci in binarized images were performed following the workflow B. Once the images were acquired, puromycin staining was filtered with the convolver applying the default normalized kernel and minimum and maximum intensities were adjusted (**steps 1** and **2**). 16-bit images were coverted to 8-bit (**step 3**) and binarized with the MaxEntropy mask (**step 4**). Neurites were selected with a segmented line (**step 5**), straighten, smoothen and binarized with the MaxEntropy mask (**steps 6** and **7**). Discrete puromycin puncta were measured (analyze particles) in neurons in 15 bins covering a distance of 150 μm from the cell nucleus or from the edge of the soma using the concentric_circles plugin (**step 8**). Graphs show the translation sites represented as Log2 (# puromycin foci + 1) vs. distance (**step 9**). Discrete puromycin foci within desired interval (soma, neurites, etc. . .) disregarding the bin position are represented as Σ (# puromycin foci; **step 10**). Scale bars, 50 μm in whole-cell micrographs and 10 μm in straighten neurites.

background, contrast and sharpness were adjusted and set the same in control and experimental conditions. Markers used as counterstain for neurite selection were adjusted for an optimal visualization in figures.

Puromycin and SYTO Intensity Analysis in Non-binarized Images

To quantify the puromycin fluorescent intensity as a measure of protein production (**Figure 1**; workflow A), the longest puromycin- and βIII tubulin-positive neurite or puromycin- and Tau-positive neurite from randomly selected cells was straightened with the Segmented Line tool in FIJI/ImageJ:

FIJI/ImageJ > File > Open (do not autoscale) > Segmented Line (**Figure 1**; workflow A; step 1) > Selection > Straighten (**Figure 1**; workflow A; step 2).

Images obtained from AxioCam measure 1038 × 1040 pixels, whereas those obtained from the Hamamatsu camera measure 512 × 512 pixels. Thus, straighten lines were 40 pixel-wide in images taken with the first camera and 20 pixel-wide in images taken with the latter. Since experiments were always compared using a randomized block design (see "Statistical Analyses"), direct comparison between neurites imaged with different cameras is never performed.

Concentric circles at 10 μm intervals emerging from the center of the cell nucleus or from the edge of the soma were generated with an in-house designed FIJI/ImageJ macro (concentric_circles, **Figure 1**; workflow A; step 3) (Quintela-Lopez et al., 2019). 15 bins were generated covering a length of 150 μm of the straighten neurites. Fluorescence intensity was measured in each bin. Background pixel intensity was measured outside the area covered by the neurite and substracted (**Figure 1**; workflow A; step 4i). To calculate the total fluorescent intensity in the soma, in neurites or in other desired interval disregarding the bin position, values retrieved from each bin of interest were summed up (**Figure 1**; workflow A; step 5i).

The same method was used to measure RNA levels in neurites stained with SYTO.

Note that workflow A (**Figure 1**) exemplifies the procedure in neurites doubly labeled for βII tubulin and puromycin, however it also applies to neurites stained for Tau and puromycin, for SYTO and Tau, for calreticulin and puromycin, etc. . .

Visual Inspection of Puromycin-Positive Translation Foci in Non-binarized Images (Manual Analyses)

As described above, the longest puromycin- and βIII-positive neurite, or puromycin- and Tau-positive neurite, etc. . . from randomly selected cells was straightened and divided into 15 10 μm-wide bins with the concentric_circles plugin (**Figure 1**; workflow A; step 3). Discrete puromycin puncta were visually scored in each bin covering a distance of 150 μm from the center of the cell nucleus or from the edge of the soma (**Figure 1**; workflow A; step 4ii). To calculate the total translation foci in the soma or in neurites or in any other desired interval disregarding the bin position, values retrieved from each bin of interest were summed up (**Figure 1**; workflow A; step 5ii). The bin ranging from 0 to 10 μm (first bin within the soma) was discarded as no discrete puncta could be visualized (N/A in **Figures 3D,E**).

Assisted Analyses of Puromycin- and SYTO-Positive Foci in Binarized Images

The assisted analysis of translation sites was performed using the following step-by-step protocol (**Figure 1**; workflow B):

FIJI/ImageJ > File > Open (do not autoscale). Go to the staining of interest (e.g., puromycin) > Process > Filter > Convolve (if a stack is opened, do not process all the images in the stack). The default normalized kernel is sufficient to enhance structures in the periphery of the neurons smaller than 5 × 5 pixels and it is thus suitable to highlight puromycin-positive translation sites distal to the center of the cell nucleus (**Figure 1**; workflow B; step 1).

Following image convolution:

Image > Adjust > Brightness/Contrast (equal min/max adjustment in all samples within the same experiment; **Figure 1**; workflow B; step 2) > Image > Type > 8-bit (**Figure 1**; workflow B; step 3) > Process > Binary > Make Binary (Method, MaxEntropy; Background, Default; Black background. Only convert current image; **Figure 1**; workflow B; step 4).

Once the image is binarized select the longest positive neurite:

Segmented Line (**Figure 1**; workflow B; step 5) > Edit > Selection > Straighten (line width: 20 pixels for Hamamatsu images; 40 pixels for AxioCam images; Process Entire Stack unclicked; **Figure 1**; workflow B; step

6) > Process > Smooth > Process > Binary > Make binary (Method, MaxEntropy; **Figure 1**; workflow B; step 7).

Straighten neurites are finally divided in 15 concentric circles at 10 μm intervals emerging from the center of the cell nucleus or from the edge of the soma with the concentric_circles plugin (**Figure 1**; workflow B; step 8). The number of objects (translation sites. . .) are scored in each interval (bin) with the Analyze Particles function (default settings; **Figure 1**; workflow B; step 9). To calculate the total translation sites in the soma or in neurites or in any other desired interval disregarding the bin position, values retrieved from each bin of interest were summed up (**Figure 1**; workflow B; step 10).

Although this procedure is described for the puromycin staining as an example, the same steps were followed to binarize and quantify SYTO-positive discrete puncta (RNA) in Tau-positive neurites. When binarization of puromycin and SYTO labeling was performed for the same neurite, colocalization between RNA and protein was performed as follows:

Process > Image Calculator > Image 1 (e.g., puromycin) AND Image 2 (e.g., SYTO; click create new window).

The resulting image is smoothen and binarized with the Mask Entropy mask. The image is finally divided in 15 concentric circles at 10 μm intervals emerging from the edge of the soma with the concentric_circles plugin. The number of objects (considered actively translating RNAs) are scored in each interval (bin) with the Analyze Particles function (default settings).

Intensity Profiles

We used intensity profiles to exemplify fluorescent signal distributions in neurites Briefly, neurites were selected with the Segmented Line tool (line width: 20 pixels for Hamamatsu images; 40 pixels for AxioCam images) and analyzed with Plot Profile.

Statistical Analyses

The sample size is specified in the figure legends. Statistical analyses were performed with Prism 7 (GraphPad Software, San Diego, CA, United States) following a randomized block design where samples from the same experiment were matched to eliminate inter-experimental variability. When comparing the means of two groups taking one variable into account, two-tailed *t*-tests were performed. When comparing the means of two groups taking two variables into account, two-way ANOVA was used. If more than two groups and more than one variable were analyzed, we performed two-way ANOVA followed by Tukey's multiple comparison test or Holm-Sidak's *post hoc* test depending on the samples requirements.

For correlation analyses we performed a normality test on the data to determine if they followed a Gaussian distribution, which most of them didn't. Thus, we chose to perform Spearman non-parametric correlation test to retrieve the correlation coefficients. In the correlation graphs, linear regression of the data was performed to evaluate the differences between slopes (ANCOVA).

Note that in some cases, Y axes are represented as Log2 of the actual measured raw values to better visualize the results. In other experiments where some values equaled zero, one unit was added to all values in order to apply a Log2 function. Regardless of the transformation, all statistical analyses were performed on raw data and not on transformed data.

RESULTS

Detection of Newly Synthesized Neuritic Proteins by Puromycilation

Based on previously published data (Baleriola et al., 2014), rat hippocampal neurons grown for 9 days *in vitro* (DIV) were treated with vehicle (DMSO) or 3 μM $A\beta_{1-42}$ oligomers for 24 h by bath application. As a first step to quantify RNA translation sites in neurites we first detected *de novo* production of neuritic proteins by puromycilation/SUnSET (Schmidt et al., 2009; **Figure 2A**). The antibiotic puromycin is an aminoacyl-tRNA analog that incorporates into the polypeptide chains during translation elongation, leading to translation termination (Yarmolinsky and Haba, 1959). The development of specific antibodies has allowed the immunodetection of puromycilated polypeptides as a measure of protein synthesis. Control and Aβ-treated cells were fed with 2 μM puromycin for 30 min prior to fixation. Following fixation with a PFA/sucrose mix, cells were stained for puromycin and counterstained with an anti-βIII tubulin antibody to visualize the neuronal cytoskeleton (**Figure 2A**). As a negative control, immunostaining was performed on neurons that had not been treated with puromycin (-puro, **Figure 2A**). Fluorescence intensity for the raw puromycin signal, represented in a colorimetric scale (**Figure 2A**), was measured along the longest puromycin- and βIII-positive neurite in randomly selected cells (1–6, **Figure 2A**). Fluorescence levels in puromycin-labeled neurites (3 and 4, **Figures 2A–C**) were well above the levels measured in negative controls (1 and 2, **Figures 2A–C**). Additionally, puromycin hotspots were readily visible in distal sites of the neurites, especially in Aβ-treated cells (4, intensity profile and heatmap in **Figure 2B**). Finally, regardless of the effect of $A\beta_{1-42}$, puromycin intensity was significantly reduced in neurites when cells were co-incubated with the translation inhibitor anisomycin (+ anis + puro, **Figure 2A**; 5 and 6, **Figures 2A–C**). Altogether these results indicate that in our system puromycin labeling can be used to detect *de novo* synthesis of neuritic proteins as previously reported in similar experimental setups (Walker et al., 2018; Rangaraju et al., 2019).

$A\beta_{1-42}$ Oligomers Increases New Synthesis of Neuritic Proteins Detected Beyond the Canonical Endoplasmic Reticulum

Then we asked whether the puromycin signal likely arose from the endoplasmic reticulum (ER). Soma-centric views consider that most protein synthesis in eukaryotic cells occurs in the ER (specifically in the rough ER). In neurons, however, the positioning of the rough ER (RER) with respect to distal sites of neurites does not explain how in some experimental

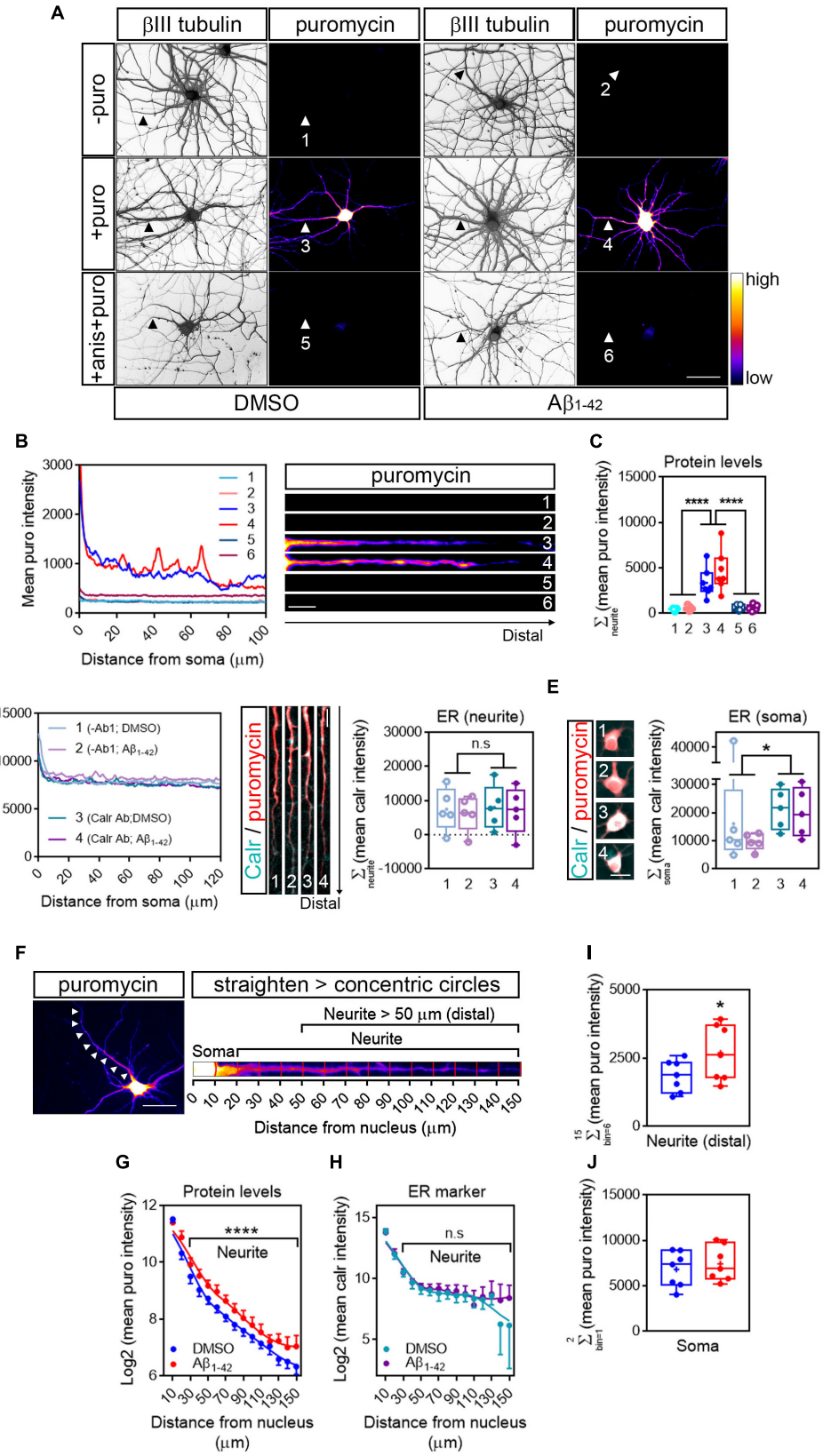

FIGURE 2 | Continued

FIGURE 2 | Detection of newly synthesized proteins by puromycilation. **(A)** Rat hippocampal neurons were grown for 9 DIV and were treated with DMSO (left panels) or $A\beta_{1-42}$ oligomers (right panels) for 24 h. Before fixing, cells were incubated with vehicle (-puro; neurites 1 and 2), with puromycin (+ puro; neurites 3 and 4) or with puromycin and anisomycin (+ anis + puro; neurites 5 and 6) for 30 mins. Cells were immunostained with an anti-βIII tubulin antibody to visualize the neuronal cytoskeleton (gray) and with an anti-puromycin antibody to analyze newly synthesized proteins (heatmaps). Scale bar, 50 μm. **(B)** Intensity profiles were measured in the longest puromycin- and βIII tubulin-positive neurite from randomly selected cells as exemplified. 1 and 2: no puromycin incubation in DMSO- and Aβ-treated neurons, respectively. 3 and 4: 30 min puromycin incubation in DMSO- and Aβ-treated cells, respectively. 5 and 6: co-incubation with anisomycin and puromycin for 30 mins in DMSO- and Aβ-treated cells, respectively. Scale bar, 10 μm in heatmaps. **(C)** Box and whisker graph representing protein levels as the total fluorescent intensity of the puromycin staining along 130 μm of βIII tubulin-positive neurites. 1 and 2: no puromycin incubation in DMSO- and Aβ-treated neurons, respectively. 3 and 4: 30 min puromycin incubation in DMSO- and Aβ-treated cells, respectively. 5 and 6: co-incubation with anisomycin and puromycin for 30 mins in DMSO- and Aβ-treated cells, respectively. Data represent the average value of 5–10 sampled cells per condition shown as individual data points, and the mean and median of 7 independent experiments ($n = 7$). $^{****}p < 0.0001$; two-way ANOVA followed by Tukey's multiple comparison test. **(D)** The "canonical" endoplasmic reticulum (ER) was defined by Calreticulin staining (Carl Ab in intensity profiles). To determine the background signal, some cells were stained only with the secondary antibody (no-primary antibody control; -Ab1 in intensity profiles). Images exemplify neurites processed for calreticulin staining (cyan) to measure the area covered by the ER and counterstained with an anti-puromycin antibody (red). Box and whisker graph representing the total fluorescent intensity of the calreticulin staining along 130 μm of calreticulin- and puromycin-positive neurites. 1 and 2: no-primary antibody control (-Ab1) in DMSO- and Aβ-treated neurons, respectively. 3 and 4: calreticulin antibody incubation (Calr Ab) in DMSO- and Aβ-treated neurons, respectively. Data represent the average value of 5–10 sampled cells per condition shown as individual data points, and the mean and median of 5 independent experiments ($n = 5$). n.s, no significant; two-way ANOVA followed by Holm-Sidak's *post hoc* test. Scale bar, 10 μm. **(E)** Calreticulin immunostaining signal (cyan) in somata from DMSO- and Aβ-treated cells and counterstained with an anti-puromycin antibody (red). Scale bar, 10 μm in images. Box and whisker graph representing the total fluorescent intensity of the calreticulin staining along the first 20 μm of calreticulin- and puromycin-positive somata. 1 and 2: no-primary antibody control (-Ab1) in DMSO- and Aβ-treated neurons, respectively. 3 and 4: calreticulin antibody incubation (Calr Ab) in DMSO- and Aβ-treated neurons, respectively. Data represent the average value of 5–10 sampled cells per condition shown as individual data points, and the mean and median of 5 independent experiments ($n = 5$). $^{*}p < 0.05$; two-way ANOVA followed by Holm-Sidak's *post hoc* test. Scale bar, 20 μm. **(F)** Cells were processed for puromycin staining to measure protein synthesis (heatmap) and counterstained with an anti-βIII tubulin antibody to visualize the neuronal cytoskeleton (not shown). The longest positive neurite (arrowheads in left micrograph) was selected with a segmented line, straighten and divided into 10 μm bins with the concentric_circles plugin (straighten neurite right) following workflow Ai in **Figure 1**. Scale bar, 50 μm. **(G)** Puromycin intensity was measured in DMSO- and Aβ-treated neurons in 15 bins covering a distance of 150 μm from the cell nucleus (as also shown in the straighten micrograph exemplified in **(F)**. The graph shows the average intensity of puromycin per condition represented as Log2 (mean puro intensity) vs. distance ± SEM measured in 7 independent experiments ($n = 7$). $^{****}p < 0.0001$; two-way ANOVA. **(H)** Calreticulin intensity was measured in DMSO- and Aβ-treated neurons in 15 bins covering a distance of 150 μm from the cell nucleus. The graph shows the average intensity of calreticulin per condition represented as Log2 (mean calr intensity) vs. distance ± SEM measured in 5 independent experiments ($n = 5$). n.s, no significant; two-way ANOVA. **(I)** Box and whisker graphs representing the total fluorescent intensity of the puromycin staining in βIII tubulin- and puromycin-positive neurites within the range of 50–150 μm from the nucleus [Neurite (distal)] as also exemplified in **(F)**. Data represent the average value of 5–10 sampled cells per condition shown as individual data points, and the mean and median of 7 independent experiments ($n = 7$). $^{*}p < 0.05$; two-tailed *t*-test. **(J)** Box and whisker graphs representing the total fluorescent intensity of the puromycin staining in βIII tubulin- and puromycin-positive somata within the range of 0–20 μm from the nucleus (Soma) as also exemplified in **(F)**. Data represent the average value of 5–10 sampled cells per condition shown as individual data points, and the mean and median of 7 independent experiments ($n = 7$).

setups that allow to study the local response of dendrites and axons (reviewed in Holt et al., 2019) newly synthesized proteins are detected peripherally, unless they are produced locally beyond the "canonical" ER. The RER is enriched in proteins involved in the folding of nascent polypeptides, being the Calnexin/Calreticulin system one the best known protein complexes (Rutkevich and Williams, 2011). After culturing hippocampal neurons for 9 days and following 24-h treatments with DMSO or $A\beta_{1-42}$, neurons were labeled with puromycin. Cells were then processed for Calreticulin (Calr) and puromycin immunostaining. As a negative control, some neurons were subjected to the immunocytochemistry procedure but were not incubated with anti-Calr antibody (no-primary antibody control). To determine the presence of Calreticulin in neurites we compared the fluorescent signal of cells incubated with anti-Carl antibody with those incubated with no primary antibody (**Figure 2D**). Results showed that both DMSO- and Aβ-treated neurites were devoid of Calreticulin, and thus of "canonical" ER (**Figure 2D**, right graph). Conversely, Calreticulin could be detected above background levels in neuronal somata of cells treated with DMSO or $A\beta_{1-42}$ oligomers (**Figure 2E**).

We then asked whether Aβ oligomers induced changes in the distribution pattern of newly synthesized proteins along neurites, beyond the canonical ER domain. The longest puromycin-positive neurite (**Figure 2F**; left micrograph) of randomly selected cells was straighten and divided into 10 μm bins following the workflow Ai (**Figure 1**). Puromycin intensity was measured in 15 bins covering a length of 150 μm from the center of the cell nucleus using the concentric_circles plugin in FIJI/ImageJ (**Figure 2F**; right micrograph). A significantly distinct distribution in the levels of newly produced proteins was observed in Aβ-treated neurites compared to controls (positions beyond 20 μm, **Figure 2G**). In line with the absence of a canonical ER in neurites, no differences were detected in the Calreticulin staining pattern between DMSO- and Aβ-treated neurites (**Figure 2H**). Finally, we focused on neuritic positions distal to the ER to increase the chances that newly synthesized proteins measured in neurites did not rely on the ER-dependent translation machinery. We summed up puromycin intensity signals in bins corresponding to the 50 to 150 μm range measured from the center of the nucleus (distal neurite; **Figure 2I**). $A\beta_{1-42}$ significantly increased the levels of newly synthesized proteins in this interval. More importantly the effect of Aβ was restricted to neurites and did not affect the neuronal soma (**Figure 2J**) in accordance with previously published data (Walker et al., 2018).

It is noteworthy pointing out that in our experimental system the effect of Aβ oligomers was not evident with puromycin pulses shorter than 30 min (e.g., 10 min. Data not shown).

Image Processing Unravels a Previously Unreported Effect of $A\beta_{1-42}$ Oligomers on Translation Foci in Neurites

Measuring puromycin intensity can give an idea of the amount of protein being produced distal from the ER within neurites and/or diffused from the actual translation site, but it does not report on the number and position of the translation sites themselves. In the case of Aβ treated cells, increased puromycin intensity might be a result of the emergence of new translation sites, a consequence of an increased rate of protein production in preexisting sites or both. To determine whether Aβ oligomers modify the amount of translation sites in neurites we quantified the number of puromycin discrete puncta. Discrete puncta in distal neuritic sites likely reflect foci of localized translation (Graber et al., 2013; Rangaraju et al., 2019). Such foci can be easily overlooked since their intensity can be ∼20 to 30 times less than somatic puromycin fluorescent levels (as implicitly shown in **Figure 2**). We have developed a strategy to enhance puromycin hotspots in neurites based solely on image processing and the assisted quantification of the resulting objects (**Figure 1**; workflow B).

The number of discrete puromycin foci was quantified along the longest puromycin- and βIII tubulin-positive neurite of randomly sampled cells (**Figure 3A**). Image acquisition was identical in control and Aβ-treated neurons. We selected neurites from raw and binarized images in order to compare quantifications performed by visual inspection of the puromycin staining (manual; **Figures 1**, **3**, workflow A) and by analyzing particles (assisted; **Figures 1**, **3**, workflow B), respectively. On the one hand DMSO- and Aβ-treated neurites were selected from raw images (represented as heatmaps; 1 and 2 in **Figure 3A**) with a segmented line 20 or 40 pixels wide and straighten (1 and 2; **Figure 3B**). On the other hand, images were filtered with the convolver in FIJI/ImageJ applying the default normalized kernel. The default kernel was sufficient to enhance structures in the periphery of the neurons and thus was suitable to highlight puromycin-positive translation foci distal to the center of the cell nucleus. Published data have reported spot quantification procedures without applying convolution filters. However, in our case image filtering prior to binarization enhanced the detection of discrete foci compared to unfiltered images, especially in Aβ-treated neurons (condition 2 in **Supplementary Figure S1**).

Following image convolution, minimum and maximum intensities (B&C menu in FIJI/ImageJ) were then manually adjusted in order to eliminate pixels outside the stained cells (background) and enhance the intensity of those inside. 16-bit images were coverted to 8-bit and binarization was performed using the MaxEntropy mask. As in the case of the raw images, DMSO- and Aβ-treated neurites were selected with a 20- or 40-pixel wide segmented line and straighten. Finally, straighten neurites were smoothen and binarized again using the MaxEntropy mask (1 and 2; **Figure 3C**). As exemplified by the number of peaks in the intensity profiles image conversion increased the number of detected sites (foci in 3B and C) and slightly enhanced the effect of Aβ oligomers, which increased from 2.7- to 3.3-fold. We then analyzed the distribution pattern of translation foci along neurites. Neurites were divided into 10 μm bins and positive puromycin puncta within each bin were visually scored prior to image conversion (1 and 2 in **Figure 3D**; wA) or were counted with the particle analyzer in binarized images (1 and 2 in **Figure 3D**; wB). In all cases 15 bins were quantified per cell, covering a distance of 150 μm from the cell nucleus. Both quantification methods revealed a significantly distinct distribution of translation sites in neurites in Aβ-treated cells compared to controls (**Figure 3E**). However, an average of almost 10-fold increase in the number of total foci in neurites was observed when using the assisted quantification method compared to visual inspection (**Figures 3E,F**).

The default matrix in FIJI's convolver is a Laplacian operator-based edge detector that allows to find discontinuities in the puromycin labeling that could result from a punctate staining arising from discrete positive foci. Laplacian operators are very accurate in finding edges in an image but also very sensitive to background noise. Thus, we quantified the amount of foci also in neurons that had not been fed with puromycin. Negative controls showed significantly less amount of foci in neurites regardless of whether quantification was performed manually in non-binarized images (**Figure 3F**; left graph) or with the particle analyzer in filtered and binarized images (**Figure 3F**; right graph). In conclusion the 5 × 5 Laplacian operator used in our approach can be successfully applied to highlight positive translation foci in distal neuritic sites.

When comparing the scores performed at each distance by manual inspection in raw images and with the assisted method in binarized images we observed a significant positive correlation between both procedures that ranged from moderate to high in DMSO- and Aβ-treated cells, respectively (**Figure 3G**). To determine which method was closer to the unbiased measurement of protein production represented by puromycin intensity (**Figure 2**), we then compared data obtained from binarized images and from raw images with the intensity values. In both cases we found a significant high positive correlation (**Figure 3H**). However, when fitting the translation sites at each distance to a regression line, a significant increase in the slope was observed when data were obtained from binarized images, suggesting increased similarities between the number of discrete puromycin foci and puromycin intensity values when using the assisted quantification method.

Finally, we focused on distal sites of the neurites (> 50 μm from the nucleus) disregarding the bin position and were unable to detect any significant change between DMSO- or Aβ-treated cells when translation foci were quantified in raw images by visual inspection (manual, **Figure 3I**; wA). Conversely, we did observe a significant effect of Aβ oligomers when quantification was performed with the particle analyzer in binarized images (assisted, **Figure 3I**; wB). In no case did we detect any changes induced by Aβ in the soma (**Figure 3I**). Altogether, results so far indicate that binarizing images from puromycin-positive cells allows the assisted quantification of neuritic translation sites yielding results that resemble those obtained from an unbiased measurement of raw puromycin intensity. Additionally, assisted quantification in binarized

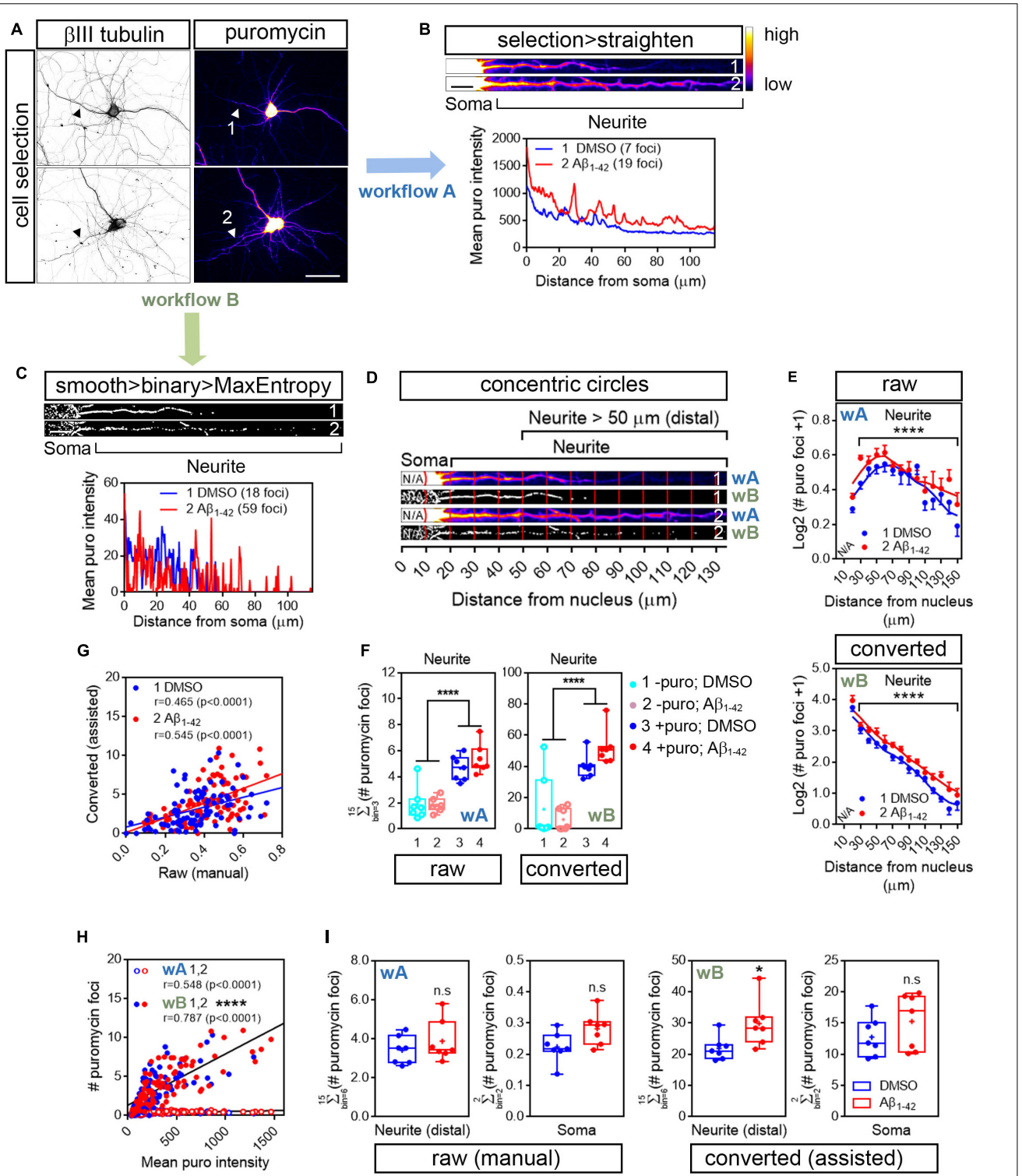

FIGURE 3 | Image processing reveals an effect of Aβ1-42 oligomers on neuritic translation sites. **(A)** Rat hippocampal neurons were grown for 9 DIV and were treated with DMSO or $A\beta_{1-42}$ oligomers for 24 h. Cells were incubated with puromycin for 30 mins and processed for βIII tubulin (gray) and puromycin immunostaining (heatmaps). Scale bar, 50 μm. **(B)** Following workflow A, the longest puromycin- and βIII-positive neurite in raw images was selected with a segmented line and straighten. Puromycin-positive discrete puncta were analyzed by visual inspection as exemplified in the intensity profiles obtained from straighten neurites (heatmaps). 1 and 2: 30 min puromycin incubation in DMSO- and Aβ-treated cells, respectively. Scale bar, 10 μm. **(C)** Following workflow B, selected neurites were straighten, smoothen and binarized with the MaxEntropy mask (smooth > binary > MaxEntropy). Puromycin-positive discrete puncta were analyzed

(Continued)

FIGURE 3 | with the particle analyzer as exemplified in the intensity profiles from straighten neurites. 1 and 2: 30 min puromycin incubation in DMSO- and Aβ-treated cells, respectively. Scale bar, 10 μm. **(D)** Discrete puromycin puncta were measured in DMSO- and Aβ-treated neurons in 15 bins covering a distance of 150 μm from the cell nucleus using the concentric_circles plugin. Measurements were performed by visual inspection in raw images (workflow Aii, wA) and with the particle analyzer in binarized images (workflow B, wB). 1: DMSO-; 2: Aβ-treated neurites. N/A, not applicable. **(E)** Graphs show the average puromycin foci per condition represented as Log2 (# puro foci + 1) vs. distance ± SEM measured in raw (wA) and binarized images (wB) from 7 independent experiments ($n = 7$). ****$p < 0.0001$; two-way ANOVA. N/A, not applicable. **(F)** Box and whisker graph representing translation sites as the total number of puromycin foci along 130 μm of βIII tubulin-positive neurites following visual inspection of raw images (raw; workflow A, wA) or assisted quantification in binarized images (converted; workflow B, wB). 1 and 2: no puromycin incubation in DMSO- and Aβ-treated neurons, respectively. 3 and 4: 30 min puromycin incubation in DMSO- and Aβ-treated cells, respectively. Data represent the average value of 5–10 sampled cells per condition shown as individual data points, and the mean and median of 7 independent experiments ($n = 7$). ****$p < 0.0001$; two-way ANOVA followed by Holm-Sidak's *post hoc* test. **(G)** Spearman correlation between quantifications in raw and in binarized images. Graphs represent each scored value per distance using both methods in DMSO- (1, blue) and Aβ-treated neurons (2, red) cultured in 7 independent experiments ($n = 7$). $p < 0.05$ indicate a significant correlation. **(H)** Spearman correlation between non-assisted (wA; 1, DMSO-; 2, Aβ-treated cells) or assisted quantification (wB; 1, DMSO-; 2, Aβ-treated neurons) of translation sites (# puromycin foci) and protein production (mean puro intensity). Graphs represent each scored value per distance from 7 independent experiments ($n = 7$). $p < 0.05$ indicate a significant correlation. ****$p < 0.0001$; significant differences between slopes. **(I)** Box and whisker graphs representing the total puromycin foci in βIII tubulin- and puromycin-positive neurites within the range of 50 to 150 μm [Neurite (distal)] and in the soma (soma; 10–20 μm) following visual inspection of raw images (raw (manual); workflow A, wA) or assisted quantification in binarized images (converted (assisted); workflow B, wB). Data represent the average value of 5–10 sampled cells per condition shown as individual data points, and the mean and median of 7 independent experiments ($n = 7$). *$p < 0.05$; n.s, no significant; two-tailed *t*-test.

images enhances the effect of $A\beta_{1-42}$ oligomers on discrete puromycin puncta in distal neurites.

Image Processing Reveals an Increase in Translation Foci in Axons in Response to $A\beta_{1-42}$ Oligomers

The first evidence of Aβ oligomers regulating local translation in neurons was reported in axons (Baleriola et al., 2014). Thus, we next tried our assisted quantification method in neurites positive for the axonal protein Tau. Additionally, after treatment with DMSO or Aβ oligomers for 24 h, we fed the cells with puromycin for 5, 10, or 30 min. Shorter puromycin pulses were tested to decrease the chances of protein diffusion from the actual translation site. We additionally sought to test whether the rate of puromycin incorporation in axons, unlike in all βIII tubulin-positive neurites, allowed us to detect increased translation in response to Aβ oligomers with pulses as short as 5 min. 5- and 10-min puromycin treatments have been successfully used to detect localized translation in neurites in other experimental setups (Graber et al., 2013; Walker et al., 2018; Rangaraju et al., 2019).

We first analyzed the distribution pattern of puromycin intensity along Tau-positive neurites. The longest puromycin-, Tau-positive neurite was selected from randomly sampled cells imaged with identical settings. Neurites from raw images (exemplified as heatmaps in **Figure 4A**) were straighten and divided into 10 μm bins. Puromycin intensity was measured in 15 bins covering a distance of 150 μm from the edge of the soma (**Figure 4B**). No changes in newly synthesized proteins were observed between control and Aβ-treated cells when neurons were exposed to puromycin for 5 or 10 min. However, a significantly distinct pattern in protein production induced by Aβ oligomers was detected in Tau-positive neurites following a 30-min treatment with puromycin (**Figure 4B**). Focusing on distal sites of the neurite (beyond 30 μm from the soma in these sets of experiments) we observed a significant accumulation of newly synthesized proteins after 30 min of puromycin treatment compared to shorter exposures in both DMSO- and Aβ-treated cells. A significant increase in puromycin intensity in Aβ-treated neurites compared to controls was also detected with the longest puromycin exposure (**Figure 4C**). These results, similar to the ones obtained in βIII tubulin-positive neurites, confirm that $A\beta_{1-42}$ oligomers induce *de novo* synthesis of axonal proteins as previously reported (Baleriola et al., 2014; Walker et al., 2018). We then quantified the number of discrete puromycin foci in binarized images. Images were convolved with the default normalized kernel in FIJI/ImageJ and processed like βIII tubulin neurites as described before (**Figure 4D**). Translation foci were scored with the particle analyzer in 15 bins covering a distance of 150 μm from the edge of the cell body. Again, a distinct pattern of translation was observed between DMSO- and Aβ-treated neurites only when cells were fed with puromycin for 30 min (**Figure 4E**). Similarly, despite detecting a significant accumulation of discrete puromycin foci in both control and Aβ-treated cells after 30 min of puromycin exposure compared to shorter pulses, these were significantly higher when Aβ oligomers were added to the cultures (**Figure 4F**).

To determine if our assisted scoring method correlated better than manual quantification with the unbiased measurements of fluorescence intensity also in Tau-positive neurites, two independent observers quantified the number of puromycin-positive puncta along neurites by visual inspection of raw images (**Figures 4G–J**). Both observers reported a significantly distinct distribution of discrete foci in DMSO- and Aβ-treated samples when scores were performed in 10 μm bins (**Figures 4G,I**). However, when focusing on distal sites of the neurites (> 30 μm from the soma) disregarding the bin position, none of them detected changes between controls and Aβ treatments (**Figures 4H,J**), in line with previous results (**Figure 3I**). Data retrieved from observer 1 revealed a low yet significant correlation between scores obtained in binarized images and those obtained in raw images in both control and Aβ-treated neurons, whereas the correlation between both scoring methods was only significant upon Aβ treatment based on results from observer 2 (**Figure 4K**). We then compared data obtained from binarized images and the averaged data retrieved from observers 1 and 2 with the intensity values. We found no significant correlation between the fluorescent intensity at each

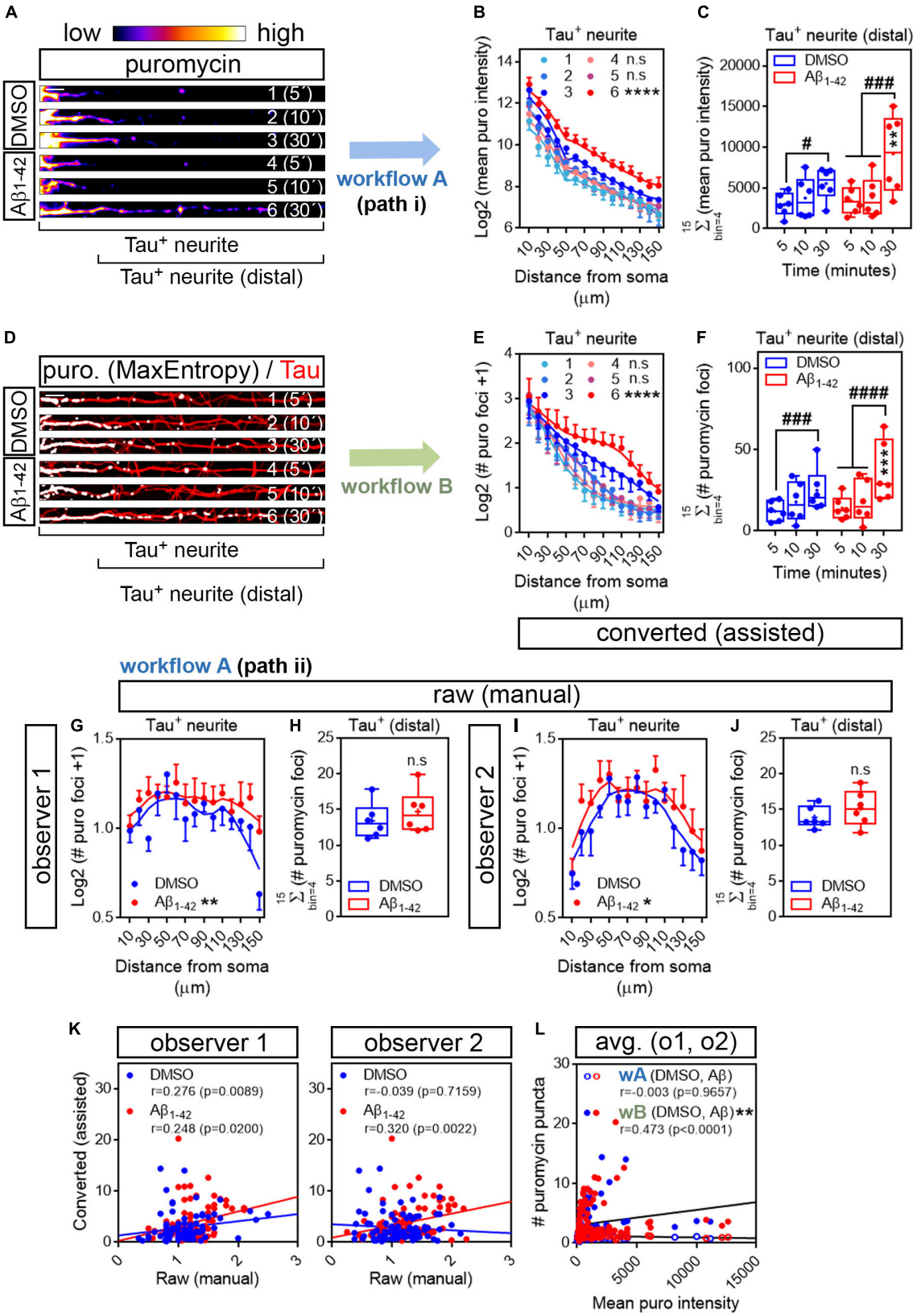

FIGURE 4 | Continued

FIGURE 4 | $A\beta_{1-42}$ oligomers increase translation sites in Tau-positive neurites. **(A)** Rat hippocampal neurons were grown for 9 DIV and treated with DMSO or with $A\beta_{1-42}$ oligomers for 24 h. Cells were fed with puromycin for 5, 10 or 30 mins, fixed and immunostained with an anti-puromycin antibody to measure protein synthesis (heatmaps) and counterstained with an anti-Tau antibody (not shown). The longest Tau-and puromycin-positive neurite was selected with a segmented line and straighten. 1, 2, and 3, DMSO-treated cells exposed to puromycin for 5, 10, and 30 mins, respectively; 4, 5 and 6, Aβ-treated cells exposed to puromycin for 5, 10, and 30 mins, respectively. Scale bar, 10 μm. **(B)** Puromycin intensity was measured in DMSO- and Aβ-treated neurons in 15 bins covering a distance of 150 μm from the edge of the soma (Tau^+ neurite) following workflow Ai in raw images. The graph shows the average intensity of puromycin per condition represented as Log2 (mean puro intensity) vs. distance ± SEM measured in 6 independent experiments ($n = 6$). 1, 2, and 3, DMSO-treated cells exposed to puromycin for 5, 10, and 30 mins respectively; 4, 5, and 6, Aβ-treated cells exposed to puromycin for 5, 10, and 30 mins, respectively. $^{****}p < 0.0001$, DMSO vs. Aβ, 30 mins puromycin; two-way ANOVA followed by Tukey's multiple comparison test. **(C)** Box and whisker graphs representing the total fluorescent intensity of the puromycin staining in Tau-positive neurites within the range of 30 to 150 μm [Tau^+ neurite (distal) as exemplified in **(A)**]. Data represent the average value of 10–20 sampled cells per condition shown as individual data points, and the mean and median of 6 independent experiments ($n = 6$). $^{\#}p < 0.05$ 5 vs. 30 mins puromycin in DMSO-treated cells; $^{\#\#\#}p < 0.001$ 5 vs. 30 mins and 10 vs. 30 mins in Aβ-treated neurons; $^{**}p < 0.01$ DMSO vs. Aβ, 30 mins puromycin; two-way ANOVA followed by Tukey's multiple comparison test. **(D)** The longest puromycin- and Tau-positive neurite was selected with a segmented line and straighten, smoothen and binarized with the MaxEntropy mask (MaxEntropy). Counterstain with the anti-Tau antibody is shown (red). 1, 2, and 3, DMSO-treated cells exposed to puromycin for 5, 10, and 30 mins, respectively; 4, 5 and 6, Aβ-treated cells exposed to puromycin for 5, 10, and 30 mins, respectively. Scale bar, 10 μm. **(E)** Puromycin-positive discrete foci were scored with the particle analyzer in 15 bins covering a distance of 150 μm from the edge of the soma (Tau^+ neurite) as explained in workflow B. The graph shows the average translation events per condition represented as Log2 (# puromycin foci + 1) vs. distance ± SEM measured in 6 independent experiments ($n = 6$). 1, 2, and 3, DMSO-treated cells exposed to puromycin for 5, 10, and 30 mins, respectively; 4, 5 and 6, Aβ-treated cells exposed to puromycin for 5, 10, and 30 mins, respectively. $^{****}p < 0.0001$ DMSO vs. Aβ, 30 mins puromycin; two-way ANOVA followed by Tukey's multiple comparison test. **(F)** Box and whisker graphs representing the total number of translation events scored in Tau-positive neurites within the range of 30 to 150 μm (Tau^+ neurite (distal) as exemplified in **(D)**). Data represent the average value of 10–20 sampled cells per condition shown as individual data points, and the mean and median of 6 independent experiments ($n = 6$). $^{\#\#\#}p < 0.001$ 5 vs. 30 mins puromycin in DMSO-treated cells; $^{\#\#\#\#}p < 0.0001$ 5 vs. 30 mins and 10 vs. 30 mins in Aβ-treated neurons; $^{***}p < 0.001$ DMSO vs. Aβ, 30 mins puromycin; two-way ANOVA followed by Tukey's multiple comparison test. **(G)** Discrete puromycin puncta scored by observer 1 in DMSO- and Aβ-treated neurons in 15 bins covering a distance of 150 μm from the edge of the soma (Tau^+ neurite) and in **(H)** distal sites of Tau-positive neurites disregarding the bin position [Tau^+ (distal)]. **(I)** Discrete puromycin puncta scored by observer 2 in DMSO- and Aβ-treated neurons in 15 bins covering a distance of 150 μm from the edge of the soma (Tau^+ neurite) and in **(J)** distal sites of Tau-positive neurites disregarding the bin position [Tau^+ (distal)]. All measurements were performed by visual inspection in raw images according to workflow Aii. Graphs in **(G)** and **(I)** show the average number of translation events per condition represented as Log2 (# puro foci + 1) vs. distance ± SEM measured following a 30-min puromycin pulse in 6 independent experiments ($n = 6$). $^{*}p < 0.05$; $^{**}p < 0.01$; two-way ANOVA followed by Tukey's multiple comparison test. Box and whisker graphs in **(H,J)** show the total number of translation events scored in Tau-positive neurites within the range of 30 to 150 μm [Tau^+ (distal)]. Data represent the average value of 10–20 sampled cells per condition shown as individual data points, and the mean and median of 6 independent experiments ($n = 6$). n.s, no significant; two-tailed *t*-tests. **(K)** Spearman correlation between quantifications in raw (manual) and in binarized (assisted) images. Graphs show values scored in raw (manual) images by observer 1 and observer 2 in DMSO- (blue) and Aβ-treated neurons (red) cultured in 6 independent experiments ($n = 6$). $p < 0.05$ indicate a significant correlation. **(L)** Spearman correlation between non-assisted [wA (DMSO, Aβ)] or assisted quantification [wB (DMSO, Aβ)] of translation sites (# puromycin foci) and protein production (mean puro intensity). Graphs represent the non-assisted counts per distance as the average score obtained by observers 1 and 2. Data correspond to 6 independent experiments ($n = 6$). $p < 0.05$ indicate a significant correlation. $^{**}p < 0.01$; significant differences between slopes.

neuritic position and the number puromycin foci scored by visual inspection (wA, **Figure 4L**). Conversely, a significant moderate positive correlation was observed between parameters when translation sites were counted in binarized images with the particle analyzer (wB, **Figure 4L**). Furthermore, when fitting the translation sites at each distance to a regression line, a significant increase in the slope was observed when data were obtained from binarized images, suggesting increased similarities between the number of puromycin foci and the puromycin intensity when using the assisted quantification method (**Figure 4L**). These results not only confirm that scoring puromycin-positive sites in neurites in binarized images by assisted means show a better fit with the unbiased measurement of raw puromycin intensity, but also reveal an effect of Aβ oligomers on discrete translation sites in neurites that was previously unreported.

Object-Based Colocalization Analyses Confirm That Peripheral Translation Sites in Axons Arise From Localized RNAs

As mentioned previously, discrete puromycin-positive puncta in distal neurites likely reflect sites of local translation. Nevertheless, we sought to determine if in our system what we had reported as neuritic translation sites did in fact colocalize with neuritic RNAs. Samples processed for puromycin detection in Tau-positive neurites were incubated for 20 min with 500 nM SYTO RNASelect, a fluorescent dye that selectively binds RNA (Savas et al., 2010). To verify that SYTO could be successfully used in our system to label neuritic RNA we compared the fluorescent intensity of the dye within Tau-positive neurites to background fluorescent levels in cells that had not been incubated with SYTO. Additionally, some fixed cells were digested with 50 μg/ml DNAse or RNAse prior to labeling. Neurites from SYTO-positive cells showed significantly higher levels of fluorescence than those not incubated with the dye (Compare dashed line with -SYTO in graph and neurites 1 and 2 in **Figure 5A**). More importantly, levels of SYTO were similar in positive neurites incubated in the presence or absence of DNAse (Compare dashed line with + SYTO + DNAse in graph and neurites 2 and 3 in **Figure 5A**), whereas incubation with RNAse moderately yet significantly reduced the fluorescence intensity (Compare dashed line with + SYTO + RNAse in graph and neurites 2 and 4 in **Figure 5A**). These results indicate that indeed neuritic RNAs can be labeled with SYTO RNASelect dye.

We then analyzed the distribution of RNA granules, measured as SYTO-stained foci, along Tau-positive neurites. For this purpose, raw images stained for SYTO were processed following the exact same protocol as for puromycin labeling (**Figure 1**;

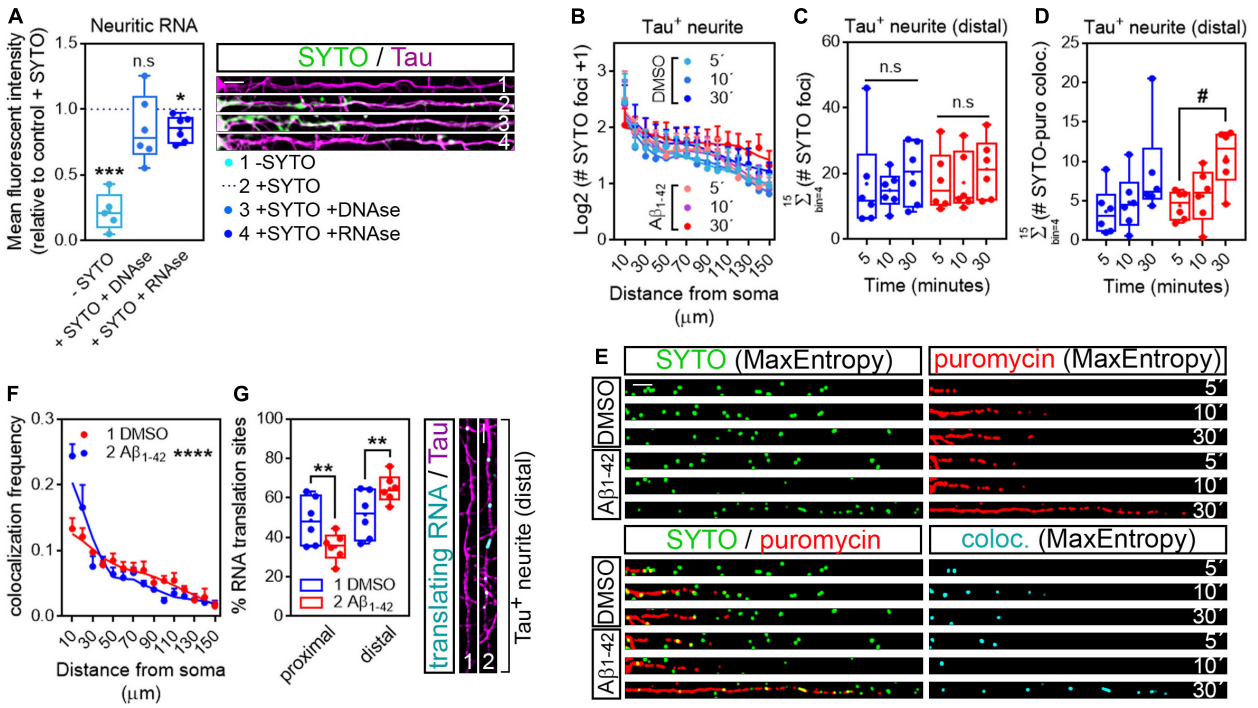

FIGURE 5 | Puromycin-positive foci in axons are a result of local protein synthesis. **(A)** Cells grown for 9 DIV and treated with DMSO for 24 h. Cells immunostained with an anti-Tau antibody (magenta) were incubated with SYTO RNASelect green fluorescent dye to label endogenous RNA (green). Total green fluorescence intensity was measured in neurites covering a distance of 150 μm from the edge of the soma (2, + SYTO). As negative control, green fluorescence was measured in cells that had not been incubated with SYTO (1, -SYTO). To determine if SYTO selectively labeled RNA, some fixed cells were digested with DNAse (3, + SYTO + DNAse) or with RNAse (4, + SYTO + RNAse). Box and whisker graphs represent the average relative fluorescence intensity of 10 neurites per condition, shown as individual data points, and the mean and median of 5 (n = 5, -SYTO negative samples compared to their corresponding + SYTO controls) or 6 (n = 6, + SYTO + DNAse and + SYTO + RNAse compared to their corresponding + SYTO controls) independent experiments. ***$p < 0.001$; *$p < 0.05$; n.s, not significant; two-tailed t-tests. Scale bar, 10 μm. **(B)** SYTO-positive staining (as represented in green in **(E)**) from randomly selected cells was filtered with the convolver, brightness and contrast were adjusted. Images were converted to 8-bit and binarized with the MaxEntropy mask. The longest Tau-positive neurite was selected with a segmented line and straighten, smoothen and binarized with the MaxEntropy mask (MaxEntropy). SYTO-positive discrete puncta were scored with the particle analyzer in 15 bins covering a distance of 150 μm from the edge of the soma. The graph shows the average number on puncta represented as Log2 (SYTO foci + 1) vs. distance ± SEM measured in 6 independent experiments (n = 6). No statistical differences were detected between DMSO- and Aβ-treated cells incubated with puromycin for 5, 10, or 30 mins. **(C)** Box and whisker graphs show the total number of RNA granules in distal sites of Tau-positive neurites [Σ (# SYTO foci)] from DMSO- and Aβ-treated cells incubated with puromycin for 5, 10, or 30 mins. Data represent the average value of 10 sampled cells per condition plotted as individual data points, and the mean and median of 6 independent experiments (n = 6). n.s, no significant; two-way ANOVA followed by Tukey's multiple comparison test. **(D)** Parallel to processing SYTO-labeled images, puromycin staining was filtered with the convolver, brightness and contrast were adjusted. Images were converted to 8-bit and binarized with the MaxEntropy mask. Same Tau-positive neurites selected for SYTO quantification (green channel) were selected in the red channel (puromycin staining in **(E)**), straighten, smoothen and binarized with the MaxEntropy mask. Co-localized objects were obtained with the AND function in the image calculator (cyan in **(E)**) and scored in distal sites of Tau-positive neurites with the particle analyzer. Box and whisker graphs show the total RNA-protein colocalized puncta in DMSO- and Aβ-treated cells incubated with puromycin for 5, 10, or 30 mins [Σ (# SYTO-puro coloc.)]. Data represent the average value of 10 sampled neurites per condition plotted as individual data points, and the mean and median of 6 independent experiments (n = 6). #$p < 0.05$ 5 vs. 30 min puromycin in Aβ-treated cells; two-way ANOVA followed by Tukey's multiple comparison test. **(E)** Micrographs from straighten, binarized neurites stained with SYTO RNASelect green fluorescent dye to label RNA (green), with an anti-puromycin antibody to label protein (red) and the resulting images when merging both channels (green, red, and yellow) and when combining both with the AND function in the image calculator (cyan). Cells treated with puromycin for 5, 10, or 30 mins are shown. Scale bar, 10 μm. **(F)** The graph represents the frequency distribution of SYTO- and puromycin-positive objects (colocalization frequency) in DMSO- and Aβ-treated neurites following 30-min puromycin exposure. Colocalized objects were measured with the particle analyzer in 15 bins covering a distance of 150 μm from the edge of the cell body. ****$p < 0.0001$ (interaction); two-way ANOVA. **(G)** Box and whisker graph representing the proportion of colocalized objects (% RNA translation sites) in proximal (0–30 μm) and distal (last 120 μm) sites of Tau-positive neurites. Data represent the average value of 10 sampled cells per condition shown as individual data points, and the mean and median of 6 independent experiments (n = 6). **$p < 0.01$; two-tailed t-test. Micrographs show colocalized objects (translating RNAs, cyan) detected within the last 120 μm (distal) of Tau positive neurites (magenta). Scale bar, 10 μm.

workflow B): images were convolved with the default normalized kernel in FIJI/ImageJ, minimum and maximum intensity values were adjusted, 16-bit images were converted to 8-bit and binarized using the MaxEntropy mask. Neurites were then selected with a segmented line, straighten, smoothen and binarized again with the MaxEntropy function (green, **Figure 5E**). The number of RNA granules was scored in 15 bins covering a distance of 150 μm from the edge of the soma and no significant differences were observed between experimental conditions, regardless of whether neurons were fed

with puromycin for 5, 10, or 30 min (**Figure 5B**). Similarly, no significant changes were detected in distal sites (> 30 μm from the soma in these sets of experiments) between DMSO- and Aβ-treated neurites (**Figure 5C**). Thus, Aβ treatment does not affect RNA recruitment to neurites. In these experiments, green and red channels corresponding to RNA (SYTO, **Figure 5E**) and protein (puromycin, **Figure 5E**) were binarized in parallel and colocalization between objects in both channels was calculated using the AND function in the FIJI/ImageJ image calculator. The resulting puncta (cyan, **Figure 5E**) were scored in 10 μm bins covering a distance of 150 μm from the edge of the cell body. No significant differences between DMSO- and Aβ-treated cells were observed in the distribution of colocalized puncta along neurites (data not shown). Given the high variability, especially in control cells, we did not detect differences between DMSO and Aβ treatments when focusing on distal sites of Tau-positive neurites either. However, we did observe an accumulation of co-localized foci in Aβ-treated cells that was not detected in controls when neurons were exposed to puromycin for 30 min compared to the 5-min treatment (**Figure 5D**). We therefore focused on the 30-min puromycin treatment and analyzed the frequency distribution of translating RNAs, measured as the proportion of colocalized puncta. Interestingly, from all translating RNAs detected, half of them were found within the first 30 μm proximal to the soma in control cells, whereas this proportion was significantly reduced in Aβ-treated cells and consequently the percentage of peripheral translating RNAs increased (**Figures 5F,G**). Altogether these results show that Aβ oligomers increase the sites of localized translation in distal Tau-positive neurites in line with previously published reports (Baleriola et al., 2014; Li and Gotz, 2017; Walker et al., 2018). Thus, the combination of RNA and protein staining techniques followed by image processing and binarization, and object-based colocalization can be successfully used to detect sites of local RNA translation in neurons which might be important to unravel the extent of local changes in early stages of AD and other neurological diseases.

DISCUSSION

Highly polarized cells like neurons heavily rely on the asymmetric distribution of their proteome for their functionality. It was classically thought that proteins that support dendritic and axonal functions are synthesized in the soma and then transported to their target destination at peripheral sites of the neuron. This soma-centric view of protein synthesis has slowly changed over the last two decades and it is now accepted that neurites contain mRNAs and components of the translation machinery and are thus able to produce proteins locally. Local protein synthesis enables neurites (both dendrites and axons) to change their proteome in an acute manner in order to adapt to fast environmental changes. Since the first studies that unambiguously demonstrated the existence of local translation in neurons (Koenig, 1967; Giuditta et al., 1968; Steward and Levy, 1982; Torre and Steward, 1992; Feig and Lipton, 1993) most work in the field has focused on understanding the role of locally produced proteins in brain physiology. For example, a subset of mRNAs translated in dendrites, which include CamK2a, Calmodulin or Bassoon, is involved in synaptic plasticity (reviewed in Holt et al., 2019). Intra-axonal synthesis of β-actin (Leung et al., 2006), RhoA (Wu et al., 2005), or Par3 (Hengst et al., 2009) is important in growth cone behavior and axon elongation during nervous system development. Proteins involved in mitochondrial function such as LaminB2 (Yoon et al., 2012) or COXIV (Aschrafi et al., 2010) are locally synthesized in axons and contribute to their maintenance in post-developmental stages. However much less is known on the role of local protein synthesis in nervous system pathologies, especially those of the CNS.

Alzheimer's disease (AD), like other neurodegenerative diseases, is characterized by synaptic dysfunction during early stages (Palop and Mucke, 2010). Understanding dynamic early changes in the local proteome (axonal, dendritic or synaptic) is in our view crucial to understand basic pathological mechanisms underlying AD and likely other neurological diseases. Recent work has shown that regulation of intra-axonal protein synthesis induced by $A\beta_{1-42}$ oligomers, whose accumulation is central to AD, contributes to neurodegeneration (Baleriola et al., 2014). These findings support a model in which retrograde transport of locally produced proteins leads to pathological, transcriptional changes in the neuronal soma. More recently, a link between intra-dendritic translation, and Tau mislocalization and hyperphosphorylation has been found (Kobayashi et al., 2017; Li and Gotz, 2017). Thus, dysregulation of the local translatome in neurons might play a more relevant role in AD than previously acknowledged. It is therefore important to know the extent and location of newly synthesized proteins in order to understand early changes in the AD brain.

Despite local translation is finally being accepted by the scientific community, the accurate measurement of this phenomenon is still challenging partly due to the limited amount of proteins that are locally produced, especially in adult axons (Rangaraju et al., 2017). There are other experimental challenges that will be not be discussed herein since the technicalities are beyond the scope of this manuscript. Our own results show that new-synthesized neuritic proteins measured at distal positions (100–150 μm from the cell nucleus) can be ∼20 to 30 times less abundant than those measured in the soma in a 30-min time frame (**Figure 2**). Thus, local translation events can be easily overlooked when visualizing *in situ* protein production under the microscope. FUNCAT (Dieterich et al., 2010), and SUnSET (Schmidt et al., 2009) are commonly used techniques in the field of local translation. Both are based on the labeling of newly synthesized proteins, with non-canonical amino acids in the case of FUNCAT or a tRNA analog in the case of SUnSET. In both cases the non-canonical molecules can be fluorescently tagged. Yet when these methods have proven very helpful to analyze the amount of newly synthesized dendritic (Dieterich et al., 2010) and axonal (Wong et al., 2017; Walker et al., 2018) proteins measured as fluorescent intensity in labeled cells, discrete foci of newly produced proteins can come unnoticed unless enhanced.

Some variations of the aforementioned techniques such as Puro-PLA or FUNCAT-PLA have been used to accurately

measure discrete translation sites of specific proteins along neurites (Tom Dieck et al., 2015). Both proximity ligation assays (PLA) are based on the spatial coincidence of two antibodies, one that recognizes the recently synthesized polypeptide chain (anti-puromycin in the case of Puro-PLA; anti-biotin for FUNCAT-PLA) and another one that recognizes a specific protein of interest. However, neither PLA approach is useful to analyze all translation foci. Other modifications of SUnSET have been recently used to evaluate overall discrete intra-neuritic and intra-dendritic translation events. For example, co-incubation of neurons with both puromycin and the translation inhibitor emetine prior to fixation prevents the puromycylated polypeptide chain release from the ribosomes. This approach is known as ribopuromycilation (RPM) and it allows the visualization of active polyribosomes in the neuronal soma and along neurites (Graber et al., 2013). Additionally, in puromycin-labeled fixed cells, proximity ligation assay (Puro-PLA) employing a single antibody against puromycin has been used to accurately identify discrete local translation sites in dendrites (Rangaraju et al., 2019). Here we describe a strategy to enhance puromycin hotspots in neurites following SUnSET, based solely on image processing and the assisted quantification of the resulting objects. Our technique does not require the incubation of the cells with any translation inhibitor besides puromycin, and it avoids the processing of the samples for proximity ligation assay, which can be pricy and time consuming.

We first performed edge detection to find discontinuities in our puromycin labeling that could result from a punctate staining arising from discrete positive foci. Instead of using the Find Edges command in FIJI/ImageJ which applies a Sobel edge detector, we used the default 5 × 5 kernel in the convolver which is a Laplacian edge detector instead. Laplacian operators are very accurate in finding edges in an image but also very sensitive to background noise (Bannister and Larkman, 1995a). We therefore adjusted the minimum and maximum intensities of our micrographs after applying the filter in order to eliminate highlighted pixels outside the area established by the neuronal/axonal markers βIII tubulin and Tau (**Figure 1**; workflow B). We additionally compared the processing workflow between puromycin-positive and puromycin-negative cells and determined that despite possible noise enhancement, positive puncta could be significantly detected over background (**Figure 3F**, right graph). Image processing with the Laplacian operator highlighted events in the periphery of neurons that could be selected and binarized with the MaxEntropy mask (**Figures 1B**, **3C**, **4D**, **5E** and **Supplementary Figure S1B**). Binarization in unprocessed images failed to detect discrete puncta in neurites to the same extent as when images were processed (**Supplementary Figure S1**).

To determine if our processing method worked in highlighting local events, we evaluated the effect of $A\beta_{1-42}$ oligomers on hippocampal neurites. Aβ oligomers are known to increase puromycin intensity when applied locally to axons, which reflects changes in local protein synthesis (Walker et al., 2018). In our case, we observed similar results in neurites following bath application of hippocampal neurons with Aβ (**Figure 2**): the effect elicited by Aβ was visible beyond the canonical ER domain and did not affect the cell body (**Figures 2C,G–J**). These results are compatible with changes in local translation but they do not address whether actual local sites of protein synthesis are affected by Aβ oligomers. Discrete puncta in distal neuritic sites likely reflect foci of localized translation (Graber et al., 2013; Rangaraju et al., 2019). We quantified discrete puromycin-positive foci in distal neuritic sites in response to $A\beta_{1-42}$ with the particle analyzer after image processing with the convolver (assisted quantification). We observed (1) an enhancement of discrete puromycin staining in both DMSO- and Aβ-treated neurites compared to visual inspection of raw puromycin staining (**Figures 3B,C**), (2) an enhancement of the effect of Aβ on newly synthesized neuritic proteins compared to controls (**Figures 3B,C,I**), and (3) a better correlation between the unbiased measurement of puromycin intensity and the number of discrete puromycin-positive sites in processed images (**Figure 3H**). Altogether these results indicate that binarizing images from puromycin-positive cells after applying a Laplacian edge detector allows the assisted quantification of neuritic translation sites yielding results that resemble those obtained from an unbiased measurement of raw puromycin intensity (**Figure 3H**). Additionally, our results unravel a previously unreported effect of Aβ oligomers on discrete translation events in neurites (**Figures 3E,I**).

Our first approach was performed in βIII tubulin-positive neurites which correspond to both dendrites and axons. We sought to increase the changes of detecting discrete translation sites since dendrites have been historically reported to have a higher translation capacity than axons (Rangaraju et al., 2017) but because changes in local neuronal translation upon Aβ treatment were first described in axons (Baleriola et al., 2014), we applied the same processing workflow to neurites stained with the axonal marker Tau. Results were very similar to those obtained for βIII tubulin-positive neurites when cells were fed with puromycin for 30 min (**Figure 4**). Shorter exposures to puromycin were also performed in order to minimize the possible detection of newly synthesized proteins diffused from the soma. Puromycin pulses as short as 10–15 min have been successfully used to detect changes in intra-axonal protein synthesis upon acute exposure of axons to Aβ oligomers (Walker et al., 2018). However, we did not observe changes between DMSO- and Aβ-treated cells possibly due to the slow pace of the translation machinery after a 24-h treatment.

In light of our results we addressed whether distal puromycin-positive events in neurites arose from localized RNAs to determine if we were actually measuring local protein synthesis. We applied the processing protocol followed for puromycin staining to SYTO-positive neurites. SYTO RNASelect green fluorescent dye selectively binds neuritic RNA (**Figure 5A**). We observed that Aβ oligomers did not change the distribution of RNA granules along neurites (**Figures 5B,E**) nor their amount in distal sites (**Figure 5C**). These results are compatible with other experiments performed in our laboratory aimed

at labeling neuritic RNAs with alternative techniques (data not shown). Taking advantage of the fact that SYTO-labeled cells were also labeled with puromycin, after binarizing the images corresponding to both stains we applied the AND function in the image calculator which essentially retrieves the colocalization between objects. In our system colocalized objects (cyan, **Figure 5E**) represent sites of actively translating RNAs. We particularly focused on colocalized objects resulting from 30-min puromycin pulses, which were higher than for shorter puromycin exposures (**Figure 5D**). Interestingly, $A\beta_{1-42}$ increased the proportion of RNA translation in distal sites of Tau-positive neurites, beyond the ER domain. Thus, the combination of RNA and protein staining techniques followed by image processing and binarization, and object-based colocalization can be successfully used to detect sites of local RNA translation in neurons.

Other edge detectors, Laplacian operators distinct to 5×5 matrices or other background subtraction methods can be used depending on the sample requirements and the researcher's criteria. However, the image processing approach described herein has proven very useful to detect discrete events with low pixel intensity, which is the expected characteristic of neuritic local translation sites.

Altogether, this study provides a simple method of quantifying local RNA translation foci using object-recognition and object-based colocalization analyses which allows a better understanding the effect of $A\beta_{1-42}$ in neurites.

DATA AVAILABILITY STATEMENT

The datasets generated for this study are available on request to the corresponding author.

ETHICS STATEMENT

The animal study was reviewed and approved by Ethics Committee for Animal Care and Use in Research (CEEA) of the University of the Basque Country (UPV/EHU).

AUTHOR CONTRIBUTIONS

JB conceived the project and designed the experiments. MG, MB-U, AB, JI, and JB performed experiments. MG, MB-U, and JB performed data analysis and wrote the manuscript.

FUNDING

JB was supported by two grants from the Spanish Ministry of Science, Innovation and Universities (RYC-2016-19837 start-up funds and SAF2016-76347-R) and start-up funds from the Basque Foundation for Science (IKERBASQUE). MG is a predoctoral fellow funded by the Basque Government. MB-U is a predoctoral fellow funded by the University of the Basque Country (UPV/EHU). AB received funding from the Portuguese Foundation for Science and Technology (FCT) in the context of the FCT funded University of Minho M.D./Ph.D. Program (SFRH/BD/52322/2013).

ACKNOWLEDGMENTS

We thank member of the Neurobiology Lab (Achucarro Basque Center for Neuroscience) for sharing the Aβ peptides with us.

SUPPLEMENTARY MATERIAL

The Supplementary Material for this article can be found online at: https://www.frontiersin.org/articles/10.3389/fnins.2020.00547/full#supplementary-material

FIGURE S1 | Workflows for image processing with or without applying the default convolution kernel (Laplacian filter). Images show the same cells used as examples for the workflow in **Figure 1**. **(B)** Represents the same step by step processing method described **Figure 1B**. **(B^{I})** Corresponds to the same workflow as in **Figure 1B** excluding **step 1** which corresponds to the application of the Laplacian filter to enhance the edges. Both workflows converge in graphs comparing both methods (green line, filter application; red line, no filter) in two experimental conditions (condition 1, blue; condition 2, red). Graphs represent Log2(#puromycin foci +1) vs. distance. Scale bars, 50 μm in whole-cell micrographs and 10 μm in straighten neurites.

REFERENCES

Aschrafi, A., Natera-Naranjo, O., Gioio, A. E., and Kaplan, B. B. (2010). Regulation of axonal trafficking of cytochrome c oxidase IV mRNA. *Mol. Cell Neurosci.* 43, 422–430. doi: 10.1016/j.mcn.2010.01.009

Baleriola, J., Walker, C. A., Jean, Y. Y., Crary, J. F., Troy, C. M., Nagy, P. L., et al. (2014). Axonally synthesized ATF4 transmits a neurodegenerative signal across brain regions. *Cell* 158, 1159–1172. doi: 10.1016/j.cell.2014.07.001

Banker, G., and Goslin, K. (1998). *Culturing Nerve Cells*, 2nd Edn. Cambridge: MIT Press.

Bannister, N. J., and Larkman, A. U. (1995a). Dendritic morphology of CA1 pyramidal neurones from the rat hippocampus: I. Branching patterns. *J. Comp. Neurol.* 360, 150–160. doi: 10.1002/cne.903600111

Bannister, N. J., and Larkman, A. U. (1995b). Dendritic morphology of CA1 pyramidal neurones from the rat hippocampus: II. Spine distributions. *J. Comp. Neurol.* 360, 161–171. doi: 10.1002/cne.903600112

Bolton, J. S. (1901). The nervous system and its constituent neurones, designed for the use of practitioners of medicine and of students of medicine and psychology. *Edinb. Med. J.* 10:4.

Dieterich, D. C., Hodas, J. J., Gouzer, G., Shadrin, I. Y., Ngo, J. T., Triller, A., et al. (2010). In situ visualization and dynamics of newly synthesized proteins in rat hippocampal neurons. *Nat. Neurosci.* 13, 897–905. doi: 10.1038/nn.2580

Feig, S., and Lipton, P. (1993). Pairing the cholinergic agonist carbachol with patterned Schaffer collateral stimulation initiates protein synthesis in hippocampal CA1 pyramidal cell dendrites via a muscarinic, NMDA-dependent mechanism. *J. Neurosci.* 13, 1010–1021. doi: 10.1523/JNEUROSCI.13-03-01010.1993

Giuditta, A., Dettbarn, W. D., and Brzin, M. (1968). Protein synthesis in the isolated giant axon of the squid. *Proc. Natl. Acad. Sci. U.S.A.* 59, 1284–1287. doi: 10.1073/pnas.59.4.1284

Graber, T. E., Hebert-Seropian, S., Khoutorsky, A., David, A., Yewdell, J. W., Lacaille, J. C., et al. (2013). Reactivation of stalled polyribosomes in synaptic

plasticity. *Proc. Natl. Acad. Sci. U.S.A.* 110, 16205–16210. doi: 10.1073/pnas.1307747110

Hafner, A. S., Donlin-Asp, P. G., Leitch, B., Herzog, E., and Schuman, E. M. (2019). Local protein synthesis is a ubiquitous feature of neuronal pre- and postsynaptic compartments. *Science* 364:6441. doi: 10.1126/science.aau3644

Hengst, U., Deglincerti, A., Kim, H. J., Jeon, N. L., and Jaffrey, S. R. (2009). Axonal elongation triggered by stimulus-induced local translation of a polarity complex protein. *Nat. Cell Biol.* 11, 1024–1030. doi: 10.1038/ncb1916

Holt, C. E., Martin, K. C., and Schuman, E. M. (2019). Local translation in neurons: visualization and function. *Nat. Struct. Mol. Biol.* 26, 557–566. doi: 10.1038/s41594-019-0263-5

Jung, H., Gkogkas, C. G., Sonenberg, N., and Holt, C. E. (2014). Remote control of gene function by local translation. *Cell* 157, 26–40. doi: 10.1016/j.cell.2014.03.005

Jung, H., Yoon, B. C., and Holt, C. E. (2012). Axonal mRNA localization and local protein synthesis in nervous system assembly, maintenance and repair. *Nat. Rev. Neurosci.* 13, 308–324. doi: 10.1038/nrn3210

Kobayashi, S., Tanaka, T., Soeda, Y., Almeida, O. F. X., and Takashima, A. (2017). Local somatodendritic translation and hyperphosphorylation of tau protein triggered by AMPA and NMDA receptor stimulation. *EBioMedicine* 20, 120–126. doi: 10.1016/j.ebiom.2017.05.012

Koenig, E. (1967). Synthetic mechanisms in the axon. IV. In vitro incorporation of [3H]precursors into axonal protein and RNA. *J. Neurochem.* 14, 437–446. doi: 10.1111/j.1471-4159.1967.tb09542.x

Leung, K. M., van Horck, F. P., Lin, A. C., Allison, R., Standart, N., and Holt, C. E. (2006). Asymmetrical beta-actin mRNA translation in growth cones mediates attractive turning to netrin-1. *Nat. Neurosci.* 9, 1247–1256. doi: 10.1038/nn1775

Li, C., and Gotz, J. (2017). Somatodendritic accumulation of Tau in Alzheimer's disease is promoted by Fyn-mediated local protein translation. *EMBO J.* 36, 3120–3138. doi: 10.15252/embj.201797724

Palop, J. J., and Mucke, L. (2010). Amyloid-beta-induced neuronal dysfunction in Alzheimer's disease: from synapses toward neural networks. *Nat. Neurosci.* 13, 812–818. doi: 10.1038/nn.2583

Quintela-Lopez, T., Ortiz-Sanz, C., Serrano-Regal, M. P., Gaminde-Blasco, A., Valero, J., Baleriola, J., et al. (2019). Abeta oligomers promote oligodendrocyte differentiation and maturation via integrin beta1 and Fyn kinase signaling. *Cell Death Dis.* 10:445. doi: 10.1038/s41419-019-1636-8

Rangaraju, V., Lauterbach, M., and Schuman, E. M. (2019). Spatially stable mitochondrial compartments fuel local translation during plasticity. *Cell* 7:e15. doi: 10.1016/j.cell.2018.12.013

Rangaraju, V., Tom Dieck, S., and Schuman, E. M. (2017). Local translation in neuronal compartments: how local is local? *EMBO Rep.* 18, 693–711. doi: 10.15252/embr.201744045

Rutkevich, L. A., and Williams, D. B. (2011). Participation of lectin chaperones and thiol oxidoreductases in protein folding within the endoplasmic reticulum. *Curr. Opin. Cell Biol.* 23, 157–166. doi: 10.1016/j.ceb.2010.10.011

Savas, J. N., Ma, B., Deinhardt, K., Culver, B. P., Restituito, S., Wu, L., et al. (2010). A role for huntington disease protein in dendritic RNA granules. *J. Biol. Chem.* 285, 13142–13153. doi: 10.1074/jbc.M110.114561

Schmidt, E. K., Clavarino, G., Ceppi, M., and Pierre, P. (2009). SUnSET, a nonradioactive method to monitor protein synthesis. *Nat. Methods* 6, 275–277. doi: 10.1038/nmeth.1314

Steward, O., and Levy, W. B. (1982). Preferential localization of polyribosomes under the base of dendritic spines in granule cells of the dentate gyrus. *J. Neurosci.* 2, 284–291. doi: 10.1523/JNEUROSCI.02-03-00284.1982

Terenzio, M., Koley, S., Samra, N., Rishal, I., Zhao, Q., Sahoo, P. K., et al. (2018). Locally translated mTOR controls axonal local translation in nerve injury. *Science* 359, 1416–1421. doi: 10.1126/science.aan1053

Tom Dieck, S., Kochen, L., Hanus, C., Heumuller, M., Bartnik, I., Nassim-Assir, B., et al. (2015). Direct visualization of newly synthesized target proteins in situ. *Nat. Methods* 12, 411–414. doi: 10.1038/nmeth.3319

Torre, E. R., and Steward, O. (1992). Demonstration of local protein synthesis within dendrites using a new cell culture system that permits the isolation of living axons and dendrites from their cell bodies. *J. Neurosci.* 12, 762–772. doi: 10.1523/JNEUROSCI.12-03-00762.1992

Walker, C. A., Randolph, L. K., Matute, C., Alberdi, E., Baleriola, J., and Hengst, U. (2018). Abeta1-42 triggers the generation of a retrograde signaling complex from sentinel mRNAs in axons. *EMBO Rep.* 19:e45435. doi: 10.15252/embr.201745435

Wong, H. H., Lin, J. Q., Strohl, F., Roque, C. G., Cioni, J. M., Cagnetta, R., et al. (2017). RNA docking and local translation regulate site-specific axon remodeling in vivo. *Neuron* 85:e858. doi: 10.1016/j.neuron.2017.07.016

Wu, K. Y., Hengst, U., Cox, L. J., Macosko, E. Z., Jeromin, A., Urquhart, E. R., et al. (2005). Local translation of RhoA regulates growth cone collapse. *Nature* 436, 1020–1024. doi: 10.1038/nature03885

Yarmolinsky, M. B., and Haba, G. L. (1959). Inhibition by puromycin of amino acid incorporation into protein. *Proc. Natl. Acad. Sci. U.S.A.* 45, 1721–1729. doi: 10.1073/pnas.45.12.1721

Yoon, B. C., Jung, H., Dwivedy, A., O'Hare, C. M., Zivraj, K. H., and Holt, C. E. (2012). Local translation of extranuclear lamin B promotes axon maintenance. *Cell* 148, 752–764. doi: 10.1016/j.cell.2011.11.064

Conflict of Interest: The authors declare that the research was conducted in the absence of any commercial or financial relationships that could be construed as a potential conflict of interest.

Copyright © 2020 Gamarra, Blanco-Urrejola, Batista, Imaz and Baleriola. This is an open-access article distributed under the terms of the Creative Commons Attribution License (CC BY). The use, distribution or reproduction in other forums is permitted, provided the original author(s) and the copyright owner(s) are credited and that the original publication in this journal is cited, in accordance with accepted academic practice. No use, distribution or reproduction is permitted which does not comply with these terms.

frontiers in Neuroscience

CORRECTION
published: 19 November 2021
doi: 10.3389/fnins.2021.792975

Corrigendum: Object-Based Analyses in FIJI/ImageJ to Measure Local RNA Translation Sites in Neurites in Response to Aβ1-42 Oligomers

María Gamarra[1,2], *Maite Blanco-Urrejola*[1,2,3], *Andreia F. R. Batista*[1,4,5], *Josune Imaz*[2] *and Jimena Baleriola*[1,3,6*]

[1] Achucarro Basque Center for Neuroscience, Leioa, Spain, [2] Department of Neurosciences, Faculty of Medicine and Nursing, University of the Basque Country, Bilbao, Spain, [3] Department of Cell Biology and Histology, Faculty of Medicine and Nursing, University of the Basque Country, Leioa, Spain, [4] Life and Health Sciences Research Institute, School of Medicine, University of Minho, Braga, Portugal, [5] ICVS/3B's, PT Associate Laboratory, Universidade Do Minho, Guimarães, Portugal, [6] IKERBASQUE Basque Foundation for Science, Bilbao, Spain

Keywords: local protein synthesis, RNA localization, neurites, fluorescence microscopy, FIJI/ImageJ analyses, colocalization analyses

OPEN ACCESS

Edited and reviewed by:
João O. Malva, University of Coimbra, Portugal

***Correspondence:**
Jimena Baleriola
jimena.baleriola@achucarro.org

Specialty section:
This article was submitted to Brain Imaging Methods, a section of the journal Frontiers in Neuroscience

Received: *11 October 2021*
Accepted: *02 November 2021*
Published: *19 November 2021*

Citation:
Gamarra M, Blanco-Urrejola M, Batista AFR, Imaz J and Baleriola J (2021) Corrigendum: Object-Based Analyses in FIJI/ImageJ to Measure Local RNA Translation Sites in Neurites in Response to Aβ1-42 Oligomers. Front. Neurosci. 15:792975. doi: 10.3389/fnins.2021.792975

A Corrigendum on

Object-Based Analyses in FIJI/ImageJ to Measure Local RNA Translation Sites in Neurites in Response to Aβ1-42 Oligomers

by Gamarra, M., Blanco-Urrejola, M., Batista, A. F. R., Imaz, J., and Baleriola, J. (2020). Front. Neurosci. 14:547. doi: 10.3389/fnins.2020.00547

In the original article, there was a mistake in **Figure 5** as published. In **Figure 5F** the blue line should correspond to the results reported from DMSO-treated cells and the red line should correspond to the results from Aβ-treated cells. The blue dot from the figure legend should therefore be labelled as "1 DMSO" and the red dot should be labelled as "2 $A\beta_{1-42}$". The corrected **Figure 5** appears below.

The authors apologize for this error and state that this does not change the scientific conclusions of the article in any way. The original article has been updated.

Publisher's Note: All claims expressed in this article are solely those of the authors and do not necessarily represent those of their affiliated organizations, or those of the publisher, the editors and the reviewers. Any product that may be evaluated in this article, or claim that may be made by its manufacturer, is not guaranteed or endorsed by the publisher.

Copyright © 2021 Gamarra, Blanco-Urrejola, Batista, Imaz and Baleriola. This is an open-access article distributed under the terms of the Creative Commons Attribution License (CC BY). The use, distribution or reproduction in other forums is permitted, provided the original author(s) and the copyright owner(s) are credited and that the original publication in this journal is cited, in accordance with accepted academic practice. No use, distribution or reproduction is permitted which does not comply with these terms.

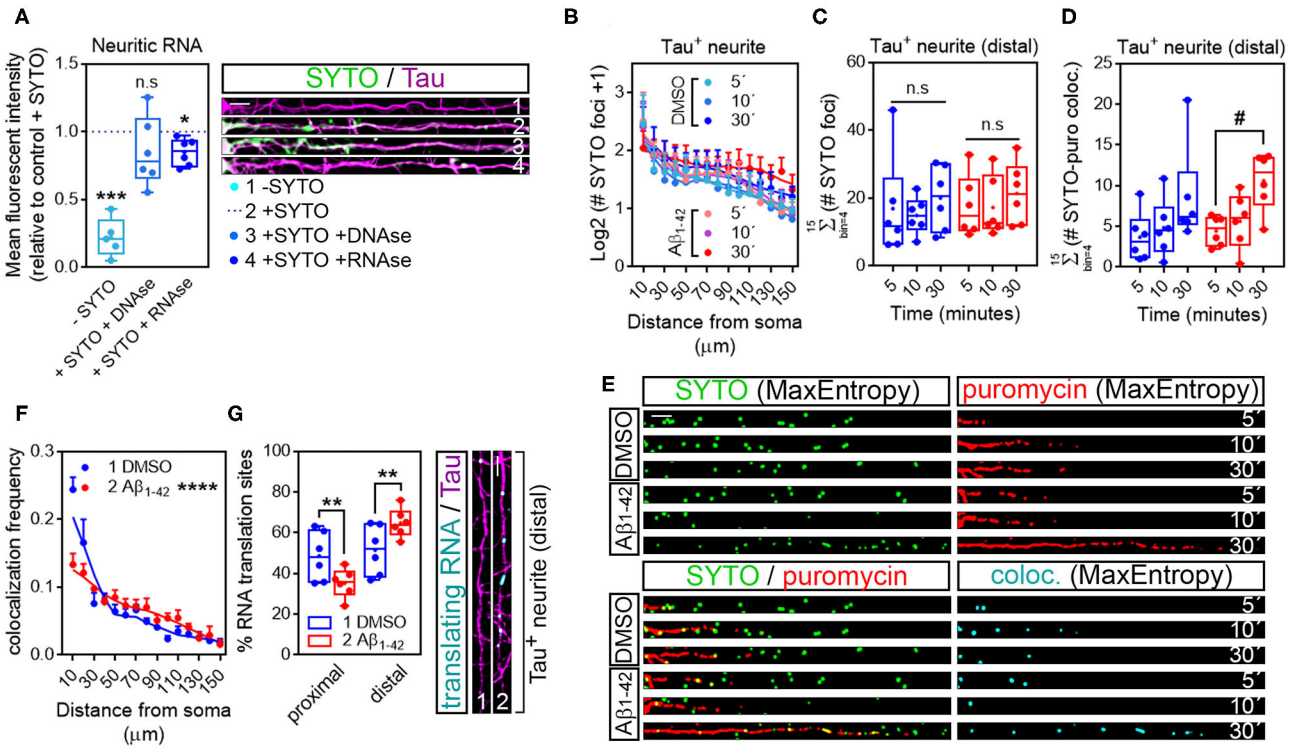

FIGURE 5 | Puromycin-positive foci in axons are a result of local protein synthesis. **(A)** Cells grown for 9 DIV and treated with DMSO for 24 h. Cells immunostained with an anti-Tau antibody (magenta) were incubated with SYTO RNASelect green fluorescent dye to label endogenous RNA (green). Total green fluorescence intensity was measured in neurites covering a distance of 150 μm from the edge of the soma (2, + SYTO). As negative control, green fluorescence was measured in cells that had not been incubated with SYTO (1, -SYTO). To determine if SYTO selectively labeled RNA, some fixed cells were digested with DNAse (3, + SYTO + DNAse) or with RNAse (4, + SYTO + RNAse). Box and whisker graphs represent the average relative fluorescence intensity of 10 neurites per condition, shown as individual data points, and the mean and median of 5 ($n = 5$, − SYTO negative samples compared to their corresponding + SYTO controls) or 6 ($n = 6$, + SYTO + DNAse and + SYTO + RNAse compared to their corresponding + SYTO controls) independent experiments. $^{***}p < 0.001$; $^{*}p < 0.05$; n.s, not significant; two-tailed *t*-tests. Scale bar, 10 μm. **(B)** SYTO-positive staining [as represented in green in **(E)**] from randomly selected cells was filtered with the convolver, brightness and contrast were adjusted. Images were converted to 8-bit and binarized with the MaxEntropy mask. The longest Tau-positive neurite was selected with a segmented line and straighten, smoothen and binarized with the MaxEntropy mask (MaxEntropy). SYTO-positive discrete puncta were scored with the particle analyzer in 15 bins covering a distance of 150 μm from the edge of the soma. The graph shows the average number on puncta represented as Log2 (SYTO foci + 1) vs. distance ± SEM measured in 6 independent experiments ($n = 6$). No statistical differences were detected between DMSO- and Aβ-treated cells incubated with puromycin for 5, 10, or 30 mins. **(C)** Box and whisker graphs show the total number of RNA granules in distal sites of Tau-positive neurites [Σ (# SYTO foci)] from DMSO- and Aβ-treated cells incubated with puromycin for 5, 10, or 30 mins. Data represent the average value of 10 sampled cells per condition plotted as individual data points, and the mean and median of 6 independent experiments ($n = 6$). n.s, no significant; two-way ANOVA followed by Tukey's multiple comparison test. **(D)** Parallel to processing SYTO-labeled images, puromycin staining was filtered with the convolver, brightness and contrast were adjusted. Images were converted to 8-bit and binarized with the MaxEntropy mask. Same Tau-positive neurites selected for SYTO quantification (green channel) were selected in the red channel [puromycin staining in **(E)**], straighten, smoothen and binarized with the MaxEntropy mask. Co-localized objects were obtained with the AND function in the image calculator [cyan in **(E)**] and scored in distal sites of Tau-positive neurites with the particle analyzer. Box and whisker graphs show the total RNA-protein colocalized puncta in DMSO- and Aβ-treated cells incubated with puromycin for 5, 10, or 30 mins [Σ (# SYTO-puro coloc.)]. Data represent the average value of 10 sampled neurites per condition plotted as individual data points, and the mean and median of 6 independent experiments ($n = 6$). #$p < 0.05$ 5 vs. 30 min puromycin in Aβ-treated cells; two-way ANOVA followed by Tukey's multiple comparison test. **(E)** Micrographs from straighten, binarized neurites stained with SYTO RNASelect green fluorescent dye to label RNA (green), with an anti-puromycin antibody to label protein (red) and the resulting images when merging both channels (green, red, and yellow) and when combining both with the AND function in the image calculator (cyan). Cells treated with puromycin for 5, 10, or 30 mins are shown. Scale bar, 10 μm. **(F)** The graph represents the frequency distribution of SYTO- and puromycin-positive objects (colocalization frequency) in DMSO- and Aβ-treated neurites following 30-min puromycin exposure. Colocalized objects were measured with the particle analyzer in 15 bins covering a distance of 150 μm from the edge of the cell body. $^{****}p < 0.0001$ (interaction); two-way ANOVA. **(G)** Box and whisker graph representing the proportion of colocalized objects (% RNA translation sites) in proximal (0–30 μm) and distal (last 120 μm) sites of Tau-positive neurites. Data represent the average value of 10 sampled cells per condition shown as individual data points, and the mean and median of 6 independent experiments ($n = 6$). $^{**}p < 0.01$; two-tailed *t*-test. Micrographs show colocalized objects (translating RNAs, cyan) detected within the last 120 μm (distal) of Tau positive neurites (magenta). Scale bar, 10 μm.

frontiers in Neuroscience

ORIGINAL RESEARCH
published: 03 June 2020
doi: 10.3389/fnins.2020.00543

Histological Correlates of Diffusion-Weighted Magnetic Resonance Microscopy in a Mouse Model of Mesial Temporal Lobe Epilepsy

Katharina Göbel-Guéniot[1,2†], Johannes Gerlach[2,3†], Robert Kamberger[4], Jochen Leupold[1,2], Dominik von Elverfeldt[1,2], Jürgen Hennig[1,2,5,6], Jan G. Korvink[7], Carola A. Haas[2,3,5,6†] and Pierre LeVan[1,2,5,8,9†]*

[1] Department of Radiology, Medical Physics, Medical Center – University of Freiburg, Freiburg, Germany, [2] Faculty of Medicine, University of Freiburg, Freiburg, Germany, [3] Experimental Epilepsy Research, Department of Neurosurgery, Medical Center – University of Freiburg, Freiburg, Germany, [4] Department of Microsystems Engineering, Technical Faculty, University of Freiburg, Freiburg, Germany, [5] BrainLinks-BrainTools Cluster of Excellence, University of Freiburg, Freiburg, Germany, [6] Center for Basics in NeuroModulation (NeuroModulBasics), Faculty of Medicine, University of Freiburg, Freiburg, Germany, [7] Institute of Microstructure Technology, Karlsruhe Institute of Technology, Karlsruhe, Germany, [8] Department of Radiology and Department of Paediatrics, Cumming School of Medicine, University of Calgary, Calgary, AB, Canada, [9] Hotchkiss Brain Institute and Alberta Children's Hospital Research Institute, University of Calgary, Calgary, AB, Canada

OPEN ACCESS

Edited by:
João O. Malva,
University of Coimbra, Portugal

Reviewed by:
He Wang,
Fudan University, China
Hidenao Fukuyama,
Kyoto University, Japan

***Correspondence:**
Pierre LeVan
pierre.levan@ucalgary.ca

† These authors have contributed equally to this work

Specialty section:
This article was submitted to Brain Imaging Methods, a section of the journal Frontiers in Neuroscience

Received: 09 March 2020
Accepted: 04 May 2020
Published: 03 June 2020

Citation:
Göbel-Guéniot K, Gerlach J, Kamberger R, Leupold J, von Elverfeldt D, Hennig J, Korvink JG, Haas CA and LeVan P (2020) Histological Correlates of Diffusion-Weighted Magnetic Resonance Microscopy in a Mouse Model of Mesial Temporal Lobe Epilepsy. Front. Neurosci. 14:543. doi: 10.3389/fnins.2020.00543

Mesial temporal lobe epilepsy (MTLE) is the most common type of focal epilepsy. It is frequently associated with abnormal MRI findings, which are caused by underlying cellular, structural, and chemical changes at the micro-scale. In the current study, it is investigated to which extent these alterations correspond to imaging features detected by high resolution magnetic resonance imaging in the intrahippocampal kainate mouse model of MTLE. Fixed hippocampal and whole-brain sections of mouse brain tissue from nine animals under physiological and chronically epileptic conditions were examined using structural and diffusion-weighted MRI. Microstructural details were investigated based on a direct comparison with immunohistochemical analyses of the same specimen. Within the hippocampal formation, diffusion streamlines could be visualized corresponding to dendrites of CA1 pyramidal cells and granule cells, as well as mossy fibers and Schaffer collaterals. Statistically significant changes in diffusivities, fractional anisotropy, and diffusion orientations could be detected in tissue samples from chronically epileptic animals compared to healthy controls, corresponding to microstructural alterations (degeneration of pyramidal cells, dispersion of the granule cell layer, and sprouting of mossy fibers). The diffusion parameters were significantly correlated with histologically determined cell densities. These findings demonstrate that high-resolution diffusion-weighted MRI can resolve subtle microstructural changes in epileptic hippocampal tissue corresponding to histopathological features in MTLE.

Keywords: MR microscopy, HARDI, tractography, hippocampus, mesial temporal lobe epilepsy, kainate

INTRODUCTION

Epilepsy is a neurological disorder characterized by epileptic seizures caused by pathologically hyper-excitable and hyper-synchronized neuronal networks (Fisher et al., 2005; Ono and Galanopoulou, 2012). The most common form of focal epilepsy is mesial temporal lobe epilepsy (MTLE), which involves the hippocampus (HC), from which seizures frequently originate (Engel, 1996). The disease may develop over the course of several years in humans (Engel, 1996), yet classical MTLE can only be identified in human patients by MRI following the complete development of so-called hippocampal sclerosis, which comprises the degeneration of certain neuronal subpopulations (esp. hilar interneurons and cornu ammonis CA1 and CA3 pyramidal cells), dispersion of the granule cell layer (GCL) and changes of the typical hippocampal innervation pattern (e.g., mossy fiber sprouting) (Haas et al., 2002; Thom et al., 2002; Blümcke et al., 2013). These effects are also mimicked by the kainate mouse model of MTLE (Suzuki et al., 1995; Bouilleret et al., 1999; Riban et al., 2002), where the disease manifests weeks following an initial epileptogenic insult. This model is frequently used to study different cellular and molecular aspects of epileptogenesis (Heinrich et al., 2006, 2011; Häussler et al., 2012; Marx et al., 2013; Janz et al., 2017). These various processes underlying the development of epilepsy are in practice not accessible in humans since they are not accompanied by obvious clinical manifestations, yet the early detection of subtle pathological biomarkers may open up novel avenues for disease treatment even before the occurrence of the first seizure.

For this purpose, high-resolution diffusion-weighted imaging (DWI) and tractography may be particularly promising due to its ability to characterize brain tissue microstructure (Pirttilä et al., 2001; Guilfoyle et al., 2003; Immonen et al., 2008; Ong et al., 2008; Ong and Wehrli, 2010; Hansen et al., 2011; Budde and Frank, 2012; Kharatishvili et al., 2014). Properties of water diffusion can notably be used to infer the presence of white matter fiber bundles, but also reflect the underlying microstructural anatomy in regions with more complex architectures (Shepherd et al., 2006). This has been further confirmed by studies of *ex vivo* samples allowing the direct comparison of diffusion tractography (DT) results with histology of the same tissue (Flint et al., 2010; Hansen et al., 2011).

The hippocampal formation has been of particular interest in MR microscopy studies (Shepherd et al., 2006; Flint et al., 2009; Wu and Zhang, 2016), where it possible to differentiate hippocampal subfields and layers according to their microstructural properties, given sufficient spatial resolutions. Several studies have shown that DWI properties differ between healthy and epileptic hippocampi (Assaf et al., 2003; Liacu et al., 2010; Rutland et al., 2018), but it is not completely clear what the various altered DWI parameters represent with respect to specific cellular-level aspects of epileptogenesis. In this study, we thus investigate the relationship between diffusion MR microscopy and the corresponding histologically determined microstructural characteristics of fixed sections of the epileptic mouse brain.

MATERIALS AND METHODS

For this study, 400 μm thick paraformaldehyde (PFA)-fixed sections of the hippocampus (21 sections/5 animals) and whole brain (5 sections/4 animals) from healthy and epileptic animals were examined by MR microscopy. Subsequently, tissue architecture and specific cellular features of the same tissue samples were visualized by histological methods to allow a direct comparison of cytoarchitectural details with the acquired MR data. A previous study had shown that MR diffusion parameters (mean diffusivity and fractional anisotropy) exhibited effect sizes of the order of several standard deviations between epileptic and control animals (Janz et al., 2017), hence a relatively low sample size was sufficient to detect these differences for the ensuing histological correlations.

Animals

Experiments were carried out with 8–9 weeks old C57BL/6N and transgenic Thy1-eGFP mice, in which enhanced green fluorescent protein (eGFP) is expressed under control of the Thy1 promoter (M-line, C57BL/6 background; Feng et al., 2000). In these mice, approximately 20% of principal neurons are eGFP-positive, wherefore their fixed tissue sections were used to visualize histological details of different brain areas following the MR scans. Mice were kept at room temperature in a 12 h light/dark cycle providing food and water *ad libitum*. All animal procedures were performed in accordance with the guidelines of the European Community's Council Directive of September 22, 2010 (2010/63/EU) and approved by the regional council (Regierungspräsidium Freiburg) and local animal welfare officer, according to the German animal protection act.

Experimental Epilepsy

Epileptogenesis was induced by unilateral kainate injection into the right dorsal HC. Mice were anesthetized using a mixture of ketamine (100 mg/kg body weight, i.p.), xylazine (5 mg/kg body weight, i.p.) and atropine (0.1 mg/kg) in 0.9% NaCl (saline) and placed in a stereotaxic frame in the prone position. 50 nl of a 20 mM kainate solution (Sigma-Aldrich, St. Louis, MO, United States) in saline were stereotaxically injected (AP = −2.0, ML = −1.5, DV = −1.9 mm, with bregma as reference) over a period of 60 s, using a micro-pump (CMA/100, Carnegie Medicine, Stockholm, Sweden) operating a 0.5 μl micro-syringe (Hamilton, Bonaduz, Switzerland). Mice were kept under observation for several hours after surgery to confirm behavioral status epilepticus, characterized by mild convulsive movements, chewing, rotations, or immobility, as previously described (Riban et al., 2002). Tissue samples were obtained from animals in the chronic phase of epilepsy (21 days after kainate injection). While many processes that are centrally involved in the pathogenesis of epilepsy (e.g., mossy fiber sprouting) are known to progress further and not reach a final state, most histopathological and electrophysiological hallmarks of MTLE with hippocampal sclerosis (e.g., granule cell dispersion, neuronal cell loss, gliosis, recurrent, spontaneous seizures) are known to have largely developed at that stage (Bouilleret et al., 1999; Suzuki

et al., 2005; Heinrich et al., 2006; Pallud et al., 2011; Häussler et al., 2012).

Sample Preparation

Hippocampal sections were prepared as follows: animals were anesthetized in isoflurane and decapitated. The hippocampus was immediately dissected in ice-cold phosphate buffer (PB), cut into thick transverse sections (400 μm) using a McIlwain Tissue Chopper. Afterward, hippocampal sections were immersion-fixed in 4% PFA over night at 4°C and, subsequently, rinsed 4–5 times, 10 min each, in 5 ml PB.

Brain sections were obtained as follows: mice were transcardially perfused for 1 min with saline, followed by 5 min of perfusion with 4% PFA in 0.1M PB. Afterwards, the brain was removed, post-fixed in 4% PFA (4–6 h at 4°C), rinsed in PB overnight and sectioned on a vibratome (400 μm coronal plane).

Considering the use of multiple sections at different positions along the hippocampal septotemporal axis from the same animals, a total of 21 hippocampal sections (six from control animals as well as nine from the ipsilateral hippocampus and six from the contralateral hippocampus of epileptic animals) and five whole-brain sections (one from a control animal and four from epileptic animals) were investigated.

MRI Data Acquisition

MR Setup

All MR experiments were performed on a horizontal preclinical 7.0 T Bruker BioSpec 70/20 USR system (300 MHz) (BrukerBioSpin, Ettlingen, Germany) with a clear bore diameter of 200 mm and using a Bruker quadrature transmit/receive MRI CryoProbe.

Sample Containers

Small MR compatible polymethylmethacrylate (PMMA) containers were glued on a custom-built 3D-printed sample holder and then horizontally mounted on a conventional mouse bed as close as possible to the surface cryoprobe head to minimize signal loss. To avoid dehydration of the tissue, the containers were filled with an isotonic sodium chloride solution (0.9%) and sealed with adhesive tape.

Structural MR Imaging

MR protocols were empirically setup to achieve high-resolution imaging (20 μm in-plane) with a signal-to-noise ratio (SNR) of at least 10.

The fixed hippocampal sections were scanned using FLASH (TR = 300 ms, TE = 18 ms, flip angle = 50°, 20 μm × 20 μm × 104 μm resolution, matrix size 650 × 550, FOV 13 mm × 11 mm, four slices, NEX = 32, scan duration 1 h 28 min) and RARE sequences (TR = 2000 ms, TE = 17 ms, RARE factor 6, 20 μm × 20 μm × 104 μm resolution, matrix size 512 × 480, FOV 10.24 mm × 9.6 mm, four slices, NEX = 32, scan duration 1 h 25 min).

The same scan parameters were used for the whole-brain sections, except with a slightly modified field of view and corresponding matrix size in order to avoid foldover artifacts within the imaged tissue: FLASH (matrix size 670 × 500, FOV 13.4 mm × 10 mm, scan duration 1 h 20 min), RARE (matrix size 450 × 750, FOV 9 mm × 15 mm, scan duration 2 h 13 min).

Diffusion-Weighted MR Imaging

High angular resolution diffusion imaging (HARDI) data was acquired using a 2D diffusion-weighted segmented EPI sequence with one b-value at 1000 s/mm^2 as a compromise between diffusion contrast and SNR. Given the observed mean diffusivities of the order of 0.5×10^{-3} mm^2/s in the investigated fixed tissue (see **Figure 5** and **Supplementary Table S1**), this would result in a theoretical ∼18% loss in contrast compared to a b-value of 2000 s/mm^2, but also a ∼65% gain in SNR due to diffusion signal attenuation. Since we were mainly interested in in-plane substructures, we also used slices thicker than the in-plane resolution to improve SNR. The resulting raw images exhibited clear contrast in regions of higher diffusivity such as the pyramidal cell layer, while maintaining acceptable SNR > 10 in the diffusion-weighted images to allow for a reliable estimation of diffusion parameters (**Figures 1A,B**).

For the hippocampal sections the scan parameters were as follows: TR = 3000 ms, TE = 46 ms, 4 segments, 60 directions, 6 b = 0 images, 40 μm × 40 μm × 100 μm resolution, matrix size 320 × 255, FOV 12.8 mm × 10.2 mm, four slices, NEX = 16, scan duration 3 h 31 min.

The same parameters were used for the healthy whole-brain sections, with the exception of a larger field of view and corresponding matrix size to account for the larger sample: matrix size 320 × 400, FOV 12.8 mm × 16 mm. This resulted in a TE of 63 ms.

For the imaging of sections from epileptic mice, the protocol was adapted with more EPI segments to reduce distortions: 6 segments, matrix size 320 × 340, FOV 12.8 mm × 13.6 mm. This resulted in a TE of 56 ms and a total scan duration of 5 h 16 min.

The diffusion images were coregistered to each other using the FSL toolbox (Smith et al., 2004) to compensate for potential image shifts caused by eddy currents. Based on the 60-direction diffusion-weighted data, microstructural pathways were reconstructed by a global tractography algorithm freely available within the Fiber Tool package[1] running under MATLAB (Reisert et al., 2011). Default parameters were used. Briefly, this method uses simulated annealing optimization to reconstruct a distribution of streamlines within each voxel that best matches the acquired data.

Histological Examination

Following the MRI measurements, histological details were visualized by three different staining methods: fluorescence immunohistochemistry (IHC), Golgi-Cox impregnation, and DiI-based tracing of neuronal processes. Microscopical analysis was performed with an AxioImager 2 (ZENsoftware; Zeiss, Göttingen, Germany). Images were taken with a digital camera (AxioCam MRm for fluorescence, AxioCam MRc5 for bright field, both Zeiss).

[1]https://www.uniklinik-freiburg.de/mr-en/research-groups/diffperf/fibertools.html

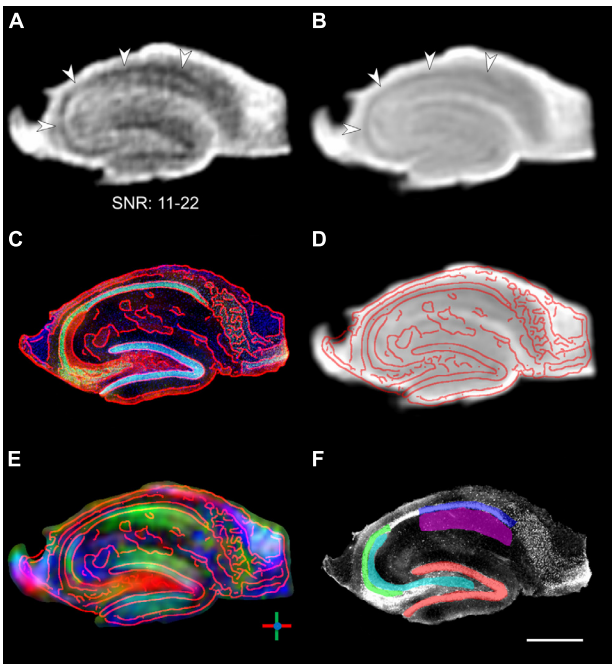

FIGURE 1 | Segmentation of DWI images. **(A)** Raw DWI image of a fixed hippocampal slice with randomly chosen diffusion direction. The b-value of 1000 s/mm^2 is relatively low for fixed tissue, but nevertheless results in clearly visible signal attenuation in the pyramidal cell layer (arrowheads) and yields acceptable SNR ranging from 11 to 22 across the slice. **(B)** Average DWI images across all 60 directions. **(C)** Corresponding histological image with overlaid contours in red. **(D,E)** Same histological contours overlaid on the mean DWI image and the image of primary diffusion orientations, demonstrating the coregistration of the DWI and histological images. In the diffusion orientation image, dorso-ventral diffusion is shown in green, left–right diffusion is shown in red, and through-plane anterior–posterior streamlines are shown in blue. **(F)** Manual ROI segmentation overlaid on the histological image (same image as in **C**, but displayed in grayscale for clarity): Red: granule cell layer of the dentate gyrus; Cyan: hilus extending into the CA3 stratum lucidum (mossy fibers); Green: CA3 pyramidal cell layer; Blue: CA1 pyramidal cell layer; Magenta: CA1 stratum radiatum (Schaffer collaterals). Scale bar: 500 μm.

For IHC, sections were cryoprotected in 25% sucrose over night at 4°C, embedded and frozen in Tissue-Tek^{TM} O.C.T Compound (Sakura Finetek Europe B.V., Alphen aan den Rijn, Netherlands) and re-sliced (50 μm) using a Leica CM3050 S cryostat (Leica, Wetzlar, Germany). Cryosections were washed three times, 5 min each in PB and IHC was performed according to standard procedures, using antibodies against neuronal nuclei (NeuN, Merck KGaA, Darmstadt, Germany), neurofilament H (SMI-32, Covance, Inc., Princeton, NJ, United States) and zinc transporter 3 (ZnT3, Synaptic Systems, Göttingen, Germany). Primary antibodies were detected by fluorophore-coupled secondary antibodies (Cy2, Cy3, or Cy5, Jackson ImmunoResearch Laboratories). Sections were counterstained with DAPI and coverslipped with fluorescence mounting medium (Dako, Glostrup, Denmark). Only sections from the center of the initially 400 μm thick tissue samples were used in order to achieve the highest possible comparability with the previously acquired MR data in the same specimen (see below).

Golgi staining was performed on hippocampal sections using the FD Rapid GolgiStain^{TM} Kit. Briefly, after impregnation in solutions containing mercuric chloride, potassium dichromate and potassium chromate, the sections were re-sliced (100–200 μm) on a cryostat, developed, dehydrated and, coverslipped with Hypermount (Thermo Fisher Scientific, Waltham, MA, United States).

For DiI tracing of CA1 pyramidal cells and their axonal inputs from Schaffer collaterals, a solid DiI crystal (diameter approximately 30–50 μm) (Thermo Fisher Scientific, Waltham, MA, United States) was placed into the CA1 stratum radiatum (SR) of a fixed hippocampal section, using a micromanipulator (H. Saur, Reutlingen, Germany). Sufficient diffusion of the dye was achieved by incubation over 1 to 2 weeks in the dark at room temperature, followed by several washing steps in PB and counterstaining with DAPI. Sections were then coverslipped with fluorescence mounting medium (Dako, Glostrup, Denmark) and analyzed.

For quantitative analysis, the images were manually segmented into the following regions of interests (ROIs) using ImageJ software: pyramidal cell layers of CA1 and of CA3, as well as granule cell layer (GCL) of the dentate gyrus (DG). Cell density within each ROI was approximated by the mean intensity of the DAPI channel after background subtraction. The average GCL width was also measured as a marker for epileptogenicity.

Quantification and Validation of Diffusion Parameters

To allow a direct comparison and validation of the measured MR parameters with histological features, the MR and histological images were realigned to each other by a 2D rigid-body coregistration using the FSL toolbox (Smith et al., 2004), which automatically aligned both datasets using by finding the rigid-body transformation that minimized mutual information as a cross-modality distance measure (**Figures 1C–E**). The use of tissue samples that were already relatively thinly sliced (400 μm) for the MRI minimized any mismatch in the slice direction. Moreover, while the imaging slices for MRI (100 μm) and the histological slices for IHC (50 μm) had different thicknesses, care was taken to select those slices from the center of the sample for both MRI and IHC, thus ensuring that the histological slice was fully contained within the MRI slice. The following additional ROIs were then defined on the coregistered images: the hilar region extending into the stratum lucidum of CA3 (where we would expect mossy fibers), and the stratum radiatum of CA1 (srCA1, where Schaffer collaterals are expected) (**Figure 1F**).

Within all ROIs, the fractional anisotropy (FA), mean diffusivity (MD), and primary diffusion orientation were computed from the diffusion tensor fitted to the MR data at each voxel. Additionally, the diffusivity along the dorso-ventral axis (dvD), the diffusivity along the left–right axis (lrD), and the ratio between the two (dvlr_ratio) were computed by fitting a spherical harmonic basis to the acquired HARDI data to interpolate the apparent diffusion coefficient (ADC) profile along the given axes.

Statistical comparisons of the diffusion parameters across ROIs and across groups (control, epileptic ipsilateral, and

epileptic contralateral) were performed by ANOVA and *post hoc* Tukey tests. Primary diffusion orientations were tested for uniformity by the V-test. Concordance between the diffusion parameters and the corresponding histological quantities was assessed by Pearson correlation coefficients. In all cases, the statistical significance threshold was set at $p < 0.05$.

RESULTS

Imaging of Hippocampal Slices

Representative examples of images of control and epileptic slices are shown in **Figures 2**, 3. In control slices, cell layers of principal neurons were clearly visible in the structural MR images (**Figures 2A,B,F,G**). Moreover, the diffusion tractography images showed diffusion streamlines with strong directional conformity (**Figures 2C,H**, big arrowheads) corresponding to radially aligned pyramidal and granule cell dendrites in stratum radiatum and the molecular layer, respectively. These dendritic arborizations could be confirmed by Golgi staining of adjacent sections (**Figure 2E**, blue arrowheads).

Coherent streamlines were also seen in the stratum oriens, where hippocampal long-range projections are localized, as well as in the stratum lucidum of CA3, into which granule cell axons (mossy fibers) extend, innervating CA3 pyramidal cells. To check potential correspondence with mossy fibers, ZnT3 immunostaining was performed (**Figure 2I**, red signal, small arrowheads). Parts of the mossy fiber tract could also be found in the Golgi staining (**Figure 2E**, red arrowheads). Tractography within the region of hilus and CA3 exhibited strong conformity in terms of distribution and directional preference with the corresponding ZnT3 and Golgi staining of mossy fibers (**Figures 2C,D,H,I, small arrowheads** and **E**, red arrowheads).

DWI also revealed tracts in the stratum radiatum of CA1, which were oriented orthogonally to the previously identified dorso-ventral streamlines of CA1 pyramidal cell dendrites, and likely correspond to CA3 pyramidal cell axons (Schaffer collaterals, **Figures 2C,H**, color-coded in red and marked by an asterisk). Since these fibers cannot be labeled specifically by antibodies, we placed a DiI crystal into the stratum radiatum of CA1 to stain CA1 pyramidal cells and the innervating Schaffer collaterals (**Figure 2J, asterisk** and **arrowheads**). In the representative photomicrograph shown in **Figure 2J**, the area of the sections in which the DiI crystal was placed is overexposed due to the high concentration of the dye. Nevertheless, CA1 pyramidal cell dendrites orthogonal to the CA1 pyramidal cell layer can be seen (**Figure 2J**, asterisk). Additionally, single Schaffer collaterals are stained (**Figure 2J**, arrowheads), which arise from CA3 pyramidal cells and extend parallel to the CA1 pyramidal cell layer to innervate the CA1 pyramidal cell dendrites.

In epileptic slices, extensive structural changes can already be seen on structural MR images (**Figures 3A,B**), with strongly reduced contrast in CA1, CA3, and hilar regions along with a dispersed GCL. Double immunostaining for NeuN and ZnT3 revealed the associated neuropathological changes (**Figure 3E**): a massive thickening of the GCL was apparent (two arrowheads), while CA1 and CA3 pyramidal cells had degenerated (asterisk in CA1). Since CA3 pyramidal cells are target cells of ZnT3-positive mossy fibers, the ZnT3 pattern also changed: some mossy fibers extended to residual CA2 pyramidal cells (**Figure 3E**, group of three arrowheads), whereas other mossy fibers started to sprout into the dispersed GCL, forming a presumably pro-epileptic positive feedback loop (**Figure 3E**, two arrowheads). CA2 pyramidal cells were shown to survive after kainate injection and to be innervated by mossy fibers (Häussler et al., 2016). The loss of pyramidal cells could also be seen in the Golgi staining of an adjacent section (**Figure 3C**, asterisk), where pyramidal cell dendrites are absent. In this region, only a high density of small glial cells was detected.

As in control slices, DWI again provided a more detailed view of these structural features. Streamlines were elongated along the dorsoventral axis in regions of the GCL and molecular layer, most likely originating from granule cell dispersion, mossy fiber sprouting and/or gliosis (**Figure 3D**, two arrowheads). In the CA2 region, streamlines parallel to the residual CA2 pyramidal cell layer could still be found (**Figure 3D**, group of three arrowheads). These features could correspond to the portion of mossy fibers which innervate these CA2 cells. In contrast, streamlines were strongly reduced in the stratum radiatum of CA1. Dorsoventral streamlines (green) corresponding to CA1 pyramidal cell dendrites largely disappeared. This reflects the underlying structural state, since pyramidal cells are known to be subject to massive neurodegeneration after kainate injection.

The features described above were highly consistent across the studied samples. Primary diffusion orientations were tested against the hypothesis that they mostly lied at specific angles with respect to the left–right axis on the coronal slices: 90 degrees (i.e., dorso-ventral orientation) for diffusion in CA1 and the GCL, corresponding to pyramidal cell and granule cell dendrites, respectively; 0 degrees (i.e., left–right orientation) in the hilus and the stratum radiatum of CA1, corresponding to mossy fibers and Schaffer collaterals, respectively; and 45 degrees in CA3, corresponding to pyramidal cell dendrites. Although it should be noted that these hypothesized orientations were only meant to be approximate, considering that the investigated structures were curved and therefore did not have a truly fixed orientation, the statistical analysis revealed that the measured orientations were concordant with the hypotheses in all cases except in CA1, where the orientations marginally failed to reach significance ($p = 0.07$) (**Figure 4A**).

However, when dividing the samples into appropriate subgroups (epileptic ipsilateral, epileptic contralateral, and control), it becomes clear that the diffusion orientations in CA1 were actually well-aligned along the dorso-ventral axis in control slices, while they were uniformly distributed in epileptic slices (**Figures 4B–D**), concordant with the loss of pyramidal cells in the latter. Similarly, in CA3, primary diffusion directions were only consistently oriented in control and contralateral slices, while the loss of pyramidal cells in ipsilateral slices was reflected in a loss of directional conformity (**Figure 4B**). In the dentate gyrus, all types of slices showed significant directionality along the dorso-ventral axis. In the hilus, only ipsilateral slices showed significant orientation distributions along the left–right

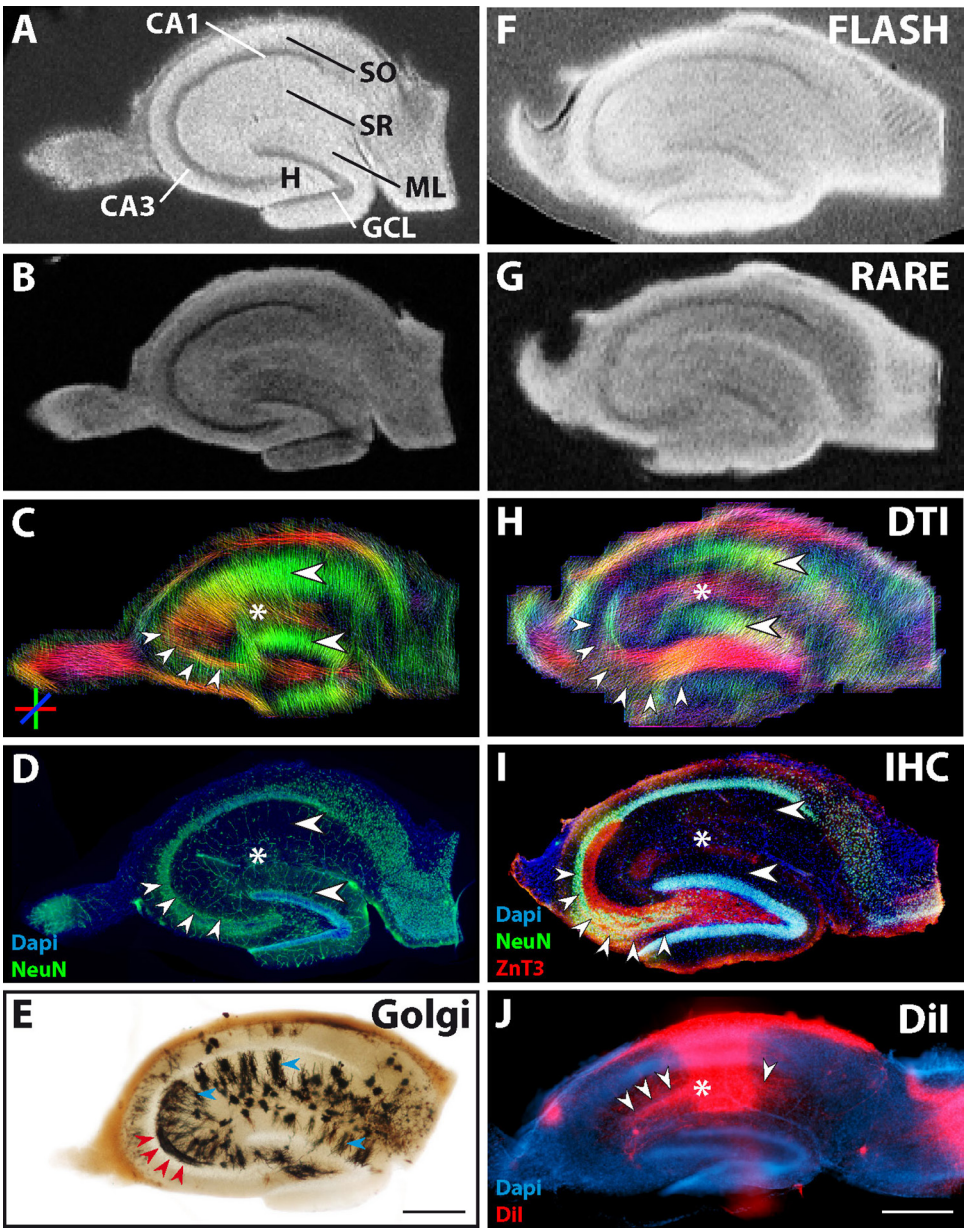

FIGURE 2 | MR and histological images of representative fixed hippocampal sections of two control animals (Section 1: **A–D**, with an adjacent section used for Golgi staining: **E**; Section 2: **F–I**). **(A,B,F,G)** Structural MRI depicts the main neuronal cell layers and tissue architecture [pyramidal cells in cornu ammonis (CA) 1 and 3; granule cell layer, GCL; molecular layer, ML; stratum oriens, SO; str. radiatum, SR; hilus, H]. Comparison of diffusion tractography images **(C,H)** to corresponding NeuN and ZnT3 immunostaining **(D,I)** shows that regions containing parallel extending dendrites of principal neurons evoke corresponding DWI streamlines (large horizontal arrowheads in the ML and CA1 stratum radiatum in **C,H,I**). Furthermore, granule cell axons, extending from the GCL into the CA3 stratum lucidum are clearly visible (small arrowheads in **C,H,I** and red arrowheads in **E**). In turn, axons from CA3 pyramidal cells project to the CA1 stratum radiatum, innervating CA1 pyramidal cell dendrites. These axons (Schaffer collaterals) could also be seen in the DWI images (asterisks in **C,H**) and could be visualized by DiI staining (small arrowheads in **J**). **(E)** Golgi staining of an adjacent section depicts the localization and orientation of principal cell dendrites (blue arrowheads in SR and ML) and parts of mossy fibers in CA3 (red arrowheads). **(J)** DiI crystal placed into the CA1 stratum radiatum, showing the orientation of CA1 pyramidal cells as well as of innervating CA3 Schaffer collaterals (asterisk and arrowheads, respectively). Scale bar: 500 μm.

axis, consistent with mossy fibers, although control slices only barely failed to reach statistical significance ($p = 0.07$). Finally, in the CA1 stratum radiatum, the loss of pyramidal cell dendrites in ipsilateral slices left Schaffer collaterals as the main source of diffusion anisotropy, thus yielding a statistically significant directional conformity along the left–right axis. This would be consistent with the observation that despite the extensive neuronal cell loss in CA1 and CA3, there is a sprouting response of new Schaffer collaterals between the spared neurons (Siddiqui and Joseph, 2005).

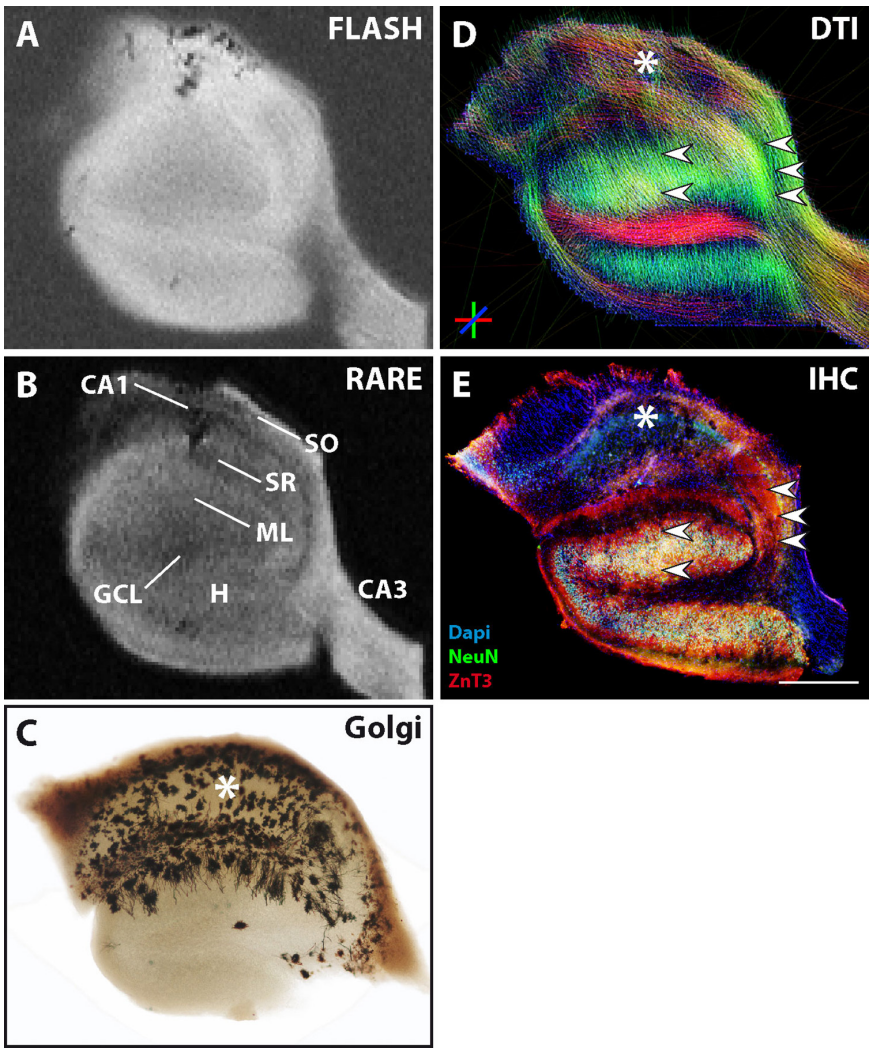

FIGURE 3 | MR and histological images of a representative fixed ipsilateral hippocampal section from a chronically epileptic mouse. **(A,B)** Structural MRI reveals decreased contrast in the pyramidal cell layers compared to control sections (see **Figure 2**), while the granule cell layer appears thickened. **(E)** Immunostainings showing degeneration of the corresponding neurons (asterisk) and dispersion of the granule cell layer (two arrowheads). **(D,E)** These histopathological changes become even more apparent in DWI, where the loss of CA1 pyramidal cells manifests as a strong reduction in dorso-ventral diffusion streamlines (asterisks in **D,E**). Furthermore, tracts in the granule cell layer appear elongated (two arrowheads in **D**), while the typical mossy fiber streamlines extending from the granule cell layer into the hilus and further into the CA3 region are less pronounced (group of three arrowheads in **D**). These abnormalities correspond to the loss of CA3 target neurons, granule cell layer dispersion and mossy fiber sprouting, which can be seen by NeuN and ZnT3 immunostainings (arrowheads in **E**). **(C)** Golgi staining of an adjacent HC section from a kainate-treated mouse confirms these structural changes and particularly highlights the degeneration and disappearance of CA1 pyramidal cells and their respective dendrites. Instead, many star-shaped glial cells can be seen in the CA1 region (asterisk). Scale bar: 500 μm.

As for the other diffusion parameters, they also showed group-level results consistent with the previous observations. The parameters for all regions and groups are shown in **Supplementary Table S1**. When pooling all slices together, dorso-ventral diffusion was found to be significantly larger in the dentate gyrus than in CA3, the hilus, and srCA1 (**Figure 5A**). Here, the ratio between dorso-ventral and left–right diffusion was a more sensitive measure, revealing additional statistical significance between dentate gyrus and CA1, and between CA1 and the hilus (**Figure 5A**). When dividing the slices into appropriate sub-groups, CA1 showed statistically significantly less FA in ipsilateral slices than both contralateral and control slices, as well as statistically significantly less dv/lr ratio in ipsilateral than in control slices (**Figure 5B**). This again reflects the loss of pyramidal cell dendrites in ipsilateral epileptic slices. In the dentate gyrus, mean diffusion, as well as diffusion along the dorso-ventral and left–right axes, was significantly increased in ipsilateral compared to contralateral slices, possibly reflecting the reduced cell density in the dispersed GCL (**Figure 5C**). In the hilus, ipsilateral slices had significantly greater mean diffusion and left–right diffusion than contralateral slices (**Figure 5D**). Ipsilateral slices also had significantly greater FA than control

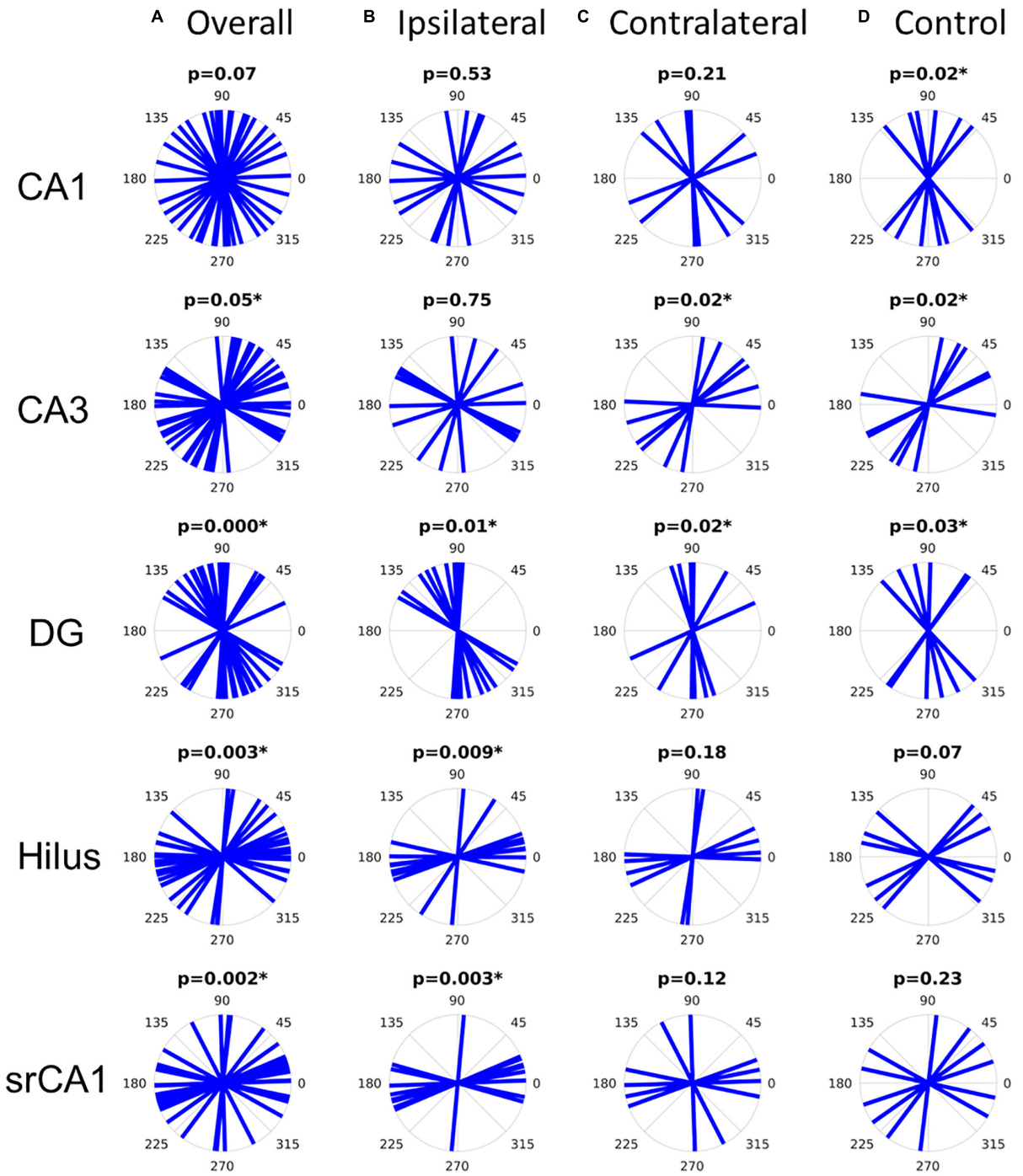

FIGURE 4 | Distribution of primary diffusion orientations in all slices **(A)**, ipsilateral epileptic slices **(B)**, contralateral epileptic slices **(C)**, or control slices **(D)**. The *p*-values refer to the V-test for non-uniformity with hypothesized diffusion orientations with respect to the left–right axis of 90 degrees for CA1 and the dentate gyrus (DG), 0 degrees for the hilus and for the CA1 stratum radiatum (srCA1), and 45 degrees for CA3. Significant *p*-values (asterisks) indicate that the diffusion orientations are not uniformly distributed and rather follow the hypothesized orientations.

slices, consistent with the emergence of mossy fibers with strong directional conformity in epileptic slices.

The previous results showed that contralateral slices sometimes showed similar alterations as ipsilateral slices in comparison to control slices. Indeed, in the kainate mouse model, structural changes may also affect the contralateral hippocampus, depending on the severity of epileptogenesis. One example of such an animal is shown in **Figure 6**. Immunostaining

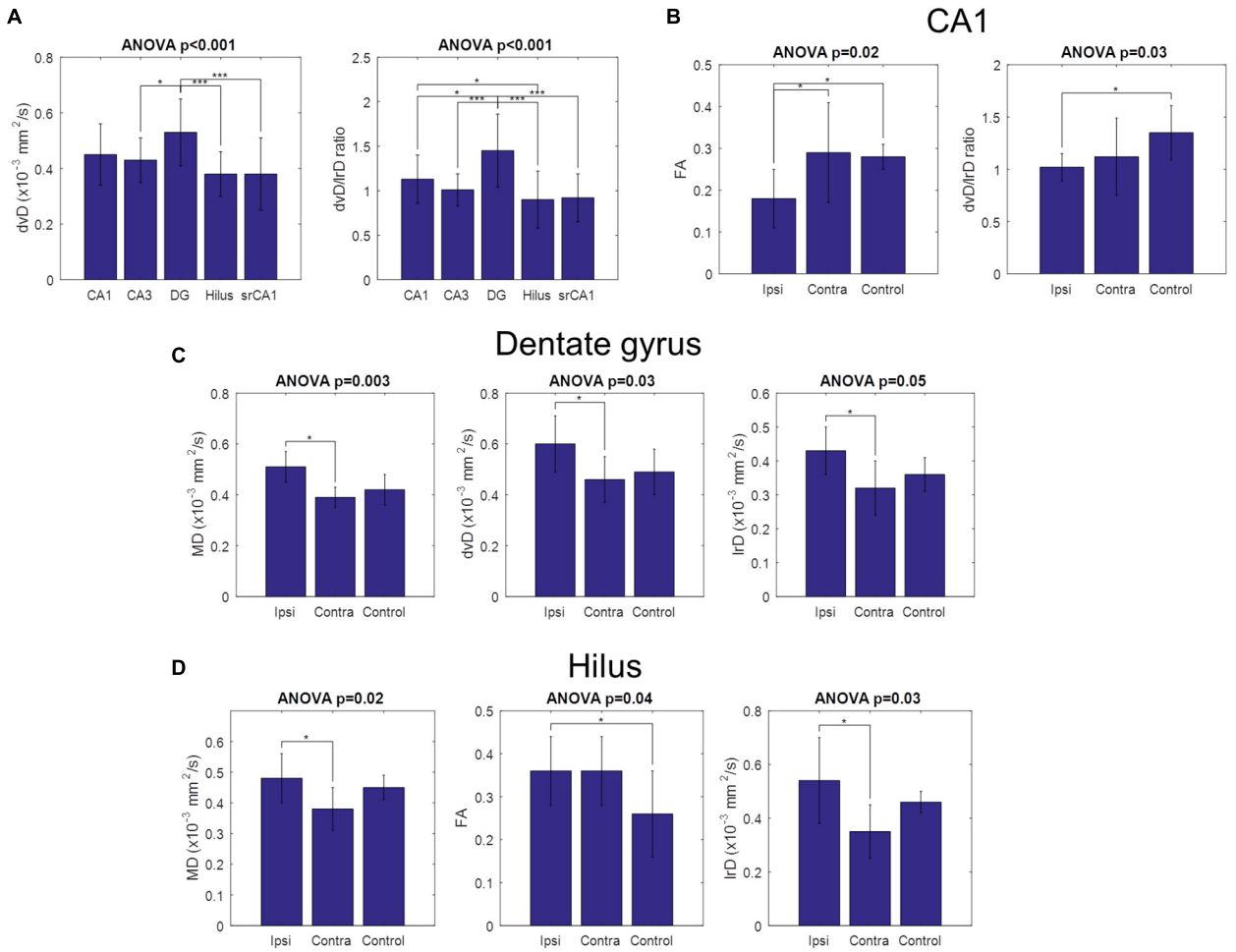

FIGURE 5 | Comparison of diffusion parameters across hippocampal regions and across slice groups. Error bars indicate the standard deviations of the measured parameters. **(A)** Dorso-ventral diffusivity was significantly higher in the dentate gyrus than in CA3, the hilus, and CA1 stratum radiatum. The ratio between dorso-ventral and left–right diffusivities showed a similar pattern, with additional significance between dentate gyrus and CA1, and between CA1 and the hilus. No other diffusion parameters were significantly different across hippocampal regions. **(B)** CA1 group differences. FA was significantly lower in ipsilateral slices than both contralateral and control slices, while the ratio between dorso-ventral and left–right diffusivities was significantly lower in ipsilateral than in control slices. **(C)** Dentate gyrus group differences. Mean diffusivity, dorso-ventral diffusivity, and left–right diffusivity were all significantly higher in ipsilateral than in contralateral slices. **(D)** Hilus group differences. Mean diffusivity and left–right diffusivity were significantly higher in ipsilateral than in contralateral slices, while FA was significantly higher in ipsilateral than in control slices. No other parameters were statistically significant. (*$p < 0.05$, ***$p < 0.001$).

for NeuN clearly showed that the contralateral side was affected by the kainate injection and that some but not all CA1 pyramidal cells had been lost (**Figure 6D**, asterisk). In contrast, all the other neuronal cell layers remained unaffected: the layers of CA3 pyramidal cells and granule cells appeared as dense and narrow bands and mossy fibers were clearly extending from the GCL into the CA3 stratum lucidum without any sprouting into the GCL (**Figure 6D**, small arrowheads). The GCL and CA3 pyramidal layer were visible on structural MRI, but not the CA1 pyramidal layer (**Figures 6A,B**). In DWI, streamlines corresponding to granule cell dendrites and mossy fibers (**Figure 6C**, single, horizontal arrowhead and small arrowheads, respectively) precisely matched the underlying cytoarchitecture, but streamlines corresponding to CA1 pyramidal cell dendrites were clearly diminished (**Figure 6C**, asterisk) and differed from the control situation (**Figures 2C,H, asterisks** and **upper**, big horizontal arrowhead). Therefore, even the impairment of only one neuronal subpopulation without extensive structural changes was clearly visible on MRI.

A direct comparison of histological and DWI parameters is shown in **Figure 7**. Significant correlations were observed between corresponding parameters in CA1 (cell density significantly correlated with MD and FA), CA3 (cell density correlated with FA), and the dentate gyrus (cell density correlated with MD). However, such correlations could be merely driven by differences between epileptic and non-epileptic slices. For example, FA of CA1, which we had previously shown to be altered in ipsilateral epileptic slices (see **Figure 5**), was significantly correlated not only with CA1 cell density, but also with CA3 cell density, GCL density, and GCL width (**Figure 7**).

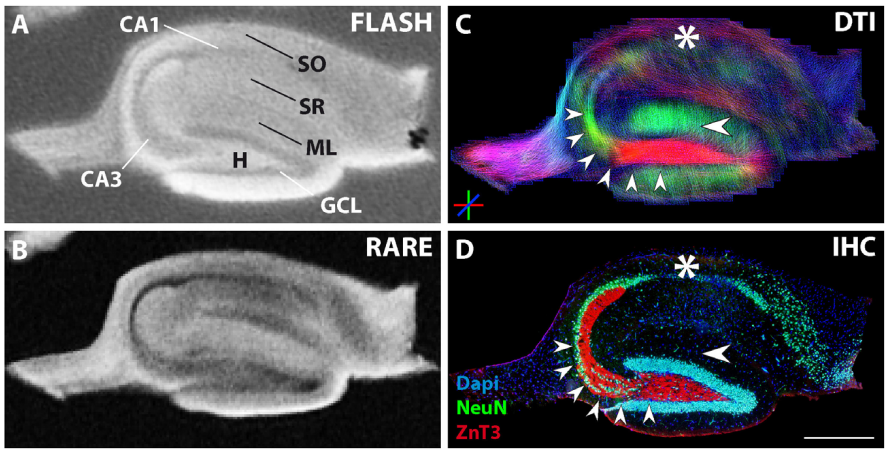

FIGURE 6 | MR and histological images of a representative fixed contralateral hippocampal section from a chronically epileptic mouse with restricted neuronal cell loss in CA1. **(A,B)** Structural MRI shows high contrast in CA3 and the granule cell layer, but diminished contrast in the CA1 pyramidal cell layer. **(C)** The corresponding DWI images show reduced dorso-ventral streamlines within CA1 (asterisk). **(D)** Immuhistochemistry reveals the exclusive degeneration of some but not all CA1 pyramidal cells (asterisk). Other neuronal cell layers or structures like CA3 pyramidal cells, granule cells, and the respective innervation pattern by mossy fibers (small arrowheads) are unaffected. Scale bar: 500 μm.

Similarly, MD of the dentate gyrus was also significantly correlated with multiple histological quantities (**Figure 7**). As all of these parameters are known to be altered in epilepsy, it is not surprising that significant correlations were observed. Nevertheless, when considering only ipsilateral epileptic slices, significant correlations notably remained between CA1 cell density and both FA and MD of CA1, as well as between CA3 cell density and FA of CA3, thus demonstrating that the DWI parameters directly reflect the underlying cellular microstructure. However, in ipsilateral epileptic slices, GCL density was not significantly correlated with DWI measures in the dentate gyrus, indicating that the diffusion alterations may be driven by features other than granule cells.

Imaging of Whole-Brain Sections

Analysis of a whole-brain section of a Thy1-eGFP mouse is shown in **Figure 8**. In addition to the features previously identified in hippocampal slices (**Figures 8B,E,H,K,N**), photomicrographs of the eGFP expression confirmed that both pyramidal and granule cells exhibit dendritic processes aligned in a very strict and parallel order, extending radially from their respective neuronal cell layer (**Figure 8K**, arrowheads). It should be noted that the whole-brain slices allowed to visualize other structural features in DWI, such as neocortical parallel streamlines oriented radially to the brain surface (**Figure 8O**, color-coded in green, arrowheads) matching the orientation of dendrites of principal neurons (**Figure 8L**).

One representative section from an epileptic mouse is shown in **Figure 9**. NeuN immunostaining and eGFP expression revealed the typical features of hippocampal sclerosis: dispersion of the GCL (**Figures 9F,H**, arrows) and the pronounced loss of CA1 and CA3 pyramidal cells (**Figures 9F,H**, arrowheads). As in the previous investigations in hippocampal slices, the increased thickness of the GCL and the neuronal cell loss in CA1 and CA3 pyramidal cell layers could be seen in structural MRI on the ipsilateral (kainate-injected) side (**Figures 9B,D**).

On the contralateral hippocampus, DWI showed dorso-ventral (DV) diffusion streamlines (color-coded in green) mainly in the molecular layer of the dentate gyrus and in the stratum radiatum of CA1. In the ipsilateral dentate gyrus, the streamlines appeared elongated (**Figure 9J**, two horizontal arrows), while in the region of CA1 stratum radiatum, DV streamlines could not be detected (**Figure 9J**, asterisks).

Ipsilateral and contralateral DWI features within the same slices could then be compared by paired *t*-tests. This confirmed previous results that FA of CA1 was significantly lower on the ipsilateral side ($p = 0.01$). Moreover, left–right diffusivity was significantly higher ipsilaterally, in accordance with the loss of anisotropy ($p = 0.04$). In the dentate gyrus, mean ($p = 0.004$), dorso-ventral ($p = 0.009$), and left–right ($p = 0.004$) diffusivities were all higher on the ipsilateral side, again in concordance with previous results (**Figure 5**), and thus demonstrating that DWI features could be used as a biomarker to identify the epileptogenic hippocampus in unilateral MTLE.

DISCUSSION

This study investigated high resolution MRI biomarkers of histological details of mouse brain tissue in epilepsy. The use of fixed samples greatly facilitated the validation of our acquired MR data by direct histological comparison of the same specimen, while circumventing issues of intra-scan variations such as physiological motion. Importantly, we made use of a MTLE mouse model in order to test the extent to which histopathological changes could be visualized by this method. While fixed tissue differs from living tissue in diffusion and relaxation parameters (Purea and Webb, 2006;

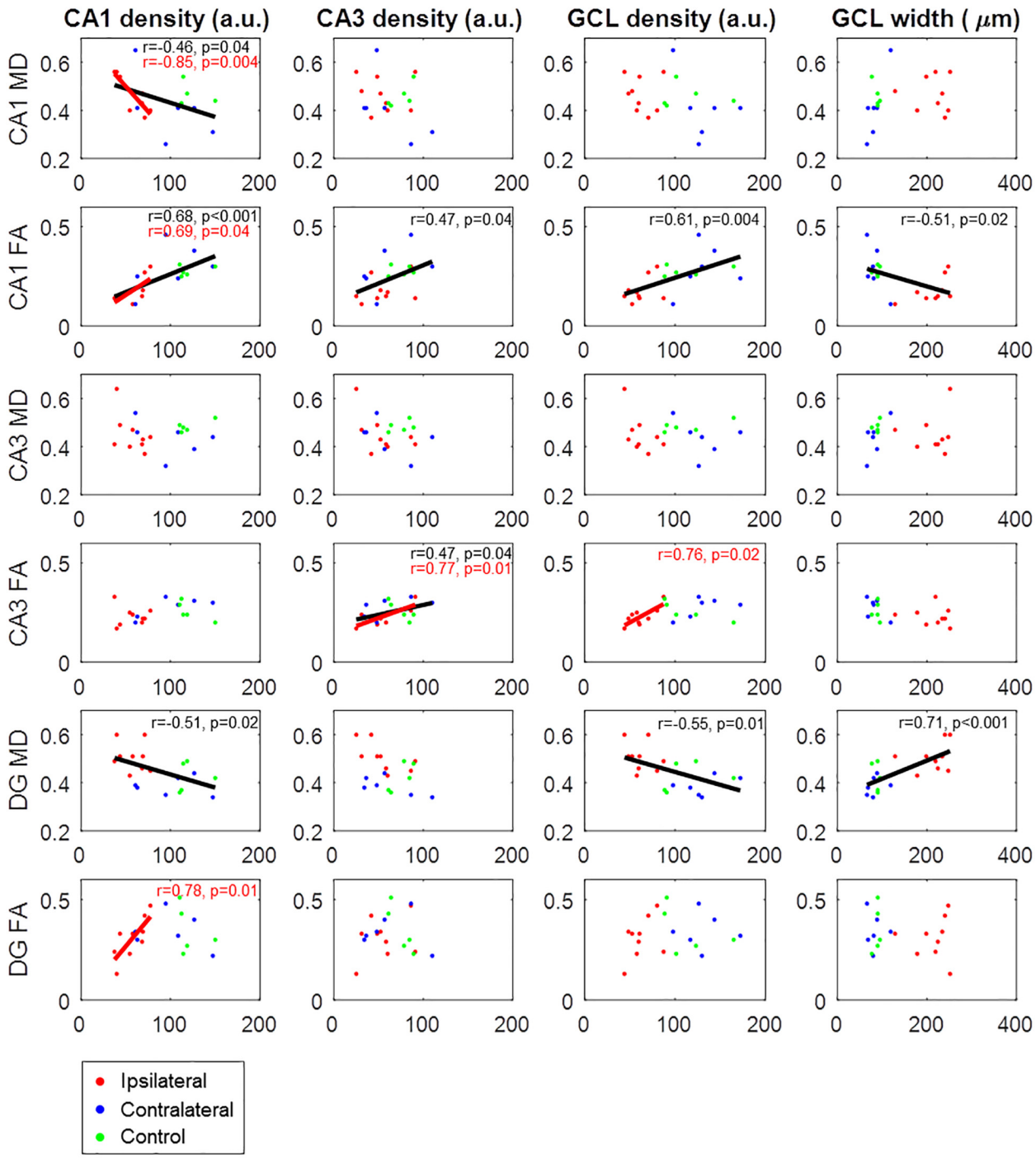

FIGURE 7 | Correlations between histological parameters (columns) and DWI parameters (rows). Cell densities were calculated from the normalized histological image intensities and are thus in arbitrary units (a.u.). Data points are from ipsilateral slices (red), contralateral slices (blue), and control slices (green). Regression lines with Pearson correlation coefficients and corresponding *p*-values are only shown for statistically significant correlations ($p < 0.05$), either across all slices (black) or only considering ipsilateral epileptic slices (red).

Schmierer et al., 2008; Richardson et al., 2014; Birkl et al., 2016), the presented work still provides important clues on the cellular-level correlates of MR features that may be observed *in vivo* (Janz et al., 2017).

DWI of tissue sections from healthy control and kainate-injected, epileptic animals revealed distinct features arising from highly organized neuronal dendrites and axons. In detail, radially oriented neuronal dendrites with high density extending

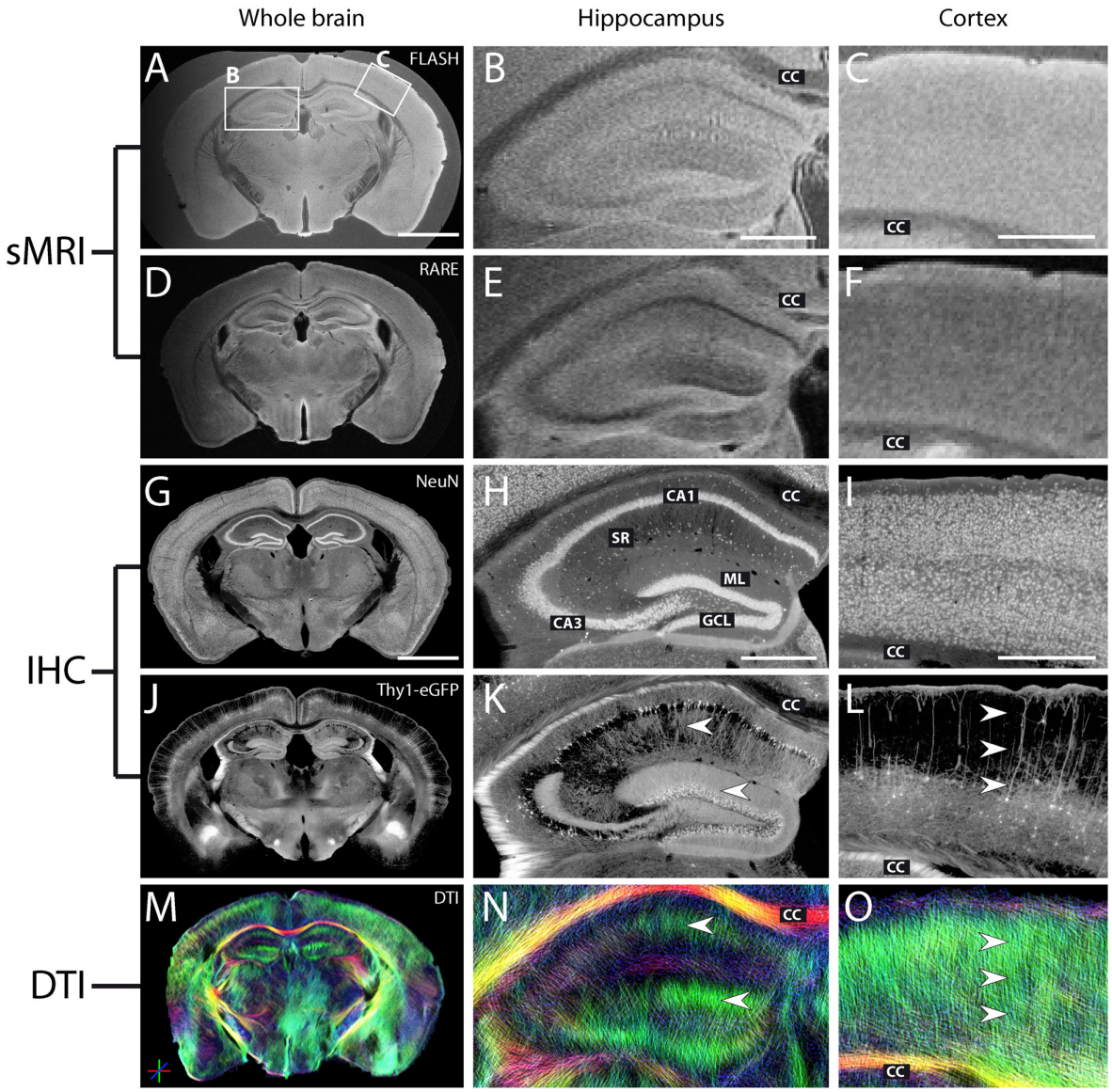

FIGURE 8 | MR and histological images of a representative fixed whole-brain section. **(A–F)** Structural MRI reveals densely packed neuronal cell layers in the hippocampus with a thickness as low as 50 μm, as confirmed by comparison with the corresponding NeuN staining **(G–I)**. Middle and right columns show magnifications of the hippocampus and the neocortex. **(G–I)** NeuN staining highlights regions with high neuronal cell density. While some neurons are arranged in densely packed cell layers (hippocampus, H: pyramidal cells in cornu ammonis CA1-3, GCL: granule cell layer), others can be found in more loosely packed cell layers (cortex, I). **(H,I)** CC, corpus callosum; ML, molecular layer; SR, stratum radiatum. **(J–L)** eGFP expression in single principal neurons illustrates the neuronal cytoarchitecture within different brain regions and highlights major fiber pathways and long-range projections. **(M–O)** DWI shows the well-ordered orientation of neuronal dendritic processes, namely radially oriented dendrites of principal neurons within the hippocampus (**K,N**, arrowheads) and cortex (**L,O**, arrowheads) along the dorso-ventral axis (highlighted in green). Note that the slightly distorted shape of the brain sections in the DWI image **(M)** is a consequence of the relatively long EPI readout of the measurement sequence. However, this only resulted in local geometrical shifts and does not invalidate the observed contrasts in diffusion measures. Scale bar: 2 mm (whole brain) and 500 μm (magnifications).

from CA1 and CA3 pyramidal cell layers and the granule cell layer of the dentate gyrus elicited strongly anisotropic water diffusion corresponding to the underlying neuronal morphology. In contrast to previous studies from, e.g., Zhang et al. (2002; Shepherd et al., 2007; Bohlen et al., 2014; Calabrese et al., 2015; Sierra et al., 2015), we could also show Schaffer collaterals as well as mossy fibers even in combination with tractography without any contrast agent. In particular, granule cell mossy fibers were seen as distinct DWI tracts, in accordance with a recent study demonstrating the ability of diffusion tractography to visualize hippocampal network organization (Wu and Zhang, 2016).

In the current work, we show that these features can be used for the detection of pathological alterations in epilepsy. The recent study of Stefanits et al. (2017) shows the

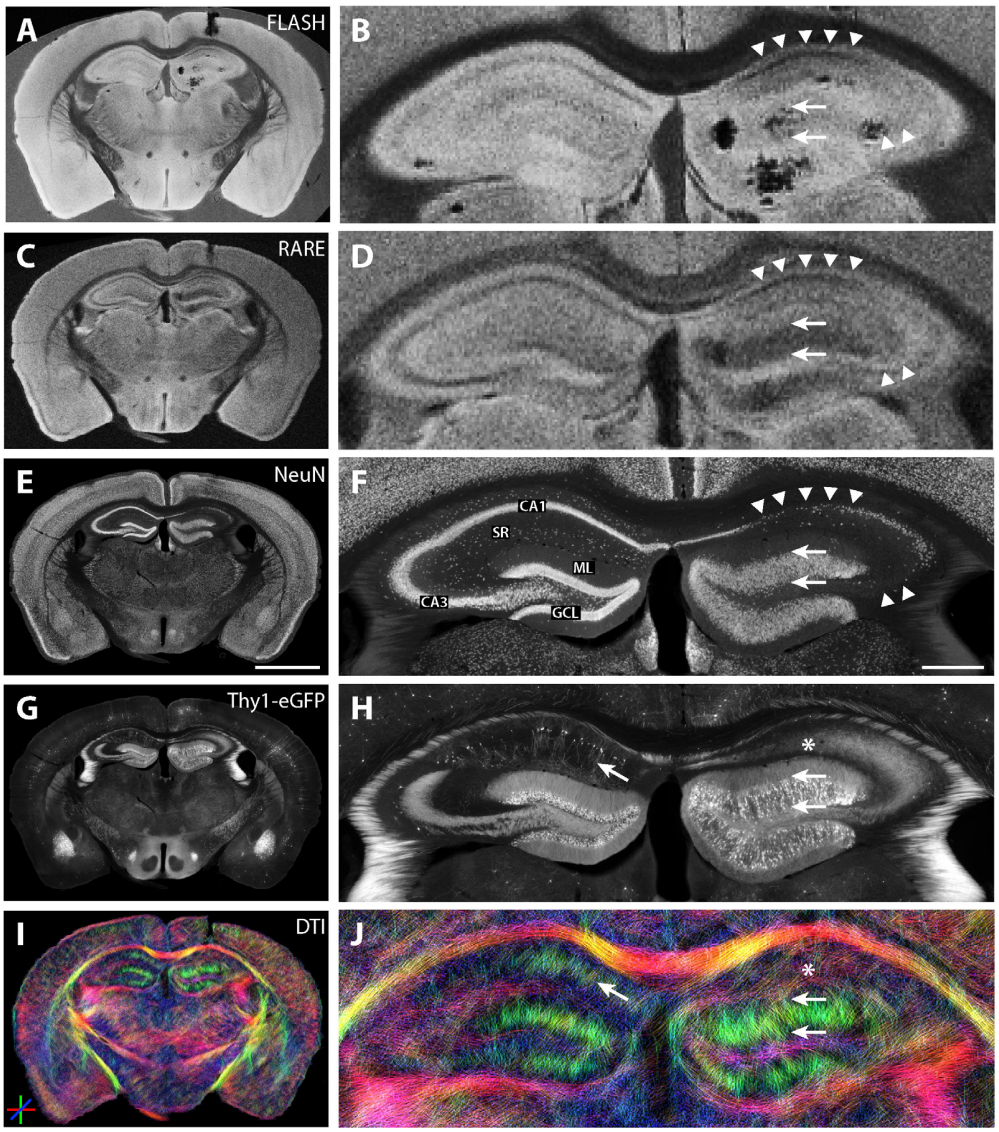

FIGURE 9 | MR and histological images of a representative fixed whole-brain section from a chronically epileptic Thy1-eGFP mouse. **(A–D)** Structural MRI highlights morphological differences between the contralateral and the kainate-injected hippocampus **(B,D)**. While the granule cell layer thickness strongly increased on the ipsilateral side (arrows), contrast was reduced in the pyramidal cell layers CA1 and CA3 (arrowheads). Darker areas in **(B)** are susceptibility artifacts due to metal fragments from the injection needle after kainate injection – tissue is actually intact as seen in the corresponding immunohistochemical stainings (see **F,H**). NeuN staining **(E,F)** and eGFP expression **(G,H)** reveal the typical hallmarks of hippocampal sclerosis: dispersion of the GCL (arrows), loss of CA1 and CA3 pyramidal cells (arrowheads; CA, cornu ammonis; SR, stratum radiatum; GCL, granule cell layer; ML, molecular layer). **(I,J)** DWI shows elongated streamlines in the ipsilateral granule cell layer and molecular layer, most likely corresponding to granule cell dispersion, mossy fiber sprouting and gliosis (two arrows, see also Heinrich et al., 2006) for reference to astrogliosis after kainate injection) whereas dorso-ventral streamlines within areas of CA1 and CA3 pyramidal cell dendrites disappeared, reflecting the degeneration of these cells (asterisk). Other brain regions do not exhibit strong morphological changes after the KA treatment. Scale bars: 2 mm (whole brain: left column) and 500 μm (magnifications: right column).

importance of high-resolution imaging of hippocampal sclerosis for clinical aspects. In chronically epileptic animals, we found that histological features of the underlying neuronal network caused consistent and reproducible changes in the corresponding MR data. In detail, DWI was able to detect the degeneration of CA1 and CA3 pyramidal cells, dispersion of granule cells and the associated network rearrangement. Crucially, even more subtle modulations, such as the exclusive degeneration of CA1 pyramidal cells in the contralateral hippocampus, could be clearly detected by DWI as reduced fractional anisotropy in CA1 (**Figures 4**, **6**). Overall, this study thus provided a better understanding of the cellular-level correlates of the diffusion alterations that manifest during epileptogenesis (Immonen et al., 2008; Sierra et al., 2015). Here, the validation of such features was made possible by using the exact same tissue samples for the MR experiments and histological examinations, given that

pathological alterations are inherently variable across epileptic animals, and also show variations along the hippocampus within individual animals (Häussler et al., 2012).

Importantly, while DWI and histological correlations have been reported previously when pooling healthy and epileptic animals (Laitinen et al., 2010), here we also show that these correlations were also significant when considering only intra-group correlations within ipsilateral epileptic slices (**Figure 7**). Indeed, in addition to the specific structural differences associated with the pathology, localized damage due to the intrahippocampal kainate injection in the mouse model may drive common variance in the DWI and histological parameters, especially considering that control animals did not undergo sham injections. However, the observation of significant correlations within the epileptic group, in which all animals underwent the exact same experimental procedures, shows that the DWI features in CA1 and CA3 directly reflect the underlying cellular microstructure, i.e., the severity of the pathological changes, rather than being driven by other between-group differences. Interestingly, there was no significant intra-group correlation between GCL density and either MD or FA of the dentate gyrus. This suggests that changes in diffusion properties in the GCL are mainly driven by processes other than granule cell dendrites. Indeed, previous studies have reported the emergence of radial glial fibers in the GCL of epileptic animals, contributing to DWI metrics (Heinrich et al., 2006; Janz et al., 2017). While histological examinations remain the gold standard to study structural dynamics of neuronal networks in animal models, such longitudinal investigations require large numbers of animals in order to cover multiple time points (Bohlen et al., 2014; Richards et al., 2014; Suero-Abreu et al., 2014; Wu and Zhang, 2016). MRI offers the advantage of mapping cyto- and axonal architecture non-invasively (Calabrese et al., 2015), allowing longitudinal *in vivo* measurements in the same animals (Janz et al., 2017).

While it is clear that the spatial resolution of MRI cannot be expected to match that of histology, even when considering the ability of DWI to infer microstructural features occurring at the sub-voxel level, the identification of DWI biomarkers of neuropathological changes, particularly early in the course of epileptogenesis before first clinical manifestations, would be especially relevant. Our results show that diffusion parameters can be directly ascribed to microstructural features such as well-ordered neuronal cell layers and their respective cellular processes in pathologically altered tissue. It should however be noted that these findings are specific to the intrahippocampal kainate model and to MTLE. While this model has been extensively studied and mimics many of the histopathological and MR imaging features of human MTLE (Janz et al., 2017), it is clear that the modeling procedure notably involving an invasive intrahippocampal injection does not fully reflect the real situation in humans. Further studies will thus be required to determine to which extent the results are applicable to other types and models of epilepsy, and ultimately to human epilepsy patients. While investigating the relevance of DWI as an early biomarker in humans before the emergence of the first clinical symptoms would require extensive long-term prospective studies, a more accessible alternative would be the examination of resection samples in patients having undergone epilepsy surgery, which is also amenable to histological comparisons (Janz et al., 2017). This could provide first indications on the feasibility of detecting pathological microstructural alterations in human patients and could also guide the development of MR imaging protocols that would be ultimately applicable *in vivo*. Moreover, while the current study employed a simple mono-exponential diffusion model emphasizing typical features such as the orientation and amplitude of the diffusivity, more complex diffusion models have shown great potential in inferring even more details about the underlying microstructure of the imaged tissue (Bonilha et al., 2015; Gatto et al., 2019). An investigation of the benefits of this additional information would be well worth pursuing.

CONCLUSION

We investigated fixed specimens of mouse brain tissue, which allowed the same tissue slices to be imaged using various MR protocols as well as subsequent fluorescence microscopy to achieve maximum comparability. The results show that high-resolution DWI parameters are associated with specific features of cellular architecture and neurodegeneration in MTLE.

The next step will be to monitor the described MR biomarkers in longitudinal studies to characterize the temporal evolution of these neuropathological cellular processes during epileptogenesis. In humans, *in vivo* measurements at sub-millimeter resolutions are gradually becoming more common (Yassa et al., 2010; Van Veluw et al., 2013; Chang et al., 2015) and a better understanding of the relation between MR signals and cellular-level microstructural effects will be of high relevance for clinical diagnostics.

DATA AVAILABILITY STATEMENT

The datasets generated for this study are available upon request to the corresponding author.

ETHICS STATEMENT

The animal study was reviewed and approved by the regional council (Regierungspräsidium Freiburg) and local animal welfare officer, according to the German animal protection act.

AUTHOR CONTRIBUTIONS

KG-G, JG, RK, JH, JK, CH, and PL: conceived and designed the study. KG-G, JL, and DE: designed the MR protocols and performed MR data acquisition. KG-G and PL: MR data analysis. RK and JK: designed and manufactured hardware used in the study. JG and CH: performed animal handling, tissue

preparation, and histological examination. KG-G, JG, CH, and PL: interpreted the data and wrote the manuscript. All authors read and approved the final manuscript.

The article processing charge was funded by the Baden-Wuerttemberg Ministry of Science, Research and Art and University of Freiburg in the funding programme Open Access Publishing.

FUNDING

This work was supported by BrainLinks-BrainTools, Cluster of Excellence funded by the German Research Foundation [DFG, grant number EXC 1086] and ERC grant number 290586.

SUPPLEMENTARY MATERIAL

The Supplementary Material for this article can be found online at: https://www.frontiersin.org/articles/10.3389/fnins.2020.00543/full#supplementary-material

REFERENCES

Assaf, B. A., Mohamed, F. B., Abou-Khaled, K. J., Williams, J. M., Yazeji, M. S., Haselgrove, J., et al. (2003). Diffusion tensor imaging of the hippocampal formation in temporal lobe epilepsy. *Am. J. Neuroradiol.* 24, 1857–1862.

Birkl, C., Langkammer, C., Golob-Schwarzl, N., Leoni, M., Haybaeck, J., Goessler, W., et al. (2016). Effects of formalin fixation and temperature on mr relaxation times in the human brain. *NMR Biomed.* 29, 458–465. doi: 10.1002/nbm.3477

Blümcke, I. M., Thom, E., Aronica, D. D., Armstrong, F., Bartolomei, A., Bernasconi, N. B., et al. (2013). International consensus classification of hippocampal sclerosis in temporal lobe epilepsy: a task force report from the ilae commission on diagnostic methods. *Epilepsia* 54, 1315–1329. doi: 10.1111/epi.12220

Bohlen, U. H., Von, O., Lotze, M., and Pfannmöller, J. P. (2014). Post-Mortem magnetic resonance microscopy (MRM) of the murine brain at 7 tesla results in a gain of resolution as compared to in vivo MRM. *Front. Neuroanat.* 8:47. doi: 10.3389/fnana.2014.00047

Bonilha, L., Lee, C. Y., Jensen, J. H., Tabesh, A., Spampinato, M. V., Edwards, J. C., et al. (2015). Altered microstructure in temporal lobe epilepsy: a diffusional kurtosis imaging study. *AJNR Am. J. Neuroradiol.* 36, 719–724. doi: 10.3174/ajnr.A4185

Bouilleret, V., Ridoux, V., Depaulis, A., Marescaux, C., Nehlig, A., Gal, G. L., et al. (1999). Recurrent seizures and hippocampal sclerosis following intrahippocampal kainate injection in adult mice: electroencephalography, histopathology and synaptic reorganization similar to mesial temporal lobe epilepsy. *Neuroscience* 89, 717–729. doi: 10.1016/s0306-4522(98)00401-1

Budde, M. D., and Frank, J. A. (2012). Examining brain microstructure using structure tensor analysis of histological sections. *Neuroimage* 63, 1–10. doi: 10.1016/j.neuroimage.2012.06.042

Calabrese, E., Badea, A., Cofer, G., Qi, Y., and Johnson, G. A. (2015). A Diffusion MRI tractography connectome of the mouse brain and comparison with neuronal tracer data. *Cerebral Cortex* 25:bhv121. doi: 10.1093/cercor/bhv121

Chang, H.-C. M., Sundman, L., Petit, S., Guhaniyogi, M.-L., Chu, C., Petty, A. W., et al. (2015). Human brain diffusion tensor imaging at submillimeter isotropic resolution on a 3tesla clinical MRI scanner. *Neuroimage* 118, 667–675. doi: 10.1016/j.neuroimage.2015.06.016

Engel, J. (1996). Introduction to temporal lobe epilepsy. *Epilepsy Res.* 26, 141–150.

Feng, G., Mellor, R. H., Bernstein, M., Keller-Peck, C., Nguyen, Q. T., Wallace, M., et al. (2000). Imaging neuronal subsets in transgenic mice expressing multiple spectral variants of GFP. *Neuron* 28, 41–51. doi: 10.1016/s0896-6273(00)00084-2

Fisher, R. S., Van Emde Boas, W., Blume, W., Elger, C., Genton, P., Lee, P., et al. (2005). Epileptic seizures and epilepsy: definitions proposed by the international league against epilepsy (ILAE) and the international bureau for epilepsy (IBE). *Epilepsia* 46, 470–472. doi: 10.1111/j.0013-9580.2005.66104.x

Flint, J., Hansen, B., Vestergaard-Poulsen, P., and Blackband, S. J. (2009). Diffusion weighted magnetic resonance imaging of neuronal activity in the hippocampal slice model. *Neuroimage* 46, 411–418. doi: 10.1016/j.neuroimage.2009.02.003

Flint, J. J., Hansen, B., Fey, M., Schmidig, D., King, M. A., Vestergaard-Poulsen, P., et al. (2010). Cellular-level diffusion tensor microscopy and fiber tracking in mammalian nervous tissue with direct histological correlation. *Neuroimage* 52, 556–561. doi: 10.1016/j.neuroimage.2010.04.031

Gatto, R. G., Amin, M., Finkielsztein, A., Weissmann, C., Barrett, T., Lamoutte, C., et al. (2019). Unveiling early cortical and subcortical neuronal degeneration in ALS mice by ultra-high field diffusion MRI. *Amyotr. Later. Scler Front. Degener* 20, 549–561. doi: 10.1080/21678421.2019.1620285

Guilfoyle, D. N., Helpern, J. A., and Lim, K. O. (2003). Diffusion tensor imaging in fixed brain tissue at 7.0 T. *NMR Biomed.* 16, 77–81. doi: 10.1002/nbm.814

Haas, C. A., Dudeck, O., Kirsch, M., Huszka, C., Kann, G., Pollak, S., et al. (2002). Role for reelin in the development of granule cell dispersion in temporal lobe epilepsy. *J. Neurosci.* 22, 5797–5802. doi: 10.1523/JNEUROSCI.22-14-05797.2002

Hansen, B., Flint, J. J., Heon-Lee, C., Fey, M., Vincent, F., King, M. A., et al. (2011). Diffusion tensor microscopy in human nervous tissue with quantitative correlation based on direct histological comparison. *Neuroimage* 57, 1458–1465. doi: 10.1016/j.neuroimage.2011.04.052

Häussler, U., Bielefeld, L., Froriep, U. P., Wolfart, J., and Haas, C. A. (2012). Septotemporal position in the hippocampal formation determines epileptic and neurogenic activity in temporal lobe epilepsy. *Cerebral Cortex (New York, N.Y.)* 22, 26–36. doi: 10.1093/cercor/bhr054

Häussler, U., Rinas, K., Kilias, A., Egert, U., and Haas, C. A. (2016). Mossy fiber sprouting and pyramidal cell dispersion in the hippocampal CA2 region in a mouse model of temporal lobe epilepsy. *Hippocampus* 26, 577–588. doi: 10.1002/hipo.22543

Heinrich, C., Lähteinen, S., Suzuki, F., Anne-Marie, L., Huber, S., Häussler, U., et al. (2011). Increase in BDNF-mediated trkb signaling promotes epileptogenesis in a mouse model of mesial temporal lobe epilepsy. *Neurobiol. Dis.* 42, 35–47. doi: 10.1016/j.nbd.2011.01.001

Heinrich, C., Nitta, N., Flubacher, A., Müller, M., Fahrner, A., Kirsch, M., et al. (2006). Reelin deficiency and displacement of mature neurons, but not neurogenesis, underlie the formation of granule cell dispersion in the epileptic hippocampus. *J. Neurosci.* 26, 4701–4713. doi: 10.1523/JNEUROSCI.5516-05.2006

Immonen, R. J., Kharatishvili, I., Sierra, A., Einula, C., Pitkänen, A., and Gröhn, O. H. J. (2008). Manganese enhanced MRI detects mossy fiber sprouting rather than neurodegeneration. Gliosis or seizure-activity in the epileptic rat hippocampus. *Neuroimage* 40, 1718–1730. doi: 10.1016/j.neuroimage.2008.01.042

Janz, P., Schwaderlapp, N., Heining, K., Häussler, U., Von Elverfeldt, J. G. K. D., Hennig, J., et al. (2017). Early tissue damage and microstructural reorganization predict disease severity in experimental epilepsy. *ELife* 6:e25742. doi: 10.7554/eLife.25742

Kharatishvili, I., Shan, Z. Y., She, D. T., Nyoman, S. F., and Reutens, D. C. (2014). MRI changes and complement activation correlate with epileptogenicity in a mouse model of temporal lobe epilepsy. *Brain Struct. Funct.* 219, 683–706. doi: 10.1007/s00429-013-0528-4

Laitinen, T., Sierra, A., Pitkänen, A., and Gröhn, O. (2010). Diffusion tensor MRI of axonal plasticity in the rat hippocampus. *Neuroimage* 51, 521–530. doi: 10.1016/j.neuroimage.2010.02.077

Liacu, D., Marco De, G., Ducreux, D., Bouilleret, V., Masnou, P., and Idy-Peretti, I. (2010). Diffusion tensor changes in epileptogenic hippocampus of TLE patients. *Neurophysiol. Clin. Clin. Neurophysiol.* 40, 151–157. doi: 10.1016/j.neucli.2010.01.003

Marx, M., Haas, C. A., and Häussler, U. (2013). Differential vulnerability of interneurons in the epileptic hippocampus. *Front. Cell. Neurosci.* 7:167. doi: 10.3389/fncel.2013.00167

Ong, H. H., and Wehrli, F. W. (2010). Quantifying axon diameter and intracellular volume fraction in excised mouse spinal cord with q-space imaging. *Neuroimage* 51, 1360–1366. doi: 10.1016/j.neuroimage.2010.03.063

Ong, H. H., Wright, A. C., Wehrli, S. L., Souza, A., Eric, D. S., Scott, N. H., et al. (2008). Indirect measurement of regional axon diameter in excised mouse spinal cord with Q-space imaging: simulation and experimental studies. *Neuroimage* 40, 1619–1632. doi: 10.1016/j.neuroimage.2008.01.017

Ono, T., and Galanopoulou, A. S. (2012). Epilepsy and epileptic syndrome. *Adv. Exp. Med. Biol.* 724, 99–113. doi: 10.1007/978-1-4614-0653-2_8

Pallud, J., Häussler, U., Langlois, M., Hamelin, S., Devaux, B., Deransart, C., et al. (2011). Dentate gyrus and hilus transection blocks seizure propagation and granule cell dispersion in a mouse model for mesial temporal lobe epilepsy. *Hippocampus* 21, 334–343. doi: 10.1002/hipo.20795

Pirttilä, T. R., Pitkänen, A., Tuunanen, J., and Kauppinen, R. A. (2001). Ex vivo MR microimaging of neuronal damage after kainate-induced status epilepticus in rat: correlation with quantitative histology. *Magnet. Reson. Med.* 46, 946–954. doi: 10.1002/mrm.1281

Purea, A., and Webb, A. G. (2006). Reversible and irreversible effects of chemical fixation on the NMR properties of single cells. *Magnet. Reson. Med.* 56, 927–931. doi: 10.1002/mrm.21018

Reisert, M., Mader, I., Anastasopoulos, C., Weigel, M., Schnell, S., and Kiselev, V. (2011). Global fiber reconstruction becomes practical. *Neuroimage* 54, 955–962. doi: 10.1016/j.neuroimage.2010.09.016

Riban, V., Bouilleret, V., Pham-Lê, B. T., Fritschy, J.-M., Marescaux, C., and Depaulis, A. (2002). Evolution of hippocampal epileptic activity during the development of hippocampal sclerosis in a mouse model of temporal lobe epilepsy. *Neuroscience* 112, 101–111. doi: 10.1016/s0306-4522(02)00064-7

Richards, K., Calamante, F., Tournier, J.-D., Kurniawan, N. D., Sadeghian, F., Retchford, A. R., et al. (2014). Mapping somatosensory connectivity in adult mice using diffusion MRI tractography and super-resolution track density imaging. *Neuroimage* 102(Pt 2), 381–392. doi: 10.1016/j.neuroimage.2014.07.048

Richardson, S., Siow, B., Panagiotaki, E., Schneider, T., Lythgoe, M. F., and Alexander, D. C. (2014). Viable and fixed white matter: diffusion magnetic resonance comparisons and contrasts at physiological temperature. *Magnet. Reson. Med.* 72, 1151–1161. doi: 10.1002/mrm.25012

Rutland, J. W., Feldman, R. E., Delman, B. N., Panov, F., Fields, M. C., Marcuse, L. V., et al. (2018). Subfield-specific tractography of the hippocampus in epilepsy patients at 7 tesla. *Seizure* 62, 3–10. doi: 10.1016/j.seizure.2018.09.005

Schmierer, K., Wheeler-Kingshott, C. A. M., Tozer, D. J., Boulby, P. A., Parkes, H. G., Yousry, T. A., et al. (2008). Quantitative magnetic resonance of postmortem multiple sclerosis brain before and after fixation. *Magne. Resona. Med.* 59, 268–277. doi: 10.1002/mrm.21487

Shepherd, T. M., Ozarslan, E., King, M. A., Mareci, T. H., and Blackband, S. J. (2006). Structural insights from high-resolution diffusion tensor imaging and tractography of the isolated rat hippocampus. *Neuroimage* 32, 1499–1509. doi: 10.1016/j.neuroimage.2006.04.210

Shepherd, T. M., Ozarslan, E., Yachnis, A. T., King, M. A., and Blackband, S. J. (2007). Diffusion tensor microscopy indicates the cytoarchitectural basis for diffusion anisotropy in the human hippocampus. *Am. J. Neuroradiol.* 28, 958–964.

Siddiqui, A. H., and Joseph, S. A. (2005). CA3 axonal sprouting in kainate-induced chronic epilepsy. *Brain Res.* 1066, 129–146. doi: 10.1016/j.brainres.2005.10.066

Sierra, A., Laitinen, T., Gröhn, O., and Pitkänen, A. (2015). Diffusion tensor imaging of hippocampal network plasticity. *Brain Struct. Funct.* 220, 781–801. doi: 10.1007/s00429-013-0683-7

Smith, S. M., Jenkinson, M., Woolrich, M. W., Beckmann, C. F., Behrens, T. E. J., Johansen-Berg, H., et al. (2004). Advances in functional and structural MR image analysis and implementation as FSL. *Neuroimage* 23(Suppl. 1), S208–S219. doi: 10.1016/j.neuroimage.2004.07.051

Stefanits, H., Springer, E., Pataraia, E., Baumgartner, C., Hainfellner, J. A., Prayer, D., et al. (2017). Seven-tesla MRI of hippocampal sclerosis: an in vivo feasibility study with histological correlations. *Investigat. Radiol.* 52, 666–671. doi: 10.1097/RLI.0000000000000388

Suero-Abreu, G. A., Raju, G. P., Aristizábal, O., Volkova, E., Wojcinski, A., Houston, E. J., et al. (2014). In vivo mn-enhanced mri for early tumor detection and growth rate analysis in a mouse medulloblastoma model. *Neoplasia (New York, N.Y.)* 16, 993–1006. doi: 10.1016/j.neo.2014.10.001

Suzuki, F., Heinrich, C., Boehrer, A., Mitsuya, K., Kurokawa, K., Matsuda, M., et al. (2005). Glutamate receptor antagonists and benzodiazepine inhibit the progression of granule cell dispersion in a mouse model of mesial temporal lobe epilepsy. *Epilepsia* 46, 193–202. doi: 10.1111/j.0013-9580.2005.35504.x

Suzuki, F., Junier, M. P., Guilhem, D., Sørensen, J. C., and Onteniente, B. (1995). Morphogenetic effect of kainate on adult hippocampal neurons associated with a prolonged expression of brain-derived neurotrophic factor. *Neuroscience* 64, 665–674. doi: 10.1016/0306-4522(94)00463-f

Thom, M., Sisodiya, S. M., Beckett, A., Martinian, L., Lin, W.-R., Harkness, W., et al. (2002). Cytoarchitectural abnormalities in hippocampal sclerosis. *J. Neuropathol. Exp. Neurol.* 61, 510–519.

Van Veluw, S. J., Wisse, L. E. M., Kuijf, H. J., Spliet, W. G. M., Hendrikse, J., Luijten, P. R., et al. (2013). Hippocampal T2 hyperintensities on 7 Tesla MRI. *Neuroimage Clin.* 3, 196–201. doi: 10.1016/j.nicl.2013.08.003

Wu, D., and Zhang, J. (2016). In vivo mapping of macroscopic neuronal projections in the mouse hippocampus using high-resolution diffusion MRI. *Neuroimage* 125, 84–93. doi: 10.1016/j.neuroimage.2015.10.051

Yassa, M. A., Muftuler, L. T., and Stark, C. E. L. (2010). Ultrahigh-resolution microstructural diffusion tensor imaging reveals perforant path degradation in aged humans in vivo. *Proc. Natl. Acad. Sci. U.S.A.* 107, 12687–12691. doi: 10.1073/pnas.1002113107

Zhang, J., Peter Van, Z. C. M., and Mori, S. (2002). Three-dimensional diffusion tensor magnetic resonance microimaging of adult mouse brain and hippocampus. *Neuroimage* 15, 892–901. doi: 10.1006/nimg.2001.1012

Conflict of Interest: The authors declare that the research was conducted in the absence of any commercial or financial relationships that could be construed as a potential conflict of interest.

Copyright © 2020 Göbel-Guéniot, Gerlach, Kamberger, Leupold, von Elverfeldt, Hennig, Korvink, Haas and LeVan. This is an open-access article distributed under the terms of the Creative Commons Attribution License (CC BY). The use, distribution or reproduction in other forums is permitted, provided the original author(s) and the copyright owner(s) are credited and that the original publication in this journal is cited, in accordance with accepted academic practice. No use, distribution or reproduction is permitted which does not comply with these terms.

frontiers in Neuroscience

ORIGINAL RESEARCH
published: 16 June 2020
doi: 10.3389/fnins.2020.00622

Improved Visualization of Focal Cortical Dysplasia With Surface-Based Multiparametric Quantitative MRI

*Michelle Maiworm[1,2,3,4], Ulrike Nöth[3,4], Elke Hattingen[2,4], Helmuth Steinmetz[1,4], Susanne Knake[4,5], Felix Rosenow[1,4,6], Ralf Deichmann[3,4], Marlies Wagner[2,4] and René-Maxime Gracien[1,3,4]**

[1] Department of Neurology, Goethe University, Frankfurt, Germany, [2] Department of Neuroradiology, Goethe University, Frankfurt, Germany, [3] Brain Imaging Center, Goethe University, Frankfurt, Germany, [4] Center for Personalized Translational Epilepsy Research Consortium (CePTER), Frankfurt, Germany, [5] Department of Neurology, Philipps University of Marburg, Marburg, Germany, [6] Epilepsy Center Frankfurt Rhine-Main, Center of Neurology and Neurosurgery, Goethe University, Frankfurt, Germany

OPEN ACCESS

Edited by:
Alard Roebroeck, Maastricht University, Netherlands

Reviewed by:
Pierre Besson, Northwestern University, United States
Stefan Schob, Universitätsklinikum Leipzig, Germany

***Correspondence:**
René-Maxime Gracien
Rene-Maxime.Gracien@kgu.de

Specialty section:
This article was submitted to Brain Imaging Methods, a section of the journal Frontiers in Neuroscience

Received: *15 April 2020*
Accepted: *19 May 2020*
Published: *16 June 2020*

Citation:
Maiworm M, Nöth U, Hattingen E, Steinmetz H, Knake S, Rosenow F, Deichmann R, Wagner M and Gracien R-M (2020) Improved Visualization of Focal Cortical Dysplasia With Surface-Based Multiparametric Quantitative MRI. Front. Neurosci. 14:622. doi: 10.3389/fnins.2020.00622

Purpose: In the clinical routine, detection of focal cortical dysplasia (FCD) by visual inspection is challenging. Still, information about the presence and location of FCD is highly relevant for prognostication and treatment decisions. Therefore, this study aimed to develop, describe and test a method for the calculation of synthetic anatomies using multiparametric quantitative MRI (qMRI) data and surface-based analysis, which allows for an improved visualization of FCD.

Materials and Methods: Quantitative T1-, T2- and PD-maps and conventional clinical datasets of patients with FCD and epilepsy were acquired. Tissue segmentation and delineation of the border between white matter and cortex was performed. In order to detect blurring at this border, a surface-based calculation of the standard deviation of each quantitative parameter (T1, T2, and PD) was performed across the cortex and the neighboring white matter for each cortical vertex. The resulting standard deviations combined with measures of the cortical thickness were used to enhance the signal of conventional FLAIR-datasets. The resulting synthetically enhanced FLAIR-anatomies were compared with conventional MRI-data utilizing regions of interest based analysis techniques.

Results: The synthetically enhanced FLAIR-anatomies showed higher signal levels than conventional FLAIR-data at the FCD sites ($p = 0.005$). In addition, the enhanced FLAIR-anatomies exhibited higher signal levels at the FCD sites than in the corresponding contralateral regions ($p = 0.005$). However, false positive findings occurred, so careful comparison with conventional datasets is mandatory.

Conclusion: Synthetically enhanced FLAIR-anatomies resulting from surface-based multiparametric qMRI-analyses have the potential to improve the visualization of FCD and, accordingly, the treatment of the respective patients.

Keywords: epilepsy, focal cortical dysplasia, quantitative magnetic resonance imaging, neuroimaging, brain imaging

INTRODUCTION

Focal cortical dysplasia (FCD) is a developmental cortical malformation with a high epileptogenic potential, often causing drug-refractory epilepsy (Gaitanis and Donahue, 2013). Accordingly, surgical treatment is often required for these patients. Diagnostics and pre-surgical evaluation include MRI to identify the FCD and estimate its extent and localization. This information is crucial as the complete resection of the lesion is an important factor for postsurgical outcome (Fauser et al., 2004; Lerner et al., 2009; Kabat and Król, 2012).

Typical MRI features of FCD include a blurring of the junction between cortical gray matter (GM) and white matter (WM), a thickening of the cortical layer, hyperintensities in subcortical WM in T2-weighted datasets and abnormal patterns of gyri and sulci (Colombo et al., 2003; Kabat and Król, 2012). However, MR-changes are often subtle and detection and evaluation of the location and extent of the lesions can be challenging with conventional MRI-techniques (Colombo et al., 2003; Kabat and Król, 2012; Hong et al., 2016). Still, clinicians need this information for treatment decisions.

Thus, post-processing techniques for conventional MRI-data have been developed to optimize the visualization of FCD. Methods described by Kassubek et al. (2002) and Huppertz et al. (2005) analyze the junction between GM and WM and the extension of the GM by normalizing T1-weighted datasets of patients with epilepsy to allow for a comparison with a control cohort. Furthermore, machine learning was used in a previous study for automated FCD detection, analyzing conventional MRI parameters (Hong et al., 2014).

Approaches using conventional MRI-data usually require steps for intensity-standardization. In contrast to conventional MRI-techniques, quantitative MRI (qMRI) measures tissue-parameters such as the T1- and T2-relaxation times or the proton density (PD) free from hardware-effects (Cercignani et al., 2018) and the resulting inhomogeneities. Accordingly, qMRI could serve as a promising basis for FCD-visualization. Nöth et al. (2020) developed a method for FCD-detection based solely on quantitative T1-data and on voxel-wise analysis of the whole brain.

In the present preliminary technical study, it was aimed to develop a method which allows for an improved visualization of FCD, using a multimodal qMRI-approach. The potential advantage is that the technique integrates information from different complementary parameters (T1, T2, and PD). The method utilizes a reconstruction of WM and pial surfaces and boundary-based analysis techniques which integrate information about the course and orientation of the WM and pial surfaces when reading parameter values and measuring the cortical thickness. The results of the calculation are used to highlight FCD areas in FLAIR datasets. As a consequence, this method has the potential to aid visual assessment of image data, thus helping to reduce the number of undetected lesions, potentially allowing for a more effective treatment.

In summary, the purpose of this study was to develop and describe the method, to show representative data and to quantify the improvement in image contrast via comparison with conventional MRI datasets, using a regions of interest (ROI) based analysis.

Abbreviations: CSF, cerebrospinal fluid; FCD, focal cortical dysplasia; FLAIR, fluid-attenuated inversion recovery; GE, gradient echo; GM, gray matter; ILAE, international league against epilepsy; MP-RAGE, magnetization-prepared rapid gradient-echo; PD, proton density; qMRI, quantitative MRI; RCP, receive coil profile; RF, radiofrequency; ROI, region of interest; SD, standard deviation; VFA, variable flip angle; WM, white matter.

MATERIALS AND METHODS

Participants

MRI-acquisition was performed for 10 patients with neuroradiologically diagnosed FCD based on clinical MRI-data (three females, age: range 18–55 years, mean ± SD: 29.6 ± 11.7 years) and five healthy subjects (three females, age: range 19–34 years, mean ± SD: 24.4 ± 5.1 years). The studies involving human participants were reviewed and approved by the respective local board (Ethik-Kommission des Fachbereichs Medizin des Universitätsklinikums der Goethe-Universität). The patients/participants provided written informed consent to participate in this study. The study was performed according to the principles formulated in the Declaration of Helsinki.

The investigated cohort and the data obtained overlap with a previous study presenting a different method for FCD-detection based solely on T1-maps and on a voxel-wise analysis across the whole brain (Nöth et al., 2020). In the current study, a completely different approach is described which utilizes multiparametric qMRI data and a surface-based analysis. Furthermore, some data obtained on subjects with FCD overlap with previous studies with different aims evaluating improved synthetic T1-weighted datasets for tissue-segmentation (Gracien et al., 2019) and assessing normal-appearing cortical tissue in patients with FCD via T2-relaxometry (Ahmad et al., 2020).

Data Acquisition and qMRI-Mapping

A 3 Tesla (T) MRI-scanner "Magnetom TRIO" (Siemens Medical Solutions, Erlangen, Germany) was used for data acquisition. Signal reception was performed with an 8-channel phased-array head coil and radiofrequency (RF) transmission with a body coil.

Functions included in MatLab (MathWorks, Natick, MA, United States), the FMRIB-Software-Library version 5.0.7 (FSL, Oxford) (Smith et al., 2004) and FreeSurfer version 6.0.1 (Athinoula A. Martinos Center for Biomedical Imaging, Boston) (Fischl et al., 2004) were used for analysis.

For B0 mapping, two gradient echo (GE)-datasets with different TE were acquired and processed with FSL PRELUDE and FUGUE: TE [1,2] = [4.89 ms,7.35 ms], TR = 560 ms, bandwidth = 200 Hz/pixel, field of view (FoV): 256 × 224 mm^2, matrix size: 64 × 56, isotropic resolution = 4 mm, 40 sagittal slices (thickness: 4 mm, no gap), $\alpha = 60°$, duration: 1:03 min.

B1-mapping was performed as reported in the literature (Volz et al., 2010). In summary, two GE-datasets were recorded (reference and magnetization prepared). The magnetization preparation consisted in an RF-pulse rotating the longitudinal magnetization by an angle β (nominal value: $\beta_0 = 45°$), followed by a gradient spoiler. Thus, comparison of this dataset with the reference-data allows for the determination of the local β and B1 follows from deviations of β from β_0. The other parameters were: TE = 5 ms, TR = 11 ms, $\alpha = 11°$, bandwidth = 260 Hz/pixel, FoV, resolution and volume coverage as for B0-mapping, duration: 0:53 min.

For voxel-wise mapping of T1, the variable flip angle (VFA) method was used (Venkatesan et al., 1998), acquiring two spoiled GE-datasets at different excitation angles $\alpha_{1,2}$, resulting in different signal intensities (SI) in both datasets. The parameters were: TE = 6.7 ms, TR = 16.4 ms, $\alpha_{1,2} = [4°,24°]$, bandwidth = 222 Hz/pixel, FoV: 256 × 224 × 160 mm^3, matrix size: 256 × 224 × 160, isotropic resolution = 1 mm, same volume coverage as for B0 and B1-mapping, duration (for both datasets): 9:48 min. Plotting of $SI_i/\tan(\alpha_i)$ versus $SI_i/\sin(\alpha_i)$ allowed for the calculation of T1 (Venkatesan et al., 1998). The respective preliminary T1-maps were corrected for inhomogeneities of B0 and B1, and for insufficient spoiling of the transverse magnetization (Preibisch and Deichmann, 2009).

T2-mapping was based on the acquisition of four T2-weighted fast spin echo datasets with different TE: TE = [13,67,93,106] ms, TR = 10 s, refocusing angle = 160°, bandwidth = 176 Hz/pixel, FoV: 256 × 176 mm^2, matrix size: 256 × 176, 69 axial slices (thickness = 2 mm, no gap), spatial resolution = 1 × 1 × 2 mm^3, turbo factor: 13, duration per dataset: 1:32 min. Each dataset was acquired twice for subsequent averaging, yielding a total duration of 12:16 min. T2 was determined by exponential fitting of the TE-dependence of signal intensities in the four averaged datasets and corrected for the influence of stimulated echoes as described in the literature (Nöth et al., 2017).

For PD-mapping, a method described in the literature (Volz et al., 2012a) was used. To this aim, the PD-weighted datasets resulting from the VFA-acquisition with the lower excitation angle were corrected for T1-, T2*- and B1-effects and for inhomogeneities of the receive-coil profile (RCP). For the correction of signal-losses in the VFA-data induced by T2*-relaxation effects during the finite TE of 6.7 ms, two GE-datasets with different TE were acquired: TE [1,2] = [4.3 ms,11 ms], TR = 1336 ms, $\alpha = 50°$, bandwidth = 292 Hz/pixel, FoV: 256 × 224 mm^2, matrix-size: 128 × 112, 80 sagittal slices (thickness: 2 mm, no gap), same volume coverage as for B0-, B1-, and T1-mapping, isotropic resolution = 2 mm, duration for both datasets: 5 min.

Synthetic T1-weighted magnetization-prepared rapid gradient-echo (MP-RAGE) anatomies were obtained as described previously (Gracien et al., 2019), using B0-corrected T1-maps and pseudo-PD-maps derived from T1-data via the Fatouros equation (Fatouros et al., 1991; Volz et al., 2012b). The virtual acquisition-parameters assumed for the synthetic data were: TR = 1900 ms, TI = 900 ms, $\alpha = 9°$, echo-spacing = 8.1 ms. All geometrical parameters (FoV, matrix size, spatial resolution, volume coverage) were identical to the respective parameters of the underlying T1-maps.

Additional conventional MRI-acquisitions comprised MP-RAGE (Mugler and Brookeman, 1990) and FLAIR-datasets obtained with the following parameters:

MP-RAGE: TE = 3.04 ms, TR = 1900 ms, TI = 900 ms, $\alpha = 9°$, bandwidth = 170 Hz/pixel, FoV: 256 × 256 × 192 mm^3, matrix-size: 256 × 256 × 192, isotropic resolution = 1 mm, duration 4:28 min.

FLAIR: TE = 353 ms, TR = 5000 ms, TI = 1800 ms, bandwidth = 930 Hz/pixel, FoV: 256 × 220 × 160 mm^3, matrix size: 256 × 220 × 160, isotropic resolution = 1 mm, duration 7:12 min.

All datasets were inspected by a senior neuroradiologist and by an experienced neurologist to assure absence of artifacts, e.g., related to subject movement.

Method for Improved FCD-Detection

Segmentation of the cerebral cortex and WM, identification of the boundary between WM and the cortex and measurement of the cortical thickness were conducted by applying the Freesurfer script "recon-all" to the synthetic MP-RAGE-data.

Since a previous study has shown that data smoothing facilitates FCD-detection (House et al., 2013), the method for FCD-detection described below was performed twice, using either the original qMRI maps or smoothed versions of these maps as input data. For each map (T1, PD or T2), smoothing was performed separately for WM- and non-WM-voxels with a subsequent combination of the smoothed subparts. To this aim, the WM-masks computed via Freesurfer and the corresponding non-WM-masks, obtained by logical negation of the WM-masks, were applied to the qMRI-maps for each subject to isolate WM and non-WM voxels. To further improve the non-WM T1- and PD-maps and the respective masks, voxels with T1-values above 2000 ms were excluded, since GM T1-values range from 1200 to 1600 ms (Volz et al., 2012a). This step reduces partial volume effects with CSF. For the same reason, voxels with T2-values above 300 ms (Gracien et al., 2016) were eliminated from the non-WM T2-maps and masks. To avoid edge errors by including zero voxels in the smoothing process, an edge preserving algorithm was used: both the respective qMRI-map (WM or non-WM) and its corresponding mask were smoothed separately (kernel with full width at half maximum of 1.5 mm), calculating subsequently the quotient (smoothed map divided by smoothed mask). Voxels outside of the respective masks were excluded. Finally, voxels of the WM- and non-WM maps were recombined.

The following algorithm was applied twice with different input data, using either the original qMRI-maps or smoothed versions of these maps:

After boundary-based coregistration of the T2-maps to the synthetic MP-RAGE-anatomies with BBRegister, original or smoothed versions of the qMRI-maps were used to obtain values of the three investigated parameters (T1, T2, PD) at four different positions:

(i) Inside the cortex, avoiding areas close to the inner and outer cortex boundary. For this purpose, the cortex was subdivided into layers which were labeled according to their respective positions inside the cortex, given in percent of the cortical thickness (0% corresponding to the WM/cortex-boundary and 100% to the outer surface of the cortex). This subdivision was performed with a resolution of 1%. Only qMRI values from layers between the 20% and the 40% mark were read and averaged.

(ii) Inside the cortex, from layers between the 60 and 80% mark, as described above.

(iii, iv) At the corresponding positions in WM, mirroring the cortex at the WM/cortex-boundary.

Standard deviations (SD) of these four values were calculated for each qMRI-parameter, each cortical vertex, and each subject and were saved in surface-datasets. Furthermore, the cortical thickness (T) was obtained vertex-wise by applying Freesurfer to the synthetic MP-RAGE-anatomies. The SD-values and T were then combined according to the following formula in a surface-based analysis:

$$Q = \frac{SD(T1) \times SD(T2) \times SD(PD)}{T}$$

A representative surface-based Q-map is demonstrated in **Figure 1**. The low values (hot colors) above the lateral sulcus corresponded to the location of an FCD. **Figure 1** shows two different ranges for Q: 0–500 (top) and 0–1000 (bottom), the latter resulting in increased noise. Visual inspection revealed that FCD-areas are characterized by low *Q*-values. Thus, these datasets would already be suitable for visual FCD-detection. Still, as the Q-maps do not show anatomical information, they were rather used to enhance the signal in conventional FLAIR-datasets as described in the following paragraph.

To avoid zero-values for the subsequent division step, Q-values were increased by a minimal constant value of 0.0001. The surface-datasets were then projected into 3D-space with mri_surf2vol. To reduce effects of values above a threshold $Q_0 = 500$, which had been empirically chosen (cf. **Figure 1**), the datasets were filtered by calculating the quotient Q_0/Q, resulting in high or low values for $Q < Q_0$ or $Q > Q_0$, respectively. Very high values of the resulting quotient-maps above 1000 (corresponding to very low *Q*-values) were excluded to reduce artifacts in regions where cortical values cannot be read, such as areas of the medial hemispheres (corpus callosum and the third ventricle). Datasets were smoothed with a Gaussian kernel (sigma: 3 mm) and a constant value of 1.0 was added, resulting in the parameter R. The parameter R can be assumed to be approximately 1.0 in normal tissue and to be increased in FCD-areas (where Q is low). Thus, R is a suitable parameter for enhancing signal intensities in the clinical FLAIR-images.

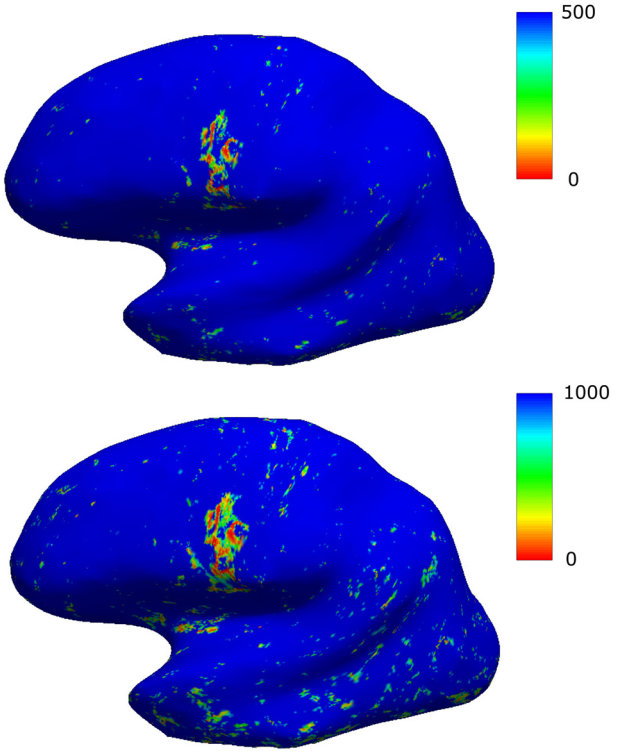

FIGURE 1 | Results of the surface-based analysis demonstrated for a representative patient. Two different scalings are presented, the scaling in the first row resulting in an improved signal-to-noise-ratio. The area with focally decreased values (hot colors) corresponds to the location of an FCD.

The R-map was obtained twice, either with (R_s) or without (R_u) initial smoothing. The average of both R-maps was then multiplied with the conventional FLAIR-anatomy, which had previously been coregistered to the synthetic MP-RAGE-dataset, yielding signal enhancement in FCD-areas.

For an analysis of signal intensities, ROIs with the dimensions $2 \times 2 \times 1$ mm³ were manually chosen in the conventional FLAIR-datasets, representing regions where the FCDs are located and the corresponding contralateral cerebral control areas. ROIs were placed by an experienced neurologist and by a senior specialist in neuroradiology deciding by consensus. In these ROIs, mean values of signal intensities were read from the conventional and enhanced FLAIR-datasets, averaged across the group and compared via Wilcoxon tests. *P*-values below 0.05 were considered significant for all tests.

RESULTS

To visualize the effect of FCD (marked with an arrow) on quantitative parameter values at the WM/cortex-junction, **Figure 2** shows, for a representative patient, the result of the

tissue segmentation superimposed on the T2-map. The blue line indicates the junction between cortex and WM and the red line the cortical surface. At the localization of the FCD, subcortical T2-values are increased, as a result of a smooth WM/cortex-junction.

For the group of patients with epilepsy, signal intensities across the FCD-ROIs were higher in the enhanced FLAIR-datasets (mean ± standard error of the mean: 202.41 ± 45.90) than in the conventional FLAIR-datasets (77.38 ± 6.16, $p = 0.005$) and higher than in the corresponding contralateral regions in the enhanced FLAIR-data (55.22 ± 2.35, $p = 0.005$). The FCD-signal in the enhanced in comparison to the conventional datasets was increased in 9/10 patients (relative increase: 66.27 ± 16.19%, range 22.53–146.90%), while no relevant increase could be observed for one patient (0.80%).

The final enhanced anatomies generated with this method for improved visualization of FCD and three clinical gold standard datasets (Wellmer et al., 2013) are presented in **Figure 3** for four representative patients (rows), showing (from left to right) the conventional T2-weighted (TE = 67 ms), the FLAIR- and the MP-RAGE-datasets and the enhanced FLAIR-datasets. The subject in the first row corresponds to the subject shown in **Figure 2**. The FCD-areas are marked with arrows.

For the subjects shown in the first three rows, focal cortical (rows 1 and 2 in the conventional FLAIR-datasets, row 2 in the T2-weighted dataset) and subcortical (FLAIR/T2-weighted: rows 1 and 3) hyperintensities and cortical thickening (FLAIR/T2-weighted: row 2) were observed, indicative of FCD. Subcortical hypointensities (rows 1 and 3) and slight cortical thickening (rows 2 and 3) were observed in the conventional MP-RAGE datasets. For these three subjects, the signal intensity is strongly increased in the enhanced FLAIR-datasets in the FCD areas. The FCDs of the participants in the first and third row are clearly visible in the conventional MRI-datasets. In contrast, the lesion in the second row is less prominent. In this case, the strong signal in the enhanced dataset could help to guide the physician's eyes when analyzing the images.

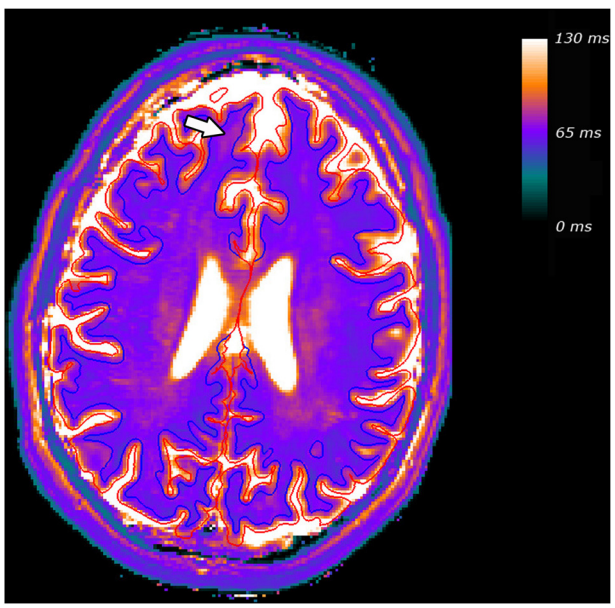

FIGURE 2 | Tissue segmentation for a representative patient, superimposed on the T2 map. The blue line indicates the junction between cortex and WM and the red line the cortical surface. The FCD and the resulting increased subcortical T2-values are marked with an arrow.

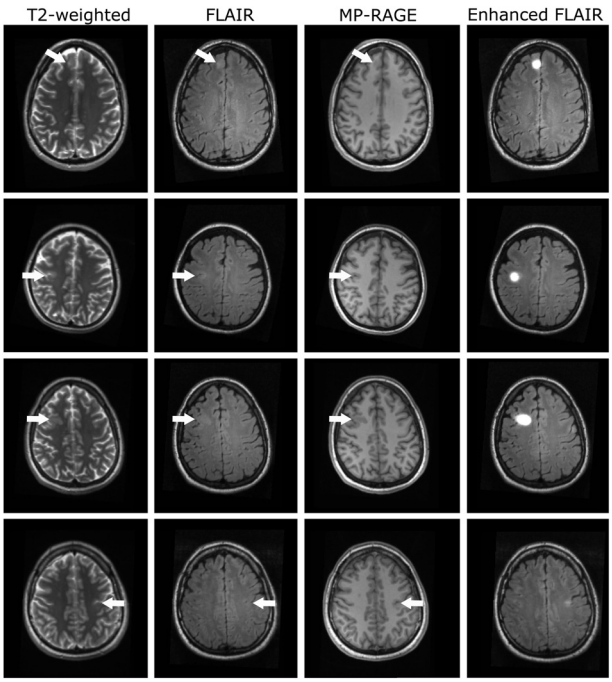

FIGURE 3 | Representative datasets of four patients with FCD (rows). From left to right: T2-weighted, FLAIR-, MP-RAGE- and enhanced FLAIR-datasets. Arrows indicate the locations of the FCDs.

For the subject in the last row of **Figure 3**, diagnosed with an FCD in the left praecentral sulcus, only subtle cortical thickening was visible in the MP-RAGE dataset and a slight hyperintensity in the conventional FLAIR-image. However, such subtle changes might be easily missed when assessing the conventional clinical data. In contrast, the stronger signal in the synthetically enhanced FLAIR-dataset as demonstrated in the fourth column is indicative of this FCD.

The patients, whose data are shown in the first and second row, underwent surgical resection of the lesions after data acquisition and analysis. Histopathological assessment revealed FCDs type IIa (row 1) and type IIb (row 2).

Some results, for which no correlate could be observed in the conventional clinical datasets, occurred both in patients and in the healthy control group. It is likely that most of these findings are false positive. Representative datasets of healthy subjects are presented in **Figure 4**: In particular, some false positive hyperintensities occurred in the enhanced FLAIR-images in regions where physiological properties such as closely spaced gyri result in a smooth WM/cortex-junction (**Figure 4**, first

row). Furthermore, despite B0 correction of T1-data, residual B0-effects affecting T1-quantification and the segmentation in basal regions, resulted in some false positive results. A representative example is displayed in **Figure 4** (second row).

DISCUSSION

The method presented in this preliminary technical study utilizes multiparametric qMRI-acquisition and surface-based analysis and combines assessment of the non-uniformity of qMRI-values across the junction between cortical GM and WM with vertex-wise measurements of the cortical thickness. This information is used to enhance the signal in conventional FLAIR-datasets in regions with a blurring at the WM/cortex-border or increased cortical thickness. We observed an increased signal in the enhanced FLAIR-datasets in regions where FCDs are located. Accordingly, the method might be helpful to visualize and detect FCD. Since the method was built utilizing the presented patients' data, a clinical evaluation of the method based on this group of patients would not be appropriate and was beyond the scope of this study.

Importantly, qMRI-maps are intrinsically corrected for hardware effects such as inhomogeneities of the static magnetic field B0, the transmitted RF field B1 and the RCP (Cercignani et al., 2018). The respective hardware-effects in conventional datasets are problematic for FCD-detection because they yield signal non-uniformities which may impair tissue segmentation or the analysis of properties of the cortex and of the WM/cortex-border. In particular, pooled data acquired with different hardware may display different signal non-uniformities, thus rendering the analysis more difficult and requiring appropriate correction procedures. When using conventional MRI-data for improved FCD-visualization, such effects can be reduced with intensity correction/normalization-procedures, but a complete elimination is problematic. Accordingly, the use of qMRI-data which are free from such hardware effects should be particularly advantageous for FCD-detection.

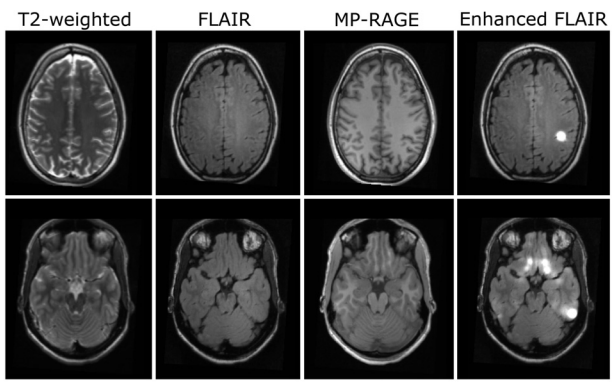

FIGURE 4 | Examples for artifacts in datasets of two healthy subjects (rows). From left to right: T2-weighted, FLAIR-, MP- RAGE-, and enhanced FLAIR-datasets.

A method using solely T1-data to derive maps of the cortical extent and of the smoothness at borders between WM and voxels with GM-characteristics was described recently (Nöth et al., 2020). In detail, T1-maps were used for a custom-built segmentation and creation of maps of the cortical extent. Furthermore, the T1-gradients at the WM/GM-border were calculated to generate maps for identification of regions with a blurring at this junction. The cortical extent and junction-maps were used to enhance the signal of synthetic DIR-datasets. While in the previous work the analysis was performed voxel-wise across the whole brain, the multiparametric method presented here is based on the reconstruction of the cortical and WM-surfaces. Another key difference is that the method presented here analyzes the junction between the cortex and the potentially abnormal WM, while the previous method creates a GM-characteristics-mask including GM and FCD-related abnormalities in WM and investigates the border between this mask and normal-appearing WM. Furthermore, junction- and thickness-analyses were combined in the present work to simplify the clinical assessment.

It should be noted that in the approach chosen here, the surface-datasets were first projected into 3D-space before smoothing was performed. A promising alternative approach which better respects the folded topology of the cortex (Lerch and Evans, 2005) would be to apply surface-based smoothing first. However, this approach is potentially problematic if an FCD is located on both sides of a sulcus. In this case, FCD-associated changes could be more closely spaced in 3D-space, forming a relatively compact area and thus high average *R*-values upon smoothing. In contrast, the FCD region might appear expanded in the surface-based dataset, which may reduce the effect of interest. Still, for further developments of the method, both approaches should be considered and tested.

In contrast to previous studies, the presented method enhances the signal of conventional FLAIR-datasets because clinicians are used to FLAIR-contrasts, which in general provide sufficient anatomical information for localization of the FCD. To pave the way of this method or other approaches toward the clinical application, future studies with larger cohorts will need to compare different methods to evaluate whether surface-based multimodal approaches are beneficial as compared to other techniques. These studies could also integrate diffusion tensor imaging (DTI) techniques to increase the sensitivity or to confirm the findings.

The method is not without limitations. As detailed in the results section, false positive findings may occur. Therefore, the enhanced datasets need to be compared carefully with conventional anatomies to confirm or reject each potential lesion. Furthermore, as the proposed method includes smoothing steps, the spatial extent of an FCD should not be estimated from the enhanced FLAIR-dataset, for example when planning surgical treatment. Since radiological evaluation of the presented method should not be based on the data used to develop the algorithm, future studies investigating different cohorts of FCD patients are required to evaluate the sensitivity and specificity of the method.

In summary, the presented multiparametric surface-based qMRI-method seems to be helpful to improve visualization of FCD. Accurate FCD-detection is of high relevance in the clinical routine because undetected lesions might in many cases result in wrong treatment decisions. Accordingly, the presented method might help to reduce false negative findings and improve the treatment of the respective FCD patients. Still, conventional anatomies remain the gold-standard for FCD-detection and the enhanced datasets should be carefully compared with routine datasets.

DATA AVAILABILITY STATEMENT

The datasets for this article are not available publicly or upon direct request because data sharing does not comply with the institutional ethics approval.

ETHICS STATEMENT

The studies involving human participants were reviewed and approved by the Ethik-Kommission des Fachbereichs Medizin des Universitätsklinikums der Goethe-Universität. The patients/participants provided their written informed consent to participate in this study.

AUTHOR CONTRIBUTIONS

UN, SK, FR, RD, MW, and, R-MG contributed to the conception and design of the study. MM, RD, MW, and R-MG organized the study. MM, MW, and R-MG executed the study and acquired the data. RD calculated the quantitative maps. MM and R-MG designed the presented method and performed the statistical analysis. MM and R-MG wrote the first draft of the manuscript. All authors reviewed the statistical analysis and the manuscript, contributed to the manuscript revision and approved the submitted version.

FUNDING

This work was supported by the State of Hesse with a LOEWE-Grant to the CePTER-Consortium (http://www.uni-frankfurt.de/67689811) and by the Clinician Scientists program at Goethe University Frankfurt. The sponsors did not influence the study design nor the collection, analysis or interpretation of data.

REFERENCES

Ahmad, R., Maiworm, M., Nöth, U., Seiler, A., Hattingen, E., Steinmetz, H., et al. (2020). Cortical changes in epilepsy patients with focal cortical dysplasia: new insights with T2 mapping. *J. Magn. Reson. Imaging* [Epub ahead of print]. doi: 10.1002/jmri.27184

Cercignani, M., Dowell, N. G., and Tofts, P. (eds) (2018). *Quantitative MRI of the Brain: Principles of Physical Measurement*. Boca Raton FL: CRC Press.

Colombo, N., Tassi, L., Galli, C., Citterio, A., Lo Russo, G., Scialfa, G., et al. (2003). Focal cortical dysplasias: MR imaging, histopathologic, and clinical correlations in surgically treated patients with epilepsy. *Am. J. Neuroradiol.* 24, 724–733.

Fatouros, P. P., Marmarou, A., Kraft, K. A., Inao, S., and Schwarz, F. P. (1991). In vivo brain water determination by T1 measurements: effect of total water content, hydration fraction, and field strength. *Magn. Reson. Med.* 17, 402–413. doi: 10.1002/mrm.1910170212

Fauser, S., Schulze-Bonhage, A., Honegger, J., Carmona, H., Huppertz, H.-J., Pantazis, G., et al. (2004). Focal cortical dysplasias: surgical outcome in 67 patients in relation to histological subtypes and dual pathology. *Brain* 127, 2406–2418. doi: 10.1093/brain/awh277

Fischl, B., Salat, D. H., van der Kouwe, A. J., Makris, N., Ségonne, F., Quinn, B. T., et al. (2004). Sequence-independent segmentation of magnetic resonance images. *Neuroimage* 23(Suppl. 1), S69–S84. doi: 10.1016/j.neuroimage.2004.07.016

Gaitanis, J. N., and Donahue, J. (2013). Focal cortical dysplasia. *Pediatr. Neurol.* 49, 79–87. doi: 10.1016/j.pediatrneurol.2012.12.024

Gracien, R. M., Reitz, S. C., Hof, S. M., Fleischer, V., Zimmermann, H., Droby, A., et al. (2016). Assessment of cortical damage in early multiple sclerosis with quantitative T2 relaxometry. *NMR Biomed.* 29, 444–450. doi: 10.1002/nbm.3486

Gracien, R.-M., van Wijnen, A., Maiworm, M., Petrov, F., Merkel, N., Paule, E., et al. (2019). Improved synthetic T1-weighted images for cerebral tissue segmentation in neurological diseases. *Magn. Reson. Imaging* 61, 158–166. doi: 10.1016/j.mri.2019.05.013

Hong, S.-J., Bernhardt, B. C., Schrader, D. S., Bernasconi, N., and Bernasconi, A. (2016). Whole-brain MRI phenotyping in dysplasia-related frontal lobe epilepsy. *Neurology* 86, 643–650. doi: 10.1212/WNL.0000000000002374

Hong, S.-J., Kim, H., Schrader, D., Bernasconi, N., Bernhardt, B. C., and Bernasconi, A. (2014). Automated detection of cortical dysplasia type II in MRI-negative epilepsy. *Neurology* 83, 48–55. doi: 10.1212/WNL.0000000000000543

House, P. M., Lanz, M., Holst, B., Martens, T., Stodieck, S., and Huppertz, H.-J. (2013). Comparison of morphometric analysis based on T1- and T2-weighted MRI data for visualization of focal cortical dysplasia. *Epilepsy Res.* 106, 403–409. doi: 10.1016/j.eplepsyres.2013.06.016

Huppertz, H.-J., Grimm, C., Fauser, S., Kassubek, J., Mader, I., Hochmuth, A., et al. (2005). Enhanced visualization of blurred gray-white matter junctions in focal cortical dysplasia by voxel-based 3D MRI analysis. *Epilepsy Res.* 67, 35–50. doi: 10.1016/j.eplepsyres.2005.07.009

Kabat, J., and Król, P. (2012). Focal cortical dysplasia – review. *Pol. J. Radiol.* 77, 35–43.

Kassubek, J., Huppertz, H.-J., Spreer, J., and Schulze-Bonhage, A. (2002). Detection and localization of focal cortical dysplasia by voxel-based 3-D MRI analysis. *Epilepsia* 43, 596–602. doi: 10.1046/j.1528-1157.2002.41401.x

Lerch, J. P., and Evans, A. C. (2005). Cortical thickness analysis examined through power analysis and a population simulation. *Neuroimage* 24, 163–173. doi: 10.1016/j.neuroimage.2004.07.045

Lerner, J. T., Salamon, N., Hauptman, J. S., Velasco, T. R., Hemb, M., Wu, J. Y., et al. (2009). Assessment and surgical outcomes for mild type I and severe type II cortical dysplasia: a critical review and the UCLA experience. *Epilepsia* 50, 1310–1335. doi: 10.1111/j.1528-1167.2008.01998.x

Mugler, J. P., and Brookeman, J. R. (1990). Three-dimensional magnetization-prepared rapid gradient-echo imaging (3D MP RAGE). *Magn. Reson. Med.* 15, 152–157. doi: 10.1002/mrm.1910150117

Nöth, U., Gracien, R.-M., Maiworm, M., Reif, P. S., Hattingen, E., Knake, S., et al. (2020). Detection of cortical malformations using enhanced synthetic contrast images derived from quantitative T1 maps. *NMR Biomed.* 33:e4203. doi: 10.1002/nbm.4203

Nöth, U., Shrestha, M., Schure, J.-R., and Deichmann, R. (2017). Quantitative in vivo T2 mapping using fast spin echo techniques - A linear correction procedure. *Neuroimage* 157, 476–485. doi: 10.1016/j.neuroimage.2017.06.017

Preibisch, C., and Deichmann, R. (2009). Influence of RF spoiling on the stability and accuracy of T1 mapping based on spoiled FLASH with varying flip angles. *Magn. Reson. Med.* 61, 125–135. doi: 10.1002/mrm.21776

Smith, S. M., Jenkinson, M., Woolrich, M. W., Beckmann, C. F., Behrens, T. E. J., Johansen-Berg, H., et al. (2004). Advances in functional and structural MR image analysis and implementation as FSL. *Neuroimage* 23(Suppl. 1), 19. doi: 10.1016/j.neuroimage.2004.07.051

Venkatesan, R., Lin, W., and Haacke, E. M. (1998). Accurate determination of spin-density andT1 in the presence of RF-field inhomogeneities and flip-angle miscalibration. *Magn. Reson. Med.* 40, 592–602. doi: 10.1002/mrm.1910400412

Volz, S., Nöth, U., and Deichmann, R. (2012a). Correction of systematic errors in quantitative proton density mapping. *Magn. Reson. Med.* 68, 74–85. doi: 10.1002/mrm.23206

Volz, S., Nöth, U., Jurcoane, A., Ziemann, U., Hattingen, E., and Deichmann, R. (2012b). Quantitative proton density mapping: correcting the receiver sensitivity bias via pseudo proton densities. *Neuroimage* 63, 540–552. doi: 10.1016/j.neuroimage.2012.06.076

Volz, S., Nöth, U., Rotarska-Jagiela, A., and Deichmann, R. (2010). A fast B1-mapping method for the correction and normalization of magnetization transfer ratio maps at 3 T. *Neuroimage* 49, 3015–3026. doi: 10.1016/j.neuroimage.2009.11.054

Wellmer, J., Quesada, C. M., Rothe, L., Elger, C. E., Bien, C. G., and Urbach, H. (2013). Proposal for a magnetic resonance imaging protocol for the detection of epileptogenic lesions at early outpatient stages. *Epilepsia* 54, 1977–1987. doi: 10.1111/epi.12375

Conflict of Interest: EH has received speaker's honoraria from BRACCO. SK has received speaker's honoraria from Desitin and UCB and educational grants from AD-Tech, Bial, Brainlab, Desitin, Eisai, Epilog, GW, Siemens, Philipps, and UCB. FR has received honoraria for presentations and consultations from EISAI, UCB Pharma, Desitin Arzneimittel, Hexal, Novartis, Medtronic, GW-Pharma, Shire, Sandoz, and Cerbomed as well as research grants from UCB, European Union, Deutsche Forschungsgemeinschaft, European Science Foundation, and the Hessonian Ministries of Science and Arts and of Social Affairs and Integration. HS has received speaker's honoraria from Bayer, Sanofi, and Boehringer Ingelheim.

The remaining authors declare that the research was conducted in the absence of any commercial or financial relationships that could be construed as a potential conflict of interest.

Copyright © 2020 Maiworm, Nöth, Hattingen, Steinmetz, Knake, Rosenow, Deichmann, Wagner and Gracien. This is an open-access article distributed under the terms of the Creative Commons Attribution License (CC BY). The use, distribution or reproduction in other forums is permitted, provided the original author(s) and the copyright owner(s) are credited and that the original publication in this journal is cited, in accordance with accepted academic practice. No use, distribution or reproduction is permitted which does not comply with these terms.

frontiers in Neuroscience

ORIGINAL RESEARCH
published: 16 June 2020
doi: 10.3389/fnins.2020.00537

A Fully Automated Method for Segmenting Arteries and Quantifying Vessel Radii on Magnetic Resonance Angiography Images of Varying Projection Thickness

Sivakami Avadiappan[1], Seyedmehdi Payabvash[1†], Melanie A. Morrison[1], Angela Jakary[1], Christopher P. Hess[1,2] and Janine M. Lupo[1]*

[1] Department of Radiology and Biomedical Imaging, University of California, San Francisco, San Francisco, CA, United States, [2] Department of Neurology, University of California, San Francisco, San Francisco, CA, United States

OPEN ACCESS

Edited by:
Miguel Castelo-Branco, Coimbra Institute for Biomedical Imaging and Translational Research (CIBIT), Portugal

Reviewed by:
Tolga Cukur, Bilkent University, Turkey
Stefan Schob, Universitätsklinikum Leipzig, Germany

***Correspondence:**
Janine M. Lupo
janine.lupo@ucsf.edu

†Present address:
Seyedmehdi Payabvash, Department of Radiology and Biomedical Imaging, Yale School of Medicine, New Haven, CT, United States

Specialty section:
This article was submitted to Brain Imaging Methods, a section of the journal Frontiers in Neuroscience

Received: *16 December 2019*
Accepted: *01 May 2020*
Published: *16 June 2020*

Citation:
Avadiappan S, Payabvash S, Morrison MA, Jakary A, Hess CP and Lupo JM (2020) A Fully Automated Method for Segmenting Arteries and Quantifying Vessel Radii on Magnetic Resonance Angiography Images of Varying Projection Thickness. Front. Neurosci. 14:537. doi: 10.3389/fnins.2020.00537

Purpose: Precise quantification of cerebral arteries can help with differentiation and prognostication of cerebrovascular disease. Existing image processing and segmentation algorithms for magnetic resonance angiography (MRA) are limited to the analysis of either 2D maximum intensity projection images or the entire 3D volume. The goal of this study was to develop a fully automated, hybrid 2D-3D method for robust segmentation of arteries and accurate quantification of vessel radii using MRA at varying projection thicknesses.

Methods: A novel algorithm that employs an adaptive Frangi filter for segmentation of vessels followed by estimation of vessel radii is presented. The method was evaluated on MRA datasets and corresponding manual segmentations from three healthy subjects for various projection thicknesses. In addition, the vessel metrics were computed in four additional subjects. Three synthetically generated angiographic datasets resembling brain vasculature were also evaluated under different noise levels. Dice similarity coefficient, Jaccard Index, F-score, and concordance correlation coefficient were used to measure the segmentation accuracy of manual versus automatic segmentation.

Results: Our new adaptive filter rendered accurate representations of vessels, maintained accurate vessel radii, and corresponded better to manual segmentation at different projection thicknesses than prior methods. Validation with synthetic datasets under low contrast and noisy conditions revealed accurate quantification of vessels without distortions.

Conclusion: We have demonstrated a method for automatic segmentation of vascular trees and the subsequent generation of a vessel radii map. This novel technique can be applied to analyze arterial structures in healthy and diseased populations and improve the characterization of vascular integrity.

Keywords: MRA, segmentation, Frangi, vessels, radii

INTRODUCTION

Analysis of human intracranial arterial system is important for characterizing disease entities with primary or secondary involvement of cerebral vascular circulation such as arteriovenous malformations, central nervous system vasculitis, and post-radiation vascular changes (Fischer et al., 2005; Jellinger and Attems, 2006; Minagar et al., 2006). Accurate quantification of vascular features serves to enhance understanding of the role of cerebral vasculature in these pathophysiological conditions. Delineation of the vascular architecture can furthermore aid planning of minimally invasive neurosurgical procedures through the identification of narrow pathways that are free of passing arteries. Time-of-flight magnetic resonance angiography (TOF-MRA) and MR venography using susceptibility weighted imaging (SWI) are two techniques that are commonly used to probe the 3D spatial architecture of arteries and veins, respectively. In order to quantify pathological deviations from normal, cerebral arteries and veins must first be separated from background brain parenchyma using a vessel segmentation algorithm.

Segmentation of the brain's vessels is challenged by complex geometry, small vessel size, and limited contrast of TOF-MRA images. Specifically, the sensitivity to detect small arterioles proximal to the capillary bed is limited in most algorithms. These arteries are typically not clearly delineated in raw MRA images due to weak signal from slow blood flow. Our group and others have recently developed sequences for the simultaneous acquisition of TOF-MRA and SWI (Du and Jin, 2008; Deistung et al., 2009; Bae et al., 2010; Bian et al., 2015). Although the benefits of these sequences include shortened scan times and the ability to jointly display arterial and venous vessels without the need for coregistration, they often come with the tradeoff of less background suppression. Hence, there is a need for a robust method to identify both small and large arteries and accurately quantify the subtle changes in arterial diameters.

Maximum intensity projection (MIP) images (Arlart et al., 1995; Johnson et al., 1998) taken through the 3D image volumes acquired using a TOF-MRA sequence provide a more informative visual display for analysis of vessels and are typically used for segmentation. MIP is a volume rendering technique for 3D data that selects the maximum voxel value along a line from the viewpoint to the plane of projection. When performed at different thicknesses, this technique can provide volumetric images of the vasculature in the form of sequential cross-sectional images. Although MIP images can clearly depict the overall shapes and paths of the blood vessels and are computationally fast, the 2D projections do not provide a good sense of depth, i.e., the spatial relationship of overlapping vessels. In addition, the presence of overlapping non-vascular structures greatly affects the visualization of small vessels with low contrast, especially at larger projection thicknesses. To overcome these issues, vessel enhancement algorithms can be first applied in order to suppress non-vascular structures and improve delineation of small blood vessels.

Vessel enhancement may be intensity based, edge based (with strong gradients), or shape based. Sato et al. (1998) implemented a line filter that enhances tubular structures in images. Frangi et al. (1998) introduced the term "vesselness" as a measurement of tubular structures by observing the ratio of eigenvalues of the Hessian matrix. Another algorithm reported by Lorigo et al. (2001) is based on a co-dimension two level set method. Aylward and Bullitt (2001) implemented an algorithm that extracts the centerline of a tubular structure by tracking vessels from a seed point. A meta-analysis of the various vessel segmentation techniques was presented by Suri et al. (2002) who reported that the multiscale vesselness using Frangi generated the best contrast between vessels and background (Chapman and Parker, 2001). The Hessian-based filter employed by this method accentuates the contrast between tubular objects and the background, thus enhancing elongated blood vessels while suppressing other anatomical features and noise. The addition of multiscale smoothing, performed using multiple runs of Gaussian filtering with different sigma values, generates a multiscale filter response at each scale that can be used to determine the likelihood that a voxel belongs to a vessel of each particular diameter. While vessel visualization is enhanced using this approach, accurate quantification of vessel radii from resulting vessel score maps remains a challenge due to underestimation and overestimation of vessel scores at the boundaries manifesting as an artificial narrowing of thick vessels and broadening of thin vessels, respectively. In order to achieve accurate quantification of vessel radii, an alternate approach is needed.

While existing methods are limited to applying vessel enhancement filters to either the original non-projected 3D images or a single MIP through the entire imaged volume (Gao et al., 2011; Hsu et al., 2017; Phellan and Forkert, 2017), there has been little investigation of the influence of projection thickness on the effectiveness of vessel segmentation. Of the few studies reported, one showed similarity between vessel radii measurements extracted from parameter-dependent MIP MRA and digital subtraction angiography derived from high contrast x-ray images (Persson et al., 2004). Another group showed that MIP images using a slab thickness of 8 mm are superior in the detection of pulmonary nodules (Kawel et al., 2009). Since radiologists routinely adjust the projection thickness within an MIP section to aid their assessment of vessel size and location, efforts to address the influence of this parameter on segmentation and subsequent vessel radii measurements will, in addition to supporting discovery research, support the integration of automated algorithms into clinical practice. These techniques will compliment traditional subjective assessment of cerebral arteries and 2D in-plane measurements with a caliper (U-King-Im et al., 2007).

To overcome the above-mentioned limitations, we introduce a novel hybrid approach which we call an adaptive Frangi technique that incorporates a Euclidean distance transform (EDT) with the Frangi filter in order to preserve accurate vessel radii information. Using this approach, we describe a robust, automatic processing pipeline for (1) accurate segmentation of arteries from MRA images for different projection thicknesses and (2) quantification of vessel radii. We apply our technique to the MRA images of three healthy volunteers and synthetic images in order to compare the automatic segmentation with manual

and other commonly used segmentation methods for different projection thicknesses. Vessel metrics were then evaluated in four patients whose images were acquired with varying scan protocols.

MATERIALS AND METHODS

Subjects and Data Acquisition

Magnetic resonance angiography images were acquired from three healthy volunteers (mean age 25 ± 2.2 years) with no known cerebrovascular disease and four patients with juvenile pilocytic astrocytomas (mean age 15 ± 1.2 years). All subjects provided informed consent as required by our institutional review board and were imaged on a 7T MRI scanner (GE Healthcare, WI, United States) with a 32-channel phased-array coil (NOVA Medical, MA, United States) using a four-echo, gradient echo sequence (Bian et al., 2015) that was previously developed to simultaneously image arteries, veins, and cerebral microbleeds (CMBs), obviating the need for image co-registration and reducing the scan time. Scan parameters were as follows: voxel size = 0.46 × 0.46 × 1 mm using an in-plane 512 × 512 matrix, FOV = 24 cm, slice thickness = 1 mm, TR = 40 ms, flip angle = 25°, and TE = 2.7, 10.5, 13.2, and 20.9 ms. Flow compensation was performed in the readout direction, and echoes were partially acquired with 65% partial Fourier sampling. A multiple overlapping thin-slab acquisition was employed with three 36 mm slabs partitioned into 1 mm thick slices with 12 slices of overlap. The 3D acquisition was accelerated in the phase direction with autocalibrating reconstruction for Cartesian imaging (ARC) using an acceleration factor of 3, resulting in a total scan time of 10.6 min. The first echo was used to create TOF-MRA images and the remaining three echoes were combined to create a composite SWI image.

Because one of the potential applications of generating vessel radii maps is to look for variations between serial scans in longitudinal studies, we scanned two volunteers twice in order to evaluate whether the vessel radii map would change between successive scans due to head orientation and slab prescription. The two scans, separated by an interval of three weeks, were used to establish the amount of variability associated with our method by comparing the resulting vessel radii distribution between the two scans.

Clinical TOF-MRA scans at lower field strengths were also obtained for two of the juvenile pilocytic astrocytoma patients in order to demonstrate the practical application of the algorithm. The imaging parameters for these two clinical scans were as follows: field strength = 1.5/3T, voxel size = 0.43 × 0.43 × 0.5 mm/0.39 × 0.39 × 0.6 mm, in-plane matrix = 512 × 512, FOV = 20/22 cm, slice thickness = 1.2/1.0 mm, TR = 23/35 ms, flip angle = 18°/20°, and TE = 3.4/3.1 ms.

Image Pre-processing and Manual Segmentation

In order to isolate the brain, skull stripping was first performed on the MRA images using a Brain Extraction Tool (BET) that is part of the FMRIB Software Library (FSL) (Smith, 2002), The TOF-MRA images were resampled to 0.23 mm^3 resolution using bicubic interpolation in order to have better differentiation for the vessel radii map, which was followed by intensity normalization by dividing the gray scale intensity values by the maximum gray scale value. The 2D MIP was obtained by taking the projection of the entire imaged volume along the superior–inferior direction. Vessel segmentation was performed on the 2D MIP, 3D raw volume, and six other projection thicknesses (4, 8, 16, 24, 32, and 48 mm) using MATLAB. The cerebrovascular structures were manually segmented from both the entire volume of the three volunteer datasets and the central slice for each of six different projection thicknesses by a board-certified neuroradiologist (SP). Manual segmentation was performed by overlaying a thresholded image on the original scan using MRIcron software, with 50% transparency on background. This threshold of 0.5 times the maximum gray scale value was selected empirically by the neuroradiologist during manual segmentation. The segmentations were then converted to contours of each vessel for each axial slice before confirming them on coronal and sagittal planes and making any additional corrections where necessary. These manual segmentations were treated as the ground truth to determine segmentation accuracy.

Three synthetic vessel datasets were downloaded from the publicly available Vascular Synthesizer (VascuSynth) software (Hamarneh and Jassi, 2010). These datasets contain randomly generated vessel-like structures of varying widths, bifurcations, and orientations. The generated vascular volumes were rendered with MIPs. The synthetic image was resized and eroded in order to simulate the resolution and vessel sizes encountered in TOF-MRA. Since these datasets and corresponding binary ground truth segmentations were virtually generated, no manual segmentation was required.

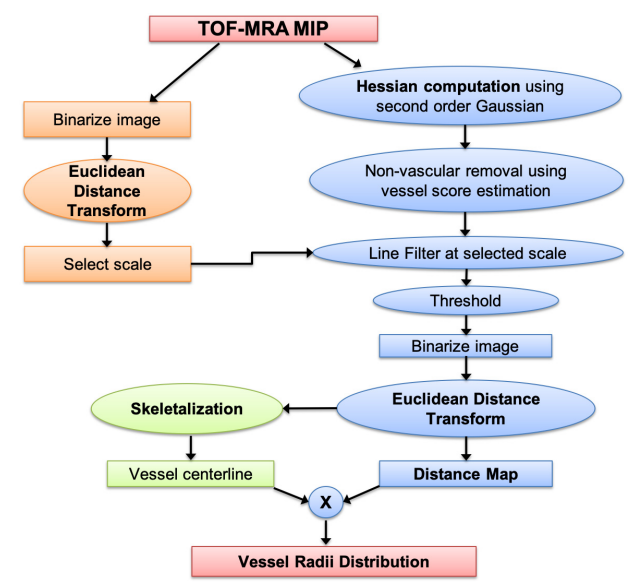

FIGURE 1 | Processing pipeline for obtaining vessel radii distribution from TOF-MRA maximum intensity projection images.

MIP Vessel Segmentation

The mathematics behind the Frangi "vesselness" filter for the purpose of vessel segmentation has been reported previously (Krissian et al., 2000). Briefly, the line intensity profile of the vessels is represented as a Gaussian function with a uniform intensity along the vessel. The Hessian matrix that is obtained by taking the second partial derivative describes the local curvature along the vessel, and its cross-section and its eigenvalues indicate the degree of curvature. The Frangi filter uses the eigenvalues to estimate the likelihood of tube-like structures. To address the need for multiscale smoothing, multiple iterations of Gaussian filtering with different sigma values were performed. Although the Frangi vessel enhancement method is an excellent technique for visualization, the accuracy of radii of vessels is not preserved. Our approach takes advantage of the vessel enhancement features provided by this method while maintaining accurate vessel shape.

A flowchart of our adaptive Frangi algorithm is shown in **Figure 1**. This algorithm is unique because it automatically determines the appropriate set of filter scales for each vessel by first calculating the radii of large vessels using intensity-based thresholding followed by discrete distance transforms. These values are then used to determine the standard deviation values for the Frangi filter (Shikata et al., 2004). The minimum sigma value (0.8) and the increment in sigma (0.2) were chosen based on prior literature (Phellan and Forkert, 2017). The maximum sigma values were then selected based on the relation sigma $_{max}$ = $\sqrt{}$ radii $_{max}$ (Krissian et al., 2000). **Figure 2** shows the sigma selection for each radii range. This adaptive scale selection ensures that large sigma values are included only for the detection of thick segments, and small sigma values are included only for the thin segments. From the output of the adaptive Frangi filter, fast marching (Sethian, 1996) with an intensity threshold of 0.001 was performed to obtain the binary image. A 2D EDT map, which labels each pixel of the image with the distance to the nearest boundary pixel, can then be obtained (Nystroem and Smedby, 2000). Voxel-wise measures of vessel radii were rapidly generated by employing a thinning procedure to obtain the vessel skeleton of the binary image followed by multiplication of the 2D-EDT with this skeleton to obtain the final vessel radii map. Histograms of the vessel radii map were then generated to depict vessel radii distribution in the MIP.

Evaluation of Segmentation Performance

For the purpose of understanding the effects of projection on quantification of vessel radii, we applied our algorithm on the continuous MIPs of varying thicknesses. Our adaptive Frangi method was able to automatically determine the optimal set of sigma values for the Frangi filter for each projection. For one of the three volunteer scans, the results of automatic segmentation method were compared to the mid-slice manual segmentation done by the neuroradiologist. Dice similarity coefficients (DSC), Jaccard Index (JI), and the F-score were used as validation metrics to evaluate the segmentation agreement between the manual and automatic segmentation for each projection thickness. The DSC is a standard measure to report the segmentation performance (Dice, 1945) and measures the spatial overlap between the manual and automatic segmentation masks. The DSC is defined as twice the size of the intersection between the two masks normalized by the sum of their volumes. The DSC varies between 0 (no overlap) and 1 (complete overlap). The JI is defined as the intersection of the two binary masks divided by the union of the two masks (Jaccard, 1901). The JI is numerically more sensitive to mismatch when there is reasonably strong overlap. The F-score measures how close the predicted boundary of an object matches the ground truth boundary (Csurka et al., 2013). Both the precision and the recall of the test are used to compute the F-score: Precision is the number of correct positive results divided by the number of all positive results returned by the classifier, and recall is the number of correct positive results divided by the number of all samples that should have been identified as positive. The F-score is the harmonic average of the precision and recall, where an F-score reaches its best value at 1 (perfect precision and recall) and worst value at 0. The above-mentioned metrics are sensitive to misplacement of the segmentation label but are relatively insensitive to volumetric under- and overestimations. Hence, in

A

Vessel radii	Sigma values
<1	0.8,1
1-1.41	0.8, 1, 1.2
1.42-2	0.8,1, 1.2, 1.4
2.01-2.8	0.8,1, 1.2, 1.4, 1.6
2.81-4	0.8,1, 1.2, 1.4, 1.6, 1.8, 2
4.01-5.65	0.8,1, 1.2, 1.4, 1.6, 1.8, 2, 2.2, 2.4
5.66-8	0.8,1, 1.2, 1.4, 1.6, 1.8, 2, 2.2, 2.4,2.6,2.8
>8	0.8,1, 1.2, 1.4, 1.6, 1.8, 2, 2.2, 2.4,2.6,2.8,3,3.2

B

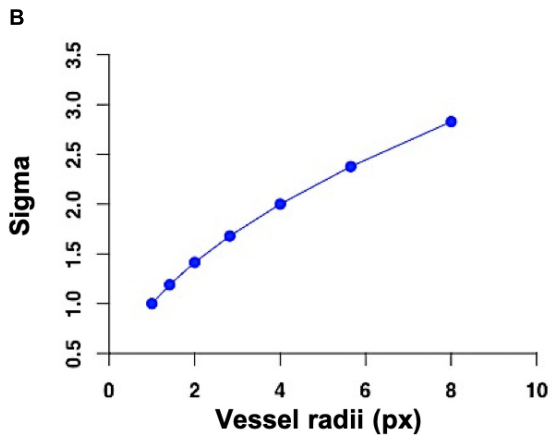

FIGURE 2 | (A) Set of sigma values for each radii range. **(B)** Selection of maximum sigma value for the maximum vessel radii.

addition, we determined the concordance correlation coefficient (CCC) (Lin, 1989)—a reproducibility index that evaluates the volume agreement between the manual and automatic segmented masks by measuring their combined variation from the line $y = x$ (i.e., the degree through which pairs of observations fall on the 45° line through the origin). In order to compare an estimate of the segmentation error between the original and our adaptive Frangi method, we also calculated the number of segmented voxels that overlapped with the manual segmentation and divided that by the number of voxels that did not overlap for each volunteer. A paired t-test was then performed to test for statistically significant difference between the two methods. Repeatability of vessel radii distributions between serial scans was also evaluated for two subjects using Bland–Altman plots.

The three synthetic datasets were also used to compare the segmentation results between the original Frangi and our adaptive Frangi methods. The segmentation metrics were calculated both between the ground truth and Frangi and also the ground truth and adaptive Frangi. The number of vessel bifurcations was also calculated for the ground truth and the automatic segmentation. In order to investigate the sensitivity of our proposed method in the presence of noise, Gaussian noise with means and standard deviations of 50, 100, 150, and 200 was added column-wise to the datasets. Increasing gray scale background with a maximum of 75% of the maximum gray scale intensity value in the image was also added horizontally across the synthetic images in order to mimic different levels of background suppression of brain parenchyma. The segmentation performance was also assessed by adding noise and varying the vessel-to-background contrast of the TOF-MRA image. The DSC was calculated for the automatically segmented noise-added images with respect to the noise-free ground truth

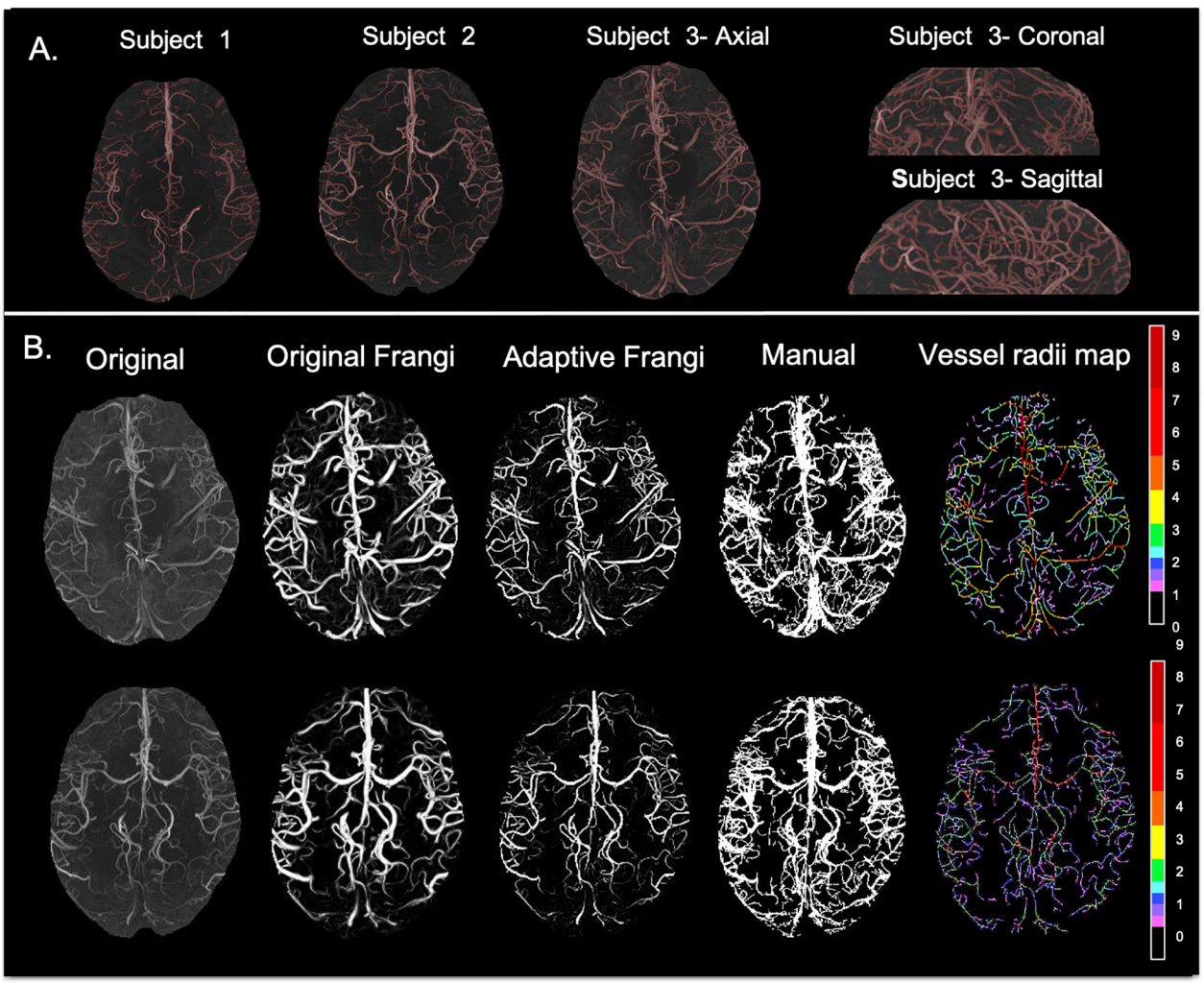

FIGURE 3 | (A) Axial maximum intensity projection images for three volunteers along with coronal and sagittal views shown for Volunteer 3. **(B)** From left to right: original TOF-MRA maximum intensity projection; Frangi filtered image where thin vessels appear broader than expected; new Adaptive Frangi filtered image where vessels maintain the radii of the original image; manual segmentation; and color-coded vessel radii map for two volunteers. Radii values are given in terms of number of pixels (1 pixel = 0.23 mm).

image for both the Frangi and adaptive Frangi methods. In order to evaluate the fidelity of the vessel radii estimation, the vessel radii distribution from the ground truth synthetic image was compared with the Frangi and adaptive Frangi. The same comparison could not be done for the TOF-MRA images because, with manual delineation, the vessel boundary may not be exactly drawn pixel-wise, especially for vessels with small radii, and it could not be considered as the ground truth for radii comparison.

RESULTS

Figure 3A shows the results of the adaptive filter overlaid on MRA on axial 2D MIPs for three volunteers and for one of the volunteers in the other two orthogonal views as well. The images demonstrate the versatility of our method and its performance in segmenting both small and large vessels. The Circle of Willis was not observed in subjects 1 and 3 because the 3-slab imaged volume was acquired more superiorly because we were interested in looking at smaller vessels closer to the periphery. In general, vessel diameters were decreasing toward the periphery and with increasing branching degree.

The DSC between the adaptive Frangi and manual segmentation for the three volunteers were found to be 0.89, 0.85, and 0.83, respectively. A comparison of the adaptive Frangi, original Frangi, and manual segmentation methods is shown in **Figures 3B,C** for two volunteers. The original Frangi filter inaccurately broadens thin vessels because it takes the maximum intensity projection across all scales, losing the thickness information of the vessels, while the manual segmentation introduces added noise after the MIP. The corresponding vessel radii distribution for the two volunteers is also shown, whereby the vessel radii map for the MIP image is color coded in terms of the number of pixels thick, where 1 pixel = 0.23 mm. Segmentation results for the two clinical MRA scans of the juvenile pilocytic astrocytoma patients acquired at lower strengths is shown in **Figure 4**. The repeatability test demonstrated a 2–14% percentage difference between the two serial scans for the same volunteer.

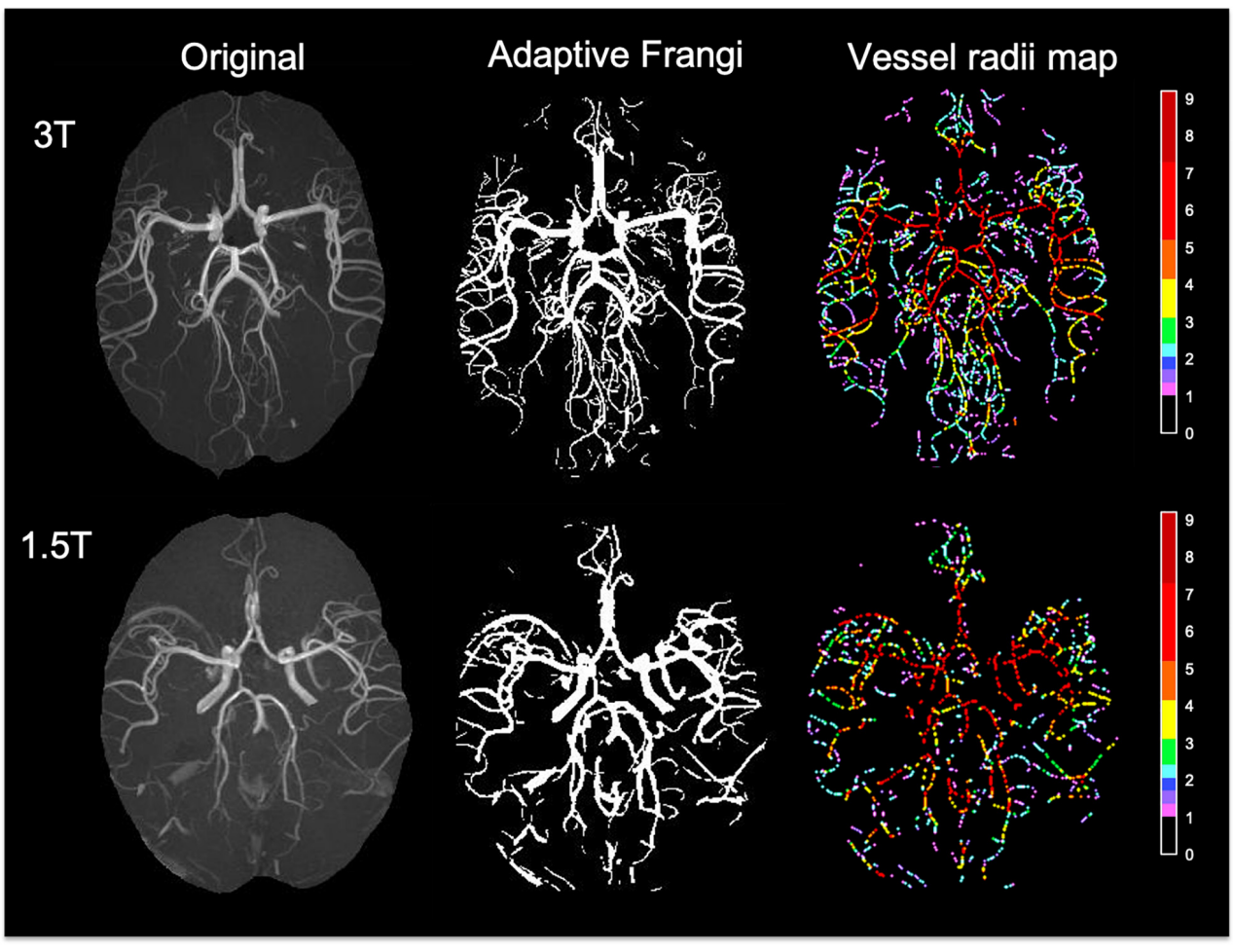

FIGURE 4 | Segmentation results and color-coded vessel radii map for two clinical MRA scans of the patients with juvenile pilocytic astrocytoma acquired at 3T **(top)** and 1.5T **(bottom)**. Radii values are given in terms of number of pixels (1 pixel = 0.23 mm).

The accuracy of the method was demonstrated by means of Bland–Altman plots with lower bias, indicating that both scans were in agreement (**Figure 5**). Histograms of the vessel radii distribution and corresponding vessel radii map for the central slice of each projection thickness are shown in **Figure 6**. The maximum radii of the vessels found in a slice increased with larger projection thicknesses, likely due to increased coverage with thicker projections. Although small vessels can be obscured as the projection thickness increases, the automatic segmentation from projected image improved the delineation of small blood vessels. The average radii measurements across the five projection thicknesses (8, 16, 24, 32, and 48) for the two region of interests displayed as white circles in **Figure 6** were 1.32 ± 0.017 and 1.70 ± 0.02 pixels, demonstrating the high level of precision of our method regardless of projection thickness.

The performance of the proposed adaptive Frangi filter was evaluated for multiple projection thicknesses (1, 4, 8, 16, and 32 mm) and compared with the corresponding manual segmentation and fixed thresholding results, as shown in **Figure 7**, for a representative central slice of each projection thickness. The color-coded difference images in the last two columns demonstrate that significantly more vessels were missed by the fixed thresholding method compared to the adaptive Frangi method, while the adaptive Frangi method was able to preserve vessel continuity more than either manual or fixed thresholding method. These trends persisted at all projection thicknesses, demonstrating the robustness of our method despite the increase in segmentation metrics (DSC, JI, F-score, and CCC) between the central slice automatic segmentation and the corresponding manual segmentation with larger projection thickness (**Figure 8**). **Table 1** displays the total arterial vessel volume and the length of arteries for all the subjects based on Frangi and adaptive Frangi filtering. A statistically significant decrease in segmentation error was found with our method compared to the original Frangi ($p < 0.003$).

In order to further evaluate the accuracy of our algorithm, both the Frangi and the adaptive Frangi algorithm were

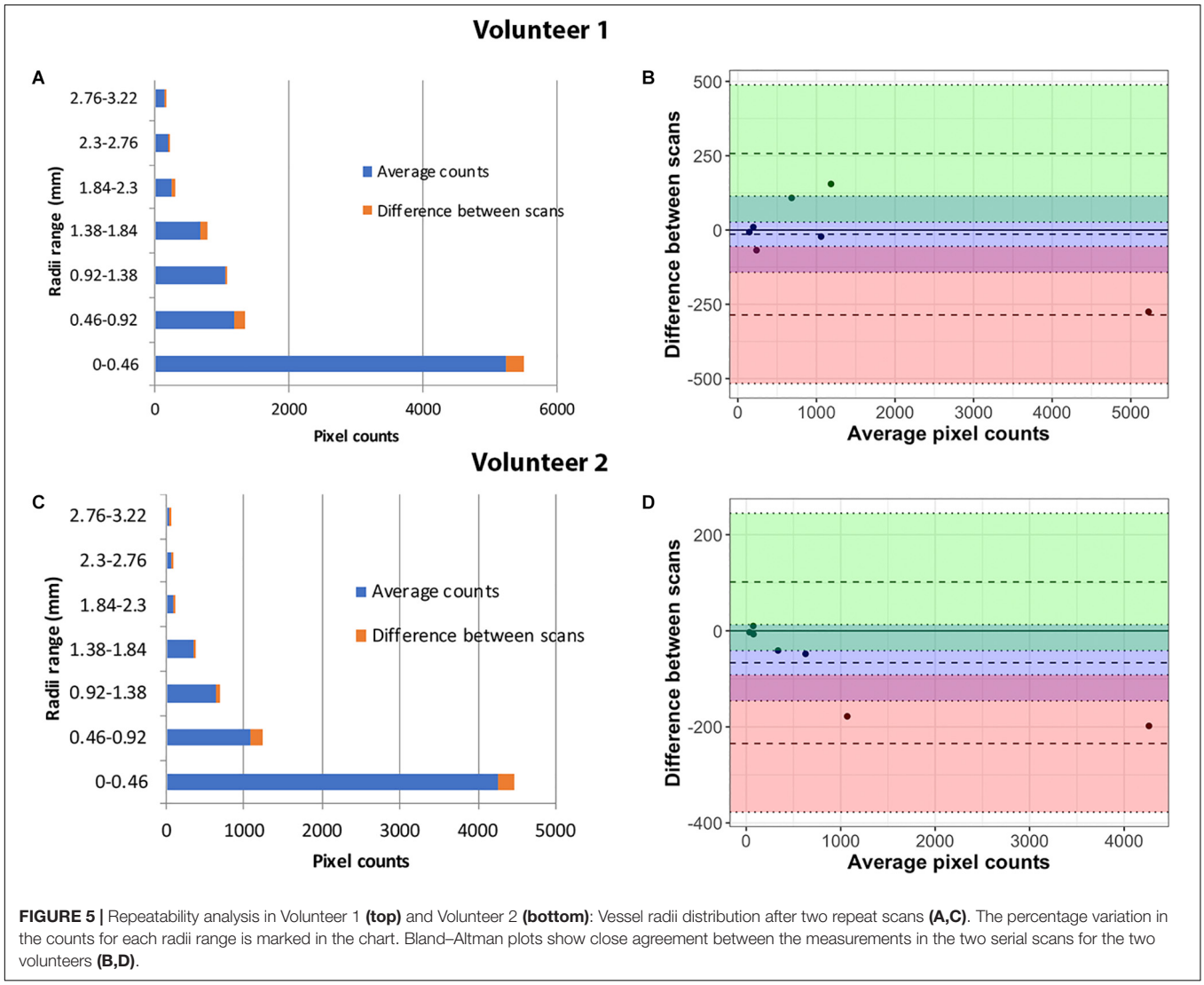

FIGURE 5 | Repeatability analysis in Volunteer 1 **(top)** and Volunteer 2 **(bottom)**: Vessel radii distribution after two repeat scans **(A,C)**. The percentage variation in the counts for each radii range is marked in the chart. Bland–Altman plots show close agreement between the measurements in the two serial scans for the two volunteers **(B,D)**.

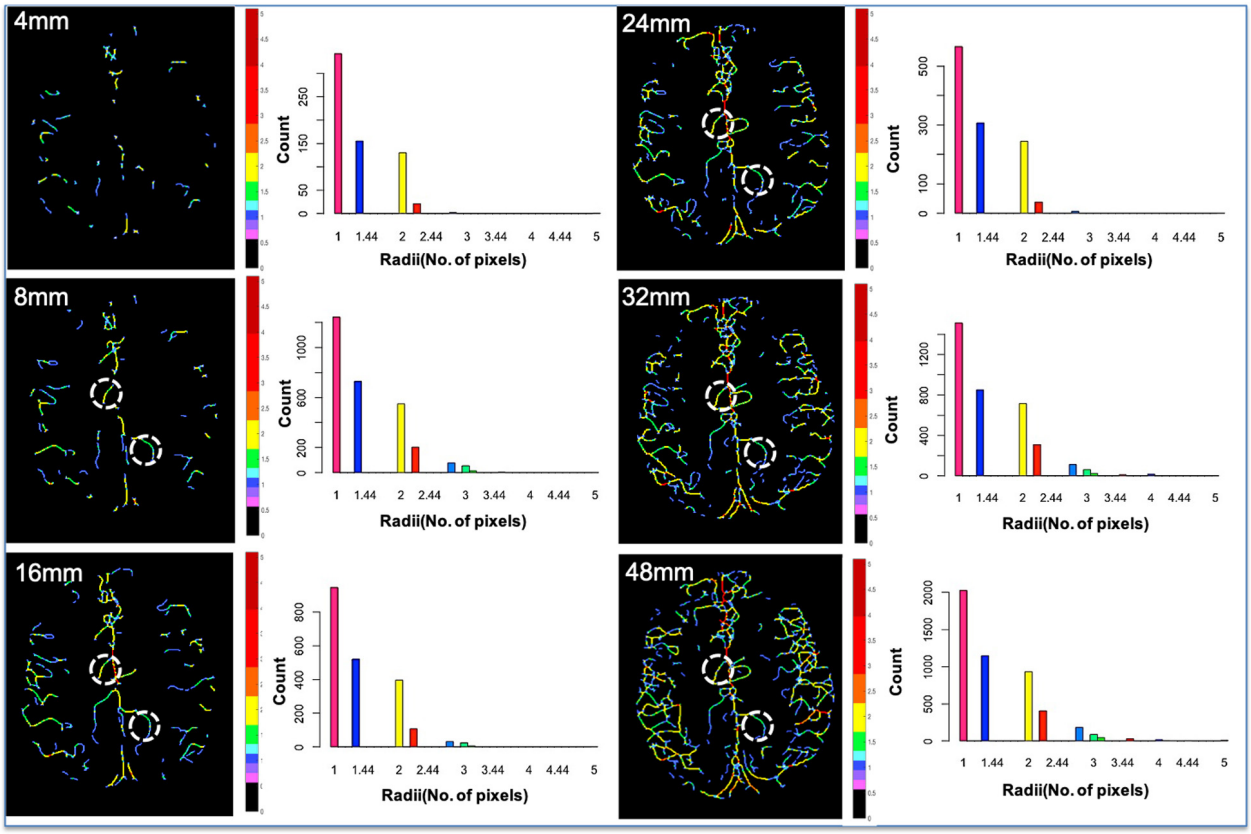

FIGURE 6 | Vessel radii map for the central slice of each projection thickness and the corresponding vessel radii distribution. As the projection thickness increases, larger vessels are preserved, and the maximum radii of the vessels found in the central slice increase due to increased coverage. Although small vessels can be obscured as the projection thickness increases, the automatic segmentation from projected image improves delineation of small blood vessels. Two identical ROIs (white circles) were overlaid on each of the five projection thicknesses (8, 16, 24, 32, and 48), and the average vessel radii within that vessel segment were evaluated. The average radii measurements for the two ROIs were 1.32 ± 0.017 and 1.70 ± 0.02 pixels. The low standard deviation demonstrates the high level of precision of our method, regardless of projection thickness.

applied to synthetic images generated from VascuSynth software. **Figure 9** shows the results of each algorithm and the difference image between the original and adaptive Frangi methods. As with the volunteer data, the adaptive Frangi method produced more accurate segmentation than the original Frangi method as shown by the minimal differences highlighted in green that only exist in cases of looped branches. The number of branches was compared in the original synthetic image and the automatically segmented image showing close agreement. The set of segmentation metrics described previously were obtained for both Frangi and adaptive Frangi compared to the ground truth synthetic image (**Table 2**). The DSC, JI, and F-scores were slightly higher for the adaptive Frangi compared to the Frangi method. The volume agreement metric, CCC, was also higher for the adaptive Frangi method.

When tested under conditions of varying contrast and noise levels, the adaptive Frangi filter maintained accurate vessel radii throughout and outperformed the Frangi filter that erroneously produces bulges at the ends of vessels (**Figure 10A**). Adding noise to the TOF-MRA reduced the DSC for the subject from 0.89 to 0.82 and 0.84 for the Frangi and adaptive Frangi methods, respectively (**Figure 10B**). Adding noise to the synthetic images reduced the DSC as expected, with more decrease observed in Frangi compared to the adaptive Frangi method (**Table 2**). Regarding the fidelity of the vessel radii measured using our algorithm, Frangi and the ground truth synthetic image were compared for the three datasets and the mean count as shown in **Figure 11A**. The Bland–Altman plots for the comparison of Frangi and ground truth (**Figure 11B**) show higher differences in the count compared to adaptive Frangi and ground truth (**Figure 11C**).

DISCUSSION

Precise characterization of vascular structures is important for the assessment and objective quantification of cerebrovascular diseases. We have devised and thoroughly evaluated a new technique for automated segmentation of cerebral vascular trees from MRA images. Although the Frangi filter has been widely

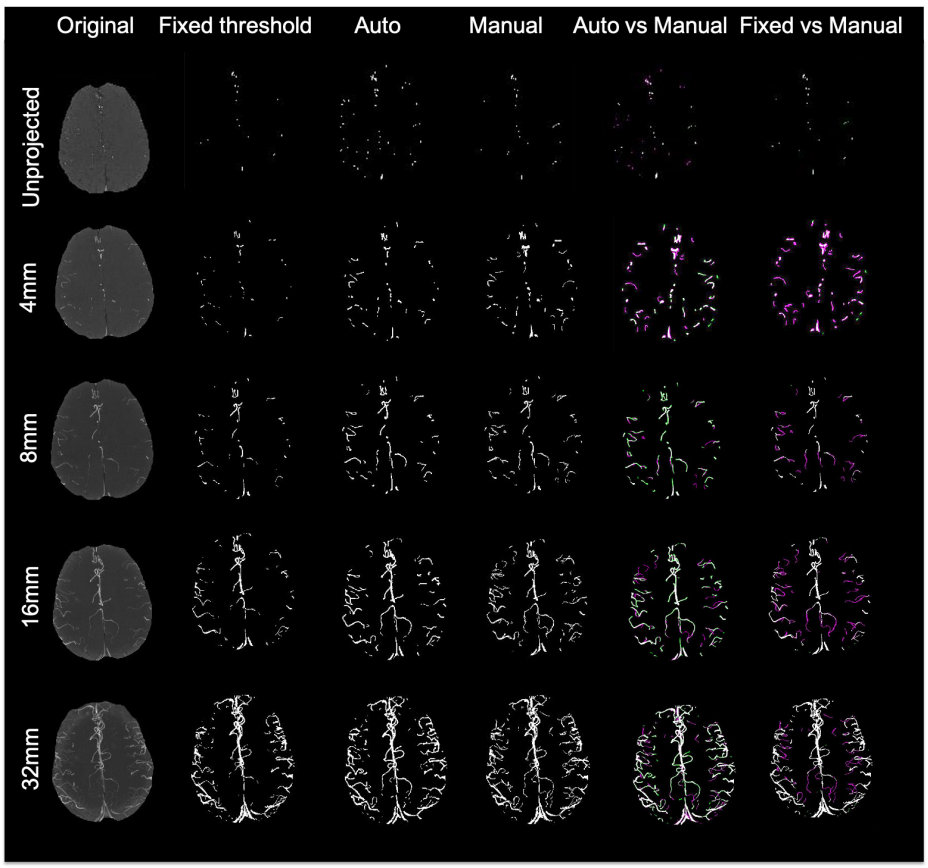

FIGURE 7 | Comparison of different segmentation methods from a central slice projected at different thicknesses. For the last 2 columns, white pixels denote overlapping areas, magenta pixels depict vessels that were only segmented manually, and green pixels missed by the manual segmentation but identified by either our adaptive Frangi **(left)** or fixed thresholding **(right)**.

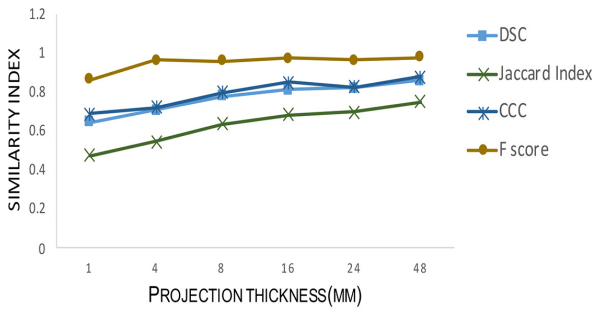

FIGURE 8 | Testing segmentation accuracy between adaptive Frangi and manual segmentation for different projection thicknesses. As the projection thickness increases, the Dice similarity coefficient, Jaccard Index, F-score, and Concordance correlation coefficient between the mid-slice automatic segmentation and the corresponding manual segmentation increase.

TABLE 1 | Vascular metrics for nine scans.

S.No.	Arterial vessel volume (ml)		Total artery length (m)	
	Frangi	Adaptive	Frangi	Adaptive
1	1.20	0.80	1.91	1.78
2	1.46	1.15	2.67	2.20
3	1.08	0.76	1.73	1.53
4	1.10	0.82	2.14	1.85
5	1.86	1.23	2.72	2.34
6	1.33	1.01	2.08	1.97
7	1.15	0.98	1.96	1.88
8	1.2	0.91	1.77	1.69
9	1.1	0.89	2.25	2.11

used in previous works, it holds limitations, and there is no standard method for determining its optimal parameters. Although Phellan and Forkert (2017) determined parameters such as minimum sigma, maximum sigma, and number of sigmas empirically, few methods (Shikata et al., 2004) have employed an EDT-based selection of scales. Our method has the advantage that it scales well for images projected at different thicknesses. The method was tested on 10 image datasets (seven from human subjects and three synthetic datasets) and validated for segmentation accuracy, flexibility, and robustness. To our knowledge, this is the first technique

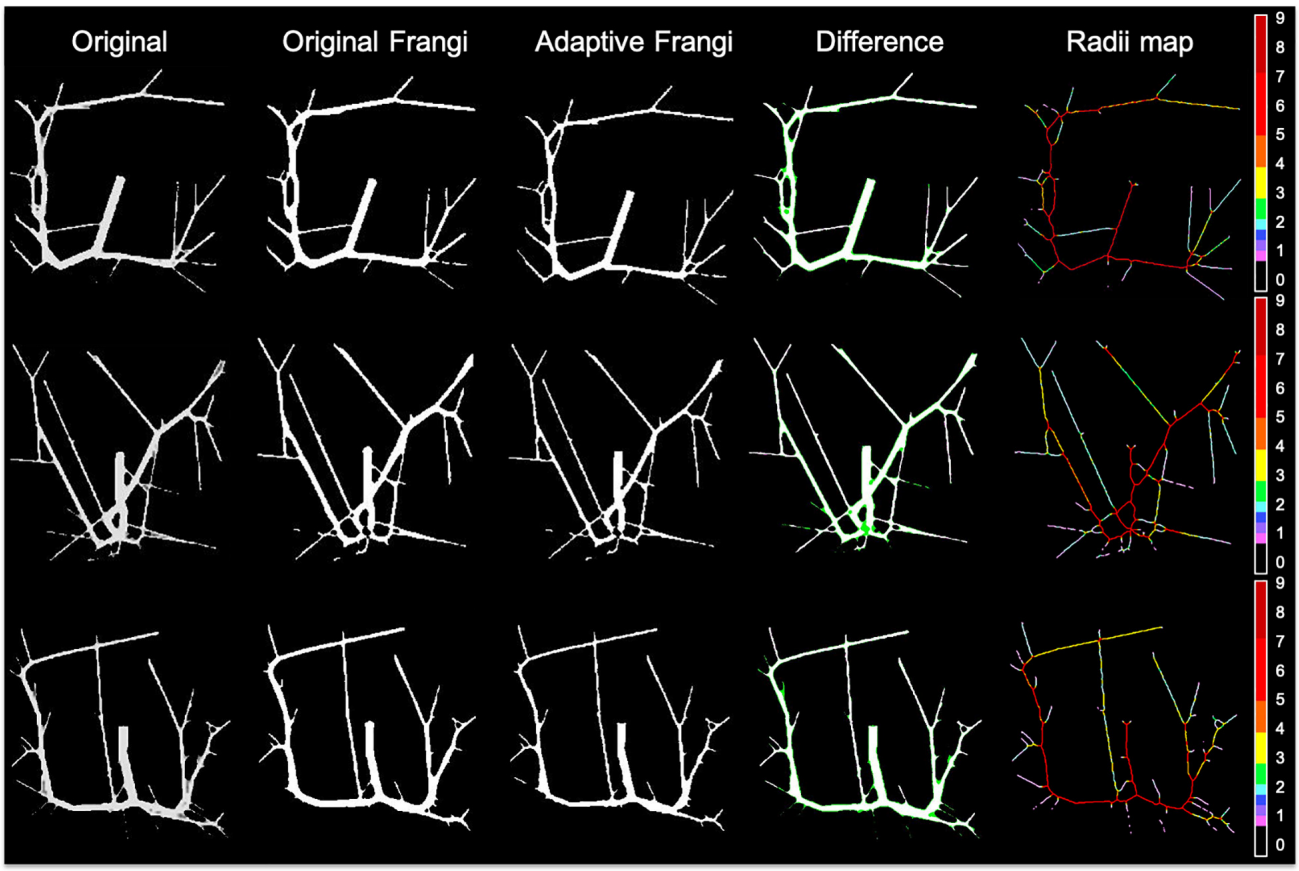

FIGURE 9 | Comparison of original Frangi filtering and adaptive Frangi filtering for a synthetic dataset. In the difference image, white pixels denote overlapping areas, while green pixels represent areas missed by the adaptive Frangi filter. Both filtering strategies missed pixels at the bifurcation points.

TABLE 2 | Testing segmentation accuracy in synthetic images.

S.No.	No. of branches		Dice		Dice with noise		Jaccard index		F1 score		CCC	
	Original	Adaptive	Frangi	Adaptive	Frangi	Adaptive	Frangi	Adaptive	Frangi	Adaptive	Frangi	Adaptive
1	38	36	0.90	0.92	0.86	0.88	0.83	0.85	0.97	0.98	0.85	0.90
2	44	40	0.90	0.90	0.83	0.86	0.82	0.83	0.99	0.99	0.90	0.91
3	56	54	0.90	0.93	0.83	0.86	0.81	0.84	0.97	0.97	0.88	0.92

CCC, concordance correlation coefficient.

to explore the effects of projection thickness on the vessel filter parameters.

The TOF-MRA images used in this work were obtained from the first echo of a multi-echo sequence that simultaneously allows acquisition of SWI images (Bian et al., 2015). As a result, the parameters used for the acquisition were optimized for the combined sequence in general and not for single echo MRA images, which resulted in a longer TR than would otherwise be considered optimal. This resulted in poorer background suppression of MRA images, necessitating the use of a more powerful vessel segmentation technique. The versatility of the algorithm was then demonstrated by applying it to standard clinical MRA scans in two pediatric patients with brain tumors acquired at 1.5T and 3T and in different imaging planes. In order to make the vessel segmentation more sensitive for a given disease application, users can expand the scale range or insert intermediate sigma values in addition to the ones used in this setting.

The manual delineation of the 2D MIP and the 3D volume of continuously projected slices was performed by a neuroradiologist. We found that some smaller branching arteries were missed by our algorithm likely due to small vessels exhibiting lower contrast than larger ones (Dehkordi et al., 2011). The smoothing applied during the vessel enhancement

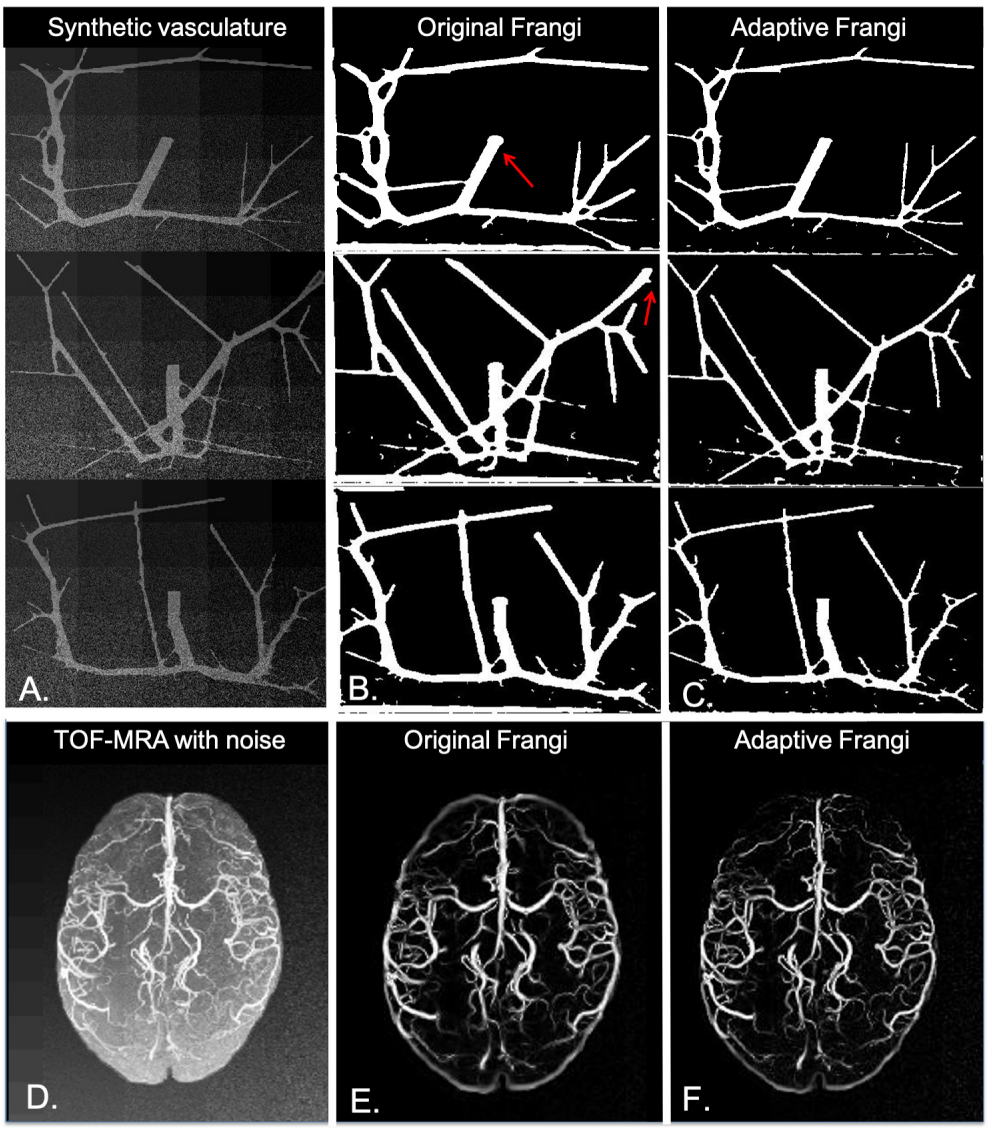

FIGURE 10 | Performance of our algorithm in the presence of noise. **(A)** Noise added synthetic dataset. **(B)** Original Frangi filtered syntetic data. **(C)** Adaptive Frangi filtered synthetic data. Red arrows denote where the Frangi filter produced some bulges at the vessel tips, and two thin vessels were not clearly delineated. **(D)** Noise added to the MIP TOF image of one subject. **(E)** Original Frangi filtered MIP TOF. **(F)** Adaptive Frangi filtered MIP TOF. Adding noise reduced the DSC for this subject from 0.85 to 0.82 for the original Frangi method and from 0.89 to 0.84 for the adaptive Frangi method.

may also contribute to this finding. Although the manual segmentation did a better job of capturing the small vessels, there were regions where our automatic segmentation visually outperformed the manual gold standard. This is because manual segmentation is prone to overestimating smaller vessels. Identification of very small, low-contrast arteries is often complicated even for expert reviewers. Manual segmentation is time-consuming as well as subject to inter-rater and intra-rater variability. In addition, the large number of arterial segments in each dataset poses a practical limit on manual segmentation by radiologists. A major issue with manual vessel diameter measurements in MRA is the variability in setting threshold levels. The estimated vessel diameter on MRA highly depends on the pixel intensity at the vessel boundaries, which is controlled by the selected image threshold (Westenberg et al., 2000).

Increasing the projection thickness has several known consequences on vessel conspicuity including the worsening of partial-volume effects, improvement of noise suppression, the preservation of larger higher-contrast vessels, and dampening of smaller vessels with lower contrast. Because increasing projection thickness improves the contrast of larger vessels, a 2D MIP is often used to increase the contrast-to-noise ratio of large vessels and accurately measure the radii of single large vessels such as the internal carotid artery or the basilar artery (Sun and Parker, 1999). Conversely, multiple non-overlapping

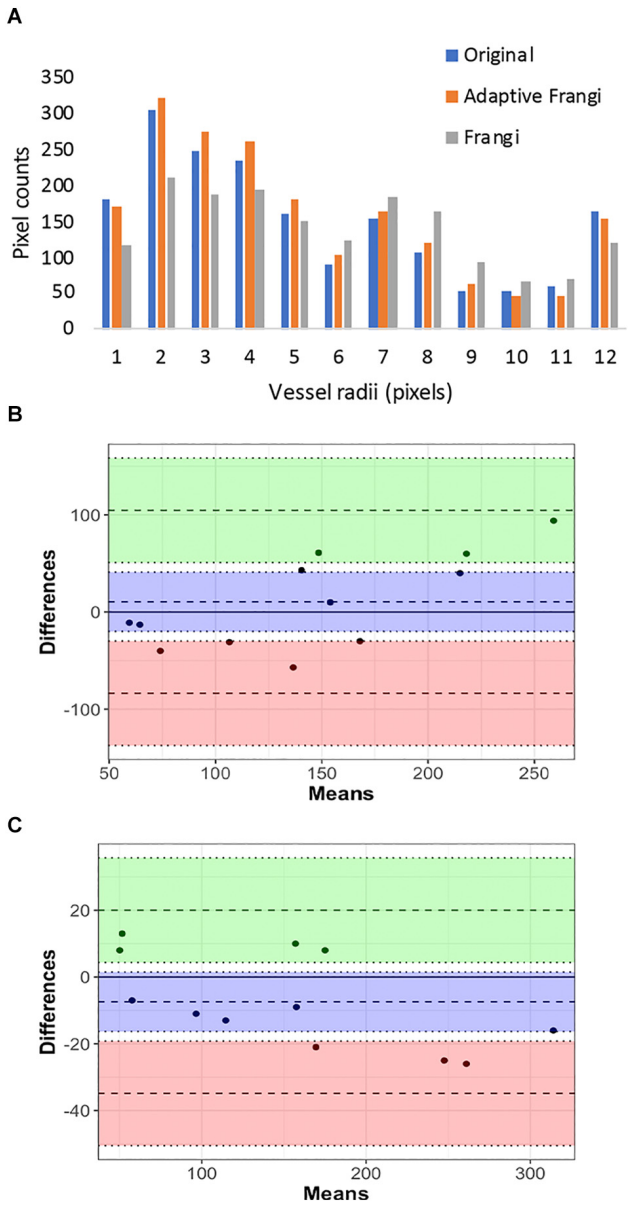

FIGURE 11 | Vessel radii comparison in synthetic images: **(A)** Pixel counts for the different vessel radii obtained using the synthetic ground truth, adaptive Frangi, and Frangi. The Bland–Altman plots for the comparison of Frangi and ground truth **(B)** shows higher differences in the count compared to adaptive Frangi and ground truth **(C)**.

8 or 16 mm projections over the entire volume are more appropriate for estimating the vessel radii distribution through the entire image volume because smaller vessels with low contrast can be obscured using larger projection thicknesses. The automatic segmentation from projected images improved delineation of small blood vessels, even at larger projection thicknesses. The observed increase in similarity metrics for larger projection thickness could be due to either increased accuracy of the manual segmentations with higher projection thickness or the fact that the Frangi filter typically looks for tubular structures with higher vesselness scores compared to blob like structures. With higher projection thickness, more volume is also covered, potentially causing more vessels to appear as tubular.

Although our algorithm scales well for images of different projection thickness, it fundamentally performs assessments on 2D projection views of inherently 3D structures. This can inevitably cause loss of important vascular structure due to varying projection angles. Although other methods that consider the full 3D structure of vessels (Ilicak et al., 2016) can overcome this limitation by utilizing a reconstruction strategy that leverages vascular maps extracted from undersampled angiographic acquisitions with higher levels of background suppression, they have not been evaluated for different projection thicknesses and are far more computationally intensive, precluding the feasibility for their incorporation in clinical practice. Our method, conversely, takes only a few minutes to produce the segmented vessels on a single CPU and corresponding vessel radii maps and can be applied for any projection thickness.

Although our method can be applied to any number of images, the results for only seven human subjects and three synthetic images are presented here to discuss performance metrics in detail. The adaptive Frangi segmentation and radii estimation method should serve as a useful tool to monitor the subtle changes in arterial structure that are expected in a variety of vascular diseases. Some examples include moyamoya, atherosclerosis, radiation-induced arteriopathy, autoimmune vasculitis, and even chronic vascular disorders such as hypertension. It can aid in the automated evaluation of cerebral vasospasm after aneurysm treatment where the magnitude and pattern of vascular injury are variable in each patient (Schob et al., 2019). Another example is the evaluation of complex arteriovenous shunts, where the quantification of lesion size, location, and pattern is highly rater-dependent (Geibprasert et al., 2010). Quantification of the severity of these complex lesions using this algorithm could help to establish a much more reliable grading system as long as lumen diameters constitute at least three pixels (Hoogeveen et al., 1998).

CONCLUSION

In conclusion, we have developed an automated tool for accurate segmentation of arteries from TOF-MRA images with suboptimal background suppression that provides accurate measures of vessel radii for a wide range of projection thicknesses. We have demonstrated the feasibility of applying an adaptive Frangi method on volunteer images from a 7T scanner. We believe that this approach can easily be extended to lower field strength data for routine clinical and research use given that its parameters are automatically calculated based on vessel radii, and it demonstrated superior performance on synthetic images of various contrasts and noise levels. Future work will apply this automated algorithm to study differences in vessel radii associated with normal aging, vessel pruning due to neurovascular disease, and the post-radiation angiitis.

DATA AVAILABILITY STATEMENT

The Matlab code and volunteer datasets generated for this study are available upon request to the corresponding author.

ETHICS STATEMENT

The studies involving human participants were reviewed and approved by UCSF Institutional Review Board. Written informed consent to participate in this study was provided by the participants' legal guardian/next of kin.

AUTHOR CONTRIBUTIONS

SA and JL conceived the study and wrote the manuscript. AJ performed the scans. SA and SP processed and analyzed the data. MM and CH helped with data analysis and interpretation.

FUNDING

The authors would like to acknowledge the support received from the NIH-NICHD grant RO1HD079568.

REFERENCES

Arlart, I. P., Bongartz, G. M., and Marchal, G. (1995). *Magnetic Resonance Angiography*. Tokyo: Springer.

Aylward, S. R., and Bullitt, E. (2001). Initialization, noise, singularities and scale in height ridge traversal for tubular object centerline extraction. *IEEE Trans. Med. Imaging* 21, 61–75. doi: 10.1109/42.993126

Bae, K. T., Park, S. H., Moon, C. H., Kim, J. H., Kaya, D., and Zhao, T. (2010). Dual-echo arteriovenography imaging with 7T MRI. *J. Magn. Reson. Imaging* 31, 255–261. doi: 10.1002/jmri.22019

Bian, W., Banerjee, S., Kelly, D. A. C., Hess, C. P., Larson, P. E. Z., Chang, S. M., et al. (2015). Simultaneous imaging of radiation-induced cerebral microbleeds, arteries and veins, using a multiple gradient echo sequence at 7 Tesla. *J Magn. Reson. Imaging* 42, 269–279. doi: 10.1002/jmri.24802

Chapman, B. E., and Parker, D. L. (2001). *Comparison of Three Multi-Scale Vessel Enhancement Filters Intended For Intracranial Mra: Initial Phantom Results*. Washington: International Society for Optics and Photonics.

Csurka, G., Larlus, D., and Perronnin, F. (2013). "What is a good evaluation measure for semantic segmentation?," in *Proceedings of the British Machine Vision Conference*, Meylan.

Dehkordi, M. T., Sadri, S., and Doosthoseini, A. (2011). A review of coronary vessel segmentation algorithms. *J. Med. Signals Sens.* 1, 49–54. doi: 10.4103/2228-7477.253755

Deistung, A., Dittrich, E., Sedlacik, J., Rauscher, A., and Reichenbach, J. R. (2009). TOF- SWI: simultaneous time of flight and fully flow compensated susceptibility weighted imaging. *J. Magn. Reson. Imaging* 29, 1478–1484. doi: 10.1002/jmri.21673

Dice, L. R. (1945). Measures of the amount of ecologic association between species. *Ecology* 26, 297–302.

Du, Y. P., and Jin, Z. (2008). Simultaneous acquisition of MR angiography and venography (MRAV). *Magn. Reson. Med.* 59, 954–958. doi: 10.1002/mrm.21581

Fischer, I., Gagner, J. P., Law, M., Newcomb, E. W., and Zagzag, D. (2005). Angiogenesis in gliomas: biology and molecular pathophysiology. *Brain. Pathol.* 15, 297–310. doi: 10.1111/j.1750-3639.2005.tb00115.x

Frangi, A. F., Niessen, W. J., Vincken, K. L., and Viergever, M. A. (1998). "Multiscale vessel enhancement filtering," in *Medical Image Computing and Computer-Assisted Intervention — MICCAI'98. MICCAI 1998. Lecture Notes in Computer Science*, Vol. 1496, eds W. M. Wells, A. Colchester, and S. Delp (Berlin: Springer).

Gao, X., Uchiyama, Y., Zhou, X., Hara, T., Asano, T., and Fujita, H. (2011). A fast and fully automatic method for cerebrovascular segmentation on time-of-flight (TOF) MRA image. *J. Digit. Imaging* 24, 609–625. doi: 10.1007/s10278-010-9326-1

Geibprasert, S., Pongpech, S., Jiarakongmun, P., Shroff, M. M., Armstrong, D. C., and Krings, T. (2010). Radiologic assessment of brain arteriovenous malformations: what clinicians need to know. *Radiographics* 30, 483–501. doi: 10.1148/rg.302095728

Hamarneh, G., and Jassi, P. (2010). Vascusynth: simulating vascular trees for generating volumetric image data with ground-truth segmentation and tree analysis. *Comput. Med. Imaging Graph.* 34, 605–616. doi: 10.1016/j.compmedimag.2010.06.002

Hoogeveen, R. M., Bakker, C. J., and Viergever, M. A. (1998). Limits to the accuracy of vessel diameter measurement in MR angiography. *J Magn. Reson. Imaging* 8, 1228–1235. doi: 10.1002/jmri.1880080608

Hsu, C. Y., Schneller, B., Alaraj, A., Flannery, M., Zhou, X. J., and Lininger, A. (2017). Automatic recognition of subject-specific cerebrovascular trees. *Magn. Reson. Med.* 77, 398–410. doi: 10.1002/mrm.26087

Ilicak, E., Cetin, S., Bulut, E., Oguz, K. K., Saritas, E. U., Unal, G., et al. (2016). Targetted vessel reconstruction in non-contrast-enhanced steady-state free precession angiography. *NMR Biomed.* 29, 532–544. doi: 10.1002/nbm.3497

Jaccard, P. (1901). 'Etude comparative de la distribution florale dans une portion des alpes et des jura. *Bull. Soc. Vaudoise Sci. Nat.* 37, 547–579.

Jellinger, K. A., and Attems, J. (2006). Prevalence and impact of cerebrovascular pathology in Alzheimer's disease and parkinsonism. *Acta Neurol. Scand.* 114, 38–46. doi: 10.1111/j.1600-0404.2006.00665.x

Johnson, D. B. S., Prince, M. R., and Chenevert, T. L. (1998). Magnetic resonance angiography: a review. *Acad. Radiol.* 5, 289–305.

Kawel, N., Seifert, B., Luetolf, M., and Boehm, T. (2009). Effect of slab thickness on the CT detection of pulmonary nodules: use of sliding thin-slab maximum intensity projection and volume rendering. *AJR Am. J. Roentgenol.* 192, 1324–1329. doi: 10.2214/AJR.08.1689

Krissian, K., Malandain, G., Ayache, N., Vaillant, R., and Trousset, Y. (2000). Model Based Detection of Tubular Structures in 3D Images. *Comput. Vis. Image Understand.* 8, 130–171.

Lin, L. (1989). A concordance correlation coefficient to evaluate reproducibility. *Biometrics* 45, 255–268.

Lorigo, L. M., Faugeras, O. D., Grimson, W. E., Keriven, R., Kikinis, R., Nabavi, A., et al. (2001). CURVES: curve evolution for vessel segmentation. *Med. Image Anal.* 5, 195–206. doi: 10.1016/s1361-8415(01)00040-8

Minagar, A., Jy, W., Jimenez, J. J., and Alexander, J. S. (2006). Multiple sclerosis as a vascular disease. *Neurol. Res.* 28, 230–235.

Nystroem, I., and Smedby, O. (2000). "A new presentation method for magnetic resonance angiography images based on skeletonization," in *Proceedings of the Volume 3976, Medical Imaging 2000: Image Display and Visualization*, San Diego, CA.

Persson, A., Dahlstrom, N., Engellau, L., Larsson, E. M., Brismar, T. B., and Smedby, O. (2004). Volume rendering compared with maximum intensity projection for magnetic resonance angiography measurements of the abdominal aorta. *Acta Radiol.* 45, 453–459. doi: 10.1080/02841850410006876

Phellan, R., and Forkert, N. D. (2017). Comparison of vessel enhancement algorithms applied to Time-of-Flight MRA images for cerebrovascular segmentation. *Med. Phys.* 44, 5901–5915. doi: 10.1002/mp.12560

Sato, Y., Nakajima, S., Shiraga, N., Atsumi, H., Yoshida, S., Koller, T., et al. (1998). Three-dimensional multi-scale line filter for segmentation and visualization of curvilinear structures in medical images. *Med. Image Anal.* 2, 143–168. doi: 10.1016/s1361-8415(98)80009-1

Schob, S., Richter, C., Scherlach, C., Lindner, D., Planitzer, U., Hamerla, G., et al. (2019). Delayed stroke after aneurysm treatment with flow diverters in small cerebral vessels: a potentially critical complication caused by subacute vasospasm. *J. Clin. Med.* 8, 1649–1667. doi: 10.3390/jcm8101649

Sethian, J. A. (1996). A fast marching level set method for monotonically advancing fronts. *Proc. Natl. Acad. Sci. U.S.A.* 93, 1591–1595. doi: 10.1073/pnas.93.4.1591

Shikata, H., Hoffman, E., and Sonka, M. (2004). Automated segmentation of pulmonary vascular tree from 3D CT images. *Proc. SPIE.* 5369, 107–116.

Smith, S. M. (2002). Fast robust automated brain extraction. *Annu. Meet. Organ. Hum. Brain Map*. 17, 143–155. doi: 10.1002/hbm.10062

Sun, Y., and Parker, D. L. (1999). Performance analysis of maximum intensity projection algorithm for display of MRA images. *IEEE Trans. Med. Imaging* 18, 1154–1169. doi: 10.1109/42.819325

Suri, J. S., Liu, K., Reden, L., and Laxminarayan, S. (2002). A review on MR vascular image processing: skeleton versus non skeleton approaches: part II. *IEEE Trans. Inf. Technol. Biomed.* 6, 338–350. doi: 10.1109/titb.2002.804136

U-King-Im, J. M., Graves, M. J., Cross, J. J., Higgins, N. J., Wat, J., Trivedi, R. A., et al. (2007). Internal carotid artery stenosis: accuracy of subjective visual impression for evaluation with digital subtraction angiography and contrast-enhanced MR angiography. *Radiology* 244, 213–222. doi: 10.1148/radiol.2441060749

Westenberg, J. J., van der Geest, R. J., Wasser, M. N., van der Linden, E. L., van Walsum, T., van Assen, H. C., et al. (2000). Vessel diameter measurements in gadolinium contrast-enhanced three-dimensional MRA of peripheral arteries. *Magn. Reson. Med.* 18, 13–22. doi: 10.1016/s0730-725x(99)00099-5

Conflict of Interest: The authors declare that the research was conducted in the absence of any commercial or financial relationships that could be construed as a potential conflict of interest.

Copyright © 2020 Avadiappan, Payabvash, Morrison, Jakary, Hess and Lupo. This is an open-access article distributed under the terms of the Creative Commons Attribution License (CC BY). The use, distribution or reproduction in other forums is permitted, provided the original author(s) and the copyright owner(s) are credited and that the original publication in this journal is cited, in accordance with accepted academic practice. No use, distribution or reproduction is permitted which does not comply with these terms.

frontiers in Neuroscience

TECHNOLOGY AND CODE
published: 14 July 2020
doi: 10.3389/fnins.2020.00712

NOSA, an Analytical Toolbox for Multicellular Optical Electrophysiology

*Sebastian Oltmanns[1], Frauke Sophie Abben[1], Anatoli Ender[2], Sophie Aimon[3], Richard Kovacs[1], Stephan J. Sigrist[2,4,5], Douglas A. Storace[6], Jörg R. P. Geiger[1] and Davide Raccuglia[1]**

[1] Institute of Neurophysiology, Charité – Universitätsmedizin Berlin, Corporate Member of Freie Universität Berlin and Humboldt-Universität zu Berlin, and Berlin Institute of Health, Berlin, Germany, [2] German Center for Neurodegenerative Diseases, Charité – Universitätsmedizin Berlin, Berlin, Germany, [3] School of Life Sciences, Technical University of Munich, Freising, Germany, [4] Institute of Biology/Genetics, Freie Universität Berlin, Berlin, Germany, [5] NeuroCure, Charité – Universitätsmedizin Berlin, Corporate Member of Freie Universität Berlin, Humboldt-Universität zu Berlin, and Berlin Institute of Health, Berlin, Germany, [6] Department of Biological Science, Florida State University, Tallahassee, FL, United States

OPEN ACCESS

Edited by:
Jorge Valero, Achucarro Basque Center for Neuroscience, Spain

Reviewed by:
Alejandro Carretero Guillén, Achucarro Basque Center for Neuroscience, Spain
Raudel Sánchez-Campusano, Universidad Pablo de Olavide, Spain
Paolo Bonifazi, Tel Aviv University, Israel

***Correspondence:**
Davide Raccuglia
davide.raccuglia@charite.de

Specialty section:
This article was submitted to Brain Imaging Methods, a section of the journal Frontiers in Neuroscience

Received: *02 April 2020*
Accepted: *12 June 2020*
Published: *14 July 2020*

Citation:
Oltmanns S, Abben FS, Ender A, Aimon S, Kovacs R, Sigrist SJ, Storace DA, Geiger JRP and Raccuglia D (2020) NOSA, an Analytical Toolbox for Multicellular Optical Electrophysiology. Front. Neurosci. 14:712. doi: 10.3389/fnins.2020.00712

Understanding how neural networks generate activity patterns and communicate with each other requires monitoring the electrical activity from many neurons simultaneously. Perfectly suited tools for addressing this challenge are genetically encoded voltage indicators (GEVIs) because they can be targeted to specific cell types and optically report the electrical activity of individual, or populations of neurons. However, analyzing and interpreting the data from voltage imaging experiments is challenging because high recording speeds and properties of current GEVIs yield only low signal-to-noise ratios, making it necessary to apply specific analytical tools. Here, we present NOSA (Neuro-Optical Signal Analysis), a novel open source software designed for analyzing voltage imaging data and identifying temporal interactions between electrical activity patterns of different origin. In this work, we explain the challenges that arise during voltage imaging experiments and provide hands-on analytical solutions. We demonstrate how NOSA's baseline fitting, filtering algorithms and movement correction can compensate for shifts in baseline fluorescence and extract electrical patterns from low signal-to-noise recordings. NOSA allows to efficiently identify oscillatory frequencies in electrical patterns, quantify neuronal response parameters and moreover provides an option for analyzing simultaneously recorded optical and electrical data derived from patch-clamp or other electrode-based recordings. To identify temporal relations between electrical activity patterns we implemented different options to perform cross correlation analysis, demonstrating their utility during voltage imaging in *Drosophila* and mice. All features combined, NOSA will facilitate the first steps into using GEVIs and help to realize their full potential for revealing cell-type specific connectivity and functional interactions.

Keywords: voltage imaging, GEVI, analytical toolbox, multicellular activity, optical electrophysiology

INTRODUCTION

One goal of The American BRAIN initiative was to develop methods to comprehend complex activity patterns in specific brain networks and even in whole brains (Alivisatos et al., 2012). One crucial step toward gaining insight into the mechanisms and interactions of neural activity patterns is the development of software that allows for measuring multicellular electrical activity and analyzing their complex datasets (Alivisatos et al., 2012).

Genetically encoded voltage indicators (GEVIs) have emerged as promising tools for measuring neural electrical activity (Lin and Schnitzer, 2016; Yang and St-Pierre, 2016). GEVIs are powerful, in part because they can be genetically targeted to specific neural populations and optically report the electrical activity from many neurons simultaneously, and even from neuropil that is otherwise inaccessible to classical electrophysiology. GEVIs have been successfully used for monitoring multicellular activity and population dynamics in *Drosophila* (Cao et al., 2013; Raccuglia et al., 2016, 2019; Aimon et al., 2019), visual and olfactory responses in mice (Gong et al., 2015; Storace et al., 2015; Storace and Cohen, 2017), cerebellar activity in Zebrafish (Miyazawa et al., 2018) and also pharyngeal activity in *C. elegans* (Azimi Hashemi et al., 2019).

Although GEVIs are being continually improved (Lin and Schnitzer, 2016; Storace et al., 2016), high recording speeds, low signal-to-noise ratios (SNR) and GEVI-specific kinetics bring about unique challenges with respect to data analysis (Yang and St-Pierre, 2016; Kulkarni and Miller, 2017) and thus require the development of adequate processing software. Yet, there is currently no freely available software, which combines processing tools addressing these challenges with analytical tools for identifying specific activity patterns, temporal relations and functional interactions.

Here we present NOSA (Neuro-Optical Signal Analysis) – an open source software designed specifically for the analysis of multicellular optical electrophysiology. NOSA features baseline fitting and filtering algorithms to extract electrical patterns from high speed recordings with low SNR. Moreover, NOSA provides analytical tools for identifying specific activity patterns and their temporal relation via functions that provide spectral and cross-correlation analysis. NOSA also includes features for spike- and burst detection, movement artifact compensation, and the ability to analyze simultaneously performed optical and electrical recordings. With these analytical tools, intuitive design, and convenient graphical interface, NOSA should greatly facilitate the first steps into using GEVIs, enabling laboratories around the world to perform and analyze multicellular voltage imaging recordings.

MATERIALS AND METHODS

NOSA Software

NOSA was written in Python 3.7.1 (see https://docs.python.org/3/license.html for license information) and only runs on Windows. Besides default packages and built in functions, NOSA uses a variety of additional packages (**Table 1**). The executable NOSA file, the master code, a manual containing additional information on the graphical user interface, the function of specific features, performance aspects and workflow examples are provided under the following GitHub repository: https://github.com/DavideR2020/NOSA. To obtain example files please send an email to the lead contact.

Optical and Classical Electrophysiology of R5 Neurons in *Drosophila melanogaster*

Flies (*Drosophila melanogaster*) were reared on standard cornmeal food at 25°C and 60% humidity under a 12 h light/dark regime. All flies were obtained from the Bloomington Stock resource center (BDRC). Experiments were performed with 3-10 d old female flies at ZT 8-12 (Zeitgeber time; during a 12/12 h light/dark cycle the onset of light is at ZT 0 h and the offset of light is at ZT 12 h). Whole-brain explant dissections and fly *in vivo* preparation were performed as previously described (Cao et al., 2013; Owald et al., 2015). During *ex vivo* experiments (**Figures 3**, **4**) external solution consisted of (in mM): 90 NaCl, 3 KCl, 1.5 $CaCl_2$, 5 $MgCl_2$, 1 NaH_2PO_4, 10 glucose, 10 sucrose, 8 trehalose, 5 TES and 26 $NaHCO_3$. During *in vivo* experiments (**Figures 5**, **6**) external solution consisted of (in mM): 70 NaCl, 3 KCl, 1.5 $CaCl_2$, 20 $MgCl_2$, 1 NaH_2PO_4, 10 glucose, 10 sucrose, 8 trehalose, 5 TES, and 26 $NaHCO_3$. For a fully functional Mg^{2+} plug, Drosophila NMDA receptors require 20 mM of Mg^{2+} (Miyashita et al., 2012). To substitute for missing sensory input in the *ex vivo* preparation, we reduced external Mg^{2+} to 5 mM which leads to spontaneous activity in R5 neurons (Raccuglia et al., 2019).

Imaging was performed on an Olympus BX51WI microscope using a Plan Apochromat 40×, numerical aperture 0.8, water-immersion objective (Olympus, Japan). ArcLight was excited at 470 nm using a Lumencor Spectra X-Light engine LED system. LED power was adjusted for each recording individually to make sure that fluorescent images were not saturated. The objective C-mount image was projected onto an Andor iXon-888 camera controlled by Andor Solis software. Imaging was performed at frame rates of 80 Hz (**Figures 3A–C**, **5**, **6**), 160 Hz (**Figures 3D–G**), 250 Hz and 1000 Hz (**Figure 4**).

In vivo (**Figure 5**) whole-cell patch-clamp recordings from R5 neurons were performed at ZT 8-12 as reported elsewhere (Wilson and Laurent, 2005; Murthy and Turner, 2013; Donlea et al., 2018). Neurons were recorded for up to 5 min. Identification of R5 neurons was based on ArcLight expression. External saline was used as described above. Patch pipettes (7–10 MΩ) were filled with internal saline containing (mM): 135 K-aspartate, 10 HEPES, 1 EGTA, 1 KCl, 4 MgATP, 0.5 Na3GTP. Internal solution was adjusted to a pH of 7.2, with an osmolarity of 265 mmol/kg.

Ca^{2+} Imaging of Hippocampal Slices

Animal care and handling was in accordance with the Helsinki declaration and institutional guidelines. Protocols for organ removal and culturing were approved by the State Office of

TABLE 1 | Packages used for NOSA.

Name	Version	License type	Copyright notice	Website
NumPy	1.16.2	BSD	Copyright© 2005-2018, NumPy Developers. All rights reserved.	https://www.numpy.org
SciPy	1.2.1	BSD	Copyright© 2001, 2002 Enthought, Inc. All rights reserved. Copyright© 2003-2013 SciPy Developers.All rights reserved.	https://www.scipy.org
PyQt5	5.11.3	GPL v3	Copyright© 2018 Riverbank Computing Limited	https: //www.riverbankcomputing.com/software/pyqt/
PyQtGraph	0.10.0	MIT	Copyright (c) 2012 University of North Carolina at Chapel Hill Luke Campagnola (luke.campagnola@gmail.com)	http://www.pyqtgraph.org
Matplotlib	3.0.3	PSF-based	©Copyright 2002 - 2012 John Hunter, Darren Dale, Eric Firing, Michael Droettboom and the Matplotlib development team; 2012 - 2018 The Matplotlib development team	http://matplotlib.org
pyStackReg	0.2.1	Custom	C + + Port of the TurboReg ImageJ Plugin. Original code by Philippe Thevenaz (Thevenaz et al., 1998). Porting by Gregor Lichtner	https://bitbucket.org/glichtner/pystackreg
DIPY (Garyfallidis et al., 2014)	0.15.0	Revised BSD-2-Clause	Copyright (c) 2008-2019, dipy developers. All rights reserved.	http://dipy.org
QDarkStyle	2.5.4	MIT	Copyright (c) 2013-2018 Colin Duquesnoy.	https://github.com/ColinDuquesnoy/QDarkStyleSheet
Neo	0.7.1	BSD-3-Clause	Copyright (c) 2010-2018, Neo authors and contributors.	http: //neuralensemble.org/neo
Quantities	0.12.3	BSD	Copyright (c) 2012, Darren Dale dsdale24@gmail.com All rights reserved.	http://python-quantities.readthedocs.io/
XlsxWriter	1.1.5	BSD	Copyright (c) 2013, John McNamara jmcnamara@cpan.org All rights reserved.	https://github.com/jmcnamara/XlsxWriter
Tifffile	2019.3.8	BSD	Copyright (c) 1994-2019, Christoph Gohlke. All rights reserved.	https://www.lfd.uci.edu/$\sim$gohlke/
PyInstaller	3.4	GPL-based	Copyright (c) 2010-2019, PyInstaller Development Team Copyright (c) 2005-2009, Giovanni Bajo Based on previous work under copyright (c) 2002 McMillan Enterprises, Inc.	http://www.pyinstaller.org/
Markdown	1.0.1	BSD-style	Copyright© 2004, John Gruber http://daringfireball.net/ All rights reserved.	https://daringfireball.net/projects/markdown/
Markdown-styles	3.1.10	BSD-3-Clause	none provided – created by GitHub user mixu (Mikito Takada)	https://github.com/mixu/markdown-styles

Health and Social Affairs Berlin, under the license number T0123/11. Organotypic hippocampal slice cultures were prepared as described previously (Kann et al., 2011; Prager et al., 2019). In short, hippocampal slices (400 μm) were obtained from Wistar rat pups at postnatal day 6–7. Slices were positioned on cell culture membrane inserts (Millicell-CM, Millipore) and maintained for 6 days in culture medium (50% MEM, 25% HBSS, 25% Horse Serum and 1 mM L-glutamine, pH set to 7.3) at 5% CO_2. At day 7, slice cultures were bulk stained with OGB-1-AM BAPTA (5 μM in DMSO, 0.01% Pluronic F-127, 0.005% Cremophor) by submerging them for 50 min at room temperature in carbogen bubbled serum free medium.

Fluorescence recordings were obtained with a spinning disk confocal microscope (Andor Revolution, BFI Optilas GmbH, Gröbenzell, Germany), equipped with an EMCCD camera (Andor iXonEM+, 60x objective N.A.1, 2 x binning, 20 Hz recording speed, laser intensity 150–200 μW at the focal level). Slice cultures were superfused with carbogen (95% O_2, 5% CO_2) saturated artificial cerebrospinal fluid containing (in mM): 129 NaCl, 3 KCl, 1.25 NaH_2PO_4, 1.8 $MgSO_4$, 1.6 $CaCl_2$, 26 $NaHCO_3$, and 10 glucose (pH 7.4, t = 30°C). For induction of synchronized epileptiform activity, Mg^{2+} was omitted and KCl was elevated to 5 mM (Prager et al., 2019).

Whole Brain Voltage Imaging in Drosophila

Whole brain recordings were performed using light field microscopy as described in detail elsewhere (Aimon et al., 2019).

FIGURE 1 | NOSA Interface. **(A)** The file manager shows imported files and contains options for movement correction, temporal cropping, offset correction and interpolation of the recording speed. **(B)** ROI manager showing added ROIs, which can be renamed and deleted. ROI masks can be generated by copying ROIs into other files. **(C)** Video panel showing currently selected frame and added ROIs. The recording can be adjusted for brightness and contrast. **(D)** Average fluorescence intensity of selected ROIs with baseline fitting curve and slide for selecting specific frames of the recording. **(E)** Processed data showing relative changes in fluorescence over time. Calculation of the relative change in fluorescence is based on recording speed, background subtraction, baseline correction and smoothing. **(F)** Panel for semi-automatic detection of spikes and bursts. Detected events are indicated with orange arrows and white lines/squares indicating spikes/bursts. **(G)** Power spectrum analysis based on processed data. If the event shape feature is selected this panel also shows the average shape of detected events. **(H)** Panel showing spike cross correlation calculated based on detected spikes and amplitude cross correlation calculated based on relative changes in fluorescence. **(I)** Control panel for adjusting the settings of each feature.

In short, a modified upright Olympus BX51W with a 20x NA 1.0 XLUMPlanFL (Olympus) was used. An adequate microlens array (RPC Photonics) positioned at the image plane and two relay lenses (50 mm f/1.4 NIKKOR-S Auto from Nikon) projected the image onto the sensor of a scientific CMOS camera (Hamamatsu ORCA-Flash 4.0). A 490 nm LED (pE100 CoolLED) at approximately 10% of its full power was used for excitation. As filter set we used a 482/25 bandpass filter, a 495-nm dichroic beam splitter, and a 520/35 bandpass emission filter (BrightLine, Semrock). The recording was performed at a frame rate of 200 Hz. The whole brain volume was reconstruction from the light field image as described in Aimon et al. (2019).

Voltage and Calcium Imaging in the Olfactory Bulb

Olfactory bulb recordings in mice were performed as described in detail elsewhere (Storace et al., 2015). In short, C57BL/6 mice (JAX, Bar Harbor, MA) were injected into the olfactory bulbs with AAV1 expressing either ArcLight- or GCaMP6f. Mice were anesthetized (ketamine/xylazine) and the bone above both olfactory bulbs was either thinned or removed. The exposure was covered with agarose and sealed with a glass coverslip. The dorsal surface of both hemispheres was illuminated with 485 ± 25 nm light using epifluorescence illumination on a Leitz Ortholux II microscope with a tungsten halogen lamp or a 150 W Xenon arc lamp (Opti Quip) and a 515 nm long-pass dichroic mirror. Fluorescence emission was recorded with a NeuroCCD-SM256 camera with 2 × 2 binning at 125 Hz using NeuroPlex software (RedShirtImaging, Decatur, GA). All surgical procedures were approved by the Yale IACUC.

RESULTS

NOSA Interface and Overview of Processing Tools

Our software package NOSA (**Figure 1**) is designed to process and analyze voltage imaging recordings. Recordings can be imported into NOSA as tif/tiff files, which can be temporally cropped (the user can select a specific time window) or corrected

for movement artifacts (**Figure 1A**). NOSA automatically calculates the relative changes in fluorescence for selected regions of interest (ROIs) (**Figures 1B,C**) after factoring in recording speed, background correction as well as selected fitting (e.g., exponential drift correction) and filtering algorithms (**Figure 1D**). Activity patterns from different ROIs (e.g., cells) can be displayed in one plot to facilitate comparisons, although the user can easily switch to a more detailed view of the currently selected ROI (**Figure 1E**).

Because most GEVIs exhibit decreases in their fluorescence in response to depolarization, NOSA provides the option to invert the relative changes in fluorescence (**Figure 1B**). To generate ROI masks, selected ROIs can be copied and pasted into other recordings (**Figure 1B**). All data extracted by NOSA can be exported as spreadsheet files (**Figure 1B**). As high recording speeds generate a larger number of frames, we included simple but efficient options to increase software performance. For example, the recording frequency can be reduced by applying different interpolation algorithms (**Figure 1B**, right-click on file name, see next chapter for details). Moreover, software performance can be increased by deselecting the live preview which will suspend processing of changes while moving the ROI. Within each uploaded recording there is a default square ROI. Additional ROIs can be added by pressing the "add" button and the ROI shape can be changed with a right click (**Figure 1B**).

NOSA features power spectrum analysis as well as spike and burst detection to analyze activity patterns (**Figures 1F,G**). The event shape feature uses detected events to display the average firing characteristics of a neuron. To analyze temporal relations and functional interactions between activity patterns, cross correlation can be performed on detected events and on the relative changes of neural activity in optical and electrical recordings (**Figure 1H**). Via the control panel all features can be controlled (**Figure 1I**) for each ROI independently and settings selected for one ROI can easily be applied to all other ROIs.

NOSA Workflow

NOSA provides an optimal workflow that facilitates the analysis of optical multicellular data (**Figure 2**), while also providing the flexibility to easily switch back and forth between different features. After uploading the data, the user should scan the recording for a time window of interest and apply the temporal cropping feature. If necessary, the processing speed can be enhanced by deactivating the live preview mode, by using a square ROI and by reducing the number of data points via resampling the recording frequency (adjust frequency, right click

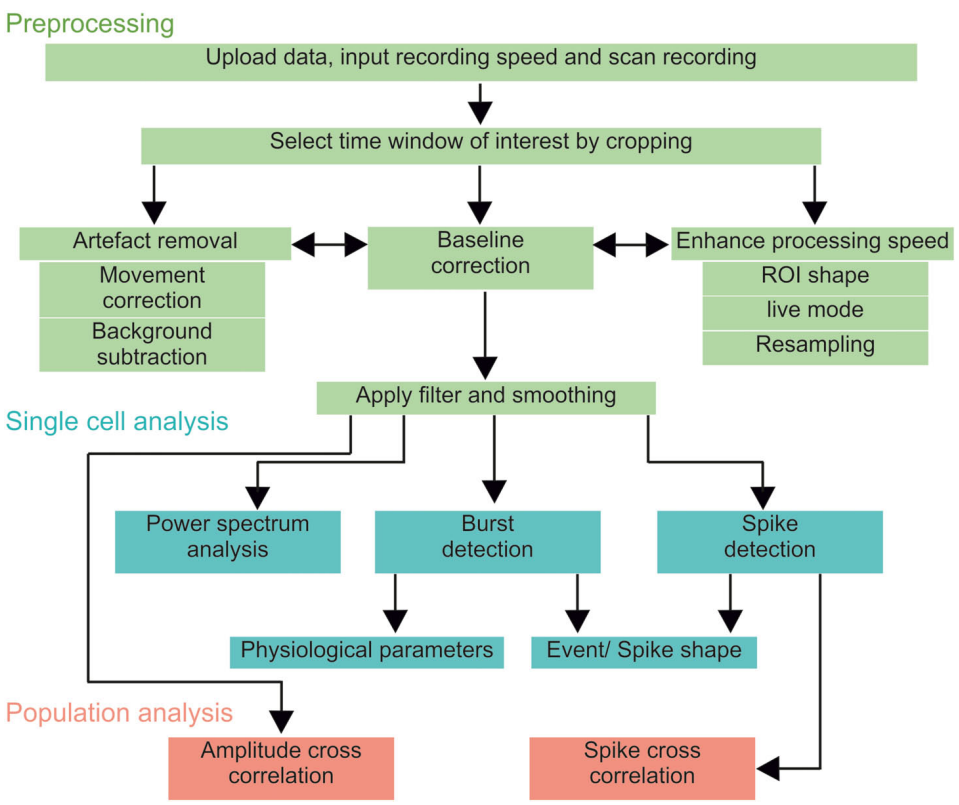

FIGURE 2 | NOSA workflow. After uploading a recording, it should first be scanned for a time window of interest and potential artifacts induced by movement or light scattering. After adjusting the processing speed, cropping and artifact removal, the user should apply the baseline correction, filtering and smoothing. After these preprocessing steps, single cell physiological parameters can be analyzed via power spectrum analysis, burst and spike detection. To identify functional interactions between neurons (population analysis) the amplitude cross correlation uses the relative changes in fluorescence while the spike cross correlation uses the temporal relation between detected spikes.

on file name). Resampling can also be used to unify different recording speeds, facilitating the simultaneous evaluation of multiple recordings. However, this method should only be used when the recording frequency is higher than needed to resolve the shape of single events or the interval between events. Therefore, NOSA will suggest a resampling frequency based on the temporal relation between detected events (spike detection) and their duration (burst detection). Based on the Nyquist theorem, the resampling frequency for resolving event intervals should be twice as high as the signal frequency. For resolving single events, the resampling frequency should not be below 10 times faster than the shortest event. At this point, light scattering artifacts can be corrected for by using the background correction function. If the light scattering artifact is due to a common source, then the ROI background subtraction should be applied. However, in multicellular recordings, light can scatter from multiple sources. In this case, the perisomatic background correction should be used. From here, movement related artifacts can be corrected by using a movement correction algorithm. The specific algorithm choice strongly depends on the type of movement. NOSA provides a side-by-side comparison of the original and corrected data for a convenient visual assessment of whether the correction was successful. For assessing how the movement correction affects the signal-to-noise ratio the corrected recording can be saved as a separate file and uploaded alongside the original file.

In the next step the user should correct for shifts in baseline fluorescence by applying the baseline correction (**Figure 2**). To help the user to pick the optimal algorithm and parameters, NOSA provides visual assistance by displaying the fitting curve next to the fluorescence intensity of the selected ROI (**Figure 1D**). Next, filtering and smoothing can be applied, although the specific choice of filter and parameter are highly dependent on the type of data and recording parameters (Widmann et al., 2015). The consequences of changing the filter and filter parameters are directly visualized in NOSA (**Figure 1E**), so that the desired frequency components can be isolated and noise can be smoothed without affecting the amplitude and shape of specific events. To facilitate a uniform analysis within and between recordings, the selected preprocessing algorithms and parameters are applied for each subsequently added ROI.

At this point, a power spectrum analysis and burst/spike detection can be applied (**Figure 2**), where static and dynamic thresholds (either set manually or based on the standard deviation of the noise and overall average) provide semi-automatic methods for detecting neural events. The optimal parameters for threshold selection depend on the variation of amplitudes and the signal-to-noise ratio and should therefore be determined empirically via visual assistance provided by NOSA (**Figure 1F**). Both burst and spike detection can be used to generate the average shape of all detected events. The burst detection can be used to quantify single cell physiological parameters such as burst duration, maximum amplitude (A_{max}), time until peak (t_{peak}) and the time constant of the decay from A_{max} (τ_{decay}) (Chamberland et al., 2017). For τ_{decay} we used non-linear least squares to fit the exponential function $f(x) = a^*e^{-b^*x}$ to the data after A_{max} and set $\tau_{decay} = 1/b$. These parameters can be used to analyze depolarization phases as well as hyperpolarization phases. The spike detection also automatically quantifies spike amplitude and τ_{decay}.

For population analysis, the spike cross correlation uses detected spikes to identify the temporal relation of activity patterns between neurons. In contrast, the amplitude cross correlation uses the relative changes in fluorescence to identify functional interactions and can therefore be performed after preprocessing. We have also implemented the option to perform a cross correlation on instantaneous amplitudes which employs the Hilbert transform of recorded activity and is particularly useful for identifying temporal relations in local field potential and compound recordings (Adhikari et al., 2010). Moreover, band pass filtering can be applied for comparing temporal relations within a specific frequency range.

Multicellular Optical Electrophysiology

To demonstrate the utility of NOSA we used *Drosophila* to express the genetically encoded voltage indicator (GEVI) ArcLight in ellipsoid body R5 ring neurons and the GEVI Varnam in fan-shaped body neurons (**Figure 3**). Both neural structures are considered to be integration centers for various sensory modalities (Seelig and Jayaraman, 2013; Green et al., 2017; Sun et al., 2017; Hu et al., 2018) and play important roles in locomotion (Strauss and Heisenberg, 1993) and sleep regulation (Donlea et al., 2014, 2018; Liu et al., 2016; Guo et al., 2018; Raccuglia et al., 2019).

After setting a ROI, the optical trace should first be corrected for shifts in baseline fluorescence (e.g., due to photoisomerization and bleaching). Several baseline correction algorithms are included (**Supplementary Figures S1–S3**), and the user can set additional baseline markers to guide the fitting curve for more complex shifts in baseline fluorescence (**Supplementary Figure S1A**). After baseline correction, smoothing and inversion of the raw fluorescence (depolarization leads to a reduction in fluorescence), the electrical patterns of single R5 neurons become apparent (**Figure 3A**, compare **Supplementary Figure S1**). A power spectrum analysis revealed that single R5 neurons oscillate between 0.5 – 1.5 Hz (**Figure 3B**). We recently reported that R5 oscillations within this spectrum are linked to the fly's sleep quality because they facilitate consolidated sleep phases (Raccuglia et al., 2019). The cross-correlation function built into NOSA provides a simple way of visualizing the temporal relation between the electrical patterns of the different cells (**Figure 3C**). The cross correlogram indicates that electrical patterns of cells 1, 2 and 3 largely overlap (main phase lag at 0) while cell 4 is out of phase (**Figure 3C**).

Due to the relatively low recording speed (78 Hz) and the slow kinetics of ArcLight we could not resolve single spikes in this example (**Figure 3A**). By increasing the recording speed to 160 Hz and taking advantage of the improved kinetics of the red-shifted GEVI Varnam (Kannan et al., 2018), we resolved single action potentials within the electrical activity of dorsal fan-shaped body neurons (**Figures 3D,E**). Compared to ArcLight, the SNR is lower and thus the detection of spikes heavily depends on the imaging conditions (**Figure 3D**), as individual spikes could not be resolved in the dimmer cells (**Figure 3D**, see cell 3).

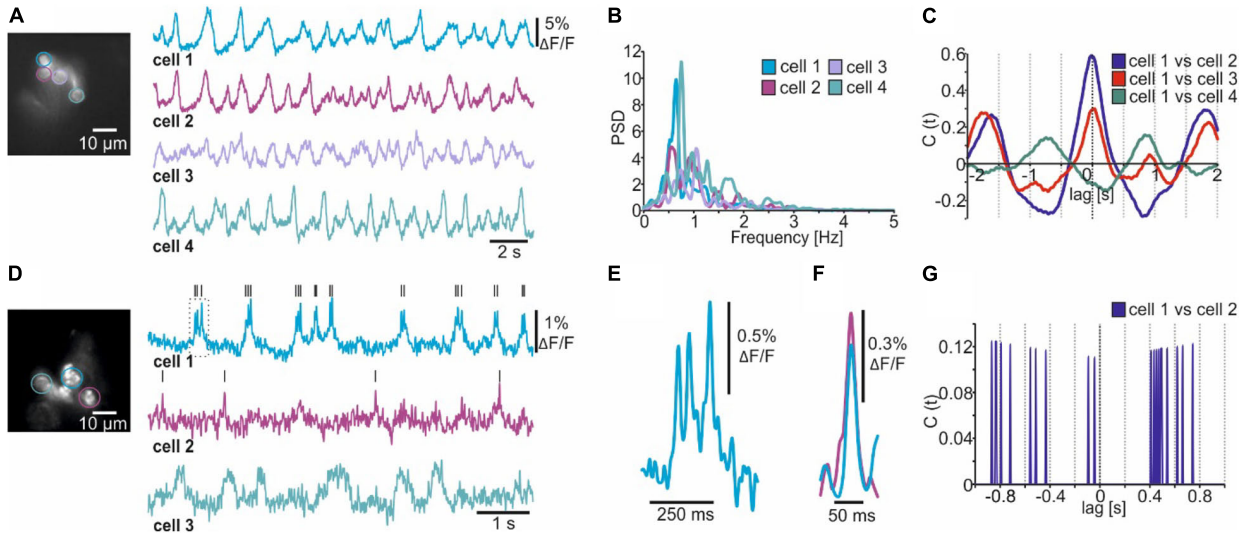

FIGURE 3 | Analyzing multicellular electrical activity from optical recordings performed in *Drosophila melanogaster*. **(A)** Wide-field image and single-cell membrane potential oscillations of *Drosophila* R5 ring neurons expressing the GEVI ArcLight. **(B)** Power spectrum analysis of R5 electrical activity shown in A. **(C)** Amplitude cross correlation indicating the temporal relation of R5 electrical patterns shown in A. **(D)** Wide-field image and single-cell electrical activity of fan-shaped body neurons expressing the GEVI Varnam. Lines indicate detected spikes using a linear threshold approach. **(E)** Burst (see dashed square in D) showing that Varnam resolves single spikes during bursting. **(F)** The event shape feature shows the average kinetics of the action potentials detected in cell 1 and 2 [see black lines in **(D)**]. **(G)** Spike cross correlation indicating no temporal relations between spikes detected in **(D)**.

That said, several functions are included to facilitate spike detection in low signal-to-noise recordings. This includes several filtering algorithms (see next chapter) as well as the ability to semi-automatically detect spikes and visualize their average shape using the event-shape feature (**Figure 3F**, compare **Supplementary Figure S2**). Moreover, the temporal relation between detected spikes can be analyzed using the spike cross correlation feature (**Figure 3G**, compare **Supplementary Figure S2**).

Spike and Burst Detection

In NOSA, electrical characteristics of single neurons as well as the kinetics of different GEVIs can be analyzed in detail using event detection features. To demonstrate this, we compare the GEVIs ArcLight and Ace2N (Gong et al., 2015) in R5 neurons in *Drosophila*. While most R5 neurons burst (∼90%), some mainly spike (Liu et al., 2016). NOSA's spike detection and event shape feature was used to analyze two spiking R5 neurons expressing either ArcLight or Ace2N (**Figures 4A,B**). While the kinetics of the depolarization are comparable, the repolarization is considerably slower in ArcLight, which is in accordance with previous findings indicating that Ace2N has faster kinetics (Gong et al., 2015).

Optical representations of action potentials do not only depend on the GEVI kinetics, but also on a sensitive interplay between recording-speed and signal-to-noise ratio. To demonstrate this, action potentials were imaged using Ace2N at either 250 Hz or 1000 Hz (**Figure 4C**). The faster recording speed resulted in a drastically reduced signal-to-noise ratio, making action potentials barely detectable (**Figure 4C**). However, filtering algorithms provided in NOSA can increase the signal-to-noise ratio and thus the spike detection fidelity, as demonstrated here by using the Savitzky-Golay algorithm (**Figure 4C**). Automatic averaging of detected spikes (event shape) indicates that the temporal features of single action potentials are well represented at 250 Hz (**Figure 4D**). Here, the limiting factors seem to be the temporal dynamics of the GEVI itself.

An advantage of enhanced temporal dynamics of a GEVI becomes apparent when analyzing high-frequency spikes in bursting neurons (**Figure 4E**). Using Ace2N, spikes riding on top of bursts are more likely to be resolved and are therefore more readily detectable (**Figure 4F**). This is likely due to the slower kinetics of ArcLight, resulting in several spikes probably merging into one "spike". However, the event shape feature indicates that the temporal characteristics of the bursts are identical, but ArcLight produces a bigger change in relative fluorescence (**Figure 4G**).

The burst detection feature can be used to directly quantify various response parameters of bursts or other detected events (**Figure 4H**). These parameters demonstrate that the maximum response amplitude (A_{max}) in ArcLight expressing neurons is significantly increased while the time to peak response (t_{peak}) is similar. Performing a regression analysis on these parameters indicates that in Ace2N A_{max} increases with t_{peak} while there is no such correlation in ArcLight (**Figure 4H**).

Movement and Background Correction

Due to a relatively small SNR, movement artifacts are especially problematic for *in vivo* voltage imaging. We therefore implemented several movement correction algorithms into NOSA. We here demonstrate the symmetric diffeomorphic algorithm, which was originally designed for detecting brain

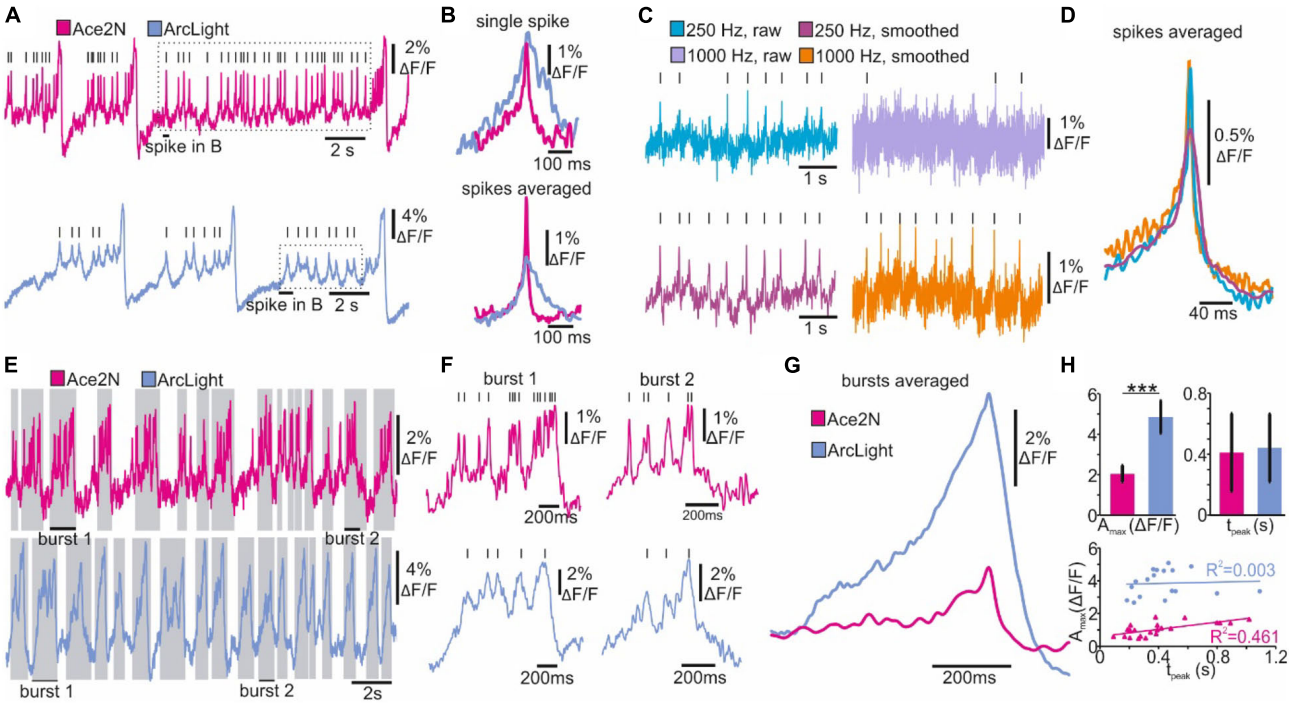

FIGURE 4 | Spike and burst detection revealing kinetic properties of GEVIs and neuron-specific firing characteristics. **(A)** Optical recordings of spiking *Drosophila* R5 neurons expressing the GEVIs Ace2N and ArcLight. Lines indicate detected spikes using a linear threshold approach. **(B)** Single and averaged spikes selected from recordings in A (dashed square indicates spikes selected for event shape). The event shape feature indicates improved kinetics of Ace2N. **(C)** Optical recordings of a spiking *Drosophila* R5 neuron (Ace2N) performed at different recording speeds. Lines indicate identified spikes. **(D)** The event shape feature shows the average kinetics of spikes detected in C. **(E, F)** Optical recordings of bursting *Drosophila* R5 neurons expressing the GEVIs Ace2N and ArcLight. Gray shaded areas and lines indicate detected bursts and spikes using the dynamic threshold approach. **(G)** The event shape feature generates the averaged kinetics of detected bursts indicating GEVI-specific differences in the optical representation of bursts. **(H)** Quantified burst parameters show increased maximum response amplitude (A_{max}) for ArcLight and a similar time to peak response (t_{peak}). Regression analysis indicates a correlation between A_{max} and t_{peak} for Ace2N but not for ArcLight. Statistics: Students *t*-test, $n = 16–20$, $p < 0.001$.

deformations during magnetic resonance imaging (Avants et al., 2008). This algorithm maximizes the cross correlation within the space of diffeomorphic maps by using inverse transformations and the Euler-Lagrange equation (Avants et al., 2008). This sophisticated algorithm is very time consuming but shows impressive results (**Figure 5A**). Single ArcLight expressing R5 neurons recorded *in vivo* in *Drosophila* show substantial movement artifacts (**Figure 5A**). However, after performing the symmetric diffeomorphic algorithm electrical activity can be recovered even during periods of heavy movement.

Scattering light can also reduce the signal-to-noise ratio in epifluorescence imaging experiments. This is especially problematic in bulk dye-loading procedures as Ca^{2+}- or voltage sensitive dyes accumulate differently in different cell-types (i.e., neurons and glial cells), leading to a large variability in fluorescence intensity. To address this issue, we implemented ROI and perisomatic background correction algorithms into NOSA (**Figures 5B,C**). To demonstrate their utility, we analyzed epileptiform activity in hippocampal slices of Wistar rats loaded with the Ca^{2+} indicator OGB-1-AM (Kovacs et al., 2001; **Figure 5B**). Here, strong and synchronized increases in fluorescence in CA3 neurons lead to increased light-scattering, contaminating the optical representation in a simultaneously recorded glial cell (**Figure 5B**). However, ROI and perisomatic background correction both successfully reduce the effects of scattered light from surrounding neurons, increasing the SNR in the activity pattern of a glial cell (**Figure 5C**). In comparison, smoothing algorithms can also eliminate the higher frequency components generated by scattering light but fail to eliminate the slower components and distort the glial Ca^{2+} responses (**Figure 5C**). Therefore, the user should first employ the background correction and then use moderate smoothing to remove residual noise (**Figure 2**).

Combined *in vivo* Optical and Classical Electrophysiology

Being able to compare optical measurements alongside ongoing electrical recordings is useful in many ways. To our knowledge, NOSA is the first open-access tool to provide the option for analyzing optical and electrical traces in parallel. For example, we performed simultaneous patch-clamp and optical *in vivo* recordings from *Drosophila* R5 neurons expressing ArcLight and uploaded recordings (abf files/axon binary file format) into NOSA (**Supplementary Figure S3**). As electrical and optical traces may be recorded with different systems,

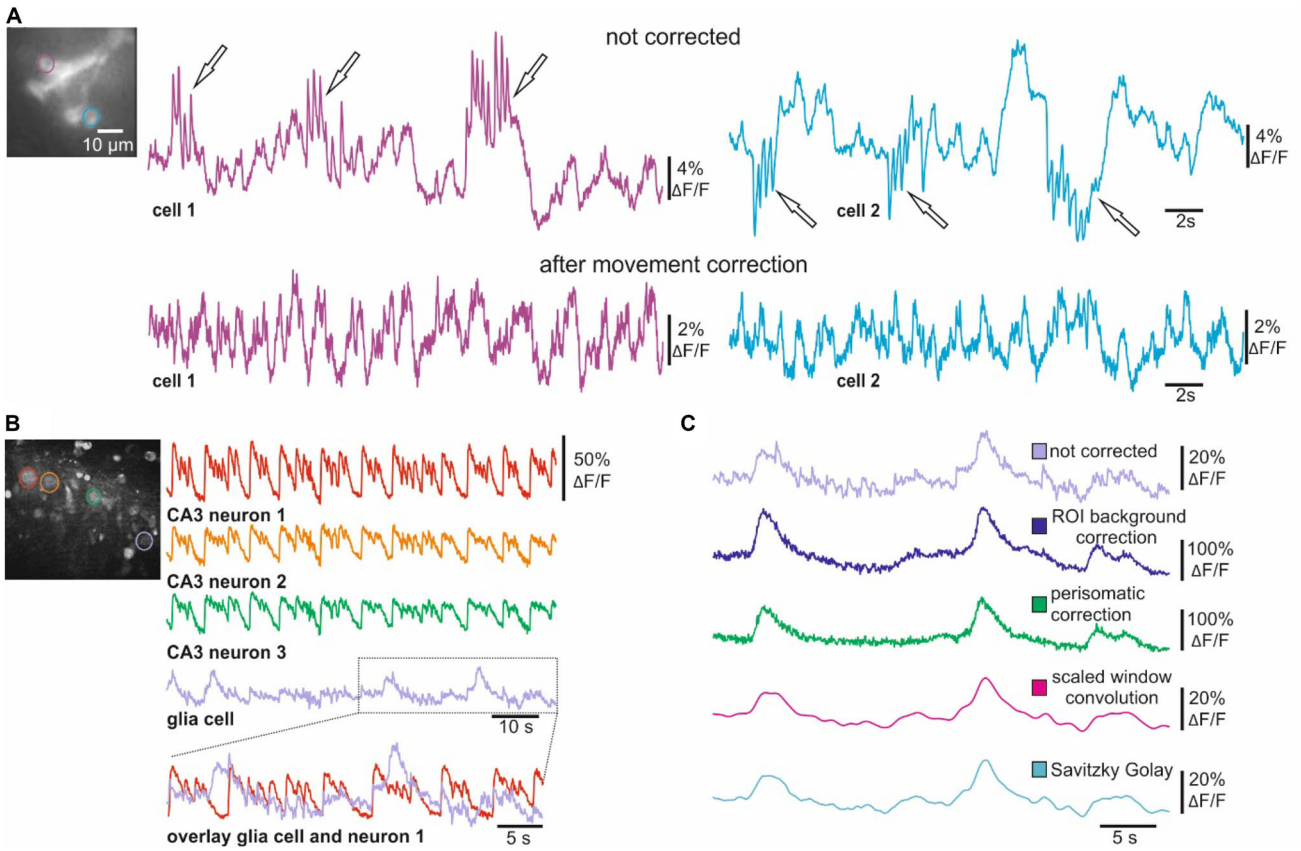

FIGURE 5 | Movement and background correction for voltage and Ca^{2+} imaging. **(A)** *In vivo* voltage imaging (ArcLight) of single *Drosophila* R5 neurons before and after performing the symmetric diffeomorphic movement correction. **(B)** Ca^{2+} imaging of CA3 neurons and glia cells from hippocampal slices of Wistar rats. CA3 neurons indicated in the wide-field image show synchronous activity of CA3 neurons after inducing epileptiform activity. The overlay demonstrates how CA3 activity contaminates the optical representation of glial activity. **(C)** Activity of glia cell indicated in B before and after ROI background correction, perisomatic background correction and smoothing with scaled window convolution as well as with the Savitzky Golay algorithm.

temporal delays between the systems could falsify a direct comparison. We therefore implemented an offset function into NOSA, which allows shifting one trace in relation to the other (**Supplementary Figure S3**). Comparing optical and electrical traces demonstrates that ArcLight faithfully represents changes in membrane potential (**Figures 6A–C**) and that a change in relative fluorescence of 2% approximates a change of 23 mV in membrane potential (**Figures 6A–C**). However, the relation between changes in fluorescence and absolute membrane potential will highly depend on the expression strength and must therefore be determined for each cell type. To simplify a direct comparison NOSA can adjust the sampling rate via interpolation of data points. In this example we reduced the sampling rate of the electrical trace from 10 kHz to 2 kHz smoothing out the spikes on top of the bursts which in this case are not represented in the optical trace (**Figure 6A**). In order to compare different current or voltage steps, several optical and electrical traces can be uploaded into NOSA and the responses can be directly visualized next to each other (**Figure 6D**). Using the burst detection feature the response kinetics of de- and hyperpolarization events can be quantified to perform a regression analysis and thus learn more about the relation between optical and electrical responses (compare **Figure 4H**).

Another important application for simultaneous patch clamp and voltage imaging is to investigate single-cell contributions to population dynamics reflected in compound recordings of neural activity. Here, we use NOSA to compare simultaneously recorded *in vivo* single-cell electrical patch-clamp of a single *Drosophila* R5 neuron expressing ArcLight with the optical compound activity of the dorsal bulb, which is comprised of the dendrites of 10-12 R5 neurons (**Figure 6E**). To clearly visualize compound activity, we used the Savitzky Golay algorithm to remove all noise. Power spectrum analysis shows that the peak frequency of the recorded R5 neuron is also represented in the dendritic compound signal (**Figure 6F**). However, the power spectrum of the compound signal is much more complex due to the fact that the electrical patterns of several R5 neurons contribute to the compound signal. Correlation analysis suggests that some depolarized states of the single R5 neuron overlap with depolarized states in the compound signal (**Figure 6G**, compare **Figure 6E**).

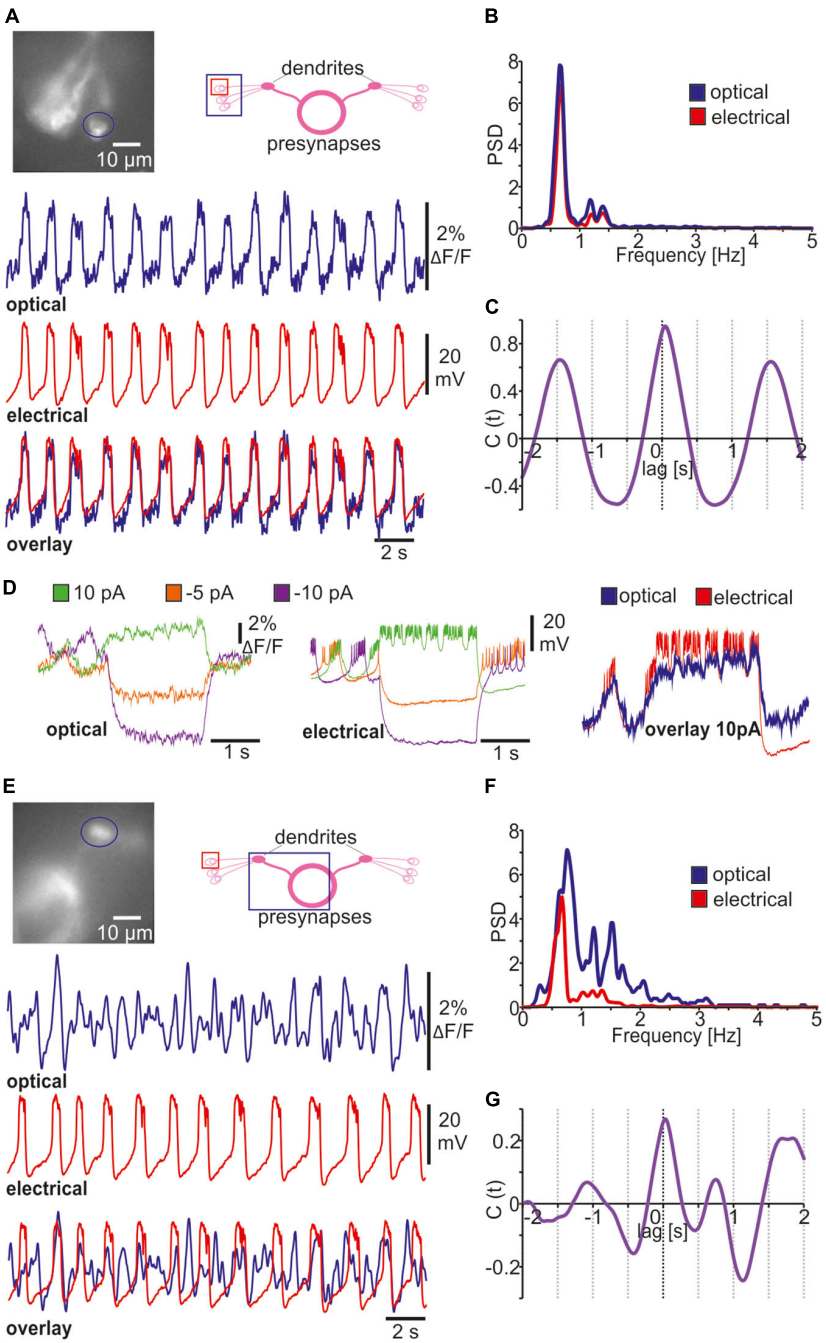

FIGURE 6 | Simultaneous optical and classical electrophysiology. **(A)** Simultaneously recorded *in vivo* single-cell electrical patch-clamp (interpolated at 2 kHz) and optical recordings (ArcLight) of bursting *Drosophila* R5 neuron indicated in the wide-field image. **(B)** Power spectrum analysis of membrane potential oscillations of R5 neuron shown in A. **(C)** Cross correlograms indicating oscillatory character and temporal overlap of optical and electrical traces shown in A. **(D)** Representation of optical and electrical traces during a series of current steps. **(E)** Simultaneously recorded *in vivo* single-cell electrical patch-clamp (interpolated at 2 kHz) and optical recordings (ArcLight) of *Drosophila* R5 dendritic area indicated in the wide-field image. **(F)** Power spectrum analysis showing more complex rhythms in the optical compound activity. **(G)** Amplitude cross correlation indicating partial temporal overlap between single-cell and compound activity.

Cross Correlation for Analyzing Event-Based Temporal Relations

When imaging electrical activity in larger brain areas or even in whole brains NOSA can easily analyze the temporal relations of specific events occurring between different neuronal populations. To demonstrate this, we analyzed *in vivo* whole brain voltage imaging recordings in *Drosophila* which panneuronally express ArcLight (Aimon et al., 2019; **Figure 7A**).

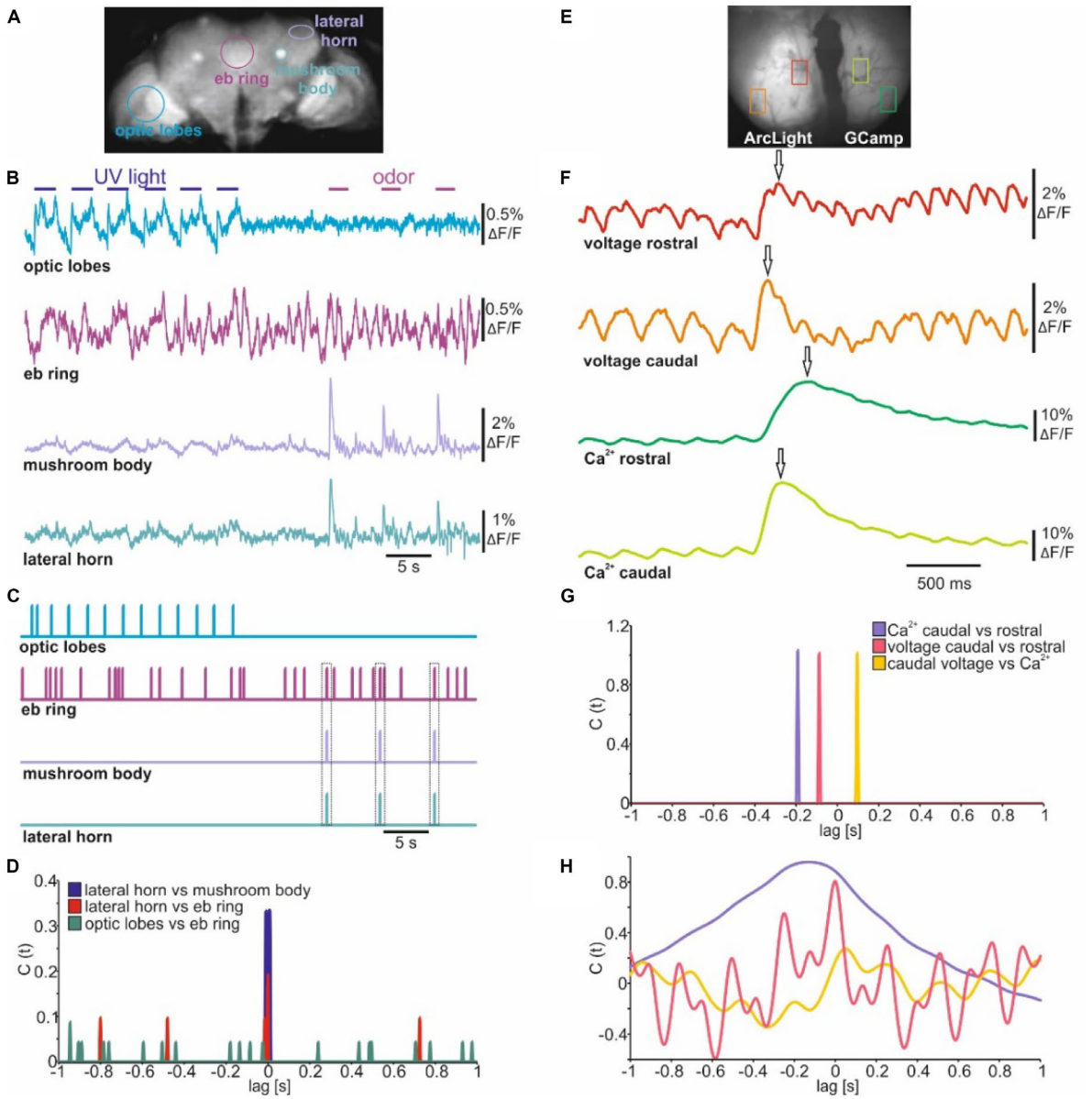

FIGURE 7 | Event cross correlation identifies temporal relations in sensory evoked population dynamics. **(A)** Wide-field image of a mid-section during whole brain voltage imaging (ArcLight) in *Drosophila*. **(B)** Electrical population activity of different neuropils during optical and olfactory stimulation. **(C)** Spike detection indicating detected events of electrical activity shown in B. **(D)** Spike cross correlation indicating temporal shifts between events shown in C. Dashed squares indicate coincidence between olfactory evoked activity and specific events detected in the central complex. **(E)** Wide-field image of the olfactory bulb of C57BL/6 mice injected with ArcLight and GCamp6f in either hemisphere. **(F)** Olfactory evoked population activity of selected caudal and rostral glomeruli. Arrows indicate detected maxima. **(G)** Spike cross correlation indicating temporal shifts between maxima indicated in **(F)**. **(H)** Amplitude cross correlation indicating oscillatory character and temporal relations of population dynamics shown in **(F)**.

Stimulation with UV light induced electrical activity in the optic lobes while olfactory stimulation induced activity around the area of the lateral horns and peduncles of the mushroom bodies (**Figure 7B**), which are both higher olfactory integration centers of the *Drosophila* brain (Heisenberg, 2003; Frechter et al., 2019). Interestingly, the central complex, which processes various sensory modalities (Green et al., 2017; Sun et al., 2017) and is important for basic locomotion (Strauss and Heisenberg, 1993; Strauss, 2002), shows spontaneous electrical activity. However, it is not clear whether some of the spontaneous activity originates from the visual or olfactory stimulation (**Figure 7B**). Rather than detecting actual spikes, NOSA's spike detection can be used to determine the temporal relation between detected events. Events can be detected using a linear or dynamic threshold (**Figure 1F**). Moreover, the threshold can be set either manually or based on the standard deviation of the whole recording. The detected

events are used to generate a time-dependent event marker (**Figure 7C**, compare **Supplementary Figure S4**). The spike cross correlation function identifies the temporal relation between detected events, demonstrating that olfactory responses in the mushroom bodies and lateral horns are temporally aligned (**Figure 7D**). Moreover, the set event markers and cross correlation analysis reveals that olfactory stimulation generates transient activity in the central complex, while visual stimulation does not lead to a detectable response (**Figure 7D**).

To analyze population dynamics in a mammalian brain we used a recording in which one hemisphere of the olfactory bulb of C57BL/6 mice expresses ArcLight while the other expresses GCaMP6f (Storace et al., 2015; **Figure 7E**). The dorsal bulb exhibits a distinct temporal organization whereby glomeruli in the caudal bulb tend to be more coupled to respiration than glomeruli in the rostral olfactory bulb (Spors et al., 2006; Wachowiak et al., 2013). To demonstrate how quickly temporal relations can be established with NOSA we used the maxima of the olfactory responses in rostral and caudal glomeruli (**Figure 7F**) to generate an event-based cross correlogram (**Figure 7G**). This shows that electrical activity requires about 84 ms to travel from the caudal side of the olfactory bulb to the rostral side (**Figure 7G**). In comparison, intracellular Ca^{2+} requires about 188 ms. Moreover, at the caudal glomeruli the delay between maxima of electrical activity and intracellular Ca^{2+} is 100 ms (**Figure 7G**). In contrast to this event-based cross correlation, the amplitude cross correlation (**Figure 7H**) considers the whole recording and is thus influenced by the rhythmic changes in voltage which are a result of the mice's breathing pattern (Storace et al., 2015).

DISCUSSION

Here, we report a novel open-source tool box, designed specifically for the analysis and interpretation of multicellular optical electrophysiology. Moreover, NOSA is the first open-access software that allows to combine the analysis of simultaneously recorded optical and electrical data. While there is sophisticated software for processing imaging recordings (Romano et al., 2017; Giovannucci et al., 2019), NOSA is an entirely open access stand-alone software that requires no installation and comes with an intuitive user-interface that allows to precisely control and comprehend each analytical step. In this manuscript we demonstrate the challenges of performing optical electrophysiology and provide hands-on solutions to extract and analyze electrical patterns from recordings with low signal-to-noise ratio (SNR).

We demonstrate how high recording speeds necessary to resolve single action potentials drastically reduce the SNR (**Figures 3**, **4**). We therefore implemented baseline fitting and filtering algorithms, which can efficiently extract single action potentials and bursts from optical recordings (**Figures 1–4**). During voltage imaging, the issue of a low SNR is aggravated by light scattering and movement artifacts for which we implemented background subtraction and movement correction algorithms (**Figure 5**). We combine these basic but essential features for processing imaging data with sophisticated analysis tools for identifying electrical characteristics (**Figure 4**) and functional interactions (**Figures 2**, **6**). NOSA can also be used to investigate the temporal relation of sensory-evoked population dynamics, as we demonstrate in whole brain recordings in *Drosophila* (**Figures 7A–D**) and in the olfactory bulb in mice (**Figures 7E–H**). We here show that NOSA can be used to quickly identify temporal relations between the activity patterns of single cells and neuronal populations, which is crucial for investigating under which conditions neural networks interact with each other.

The properties and limitations of GEVIs affect the optical representation of neuronal activity. For example, the improved kinetics of the red-shifted GEVI Varnam increases the likelihood of resolving single spikes while ArcLight generally yields higher SNR (**Figure 3**). NOSA can be used to quickly determine the properties of GEVIs. Using NOSA, we verify that the GEVI Ace2N has faster kinetics than ArcLight (Gong et al., 2015), especially with respect to the repolarization phase of an action potential (**Figure 4B**). However, the temporal representation of bursts is similar in both GEVIs (**Figure 4G**). In fact, during bursts ArcLight yields higher relative changes in fluorescence (**Figure 4G**). Performing a regression analysis on burst parameters automatically quantified by NOSA revealed that Ace2N, but not ArcLight responses, showed a correlation between peak amplitudes and burst duration (**Figure 4H**). Other important limitations of GEVIs concern the relatively slow diffusion in lipid membranes which reduces the reposition speed and thus limits the duration of imaging sessions (St-Pierre et al., 2014; Fujiwara et al., 2016). However, the bleaching kinetics strongly depend on imaging conditions and also differ between GEVIs. With specific knowledge about the properties and limitations, the adequate GEVI can be chosen for a specific experiment. A comprehensive characterization of the properties of different GEVIs are reported elsewhere (Bando et al., 2019).

NOSA's event detection can be used to extract neuron-specific firing characteristics (**Figure 4**), enabling the fast identification of specific types of neurons within a population of seemingly homogeneous neurons. This knowledge could then be used to electrically stimulate neurons with specific attributes and analyze their connectivity to other neurons (Antic et al., 2016). Such sophisticated experiments would benefit from another feature, which is provided by NOSA: the simultaneous analysis of optical and electrical data (**Figure 6**). Moreover, we show how this feature can be used to analyze single-cell contributions to population dynamics (**Figure 6E**). This is especially important when trying to understand how a multitude of neurons orchestrate their electrical activities to generate population dynamics, e.g., during sleep (Buzsaki and Draguhn, 2004).

Since NOSA is implemented in Python and available on Github[1], NOSA can easily be shared, extended to other operating systems and updated with new functions and tools. Functions that would further improve the usability of NOSA include options for hand-drawn ROIs and reliable automatic ROI detection. Implementing sophisticated artificial intelligence

[1]https://github.com/DavideR2020/NOSA

could provide internal performance indices ("figures of merit") that could help the user choose the right parameters for each feature. Based on GEVI-specific kinetics, deconvolution algorithms could be used to improve the optical representation of electrical activity. For testing the functionality and reliability of such sophisticated algorithms, simulated neuronal data could be used. Simulated data has the advantage that the user can directly test whether the chosen feature and parameters can achieve the desired outcome. Moreover, an automatic regression analysis using identified response parameters would further facilitate the identification of GEVI-specific kinetics.

GEVIs are currently improving at a rapid pace, developing toward stronger fluorescence and improved kinetics. However, currently the diverse properties of GEVIs and a missing analytical pipeline represent motivational bottlenecks preventing experimental implementation and widespread use of GEVIs. With NOSA we provide an analytical toolbox that will greatly facilitate the use of GEVIs in studying multicellular electrical patterns, inexorably improving our understanding of functional interactions within neural networks.

DATA AVAILABILITY STATEMENT

The executable NOSA file, the master code and a manual containing additional information are provided under the following GitHub repository: https://github.com/DavideR2020/NOSA. To obtain example files please send an email to the lead contact.

ETHICS STATEMENT

The animal studies were reviewed and approved by the State Office of Health and Social Affairs Berlin and the Yale Institutional Animal Case and Use Committee.

AUTHOR CONTRIBUTIONS

SO and FA designed and created NOSA. AE, SA, RK, DS, and DR performed the experiments. SS and JG provided resources and conceptualization. DR provided conceptualization and wrote the manuscript. All authors contributed to the article and approved the submitted version.

ACKNOWLEDGMENTS

We thank Eric Reynolds for comments on the manuscript. This manuscript has been released as a preprint at biorxivs (Oltmanns et al., 2020). Experimental contribution provided by DS was supported by US NIH grant DC016133. We acknowledge support from the German Research Foundation (DFG) and the Open Access Publication Fund of Charité – Universitätsmedizin Berlin.

SUPPLEMENTARY MATERIAL

The Supplementary Material for this article can be found online at: https://www.frontiersin.org/articles/10.3389/fnins.2020.00712/full#supplementary-material

REFERENCES

Adhikari, A., Sigurdsson, T., Topiwala, M. A., and Gordon, J. A. (2010). Cross-correlation of instantaneous amplitudes of field potential oscillations: a straightforward method to estimate the directionality and lag between brain areas. *J. Neurosci. Methods* 191, 191–200. doi: 10.1016/j.jneumeth.2010.06.019

Aimon, S., Katsuki, T., Jia, T., Grosenick, L., Broxton, M., Deisseroth, K., et al. (2019). Fast near-whole-brain imaging in adult *Drosophila* during responses to stimuli and behavior. *PLoS Biol.* 17:e2006732. doi: 10.1371/journal.pbio.2006732

Alivisatos, A. P., Chun, M., Church, G. M., Greenspan, R. J., Roukes, M. L., and Yuste, R. (2012). The brain activity map project and the challenge of functional connectomics. *Neuron* 74, 970–974. doi: 10.1016/j.neuron.2012.06.006

Antic, S. D., Empson, R. M., and Knopfel, T. (2016). Voltage imaging to understand connections and functions of neuronal circuits. *J. Neurophysiol.* 116, 135–152. doi: 10.1152/jn.00226.2016

Avants, B. B., Epstein, C. L., Grossman, M., and Gee, J. C. (2008). Symmetric diffeomorphic image registration with cross-correlation: evaluating automated labeling of elderly and neurodegenerative brain. *Med Image Anal.* 12, 26–41. doi: 10.1016/j.media.2007.06.004

Azimi Hashemi, N., Bergs, A. C. F., Schuler, C., Scheiwe, A. R., Steuer Costa, W., Bach, M., et al. (2019). Rhodopsin-based voltage imaging tools for use in muscles and neurons of *Caenorhabditis elegans*. *Proc. Natl. Acad. Sci. U.S.A.* 116, 17051–17060. doi: 10.1073/pnas.1902443116

Bando, Y., Sakamoto, M., Kim, S., Ayzenshtat, I., and Yuste, R. (2019). Comparative evaluation of genetically encoded voltage indicators. *Cell Rep.* 26:e804.

Buzsaki, G., and Draguhn, A. (2004). Neuronal oscillations in cortical networks. *Science* 304, 1926–1929. doi: 10.1126/science.1099745

Cao, G., Platisa, J., Pieribone, V. A., Raccuglia, D., Kunst, M., and Nitabach, M. N. (2013). Genetically targeted optical electrophysiology in intact neural circuits. *Cell* 154, 904–913. doi: 10.1016/j.cell.2013.07.027

Chamberland, S., Yang, H. H., Pan, M. M., Evans, S. W., Guan, S., Chavarha, M., et al. (2017). Fast two-photon imaging of subcellular voltage dynamics in neuronal tissue with genetically encoded indicators. *eLife* 6:e25690.

Donlea, J. M., Pimentel, D., and Miesenbock, G. (2014). Neuronal machinery of sleep homeostasis in *Drosophila*. *Neuron* 81, 860–872. doi: 10.1016/j.neuron.2013.12.013

Donlea, J. M., Pimentel, D., Talbot, C. B., Kempf, A., Omoto, J. J., Hartenstein, V., et al. (2018). Recurrent circuitry for balancing sleep need and sleep. *Neuron* 97:e374.

Frechter, S., Bates, A. S., Tootoonian, S., Dolan, M. J., Manton, J., Jamasb, A. R., et al. (2019). Functional and anatomical specificity in a higher olfactory centre. *eLife* 8:e44590.

Fujiwara, T. K., Iwasawa, K., Kalay, Z., Tsunoyama, T. A., Watanabe, Y., Umemura, Y. M., et al. (2016). Confined diffusion of transmembrane proteins and lipids induced by the same actin meshwork lining the plasma membrane. *Mol. Biol. Cell* 27, 1101–1119. doi: 10.1091/mbc.e15-04-0186

Garyfallidis, E., Brett, M., Amirbekian, B., Rokem, A., van der Walt, S., Descoteaux, M., et al. (2014). Dipy, a library for the analysis of diffusion MRI data. *Front. Neuroinform.* 8:8. doi: 10.3389/fninf.2014.00008

Giovannucci, A., Friedrich, J., Gunn, P., Kalfon, J., Brown, B. L., Koay, S. A., et al. (2019). CaImAn an open source tool for scalable calcium imaging data analysis. *eLife* 8:e38173.

Gong, Y., Huang, C., Li, J. Z., Grewe, B. F., Zhang, Y., Eismann, S., et al. (2015). High-speed recording of neural spikes in awake mice and flies with a fluorescent voltage sensor. *Science* 350, 1361–1366. doi: 10.1126/science.aab0810

Green, J., Adachi, A., Shah, K. K., Hirokawa, J. D., Magani, P. S., and Maimon, G. (2017). A neural circuit architecture for angular integration in *Drosophila*. *Nature* 546, 101–106. doi: 10.1038/nature22343

Guo, F., Holla, M., Diaz, M. M., and Rosbash, M. (2018). A circadian output circuit controls sleep-wake arousal in *Drosophila*. *Neuron* 100, 624–635.e4. doi: 10.1016/j.neuron.2018.09.002

Heisenberg, M. (2003). Mushroom body memoir: from maps to models. *Nat. Rev. Neurosci.* 4, 266–275. doi: 10.1038/nrn1074

Hu, W., Peng, Y., Sun, J., Zhang, F., Zhang, X., Wang, L., et al. (2018). Fan-shaped body neurons in the *Drosophila* brain regulate both innate and conditioned nociceptive avoidance. *Cell Rep.* 24, 1573–1584. doi: 10.1016/j.celrep.2018.07.028

Kann, O., Huchzermeyer, C., Kovacs, R., Wirtz, S., and Schuelke, M. (2011). Gamma oscillations in the hippocampus require high complex I gene expression and strong functional performance of mitochondria. *Brain* 134, 345–358. doi: 10.1093/brain/awq333

Kannan, M., Vasan, G., Huang, C., Haziza, S., Li, J. Z., Inan, H., et al. (2018). Fast, in vivo voltage imaging using a red fluorescent indicator. *Nat. Methods* 15, 1108–1116. doi: 10.1038/s41592-018-0188-7

Kovacs, R., Schuchmann, S., Gabriel, S., Kardos, J., and Heinemann, U. (2001). Ca2+ signalling and changes of mitochondrial function during low-Mg2+-induced epileptiform activity in organotypic hippocampal slice cultures. *Eur. J. Neurosci.* 13, 1311–1319. doi: 10.1046/j.0953-816x.2001.01505.x

Kulkarni, R. U., and Miller, E. W. (2017). Voltage imaging: pitfalls and potential. *Biochemistry* 56, 5171–5177. doi: 10.1021/acs.biochem.7b00490

Lin, M. Z., and Schnitzer, M. J. (2016). Genetically encoded indicators of neuronal activity. *Nat. Neurosci.* 19, 1142–1153. doi: 10.1038/nn.4359

Liu, S., Liu, Q., Tabuchi, M., and Wu, M. N. (2016). Sleep drive is encoded by neural plastic changes in a dedicated circuit. *Cell* 165, 1347–1360. doi: 10.1016/j.cell.2016.04.013

Miyashita, T., Oda, Y., Horiuchi, J., Yin, J. C., Morimoto, T., and Saitoe, M. (2012). Mg(2+) block of *Drosophila* NMDA receptors is required for long-term memory formation and CREB-dependent gene expression. *Neuron* 74, 887–898. doi: 10.1016/j.neuron.2012.03.039

Miyazawa, H., Okumura, K., Hiyoshi, K., Maruyama, K., Kakinuma, H., Amo, R., et al. (2018). Optical interrogation of neuronal circuitry in zebrafish using genetically encoded voltage indicators. *Sci. Rep.* 8:6048.

Murthy, M., and Turner, G. (2013). Whole-cell in vivo patch-clamp recordings in the *Drosophila* brain. *Cold Spring Harb. Protoc.* 2013, 140–148.

Oltmanns, S., Abben, F. S., Ender, A., Aimon, S., Kovacs, R., Sigrist, S. J., et al. (2020). NOSA, an analytical toolbox for multicellular optical electrophysiology. *bioRxiv* [Preprint]. doi: 10.1101/2020.03.15.992420

Owald, D., Felsenberg, J., Talbot, C. B., Das, G., Perisse, E., Huetteroth, W., et al. (2015). Activity of defined mushroom body output neurons underlies learned olfactory behavior in *Drosophila*. *Neuron* 86, 417–427. doi: 10.1016/j.neuron.2015.03.025

Prager, O., Kamintsky, L., Hasam-Henderson, L. A., Schoknecht, K., Wuntke, V., Papageorgiou, I., et al. (2019). Seizure-induced microvascular injury is associated with impaired neurovascular coupling and blood-brain barrier dysfunction. *Epilepsia* 60, 322–336. doi: 10.1111/epi.14631

Raccuglia, D., Huang, S., Ender, A., Heim, M. M., Laber, D., Suarez-Grimalt, R., et al. (2019). Network-specific synchronization of electrical slow-wave oscillations regulates sleep drive in *Drosophila*. *Curr. Biol.* 29:e3613.

Raccuglia, D., Yan McCurdy, L., Demir, M., Gorur-Shandilya, S., Kunst, M., Emonet, T., et al. (2016). Presynaptic GABA receptors mediate temporal contrast enhancement in *Drosophila* olfactory sensory neurons and modulate odor-driven behavioral kinetics. *eNeuro* 3:ENEURO.0080-16.2016.

Romano, S. A., Perez-Schuster, V., Jouary, A., Boulanger-Weill, J., Candeo, A., Pietri, T., et al. (2017). An integrated calcium imaging processing toolbox for the analysis of neuronal population dynamics. *PLoS Comput. Biol.* 13:e1005526. doi: 10.1371/journal.pcbi.1005526

Seelig, J. D., and Jayaraman, V. (2013). Feature detection and orientation tuning in the *Drosophila* central complex. *Nature* 503, 262–266. doi: 10.1038/nature12601

Spors, H., Wachowiak, M., Cohen, L. B., and Friedrich, R. W. (2006). Temporal dynamics and latency patterns of receptor neuron input to the olfactory bulb. *J. Neurosci.* 26, 1247–1259. doi: 10.1523/jneurosci.3100-05.2006

Storace, D., Sepehri Rad, M., Kang, B., Cohen, L. B., Hughes, T., and Baker, B. J. (2016). Toward better genetically encoded sensors of membrane potential. *Trends Neurosci.* 39, 277–289. doi: 10.1016/j.tins.2016.02.005

Storace, D. A., Braubach, O. R., Jin, L., Cohen, L. B., and Sung, U. (2015). Monitoring brain activity with protein voltage and calcium sensors. *Sci. Rep.* 5:10212.

Storace, D. A., and Cohen, L. B. (2017). Measuring the olfactory bulb input-output transformation reveals a contribution to the perception of odorant concentration invariance. *Nat. Commun.* 8:81.

St-Pierre, F., Marshall, J. D., Yang, Y., Gong, Y., Schnitzer, M. J., and Lin, M. Z. (2014). High-fidelity optical reporting of neuronal electrical activity with an ultrafast fluorescent voltage sensor. *Nat. Neurosci.* 17, 884–889. doi: 10.1038/nn.3709

Strauss, R. (2002). The central complex and the genetic dissection of locomotor behaviour. *Curr. Opin. Neurobiol.* 12, 633–638. doi: 10.1016/s0959-4388(02)00385-9

Strauss, R., and Heisenberg, M. (1993). A higher control center of locomotor behavior in the *Drosophila* brain. *J. Neurosci.* 13, 1852–1861. doi: 10.1523/jneurosci.13-05-01852.1993

Sun, Y., Nern, A., Franconville, R., Dana, H., Schreiter, E. R., Looger, L. L., et al. (2017). Neural signatures of dynamic stimulus selection in *Drosophila*. *Nat. Neurosci.* 20, 1104–1113. doi: 10.1038/nn.4581

Thevenaz, P., Ruttimann, U. E., and Unser, M. (1998). A pyramid approach to subpixel registration based on intensity. *IEEE Trans. Image Process.* 7, 27–41. doi: 10.1109/83.650848

Wachowiak, M., Economo, M. N., Diaz-Quesada, M., Brunert, D., Wesson, D. W., White, J. A., et al. (2013). Optical dissection of odor information processing in vivo using GCaMPs expressed in specified cell types of the olfactory bulb. *J. Neurosci.* 33, 5285–5300. doi: 10.1523/jneurosci.4824-12.2013

Widmann, A., Schroger, E., and Maess, B. (2015). Digital filter design for electrophysiological data–a practical approach. *J. Neurosci. Methods* 250, 34–46. doi: 10.1016/j.jneumeth.2014.08.002

Wilson, R. I., and Laurent, G. (2005). Role of GABAergic inhibition in shaping odor-evoked spatiotemporal patterns in the *Drosophila* antennal lobe. *J. Neurosci.* 25, 9069–9079. doi: 10.1523/jneurosci.2070-05.2005

Yang, H. H., and St-Pierre, F. (2016). Genetically encoded voltage indicators: opportunities and challenges. *J. Neurosci.* 36, 9977–9989. doi: 10.1523/jneurosci.1095-16.2016

Conflict of Interest: The authors declare that the research was conducted in the absence of any commercial or financial relationships that could be construed as a potential conflict of interest.

Copyright © 2020 Oltmanns, Abben, Ender, Aimon, Kovacs, Sigrist, Storace, Geiger and Raccuglia. This is an open-access article distributed under the terms of the Creative Commons Attribution License (CC BY). The use, distribution or reproduction in other forums is permitted, provided the original author(s) and the copyright owner(s) are credited and that the original publication in this journal is cited, in accordance with accepted academic practice. No use, distribution or reproduction is permitted which does not comply with these terms.

frontiers in Neuroscience

ORIGINAL RESEARCH
published: 28 July 2020
doi: 10.3389/fnins.2020.00750

Glutamate Chemical Exchange Saturation Transfer (GluCEST) Magnetic Resonance Imaging in Pre-clinical and Clinical Applications for Encephalitis

Yanlong Jia[1†], Yanzi Chen[2†], Kuan Geng[3], Yan Cheng[1], Yan Li[1], Jinming Qiu[1], Huaidong Huang[1], Runrun Wang[1], Yunping Zhang[4] and Renhua Wu[1]**

[1] Department of Radiology, The Second Affiliated Hospital of Shantou University Medical College, Shantou, China, [2] Department of Radiology, Affiliated Longhua People's Hospital, Southern Medical University, Shenzhen, China, [3] Department of Radiology, The First People's Hospital of Honghe Prefecture, Mengzi, China, [4] Department of Nuclear Medicine, Shenzhen Luohu District People's Hospital, Shenzhen, China

Background: Encephalitis is a common central nervous system inflammatory disease that seriously endangers human health owing to the lack of effective diagnostic methods, which leads to a high rate of misdiagnosis and mortality. Glutamate is implicated closely in microglial activation, and activated microglia are key players in encephalitis. Hence, using glutamate chemical exchange saturation transfer (GluCEST) imaging for the early diagnosis of encephalitis holds promise.

Methods: The sensitivity of GluCEST imaging with different concentrations of glutamate and other major metabolites in the brain was validated in phantoms. Twenty-seven Sprague–Dawley (SD) rats with encephalitis induced by *Staphylococcus aureus* infection were used for preclinical research of GluCEST imaging in a 7.0-Tesla scanner. For the clinical study, six patients with encephalitis, six patients with lacunar infarction, and six healthy volunteers underwent GluCEST imaging in a 3.0-Tesla scanner.

Results: The number of amine protons on glutamate that had a chemical shift of 3.0 ppm away from bulk water and the signal intensity of GluCEST were concentration-dependent. Under physiological conditions, glutamate is the main contributor to the GluCEST signal. Compared with normal tissue, in both rats and patients with encephalitis, the encephalitis areas demonstrated a hyper-intense GluCEST signal, while the lacunar infarction had a decreased GluCEST signal intensity. After intravenous immunoglobulin therapy, patients with encephalitis lesions showed a decrease in GluCEST signal, and the results were significantly different from the pre-treatment signal (1.34 ± 0.31 vs 5.0 ± 0.27%, respectively; $p = 0.000$).

OPEN ACCESS

Edited by:
Miguel Castelo-Branco, Coimbra Institute for Biomedical Imaging and Translational Research, Portugal

Reviewed by:
Dong-Hoon Lee, Yonsei University, South Korea
Zhongliang Zu, Vanderbilt University, United States

***Correspondence:**
Yunping Zhang
ypzhang2008@163.com
Renhua Wu
rhwu@stu.edu.cn

† These authors have contributed equally to this work

Specialty section:
This article was submitted to Brain Imaging Methods, a section of the journal Frontiers in Neuroscience

Received: *07 March 2020*
Accepted: *25 June 2020*
Published: *28 July 2020*

Citation:
Jia Y, Chen Y, Geng K, Cheng Y, Li Y, Qiu J, Huang H, Wang R, Zhang Y and Wu R (2020) Glutamate Chemical Exchange Saturation Transfer (GluCEST) Magnetic Resonance Imaging in Pre-clinical and Clinical Applications for Encephalitis. Front. Neurosci. 14:750. doi: 10.3389/fnins.2020.00750

Conclusion: Glutamate plays a role in encephalitis, and the GluCEST imaging signal has potential as an *in vivo* imaging biomarker for the early diagnosis of encephalitis. GluCEST will provide new insight into encephalitis and help improve the differential diagnosis of brain disorders.

Keywords: chemical exchange saturation transfer, encephalitis, *Staphylococcus aureus*, glutamate, magnetic resonance imaging

INTRODUCTION

Encephalitis is serious inflammatory disease of the central nervous system (CNS) that is caused by many physiological or pathological factors (Kumar, 2020). According to its etiology, encephalitis can be divided into three types, namely, infectious encephalitis (e.g., bacterial, viral, fungal, and tuberculosis), autoimmune encephalitis, and unexplained encephalitis. Encephalitis is mainly caused by the degeneration or necrosis of neurons by the invading brain parenchyma. Owing to a lack of well-defined clinical characteristics, it is easy to misdiagnose the condition and delay treatment, resulting in a higher disability and death rate, which can cause a serious burden to patients, families, and society (Dong et al., 2019). Currently, up to 85% of encephalitis is unexplained. Although the International Encephalitis Consortium (IEC) defined the diagnostic criteria of encephalitis (Venkatesan et al., 2013), some challenging problems still remain in their clinical application (Granerod et al., 2011; Regner et al., 2018; Bewersdorf et al., 2019), as follows: (i) biopsy represents the "gold standard" for encephalitis; owing to its invasive nature and high false positive rate, it is rarely performed in the clinic; (ii) symptoms are atypical and disease progression is rapid, it is easily confused with other brain disorders, and sometimes a definitive treatment is lacking; and (iii) significant cerebrospinal fluid (CSF) pleocytosis or demonstrable neuroimaging abnormalities are often regarded as surrogate markers of brain inflammation in the absence of pathologic evidence; however, there is a high false-negative rate. In addition to the consensus reached by the IEC, other consensus statements or guidelines have also proposed that imaging technology will play an important role in the early diagnosis of the disease.

Currently, multiple imaging methods are used to improve the diagnosis of encephalitis. Conventional magnetic resonance image (MRI), with the advantages of high soft tissue resolution and the non-invasive nature of the procedure, has been widely used to diagnose encephalitis in the clinic; however, it can only provide anatomical information and the physiological or biochemical information that can be acquired is limited (Zoccarato et al., 2019). Moreover, the perfusion information of lesions can be obtained by injecting gadolinium (Gd)-based contrast agents and, in turn, can increase the risk of Gd deposition and potential side effects (Rogosnitzky and Branch, 2016). Magnetic resonance spectroscopy (MRS) measurement is time-consuming and has poor spatial specificity *in vivo*, which has also limited its applicability despite the fact that it can provide unparalleled opportunities for understanding diseases in terms of metabolism information (Burger et al., 2019). In addition, positron emission tomography (PET) or single-photon emission computed tomography (SPECT) can provide energy metabolism information of diseases, but it has the disadvantages of low specificity, high cost, and the requirement for an intravenous injection of radioactive or ionizing agents (Nishiguchi et al., 2017; Muller Herde et al., 2019). Therefore, there is a need for a non-invasive molecular imaging technology with high spatial resolution that does not require the administration of contrast agents.

Chemical exchange saturation transfer (CEST) is a relatively novel MR molecular imaging approach that utilizes a frequency selective radiofrequency (RF) irradiation pulse on particular exchangeable protons (e.g., hydroxyls, amides, and amines), thus resulting in attenuated water signals that can be measured via the loss of water signal intensity to indirectly characterize the microenvironment of the solution (Ward et al., 2000; Li et al., 2017). CEST MRI has several advantages (Wu et al., 2015; Jia et al., 2019; Wang et al., 2019), as follows: (1) it allows amplified detection of low concentration agents; (2) it can be switched "on" and "off" at will by adjusting the RF irradiation pulse parameters; (3) it has the potential to provide metabolite information from biological tissues as well as anatomical features; (4) it has high spatial resolution, is non-invasive, and does not require the injection of contrast agents; and (5) it can be specifically tailored to respond to a given stimulus (e.g., pH, enzyme, temperature, metabolite levels, etc.). Given these advantages and good performance, CEST MRI has received much attention and is now widely used in preclinical and clinical research. Glutamate (Glu) is the most abundant excitatory neurotransmitter in the brain and is involved in learning, memory, emotion, and cognitive function. The fact that amine protons on Glu that show a chemical shift of 3.0 ppm away from bulk water (0 ppm) can be measured indicates that GluCEST MRI represents a feasible approach for the diagnosis of disease (Cai et al., 2012). Currently, GluCEST imaging has been widely used in psychiatric disorders. For example, Mao et al. (2019) demonstrated that GluCEST imaging could be used for the diagnosis of acute traumatic brain injury and prediction of its prognosis. Bagga et al. (2016, 2018) successfully used GluCEST MRI in a mouse model of dopamine deficiency and Parkinson's disease to measure spatial changes in Glu. Davis et al. (2015) showed that GluCEST MRI allows the visualization of cerebral Glu changes in rat models of stress-induced sleep disturbance and status epilepticus (Lee et al., 2019). Crescenzi et al. (2014) identified Glu deficits in mouse models of dementia using GluCEST imaging. All of these studies show that GluCEST MRI may represent a valuable approach for interpreting alterations in cerebral biochemical information. Recently, an abundance of evidence has indicated that Glu is implicated in microglial activation and that activated microglia play a key role in encephalitis (Takaki et al., 2012;

Zhang et al., 2016). However, the mechanism linking Glu and encephalitis is still unclear.

In this study, we hypothesized that Glu is involved in the occurrence of encephalitis and may serve as a potential biomarker for the diagnosis of incipient encephalitis. Moreover, we hypothesized that GluCEST imaging could be used to predict encephalitis progression or prognosis. Our study may provide new insight into encephalitis and help improve the differential diagnosis of brain disorders.

MATERIALS AND METHODS

Pre-clinical Research

Phantom Preparation

Glu (Sigma Aldrich, St Louis, MO, United States) phantoms were first prepared for the optimization of GluCEST MRI parameters. To evaluate whether the CEST effect of Glu was concentration-dependent, different concentrations of Glu (0, 5, 10, 20, 40, and 50 mM) were prepared and their pH was titrated to 7.0. To simulate the effect of other metabolites on GluCEST under physiological conditions, different concentrations of metabolites [*N*-acetylaspartate (NAA; 10 mM), myo-inositol (MI; 10 mM), creatine (Cr; 6 mM), glutamine (Gln; 2 mM), Glu (10 mM), and γ-aminobutyric acid (GABA; 2 mM)] were also used in our study (pH 7.0, room temperature). Before the CEST imaging scan, the nuclear magnetic resonance tubes were inserted into a phantom holder filled with 3% agarose gel to minimize susceptibility inhomogeneity.

Animal Model Preparation

All animal care and experimental procedures were approved by the Animal Care and Use Committee of Shantou University Medical College and were in accordance with guidelines from the Chinese Animal Welfare Agency. Twenty-seven adult SD rats, weighing 250–300 g, were used in the experiment and contralateral tissue was collected as a control. All rats were kept in a specific pathogen-free animal room with a temperature-controlled system and a 12-h dark–light cycle. Animals were allowed free access to water and food. *Staphylococcus aureus* (Biotechnology Institute of Beina Chuanglian, Beijing, No. GIM1.160) was cultured overnight on blood agar, with the concentration determined to be $10^7/\mu m$. Rats were anesthetized with 3∼4.0% isoflurane vaporized with 5% O_2. The animals were mounted in a stereotactic frame, the rats' skulls were exposed through a skin incision, and a hole was drilled 4 mm away from bregma in the right side. This hole was situated in the right frontal lobe. Then, 2 μm suspension containing $10^7/\mu m$ *S. aureus* was injected 2.5 mm deep into the hole, with an injection time of 3 min. At pre-injection (0 days) and 3- and 7-day post-injection of *S. aureus*, MR scans were used to observe the dynamic changes of disease in rats.

MRI Acquisitions at 7.0 T

All imaging procedures were performed on an Agilent 7.0 Tesla (7.0 T) MR scanner (Agilent Technologies, Inc., Santa Clara, CA, United States) with a standard 9563 body coil for signal transmission and reception. To eliminate signal interference of B_0 field inhomogeneity, the B_0 map was corrected prior to the experiments with the following parameters: repetition time (TR) = 40 ms, echo time (TE) = 3, 3.5, and 4 ms, slice thickness = 2 mm, field of view (FOV) = 35 mm × 35 mm, matrix size = 64 × 64, and average = 12. High-resolution T2-weighted axial slices were acquired with TR = 4000 ms, TE = 10 ms, slice thickness = 2 mm, and FOV = 35 × 35 mm. For *in vitro* and *in vivo* experiments, an improved version of continuous wave echo planar imaging sequence was used with the following parameters: TR/TE = 1500/14 ms, saturation power (B_1) = 3.6 μT (*in vitro* phantoms) and 5.9 μT (*in vivo*), saturation time = 2 s, FOV = 35 mm × 35 mm, slice thickness = 2 mm, matrix size = 64 × 64, average = 1. Z-spectra with 52 frequency offsets from -5 to +5 ppm with intervals of 0.2 ppm, and the reference image (S_0 image) were obtained.

Clinical Research

Human Subjects

This study was approved by the local institutional review board. According to procedures approved by our hospital ethics committee, informed consent was provided before MR examination. Six patients with encephalitis (4 women, 2 men, age 48.17 ± 5.53 years), six patients with lacunar infarction (LI; 3 women, 3 men, age 52.5 ± 4.6 years), and six healthy volunteers (3 women, 3 men, age 46.33 ± 7.31 years) were recruited into this study. According to the major criterion of encephalitis established by the IEC, participants with altered mental status (including decreased level of consciousness, lethargy, or personality change) lasting ≥24 h and/or laboratory examination (lumbar puncture, complete blood count) or electroencephalography consistent with inflammatory changes, were diagnosed with encephalitis. Participants were excluded from the study if any of the following conditions were met: (i) MRI revealed brain injury, hematoma, or tumor; (ii) any contraindication for MRI (e.g., claustrophobia, cardiac pacemaker, or metal in the body); and (iii) any neurological disorder (e.g., schizophrenia, depression) diagnosed by two experienced neurologists and a radiologist, according to clinical symptoms and the MRI scan.

MRI Acquisitions at 3.0 T

All MR data acquisitions were performed on a 3.0 T MR system (Sigma; GE Healthcare, Milwaukee, WI, United States) equipped with an eight-channel phased-array head coil. Anatomy images were acquired by a fast spin echo sequence with the following scanning parameters: (1) T2-weighted imaging ($T2_W$ imaging): TR = 4480 ms, TE = 120 ms, FOV = 240 mm^2 × 240 mm^2, resolution = 256 × 384, and slice thickness = 5 mm; (2) $T2_W$ imaging-fluid attenuated inversion recovery (T2Flair): TR = 8600 ms, TE = 155 ms, TI = 2100 ms, FOV = 240 mm^2 × 240 mm^2, resolution = 256 × 384, and slice thickness = 5 mm; and (3) diffusion-weighted images (DWI): TR = 6000 ms, TE = min, *b* values = 1,000, FOV = 240 mm^2 × 240 mm^2, resolution = 256 × 384, and slice thickness = 5 mm. In addition, a magnetization transfer (MT)-prepared gradient echo MRI sequence was used for CEST imaging with the following parameters: TR = 50 ms, TE = 3.1 ms,

FOV = 240 mm^2 × 240 mm^2, matrix = 128 × 128, slice thickness = 5 mm, bandwidth = 15.63 kHz. The MT saturation pulse was set to 4 ms width Fermi pulse with flip = 600° (B_1 = 1.95 μT). Forty-one equidistant frequency offsets between 5 and -5 ppm and an additional S_0 image were acquired. Z-spectra were corrected for B_0 inhomogeneity using a water saturation shift referencing map (WASSR) with the saturation power and time are 0.1 μT and 20 ms, respectively.

Image Processing and Data Analysis

All of the CEST image processing and data analyses were performed using custom-written scripts in MatLab (Math works, Natick, MA, United States, R2011b). Z-spectra were calculated from the normalized images for the region of interest (ROI) outlined in each phantom compartment. The GluCEST contrast map, also called the magnetization transfer ratio (MTR_{asym}), was defined by the following equation (Cai et al., 2012):

$$MTR_{asym} = \frac{S(-3ppm) - S(+3ppm)}{S_0}$$

where S (-3 ppm) and S (+ 3 ppm) are the water signal with a saturation pulse at offsets ± 3 ppm from the water resonance, respectively. S_0 is the water signal without the saturation pulse. The sex and electroencephalogram (EEG) proportions were tested using a chi-squared (χ^2) test. Age and education were assessed in the three groups using one-way analysis of variance (ANOVA). The MTR_{asym} data, cerebrospinal fluid white blood cell (CSF WBC) count, and disease duration were analyzed using an unpaired *t* test. Statistical evaluations were performed using GraphPad Prism software and differences with $p < 0.05$ were deemed statistically significant.

RESULTS

Phantom Studies

The Z-spectra show that the amine protons on Glu generated a CEST effect with a chemical shift of 3.0 ppm away from bulk water, and the CEST signal of Glu was increased as the concentrations increased, indicating that the GluCEST signal was concentration-dependent (**Figures 1A,B**). **Figure 1C** shows a good linear relationship with the regression equation $MTR_{asym}(\%) = 0.215 \times (\text{Glu concentration}) - 0.1568$ ($R^2 = 0.988$), indicating that the GluCEST effect increases by nearly 0.215% for every 1 mM Glu added. In addition, to simulate the effect of other metabolites on the GluCEST signal under physiological conditions, different concentrations of metabolites [Glu (10 mM), GABA (2 mM), Gln (2 mM), NAA (10 mM), Cr (6 mM), and MI (10 mM)] were used in our study. The results show that Glu is the main contributor to the GluCEST signal, GABA and Cr provide a small contribution to the GluCEST effect, while the contribution of other metabolites (NAA, MI, and Gln) to the GluCEST effect was negligible (**Figure 1D**). We also evaluated the selection of parameters from the phantoms test and applied the selected optimal parameters to the subsequent *in vivo* application.

GluCEST Imaging *in vivo* in Encephalitis Model Rats

All anatomic images clearly showed the presence of encephalitis lesions, suggesting that we successfully established the encephalitis rat model. The GluCEST imaging had high spatial resolution, which could distinguish the encephalitis lesions and separate the white matter and gray matter tissue of rats (**Figure 2A**). To evaluate whether Glu was involved in the development of encephalitis, GluCEST imaging was used to directly observe Glu *in vivo*. The results show that the mean MTR_{asym} (3.0 ppm) in the encephalitis areas was elevated 3 days after infection with *S. aureus* compared with the healthy control (HC) group (20.24 ± 1.71% vs 14.09 ± 0.79%, t = -16.985, p = 0.000), indicating that Glu was involved in the occurrence of encephalitis and that GluCEST imaging could be used for the diagnosis of encephalitis (**Figure 2B**). In addition, to acquire new insight into viable inflammation microenvironments, dynamic changes in Glu concentrations were also observed at different time points (3 and 7 days after infection) in encephalitis rats. The results show that the GluCEST signal was increased with time, and statistically significant differences were found between the various time points [26.66 ± 1.63 vs 14.09 ± 0.79%, t = -36.105, p = 0.000 (7 days vs 0 days) (**Figure 2C**); 26.66 ± 1.63 vs 20.24 ± 1.71%, t = -14.102, p = 0.000 (7 days vs 3 days) (**Figure 2D**)].

Demographics and Clinical Characteristics

All subjects successfully completed the experiment. No significant differences were noted among the three groups (encephalitis, LI, and HC) in terms of age (F = 1.737, p = 0.2097), sex (χ^2 = 0.45, p = 0.799), or education (F = 2.807, p = 0.0921). Similarly, no statistically significant difference was found in EEG (χ^2 = 3.086, p = 0.079) or disease duration (19.17 ± 2.798 vs 15.0 ± 1.461, p = 0.261) between patients with encephalitis and LI. However, the CSF WBC count in the encephalitis group was higher than that in the LI group (9.50 ± 2.432 vs 2.50 ± 0.6708, p = 0.0196), indicating that suspected encephalitis patients could be diagnosed with encephalitis without requiring biopsy. The detailed demographic characteristics of subjects are presented in **Table 1**.

GluCEST Imaging *in vivo* in Patients With Encephalitis

As shown in **Figure 3**, GluCEST MRI could clearly distinguish white matter and gray matter in a similar manner to $T2_W$ imaging, and the gray matter signal intensity of GluCEST was higher than that of white matter. In addition, it could clearly detect the lesion area. Hence, using GluCEST MRI to map the distribution of Glu in human brain structures is feasible using a 3.0 T MR system. Compared with the HC group, the signal intensity of GluCEST was elevated in patients with encephalitis, while patients with LI showed a decreased GluCEST signal intensity (**Figure 4A**). Moreover, a significant difference was found between patients with encephalitis and LI in terms of

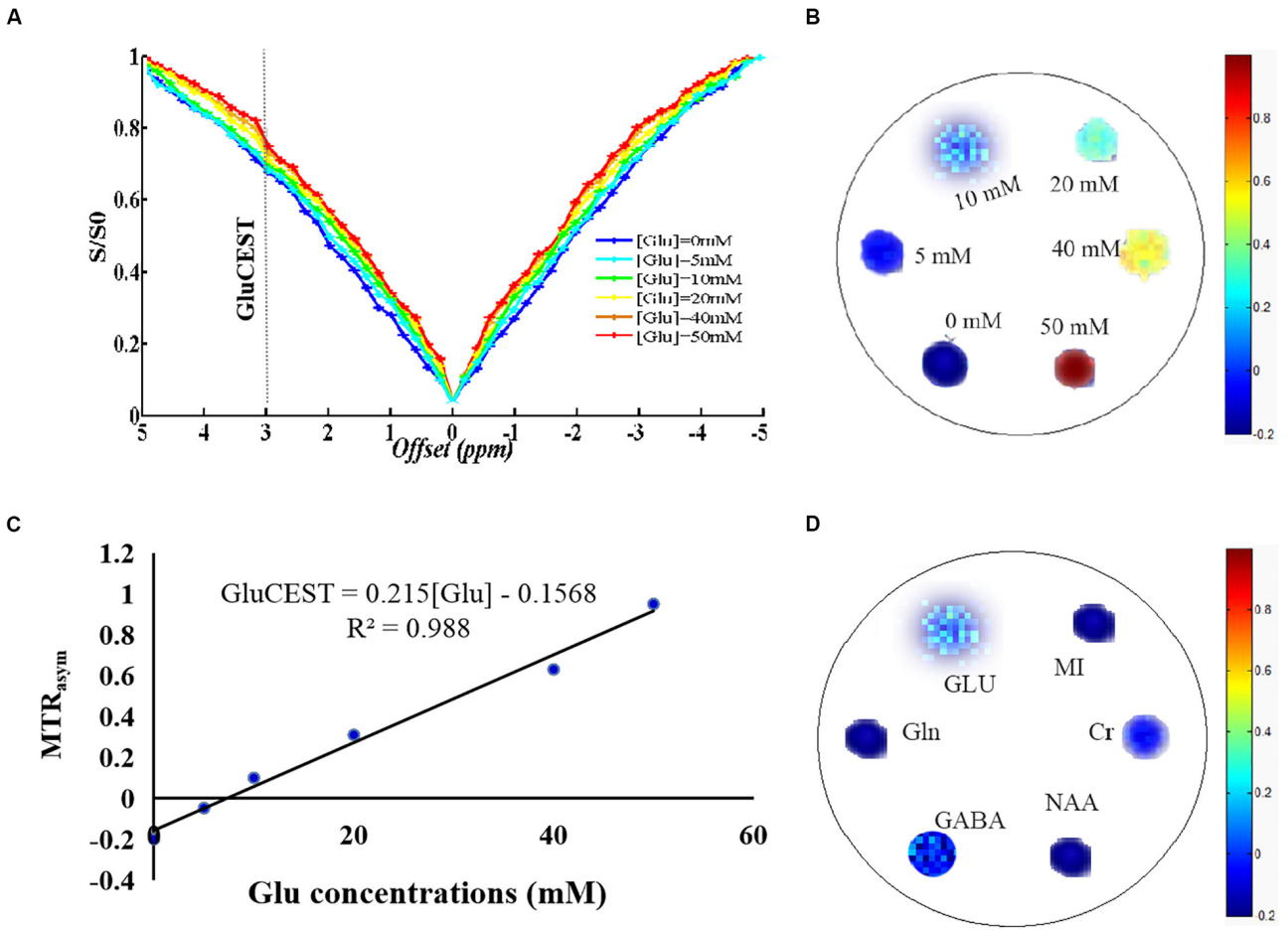

FIGURE 1 | Phantom studies performed on 7.0 T scanner. **(A)** Z-spectra show that the amine protons on glutamate (Glu) generated a chemical exchange saturation transfer (CEST) effect with a chemical shift of 3.0 ppm away from bulk water. **(B)** GluCEST map showing that the GluCEST signal was concentration-dependent. **(C)** GluCEST signal increased as the Glu concentrations increase, which appears to have a good linear relationship, indicating that the GluCEST effect increases by nearly 0.215% with every 1 mM Glu added. **(D)** Under physiological conditions, Glu is the main contributor to the GluCEST signal and γ-aminobutyric acid (GABA) and creatine (Cr) have a small contribution to the GluCEST effect, while the contribution of other metabolites [*N*-acetylaspartate (NAA), myo-inositol (MI), glutamine (Gln)] to the GluCEST effect was negligible.

the GluCEST signal (5.0 ± 0.27 vs -2.0 ± 0.11%, t = 59.745, p = 0.000) (**Figure 4C**). Z-spectrums are often used to provide qualitative insights into the CEST imaging exchange mechanism and complete understanding of the physics of the phenomenon. In our study, the average z-spectrum was also drawn based on the ROIs in the lesions. The results demonstrate that a small signal dip at 3.0 ppm was observed in the inflamed regions, but this was not observed in the LI regions, indicating that inflammation may be a cause of elevated local Glu concentrations (**Figure 4B**).

To explore the relationship between Glu concentration and the severity of lesions, we compared the changes in Glu before and after intravenous immunoglobulin treatment in both patients with encephalitis and LI. In patients with encephalitis, the results show that the signal intensity of GluCEST in encephalitis regions was obviously decreased post-treatment compared with pre-treatment (1.34 ± 0.31 vs 5.0 ± 0.27%, t = 20.205, p = 0.000), and the range of the signal intensity of the lesions was also reduced in the anatomical images ($T2_W$ imaging and T2 Flair) (**Figure 5**). However, no significant changes were found in either the GluCEST signal or morphology in patients with LI before or after treatment. This suggests that GluCEST imaging may provide new insight into encephalitis and help improve the differential diagnosis of brain disorders and the monitoring of treatment responses.

DISCUSSION

In this study, we evaluated the *in vivo* application of GluCEST imaging in both a rat model of *S. aureus*-induced encephalitis and in patients with encephalitis, as well as quantified GluCEST signals and evaluated treatment responses. GluCEST maps indicated higher glutamate concentrations in the encephalitis lesions compared with the control group. To date, several studies have demonstrated that Glu serves as the predominant

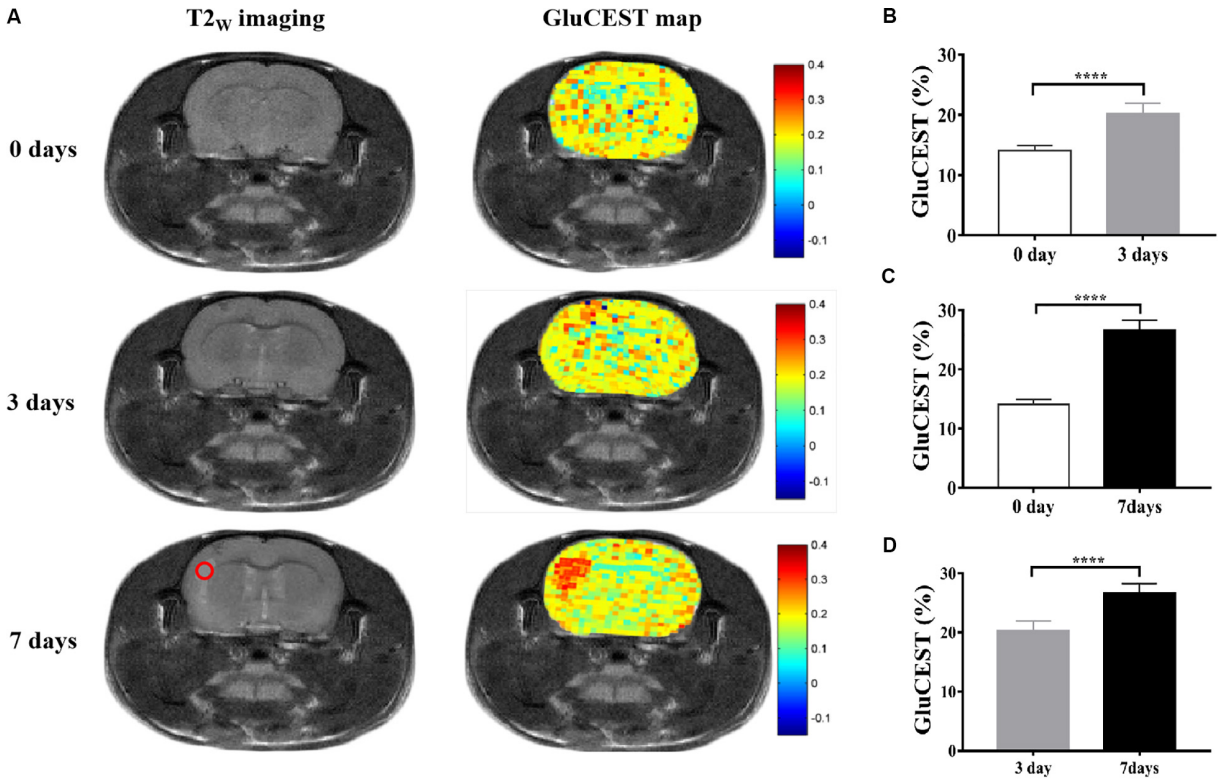

FIGURE 2 | Glutamate chemical exchange saturation transfer imaging *in vivo* in encephalitis rats. **(A)** $T2_W$ imaging and GluCEST map of encephalitis rats with *Staphylococcus aureus* infections at different time points (0, 3, and 7 days), suggesting that the GluCEST signal was increased with increasing time; statistically significant differences were found among the different time points [0 days vs 3 days **(B)**, 0 days vs 7 days **(C)**, and 3 days vs 7 days **(D)**, $n = 27$, Student's t test, two-tailed, unpaired, $^{****}p < 0.0001$].

TABLE 1 | Demographic characteristics of the subjects.

Characteristics	HC group ($n = 6$)	LI group ($n = 6$)	Encephalitis ($n = 6$)	$\chi^2/F/t$	p value
Sex (M/F)[a]	3/3	3/3	2/4	0.45	0.799
Electroencephalogram (+/-)[a]	–	2/4	5/1	3.086	0.079
Age (years)[b]	46.33 ± 7.312	52.5 ± 4.461	48.17 ± 5.529	1.737	0.2097
Education (years)[b]	9 ± 1.789	7.667 ± 1.211	10.17 ± 2.317	2.807	0.0921
CSF WBC (count/mm^3)[c]	–	2.50 ± 0.6708	9.50 ± 2.432	2.774	0.0196*
Disease duration (days)[c]	–	15.0 ± 1.461	19.17 ± 2.798	1.32	0.261

[a]*The sex and electroencephalogram (EEG) were tested using a chi-squared test.* [b]*Age and education were analyzed using one-way analysis of variance (ANOVA).* [c] *The cerebrospinal fluid white blood cell (CSF WBC) count, and disease duration were analyzed with unpaired t test. $p < 0.05$ (*) was considered statistically significant. HC, healthy control; LI, lacunar infarction.*

excitatory neurotransmitter in the brain and is involved in learning, memory, emotion, cognition, and energy metabolism (Lancaster, 2016; Nasrallah, 2017). Excessive accumulation of extracellular Glu induces excitotoxicity in CNS neurons, which may lead to various brain disorders, such as epilepsy, schizophrenia, depression, tumors, etc. (Davis et al., 2015; Roalf et al., 2017; Neal et al., 2019; Kaminski et al., 2020). It was also recently reported that glutamate is closely implicated in microglial activation and that activated microglia play a key role in encephalitis. Hence, there is significant interest in developing Glu as validated biomarker to diagnose encephalitis incipiently and precisely.

In the present study, we first explored the factors affecting the GluCEST signal and whether the GluCEST imaging signal was concentration-dependent using phantoms. We determined that glutamate is the main contributing factor to the GluCEST signal under physiological conditions, which is consistent with results from similar previous studies (Cai et al., 2012; Kogan et al., 2013). Subsequently a rat model of *S. aureus*-induced encephalitis was used to simulate the microenvironment of encephalitis, which aids in further understanding the mechanism of encephalitis. Our research team has previously shown that the GluCEST signal (at 3.0 ppm) in *S. aureus*-induced brain lesions was significantly higher than that in healthy controls (Chen et al., 2018); this

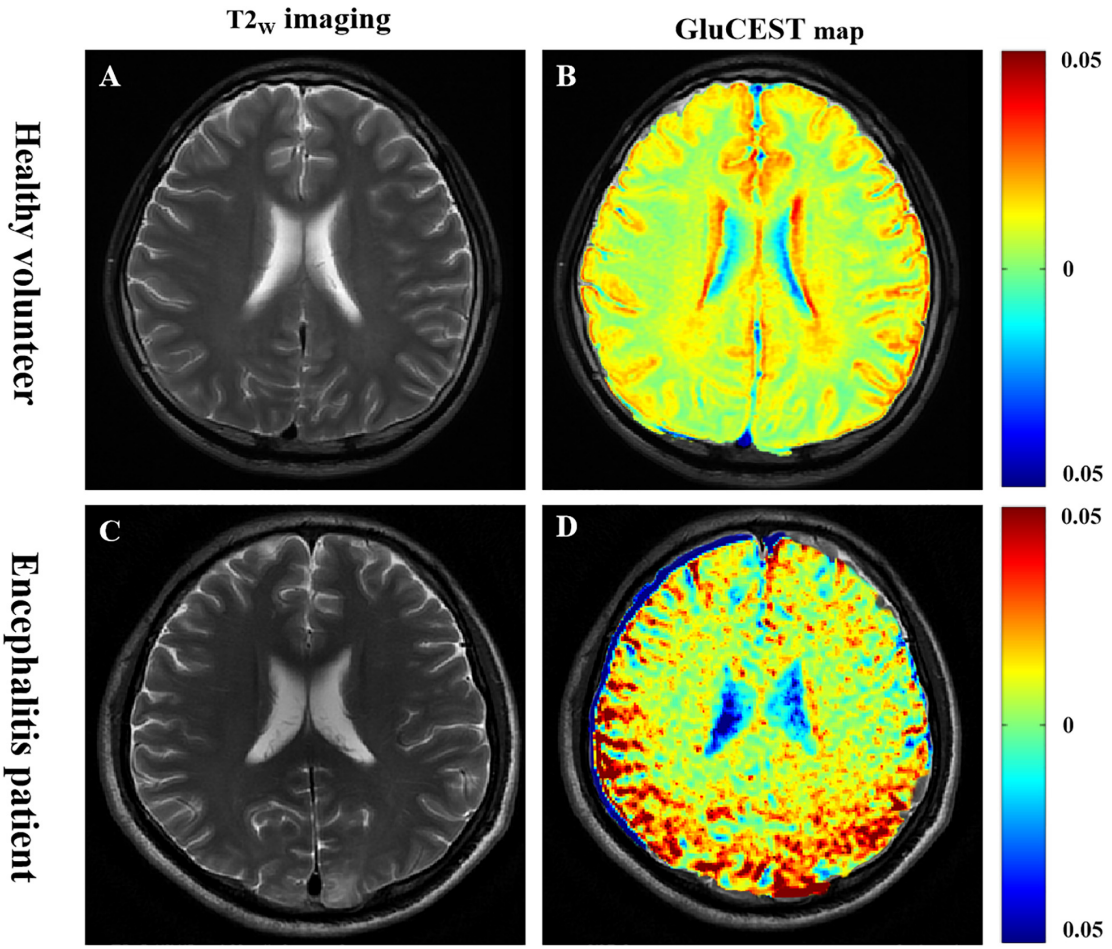

FIGURE 3 | Glutamate chemical exchange saturation transfer imaging was feasible in human brain using the 3.0 T MR system. **(A,B)** In a healthy volunteer, GluCEST magnetic resonance image (MRI) could clearly distinguish white matter and gray matter, similar to $T2_W$ imaging, and the gray matter signal intensity of GluCEST was higher than that of white matter. **(C,D)** In a patient with encephalitis, GluCEST imaging also clearly showed the left parietal cortex and subcortex lesion.

result was consistent with a previous similar study showing that the extracellular level of Glu increased 12-fold and 30-fold 8 and 20 h, respectively, after staphylococcal infection, as detected by microdialysis (Hassel et al., 2014). This may be due to the activation of microglia, astrogliosis, inflammatory cells, and pro-inflammatory factors, which can lead to the massive release of Glu into the extracellular space, as well as hindered transamination from Glu (Bagga et al., 2016; Igarashi et al., 2017; Thomas et al., 2020). However, an early MRS study showed that the Glu level is decreased in encephalitis (Lentz et al., 2008). This discrepancy might be attributed to the lower resolution of MRS, and the heterogeneous distribution of Glu may lead to its inaccurate detection. In addition, the result was not completely consistent with that of the study of Liu et al., who showed that a broad CEST contrast over a frequency range from 0.5 to 4 ppm, peaking at 2.6 ppm after injection of *S. aureus* and *Clostridium novyi*-NT (*C. novyi*-NT), respectively (Liu et al., 2013, 2018). The reason for the difference in the maximum MTR_{asym} value may be due to the fact that the MT or relaxation properties are significantly different in tissues *in vivo*, which may affect the shape of the Z-spectra (Stanisz et al., 2005). Although other neurotransmitters such as GABA or Cr also increased, their contribution to the GluCEST signals are quite limited based on the phantom results. In this study, we mainly used GluCEST imaging to directly observe the dynamic changes in Glu concentrations in encephalitis lesions, which is of vital importance for understanding the pathogenesis of encephalitis.

Recently, GluCEST imaging has attracted a lot of attention since it is a novel non-invasive MRI technique that has been widely used in the diagnosis of many diseases. For example, Zhuang et al. (2019) demonstrated that GluCEST imaging could be used to diagnose traumatic brain injury using a 7.0 T MR system. Igarashi et al. (2017) successfully used GluCEST MRI to measure spatial changes in Glu in a rat model of ischemia. However, most reports have focused on pre-clinical animal studies with high field strength. Considering the sensitivity of GluCEST and the limitation of the SAR value, few studies can be readily translated to the clinical setting using the GluCEST imaging technique, even though several researchers have proven that GluCEST MRI can be successfully used to map the Glu

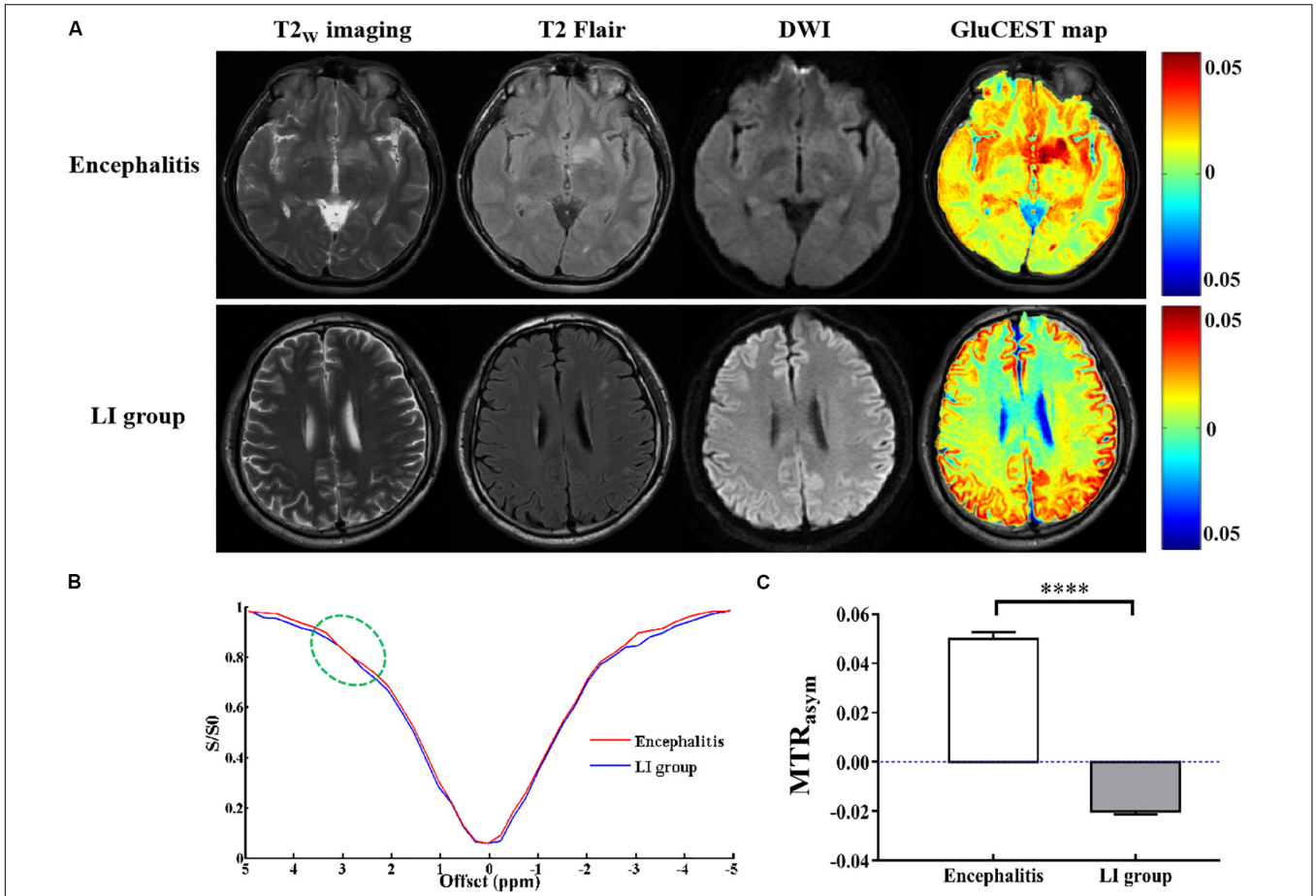

FIGURE 4 | Glutamate chemical exchange saturation transfer imaging *in vivo* of patients with encephalitis and lacunar infarction. **(A)** Conventional T2w imaging, T2Flair, and diffusion-weighted images (DWI) could not discriminate encephalitis and lacunar infarction (LI), but GluCEST MRI could distinguish between them. **(B)** Z-spectrum demonstrated that a small signal dip at 3.0 ppm (green circle) was observed in the inflamed regions but not observed in the LI regions, indicating that inflammation is a cause of the elevated local glutamate concentration. **(C)** GluCEST signal was elevated in patients with encephalitis and decreased in patients with LI (n = 6, Student's t test, two-tailed, unpaired, $^{****}p < 0.0001$).

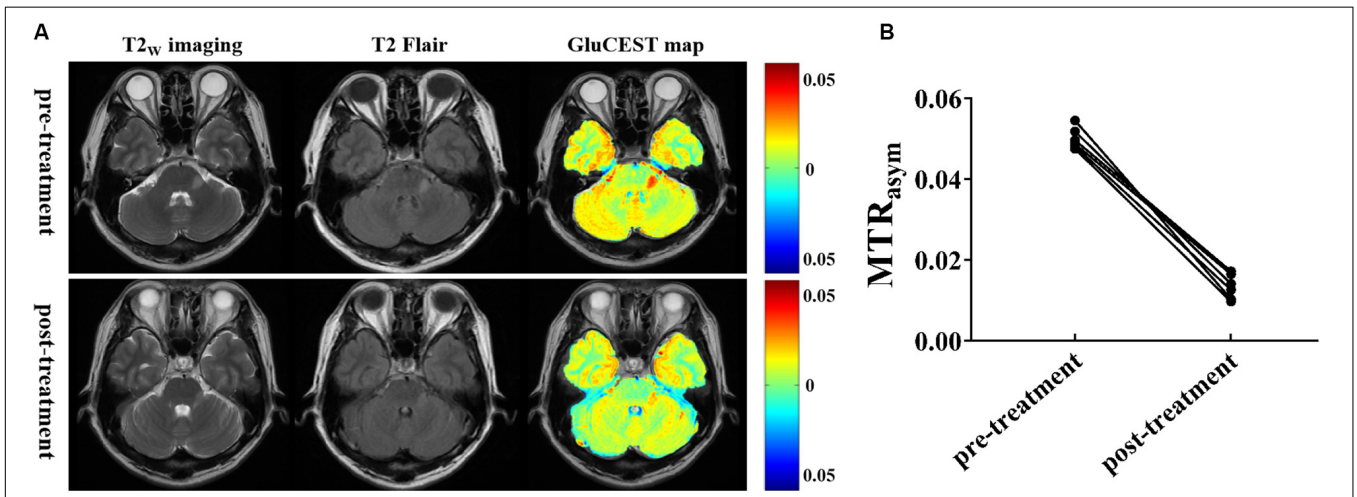

FIGURE 5 | Glutamate chemical exchange saturation transfer imaging was used for efficacy evaluation. **(A)** $T2_W$ imaging, T2Flair, and GluCEST maps of a patient with encephalitis before and after intravenous immunoglobulin therapy. **(B)** Compared with pre-treatment, the magnetization transfer ratio (MTR_{asym}) value (GluCEST signal) at post-treatment was significantly decreased (n = 6, Student's t test, two-tailed, paired).

distribution in human brain or spinal cord structures and it has high reproducibility (Kogan et al., 2013; Nanga et al., 2018). Fortunately, a preliminary study of our research team successfully used 3.0 T MRI scanner to GluCEST imaging for brain injury, compared it with MRS results, and suggested that the observed signals are highly contributed to glutamate; thus, it is feasible to detect the CEST effect from glutamate at 3.0 T (Mao et al., 2019). In our studies, we demonstrated that GluCEST imaging could be translated to the clinic without the need for contrast agents. Compared with the HC group, the signal intensity of GluCEST in patients with encephalitis was increased, while the signal was decreased in patients with LI. The result was inconsistent with that of Igarashi et al. (2017) who indicated that the Glu concentration was increased in the acute focal ischemic lesion, particularly at the border zone. This may be due to the necrosis or loss of neurons caused by occlusion of small blood vessels in LI and there was little or no microglial activation around the lesion since the amount of Glu released was too little to cause changes in the GluCEST signal. However, in acute focal ischemia, a large amount of Glu is released outside of the cells, and there is more microglial activation around the border zone, leading to an increase in the Glu concentration. Notably, the choice of ROI may also affect the quantitative analysis of the GluCEST signal. In addition, the Z-spectrum allows intuitive observation of a small peak at a specific frequency of Glu (3.0 ppm) in encephalitis and was not observed in patients with LI, indicating that encephalitis causes a mass increase in Glu and that the Glu concentration caused by LI was too low to be observed. In short, GluCEST imaging can be used to distinguish encephalitis and LI, in a similar manner to the way in which Liu et al. (2018) showed that bacCEST MRI permits the differentiation of brain abscesses from glioma tumors. Early detection of the response of a brain abscess to an antibiotic treatment is crucial for treatment planning and adjustment. Conventional MRI is unable to directly detect the treatment response, and abscesses may become initially enlarged when the antibiotic treatment is effective. GluCEST imaging has potential clinical utility for monitoring the treatment response before any morphological changes. Our results show that the GluCEST signal in patients with encephalitis was dramatically decreased after intravenous injection of immunoglobulin therapy compared with before therapy. This study demonstrates that GluCEST imaging has the potential as an imaging biomarker for predicting therapeutic outcomes. In patients with LI, however, no obvious changes were found in the GluCEST signal. The reduction in the GluCEST signal in encephalitis lesions after treatment may be due to the fact that the activation of microglia or pro-inflammatory factors was inhibited by immunoglobulin. This result is consistent with a similar previous study that reported a reduced GluCEST signal following ciliary neurotrophic factor (CNTF) injection in the brain, which was attributed to reduced astroglial cellular activity as well as a reduction in the level of glutamine, a precursor of Glu (Carrillo-De Sauvage et al., 2015). Of course, the detailed mechanism of Glu in encephalitis requires further study.

As a method to indirectly detect the solute molecules, CEST imaging often depends on multiple other tissue parameters, including direct water saturation (DS), semi-solid non-specific MT, nuclear overhauser enhancement (NOE) effect, water longitudinal relaxation time (T1w), and nearby overlapping CEST signal influences. Variation of these parameters may cause misinterpretation of the GluCEST signal in encephalitis. Thus, correction of these non-specific factors is necessary. Since the DS effects are symmetric with respect to the water resonance frequency, they can be removed by asymmetry analysis; thus, we used the GluCEST formula $S(-3ppm) - S(3ppm)/S_0$ not the $S(-3ppm) - S(3ppm)/S(-3ppm)$ to calculate the GluCEST signal. MT asymmetry is dependent on the applied saturation pulse parameters, and a strong saturation pulse (saturation power >3 μT) with short duration can largely mitigate the confounding effects of MT asymmetry. Thus, in our study, a strong saturation pulse with short saturation times was applied both in the phantom (3.6 μT, 2 s) and *in vivo* (5.9 μT, 2 s) models. In addition, a strong saturated power can reduce the interference of NOE effect. Although several post-processing techniques have been developed to increase the specificity by removing DS, semi-solid MT, NOE effect, and T1w influences, it is still challenging to remove overlapping CEST signals from other potential contaminations. For instance, proteins also have amines of approximately 3 ppm which could contaminate the GluCEST effect. Recently, Zhang et al. performed both *in vitro* and *in vivo* experiments and demonstrated that exchange-dependent relaxation rate (Rex) technology may be a good choice to address this problem (Zhang et al., 2017, 2018). In short, CEST signals are affected by other contamination factors or non-specific parameters, and this needs further study.

Despite the fact that our study confirmed that Glu was involved in the occurrence and development of encephalitis and can be quantitatively evaluated by GluCEST imaging, there are still some limitations in the present study. For example, (i) biopsy as the "gold standard" for the diagnosis of encephalitis, owing to its invasive nature and deep location, and the small scope of lesions limited its used in this study; (ii) the clinical sample sizes are small, and there was no classification of the encephalitis; and (iii) GluCEST imaging was affected by many factors, and there is a lack of unified clinical scanning and diagnostic standards, etc. In spite of these shortcomings, we are also working hard to solve them. For example, we tried our best to achieve accurate diagnosis through combined clinical symptoms, laboratory tests, and experienced neurologists. In terms of the insufficient sample size, we simulated the change in clinical encephalitis using the encephalitis rat model. Of course, we need to continue recruiting patients with encephalitis, and a grading study is also required. Finally, with the development of the MR system hardware and software as well as the efforts of scientists, a standard imaging scheme for clinical practice research will be developed in the future.

CONCLUSION

Our study demonstrates that Glu is associated with the early changes in the occurrence and development of encephalitis both in preclinical and clinical applications, and high-resolution

GluCEST imaging could be used for real-time, quantitative, and non-invasive monitoring of its dynamic change without requiring the injection of any exogenous imaging contrast agents. In addition, we could use GluCEST imaging to observe the spatial alteration of Glu before and after treatment and then evaluate the therapeutic effect. Therefore, GluCEST imaging has the potential as an *in vivo* imaging biomarker for metabolic and functional changes in the rat model of encephalitis induced by *S. aureus* and patients with encephalitis and could predict encephalitis progress or prognosis with highly clinically translatable value. Importantly, this may provide us new insight into encephalitis and help improve the differential diagnosis of brain disorders. In the future, it will be promising to develop novel agents based on Glu for targeted diagnosis and treatment of encephalitis.

DATA AVAILABILITY STATEMENT

All datasets generated for this study are included in the article/supplementary material.

ETHICS STATEMENT

The studies involving human participants were reviewed and approved by the local ethics committee of the Second Affiliated Hospital of Shantou University Medical College. The patients/participants provided their written informed consent to participate in this study. The animal study was reviewed and approved by Animal Care and Use Committee of Shantou University Medical College.

AUTHOR CONTRBUTIONS

YChen and RWu designed the study. YChen, KG, YCheng, JQ, and HH performed the experiments and collected clinical data. YL and RWa processed images. YJ carried out statistical analysis and drafted the manuscript. YZ and RWu critically reviewed and revised the manuscript. All authors contributed to the article and approved the submitted version.

FUNDING

This work was supported by the National Natural Science Foundation of China (Grant No. 31870981) and Grant for Key Disciplinary Project of Clinical Medicine under the Guangdong High-level University Development Program (Grant No. 002-18119101).

REFERENCES

Bagga, P., Crescenzi, R., Krishnamoorthy, G., Verma, G., Nanga, R. P., Reddy, D., et al. (2016). Mapping the alterations in glutamate with GluCEST MRI in a mouse model of dopamine deficiency. *J. Neurochem.* 139, 432–439. doi: 10.1111/jnc.13771

Bagga, P., Pickup, S., Crescenzi, R., Martinez, D., Borthakur, A., D'aquilla, K., et al. (2018). In vivo GluCEST MRI: reproducibility, background contribution and source of glutamate changes in the MPTP model of Parkinson's disease. *Sci. Rep.* 8:2883. doi: 10.1038/s41598-018-21035-3

Bewersdorf, J. P., Koedel, U., Patzig, M., Dimitriadis, K., Paerschke, G., Pfister, H. W., et al. (2019). Challenges in HSV encephalitis: normocellular CSF, unremarkable CCT, and atypical MRI findings. *Infection* 47, 267–273. doi: 10.1007/s15010-018-1257-7

Burger, A., Kotze, M. J., Stein, D. J., Janse Van Rensburg, S., and Howells, F. M. (2019). The relationship between measurement of in vivo brain glutamate and markers of iron metabolism: a proton magnetic resonance spectroscopy study in healthy adults. *Eur. J. Neurosci.* 51, 984–990. doi: 10.1111/ejn.14583

Cai, K., Haris, M., Singh, A., Kogan, F., Greenberg, J. H., Hariharan, H., et al. (2012). Magnetic resonance imaging of glutamate. *Nat. Med.* 18, 302–306. doi: 10.1038/nm.2615

Carrillo-De Sauvage, M. A., Flament, J., Bramoulle, Y., Ben Haim, L., Guillermier, M., Berniard, A., et al. (2015). The neuroprotective agent CNTF decreases neuronal metabolites in the rat striatum: an in vivo multimodal magnetic resonance imaging study. *J. Cereb. Blood.Flow. Metab.* 35, 917–921. doi: 10.1038/jcbfm.2015.48

Chen, Y., Dai, Z., Shen, Z., Guan, J., Zhuang, Z., Mao, Y., et al. (2018). Imaging of glutamate in brain abscess using GLUCEST at 7T. *Radiol. Infecti. Dis.* 5, 148–153. doi: 10.1016/j.jrid.2018.11.001

Crescenzi, R., Debrosse, C., Nanga, R. P., Reddy, S., Haris, M., Hariharan, H., et al. (2014). In vivo measurement of glutamate loss is associated with synapse loss in a mouse model of tauopathy. *Neuroimage* 101, 185–192. doi: 10.1016/j.neuroimage.2014.06.067

Davis, K. A., Nanga, R. P., Das, S., Chen, S. H., Hadar, P. N., Pollard, J. R., et al. (2015). Glutamate imaging (GluCEST) lateralizes epileptic foci in nonlesional temporal lobe epilepsy. *Sci. Transl. Med.* 7:309ra161. doi: 10.1126/scitranslmed.aaa7095

Dong, X., Zheng, D., and Nao, J. (2019). Clinical characteristics and factors associated with short-term prognosis in adult patients with autoimmune encephalitis of non-neoplastic etiology. *Neurol. Sci.* 40, 1567–1575. doi: 10.1007/s10072-019-03883-7

Granerod, J., Ambrose, H. E., and Davies, W. S. (2011). Causes of encephalitis and differences in their clinical presentations in England: a multicentre, population-based prospective study. *Lancet. Infect. Dise.* 11:79. doi: 10.1016/S1473-3099(10)70222-X

Hassel, B., Dahlberg, D., Mariussen, E., Goverud, I. L., Antal, E. A., Tonjum, T., et al. (2014). Brain infection with Staphylococcus aureus leads to high extracellular levels of glutamate, aspartate, γ-aminobutyric acid, and zinc. *J. Neurosci. Res.* 92, 1792–1800. doi: 10.1002/jnr.23444

Igarashi, H., Ueki, S., Ohno, K., Ohkubo, M., and Suzuki, Y. (2017). Magnetic resonance imaging of neurotransmitter-related molecules. *J. Nippon. Med. Sch.* 84, 160–164. doi: 10.1272/jnms.84.160

Jia, Y., Wang, C., Zheng, J., Lin, G., Ni, D., Shen, Z., et al. (2019). Novel nanomedicine with a chemical-exchange saturation transfer effect for breast cancer treatment in vivo. *J. Nanobiotechnol.* 17:123. doi: 10.1186/s12951-019-0557-0

Kaminski, J., Gleich, T., Fukuda, Y., Katthagen, T., Gallinat, J., Heinz, A., et al. (2020). Association of cortical glutamate and working memory activation in patients with schizophrenia: a multimodal proton magnetic resonance spectroscopy and functional magnetic resonance imaging study. *Biol. Psychiatry* 87, 225–233. doi: 10.1016/j.biopsych.2019.07.011

Kogan, F., Singh, A., Debrosse, C., Haris, M., Cai, K., Nanga, R. P., et al. (2013). Imaging of glutamate in the spinal cord using GluCEST. *Neuroimage* 77, 262–267. doi: 10.1016/j.neuroimage.2013.03.072

Kumar, R. (2020). Understanding and managing acute encephalitis. *F1000Res* 9:F1000 Faculty Rev-60. doi: 10.12688/f1000research.20634.1

Lancaster, E. (2016). The diagnosis and treatment of autoimmune encephalitis. *J. Clin. Neurol.* 12, 1–13. doi: 10.3988/jcn.2016.12.1.1

Lee, D. H., Woo, C. W., Kwon, J. I., Chae, Y. J., Ham, S. J., Suh, J. Y., et al. (2019). Cerebral mapping of glutamate using chemical exchange saturation transfer

imaging in a rat model of stress-induced sleep disturbance at 7.0T. *J. Magn. Reson. Imaging* 50, 1866–1872. doi: 10.1002/jmri.26769

Lentz, M. R., Westmoreland, S. V., Lee, V., Ratai, E. M., Halpern, E. F., and Gonzalez, R. G. (2008). Metabolic markers of neuronal injury correlate with SIV CNS disease severity and inoculum in the macaque model of neuroAIDS. *Magn. Reson. Med.* 59, 475–484. doi: 10.1002/mrm.21556

Li, C., Chen, M., Zhao, X., Wang, R., Chen, H., Su, W., et al. (2017). Chemical Exchange Saturation Transfer MRI Signal Loss of the Substantia Nigra as an Imaging Biomarker to Evaluate the Diagnosis and Severity of Parkinson's Disease. *Front. Neurosci.* 11:489. doi: 10.3389/fnins.2017.00489

Liu, G., Bettegowda, C., Qiao, Y., Staedtke, V., Chan, K. W., Bai, R., et al. (2013). Noninvasive imaging of infection after treatment with tumor-homing bacteria using Chemical Exchange Saturation Transfer (CEST) MRI. *Magn. Reson. Med.* 70, 1690–1698. doi: 10.1002/mrm.24955

Liu, J., Bai, R., Li, Y., Staedtke, V., Zhang, S., Van Zijl, P. C. M., et al. (2018). MRI detection of bacterial brain abscesses and monitoring of antibiotic treatment using bacCEST. *Magn. Reson. Med.* 80, 662–671. doi: 10.1002/mrm.27180

Mao, Y., Zhuang, Z., Chen, Y., Zhang, X., Shen, Y., Lin, G., et al. (2019). Imaging of glutamate in acute traumatic brain injury using chemical exchange saturation transfer. *Quant. Imaging. Med. Surg.* 9, 1652–1663. doi: 10.21037/qims.2019.09.08

Muller Herde, A., Schibli, R., Weber, M., and Ametamey, S. M. (2019). Metabotropic glutamate receptor subtype 5 is altered in LPS-induced murine neuroinflammation model and in the brains of AD and ALS patients. *Eur. J. Nucl. Med. Mol. Imaging* 46, 407–420. doi: 10.1007/s00259-018-4179-9

Nanga, R. P. R., Debrosse, C., Kumar, D., Roalf, D., Mcgeehan, B., D'aquilla, K., et al. (2018). Reproducibility of 2D GluCEST in healthy human volunteers at 7 T. *Magn. Reson. Med.* 80, 2033–2039. doi: 10.1002/mrm.27362

Nasrallah, H. A. (2017). Glutamate's exciting roles in body, brain, and mind: a fertile future pharmacotherapy target. *Current. Psychiatry.* 16, 17–18.

Neal, A., Moffat, B. A., Stein, J. M., Nanga, R. P. R., Desmond, P., Shinohara, R. T., et al. (2019). Glutamate weighted imaging contrast in gliomas with 7Tesla magnetic resonance imaging. *Neuroimage. Clin.* 22:101694. doi: 10.1016/j.nicl.2019.101694

Nishiguchi, N., Sato, T., Haraguchi, K., Inoue, D., Takahashi, Y., and Moriuchi, H. (2017). Diagnostic value of single photon emission computed tomography (SPECT) for patients with non-herpetic acute limbic encephalitis. *No. To. Hattatsu.* 49, 46–50.

Regner, G. G., Pereira, P., Leffa, D. T., De Oliveira, C., Vercelino, R., Fregni, F., et al. (2018). Preclinical to clinical translation of studies of transcranial direct-current stimulation in the treatment of epilepsy: a systematic review. *Front. Neurosci.* 12:189. doi: 10.3389/fnins.2018.00189

Roalf, D. R., Nanga, R. P. R., Rupert, P. E., Hariharan, H., Quarmley, M., Calkins, M. E., et al. (2017). Glutamate imaging (GluCEST) reveals lower brain GluCEST contrast in patients on the psychosis spectrum. *Mol. Psychiatry* 22, 1298–1305. doi: 10.1038/mp.2016.258

Rogosnitzky, M., and Branch, S. (2016). Gadolinium-based contrast agent toxicity: a review of known and proposed mechanisms. *Biometals* 29, 365–376. doi: 10.1007/s10534-016-9931-7

Stanisz, G. J., Odrobina, E. E., Pun, J., Escaravage, M., Graham, S. J., Bronskill, M. J., et al. (2005). T1, T2 relaxation and magnetization transfer in tissue at 3T. *Magn. Reson. Med.* 54, 507–512. doi: 10.1002/mrm.20605

Takaki, J., Fujimori, K., Miura, M., Suzuki, T., Sekino, Y., and Sato, K. (2012). L-glutamate released from activated microglia downregulates astrocytic L-glutamate transporter expression in neuroinflammation: the 'collusion' hypothesis for increased extracellular L-glutamate concentration in neuroinflammation. *J. Neuroinflam.* 9:275. doi: 10.1186/1742-2094-9-275

Thomas, A. M., Xu, J., Calabresi, P. A., Van Zijl, P. C. M., and Bulte, J. W. M. (2020). Monitoring diffuse injury during disease progression in experimental autoimmune encephalomyelitis with on resonance variable delay multiple pulse (onVDMP) CEST MRI. *Neuroimage* 204:116245. doi: 10.1016/j.neuroimage.2019.116245

Venkatesan, A., Tunkel, A. R., Bloch, K. C., Lauring, A. S., Sejvar, J., Bitnun, A., et al. (2013). Case definitions, diagnostic algorithms, and priorities in encephalitis: consensus statement of the international encephalitis consortium. *Clin. Infect. Dis.* 57, 1114–1128. doi: 10.1093/cid/cit458

Wang, R., Wang, C., Dai, Z., Chen, Y., Shen, Z., Xiao, G., et al. (2019). An Amyloid-beta targeting chemical exchange saturation transfer probe for in vivo detection of Alzheimer's disease. *ACS. Chem. Neurosci.* 10, 3859–3867. doi: 10.1021/acschemneuro.9b00334

Ward, K. M., Aletras, A. H., and Balaban, R. S. (2000). A new class of contrast agents for MRI based on proton chemical exchange dependent saturation transfer (CEST). *J. Magn. Reson.* 143, 79–87. doi: 10.1006/jmre.1999.1956

Wu, R., Longo, D. L., Aime, S., and Sun, P. Z. (2015). Quantitative description of radiofrequency (RF) power-based ratiometric chemical exchange saturation transfer (CEST) pH imaging. *NMR Biomed.* 28, 555–565. doi: 10.1002/nbm.3284

Zhang, X. Y., Wang, F., Li, H., Xu, J., Gochberg, D. F., Gore, J. C., et al. (2017). CEST imaging of fast exchanging amine pools with corrections for competing effects at 9.4 T. *NMR. Biomed* 30:e3715. doi: 10.1002/nbm.3715

Zhang, X. Y., Wang, F., Xu, J., Gochberg, D. F., Gore, J. C., and Zu, Z. (2018). Increased CEST specificity for amide and fast-exchanging amine protons using exchange-dependent relaxation rate. *NMR. Biomed.* 31:e3863. doi: 10.1002/nbm.3863

Zhang, Z., Bassam, B., Thomas, A. G., Williams, M., Liu, J., Nance, E., et al. (2016). Maternal inflammation leads to impaired glutamate homeostasis and up-regulation of glutamate carboxypeptidase II in activated microglia in the fetal/newborn rabbit brain. *Neurobiol. Dis.* 94, 116–128. doi: 10.1016/j.nbd.2016.06.010

Zhuang, Z., Shen, Z., Chen, Y., Dai, Z., Zhang, X., Mao, Y., et al. (2019). Mapping the Changes of Glutamate Using Glutamate Chemical Exchange Saturation Transfer (GluCEST) Technique in a Traumatic Brain Injury Model: a Longitudinal Pilot Study. *ACS Chem. Neurosci.* 10, 649–657. doi: 10.1021/acschemneuro.8b00482

Zoccarato, M., Valeggia, S., Zuliani, L., Gastaldi, M., Mariotto, S., Franciotta, D., et al. (2019). Conventional brain MRI features distinguishing limbic encephalitis from mesial temporal glioma. *Neuroradiology* 61, 853–860. doi: 10.1007/s00234-019-02212-1

Conflict of Interest: The authors declare that the research was conducted in the absence of any commercial or financial relationships that could be construed as a potential conflict of interest.

Copyright © 2020 Jia, Chen, Geng, Cheng, Li, Qiu, Huang, Wang, Zhang and Wu. This is an open-access article distributed under the terms of the Creative Commons Attribution License (CC BY). The use, distribution or reproduction in other forums is permitted, provided the original author(s) and the copyright owner(s) are credited and that the original publication in this journal is cited, in accordance with accepted academic practice. No use, distribution or reproduction is permitted which does not comply with these terms.

frontiers in Neuroscience

ORIGINAL RESEARCH
published: 30 July 2020
doi: 10.3389/fnins.2020.00825

Investigating the Reliability of Population Receptive Field Size Estimates Using fMRI

Agustin Lage-Castellanos[1,2], Giancarlo Valente[1], Mario Senden[1] and Federico De Martino[1,3]*

[1] Department of Cognitive Neuroscience, Faculty of Psychology and Neuroscience, Maastricht University, Maastricht, Netherlands, [2] Department of NeuroInformatics, Cuban Center for Neuroscience, Havana, Cuba, [3] Center for Magnetic Resonance Research, Department of Radiology, University of Minnesota, Minneapolis, MN, United States

In functional MRI (fMRI), population receptive field (pRF) models allow a quantitative description of the response as a function of the features of the stimuli that are relevant for each voxel. The most popular pRF model used in fMRI assumes a Gaussian shape in the features space (e.g., the visual field) reducing the description of the voxel's pRF to the Gaussian mean (the pRF preferred feature) and standard deviation (the pRF size). The estimation of the pRF mean has been proven to be highly reliable. However, the estimate of the pRF size has been shown not to be consistent within and between subjects. While this issue has been noted experimentally, here we use an optimization theory perspective to describe how the inconsistency in estimating the pRF size is linked to an inherent property of the Gaussian pRF model. When fitting such models, the goodness of fit is less sensitive to variations in the pRF size than to variations in the pRF mean. We also show how the same issue can be considered from a bias-variance perspective. We compare different estimation procedures in terms of the reliability of their estimates using simulated and real fMRI data in the visual (using the Human Connectome Project database) and auditory domain. We show that, the reliability of the estimate of the pRF size can be improved considering a linear combination of those pRF models with similar goodness of fit or a permutation based approach. This increase in reliability of the pRF size estimate does not affect the reliability of the estimate of the pRF mean and the prediction accuracy.

Keywords: population receptive fields, retinotopy, tonotopy, computational neuroscience, fMRI

OPEN ACCESS

Edited by:
Miguel Castelo-Branco, Coimbra Institute for Biomedical Imaging and Translational Research (CIBIT), Portugal

Reviewed by:
Maria Fatima Silva, University of Coimbra, Portugal
Ben Mark Harvey, Utrecht University, Netherlands
Otília C. d'Almeida, University of Coimbra, Portugal

****Correspondence:***
Agustin Lage-Castellanos
a.lagecastellanos@maastrichtuniversity.nl; mlsttin@gmail.com

Specialty section:
This article was submitted to Brain Imaging Methods, a section of the journal Frontiers in Neuroscience

Received: *07 March 2020*
Accepted: *15 July 2020*
Published: *30 July 2020*

Citation:
Lage-Castellanos A, Valente G, Senden M and De Martino F (2020) Investigating the Reliability of Population Receptive Field Size Estimates Using fMRI. Front. Neurosci. 14:825. doi: 10.3389/fnins.2020.00825

INTRODUCTION

In sensory cortical (and subcortical) areas, processing is organized in maps whose topography depends on the preferences of neuronal populations to the information carried by external stimuli (i.e., the receptive field – RF). Using computational approaches and functional magnetic resonance imaging (fMRI) data, the receptive field of the neuronal population within each voxel (population receptive field, pRF) can be estimated non-invasively at the level of individual subjects. That is, pRF modeling approaches parametrically characterize the measured fMRI response in the space of a chosen set of features that represent the stimuli. Over the last decade, these approaches have become mainstream in neuroscientific fMRI research (Wandell and Winawer, 2015).

Population receptive field modeling has been introduced to study visual information processing building on early techniques for visual field mapping (Engel et al., 1994; Sereno et al., 1995). The pioneering model of Dumoulin and Wandell (Dumoulin and Wandell, 2008) underlies the majority of the current pRF modeling approaches. This model assumes that the pRF characterizing neuronal populations in the visual cortex is a two-dimensional Gaussian function that is defined in the visual space spanned by the stimuli. The Gaussian in the visual field coordinates is described by three parameters, the distance to the fovea (eccentricity), the angle of the pRF mean with respect to the horizontal axis and the standard deviation (pRF size). A number of extensions of this initial model, varying the function that describes the pRF, have been considered. For example the effect of suppressive surround in the visual pRF has been introduced by combining two Gaussian functions (Zuiderbaan et al., 2012; Harvey et al., 2013), and compressive spatial summation has been introduced considering non-linear effects in the pRF model (Kay et al., 2013). Apart from variations on the model shape or properties, different estimation approaches have also been considered. A Bayesian framework for the estimation of the pRF parameters has been introduced allowing model comparison using the posterior probability (Zeidman et al., 2018). Furthermore, using a Bayesian approach, the incorporation of prior anatomical information in the pRF estimation procedure has also been considered (Benson and Winawer, 2018). Another possibility for fitting the Gaussian model is to select the best combination of Gaussian basis functions using LASSO regression. The pRF can also be estimated directly from the features matrix using regularized linear regression, without making *a priori* assumptions about the pRF shape (Moerel et al., 2012; Lee et al., 2013). Apart from characterizing the properties of voxels in response to external stimulation, the pRF modeling approach has also been extended to study resting state connectivity (Gravel et al., 2014). Outside the study of visual areas, pRF modeling approaches have been successfully applied to map the spatial organization of the somatosensory cortex (Puckett et al., 2020) as well as the preference and selectivity (i.e., tuning) to sound frequency in auditory cortical areas (Thomas et al., 2015).

Despite the widespread application of the pRF modeling methodology (Gravel et al., 2014; Zuiderbaan et al., 2017; Dumoulin and Knapen, 2018), there are challenges concerning model fitting that require careful consideration. In fact, finding the best Gaussian pRF representing the responses of an fMRI voxel is a non-convex optimization problem. As a consequence, the cost function (e.g., the minimum squared error or the correlation between the actual voxel response and the response predicted by the pRF model) presents a constellation of local minima and maxima that compromise the convergence of the optimization algorithms conditioned to the signal-to-noise ratio (SNR) of the fMRI data. While this issue has been noted experimentally, here we describe the pRF optimization landscape and show that these local optima appear in a subspace of the cost function space that is populated by very narrow pRFs. This problem is particularly relevant in noisy voxels, where one of the local minima can become the global minimum, and thus result in compromised estimates of the pRF size in particular, but also of the pRF mean. This issue is apparent from the analysis of *in vivo* data where the estimates of pRF size appear to have low consistency both across subjects and within subject (using split-half reliability metrics) (Benson et al., 2018), in contrast with the higher consistency of the pRF eccentricity and polar angle in different areas of the visual cortex. The same issue has been previously highlighted by studies that reported the reliability of pRF parameter estimates in visual cortical areas across sessions (van Dijk et al., 2016) or runs (Zeidman et al., 2018). In addition the estimates of the pRF size have been shown to be more sensitive to changes in the experimental design and the stimuli compared to the estimates of the pRF mean (Alvarez et al., 2015). Different heuristic approaches have been used to mitigate the problem. For example, spatial smoothing can be used to increase the SNR in the fMRI data (Dumoulin and Wandell, 2008) or the analyses can be limited to voxels whose variance explained by the model exceeds a pre-determined threshold (Dumoulin and Wandell, 2008; Thomas et al., 2015). Alternatively, constraints can be introduced to the size of the pRF (i.e., allowing only pRF broader than a certain value) (Zeidman et al., 2018) and a combination of all these approaches has also been considered (Thomas et al., 2015).

These algorithmic alternatives come with multiple software implementations which complicates the validation of the pRF estimation. With the aim of evaluating the reproducibility of these software alternatives a computational framework has been recently developed (Lerma-Usabiaga et al., 2020). Following a similar but complementary aim, this article focuses on the algorithmic principles rather than the software alternatives for estimating the pRF. In particular, we focus on understanding the theoretical difficulties underlying the estimation of the Gaussian pRF model and their interaction with the noise in the signal. To do this, here we first consider simulated data and study the sensitivity of the pRF cost function under variations of the pRF parameters. We focus on the reasons underling the instability (inconsistency) in the estimation of the pRF size. On simulated data that represent the response to traveling bars in the visual field, we compare five pRF estimation methods in terms of bias and variance of the pRF parameters. Four of them are approaches that have been previously introduced. In particular we consider the pRF estimation procedure and an estimation procedure based on grid search extracted from the procedure reported in Benson et al. (2018), the convex estimation procedure introduced by COpRF and the linearized encoding procedure proposed by Lee et al. (2013). The fifth approach consists in a heuristic procedure, that we introduce here, that averages pRF models with similar training error. The advantage of this procedure is a reduction in the variance of the estimated pRF sizes, increasing the reliability of pRFs parameters.

The results obtained in simulations are then validated on real fMRI (visual and auditory fMRI experiments) data by considering the split-half reliability of the pRF parameter. We used the retinotopic experiment from the 7 Tesla Human Connectome Project (HCP) (consisting in 181 subjects – Benson et al., 2018) to evaluate the different methods in their ability of estimating visual pRFs. In this dataset, the Gaussian pRF model

is estimated from the response elicited by visual stimuli that smoothly travel across the visual field (see (Senden et al., 2014) for alternatives design that can be used for pRF mapping). In this case the estimation of the pRF occurs in the domain of the fMRI time series by convolving the neural response predicted by the Gaussian pRF model with the hemodynamic response function. However, when the experimental design allows (i.e., when the temporal sequence of the stimuli allows for the estimation of the response to each individual stimulus) the pRF can also be estimated based on a response vector that does not include the effect of the hemodynamic response and constructed by the Beta coefficients estimated with a General Linear Model. In this case, we show that, when the responses to individual stimuli are exchangeable under the null hypothesis, a modification of the grid-search algorithm can be used that leverages a permutation test to estimate the distribution of the cost function under the null hypothesis which is the one of no relationship between the voxel's pRF model and the observed data. We test this approach on auditory pRFs estimated from the response to natural sounds. In this dataset, selecting the auditory pRF with the smallest probability of occurring by chance results in more reliable estimates than any of the standard methods.

MATERIALS AND METHODS

In pRF modeling, the observed fMRI response y is assumed to be a function of the pRF (w) and a matrix X that represents the stimuli (e.g., images or sounds) in the feature space (e.g., pixels or sound frequencies), convolved with the hemodynamic response function:

$$y = \alpha\ (Xw)^{\gamma} + \varepsilon \tag{1}$$
$$\varepsilon \sim \mathrm{N}(0,\ \Sigma)$$

The measurement noise is represented by ε which is assumed to be Gaussian with zero mean and covariance matrix Σ. In the visual field the features are measured in degrees of the visual field (Engel et al., 1994) while in the auditory domain the features could represent (logarithmically spaced) frequency bands measured in Hertz (Moerel et al., 2015). The parameter α (usually referred to as pRF gain) adjusts the predicted and observed responses to the same scale. The exponent γ introduces a non-linear relationship between the response and the voxel's pRF allowing to model compressive summation in the visual field (Kay et al., 2013). The simultaneous estimation of the exponent and the pRF size is hampered by their interaction on the cost function and, for this reason, it is common practice to assume a fixed value for γ (Thomas et al., 2015; Benson et al., 2018). In all subsequent analyses we will use a value of $\gamma = 1$ unless otherwise stated. Commonly, the shape of the receptive field is assumed to be an isotropic Gaussian $w(r|\mu, \sigma)$, which is a function of two parameters, the pRF mean μ and the pRF size (standard deviation σ).

$$w_i = e^{-\frac{(r_i-\mu)^T(r_i-\mu)}{2\sigma^2}} \tag{2}$$

In the visual domain, this function describes the response of a voxel to a stimulus presented at position r_i in the feature space (Dumoulin and Wandell, 2008). In the auditory domain r typically refer to spectral characteristics of the sounds. Note that in Eq. 2 the pRF is described by a multidimensional Gaussian (r and μ are vectors) whereas the intensity of the response at a particular location is a scalar value resulting from the multiplication between the matrix X and the vector w.

Real Data

The HCP Dataset

The retinotopy data from the Young Adult Human Connectome Project (HCP) contains pre-processed fMRI data from 181 subjects acquired at 7T with isotropic voxels of 1.6 mm. The dataset and the codes for retinotopic analysis are available from[1] and[2] respectively. In this dataset, after preprocessing, the voxel size was resampled to 2 mm isotropic and projected on the cortical surface. The experimental design consisted of six fMRI runs of 300 s each acquired with a TR of one second, in which visual stimuli (bars) where presented traveling smoothly across the visual field. To evaluate the reliability of the pRF parameter estimates we have split each of the runs in two halves (150 fMRI volumes each). Following a previous report (Benson et al., 2018), we analyzed the data coming from four regions of interest in visual cortex defined as posterior (V1-V3), dorsal (V3A/B, IPS0-5), lateral (LO-1/2, TO-1/2), and ventral (VO-1/2, PHC-1/2), with a total of 5012 voxels in each subject. A detailed description of the experiment can be found in Benson et al. (2018). Due to its large number of subjects and the standardization of the preprocessing pipeline this dataset is an excellent benchmark sample for a wide range of applications, including the validation of pRF methods.

Natural Sounds Experiment

Subjects with no history of neurological disease took part in the experiment and gave informed consent before commencement of the measurements. The Ethical Committee of the Faculty for Psychology and Neuroscience at Maastricht University granted approval for the study. Magnetic resonance imaging data were acquired on an actively shielded MAGNETOM 7T whole body system driven by a Siemens console at Scannexus https://scannexus.nl/. Functional (T2* weighted) data (1.1 mm isotropic) were acquired using a clustered Echo Planar Imaging (EPI) technique. The experiments were designed according to a fast event-related scheme. A total of 168 natural sounds were presented six times across 24 runs in silent gaps in between volume acquisitions using magnetic compatible earbuds (Sensimetrics inc.). The 168 sounds were divided into four training and testing sets (126 and 42 sounds respectively) without overlapping sounds between the training and test set. For more details on the acquisition and stimulation paradigm we refer to (Sitek et al., 2019). We analyzed data in the original volume space (without projection on the cortical surface) confined to an anatomical mask covering the auditory cortex (Heschl's gyrus,

[1] https://db.humanconnectome.org/app/action/DownloadPackagesAction
[2] https://osf.io/bw9ec/

planum temporale and planum polare) bilaterally. We estimated pRFs from the voxels' beta time series (i.e., the estimated response to all individual natural sounds in the experiment). Beta series estimation followed the procedure detailed in Sitek et al. (2019), the codes are publicly available at https://github.com/sitek/subcortical-auditory-atlas. Only voxels that belonged to the top 10% of the distribution of F-values estimated on the training data were submitted to the pRF analysis. On average this selection criterion produced a set of 20000 voxels in the sample of 10 subjects. Note this number is approximately five times larger than the number of voxels that were submitted to the pRF analysis in the visual dataset example. The unprocessed fMRI time series for the 10 subjects can be downloaded from https://openneuro.org/datasets/ds001942/versions/1.2.0. To estimate a Gaussian pRF in the sound frequency space, natural sounds were analyzed in order to extract the norm (energy) of the Fourier transform at 2048 logarithmically scale frequency partitions from 180 Hz to 7040 Hz.

Simulations

We used simulations to compare pRF estimation procedures. The first simulation corresponds to a one dimensional pRF characterizing the preference to sound frequencies that can be estimated in auditory fMRI experiments. We used this simulation to introduce the optimization landscape typical of pRF modeling. The second simulation considers the case of a two dimensional pRF representing the retinotopic preference that can be estimated from visual fMRI experiments. We used this simulation both for introducing issues relating to the optimization of the pRF paramters as well as for a comparison between estimation approaches.

To introduce the optimization landscape and provide a simple graphical representation, we started with simulating a one-dimensional pRF, modeling the response of a voxel to 240 equally spaced tones between 88–8000 Hz presented randomly in one single fMRI run. This simulation followed the experimental design adopted by Thomas et al. (2015), in which one fMRI run contains 260 volumes (TR = 2000 ms). We simulated the response elicited by a pRF with mean and size defined by [$\mu_0 = 120$ (4.04 KHz), $\sigma_0 = 16.2$ (534 Hz)] and a scaling parameter of $\alpha = 1$. To the simulated fMRI response (obtained following Eq. 1) we added realistic fMRI noise generated with a first order autoregressive processes with an autoregressive coefficient of 0.36 (implemented using the Matlab function arima.m) (Worsley and Friston, 1995). The standard deviation of the noise defines the SNR, and it affects the maximum performance that a model can attain in predicting fMRI responses. In reporting the results of our simulations we quantified the noise level by computing the split-half noise ceiling (SHnc) between two signals generated under the same simulation framework (Lage-Castellanos et al., 2019). We used the SHnc as to quantify signal to noise ratio as it relates to the reproducibility of the data and is an estimator of the maximum prediction accuracy that a pRF model can attain given the noise in the data. As we have previously shown this is a robust estimate that does not rely on specific assumptions with respect to the noise structure (Lage-Castellanos et al., 2019). We used this simulated data to analyze the effect of the noise on the estimation of the pRF parameters in two representative scenarios with high and low noise ceiling (i.e., SHnc values of 0.63 and 0.11 respectively).

In a second set of simulations, we considered a two-dimensional pRF, modeling the responses of a voxel in visual cortex to retinotopic mapping stimuli. We followed the experimental design of the retinotopic experiment of Human Connectome Project (see e.g., Benson et al., 2018). We simulated the response of two voxels with different pRFs (eccentricity: 1.79°; angle: 0.59 radians, 33.8°), one narrow and one broad (size: 0.23° and 1.81°, respectively). In **Figure 1** we present the values of the simulated pRF parameters in the second simulated dataset in the context of the pRF parameters estimated from the HCP data. To evaluate the effect of SNR we considered three scenarios with different noise ceilings: high (0.6 SHnc), medium (0.35 SHnc), and low (0.1 SHnc). These noise levels match the distribution of the SHnc in the real data used in this article (see **Supplementary Figure S1**). In order to evaluate the bias and variance of the estimated pRF parameters by different procedures, the second set of simulations was repeated 1000 times.

pRF Model Estimation

To estimate the pRF, most applications use as cost function either the sum of squared error (C_{SSE}) or one minus the correlation (C_{1-corr}). In the case of a linear model (i.e., $\gamma = 1$), these cost functions are defined as:

$$C_{SSE} = \left(y - \alpha X w\left(\mu, \sigma\right)\right)^{\mathrm{T}} \left(y - \alpha X w\left(\mu, \sigma\right)\right) \tag{3}$$

$$C_{1-corr} = 1 - \frac{y^{\mathrm{T}} X w(\mu,\sigma)}{\sqrt{w^T X^T X w}}$$

$$\alpha^*, \mu^*, \sigma^{2*} = \mathrm{argmin}^2_{\alpha,\mu,\sigma}\, C\left(\alpha, \mu, \sigma^2\right)$$

Here, without loss of generality, we assumed y and the columns of $\mathbf{X}$ to have zero mean, which makes the definition of C_{1-corr} simpler and have omitted the variance of y in the definition of C_{1-corr} since it is not a function of the pRF parameters and only acts as a scaling parameter for the cost function of each voxel. If the variance of y is not unitary the value of C_{1-corr} is a linear function of one minus the correlation coefficient and is not bounded in the interval [0 2]. Note that the minimum of the cost function is invariant to this linear transformation.

In the original (Dumoulin and Wandell, 2008) procedure, the pRF parameters(μ, σ) are optimized in a two-step approach using C_{SSE} as a cost function. The scaling factor (α) was linearly solved to account for the unknown units of the fMRI signal. For $\alpha = \left(w^T X^T X\, w\right)^{-\frac{1}{2}}$ both cost functions C_{SSE} and C_{1-corr} are equivalent (see **Supplementary Material 1.1**), but not equivalent to the original procedure in which α is used to adjust the scale of y (Dumoulin and Wandell, 2008). Note that for C_{1-corr} the scale of y is not relevant. Trying to optimize μ, σ and α at the same time increases the number of local extrema since varying either α or σ have similar effect on the cost function, and results in imprecise estimations for α and/or σ (Zeidman et al., 2018). Finally, minimizing C_{1-corr} is equivalent to maximizing the

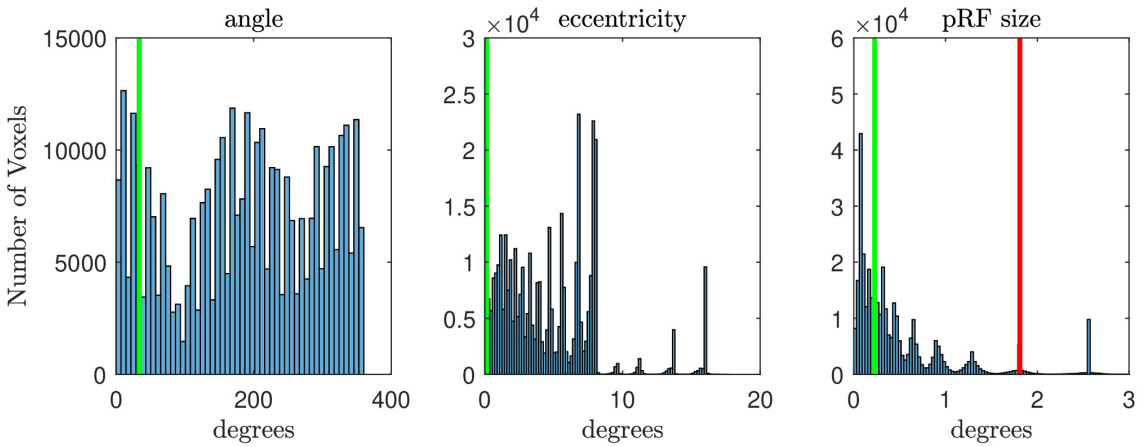

FIGURE 1 | Distribution of the estimated pRF parameters (angle, eccentricity and pRF size) from the retinotopy experiment of the HCP database (Benson et al., 2018). The vertical lines denote the values of the parameters of the pRF used in the second simulation. In the extreme right the green and the red lines denote the pRF sizes used for simulating the narrow and the broad pRFs respectively.

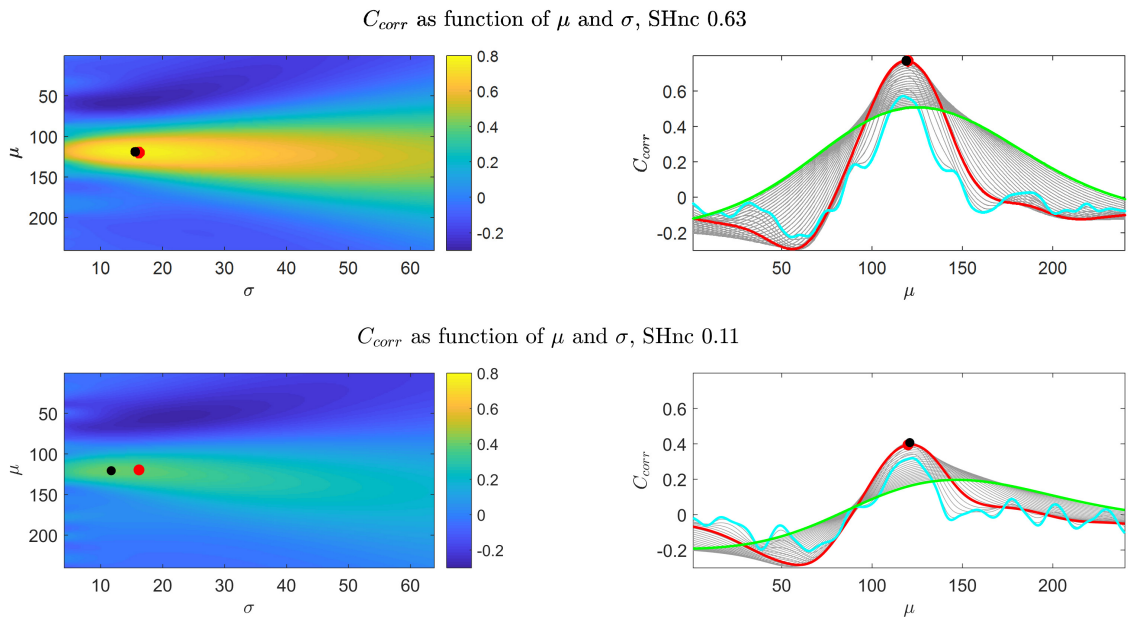

FIGURE 2 | Results obtained from the simulations of the one dimensional pRF characterizing the preference to sound frequencies (i.e., auditory fMRI data). Upper and bottom **left panels** show C_{corr} as a function of μ and σ for high and low SHnc respectively. The **right panels** show the corresponding profiles with respect to μ, while the different (gray) curves are obtained with different σ values. The values of C_{corr} as a function of μ for the broadest and narrowest possible pRFs are displayed in green and cyan respectively. The values of C_{corr} as a function of μ for the pRF that generated the data are depicted in red. Red dots and black dots denote the μ, σ used to generate the data and the global minimum respectively. In the high SHnc scenario the generative pRF (red) and the global minimum (black) are in the same location in the (μ, σ) space (the dots are superimposed).

correlation coefficient between the predicted and observed data (C_{corr}) and in this manuscript when presenting the results of our analyses we will use C_{corr}.

Figure 2 (left panels) shows for the first simulation (auditory data experimental design) the value of the cost function (C_{corr}) for every possible combination of the pRF mean (μ - scalar for the one dimensional Gaussian simulation) and size (σ) obtained with high (top) and low (bottom) noise ceiling. The right panels of **Figure 2** show the dependence of the cost function C_{corr} on μ, with different curves corresponding to different σ values (depicted in gray). The results for C_{SSE} are presented in the **Supplementary Figure S2**. Both when using the correlation or

the residual sum of squares, the cost function varies little along the σ axis in comparison to the μ axis (note the left panels of **Figure 2** and **Supplementary Figure S2**), and, as a result, is more sensitive to variations in the pRF mean than in the pRF size. An interesting observation can be made when comparing the right panels of **Figure 2** and **Supplementary Figure S2**. When considering the behavior across a large range of possible pRF means, the C_{corr} of narrow models (cyan line) is generally worse than the one of broad models (i.e., the cyan line is above the green one and C_{corr} is better when is higher). This behavior is opposite for C_{SSE}. Importantly, around the optimal pRF mean narrow and broad models result in a similar behavior when using both C_{corr} and C_{SSE}. In what follows for simplicity we will present results obtained using the correlation as cost function, but the conclusions we take apply to the use of the sum of square errors given that both cost functions present the same behavior with respect to changes in the pRF size. In **Supplementary Figure S3** we present the ratio between the derivatives of the cost function (C_{corr}) with respect to μ and σ for two different noise levels as it allows to visualize the regions of the optimization landscape in which either of the parameters (the pRF mean or size) have more influence on the cost function. The formulas for the derivatives with respect to μ and σ are presented in the **Supplementary Material 1.2**. It is important to note that, in low noise ceiling conditions (bottom in **Figure 2** and **Supplementary Figure S2**), the global minimum of the cost function shifts away from the true pRF mean and sigma and local extrema emerge compromising the convergence of pRF estimation. The number of local extrema (with respect to μ) increases with decreasing values of σ (narrowest pRF, cyan curve in the bottom right panel of **Figure 2**). In **Supplementary Material 1.3** we show that when $\sigma \rightarrow 0$ the derivative of the cost function tends to zero. That is, for $\sigma \rightarrow 0$ the cost function corresponds to either a local minimum or a local maximum. As a result the minimization of the cost function in noisy voxels may be biased toward narrow pRFs, and to the limit the pRFs can result in selecting a single feature in the stimulus space. In particular high frequency noise with sharp spikes can bias the estimation in the direction of narrow pRFs as the prediction of a pRF selecting a single feature in stimulus space result in a prediction with sharp peaks (every time this feature is stimulated).

For gradient-based optimization methods, whether the algorithm asymptotically approaches the global minimum as the iterations proceed (i.e., convergence) crucially depends on the initial conditions. In **Figure 3** we show the distance (measured as squared Euclidean norm) between simulated pRF parameter values (μ and σ defined by the red dot in correspondence with **Figure 2**, auditory data) and the estimates obtained from the Levenberg-Marquardt algorithm (LMA) as a function of the initial conditions averaged over 30 realizations of the noise (high and low SHnc in left and right panels of **Figure 3** respectively). We used here C_{corr} as cost function and the Levenberg-Marquardt algorithm for optimization. The pRF size was constrained to be a positive number. The same results were obtained when the estimation was carried on using gradient-descend (data not shown). The turquoise (pink) region indicates for which initial conditions the estimation procedure converges to the global minimum. In line with the results reported in **Figure 2** indicating that the number of local minima depends on the pRF size, the region of convergence narrows as σ decreases. This renders the choice of a large sigma as initial condition safe irrespective of the true size of the receptive field. Typically, initial conditions for pRF parameter estimation are obtained from grid-search. In our simulation the initial conditions obtained from grid-search (black dots in **Figure 3**) are always falling within the region of convergence for the subsequent LMA optimization even at the highest level of simulated noise.

We tested the insights on the behavior of the optimization method gathered on simulated data on real fMRI data. **Figure 4** displays C_{corr} for different values of μ [defined by (x, y)] and σ from a voxel in the HCP dataset. Note that, consistently with the simulations presented in **Figure 2**, the cost function varies mainly with respect to μ (for a fixed value of σ ; i.e., within each plot) while the variability between plots (i.e., for different σ) is smaller. **Figure 5** presents the variation of C_{corr} with respect to σ for the optimal pRF position (μ) for the two independent data splits in real fMRI data (same voxel from the HCP data set presented in **Figure 4**). For a range of σ between [0 – 2.5] the cost function is constrained in the small interval of [0.63 – 0.65] and [0.59 – 0.61] (correlation coefficient) for the first and second splits respectively. The global optimum occurs at locations $\sigma_1 = 1.81$ and $\sigma_2 = 1.28$ that is a change in width of the pRF across the two splits of 1.4 times. The corresponding estimated pRFs are displayed in the right panels of **Figure 5**. The ratio between σ_1 and σ_2 for all voxels in the visual cortex (subject code 100610) is presented in the **Supplementary Figure S4**.

These analyses in both simulated and real data illustrate the low sensitivity of the cost function (both the correlation and the residual sum of squares) to variations in σ resulting in the large variability in the estimated pRF size that has been previously reported. We show that this problem is amplified by the noise in the fMRI data and that the variability in the estimate of the pRF size is contrasted by the relative robustness of the estimate of the pRF mean.

pRF Estimation Methods

In this section we briefly describe the algorithmic principles used by different pRF estimation methods. Note that different software implementations of the same algorithm are available and they may differ in computational efficiency, number of hyperparameters and programming language. For an exhaustive comparison between software tools for estimating the pRF see (Lerma-Usabiaga et al., 2020).

Two-Steps Optimization [GridSearch-Gradient Based] (HCP7pRF)

Here we used the implementation of the method presented in Benson et al. (2018) which is available at https://osf.io/bw9ec/. Following the approach of Dumoulin and Wandell (2008) this method estimates the pRFs in two-steps. A grid-search is used for selecting initial values for the pRF parameters for subsequent non-linear optimization. The grid search optimization uses the correlation coefficient as the cost function. The initial conditions are selected within a dictionary

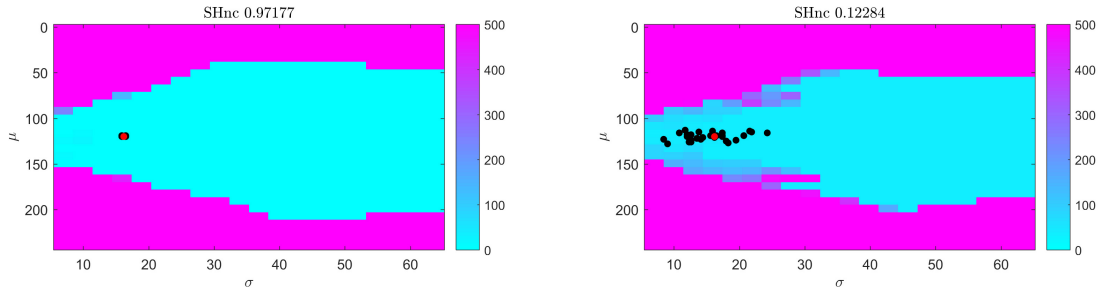

FIGURE 3 | Results of the convergence of the optimization of a one simulated dimensional pRF characterizing the preference to sound frequencies (i.e., auditory fMRI data; high **(left)** and low **(right)** split-half noise ceiling). Colors indicate the distance (squared Euclidean norm) between true parameter values (red dot) and the solution obtained from starting Levenberg-Marquardt optimization at each location in parameter space. Distance values are averaged over 30 realizations. Black dots indicate the initial conditions (for pRF estimation using LMA) estimated from grid-search. In particular a cyan color indicates the starting values for pRF mean and size that resulted in the Levenberg-Marquardt algorithm to converge to the simulated value.

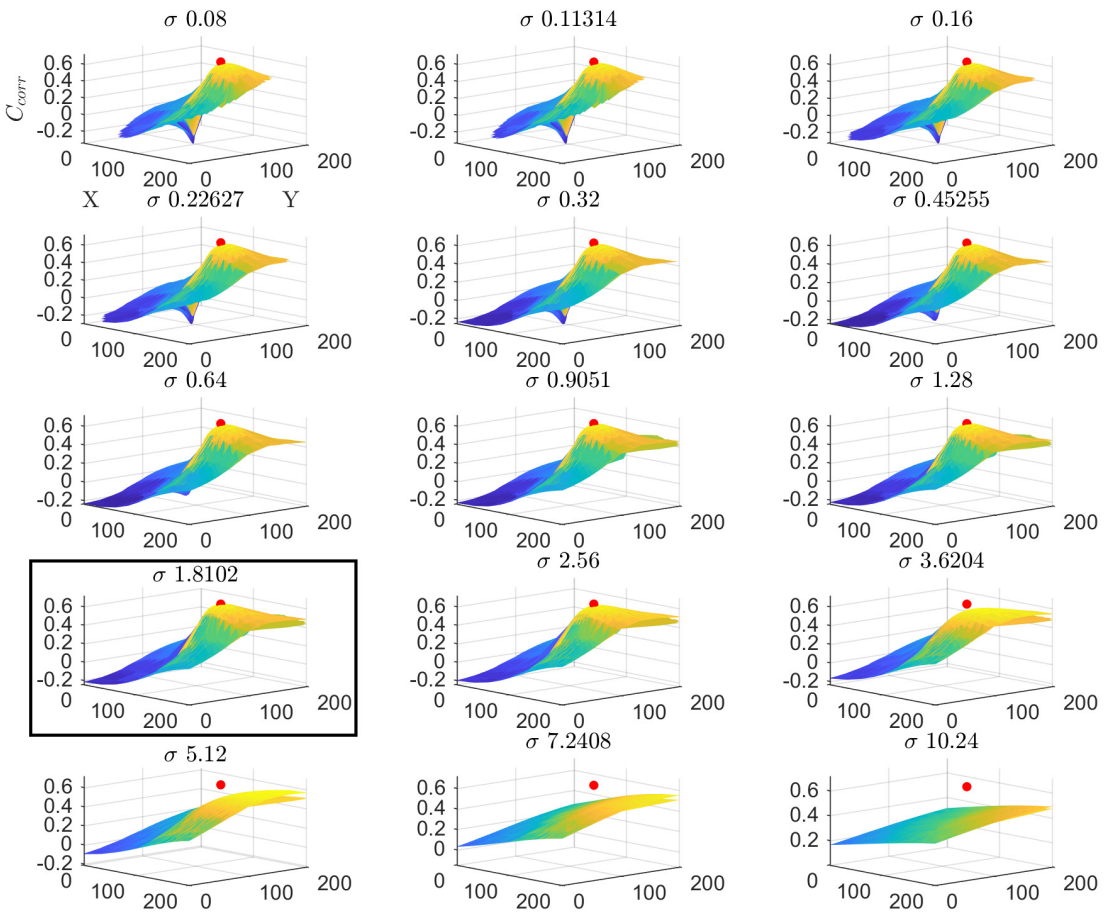

FIGURE 4 | Cost function (C_{corr}) in the space of the pRF paramters (x, y, σ) for a voxel from the HCP dataset in the first split of the data (subject code 100610, first split, voxel index 5). The location of the global maximum is represented by a red dot and is obtained σ = 1.81. Each subplot represents the cost function at varying values of μ (defined by (x, y)) while the different subplots are obtained varying the value of the pRF size (σ). For visualization clarity in this figure we used cartesian coordinates instead of eccentricity and angle.

of plausible pRFs. In this dictionary the angles of all possible pRFs are uniformly distributed between [0° and 360°]. On the other hand, eccentricity and pRF size are characterized by non-uniform distributions with the density of pRFs decreasing with eccentricity and more seeds characterized by a small σ (i.e., narrow pRF). The scaling parameter α is computed using linear regression between the observed and predicted fMRI time series (the latter obtained after selecting the best seed with grid search

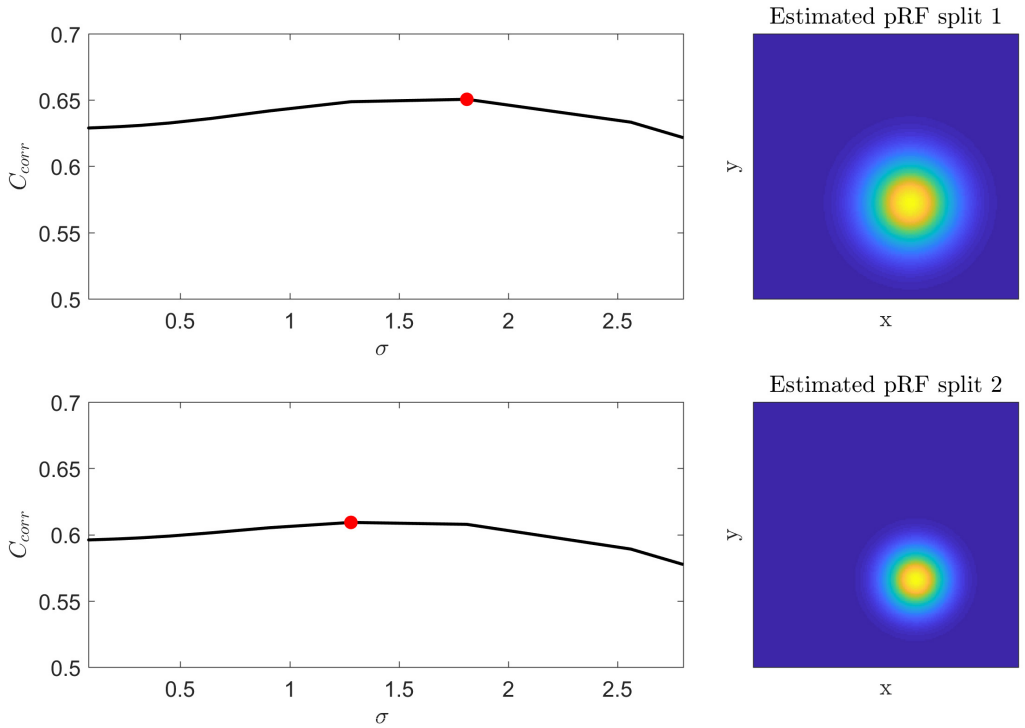

FIGURE 5 | Left: Cost function (correlation coefficient) as a function of the pRF size (σ) for the two splits of a voxel in the HCP dataset. The cost function was computed by fixing the voxel's pRF mean (x, y) to the value of the best fit model that corresponds to the global maximum (red dot in the figure). **Right:** The corresponding estimated pRFs for each split.

optimization). The pRF parameters obtained in the first pass (using grid search) are then submitted to a second non-linear optimization pass using the Levenberg-Marquardt algorithm implemented by the Matlab function lsqcurvefit. This second optimization pass uses the C_{SSE} as the cost function. In this approach, the observed voxel's fMRI time series is standardized to have zero mean and unitary variance. The non-linear optimizer also allows for the eventual optimization of the compressive non-linearity (γ) (Kay et al., 2013). Here, we used default setting for all functions in this toolbox.

Two-Steps Optimization [GridSearch-Gradient Based] for Auditory Data (GS + Gb)

A two-steps optimization approach has also been developed to estimate auditory pRFs (Thomas et al., 2015). Here when analyzing auditory fMRI (or the simulated auditory responses) we used this approach whose implementation is available at https://github.com/kellychang4/pRF. This approach, firsts uses grid-search to obtain an estimate of the initial conditions to be refined in a second step. The dictionary used in the grid-search considers pRFs with logarithmically spaced (tonotopic) preferences (i.e., the mean of the pRFs) between 180 Hz and 7040 Hz, while the pRF size varies linearly from 10 to 100 in full width at half-maximum (FWHM) of the logarithmic spaced bins. After the grid-search, the estimation of the model is refined using the Nelder-Mead algorithm (Lagarias et al., 1998 implemented by the fminsearch Matlab function) which is a direct search method and does not rely on the gradient of the cost function. It is important to note that in this procedure both the grid search and the finer optimization step are carried on using C_{corr} as the cost function (which is a difference with respect to the two-step procedure outlined above for the analysis of visual data which uses C_{SSE} in the second optimization step).

Grid-Search (GS)

Grid-search automatically imposes a form of regularization on the models avoiding the optimization to converge into to the subset of the local minima not included in the grid. For this reason, we included here the estimation of pRF using only grid-search and used, for the auditory and visual data, the grid-search module from the HCP7pRF procedure. The regularization is given by the coarseness of the grid. A coarse grid will reduce the variability of the estimated pRF while paying the cost of introducing an estimation bias. A very fine grid will produce unbiased estimates however increasing the risk of landing in local minima. Consistently with the implementation of grids search available in the two-step optimization procedures for both visual and auditory data (see above) we used C_{corr} as the cost function.

Convex pRF Estimation (COpRF)

We used the implementation available at https://github.com/davesl/COpRF. The algorithm estimates the voxel's pRF as a linear combination of the pRF seeds available in a large pRF dictionary using LASSO regression (Bishop, 2006). The Lasso

regression minimizes C_{SSE} where the voxel's fMRI time series and the pRF dictionary have been standardized to have zero mean and unitary norm. As Lasso imposes sparsity on the regression coefficients only a small subset of the pRF dictionary will be selected for obtaining the voxel's pRF. Interestingly, two consecutive regressions are performed using different dictionary sizes. The first regression uses a reduced dictionary of around 3000 seeds. Then the seeds from the large dictionary that are contained within a radius from the center of the pRF estimated in the first pass are submitted into the second regression. It is important to note that estimated pRF parameters for the voxel's pRF are derived by the weighted sum of the pRF parameters of the selected seeds using the LASSO coefficients. Here we used the default values in the toolbox for the search radius and the LASSO regularization parameter.

Linearized Encoding (LinEnc)

We used the implementation available at: https://sites.google.com/site/leesangkyun/prf/codes.zip, (Lee et al., 2013). Linearized encoding models do not assume a specific shape for the pRF, instead using the General Linear Model (GLM) the (linear) contribution of each model feature to the fMRI time series (or Beta series) is estimated using ridge regression (Bishop, 2006) which uses C_{SSE} on the space of the original variables (untransformed). Regularization is required as the number of model features (e.g., points in the visual field, or frequencies of a sound) is often larger than the number of time points in the fMRI time series (or the number of stimuli that define the length of the Beta series). In the original settings of this toolbox the voxel's pRF is estimated only if the explained variance is larger than 0.3 after ridge regression. Here, to compare all methods under the same conditions, we performed the estimation for all voxels. For the estimation of visual pRFs we down sampled the visual stimuli to a square of 101×101 pixels. We used the default parameters of the toolbox (i.e., the grid of regularization parameters (λ) to be used in the ridge regression). To estimate a preferred feature and the size of the pRF, in a second step a Gaussian function is fit (using the Matlab function lsqcurvefit) to the estimated linear coefficients after imposing a threshold for discarding noisy coefficients. We used the default setting for this second step by considering three different thresholds (0.3, 0.5, and 0.7; relative to the value of maximum coefficient) and selecting the Gaussian model that explained the highest amount of variance of the linear coefficients obtained from the first step.

Modifications to the Grid Search Procedure

In this section we describe the two variants of the grid search algorithm. We propose these modifications with the purpose of increasing the reliability of the estimate of the pRF size. The first approach combines the pRF models in the search space that result in similar goodness of fit to the data. The second modifies the criterion for selecting the best pRF model. In particular, instead of selecting the pRF model that maximizes the correlation to the observed data, we select the model with minimum probability of being obtained under the null hypothesis of no relationship between the observed and predicted responses.

Averaging pRF Models Explored With Grid-Search (ModelAve)

To reduce the variability of the pRF estimates, we propose to average pRFs models obtained from a grid-search and that have similar goodness of fit using C_{corr} as the cost function. We used the grid-search module of the two-step optimization procedure. However, instead of selecting the pRF model that produces the maximum correlation with the observed response (as in the grid-search procedure described above), we propose to consider all pRFs models within a range of 1% of the goodness of fit of the best model. The voxel's pRF can then be obtained as the average of the pRF models in this interval. Note that the average is performed in the pRF space instead of the parameters space (as done by the COpRF procedure). Despite the resulting averaged pRF not being necessarily a Gaussian function, to estimate pRF parameters (μ and σ) we fitted a Gaussian to the averaged pRF. This approach can be used both on the original fMRI time series (for experimental designs such as the traveling bars in the visual field that do not allow the estimation of single stimuli) as well as on Beta time series. Here we used this approach to analyze both visual and auditory fMRI data.

Permutation Based Model Grid-Search for Separable Betas Design (PermGS)

This procedure can only be implemented when the Beta responses are exchangeable under the null hypothesis. The experimental design of the retinotopy HCP dataset consists of visual stimuli that smoothly travels across the visual field. This experimental design prevents the estimation of separate betas associated with each stimulus and, as a consequence, the permutation procedure cannot be used. For this reason, here we used this method only when analyzing the auditory data. The distribution of local minima in the optimization space that we have highlighted in simulations (**Figures 2–4**) results in a large probability for the best model to be characterized by small σ just by chance. Such probability can be estimated by empirically determining the null distribution of the cost function (C_{corr}) for every possible combination of pRF mean and size using permutations. The permutation procedure consists in randomizing the response vector (here the beta series estimated from the fMRI time series as the response to all the stimuli) while keeping the pRF model fixed. By defining the empirical null distribution we selected, for every voxel, the pRF model (i.e., selecting the pRF mean and size) with the smallest probability of occurring by chance.

Statistical Analysis

The results obtained on simulated data were statistically assessed using bootstrapping in order to evaluate the bias of the pRF estimates as well as for comparing the variance of the estimates across methods. In particular, the distributions of pRF parameters (angle, eccentricity and size in the case of the simulated visual data) obtained from the 1000 simulations were bootstrapped 10000 times (i.e., we derived 10000 bootstrap samples each one representing the distribution of a given pRF parameter over 1000 simulations). To statistically evaluate the bias in the estimated parameters we computed the $\alpha = 0.05$ (two tailed)

confidence intervals of the mean of each bootstrap sample. The bootstrapping procedure for the pRF was implemented using R and a package (circular) allowing to account for circular data[3]. When the value of the pRF parameter used for simulating the data (e.g., the simulated parameter) fell outside the confidence intervals we concluded that the method is biased and estimated the bias as the distance between the simulated parameter and the mean across all bootstrap samples. When a significant bias was observed, we reported the effect in terms of the original units (e.g., degrees of the visual field). To compare the variability of the estimates (for each pRF parameter), we computed the ratio of the variance between bootstrap samples (paired) obtained using different approaches. This results in 10000 values of the ratio between two methods. Estimating the $\alpha = 0.05$ confidence interval of this distribution allowed us to evaluate if there were significant differences between methods (i.e., when the value 1 indicating identical variability between two methods was not included within the confidence interval).

The statistical analyses of the estimates obtained on the HCP dataset were performed using bootstrapping. In particular, we bootstrapped 10000 times the 181 values of reliability (one value per subject) obtained by correlating the estimates of each of the pRF parameters obtained across the two splits of the data. By estimating confidence intervals ($\alpha = 0.05$) for the difference between each pair of methods we determined the significance of the differences and report the effect size as the mean differences in reliability between methods. We followed a similar approach to compare prediction accuracy between methods.

For the auditory data, we tested for statistical differences (in reliability of the estimates measured as the Spearman correlation between independent estimates of the pRF parameters) using permutation tests. The empirical null distribution of the difference in reliability between each pair of methods was obtained by exchanging the values between methods. The p-values (threshold at $\alpha = 0.05$, two tailed) were computed as the cumulative probability of obtaining a reliability greater or equal (smaller or equal for the left tail) than the observed difference under the distribution of the null hypothesis.

[3]https://cran.r-project.org/web/packages/circular/circular.pdf

RESULTS

The different estimation methods use different cost functions (some the correlation and some the sum of squares). Our previous analyses showed that the sensitivity of these cost functions to variations in the pRF size (and mean) is similar (see **Figure 2** and **Supplementary Figure S2**) and in **Supplementary Material** (**Supplementary Figure S5**) we present the results on simulated data in which we changed the cost function for the Grid Search from the correlation to the sum of squares. These results show that the choice of the cost function does not influence our evaluation on the reliability of the estimates of the pRF size.

Results for Simulated Visual Data

Figures 6, **7** report the comparison between the tested pRF estimation procedures in terms of bias and variance of the estimates on the second simulated dataset (i.e., two visual pRFs, one narrow and one broad) at three levels of noise (high, medium, and low).

For a narrow pRF (**Figure 6** and **Table 1**), COpRF and ModelAve showed biased estimates of the eccentricity and the pRF size. LinEnc produced biased estimates as well, but, in particular for eccentricity and pRF size the bias was larger in effect size compared to the bias introduced by ModelAve and COpRF (at all considered noise levels). We did not detect a significance bias for HCP7pRF and grid-search. However,

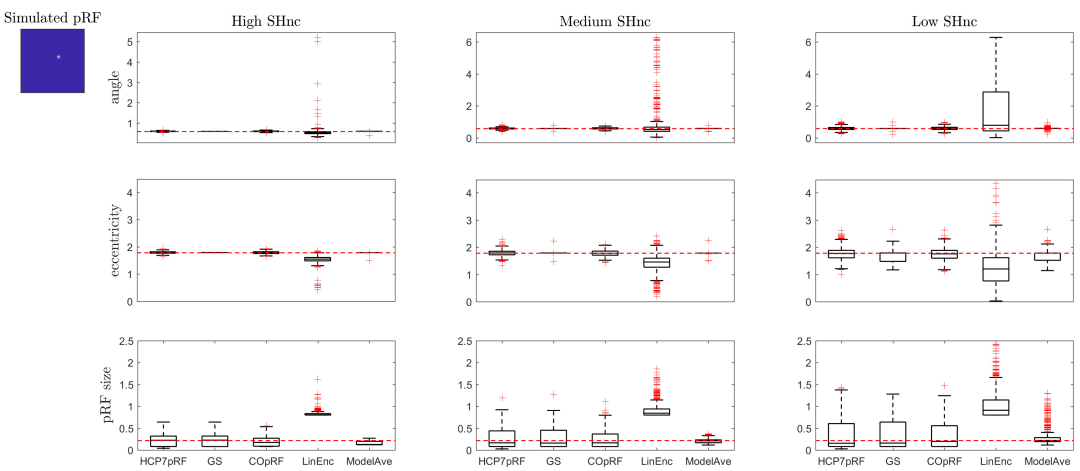

FIGURE 6 | Boxplots ([25, 50, 75] percentiles over 1000 simulated datasets) represents the estimated pRF parameters using different estimation procedures for a narrow two-dimensional pRF (presented in extreme left). Each column refers to a different split-half noise ceiling level from high to low: High SHnc = 0.63, Medium SHnc = 0.35, Low SHnc = 0.1. Each row presents the results for each of the pRF parameters: angle, eccentricity and pRF size. Outliers (in the estimated pRF parameters) are denoted by red + symbols and defined by the condition of being outside the 1.5 interquartile range. The horizontal red line indicates the pRF parameters used to simulate the data.

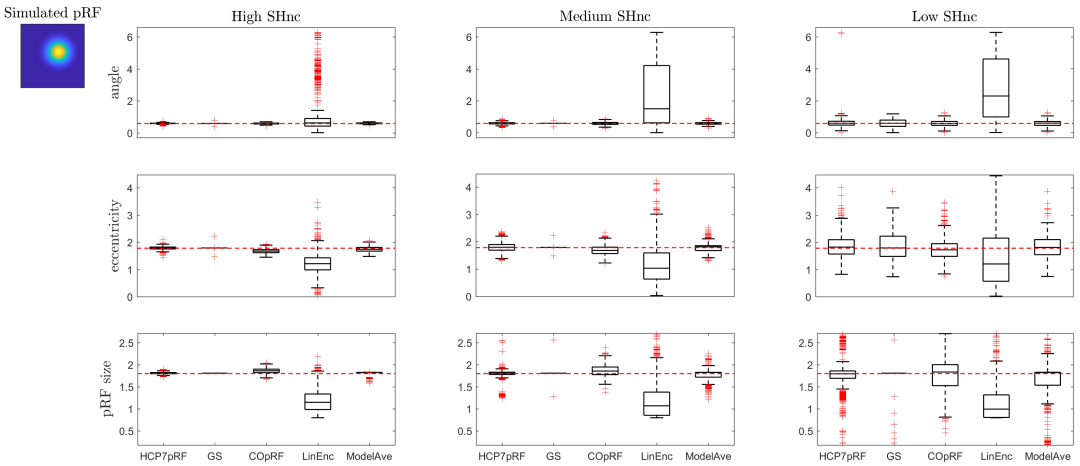

FIGURE 7 | Boxplots ([25, 50, 75] percentiles over 1000 simulated datasets) represents the estimated pRF parameters using different estimation procedures for a broad two-dimensional pRF (presented in extreme left). Each column refers to a different split-half noise ceiling level from high to low: High SHnc = 0.63, Medium SHnc = 0.35, Low SHnc = 0.1. Each row presents the results for each of the pRF parameters: angle, eccentricity and pRF size. Outliers (in the estimated pRF parameters) are denoted by red + symbols and defined by the condition of being outside the 1.5 interquartile range. The horizontal red line indicates the pRF parameters used to simulate the data.

TABLE 1 | Statistical analysis of the bias of the estimates of the angle, eccentricity and pRF size obtained when simulating a narrow visual pRF (angle = 0.59 radians, eccentricity = 1.79°, pRF size σ = 0.23°) at different noise levels.

	Low Noise			**Medium Noise**			**High Noise**		
	Angle	**Ecc.**	**Size**	**Angle**	**Ecc.**	**Size**	**Angle**	**Ecc.**	**Size**
HCP7pRF	n.s.	n.s.	n.s.	n.s.	n.s.	n.s.	n.s.	n.s.	n.s.
GS	n.s.	n.s.	n.s.	n.s.	n.s.	n.s.	n.s.	n.s.	n.s.
COpRF	n.s.	−0.007	−0.05	n.s.	−0.01	−0.06	n.s.	−0.03	n.s.
LinEnc	n.s.	−0.24	0.57	n.s.	−0.33	0.61	n.s.	−0.59	0.68
ModelAve	n.s.	−0.006	−0.09	n.s.	−0.006	−0.01	n.s.	−0.006	n.s.

For every noise level, columns represent the different parameters while rows represent the different estimation methods. For significant effects ($p < 0.05$) we report the effect size (in units of the parameter), while n.s. indicates a non-significant effect. When significant bias was observed, the corresponding cell displays the mean of the estimated parameter minus the its true value.

TABLE 2 | Pairwise comparison of the variability of the estimates of the pRF size between estimation methods at different levels of noise (narrow pRF: angle = 0.59 radians, eccentricity = 1.79°, pRF size σ = 0.23°).

	Low Noise				**Medium Noise**				**High Noise**			
	GS	***COpRF***	***LinEnc***	***ModelAve***	***GS***	***COpRF***	***LinEnc***	***ModelAve***	***GS***	***COpRF***	***LinEnc***	***ModelAve***
HCP7pRF	n.s.	1.24	5.56	9.10	n.s.	1.12	1.67	12.53	n.s.	1.13	n.s.	3.93
GS		1.24	5.61	9.16		1.12	1.68	12.62		1.14	n.s.	3.87
COpRF			4.48	7.33			1.48	11.17			n.s.	3.47
LinEnc				n.s.				7.45				3.84

Every cell displays (for significant effects) the variance of the pRF size estimated by the method in the row divided by the variance of the method in the column ($\frac{Var(\sigma)_{row}}{Var(\sigma)_{col}}$), while n.s. indicates a non-significant effect.

HCP7pRF is two orders of magnitude more computationally demanding than grid-search (see **Supplementary Table S1**). This pattern was largely confirmed when considering large pRFs (**Figure 7** and **Supplementary Table S2**). In this case, we did not detect a significance bias for grid-search (all parameters). LinEnc produced biased estimates of the eccentricity and pRF size which were larger in effect size compared to the bias introduced by ModelAve and COpRF (at all considered noise levels). We compared the variability of the estimates of the pRF between pairs of methods by statistically assessing (with bootstrapping – see section "MATERIALS AND METHODS") the ratio between the variance of the estimates. The results of this statistical analysis are reported in **Table 2** for a narrow pRF and **Supplementary Table 3** for a broad pRF. Averaging models

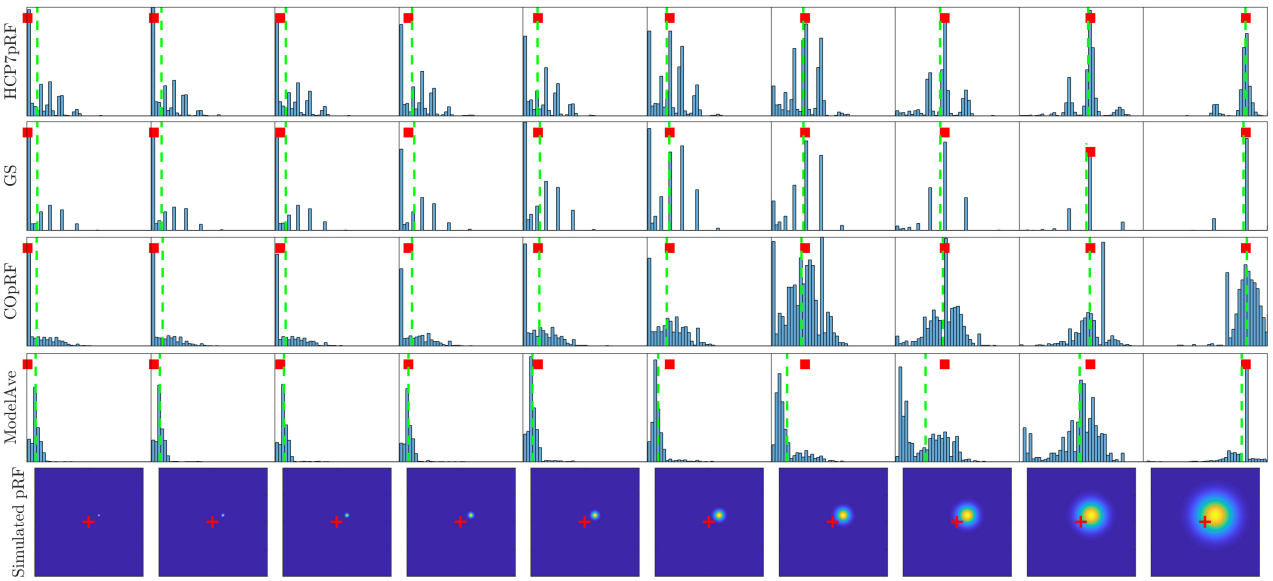

FIGURE 8 | Histograms of the estimated pRF size for HCP7pRF, GS, COpRF and ModelAve. The bottom row shows the simulated pRF (the fovea is marked in red). In all other plots, the red square denotes the pRF size value used to simulate the data (i.e., the targeted value to be estimated). The vertical green lines denote the median of the distribution of the estimated pRF size.

with similar goodness of fit (ModelAve) prior to the estimation of the pRF size resulted in a smaller variability of the estimates at all the considered noise levels for narrow pRFs (**Table 2**). When considering broad pRFs (**Supplementary Table S3**) the advantage of using model averaging with respect to the variability of the estimates was less noticeable. Note that reducing the variability of the pRF size estimates for narrow pRFs will have a large impact on the analysis of real data, as the largest proportion of voxels in visual cortex present narrow pRFs (see **Figure 1**). Linearized encoding showed the larger bias in the estimate of the pRF parameters (eccentricity and size) for all considered noise levels and this bias did not correspond to a significant gain in variance reduction when comparing its estimates to e.g., model averaging.

A more refined evaluation of the estimated pRF size for monotonically increasing simulated pRF sizes and moderate noise level (SHnc = 0.35) is presented in **Figure 8**. Each simulation was repeated 1000 times and the empirical distribution of the estimated pRF size is presented for HCP7pRF, GS, COpRF and ModelAve. The LinEnc algorithm was discarded as this method showed the largest bias and not significantly improved variability of the estimates when comparing it to model averaging (see **Tables 1**, **2** and **Supplementary Tables S2, S3**). Our results indicate that, within the range of the pRF size we considered here, combining models with similar performances (ModelAve) reduced the variance of the estimates for pRF size smaller than $\sigma = 0.91$ (see **Supplementary Table S4**). While model averaging resulted in a reduction in variance, for a large range of pRF sizes, it was also associated with an increased bias of the estimated of the pRF size as evidenced by the separation between the median (green lines in **Figure 8**) and the value of the pRF size used for simulating the data (red square).

Computational times for all tested approaches relative to GS are presented in **Supplementary Table S1** for the estimation of a narrow (visual) pRF (for a varying number of simulated voxels), and at a medium noise level (SHnc = 0.35). The results indicate that the two step optimization procedure (HCP7pRF) is the most computationally demanding approach (at least two orders of magnitude slower than GS).

Visual pRFs Estimated From the Human Connectome Dataset

We evaluated the reliability of the pRF parameter estimates obtained with each of the approaches by computing the (Spearman) correlation (across voxels) of the pRF parameters estimated in two (independent) halves of the dataset (**Figure 9**). For the eccentricity and the pRF size we used the Spearman correlation to account for non-normal distributions while for the angle we used the circular correlation coefficient (Mardia, 1975).We performed this analysis in four regions of interest within the visual system: posterior, dorsal, lateral and ventral (see Benson et al., 2018 for more details on the definition of the regions) and in 181 subjects. We chose to perform the analysis within predefined regions of interest in order to be consistent with the analyses reported in Benson et al. (2018). In **Figure 9** we report the results across the four ROIs combined. Note that, in order to compare our results to a previous analysis reported in Benson et al. (2018) we report here also the results obtained by the HCP7pRF approach using an exponent of 0.05 (HCP7pRF05). All methods except for linearized encoding showed similar reliability for the estimates of the pRF eccentricity and angle (i.e., the position in the visual field). In agreement with our simulations, the estimate of the pRF size obtained using model

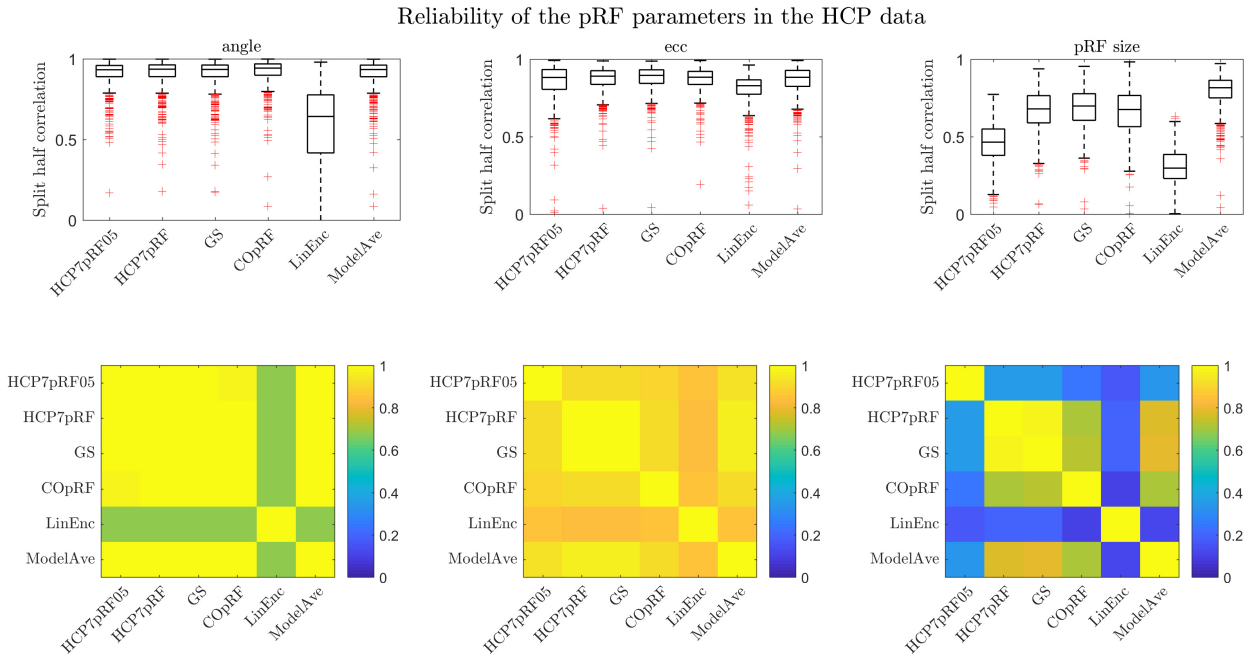

FIGURE 9 | The split-half reliability ([25, 50, 75] percentiles of the distribution across 181 subjects) for pRF parameters estimates for different methods. The correlation between the parameters estimated by the different methods (across all ROIs) is presented in the bottom row.

averaging was most reliable ($\rho^{\text{ModelAve}}_{\text{pRF size}} = 0.81$ vs $\rho^{\text{HCP7pRF}}_{\text{pRF size}} = 0.67$, mean values across the four ROIs, see **Supplementary Table S5** for the results of the statistical comparisons between methods). Note that the reliability of the estimate of the pRF size obtained with the compressive non-linearity fixed to 0.05 was significantly lower than the one obtained using a fixed value of 1 (**Supplementary Table S5**). Linearized encoding resulted in the overall lowest reliability for the estimated pRF parameters ($\rho_{\text{angle}} = 0.56$, $\rho_{\text{ecc}} = 0.83$, $\rho_{\text{pRF size}} = 0.39$, mean values across the four ROIs) and accuracy of the predictions (**Supplementary Table S5**). In terms of mean prediction accuracy all other methods performed similarly (prediction accuracy [correlation]: HCP7pRF05 = 0.37, HCP7pRF = 0.36, GS = 0.36, COpRF = 0.36, ModelAve = 0.36, LinEnc = 0.24). Note that despite the small effect size the small increase in prediction accuracy attainable when using a non-linear model (HCP7pRF05) was statistically significant (**Supplementary Table S5**).

By combining voxels across all regions of interest and averaging across all 181 subjects in the dataset, we computed the similarity (Spearman correlation) between the parameters estimated between the different methods (**Figure 9** bottom row). All methods except linearized encoding resulted in similar estimates of the angle (with correlations above 0.85). Estimates of eccentricity were similar across all methods (with the minimum correlation of 0.79 between HCP7pRF05 and linearized encoding). As expected, the pRF size showed largest variability in its estimate across methods. Note that large correlation between the pRF parameters obtained with HCP7pRF and grid-search (above 0.9 for ecc, angle and the pRF size), which is an argument in favor of using grid-search over HCP7pRF considering their large difference in computational efficiency. The estimate of the pRF size obtained by fixing the compressive non-linearity to 0.05 was the least similar to all other approaches (that instead used a fixed value of 1).

Auditory pRFs

Figure 10 shows the mean reliability (Spearman correlation between estimates obtained in two separate halves of the data) in the auditory data (10 subjects) as a function of the prediction accuracy. The pRF estimation using COpRF and LinEnc were not included in this analysis since these toolboxes were designed specifically for visual stimuli. We report reliability as a function of prediction accuracy as we hypothesize that evaluating the estimates of the model parameters should be limited to those voxels in which the model is a good descriptor of the response. As we are limiting the investigation to a simple model of sound frequency, high prediction accuracy is expected in early auditory cortical regions (Norman-Haignere and McDermott, 2018). It is relevant to note that previous studies (Santoro et al., 2014) have shown that feature spaces that are more complex than the use of only sound frequencies (e.g., the combination of frequency, spectral modulations and temporal modulations) may better describe the response in secondary cortical areas.

Our results indicate that the permutation based grid-search outperformed all other methods in terms of reliability of the estimated pRF mean and size. The statistical comparison of the reliability of the pRF mean and size across voxels whose prediction accuracy was larger than 0.2 (measured as the correlation between predicted and actual responses to the test sounds) is reported in **Supplementary Table S6** (similar results

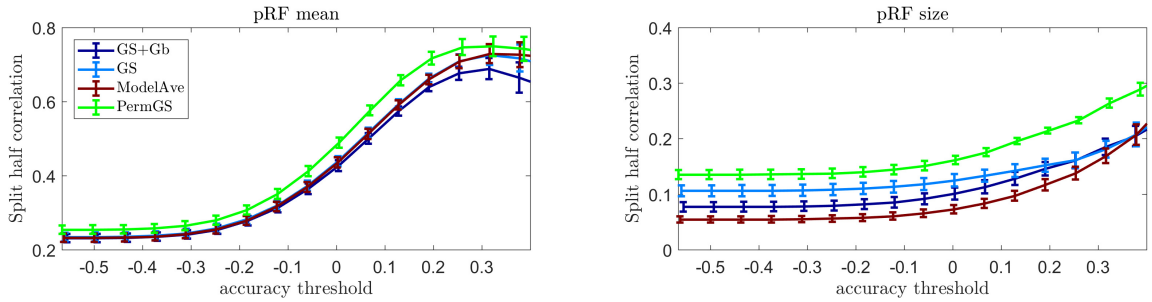

FIGURE 10 | Reliability analysis for the auditory data. The mean reliability across 10 subjects is presented as a function of the mean prediction accuracy for four pRF estimation methods for the pRF mean (left) and size (central). In the right panel display the mean prediction accuracy (across 20000 voxels), for every subject.

were obtained when testing for differences between methods considering voxels thresholded at higher value of prediction accuracy). As when analyzing the visual data, also for the auditory data the two-steps optimization procedure (GS + Gb) was more computationally demanding (requiring over 24 h compared to the few minutes of GS alone). Note that the permutation approach will be more computationally demanding than the grid search alone. In particular considering a set of 42286 voxels, the permutation based approach was 21 times more expensive than grid search.

DISCUSSION AND CONCLUSION

The use of computational approaches such as population receptive field modeling has become an established method for analyzing fMRI data (Gravel et al., 2014; Zuiderbaan et al., 2017; Dumoulin and Knapen, 2018). Despite the widespread application of this methodology, the analysis of *in vivo* data in a large sample (the Human Connectome) has highlighted low consistency in the estimate of the pRF size in comparison with the pRF mean (Benson et al., 2018). In this article we examined the influence of the optimization procedure on the variability of the pRF parameters and proposed modifications to the algorithms in order to improve the reliability of the pRF parameters in noisy scenarios. Following previous research, we considered as cost function the correlation and sum of squared errors. Both of these are strongly affected by outliers. The sensitivity to outliers of pRF estimation methods has not been considered in the literature, and in future studies it would be of interest to investigate pre-processing strategies or alternative cost functions that could limit such sensitivity.

The Gaussian model for the pRF and the cost function (correlation or minimum squared error) used to derive it define the optimization landscape. This optimization landscape, common to all estimation procedures, is at the basis of the large variability in the estimates of the pRF size that has been previously reported (Benson et al., 2018). In particular, estimates of the pRF size have higher variance because of the weaker sensitivity of the cost function to variations in the pRF size than to variations in the pRF mean. Here, we illustrate this issue using simulations (**Figures 2**, **3**) as well as theoretically (**Supplementary Material**). We performed simulations at different noise levels and quantified SNR (of simulated and real data) using the split-half noise ceiling (an estimate of the maximum prediction accuracy that a pRF model can attain given the noise in the data) which is computationally efficient and is not based on assumptions about the noise structure (Lage-Castellanos et al., 2019). Computing the SHnc only requires that the data can be split in two identical partitions for computing the correlations between the observed responses.

When considering established pRF estimation procedures, our simulations showed that some approaches produce biased estimates of the pRF parameters across the different levels of noise and independently of the pRFs size (see the statistical comparisons reported in **Table 1** as well as **Supplementary Table S2**). In particular, estimating pRFs with linearized encoding resulted in larger biases compared to all other approaches. With respect to the variability of the pRF size estimates previously reported (Benson et al., 2018), our simulations indicate that the difference in variability of the estimates between methods was more noticeable when considering narrow pRFs. For narrow pRFs, linearized approach produced more reliable estimates compared to grid search, HCP7pRF and COpRF at medium and low noise levels (**Table 2**). Taken together the analyses of the bias and variability in simulated data indicate that estimating pRFs with linearized encoding trades off bias in the pRF parameters for stability of the estimated pRF size. The weaker sensitivity of the cost function to changes in pRF size noticeable in simulated data was apparent also when estimating pRFs from real fMRI data obtained in response to visual stimulation (**Figure 4**). This weaker sensitivity resulted in different estimates of the pRF size when using independent splits of the fMRI data (**Figure 5**). Both the bias in the estimation of pRF parameters introduced by some of the approaches as well as the variability in the estimates of the pRF size may affect studies that aim at comparing the pRF size across brain regions or between experimental conditions. A bias in the estimated pRF parameters compromises accuracy and reproducibility especially in low SNR datasets (e.g., using high spatial resolution), while the increased variance of the estimates of the pRF size compromises statistical power. These issues highlight the relevance of controlling for the SNR in the data. Previous approaches have used a combination of heuristics to this end, ranging from smoothing the fMRI data to increase

SNR (Dumoulin and Wandell, 2008) as well as considering only voxels (or regions) in which the pRF model explains a sufficient amount of variance in the signal (Dumoulin and Wandell, 2008; Thomas et al., 2015). In addition, constraints have been introduced allowing only pRFs broader than a certain value (Thomas et al., 2015; Zeidman et al., 2018). Interestingly, our results show that initiating the search for the pRF from regions of the parameter landscape with broad pRF may help obtain unbiased estimates (see e.g., **Figure 3** where we show that the region of convergence for the optimization procedure is larger when the initial pRF size is set to larger values). When algorithms other than a simple grid-search are used, initial conditions for the optimization of pRF parameter are typically obtained from an initial grid-search. While in our simulations this resulted to be an effective strategy even in the case of low SNR, the development of an optimization strategy that moves specifically from broad to narrow pRFs could represent an interesting alternative for low SNR data (e.g., high resolution functional data) that to our knowledge has not been explored yet. It is important to note that here we used default hyperparameters values when using previously introduced estimation approaches (e.g., the regularization parameters in the ridge regression of the linearized encoding approach was fixed for all voxels to a value of equal to one). Fine-tuning hyperparameters may result in improved reliability of the estimated pRF parameters, but it is a data set specific problem that could be addressed in follow up studies. One interesting observation that derives from the results of our simulations is that performing a second optimization step (e.g., using Levenberg-Marquardt as in the implementation of the pRF method Benson et al., 2018) did not improve the reliability of the estimated parameters compared to grid-search (see **Table 2** and **Supplementary Table S3**). This is particularly relevant considering the higher computational efficiency of grid-search compared to the rest of the algorithms (see **Supplementary Table S1**). We considered computational time for the estimation of the pRF of voxels with a medium level of noise (SHnc = 0.35). We expect this time to increase for all approaches except grid search when the noise in the data increases. It is plausible to assume that the absence of an improvement in the reliability of the estimates obtained with a second optimization step is caused by the effect of noise on the optimization routine resulting in non-replicable estimates. It is important to note that the computational complexity of grid-search increases rapidly with the number of pRF parameters to be estimated. In this article the number of parameters were limited to the pRF mean and size (e.g., the inclusion of the non-linearity term or the increase in dimensionality of the pRF mean).

With the aim of reducing the variability of the estimated pRF size in noisy scenarios here we introduced two specific modifications of the grid-search algorithm. It is important to note that, while these approaches improved the reliability of the pRF size estimates in simulated and real data, they do not constitute a principled solution to the low sensitivity of the cost function to the pRF size (as they are still based on the use of the same cost function). The first approach averages pRF models (obtained from grid-search) that result in similar goodness of fit to the data. This procedure can be interpreted as a Bayesian Model Average under a uniform prior. Here, we averaged models whose goodness of fit was within an interval of 1% of the minimum. The threshold of goodness of fit defining this interval has direct influence on the bias-variance tradeoff of the Model Average approach. Averaging more models will decrease the variance of the estimates but at the cost of increased bias. In addition, this hyperparameter should be carefully set depending on data quality. Noisier fMRI data will require averaging more models (i.e., considering a larger interval of goodness of fit) to achieve similar reductions of the variance of the estimates. How to calibrate this threshold conditioned to the noise in the data should be considered in the future. For narrow PRFs, model averaging resulted in improved reliability of the estimate of the pRF size compared to the previously introduced approaches we tested (**Table 2**). This improved reliability came at the cost of a small but significant bias in the estimate of the pRF parameters (**Figure 8**, **Table 1** and **Supplementary Table S2**). A more systematic analysis of the reliability of the PRF size estimate in dependence with the pRF size indicated that using model averaging is advantageous when the pRF size generating the data is smaller than $\sigma = 0.91$. This indicates that using model averaging may be preferable when considering early visual cortical regions (see **Figure 1** for a distribution of the pRF size in visual cortical areas in the HCP dataset). The improved reliability we observed in simulations was confirmed by the analysis of the HCP dataset, where model averaging resulted in a significant reduction of the variability of the pRF size estimates (**Supplementary Table S5**).

The second modification to the standard grid-search procedure that we introduce here is a permutation based procedure. This approach was motivated by the observation that, under the null hypothesis, the probability of obtaining a given fit is not independent of the pRF size. In particular, considering the two limit cases of infinite pRF size (i.e., a pRF with no preferred feature) and a pRF selecting a single feature, the first produces the same prediction regardless of the pRF mean, while pRFs selecting a single feature produce different (uncorrelated) predictions. As a result, the probability of selecting a narrow pRF model under the null hypothesis is higher than the probability of selecting a broader pRF model. The empirical null distribution of values of the cost function (e.g., correlation) for all the pRF parameters in a grid can be obtained using permutations. The selection of the pRF parameters is then based on the probability of observing under the null hypothesis a value of the cost function more extreme than that obtained in the original case. Importantly, the permutation procedure limits the applicability of this approach as it requires the observed data to be exchangeable under the null hypothesis, thus it can only be applied to particular stimulation designs (i.e., not in the case of the classical traveling wave retinotopic stimulation). While outside of the scope of our publication, it is worth noting that the experimental setup has been shown to have an effect on the estimation of pRF parameters even when controlling for the experimental time. The ordered presentation of tones (ascending and descending) resulted in higher goodness of fit to the observed fMRI data compared to a random presentation, and the random presentation of bars on the visual screen has been found to produce more reliable pRF

estimates as evidenced by higher prediction accuracy (Senden et al., 2014). In addition, previous reports have in some cases discouraged the estimation of pRF size (bandwidth in the case of auditory pRFs) from ordered stimulus designs as it may be affected by the overemphasis of the response near the beginning or the end of the sweep (Thomas et al., 2015). These results justify the comparison of the permutation based approach to previously introduced estimation procedures on a design that like a random stimulus order design allows for the estimation of individual stimulus responses. In particular, we applied the permutation based approach to an auditory data in which natural sounds were presented and from which we estimated, per voxel, a vector representing the response to all the individual (natural) stimuli (Sitek et al., 2019). In this dataset, the permutation based approach resulted in improved reliability of the estimated pRF parameters (mean and size) compared to both model averaging and a two-step optimization procedure that has been previously introduced (Thomas et al., 2015). The improved reliability for the permutation approach came at the cost of computational time.

It is important to note that in all our investigations we considered a fixed non-linearity (fixed to 1 – a linear model) for the pRF model. We did not systematically consider the effect that either optimizing the non-linearity, or considering a term other than 1, would have on the estimates of the pRF mean and size. The simultaneous optimization of the pRF mean, size and non-linearity increases the number of local minima (Zeidman et al., 2018) and is expected to result in increased variability of the estimates. Here, when analyzing real visual data, we compared models estimated with an non-linearity fixed to one to the procedure previously reported that used a non-linearity fixed to 0.05 (Benson et al., 2018). Our results indicate that a non-linearity of 0.05 results in more variable estimates of the pRF parameters (angle, eccentricity and in particular size) despite a small advantage in prediction accuracy (**Supplementary Table S5**).

While our results on the validity of the estimates are in line with the results reported previously (Lerma-Usabiaga et al., 2020), here we focused on understanding how the interaction between the pRF model (e.g., Gaussian) and cost function underlie the previously reported variability of the pRF size. In this respect, while interesting, we did not consider the effect that the hemodynamic response function has on the estimates (which we considered fixed and equal across methods). The issues we highlight here of the sensitivity of the cost function to variations in the pRF size are thus general in nature and affect all estimation procedures similarly. This variability requires careful considerations when comparing the estimated pRF size across regions or experimental conditions. To limit this effect, previous approaches introduced heuristics based on imposing a threshold on the signal to noise ratio of the data or constraining the search of plausible pRF sizes. Here we introduce two modification of the grid-search optimization method based on model averaging and selecting the best model based on permutation testing. Both approaches showed improved reliability of the estimates of the pRF size in both simulated and real data.

DATA AVAILABILITY STATEMENT

Publicly available datasets were analyzed in this study. This data can be found here: https://db.humanconnectome.org/app/action/DownloadPackagesAction.

ETHICS STATEMENT

The studies involving human participants were reviewed and approved by Ethics Review Committee Psychology and Neuroscience (ERCPN), Maastricht University. The patients/participants provided their written informed consent to participate in this study.

AUTHOR CONTRIBUTIONS

AL-C, GV, and FD performed the conceptualization. AL-C, GV, MS, and FD did the methodology and wrote, reviewed, and edited the manuscript. AL-C did the software, formal analysis, and wrote the original draft. All authors contributed to the article and approved the submitted version.

FUNDING

This work was supported by the Netherlands Organization for Scientific Research (NWO; VIDI grant 864-13-012 to FD). The funders had no role in study design, data collection and analysis, decision to publish, or preparation of the manuscript.

SUPPLEMENTARY MATERIAL

The Supplementary Material for this article can be found online at: https://www.frontiersin.org/articles/10.3389/fnins.2020.00825/full#supplementary-material

REFERENCES

Alvarez, I., De Haas, B., Clark, C., Rees, G., and Schwarzkopf, D. (2015). Comparing different stimulus configurations for population receptive field mapping in human fMRI. *Front. Hum. Neurosci.* 9:96. doi: 10.3389/fnhum.2015.00096

Benson, N. C., Jamison, K. W., Arcaro, M. J., Vu, A. T., Glasser, M. F., Coalson, T. S., et al. (2018). The human connectome project 7 Tesla retinotopy dataset: description and population receptive field analysis. *J. Vis.* 18:23. doi: 10.1167/18.13.23

Benson, N. C., and Winawer, J. (2018). Bayesian analysis of retinotopic maps. *eLife* 7:e40224. doi: 10.7554/eLife.40224

Bishop, C. M. (2006). *Pattern Recognition and Machine Learning*. New York, NY: Springer-Verlag.

Dumoulin, S. O., and Knapen, T. (2018). How visual cortical organization is altered by ophthalmologic and neurologic disorders. *Annu. Rev. Vis. Sci.* 4, 357–379.

Dumoulin, S. O., and Wandell, B. A. (2008). Population receptive field estimates in human visual cortex. *Neuroimage* 39, 647–660. doi: 10.1016/j.neuroimage.2007.09.034

Engel, S. A., De, R., Ba, W., At, L., Gh, G., Ej, C., et al. (1994). fMRI of human visual cortex. *Nature* 369:525.

Gravel, N., Harvey, B., Nordhjem, B., Haak, K. V., Dumoulin, S. O., and Renken, R. (2014). Cortical connective field estimates from resting state fMRI activity. *Front. Neurosci.* 8:339. doi: 10.3389/fnins.2014.00339

Harvey, B. M., Vansteensel, M. J., Ferrier, C. H., Petridou, N., Zuiderbaan, W., Aarnoutse, E. J., et al. (2013). Frequency specific spatial interactions in human electrocorticography: v1 alpha oscillations reflect surround suppression. *Neuroimage* 65, 424–432. doi: 10.1016/j.neuroimage.2012.10.020

Kay, K. N., Winawer, J., Mezer, A., and Wandell, B. A. (2013). Compressive spatial summation in human visual cortex. *J. Neurophysiol.* 110, 481–494. doi: 10.1152/jn.00105.2013

Lagarias, J., Reeds, J., Wright, M., and Wright, P. (1998). Convergence properties of the nelder–mead simplex method in low dimensions. *SIAM J. Optim.* 9, 112–147. doi: 10.1137/S1052623496303470

Lage-Castellanos, A., Valente, G., Formisano, E., and De Martino, F. (2019). Methods for computing the maximum performance of computational models of fMRI responses. *PLoS Comput. Biol.* 15:e1006397. doi: 10.1371/journal.pcbi.1006397

Lee, S., Papanikolaou, A., Logothetis, N. K., Smirnakis, S. M., and Keliris, G. A. (2013). A new method for estimating population receptive field topography in visual cortex. *Neuroimage* 81, 144–157. doi: 10.1016/j.neuroimage.2013.05.026

Lerma-Usabiaga, G., Benson, N., Winawer, J., and Wandell, B. A. (2020). A validation framework for neuroimaging software: the case of population receptive fields. *PLoS Comput. Biol* 16:e1007924. doi: 10.1371/journal.pcbi.1007924

Mardia, K. V. (1975). Statistics of directional data. *J. R. Stat. Soc. Ser. B* 37, 349–393.

Moerel, M., De Martino, F., and Formisano, E. (2012). Processing of natural sounds in human auditory cortex: tonotopy, spectral tuning, and relation to voice sensitivity. *J. Neurosci.* 32, 14205–14216. doi: 10.1523/jneurosci.1388-12.2012

Moerel, M., De Martino, F., Ugurbil, K., Yacoub, E., and Formisano, E. (2015). Processing of frequency and location in human subcortical auditory structures. *Sci. Rep.* 5, 1–15. doi: 10.1038/srep17048

Norman-Haignere, S. V., and McDermott, J. H. (2018). Neural responses to natural and model-matched stimuli reveal distinct computations in primary and nonprimary auditory cortex. *PLoS Biol.* 16:e2005127. doi: 10.1371/journal.pbio.2005127

Puckett, A. M., Bollmann, S., Junday, K., Barth, M., and Cunnington, R. (2020). Bayesian population receptive field modeling in human somatosensory cortex. *Neuroimage* 208:116465. doi: 10.1016/j.neuroimage.2019.116465

Santoro, R., Moerel, M., De Martino, F., Goebel, R., Ugurbil, K., Yacoub, E., et al. (2014). Encoding of natural sounds at multiple spectral and temporal resolutions in the human auditory cortex. *PLoS Comput. Biol.* 10:e1003412. doi: 10.1371/journal.pcbi.1003412

Senden, M., Reithler, J., Gijsen, S., and Goebel, R. (2014). Evaluating population receptive field estimation frameworks in terms of robustness and reproducibility. *PLoS One* 9:e114054. doi: 10.1371/journal.pone.0114054

Sereno, M. I., Dale, A. M., Reppas, J. B., Kwong, K. K., Belliveau, J. W., Brady, T. J., et al. (1995). Borders of multiple visual areas in humans revealed by functional magnetic resonance imaging. *Science* 268, 889–893. doi: 10.1126/science.7754376

Sitek, K. R., Gulban, O. F., Calabrese, E., Johnson, G. A., Lage-Castellanos, A., Moerel, M., et al. (2019). Mapping the human subcortical auditory system using histology, postmortem MRI and in vivo MRI at 7T. *eLife* 8:e48932. doi: 10.7554/eLife.48932

Thomas, J. M., Huber, E., Stecker, G. C., Boynton, G. M., Saenz, M., and Fine, I. (2015). Population receptive field estimates of human auditory cortex. *Neuroimage* 105, 428–439. doi: 10.1016/j.neuroimage.2014.10.060

van Dijk, J. A., de Haas, B., Moutsiana, C., and Schwarzkopf, D. S. (2016). Intersession reliability of population receptive field estimates. *Neuroimage* 143, 293–303. doi: 10.1016/j.neuroimage.2016.09.013

Wandell, B. A., and Winawer, J. (2015). Computational neuroimaging and population receptive fields. *Trends Cogn. Sci.* 19, 349–357. doi: 10.1016/j.tics.2015.03.009

Worsley, K. J., and Friston, K. J. (1995). Analysis of fMRI time-series revisited. *Neuroimage* 2, 45–53. doi: 10.1006/nimg.1995.1007

Zeidman, P., Silson, E. H., Schwarzkopf, D. S., Baker, C. I., and Penny, W. (2018). Bayesian population receptive field modelling. *Neuroimage* 180, 173–187. doi: 10.1016/j.neuroimage.2017.09.008

Zuiderbaan, W., Harvey, B. M., and Dumoulin, S. O. (2012). Modeling center-surround configurations in population receptive fields using fMRI. *J. Vis.* 12:10. doi: 10.1167/12.3.10

Zuiderbaan, W., Harvey, B. M., and Dumoulin, S. O. (2017). Image identification from brain activity using the population receptive field model. *PLoS One* 12:e0183295. doi: 10.1371/journal.pone.0183295

Conflict of Interest: The authors declare that the research was conducted in the absence of any commercial or financial relationships that could be construed as a potential conflict of interest.

Copyright © 2020 Lage-Castellanos, Valente, Senden and De Martino. This is an open-access article distributed under the terms of the Creative Commons Attribution License (CC BY). The use, distribution or reproduction in other forums is permitted, provided the original author(s) and the copyright owner(s) are credited and that the original publication in this journal is cited, in accordance with accepted academic practice. No use, distribution or reproduction is permitted which does not comply with these terms.

frontiers in Neuroscience

ORIGINAL RESEARCH
published: 30 July 2020
doi: 10.3389/fnins.2020.00793

In vivo PET Imaging of Gliogenesis After Cerebral Ischemia in Rats

*María Ardaya[1,2], Ana Joya[1,3], Daniel Padro[3], Sandra Plaza-García[3], Vanessa Gómez-Vallejo[3], Mercedes Sánchez[1], Maider Garbizu[1], Unai Cossío[3], Carlos Matute[1,2], Fabio Cavaliere[1,2], Jordi Llop[3,4] and Abraham Martín[1,5]**

[1] Achucarro Basque Center for Neuroscience, Leioa, Spain, [2] Department of Neuroscience, University of Basque Country (UPV/EHU) and CIBERNED, Leioa, Spain, [3] CIC biomaGUNE, Basque Research and Technology Alliance, San Sebastian, Spain, [4] Centro de Investigación Biomédica en Red – Enfermedades Respiratorias, CIBERES, Madrid, Spain, [5] Ikerbasque Basque Foundation for Science, Bilbao, Spain*

In vivo positron emission tomography of neuroinflammation has mainly focused on the evaluation of glial cell activation using radiolabeled ligands. However, the non-invasive imaging of neuroinflammatory cell proliferation has been scarcely evaluated so far. *In vivo* and *ex vivo* assessment of gliogenesis after transient middle cerebral artery occlusion (MCAO) in rats was carried out using PET imaging with the marker of cell proliferation 3′-Deoxy-3′-[18F] fluorothymidine ([^{18}F]FLT), magnetic resonance imaging (MRI) and fluorescence immunohistochemistry. MRI-T_2W studies showed the presence of the brain infarction at 24 h after MCAO affecting cerebral cortex and striatum. *In vivo* PET imaging showed a significant increase in [^{18}F]FLT uptake in the ischemic territory at day 7 followed by a progressive decline from day 14 to day 28 after ischemia onset. In addition, immunohistochemistry studies using Ki67, CD11b, and GFAP to evaluate proliferation of microglia and astrocytes confirmed the PET findings showing the increase of glial proliferation at day 7 after ischemia followed by decrease later on. Hence, these results show that [^{18}F]FLT provides accurate quantitative information on the time course of glial proliferation in experimental stroke. Finally, this novel brain imaging method might guide on the imaging evaluation of the role of gliogenesis after stroke.

Keywords: Cerebral ischemia, PET, [^{18}F]FLT, gliogenesis, glia

OPEN ACCESS

Edited by:
João O. Malva, University of Coimbra, Portugal

Reviewed by:
Antero Abrunhosa, University of Coimbra, Portugal
Andre Obenaus, University of California, Irvine, United States

***Correspondence:**
Abraham Martín
abraham.martin@achucarro.org

Specialty section:
This article was submitted to Brain Imaging Methods, a section of the journal Frontiers in Neuroscience

Received: *17 May 2020*
Accepted: *06 July 2020*
Published: *30 July 2020*

Citation:
Ardaya M, Joya A, Padro D, Plaza-García S, Gómez-Vallejo V, Sánchez M, Garbizu M, Cossío U, Matute C, Cavaliere F, Llop J and Martín A (2020) In vivo PET Imaging of Gliogenesis After Cerebral Ischemia in Rats. Front. Neurosci. 14:793. doi: 10.3389/fnins.2020.00793

INTRODUCTION

Gliogenesis is the process by which glial progenitor cells differentiate into mature glia during development, and in the adult brain to maintain and regulate brain function (Lee et al., 2000). Following stroke, neurovascular disturbances lead to a massive neuroinflammatory reaction through the activation of glial cells such as microglia and astrocytes that amplifies ischemic damage and neuronal death (Moskowitz et al., 2010). In turn, proliferation of glial cells underlies compensatory mechanisms that likely contributes to neuronal restoration after brain injury (Rusznak et al., 2016).

In vivo positron emission tomography (PET) of neuroinflammation has been mainly focused on the evaluation of microglia/macrophage and astrocytic activation using radiolabeled ligands for the Translocator protein 18 kDa (TSPO) (Martin et al., 2010; Dupont et al., 2017; Pulagam et al., 2017). TSPO, a mitochondrial protein expressed in reactive glial cells, is considered the hallmark for neuroinflammation, as it is highly expressed after inflammatory reaction while low

expression is shown in the healthy brain (Martin et al., 2010). For this reason, this biomarker has been widely used to monitor neuroinflammatory activation in major neurological diseases i.e., stroke, Alzheimer's disease, Parkinson's disease and multiple sclerosis, among others (Dupont et al., 2017). Despite the imaging of glial activation has been fully characterized with TSPO radiotracers during the last decade, the investigation of glial cell proliferation using PET imaging still remains unexplored. PET imaging of cellular proliferation has been mainly limited to the use of 3′-Deoxy-3′-[^{18}F]fluorothymidine ([^{18}F]FLT) in both preclinical and clinical routine (McHugh et al., 2018; Schelhaas et al., 2018; Bashir et al., 2020). [^{18}F]FLT is an analog of thymidine which is phosphorylated by thymidine kinase-1 (TK-1), an enzyme expressed during the DNA synthesis and up-regulated during the S phase of the cell cycle (Shields et al., 1998). Once phosphorylated, [^{18}F]FLT cannot be incorporated into the DNA and is metabolically trapped inside the cells. For this reason, the uptake and accumulation of [^{18}F]FLT are used as surrogate of cellular proliferation (Cieslak et al., 2016). [^{18}F]FLT has been extensively used in the field of oncology to characterize tumors and predict the response to personalized therapeutic approaches (Schelhaas et al., 2017). Therefore, the main application of this radiotracer in neurology has been restricted to the diagnosis of glioblastoma (Nikaki et al., 2017; Brahm et al., 2018). Nevertheless, few studies have reported the visualization of endogenous neural stem cells in living animals using [^{18}F]FLT after focal cerebral ischemia, that could be used to monitor the effect of drugs aimed at expanding the neural stem cell niche (Rueger et al., 2010, 2012). Moreover, previous studies from our group and others showed that the lack of toll-like receptor 4 which is mainly expressed in microglia and astrocytes after brain ischemia, was able to increase neurogenesis using [^{18}F]FLT-PET in the subventricular area after focal ischemia in mice (Caso et al., 2007, 2008; Moraga et al., 2016). Despite these findings, the use of [^{18}F]FLT to monitor proliferation of glial cells has not been explored before. The purpose of the present study was to investigate non-invasively gliogenesis in the rat brain after cerebral ischemia using [^{18}F]FLT-PET and immunohistochemistry. In particular, we were interested in clarifying the relationship of the [^{18}F]FLT uptake and proliferative microglia/macrophages and astrocytes in a preclinical model of ischemic stroke in rats. Hence, these results provide valuable information about the use of a novel imaging methodology to follow up proliferation of glial cells *in vivo* after cerebral ischemia. This research might ultimately contribute to a better design of novel diagnostic and therapeutic strategies for neurologic diseases such as stroke.

MATERIALS AND METHODS

Cerebral Ischemia and Experimental Set-Up

Eight-weeks old male Sprague-Dawley rats (n = 32; 307 ± 4.3 g body weight; Janvier, France) were used for both non-invasive imaging and immunohistochemical studies. Animal experimental protocols and relevant details regarding welfare were approved by the animal ethics committee of CIC biomaGUNE and were conducted in accordance with the ARRIVE guidelines and Directives of the European Union on animal ethics and welfare. Rats were anaesthetized with 2.5% isoflurane in 100% O_2 and transient focal ischemia was produced by a 90 min intraluminal occlusion of the middle cerebral artery (MCAO) followed by reperfusion as described previously (Justicia et al., 2001). Ischemic rats were subjected to T_2-weighted (T_2W) MRI scans at 24 h after reperfusion to select rats presenting cortico-striatal infarction for inclusion in the PET studies. 16 rats were used to carry out [^{18}F]FLT-PET imaging studies. Eight of them were only scanned before ischemic insult. A different set of rats (n = 8) was scanned at 7 days after ischemia; of these, five animals were re-scanned at days 14 and 28 after ischemia. Overall, five animals were subjected to the three PET imaging sessions. Not all animals were subjected to the complete PET imaging protocol due to technical issues with the PET scanner at day 14 (n = 5) after stroke. In addition, one animal died before last PET session at day 28 (n = 7) after ischemia. In all cases, [^{18}F]FLT uptake in the brain was determined. In addition, additional 16 rats were used to perform immunohistochemical studies for proliferation of glial cells before (control) and at days 7, 14, and 28 after ischemia.

Magnetic Resonance Imaging

T_2W-MRI scans were used to include rats in the PET study and to evaluate the infarction volume. Scans were performed in rats anaesthetized with 4% isoflurane and maintained by 2–2.5% of isoflurane in a 30/70% mixture of O_2/N_2. Animals were placed into a rat holder compatible with the MRI acquisition system and maintained normothermia using a water-based heating blanket at 37°C. To ensure animal welfare, temperature and respiration rate were continuously monitored while they remain in the MRI magnet, using a SAII M1030 system (SA Instruments, NY, United States). MRI *in vivo* studies were performed on a 7T horizontal bore Bruker Biospec USR 70/30 MRI system (Bruker Biospin GmbH, Ettlingen, Germany), interfaced to an AVANCE III console, and with a BGA12-S imaging gradient insert (maximal gradient strength 400 mT/m, switchable within 80 μs). These measurements were performed with a 72 mm volumetric quadrature coil for excitation and a 20 mm rat brain surface coil for reception. The imaging session started with the acquisition of a scout scan, which was used to plan the whole study focusing on the region of interest. T2-W images were acquired with a Bruker's RARE (Rapid Acquisition with Relaxation Enhancement) sequence (Effective TE = 40 ms, TR = 4400 ms, NA = 2; Matrix = 256 × 256 points; FOV = 25.6 mm × 25.6 mm; spatial resolution = 100 μm × 100 μm; 24 contiguous slices of 1 mm thickness covering the whole brain), which was used to quantify the volume of the lesion. For the image analysis, regions of interest (ROIs) were manually defined by the same researcher a blind fashion using the open source software 3D Slicer image analysis software (version 4.8[1]) for each rat on the region of increased signal in the ipsilateral hemisphere. The total lesion

[1]http://www.slicer.org

volume was calculated by summing the area of the infarcted regions of all slices affected by the lesion.

Radiochemistry

The synthesis of 3′-Deoxy-3′-[^{18}F]fluorothymidine ([^{18}F]FLT) was performed as described earlier (Machulla et al., 2000), using a TRACERlab FXFN synthesis module (GE Healthcare). In brief, [^{18}F]Fluoride was produced via the ^{18}O(p,n)^{18}F nuclear reaction in 2.9 ml of 98% ^{18}O-enriched water. The [^{18}F]F^{-} was trapped in a pre-conditioned QMA cartridge and transferred to the reactor by sequential elution with a solution of K_2CO_3 (3.5 mg) in water (0.5 ml) and a solution of Kryptofix $K_{2.2.2}$ (15 mg) in acetonitrile (1 ml). After azeotropic evaporation, a solution containing the precursor (10 mg of 5′-O-Benzoyl-2,3′-anhydrothymidine in 1 ml of dimethylsulfoxide) was added and the fluorination reaction was allowed to occur at 100°C for 10 min. The reactor was then cooled at room temperature and 0.35 ml of 1% NaOH aqueous solution were added for the hydrolysis of protecting groups (5 min at 50°C). Finally, 0.75 ml of 0.2 M NaH_2PO_4 aqueous solution and 1.75 ml of mobile phase, consisting of 0.01 M NaH_2PO_4 solution (90%) and ethanol (10%), were added and the mixture was purified by HPLC, using a VP125/10 Nucleosil 100-7C18 semipreparative column (Macherey-Nagel) as stationary phase. The collected fraction (retention time = 13,14 min) was filtered through a 0.22 μm sterile filter to yield the final [^{18}F]FLT solution. Average radiochemical yield was 7.5 ± 1.1% (EOS) in an overall production time of ca. 60 min. Radiochemical purity was higher than 95% in all cases.

Positron Emission Tomography Scans and Data Acquisition

PET scans were performed using an eXplore Vista PET-CT camera (GE Healthcare, Waukesha, WI, United States). Scans were performed in rats anaesthetized with 4% isoflurane and maintained by 2–2.5% of isoflurane in 100% O_2. Animals were placed into a rat holder compatible with the PET acquisition system and maintained normothermia using a water-based heating blanket at 37°C. To ensure animal welfare, temperature and respiration rate were continuously monitored while they remain in the PET scanner, using a SAII M1030 system (SA Instruments, NY, United States). The tail vein was catheterized with a 24-gage catheter for intravenous administration of the radiotracer. For longitudinal assessment of [^{18}F]FLT uptake after ischemia, control animals (n = 8) and ischemic animals at days 7 (n = 8), 14 (n = 5), and 28 (n = 7) after ischemia were scanned. The radioactivity (±70 MBq) controlled for animal weight was injected and dynamic brain images were acquired for 18 frames and 60 min in the 400–700 keV energetic window. After each PET scan, CT acquisitions were also performed (140 mA intensity, 40 kV voltage), to provide anatomical information of each animal as well as the attenuation map for the later PET image reconstruction. Dynamic acquisitions were reconstructed (decay and CT-based attenuation corrected) with filtered back projection (FBP) using a Ramp filter with a cutoff frequency of 0.5 mm^{-1}.

Positron Emission Tomography Image Analysis

PET images were analyzed using PMOD image analysis software (version 3.5, PMOD Technologies Ltd., Zurich, Switzerland). To verify the anatomical location of the signal, PET images were co-registered to the anatomical data of a MRI rat brain template. Two type of Volumes of Interest (VOIs) were established as follows: (1) A first set of VOIs was defined to study the whole brain [^{18}F]FLT PET signal. Whole brain VOIs were manually drawn in both the entire ipsilateral and contralateral hemispheres on slices of a MRI (T_2W) rat brain template provided by PMOD software. (2) A second set of VOIs was automatically generated in the cerebral cortex and the striatum by using the regions proposed by the PMOD rat brain template, to study the evolution of [^{18}F]FLT PET signal in these specific regions in both the ipsilateral and contralateral cerebral hemispheres. The last five frames (last 15 min of acquisition) were summed to quantify radiotracer uptake. Average values in each ROI were determined and expressed as percentage of injected dose per cubic centimeter (%ID/cc).

Immunohistochemistry and Cell Counting

Immunohistochemistry staining was carried out at control (n = 4), day 7 (n = 4), day 14 (n = 4), and day 28 (n = 4) after reperfusion and the "n" of each group was randomly assigned. The brain was removed, frozen and cut in 5-μm-thick sections in a cryostat. Sections were fixed in 4% paraformaldehyde during 15 min, washed with phosphate-buffered saline (PBS) and incubated 5 min in NH_4Cl, following by two PBS rinse and methanol-acetone (1:1) permeabilization during 5 min at −20°C. After PBS washing, samples were saturated with a solution of bovine serum albumin (BSA) 5%/Tween 0.5% in PBS during 15 min at room temperature, and incubated during 2 h at room temperature with primary antibodies BSA (5%)/Tween (0.5%) in PBS. Sections were stained for Ki67 with rabbit anti-rat Ki67 (1:400, AbCam, Cambridge, United Kingdom), for CD11b with mouse anti-rat CD11b (1:300; Serotec, Raleigh, NC, United States) and for the glial fibrillary acidic protein (GFAP) with chicken anti-rat GFAP (1:500; AbCam, Cambridge, United Kingdom). Sections were washed (3 × 10 min) in PBS and incubated for 1 h at room temperature with secondary antibodies Alexa Fluor 594 goat anti-rabbit IgG, Alexa Fluor 488 goat anti-mouse IgG and Alexa Fluor 647 goat anti-chicken IgG (Molecular Probes, Life Technologies, Madrid, Spain, 1:1,000) in BSA 5%/Tween 0.5% in PBS, washed again (3 × 10 min) in PBS, and mounted with a prolong antifade kit with DAPI in slices (Molecular Probes Life Technologies, Madrid). Standardized images acquisition was performed with the Panoramic MIDI II automated digital slide scanner (3DHistech Ltd., Hungary) and the Leica SP8 microscope (Hospitalet de Llobregat, Spain). Cells were manually counted in ten representative and different fields at Bregma: circa 0.50 mm and 40× magnification in a blind-fashion to avoid bias by using Image J (Version 2.0.0-rc-69/11.52p, NIH) software.

Statistical Analyses

For PET, the percentage of injected dose per cubic centimeter (%ID/cc) within each region and time point following cerebral ischemia were averaged and compared with the averaged baseline control values (day 0) using one-way ANOVA followed by Dunnet's multiple-comparison tests for *post hoc* analysis. Likewise, cellular expression of both $Ki67^+/CD11b^+$ and $Ki67^+/GFAP^+$ at control and days 7, 14, and 28 after ischemia were compared using the same statistical analysis than that for PET imaging. The level of significance was regularly set at $p < 0.05$. Statistical analyses were performed with GraphPad Prism version 8 software.

RESULTS

The evaluation of *in vivo* gliogenesis was explored by PET using the radiotracer [^{18}F]FLT during the first month after transient focal ischemia in rats. All the images were quantified in standard units, i.e.,%ID/cc of [^{18}F]FLT. The images with normalized color scale illustrate the evolution of the PET signals before (control) and at 7, 14, and 28 days after ischemia onset (**Figures 1A,C–E**). Hyperintensity of MRI-T_2W images showed the edema formation as result of the evolution of the brain infarction at day 1 after reperfusion (**Figure 1B**). All animals subjected to PET studies showed cortico-striatal MRI alterations (mean ± sd: 298 ± 71 mm^3, $n = 8$).

Imaging Glial Proliferation Using [^{18}F]FLT PET After Cerebral Ischemia

In vivo imaging of glial proliferation was evaluated with the uptake of [^{18}F]FLT in the ipsilateral and contralateral whole brain, cerebral cortex and striatum before (control) and at 7, 14, and 28 days after MCAO (**Figure 2**). All brain regions evaluated in both brain hemispheres showed a similar PET signal evolution after ischemia. In the ipsilateral whole brain, [^{18}F]FLT uptake showed a significant increase at day 7 after ischemia in comparison to baseline ($p < 0.05$, **Figure 2A**). Subsequently, the PET signal displayed a decline during days 14 and 28 after stroke. In the contralateral whole brain, [^{18}F]FLT signal showed similar values along the different days evaluated (**Figure 2B**). The ischemic cerebral cortex showed a significant PET signal increase at day 7 after ischemia in comparison to control rats followed a progressive decrease from days 14 to 28 after MCAO ($p < 0.001$, **Figure 2C**). The contralateral cerebral cortex showed similar values at different days after ischemia in relation to control values (**Figure 2D**). Moreover, cerebral cortex showed higher PET signal values (0.15–0.20%ID/cc) in relation to striatum (circa 0.10% ID/cc) in control rats, probably due to spill-over effects from the [^{18}F]FLT PET signal coming from boundary tissues outside the brain. The injured striatum showed [^{18}F]FLT PET signal uptake during the first week after reperfusion followed by a sharp decrease at the third and fourth week after ischemia ($p < 0.001$ with respect to control animals, **Figure 2E**). Finally, the contralateral striatum displayed non-significant PET signal changes at different days after MCAO (**Figure 2F**).

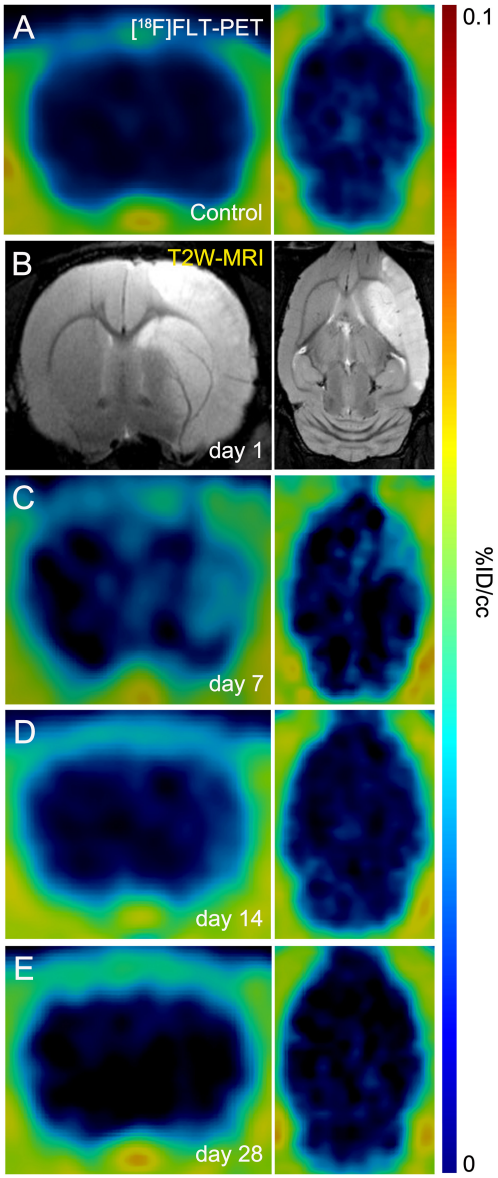

FIGURE 1 | Positron emission tomography (PET) images of [^{18}F]FLT and Magnetic resonance imaging (MRI) [T_2-weighthing (T_2W)] before (control) and at days 1, 7, 14, and 28 after cerebral ischemia in rats. [^{18}F]FLT PET **(A, C–E)** and MRI-T_2W **(B)** images of axial and coronal planes at the level of the lesion are shown. Images correspond to representative animals for each time point.

Brain Lesion Evolution After Ischemia

MRI-T_2W image hyperintensities showed the formation of vasogenic edema as the consequence of brain infarction evolution at day 1 after ischemia onset (**Figure 3A**). Cortical and striatal MRI alterations coincided with the increase of [^{18}F]FLT PET as potential marker for gliogenesis and the activation of microglia and infiltrated macrophages at day 7 (**Figure 3B**) followed by

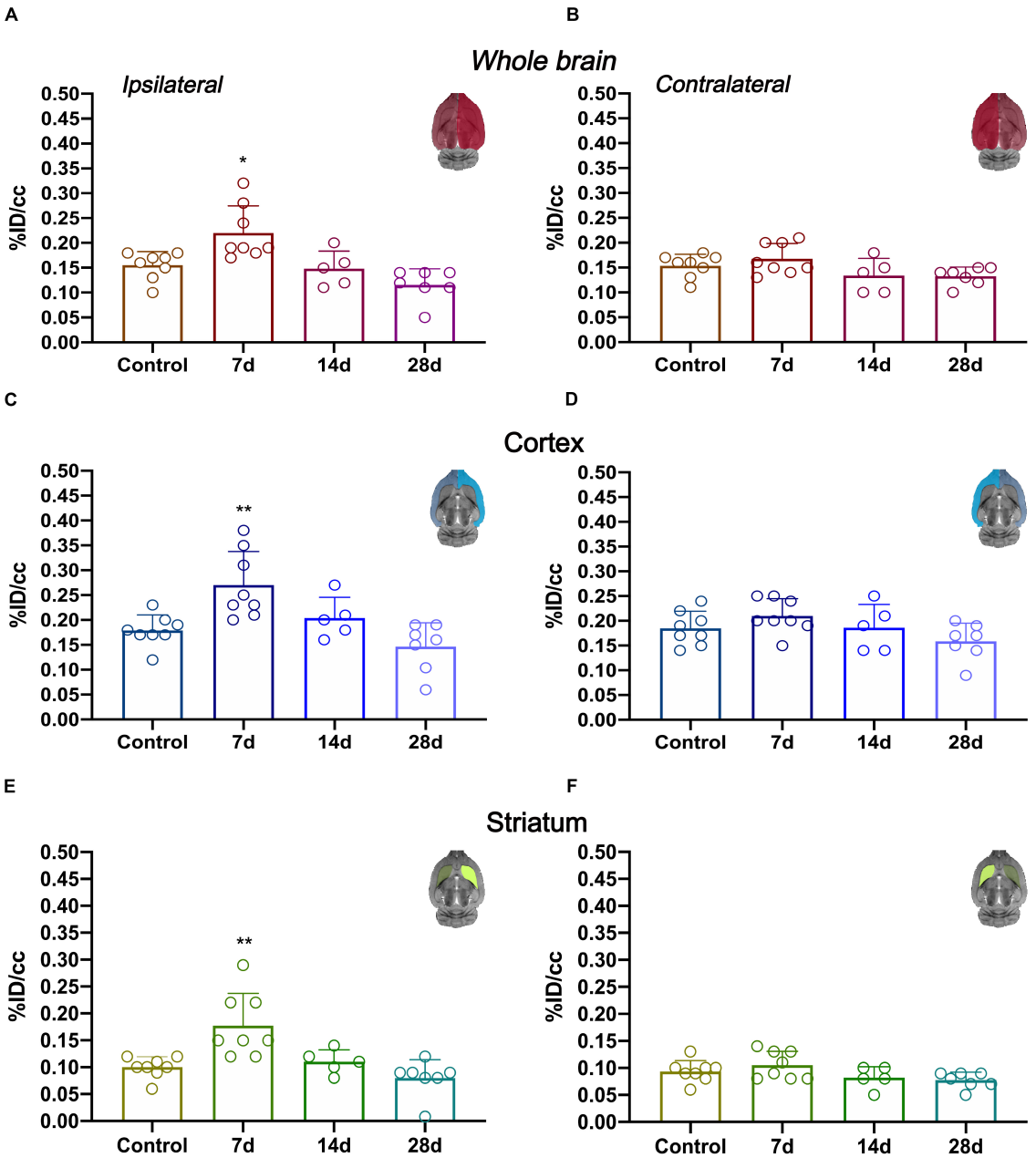

FIGURE 2 | Time course of the progression of [^{18}F]FLT PET signals at before (control) and after cerebral ischemia.%ID/cc (mean ± SD) of [^{18}F]FLT was quantified in six VOIs. The entire ipsilateral cerebral hemisphere **(A)**, contralateral hemisphere **(B)**, ipsilateral cerebral cortex **(C)**, contralateral cerebral cortex **(D)**, ipsilateral striatum **(E)** and contralateral striatum **(F)** are shown. The upper right panels of each figure show the selected brain ROIs for the quantification defined on a slice of a MRI (T_2W) template. Rats were examined by PET at control (n = 8) and at 7 (n = 8), 14 (n = 5), and 28 (n = 7) days after ischemia. *$p < 0.05$, **$p < 0.01$ compared with control.

a decrease at day 28 (**Figure 3C**) after ischemia. The infarcted area (cerebral cortex and striatum) was occupied by cells with the morphology of amoeboid reactive microglia/macrophages showing intense CD11b immunoreactivity flanked by reactive astrocytes (GFAP$^+$ cells) at day 7 after MCAO (**Figure 3D**). Some of these glial cells were positive for the proliferation marker Ki67, supporting the detection of glial proliferation by PET using [^{18}F]FLT. During following weeks, brain infarction evolved into a cystic cavity surrounded by the formation of the astrocytic scar (**Figure 3E**).

Ex vivo Evaluation of Glial Proliferation After MCAO

The ischemic cerebral cortex showed a significant increase of proliferative microglia/infiltrated macrophages (in red-CD11b

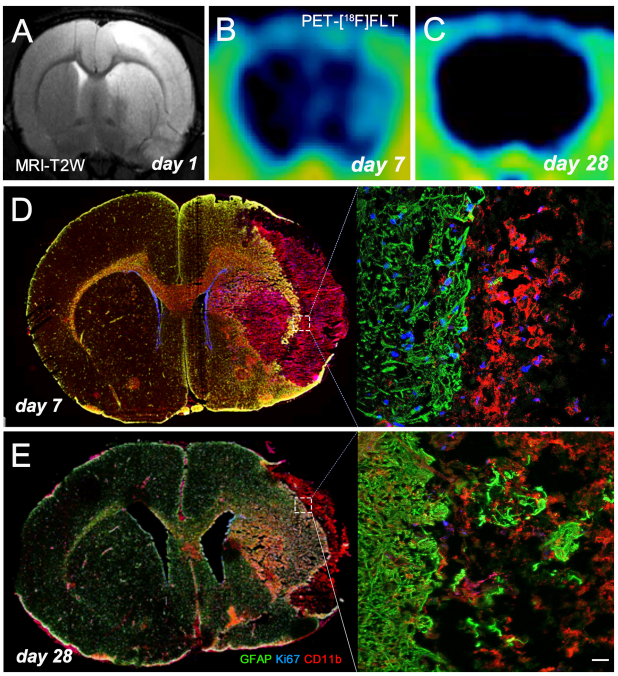

FIGURE 3 | MRI-T_2W and [^{18}F]FLT PET signal shows the vasogenic edema and the evolution of cerebral proliferation at days 1 **(A)**, 7 **(B)**, and 28 **(C)** after MCAO. Images correspond to the same animal. Immunofluorescent labeling of GFAP (green), Ki67 (blue) and CD11b (red) of an axial section at days 7 **(D)** and 28 **(E)** shows gliogenesis after cerebral ischemia. Scale bar, 20 μm.

and blue-Ki67; **Figure 4**) at day 7 in comparison to control brains followed by a slight decrease at day 14 and a sharp decline at day 28 after ischemia ($p < 0.001$, **Figure 6A**), In contrast, the number of proliferative astrocytes (in green-GFAP and blue-Ki67; **Figure 4**) showed pseudo-control values at day 7 followed by a mild non-significant increase at 14 and 28 days after cerebral ischemia (**Figure 6A**). Despite the number of $CD11^+/Ki67^+$ was much higher than $GFAP^+/ki67^+$ cells at days 7 and 14, the values of both proliferative glial cells were similar at day 28 after MCAO (**Figure 6A**). In the non-ischemic cerebral cortex (contralateral), both proliferative microglia and astrocytes showed low values at different days after ischemia (**Figure 6B**).

Similarly, the ischemic striatum showed a significant increase of $CD11^+/Ki67^+$ (in red and blue; **Figure 5**) followed by a progressive decrease from days 14 to 28 after cerebral ischemia ($p < 0.05$; $p < 0.01$, **Figure 6C**). Likewise, the number of proliferative astrocytes showed a progressive mild increase from days 7 to 14 followed by the highest value reached at day 28 after MCAO ($p < 0.05$; $p < 0.001$, **Figure 6C**). In contrast, very low proliferative glial was observed in the contralateral striatum at the different time points after ischemia (**Figure 6D**). Cerebral cortex showed non-significant higher values of proliferative microglia and infiltrated macrophages at days 7 and 14 in relation to the striatum, while this situation was reverted at day 28 (**Figure 6E**). In the other hand, striatum showed non-significant increase of proliferative astrocytes in comparison to cerebral cortex at different days after stroke (**Figure 6F**).

DISCUSSION

The neuroinflammatory reaction, firstly led by the activation of microglia and the infiltration of macrophages and later by the over-reactivity of astrocytes, has been extensively monitored with PET after ischemic stroke (Rojas et al., 2007; Martin et al., 2010). However, new functions and properties of proliferative glia that might account for neuronal restoration (Rusznak et al., 2016) after brain ischemia have been barely studied so far. To fill this gap, we explored a novel non-invasive *in vivo* imaging method able to detect proliferation of microglia/macrophages and astrocytes after stroke in rats by using [^{18}F]FLT PET.

Previously, Rueger and colleagues described the use of [^{18}F]FLT PET as imaging method of endogenous neural stem cells (NSCs) after cerebral ischemia in rats (Rueger et al., 2010). This study showed for the first time the uptake of [^{18}F]FLT in both NSC niches, the subventricular area and the hippocampus that correlated with a high bromodeoxyuridine (BrdU) accumulation in those brain regions. Additionally, these authors also described a cellular proliferation enhancement within the infarcted region with both [^{18}F]FLT and BrdU staining at 1 week after preclinical stroke. However, these results were not directly related to the proliferation of glial cells rather than a merely increase of cellular proliferation after stroke (Rueger et al., 2010). Therefore, these latter findings are fully consistent with PET imaging results observed in our work (**Figure 1**). In the present study, the PET [^{18}F]FLT signal uptake showed a significant increase at day 7 after ischemia that was followed by a progressive decline to pseudo-control values at day 28 after reperfusion (**Figure 2**). In fact, these results stand in agreement with the *in vivo* PET imaging distribution of TSPO, a well-known marker of neuroinflammation, after cerebral ischemia (Domercq et al., 2016). Hence, taking into account that the TSPO overexpression is principally due to the activation of microglia/infiltrated macrophages and astrocytes (Martin et al., 2010), our results could suggest that [^{18}F]FLT signal in the region of infarction can be linked to the inflammatory reaction. To verify this hypothesis, we performed the immunohistochemical characterization of proliferative microglia/macrophages and astrocytes at days 7, 14, and 28 after ischemia (**Figures 3–5**).

In the present study, we evaluated the proliferative glial cells using the marker Ki67, a nuclear protein expressed in all phases of the cell cycle except the resting state. A previous study showed higher numbers of Ki67 positive cells in comparison to BrdU expression pattern in the rat brain. In fact, these findings might be due to BrdU is incorporated to DNA during the S-phase of the mitotic process, whereas Ki67 might be incorporated during all phases (Kee et al., 2002). Additionally, [^{18}F]FLT has shown to be a thymidine analog that is trapped inside proliferative cells during the S-phase in a similar manner than BrdU. However, previous works showed lower [^{18}F]FLT values in comparison to BrdU positive cells based on differences in their incubation times (i.e., from 1.5 to 6 h, respectively) (Rueger et al., 2010, 2012). Therefore, all these previous findings may explain the higher events observed in our study by immunohistochemistry with Ki67 positive cells in comparison to the PET signal with [^{18}F]FLT (**Figures 4–6**). Despite this, these results showed a

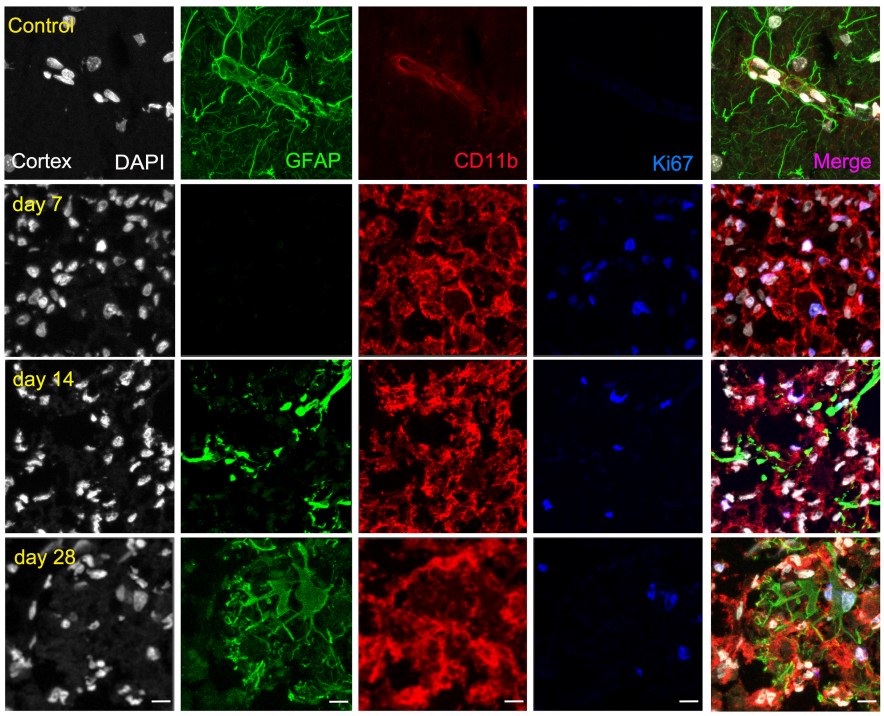

FIGURE 4 | Immunofluorescent labeling of DAPI (white), GFAP (green), CD11b (red) and Ki67 (blue) in the ischemic cortex, shown as four channels. The data show temporal evolution of cortical proliferative (Ki^+) microglia/macrophages ($CD11b^+$) and astrocytes ($GFAP^+$) at day 0 (control; first row), day 7 (second row), day 14 (third row), and day 28 (fourth row) after ischemia. Scale bars, 10 μm.

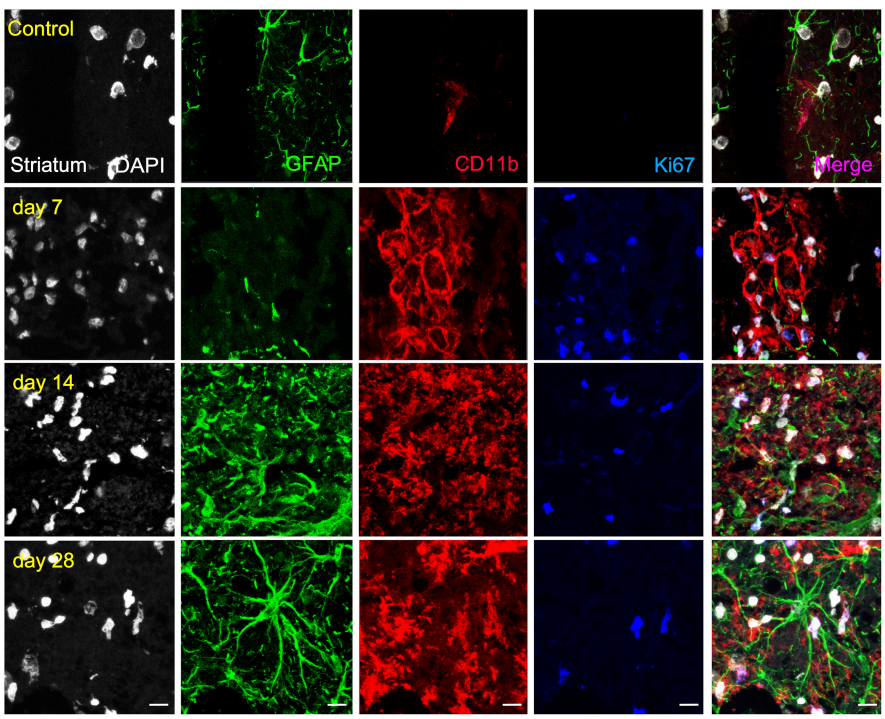

FIGURE 5 | Immunofluorescent labeling of DAPI (white), GFAP (green), CD11b (red) and Ki67 (blue) in the ischemic striatum, shown as four channels. The data show temporal evolution of striatal proliferative (Ki^+) microglia/macrophages ($CD11b^+$) and astrocytes ($GFAP^+$) at day 0 (control; first row), day 7 (second row), day 14 (third row), and day 28 (fourth row) after ischemia. Scale bars, 10 μm.

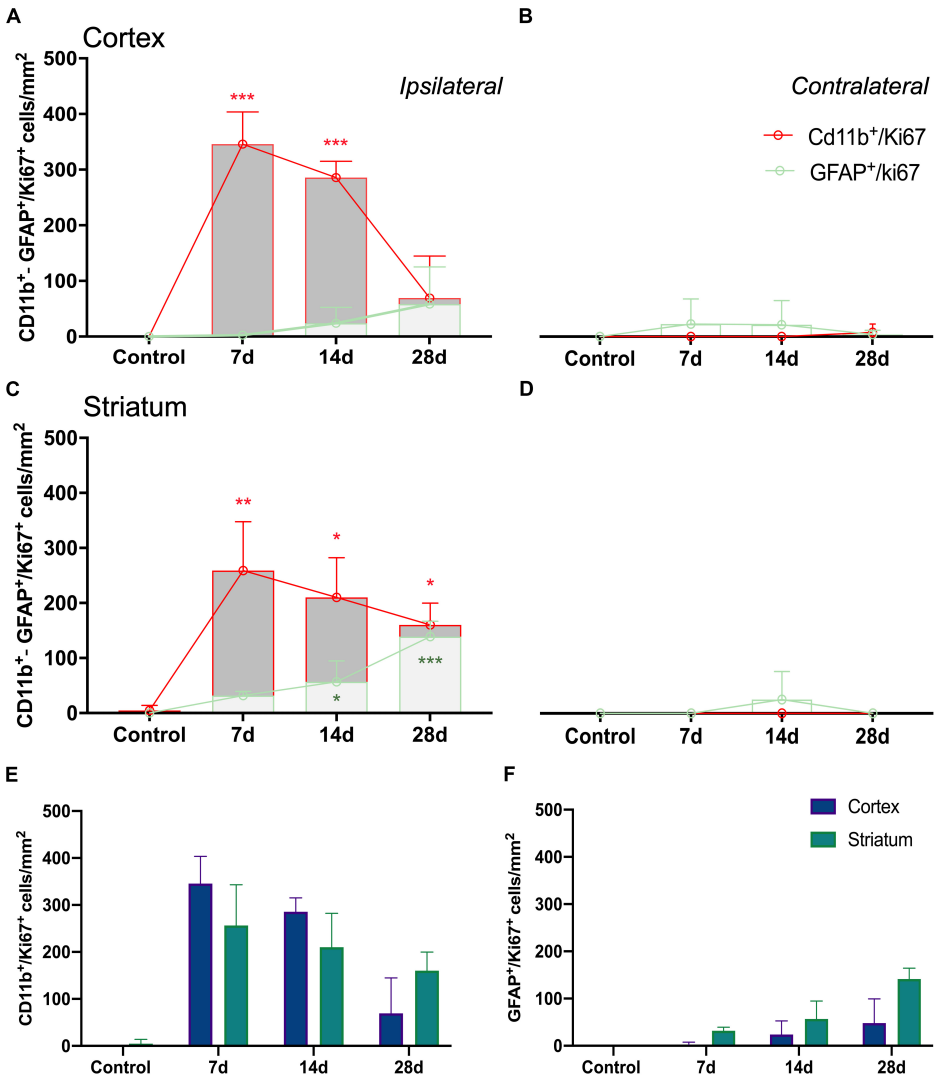

FIGURE 6 | Temporal profiles of CD11b$^+$/Ki67$^+$ and GFAP$^+$/Ki67$^+$ cells in four brain regions after ischemia onset. Ipsilateral cerebral cortex **(A)**, contralateral cerebral cortex **(B)**, ipsilateral striatum **(C)** and contralateral striatum **(D)** are shown. CD11b$^+$/Ki67$^+$ **(E)** and GFAP$^+$/Ki67$^+$ **(F)** cells show evolution of proliferative glial cells in cerebral cortex and striatum. Cell counts/mm^2 were counted before (control) and days 7, 14, and 28 (n = 12, 4 rats/time point) after ischemia. *p < 0.05, **p < 0.01, ***p < 0.001 compared with control.

significant increase of proliferative microglia/macrophages at day 7 followed by a decrease from days 14 to 28 supporting the findings observed with [^{18}F]FLT. In contrast, the number of proliferative astrocytes showed low levels during the first two weeks that was significantly increased at day 28 after ischemia. The increase of proliferative astroglial cells at day 28 was not paralleled by increased [^{18}F]FLT uptake, which displayed pseudo-control values in both cerebral cortex and striatum one month after ischemia. In fact, these differences could be explained by the higher resolution showed by confocal microscopy in relation to PET imaging which allows for a more accurate detection of proliferative cells in the region of infarction (Tichauer et al., 2015).

Overall, our study showed that [^{18}F]FLT PET was able to detect mainly proliferative CD11b positive cells (microglia and infiltrated macrophages) that accounted for the highest proliferative cellular population in the ischemic area at day 7 after stroke.

Summary and Conclusion

In summary, we report here for the first time a novel imaging tool to evaluate glial proliferation using PET imaging. We describe a novel imaging tool to evaluate glial proliferation with PET since [^{18}F]FLT is a radiotracer able to detect cellular proliferation *in vivo*. Following cerebral ischemia, a massive amount of glial cells become activated and others proliferate too. Since neuronal population dies in the region of the infarction after stroke, we might be able to monitor proliferative glial cells involved in the immune response. Therefore, these results provide valuable information regarding the *in vivo* detection of proliferative glia

after stroke that might contribute to the discovery of novel diagnostic tools for stroke care.

Limitation Section

The main limitations of the present study are as follows: (i) the resolution of current PET cameras might certainly limit the use of this imaging technique for the evaluation of low proliferative glial density, (ii) the no correction to compensate for the effect of the surface coil in MRI studies, (iii) the regions of interest of MRI images were drawn by less than two researchers, and (iv) the count of cells was carried out manually.

DATA AVAILABILITY STATEMENT

The raw data supporting the conclusions of this article will be made available by the authors, without undue reservation.

ETHICS STATEMENT

The animal study was reviewed and approved by Ethics committee of CIC biomaGUNE.

AUTHOR CONTRIBUTIONS

MA, AJ, DP, SP-G, VG-V, MS, MG, and UC performed the experiments and acquired the data. FC, CM, JL, and AM designed the experiments and analyzed the data, prepared the manuscript, and approved the final version of the manuscript. All authors contributed to the article and approved the submitted version.

FUNDING

The authors would like to thank A. Leukona, X. Ríos-Anglada, and V. Salinas for technical support in the radiosynthesis. This study was funded by grants from the Spanish Ministry of Education and Science/FEDER RYC-2017-22412, SAF2016-75292-R, PID2019-107989RB-I00, the Basque Government (IT1203/19, BIO18/IC/006) and CIBERNED. María Ardaya holds a fellowship from the University of País Vasco. Ana Joya acknowledges funding from Fundació La Marató de TV3 (17/C/2017). Part of the work has been performed under the Maria de Maeztu Units of Excellence Program from the Spanish State Research Agency (Grant No. MDM-2017-0720).

REFERENCES

Bashir, A., Binderup, T., and Vestergaard, M. B. (2020). In vivo imaging of cell proliferation in meningioma using 3′-deoxy-3′-[(18)F]fluorothymidine PET/MRI. *Eur. J. Nuclear Med. Mol. Imag.* 47, 1496–1509.

Brahm, C. G., den Hollander, M. W., Enting, R. H., de Groot, J. C., Solouki, A. M., den Dunnen, W. F. A., et al. (2018). Serial FLT PET imaging to discriminate between true progression and pseudoprogression in patients with newly diagnosed glioblastoma: a long-term follow-up study. *Eur. J. Nuclear Med. Mol. Imag.* 45, 2404–2412.

Caso, J. R., Pradillo, J. M., Hurtado, O., Leza, J. C., Moro, M. A., and Lizasoain, I. (2008). Toll-like receptor 4 is involved in subacute stress-induced neuroinflammation and in the worsening of experimental stroke. *Stroke* 39, 1314–1320.

Caso, J. R., Pradillo, J. M., Hurtado, O., Lorenzo, P., Moro, M. A., and Lizasoain, I. (2007). Toll-like receptor 4 is involved in brain damage and inflammation after experimental stroke. *Circulation* 115, 1599–1608.

Cieslak, J. A., Sibenaller, Z. A., and Walsh, S. A. (2016). Fluorine-18-labeled thymidine positron emission tomography (FLT-PET) as an index of cell proliferation after pharmacological ascorbate-based therapy. *Rad. Res.* 185, 31–38.

Domercq, M., Szczupak, B., and Gejo, J. (2016). PET imaging with [(18)F]FSPG evidences the role of system xc(-) on brain inflammation following cerebral ischemia in rats. *Theranostics* 6, 1753–1767.

Dupont, A. C., Largeau, B., Santiago Ribeiro, M. J., Guilloteau, D., Tronel, C., and Arlicot, N. (2017). Translocator protein-18 kDa (TSPO) positron emission tomography (PET) imaging and its clinical impact in neurodegenerative diseases. *Intern. J. Mol. Sci.* 18:785.

Justicia, C., Perez-Asensio, F. J., Burguete, M. C., Salom, J. B., and Planas, A. M. (2001). Administration of transforming growth factor-alpha reduces infarct volume after transient focal cerebral ischemia in the rat. *J. Cereb. Blood Flow Metab.* 21, 1097–1104.

Kee, N., Sivalingam, S., Boonstra, R., and Wojtowicz, J. M. (2002). The utility of Ki-67 and BrdU as proliferative markers of adult neurogenesis. *J. Neurosci. Methods* 115, 97–105.

Lee, J. C., Mayer-Proschel, M., and Rao, M. S. (2000). Gliogenesis in the central nervous system. *Glia* 30, 105–121.

Machulla, H. J., Blocher, A., Kuntzsch, M., Piert, M., Wei, R., and Grierson, J. R. (2000). Simplified labeling approach for synthesizing 3′-Deoxy-3′-[18F]fluorothymidine ([18F]FLT). *J. Radioanalyt. Nuclear Chem.* 243, 843–846.

Martin, A., Boisgard, R., Theze, B., Van Camp, N., Kuhnast, B., Damont, A., et al. (2010). Evaluation of the PBR/TSPO radioligand [(18)F]DPA-714 in a rat model of focal cerebral ischemia. *J. Cereb. Blood Flow Metab.* 30, 230–241.

McHugh, C. I., Thipparthi, M. R., Lawhorn-Crews, J. M., Polin, L., Gadgeel, S., Akoury, J., et al. (2018). Using radiolabeled 3′-Deoxy-3′-(18)F-fluorothymidine with PET to monitor the effect of dexamethasone on non-small cell lung cancer. *J. Nuclear Med.* 59, 1544–1550.

Moraga, A., Gomez-Vallejo, V., Cuartero, M. I., Szczupak, B., Sebastián, E. S., Markuerkiaga, I., et al. (2016). Imaging the role of toll-like receptor 4 on cell proliferation and inflammation after cerebral ischemia by positron emission tomography. *J. Cereb. Blood Flow Metab.* 36, 702–708.

Moskowitz, M. A., Lo, E. H., and Iadecola, C. (2010). The science of stroke: mechanisms in search of treatments. *Neuron* 67, 181–198.

Nikaki, A., Angelidis, G., Efthimiadou, R., Tsougos, I., Valotassiou, V., Fountas, K., et al. (2017). (18)F-fluorothymidine PET imaging in gliomas: an update. *Ann. Nuclear Med.* 31, 495–505.

Pulagam, K. R., Colas, L., Padro, D., Plaza-García, S., Gómez-Vallejo, V., Higuchi, M., et al. (2017). Evaluation of the novel TSPO radiotracer [(18)F] VUIIS1008 in a preclinical model of cerebral ischemia in rats. *EJNMMI Res.* 7:93.

Rojas, S., Martin, A., and Arranz, M. J. (2007). Imaging brain inflammation with [(11)C]PK11195 by PET and induction of the peripheral-type benzodiazepine receptor after transient focal ischemia in rats. *J. Cereb. Blood Flow Metab.* 27, 1975–1986.

Rueger, M. A., Backes, H., Walberer, M., Neumaier, B., Ullrich, R., Simard, M. L., et al. (2010). Noninvasive imaging of endogenous neural stem cell mobilization in vivo using positron emission tomography. *J. Neurosci.* 30, 6454–6460.

Rueger, M. A., Muesken, S., Walberer, M., Jantzen, S. U., Schnakenburg, K., Backes, H., et al. (2012). Effects of minocycline on endogenous neural stem cells after experimental stroke. *Neuroscience* 215, 174–183.

Rusznak, Z., Henskens, W., Schofield, E., Kim, W. S., and Fu, Y. (2016). Adult neurogenesis and gliogenesis: possible mechanisms for neurorestoration. *Exper. Neurobiol.* 25, 103–112.

Schelhaas, S., Heinzmann, K., Bollineni, V. R., Kramer, G. M., Liu, Y., Waterton, J. C., et al. (2017). Preclinical applications of 3′-Deoxy-3′-[(18)F]fluorothymidine in oncology - a systematic review. *Theranostics* 7, 40–50.

Schelhaas, S., Wachsmuth, L., and Hermann, S. (2018). Thymidine metabolism as a confounding factor for 3′-deoxy-3′-(18)F-fluorothymidine uptake after therapy in a colorectal cancer model. *J. Nuclear Med.* 59, 1063–1069.

Shields, A. F., Grierson, J. R., Dohmen, B. M., Machulla, H. J., Stayanoff, J. C., Lawhorn-Crews, J. M., et al. (1998). Imaging proliferation in vivo with [F-18]FLT and positron emission tomography. *Nat. Med.* 4, 1334–1336.

Tichauer, K. M., Wang, Y., Pogue, B. W., and Liu, J. T. (2015). Quantitative in vivo cell-surface receptor imaging in oncology: kinetic modeling and paired-agent principles from nuclear medicine and optical imaging. *Phys. Med. Biol.* 60, R239–R269.

Conflict of Interest: The authors declare that the research was conducted in the absence of any commercial or financial relationships that could be construed as a potential conflict of interest.

Copyright © 2020 Ardaya, Joya, Padro, Plaza-García, Gómez-Vallejo, Sánchez, Garbizu, Cossío, Matute, Cavaliere, Llop and Martín. This is an open-access article distributed under the terms of the Creative Commons Attribution License (CC BY). The use, distribution or reproduction in other forums is permitted, provided the original author(s) and the copyright owner(s) are credited and that the original publication in this journal is cited, in accordance with accepted academic practice. No use, distribution or reproduction is permitted which does not comply with these terms.

frontiers in Neuroscience

REVIEW
published: 11 August 2020
doi: 10.3389/fnins.2020.00819

Deciphering Brain Function by Miniaturized Fluorescence Microscopy in Freely Behaving Animals

Sarah Malvaut[1,2†], Vlad-Stefan Constantinescu[1,2†], Harold Dehez[3], Sead Doric[3] and Armen Saghatelyan[1,2]*

[1] CERVO Brain Research Center, Quebec City, QC, Canada, [2] Department of Psychiatry and Neuroscience, Universite Laval, Quebec City, QC, Canada, [3] Doric Lenses Inc., Quebec City, QC, Canada

Animal behavior is regulated by environmental stimuli and is shaped by the activity of neural networks, underscoring the importance of assessing the morpho-functional properties of different populations of cells in freely behaving animals. In recent years, a number of optical tools have been developed to monitor and modulate neuronal and glial activity at the protein, cellular, or network level and have opened up new avenues for studying brain function in freely behaving animals. Tools such as genetically encoded sensors and actuators are now commonly used for studying brain activity and function through their expression in different neuronal ensembles. In parallel, microscopy has also made major progress over the last decades. The advent of miniature microscopes (mini-microscopes also called mini-endoscopes) has become a method of choice for studying brain activity at the cellular and network levels in different brain regions of freely behaving mice. This technique also allows for longitudinal investigations while animals carrying the microscope on their head are performing behavioral tasks. In this review, we will discuss mini-endoscopic imaging and the advantages that these devices offer to research. We will also discuss current limitations of and potential future improvements in mini-endoscopic imaging.

Keywords: miniature endoscopes, mini-endoscopic imaging, animal behavior, GRIN lenses, GCaMP, GECI, Ca^{2+} imaging

OPEN ACCESS

Edited by:
João O. Malva, University of Coimbra, Portugal

Reviewed by:
Daniel Benjamin Aharoni, University of California, Los Angeles, United States
Alberto L. Vazquez, University of Pittsburgh, United States

***Correspondence:**
Armen Saghatelyan
armen.saghatelyan@fmed.ulaval.ca; armen.saghatelyan@crulrg.ulaval.ca

† These authors have contributed equally to this work

Specialty section:
This article was submitted to Brain Imaging Methods, a section of the journal Frontiers in Neuroscience

Received: *20 April 2020*
Accepted: *14 July 2020*
Published: *11 August 2020*

Citation:
Malvaut S, Constantinescu V-S, Dehez H, Doric S and Saghatelyan A (2020) Deciphering Brain Function by Miniaturized Fluorescence Microscopy in Freely Behaving Animals. Front. Neurosci. 14:819. doi: 10.3389/fnins.2020.00819

INTRODUCTION

Understanding how brain functions are shaped by experience and, in turn, how neural networks regulate animal behavior has always been of great interest to the scientific community as well as the general public. One of the long-term aims of neuroscience research is to understand how specific spatio-temporal activity patterns emerging from local neural networks regulate specific animal behaviors. Recording neural activity at the microcircuit level from distinct subsets of neurons and glia in freely behaving animals has thus become essential for studying how experience is represented and processed by the brain. The function of these networks can be interrogated using extracellular multi-electrode recordings (Nicolelis and Ribeiro, 2002), large-scale brain imaging techniques such as functional magnetic resonance imaging (fMRI), voltage-sensitive dye-based imaging, intrinsic optical signal imaging, and positron emission tomography (PET) (Grinvald et al., 1988;

Shoham et al., 1999; Logothetis et al., 2002), or *in vivo* Ca^{2+} imaging using one- and two-photon mini-endoscopes (Dombeck et al., 2007; Kerr et al., 2007; Grewe and Helmchen, 2009). The technique of choice for these types of experiments has mostly involved taking electrophysiological recordings in either awake head-restrained or freely behaving rodents (Wilson and Mcnaughton, 1993; Houweling and Brecht, 2008; Harvey et al., 2009; Niell and Stryker, 2010). This approach has provided a great number of important insights into how neuronal ensembles orchestrate behavior such as the discovery of spatial representation by place and grid cells, for instance (O'keefe and Dostrovsky, 1971; Hafting et al., 2005). However, despite the tremendous value of this technique, the number of cells that can be recorded at a given time is limited by the small number of electrodes that can be used simultaneously. In theory, increasing the number of electrodes should make it possible to record electrophysiological activity in more cells, but the spacing between the electrodes is limited. Electrophysiological recordings also exclude electrically silent cells from the subsequent analysis of network dynamics (Shoham et al., 2006). To address some of these caveats, researchers can now take advantage of dense recordings using multi-tetrode arrays or silicone probes that make it possible to take recordings from large neuronal populations rather than from individual cells. Such large population-level recordings can be used to address questions that otherwise could not have been investigated using data from individual cell recordings (Csicsvari et al., 2003; Harris et al., 2003; Buzsaki, 2004; Dupret et al., 2010; Stensola et al., 2012). However, even with advances in electrophysiological recordings of large subsets of cells, there remain some important aspects that cannot be studied using such techniques. Although electrophysiology allows for distinct cell populations to be differentiated based on waveform shapes (Trainito et al., 2019), it is much more challenging to assess the individual contribution of each subset of recorded cells to the observed network dynamics. Recordings from subcellular structures such as dendrites can be also obtained in freely behaving mice using electrophysiological approaches (Moore et al., 2017). By taking advantage of the immune response that follows a tetrode implant, which allows a dendrite to get trapped between the tetrode tips and the glial encapsulation, it is possible to measure the dendritic membrane voltage in freely behaving rodents (Moore et al., 2017). This methodology could also provide important insights into the electrophysiological correlates of dendritic action potential integration, but has a low success rate and low yield.

The study of brain function has taken a step further with the advent of new optical tools designed to investigate neuronal activity at the protein, cellular, or network level. These include genetically encoded Ca^{2+} indicators (GECIs). Ca^{2+} is an important second messenger involved in the homeostasis of essentially all cells in the brain (Clapham, 1995; Berridge et al., 2000) and GECI-recorded Ca^{2+} fluctuations can be used to study the activity and coding of neural ensembles in basal conditions and in response to stimuli (Tian et al., 2012; Lin and Schnitzer, 2016). Many different versions of GECIs exist, and their repertoire and properties are constantly improving (Dana et al., 2016, 2019; Shen et al., 2020). The green and red Ca^{2+} indicators (GCaMP and RCaMP, respectively) are the most common (Lin and Schnitzer, 2016; Shen et al., 2020). More recently, a quadricolor GECI suite (XCaMP) (Inoue et al., 2019) and a near-infrared Ca^{2+} indicator (Qian et al., 2019) were designed to further expand the palette of GECIs and to study more complex neural dynamics. Using viral or transgenic labeling, GECIs can be expressed all over the brain or in specific neuronal/glial subtypes and are now widely used in the context of learning, memory formation, and plasticity (Jercog et al., 2016). They also allow for long-term investigations of brain activity for up to several weeks and even months (Jercog et al., 2016). In addition to GECIs, current efforts to develop genetically encoded voltage indicators (GEVIs) will eventually make it possible to monitor individual spikes during high-frequency trains of action potentials or subthreshold changes in the membrane potential in selected populations of cells (Bando et al., 2019). This will further increase the palette of functional assessments of neural networks during animal behavior. In addition to functional changes, several morphological modifications such as spine formation/elimination, the dynamics of glia processes, and microglia migration occur in response to environmental stimuli. Furthermore, several regions of the adult brain retain the capacity to renew their cellular populations during injury (Torper and Gotz, 2017) or under homeostatic conditions through adult neurogenesis (Gengatharan et al., 2016; Obernier and Alvarez-Buylla, 2019; Vicidomini et al., 2020). All these morphological changes can be also monitored *in vivo* using live imaging approaches (Berry and Nedivi, 2017; Pilz et al., 2018; Wallace et al., 2020).

In vivo imaging of morpho-functional changes in zebra fish larvae and nematodes has been performed in whole organisms (Ahrens et al., 2012; Nguyen et al., 2016). In rodents, *in vivo* imaging of a given brain region has traditionally been performed by two-photon microscopy in anesthetized or awake head-restrained animals performing specific behavioral tasks. While this allows for long-term and longitudinal recording of brain activity, it is limited to a restricted number of behavioral tasks and cannot be used to study deep brain structures unless the overlying brain regions are removed, which may affect cellular activity and animal behavior. The last two decades saw the advent of miniaturized fluorescent microscopes (also called mini-microscopes or mini-endoscopes) that enable *in vivo* recordings of brain structure and function of freely behaving animals to be taken at the cellular and network levels. These devices, which are similar to benchtop microscopes in their optical designs, contain miniaturized optical parts (mirrors, filters, or even a camera) and can be carried by animals that freely displace in an arena. Displays and recordings of acquired images are then computer assisted, allowing for the modulation of different parameters such as acquisition frame rate, exposure, and illumination power, without any additional manipulation of the recorded animal. Mini-endoscopes have evolved considerably in recent years since the first miniaturized versions were developed (Helmchen et al., 2001) and are still being refined and improved. They have helped provide answers to several unresolved questions regarding brain activity and structure. In this review, we will first present the various models of currently available mini-endoscopes and

provide an overview of their specifications, advantages, and limitations. We will then discuss the *in vivo* applications of mini-endoscopy and the limitations of existing devices as well as future avenues for improving mini-endoscopic microscopy.

CURRENT STATE OF THE ART FOR RECORDING BRAIN ACTIVITY AND STRUCTURE USING MINI-ENDOSCOPES

One-Color Mini-Endoscopes

The first versions of mini-endoscopes were based on two-photon excitation, and some microscope components such as lasers and photomultipliers (PMT) were converted to transmit the excitation light to the head of the animal or to collect emissions through optic fibers. These systems were used for imaging at the surface of the brain (Helmchen et al., 2001; Helmchen, 2002; Flusberg et al., 2005). They were bulky and heavy (25 g, 70 mm high), limiting applications involving naturalistic behavior. Also, the devices could not compensate very well for strong motion artifacts (Helmchen et al., 2001; Helmchen, 2002). Subsequent improvements led to the creation of lighter portable two-photon excitation microscopes (Gobel et al., 2004; Flusberg et al., 2008; Sawinski et al., 2009) that were used to image neural networks in freely moving mice and rats. A promising approach using a portable two-photon excitation-scanning microscope that weighs as little as 2 g was recently introduced to study activity in the entorhinal cortex of freely behaving mice (Zong et al., 2017; Rowland et al., 2018). These systems provide the obvious advantages of two-photon excitation microscopy such as a small excitation volume, increased tissue penetration, reduced phototoxicity, and the possibility of imaging subcellular structures. However, the low two-photon absorption cross-section also imposes high spatial (small focal spot) and temporal (short laser pulse) constraints on two-photon microscopy systems. To get sufficient excitation intensity at focus, it requires high numerical aperture diffraction-limited optics as well as expensive table-top femtosecond pulse lasers with proper dispersion compensation. Laser scanning two-photon microscopes should also be properly stabilized to avoid motion artifacts as the pixels of each image are not recorded simultaneously. It is thus more challenging to use two-photon excitation in a context of mini-endoscopes, suggesting that miniaturized epifluorescence microscopy tends to represent a simpler and more affordable method for imaging activity in neural networks at the cellular level, particularly in deep brain regions while animals are freely behaving.

Several groups have taken advantage of small optical rod lenses [gradient refractive index (GRIN) lenses] (Jung and Schnitzer, 2003; Levene et al., 2004) to build mini-endoscopes. These lenses have a short working distance and can be fixed either at the surface of the brain or inserted into deep brain regions to perform imaging in the superficial or deep brain regions, respectively (Helmchen et al., 2001; Helmchen, 2002; Flusberg et al., 2005). GRIN lenses, which can have different diameters and customizable lengths, have been used for *in vivo* imaging of previously unreachable deep brain structures such as the substantia nigra, the hypothalamus, the parabrachial nucleus, and the basal forebrain (Bocarsly et al., 2015; Fu et al., 2019; Patel et al., 2019). GRIN lenses are usually flat at the tip, making it possible to image cells just below the tip. However, they can also be coupled with a prism mirror allowing for "side-view" imaging. This configuration, in our experience, significantly reduces tissue damage and immune responses compared to blunt probes. In line with this, less tissue damage and better neuronal preservation is observed for well-sharpened and small tip angle silicone probes used for *in vivo* electrophysiological recordings (Edell et al., 1992). The GRIN coupled with a prism has been used for imaging neurons located in different cortical layers (Gulati et al., 2017).

Gradient refractive index implantation is minimally invasive, and the presence of the lens in an animal's brain does not alter the locomotion or behavior of the animal in selected tasks commonly used in neuroscience research (Lee et al., 2016), although this largely depends on the diameter and type of GRIN lens (Resendez et al., 2016). Larger diameter (1 mm) GRIN lenses have been described as being more suitable for an implantation in superficial brain regions such as the cortex or the hippocampus, whereas smaller diameter GRINs are more suitable for deeper brain regions such as the hypothalamus or the ventral tegmental area (Resendez et al., 2016). Slow insertion of probes during implantation or using probes coupled with a prism can minimize possible compression of the brain, restricting it to the front of the GRIN and reducing possible damage (Edell et al., 1992; Levene et al., 2004). For deep brain region imaging, a track in the brain is often created using a sharp needle or blade. Brain tissue aspiration is also used in some cases (Resendez et al., 2016; Gulati et al., 2017; Gonzalez et al., 2019; De Groot et al., 2020). The inflammatory response resulting from implant insertion normally largely clears up after 4 weeks (Bocarsly et al., 2015), or less for sharp-ended implants (Edell et al., 1992; Turner et al., 1999). This observation highlights the need to start recording with miniature endoscopes several weeks post-implantation. A minimal period ranging from 2 to 4 weeks is required before acquiring data using GRIN lenses (Barbera et al., 2019; Fu et al., 2019; Gonzalez et al., 2019). To confirm the correct implantation of a GRIN lens, a *post hoc* analysis in post-mortem brain tissues can be used. This step makes it possible to adapt the stereotaxic coordinates used in different animals (Lee et al., 2016; Resendez et al., 2016). When viral vectors are injected in a defined brain region a few weeks before GRIN implantation, changes in background fluorescence may be also used to ascertain the correct positioning.

As for animals becoming habituated to the imaging device, it is common practice to try to reduce the weight of mini-endoscopes as much possible so as to not interfere with naturalistic behavior of the animals (Resendez et al., 2016). Chronic GRIN implants do not alter animal performance in standard behavioral procedures such as the rotarod test or the Morris water maze (Lee et al., 2016). However, no comparative studies have been reported with regard to the adaptation of animals to mini-endoscopes of different weights and configurations. Further behavioral investigations will be required to accurately evaluate the maximal weight that small rodents like mice can carry on their head without an impact on their behavior and to compare different

mini-endoscopes, some of which are bulkier than others. Also, not all available versions of mini-endoscopes can reach very lateral or anterior brain regions such as the olfactory bulb. In fact, due to size constraints, placing a mini-endoscope in such regions could potentially alter the normal behavior of the animals or even their vision if placed too close to their eyes. Smaller footprint mini-endoscopes may help to resolve this issue.

An important step in the conception of mini-endoscopes is thus the miniaturization of microscope parts. Ghosh et al. (2011), in their first version of a fully miniaturized epifluorescence mini-endoscope, replaced larger external light sources (e.g., Xenon lamps, mercury lamps, high power LEDs, and lasers) with smaller internal LEDs that are efficient and low-cost alternatives. This approach is now widely used in different open source mini-endoscopes designed to image in freely behaving rodents or songbirds. These include the UCLA Miniscope (Cai et al., 2016), the National Institute of Drug Abuse MiniScope (Barbera et al., 2016), the Boston University FinchScope that was developed for imaging in songbirds (Liberti et al., 2017), and the University of Toronto CHEndoscope (Jacob et al., 2018). Although very practical in terms of cost, availability, and size, installing LEDs directly in the microscope body can have some drawbacks. Because of its location in the microscope body, maximum output power is limited in order to minimize potential excessive heat on the animal's head at higher powers normally used for optogenetic stimulations. To alleviate these issues, some commercial one-color mini-endoscopes can be connected to adjustable, exchangeable external light sources such as lasers, laser pumped incoherent sources (Ce:YAG), or LEDs using an optical fiber. However, this has the disadvantage of adding an extra optical fiber above the animal's head.

Mini-endoscopes also take advantage, in their design, of off-the-shelf miniature electronic components such as complementary metal oxide semiconductor (CMOS) sensors for image detection. These sensors support high acquisition frame rates (higher than 30 Hz) and can, in some cases, be coupled to a microphone to record songbird vocalizations (Liberti et al., 2017). Improved versions of mini-endoscopes are currently available from commercial sources (Doric Lenses, Inscopix, and Neurescence) as well as open-source platforms (UCLA Miniscope, NINscope, and FinchScope).

It should be also mentioned that because of their miniaturization and their use in freely behaving animals, device failure may also occur. Unlike tabletop microscopy systems, miniaturized fluorescence microscopes are operated in challenging environments, with the animal moving in different directions and potentially applying some constraints on the microscope and optical fibers. Several approaches have been investigated to reduce the risks of experiment interruption due to microscope failure, including sturdier bodies in hard plastic (Cai et al., 2016) and metal frames (Zong et al., 2017), protected electronics, and connectorized systems with interchangeable cables (Barbera et al., 2016; Cai et al., 2016; Liberti et al., 2017; Jacob et al., 2018; De Groot et al., 2020). Optical components used in miniature endoscopes can be costly and, because of their size, failure can happen during surgical implantation or extraction. To counteract this, Bocarsly et al. (2015) proposed a version of the device, including the implantation in animal's brain of a guide cannula, allowing for the insertion of a GRIN lens for each imaging session. However, it should be noted that the resulting diameter of the imaging probe is larger, which has an impact on brain tissue, as previously reported (Bocarsly et al., 2015; Resendez et al., 2016).

Two-Color Mini-Endoscopes

Functional and structural imaging in a given brain region was, for a long time, restricted to a general cell population or a subset of cells expressing a particular Ca^{2+} indicator or fluorescent marker. More recently, two-color versions of mini-endoscopes have been developed that allow two different fluorophores with different emission and excitation wavelengths to be imaged. However, GRIN lenses have large chromatic aberrations that induce a shift (sometimes up to several tens of microns) in the imaged focal plane when comparing the fluorescence of two different fluorophores. To counteract these aberrations, one solution is to place two CMOS sensors in the microscope body at a specific location to compensate for the focal shift induced by the GRIN lens when imaging the two spectrally distinct fluorophores. Another solution for counteracting chromatic aberrations is to use achromatic lenses. The availability of several versions and colors of GECIs (Dana et al., 2016, 2019; Shen et al., 2020), each with its own emission/excitation spectra, means that it is now possible to image using both green and red Ca^{2+} indicators with similar kinetics (Shen et al., 2020). Two-color mini-endoscopes have a number of advantages. First, when combined with Ca^{2+} indicators of spectrally distinguishable colors (GCaMP and RCaMP, for instance), it is possible to compare the activity of two different cell populations in the same brain region of freely behaving animals. In addition, two-color mini-endoscopes can be used for motion correction. In fact, *xy* and *z* drift can occur when animals are moving, which may create some bias in data analysis and interpretation. This issue can be addressed by performing functional Ca^{2+} imaging combined with morphological fluorescent marker imaging followed by open-source plugin or software processing for motion and drift correction. These systems can be also used for imaging cell populations that can be defined only based on the combinatory genetic labeling approaches, leading to the expression of two different fluorophores (or sensors) by the same cell. Two-color mini-endoscopes can be also used for assessing the interplay between different cellular populations in a given brain region. It should be noted, however, that because of their optical design, two-color mini-endoscopes are bulkier and a longer habituation period for the animal may be required before starting the experiments.

Combined Optogenetic and Imaging Mini-Endoscopes for Studying Brain Connectivity and Disease Pathogenesis

The discovery that neuronal activity can be modulated using light-sensitive ion channels or opsins was a breakthrough in the field of neuroscience (Kim et al., 2017). *In vivo* optogenetic approaches are now widely used to modulate

neuronal activity and to investigate the impact on animal behavior (Kim et al., 2017). It is possible to modulate neuronal activity by either stimulating or inhibiting the activity of a cell population in a given structure while simultaneously imaging the responses of the same or neighboring populations of cells in the same structure or even in a very different, remote structure (Stamatakis et al., 2018). However, the opsin and Ca^{2+} indicators have to be carefully chosen as crosstalk between the channels may affect the recordings (Stamatakis et al., 2018). In addition, the imaging light source attenuates the optogenetic response (Stamatakis et al., 2018), which means that care must be taken in choosing the excitation light source for imaging in order to provide a better signal-to-noise ratio and minimal crosstalk.

De Groot et al. (2020) developed the NINscope, which can be used to simultaneously record and optogenetically stimulate two distant brain structures. The authors reduced the footprint of the mini-endoscope, making it possible to record the Ca^{2+} activity of a subset of cells in a given brain region while optogenetically stimulating cells in many other brain areas using small LEDs installed on the surface of the brain (De Groot et al., 2020). For experiments requiring optogenetic manipulation of deeper brain regions that cannot be targeted with the NINscope, a micro-LED can be implanted inside the brain. The stimulation can then be synchronized with the endoscope imaging (Shin et al., 2017). Combined optogenetic and imaging mini-endoscope baseplates composed of a GRIN relay lens for fluorescence imaging and an optical fiber for opsin activation are also commercially available. These systems offer a customizable length and distance between the imaging cannula and the implanted optical fiber. We used one of these mini-endoscope baseplates to optogenetically induce α-synuclein aggregation in the substantia nigra and to monitor changes in striatal neurons using Ca^{2+} imaging (Bérard et al., 2019).

Multi-Region Imaging With Mini-Endoscopes

The NINscope developed by De Groot et al. (2020) also allows the simultaneous and synchronous imaging of two separate brain regions because of its reduced footprint. This is of particular relevance in a context of brain connectivity as the activity of two distinct regions can be correlated at the cellular level depending on the selected behaviors or stimuli. Simultaneous recording using two separate mini-endoscopes can also be performed in both hemispheres of the same structure (Gonzalez et al., 2019; De Groot et al., 2020). These recordings can be used to investigate the lateralization of brain activity (Gonzalez et al., 2019) and to compare, in the same subject, the activity of two hemispheres to which a different treatment may have been applied. A device allowing for simultaneous imaging of different brain regions is now also commercially available. In fact, because of it small footprint, the fiber bundle-based device from Neurescence (quartet mini-microscope) can record neuronal activity from up to four different brain regions as well as from different animals that are socially interacting, for instance.

Mini-Endoscopes With Dual-Modality Recordings

Mini-endoscopes also allow for dual-modality recording of neuronal activity. Yashiro et al. (2017) used a mini-endoscope system coupled with electrophysiological recordings of neural activity to make simultaneous optical recordings from large neuronal subsets. Such simultaneous optical and electrical recordings may prove to be extremely useful in correlating electrically recorded phenomena (multi-unit activity and local field potentials) with optically recorded Ca^{2+} fluctuations. Combined electrical and Ca^{2+} signal recordings from a single fluorescent neuron *in vivo* have also been made and allow the spiking activity of recorded cells to be correlated with changes in Ca^{2+} dynamics (Lechasseur et al., 2011). In addition to combining imaging and electrophysiological recordings, commercially available dual implant baseplates composed of a GRIN lens and an optical fiber allow Ca^{2+} imaging and photometry recordings in two different brain regions located as close together as 1 mm to be performed. Another potential new application for mini-endoscopes involves combining Ca^{2+} imaging with intrinsic optical signals (Senarathna et al., 2019). This device can be used to monitor neuronal activity in large areas of the brain and subtract the hemodynamic signal, providing insights into neurovascular coupling (Senarathna et al., 2019). Other types of dual-modality recording mini-endoscopes are also available, such as those that allow for combined Ca^{2+} imaging and bird vocalization recording (Liberti et al., 2017). It is likely that in coming years other dual-modality mini-endoscopes will be developed. These systems could allow for combining imaging and local drug delivery via integrated cannula, Ca^{2+} activity recordings and respiration/sniffing assessments, or simultaneous Ca^{2+} and voltage imaging, for instance. This in turn will make it possible to perform multi-modal assesments of neural networks during unrestricted animal behavior.

Electronic Modulation of the Field of View: eFocus Mini-Endoscopes

A non-negligible drawback of traditional mini-endoscopes was, for a long time, the inability to change the focus prior to or during image acquisition, limiting imaging to a single focal plane (Barretto and Schnitzer, 2012; Hamel et al., 2015). Indeed over time, following consecutive imaging sessions, the focal plane can change slightly and tracking the same cells can become challenging. To counteract this, the first versions of commercial and open-source mini-endoscopes offered the possibility to manually and mechanically adjust the image focus with a slider, screw, or turret before starting a recording, which resulted in additional manipulations of both the device and the animal (Ghosh et al., 2011; Barbera et al., 2016; Cai et al., 2016; Liberti et al., 2017; Jacob et al., 2018). To deal with this issue, updated electronically focused versions of endoscopes have been released by several companies such as Inscopix and Doric Lenses or were built from open-source designs (e.g., UCLA miniscope version 4). These versions make it possible to adjust the focus remotely and thus avoid mechanical manipulations of the endoscope while the animals are freely behaving. To that end, several groups

have taken advantage of different strategies. For example, electro-wetting liquid lenses, which are small devices containing two non-miscible liquids, have been used. They allow for the rapid deformation of the lenses and thus the electronic focusing of the field of view by applying a voltage (Grewe et al., 2011; Zou et al., 2015; Ozbay et al., 2018). Electronically tunable liquid crystal lenses have also been used (Bagramyan et al., 2017). These lenses, which are traditionally used in liquid crystal displays, consume little energy and are lighter than electro-wetting liquid lenses, two important parameters for improving mini-endoscopes without compromising their size and weight.

IN VIVO APPLICATIONS OF MINI-ENDOSCOPIC IMAGING

As discussed above, two main approaches for optical brain imaging studies on live animals have emerged—those that require the experimental subjects to be head-fixed, such as two-photon excitation microscopy, and those that allow for unrestrained behavior, such as mini-endoscopes. Each technique has its share of advantages and drawbacks. Depending on the nature of the study, researchers can now use a variety of methods that can accommodate either imaging approach. New advancements in fluorescent reporter proteins, in particular GECIs and GEVIs, mean that neuroscientists can perform two-color fluorescence imaging and can distinguish the activity of a dual-labeled subset within a broad population of indicator-labeled cells (Chen et al., 2013; Inoue et al., 2015; Malvaut et al., 2017). The head-fixed imaging approaches that use high-performance lenses and the optical sectioning provided by two-photon microscopy allow for the interrogation of activity patterns during animal behavior at subcellular levels such as in dendrites, dendritic spines, and even axonal boutons (Petreanu et al., 2012; Xu et al., 2012; Boyd et al., 2015; Sheffield and Dombeck, 2015). The head-fixed paradigm can also make intracranial drug delivery easier (Nimmerjahn et al., 2009; Lovett-Barron et al., 2014). Behavioral assays, including adapted fear conditioning paradigms (Lovett-Barron et al., 2014), controlled delivery of sensory stimuli (Verhagen et al., 2007; Carey et al., 2009; Andermann et al., 2011; Blauvelt et al., 2013; Patterson et al., 2013; Miller et al., 2014), and perceptual discrimination tasks (Andermann et al., 2010; Komiyama et al., 2010; O'connor et al., 2010) can now be done in a head-restrained configuration to study changes at subcellular levels during complex behavioral tasks. Another exciting avenue for head-restrained optical imaging in live animals involves the use of virtual reality approaches (Harvey et al., 2009, 2012; Dombeck et al., 2010), which could provide new information about an animal's spatial navigation.

However, even with the enrichment of the behavioral repertoire that can be tested during head-restrained experiments, the array of behavioral manipulations is still restricted and is associated with the stress that the animals may encounter during head fixation and imaging. This stress can have an adverse effect on the outcome of the behavioral analysis and is likely to affect the neuronal activity patterns recorded (Thurley and Ayaz, 2017). Miniaturized head-mounted imaging devices were designed to circumvent these shortcomings. The main motivation for these devices was first and foremost their ability to record activity from many neurons in an animal that is unrestrained and that can display natural innate behavior as well as a broad array of social behaviors such as fighting, mating, care-giving, and other forms of interaction. The need to accurately monitor cell activity in freely behaving experimental subjects has led to recent advances in mini-endoscopic imaging that make it possible to record neuronal activity simultaneously from different brain regions (De Groot et al., 2020), to combine Ca^{2+} imaging and recordings of other modalities such as electrical recordings of neural activity (Yashiro et al., 2017) or sound vocalizations (Liberti et al., 2017), and to image activity in neural networks at different focal planes and in different neuronal populations using efocus and two-color versions of mini-endoscopes. Also, the versatility of mini-endoscopes enables cell activity to be tracked across a large array of behavioral paradigms established over the last decades (Morris, 1984; Graeff et al., 1998; Nadler et al., 2004).

The main *in vivo* application for mini-endoscopes is the imaging of GECIs in large subsets of neurons in freely behaving animals. As mini-endoscopes have many useful characteristics such as relative ease of use, scalability, and commercial availability, they have seen a significant spread to numerous research fields. The use of mini-endoscopes in neuroscience-related fields such as learning and memory, neuropsychiatric disorders, and drug discovery has enabled scientists to accurately describe temporal changes that neuronal circuits exhibit during memory formation and retention as well as modifications due to a pathology. The field of learning and memory has in particular been directly influenced by the development of mini-endoscopes. Tracking the formation and subsequent modification of cellular ensembles that retain learned information, or engrams, over long periods of time has allowed neuroscientists to answer questions about the coding dynamics underlying the neurobiology of long-term memory (Tian et al., 2009; Cai et al., 2016). Established behavioral assays coupled with long-term monitoring of cellular activity has revealed that activity-induced modifications in neuronal CREB (cAMP response element-binding protein) levels are encoded by a shared neural ensemble in the CA1 part of the hippocampus that links distinct contextual memories occurring close in time (Cai et al., 2016). Neuronal activity in the spinal cord of freely behaving mice has also been recorded using a vertebra-affixed mini-endoscope (Sekiguchi et al., 2016). Implanting a mini-endoscope in the spinal cord is technically more challenging than anchoring an implant on top of the skull due to the pronounced movement of the spine within the vertebral column. Although fewer cells can be imaged due the curvature of the spinal cord, these experiments showed that distinct cutaneous stimuli activate overlapping ensembles of dorsal horn neurons and that stimulus type and intensity are encoded at the single-cell level (Sekiguchi et al., 2016).

Mini-endoscopic applications are not limited to the field of learning and memory. Mouse models of diseases are very important for studying the neurobiological basis of a myriad of brain disorders. As most of these diseases are, to some extent, characterized by a deficit in information processing, imaging neural activity in transgenic and knockout mice could

be very advantageous for elucidating the underpinnings of the disease mechanisms (Nestler and Hyman, 2010). For example, much more information about alterations in coding dynamics in animal disease models can be inferred from large-scale imaging in freely behaving animals than is possible with electrophysiological measurements. These approaches could also narrow the gap between molecular and behavioral analyses. This concept becomes clear in the context of Alzheimer's disease (AD), where much progress in understanding the molecular pathology underlying the neurodegeneration observed in human patients has led to the emergence of different mouse models that exhibit one or more AD hallmarks (b-amyloid, presenilins, apolipoprotein E, and Tau) (Knowles et al., 2009; Sterniczuk et al., 2010; Filali et al., 2012; Youmans et al., 2012). However, little is known about how these molecular pathways influence population dynamics during memory encoding and retrieval. With the advent of mini-endoscopy, longitudinal imaging in different AD models during the performance of memory tests is now feasible and could shed new light on memory coding dysfunctions in AD as well as in other neurological and psychiatric disorders (Ziv and Ghosh, 2015). As in the case of AD, the use of mini-endoscopes in animal models of other neurodegenerative disorders and brain trauma may allow the early hallmarks of disease manifestation to be deciphered. These mini-endoscopes combined with optogenetic stimulation can also be used to induce molecular alterations in cells and study disease progression. For example, it is now possible to optogenetically induce the aggregation of α-synuclein in dopaminergic neurons in the substantia nigra and to study alterations in the nigrostriatal pathway and in the network activity of striatal neurons using longitudinal mini-endoscopic Ca^{2+} imaging (Bérard et al., 2019).

Drug discovery could also benefit from mini-endoscopic imaging. Although much research has focused on the pharmacological and molecular mechanisms of drugs at the cellular level, much less attention has been directed at understanding the effect of drugs on neuronal coding. Berdyyeva et al. (2014) showed that a GABA-A agonist used for treating insomnia reduces hippocampal neuronal firing in freely behaving mice. This result, although not surprising, shed light on the need to correlate neuronal dynamics with the effects of chronic drug administration and to identify the effects of the drugs on the overall neuronal network. Addressing these issues would further advance our ability to design future therapies for treating brain diseases (Ziv and Ghosh, 2015).

The capability of mini-endoscopes to record neural activity in freely behaving animals can be further enhanced by using optogenetic stimulations (Stamatakis et al., 2018) or by combining two different recording techniques such as extracellular electrophysiological recordings with Ca^{2+} imaging in freely behaving animals (Yashiro et al., 2017). Stamatakis et al. (2018) used a mini-endoscope that jointly records optical neural activity and light-induced alterations of cellular ensemble activity in the same field-of-view. Other researchers have used a device to optogenetically stimulate brain regions away from the imaging field-of-view (Shin et al., 2017; Bérard et al., 2019; Senarathna et al., 2019). Engineering advances in the manufacture of mini-endoscopes have led to a reduction in the weight and size of these devices, making it possible to simultaneously record cellular activities in different brain regions as was done using the NINscope (De Groot et al., 2020). Such types of experiments will yield new data subsets that can be used to analyze the extent to which lateralization occurs during behavior and learning and to track the network stability of multi-region cellular ensembles over long periods of time (Gonzalez et al., 2019).

Mini-endoscopes are mostly used to investigate *in vivo* brain function in freely behaving animals by Ca^{2+} imaging of cell populations in a given region and are evolving in parallel with improvements in GECIs. The use of such powerful tools will likely expand to the study of other processes underlying brain activity. For instance, an *in vivo* two-photon investigation of adult neurogenesis and, more particularly, stem cell division has been already performed in anesthetized head-restrained animals (Pilz et al., 2018). Mini-endoscopes could help unravel this process in freely behaving animals and to correlate stem cell division with naturalistic patterns of animal behavior. These experiments can be performed under homeostatic conditions in known neurogenic regions of the brain like the dentate gyrus or the subventricular zone, as well as after injury and neuronal regeneration. In line with this, mini-endoscopic imaging has shown that coupling pre-existing neurons to the cerebrovascular system regulates adult hippocampal neurogenesis (Shen et al., 2019) and that newborn neurons in the adult dentate gyrus migrate laterally first to increase their dispersion (Wang et al., 2019). The migration of neuronal progenitors and microglial cells following different neurodegenerative disorders and brain trauma can also be recorded by mini-endoscopic imaging. In addition, the use of miniaturized two-photon microscopes makes it possible to image Ca^{2+} activity in dendrites (Zong et al., 2017) and may be used in the future to image other sub-cellular structures. Future studies will certainly deepen our understanding of the cellular and molecular mechanisms operating in homeostatic and diseased conditions.

LIMITATIONS AND FUTURE AVENUES FOR MINI-ENDOSCOPIC IMAGING

Given the experimentally proven benefits and versatility of mini-endoscopes for neuroscience research, it has become increasingly clear that the impact of these devices will grow exponentially. However, they still have some limitations and drawbacks and further improvements are needed. The weight and size of mini-endoscopes are crucial and should be further improved to enable unrestrained one- and two-photon mini-endoscopic imaging in freely behaving mice and other small animal models. Similarly, the footprint of mini-endoscopes should be reduced for multi-region imaging in order to record activity from adjacent brain areas. Another caveat is that most of the mini-endoscopes used in freely behaving animals need to be tethered to optical components that are too big and too heavy to be mounted on an animal's head, which means that more complex social behaviors

such as social interactions, mating, and mate aggression cannot be fully investigated due to the obvious physical constraints. The poor optical sectioning of one-photon mini-endoscopes and the major aberrations caused by their optical components (GRIN lenses) should also be taken into consideration and be improved. Below we discuss some of the avenues for addressing these issues.

Optical Sectioning

Despite the advantages of wide-field epifluorescence mini-endoscopy (large field of view, small dimensions, and technical simplicity), these systems do not provide the optical sectioning of widely used tabletop systems such as confocal or two-photon microscopes or two-photon mini-endoscopes. As a consequence, image contrast in the focal plane is strongly attenuated by the out-of-focus fluorescent background when imaging densely labeled structures, especially in scattering media. The strong background limits neuronal and glial activity recording to the soma, as smaller structures such as dendrites, dendritic spines, and glial processes are too dim to be resolved. One of the key avenues for future developments is thus the integration and miniaturization of non-scanning optical sectioning systems already offered in large-scale microscopes.

Among non-scanning techniques, the tabletop version of the HiLo microscope has generated a great deal of interest (Lim et al., 2011; Lauterbach et al., 2015). The HiLo microscopy technique is based on epifluorescence microscopy and makes it possible to reject the out-of-focus fluorescent background by processing two images, one recorded with a uniform illumination and the other recorded with a high contrast pattern. HiLo microscopy provides high contrast images with optical sectioning similar to confocal microscopy at the expense of half the camera frame rate. The use of speckle illumination for the high contrast illumination has been proposed, as fast switching from uniform to speckle illumination can be obtained with the simple addition of a diffuser and a galvanometric scanner. HiLo microscopy has already been used for endoscopic applications using a flexible fiber bundle to deliver shaped illumination to the sample and to collect the fluorescence (Ford et al., 2012). Although fiber bundles allow images and illumination patterns to be relayed over long distances (up to meters), they are more rigid than the smaller diameter multi-mode fibers used to deliver light in experiments on freely behaving animals. They also have a small core fill factor, which results in low optical transmission. These properties limit their use for dimmer fluorescent signal recording in freely behaving small animals. Generating both illumination types in the microscope body at the expense of the size of the system is a good alternative to fiber bundles, and the technical simplicity of the HiLo microscopy technique makes it a good candidate for miniaturization.

More recently, it has been proposed that the light field microscopy (LFM) and seeded iterative demixing (SID) techniques can be integrated into miniaturized microscopes (Nobauer et al., 2017; Skocek et al., 2018). These computational methods only require minor hardware modifications to the microscope body by inserting a microlens array in the detection pathway of a miniaturized epifluorescence microscope. A 700 μm $\times$ 600 μm $\times$ 360 μm volume has been imaged at a frequency of 16 Hz with a discrimination threshold between cells of 15 microns. Despite the complex analytics and lower spatial resolution of this method, the reduced number of optical components and the extraction of a large volumetric amount of data makes it a good candidate for Ca^{2+} activity recording in freely behaving animals with improved optical sectioning.

As mentioned above, the first versions of mini-endoscopes were based on a two-photon excitation principle that provides superior optical sectioning (Helmchen et al., 2001; Helmchen, 2002; Flusberg et al., 2005). However, these systems are bulkier and heavier, which limits the behavioral paradigms that can be studied. In these versions, the laser scanning mechanism is either located proximally on the animal for higher resolution and sensitivity, or remotely and is connected to the animal with a fiber bundle to limit the number of optical components on the animal (Ozbay et al., 2015, 2018). To reduce the weight of the imaging systems, miniaturized scanning systems were developed based on micro-mechanical systems (MEMS), scanning mirrors (Piyawattanametha et al., 2006; Zong et al., 2017), and piezoelectric actuators (Engelbrecht et al., 2008). High resolution miniaturized two-photon mini-endoscopes capable of imaging a 130 μm $\times$ 130 μm-field of view at 40 Hz have been used to record Ca^{2+} activity in dendrites and spines in freely behaving animals (Zong et al., 2017). In this system, a hollow core photonic crystal fiber and an achromatic objective lens are used to minimize light pulse broadening and maintain the high intensity at focus essential for two-photon excitation. However, this work was done in the first layers of the brain (visual cortex). Minimizing pulse broadening remains one of the main challenges of deep brain imaging. To achieve this, the chromatic aberration of the GRIN lenses used for deep brain imaging has to be properly compensated without increasing the outer diameter of the implant. This will require the development of new minimally invasive achromatic optical probes. Another interesting approach to increase the imaging depth without using GRIN lenses is miniaturized three-photon microscopy. Klioutchnikov et al. (2020) recently designed a three-photon microscope capable of recording calcium transients at multiple cortical depths of up to 1120 microns in freely behaving animals. However, the weight of the device developed by Klioutchnikov et al. (2020) (around 5 g) restricts its use for now to bigger rodents such as rats.

Miniaturized confocal microscopes with a scanning system placed on the animal would provide optical sectioning without a complex laser system and non-linear effect management. The main drawback of confocal microscopy compared to two-photon microscopy is its lower excitation wavelength, which creates more scattering and higher phototoxicity. The chromatic aberrations of the optical system, including the GRIN relay lens, will also have to be properly compensated to ensure that the pinhole and object plane remain in conjugated planes.

Optical Aberration Compensation

The high numerical aperture and the small outer diameter of GRIN lenses (0.5–1 mm) allow the imaging of structures located several millimeters deep in tissue with minimal invasiveness. In comparison, relay lenses made of optically homogenous materials

with a similar numerical aperture are at least five times larger in diameter. Given this, GRIN lenses have become the preferred option for *in vivo* deep structure imaging. However, GRIN lenses also suffer from high intrinsic on-axis and off-axis optical aberrations (astigmatism and chromatic) and have the highest optical aberrations in miniaturized microscopy systems, leading to lower spatial resolutions and smaller effective fields of view, especially with high numerical aperture GRIN lenses. To solve this issue, adaptive optics methods have been used in two-photon mini-endoscopes. One of these methods allows the recovery of diffraction-limited resolution in a large field of view by measuring and correcting off-axis aberrations using pupil segmentation-based adaptive optics (Wang and Ji, 2012). Future developments in miniature microscopy would also benefit from the use of miniature tunable liquid crystal lenses and miniaturization of the phase modulators used in adaptive optics methods such as phase liquid crystal spatial light modulators. Adding adaptive optics to miniaturized microscopes would also help reduce the impact of light scattering in tissue. The inhomogeneity created by the different components of the sample (water, proteins, and lipids, etc.) distorts the fluorescence wavefront, resulting in lower resolution and contrast.

Wireless Imaging Systems

With the development of tethered miniaturized microscopes, it became possible to correlate brain activity and behavior recordings. However, despite several attempts to reduce the impact of the cables on animal behavior (very flexible cables, motor-assisted rotary-joints, etc.), some complex behavioral studies such as social interaction studies with multiple animals cannot be performed with these systems due to cable entanglement. To overcome these issues, several wireless models have been proposed (Liberti et al., 2017; Barbera et al., 2019; Shuman et al., 2020). One of the main challenges in developing wireless systems is minimizing their size and weight by, for instance, reducing the size of the lithium polymer (LiPo) batteries. Several avenues have been explored to reduce power consumption and use lighter batteries: limiting the number of on-board electronic components with on-site recording (Barbera et al., 2019; Shuman et al., 2020) and using low resolution sensors to restrict the amount of transferred data (Liberti et al., 2017). Using a battery backpack for a better distribution of the weight has also been explored (Barbera et al., 2019). For example, Liberti et al. (2017) introduced the FinchScope, a wireless mini-endoscope that uses a 2 g wireless transmitter and a LiPo battery. Barbera et al. (2019) also introduced a wireless mini-endoscope that is powered by a battery backpack anchored on the animal's back and that is equipped with Micro SD card storage. They were able to record the activity of medium spiny neurons (MSNs) in the dorsal striatum of two freely behaving and interacting mice. In both studies, power was supplied to the microscope by miniature LiPo batteries, which depending on their size, can provide power for 30 min to 1 h at the expense of increasing the weight of the microscope to several grams (Liberti et al., 2017). For future developments, local recording remains a very good solution for reducing the weight of the system. Transferring data samples at a very low frame rate (0.2–1 Hz) and adding a communication interface for the synchronization with external components such as behavior cameras would improve system feedback. The development of new wireless systems should also take into account future behavioral studies aiming to assess the impact of the weight and its distribution (e.g., backpack battery versus integrated battery) on animal behavior. Further improvements are required to optimize wireless mini-endoscopes, improvements that will largely benefit the neuroscience field by expanding the number of possible behavioral experiments that can be performed while monitoring brain activity. The potential of this technique can also be extended to animals that exhibit more complex social behavior like monkeys and small primates. In addition, more complex social behaviors can be assessed without the constraints of the cable from the imaging device.

GENERAL CONCLUSION

Imaging neuronal activity using various sensors and actuators has emerged as a powerful tool that allows neuroscientists to record large-scale neuronal activity in freely behaving animals. Traditional tools used for imaging such as two-photon excitation microscopy have opened up the possibility of imaging Ca^{2+} activity patterns at the cellular and subcellular levels with unprecedented optical resolution. But these experimental setups are costly and require specific infrastructures that limit their dissemination among large numbers of laboratories. Also, these setups require the animals to be head-restrained during the imaging phase, which markedly limits the behavioral repertoire that can be tested. The development of mini-endoscopes has given rise to a new class of devices that have proven to be very useful in acquiring and correlating functional cellular signals from cortical and deep brain regions to animal behavior. The ease of use coupled with the portability and relative low cost of mini-endoscopes has provided a much-needed technical alternative. The capacity to take recordings from large neuronal populations in freely behaving animals has made it possible to analyze large-scale Ca^{2+} imaging data with higher statistical power and to discover different types of coding dynamics related to animal behavior. The versatility of these devices also provides a good platform for improvements to the original design based on research requirements. Designs that incorporate parallel electrophysiological recordings or that allow all-optical circuit-level investigations by combining imaging with optogenetic manipulations can be used to further dissect activity at the microcircuit level and increase our understanding of neural processes underlying animal behavior. The ability to construct lightweight small mini-endoscopes will contribute to animal well-being, will improve the read-out of neural activity under natural conditions, and will expand research to other animal models. By decreasing the size of these devices, mini-endoscopes now also permit the use of multiple devices on the same experimental subject, which allows for the imaging of multiple brain areas in mice and other larger animals such as rats and primates. This multi-site recording approach will open up new avenues

for systems neuroscience research, where longitudinal large-scale recordings beyond a single local circuit can be performed and may uncover exciting new information related to circuit activity patterns governing brain-wide functional circuitry and synchronicity. Further improvements to these devices aiming to increase the depth of penetration in living tissue, fine tune spatial and temporal resolution, and add a wireless option for even less restrictive behavioral repertoires are needed to make functional imaging in freely behaving animals more widely accessible. The traditional use of mini-endoscopy is to image Ca^{2+} activity at the neuronal level. However, the advances in fluorescent reporters, onsite lens focus technologies, and two- and three-photon miniaturization will enable scientists to image cellular and subcellular compartments such as dendrites and dendritic spines. Further development of GEVIs, which have much more temporal resolution than GECIs, will push the use of mini-endoscopes even further, giving scientists the means to optically assess voltage changes across membranes and dendritic compartments. This will most likely revolutionize neuroscience research, giving scientists a tool to record, stimulate, and differentiate between the fast electrophysiological events associated with synaptic activity and the slow Ca^{2+} events associated with the various biomolecular processes that occur during learning and memory. In addition, mini-endoscopic imaging approaches may allow scientists to monitor activity related to spine formation/elimination, the dynamics of glia processes, microglia migration, and adult neurogenesis in freely behaving animals. The flexible methodological approach provided by mini-endoscopes will continue to afford neuroscientists with better tools to image large neuronal populations during increasingly less restrained behavioral paradigms. This, in turn, will lead to new datasets that will more accurately depict the relationship between recorded functional and structural activities and animal behavior.

AUTHOR CONTRIBUTIONS

All authors listed have made a substantial, direct and intellectual contribution to the work, and approved it for publication.

FUNDING

This work was supported by a postdoctoral fellowship from Mitacs to SM and an operating grant from the Natural Sciences and Engineering Research Council of Canada (NSERC) to AS.

REFERENCES

Ahrens, M. B., Li, J. M., Orger, M. B., Robson, D. N., Schier, A. F., Engert, F., et al. (2012). Brain-wide neuronal dynamics during motor adaptation in zebrafish. *Nature* 485, 471–477. doi: 10.1038/nature11057

Andermann, M. L., Kerlin, A. M., and Reid, R. C. (2010). Chronic cellular imaging of mouse visual cortex during operant behavior and passive viewing. *Front. Cell Neurosci.* 4:3. doi: 10.3389/fncel.2010.00003

Andermann, M. L., Kerlin, A. M., Roumis, D. K., Glickfeld, L. L., and Reid, R. C. (2011). Functional specialization of mouse higher visual cortical areas. *Neuron* 72, 1025–1039. doi: 10.1016/j.neuron.2011.11.013

Bagramyan, A., Galstian, T., and Saghatelyan, A. (2017). Motion-free endoscopic system for brain imaging at variable focal depth using liquid crystal lenses. *J Biophoton.* 10, 762–774. doi: 10.1002/jbio.201500261

Bando, Y., Sakamoto, M., Kim, S., Ayzenshtat, I., and Yuste, R. (2019). Comparative evaluation of genetically encoded voltage indicators. *Cell Rep* 26, e804.

Barbera, G., Liang, B., Zhang, L., Gerfen, C. R., Culurciello, E., Chen, R., et al. (2016). Spatially compact neural clusters in the dorsal striatum encode locomotion relevant information. *Neuron* 92, 202–213. doi: 10.1016/j.neuron.2016.08.037

Barbera, G., Liang, B., Zhang, L., Li, Y., and Lin, D. T. (2019). A wireless miniScope for deep brain imaging in freely moving mice. *J. Neurosci. Methods* 323, 56–60. doi: 10.1016/j.jneumeth.2019.05.008

Barretto, R. P., and Schnitzer, M. J. (2012). In vivo optical microendoscopy for imaging cells lying deep within live tissue. *Cold Spring. Harb. Protoc.* 2012, 1029–1034.

Bérard, M., Sheta, R., Malvaut, S., Turmel, R., Alpaugh, M. J., Dubois, M., et al. (2019). *Optogenetic-Mediated Spatiotemporal Control of α-Synuclein Aggregation Disrupts Nigrostriatal Transmission and Precipitates Neurodegeneration. NEURON-D-19-01059*. Available online at: https://ssrn.com/abstract=3416893 (accessed July 9, 2019).

Berdyyeva, T., Otte, S., Aluisio, L., Ziv, Y., Burns, L. D., and Dugovic, C. (2014). Zolpidem reduces hippocampal neuronal activity in freely behaving mice: a large scale calcium imaging study with miniaturized fluorescence microscope. *PLoS ONE* 9:e112068. doi: 10.1371/journal.pone.0112068

Berridge, M. J., Lipp, P., and Bootman, M. D. (2000). The versatility and universality of calcium signalling. *Nat. Rev. Mol. Cell Biol.* 1, 11–21. doi: 10.1038/35036035

Berry, K. P., and Nedivi, E. (2017). Spine dynamics: are they all the same? *Neuron* 96, 43–55. doi: 10.1016/j.neuron.2017.08.008

Blauvelt, D. G., Sato, T. F., Wienisch, M., Knopfel, T., and Murthy, V. N. (2013). Distinct spatiotemporal activity in principal neurons of the mouse olfactory bulb in anesthetized and awake states. *Front. Neural Circuits* 7:46. doi: 10.3389/fncir.2013.00046

Bocarsly, M. E., Jiang, W. C., Wang, C., Dudman, J. T., Ji, N., and Aponte, Y. (2015). Minimally invasive microendoscopy system for in vivo functional imaging of deep nuclei in the mouse brain. *Biomed. Opt. Express* 6, 4546–4556.

Boyd, A. M., Kato, H. K., Komiyama, T., and Isaacson, J. S. (2015). Broadcasting of cortical activity to the olfactory bulb. *Cell Rep.* 10, 1032–1039. doi: 10.1016/j.celrep.2015.01.047

Buzsaki, G. (2004). Large-scale recording of neuronal ensembles. *Nat. Neurosci.* 7, 446–451. doi: 10.1038/nn1233

Cai, D. J., Aharoni, D., Shuman, T., Shobe, J., Biane, J., Song, W., et al. (2016). A shared neural ensemble links distinct contextual memories encoded close in time. *Nature* 534, 115–118. doi: 10.1038/nature17955

Carey, R. M., Verhagen, J. V., Wesson, D. W., Pirez, N., and Wachowiak, M. (2009). Temporal structure of receptor neuron input to the olfactory bulb imaged in behaving rats. *J. Neurophysiol.* 101, 1073–1088. doi: 10.1152/jn.90902.2008

Chen, T. W., Wardill, T. J., Sun, Y., Pulver, S. R., Renninger, S. L., and Baohan, A. (2013). Ultrasensitive fluorescent proteins for imaging neuronal activity. *Nature* 499, 295–300. doi: 10.1038/nature12354

Clapham, D. E. (1995). Calcium signaling. *Cell* 80, 259–268.

Csicsvari, J., Henze, D. A., Jamieson, B., Harris, K. D., Sirota, A., Bartho, P., et al. (2003). Massively parallel recording of unit and local field potentials with silicon-based electrodes. *J. Neurophysiol.* 90, 1314–1323. doi: 10.1152/jn.00116.2003

Dana, H., Mohar, B., Sun, Y., Narayan, S., Gordus, A., Hasseman, J. P., et al. (2016). Sensitive red protein calcium indicators for imaging neural activity. *Elife* 5:e12727.

Dana, H., Sun, Y., Mohar, B., Hulse, B. K., Kerlin, A. M., Hasseman, J. P., et al. (2019). High-performance calcium sensors for imaging activity in neuronal populations and microcompartments. *Nat. Methods* 16, 649–657. doi: 10.1038/s41592-019-0435-6

De Groot, A., Van Den Boom, B. J., Van Genderen, R. M., Coppens, J., Van Veldhuijzen, J., Bos, J., et al. (2020). NINscope, a versatile miniscope for multi-region circuit investigations. *Elife* 9:e49987.

Dombeck, D. A., Harvey, C. D., Tian, L., Looger, L. L., and Tank, D. W. (2010). Functional imaging of hippocampal place cells at cellular resolution during virtual navigation. *Nat. Neurosci.* 13, 1433–1440. doi: 10.1038/nn.2648

Dombeck, D. A., Khabbaz, A. N., Collman, F., Adelman, T. L., and Tank, D. W. (2007). Imaging large-scale neural activity with cellular resolution in awake, mobile mice. *Neuron* 56, 43–57. doi: 10.1016/j.neuron.2007.08.003

Dupret, D., O'neill, J., Pleydell-Bouverie, B., and Csicsvari, J. (2010). The reorganization and reactivation of hippocampal maps predict spatial memory performance. *Nat. Neurosci.* 13, 995–1002. doi: 10.1038/nn.2599

Edell, D. J., Toi, V. V., Mcneil, V. M., and Clark, L. D. (1992). Factors influencing the biocompatibility of insertable silicon microshafts in cerebral cortex. *IEEE Trans. Biomed. Eng.* 39, 635–643. doi: 10.1109/10.141202

Engelbrecht, C. J., Johnston, R. S., Seibel, E. J., and Helmchen, F. (2008). Ultra-compact fiber-optic two-photon microscope for functional fluorescence imaging in vivo. *Opt Express* 16, 5556–5564.

Filali, M., Lalonde, R., Theriault, P., Julien, C., Calon, F., and Planel, E. (2012). Cognitive and non-cognitive behaviors in the triple transgenic mouse model of Alzheimer's disease expressing mutated APP, PS1, and Mapt (3xTg-AD). *Behav. Brain Res.* 234, 334–342. doi: 10.1016/j.bbr.2012.07.004

Flusberg, B. A., Jung, J. C., Cocker, E. D., Anderson, E. P., and Schnitzer, M. J. (2005). In vivo brain imaging using a portable 3.9 gram two-photon fluorescence microendoscope. *Opt. Lett.* 30, 2272–2274.

Flusberg, B. A., Nimmerjahn, A., Cocker, E. D., Mukamel, E. A., Barretto, R. P., Ko, T. H., et al. (2008). High-speed, miniaturized fluorescence microscopy in freely moving mice. *Nat. Methods* 5, 935–938. doi: 10.1038/nmeth.1256

Ford, T. N., Lim, D., and Mertz, J. (2012). Fast optically sectioned fluorescence HiLo endomicroscopy. *J. Biomed. Opt.* 17, 021105. doi: 10.1117/1.jbo.17.2.021105

Fu, O., Iwai, Y., Kondoh, K., Misaka, T., Minokoshi, Y., and Nakajima, K. I. (2019). SatB2-expressing neurons in the parabrachial nucleus encode sweet taste. *Cell Rep.* 27, 1650–1656.e1654.

Gengatharan, A., Bammann, R. R., and Saghatelyan, A. (2016). The role of astrocytes in the generation, migration, and integration of new neurons in the adult olfactory bulb. *Front. Neurosci.* 10:149. doi: 10.3389/fnins.2016.00149

Ghosh, K. K., Burns, L. D., Cocker, E. D., Nimmerjahn, A., Ziv, Y., Gamal, A. E., et al. (2011). Miniaturized integration of a fluorescence microscope. *Nat. Methods* 8, 871–878. doi: 10.1038/nmeth.1694

Gobel, W., Kerr, J. N., Nimmerjahn, A., and Helmchen, F. (2004). Miniaturized two-photon microscope based on a flexible coherent fiber bundle and a gradient-index lens objective. *Opt. Lett.* 29, 2521–2523.

Gonzalez, W. G., Zhang, H., Harutyunyan, A., and Lois, C. (2019). Persistence of neuronal representations through time and damage in the hippocampus. *Science* 365, 821–825. doi: 10.1126/science.aav9199

Graeff, F. G., Netto, C. F., and Zangrossi, H. Jr. (1998). The elevated T-maze as an experimental model of anxiety. *Neurosci. Biobehav. Rev.* 23, 237–246. doi: 10.1016/s0149-7634(98)00024-4

Grewe, B. F., and Helmchen, F. (2009). Optical probing of neuronal ensemble activity. *Curr. Opin. Neurobiol.* 19, 520–529. doi: 10.1016/j.conb.2009.09.003

Grewe, B. F., Voigt, F. F., van 't Hoff, M., and Helmchen, F. (2011). Fast two-layer two-photon imaging of neuronal cell populations using an electrically tunable lens. *Biomed. Opt. Express* 2, 2035–2046.

Grinvald, A., Frostig, R. D., Lieke, E., and Hildesheim, R. (1988). Optical imaging of neuronal activity. *Physiol. Rev.* 68, 1285–1366.

Gulati, S., Cao, V. Y., and Otte, S. (2017). Multi-layer cortical Ca2+ imaging in freely moving mice with prism probes and miniaturized fluorescence microscopy. *J. Vis. Exp.* 55579.

Hafting, T., Fyhn, M., Molden, S., Moser, M. B., and Moser, E. I. (2005). Microstructure of a spatial map in the entorhinal cortex. *Nature* 436, 801–806. doi: 10.1038/nature03721

Hamel, E. J., Grewe, B. F., Parker, J. G., and Schnitzer, M. J. (2015). Cellular level brain imaging in behaving mammals: an engineering approach. *Neuron* 86, 140–159. doi: 10.1016/j.neuron.2015.03.055

Harris, K. D., Csicsvari, J., Hirase, H., Dragoi, G., and Buzsaki, G. (2003). Organization of cell assemblies in the hippocampus. *Nature* 424, 552–556. doi: 10.1038/nature01834

Harvey, C. D., Coen, P., and Tank, D. W. (2012). Choice-specific sequences in parietal cortex during a virtual-navigation decision task. *Nature* 484, 62–68. doi: 10.1038/nature10918

Harvey, C. D., Collman, F., Dombeck, D. A., and Tank, D. W. (2009). Intracellular dynamics of hippocampal place cells during virtual navigation. *Nature* 461, 941–946. doi: 10.1038/nature08499

Helmchen, F. (2002). Miniaturization of fluorescence microscopes using fibre optics. *Exp. Physiol.* 87, 737–745. doi: 10.1113/eph8702478

Helmchen, F., Fee, M. S., Tank, D. W., and Denk, W. (2001). A miniature head-mounted two-photon microscope. High-resolution brain imaging in freely moving animals. *Neuron* 31, 903–912. doi: 10.1016/s0896-6273(01)00421-4

Houweling, A. R., and Brecht, M. (2008). Behavioural report of single neuron stimulation in somatosensory cortex. *Nature* 451, 65–68. doi: 10.1038/nature06447

Inoue, M., Takeuchi, A., Horigane, S., Ohkura, M., Gengyo-Ando, K., and Fujii, H. (2015). Rational design of a high-affinity, fast, red calcium indicator R-CaMP2. *Nat. Methods* 12, 64–70. doi: 10.1038/nmeth.3185

Inoue, M., Takeuchi, A., Manita, S., Horigane, S. I., Sakamoto, M., and Kawakami, R. (2019). Rational engineering of XCaMPs, a multicolor GECI suite for in vivo imaging of complex brain Circuit dynamics. *Cell* 177, 1346–1360.e1324.

Jacob, A. D., Ramsaran, A. I., Mocle, A. J., Tran, L. M., Yan, C., Frankland, P. W., et al. (2018). A compact head-mounted endoscope for in vivo calcium imaging in freely behaving mice. *Curr. Protoc. Neurosci.* 84:e51. doi: 10.1002/cpns.51

Jercog, P., Rogerson, T., and Schnitzer, M. J. (2016). Large-scale fluorescence calcium-imaging methods for studies of long-term memory in behaving mammals. *Cold Spring Harb. Perspect. Biol.* 8, a021824. doi: 10.1101/cshperspect.a021824

Jung, J. C., and Schnitzer, M. J. (2003). Multiphoton endoscopy. *Opt. Lett.* 28, 902–904.

Kerr, J. N., De Kock, C. P., Greenberg, D. S., Bruno, R. M., Sakmann, B., and Helmchen, F. (2007). Spatial organization of neuronal population responses in layer 2/3 of rat barrel cortex. *J. Neurosci.* 27, 13316–13328. doi: 10.1523/jneurosci.2210-07.2007

Kim, C. K., Adhikari, A., and Deisseroth, K. (2017). Integration of optogenetics with complementary methodologies in systems neuroscience. *Nat. Rev. Neurosci.* 18, 222–235. doi: 10.1038/nrn.2017.15

Klioutchnikov, A., Wallace, D. J., Frosz, M. H., Zeltner, R., Sawinski, J., Pawlak, V., et al. (2020). Three-photon head-mounted microscope for imaging deep cortical layers in freely moving rats. *Nat. Methods* 17, 509–513. doi: 10.1038/s41592-020-0817-9

Knowles, J. K., Rajadas, J., Nguyen, T. V., Yang, T., Lemieux, M. C., Vander Griend, L., et al. (2009). The p75 neurotrophin receptor promotes amyloid-beta(1-42)-induced neuritic dystrophy in vitro and in vivo. *J. Neurosci.* 29, 10627–10637. doi: 10.1523/jneurosci.0620-09.2009

Komiyama, T., Sato, T. R., O'connor, D. H., Zhang, Y. X., Huber, D., Hooks, B. M., et al. (2010). Learning-related fine-scale specificity imaged in motor cortex circuits of behaving mice. *Nature* 464, 1182–1186. doi: 10.1038/nature08897

Lauterbach, M. A., Ronzitti, E., Sternberg, J. R., Wyart, C., and Emiliani, V. (2015). Fast calcium imaging with optical sectioning via HiLo microscopy. *PLoS ONE* 10:e0143681. doi: 10.1371/journal.pone.0143681

Lechasseur, Y., Dufour, S., Lavertu, G., Bories, C., Deschenes, M., Vallee, R., et al. (2011). A microprobe for parallel optical and electrical recordings from single neurons in vivo. *Nat. Methods* 8, 319–325. doi: 10.1038/nmeth.1572

Lee, S. A., Holly, K. S., Voziyanov, V., Villalba, S. L., Tong, R., Grigsby, H. E., et al. (2016). Gradient index microlens implanted in prefrontal cortex of mouse does not affect behavioral test performance over time. *PLoS ONE* 11:e0146533. doi: 10.1371/journal.pone.0146533

Levene, M. J., Dombeck, D. A., Kasischke, K. A., Molloy, R. P., and Webb, W. W. (2004). In vivo multiphoton microscopy of deep brain tissue. *J. Neurophysiol.* 91, 1908–1912. doi: 10.1152/jn.01007.2003

Liberti, W. A., Perkins, L. N., Leman, D. P., and Gardner, T. J. (2017). An open source, wireless capable miniature microscope system. *J. Neural Eng.* 14:045001. doi: 10.1088/1741-2552/aa6806

Lim, D., Ford, T. N., Chu, K. K., and Mertz, J. (2011). Optically sectioned in vivo imaging with speckle illumination HiLo microscopy. *J. Biomed. Opt.* 16:016014. doi: 10.1117/1.3528656

Lin, M. Z., and Schnitzer, M. J. (2016). Genetically encoded indicators of neuronal activity. *Nat. Neurosci.* 19, 1142–1153. doi: 10.1038/nn.4359

Logothetis, N., Merkle, H., Augath, M., Trinath, T., and Ugurbil, K. (2002). Ultra high-resolution fMRI in monkeys with implanted RF coils. *Neuron* 35, 227–242. doi: 10.1016/s0896-6273(02)00775-4

Lovett-Barron, M., Kaifosh, P., Kheirbek, M. A., Danielson, N., Zaremba, J. D., and Reardon, T. R. (2014). Dendritic inhibition in the hippocampus supports fear learning. *Science* 343, 857–863. doi: 10.1126/science.1247485

Malvaut, S., Gribaudo, S., Hardy, D., David, L. S., Daroles, L., Labrecque, S., et al. (2017). CaMKIIalpha expression defines two functionally distinct populations of granule cells involved in different types of odor behavior. *Curr. Biol.* 27:e3316.

Miller, J. E., Ayzenshtat, I., Carrillo-Reid, L., and Yuste, R. (2014). Visual stimuli recruit intrinsically generated cortical ensembles. *Proc. Natl. Acad. Sci. U.S.A.* 111, E4053–E4061.

Moore, J. J., Ravassard, P. M., Ho, D., Acharya, L., Kees, A. L., Vuong, C., et al. (2017). Dynamics of cortical dendritic membrane potential and spikes in freely behaving rats. *Science* 355:eaaj1497. doi: 10.1126/science.aaj1497

Morris, R. (1984). Developments of a water-maze procedure for studying spatial learning in the rat. *J. Neurosci. Methods* 11, 47–60. doi: 10.1016/0165-0270(84)90007-4

Nadler, J. J., Moy, S. S., Dold, G., Trang, D., Simmons, N., Perez, A., et al. (2004). Automated apparatus for quantitation of social approach behaviors in mice. *Genes Brain Behav.* 3, 303–314. doi: 10.1111/j.1601-183x.2004.00071.x

Nestler, E. J., and Hyman, S. E. (2010). Animal models of neuropsychiatric disorders. *Nat. Neurosci.* 13, 1161–1169.

Nguyen, J. P., Shipley, F. B., Linder, A. N., Plummer, G. S., Liu, M., Setru, S. U., et al. (2016). Whole-brain calcium imaging with cellular resolution in freely behaving Caenorhabditis elegans. *Proc. Natl. Acad. Sci. U.S.A.* 113, E1074–E1081.

Nicolelis, M. A., and Ribeiro, S. (2002). Multielectrode recordings: the next steps. *Curr. Opin. Neurobiol.* 12, 602–606. doi: 10.1016/s0959-4388(02)00374-4

Niell, C. M., and Stryker, M. P. (2010). Modulation of visual responses by behavioral state in mouse visual cortex. *Neuron* 65, 472–479. doi: 10.1016/j.neuron.2010.01.033

Nimmerjahn, A., Mukamel, E. A., and Schnitzer, M. J. (2009). Motor behavior activates Bergmann glial networks. *Neuron* 62, 400–412. doi: 10.1016/j.neuron.2009.03.019

Nobauer, T., Skocek, O., Pernia-Andrade, A. J., Weilguny, L., Traub, F. M., Molodtsov, M. I., et al. (2017). Video rate volumetric Ca(2+) imaging across cortex using seeded iterative demixing (SID) microscopy. *Nat. Methods* 14, 811–818. doi: 10.1038/nmeth.4341

Obernier, K., and Alvarez-Buylla, A. (2019). Neural stem cells: origin, heterogeneity and regulation in the adult mammalian brain. *Development* 146:dev156059. doi: 10.1242/dev.156059

O'connor, D. H., Peron, S. P., Huber, D., and Svoboda, K. (2010). Neural activity in barrel cortex underlying vibrissa-based object localization in mice. *Neuron* 67, 1048–1061. doi: 10.1016/j.neuron.2010.08.026

O'keefe, J., and Dostrovsky, J. (1971). The hippocampus as a spatial map. Preliminary evidence from unit activity in the freely-moving rat. *Brain Res.* 34, 171–175. doi: 10.1016/0006-8993(71)90358-1

Ozbay, B. N., Futia, G. L., Ma, M., Bright, V. M., Gopinath, J. T., Hughes, E. G., et al. (2018). Three dimensional two-photon brain imaging in freely moving mice using a miniature fiber coupled microscope with active axial-scanning. *Sci. Rep.* 8:8108.

Ozbay, B. N., Losacco, J. T., Cormack, R., Weir, R., Bright, V. M., Gopinath, J. T., et al. (2015). Miniaturized fiber-coupled confocal fluorescence microscope with an electrowetting variable focus lens using no moving parts. *Opt. Lett.* 40, 2553–2556.

Patel, J. M., Swanson, J., Ung, K., Herman, A., Hanson, E., Ortiz-Guzman, J., et al. (2019). Sensory perception drives food avoidance through excitatory basal forebrain circuits. *Elife* 8:e44548.

Patterson, M. A., Lagier, S., and Carleton, A. (2013). Odor representations in the olfactory bulb evolve after the first breath and persist as an odor afterimage. *Proc. Natl. Acad. Sci. U.S.A.* 110, E3340–E3349.

Petreanu, L., Gutnisky, D. A., Huber, D., Xu, N. L., O'connor, D. H., Tian, L., et al. (2012). Activity in motor-sensory projections reveals distributed coding in somatosensation. *Nature* 489, 299–303. doi: 10.1038/nature11321

Pilz, G. A., Bottes, S., Betizeau, M., Jorg, D. J., Carta, S., Simons, B. D., et al. (2018). Live imaging of neurogenesis in the adult mouse hippocampus. *Science* 359, 658–662. doi: 10.1126/science.aao5056

Piyawattanametha, W., Barretto, R. P., Ko, T. H., Flusberg, B. A., Cocker, E. D., Ra, H., et al. (2006). Fast-scanning two-photon fluorescence imaging based on a microelectromechanical systems two- dimensional scanning mirror. *Opt. Lett.* 31, 2018–2020.

Qian, Y., Piatkevich, K. D., Mc Larney, B., Abdelfattah, A. S., Mehta, S., Murdock, M. H., et al. (2019). A genetically encoded near-infrared fluorescent calcium ion indicator. *Nat. Methods* 16, 171–174.

Resendez, S. L., Jennings, J. H., Ung, R. L., Namboodiri, V. M., Zhou, Z. C., Otis, J. M., et al. (2016). Visualization of cortical, subcortical and deep brain neural circuit dynamics during naturalistic mammalian behavior with head-mounted microscopes and chronically implanted lenses. *Nat. Protoc.* 11, 566–597. doi: 10.1038/nprot.2016.021

Rowland, D. C., Obenhaus, H. A., Skytoen, E. R., Zhang, Q., Kentros, C. G., Moser, E. I., et al. (2018). Functional properties of stellate cells in medial entorhinal cortex layer II. *Elife* 7:e36664.

Sawinski, J., Wallace, D. J., Greenberg, D. S., Grossmann, S., Denk, W., and Kerr, J. N. (2009). Visually evoked activity in cortical cells imaged in freely moving animals. *Proc. Natl. Acad. Sci. U.S.A.* 106, 19557–19562. doi: 10.1073/pnas.0903680106

Sekiguchi, K. J., Shekhtmeyster, P., Merten, K., Arena, A., Cook, D., Hoffman, E., et al. (2016). Imaging large-scale cellular activity in spinal cord of freely behaving mice. *Nat. Commun.* 7:11450.

Senarathna, J., Yu, H., Deng, C., Zou, A. L., Issa, J. B., Hadjiabadi, D. H., et al. (2019). A miniature multi-contrast microscope for functional imaging in freely behaving animals. *Nat. Commun.* 10:99.

Sheffield, M. E., and Dombeck, D. A. (2015). Calcium transient prevalence across the dendritic arbour predicts place field properties. *Nature* 517, 200–204. doi: 10.1038/nature13871

Shen, J., Wang, D., Wang, X., Gupta, S., Ayloo, B., Wu, S., et al. (2019). Neurovascular coupling in the dentate gyrus regulates adult hippocampal neurogenesis. *Neuron* 103:e873.

Shen, Y., Nasu, Y., Shkolnikov, I., Kim, A., and Campbell, R. E. (2020). Engineering genetically encoded fluorescent indicators for imaging of neuronal activity: progress and prospects. *Neurosci. Res.* 152, 3–14. doi: 10.1016/j.neures.2020.01.011

Shin, G., Gomez, A. M., Al-Hasani, R., Jeong, Y. R., Kim, J., Xie, Z., et al. (2017). Flexible near-field wireless optoelectronics as subdermal implants for broad applications in optogenetics. *Neuron* 93, 509–521.e503.

Shoham, D., Glaser, D. E., Arieli, A., Kenet, T., Wijnbergen, C., Toledo, Y., et al. (1999). Imaging cortical dynamics at high spatial and temporal resolution with novel blue voltage-sensitive dyes. *Neuron* 24, 791–802. doi: 10.1016/s0896-6273(00)81027-2

Shoham, S., O'connor, D. H., and Segev, R. (2006). How silent is the brain: is there a "dark matter" problem in neuroscience? *J. Compar. Physiol. A Neuroethol. Sens. Neural Behav. Physiol.* 192, 777–784. doi: 10.1007/s00359-006-0117-6

Shuman, T., Aharoni, D., Cai, D. J., Lee, C. R., Chavlis, S., Page-Harley, L., et al. (2020). Breakdown of spatial coding and interneuron synchronization in epileptic mice. *Nat. Neurosci.* 23, 229–238. doi: 10.1038/s41593-019-0559-0

Skocek, O., Nobauer, T., Weilguny, L., Martinez Traub, F., Xia, C. N., Molodtsov, M. I., et al. (2018). High-speed volumetric imaging of neuronal activity in freely moving rodents. *Nat. Methods* 15, 429–432. doi: 10.1038/s41592-018-0008-0

Stamatakis, A. M., Schachter, M. J., Gulati, S., Zitelli, K. T., Malanowski, S., Tajik, A., et al. (2018). Simultaneous optogenetics and cellular resolution calcium imaging during active behavior using a miniaturized microscope. *Front. Neurosci.* 12:496. doi: 10.3389/fnins.2018.00496

Stensola, H., Stensola, T., Solstad, T., Froland, K., Moser, M. B., and Moser, E. I. (2012). The entorhinal grid map is discretized. *Nature* 492, 72–78. doi: 10.1038/nature11649

Sterniczuk, R., Antle, M. C., Laferla, F. M., and Dyck, R. H. (2010). Characterization of the 3xTg-AD mouse model of Alzheimer's disease: part 2. Behavioral and cognitive changes. *Brain Res.* 1348, 149–155. doi: 10.1016/j.brainres.2010.06.011

Thurley, K., and Ayaz, A. (2017). Virtual reality systems for rodents. *Curr. Zool.* 63, 109–119. doi: 10.1093/cz/zow070

Tian, L., Hires, S. A., and Looger, L. L. (2012). Imaging neuronal activity with genetically encoded calcium indicators. *Cold Spring Harb Protoc.* 2012, 647–656.

Tian, L., Hires, S. A., Mao, T., Huber, D., Chiappe, M. E., Chalasani, S. H., et al. (2009). Imaging neural activity in worms, flies and mice with improved GCaMP calcium indicators. *Nat. Methods* 6, 875–881. doi: 10.1038/nmeth.1398

Torper, O., and Gotz, M. (2017). Brain repair from intrinsic cell sources: turning reactive glia into neurons. *Prog. Brain Res.* 230, 69–97. doi: 10.1016/bs.pbr.2016.12.010

Trainito, C., Von Nicolai, C., Miller, E. K., and Siegel, M. (2019). Extracellular spike waveform dissociates four functionally distinct cell classes in primate cortex. *Curr Biol* 29, 2973–2982.e2975.

Turner, J. N., Shain, W., Szarowski, D. H., Andersen, M., Martins, S., Isaacson, M., et al. (1999). Cerebral astrocyte response to micromachined silicon implants. *Exp. Neurol.* 156, 33–49. doi: 10.1006/exnr.1998.6983

Verhagen, J. V., Wesson, D. W., Netoff, T. I., White, J. A., and Wachowiak, M. (2007). Sniffing controls an adaptive filter of sensory input to the olfactory bulb. *Nat. Neurosci.* 10, 631–639. doi: 10.1038/nn1892

Vicidomini, C., Guo, N., and Sahay, A. (2020). Communication, cross talk, and signal integration in the adult hippocampal neurogenic niche. *Neuron* 105, 220–235. doi: 10.1016/j.neuron.2019.11.029

Wallace, J., Lord, J., Dissing-Olesen, L., Stevens, B., and Murthy, V. N. (2020). Microglial depletion disrupts normal functional development of adult-born neurons in the olfactory bulb. *Elife* 9, e50531.

Wang, C., and Ji, N. (2012). Pupil-segmentation-based adaptive optical correction of a high-numerical-aperture gradient refractive index lens for two-photon fluorescence endoscopy. *Opt. Lett.* 37, 2001–2003.

Wang, J., Shen, J., Kirschen, G. W., Gu, Y., Jessberger, S., and Ge, S. (2019). Lateral dispersion is required for circuit integration of newly generated dentate granule cells. *Nat. Commun.* 10:3324.

Wilson, M. A., and Mcnaughton, B. L. (1993). Dynamics of the hippocampal ensemble code for space. *Science* 261, 1055–1058. doi: 10.1126/science.8351520

Xu, N. L., Harnett, M. T., Williams, S. R., Huber, D., O'connor, D. H., Svoboda, K., et al. (2012). Nonlinear dendritic integration of sensory and motor input during an active sensing task. *Nature* 492, 247–251. doi: 10.1038/nature11601

Yashiro, H., Nakahara, I., Funabiki, K., and Riquimaroux, H. (2017). Micro-endoscopic system for functional assessment of neural circuits in deep brain regions: simultaneous optical and electrical recordings of auditory responses in mouse's inferior colliculus. *Neurosci. Res.* 119, 61–69. doi: 10.1016/j.neures.2017.01.002

Youmans, K. L., Tai, L. M., Nwabuisi-Heath, E., Jungbauer, L., Kanekiyo, T., and Gan, M. (2012). APOE4-specific changes in Abeta accumulation in a new transgenic mouse model of Alzheimer disease. *J. Biol. Chem.* 287, 41774–41786. doi: 10.1074/jbc.m112.407957

Ziv, Y., and Ghosh, K. K. (2015). Miniature microscopes for large-scale imaging of neuronal activity in freely behaving rodents. *Curr. Opin. Neurobiol.* 32, 141–147. doi: 10.1016/j.conb.2015.04.001

Zong, W., Wu, R., Li, M., Hu, Y., Li, Y., Li, J., et al. (2017). Fast high-resolution miniature two-photon microscopy for brain imaging in freely behaving mice. *Nat. Methods* 14, 713–719. doi: 10.1038/nmeth.4305

Zou, Y., Zhang, W., Chau, F. S., and Zhou, G. (2015). Miniature adjustable-focus endoscope with a solid electrically tunable lens. *Opt. Express* 23, 20582–20592.

Conflict of Interest: SD and HD declare a conflict of interest. SD is the owner of Doric Lenses and HD is an R&D scientist at Doric Lenses.

The remaining authors declare that the research was conducted in the absence of any commercial or financial relationships that could be construed as a potential conflict of interest.

Copyright © 2020 Malvaut, Constantinescu, Dehez, Doric and Saghatelyan. This is an open-access article distributed under the terms of the Creative Commons Attribution License (CC BY). The use, distribution or reproduction in other forums is permitted, provided the original author(s) and the copyright owner(s) are credited and that the original publication in this journal is cited, in accordance with accepted academic practice. No use, distribution or reproduction is permitted which does not comply with these terms.

frontiers in Neuroscience

TECHNOLOGY AND CODE
published: 15 September 2020
doi: 10.3389/fnins.2020.00900

Pyneal: Open Source Real-Time fMRI Software

*Jeff J. MacInnes[1], R. Alison Adcock[2], Andrea Stocco[1,3], Chantel S. Prat[1,3], Rajesh P. N. Rao[4] and Kathryn C. Dickerson[2]**

[1] Institute for Learning and Brain Sciences, University of Washington, Seattle, WA, United States, [2] Department of Psychiatry and Behavioral Sciences, Center for Cognitive Neuroscience, Duke Institute for Brain Sciences, Duke University, Durham, NC, United States, [3] Department of Psychology, University of Washington, Seattle, WA, United States, [4] Department of Computer Science and Engineering, Center for Neurotechnology, University of Washington, Seattle, WA, United States

Increasingly, neuroimaging researchers are exploring the use of real-time functional magnetic resonance imaging (rt-fMRI) as a way to access a participant's ongoing brain function throughout a scan. This approach presents novel and exciting experimental applications ranging from monitoring data quality in real time, to delivering neurofeedback from a region of interest, to dynamically controlling experimental flow, or interfacing with remote devices. Yet, for those interested in adopting this method, the existing software options are few and limited in application. This presents a barrier for new users, as well as hinders existing users from refining techniques and methods. Here we introduce a free, open-source rt-fMRI package, the Pyneal toolkit, designed to address this limitation. The Pyneal toolkit is python-based software that offers a flexible and user friendly framework for rt-fMRI, is compatible with all three major scanner manufacturers (GE, Siemens, Phillips), and, critically, allows fully customized analysis pipelines. In this article, we provide a detailed overview of the architecture, describe how to set up and run the Pyneal toolkit during an experimental session, offer tutorials with scan data that demonstrate how data flows through the Pyneal toolkit with example analyses, and highlight the advantages that the Pyneal toolkit offers to the neuroimaging community.

Keywords: real-time, functional magnetic resonance imaging, neurofeedback, open source software, python (programming language), neuroimaging methods, rt-fMRI

OPEN ACCESS

Edited by:
Alard Roebroeck, Maastricht University, Netherlands

Reviewed by:
Shijie Zhao, Northwestern Polytechnical University, China
Mark S. Bolding, The University of Alabama at Birmingham, United States

***Correspondence:**
Kathryn C. Dickerson
kathryn.dickerson@duke.edu

Specialty section:
This article was submitted to Brain Imaging Methods, a section of the journal Frontiers in Neuroscience

Received: *20 January 2020*
Accepted: *03 August 2020*
Published: *15 September 2020*

Citation:
MacInnes JJ, Adcock RA, Stocco A, Prat CS, Rao RPN and Dickerson KC (2020) Pyneal: Open Source Real-Time fMRI Software. Front. Neurosci. 14:900. doi: 10.3389/fnins.2020.00900

INTRODUCTION

Real-time functional magnetic resonance imaging (rt-fMRI) is an emerging technique that expands the scope of research questions beyond what traditional neuroimaging methods can offer (Sulzer et al., 2013a; Stoeckel et al., 2014; Sitaram et al., 2017; MacInnes and Dickerson, 2018). With traditional fMRI, brain activation is measured concurrently but independently from the experiment. All analyses (e.g., correlating behavior or cognitive state with brain activations)

therefore, take place after the scan[1] is completed, once the brain images and behavioral data have been saved and transferred to a shared location. In contrast, *real-time fMRI* is an approach whereby MRI data is accessed and analyzed throughout an ongoing scan, and can be incorporated directly into the experiment. Technological advances over the last decade have made it feasible to reconfigure an MRI environment to allow researchers to access and analyze incoming data at a rate that matches data acquisition. A few key advantages that rt-fMRI provides over traditional fMRI include the ability to: (1) monitor data quality in real time, thereby saving time and money, (2) provide participants with feedback from a region or network of regions in cognitive training paradigms, and (3) use ongoing brain activation as an independent variable to dynamically control the flow of an experimental task.

While rt-fMRI has risen in popularity over the past decade (Sulzer et al., 2013a), the majority of imaging centers around the world remain unequipped to support this technique. In the past, this was primarily due to the computational demands exceeding scanner hardware capabilities [e.g., reconstructing and analyzing datasets composed of >100 k voxels at a rate that matched data acquisition was not feasible (Voyvodic, 1999)]. Excitingly, modern day scanners available from each of the major MRI manufacturers – GE, Philips, and Siemens – are now outfitted with multicore processors, capable of operating in parallel to reconstruct imaging data and write files to disk while a scan is ongoing.

The availability of fMRI data in real time presents novel opportunities to design experiments that incorporate information about ongoing brain activation. However, finding the right software tool to read images across multiple data formats, support flexible analyses, and integrate the results into an ongoing experimental presentation is a challenge. To date, the existing software options are limited for one or more reasons, including: cost (requiring a commercial license or dependent upon commercially licensed software such as Matlab) or a constrained choice of analysis options [e.g., region of interest (ROI) analysis only].

In this article, we describe the Pyneal toolkit, an open source and freely available software package that was developed to address these limitations and support real-time fMRI. It is written entirely in Python, a programming language that offers flexibility and performance, balanced with readability and widespread support among the neuroimaging community. The Pyneal toolkit was built using a modular architecture to support a variety of different data formats, including those used across all three major MRI scanner manufacturers – GE, Philips, and Siemens. It offers built-in routines for basic data quality measures and single ROI summary statistics, as well as a web-based dashboard for monitoring the progress of ongoing scans. Its primary advantage, however, is that it offers an easy-to-use scaffolding on which users can design fully customized analyses to meet their unique experimental needs (e.g., neurofeedback from multiple ROIs, dynamic experimental control, classification of brain states, brain-computer interaction). This flexibility allows researchers full control over which neural regions to include, which analyses to carry out, and how the results of those analyses may be incorporated into the overall experimental flow. Moreover, computational and technological advances have ushered in new and more sensitive approaches to fMRI analyses. As the field continues to evolve, the ability to customize analyses within the Pyneal toolkit will allow researchers to quickly adapt new analytic methods to real-time experiments.

The Pyneal toolkit was designed to offer a powerful and flexible tool to existing rt-fMRI practitioners as well as to lower the burden of entry for new researchers or imaging centers looking to add this capability to their facilities. Here we provide an overview of the software architecture, describe how it is used, offer tutorial data and analyses demonstrating how to use the Pyneal toolkit, and discuss the advantages of the Pyneal toolkit. We conclude by describing both limitations of and future directions for the Pyneal toolkit.

METHOD

The Pyneal toolkit is available at https://github.com/jeffmacinnes/pyneal and full documentation is online at https://jeffmacinnes.github.io/pyneal-docs/.

Overview

The Pyneal toolkit was created as a flexible and open-source option for researchers interested in pursuing real-time fMRI methods. The entire codebase is written in Python 3[2] and integrates commonly used neuroimaging libraries (e.g., Nipy, NiBabel). For users developing customized real-time analyses, Python has a low burden of entry (compared to languages like Java or C++), while at the same time offers performance measures that meet or exceed the needs of basic research applications, in part due to backend numeric computing libraries (e.g., Numpy, Scipy) that are wrapped on top of a fast, C-based architecture.

In order to support a wide range of data types and computing environments, the software is divided into two primary components: Pyneal Scanner and Pyneal[3] (see **Figure 1**). The two components communicate via TCP/IP connections, allowing users the flexibility to run the components on the same or different machines as required by their individual scanning environments[4]. Internally, Pyneal uses ZeroMQ[5], a performant and reliable messaging framework, for all TCP/IP-based communication among its core processes.

[1]Throughout this article we use the term *scan* or *run* to refer to a single, discrete 4D acquisition, and the terms *experimental session* to refer to a collection of scans that are administered to a particular participant in a continuous time window.

[2]https://docs.python.org/3.6

[3]Throughout this article we will use the phrase "Pyneal toolkit" when referring to the overall toolkit and "Pyneal" when referencing the specific software component comprising Pyneal (as opposed to Pyneal Scanner for example).

[4]The Pyneal toolkit documentation, and the figures shown throughout this section, use the terms "Scanner Computer" and "Analysis Computer" to refer to the machines that are running Pyneal Scanner and Pyneal, respectively. However, it is important to note that these terms refer to functional roles: there is no conflict in having the Pyneal Scanner and Pyneal running on the same physical machine.

[5]ZeroMQ, a powerful open source library for messaging, is available at https://zeromq.org/ and https://github.com/zeromq.

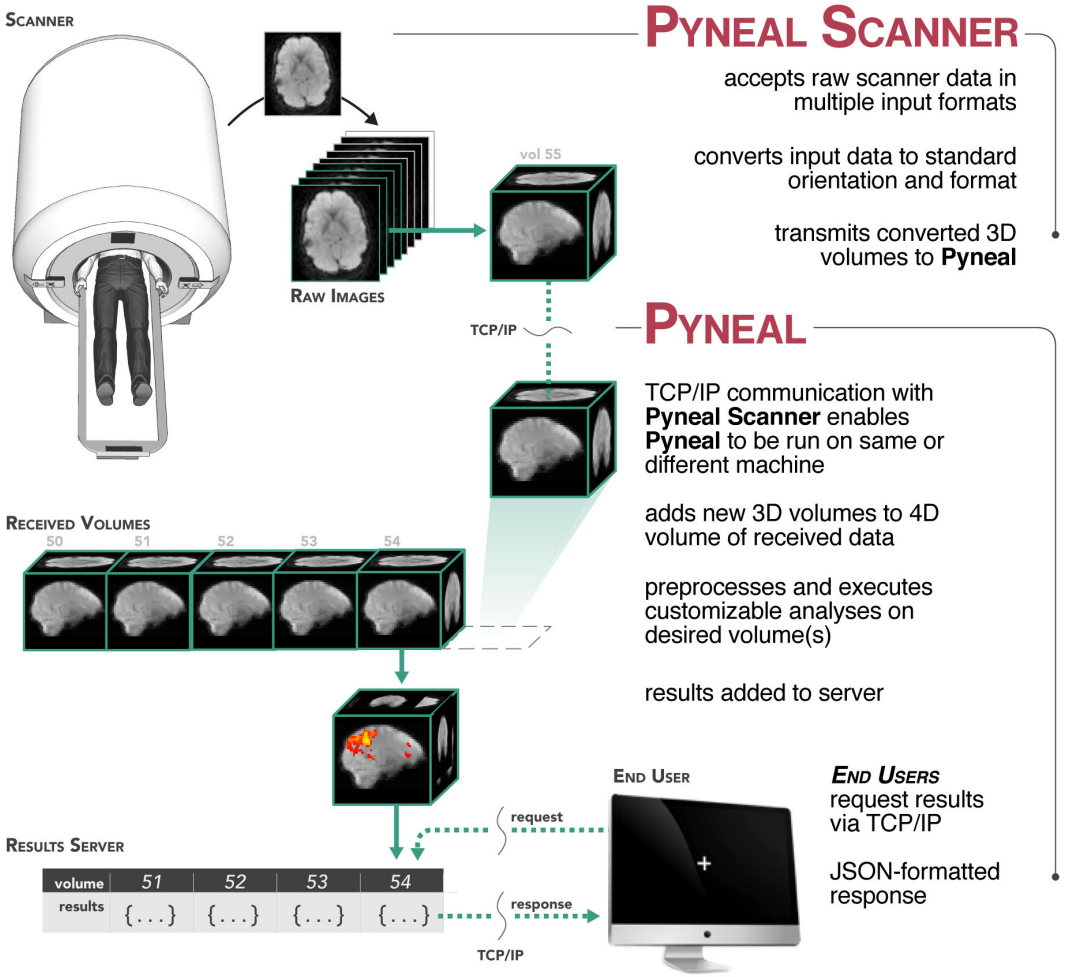

FIGURE 1 | Overview of the Pyneal toolkit. The Pyneal toolkit consists of two modules: Pyneal Scanner and Pyneal. Pyneal Scanner receives the raw data and transforms it into a standardized format for Pyneal to use. Pyneal analyzes the data in real time and makes it available for subsequent use (e.g., by a remote End User for experimental display). Pyneal Scanner and Pyneal can operate on the same computer (e.g., dedicated analysis computer) or separate computers (as required by the specific scanning environment).

During a scan, Pyneal Scanner is responsible for converting data into a standardized format and passing it along to Pyneal (see **Figure 2**). Pyneal receives incoming data, carries out the specified preprocessing and analysis steps, and stores the results of the analysis on a locally running server. Throughout the scan, any remote End User (e.g., a workstation running the experimental task) can retrieve analysis results from Pyneal at any point. Each of these components is discussed in greater detail below.

Pyneal Scanner

Given the range of potential input data formats, depending on the scanning environment, we aimed to standardize the incoming data in a way that allows subsequent processing steps to be environment agnostic. Thus we divided the overall Pyneal toolkit architecture into two components that operate independently, enabling one component, Pyneal Scanner, to adapt to the idiosyncrasies of the local scanning environment without affecting the downstream processing and analysis stages of the Pyneal component (see **Figure 2**).

Architecturally, Pyneal Scanner uses a multithreaded design with one thread *monitoring* for the appearance of new image data, and a second thread *processing* image data as it appears. This design allows Pyneal Scanner to efficiently process incoming scan data with minimal latency (in practice, under typical scanning conditions, the latency between when new image data arrives and is processed is on the order of tens of milliseconds). Throughout a scan, new images that appear from the scanner are placed into a queue. The processing thread pulls individual files from that queue and converts the data to a standardized format. In addition, header information from the first images to arrive is processed to determine key metadata about the current scan, including total volume dimensions, voxel spacing, total number of expected time points, and the affine transformation needed to reorient the data to RAS+ format (axes increase from left to right, posterior to anterior, inferior to superior).

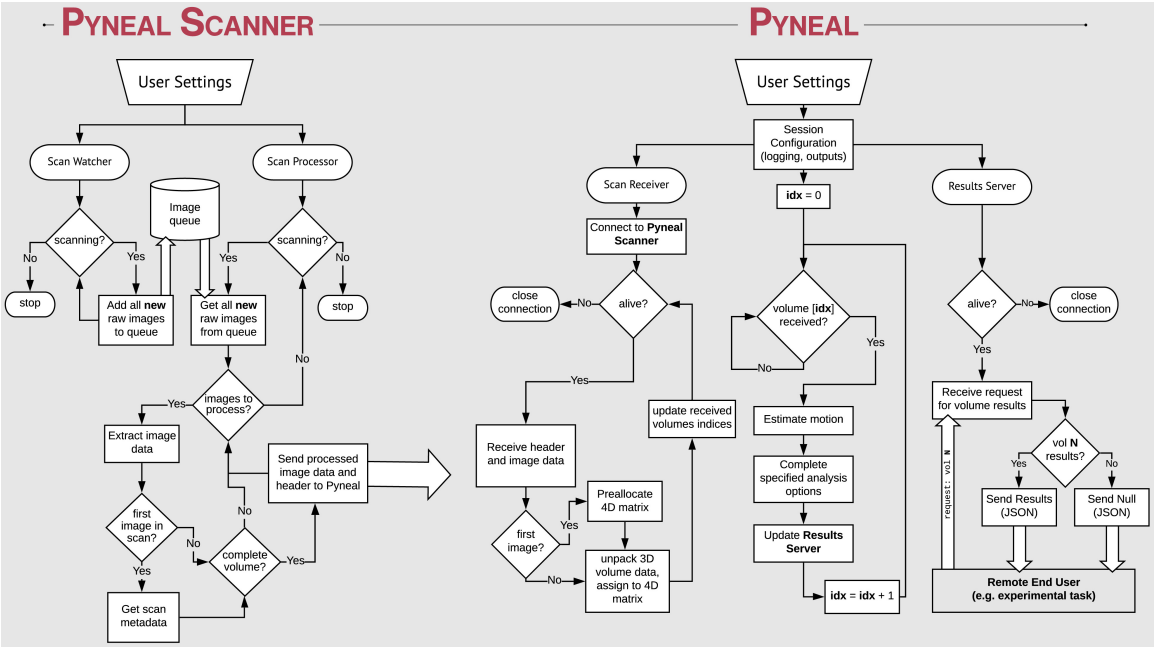

FIGURE 2 | Process flow diagram illustrating the multi-threaded nature of the Pyneal toolkit. Pyneal Scanner has two sub-modules: a scan watcher and scan processor. The scan watcher monitors and adds all new raw images to a queue. The scan processor receives all new raw images from the queue, extracts the image data, transforms it to a standardized format, and sends it to Pyneal for analysis. Pyneal operates as an independent, multi-threaded component and has three sub-modules: scan receiver, scan processor, and results server. The scan receiver receives formatted data from Pyneal Scanner and sends it to the scan processor, which completes the specified analyses and sends them to the results server. The results server listens to incoming requests from End Users (e.g., experimental task).

Pyneal Scanner is initialized through a simple configuration text file specifying the scanner type and paths to where data files are expected to appear throughout a scan. Users can create this file manually, or follow the command line prompts when first launching; in either case, once Pyneal Scanner is configured at the start of a session, it does not need to be modified, unless the scanning environment itself is modified. In that case, users can update Pyneal Scanner without having to add any additional modifications to downstream processes in Pyneal. Regardless of how and where the data arrives from the scanner, as long as Pyneal Scanner continues to output data in the expected format, subsequent stages in the pipeline will proceed unaffected. This is a significant advantage that provides researchers the necessary latitude to customize the installation to their unique environment.

Pyneal Scanner has built-in routines for handling common data formats used in GE (e.g., 2D dicom slice files), Siemens (e.g., 3D dicom mosaic files), and Philips scanners (e.g., PAR/REC files), and is easily extensible to incorporate additional formats that may emerge in the future.

As soon as a complete volume (i.e., 3D array of voxel values from a single time point) has arrived, it is passed along to Pyneal via a dedicated TCP/IP socket interface. This arrangement allows Pyneal Scanner and Pyneal to run on separate machines or as separate processes on the same machine, depending on the particular requirements of the local scanning environment. For instance, if newly arriving images are only accessible from the scanner console itself, Pyneal Scanner can run on that machine, monitoring the local directory where new images appear, and then transferring processed volumes to Pyneal running on a separate dedicated machine. Alternatively, the scanner network configuration may be such that it is possible to remotely mount the directory where new images appear, allowing Pyneal Scanner and Pyneal to run concurrently on the same machine.

Each transmitted volume from Pyneal Scanner to Pyneal occurs in two waves: First, Pyneal Scanner sends a JSON-formatted header that contains relevant metadata about the current volume, including the time point index and volume dimensions. Second, it sends the numeric array representing the volume data itself. Pyneal uses the information from the header to reconstruct the incoming array, store it as a memory- and computation-efficient Numpy array, and index the volume in a way to facilitate subsequent processing and analysis steps.

Pyneal

Pyneal is divided up into three distinct submodules that operate efficiently in a multithreaded configuration: submodule 1: the scan receiver, accepts incoming data from Pyneal Scanner; submodule 2: the processing module, oversees the preprocessing and analysis stages on each incoming volume, and submodule 3: the results server fields requests for data from remote End Users throughout the scan (see **Figure 2**).

As described above, throughout a scan Pyneal's submodule 1 (scan receiver) receives re-formatted data from Pyneal Scanner. Each new data point is represented as a 3D matrix of voxel values corresponding to a single sample (i.e., one TR). The JSON header

that Pyneal Scanner provides with every transmission allows Pyneal to reconstruct the 3D volume with the correct dimensions, as well as assign it the proper index location in time. Each new volume is passed to the proper location of a preallocated 4D matrix that incrementally fills in throughout the scan.

Submodule 2 (processing module) accepts each 3D volume and submits it through preprocessing and analysis stages. The preprocessing stage estimates motion using a histogram registration algorithm and yields mean displacement in millimeters relative to a fixed reference volume from the start of the run (absolute motion), as well as relative to the previous time point (relative motion) (Jenkinson, 2000).

The analysis stage takes the preprocessed volume and runs the specified analyses or computations on the volume. Users have the option of selecting from built-in analysis routines (including calculating a weighted or unweighted mean signal within a supplied ROI mask), or, importantly, can generate and include their own custom analysis script (written in Python) that will be executed on each volume. The ability to design and execute customized analyses in real-time provides researchers the freedom to measure and use ongoing brain activations however they desire. See *Using Pyneal* below for more details on selecting an analysis or building a custom analysis script.

The analysis stage is capable of computing and returning multiple results on each volume (e.g., mean signal from multiple distinct ROIs). The computed results are tagged with the corresponding volume index, and passed along to the third submodule: the results server.

Submodule 3, (the results server), listens for and responds to incoming requests for specific results from an End User throughout the scan. An End User is anything that may wish to access real-time results throughout an on-going scan (e.g., experimental presentation software that will present results as neurofeedback to the participant in the scanner). To request results, the End User sends a specific volume index to the results server via a TCP/IP socket interface. The result server receives the request and checks to see if the requested volume has arrived and been analyzed. Responses are sent as a JSON-formatted reply to the End User. If the requested volume has not been processed yet, the reply message from the Result Server will contain the entry foundResults: False; if the requested volume exists, the Results Server retrieves the requested results for that volume, and sends a reply message to the End User that contains foundResults: True as well as the full set of results for that volume. The End User can then parse and make use of the results as needed (e.g., update a graphical display showing mean percent signal change in an ROI).

At the completion of each run, Pyneal creates a unique output directory for the current scan. The scan data is written to this directory as a 4D NIFTI image, along with a JSON file containing all computed results as well as log files.

Using Pyneal

Once installed, users can interact with and customize Pyneal via configuration files and graphical user interfaces (GUIs). At the start of a new scan, the user needs to launch both Pyneal Scanner and Pyneal.

Launching Pyneal Scanner is done via the command line. Pyneal Scanner uses a configuration text file to obtain parameters specific to the current computing environment, including the scanner make and the directory path where new incoming data is expected to appear (see example in the Full Pipeline tutorial below, section "Pyneal Toolkit – Full Pipeline Tutorial"). Users can manually create this configuration file ahead of time, or, if no file exists, the user will be prompted to specify the parameters via the command line when launching. Parameters specified via the command line will be written into the configuration file and saved to disk. Pyneal Scanner will automatically read this configuration file at the start of every scan. Thus, Pyneal Scanner needs to be configured only once at the beginning of each experimental session.

Launching Pyneal is also done via the command line. Upon launching Pyneal at the start of each scan (run), the user is presented with a setup GUI for configuring Pyneal to the current scan (see **Figure 3**). The setup GUI includes sections for socket communication parameters (e.g., IP address), selecting an input mask, setting preprocessing parameters, choosing analyses, and specifying an output directory. Some parameters, like the socket communication host address and ports, are unlikely to change from experimental session to session, while other parameters, most notably the input mask and output directory, will be specific to experimental session and/or each individual scan. The GUI is populated with the last used settings to minimize set-up time, however, the GUI must be launched before each scan.

The setup GUI asks users to specify the path to an input mask, which will be used during the analysis stage of a scan. If the user selects one of the built-in analysis options (i.e., calculate an *average* or *median*), the mask will define which voxels are included in the calculation. Alternatively, if the user chooses to use a custom analysis, a reference to this mask will be passed into the custom analysis script, which the user is free to use or ignore as needed. In addition, the mask panel also allows users to specify whether or not to use voxel values from the mask as weights in subsequent analyses.

All analyses in Pyneal take place in the native functional space of the current scan, and as such, this mask is required to match the dimensions and orientation of the incoming functional data. For cases where the user wishes to use an existing anatomical mask in a different imaging space (e.g., MNI space), the Pyneal toolkit includes a Create Mask tool (*utils/createMask.py*) for transforming masks to the functional space of the current subject [see **Figure 4**; Note that this functionality requires FSL (Jenkinson et al., 2012) to be installed].

Pyneal includes built-in analysis options for calculating the average and median activation levels across all voxels in the supplied mask. For experiments that wish to present neurofeedback from a single ROI, these options may be appropriate. However, one of Pyneal's primary advantages is the ability to run fully customized analyses. By selecting "custom" in the analysis panel, the user will be prompted to choose a python-based analysis script they have composed. Pyneal requires that a custom script contain certain functions in order to integrate with the rest of the Pyneal pipeline throughout a scan. However, beyond that basic structure, there are few limitations on what

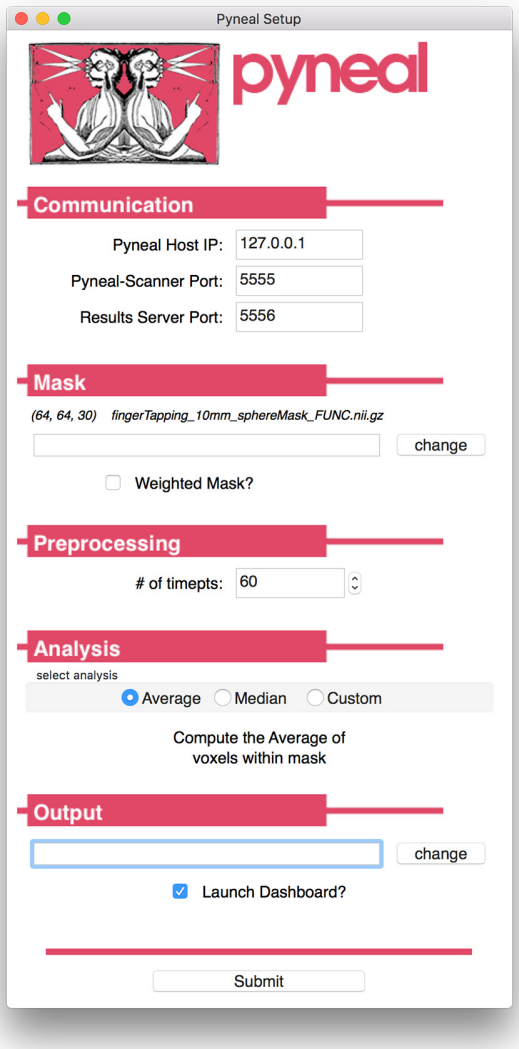

FIGURE 3 | Pyneal Graphical User Interface (GUI). The Pyneal GUI contains the following sections: (1) Communication: allows Pyneal to communicate with Pyneal Scanner and any End Users. This includes the IP address of the computer running Pyneal as well as the port numbers for Pyneal Scanner and End Users to communicate with Pyneal. (2) Mask: users have the option of loading a mask to use during real-time fMRI runs (weighted or unweighted). (3) Preprocessing: users specify the number of timepoints (volumes) in the run. (4) Analysis: users may choose between one of the default options (calculating the average or median of a mask) or importantly can upload a custom analysis script (e.g., correlation between two regions). (5) Output: users specify a location where the output files are saved.

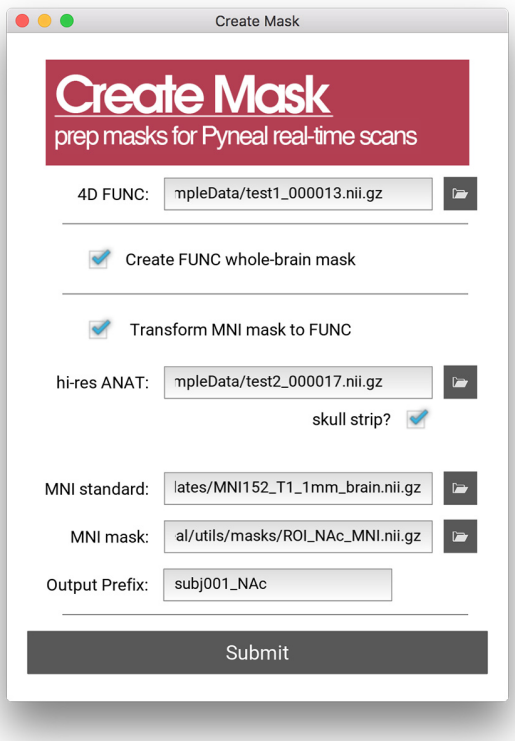

FIGURE 4 | Create Mask GUI. This GUI assists users in making a mask that can be used in analysis during the real-time fMRI runs. Users can choose between making a whole brain mask or a mask from a pre-specified MNI template (e.g., amygdala ROI). Users must load an example functional data file for both mask types. When creating a mask from an MNI template, users must additionally load an anatomical data file, specify the path to the MNI standard brain file, the MNI mask file, and specify the new file name (output prefix). Note, this tool requires FSL.

users may wish to include. To assist users in designing a custom analysis script, we include a basic template file[6] with the required named functions and input/output variable names that users can expand upon as needed. The benefit of this approach is that it liberates users to design analysis approaches that are best suited to their experimental questions, all while fully integrating into the existing Pyneal pipeline.

Lastly, users are able to specify an output directory for the current experimental session. During an experimental session, the output from each scan will be saved to its own unique subdirectory within this output directory. The saved output from each scan includes a log file showing all settings and messages recorded throughout the scan, a JSON file containing all of the computed analysis results, and a 4D NIFTI image containing the functional data as received by Pyneal.

Once the user hits "submit," Pyneal will establish communication with Pyneal Scanner, launch the results server, and wait for the scan to start and data to appear.

Web-Based Dashboard

Once the scan begins, users are presented with a web-based dashboard (see **Figure 5**) viewable in an internet browser. The dashboard updates in real-time allowing users to view the progress of the scan, and monitor the status via four separate components. A plot in the top-left displays ongoing head motion estimates expressed in millimeters relative

[6]https://github.com/jeffmacinnes/pyneal/blob/master/utils/customAnalyses/customAnalysisTemplate.py

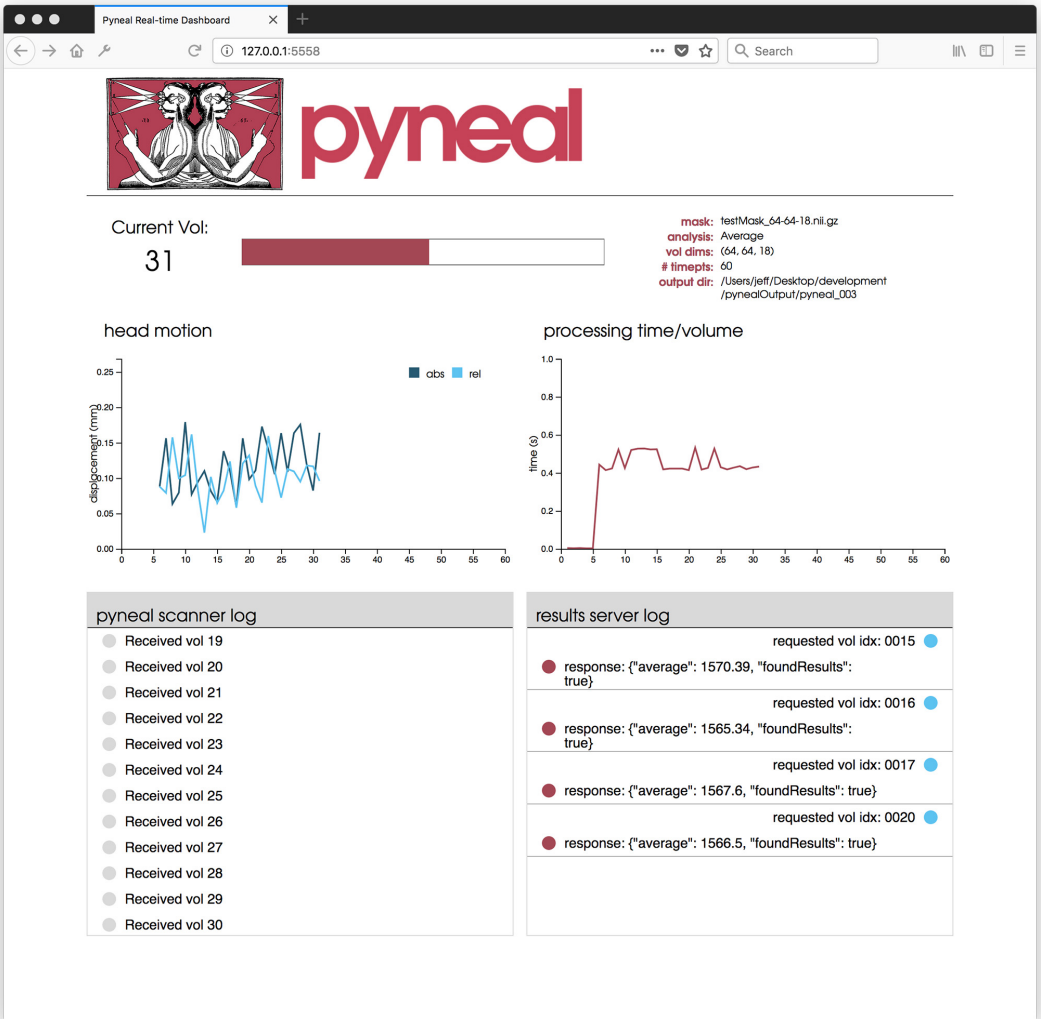

FIGURE 5 | Pyneal Dashboard. This web-based dashboard allows users to monitor analysis and progress during real-time runs. The current volume is displayed along with basic information about the scan (e.g., mask, analysis, etc.). Two plots indicate: (1) head motion (top left) – both relative (compared to previous volume) and absolute (compared to the start of the scan) and (2) processing time for each volume (top right). Two log windows display: (1) messages from Pyneal Scanner (bottom left) and (2) communication between Pyneal and the End User (bottom right).

to both a fixed reference volume (absolute displacement) and the previous volume (relative displacement). In the top-right, a separate plot shows the processing time for each volume. By monitoring this plot, users can ensure that all analyses are completing at a rate that keeps pace with data acquisition. At the bottom, two log windows allow users to watch incoming messages from Pyneal Scanner (bottom left) and communication between Pyneal's results server and any End User (bottom right).

RESULTS

Here we present two complementary tutorials and results using real fMRI data. Section "Pyneal Toolkit – Full Pipeline Tutorial" details how to set up and use the Pyneal toolkit. It demonstrates the full pipeline of data flow throughout the Pyneal Toolkit. Section "Pyneal Analysis Tutorial" describes in more detail how to run two example analyses in Pyneal – one using the default built-in ROI-averaging tool in the toolkit and the second using a custom analysis script. Please see: https://github.com/jeffmacinnes/pyneal-tutorial for full access to the data and scripts for both tutorials.

Both tutorials assume the user has downloaded and installed the Pyneal toolkit and the Pyneal Tutorial repositories in their local folder. If so, the following directories should be located in the user's home directory:

~/pyneal
~/pyneal-tutorial

Pyneal Toolkit – Full Pipeline Tutorial

The goal of this tutorial is to test the Pyneal toolkit's complete pipeline using conditions similar to what is available at the three major scanner manufacturers. This tutorial uses the Scanner Simulator command line tool that comes with the Pyneal toolkit. This tool mimics the behavior of an actual scanner by writing image data to an output directory at a steady rate (directory and rate specified by the user). The source data (included) are actual scan images from GE, Philips, and Siemens scanners. These data are meant to simulate the format and directory structure typical of each of these platforms. This tutorial allows users to test the complete Pyneal toolkit's pipeline on any of these platforms prior to actual data collection.

Regardless of scanner type, each platform follows the same general steps:

- Set up the Scan Simulator.
- Set up Pyneal Scanner.
- Set up Pyneal.

Below we provide a complete example using the Siemens' scanner setup. Please see https://github.com/jeffmacinnes/pyneal-tutorial for source data and information for all scanner types, including examples using GE and Philips scanners.

Siemens Full Pipeline Tutorial:

Inside the Siemens_demo folder, there is a directory named scanner. This directory serves as the mock scanner for this tutorial, and follows a structure similar to what is observed on actual Siemens scanners. There's a single session directory (data) that contains all of the dicom files for two functional series (000013, 000015) and an anatomical series (for more source data detail, see Appendix: Siemens source data within: https://github.com/jeffmacinnes/pyneal-tutorial/blob/master/FullPipelineTutorial.md).

We will use the Scanner Simulator tool to simulate a new functional series, using 000013 as our source data. The new series will appear in the session directory alongside the existing series files, and dicom files will contain the series name 000014.

To perform this tutorial the following steps are required:

I. Launch `Siemens_sim.py` with the desired input data
- Open a new terminal window and navigate to the Scanner Simulator tool: `cd ~ /pyneal/pyneal_scanner/simulation/scannerSimulators`
- launch `Siemens_sim.py`, specifying paths to the source directory (`~/pyneal-tutorial/Siemens_demo/scanner/data`) and series numbers (`000013`). The user can also specify the new series number (`-n 000014`), and TR (`-t 1000`) if desired.

```
python Siemens_sim.py ~/pyneal-tutorial/Siemens_demo/scanner/data 000013 -t 1000 -n 000014
```

The user should see details about the current scan, and an option to press ENTER to begin the scan:

```
————————
Source dir: ~/pyneal-tutorial/Siemens_demo/scanner/data
Total Mosaics Found: 60
TR: 1000
Press ENTER to begin the "scan"
```

Before starting the simulator, first complete the following two steps: setting up Pyneal Scanner and Pyneal.

II. Configure Pyneal Scanner to watch for new scan data in the session directory for the Siemens mock scanner.
- open a second terminal window, and navigate to Pyneal Scanner:
  `cd ~/pyneal/pyneal_scanner`
- create (or edit the existing) scannerConfig.yaml file in this directory to set the scannerMake to Siemens and the scannerBaseDir to the mock scanner folder. The contents of the scannerConfig.yaml file should be:

```
pynealSocketHost: 127.0.0.1
pynealSocketPort: '5555'
scannerBaseDir: ~/pyneal-tutorial/Siemens_demo/scanner/data
scannerMake: Siemens
```

- launch Pyneal Scanner:
  `python pynealScanner.py`

The user should see details about the current session, and an indication that Pyneal Scanner is attempting to connect to Pyneal:

```
================
Session Dir:
~/pyneal-tutorial/Siemens_demo/scanner/data
Unique Series:

  000013 60 files 1113170 min, 51 s ago
  000015 60 files 1113170 min, 51 s ago
  000017 52 files 1113170 min, 51 s ago

MainThread - Connecting to pynealSocket...
```

There is nothing more to do in this terminal window. Once Pyneal is set up and the Scan Simulator tool starts, Pyneal Scanner will begin processing new images as they appear and sending the data to Pyneal. The user can monitor the progress via the log messages that appear in this terminal.

III. Configure and launch Pyneal
- Open a third terminal window, navigate to and launch Pyneal.

```
cd ~/pyneal
python pyneal.py
```

- Configure Pyneal for the Siemens tutorial demo:
  - Communication: Set the `Pyneal Host IP` to `127.0.0.1`, the `Pyneal-Scanner Port` to `5555`, and the `Results Server Port` to `5558`.
  - Mask: In the `Siemens_demo` directory, there is a file named `dummyMask_64-64-18.nii.gz`. Set the mask value in Pyneal to use this file. This mask

was pre-made to match the volume dimensions of the `Siemens_demo` scan data. This mask is simply a rectangle positioned in the middle slice of the 3D volume, and is for demonstration purposes only. The user can unselect the `Weighted Mask?` option
  - Preprocessing: Set `# of timepts` to: `60`. The user can keep the `Estimate Motion?` option selected if preferred.
  - Analysis: Select the `Average` option.
  - Output: Set the output directory to `~/pyneal-tutorial/Siemens_demo/output`. Check `Launch Dashboard?`

- Start Pyneal by pressing `Submit`.
  - In the Pyneal Scanner terminal, the user will see messages indicating that Pyneal Scanner has successfully set up a connection to Pyneal and that it is waiting for a new `seriesDir` (which will be created once the scan starts).
  - In addition, the user can open a browser window and enter `127.0.0.1:5558` in the URL bar to see the Pyneal dashboard.

IV. Start demo
- In the first terminal window, where the Scan Simulator tool is running, press `ENTER` to begin the scan.
- As the scan is progressing, each of the three terminal windows will update with new log messages. In addition, the user can monitor the progress from the dashboard in a web browser at `127.0.0.1:5558`.
- As soon at the scan finishes, the user can find the Pyneal output at `~/pyneal-tutorial/Siemens_demo/output/pyneal_001`. This directory will have:
  - *pynealLog.log:* log file from the current scan.
  - *receivedFunc.nii.gz:* 4D nifti file of the data, as received by Pyneal * *results.json:* JSON file containing the analysis results from the current scan.

Pyneal Analysis Tutorial

The goal of this tutorial is to guide users through two different analyses using Pyneal. We provide real fMRI data (note – this tool also allows for use of randomly generated data). This tutorial uses the `pynealScanner_sim.py` command line tool that comes with the Pyneal toolkit. This tool takes real or generated data, breaks it apart, and sends it to Pyneal for analysis. The source data (included) is a nifti file from one run of a hand squeezing task. It alternates between blocks of squeeze and rest (each 20 s, repeated five times). The first analysis demonstrates Pyneal's built-in ROI neurofeedback tool. The second demonstrates use of a custom analysis script: correlating the activation of two ROIs and using it for neurofeedback.

Neurofeedback: Single ROI Averaging Using Built-in Analysis Functions

Example: A researcher wishes to provide participants with neurofeedback from the primary motor cortex (M1) in a hand-squeezing task. The M1 ROI is defined on the basis of an anatomical mask using the Juelich atlas in FSL.

Tutorial: Ordinarily, the first step is to create a unique mask in functional space of the target ROI (M1). For the purposes of this tutorial, we provide the ROI in subject-specific space for users. We used the left M1 ROI from the Juelich atlas freely available in FSL. We thresholded the mask at 10% and binarized it using `fslmaths`. Then using `flirt`, we converted the left M1 mask (in MNI space) to functional space (subject-specific). The resulting mask, `L_MotorCortex.nii.gz` is now ready to use in this tutorial.

This tutorial uses the Pyneal Scanner simulation script, which is located in:

```
~/pyneal/utils/simulation/pyneal
Scanner_sim.py
```

Usage includes:

```
python pynealScanner_sim.py [-filePath]
[-random] [-dims] [-TR] [-sockethost]
[-socketport]
```

Input arguments:

- `-f/-filePath: path to 4D nifti image the user wants to use as the "scan" data. Here we are using "func.nii.gz" provided in ~/pyneal-tutorial/analysis Tutorial as our input data.`
- `-r/-random: flag to generate random data instead of using a pre-existing nifti image`
- `-d/-dims: desired dimensions of randomly generated dataset [default: 64 64 18 60]`
- `-t/-TR: set the TR in ms [default: 1000]`
- `-sh/-sockethost: IP address Pyneal host [default: 127.0.0.1]`
- `-sp/-socketport: port number to send 3D volumes over to Pyneal [default: 5555]`

To run the tutorial, the following steps are required:

I. Launch pynealScanner_sim.py script

```
python pynealScanner_sim.py -f ~/pyneal
-tutorial/analysisTutorial/func.
nii.gz -t 1000 -sh 127.0.0.1 -sp 5555
```

Here we are setting the TR to 1000 ms, the host socket number to 127.0.0.1 and the port number to 5555. This tool will simulate the behavior of Pyneal Scanner. During a real scan, Pyneal Scanner will send data to Pyneal over a socket connection. Each transmission comes in two phases: (1) a json header with metadata about the volume and (2) the volume itself.

Once the user hits enter, she should see the following:

```
Prepping dataset: ~/pyneal-tutorial/
analysisTutorial/func.nii.gz
Dimensions: (64, 64, 18, 208)
TR: 1000
```

```
Connecting to Pyneal at 127.0.0.1:5555
waiting for connection...
```

II. Launch Pyneal using the appropriate configurations. In a new terminal window type:

```
cd ~/pyneal
python pyneal.py
```

This will launch the Pyneal GUI. Configure Pyneal with the following:

- Communication: Set the `Pyneal Host IP` to `127.0.0.1`, the `Pyneal-Scanner Port` to `5555`, and the `Results Server Port` to `5558`.
- Mask: In the `~/pyneal-tutorial/analysisTutorial/masks/` directory, there is a file named `L_MotorCortex.nii.gz`. Set the mask value in Pyneal to use this file. The user can unselect the `Weighted Mask?` option. Once the mask is loaded, the GUI should display the volume dimensions of the selected mask (here 64, 64, 18), allowing us to confirm a match with the dimensions of the upcoming scan.
- Preprocessing: Set `# of timepts` to: `208`. The user can keep the `Estimate Motion?` option selected if preferred.
- Analysis: Select the `Average` option.
- Output: Set the output directory to `~/pyneal-tutorial/analysisTutorial/output`. Check `Launch Dashboard?`

The user can then hit `Submit` to start Pyneal.

III. Start the scan

Back in the Scan Simulator terminal, the user should see a successful connection to Pyneal

```
connected to pyneal
Press ENTER to begin the "scan"
```

IV. Hit Enter to begin the simulated scan

As soon as the scan simulation begins, Pyneal Scanner begins processing and transmitting volumes of the provided data (`func.nii.gz`) to Pyneal, which calculates the mean activation within the target region on each volume and stores the results on the Pyneal's Results Server. As the scan is progressing, the user should see information about each volume appear in both the Scan Simulator and Pyneal terminals, indicating the volumes are being successfully transmitted and processed.

V. Results

- At the completion of the scan, the user can find the following Pyneal output files in `~/pyneal-tutorial/analysisTutorial/output/pyneal_001` (*Note*: the directory names increase in sequence. If this is the first time saving output to this directory, it will be `_001`, otherwise it will be a larger number):
  - `pynealLog.log`: complete log file from the scan.
  - `receivedFunc.nii.gz`: 4D Nifti of the data, as received by Pyneal.
  - `results.json`: JSON-formatted file containing the computed analysis results at each timepoint.
- Since the input data here came from a simple hand squeezing task where we computed the average signal within the Left Motor Cortex, we expect to see a fairly robust signal in the results, following the alternating blocks design of the task.
  - To confirm, the user can open the results.json file and plot the results at each timepoint using the user's preferred tools (e.g., Python, Matlab).

Note – it is also possible to use this setup to test communication with an End User (e.g., experimental presentation script) if desired. See https://jeffmacinnes.github.io/pyneal-docs/simulations/ for more details.

See *MacInnes et al. (2016) for an example of a single ROI analysis using built-in tools in the Pyneal toolkit. For additional examples of rt-fMRI single-ROI neurofeedback studies, see deCharms et al. (2005), Caria et al. (2010), Sulzer et al. (2013b), Greer et al. (2014), Young et al. (2017).*

Neurofeedback: Correlation Between Two ROIs Using a Custom Analysis Script

Example: Using a custom analysis script to calculate the correlation between two ROIs and use the correlation as feedback during a task. *E.g., A researcher wishes to calculate the correlation between the primary motor cortex and the caudate nucleus and use that correlated signal as neurofeedback in a hand squeezing task.*

This tutorial uses the Pyneal Scanner simulation script, which is located in:

```
~/pyneal/utils/simulation/pyneal_scanner_sim.py
```

To perform this tutorial the following steps are required:

I. Setup Scan Simulator

Like in the example in "Neurofeedback: Single ROI Averaging Using Built-in Analysis Functions," the first step is to set up Pyneal Scanner Simulator, which will send our sample dataset to Pyneal for analysis.

Open a new terminal and navigate to the Simulation Tools directory: `cd ~/pyneal/utils/simulation`

Run `pynealScanner_sim.py` and pass in the path to our sample dataset.

Type:

```
python pynealScanner_sim.py -f ~/pyneal-tutorial/analysisTutorial/func.nii.gz -t 1000 -sh 127.0.0.1 -sp 5555
```

Hit enter. The user should see the simulator prepare the data and wait for a connection to Pyneal:

```
Prepping dataset: ~/pyneal-tutorial/analysisTutorial/func.nii.gz
```

```
Dimensions: (64, 64, 18, 208)
TR: 1000
Connecting to Pyneal at 127.0.0.1:5555
waiting for connection...
```

II. Setup Custom Analysis Script

This tutorial includes a custom analysis script that the user will load into pyneal. This script can be found at: ~/pyneal-tutorial/analysisTutorial/customAnalysis_ROI_corr.py. Open this file to follow along below. This script is adapted from the customAnalysisTemplate.py that is included in the Pyneal toolkit.

There are two relevant sections to this script:

initialize

The analysis script includes an __init__ method that runs once Pyneal is launched. This section should be used to load any required files and initialize any variables needed once the scan begins.

In the __init__ method in the tutorial script, the user will find the following code block:

```
## Load the mask files for the 2 ROIs
we will compute the correlation between
# Note: we will be ignoring the mask
that is passed in from the Pyneal GUI
mask1_path = join(self.customAnalysis
Dir, 'masks/L_Caudate.nii.gz')
mask2_path = join(self.customAnalysis
Dir, 'masks/L_MotorCortex.nii.gz')
mask1_img = nib.load(mask1_path)
mask2_img = nib.load(mask2_path)
self.masks = {
  'mask1': {
    'mask': mask1_img.get_data() > 0,
    # creat boolean mask
    'vals': np.zeros(self.numTimepts)
    # init array to store mean signal
    on each timept
  },
  'mask2': {
    'mask': mask2_img.get_data() > 0,
    'vals': np.zeros(self.numTimepts)
  }
}
## Correlation config
self.corr_window = 10 # number of
timepts to calculate correlation over
```

The above block of code does the following:

- Loads each mask file. Note that while the template provides a reference to the mask file loaded via the Pyneal GUI, we are ignoring that mask and instead loading each mask manually.
- Pre-allocates an array for each mask where we will store the mean signal within that mask on each timepoint.
- Sets the correlation window to 10 timepoints, meaning that, with each new volume that arrives, the correlation between the two ROIs will be computed over the previous 10 timepoints.

compute

The compute method will be executed on each incoming volume throughout the scan, and provides the image data (vol) and volume index (volIdx) as inputs. This method should be used to define analysis steps.

In the compute method in the tutorial script, the user will find the following code block:

```
## Get the mean signal within each mask
at this timept
for roi in self.masks:
   mask = self.masks[roi]['mask']
   meanSignal = np.mean(vol[mask])
   self.masks[roi]['vals'][volIdx] =
   meanSignal
## Once enough timepts have
accumulated, start calculating rolling
correlation
if volIdx > self.corr_window:
   # get the timeseries from each ROI
   over the correlation window
   roi1_ts = self.masks['mask1']['vals']
   [volIdx-self.corr_window:volIdx]
   roi2_ts = self.masks['mask2']['vals']
   [volIdx-self.corr_window:volIdx]
   # compute correlation,
   return r-value only
   Corr = stats.pearsonr(roi1_ts,
   roi2_ts)[0]
else:
   corr = None
return {'corr': corr }
```

The above block of code does the following:

- Computes the mean signal within each mask at the current timepoint.
- Once enough volumes have arrived, computes the correlation between the two ROIs over the specified correlation window.
- Returns the result of the correlation as a dictionary.

The results of any custom script need to be returned as a dictionary. The Pyneal will integrate these results into the existing pipeline and the results will be available via the Pyneal Results Server (for requests from an End User if desired) in the same manner as with the built-in analysis options.

III. Set up Pyneal

Next, configure Pyneal to use the custom analysis script developed above.

In a new terminal, launch Pyneal:

```
cd ~/pyneal
python pyneal.py
```

- Configure Pyneal:
  - Communication: Set the `Pyneal Host IP` to `127.0.0.1`, `Pyneal-Scanner Port` to `5555`, and the `Results Server Port` to `5558`.
  - Mask: In the `~/pyneal-tutorial/analysis Tutorial/masks/` directory, select `L_Motor Cortext.nii.gz`. Note that although the custom analysis script overrides the mask supplied here, a valid mask file is required nonetheless.
  - Preprocessing: Set `# of timepts` to: `208`. The user can keep the Estimate Motion? option selected if preferred.
  - Analysis: Select the `Custom` option. The user will be presented with a file dialog. Select the custom analysis script at `~/pyneal-tutorial/analysisTutorial/custom Analysis_ROI_corr.py`.
  - Output: Set the output directory to `~/pyneal-tutorial/analysisTutorial/output`. Check `Launch Dashboard?`
- Hit `Submit` to start Pyneal.

IV. Start the scan

Back in the Scan Simulator terminal, the user should see a successful connection to Pyneal

```
connected to pyneal
Press ENTER to begin the "scan"
```

- Hit `Enter` to begin the simulated scan

As the scan is progressing, the user should see information about each volume appear in both the Scan Simulator and the Pyneal terminals, indicating the volumes are being successfully transmitted and processed.

V. Results

- At the completion of the scan, the user can find the following Pyneal output files in `~/pyneal-tutorial/analysisTutorial/output/pyneal_002` (Note: the directory names increase in sequence. If the user completed the single ROI NF tutorial first, it'll be `_002`, otherwise it'll be a different number):
  - `pynealLog.log`: complete log file from the scan.
  - `receivedFunc.nii.gz`: 4D Nifti of the data, as received by the Pyneal.
  - `results.json`: JSON-formatted file containing the computed analysis results at each timepoint.
- The custom analysis script computed a sliding window correlation between the Left Motor Cortex and the Left Caudate throughout the task.
  - To visualize these results, the user can open the `results.json` file and plot the results at each timepoint using their preferred tools (e.g., Python, Matlab).

DISCUSSION

Advantages of the Pyneal Toolkit rt-fMRI Software

A variety of tools currently exist that support real-time fMRI to varying degrees, including AFNI (Cox and Jesmanowicz, 1995), FIRE (Gembris et al., 2000), scanSTAT (Cohen, 2001), STAR (Magland et al., 2011), FieldTrip toolbox extension (Oostenveld et al., 2011), Turbo-BrainVoyager (Goebel, 2012), FRIEND (Sato et al., 2013), BART (Hellrung et al., 2015), OpenNFT (Koush et al., 2017), and Neu3CA-RT (Heunis et al., 2018). At a time when implementing real-time fMRI meant researchers had to develop custom in-house software solutions, these tools presented a valuable alternative, catalyzing new experiments, and supporting pioneering early research with real-time fMRI. Nevertheless, the existing software options are limited in one or more ways that fundamentally restricts who can use them and where, and what types of experiments they support. Please see **Table 1** for a comparison of the Pyneal toolkit to the other main rt-fMRI software packages currently available. For example, some of these tools require users to purchase licensing agreements for the package itself (e.g., Turbo-BrainVoyager), or are designed to work inside of commercial software packages like Matlab[7]. In addition, a number of these tools are designed to only support a particular usage of real-time fMRI, like neurofeedback, while not supporting other uses of rt-fMRI. And lastly, even in cases where the underlying code *is* customizable, it often requires proficiency with advanced computer languages like C++. We built the Pyneal toolkit to directly address these limitations.

Free and Open-Source

The Pyneal toolkit offers a number of key features that make it an appealing package for existing real-time fMRI practitioners as well as those new to the field. First, in support of the growing movement toward open-science, the Pyneal toolkit is free and open source. It is written entirely in Python (see text footnote 2), and all required dependencies are similarly cost-free and open. We chose to use Python specifically because it is sufficiently powerful to handle the computational demands of fMRI analysis in real-time and the language is comparatively easy for users to read and write, an important consideration when designing a package that encourages customization by researchers. Furthermore, the number of libraries designed to aid scientific computing (e.g., Numpy, Scipy, Scikit-learn), and the large user support community worldwide, have lead Python to surge in popularity among the sciences (see Perez et al., 2011), and neuroscience in particular (see Gleeson et al., 2017 and Muller et al., 2015). The Pyneal toolkit follows style and documentation guidelines of scientific python libraries, and when possible uses the same data formats and image orientation conventions as popular neuroimaging libraries (e.g., NiBabel). Moreover, the source code for the Pyneal toolkit is hosted via a GitHub repository, which ensures users can access the most up-to-date code releases, as well as track modifications and revisions to the codebase across time (Perkel, 2016).

[7]https://www.mathworks.com/help/matlab/

TABLE 1 | Comparison of common, currently available real-time fMRI software packages.

Software	Commercial license required?	Cost	Source code available?	Base software language	Network requirements	Main types of built in analyses	Limitations
Pyneal	No	Free	Yes	Python	TCP/IP socket communication	Out of the box ROI neurofeedback analyses; *allows fully custom analysis scripts written by users in Python*	Not compatible with multiband data yet; no online data preprocessing yet; has not been tested on Windows environment (no known incompatibilities)
AFNI plug_realtime	No (GNU GPL v2.0 license)	Free	Yes	C	TCP/IP socket communication	Data quality assessment (e.g., motion) and neurofeedback	Limited documentation online; limited built-in functions
Turbo-Brain Voyager	Yes	Price varies across countries; see https://www.brainvoyager.com/products/purchase.html for current pricing	Not for main software; may be available for plugins and remote extensions	C++	Depends on the MRI manufacturer. Siemens: TCP/IP connection to the imager and default dicom export to the TBV analysis computer. GE/Philips: supports reading the exported files	Incremental: GLM, ERA, motion correction, spatial smoothing, and drift removal; multi-voxel pattern classification; ICA; ROI NF	Commercial license required. Requires sophisticated software knowledge: custom analyses are allowed via user development of plugins; must be in C++. (Note – TBV provides a network interface build on top of the plugin interface. The network interface is available for all programming languages.)
FRIEND	No	Free	Yes	C++	TCP/IP socket communication for communicating with End Users via Friend Engine	Image preprocessing, NF, ROI analysis (PSC), and multivoxel pattern decoding	Requires sophisticated software knowledge: custom plugins must be written in C++. Frontend is fully customizable, but users must be comfortable writing socket protocols.
OpenNFT	No (GNU GPL v3.0 license)	Free	Yes	Python and Matlab	TCP/IP socket communication	Built-in key volume and time series preprocessing and processing procedures (e.g., spatial smoothing, high pass filtering, despiking); rt QA; incremental and cummulative GLM; the following types of NF: continuous and intermittent activation-based NF; intermittent effective connectivity NF, continuous classification-based NF.	Requires Matlab license (commercial); tested with Siemens and Philips, but should be compatible with other scanner types. Has not been tested on GE to our knowledge.

ROI, region of analysis; GLM, general linear model; ERA, event related averaging; ICA, independent component analysis; NF, neurofeedback; IP, internet protocol; TCP, transmission control protocol. Note, in this table we exclude packages that are exclusively quality control (for example see rtQC: https://github.com/rtQC-group/rtQC).

Flexibility in Handling Multiple Data Formats and Local Computing Configurations

A second advantage the Pyneal toolkit offers is flexibility in handling multiple different data formats and directory structures. MRI data can be represented via a number of different file formats, depending in part on the particular scanner manufacturer and/or automated processing pipelines that modify data before it gets written to disk. For instance, the scanner may store images using a universal medical imaging standard like DICOM, a more specific neuroimaging standard like Nifti, or a proprietary format like the PAR/REC file convention currently seen with Philips scanners. Moreover, even within a given file format, there is considerable variation in *how* data are represented. For instance, a single DICOM image file may represent a 2D slice (GE scanners) or a 3D volume arranged as a 2D mosaic grid (Siemens scanners). Lastly, even when two imaging centers have the same scanners and use the same data formats, there can be differences in how the local computing networks are configured. This affects where data is saved, and how the Pyneal toolkit can access existing pipelines. The Pyneal toolkit was designed to be robust to these differences across scanning environments.

Relatedly, a third advantage is the ability of the Pyneal toolkit to accommodate multiple different environmental variations. Importantly, the Pyneal toolkit splits data handling from real-time analysis tasks into modular components that run via independent processes. Pyneal Scanner is responsible for reading incoming MRI data in whatever form it takes, accessing the raw data, and reformatting to a standardized form that is compatible with subsequent analysis stages of Pyneal. The re-formatted data is then passed to the preprocessing and analysis stage of Pyneal via TCP/IP based interprocess communications. The modular nature of this configuration offers important advantages. For one, Pyneal Scanner and Pyneal are able (though not required) to run on separate workstations. This is important as researchers may lack the administrative permissions needed to significantly modify the computing environment of a shared scanning suite. For example, in a situation where the scanner console does not export images to a shared network directory, Pyneal Scanner can run on the scanner console and pass data to a remote workstation running Pyneal, minimizing the risk of interfering with normal scanner operations. In other situations where the scanner *does* export images to a shared network directory, Pyneal Scanner and Pyneal can run on the same workstation.

The modular nature of the Pyneal toolkit's design means that it can be modified to support new data formats in the future without having to drastically alter the core codebase. Importantly, if the Pyneal toolkit does not currently support a desired data format, researchers can modify Pyneal Scanner to accommodate their needs without having to modify the rest of the Pyneal toolkit core utilities. As the entire toolkit is free and open-source, users and welcome and encouraged to do so.

Fully Customizable Analyses

A fourth, and chief, advantage that the Pyneal toolkit offers is flexibility of analyses. The ability to design and implement uniquely tailored analysis routines via custom analysis scripts means that users can adapt the method to their research question rather than having to constrain their research questions based on the methodology. This flexibility means that the Pyneal toolkit can be used to accommodate a broader and more diverse spectrum of research and experimental goals, offering numerous benefits to the real-time neuroimaging community and general scientific advancement. Importantly, in the Pyneal toolkit, the entire incoming data stream is made available, and by using custom analysis scripts, researchers can extract, manipulate and interrogate whichever portions of that data are most relevant to their question. In addition, researchers are able to use these results in real-time for whatever purpose they choose, including neurofeedback, experimental control, quality-assurance monitoring, etc.

The ability to design and test one's own analyses will expedite the growth and maturation of real-time neuroimaging more broadly. It is worth highlighting that real-time fMRI is still a comparatively new approach, with many open questions regarding imaging parameters, experimental design, effect sizes, subject populations, long-term outcomes, and general best practices (Sulzer et al., 2013a). Determining satisfactory answers to these questions has been slow, in part due to the limitations of existing software and a small community of users. Customizing analyses in the Pyneal toolkit allows researchers to work in a rapid and iterative way to explore new methods, addressing these questions, and establishing a framework for future studies. It also means that researchers can keep up with the latest analytic advances in their domain without having to rely on external software developers to release new updates for their real-time tools.

In short, the Pyneal toolkit is powerful precisely because it does not presuppose how researchers intend to use it; our conviction is that advances in real-time neuroimaging are best achieved by empowering the community to develop those advances itself.

Limitations

While the Pyneal toolkit offers a convenient and flexible infrastructure for accessing and using fMRI data in real-time, there are a few limitations with the software presently. First, the Pyneal toolkit does not currently include built-in online denoising of the raw fMRI data. Depending on the application, a user may find that simple denoising steps prior to analysis, such as slow-wave drift removal or head motion correction, may increase the signal-to-noise ratio and improve the statistical power of the analysis. We plan to include built-in options for basic denoising in forthcoming software releases. In the meantime, the current version of the Pyneal toolkit allows users to implement their own denoising steps as part of a customized processing pipeline via a custom analysis script.

Second, the Pyneal toolkit offers built-in support for standard data formats found across the three main scanner manufacturers, but does not currently support multiband acquisitions. As imaging technology advances, multiband acquisitions are becoming increasingly common as a way to increase coverage while maintaining short TRs. As such, we plan to offer built-in multiband support in an upcoming software update. Due to the

modular nature of the Pyneal toolkit, multiband support can be integrated as a component of Pyneal Scanner without requiring significant changes to the bulk of the code base.

Third, the Pyneal toolkit was built and tested using Python 3 on Linux and macOS environments. While there are no obvious incompatibilities with a Windows environment, we have not had the resources to thoroughly test the Pyneal toolkit across multiple platforms. We encourage Windows users to run the Pyneal toolkit via a virtual machine configured as a Linux operating system. In future versions of the Pyneal toolkit we hope to offer broader support across platforms, or containerize the application using a tool like Docker[8] in order to be platform agnostic.

While our team is working to improve the aforementioned limitations, we would also like to extend an invitation to the neuroimaging community to contribute directly to the Pyneal toolkit. The Pyneal toolkit was developed with the open source ethos of sharing and collaboration. It lives in the GitHub ecosystem, which facilitates collaborative work across multiple teams and/or individuals, and offers an easy way for users to submit new features, discuss code modifications in detail, and log bugs as they are discovered. Working collaboratively in this manner ensures efficiency in expanding the software's capabilities and improving stability. Anyone interested in working on the Pyneal toolkit can find information in the *Contributor Guidelines* and *Contributor Code of Conduct* outlined in the documentation at the Pyneal toolkit GitHub repository at: https://github.com/jeffmacinnes/pyneal.

CONCLUSION

In this article we describe the Pyneal toolkit, a free and open-source software platform for rt-fMRI. The Pyneal toolkit provides seamless access to incoming MRI data across a variety of formats, a flexible basis to carry out preprocessing and analysis in real-time, a mechanism to communicate results in real-time with remote devices, and interactive tools to monitor the quality and status of an on-going real-time fMRI experimental session. In addition to a number of basic built-in analysis options, the Pyneal toolkit offers users the flexibility to design and implement fully customized processing pipelines, allowing real-time fMRI analyses to be tailored to the experimental question instead of the other way around [for two examples using the Pyneal toolkit with different experimental approaches see (MacInnes et al., 2016) and (MacDuffie et al., 2018)]. As the rt-fMRI community grows worldwide, new tools are needed that allow researchers to flexibly adapt to suit their unique needs, be that neurofeedback from a single or multiple regions, triggering task flow, or online multivariate classification. The Pyneal toolkit offers researchers a powerful way to address the current open questions in the field, and the flexibility necessary to adapt to answer future questions.

[8] https://www.docker.com/

DATA AVAILABILITY STATEMENT

Pyneal is available at https://github.com/jeffmacinnes/pyneal and full documentation is online at https://jeffmacinnes.github.io/pyneal-docs/.

AUTHOR CONTRIBUTIONS

JM designed and developed the software and documentation, and co-wrote the manuscript. KD consulted on software design, provided material support, and co-wrote the manuscript. RA and AS consulted on software design and implementation, provided material support, and revised the manuscript. RR and CP provided material support and revised the manuscript. All authors contributed to the article and approved the submitted version.

FUNDING

Funding support came from W.M. Keck Foundation (AS, CP, and RR), NCATS 1KL2TR002554 (KD), NIMH R01 MH094743 (RA), NSF EEC-1028725 (RR), as well as the Alfred P. Sloan Foundation (RA), Klingenstein Fellowship Award in the Neurosciences (RA), and the Dana Foundation Brain and Immuno-Imaging Program (RA). The content is solely the responsibility of the authors and does not necessarily represent the official views of the NIH or the NSF.

ACKNOWLEDGMENTS

The authors would like to thank Ian Ballard for helpful comments on the manuscript.

REFERENCES

Caria, A., Ranganatha, S., Ralf, V., Chiara, B., and Niels, B. (2010). Volitional control of anterior insula activity modulates the response to aversive stimuli. a real-time functional magnetic resonance imaging study. *Biol. Psychiatry* 68, 425–432. doi: 10.1016/j.biopsych.2010.04.020

Cohen, M. S. (2001). Real-time functional magnetic resonance imaging. *Methods* 25, 201–220. doi: 10.1006/meth.2001.1235

Cox, R. W., and Jesmanowicz, A. (1995). Real-time functional magnetic resonance imaging. *Magn. Reson. Insights* 33, 230–236. doi: 10.1002/mrm.1910330213

deCharms, R. C., Fumiko, M., Gary, H. G., David, L., John, M. P., Deepak, S., et al. (2005). Control over brain activation and pain learned by using real-time functional MRI. *Proc. Natl. Acad. Sci. U.S.A.* 102, 18626–18631. doi: 10.1073/pnas.0505210102

Gembris, D., John, G. T., Stefan, S., Wolfgang, F., Dieter, S., and Stefan, P. (2000). Functional magnetic resonance imaging in real time (FIRE): sliding-window correlation analysis and reference-vector optimization. *Magn. Reson. Med.* 43, 259–268. doi: 10.1002/(sici)1522-2594(200002)43:2<259::aid-mrm13>3.0.co;2-p

Gleeson, P., Andrew, P. D., Silver, R. A., and Giorgio, A. A. (2017). A commitment to open source in neuroscience. *Neuron* 96, 964–965. doi: 10.1016/j.neuron.2017.10.013

Goebel, R. (2012). BrainVoyager–past, present, future. *NeuroImage* 62, 748–756. doi: 10.1016/j.neuroimage.2012.01.083

Greer, S. M., Andrew, J. T., Gary, H. G., and Brian, K. (2014). Control of nucleus accumbens activity with neurofeedback. *NeuroImage* 96, 237–244. doi: 10.1016/j.neuroimage.2014.03.073

Hellrung, L., Maurice, H., Oliver, Z., Torsten, S., Christian, K., and Elisabeth, R. (2015). Flexible adaptive paradigms for fMRI using a novel software package 'Brain Analysis in Real-Time' (BART). *PLoS One* 10:e0118890. doi: 10.1371/journal.pone.0118890

Heunis, S., René, B., Rolf, L., Anton, D. L., Marcel, B., Bert, A., et al. (2018). Neu3CA-RT: a framework for real-time fMRI analysis. *Psychiatry Res.* 282, 90–102. doi: 10.1016/j.pscychresns.2018.09.008

Jenkinson, M. (2000). *Measuring Transformation Error by RMS Deviation. TR99MJ1*. Oxford: Oxford University.

Jenkinson, M., Christian, F. B., Timothy, E. J. B., Mark, W. W., and Stephen, M. S. (2012). FSL. *NeuroImage* 62, 782–790.

Koush, Y., John, A., Evgeny, P., Ronald, S., Peter, Z., and Sergei, B. (2017). OpenNFT: an open-source python/matlab framework for real-time fMRI neurofeedback training based on activity, connectivity and multivariate pattern analysis. *NeuroImage* 156, 489–503. doi: 10.1016/j.neuroimage.2017.06.039

MacDuffie, K. E., Jeff, M., Kathryn, C. D., Kari, M. E., Timothy, J. S., and Alison, R. A. (2018). Single session real-time fMRI neurofeedback has a lasting impact on cognitive behavioral therapy strategies. *NeuroImage Clin.* 19, 868–875. doi: 10.1016/j.nicl.2018.06.009

MacInnes, J. J., and Dickerson, K. C. (2018). *Real-Time Functional Magnetic Resonance Imaging. eLS*. Hoboken, NJ: John Wiley & Sons, Ltd.

MacInnes, J. J., Dickerson, K. C., Nan-Kuei, C., and Adcock, R. A. (2016). Cognitive neurostimulation: learning to volitionally sustain ventral tegmental area activation. *Neuron* 89, 1331–1342. doi: 10.1016/j.neuron.2016.02.002

Magland, J. F., Christopher, W. T., and Anna, R. C. (2011). Spatio-temporal activity in real time (STAR): optimization of regional fMRI feedback. *NeuroImage* 55, 1044–1053. doi: 10.1016/j.neuroimage.2010.12.085

Muller, E., James, A. B., Markus, D., Marc-Oliver, G., Michael, H., and Davison, A. P. (2015). Python in neuroscience. *Front, Neuroinform.* 9:11. doi: 10.3389/fninf.2015.00011

Oostenveld, R., Pascal, F., Eric, M., and Jan-Mathijs, S. (2011). FieldTrip: open source software for advanced analysis of meg, eeg, and invasive electrophysiological data. *Comput. Intell. Neurosci.* 2011:156869.

Perez, F., Granger, B. E., and Hunter, J. D. (2011). Python: an ecosystem for scientific computing. *Comput. Sci. Eng.* 13, 13–21. doi: 10.1109/mcse.2010.119

Perkel, J. (2016). Democratic databases: science on GitHub. *Nature* 538, 127–128. doi: 10.1038/538127a

Sato, J. R., Rodrigo, B., Fernando, F. P., Griselda, J. G., Ivanei, E. B., and Patricia, B. (2013). Real-Time fMRI pattern decoding and neurofeedback using FRIEND: an FSL-Integrated BCI toolbox. *PLoS One* 8:e81658. doi: 10.1371/journal.pone.0081658

Sitaram, R., Ros, T., Stoeckel, L., Haller, S., Scharnowski, F., Lewis-Peacock, J., et al. (2017). Closed-loop brain training: the science of neurofeedback. *Nat. Rev. Neurosci.* 18, 86–100. doi: 10.1038/nrn.2016.164

Stoeckel, L. E., Garrison, K. A., Ghosh, S., Wighton, P., Hanlon, C. A., Gilman, J. M., et al. (2014). Optimizing real time fMRI neurofeedback for therapeutic discovery and development. *NeuroImage Clin.* 5, 245–255. doi: 10.1016/j.nicl.2014.07.002

Sulzer, J., Haller, S., Scharnowski, F., Weiskopf, N., Birbaumer, N., Blefari, M. L., et al. (2013a). Real-Time fMRI neurofeedback: progress and challenges. *NeuroImage* 76, 386–399.

Sulzer, J., Ranganatha, S., Maria, L. B., Spyros, K., Niels, B., and Klaas, E. S. (2013b). Neurofeedback-mediated self-regulation of the dopaminergic midbrain. *NeuroImage* 83, 817–825. doi: 10.1016/j.neuroimage.2013.05.115

Voyvodic, J. T. (1999). Real-Time fMRI paradigm control, physiology, and behavior combined with near real-time statistical analysis. *NeuroImage* 10, 91–106. doi: 10.1006/nimg.1999.0457

Young, K. D., Greg, J. S., Vadim, Z., Raquel, P., Masaya, M., and Han, Y. (2017). Randomized clinical trial of real-time fMRI amygdala neurofeedback for major depressive disorder: effects on symptoms and autobiographical memory recall. *Am. J. Psychiatry* 174, 748–755. doi: 10.1176/appi.ajp.2017.16060637

Conflict of Interest: The authors declare that the research was conducted in the absence of any commercial or financial relationships that could be construed as a potential conflict of interest.

Copyright © 2020 MacInnes, Adcock, Stocco, Prat, Rao and Dickerson. This is an open-access article distributed under the terms of the Creative Commons Attribution License (CC BY). The use, distribution or reproduction in other forums is permitted, provided the original author(s) and the copyright owner(s) are credited and that the original publication in this journal is cited, in accordance with accepted academic practice. No use, distribution or reproduction is permitted which does not comply with these terms.

frontiers in Neuroscience

ORIGINAL RESEARCH
published: 16 September 2020
doi: 10.3389/fnins.2020.535441

Initial Experience of Challenge-Free MRI-Based Oxygen Extraction Fraction Mapping of Ischemic Stroke at Various Stages: Comparison With Perfusion and Diffusion Mapping

Shun Zhang[1], Junghun Cho[2,3], Thanh D. Nguyen[2], Pascal Spincemaille[2], Ajay Gupta[2], Wenzhen Zhu[1] and Yi Wang[2,3]**

[1] Department of Radiology, Tongji Hospital, Tongji Medical College, Huazhong University of Science and Technology, Wuhan, China, [2] Department of Radiology, Weill Cornell Medicine, New York, NY, United States, [3] Department of Biomedical Engineering, Cornell University, Ithaca, NY, United States

OPEN ACCESS

Edited by:
Alard Roebroeck, Maastricht University, Netherlands

Reviewed by:
Ives R. Levesque, McGill University, Canada
Jean Chen, University of Toronto, Canada
Chunmei Li, Beijing Hospital, China
Kamil Uludag, Maastricht University, Netherlands
Lirong Yan, University of Southern California, Los Angeles, United States

***Correspondence:**
Wenzhen Zhu
zhuwenzhen8612@163.com
Yi Wang
yiwang@med.cornell.edu

Specialty section:
This article was submitted to Brain Imaging Methods, a section of the journal Frontiers in Neuroscience

Received: *16 February 2020*
Accepted: *18 August 2020*
Published: *16 September 2020*

Citation:
Zhang S, Cho J, Nguyen TD, Spincemaille P, Gupta A, Zhu W and Wang Y (2020) Initial Experience of Challenge-Free MRI-Based Oxygen Extraction Fraction Mapping of Ischemic Stroke at Various Stages: Comparison With Perfusion and Diffusion Mapping. Front. Neurosci. 14:535441. doi: 10.3389/fnins.2020.535441

MRI-based oxygen extraction fraction imaging has a great potential benefit in the selection of clinical strategies for ischemic stroke patients. This study aimed to evaluate the performance of a challenge-free oxygen extraction fraction (OEF) mapping in a cohort of acute and subacute ischemic stroke patients. Consecutive ischemic stroke patients (a total of 30 with 5 in the acute stage, 19 in the early subacute stage, and 6 in the late subacute stage) were recruited. All subjects underwent MRI including multi-echo gradient echo (mGRE), diffusion weighted imaging (DWI), and 3D-arterial spin labeling (ASL). OEF maps were generated from mGRE phase + magnitude data, which were processed using quantitative susceptibility mapping (QSM) + quantitative blood oxygen level-dependent (qBOLD) imaging with cluster analysis of time evolution. Cerebral blood flow (CBF) and apparent diffusion coefficient (ADC) maps were reconstructed from 3D-ASL and DWI, respectively. Further, cerebral metabolic rate of oxygen ($CMRO_2$) was calculated as the product of CBF and OEF. OEF, $CMRO_2$, CBF, and ADC values in the ischemic cores (absolute values) and their contrasts to the contralateral regions (relative values) were evaluated. One-way analysis of variance (ANOVA) was used to compare OEF, $CMRO_2$, CBF, and ADC values and their relative values among different stroke stages. The OEF value of infarct core showed a trend of decrease from acute, to early subacute, and to late subacute stages of ischemic stroke. Significant differences among the three stroke stages were only observed in the absolute OEF ($F = 6.046$, $p = 0.005$) and relative OEF ($F = 5.699$, $p = 0.009$) values of the ischemic core, but not in other measurements (absolute and relative $CMRO_2$, CBF, ADC values, all values of $p > 0.05$). In conclusion, the challenge-free QSM + qBOLD-generated OEF mapping can be performed on stroke patients. It can provide more information on tissue viability that was not available with CBF and ADC and, thus, may help to better manage ischemic stroke patients.

Keywords: ischemic stroke, MRI, oxygen extraction fraction, cerebral metabolic rate of oxygen, quantitative susceptibility mapping, cerebral blood flow

INTRODUCTON

Ischemic stroke due to impaired blood flow to the brain is one of the leading causes of mortality and morbidity all over the world (Benjamin et al., 2017; Wang et al., 2017). A major therapy objective is to salvage tissue in the ischemic penumbra, a region with perfusion below a functional threshold but above a preservation threshold (Dirnagl et al., 1999; Pushie et al., 2018; Thirugnanachandran et al., 2018). The penumbra is estimated using MRI according to the mismatch between perfusion weighted imaging (PWI, indicating a functional threshold) and diffusion weighted imaging (DWI, non-hyperintensity indicating a preservation threshold). However, the difficulty in perfusion quantification makes it problematic to define a PWI threshold (Wouters et al., 2017; Zaro-Weber et al., 2017). The PWI–DWI mismatch may overestimate the penumbral tissue with the mismatch volume varying with quantification methods (Sobesky et al., 2005).

Penumbra evolves rapidly within the first few hours (Dirnagl et al., 1999; Pushie et al., 2018; Thirugnanachandran et al., 2018), and 24 h may be the threshold time window beyond which ischemic lesion becomes irreversible (Bonova et al., 2013). Accordingly, therapy of ischemic stroke is guided by the time from stroke onset. In current guidelines, intravenous administration of thrombolytic tissue plasminogen activator can be performed within 4.5 h (Davis and Donnan, 2009), and endovascular thrombectomy guided by advanced imaging of penumbral pattern can be performed within 24 h (Saver et al., 2016; Albers et al., 2018; Nogueira et al., 2018; Powers et al., 2018; Adeoye et al., 2019). Additionally, about 14% of strokes are wake-up types without known onset time (Mackey et al., 2011). Therefore, it is important for stroke therapy to assess tissue viability in ischemic lesions and differentiate stroke stages (Allen et al., 2012).

Oxygen extraction fraction (OEF) mapping reflects tissue metabolic state and is regarded as a very sensitive parameter in characterizing neural damage as tissue evolves from oligemia, to penumbra, and finally to death during ischemia (Powers, 1991; Leigh et al., 2018). The ^{15}O positron emission tomography (^{15}O-PET) is the gold standard for quantitatively assessing OEF and cerebral metabolic rate of oxygen ($CMRO_2$). However, the 2 min half-life of ^{15}O requires a cyclotron in the PET room, which is not available in almost all clinical practices, and PET is too expensive for routine use (Heiss, 2012; Leigh et al., 2018).

MRI-based OEF and $CMRO_2$ mapping techniques have recently been developed to evaluate oxygen consumption in tissue using quantitative blood oxygenation level-dependent (BOLD) contrast (He and Yablonskiy, 2007; Yablonskiy et al., 2013a), quantitative imaging of extraction of oxygen and tissue consumption (QUIXOTIC) (Bolar et al., 2011), calibrated BOLD (Davis et al., 1998; Gauthier and Hoge, 2012; Hoge, 2012; Blockley et al., 2013), and quantitative susceptibility mapping (QSM) (Zhang et al., 2015, 2017, 2018; Cho et al., 2018, 2020). In QSM, post-processing of complex 3D multi-echo gradient echo (mGRE) data (de Rochefort et al., 2010), tissue iron (ferritin, diffuse), and blood deoxyheme iron (in venioles, cylinders) can be separated using vascular challenges or prior knowledge (Zhang et al., 2015, 2017, 2018). Recently, OEF mapping can be achieved by combining QSM processing of phase and quantitative blood oxygen level-dependent (qBOLD) modeling of magnitude (Ogawa et al., 1990; Yablonskiy and Haacke, 1994b) of mGRE data without any vascular challenge administration (Cho et al., 2018, 2020), making it ready for routine use in imaging acute ischemic patients. When 3D OEF is multiplied by cerebral blood flow (CBF) from 3D arterial spin labeling (ASL) images, $CMRO_2$ can be generated from MRI examinations.

In this work, we report an initial experience using challenge-free OEF mapping from mGRE (Cho et al., 2020) in a cohort of acute and subacute ischemic stroke patients, and compared it with apparent diffusion coefficient (ADC), CBF, and $CMRO_2$ mapping.

MATERIALS AND METHODS

Patient Cohort

This was a retrospective study for which written informed consent from patients was waived by the local institutional review board.

A total of 30 consecutive patients with ischemic stroke from January 2014 to January 2015 were recruited according to the following inclusion criteria: (1) the time interval between stroke onset and MRI examination was quantifiable and ranged between 6 h and 15 days; (2) ischemic lesion caused by the stenosis or occlusion of the middle cerebral artery; (3) MRI scan protocol included 3D mGRE and 3D-ASL, in addition to conventional T1 weighted (T1w), T2 weighted (T2w), T2w FLAIR, and DWI sequences; (4) patients did not receive therapy of intravenous thrombolysis or mechanical thrombectomy before the MRI scan; and (5) patients did not show hemorrhage transformation in subsequent MRI scans. A detailed description of the patient characteristics is shown in **Table 1**.

The included ischemic stroke patients were classified into three groups (Fung et al., 2011) based on the time interval between stroke onset and MRI examination: (1) acute stage (6–24 h, $n = 5$); (2) early subacute stage (1–7 days, $n = 19$); and (3) late subacute stage (7–15 days, $n = 6$) (**Table 1**).

MRI Protocol and Image Processing

Brain MRIs were performed on a GE 3.0T scanner (Discovery MR750, GE Healthcare) with a 32-channel head coil. The image protocol consisted of 3D mGRE, 3D-ASL, and conventional sequences (T1w, T2w, T2w FLAIR, and DWI). The acquisition parameters for mGRE were field of view = 24 × 24 cm, TR = 42.8 m, TE1/ΔTE = 4.5/4.9 m, number of TEs = 8, acquisition matrix = 416 × 320, readout bandwidth = 244 Hz/pixel, slice thickness = 2 mm, flip angle = 20°, number of averages = 1, and scan time = 5 min 15 s Parameters for 3D-ASL were field of view = 24 × 24 cm, TR = 4,787 m, TE = 14.6 m, acquisition matrix = 128 × 128, slice thickness = 4 mm, post-labeling delay time = 1,525 m, and number of averages = 3. Parameters for DWI were field of view = 24 × 24 cm, TR = 3,000 m, TE = 71 m, acquisition matrix = 160 × 160, flip angle = 90°, slice thickness = 5 mm, number of averages = 4, *b*-value = 0,

TABLE 1 | Patient characteristics and demographics.

	No. of patients	Gender (M/F)	Age (years, mean ± SD)	Time between stroke onset and MRI examination (days, mean ± *SD*)	NIHSS (mean ± *SD*)	Causative subtypes (no. of 1/2/3/4/5*)
Acute	5	4/1	57.6 ± 8.6	0.7 ± 0.4	8.4 ± 7.0	3/0/2/0/0
Early subacute	19	15/4	58.7 ± 11.4	3.7 ± 1.7	7.5 ± 4.0	6/1/4/1/7
Late subacute	6	6/0	52.5 ± 8.9	9.8 ± 2.8	8.2 ± 3.9	3/1/2/0/0

*NIHSS, National Institutes of Health Stroke Scale. *Causative subtypes of ischemic stroke (Ay et al., 2005): 1, large artery atherosclerosis; 2, cardioaortic embolism; 3, small-artery occlusion; 4, other causes; 5, undetermined causes.*

1,000 s/mm^2. The 3D-ASL and DWI images were sent to a GE workstation (GE Healthcare, AW4.5 workstation) for cerebral blood flow (CBF) and apparent diffusion coefficient (ADC) calculation. QSM was reconstructed from mGRE images using a fully automated zero-referenced morphology enabled dipole inversion (MEDI + 0) method with the ventricular cerebrospinal fluid as a zero reference according to the following optimization (Liu et al., 2018):

$$\begin{aligned}\underset{\chi(r)}{\operatorname{argmin}} &||w(r)\left(e^{-iSMV*d*\chi(r)}-e^{-iSMV*b(r)}\right)||_2^2\\ &+\lambda_1||M_G(r)\nabla\chi(r)||_1+\lambda_2 M_{CSF}(r)\left(\chi(r)-\overline{\chi_{CSF}}\right)_2^2 \qquad (1)\end{aligned}$$

where SMV is the spherical mean value operator (radius 5 mm), $w(r)$ reflects the reliability of the local field $b(r)$, $M_G(r)$ is the edge mask, ∇ is the 3D gradient operator, and $\overline{\chi_{CSF}}$ is the average of $\chi(r)$ over the mask M_{CSF}. All the images were co-registered to the magnitude image, which is the geometric mean of the magnitude of mGRE along the time direction and has the same space with QSM, using the FMRIB's Linear Image Registration Tool algorithm (Jenkinson et al., 2002).

To decompose the susceptibility source into cylindrical deoxyheme iron and diffuse susceptibility source, QSM susceptibility sources was modeled as

$$\begin{aligned}&\chi_{QSM}(Y,\nu,\chi_{nb})\\ &=\left[\frac{\chi_{ba}}{\alpha}+\psi_{Hb}\cdot\Delta\chi_{Hb}\cdot\left(-Y+\frac{1-(1-\alpha)\cdot Y_a}{\alpha}\right)\right]\cdot\nu\\ &\quad+\left(1-\frac{\nu}{\alpha}\right)\cdot\chi_{nb} \qquad (2)\end{aligned}$$

where α is the vein volume fraction assumed to be constant (0.77), ψ_{Hb} is the hemoglobin volume fraction (0.0909 for tissue and 0.1197 for vein), and $\Delta\chi_{Hb}$ is the susceptibility difference between deoxy- and oxy-hemoglobin (12,522 ppb). The qBOLD model of the magnitude signal $|s_j|$ for the jth echo at echo time $j\Delta TE$ in multi-echo magnitude time evolution was (Yablonskiy et al., 2013b)

$$\begin{aligned}|s_j| &= F_{qBOLD}\left(Y,\nu,\chi_{nb},s^0,R_2,\ j\Delta TE\right)\\ &= s^0 e^{-R_2\cdot j\Delta TE}e^{-\nu f\left(\delta\omega(Y,\chi_{nb})\cdot j\Delta TE\right)}g\left(j\Delta TE\right) \qquad (3)\end{aligned}$$

where $f(\delta\omega\cdot TE)={}_1F_2\left(\left[-\frac{1}{2}\right];\left[\frac{3}{4},\frac{5}{4}\right];-\frac{9}{16}(\delta\omega\cdot TE)^2\right)-1$ with ${}_1F_2$is the generalized hypergeometric function, $\delta\omega(Y,\chi_{nb})=\frac{1}{3}\cdot\gamma\cdot B_0\cdot\left[\mathrm{Hct}\cdot\Delta\chi_0\cdot(1-Y)+\chi_{ba}-\chi_{nb}\right]$, and g accounts for the macroscopic contributions due to voxel sensitivity function. Here, γ is the gyromagnetic ratio (267.513 MHz/T), B_0 is the main magnetic field (3T in our study), Hct is the hematocrit (0.357), $\Delta\chi_0$ is the susceptibility difference between fully oxygenated and fully deoxygenated blood ($4\pi\times 0.27$ ppm) (Yablonskiy and Haacke, 1994a), χ_{ba} is the purely oxygenated blood susceptibility (-108.3 ppb), $Y$is the oxygenation, χ_{nb} is the non-blood susceptibility, and ν is the vein blood volume fraction. In determining $OEF=1-\frac{Y}{Y_a}$ with Y_a, the arterial oxygen saturation (0.98), the reconstruction problem from the multi-echo data is to combine the QSM value χ of the phase analysis and the qBOLD data fitting of the magnitude analysis using denoising regularization $R\left(Y,\nu,\chi_{nb},s^0,R_2\right)$ (Cho et al., 2018):

$$\begin{aligned}\underset{Y,\nu,\chi_{nb},s^0,R_2}{\operatorname{argmin}} &\sum_j\left|\left|s_j\right|-F_{qBOLD}\left(Y,\nu,\chi_{nb},s^0,R_2,\ j\Delta TE\right)\right|_2^2\\ &+w\left|\left|\chi-\chi_{QSM}(Y,\nu,\chi_{nb})\right|\right|_2^2+\lambda R\left(Y,\nu,\chi_{nb},s^0,R_2\right) \qquad (4)\end{aligned}$$

The above minimization problem is solved using a strong denoising algorithm called a cluster analysis of time evolution (CAT) where voxels with similar mGRE magnitude time evolutions are assumed to have similar model parameter values, including OEF, and are grouped into a cluster (Cho et al., 2020). For the grouping, X-means, a modified K-means method that provides an optimal number of clusters, was used with the squared Euclidean distance of the magnitude time evolution across echoes as the similarity measurement. CBF maps were used to further generate the $CMRO_2$ maps using the equation: $CMRO_2 = CBF \times OEF \times [H]_a$, where $[H]_a = 7.377$ μmol/ml is the oxygenated heme molar concentration in the arteriole.

Image Analysis

The ischemic core region was manually segmented on co-registered DWI and ADC images by an experienced neuroradiologist (7 years of experience), and the contralateral mirror area with a similar size was also drawn. Infarct cores were defined by identifying the hyperintense regions on the DWI maps and confirmed to be hypointense on the corresponding ADC map. The hypoperfused region on CBF was identified by comparison with the contralateral region. A mismatch region between the hypoperfused region on CBF and the ischemic core on DWI/ADC was also segmented when existed. For each patient, OEF, $CMRO_2$, CBF, and ADC were measured on a segmented ischemic core region of interest (ROI) as their absolute values. The differences in OEF, $CMRO_2$, CBF, and ADC

between an ischemic core and its contralateral ROI were also computed using their contrasts or relative values.

Statistical Analysis

Statistical analyses were performed with SPSS for Windows (version 22.0, Chicago, IL, United States). The differences among the three ischemic stages for absolute OEF, $CMRO_2$, CBF, and ADC values and relative OEF, $CMRO_2$, CBF, and ADC were performed using one-way analysis of variance (ANOVA), followed by the least significant difference (LSD) multiple comparison *post hoc* tests. A value of $p < 0.05$ was recognized as statistically significant.

RESULTS

In three of five acute stroke cases (6, 18, and 24 h from stroke symptom onset), there was a mismatch between the hypoperfused region on CBF and the ischemic core region on DWI/ADC (**Figure 1** and **Supplementary Figure 1**), and the hypoperfused mismatch region had a slightly higher OEF value than the ischemic core region (yellow ROI in **Figure 1**). The matched region had a similar signal or scattered hypointense signal on OEF when compared to the contralateral region. On $CMRO_2$ and CBF maps, the ischemic core region showed a low signal in every stage. There existed no mismatch region in the other two acute stroke cases. The ischemic core region had a decreased ADC for all the five acute cases. The OEF, $CMRO_2$, and the relevant CBF, QSM, DWI, and ADC maps of one acute ischemic stroke patient are shown in **Figure 1**. In early subacute and late subacute stages, the OEF of the ischemic core region manifested as a heterogeneously low signal, compared to the contralateral region.

The absolute OEF, $CMRO_2$, CBF, and ADC values of the ischemic core and the contralateral region in each individual case, averaged values, and their differences or relative values in each stage are shown in **Figures 2**–**5**. The OEF and $CMRO_2$ values in the ischemic core showed a decreasing trend as the time between symptom onset and MRI examination increased (**Figures 2**, **3**, respectively), while the CBF and ADC values showed a slight increasing trend (**Figures 4**, **5**, respectively). There were significant changes among the three stages for the absolute OEF value ($F = 6.046$, $p = 0.005$) in the ischemic core and the relative OEF ($F = 5.699$, $p = 0.009$). *Post hoc* tests showed that the changes in absolute OEF values from acute to early subacute phase ($p = 0.003$), and from acute to late subacute phase ($p = 0.004$) were significant, but not significant from early subacute to late subacute phase ($p = 0.555$); the changes in the

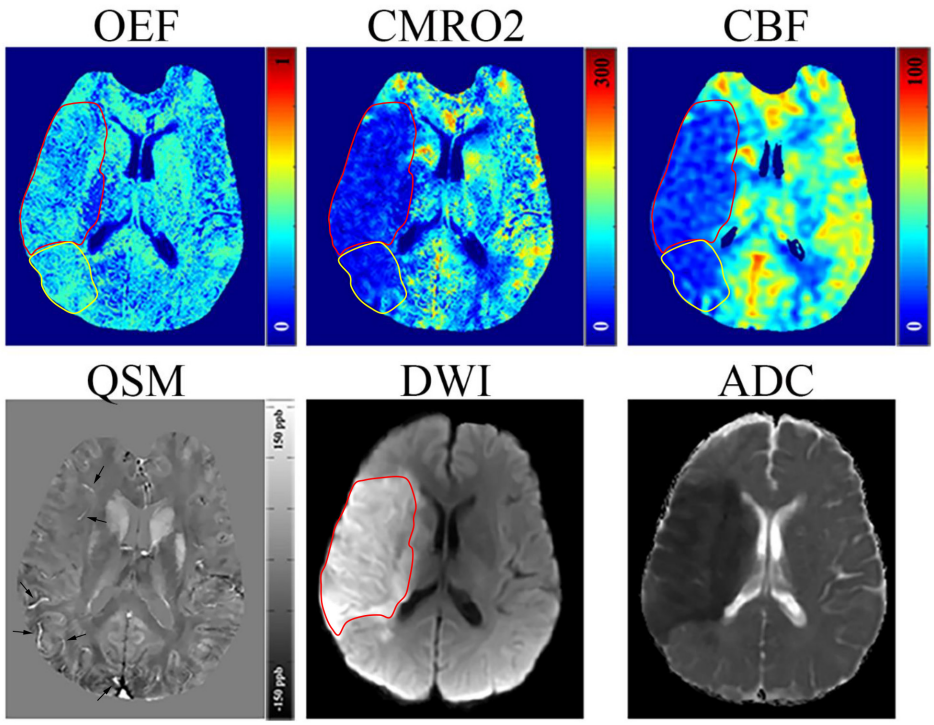

FIGURE 1 | Representative images of an acute ischemic stroke patient with 18 h between MRI examination and stroke symptom onset. The ischemic lesion was caused by the occlusion of the right middle cerebral artery. The ischemic core (red circle) identified on diffusion weighted imaging (DWI) and apparent diffusion coefficient (ADC) maps manifested as a slight decrease (30.38%) in oxygen extraction fraction (OEF) by comparing to the contralateral region (32.12%); some scattered dots within the ischemic core showed a higher OEF. A mismatch (yellow circle) is seen between the cerebral blood flow (CBF) and DWI maps near the ischemic core showing a relatively high OEF (32.15%), slightly higher than the contralateral region, which may represent salvageable ischemic tissue or benign oligemia tissue. Both the ischemic core and mismatch region showed a decrease in cerebral metabolic rate of oxygen ($CMRO_2$). On the quantitative susceptibility mapping (QSM) map, some hyperintense veins (arrow) can be seen surrounding the ischemic core.

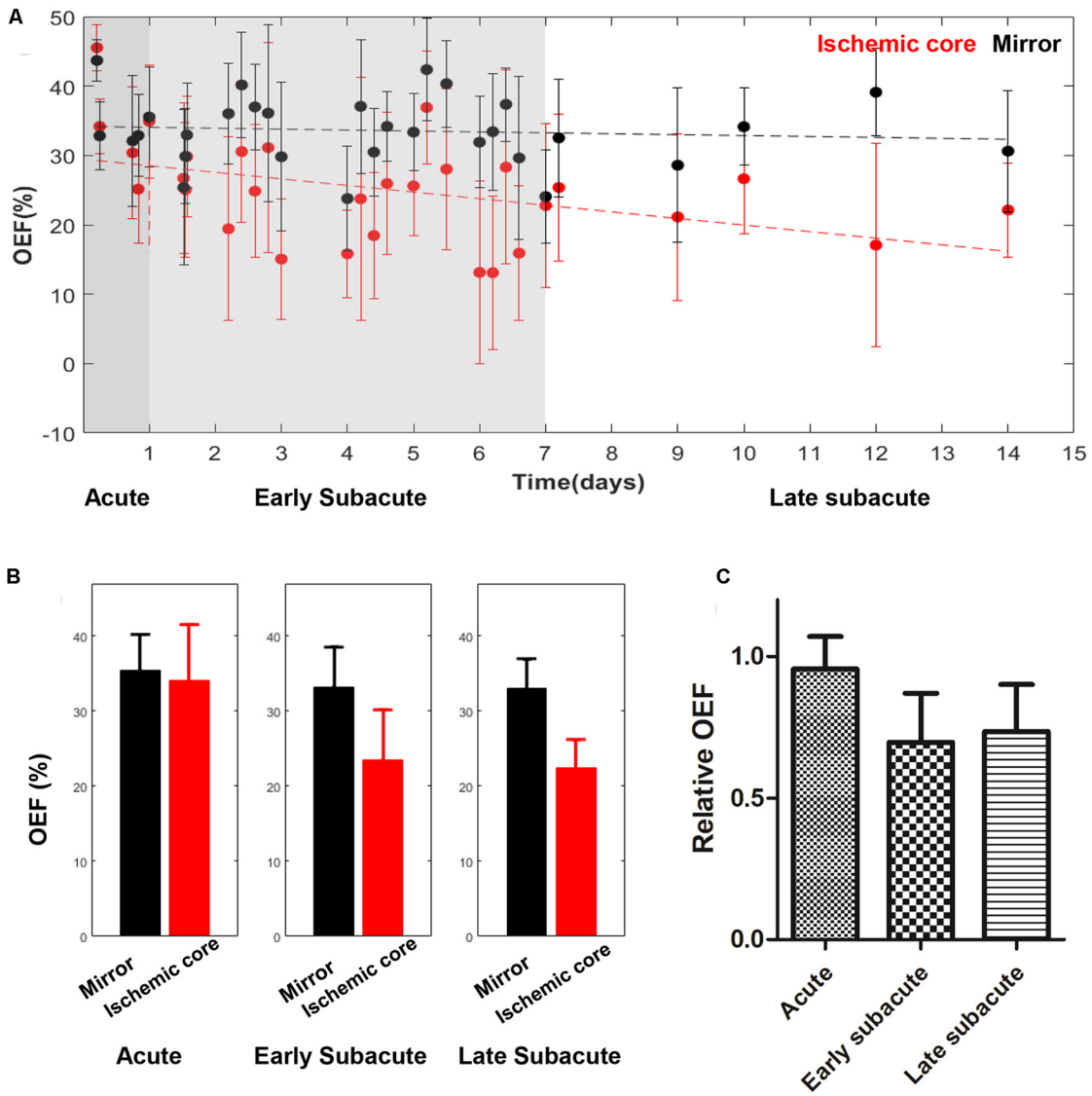

FIGURE 2 | Absolute OEF values in the ischemic core and the contralateral region of the 30 included cases **(A)** and averaged OEF value **(B)**, relative OEF **(C)** in every stage. The absolute OEF value in the ischemic core showed a trend of decrease as the time between symptom onset and MRI examination increased, while OEF values of contralateral regions were relatively stable. Relative OEF also showed a trend of decrease.

relative OEF from acute to early subacute phase ($p = 0.003$) and from acute to late subacute phase ($p = 0.009$) were significant, but not significant from early subacute to late subacute phase ($p = 0.867$). No significant changes among the three stages were found for absolute and relative $CMRO_2$, CBF, and ADC values (all values of $p > 0.05$) (**Table 2**).

DISCUSSION

Our preliminary results demonstrate that challenge-free oxygen extraction fraction (OEF) mapping can be performed in a clinical setting. OEF is the most sensitive imaging for measuring tissue functional changes in stroke stages compared to cerebral blood flow (CBF), apparent diffusion coefficient (ADC), and cerebral metabolic rate of oxygen consumption ($CMRO_2$). The challenge-free OEF mapping is achieved from quantitative susceptibility mapping (QSM) and quantitative blood oxygen level-dependent (qBOLD) modeling of 3D multi-echo gradient echo data, using cluster analysis of time evolution (CAT) to denoise QSM + qBOLD estimation of OEF. Challenge-free OEF mapping can be used to assess vital oxygen metabolism information of the ischemic tissue for comprehensive stratification of stroke therapy.

The current guidelines (Powers et al., 2018) in selecting eligible acute ischemic stroke patients to receive intravenous thrombolysis therapy are time dependent: the patient should be treated within 3 and 4.5 h of ischemic stroke symptom onset. Now, several studies (Sobesky et al., 2005;

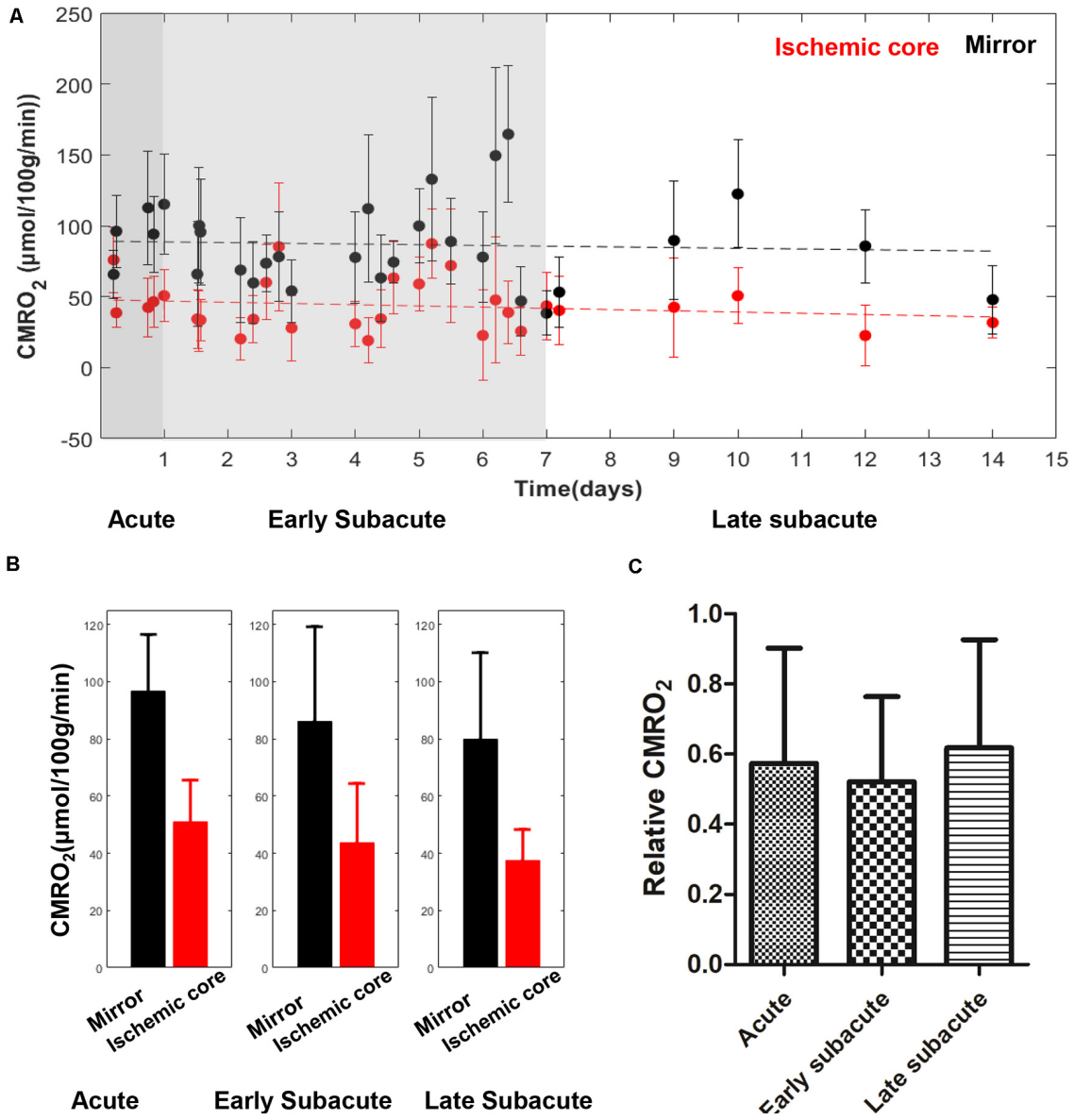

FIGURE 3 | Absolute $CMRO_2$ values in the ischemic core and the contralateral region of the 30 included cases **(A)** and averaged $CMRO_2$ value **(B)**, relative $CMRO_2$ **(C)** in every stage. The absolute $CMRO_2$ value in the ischemic core showed a trend of slight decrease with time increase. Relative $CMRO_2$ were relatively stable in the three stages.

Heidenreich et al., 2008; Heiss and Zaro Weber, 2017; Zaro-Weber et al., 2017; Leslie-Mazwi et al., 2018) have reported that identifying the existence of ischemic penumbra using MRI techniques, such as PWI/DWI mismatch approach, can prolong the time window to 24 h, or help change the treatment plan for intra-arterial thrombectomy (Albers et al., 2018). The ischemic penumbra region (Wu et al., 2018), which has preserved neuronal integrity, but impaired function due to hypoperfusion, can recover completely if it receives blood supply in a timely manner but will die otherwise. In the small patient cohort of this study, some of the acute ischemic stroke patients were found to have a slightly elevated OEF in some scattered areas of the ischemic core compared to the contralateral region. This implies that the ischemic core may contain some penumbral tissues even at 4.5 h after the stroke onset.

The CBF/DWI mismatch region in three acute cases was found to have a higher OEF than the ischemic core. The elevated OEF indicates that the ischemic tissue is probably struggling to survive by maintaining energy consumption under reduced blood flow. This information is useful in addressing the ASL-CBF underestimation of the hypoperfused ischemic tissue, due to the presence of a prolonged transit delay resulting from arterial occlusion (Wolf and Detre, 2007; Wang et al., 2012; Bivard et al., 2014). The CBF/DWI mismatch region is difficult

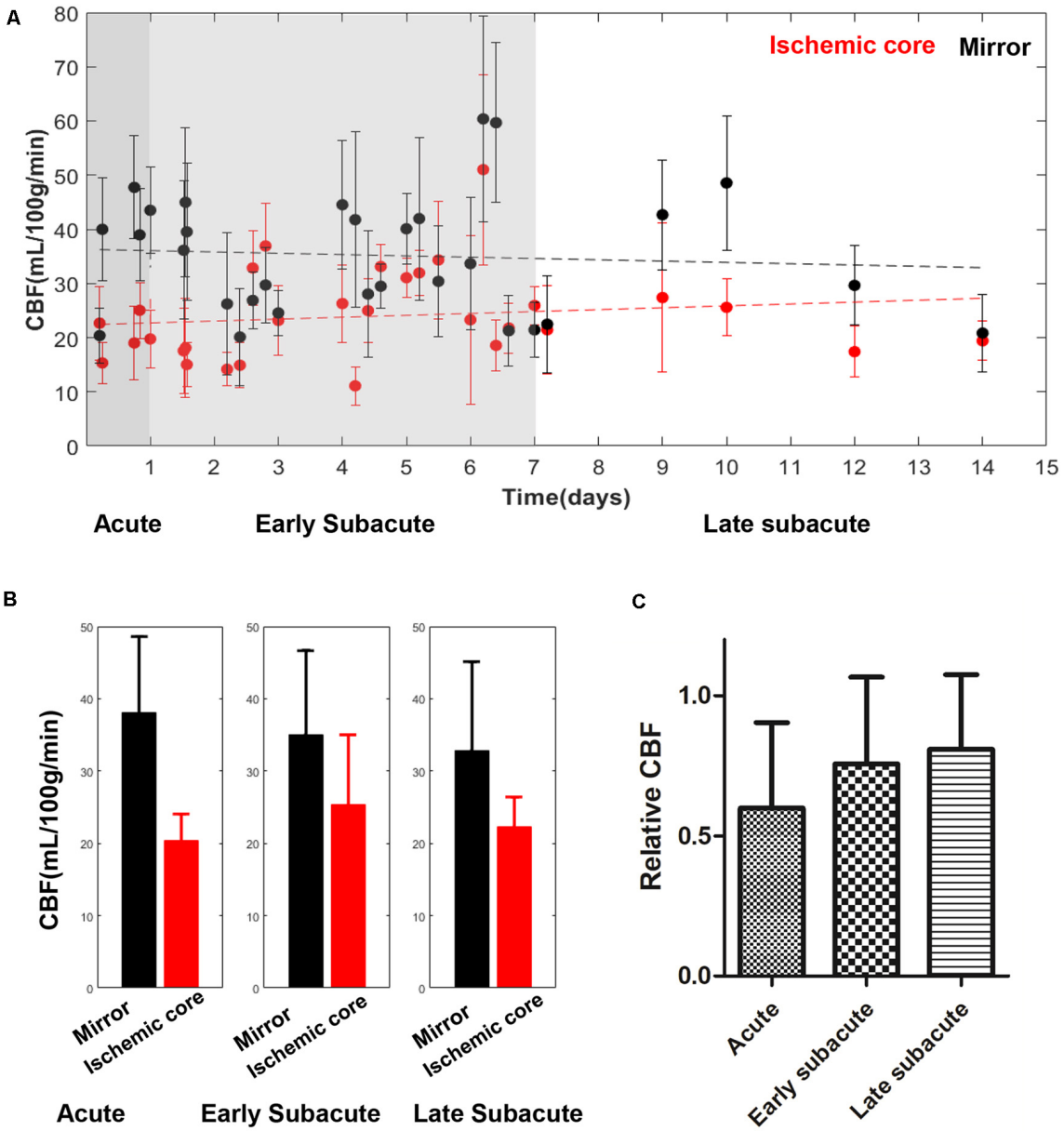

FIGURE 4 | Absolute CBF values in the ischemic core and the contralateral region of the 30 included cases **(A)** and averaged CBF value **(B)**, relative CBF **(C)** in every stage. The absolute CBF value in the ischemic core showed a trend of increase with time increase. Relative CBF also showed a trend of increase.

to interpret, as it may correspond to ischemic penumbra that benefits from timely revascularization or benign oligemia that does not progress to infarction and does not benefit from thrombotic therapy (Leigh et al., 2018; Wu et al., 2018). The risks of thrombolysis or intra-arterial thrombectomy may outweigh the benefits, if the ischemic core has a substantially decreased OEF, such as in case 5 in **Supplementary Figure 1**. Therefore, the challenge-free QSM + qBOLD-based OEF mapping that can be performed in clinical settings to assess tissue viability may be included in the routine MRI of ischemic stroke patients for comprehensive evaluation in therapy decision making.

OEF mapping captured the metabolic changes in different ischemic stages that are difficult to detect in CBF and ADC mapping. As the time between stroke symptom onset and MRI examination prolongs, OEF decreases, indicating that the ischemic tissue becomes functionally impaired without timely reperfusion, ending with cell death, consistent with the dynamic process of the pathophysiological change (Dirnagl et al., 1999; Tian et al., 2016). Our observed data on the trend of CBF increase with stroke onset time is consistent with the cerebral perfusion temporal changes measured on CT (Yang et al., 2015), usually as a result of the formation of collateral flow surrounding

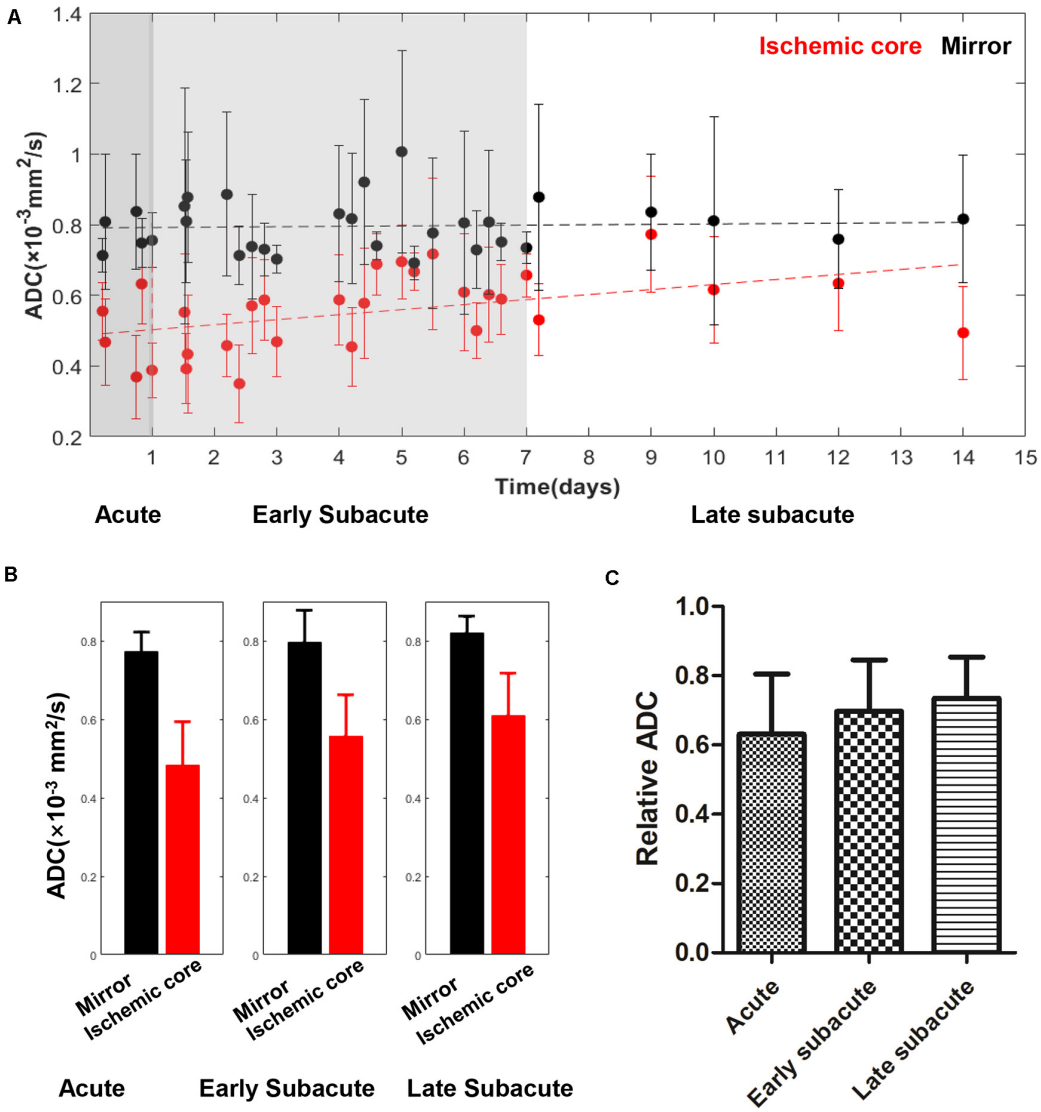

FIGURE 5 | Absolute ADC values in the ischemic core and the contralateral region of the 30 included cases **(A)** and averaged ADC value **(B)**, relative ADC **(C)** in every stage. The absolute ADC value in the ischemic core showed a trend of increase with the time between symptom onset and MRI examination increased, while the ADC value of the contralateral region was relatively stable. Relative ADC also showed a trend of increase.

TABLE 2 | The absolute OEF, oxygen extraction fraction; $CMRO_2$, cerebral metabolic rate of oxygen; CBF, cerebral blood flow and ADC, apparent diffusion coefficient values of ischemic core, and the relative OEF, $CMRO_2$, CBF, and ADC in different stages.

	Absolute OEF (%)	Relative OEF	Absolute $CMRO_2$ (μmol/100 g/min)	Relative $CMRO_2$	Absolute CBF (ml/100 g/min)	Relative CBF	Absolute ADC (× $10^{-3}mm^2/s$)	RelativeADC
Acute	34.03 ± 7.51	0.96 ± 0.11	50.82 ± 14.74	0.57 ± 0.33	20.36 ± 3.70	0.60 ± 0.31	0.48 ± 0.11	0.63 ± 0.17
Early subacute	23.56 ± 6.84	0.70 ± 0.17	43.63 ± 21.32	0.52 ± 0.24	25.27 ± 9.98	0.76 ± 0.31	0.55 ± 0.11	0.70 ± 0.15
Late subacute	21.73 ± 3.82	0.68 ± 0.13	38.54 ± 9.91	0.62 ± 0.31	22.86 ± 4.03	0.81 ± 0.27	0.59 ± 0.11	0.74 ± 0.13
F, P value	6.046, 0.005*	5.699, 0.009*	0.585, 0.564	0.316, 0.732	0.733, 0.490	0.738, 0.488	1.508, 0.239	0.734, 0.489

**Significant difference among three different stages using the one-way analysis of variance (ANOVA).*

the ischemic core; a few acute/early subacute cases of CBF at ischemic cores larger than contralateral regions (**Figure 4**) may reflect the extremes of collateral vascular remodeling or measurement errors. The available CBF map multiplied by the OEF map generates the $CMRO_2$ map, which in our results showed a relatively homogenous low signal. $CMRO_2$

errors might be mainly driven by the underestimation of ASL–CBF, which was, in part, caused by the short postlabel time (1,525 min) used in our study (Zaharchuk, 2011; Wang et al., 2012; Bivard et al., 2014) and, consequently, were not as sensitive as OEF in detecting metabolic changes in ischemic stroke stages. Accurate computation of $CMRO_2$ requires improvements in the accuracy of CBF mapping.

The CAT algorithm based on X-means machine learning has made QSM + qBOLD post-processing of the available multi-echo gradient echo MRI (mGRE) data for OEF mapping robust against noise. This CAT QSM + qBOLD OEF mapping eliminates assumptions in and, therefore, is theoretically more accurate than other OEF mapping methods (Kudo et al., 2016; Uwano et al., 2017; Zhang et al., 2017, 2018). QSM (de Rochefort et al., 2010; Wang and Liu, 2015; Liu et al., 2018) has been shown to be highly reproducible (Deh et al., 2015; Spincemaille et al., 2019), and recent technical developments in preconditioning for optimization execution (Liu et al., 2016) and in phase unwrapping (Dong et al., 2015) promise to make QSM robust even in brain regions near the air–tissue interface. The challenge of qBOLD prone to noise is effectively addressed by the CAT algorithm. The OEF map is generated from mGRE within 25 min on a standard desktop computer, which can be further shortened to a few minutes by optimizing the processing codes and using more powerful computers. Therefore, rapid OEF mapping can be included in routine clinical MRI protocols to accurately evaluate tissue viability in acute ischemic stroke patients, and upon further validation, would help patient management stratification for a timely beneficial therapy.

There are some limitations in this study. The small number of patients, particularly in the acute phase, only allowed a limited demonstration of the broad possible manifestations of the metabolic changes of stroke. The results here may not be generalized without further studies in larger cohorts of stroke patients. The delineation of penumbra tissue at risk, which is of great importance in guiding therapy stratification, could only be shown in three patients. The patients in this cross-section study only had one MRI, and there was an imbalanced gender distribution. Therefore, the benefits of the presented OEF mapping method illustrated here should be understood with caution. Future studies including more acute cases and longitudinal MRI scans are needed to validate our preliminary results. Finally, ischemic stroke patients with hemorrhagic transformation were not included. As further improvements are being developed to account for the strong susceptibility sources of hemorrhages for accurate OEF estimation, OEF mapping using the method described here should become feasible in these patients.

In conclusion, the challenge-free OEF mapping using CAT QSM + qBOLD modeling of mGRE data can be performed in clinical practice to assess oxygen metabolic information, which is helpful in evaluating tissue viability in acute ischemic stroke patients.

DATA AVAILABILITY STATEMENT

The datasets generated for this study are available on request to the corresponding author.

ETHICS STATEMENT

The studies involving human participants were reviewed and approved by the Institutional Review Board of Tongji Hospital, Tongji Medical College, Huazhong University of Science and Technology, Wuhan, China. Written informed consent for participation was not required for this study in accordance with the national legislation and the institutional requirements.

AUTHOR CONTRIBUTIONS

SZ, WZ, and YW were responsible for the study concepts and design. SZ, AG, WZ, and YW were responsible for literature research. SZ, AG, and WZ were responsible for the clinical studies. SZ, JC, TN, and PS were responsible for the statistical analysis. All authors were guarantors of integrity of the entire study and responsible for the experimental studies and data analysis, manuscript preparation and editing, and final approval.

FUNDING

This work was supported, in part, by grants from the National Natural Science Foundation of China (Grant Nos. 81801666, 81570462, and 81730049) and the National Institutes of Health (R01NS090464, R01NS095562, R21EB024366, S10OD021782, and R01CA181566).

SUPPLEMENTARY MATERIAL

The Supplementary Material for this article can be found online at: https://www.frontiersin.org/articles/10.3389/fnins.2020.535441/full#supplementary-material

REFERENCES

Adeoye, O., Nystrom, K. V., Yavagal, D. R., Luciano, J., Nogueira, R. G., Zorowitz, R. D., et al. (2019). Recommendations for the Establishment of Stroke Systems of Care: A 2019 Update. *Stroke* 50, e187–e210. doi: 10.1161/STR.0000000000000173

Albers, G. W., Marks, M. P., Kemp, S., Christensen, S., Tsai, J. P., Ortega-Gutierrez, S., et al. (2018). Thrombectomy for Stroke at 6 to 16 Hours with Selection by Perfusion Imaging. *New England Journal of Medicine* 378, 708–718. doi: 10.1056/NEJMoa1713973

Allen, L. M., Hasso, A. N., Handwerker, J., and Farid, H. (2012). Sequence-specific MR imaging findings that are useful in dating ischemic stroke. *Radiographics* 32, 1285–1297. doi: 10.1148/rg.325115760

Ay, H., Furie, K. L., Singhal, A., Smith, W. S., Sorensen, A. G., and Koroshetz, W. J. (2005). An evidence-based causative classification system for acute ischemic stroke. *Ann. Neurol.* 58, 688–697. doi: 10.1002/ana.20617

Benjamin, E. J., Blaha, M. J., Chiuve, S. E., Cushman, M., Das, S. R., Deo, R., et al. (2017). Heart Disease and Stroke Statistics-2017 Update A Report From the American Heart Association. *Circulation* 135, E146–E603. doi: 10.1161/Cir.0000000000000485

Bivard, A., Krishnamurthy, V., Stanwell, P., Levi, C., Spratt, N. J., Davis, S., et al. (2014). Arterial spin labeling versus bolus-tracking perfusion in hyperacute stroke. *Stroke* 45, 127–133. doi: 10.1161/STROKEAHA.113.003218

Blockley, N. P., Griffeth, V. E., Simon, A. B., and Buxton, R. B. (2013). A review of calibrated blood oxygenation level-dependent (BOLD) methods for the measurement of task-induced changes in brain oxygen metabolism. *NMR Biomed.* 26, 987–1003. doi: 10.1002/nbm.2847

Bolar, D. S., Rosen, B. R., Sorensen, A., and Adalsteinsson, E. (2011). QUantitative Imaging of eXtraction of oxygen and TIssue consumption (QUIXOTIC) using venular-targeted velocity-selective spin labeling. *Magn. Reson. Med.* 66, 1550–1562. doi: 10.1002/mrm.22946

Bonova, P., Burda, J., Danielisova, V., Nemethova, M., and Gottlieb, M. (2013). Development of a pattern in biochemical parameters in the core and penumbra during infarct evolution after transient MCAO in rats. *Neurochem. Int.* 62, 8–14. doi: 10.1016/j.neuint.2012.10.015

Cho, J., Kee, Y., Spincemaille, P., Nguyen, T. D., Zhang, J., Gupta, A., et al. (2018). Cerebral metabolic rate of oxygen (CMRO2) mapping by combining quantitative susceptibility mapping (QSM) and quantitative blood oxygenation level-dependent imaging (qBOLD). *Magn. Reson. Med.* 80, 1595–1604. doi: 10.1002/mrm.27135

Cho, J., Zhang, S., Kee, Y., Spincemaille, P., Nguyen, T. D., Hubertus, S., et al. (2020). Cluster analysis of time evolution (CAT) for quantitative susceptibility mapping (QSM) and quantitative blood oxygen level-dependent magnitude (qBOLD)-based oxygen extraction fraction (OEF) and cerebral metabolic rate of oxygen (CMRO2) mapping. *Magn. Reson. Med.* 83, 844–857. doi: 10.1002/mrm.27967

Davis, S. M., and Donnan, G. A. (2009). 4.5 *hours: the new time window for tissue plasminogen activator in stroke*. *Stroke* 40, 2266–2267. doi: 10.1161/STROKEAHA.108.544171

Davis, T. L., Kwong, K. K., Weisskoff, R. M., and Rosen, B. R. (1998). Calibrated functional MRI: mapping the dynamics of oxidative metabolism. *Proc. Natl. Acad. Sci. USA* 95, 1834–1839. doi: 10.1073/pnas.95.4.1834

de Rochefort, L., Liu, T., Kressler, B., Liu, J., Spincemaille, P., Lebon, V., et al. (2010). Quantitative susceptibility map reconstruction from MR phase data using bayesian regularization: validation and application to brain imaging. *Magn. Reson. Med.* 63, 194–206. doi: 10.1002/mrm.22187

Deh, K., Nguyen, T. D., Eskreis-Winkler, S., Prince, M. R., Spincemaille, P., Gauthier, S., et al. (2015). Reproducibility of quantitative susceptibility mapping in the brain at two field strengths from two vendors. *J. Magn. Reson. Imaging* 42, 1592–1600. doi: 10.1002/jmri.24943

Dirnagl, U., Iadecola, C., and Moskowitz, M. A. (1999). Pathobiology of ischaemic stroke: an integrated view. *Trends Neurosci* 22, 391–397. doi: 10.1016/s0166-2236(99)01401-0

Dong, J., Liu, T., Chen, F., Zhou, D., Dimov, A., Raj, A., et al. (2015). Simultaneous phase unwrapping and removal of chemical shift (SPURS) using graph cuts: application in quantitative susceptibility mapping. *IEEE Trans. Med. Imaging* 34, 531–540. doi: 10.1109/TMI.2014.2361764

Fung, S. H., Roccatagliata, L., Gonzalez, R. G., and Schaefer, P. W. (2011). MR diffusion imaging in ischemic stroke. *Neuroimaging Clin. N. Am.* 21, 345–377. doi: 10.1016/j.nic.2011.03.001

Gauthier, C. J., and Hoge, R. D. (2012). Magnetic resonance imaging of resting OEF and CMRO2 using a generalized calibration model for hypercapnia and hyperoxia. *Neuroimage* 60, 1212–1225. doi: 10.1016/j.neuroimage.2011.12.056

He, X., and Yablonskiy, D. A. (2007). Quantitative BOLD: mapping of human cerebral deoxygenated blood volume and oxygen extraction fraction: default state. *Magn. Reson. Med.* 57, 115–126. doi: 10.1002/mrm.21108

Heidenreich, J. O., Hsu, D., Wang, G., Jesberger, J. A., Tarr, R. W., Zaidat, O. O., et al. (2008). Magnetic resonance imaging results can affect therapy decisions in hyperacute stroke care. *Acta Radiol.* 49, 550–557. doi: 10.1080/02841850801958320

Heiss, W. D. (2012). David sherman lecture 2012: the role of positron emission tomography for translational research in stroke. *Stroke* 43, 2520–2525. doi: 10.1161/STROKEAHA.112.658237

Heiss, W. D., and Zaro Weber, O. (2017). Validation of MRI Determination of the Penumbra by PET Measurements in Ischemic Stroke. *J Nucl Med* 58, 187–193. doi: 10.2967/jnumed.116.185975

Hoge, R. D. (2012). Calibrated FMRI. *Neuroimage* 62, 930–937. doi: 10.1016/j.neuroimage.2012.02.022

Jenkinson, M., Bannister, P., Brady, M., and Smith, S. (2002). Improved optimization for the robust and accurate linear registration and motion correction of brain images. *NeuroImage* 17, 825–841. doi: 10.1006/nimg.2002.1132

Kudo, K., Liu, T., Murakami, T., Goodwin, J., Uwano, I., Yamashita, F., et al. (2016). Oxygen extraction fraction measurement using quantitative susceptibility mapping: Comparison with positron emission tomography. *J. Cereb. Blood Flow Metab.* 36, 1424–1433. doi: 10.1177/0271678x15606713

Leigh, R., Knutsson, L., Zhou, J., and van Zijl, P. C. (2018). Imaging the physiological evolution of the ischemic penumbra in acute ischemic stroke. *J. Cereb. Blood Flow Metab.* 38, 1500–1516. doi: 10.1177/0271678X17700913

Leslie-Mazwi, T. M., Lev, M. H., Schaefer, P. W., Hirsch, J. A., and Gonzalez, R. G. (2018). MR Imaging Selection of Acute Stroke Patients with Emergent Large Vessel Occlusions for Thrombectomy. *Neuroimaging Clin. N. Am.* 28, 573–584. doi: 10.1016/j.nic.2018.06.003

Liu, Z., Kee, Y., Zhou, D., Wang, Y., and Spincemaille, P. (2016). Preconditioned total field inversion (TFI) method for quantitative susceptibility mapping*. *Magn Reson Med.* doi: 10.1002/mrm.26331

Liu, Z., Spincemaille, P., Yao, Y., Zhang, Y., and Wang, Y. (2018). MEDI+0: Morphology enabled dipole inversion with automatic uniform cerebrospinal fluid zero reference for quantitative susceptibility mapping. *Magn. Reson. Med.* 79, 2795–2803. doi: 10.1002/mrm.26946

Mackey, J., Kleindorfer, D., Sucharew, H., Moomaw, C. J., Kissela, B. M., Alwell, K., et al. (2011). Population-based study of wake-up strokes. *Neurology* 76, 1662–1667. doi: 10.1212/WNL.0b013e318219fb30

Nogueira, R. G., Jadhav, A. P., Haussen, D. C., Bonafe, A., Budzik, R. F., Bhuva, P., et al. (2018). Thrombectomy 6 to 24 Hours after Stroke with a Mismatch between Deficit and Infarct. *N. Engl. J. Med.* 378, 11–21. doi: 10.1056/NEJMoa1706442

Ogawa, S., Lee, T. M., Kay, A. R., and Tank, D. W. (1990). Brain magnetic resonance imaging with contrast dependent on blood oxygenation. *Proc. Natl. Acad. Sci. U.S.A.* 87, 9868–9872. doi: 10.1073/pnas.87.24.9868

Powers, W. J. (1991). Cerebral hemodynamics in ischemic cerebrovascular disease. *Ann. Neurol.* 29, 231–240. doi: 10.1002/ana.410290302

Powers, W. J., Rabinstein, A. A., Ackerson, T., Adeoye, O. M., Bambakidis, N. C., Becker, K., et al. (2018). 2018 Guidelines for the Early Management of Patients With Acute Ischemic Stroke: A Guideline for Healthcare Professionals From the American Heart Association/American Stroke Association. *Stroke* 49, e46–e110. doi: 10.1161/STR.0000000000000158

Pushie, M. J., Crawford, A. M., Sylvain, N. J., Hou, H., Hackett, M. J., George, G. N., et al. (2018). Revealing the Penumbra through Imaging Elemental Markers of Cellular Metabolism in an Ischemic Stroke Model. *ACS Chem Neurosci* 9, 886–893. doi: 10.1021/acschemneuro.7b00382

Saver, J. L., Goyal, M., van der Lugt, A., Menon, B. K., Majoie, C. B. L. M., Dippel, D. W., et al. (2016). Time to Treatment With Endovascular Thrombectomy and Outcomes From Ischemic Stroke: A Meta-analysis. *Jama-Journal of the American Medical Association* 316, 1279–1288. doi: 10.1001/jama.2016.13647

Sobesky, J., Zaro-Weber, O., Lehnhardt, F. G., Vaaa, H., Neveling, M., Jacobs, A., et al. (2005). Does the mismatch match the penumbra? Magnetic resonance imaging and positron emission tomography in early ischemic stroke**. *Stroke* 36, 980–985. doi: 10.1161/01.STR.0000160751.79241.a3

Spincemaille, P., Liu, Z., Zhang, S., Kovanlikaya, I., Ippoliti, M., Makowski, M., et al. (2019). Clinical Integration of Automated Processing for Brain Quantitative Susceptibility Mapping: Multi-Site Reproducibility and Single-Site Robustness. *J. Neuroimaging* 29, 689–698. doi: 10.1111/jon.12658

Thirugnanachandran, T., Ma, H., Singhal, S., Slater, L. A., Davis, S. M., Donnan, G. A., et al. (2018). Refining the ischemic penumbra with topography. *Int J Stroke* 13, 277–284. doi: 10.1177/1747493017743056

Tian, T., Guo, L., Xu, J., Zhang, S., Shi, J., Liu, C., et al. (2016). Brain white matter plasticity and functional reorganization underlying the central pathogenesis of trigeminal neuralgia. *Sci Rep* 6, 36030. doi: 10.1038/srep36030

Uwano, I., Kudo, K., Sato, R., Ogasawara, K., Kameda, H., Nomura, J. I., et al. (2017). Noninvasive Assessment of Oxygen Extraction Fraction in Chronic

Ischemia Using Quantitative Susceptibility Mapping at 7 Tesla. *Stroke* 48, 2136–2141. doi: 10.1161/STROKEAHA.117.017166

Wang, D. J., Alger, J. R., Qiao, J. X., Hao, Q., Hou, S., Fiaz, R., et al. (2012). The value of arterial spin-labeled perfusion imaging in acute ischemic stroke: comparison with dynamic susceptibility contrast-enhanced MRI. *Stroke* 43, 1018–1024. doi: 10.1161/STROKEAHA.111.631929

Wang, W. Z., Jiang, B., Sun, H. X., Ru, X. J., Sun, D. L., Wang, L. H., et al. (2017). Prevalence, Incidence, and Mortality of Stroke in China Results from a Nationwide Population-Based Survey of 480 687 Adults. *Circulation* 135, 759. doi: 10.1161/Circulationaha.116.025250

Wang, Y., and Liu, T. (2015). Quantitative susceptibility mapping (QSM): Decoding MRI data for a tissue magnetic biomarker. *Magn. Reson. Med.* 73, 82–101. doi: 10.1002/mrm.25358

Wolf, R. L., and Detre, J. A. (2007). Clinical neuroimaging using arterial spin-labeled perfusion magnetic resonance imaging. *Neurotherapeutics* 4, 346–359. doi: 10.1016/j.nurt.2007.04.005

Wouters, A., Christensen, S., Straka, M., Mlynash, M., Liggins, J., Bammer, R., et al. (2017). A Comparison of Relative Time to Peak and Tmax for Mismatch-Based Patient Selection. *Front Neurol* 8:539. doi: 10.3389/fneur.2017.00539

Wu, L., Wu, W., Tali, E. T., and Yuh, W. T. (2018). Oligemia, Penumbra, Infarction: Understanding Hypoperfusion with Neuroimaging. *Neuroimaging Clin. N. Am.* 28, 599–609. doi: 10.1016/j.nic.2018.06.013

Yablonskiy, D. A., and Haacke, E. M. (1994a). Theory of NMR signal behavior in magnetically inhomogeneous tissues: the static dephasing regime. *Magn. Reson. Med.* 32, 749–763. doi: 10.1002/mrm.1910320610

Yablonskiy, D. A., and Haacke, E. M. (1994b). Theory of NMR signal behavior in magnetically inhomogeneous tissues: the static dephasing regime. *Magn. Reson. Med.* 32, 749–763. doi: 10.1002/mrm.1910320610

Yablonskiy, D. A., Sukstanskii, A. L., and He, X. (2013a). BOLD-based Techniques for Quantifying Brain Hemodynamic and Metabolic Properties – Theoretical Models and Experimental Approaches. *NMR Biomed.* 26, 963–986. doi: 10.1002/nbm.2839

Yablonskiy, D. A., Sukstanskii, A. L., Luo, J., and Wang, X. (2013b). Voxel spread function method for correction of magnetic field inhomogeneity effects in quantitative gradient-echo-based MRI. *Magn. Reson. Med.* 70, 1283–1292. doi: 10.1002/mrm.24585

Yang, J., d'Esterre, C., Ceruti, S., Roversi, G., Saletti, A., Fainardi, E., et al. (2015). Temporal changes in blood-brain barrier permeability and cerebral perfusion in lacunar/subcortical ischemic stroke. *BMC Neurol.* 15:214. doi: 10.1186/s12883-015-0468-460

Zaharchuk, G. (2011). Arterial spin label imaging of acute ischemic stroke and transient ischemic attack. *Neuroimaging Clin. N. Am.* 21, 285–301. doi: 10.1016/j.nic.2011.01.003

Zaro-Weber, O., Moeller-Hartmann, W., Siegmund, D., Kandziora, A., Schuster, A., Heiss, W. D., et al. (2017). MRI-based mismatch detection in acute ischemic stroke: Optimal PWI maps and thresholds validated with PET. *J. Cereb. Blood Flow Metab.* 37, 3176–3183. doi: 10.1177/0271678x16685574

Zhang, J., Cho, J., Zhou, D., Nguyen, T. D., Spincemaille, P., Gupta, A., et al. (2018). Quantitative susceptibility mapping-based cerebral metabolic rate of oxygen mapping with minimum local variance. *Magn. Reson. Med.* 79, 172–179. doi: 10.1002/mrm.26657

Zhang, J., Liu, T., Gupta, A., Spincemaille, P., Nguyen, T. D., and Wang, Y. (2015). Quantitative mapping of cerebral metabolic rate of oxygen (CMRO2) using quantitative susceptibility mapping (QSM). *Magn. Reson. Med.* 74, 945–952. doi: 10.1002/mrm.25463

Zhang, J., Zhou, D., Nguyen, T. D., Spincemaille, P., Gupta, A., and Wang, Y. (2017). Cerebral metabolic rate of oxygen (CMRO2) mapping with hyperventilation challenge using quantitative susceptibility mapping (QSM). *Magn. Reson. Med.* 77, 1762–1773. doi: 10.1002/mrm.26253

Conflict of Interest: QSM post-processing software has been developed by Medimagemetric LLC, a Cornell spinoff company that YW owns shares. AG reports non-financial support from GE Healthcare and non-financial support from Siemens Medical Solutions USA, Inc., outside the submitted work.

The remaining authors declare that the research was conducted in the absence of any commercial or financial relationships that could be construed as a potential conflict of interest.

Copyright © 2020 Zhang, Cho, Nguyen, Spincemaille, Gupta, Zhu and Wang. This is an open-access article distributed under the terms of the Creative Commons Attribution License (CC BY). The use, distribution or reproduction in other forums is permitted, provided the original author(s) and the copyright owner(s) are credited and that the original publication in this journal is cited, in accordance with accepted academic practice. No use, distribution or reproduction is permitted which does not comply with these terms.

frontiers in Neuroscience

ORIGINAL RESEARCH
published: 18 September 2020
doi: 10.3389/fnins.2020.569657

Snowball ICA: A Model Order Free Independent Component Analysis Strategy for Functional Magnetic Resonance Imaging Data

Guoqiang Hu[1,2,3], Abigail B. Waters[2,4], Serdar Aslan[2,3], Blaise Frederick[2,3], Fengyu Cong[1,5,6,7] and Lisa D. Nickerson[2,3]**

[1] School of Biomedical Engineering, Faculty of Electronic Information and Electrical Engineering, Dalian University of Technology, Dalian, China, [2] Brain Imaging Center, Mclean Hospital, Belmont, MA, United States, [3] Department of Psychiatry, Harvard Medical School, Boston, MA, United States, [4] Department of Psychology, Suffolk University, Boston, MA, United States, [5] School of Artificial Intelligence, Faculty of Electronic Information and Electrical Engineering, Dalian University of Technology, Dalian, China, [6] Key Laboratory of Integrated Circuit and Biomedical Electronic System of Liaoning Province, Dalian University of Technology, Dalian, China, [7] Faculty of Information Technology, University of Jyvaskyla, Jyvaskyla, Finland

OPEN ACCESS

Edited by:
Miguel Castelo-Branco,
Coimbra Institute for Biomedical Imaging and Translational Research (CIBIT), Portugal

Reviewed by:
Li Dong,
University of Electronic Science and Technology of China, China
Xi Jiang,
University of Electronic Science and Technology of China, China

***Correspondence:**
Fengyu Cong
cong@dlut.edu.cn
Lisa D. Nickerson
lisa_nickerson@hms.harvard.edu

Specialty section:
This article was submitted to Brain Imaging Methods, a section of the journal Frontiers in Neuroscience

Received: 04 June 2020
Accepted: 31 August 2020
Published: 18 September 2020

Citation:
Hu G, Waters AB, Aslan S, Frederick B, Cong F and Nickerson LD (2020) Snowball ICA: A Model Order Free Independent Component Analysis Strategy for Functional Magnetic Resonance Imaging Data. Front. Neurosci. 14:569657. doi: 10.3389/fnins.2020.569657

In independent component analysis (ICA), the selection of model order (i.e., number of components to be extracted) has crucial effects on functional magnetic resonance imaging (fMRI) brain network analysis. Model order selection (MOS) algorithms have been used to determine the number of estimated components. However, simulations show that even when the model order equals the number of simulated signal sources, traditional ICA algorithms may misestimate the spatial maps of the signal sources. In principle, increasing model order will consider more potential information in the estimation, and should therefore produce more accurate results. However, this strategy may not work for fMRI because large-scale networks are widely spatially distributed and thus have increased mutual information with noise. As such, conventional ICA algorithms with high model orders may not extract these components at all. This conflict makes the selection of model order a problem. We present a new strategy for model order free ICA, called Snowball ICA, that obviates these issues. The algorithm collects all information for each network from fMRI data without the limitations of network scale. Using simulations and *in vivo* resting-state fMRI data, our results show that component estimation using Snowball ICA is more accurate than traditional ICA. The Snowball ICA software is available at https://github.com/GHu-DUT/Snowball-ICA.

Keywords: independent component analysis, functional magnetic resonance imaging, model order, dimension reduction, mutual information

INTRODUCTION

Functional connectivity and network-based analysis of functional magnetic resonance imaging (fMRI) have revolutionized our understanding of the overall functional organization of the brain (Beaty et al., 2018; Pedersen et al., 2018; Sokolov et al., 2018). Independent component analysis (ICA), a commonly used data-driven approach for fMRI data analysis, has been effectively used for functional network studies (Seifritz et al., 2002; Hermans et al., 2011; Freeman et al., 2014;

Richiardi et al., 2015; Constantinescu et al., 2016; Glasser et al., 2016; Rose et al., 2016; Tavor et al., 2016). However, there remains significant variation in spatial characteristics of networks between datasets and between ICA methods used to identify optimal configuration of components.

Model order selection (MOS – choosing the number of extracted components) in ICA is a significant methodological concern that contributes to this variation in fMRI brain network analysis (Abou-Elseoud et al., 2010; Beckmann, 2012; Kuang et al., 2018). Allen and colleagues (Allen et al., 2012) found that when the model order is too low, ICA distorts the estimation of sources. However, increasing the model order beyond the true dimensionality can result in certain sources being split into multiple components. In fact, most conventional signal processing applications used to estimate the number of source signals cannot reliably model the exact spatial characteristics of these signals, even when the true model order is known. This remains a significant problem for neuroscience researchers.

Many solutions have been proposed to address this issue. Information-theoretic criteria (ITC) have been used in numerous signal processing applications to estimate model order, including minimum code length based minimum description length (MDL) criterion (Rissanen, 1978), Akaike information criterion (AIC) (Akaike, 1998), and Bayesian information criterion (BIC) (Rissanen, 1978). Combining ITC with a resampling method was proposed for subsampling a set of effectively independent and identically distributed (i.i.d.) samples from dependent data samples (Li et al., 2007). The Laplace approximation (LAP) algorithm (Minka, 2000) was improved based on the empirical distribution function of the eigenvalues developed in random matrix theory (Beckmann and Smith, 2004). Entropy-rate-based order selection by finite memory length model (ER-FM) and entropy-rate-based order selection by AR model (ER-AR) are two likelihood estimators-based methods, which use all available samples instead of down sampling data (Fu et al., 2014). All of these methods attempt to accurately estimate the number of intrinsic source signals, which is then used as the optimal model order before ICA decomposition is performed.

In the field of fMRI data processing, the Group ICA of fMRI Toolbox(GIFT[1]; Calhoun et al., 2001a) and the Multivariate Exploratory Linear Optimized Decomposition into Independent Components (MELODIC[2]; Beckmann and Smith, 2004) are the two most popular software tools used for ICA. Both of these tools implement a principal component analysis (PCA)-based data reduction step prior to ICA. Moreover, for fMRI data, ICA can be performed on single-subject fMRI data, or on multi-subject data (by either stacking the fMRI data across subjects or by temporally concatenating data across subjects). For resting state fMRI, which is most commonly used for network analysis, data are temporally concatenated across subjects prior to the analysis. In GIFT, the default option for data reduction of temporally concatenated multi-subject data proceeds by first reducing data at the individual subject-level with PCA, then applying PCA to the group-level (concatenated) reduced fMRI data for further data reduction prior to ICA. As the number of subjects and the length of the time series increases, in order to reduce required memory, several dimension reduction methods have been proposed (Calhoun et al., 2015). For example, multi power iteration (MPOWIT) was designed to estimate a subspace larger than the desired one (Rachakonda et al., 2016). In contrast, the default in MELODIC utilizes an incremental approach called Incremental Group PCA (MIGP) (Smith et al., 2014) to perform data reduction (although this option can be turned off to implement a two-stage group PCA-based data reduction). Even though initial data reduction differs between these methods, the model order is selected from the group PCA, and therefore determined prior to the ICA decomposition. The order of steps in the data reduction process may contribute to premature removal of data as "noise," when it in fact contributes meaningful information.

In this article, we propose a new ICA strategy that does not require MOS before ICA decomposition, the Snowball ICA. This approach differs from traditional ICA algorithms by iteratively collecting information about source signals from the fMRI data. First, we demonstrate how conventional MOS procedures contribute to inaccurate estimation of signal sources. Our Snowball ICA will then be compared with standard implementations using MELODIC and GIFT to determine the accuracy of spatial quality estimation using simulated data and *in vivo* fMRI data.

MATERIALS AND METHODS

Conventional Spatial Group ICA

For conventional multi-subject fMRI data analysis, both noise free ICA (Calhoun et al., 2001b) and probabilistic ICA (Beckmann and Smith, 2004) are widely used. Both of these ICA models suffer the effect of MOS (Abou-Elseoud et al., 2010; Beckmann, 2012). For simplicity, the spatial group ICA algorithm (Calhoun et al., 2001a) implemented as in GIFT is used to show how MOS will impact the extracted components. First, data reduction is performed for each subject:

$$X_s = V_s^{-1} Z_s, \tag{1}$$

where $Z_s \in \mathbb{R}^{T \times M}$ represents the s-th subject's fMRI data after preprocessing, T is the number of volumes, M is the number of voxels of each scan. V_s^{-1} is the dimension reduction matrix, which is usually obtained from eigen decomposition of covariance matrix of Z_s. At this stage, components that explain 90% variance are typically used to construct the reduced data. For group ICA, data from different subjects is temporally concatenated after the data reduction, as follows:

$$D = \begin{bmatrix} X_1 \\ \vdots \\ X_S \end{bmatrix} = \begin{bmatrix} V_1^{-1} Z_1 \\ \vdots \\ V_S^{-1} Z_S \end{bmatrix}. \tag{2}$$

[1]https://trendscenter.org/software/gift/

[2]http://fsl.fmrib.ox.ac.uk/fsl/fslwiki/MELODIC/

Singular value decomposition of the aggregate data is as follows:

$$D = G \sum U, \tag{3}$$

where $D \in \mathbb{R}^{N \times M}$ is the aggregate matrix of all subjects fMRI data. G is a unitary $N \times N$ dimension reduction matrix. $\sum$ is a diagonal $N \times N$ matrix. Each value δ_k on diagonal of $\sum$ is the square root of variance of each component. U is an $N \times M$ matrix consisting of N unit row-vectors. $\sum U$ represents the group PCA components.

Based on PCA theory, the dimensionality of the aggregate matrix after concatenation is reduced again:

$$X = \left(G_{:,\,1:R}\right)^T D, \tag{4}$$

where R is the model order. The formula in Eq. 4 is therefore selecting the first R vectors of $\sum U$. The information contained in the $N - R$ components is labeled as "noise" and removed as shown in **Figure 1**. In this study, we investigate whether or not these components are noise using simulated data.

Noise-free ICA is given by the following:

$$Y = WX, \tag{5}$$

where $X \in \mathbb{R}^{R \times M}$ is the matrix to be fed into ICA unmixing program. $W \in \mathbb{R}^{R \times R}$ represents the unmixing matrix. $Y \in \mathbb{R}^{R \times M}$ is the independent component matrix that is used to estimate the source matrix.

$$GW^{-1}Y = \begin{bmatrix} V_1^{-1}Z_1 \\ \vdots \\ V_s^{-1}Z_s \end{bmatrix} = \begin{bmatrix} G_1 \\ \vdots \\ G_s \end{bmatrix} W^{-1}Y. \tag{6}$$

Reconstruction of time courses is done as follows:

$$Z_s = V_s G_s W^{-1} Y. \tag{7}$$

With $\left[V_m G_m W^{-1}\right]$, $(m = 1, 2, \cdots, M)$, containing the time course information of each component for each subject. Y represents the estimation of the source signals, including the spatial distribution of each component. The results from temporal concatenated Group ICA result in shared spatial distributions across subjects, with different temporal courses for each subject.

Quantifying the Information Used in the ICA at a Given Model Order

Information included in the ICA algorithm is represented by the sum of the first R PCA components. When PCA is used as the data reduction procedure, the ratio of information used for ICA can be calculated with the following formula:

$$\text{Ratio}\,(R) = \frac{\sum_{r=1}^{R} \delta_r}{\sum_{k=1}^{K} \delta_k}, \tag{8}$$

where R is the model order and K is the dimensionality of the latent data contained in the algorithm. This index is used to describe the ratio of information included in the ICA procedure.

Pseudo-ICA for Simulations

In order to study the distribution of the meaningful source information that may be contained in the PCA components labeled "noise," a "pseudo-ICA" approach is used. In these simulations, the spatial correlation coefficient, C, between PCA components U and the ground truth signal sources is calculated, giving the following formula for pseudo-ICA:

$$Y_p = C_{:,1:R} U_{1:R,:}, \tag{9}$$

where Y_p represents the components matrix estimated by Pseudo-ICA. Each row of Y_p represents one component estimated by Pseudo-ICA. The order of the component matrix is exactly same as that of sources matrix. R represents the results calculated based on R PCA components. $U_{1:R,:}$ is exactly the same with what would be fed into conventional ICA algorithms. $C_{:,1:R}$ works as the unmixing matrix but without the limitation of independent constrain. Pseudo-ICA is therefore able to examine the effect of the number of PCA components on the accuracy of estimated results, neglecting the restriction of independence between components.

The correlation between the ground truth and PCA components represents the information ratio for each source signal for PCA components. Both the distribution of source information throughout the PCA components labeled "noise" and the accuracy of Pseudo-ICA components were used to evaluate performance of the PCA.

Mutual Information Between Sources and Noise

Mutual information is a criterion used to describe the dependence between two variables. Under the independence constraint of spatial ICA, components with high mutual information will not be extracted appropriately. For two discrete random variables Y_1 and Y_2, the mutual information is defined as (Cover and Thomas, 2012):

$$I\left(Y_1, Y_2\right) = \sum_{y_1 \in \mathcal{Y}_1} \sum_{y_2 \in \mathcal{Y}_2} p_{(Y_1, Y_2)}\left(y_1,\ y_2\right) \log\left(\frac{p_{(Y_1, Y_2)}\left(y_1,\ y_2\right)}{p_{Y_1}\left(y_1\right) p_{Y_2}\left(y_2\right)}\right). \tag{10}$$

Once the model order was selected for the conventional ICA procedure, the PCA data reduction limits the resulting information for each source that is fed into ICA. For example, R PCA components will consist of information from N signal sources and R-N noise sources. However, the mutual information between different sources and the same noise will be different, with more spatially distributed sources having higher the mutual information with noise. This is demonstrated in section "Results" for the Simulations. As the number of PCA components increases, the number of noise signals increases, and the existence of spatially distributed sources sharing mutual information with noise also grows. In turn, because of the spatial independence constraint of ICA, large-scale sources may not be estimated. This effect is illustrated with simulations.

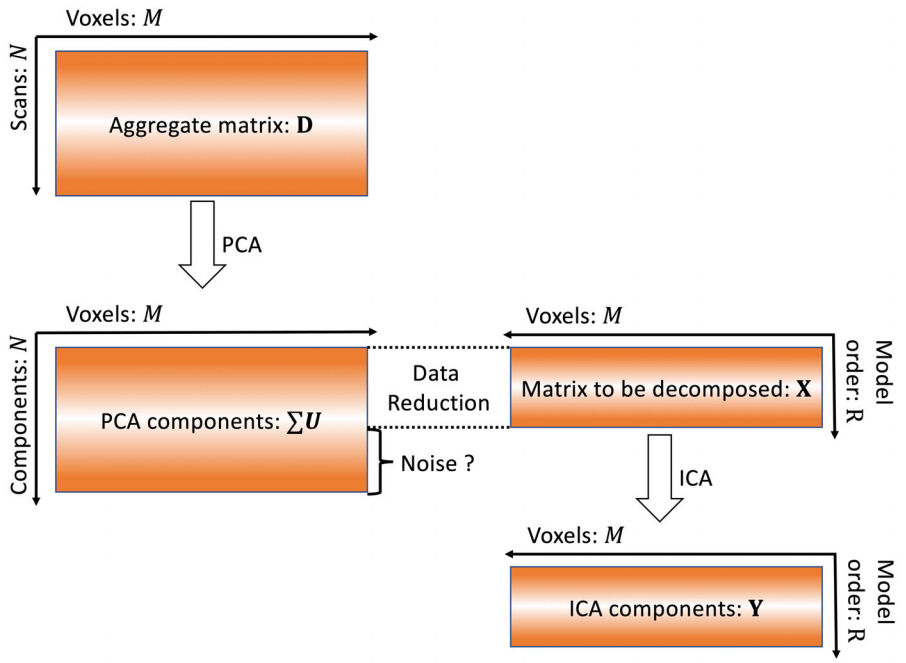

FIGURE 1 | Conventional ICA algorithm. In conventional ICA, the model order is determined and then data reduction is applied prior to ICA. The removal of this information as "noise" may also result in removal of meaningful signals.

Snowball ICA

The overall workflow of Snowball ICA is illustrated in **Figure 2**. In Snowball ICA, the purpose is exactly the same as using conventional ICA to estimate independent component networks from fMRI data that are linear combination of network signals plus artifact (noise) signals. The aggregate fMRI data is denoted by $Z \in \mathbb{R}^{T \times M}$, which is organized with subjects' fMRI data temporally concatenated without data reduction. T represents total number of scans across all subjects runs of fMRI data. M denotes the number of voxels. T is larger than the number of independent components R to be estimated, which means the model is overdetermined. However, all widely used ICA algorithms are determined (Bell and Sejnowski, 1995; Hyvarinen, 1999), made so by applying one of several dimension reduction methods. This data reduction step results in a loss of information. In contrast to conventional ICA, our proposed approach analyses aggregate fMRI data separated into different blocks to make the model determined. In order to combine blocks together, the Snowball ICA is divided into two parts. The first stage is seed creation, and the second stage is information collection. Seed creation is used to make sure the estimation is stable and information collection is then done to collect information from all blocks of data.

Seed Creation

The first stage is seed creation, in which a randomly selected individual subject's fMRI data is selected from the group fMRI dataset. Since the information about each component from different subjects will be collected in the next stage (Information Collection), the initial seed creation is not that critical. It can be created only from a single subject, from large chunks of randomly selected data, or from conventional spatial group ICA results. In order to save time, we use a randomly selected subject to create the seed in this study. Once the data have been selected, ICA is repeated many times. The most stable component from these ICAs is selected as the seed. ICASSO (ICASSO-software package[3]) was used to evaluate component stability. The algorithm was run for ICA repeatedly with the same parameters and the same algorithm. Then hierarchical clustering was implemented to cluster all of the extracted components (Himberg et al., 2004; Zhang et al., 2018; Hu et al., 2019). Hierarchical clustering has been widely applied for the assessment of reproducibility of ICA components. The clustering method is the process for transforming a proximity matrix into a nested partition, which can be graphically represented by a tree called dendrogram. In this study, the dendrogram is formed from the bottom up. For this clustering method, at the first iteration, the number of clusters is same as the number of total independent components N. At the second iteration, the most similar clusters will merge as a new cluster, so the number of clusters will become N-1. At the third iteration, the number of clusters will become N-2. As the clustering goes forward, at the top level of the hierarchy, the number of clusters converges to a single cluster. Using this approach, the hierarchical organization of the data fed into the algorithm can be established. When hierarchical clustering is applied for ICA algorithm stability analysis, the cluster result is the dendrogram at the level of number of independent components. So, once the independent

[3]http://www.cis.hut.fi/projects/ica/icasso/

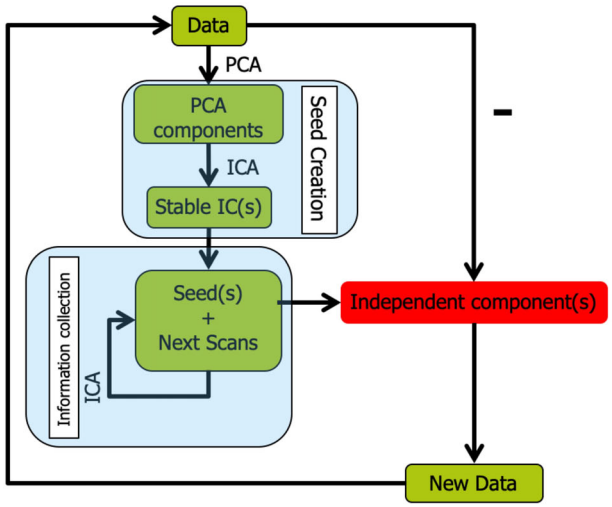

FIGURE 2 | Snowball ICA algorithm. In order to avoid the necessity of specifying model order in conventional ICA, Snowball ICA estimates components one by one (or a few at a time) until no stable components can be further estimated from the data. After seed creation for a new component(s) to be estimated via information collection, the estimated snowball component(s) are removed from the multi-subject data and seed creation is repeated to determine the next seed pattern(s). The Snowball ICA will stop when there are no more stable components estimated during the seed creation step.

components from multiple runs are computed, no matter how many hierarchical clustering runs, the clustering results would be exactly same. After clustering, the difference between the average intra-class similarities and average inter-class similarities is used as an index to evaluate the stability of the components:

$$Iq\,(r) = \bar{S}\,(r)_{int} - \bar{S}\,(r)_{ext}\,. \tag{11}$$

In order to ensure the stability of results, the most stable component was selected as the seed to feed into the information collection stage. Y_{seed} denotes the stable component estimated from Seed Creation. The Snowball ICA algorithm stops once stable components are no longer extracted.

Information Collection

In the second stage, information collection, the seed component is concatenated with randomly selected new scans, and these new aggregate data are then fed into the ICA unmixing algorithm. The resulting ICA component that most closely matches the seed is then used as the new seed to be concatenated with more of the original data in the next iteration. Gradually, the seed will collect all information about the signal it represents from each scan, resulting in accurate ICA components.

First, the aggregate data Z is separated into K blocks:

$$Z = \begin{bmatrix} Z_1 \\ Z_2 \\ \vdots \\ Z_K \end{bmatrix}, \tag{12}$$

where $Z_{\text{k}} \in \mathbb{R}^{T/K \times M}$. Then for the first block, Z_1, ICA with reference (ICA-R) (Lu and Rajapakse, 2005; Huang and Mi, 2007; Lin et al., 2007; Du and Fan, 2013) is implemented, with Y_{seed} being selected as the most stable component after repeated ICAs. Once the information belonging to the first block is collected, the estimated component is designated Y_{seed}. Then the next block of data, Z_{k}, goes through the same procedure to create an updated $Y_{\text{seed_new}}$ as reference for the next block, with remaining blocks going through the same procedure iteratively until all blocks are used. The order of processing blocks may be random. Once all blocks have been used, the resulting component is Y_1, the first extracted ICA spatial map (SM). This process then repeats, after removing the estimated Y_1 component from the original data, to identify the next component Y_2, and so on. For each Z_{k}, the implementation of ICA-R is as follow:

$$\begin{bmatrix} Y_{seed_new} \\ Y_1 \\ \vdots \\ Y_{T/K} \end{bmatrix} \leftarrow A_k \begin{bmatrix} Y_{\text{seed}} \\ Z_k \end{bmatrix}, \tag{13}$$

where A_{k} is unmixing matrix estimated with independence constraint. $Y_{\text{seed_new}}$ is updated seed that represents network information collected about Y_{seed} from Z_{k}. It will replace Y_{seed} in the next block iteration. The seed component, Y_{seed}, works as a reference and the information belonging to this reference network is gradually collected as more and more blocks are used. Once K blocks are used, the final Y_{seed} is the SM of estimated component of Snowball ICA and is represented by S_{snowball}.

Removal of Estimated Components

As shown in **Figure 2**, once a component is accurately estimated, it is then removed from each subject's fMRI data prior to determining the next seed to feed into Stage 2, as follows:

$$Z_{s_new} = Z_s - T_{snowball} \times S_{snowball}, \tag{14}$$

where S_{snowball} is the accurate component estimated via the information collection stage of the Snowball ICA. There are several ways to reconstruct subject components from group ICA results (Erhardt et al., 2011; Du and Fan, 2013). Unlike the conventional ICA procedure, the unmixing matrix for each subject is difficult to obtain using Snowball ICA. However, Allen et al. (2012) showed that without any PCA dimension reduction prior to ICA (e.g., PCA is only used for rotation and whitening), the difference between back-projection and dual regression for reconstructing subject components is within computational precision. Hence, T_{snowball} represents time series that is calculated with the first stage of dual regression (Nickerson et al., 2017). Z_{s} represents the s-th subject's fMRI data. For each subject, $Z_{\text{s_new}}$ replaces Z_{s} in the next iteration of Snowball ICA to identify subsequent components. With this method, the information from components that has been estimated accurately will not be considered during creation of the next seed for new component estimation. Note that $Z_{\text{s_new}}$ is *only* used for seed creation, whereas the original data are used for information collection. This is done to account for the fact that different

components may have some spatial overlap. In this case, the information from estimated components is only removed for seed creation, but not for information collection. Therefore, even though the overlapping signals are not included in the seed, the overlapping information will still be estimated during Information Collection.

The steps of Snowball ICA are as follows:

Step (1) Identify the seeds Y_{seed} as most stable ICA component (Iq > 0.9) from a small amount of the total data.
Step (2) Aggregate Y_{seed} with randomly selected scans chosen from all scans of all subjects to form a new data matrix and apply the ICA algorithm to decompose the new data matrix. Each scan is selected only once.
Step (3) The most similar IC(s) to the seed(s) are selected as new seed(s) Y_{seed}.
Step (4) Repeat Steps 2 and 3 until all scans of all subjects have been used and the components are estimated accurately.
Step (5) Remove the resulting snowball ICA components ($S_{snowball}$) from the multi-subject data and repeat to determine the next seed pattern. The Snowball ICA will stop when there are no more stable components estimated in Step 1.

Evaluation of ICA Components Visualization

The ICA SMs are thresholded using a Z-threshold criterion ($|z| > 2.3$) (McKeown and Sejnowski, 1998; Calhoun et al., 2001a). These thresholded SMs are overlaid onto a transparent standard brain template to visualize the results. The MATLAB scripts used for this procedure can be downloaded from: https://github.com/GHu-DUT/Show_3D_GlassBrain.

Assessing the Snowball Component Spatial Patterns

For processing of real data that lack ground truth, the pros and cons of different algorithms can be compared as to whether they meet the ICA assumption. In theory, the purpose of ICA is to extract non-Gaussian signals. The stronger the non-Gaussianity of the signals, the more this assumption of ICA is satisfied. The standard measure of non-Gaussianity is kurtosis (Hyvärinen and Oja, 2000). The kurtosis of signal y with mean value μ and standard deviation σ is defined by:

$$Kurt\left(y\right) = E\left[\left(\frac{y-\mu}{\sigma}\right)^4\right] = \frac{\mu_4}{\sigma_4}. \quad (15)$$

Independent component analysis spatial components are estimated by maximizing non-Gaussianity, therefore we use Kurt to evaluate the "goodness" of independence components. The higher the index is, the easier a network is distinguished from background (Gaussian) noise.

Simulations

Simulated phantom fMRI data experiment aims to explore the reason that MOS effect the ICA decomposition. Simulated data were generated with the MATLAB toolbox, SimTB (Erhardt et al., 2012), which was developed to facilitate the testing of different analytic methods for multi-subject data and is freely available for download[4]. In SimTB, we adopt a data generation model that is largely consistent with the assumption of spatial ICA. In other words, data can be expressed as the product of activation temporal courses (TCs) and non-Gaussian sources, which we refer to as SMs. For subjects $i = 1, \cdots, M$, we created n components, each consisting of an SM and corresponding TC. In our simulation, there are $M = 10$ subjects and $n = 29$ components. SMs have $V = 148 \times 148$ voxels and TCs are $T = 150$ time points in length with a repetition time (TR) of 2s/sample. Rician noise with random contrast-to-noise ratio (CNR), selected according to a uniform distribution, for each subject was added for each time course (across subjects, mean ± SD: 0.32 ± 0.23). The simulated sources are shown in **Figure 3**. Voxels with values larger than 2.3 after standard normalization are defined as the signal represented by the component. The spatial extent of each network is defined as the number of voxels in the thresholded regions. Readers are pointed to (Erhardt et al., 2012) for more details of the spatial and temporal properties of the simulated sources.

In the traditional ICA algorithm, it is generally true that the first R PCA components will contain almost all of the information about all of the signal sources (the rest will correspond to noise/artifacts). PCA components are orthogonal, and the spatial cross correlation between PCA components and the ground truth signals can be used to identify the information about each signal contained in a PCA component.

For the simulated data, Matlab FastICA (Hyvärinen and Oja, 2000) was used as a representative traditional approach with model orders of 10, 29, 50, 100, 200, 400, 500, 800, and 1000, in order to compare the results under different model orders. The mutual information of sources with noise was also calculated. In Snowball ICA, for seed creation the model order was chosen as 10 and ICA was run 10 times with ICASSO. The stable components (Iq > 0.9) were used as seeds.

In order to test the performance of Snowball ICA, MELODIC, and GIFT under different CNR levels, a range of CNR (0.1–20) was also applied when subjects' data generated. All the other parameters were kept exactly same. All three methods were then applied to the same dataset. In MELODIC and GIFT, the number of independent components was set to equal the number of sources (29 for the simulated data). Estimation accuracy is calculated as the average over all components of the spatial cross correlation between the independent components and their corresponding ground truth signals.

Resting-State fMRI Data

Resting state fMRI for 50 healthy unrelated subjects were utilized from the WU-Minn Human Connectome Project (HCP: Van Essen et al., 2013) to demonstrate our new method. Each subject completed resting state fMRI with the following scan parameters: TE/TR/FA = 33.1 ms/720 ms/52°, 72 slices, 2 mm isotropic, eyes open fixation. The data was then temporally preprocessed and de-noised using the FIX approach (Griffanti et al., 2014; Salimi-Khorshidi et al., 2014). The resulting images were then aligned

[4]https://trendscenter.org/software/

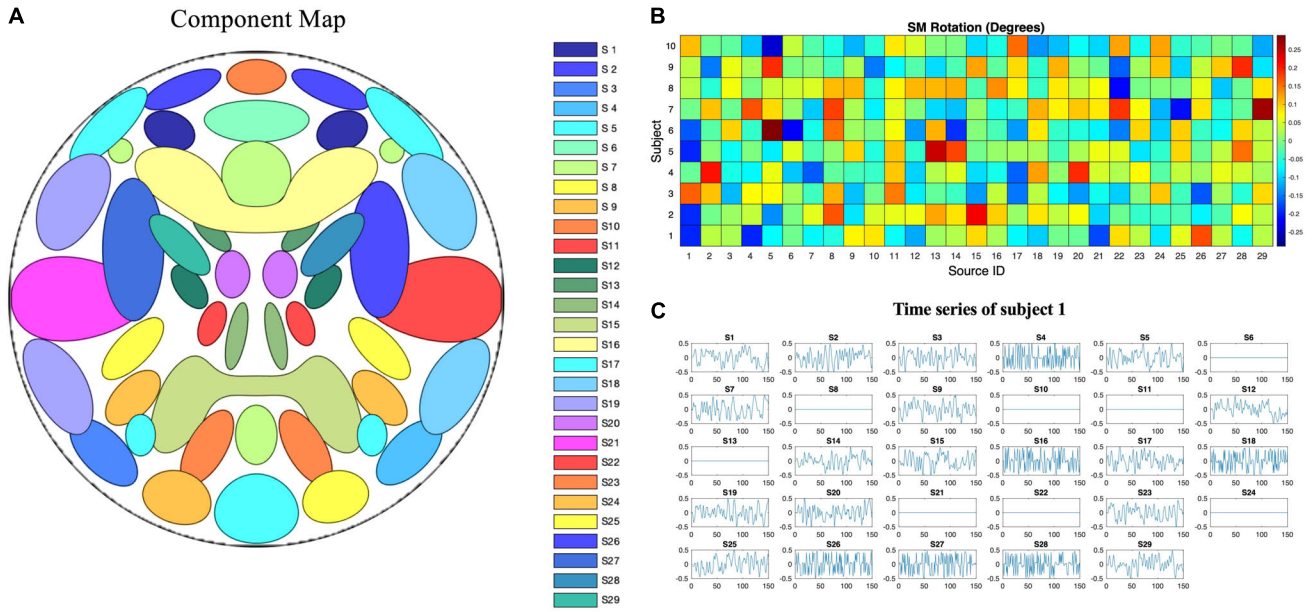

FIGURE 3 | Ground truth spatiotemporal signal sources used in the simulations for simulated phantom fMRI data. **(A)** Spatial map showing the spatial configuration of the 29 signal sources. **(B)** To mimic between-subject spatial variability, the sources for each subject were given a small amount of random rotation and some sources were randomly excluded. **(C)** Temporal course of each signal source for a single subject. Straight lines with zero values indicate that the component is not present in that subject's simulated data.

using MSM registration (Robinson et al., 2014). Full details of the HCP resting state data can be found in publications from the project (Smith et al., 2013; Van Essen et al., 2013).

Independent component analysis components estimated using the traditional ICA algorithm and the Snowball ICA strategy were compared. To apply the FastICA algorithm to the *in vivo* resting state fMRI data, FastICA as implemented in GIFT and in FSL MELODIC were both used with an empirical model order = 40. In Snowball ICA, FastICA was used for seed creation with a model order of 10 for Step 1. Stable components ($Iq > 0.9$) were used as seeds. In information collection, 20 scans were considered at the same time for Step 2. The estimated components from GIFT, MELODIC, and Snowball ICA were compared using visualization, kurtosis, and representativeness of network TCs.

To assess how selection of the initial parameters affects estimation, estimation consistency was tested across model orders in seed creation and across block sizes of information collection. For seed creation, model orders of 20, 40, and 60 were used to estimate seeds from randomly selected single subject's fMRI data or from conventional group ICA SMs. The right frontoparietal network was then selected as the seed. For information collection, the block size was set to 20, 40, and 60. The consistency of the estimated networks with these parameter combinations was then assessed by visual inspection and similarity score, as shown in **Figure 12**. The similarity score is defined as the average Pearson correlation coefficient of SMs estimated with different parameters.

RESULTS

Simulation Results

Ideally, the PCA data reduction procedure will be able to retain all information related to signal sources while removing only noise. **Figure 4** shows that PCA data reduction is not effective for this purpose. Even for approximately the 200th and 1250th PCA components, they still contain meaningful information about signal sources. If the model order is chosen to be 29, which is exactly the number of sources in the simulated data, much of the information from signal sources is removed.

The second simulated signal source was selected as an example to show the Pseudo-ICA results under different model orders (**Figure 5**). **Figure 5** shows that without the restriction of independence between components, when more PCA components are retained, the estimated component is more accurate.

The components estimated by Matlab FastICA under different model orders are shown in **Figure 6**. For each component, as model order increases, the accuracy of the estimated components also increases. However, when the model order is higher than 200, even though some new components are estimated, other components disappear. The disappearing components have relatively large scales.

The disappeared component under each model order is defined as the component that cannot be estimated under the model order but can be estimated with lower model order. This means that the disappearance is caused by independent constraint but not information insufficient of the component. As shown in **Figure 7A**, the mutual information of network

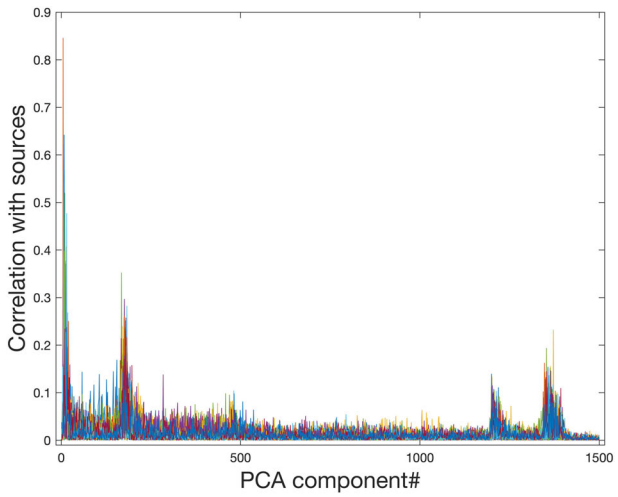

FIGURE 4 | Correlation of PCA spatial maps with simulated signal source maps. Group PCA was applied to the simulated group data (N = 10) with 1500 components extracted in order of most variance accounted for. Even components extracted after approximately the first 200 and the first 1250 components still show a correlation with the simulated signal sources and therefore contain meaningful information about signal sources. When PCA is used for data reduction of group fMRI data, model orders may range from 20 to approximately 100–200, therefore this meaningful information will be lost during data reduction.

is significant correlated with network size. As the network size becomes larger, the mutual information between network and noise also increases. The average of mutual information with noise of estimated networks under different model order are shown in **Figure 7B**. The result shows that the mutual information with noise of estimated networks is decreasing as the model order increases. When the change of model order is relatively small, the mutual information with noise does not change much such as model order from 10 to 100. But when the change of model order value is relatively large, mutual information with noise also drops sharply, such as model order from 100 to 1000. The color dots represent the mutual information with noise of disappeared components at each model order. Almost all the disappeared components have higher mutual information with noise. We draw the conclusion that the scale of the estimated components is different under different model order. Limited with mutual information with noise, the higher the model order, the smaller the scale.

The comparison of Snowball ICA and traditional FastICA results are shown in **Figure 6**. For Snowball ICA, almost every component shows accurate estimation of sources with high correlation with ground truth. In order to compare the performance of Snowball ICA and conventional ICA, the number of extracted components that significant correlated ground truth was counted, with the threshold of 0.4 of Pearson correlation coefficient. In order to make sure the source was not split as several components, the components with the highest similarity correlated with ground truth are identified by eyes. Compared with the traditional ICA algorithm, Snowball ICA is able to estimate almost all signal sources (26/29) with high spatial accuracy. The signal sources include both large-scale networks (e.g., source #15, #16, #18, #21, #22) and small-scale networks (e.g., source #11, #12, #13, #28) can be estimated with Snowball ICA. For conventional ICA, a model order of 400, results in the most components being extracted (20/29). But this is still less than Snowball, and the accuracy is also lower. Meanwhile, 400 is much higher than the actual number of ground truth components. However, when the model order = 29, which is exactly same with the number of ground truth, the number of components obtained with conventional ICA are still few and the accuracy is also no better than the components that estimated with higher model order. From the results of Pseudo-ICA, for each source, when the PCA component contain more information of the source signals, the accuracy of estimated components shows significant improvement. For traditional ICA, limited by the restriction of independence for extracted components and influence of noise, the accuracy of its results is worse than Pseudo-ICA results. The higher the model order, the more pronounced the effect.

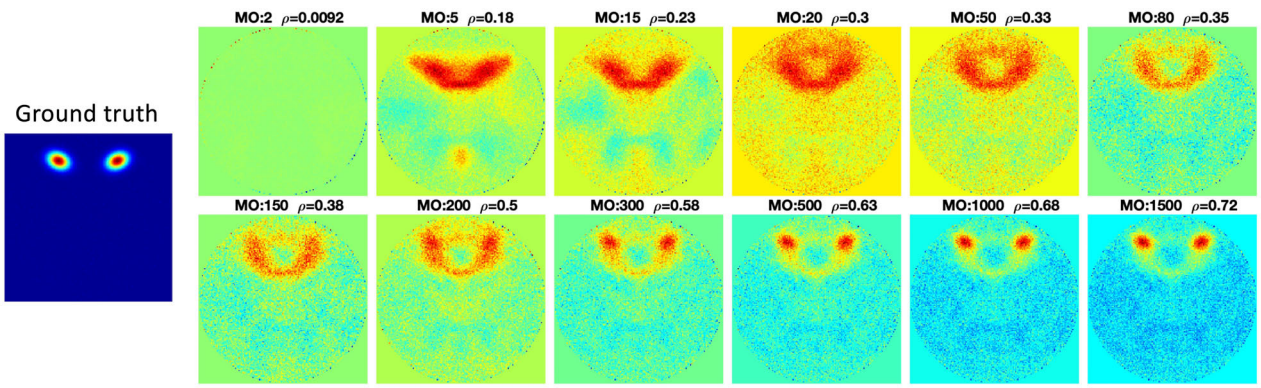

FIGURE 5 | Pseudo-ICA results with different model orders. Without limitations of the spatial independence constraint of spatial ICA, the ICA estimation would be more accurate as more PCA components are retained with increasing model order (MO).

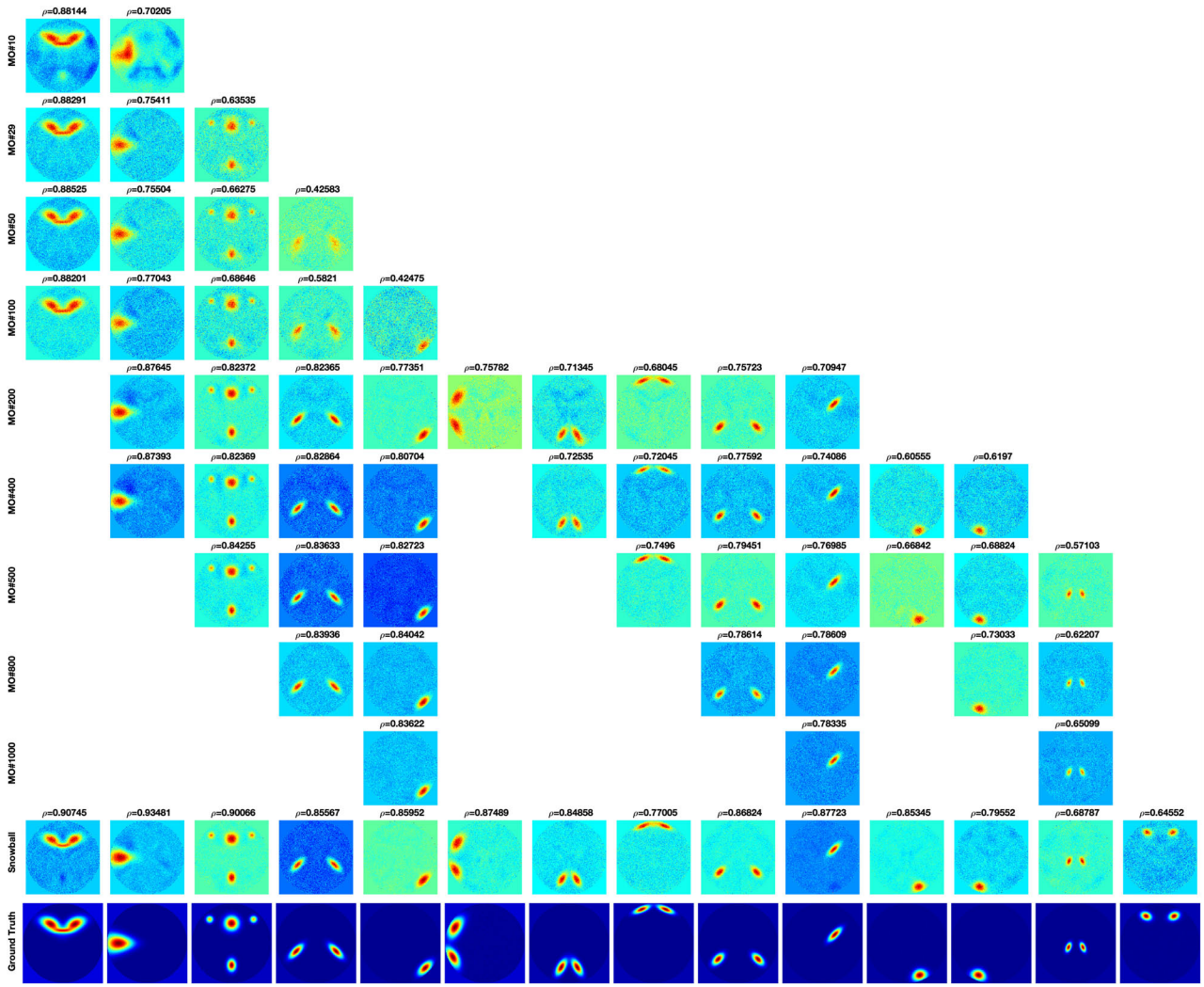

FIGURE 6 | FastICA results under different model orders, MO (shown on the far left side of the figure). Snowball ICA results are shown in the row above the ground truth signals (shown in the bottom row). As model order increases for FastICA, the accuracy of estimation of individual networks increases but some networks with wide spatial distributions disappear at higher MO. In addition, FastICA only identifies a maximum of about 65% of the simulated sources, and only 9/29 at the true MO of the simulated data. In contrast, Snowball ICA estimates 26/29 ground truth signal sources, including widely distributed and highly focal networks, with high accuracy. Additional details on this figure can be found in the **Supplementary Material**.

The performance of Snowball ICA, MELODIC, and GIFT under different CNR levels are compared in terms of spatial estimation accuracy, as shown in **Figure 8**. Snowball ICA demonstrates greater accuracy across the ranges of CNR that may be observed in BOLD fMRI signals (Welvaert and Rosseel, 2013) as GIFT and MELODIC.

Resting State fMRI Data Results

The model order was chosen from 25 to 50 for fMRI data processing (Beckmann et al., 2005; Damoiseaux et al., 2006; Luca et al., 2010). **Figure 9** shows the information used under different model orders. Even when model order is 100, the information used is no more than 40%. That means more than 60% of the information was removed, reducing potential accuracy.

For the dataset, the estimated model order is found to be 16 using the MDL criteria, 648 using the LAP, 830 using ER_AR and 806 using ER_FM. The wide range of estimated model order when using different criteria makes MOS a big problem in real-world applications. The explained information under model order 16 is only 22.36%. Under the model order of 648, 830, or 806, based on simulation results, some components with large scale could not be extracted. Even though model order 830 is very high, the information used is only 71.34%.

The corresponding components estimated by Snowball ICA, GIFT, and MELODIC were compared by visual inspection and kurtosis. Visual inspection of components estimated by each method suggests that Snowball ICA produces SMs with the cleanest spatial distribution (**Figure 10**). **Figure 11** shows that components estimated by Snowball ICA exhibit the greatest

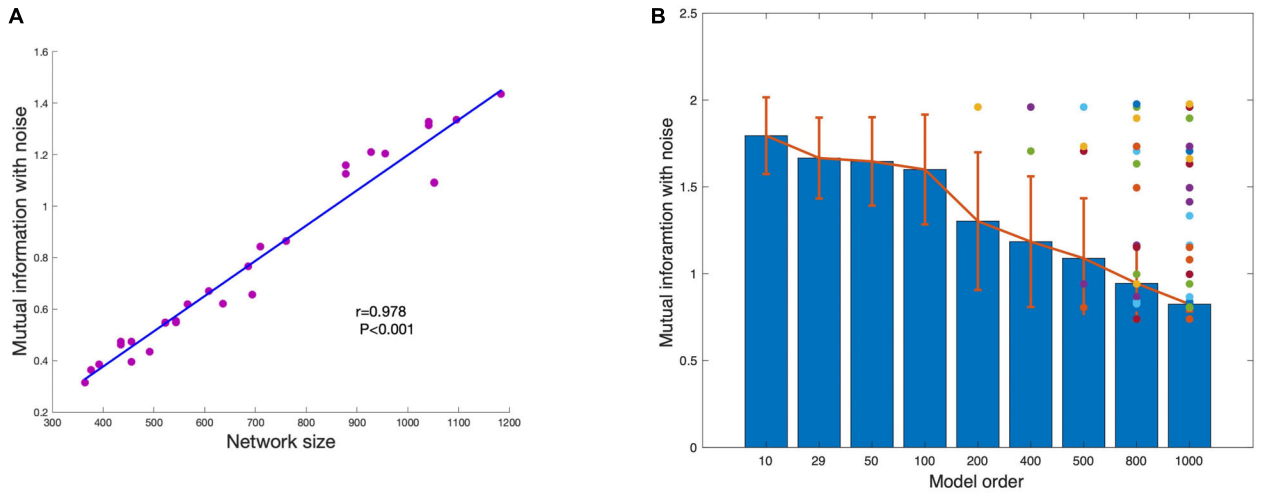

FIGURE 7 | (A) The strong association between network size and shared mutual information with noise shows that more spatially extensive brain networks share greater mutual information with background noise. **(B)** The average mutual information of estimated networks under each model order. The colored dots represent the mutual information with noise of networks that disappear at higher MO with FastICA.

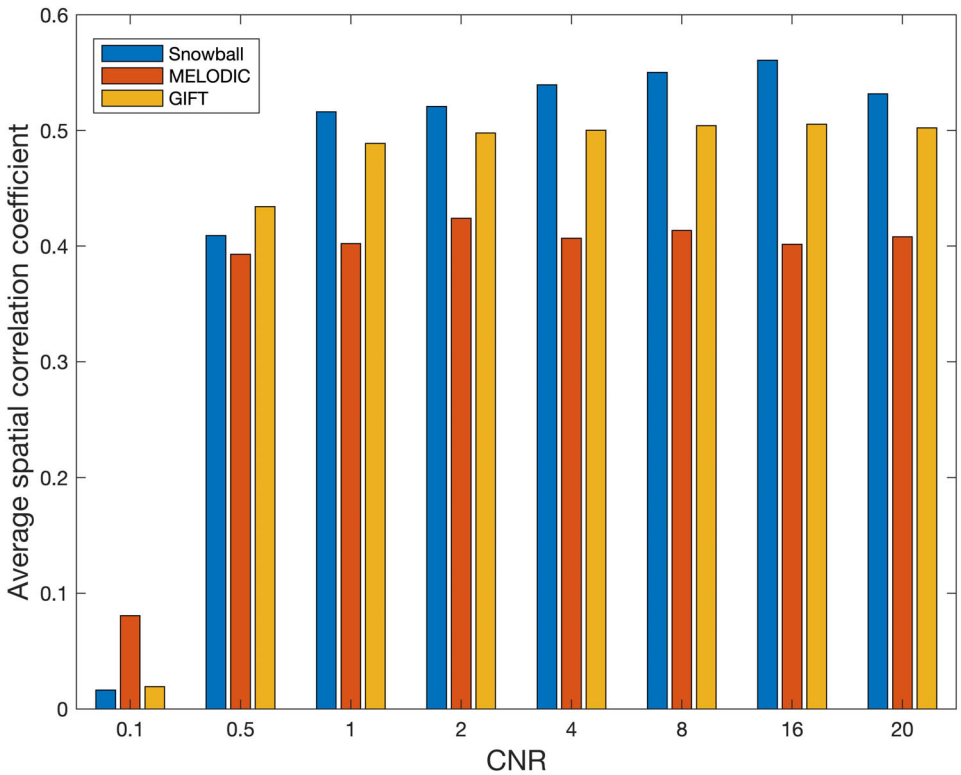

FIGURE 8 | Spatial estimation accuracy of Snowball, MELODIC, and GIFT across different levels of contrast-to-noise ratio (CNR). Snowball ICA demonstrates greater accuracy across the ranges of CNR that may be observed in BOLD fMRI signals as GIFT and MELODIC.

kurtosis, e.g., non-Gaussianity. However, Snowball ICA is a time-consuming strategy. MELODIC, GIFT, and Snowball were run on a computing cluster with 5 Linux-X64 nodes. The configuration of each node is: Intel(R) Xeon(R) Gold CPU 6130 2.10 GHz and 187.5 GB of random-access memory (RAM). The time costs of each method to estimate the same number of components are as follows: GIFT: 17 min, MELODIC: 50 min, Snowball: 30 h and 11 min. Further optimization of Snowball will be needed to reduce the computing time, however computing clusters are becoming more widely available and balance the need

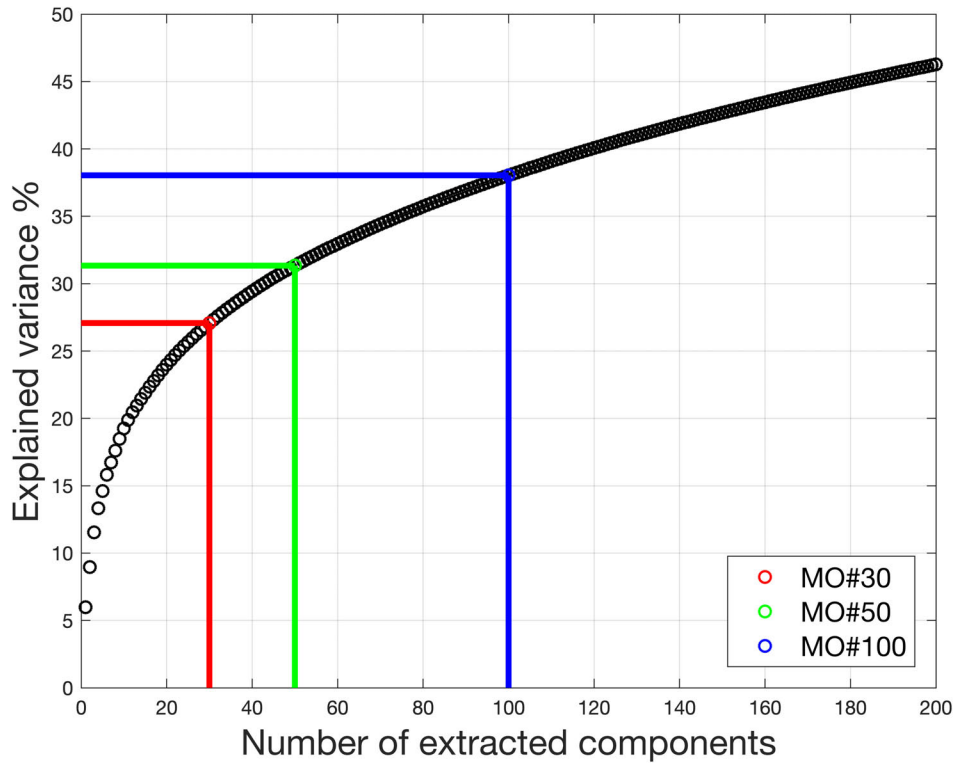

FIGURE 9 | Real *in vivo* fMRI data result: variance retained under different model order. With model order equal to 30, only 27% of the variance is retained for the ICA. Even with model order equal to 100, the variance retained for the ICA is no more than 40%.

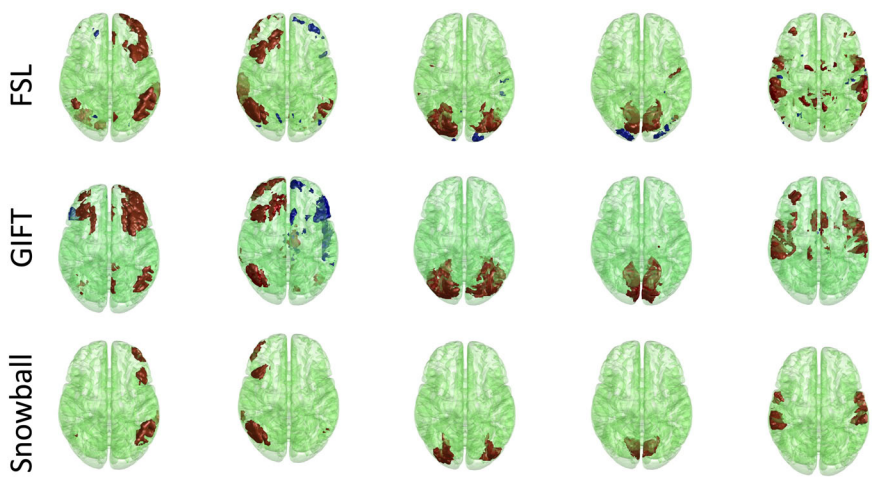

FIGURE 10 | Real *in vivo* fMRI data results: assessing the Snowball component via visualization. Spatial maps of five networks extracted by FSL, GIFT, and Snowball. The threshold is 2.3 for all spatial maps, after standardization of spatial maps. Spatial maps of all components estimated from each method are shown in the **Supplementary Material**.

for improved methods for network estimation with intensive computational needs for our method.

The results of different parameter choices are shown in **Figure 12**. The seeds estimated with different model orders in seed creation from different subjects vary greatly, with an average similarity across three different seeds equal to 0.25. However, the final estimates of the right frontoparietal network after information collection are all highly similar, with an average similarity equal to 0.82, even when different block sizes are applied. As shown in **Figure 12**, after thresholding, the visualized results are nearly identical. Our findings demonstrate that different seeds constructed with different parameters in the

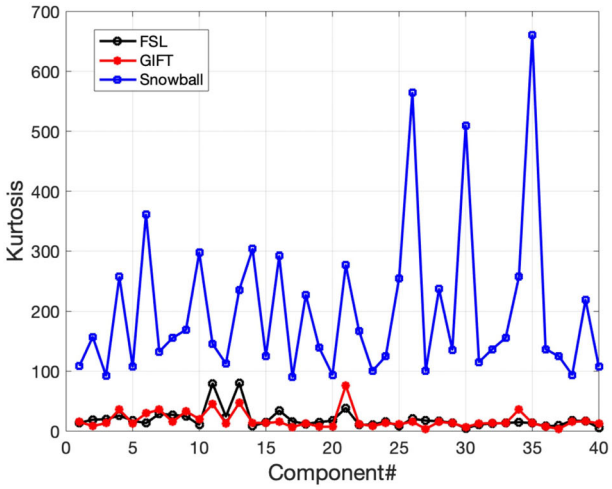

FIGURE 11 | Real *in vivo* fMRI data results: assessing the Snowball component via kurtosis. Kurtosis for the set of spatial maps extracted by FSL, GIFT, and Snowball ICA. The results of Snowball ICA have the highest kurtosis and are thus most consistent with the assumptions of the ICA model.

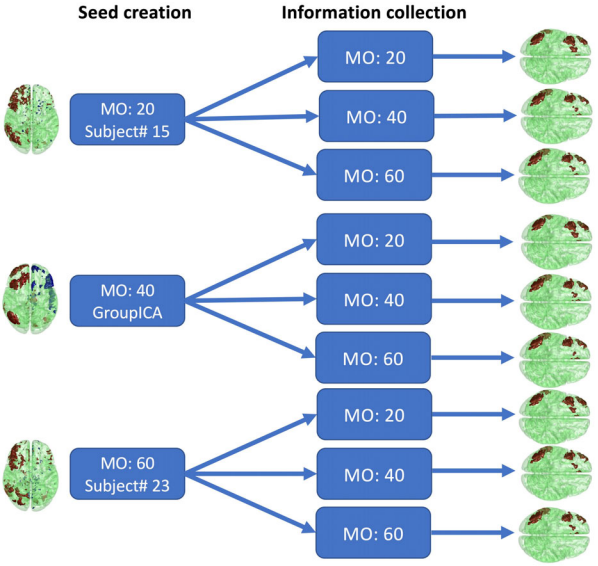

FIGURE 12 | Real *in vivo* fMRI data results: Snowball ICA parameter selection. Comparison of the estimated right frontoparietal network obtained using different parameters for seed creation and information collection shows that although considerable differences exist between seeds estimated with different model orders in seed creation and in block sizes, the final estimated networks are highly similar.

seed creation step, and information collection with different parameters, will still converge to the same solution for a given network. As such, initial parameter selection is not a crucial step in implementing Snowball ICA.

DISCUSSION

The main findings of this study are that (1) traditional ICA methods have significant limitations in estimation of signal source number and spatial component quality, (2) information is lost during data reduction, and (3) large and small scale components cannot be accurately estimated with the same model order due to independence constraints. Furthermore, our proposed method, the Snowball ICA, addresses these limitations and outperforms traditional ICA algorithms on a number of metrics. We believe these findings are important for a number of reasons.

Information is lost by data reduction. When the model order is different, different numbers of PCA components are used, and the information fed into ICA unmixing program is markedly different. Therefore, the accuracy of components varies based on model order. Traditional ICA presumes that PCA data reduction reduces redundant information and only leaves useful information. This is easy to implement when the signal-to-noise ratio is high, such as mixed high-quality acoustic signals. However, because fMRI data is much more complex than acoustic signals, the removal of this information as "noise" may be obscuring meaningful signals in the brain and contributing to issues with reproducibility. While increasing the number of PCA components used increases the accuracy of components and the percentage of information used, traditional methods are unable to include all of the meaningful information. Snowball ICA is able to estimate these components accurately, represent higher proportions of information, and do so without increasing model order to unreasonable levels. Even though PCA is also applied in Snowball ICA seed creation part, the lost information would be collected in the information collection stage.

The spatial scale of estimated components decreases as the model order increases with conventional approaches. Based on information theory with independence constraints, the mutual information between components should be low (Hyvarinen, 1999; Hyvärinen and Oja, 2000). Each signal has intrinsic mutual information with noise. Larger-scale network has higher mutual information with noise. However, inevitably, once model order is selected both source information and noise components will also be extracted. Limited by mutual information with those noise, some components with large shape may not be extracted. From the simulations, when the model order is smaller, components with a larger scale can be extracted, but this is less accurate due to data reduction limitations. In contrast, Snowball ICA is able to extract both large- and small-scale components. This is especially important given the variation in network composition in the brain. Snowball ICA is not limited to research questions involving similarly scaled network interactions – it can be used to simultaneously study the large- and small-scale networks that coexist in the brain.

The information collection step of Snowball can be followed with any kind of current ICA. There are two kinds of ICA algorithms in fMRI data processing. The first is GIFT, based on the ICASSO, the conventional method introduced in this article. The other is probabilistic ICA (Beckmann and Smith, 2004), also known as noise ICA, which attempts to generalize ICA to include noise. The mechanism of model order effect of noise

free ICA is explored in study. Probabilistic ICA leverages some information from noise, which may improve the accuracy of estimation to some extent. Further work is needed to investigate the how model order affects probabilistic ICA. Both of these two algorithms could be followed by Snowball ICA information collection, to improve the accuracy of the components and strengthen confidence of fMRI findings.

In addition to the application of ICA for fMRI data analyses, ICA is also widely used in the analysis and processing of electroencephalogram (EEG) and EEG-fMRI data fusion (Calhoun et al., 2009; Lei et al., 2012; Dong et al., 2014, 2016). For data fusion, spatial ICA of fMRI and temporal ICA of EEG has been used to extract features that are matched across the modalities. The number of independent components impacts the final estimations for both spatial ICA and temporal ICA. With Snowball ICA, the intrinsic embedded components can be estimated more accurately without the need to specify the model order for either EEG or fMRI, which may lead to improvements in fusion of high spatial and temporal resolution information.

When Snowball ICA is applied for group wise fMRI decomposition, there are several factors that may influence the accuracy of estimation. First, differences in brain shapes of different subjects may result in misalignment of the network SMs across subjects. Second, it is logical to assume some components are stronger in some subjects/scans. So, if iteration in information collection is not stable, the order where these scans are fed into Snowball may impact the estimation of components. Third, there are a number of parameters that are important for snowball ICA (seed model order, threshold Iq, block size of information collection iterations). In this study, theses parameters are selected based on our experience. The threshold Iq was also selected as 0.9 based on our experience and on previous published studies. Abou-Elseoud et al. (2010) who found that when the value of Iq is greater than 0.8, the results are repeatable. A study by Allen et al. (2011) also demonstrated that the Iq of meaningful components was typically larger than 0.9. In the present study, although the choice of specific Iq may affect the number of extracted components, use of a higher Iq ensures that the extracted components are reliable. In addition, the specific choice of Iq does not affect the accuracy of the estimated components. We also observed that the slight change of the model order will not have much influence on the estimated components (**Figure 7B**), which is also demonstrated with parameter selection (**Figure 12**). Hence, the selection of the seed model order and the block size of information collection iterations is not fatal.

Model order selection is also a crucial step in temporal ICA. Theoretically, Snowball ICA can also be applied for temporal ICA. However, it is not clear if the improvements we observe with spatial ICA will be realized with temporal ICA. In the case of spatial ICA, Snowball is effective at estimating networks without specifying a model order because it utilizes more information in the data (e.g., it obviates loss of information during data reduction with PCA) and is better able to identify networks that share large degree of mutual information with the noise. It is likely that temporal ICA will have different factors that may impact whether improvements in estimation would be seen with Snowball ICA.

While Snowball ICA is time-consuming due to the iterative process, it will be important for researchers determine the cost-benefit based on their hypothesized source signal scale. Further research will be necessary to explore ways to decrease computational costs for Snowball ICA. Besides, Snowball ICA is an empirical strategy that combining the conventional ICA and iteration of ICA with reference to solve the mode order problem. New algorithm with overall theoretical principles to solve the model order problem worth further investigation. Due to the lack of acknowledge of ground truth in real-world application, even though Snowball ICA can be identified with better performance compared with conventional ICA in some sense, more comparison of them in terms of neuroscience such as assessing relative heritability, or behavioral prediction accuracy, or split-half reproducibility is needed.

CONCLUSION

In this article, we present a novel strategy, called Snowball ICA, to solve the MOS problem of ICA for applications to fMRI data processing. Choice of model order for ICA, and the PCA data reduction step prior to the ICA, directly impacts how much variance in the data is utilized for ICA estimation. In addition, shared mutual information between estimated sources and noise varies with the network spatial scale, making optimization of model order a challenging problem. Snowball ICA ultimately utilizes much more information contained in the data for the ICA decomposition, and is able to estimate signal sources that share mutual information with noise, which results in improved network estimation when compared with traditional ICA. The effectiveness of the proposed method is demonstrated through extensive simulations and by application to *in vivo* fMRI data.

DATA AVAILABILITY STATEMENT

Publicly available datasets were analyzed in this study. This data can be found here: https://www.humanconnectome.org.

AUTHOR CONTRIBUTIONS

GH, FC, and LN: conceptualization. GH: methodology, software, formal analysis, and writing—original draft preparation. GH, SA, and BF: validation. GH and LN: investigation. GH, AW, and LN: writing—review and editing. AW: visualization. FC and LN: supervision and project administration. FC, LN, and BF: funding acquisition. All authors contributed to the article and approved the submitted version.

FUNDING

This work was supported by National Natural Science Foundation of China (Grant No. 91748105), National Foundation in China (No. JCKY2019110B009), and the Fundamental Research Funds for the Central Universities

(DUT2019) in Dalian University of Technology in China. This work was also supported by China Scholarship Council (No. 201806060038). LN was supported by the National Institutes of Health (PI: LN, DA037265, AA024565). SA and BF were supported by NS097512 (PI: BF).

SUPPLEMENTARY MATERIAL

The Supplementary Material for this article can be found online at: https://www.frontiersin.org/articles/10.3389/fnins.2020.569657/full#supplementary-material

REFERENCES

Abou-Elseoud, A., Starck, T., Remes, J., Nikkinen, J., Tervonen, O., and Kiviniemi, V. (2010). The effect of model order selection in group PICA. *Hum. Brain Mapp.* 31, 1207–1216. doi: 10.1002/hbm.20929

Akaike, H. (1998). "Information theory and an extension of the maximum likelihood principle," in *Selected Papers of Hirotugu Akaike. Springer Series in Statistics (Perspectives in Statistics)*, eds E. Parzen, K. Tanabe, and G. Kitagawa (New York, NY: Springer).

Allen, E. A., Erhardt, E. B., Wei, Y., Eichele, T., and Calhoun, V. D. (2012). Capturing inter-subject variability with group independent component analysis of fMRI data: a simulation study. *Neuroimage* 59, 4141–4159. doi: 10.1016/j.neuroimage.2011.10.010

Allen, E. A., Liu, J., Kiehl, K. A., Gelernter, J., Pearlson, G. D., Perrone-Bizzozero, N. I., et al. (2011). Components of cross-frequency modulation in health and disease. *Front. Syst. Neurosci.* 5:59. doi: 10.3389/fnsys.2011.00059

Beaty, R. E., Kenett, Y. N., Christensen, A. P., Rosenberg, M. D., Benedek, M., Chen, Q., et al. (2018). Robust prediction of individual creative ability from brain functional connectivity. *Proc. Natl. Acad. Sci.* 115, 1087–1092. doi: 10.1073/pnas.1713532115

Beckmann, C. F. (2012). Modelling with independent components. *Neuroimage* 62, 891–901. doi: 10.1016/j.neuroimage.2012.02.020

Beckmann, C. F., DeLuca, M., Devlin, J. T., and Smith, S. M. (2005). Investigations into resting-state connectivity using independent component analysis. *Philos. Trans. R. Soc. B Biol. Sci.* 360, 1001–1013. doi: 10.1098/rstb.2005.1634

Beckmann, C. F., and Smith, S. M. (2004). Probabilistic independent component analysis for functional magnetic resonance imaging. *IEEE Trans. Med. Imag.* 23, 137–152. doi: 10.1109/TMI.2003.822821

Bell, A., and Sejnowski, T. (1995). Information-maximization approach to blind separation and blind deconvolution. *Technology* 1159, 1129–1159. doi: 10.1162/neco.1995.7.6.1129

Calhoun, V. D., Adali, T., Pearlson, G. D., and Pekar, J. J. (2001a). A method for making group inferences from functional MRI data using independent component analysis. *Hum. Brain Mapp.* 14, 96–107. doi: 10.1002/hbm

Calhoun, V. D., Adali, T., Pearlson, G. D., and Pekar, J. J. J. (2001b). Spatial and temporal independent component analysis of functional MRI data containing a pair of task-related waveforms. *Hum. Brain Mapp.* 13, 43–53. doi: 10.1002/hbm.1024

Calhoun, V. D., Liu, J., and Adali, T. (2009). A review of group ICA for fMRI data and ICA for joint inference of imaging, genetic, and ERP data. *Neuroimage* 45, 163–172. doi: 10.1016/j.neuroimage.2008.10.057

Calhoun, V. D., Silva, R. F., Adali, T., and Rachakonda, S. (2015). Comparison of PCA approaches for very large group ICA. *Neuroimage* 118, 662–666. doi: 10.1016/j.neuroimage.2015.05.047

Constantinescu, A. O., Reilly, J. X. O., and Behrens, T. E. J. (2016). Organizing conceptual knowledge in humans with a grid-like code. *Science* 352, 1464–1468. doi: 10.1126/science.aaf0941.Organizing

Cover, T. M., and Thomas, J. A. (2012). *Elements of Information Theory*. Hoboken, NJ: John Wiley & Sons.

Damoiseaux, J. S., Rombouts, S. A. R. B., Barkhof, F., Scheltens, P., Stam, C. J., Smith, S. M., et al. (2006). Consistent resting-state networks across healthy subjects. *Proc. Natl. Acad. Sci. U.S.A.* 103, 13848–13853. doi: 10.1073/pnas.0601417103

Dong, L., Gong, D., Valdes-Sosa, P. A., Xia, Y., Luo, C., Xu, P., et al. (2014). Simultaneous EEG-fMRI: trial level spatio-temporal fusion for hierarchically reliable information discovery. *Neuroimage* 99, 28–41. doi: 10.1016/j.neuroimage.2014.05.029

Dong, L., Luo, C., Zhu, Y., Hou, C., Jiang, S., Wang, P., et al. (2016). Complex discharge-affecting networks in juvenile myoclonic epilepsy: a simultaneous EEG-fMRI study. *Hum. Brain Mapp.* 37, 3515–3529. doi: 10.1002/hbm.23256

Du, Y., and Fan, Y. (2013). Group information guided ICA for fMRI data analysis. *Neuroimage* 69, 157–197. doi: 10.1016/j.neuroimage.2012.11.008

Erhardt, E. B., Allen, A. E., Wei, Y., Eichele, T., and Calhoun, D. V. (2012). SimTB, a simulation toolbox for fMRI data under a model of spatiotemporal separability. *Neuroimage* 59, 4160–4167. doi: 10.1016/j.dcn.2011.01.002.The

Erhardt, E. B., Rachakonda, S., Bedrick, E. J., Allen, E. A., Adali, T., and Calhoun, V. D. (2011). Comparison of multi-subject ICA methods for analysis of fMRI data. *Hum. Brain Mapp.* 32, 2075–2095. doi: 10.1002/hbm.21170

Freeman, J., Vladimirov, N., Kawashima, T., Mu, Y., Sofroniew, N. J., Bennett, D. V., et al. (2014). Mapping brain activity at scale with cluster computing. *Nat. Methods* 11, 941–950. doi: 10.1038/nmeth.3041

Fu, G. S., Anderson, M., and Adali, T. (2014). Likelihood estimators for dependent samples and their application to order detection. *IEEE Trans. Signal Process.* 62, 4237–4244. doi: 10.1109/TSP.2014.2333551

Glasser, M. F., Coalson, T. S., Robinson, E. C., Hacker, C. D., Yacoub, E., Ugurbil, K., et al. (2016). A multi-modal parcellation of human cerebral cortex. *Nature* 536, 171–178. doi: 10.1038/nature18933.A

Griffanti, L., Salimi-Khorshidi, G., Beckmann, C. F., Auerbach, E. J., Douaud, G., Sexton, C. E., et al. (2014). ICA-based artefact removal and accelerated fMRI acquisition for improved resting state network imaging. *Neuroimage* 95, 232–247. doi: 10.1016/j.neuroimage.2014.03.034

Hermans, E. J., Marle, H. J. F., Van, Ossewaarde, L., Henckens, M. J. A. G., Qin, S., et al. (2011). Stress-Related noradrenergic activity prompts large-scale neural network reconfiguration. *Science* 334, 1151–1153. doi: 10.1126/science.1209603

Himberg, J., Hyvärinen, A., and Esposito, F. (2004). Validating the independent components of neuroimaging time series via clustering and visualization. *Neuroimage* 22, 1214–1222. doi: 10.1016/j.neuroimage.2004.03.027

Hu, G., Zhang, Q., Waters, A. B., Li, H., Zhang, C., Wu, J., et al. (2019). Tensor clustering on outer-product of coefficient and component matrices of independent component analysis for reliable functional magnetic resonance imaging data decomposition. *J. Neurosci. Methods* 325:108359. doi: 10.1016/j.jneumeth.2019.108359

Huang, D. S., and Mi, J. X. (2007). A new constrained independent component analysis method. *IEEE Trans. Neural Networks* 18, 1532–1535. doi: 10.1109/TNN.2007.895910

Hyvarinen, A. (1999). Fast and robust fixed-point algorithm for independent component analysis. *IEEE Trans. Neural Networks Learn. Syst.* 10, 626–634. doi: 10.1109/72.761722

Hyvärinen, A., and Oja, E. (2000). Independent component analysis: algorithms and applications. *Neural Networks* 13, 411–430. doi: 10.13031/trans.56.9922

Kuang, L. D., Lin, Q. H., Gong, X. F., Cong, F., Sui, J., and Calhoun, V. D. (2018). Model order effects on ICA of resting-state complex-valued fMRI data: application to schizophrenia. *J. Neurosci. Methods* 304, 24–38. doi: 10.1016/j.jneumeth.2018.02.013

Lei, X., Valdes-Sosa, P. A., and Yao, D. (2012). EEG/fMRI fusion based on independent component analysis: integration of data-driven and model-driven methods. *J. Integr. Neurosci.* 11, 313–337. doi: 10.1142/S0219635212500203

Li, Y.-O., Adali, T., Calhoun, V. D., Li, Y.-O., Adali, T., Calhoun, V. D., et al. (2007). Estimating the number of independent components for functional magnetic resonance imaging data. *Hum. Brain Mapp.* 28, 1251–1266. doi: 10.1002/hbm.20359

Lin, Q. H., Zheng, Y. R., Yin, F. L., Liang, H., and Calhoun, V. D. (2007). A fast algorithm for one-unit ICA-R. *Inf. Sci. (Ny).* 177, 1265–1275. doi: 10.1016/j.ins.2006.09.011

Lu, W., and Rajapakse, J. C. (2005). Approach and applications of constrained ICA. *IEEE Trans. Neural Networks* 16, 203–212. doi: 10.1109/TNN.2004.836795

Luca, M. D., Beckmann, C. F., Stefano, D., Matthews, P. M., and Smith, S. M. (2010). fMRI resting state networks define distinct modes of long-distance interactions in the human brain. *Neuroimage* 7, 436–438. doi: 10.1016/j.neuroimage.2005.08.035

McKeown, M. J., and Sejnowski, T. J. (1998). Independent component analysis of fMRI data: examining the assumptions. *Hum. Brain Mapp.* 6, 368–372. doi: 10.1002/(sici)1097-0193(1998)6:5/6<368::aid-hbm7>3.0.co;2-e

Minka, T. P. (2000). *Automatic choice of dimensionality for PCA* Technical Report No. TR514, Cambridge, MA: M.I.T. Media Laboratory Perceptual Computing Section.

Nickerson, L. D., Smith, S. M., Öngür, D., and Beckmann, C. F. (2017). Using dual regression to investigate network shape and amplitude in functional connectivity analyses. *Front. Neurosci.* 11:115. doi: 10.3389/fnins.2017.00115

Pedersen, M., Zalesky, A., Omidvarnia, A., and Jackson, G. D. (2018). Multilayer network switching rate predicts brain performance. *Proc. Natl. Acad. Sci.* 115, 13376–13381. doi: 10.1073/pnas.1814785115

Rachakonda, S., Silva, R. F., Liu, J., and Calhoun, V. D. (2016). Memory efficient PCA methods for large group ICA. *Front. Neurosci.* 10:17. doi: 10.3389/fnins.2016.00017

Richiardi, J., Altmann, A., Milazzo, A., Chang, C., Mallar, M., Banaschewski, T., et al. (2015). Correlated gene expression supports synchronous activity in brain networks. *Science* 348, 1241–1244. doi: 10.1126/science.1255905.Correlated

Rissanen, J. (1978). Modelling by the shortest data description. *Automatica* 14, 465–471. doi: 10.1016/0005-1098(78)90005-5

Robinson, E. C., Jbabdi, S., Glasser, M. F., Andersson, J., Burgess, G. C., and Harms, M. P. (2014). Msm: a new flexible framework for multimodal surface matching. *Neuroimage* 100, 414–426. doi: 10.1016/j.neuroimage.2014.05.069.MSM

Rose, N. S., LaRocque, J. J., Riggall, A. C., Gosseries, O., Starrett, M. J., Meyering, E. E., et al. (2016). Reactivation of latent working memories with transcranial magnetic stimulation. *Science* 354, 1136–1139. doi: 10.1021/acsnano.5b07425. Molecular

Salimi-Khorshidi, G., Douaud, G., Beckmann, C. F., Glasser, M. F., Griffanti, L., and Smith, S. M. (2014). Automatic denoising of functional MRI data: combining independent component analysis and hierarchical fusion of classifiers. *Neuroimage* 90, 449–468. doi: 10.1016/j.neuroimage.2013.11.046

Seifritz, E., Esposito, F., Hennel, F., Mustovic, H., Neuhoff, J., Bilecen, D., et al. (2002). Spatiotemporal pattern of neural processing in the human auditory cortex. *Sci. (New York, NY)* 297, 1706–1708. doi: 10.1126/science.1074355

Smith, S. M., Beckmann, C. F., Andersson, J., Auerbach, E. J., Bijsterbosch, J., Douaud, G., et al. (2013). Resting-state fMRI in the human connectome project. *Neuroimage* 80, 144–168. doi: 10.1016/j.neuroimage.2013.05.039

Smith, S. M., Hyvaŕinen, A., Varoquaux, G., Miller, K. L., and Beckmann, C. F. (2014). Group-PCA for very large fMRI datasets. *Neuroimage* 101, 738–749. doi: 10.1016/j.neuroimage.2014.07.051

Sokolov, A. A., Zeidman, P., Erb, M., Ryvlin, P., Friston, K. J., and Pavlova, M. A. (2018). Structural and effective brain connectivity underlying biological motion detection. *Proc. Natl. Acad. Sci.* 115, E12034–E12042. doi: 10.1073/pnas.1812859115

Tavor, I., Jones, O. P., Mars, R. B., Smith, S. M., Behrens, T. E. J., Jbabdi, S., et al. (2016). Task-free MRI predicts individual differences in brain activity during task performance. *Science* 352, 216–220. doi: 10.1126/science.aad8127

Van Essen, D. C., Smith, S. M., Barch, D. M., Behrens, T. E. J., Yacoub, E., Ugurbil, K., et al. (2013). The WU-Minn human connectome project: an overview. *Neuroimage* 80, 62–79. doi: 10.1016/j.neuroimage.2013.05.041

Welvaert, M., and Rosseel, Y. (2013). On the definition of signal-to-noise ratio and contrast-to-noise ratio for fMRI data. *PLoS One* 8:e77089. doi: 10.1371/journal.pone.0077089

Zhang, Q., Hu, G., Tian, L., Ristaniemi, T., Huili Wang, Chen, H., et al. (2018). Examining stability of independent component analysis based on coefficient and component matrices for voxel-based morphometry of structural magnetic resonance imaging. *Cogn. Neurodyn.* 12, 461–470. doi: 10.1007/s11571-018-9484-9482

Conflict of Interest: The authors declare that the research was conducted in the absence of any commercial or financial relationships that could be construed as a potential conflict of interest.

Copyright © 2020 Hu, Waters, Aslan, Frederick, Cong and Nickerson. This is an open-access article distributed under the terms of the Creative Commons Attribution License (CC BY). The use, distribution or reproduction in other forums is permitted, provided the original author(s) and the copyright owner(s) are credited and that the original publication in this journal is cited, in accordance with accepted academic practice. No use, distribution or reproduction is permitted which does not comply with these terms.

frontiers in Neuroscience

REVIEW
published: 23 September 2020
doi: 10.3389/fnins.2020.00903

Imaging the Neuroimmune Dynamics Across Space and Time

*Micaël Carrier[1], Marie-Ève Robert[1], Fernando González Ibáñez[1], Michèle Desjardins[2,3] and Marie-Ève Tremblay[1,4,5]**

[1] Axe Neurosciences, Centre de Recherche du CHU de Québec, Université Laval, Québec City, QC, Canada, [2] Axe Oncologie, Centre de Recherche du CHU de Québec, Université Laval, Québec City, QC, Canada, [3] Department of Physics, Physical Engineering and Optics, Université Laval, Québec City, QC, Canada, [4] Department of Molecular Medicine, Université Laval, Québec City, QC, Canada, [5] Division of Medical Sciences, University of Victoria, Victoria, BC, Canada

The immune system is essential for maintaining homeostasis, as well as promoting growth and healing throughout the brain and body. Considering that immune cells respond rapidly to changes in their microenvironment, they are very difficult to study without affecting their structure and function. The advancement of non-invasive imaging methods greatly contributed to elucidating the physiological roles performed by immune cells in the brain across stages of the lifespan and contexts of health and disease. For instance, techniques like two-photon *in vivo* microscopy were pivotal for studying microglial functional dynamics in the healthy brain. Through these observations, their interactions with neurons, astrocytes, blood vessels and synapses were uncovered. High-resolution electron microscopy with immunostaining and 3D-reconstruction, as well as super-resolution fluorescence microscopy, provided complementary insights by revealing microglial interventions at synapses (phagocytosis, trogocytosis, synaptic stripping, etc.). In addition, serial block-face scanning electron microscopy has provided the first 3D reconstruction of a microglial cell at nanoscale resolution. This review will discuss the technical toolbox that currently allows to study microglia and other immune cells in the brain, as well as introduce emerging methods that were developed and could be used to increase the spatial and temporal resolution of neuroimmune imaging. A special attention will also be placed on positron emission tomography and the development of selective functional radiotracers for microglia and peripheral macrophages, considering their strong potential for research translation between animals and humans, notably when paired with other imaging modalities such as magnetic resonance imaging.

Keywords: microscopy, microglia, fluorescence microscopy, electron microscopy, positron emission tomography, magnetic resonance imaging

OPEN ACCESS

Edited by:
João O. Malva, University of Coimbra, Portugal

Reviewed by:
Alejandra Sierra, University of Eastern Finland, Finland
Raquel Ferreira, University of Beira Interior, Portugal

****Correspondence:***
Marie-Ève Tremblay
evetremblay@uvic.ca

Specialty section:
This article was submitted to Brain Imaging Methods, a section of the journal Frontiers in Neuroscience

Received: *09 June 2020*
Accepted: *04 August 2020*
Published: *23 September 2020*

Citation:
Carrier M, Robert M-È, González Ibáñez F, Desjardins M and Tremblay M-È (2020) Imaging the Neuroimmune Dynamics Across Space and Time. Front. Neurosci. 14:903. doi: 10.3389/fnins.2020.00903

INTRODUCTION

The immune system of the central nervous system (CNS) is essential to maintain its homeostasis [reviewed in Tay et al. (2017)]. Typically, this task is mainly performed by the resident immune cell population, microglia (Ginhoux et al., 2010; Tay et al., 2019). The role of microglia and other immune cells in the brain was uncovered using innovative methods allowing to image them *in situ* (Savage et al., 2019a) and *in vivo* (Davalos et al., 2005; Herz et al., 2012). Considering

that immune cells like microglia are highly sensitive to changes in their microenvironment, non-invasive techniques that prevent their reaction during tissue preparation and imaging are necessary (Cătălin et al., 2017; Augusto-Oliveira et al., 2019). Immune cell reactivity can be assessed using morphological features (Savage et al., 2019a) or more sensitively by ultrastructure (El Hajj et al., 2019; Savage et al., 2019c). Overall, imaging techniques revealed that microglia play essential roles in the brain: as immune sentinels that clean toxic extracellular debris and repair damage to neighboring cells, but also as glial cells regulating neuronal and astrocytic/oligodendrocytic cell survival, differentiation, maturation, migration, as well as network formation and refinement with relation to neuronal activity (Ter Veer et al., 2017; Bordeleau et al., 2019; Tay et al., 2019). Once reactive, microglia play important roles in neuroinflammation –beneficial or detrimental depending on the context of disease or injury (Plemel et al., 2020). These roles of reactive microglia are exerted in cooperation with other glial and other innate immune cells (e.g., monocytes, neutrophils) as well as endothelial cells forming the blood-brain-barrier (BBB) (Sofroniew, 2015; Van Dyken and Lacoste, 2018; Bellver-Landete et al., 2019). Although monocytes were not shown to be present in the healthy adult mouse brain (Ginhoux et al., 2013; Prinz and Priller, 2014, 2017) they can be recruited rapidly in a wide panoply of contexts (D'Mello et al., 2009; Wohleb et al., 2015; Varvel et al., 2016; Niraula et al., 2018; Schneider et al., 2019). Once in the brain, monocytes tend to adopt a similar morphology as microglia and are often referred to as microglia-like cells even if they have a different origin, from the bone marrow while microglia come from the embryonic yolk sac (Leone et al., 2006; Varvel et al., 2012; Katsumoto et al., 2014). The adaptive immune system is also highly complex, with multiple cell types such as lymphocytes (T cells, B cells, and NK cells) playing a possibly important role in brain development, activity and plasticity notably through their secretion of neurotrophins (Kipnis et al., 2004; Lewitus and Schwartz, 2009; Morimoto and Nakajima, 2019). T cells in particular are often seen in the brain parenchyma in multiple sclerosis, both in human samples and its animal models of experimental autoimmune encephalomyelitis. In these autoimmune diseases, T cells are considered to change their behavior in a destructive way that causes demyelination and inflammation (Lehmann, 1998). Here, we will review the main imaging techniques that are currently available to study brain immunity, focusing on microglia as they are mainly studied, but also on monocytes and T cells, while providing examples of their complementary applications, and discuss the power of their combination into integrative studies.

IMAGING THE HOMEOSTATIC BRAIN USING PHOTONS

Microscopy techniques (brightfield, fluorescence, confocal, multiphoton, etc.) are commonly used in neuroimmunology to analyze the density, distribution and morphology of different cell types, including microglia, and their interactions one with another (Savage et al., 2019a). The examined cells often require markers to be visualized. Immunostaining is widely used to label the cells of interest across various types of samples, from animal models to human *postmortem* CNS. For example, double immunostaining against IBA1 and TMEM119 can be used to distinguish microglia (double positive; derived from embryonic yolk sac) from infiltrating peripheral macrophages (expressing IBA1 but not TMEM119; from bone marrow) (González Ibanez et al., 2019). One should note that TMEM119 expression is not stable in early development (until P20 in mouse) and can change in disease context such as multiple sclerosis, highlighting the importance of using a combination of markers including Fcrls, siglec-h, sall1, P2RY12 and more recently HEXB to identify microglia (Butovsky et al., 2014; Buttgereit et al., 2016; Konishi et al., 2017; Zrzavy et al., 2017; Masuda et al., 2020). Fluorescence can also label immune cells directly, without immunostaining, when markers are biologically expressed in transgenic animals (Martell et al., 2017; Daigle et al., 2018). Fate mapping of immune cells origin and trajectory, from the embryonic yolk sac or bone marrow to the CNS, and then function in the CNS can then be performed (Gomez Perdiguero et al., 2015). Reporter mice are especially useful when they are crossed one with another. As an example, the CX3CR1$^{+/GFP}$;Thy1H$^{+/YFP}$ model (Feng et al., 2000; Jung et al., 2000) labels microglia and neurons including synapses in two different colors. It allows to study dynamic relationships between the two cell types, which is particularly relevant for studying microglia-synapse structural interactions (Tremblay et al., 2010). Furthermore, fluorescent dyes can be injected *in vivo*, while cells can be stained *ex vivo* and introduced back into animals, which can be transgenic, to allow for their discrimination (Helmchen and Denk, 2005). Many different mouse models, discussed in detail in a comprehensive review (Theret et al., 2019), were developed to study the function of resident microglia and macrophages within the CNS. Parallel to this, photonic microscopy greatly evolved, providing always improved images, bypassing the spatial resolution limit from 350 nm to around 65 nm with super-resolution microscopy (Klar et al., 2001; Evilsizor et al., 2015), which is especially useful for studying synaptic interactions. We will next explore the main microscopy techniques that are commonly used in neuroimmunology and present emerging ones that could provide new insights. Advantages and limitations are compared in **Table 1**.

Slide Scanning

When answering questions about immune cell functions without knowing the specific CNS regions of interest involved, one can turn to high throughput imaging techniques such as slide scanning. This very convenient technique uses a mobile stage to automatically image regions of interest, from a series of CNS sections mounted on an entire microscopy glass slide, with a theoretical resolution of 900 nm (x-y). Whole mounts of mouse brain (Roetzer et al., 2019) and spinal cord (Bellver-Landete et al., 2019) were successfully imaged using this technique. It is ideal to perform quantitative analysis of microglial density and distribution, for instance, across large CNS tissue areas, as proposed within an experimental workflow in **Figure 1A**. One edge of the technique is the large amount of information

TABLE 1 | Comparison of light microscopy techniques based on their advantages and limitations.

Method	Tissue preparation	Spatial resolution	Depth	Main uses	*In vivo* imaging	Advantages	Limitations	References
Epifluorescence	-Fixation -*In vivo*: cranial window	350–500 nm	<200 μm	Rapid verifications (i.e. staining outcome, morphology, distribution)	Possible, but not typically used	-Easy use -Low cost -Rapid -Multi-channels -Optical sectioning not required	-Light diffraction limit -Out-of-focus background fluorescence detection	Yang and Yuste, 2017; Bayerl et al., 2019
Slide scanner microscopes (brightfield or fluorescent)	-Fixation -Slide-mounted	350–500 nm	<200 μm	-Cell distribution, density and morphology -Surface area -3D reconstructions (whole brain or serial sections)	No	-Easy use -High-speed scanning of large tissue sections -Multi-channel	-Light diffraction limit -Out-of-focus background fluorescence detection	Mikula et al., 2007; Chen et al., 2014; Yang and Yuste, 2017; Roetzer et al., 2019
Confocal	-Fixation -Tissue clearing	200–800 nm	<100 μm	-2D imaging of tissue sections -3D reconstructions (z stacks)	Possible, but not typically used	-Reduction of out of focus background fluorescence detection -Multi-channels	-Photobleaching -Slow speed: not suitable for following rapid changes in dynamic phenomena	Graf and Boppart, 2010; Pérez-Alvarez et al., 2013; Oreopoulos et al., 2014; Villaseñor and Collin, 2017
2-photon	-Fixation -*In vivo*: thinned-skull or cranial window -Chronic *in vivo*: canula insertion	400–900 nm	>300 μm >500 μm in vitro	-Live *in vivo* imaging -Time-lapse imaging -3D reconstructions	Yes	-Reduction of out of focus background fluorescence detection -Reduction of light scattering -Increased spatial and temporal resolution -Multi-channels	-Photobleaching (less than confocal microscopes) -Slightly decreased resolution due the use of larger wavelengths	Santi, 2011; Pérez-Alvarez et al., 2013; Oreopoulos et al., 2014
STED	-Fixation -*In vivo*: thinned-skull or cranial window -Chronic *in vivo*: canula insertion	65–100 nm	10–15 μm	-Synapse and dendritic spine dynamics	Yes	-Subcellular resolution -Multi-channels	-High cost and difficult equipment accessibility -Low tissue-penetration depth	Klar et al., 2001; Westphal et al., 2008; Berning et al., 2012; Chéreau et al., 2015
Light-sheet	-Fixation -Tissue clearing -Organotypic cultures	270–1000 nm	750 μm (live tissue) 2 mm (cleared tissue)	-Whole small organisms imaging (i.e. mouse embryos) or brain -Overview of cellular networks -3D reconstructions	No	-High-speed scanning of large tissue sections -Reduced photobleaching -High tissue-penetration depth	-Not suitable for large organisms such as adult mice (i.e. suitable for mice up to P14) -Depth limit established by autofluorescence -Limited number of channels (max. 2–3)	Dodt et al., 2007; Santi, 2011; Fiolka, 2019; Wang et al., 2019

provided in slide scanning images. Being formed of multiple tiles, these images allow the user to zoom in and out to visualize cellular density, distribution, morphology, intercellular relationships and other features of interest. The mosaic can be used to see the bigger picture of the cellular alterations or phenotypic changes as mentioned in **Figure 1B**. It can also be used to create new files containing smaller regions of interest with softwares such as QUPATH that could also be used for automatic analysis of density, distribution or morphology and intercellular relationships with machine learning (Bankhead et al., 2017). For instance, automatic analysis of slide scanning images was performed to characterize IBA1-immunopositive microglia/monocytes in traumatic brain injured mice at the site of injuries. The mosaic generated was used to count and classify these cells as "ramified" or "amoeboid" using machine learning, in less than 15 min compared to 5 h for a manual analyst. This faster

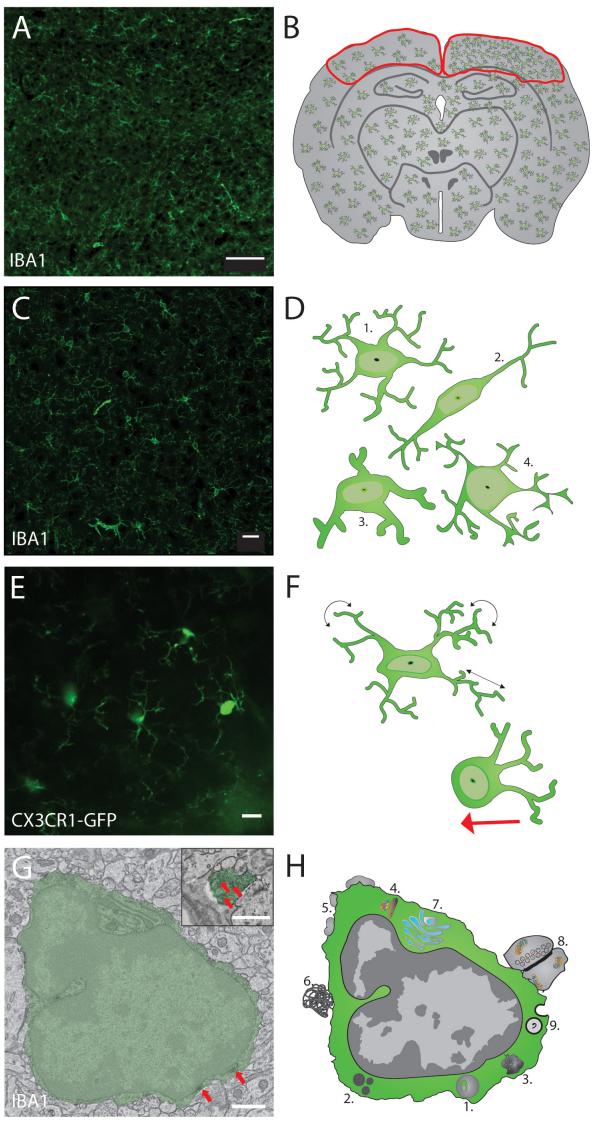

FIGURE 1 | Proposed thorough structural analysis of the immune cells in the brain, exemplified with microglia. Optimal analysis of microglial density, distribution, morphology and ultrastructure using 4 different imaging modalities can allow to evaluate their cellular network, organellar function and health status. **(A)** Slide scanning can be performed to image microglial density and distribution throughout the brain (scale bar = 100 μm) while discriminating between different regions and layers of interest **(B)**. Microglial morphology can be assessed in **(C)** using confocal microscopy to measure quantitative changes in their cell body and arborization area (scale bar = 20 μm) to be then classified, as illustrated starting from the top in **(D)** into ramified, rod shape, hypertrophic and dystrophic phenotypes, an assessment not always feasible by slide scanner imaging due to the lower resolution and lack of 3D information. Microglial dynamics can be investigated using non-invasive two-photon *in vivo* imaging of CX3CR1+/GFP reporter mice (scale bar = 10 μm), as shown in **(E)** with a thinned-skull preparation allowing to assess microglial cell body mobility (red arrow in **F**) and process motility (black arrows) during normal physiological conditions in the intact mouse cerebral cortex. The ultrastructure of microglial cell body and processes can be analyzed using **(G)** transmission electron microscopy, as illustrated by a pseudocolored microglia (scale bar = 1 μm) that displays peroxidase staining in its cell body and processes against the IBA1 protein (red arrows). Cytologic events that can

(Continued)

FIGURE 1 | Continued
be quantified in microglia using different electron microscopy techniques are illustrated in **(H)** and include, notably, 1. Lysosomal inclusions, 2. Lipid bodies, 3. Lipofuscin granules, 4. Elongated or altered mitochondria, 5. Extracellular space pockets, 6. Extracellular digestion, 7. Endoplasmic reticulum/Golgi dilation, 8. Synaptic contacts, and 9. Phagolysosomal inclusions.

process suggests strong potential for similar high-throughput analysis using human brain slices (Kyriazis et al., 2019). Slide scanning combined with machine learning is then a prime choice method for whole slices imaging in animal and human *postmortem* samples (Budde and Annese, 2013), considering that it removes the human bias when counting or tracing the contour of infiltrating monocytes or microglia from hundreds of slices.

Confocal Microscopy

The biggest foe of fluorescent microscopy is light scattering, which limits its spatial resolution to about 300 nm (x-y) and 600 nm (z) at best. To circumscribe this problem, confocal microscopes increase resolution by only detecting the fluorescence emitted by the sample at the focal point. This feat is achieved by using a pinhole to reject light originating from outside the focal plane (Elliott, 2020). In neuroimmunology, confocal microscopy is commonly used to image the morphology of immune cells in three dimensions (3D), by acquiring z-stacks as presented in **Figure 1C**. Z-stacks are the key functionality of confocal microscopy. Allowing the 3D analysis of immune cells can give deeper insight when characterizing the shape of microglia, monocytes and T cells (Perego et al., 2013; Mittal et al., 2019). In Alzheimer's disease pathology, for instance, T cell morphology can be 3D rendered in relation to neurons, which allowed the identification of "emperipolesis," a phenomenon by which the T cell is actually inside the neuron, which might suggest neuronal damage associated with the foreign cell entry (Lodygin et al., 2019). In injuries, the morphology of microglia can also be effectively assessed from 3D reconstruction where the ramification density and arborization area can be analyzed for microglia close to injury site *versus* located in the periphery (Otxoa-de-Amezaga et al., 2019). Such changes in morphology, associated with microglial surveillance capacity and interactions with other parenchymal elements, including synapses, can be missed in typical epifluorescence images as smaller ramifications are difficult to discern with the reduced resolution. Thus, confocal microscopy is an effective tool to reveal the morphology of microglia and other cell types in 3D, as required to identify phenotypic changes, cellular alterations and functions, as illustrated in **Figure 1D**. In the case of microglia, their morphology is considered a direct indicator of their activity. For instance, amoeboid microglia tend to migrate in the brain while hypertrophic microglia tend to perform more phagocytosis than surveillant ones (Savage et al., 2019a; Tay et al., 2019). Using confocal microscopy, researchers can analyze various morphological changes like the formation of phagocytic cups at the end of microglia/monocyte processes, associated with the removal of engulfed newly proliferated cells and responsible for the development of juvenile play in adolescent rat (Sierra et al.,

2010; VanRyzin et al., 2019). However, confocal microscopy is not often used in *in vivo* applications because of its limited penetration depth, which depends on the usable excitation wavelength (Graf and Boppart, 2010).

Stimulated Emission Depletion (STED)

Microscopy increases image resolution by overcoming the light diffraction limit. Similar to other commonly used fluorescence microscopy approaches, STED involves the detection of fluorescence by point-scanning. A doughnut-like shape beam is used to deplete surrounding fluorophores in order to only read the fluorescence of the fluorophore of interest (Hell and Wichmann, 1994; Tardif et al., 2019) STED microscopy's nanoscale resolution (65 nm in x-y and 150 nm in z) resulted in multiple applications, including the structural imaging of microglial and synaptic dynamics in fixed and live thick brain slices (Hein et al., 2008; Chéreau et al., 2015). Recent progresses further allowed to generate the first STED able to image efficiently *in vivo*, by adding components of a two-photon system. The use of a pulsed laser source provided better penetration, combined with the high spatial resolution of STED microscopy. With this approach, a greater number of small dendritic spines was imaged than with conventional two-photon microscopy, thus allowing to show a higher turnover of dendritic spines than previously envisioned (Pfeiffer et al., 2018). Other high-resolution microscopy techniques have been developed such as structured illumination microscopy (SIM) that uses a spatial modulation pattern to illuminate the sample, in which a software demodulation and filtering allows to overcome the diffraction limit with a factor two (Schermelleh et al., 2008). Stochastic optical reconstruction microscopy (STORM), where only a portion of fluorophores are excited on each cycle of laser emission, gives insight into their precise location at the nanoscale (Rust et al., 2006).

Light-Sheet

While super-resolution techniques revolutionized the use of fluorescence microscopy by increasing its spatial resolution, light-sheet microscopy is a technique that was developed for faster imaging. It allows to perform high speed scanning of large CNS tissue volumes. The system requires a fluorescence detection setup that differs slightly from epifluorescence microscopy, since detection is performed transverse to the illumination by a thin sheet of laser light (Keller and Ahrens, 2015). This non-destructive imaging technique prevents sectioning interpretation artifacts. These artifacts arise when cells are cut in cross-section by vibratome, freezing microtome or cryostat. In addition, it offers the possibility to perform molecular analyses after imaging the fixed tissue (Glaser et al., 2017). Light-sheet fluorescence microscopy achieves a resolution of ∼26 μm (x-y) (Colombelli and Lorenzo, 2014) with 3D optical sectioning (up to ∼300 nm in *z*) and high-speed of imaging (2.7×10^4 $\mu m^3 s^{-1}$) (Lu C.-H. et al., 2019) that limits the effects of photobleaching compared to confocal microscopy (Santi, 2011; Power and Huisken, 2017). Light-sheet microscopy was used to visualize the entire adult mouse brain in health (Qi et al., 2019) and Alzheimer's disease pathology (Liebmann et al., 2016). This emerging technique showed the 3D-distribution of neurons, microglia, the vasculature and tau proteins, throughout the entire brain parenchyma, using IDISCO to clear the tissue (Qi et al., 2019). Further iterations of IDISCO such as FDISCO or SHIELD could be employed as well (Renier et al., 2014; Park et al., 2018). However, light-sheet imaging techniques with *in vivo* whole mouse brain imaging capacity were not yet proposed (Dodt et al., 2007; Susaki et al., 2014).

Multiphoton Microscopy

Is currently the technique of choice in neuroimmunology for *in vivo* studies. This technique uses a femtosecond pulsed laser that produces a very high density of photons in a very short time allowing for 2 or 3 photons, respectively, to play the same excitation role as a single photon of full energy. These 2 or 3 photons have half or one third of the quantum energy of a single photon since their wavelength is about two or three times longer than a single excitation photon (typically 800–950 nm for two-photon and 1100–1300 nm for three-photon microscopy) (Svoboda and Yasuda, 2006). Because longer wavelengths are more penetrating, one can explore phenomena deeper into biological tissues (Wang et al., 2018). The addition of energy from several photons takes place at the focal plane of the objective where a large number of photons is needed to make emerge this rare phenomenon, in a single point instead of a large double cone-like structure for single photon excitation. Therefore, the multiphoton technique preserves tissue integrity outside of the focal plane. With two-photon microscopy, the single focal point achieves a spatial resolution approximating 0.42 μm (x-y) and 0.81 μm (z) according to the numerical aperture of the objective (Soeller and Cannell, 1996; Diaspro et al., 2005; Zheng et al., 2019).

Seminal findings that dramatically changed the field of neuroimmunology were obtained with two-photon *in vivo* microscopy. A pioneer experiment conducted with this technique, in healthy conditions *versus* after a focal lesion generated with a two-photon laser, debunked the previous paradigm. Microglia are not resting cells in the absence of injury. Instead, they are extremely dynamic, with their processes constantly surveying the entire brain parenchyma with a time course that reaches 5.5 h in adult mice (Davalos et al., 2005; Nimmerjahn et al., 2005). In this seminal work conducted in anesthetized CX3CR1$^{+/GFP}$ reporter mice, time-lapse images of fluorescent microglia were obtained through the skull, using minimally invasive thinned-skull method (Marker et al., 2010; Parkhurst et al., 2013). This achievement is reproduced in **Figure 1E**. A growing technology for two-photon microscopy is the resonant scanner, which allows acquisition speed to reach 30 frames per second. This high imaging speed is particularly useful for studying the real time activity of neuronal and glial cell populations via *in vivo* calcium imaging (Grewe et al., 2011; Olmedillas del Moral et al., 2019; Verkhratsky et al., 2019). Other types of microscopy techniques providing time-lapse imaging

with high temporal resolution are extensively reviewed here (Mondal, 2014; Ueda et al., 2020).

BEATING THE SPATIAL RESOLUTION LIMIT USING ELECTRONS

Electron microscopy (EM) generates images by interrogating a dehydrated sample with a beam of electrons, which are transmitted (transmission electron microscopy; TEM) or bounced back (scanning electron microscopy; SEM) using specialized detectors. The resulting beam reveals the ultrastructure of the investigated object, e.g., structure of protein, organelle, subcellular compartment or cell. By uncovering these elements from the atomic to the millimeter (and even centimeter) level, ultrastructural techniques have provided important information in neuroscience and neuroimmunology (Genoud et al., 2006; Knott and Genoud, 2013; Savage et al., 2018, 2019a). EM has allowed to shed light on microglia-neuron communication, revealing that 94% of microglial processes directly contact synaptic elements in the healthy adolescent mouse visual cortex (Tremblay et al., 2010). These ultrastructural insights and others contributed to defining the role of microglia in developmental synaptic pruning (Tremblay et al., 2010; Paolicelli et al., 2011; Schafer et al., 2012). The quadripartite synapse model, in which microglia and astrocytes regulate together synaptic function and plasticity, also arose from ultrastructural observations (Bennett, 2007; Tremblay et al., 2011, 2014; Schafer et al., 2013; Sierra and Tremblay, 2014).

TEM

Electron microscopy can reach the resolution at <50 pm (x-y) for TEM compared to 3 Å for cryo-EM (Earl et al., 2017). This allows TEM to provide fine details regarding immune cells morphology, from cell body to finest and most distal processes. As illustrated in **Figures 1G,H**, this nanoscale resolution allows to identify signs of 'intracellular' activity (e.g., organellar changes, phagosomal inclusions) and extracellular activity (e.g., extracellular digestion of cellular debris, intercellular contacts with other glial cells, neurons, and synapses). The quantification of events for each cell type studied is essential to assess the situation of the cell, whether it is in steady state or overwhelmed by phagocytic inclusions requiring digestion, accumulated misfolded proteins in the endoplasmic reticulum or Golgi apparatus, stressed mitochondria or making increased synaptic contacts as previously evaluated for microglia across a range of contexts, including Huntington's disease pathology (Savage et al., 2020). Additionally, an increasing body of evidence supports the idea that the microglial population is composed of diverse subpopulations endowed with unique intrinsic properties that perform different functions, and display a high degree of spatial and temporal specialization (Stratoulias et al., 2019). Evidence of this microglial heterogeneity was notably provided with TEM. The dark microglia, identified at the ultrastructural level by their electron dense cytoplasm and other markers of cellular stress, as well as extensive interactions with synapses (Bisht et al., 2016b), are rare in healthy young adult mice, but increase in number up to 10-fold with chronic unpredictable or social defeat stress, aging and other pathological contexts, including Alzheimer's disease pathology (St-Pierre et al., 2020), showing the importance of this approach for the *in situ* study of microglial functional diversity.

SBF-SEM

3D-EM allows to reconstruct organelles, cytoskeletal elements, subcellular compartments, and cellular relationships, among different cell types including immune cells *in situ* (Bolasco et al., 2018). Blocks of CNS tissue can be imaged using serial block face SEM, in which the tissue is sequentially imaged at a resolution of ∼10 nm (x-y), cut (25–50 nm thick)(z) with an ultramicrotome mounted inside the SEM chamber, realigned and imaged, to automatically generate z-stacks of serial images (Denk and Horstmann, 2004; Briggman and Bock, 2012; Peddie and Collinson, 2014; Yamasaki et al., 2014). This allows SBF-SEM to reconstruct multiple immune cells, neurons and astrocytes at the nanoscale (Calì et al., 2019). This technique is much faster than the method used in pioneering studies: serial section TEM to image synapses (Fiala and Harris, 2001) or microglial processes interacting with synapses (Tremblay et al., 2010), by aligning and segmenting series of ultrathin sections cut manually and reconstructed semi-manually with Reconstruct (Fiala, 2005). This method allowed the accurate comparison of nucleus to cell body ratio and mitochondrial distribution among the different brain cells, including between individual microglial cells, giving insight into the functional status of microglia and other cells in their 3D microenvironment (Savage et al., 2018). Microglial mitochondria analysis is promising based on reports of mitochondria defects in multiple neurodegenerative disease such as Parkinson's disease, Huntington's disease, Alzheimer's disease and amyotrophic lateral sclerosis (Chaturvedi and Flint Beal, 2013). This whole cell analysis was further used to discriminate monocyte-derived cells from microglia based on their distinctive ultrastructural features in the brain of experimental autoimmune encephalomyelitis mouse models of multiple sclerosis. This distinction between microglia and monocyte-derived cells is normally difficult to achieve in a 2D plane but was possible in 3D while showing the specific interaction of monocytes at the Ranvier node, where they could be initiating the demyelination (Yamasaki et al., 2014).

FIB-SEM

3D-EM is also possible using focused ion beam scanning electron microscopy (FIB-SEM) that removes as little as 3 nm of tissue after each block face image acquisition to create z-stack of images. FIB-SEM produces a higher 3D resolution reaching 3–5 nm (x, y, and z) (Briggman and Bock, 2012), which is required to study the fine geometry of organelles, phagosomes and autophagosomes and cytoskeletal elements at the expense of having a reduced field of view and slower acquisition speed compared with SBF-SEM (Heymann et al., 2006; Knott and Genoud, 2013; Peddie and Collinson, 2014; Savage et al., 2019b). With this level of resolution, FIB-SEM imaging of immune cells allows to discern between cellular elements that are partially surrounded by a

microglial process, for instance during synaptic stripping, from the ones that are fully engulfed and internalized (phagocytosed). Different steps of phagocytosis process could be identified, from partial to complete engulfment, given the observation of microglia nibbling small pieces of axon terminals (i.e., performing trogocytosis) in the postnatal mouse hippocampus (Weinhard et al., 2018).

Correlative Light and Electron Microscopy (CLEM)

Has seen its usage escalating over the past years (Begemann and Galic, 2016). Combining the minimally invasive *in vivo* imaging capacity of two-photon imaging with the nanometer resolution of serial section TEM revealed microglial ability to interact actively with pre- and post-synaptic elements, while some microglial cells had synaptic elements inside their phagosomes under normal physiological conditions (Tremblay et al., 2010). In the context of studying Alzheimer's disease pathology, brightfield microscopy combined with TEM also allowed to image microglial diversity around amyloid plaques (Bisht et al., 2016a; El Hajj et al., 2019). **Figure 1** proposes a correlative approach that combines four different modalities of microscopy to paint the most insightful portrait of microglial diversity. CLEM is a most promising method for investigating in 2D and even 3D microglial relationships with synapses throughout life, from development (Schafer et al., 2012) to aging (Beckman et al., 2019). Synapses can be imaged using confocal microscopy and their ultrastructural relationships with microglia and other immune cells can be imaged using TEM or even SEM with array tomography. This workflow with array tomography allows the captured images to be stitched into larger 2D mosaic, thus providing a better view of their general organization within CNS regions and layers. These images can be correlated with the evaluation of cognitive decline by measuring the loss of synapses but also the integrity of their structure in the prefrontal cortex of human donors (Henstridge et al., 2018). Other important protocols such as the Nanobody-Assisted Tissue Immunostaining for Volumetric Electron microscopy (NATIVE) can provide enhanced staining using single-domain nanobodies with better penetration into the tissue for large scale 3D reconstruction over the entire mouse hippocampus (Fang et al., 2018), and would allow to correlate data from the nanoscale to the brain-region level.

CLINICAL VIEW ON NEUROIMMUNE IMAGING

Studying the human brain offers a different set of challenges compared to studying animal models. Several non-invasive techniques developed between 1960 and 1980 (Nutma et al., 2019), especially, allow to have a look at immune system activity inside the human brain. Some of the techniques currently used are positron emission tomography (PET) (Harrison et al., 2014) and magnetic resonance imaging (MRI) (Arnò et al., 2014; Harrison et al., 2015; Rollins et al., 2018) to analyze the integrity of the brain parenchyma and BBB (Kenk et al., 2015; Montagne et al., 2016).

PET

Allows to visualize microglial activity by measuring the dynamic coupling of the radiotracer [11C]PBR28 or [11C]PK11195 to the translocator protein (TSPO). This protein localized to microglial mitochondria can be used as a proxy of their neuroinflammatory and phagocytic activity (Sandiego et al., 2015; Sucksdorff et al., 2019). This makes PET imaging useful to study immune cells *in vivo* using these radiolabels, but it lacks in spatial resolution (Albrecht et al., 2016). While [11C]PBR28 or [11C]PK11195 tracers are widely used, a range of different microglial receptors and signaling proteins can be targeted via PET radiotracers (Tronel et al., 2017). This approach allowed to observe live changes in microglial activity (notably associated with phagocytosis and/or release of pro-inflammatory mediators) in the human brain after peripheral injection of lipopolysaccharide, a bacterial endotoxin, that was studied to determine how the adaptive immune response exerts a direct effect on behavior between health and disease (Sandiego et al., 2015). For PET imaging, the nature of the radiotracer targets and their low expression levels at steady-state generally limit their use to study reactive functions (e.g., neuroinflammation and exacerbated phagocytosis), and not microglial functions in normal homeostatic conditions (Owen et al., 2012). Using PET in schizophrenic patients with [18 F]-FEPPA, another ligand for TSPO, neuroinflammation was assessed in schizophrenia patients after antipsychotic treatment, revealing no difference, thus suggesting that neuroinflammation happens in earlier stages of the pathology (Kenk et al., 2015). Efforts to find and develop new tracers for the study of non-inflamed microglia would represent a step of major importance for the future investigation of the microglial subpopulations engaged in different functions across a variety of homeostatic and neuroinflammatory states (Beaino et al., 2017; Villa et al., 2018). Other innate immune cells such as monocytes have also been imaged using PET with the tracer [111Indium] oxyquinoline which enters leukocyte cell membrane and provides an effective visualization in the mouse and human blood (Kircher et al., 2008). More mouse PET investigations have shown T cells which can also be labeled by [111Indium] oxyquinoline in animal models (Gong et al., 2011). Further investigation of monocytes and T cells is required in human to translate the findings from animal research. Clinical investigation using high spatial resolution imaging typically uses MRI.

MRI

Is an established non-invasive imaging technique that is used in clinical and preclinical research studies, with various animal models, making it an excellent tool for translational research (Desjardins et al., 2019). MRI with gadolinium has been used in rodents to study BBB integrity and its role in depression together with blood oxygenation dynamics. This is particularly interesting as the BBB is emerging as an active interface between the periphery and the brain that modulates neuroimmune interactions differently between health and disease conditions (Menard et al., 2017). Further than BBB investigation, MRI is a crucial tool that provides a high-resolution view of brain structures across the whole parenchyma in the same session

(Ladd et al., 2018). While it is not able to directly image immune cells, MRI is used to image the whole human or animal brain during neuroinflammation, giving insight into immune cells effects on the disruption of the neurovascular unit, demyelination as well as gray and white matter volume reduction (Quarantelli, 2015; Albrecht et al., 2016). One MRI imaging method, diffusion MRI, is widely used to image white matter tracts. This is achieved by measuring water molecule arbitrary movements in the parenchyma to map the cellular architecture of the white matter (Le Bihan and Iima, 2015). This technique was used similarly to PET for the analysis of neuroinflammation in schizophrenia patients. By measuring free-water abnormities with the MRI machine, authors showed limited extracellular space indicating less inflammation in the parenchyma during late schizophrenia stages (Pasternak et al., 2015), which supports the previous evidence.

With its ability to image during the lifetime of the subject, whether animal or human, MRI can be used in experimental settings to investigate disease progression longitudinally, which can then be correlated with *postmortem* immunostaining for microglia and monocytes (Neuwelt et al., 2009), in addition to various disease hallmarks (Justicia et al., 2008; Jacobs et al., 2012; Tang et al., 2018; Yi et al., 2019). In a rat model of glioma, tumors were imaged during growth progression while studying the microglial/macrophagic changes visualized using ultrasmall superparamagnetic iron oxides (USPIOs). Microglia/macrophages store iron, a mineral necessary for oxidative metabolism, synaptic plasticity, myelination and neurotransmitter synthesis (Nnah and Wessling-Resnick, 2018). USPIOs is also internalized by microglia and macrophages, making the USPIOs-filled cells appearing as dark spots on MRI images. The observations were then correlated with confocal imaging of microglia/macrophages taking up Texas Red-labeled USPIOs in the tumor zone using high spatial resolution confocal imaging (Fleige et al., 2001). Ultimately, correlative [18F]DPA-714-PET and MRI-USPIOs together with confocal imaging allowed to investigate microglia/macrophage properties in an experimental autoimmune encephalomyelitis mouse model of multiple sclerosis. This work showed that microglia/macrophages upregulate TSPO and IBA1 in the demyelinating regions during acute phases, suggesting their dysfunction as a contributing factor to the inflammation seen in multiple sclerosis (Coda et al., 2020).

CONCLUSION

A Case for Correlative Microscopy and New Development

Research focusing on the neuroimmune component of the CNS is fundamental to provide further information on the properly functioning system with the goal of identifying and understanding the complex subcellular, cellular and intercellular processes that become compromised, dysregulated, or exacerbated in disease, whether the involved cells are stressed, degenerating or senescent. There is a tremendous need to pair clinical PET and MRI together with *postmortem* CLEM, notably using slide scanning, confocal, TEM or SEM together within an integrative investigation. CLEM can bring researchers closer to the goal of providing further insights into the mechanisms that govern brain immunity and its important consequences on neuronal circuits and behavior across life. This collaborative endeavor aims to maintain health, as well as prevent and treat cancer, but also neurodevelopmental, neuropsychiatric, neurological and neurodegenerative diseases, in which the innate and adaptive immune cells have been critically implicated (Sierra and Tremblay, 2014; Rangachari et al., 2017; Lecours et al., 2018; Bordeleau et al., 2019). By bringing together complementary imaging approaches CLEM can allow researchers to pair the observations in order to provide unprecedented insights into the mechanistic underpinnings of CNS development, function and plasticity. From slide scanning and confocal microscopy to more specialized tools like two-photon imaging and the different emerging types of 3D-EM modalities (Briggman and Bock, 2012; Peddie and Collinson, 2014), STED and light-sheet microscopy, which are now on the rise, will likely become common practice as the technology becomes more accessible.

The perspective of the field is now at a point where several new technologies are just waiting to be used in neuroimmunology. One example of new technology that could provide insights into the role of T cells, in particular, is 4D electron microscopy. This cutting-edge type of microscopy detects photon-induced near-field signals measured at T cell surfaces. This principle allowed the evaluation by electromagnetic measurement of T cell activation and to correlate this finding with the major compatibility binding complexes measured from the near-field signals at the cell surface. These results demonstrated structural changes that serve as biomarkers of T cell sensitivity to immune challenges (Lu Y. et al., 2019). Other techniques are still not offering their advantages in neuroimmunology yet, such as holographic microscopy which brings the resolution of electron microscopy to the order of the Armstrong. This would raise the imaging of phagosomal inclusions highlighted in **Figure 1H** to a new level, where could be determined the content of these vesicles. Multi-isotope imaging mass spectrometry would also bring many possibilities to the field. This imaging technique is able to image and quantify molecules in the samples, which presents great potential to identify new molecular targets in the neuroimmunology field (Arrojo E Drigo et al., 2019; Madan et al., 2019).

AUTHOR CONTRIBUTIONS

MC was responsible for the manuscript plan and management, writing of the correlative and clinical imaging sections while taking care of the overall revision and formatting of the manuscript, and creating the figure included in the manuscript. M-ÈR was responsible for writing the fluorescent imaging section and creating the table. FG was in charge of writing the electron microscopy section of the manuscript. MD and M-ÈT were in charge of revising the manuscript and providing theoretical and writing support to all authors while M-ÈT contributed significantly to the structure and ideas content of the manuscript.

FUNDING

This work was supported by grants from the Canadian Institutes of Health Research (CIHR; Foundation Scheme), Natural Sciences and Engineering Research Council of Canada (Discovery Grant), and NEURON-ERANET Synaptic Dysfunction in Disorders of the Nervous System (MicroSynDep consortium) to M-ÈT. MC was supported by a Master's Training Award from Fonds de Recherche du Québec – Santé (FRQS). FG was supported by a Mexican Council of Science and Technology (CONACYT) training grant. M-ÈT holds a Canada Research Chair (Tier 2) in Neurobiology of Aging and Cognition.

ACKNOWLEDGMENTS

We are grateful to our colleagues Sammy Weiser Novak and Jean-Christophe Comte for sharing their insights and contributing to our manuscript through their expertise in electron microscopy and multiphoton microscopy.

REFERENCES

Albrecht, D. S., Granziera, C., Hooker, J. M., and Loggia, M. L. (2016). In vivo imaging of human neuroinflammation. *ACS Chem. Neurosci.* 7, 470–483. doi: 10.1021/acschemneuro.6b00056

Arnò, B., Grassivaro, F., Rossi, C., Bergamaschi, A., Castiglioni, V., Furlan, R., et al. (2014). Neural progenitor cells orchestrate microglia migration and positioning into the developing cortex. *Nat. Commun.* 5:5611. doi: 10.1038/ncomms6611

Arrojo E Drigo, R., Lev-Ram, V., Tyagi, S., Ramachandra, R., Deerinck, T., Bushong, E., et al. (2019). Age mosaicism across multiple scales in adult tissues. *Cell Metab.* 30, 343–351.e3. doi: 10.1016/j.cmet.2019.05.010

Augusto-Oliveira, M., Arrifano, G. P., Lopes-Araújo, A., Santos-Sacramento, L., Takeda, P. Y., Anthony, D. C., et al. (2019). What do microglia really do in healthy adult brain? *Cells* 8:1293. doi: 10.3390/cells8101293

Bankhead, P., Loughrey, M. B., Fernández, J. A., Dombrowski, Y., McArt, D. G., Dunne, P. D., et al. (2017). QuPath: open source software for digital pathology image analysis. *Sci. Rep.* 7:16878. doi: 10.1038/s41598-017-17204-5

Bayerl, S. H., Ghori, A., Nieminen-Kelhä, M., Adage, T., Breitenbach, J., Vajkoczy, P., et al. (2019). *In vitro* and *in vivo* testing of a novel local nicardipine delivery system to the brain: a preclinical study. *J. Neurosurg.* 132, 465–472. doi: 10.3171/2018.9.JNS173085

Beaino, W., Janssen, B., Kooij, G., van der Pol, S. M. A., van Het Hof, B., van Horssen, J., et al. (2017). Purinergic receptors P2Y12R and P2X7R: potential targets for PET imaging of microglia phenotypes in multiple sclerosis. *J. Neuroinflammation* 14:259. doi: 10.1186/s12974-017-1034-z

Beckman, D., Ott, S., Donis-Cox, K., Janssen, W. G., Bliss-Moreau, E., Rudebeck, P. H., et al. (2019). Oligomeric Aβ in the monkey brain impacts synaptic integrity and induces accelerated cortical aging. *Proc. Natl. Acad. Sci. U.S.A.* 116, 26239–26246. doi: 10.1073/pnas.1902301116

Begemann, I., and Galic, M. (2016). Correlative light electron microscopy: connecting synaptic structure and function. *Front. Synaptic Neurosci.* 8:28. doi: 10.3389/fnsyn.2016.00028

Bellver-Landete, V., Bretheau, F., Mailhot, B., Vallières, N., Lessard, M., Janelle, M.-E., et al. (2019). Microglia are an essential component of the neuroprotective scar that forms after spinal cord injury. *Nat. Commun.* 10:518. doi: 10.1038/s41467-019-08446-0

Bennett, M. R. (2007). Synaptic P2X7 receptor regenerative-loop hypothesis for depression. *Aust. N. Z. J. Psychiatry* 41, 563–571. doi: 10.1080/00048670701399994

Berning, S., Willig, K. I., Steffens, H., Dibaj, P., and Hell, S. W. (2012). Nanoscopy in a living mouse brain. *Science* 335:551. doi: 10.1126/science.1215369

Bisht, K., El Hajj, H., Savage, J. C., Sánchez, M. G., and Tremblay, M. -È (2016a). Correlative light and electron microscopy to study microglial interactions with β-Amyloid plaques. *J. Vis. Exp. JoVE* 112:54060. doi: 10.3791/54060

Bisht, K., Sharma, K. P., Lecours, C., Gabriela Sánchez, M., El Hajj, H., Milior, G., et al. (2016b). Dark microglia: a new phenotype predominantly associated with pathological states. *Glia* 64, 826–839. doi: 10.1002/glia.22966

Bolasco, G., Weinhard, L., Boissonnet, T., Neujahr, R., and Gross, C. T. (2018). Three-dimensional nanostructure of an intact microglia cell. *Front. Neuroanat.* 12:105. doi: 10.3389/fnana.2018.00105

Bordeleau, M., Carrier, M., Luheshi, G. N., and Tremblay, M. -È (2019). Microglia along sex lines: from brain colonization, maturation and function, to implication in neurodevelopmental disorders. *Semin. Cell Dev. Biol.* 94, 152–163. doi: 10.1016/j.semcdb.2019.06.001

Briggman, K. L., and Bock, D. D. (2012). Volume electron microscopy for neuronal circuit reconstruction. *Curr. Opin. Neurobiol.* 22, 154–161. doi: 10.1016/j.conb.2011.10.022

Budde, M. D., and Annese, J. (2013). Quantification of anisotropy and fiber orientation in human brain histological sections. *Front. Integr. Neurosci.* 7:3. doi: 10.3389/fnint.2013.00003

Butovsky, O., Jedrychowski, M. P., Moore, C. S., Cialic, R., Lanser, A. J., Gabriely, G., et al. (2014). Identification of a unique TGF-β dependent molecular and functional signature in microglia. *Nat. Neurosci.* 17, 131–143. doi: 10.1038/nn.3599

Buttgereit, A., Lelios, I., Yu, X., Vrohlings, M., Krakoski, N. R., Gautier, E. L., et al. (2016). Sall1 is a transcriptional regulator defining microglia identity and function. *Nat. Immunol.* 17, 1397–1406. doi: 10.1038/ni.3585

Calì, C., Agus, M., Kare, K., Boges, D. J., Lehväslaiho, H., Hadwiger, M., et al. (2019). 3D cellular reconstruction of cortical glia and parenchymal morphometric analysis from serial block-face electron microscopy of juvenile rat. *Prog. Neurobiol.* 183:101696. doi: 10.1016/j.pneurobio.2019.101696

Cătălin, B., Stopper, L., Bălşeanu, T.-A., and Scheller, A. (2017). The in situ morphology of microglia is highly sensitive to the mode of tissue fixation. *J. Chem. Neuroanat.* 86, 59–66. doi: 10.1016/j.jchemneu.2017.08.007

Chaturvedi, R. K., and Flint Beal, M. (2013). Mitochondrial diseases of the brain. *Free Radic. Biol. Med.* 63, 1–29. doi: 10.1016/j.freeradbiomed.2013.03.018

Chen, Z., Shin, D., Chen, S., Mikhail, K., Hadass, O., Tomlison, B. N., et al. (2014). Histological quantitation of brain injury using whole slide imaging: a pilot validation study in mice. *PLoS One* 9:e92133. doi: 10.1371/journal.pone.0092133

Chéreau, R., Tønnesen, J., and Nägerl, U. V. (2015). STED microscopy for nanoscale imaging in living brain slices. *Methods San Diego Calif.* 88, 57–66. doi: 10.1016/j.ymeth.2015.06.006

Coda, A. R., Anzilotti, S., Boscia, F., Greco, A., Panico, M., Gargiulo, S., et al. (2020). In vivo imaging of CNS microglial activation/macrophage infiltration with combined [18F]DPA-714-PET and SPIO-MRI in a mouse model of relapsing remitting experimental autoimmune encephalomyelitis. *Eur. J. Nucl. Med. Mol. Imaging* doi: 10.1007/s00259-020-04842-7 [Epub ahead of print].

Colombelli, J., and Lorenzo, C. (2014). "Light sheet fluorescence microscopy applications for multicellular systems," in *Fluorescence Microscopy*, ed. Academic Press (Amsterdam: Elsevier), 109–120. doi: 10.1016/B978-0-12-409513-7.00008-7

Daigle, T. L., Madisen, L., Hage, T. A., Valley, M. T., Knoblich, U., Larsen, R. S., et al. (2018). A suite of transgenic driver and reporter mouse lines with enhanced brain-cell-type targeting and functionality. *Cell* 174, 465–480.e22. doi: 10.1016/j.cell.2018.06.035

Davalos, D., Grutzendler, J., Yang, G., Kim, J. V., Zuo, Y., Jung, S., et al. (2005). ATP mediates rapid microglial response to local brain injury in vivo. *Nat. Neurosci.* 8, 752–758. doi: 10.1038/nn1472

Denk, W., and Horstmann, H. (2004). Serial block-face scanning electron microscopy to reconstruct three-dimensional tissue nanostructure. *PLoS Biol.* 2:e329. doi: 10.1371/journal.pbio.0020329

Desjardins, M., Kılıç, K., Thunemann, M., Mateo, C., Holland, D., Ferri, C. G. L., et al. (2019). Awake mouse imaging: from two-photon microscopy to blood oxygen level-dependent functional magnetic resonance imaging. *Biol.*

Psychiatry Cogn. Neurosci. Neuroimaging 4, 533–542. doi: 10.1016/j.bpsc.2018.12.002

Diaspro, A., Chirico, G., and Collini, M. (2005). Two-photon fluorescence excitation and related techniques in biological microscopy. *Q. Rev. Biophys.* 38, 97–166. doi: 10.1017/S0033583505004129

D'Mello, C., Le, T., and Swain, M. G. (2009). Cerebral microglia recruit monocytes into the brain in response to tumor necrosis Factorα signaling during peripheral organ inflammation. *J. Neurosci.* 29, 2089–2102. doi: 10.1523/JNEUROSCI.3567-08.2009

Dodt, H.-U., Leischner, U., Schierloh, A., Jährling, N., Mauch, C. P., Deininger, K., et al. (2007). Ultramicroscopy: three-dimensional visualization of neuronal networks in the whole mouse brain. *Nat. Methods* 4, 331–336. doi: 10.1038/nmeth1036

Earl, L. A., Falconieri, V., Milne, J. L., and Subramaniam, S. (2017). Cryo-EM: beyond the microscope. *Curr. Opin. Struct. Biol.* 46, 71–78. doi: 10.1016/j.sbi.2017.06.002

El Hajj, H., Savage, J. C., Bisht, K., Parent, M., Vallières, L., Rivest, S., et al. (2019). Ultrastructural evidence of microglial heterogeneity in Alzheimer's disease amyloid pathology. *J. Neuroinflammation* 16:87. doi: 10.1186/s12974-019-1473-9

Elliott, A. D. (2020). Confocal microscopy: principles and modern practices. *Curr. Protoc. Cytom.* 92:e68. doi: 10.1002/cpcy.68

Evilsizor, M. N., Ray-Jones, H. F., Lifshitz, J., and Ziebell, J. (2015). Primer for immunohistochemistry on cryosectioned rat brain tissue: example staining for microglia and neurons. *J. Vis. Exp. JoVE* 99:e52293. doi: 10.3791/52293

Fang, T., Lu, X., Berger, D., Gmeiner, C., Cho, J., Schalek, R., et al. (2018). Nanobody immunostaining for correlated light and electron microscopy with preservation of ultrastructure. *Nat. Methods* 15, 1029–1032. doi: 10.1038/s41592-018-0177-x

Feng, G., Mellor, R. H., Bernstein, M., Keller-Peck, C., Nguyen, Q. T., Wallace, M., et al. (2000). Imaging neuronal subsets in transgenic mice expressing multiple spectral variants of GFP. *Neuron* 28, 41–51. doi: 10.1016/s0896-6273(00)00084-2

Fiala, J. C. (2005). Reconstruct: a free editor for serial section microscopy. *J. Microsc.* 218, 52–61. doi: 10.1111/j.1365-2818.2005.01466.x

Fiala, J. C., and Harris, K. M. (2001). Extending unbiased stereology of brain ultrastructure to three-dimensional volumes. *J. Am. Med. Inform. Assoc. JAMIA* 8, 1–16. doi: 10.1136/jamia.2001.0080001

Fiolka, R. (2019). Resolution upgrades for light-sheet microscopy. *Nat. Methods* 16, 813–814. doi: 10.1038/s41592-019-0542-4

Fleige, G., Nolte, C., Synowitz, M., Seeberger, F., Kettenmann, H., and Zimmer, C. (2001). Magnetic labeling of activated microglia in experimental gliomas. *Neoplasia N.Y.N* 3, 489–499. doi: 10.1038/sj.neo.7900176

Genoud, C., Quairiaux, C., Steiner, P., Hirling, H., Welker, E., and Knott, G. W. (2006). Plasticity of astrocytic coverage and glutamate transporter expression in adult mouse cortex. *PLoS Biol.* 4:e343. doi: 10.1371/journal.pbio.0040343

Ginhoux, F., Greter, M., Leboeuf, M., Nandi, S., See, P., Gokhan, S., et al. (2010). Fate mapping analysis reveals that adult microglia derive from primitive macrophages. *Science* 330, 841–845. doi: 10.1126/science.1194637

Ginhoux, F., Lim, S., Hoeffel, G., Low, D., and Huber, T. (2013). Origin and differentiation of microglia. *Front. Cell. Neurosci.* 7:45. doi: 10.3389/fncel.2013.00045

Glaser, A. K., Reder, N. P., Chen, Y., McCarty, E. F., Yin, C., Wei, L., et al. (2017). Light-sheet microscopy for slide-free non-destructive pathology of large clinical specimens. *Nat. Biomed. Eng.* 1:0084. doi: 10.1038/s41551-017-0084

Gomez Perdiguero, E., Klapproth, K., Schulz, C., Busch, K., Azzoni, E., Crozet, L., et al. (2015). Tissue-resident macrophages originate from yolk-sac-derived erythro-myeloid progenitors. *Nature* 518, 547–551. doi: 10.1038/nature13989

Gong, N., Liu, J., Reynolds, A. D., Gorantla, S., Mosley, R. L., and Gendelman, H. E. (2011). Brain ingress of regulatory T cells in a murine model of HIV-1 encephalitis. *J. Neuroimmunol.* 230, 33–41. doi: 10.1016/j.jneuroim.2010.08.014

González Ibanez, F., Picard, K., Bordelau, M., Sharma, K., Bisht, K., and Tremblay, M.-È. (2019). Immunofluorescence staining using IBA1 and TMEM119 for microglial density, morphology and peripheral myeloid cell infiltration analysis in mouse brain. *J. Vis. Exp. JoVE.* doi: 10.3791/60510

Graf, B. W., and Boppart, S. A. (2010). Imaging and analysis of three-dimensional cell culture models. *Methods Mol. Biol. Clifton NJ* 591, 211–227. doi: 10.1007/978-1-60761-404-3_13

Grewe, B. F., Voigt, F. F., van't Hoff, M., and Helmchen, F. (2011). Fast two-layer two-photon imaging of neuronal cell populations using an electrically tunable lens. *Biomed. Opt. Express* 2, 2035–2046. doi: 10.1364/BOE.2.002035

Harrison, N. A., Cooper, E., Dowell, N. G., Keramida, G., Voon, V., Critchley, H. D., et al. (2015). Quantitative magnetization transfer imaging as a biomarker for effects of systemic inflammation on the brain. *Biol. Psychiatry* 78, 49–57. doi: 10.1016/j.biopsych.2014.09.023

Harrison, N. A., Doeller, C. F., Voon, V., Burgess, N., and Critchley, H. D. (2014). Peripheral inflammation acutely impairs human spatial memory via actions on medial temporal lobe glucose metabolism. *Biol. Psychiatry* 76, 585–593. doi: 10.1016/j.biopsych.2014.01.005

Hein, B., Willig, K. I., and Hell, S. W. (2008). Stimulated emission depletion (STED) nanoscopy of a fluorescent protein-labeled organelle inside a living cell. *Proc. Natl. Acad. Sci. U.S.A.* 105, 14271–14276. doi: 10.1073/pnas.0807705105

Hell, S. W., and Wichmann, J. (1994). Breaking the diffraction resolution limit by stimulated emission: stimulated-emission-depletion fluorescence microscopy. *Opt. Lett.* 19, 780–782. doi: 10.1364/ol.19.000780

Helmchen, F., and Denk, W. (2005). Deep tissue two-photon microscopy. *Nat. Methods* 2, 932–940. doi: 10.1038/nmeth818

Henstridge, C. M., Sideris, D. I., Carroll, E., Rotariu, S., Salomonsson, S., Tzioras, M., et al. (2018). Synapse loss in the prefrontal cortex is associated with cognitive decline in amyotrophic lateral sclerosis. *Acta Neuropathol. (Berl.)* 135, 213–226. doi: 10.1007/s00401-017-1797-4

Herz, J., Zinselmeyer, B. H., and McGavern, D. B. (2012). Two-photon imaging of microbial immunity in living tissues. *Microsc. Microanal. Off. J. Microsc. Soc. Am. Microbeam Anal. Soc. Microsc. Soc. Can.* 18, 730–741. doi: 10.1017/S1431927612000281

Heymann, J. A. W., Hayles, M., Gestmann, I., Giannuzzi, L. A., Lich, B., and Subramaniam, S. (2006). Site-specific 3D imaging of cells and tissues with a dual beam microscope. *J. Struct. Biol.* 155, 63–73. doi: 10.1016/j.jsb.2006.03.006

Jacobs, A. H., Tavitian, B., and INMiND consortium (2012). Noninvasive molecular imaging of neuroinflammation. *J. Cereb. Blood Flow Metab. Off. J. Int. Soc. Cereb. Blood Flow Metab.* 32, 1393–1415. doi: 10.1038/jcbfm.2012.53

Jung, S., Aliberti, J., Graemmel, P., Sunshine, M. J., Kreutzberg, G. W., Sher, A., et al. (2000). Analysis of fractalkine receptor CX(3)CR1 function by targeted deletion and green fluorescent protein reporter gene insertion. *Mol. Cell. Biol.* 20, 4106–4114. doi: 10.1128/mcb.20.11.4106-4114.2000

Justicia, C., Ramos-Cabrer, P., and Hoehn, M. (2008). MRI detection of secondary damage after stroke: chronic iron accumulation in the thalamus of the rat brain. *Stroke* 39, 1541–1547. doi: 10.1161/STROKEAHA.107.503565

Katsumoto, A., Lu, H., Miranda, A. S., and Ransohoff, R. M. (2014). Ontogeny and functions of CNS macrophages. *J. Immunol. Baltim. Md* 1950, 2615–2621. doi: 10.4049/jimmunol.1400716

Keller, P. J., and Ahrens, M. B. (2015). Visualizing whole-brain activity and development at the single-cell level using light-sheet microscopy. *Neuron* 85, 462–483. doi: 10.1016/j.neuron.2014.12.039

Kenk, M., Selvanathan, T., Rao, N., Suridjan, I., Rusjan, P., Remington, G., et al. (2015). Imaging neuroinflammation in gray and white matter in schizophrenia: an in-vivo PET study with [18F]-FEPPA. *Schizophr. Bull.* 41, 85–93. doi: 10.1093/schbul/sbu157

Kipnis, J., Cohen, H., Cardon, M., Ziv, Y., and Schwartz, M. (2004). T cell deficiency leads to cognitive dysfunction: implications for therapeutic vaccination for schizophrenia and other psychiatric conditions. *Proc. Natl. Acad. Sci. U.S.A.* 101, 8180–8185. doi: 10.1073/pnas.0402268101

Kircher, M. F., Grimm, J., Swirski, F. K., Libby, P., Gerszten, R. E., Allport, J. R., et al. (2008). Noninvasive in vivo imaging of monocyte trafficking to atherosclerotic lesions. *Circulation* 117, 388–395. doi: 10.1161/CIRCULATIONAHA.107.719765

Klar, T. A., Engel, E., and Hell, S. W. (2001). Breaking Abbe's diffraction resolution limit in fluorescence microscopy with stimulated emission depletion beams of various shapes. *Phys. Rev. E Stat. Nonlin. Soft Matter Phys.* 64:066613. doi: 10.1103/PhysRevE.64.066613

Knott, G., and Genoud, C. (2013). Is EM dead? *J. Cell Sci.* 126, 4545–4552. doi: 10.1242/jcs.124123

Konishi, H., Kobayashi, M., Kunisawa, T., Imai, K., Sayo, A., Malissen, B., et al. (2017). Siglec-H is a microglia-specific marker that discriminates microglia from CNS-associated macrophages and CNS-infiltrating monocytes. *Glia* 65, 1927–1943. doi: 10.1002/glia.23204

Kyriazis, A. D., Noroozizadeh, S., Refaee, A., Choi, W., Chu, L.-T., Bashir, A., et al. (2019). An end-to-end system for automatic characterization of Iba1 immunopositive microglia in whole slide imaging. *Neuroinformatics* 17, 373–389. doi: 10.1007/s12021-018-9405-x

Ladd, M. E., Bachert, P., Meyerspeer, M., Moser, E., Nagel, A. M., Norris, D. G., et al. (2018). Pros and cons of ultra-high-field MRI/MRS for human application. *Prog. Nucl. Magn. Reson. Spectrosc.* 109, 1–50. doi: 10.1016/j.pnmrs.2018.06.001

Le Bihan, D., and Iima, M. (2015). Diffusion magnetic resonance imaging: what water tells us about biological tissues. *PLoS Biol.* 13:e1002203. doi: 10.1371/journal.pbio.1002203

Lecours, C., Bordeleau, M., Cantin, L., Parent, M., Paolo, T. D., and Tremblay, M. -È (2018). Microglial implication in Parkinson's disease: loss of beneficial physiological roles or gain of inflammatory functions? *Front. Cell. Neurosci.* 12:282. doi: 10.3389/fncel.2018.00282

Lehmann, P. V. (1998). The fate of T cells in the brain. *Am. J. Pathol.* 153, 677–680.

Leone, C., Le Pavec, G., Même, W., Porcheray, F., Samah, B., Dormont, D., et al. (2006). Characterization of human monocyte-derived microglia-like cells. *Glia* 54, 183–192. doi: 10.1002/glia.20372

Lewitus, G. M., and Schwartz, M. (2009). Behavioral immunization: immunity to self-antigens contributes to psychological stress resilience. *Mol. Psychiatry* 14, 532–536. doi: 10.1038/mp.2008.103

Liebmann, T., Renier, N., Bettayeb, K., Greengard, P., Tessier-Lavigne, M., and Flajolet, M. (2016). Three-dimensional study of Alzheimer's disease Hallmarks using the iDISCO clearing method. *Cell Rep.* 16, 1138–1152. doi: 10.1016/j.celrep.2016.06.060

Lodygin, D., Hermann, M., Schweingruber, N., Flügel-Koch, C., Watanabe, T., Schlosser, C., et al. (2019). β-Synuclein-reactive T cells induce autoimmune CNS grey matter degeneration. *Nature* 566, 503–508. doi: 10.1038/s41586-019-0964-2

Lu, C.-H., Tang, W.-C., Liu, Y.-T., Chang, S.-W., Wu, F. C. M., Chen, C.-Y., et al. (2019). Lightsheet localization microscopy enables fast, large-scale, and three-dimensional super-resolution imaging. *Commun. Biol.* 2:177. doi: 10.1038/s42003-019-0403-9

Lu, Y., Yoo, B.-K., Ng, A. H. C., Kim, J., Yeom, S., Tang, J., et al. (2019). 4D electron microscopy of T cell activation. *Proc. Natl. Acad. Sci. U.S.A.* 116, 22014–22019. doi: 10.1073/pnas.1914078116

Madan, I., Vanacore, G. M., Pomarico, E., Berruto, G., Lamb, R. J., McGrouther, D., et al. (2019). Holographic imaging of electromagnetic fields via electron-light quantum interference. *Sci. Adv.* 5:eaav8358. doi: 10.1126/sciadv.aav8358

Marker, D. F., Tremblay, M.-E., Lu, S.-M., Majewska, A. K., and Gelbard, H. A. (2010). A thin-skull window technique for chronic two-photon in vivo imaging of murine microglia in models of neuroinflammation. *J. Vis. Exp. JoVE* 43, 2059. doi: 10.3791/2059

Martell, J. D., Deerinck, T. J., Lam, S. S., Ellisman, M. H., and Ting, A. Y. (2017). Electron microscopy using the genetically encoded APEX2 tag in cultured mammalian cells. *Nat. Protoc.* 12, 1792–1816. doi: 10.1038/nprot.2017.065

Masuda, T., Amann, L., Sankowski, R., Staszewski, O., Lenz, M., and Errico, D. (2020). Novel Hexb-based tools for studying microglia in the CNS. *Nat. Immunol.* 21, 802–815. doi: 10.1038/s41590-020-0707-4

Menard, C., Pfau, M. L., Hodes, G. E., Kana, V., Wang, V. X., Bouchard, S., et al. (2017). Social stress induces neurovascular pathology promoting depression. *Nat. Neurosci.* 20, 1752–1760. doi: 10.1038/s41593-017-0010-3

Mikula, S., Trotts, I., Stone, J. M., and Jones, E. G. (2007). Internet-enabled high-resolution brain mapping and virtual microscopy. *NeuroImage* 35, 9–15. doi: 10.1016/j.neuroimage.2006.11.053

Mittal, K., Eremenko, E., Berner, O., Elyahu, Y., Strominger, I., Apelblat, D., et al. (2019). CD4 T cells induce a subset of MHCII-expressing microglia that attenuates alzheimer pathology. *iScience* 16, 298–311. doi: 10.1016/j.isci.2019.05.039

Mondal, P. P. (2014). Temporal resolution in fluorescence imaging. *Front. Mol. Biosci.* 1:11. doi: 10.3389/fmolb.2014.00011

Montagne, A., Toga, A. W., and Zlokovic, B. V. (2016). Blood-brain barrier permeability and gadolinium: benefits and potential pitfalls in research. *JAMA Neurol.* 73, 13–14. doi: 10.1001/jamaneurol.2015.2960

Morimoto, K., and Nakajima, K. (2019). Role of the immune system in the development of the central nervous system. *Front. Neurosci.* 13:916. doi: 10.3389/fnins.2019.00916

Neuwelt, E. A., Hamilton, B. E., Varallyay, C. G., Rooney, W. R., Edelman, R. D., Jacobs, P. M., et al. (2009). Ultrasmall superparamagnetic iron oxides (USPIOs): a future alternative magnetic resonance (MR) contrast agent for patients at risk for nephrogenic systemic fibrosis (NSF)? *Kidney Int.* 75, 465–474. doi: 10.1038/ki.2008.496

Nimmerjahn, A., Kirchhoff, F., and Helmchen, F. (2005). Resting microglial cells are highly dynamic surveillants of brain parenchyma in vivo. *Science* 308, 1314–1318. doi: 10.1126/science.1110647

Niraula, A., Wang, Y., Godbout, J. P., and Sheridan, J. F. (2018). Corticosterone production during repeated social defeat causes monocyte mobilization from the bone marrow, glucocorticoid resistance, and neurovascular adhesion molecule expression. *J. Neurosci. Off. J. Soc. Neurosci.* 38, 2328–2340. doi: 10.1523/JNEUROSCI.2568-17.2018

Nnah, I. C., and Wessling-Resnick, M. (2018). Brain iron homeostasis: a focus on microglial iron. *Pharm. Basel Switz.* 11:129. doi: 10.3390/ph11040129

Nutma, E., Willison, H., Martino, G., and Amor, S. (2019). Neuroimmunology – the past, present and future. *Clin. Exp. Immunol.* 197, 278–293. doi: 10.1111/cei.13279

Olmedillas del Moral, M., Asavapanumas, N., Uzcátegui, N., and Garaschuk, O. (2019). Healthy brain aging modifies microglial calcium signaling in vivo. *Int. J. Mol. Sci.* 20:589. doi: 10.3390/ijms20030589

Oreopoulos, J., Berman, R., and Browne, M. (2014). Spinning-disk confocal microscopy: present technology and future trends. *Methods Cell Biol.* 123, 153–175. doi: 10.1016/B978-0-12-420138-5.00009-4

Otxoa-de-Amezaga, A., Miró-Mur, F., Pedragosa, J., Gallizioli, M., Justicia, C., Gaja-Capdevila, N., et al. (2019). Microglial cell loss after ischemic stroke favors brain neutrophil accumulation. *Acta Neuropathol. (Berl.)* 137, 321–341. doi: 10.1007/s00401-018-1954-4

Owen, D. R., Yeo, A. J., Gunn, R. N., Song, K., Wadsworth, G., Lewis, A., et al. (2012). An 18-kDa translocator protein (TSPO) polymorphism explains differences in binding affinity of the PET radioligand PBR28. *J. Cereb. Blood Flow Metab. Off. J. Int. Soc. Cereb. Blood Flow Metab.* 32, 1–5. doi: 10.1038/jcbfm.2011.147

Paolicelli, R. C., Bolasco, G., Pagani, F., Maggi, L., Scianni, M., Panzanelli, P., et al. (2011). Synaptic pruning by microglia is necessary for normal brain development. *Science* 333, 1456–1458. doi: 10.1126/science.1202529

Park, Y.-G., Sohn, C. H., Chen, R., McCue, M., Yun, D. H., Drummond, G. T., et al. (2018). Protection of tissue physicochemical properties using polyfunctional crosslinkers. *Nat. Biotechnol.* doi: 10.1038/nbt.4281 [Epub ahead of print].

Parkhurst, C. N., Yang, G., Ninan, I., Savas, J. N., Yates, J. R., Lafaille, J. J., et al. (2013). Microglia promote learning-dependent synapse formation through BDNF. *Cell* 155, 1596–1609. doi: 10.1016/j.cell.2013.11.030

Pasternak, O., Westin, C.-F., Dahlben, B., Bouix, S., and Kubicki, M. (2015). The extent of diffusion MRI markers of neuroinflammation and white matter deterioration in chronic schizophrenia. *Schizophr. Res.* 161, 113–118. doi: 10.1016/j.schres.2014.07.031

Peddie, C. J., and Collinson, L. M. (2014). Exploring the third dimension: volume electron microscopy comes of age. *Micron Oxf. Engl.* 1993, 9–19. doi: 10.1016/j.micron.2014.01.009

Perego, C., Fumagalli, S., and De Simoni, M.-G. (2013). Three-dimensional confocal analysis of microglia/macrophage markers of polarization in experimental brain injury. *J. Vis. Exp. JoVE* 79:50605. doi: 10.3791/50605

Pérez-Alvarez, A., Araque, A., and Martín, E. D. (2013). Confocal microscopy for astrocyte *in vivo* imaging: Recycle and reuse in microscopy. *Front. Cell. Neurosci.* 7:51. doi: 10.3389/fncel.2013.00051

Pfeiffer, T., Poll, S., Bancelin, S., Angibaud, J., Inavalli, V. K., Keppler, K., et al. (2018). Chronic 2P-STED imaging reveals high turnover of dendritic spines in the hippocampus in vivo. *eLife* 7:e34700. doi: 10.7554/eLife.34700

Plemel, J. R., Stratton, J. A., Michaels, N. J., Rawji, K. S., Zhang, E., Sinha, S., et al. (2020). Microglia response following acute demyelination is heterogeneous and limits infiltrating macrophage dispersion. *Sci. Adv.* 6:eaay6324. doi: 10.1126/sciadv.aay6324

Power, R. M., and Huisken, J. (2017). A guide to light-sheet fluorescence microscopy for multiscale imaging. *Nat. Methods* 14, 360–373. doi: 10.1038/nmeth.4224

Prinz, M., and Priller, J. (2014). Microglia and brain macrophages in the molecular age: from origin to neuropsychiatric disease. *Nat. Rev. Neurosci.* 15, 300–312. doi: 10.1038/nrn3722

Prinz, M., and Priller, J. (2017). The role of peripheral immune cells in the CNS in steady state and disease. *Nat. Neurosci.* 20, 136–144. doi: 10.1038/nn.4475

Qi, Y., Yu, T., Xu, J., Wan, P., Ma, Y., Zhu, J., et al. (2019). FDISCO: advanced solvent-based clearing method for imaging whole organs. *Sci. Adv.* 5:eaau8355. doi: 10.1126/sciadv.aau8355

Quarantelli, M. (2015). MRI/MRS in neuroinflammation: methodology and applications. *Clin. Transl. Imaging* 3, 475–489. doi: 10.1007/s40336-015-0142-y

Rangachari, M., Kerfoot, S. M., Arbour, N., and Alvarez, J. I. (2017). Editorial: lymphocytes in MS and EAE: more than just a CD4+ World. *Front. Immunol.* 8:133. doi: 10.3389/fimmu.2017.00133

Renier, N., Wu, Z., Simon, D. J., Yang, J., Ariel, P., and Tessier-Lavigne, M. (2014). iDISCO: a simple, rapid method to immunolabel large tissue samples for volume imaging. *Cell* 159, 896–910. doi: 10.1016/j.cell.2014.10.010

Roetzer, T., Leskovar, K., Peter, N., Furtner, J., Muck, M., Augustin, M., et al. (2019). Evaluating cellularity and structural connectivity on whole brain slides using a custom-made digital pathology pipeline. *J. Neurosci. Methods* 311, 215–221. doi: 10.1016/j.jneumeth.2018.10.029

Rollins, C. P. E., Gallino, D., Kong, V., Ayranci, G., Devenyi, G. A., Germann, J., et al. (2018). Contributions of a high-fat diet to Alzheimer's disease-related decline: a longitudinal behavioural and structural neuroimaging study in mouse models. *Neuroimage Clin.* 21:101606. doi: 10.1016/j.nicl.2018.11.016

Rust, M. J., Bates, M., and Zhuang, X. (2006). Sub-diffraction-limit imaging by stochastic optical reconstruction microscopy (STORM). *Nat. Methods* 3, 793–795. doi: 10.1038/nmeth929

Sandiego, C. M., Gallezot, J.-D., Pittman, B., Nabulsi, N., Lim, K., Lin, S.-F., et al. (2015). Imaging robust microglial activation after lipopolysaccharide administration in humans with PET. *Proc. Natl. Acad. Sci. U.S.A.* 112, 12468–12473. doi: 10.1073/pnas.1511003112

Santi, P. A. (2011). Light sheet fluorescence microscopy: a review. *J. Histochem. Cytochem. Off. J. Histochem. Soc.* 59, 129–138. doi: 10.1369/0022155410394857

Savage, J. C., Carrier, M., and Tremblay, M.-E. (2019a). Morphology of microglia across contexts of health and disease. *Methods Mol. Biol. Clifton NJ* 2034, 13–26. doi: 10.1007/978-1-4939-9658-2_2

Savage, J. C., Novak, S. W., and Tremblay, M.-E. (2019b). Imaging and reconstructing microglia in 3 dimensions using FIB-SEM. *Microsc. Microanal.* 25, 1316–1317. doi: 10.1017/S1431927619007311

Savage, J. C., Picard, K., González-Ibáñez, F., and Tremblay, M. -È (2018). A brief history of microglial ultrastructure: distinctive features, phenotypes, and functions discovered over the past 60years by electron microscopy. *Front. Immunol.* 9:803. doi: 10.3389/fimmu.2018.00803

Savage, J. C., St-Pierre, M.-K., Carrier, M., El Hajj, H., Novak, S. W., Sanchez, M. G., et al. (2020). Microglial physiological properties and interactions with synapses are altered at presymptomatic stages in a mouse model of Huntington's disease pathology. *J. Neuroinflammation* 17:98. doi: 10.1186/s12974-020-01782-9

Savage, J. C., St-Pierre, M.-K., Hui, C. W., and Tremblay, M.-E. (2019c). Microglial ultrastructure in the hippocampus of a lipopolysaccharide-induced sickness mouse model. *Front. Neurosci.* 13:1340. doi: 10.3389/fnins.2019.01340

Schafer, D. P., Lehrman, E. K., Kautzman, A. G., Koyama, R., Mardinly, A. R., Yamasaki, R., et al. (2012). Microglia sculpt postnatal neural circuits in an activity and complement-dependent manner. *Neuron* 74, 691–705. doi: 10.1016/j.neuron.2012.03.026

Schafer, D. P., Lehrman, E. K., and Stevens, B. (2013). The "quad-partite" synapse: microglia-synapse interactions in the developing and mature CNS. *Glia* 61, 24–36. doi: 10.1002/glia.22389

Schermelleh, L., Carlton, P. M., Haase, S., Shao, L., Winoto, L., Kner, P., et al. (2008). Subdiffraction multicolor imaging of the nuclear periphery with 3D structured illumination microscopy. *Science* 320, 1332–1336. doi: 10.1126/science.1156947

Schneider, C. A., Velez, D. X. F., Azevedo, R., Hoover, E. M., Tran, C. J., Lo, C., et al. (2019). Imaging the dynamic recruitment of monocytes to the blood–brain barrier and specific brain regions during Toxoplasma gondii infection. *Proc. Natl. Acad. Sci. U.S.A.* 116, 24796–24807. doi: 10.1073/pnas.1915778116

Sierra, A., Encinas, J. M., Deudero, J. J. P., Chancey, J. H., Enikolopov, G., Overstreet-Wadiche, L. S., et al. (2010). Microglia shape adult hippocampal neurogenesis through apoptosis-coupled phagocytosis. *Cell Stem Cell* 7, 483–495. doi: 10.1016/j.stem.2010.08.014

Sierra, A., and Tremblay, M. -È (2014). *Microglia in Health and Disease*, eds M. -È Tremblay and A. Sierra (New York, NY: Springer New York), 3–6. doi: 10.1007/978-1-4939-1429-6_1

Soeller, C., and Cannell, M. B. (1996). Construction of a two-photon microscope and optimisation of illumination pulse duration. *Pflugers Arch.* 432, 555–561. doi: 10.1007/s004240050169

Sofroniew, M. V. (2015). Astrocyte barriers to neurotoxic inflammation. *Nat. Rev. Neurosci.* 16, 249–263. doi: 10.1038/nrn3898

St-Pierre, M.-K., Šimončičová, E., Bögi, E., and Tremblay, M. -È (2020). Shedding light on the dark side of the microglia. *ASN Neuro* 12:1759091420925335. doi: 10.1177/1759091420925335

Stratoulias, V., Venero, J. L., Tremblay, M., and Joseph, B. (2019). Microglial subtypes: diversity within the microglial community. *EMBO J.* 38:e101997. doi: 10.15252/embj.2019101997

Sucksdorff, M., Tuisku, J., Matilainen, M., Vuorimaa, A., Smith, S., Keitilä, J., et al. (2019). Natalizumab treatment reduces microglial activation in the white matter of the MS brain. *Neurol. Neuroimmunol. Neuroinflammation* 6:e574. doi: 10.1212/NXI.0000000000000574

Susaki, E. A., Tainaka, K., Perrin, D., Kishino, F., Tawara, T., Watanabe, T. M., et al. (2014). Whole-brain imaging with single-cell resolution using chemical cocktails and computational analysis. *Cell* 157, 726–739. doi: 10.1016/j.cell.2014.03.042

Svoboda, K., and Yasuda, R. (2006). Principles of two-photon excitation microscopy and its applications to neuroscience. *Neuron* 50, 823–839. doi: 10.1016/j.neuron.2006.05.019

Tang, T., Valenzuela, A., Petit, F., Chow, S., Leung, K., Gorin, F., et al. (2018). In vivo MRI of functionalized iron oxide nanoparticles for brain inflammation. *Contrast Media Mol. Imaging* 2018:3476476. doi: 10.1155/2018/3476476

Tardif, C., Nadeau, G., Labrecque, S., Côté, D., Lavoie-Cardinal, F., and De Koninck, P. (2019). Fluorescence lifetime imaging nanoscopy for measuring Förster resonance energy transfer in cellular nanodomains. *Neurophotonics* 6:015002. doi: 10.1117/1.NPh.6.1.015002

Tay, T. L., Carrier, M., and Tremblay, M. -È (2019). Physiology of microglia. *Adv. Exp. Med. Biol.* 1175, 129–148. doi: 10.1007/978-981-13-9913-8_6

Tay, T. L., Savage, J. C., Hui, C. W., Bisht, K., and Tremblay, M. -È (2017). Microglia across the lifespan: from origin to function in brain development, plasticity and cognition. *J. Physiol.* 595, 1929–1945. doi: 10.1113/JP272134

Ter Veer, M. J. T., Pfeiffer, T., and Nägerl, U. V. (2017). Two-photon STED microscopy for nanoscale imaging of neural morphology in vivo. *Methods Mol. Biol. Clifton NJ* 1663, 45–64. doi: 10.1007/978-1-4939-7265-4_5

Theret, M., Mounier, R., and Rossi, F. (2019). The origins and non-canonical functions of macrophages in development and regeneration. *Dev. Camb. Engl.* 146:dev156000. doi: 10.1242/dev.156000

Tremblay, M. -È, Lowery, R. L., and Majewska, A. K. (2010). Microglial interactions with synapses are modulated by visual experience. *PLoS Biol.* 8:e1000527. doi: 10.1371/journal.pbio.1000527

Tremblay, M. -È, Paolicelli, R., Stevens, B., Wake, H., and Bessis, A. (2014). "Chapter 9. Developing and mature synapses," in *Microglia in Health and Disease*, eds M. È Tremblay and A. Sierra (New York, NY: Springer).

Tremblay, M. -È, Stevens, B., Sierra, A., Wake, H., Bessis, A., and Nimmerjahn, A. (2011). The role of microglia in the healthy brain. *J. Neurosci. Off. J. Soc. Neurosci* 31, 16064–16069. doi: 10.1523/JNEUROSCI.4158-11.2011

Tronel, C., Largeau, B., Santiago Ribeiro, M. J., Guilloteau, D., Dupont, A.-C., and Arlicot, N. (2017). Molecular targets for PET imaging of activated microglia: the current situation and future expectations. *Int. J. Mol. Sci.* 18:802. doi: 10.3390/ijms18040802

Ueda, H. R., Ertürk, A., Chung, K., Gradinaru, V., Chédotal, A., Tomancak, P., et al. (2020). Tissue clearing and its applications in neuroscience. *Nat. Rev. Neurosci.* 21, 61–79. doi: 10.1038/s41583-019-0250-1

Van Dyken, P., and Lacoste, B. (2018). Impact of metabolic syndrome on neuroinflammation and the blood-brain barrier. *Front. Neurosci.* 12:930. doi: 10.3389/fnins.2018.00930

VanRyzin, J. W., Marquardt, A. E., Argue, K. J., Vecchiarelli, H. A., Ashton, S. E., Arambula, S. E., et al. (2019). Microglial phagocytosis of newborn cells is induced by endocannabinoids and sculpts sex differences in juvenile rat social play. *Neuron* 102, 435–449.e6. doi: 10.1016/j.neuron.2019.02.006

Varvel, N. H., Grathwohl, S. A., Baumann, F., Liebig, C., Bosch, A., Brawek, B., et al. (2012). Microglial repopulation model reveals a robust homeostatic process for replacing CNS myeloid cells. *Proc. Natl. Acad. Sci. U.S.A.* 109, 18150–18155. doi: 10.1073/pnas.1210150109

Varvel, N. H., Neher, J. J., Bosch, A., Wang, W., Ransohoff, R. M., Miller, R. J., et al. (2016). Infiltrating monocytes promote brain inflammation and exacerbate neuronal damage after status epilepticus. *Proc. Natl. Acad. Sci. U.S.A.* 113, E5665–E5674. doi: 10.1073/pnas.1604263113

Verkhratsky, A., Parpura, V., Vardjan, N., and Zorec, R. (2019). "Physiology of astroglia," in *Neuroglia in Neurodegenerative Diseases Advances in Experimental Medicine and Biology*, eds A. Verkhratsky, M. S. Ho, R. Zorec, and V. Parpura (Singapore: Springer Singapore), 45–91. doi: 10.1007/978-981-13-9913-8_3

Villa, A., Gelosa, P., Castiglioni, L., Cimino, M., Rizzi, N., Pepe, G., et al. (2018). Sex-specific features of microglia from adult mice. *Cell Rep.* 23, 3501–3511. doi: 10.1016/j.celrep.2018.05.048

Villaseñor, R., and Collin, L. (2017). High-resolution confocal imaging of the blood-brain barrier: imaging, 3D reconstruction, and quantification of transcytosis. *J. Vis. Exp. JoVE*. doi: 10.3791/56407

Wang, F., Wan, H., Ma, Z., Zhong, Y., Sun, Q., Tian, Y., et al. (2019). Light-sheet microscopy in the near-infrared II window. *Nat. Methods* 16, 545–552. doi: 10.1038/s41592-019-0398-7

Wang, T., Ouzounov, D. G., Wu, C., Horton, N. G., Zhang, B., Wu, C.-H., et al. (2018). Three-photon imaging of mouse brain structure and function through the intact skull. *Nat. Methods* 15, 789–792. doi: 10.1038/s41592-018-0115-y

Weinhard, L., di Bartolomei, G., Bolasco, G., Machado, P., Schieber, N. L., Neniskyte, U., et al. (2018). Microglia remodel synapses by presynaptic trogocytosis and spine head filopodia induction. *Nat. Commun.* 9:1228. doi: 10.1038/s41467-018-03566-5

Westphal, V., Rizzoli, S. O., Lauterbach, M. A., Kamin, D., Jahn, R., and Hell, S. W. (2008). Video-rate far-field optical nanoscopy dissects synaptic vesicle movement. *Science* 320, 246–249. doi: 10.1126/science.1154228

Wohleb, E. S., McKim, D. B., Sheridan, J. F., and Godbout, J. P. (2015). Monocyte trafficking to the brain with stress and inflammation: a novel axis of immune-to-brain communication that influences mood and behavior. *Front. Neurosci.* 8:447. doi: 10.3389/fnins.2014.00447

Yamasaki, R., Lu, H., Butovsky, O., Ohno, N., Rietsch, A. M., Cialic, R., et al. (2014). Differential roles of microglia and monocytes in the inflamed central nervous system. *J. Exp. Med.* 211, 1533–1549. doi: 10.1084/jem.20132477

Yang, W., and Yuste, R. (2017). *In vivo* imaging of neural activity. *Nat. Methods* 14, 349–359. doi: 10.1038/nmeth.4230

Yi, S. Y., Barnett, B. R., Torres-Velázquez, M., Zhang, Y., Hurley, S. A., Rowley, P. A., et al. (2019). Detecting microglial density with quantitative multi-compartment diffusion MRI. *Front. Neurosci.* 13:81. doi: 10.3389/fnins.2019.00081

Zheng, Y., Chen, J., Shi, X., Zhu, X., Wang, J., Huang, L., et al. (2019). Two-photon focal modulation microscopy for high-resolution imaging in deep tissue. *J. Biophotonics* 12:e201800247. doi: 10.1002/jbio.201800247

Zrzavy, T., Hametner, S., Wimmer, I., Butovsky, O., Weiner, H. L., and Lassmann, H. (2017). Loss of 'homeostatic' microglia and patterns of their activation in active multiple sclerosis. *Brain* 140, 1900–1913. doi: 10.1093/brain/awx113

Conflict of Interest: The authors declare that the research was conducted in the absence of any commercial or financial relationships that could be construed as a potential conflict of interest.

Copyright © 2020 Carrier, Robert, González Ibáñez, Desjardins and Tremblay. This is an open-access article distributed under the terms of the Creative Commons Attribution License (CC BY). The use, distribution or reproduction in other forums is permitted, provided the original author(s) and the copyright owner(s) are credited and that the original publication in this journal is cited, in accordance with accepted academic practice. No use, distribution or reproduction is permitted which does not comply with these terms.

frontiers in Neuroscience

REVIEW
published: 01 October 2020
doi: 10.3389/fnins.2020.00871

Rapidly (and Successfully) Translating Novel Brain Radiotracers From Animal Research Into Clinical Use

Robert C. Shaw[1,2], *Gilles D. Tamagnan*[3] *and Adriana Alexandre S. Tavares*[1,2]*

[1] BHF Centre for Cardiovascular Sciences, University of Edinburgh, Edinburgh, United Kingdom, [2] Edinburgh Imaging, University of Edinburgh, Edinburgh, United Kingdom, [3] XingImaging, LLC, New Haven, CT, United States

The advent of preclinical research scanners for *in vivo* imaging of small animals has added confidence into the multi-step decision-making process of radiotracer discovery and development. Furthermore, it has expanded the utility of imaging techniques available to dissect clinical questions, fostering a cyclic interaction between the clinical and the preclinical worlds. Significant efforts from medicinal chemistry have also made available several high-affinity and selective compounds amenable for radiolabeling, that target different receptors, transporters and enzymes *in vivo*. This substantially increased the range of applications of molecular imaging using positron emission tomography (PET) or single photon emission computed tomography (SPECT). However, the process of developing novel radiotracers for *in vivo* imaging of the human brain is a multi-step process that has several inherent pitfalls and technical difficulties, which often hampers the successful translation of novel imaging agents from preclinical research into clinical use. In this paper, the process of radiotracer development and its relevance in brain research is discussed; as well as, its pitfalls, technical challenges and future promises. Examples of successful and unsuccessful translation of brain radiotracers will be presented.

Keywords: novel radiotracer, translational, brain, animal research, development and discovery

OPEN ACCESS

Edited by:
Miguel Castelo-Branco, Coimbra Institute for Biomedical Imaging and Translational Research (CIBIT), Portugal

Reviewed by:
Thierry Billard, UMR 5246 Institut de Chimie et Biochimie Moléculaires et Supramoléculaires (ICBMS), France
Geoffrey Warnock, University Hospital Zürich, Switzerland

***Correspondence:**
Adriana Alexandre S. Tavares
adriana.tavares@ed.ac.uk

Specialty section:
This article was submitted to Brain Imaging Methods, a section of the journal Frontiers in Neuroscience

Received: *10 December 2019*
Accepted: *27 July 2020*
Published: *01 October 2020*

Citation:
Shaw RC, Tamagnan GD and Tavares AAS (2020) Rapidly (and Successfully) Translating Novel Brain Radiotracers From Animal Research Into Clinical Use. Front. Neurosci. 14:871. doi: 10.3389/fnins.2020.00871

INTRODUCTION

Single photon emission computed tomography (SPECT) and positron emission tomography (PET) rely on the *in vivo* detection and quantification of the radiotracer distribution and binding to a specific biological target in the living body (Salvadori, 2008). These techniques are at the leading edge of molecular imaging and allow for exceptional target specificity and high sensitivity (Haberkorn and Eisenhurt, 2005; Salvadori, 2008; Kemp et al., 2010). PET and SPECT imaging is based on the radiotracer principle, which states that the radiotracer does not alter or perturb the biological system under investigation. This is only possible when the injected mass of a radiotracer occupies a small percentage of the target, i.e., the microdosing principle (Ruth, 2009). Radiotracer imaging allows for studies investigating neurotransmission, metabolism, regional cerebral blood flow and pharmacology *in vivo*. Consequently, PET and SPECT imaging can assist in diagnosing multiple neurodegenerative and neuropsychiatric disorders. They also provide imaging biomarkers

to track disease development and monitor the effects of drugs on disease progression. Finally, radionuclide molecular imaging techniques can be used to determine optimal dosing for new drugs via microdosing experimental set-up and can aid with accelerating the implementation of personalized medicine (Brooks, 2005; Agdeppa and Spiker, 2009; Van de Bittner et al., 2014).

Despite the tremendous potential of PET and SPECT imaging, only a limited number of central nervous system (CNS) targets are currently used in humans; yet there are thousands of potential brain proteins not yet explored. This limited availability may in part be explained by the wide range of ever-growing, strict, criteria that must be fulfilled prior to radiotracer regulatory approval and by the empirical nature of radiotracer discovery (Brust et al., 2014; Van de Bittner et al., 2014). In this review, different aspects associated with brain radiotracer discovery and development will be discussed. Suggestions of alternative approaches to improve the flow through the pipeline will be also provided, alongside examples of radiotracers successful and unsuccessful in their translation to human research.

THE PROCESS OF RADIOTRACER DISCOVERY AND DEVELOPMENT

Despite the similarities between drug and radiotracer discovery and development processes, imaging agent development has the flexibility to aim at investigating functional and non-functional targets, as long as they play a role on a given disorder or mechanism of interest and meet imageability requirements (Agdeppa and Spiker, 2009). Unfortunately, the relatively small market sizes for radiotracer commercialization compared with the drug market, together with radiolabeling constrains and regulatory/intellectual property challenges, represent restrictions to the innovation potential in radiotracer discovery and development. In fact, based on 2004 estimates, the total imaging market was only 1% of the total therapeutic market (Nunn, 2006a). This demonstrates that the majority of the radiotracers developed will fall into a small/specialty market size. Furthermore, in 2006, it was estimated that a diagnostic imaging agent takes ˜8–10 years to develop at a cost of between $100 and $150 million with a potential return in sales of only $200–400 million per year, even for highly used diagnostic agents, such as the nuclear cardiology radiotracer Cardiolite^{TM}, Lantheus. This value was gained through associated costs from therapeutic drug development as there were not publicly available data at this time on costs for developing imaging agents (Nunn, 2006b). Conversely, costs to develop a novel therapeutic drug are around $850 million over 14 years with a potential return of up to as much as $3.4 billion (Nunn, 2006a,b). Later, in Zimmermann (2013) estimated the cost of a conventional drug development at €82–300 million over 10–15 years; while the development of novel radiotracers for diagnostic purposes was calculated to be €20–60 million over 7–9 years (**Figure 1**). However, this is a conservative measure looking at money invested in a successful candidate not taking into account the investment in failed candidates or candidates that did not make it to completion. If the cost of investment in research into unsuccessful targets was included this figure could be as much as 300% higher (Zimmermann, 2013). In March, Wouters et al. (2020) reported that when accounting for the costs of failed drug trials (between 2009 and 2018), the mean investment was $1,335.9 million. Analysis of the success rate of new drugs per stage of development, excluding regulatory approval, shows that the lowest success is achieved at the preclinical stages with only ∼30% success rate. This is lower than first in human success rate that averages at ˜75% (Takebe et al., 2018). It is possible that the drop in development costs of successful drugs and radiotracers relates with improvement of preclinical methods, which in the case of PET/SPECT imaging might stem from the development of dedicated preclinical imaging platforms. Notwithstanding, the overall cost (i.e., corrected for failed candidates) has not reduced with time. From these data, it is clear that the commercialization of diagnostic imaging agents will not generate the same return as pharmaceutical drugs. Thus, partnerships between academia, the pharmaceutical industry and imaging companies improves the viability of radiotracer discovery and development in light of the increasing demand for personalized medicine. Over the years, the academic community has been invaluable to explore new high risk/high gain areas; demonstrating the feasibility of new imaging approaches. Unsurprisingly, academia has been credited for the majority of PET and SPECT radiotracers discovery to date. In turn, industry can facilitate the route to commercialization for radiotracers discovered in academia (Agdeppa and Spiker, 2009). Furthermore, partnering between pharmaceutical companies, imaging companies and academia can allow for the conversion of failed therapeutic agents into radiotracers. Abandoned drug candidates and families of compounds, which failed due to toxicity or short biological half-life, can sometimes be repurposed as PET or SPECT radiotracers. This is due to the radiotracer principle allowing for the safe use of very low (picomolar) concentrations of compounds that are toxic at higher concentrations. Furthermore, the rapid clearance of a given compound, which is suboptimal for drug candidates, may be suitable and even desirable, for a PET or SPECT radiotracer (Willmann et al., 2008).

The process of radiotracer discovery and development has been described in various ways, however, one aspect of this process is consistent across the field: developing radiotracers is a multidisciplinary iterative process. Each stage of the process can feedback to a prior stage and/or input the subsequent stage (Salvadori, 2008; Agdeppa and Spiker, 2009; Barth and Need, 2014; Van de Bittner et al., 2014). Below we provide an overview of the key stages in the process of radiotracer discovery and development.

Evaluation of Market Opportunities and Prioritization of Research Questions to Target

At early stages of radiotracer discovery, multiple factors must be considered beyond the scientific challenges alone (**Figure 1**). It is important to understand from the outset how the radiotracer would be used and then established predefined performance

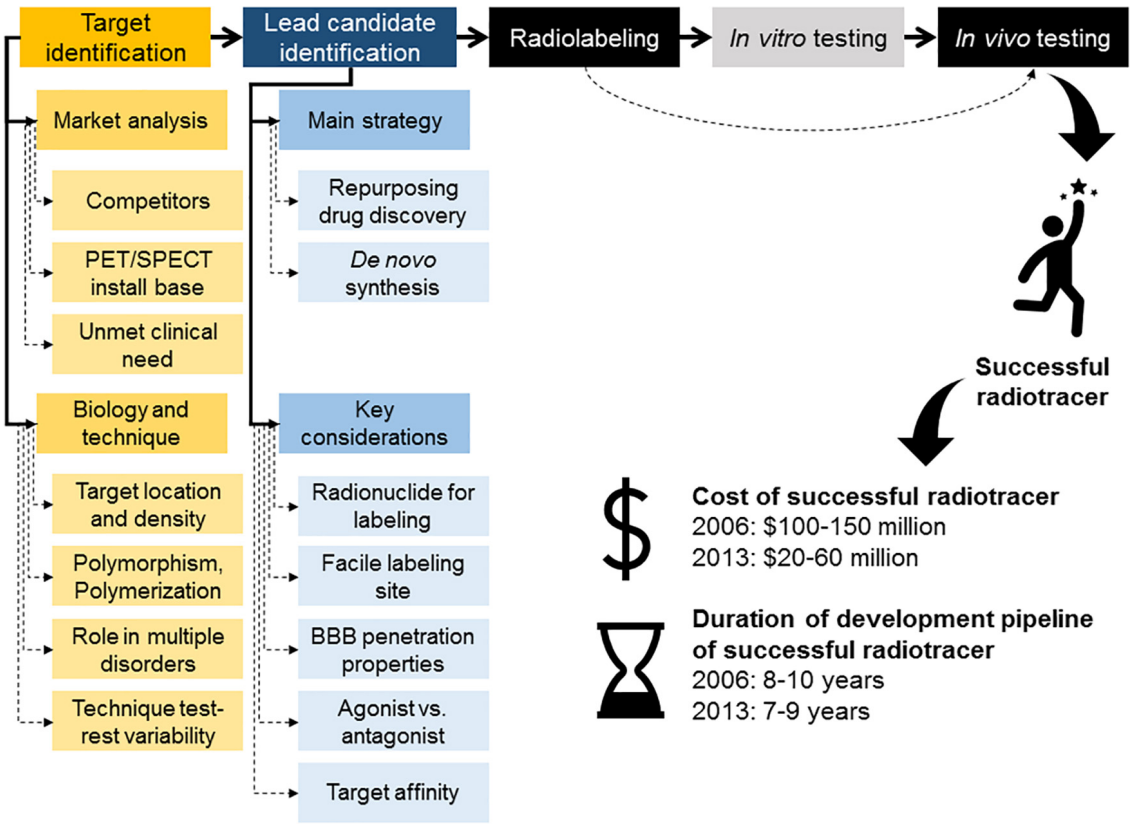

FIGURE 1 | Overview of radiotracer discovery and development pipeline. Main steps in the radiotracer discovery and development pipeline, including typical development costs and timelines for development of a successful radiotracer. A strategy to accelerate the process of radiotracer development involves removal of the *in vitro* testing of the radiolabeled compound and instead progress with the radiolabeled compound straight into *in vivo* testing.

criteria required for success. For example, one could ask whether the development of a novel radiotracer for a given target would enhance the ability to image such target by improving target:non-target ratios, reducing off target binding or kinetics *in vivo*. For previously unexplored targets, it would be important to provide convincing evidence that the novel radiotracer will specifically label the target or mechanism that they are designed to measure (Agdeppa and Spiker, 2009).

Given the expensive and time-consuming nature of radiotracer discovery and development, which ultimately culminates with a small/specialty market, it is also important to perform a "market search" at the inception of radiotracer discovery. Obtaining insights from physicians can be useful to understand the need for a given imaging tool in clinical practice or research. In short, if imaging with a radiotracer for an unmet clinical need would not be "prescribed," then the development of such radiotracer may be unnecessary. In the basic research context, which accounts for the majority of these PET and SPECT imaging, the utility of a radiotracer can be difficult to anticipate. Potential use can be appraised by discussing this among colleagues, preclinical scientists and experts from pharmaceutical companies, in order to determine preclinical use and human translational potential of a given radiotracer (Van de Bittner et al., 2014). Commercialization potential is important when selecting projects and in practice; technically feasible projects may not be a priority due to a limited potential return on investment (Nunn, 2006a). A careful evaluation of the market size may also be driven by current/future install bases in clinical use and modality constrains. For example, SPECT equipment is more widely distributed and numerous in comparison with PET (around 12 530 multi-head SPECT scanners vs. around 1000 PET scanners in the United States of America in 2008) (Agdeppa and Spiker, 2009). Thus, the development of a novel SPECT radiotracer might be preferred over a PET radiotracer if the SPECT imaging performance is adequate. This is especially true as the physical limits of PET and SPECT detection are approached in the clinical setting as they have been approached in the preclinical setting (Mariani et al., 2008; Seo et al., 2008; Ruth, 2009). For example, in the preclinical setting, small animal SPECT scanners have higher resolution than PET scanners, although this comes at the expense of relatively lower sensitivity (de Kemp et al., 2010; Koba et al., 2013). PET is arguably superior to SPECT in regards to being able to directly measure the attenuation effect of the object being viewed; as well as having a higher resolution and accuracy in quantitative assessment of regional concentrations of a radiotracer (Alavi and Basu, 2008; Ruth, 2009). The higher sensitivity gives PET the ability to measure targets with lower expression. However, PET does still

have limitations and challenges. Short-lived PET radionuclides, such as ^{15}O and ^{11}C, require a cyclotron in close proximity to the PET scanner. This may limit widespread market distribution, but it can be advantageous during early stages of radiotracer discovery and development as it will be detailed below. PET scanning also incurs higher costs in comparison with SPECT scanning (Ottobrini et al., 2006; von Schulthess and Burger, 2010). Targeting specific molecules so that they can be easily labeled for both PET and SPECT imaging should be considered in the early stages of radiotracer design in order to reach users in both modalities. This keeps options open and can save time and money in long term development.

From a commercialization point of view, similarly to therapeutic drugs, knowing the intellectual property (IP) landscape before project conception can help identify opportunities and competition. It is important to be up to date on the status of technology, other applicable imaging agents and non-imaging biomarkers, regardless of the imaging modality. For example, magnetic resonance imaging (MRI) research is improving endogenous signal without the use of contrast agents. Blood biomarkers and non-imaging biomarkers are other forms of competition and could limit the use of novel imaging agent, although these diagnostics lack spatial information that can be obtained with imaging. If a cheap blood test can give the same information as an expensive time consuming scan then it is unlikely that it will be adopted in the clinical setting. These aspects are important to consider, especially due to the long times associated with the development of novel radiotracers. Moreover, consideration of the impact of a novel radiotracer on health economics, in light of the reimbursement issues, may be valuable when aiming at commercialization of a novel radiotracer (Agdeppa and Spiker, 2009). Alternative approaches, less focused on the commercialization of the novel radiotracer, have suggested to start the brain radiotracer development program based on assessing an unmet medical need or based on an expectation in human disease imaging (Van de Bittner et al., 2014).

In summary, when initiating the journey of radiotracer discovery and development, the researcher must look beyond purely the scientific scope and should address important questions. If the purpose of that radiotracer development is to attract investment and lead to commercialization: (1) is there a market or a medical need that justifies the development of this radiotracer?; (2) will the quality of the science and technology behind the new molecule be attractive to an investor?; (3) is it feasible and will it comply with regulations?; and (4) in this limited competitive landscape, will the novel radiotracer stand a chance? An example of a recently developed successful radiotracer with potential to have wider impact in the field of brain research and clinical imaging is ^{18}F-MNI1126, a radiotracer targeting the synaptic vesicle glycoprotein 2A (SV2A) (Mercier et al., 2017; Constantinescu et al., 2019).

Target Identification

Traditionally, therapeutic drug targets have an important mechanistic effect in disease processes, such as, inhibiting the target may alter/reduce disease severity or progression (Pritchard et al., 2003). An important difference between therapeutic drugs and diagnostic radiotracers' target identification step is that the latter can be developed for targets that play an important role in a given disease, yet have no functional effect in modifying disease processes. A pivotal example of these so called "non-functional" targets is amyloid imaging, where structural proteins are targeted (Klunk et al., 2004). This means that a radiotracer target needs only have altered expression, occupancy or function in a given disorder, resulting in a wide range of potential targets for *in vivo* imaging, which in turn will allow for a given radiotracer to be applied to investigate several different medical or biological questions (Agdeppa and Spiker, 2009; Van de Bittner et al., 2014).

To assist with the target identification during radiotracer discovery, it is also important to consider the location and amount of target assessable for high quality *in vivo* imaging. An essential property for *in vivo* imaging using radiotracers is the concept of binding potential (*BP*), which provide a measurement of radiotracer-target interaction as a function of the total target density (B_{max}) and the radiotracer binding affinity (K_D). The suggested ideal *BP* values for *in vivo* imaging in the literature can vary considerably from 1.5 (Barth and Need, 2014) up to 10 (Patel and Gibson, 2008). Some have proposed, as a rule of thumb, that a *BP* of 5 is a suitable value for quantitative PET imaging, especially in the clinical setting where kinetic modeling techniques are not always available (Van de Bittner et al., 2014). When assessing which target to tackle during radiotracer discovery, it is possible to estimate the ideal K_D value for the prospective candidate radiotracer from the known B_{max}. When the B_{max} is unknown, it can be measured using autoradiography, binding assays or quantitative immunohistochemistry methods. *In vivo, BP* can be expressed in three different forms depending on the reference used, BP_{ND}, BP_F, and BP_P. BP_{ND} refers to the ratio of radioligand specifically bound to its target vs the amount binding non-specifically (the non-displaceable amount). BP_F refers to the ratio of specifically bound radiotracer to free fraction and BP_P refers to the total concentration in the plasma that is available (excluding ligand irreversibly bound to plasma proteins) (Innis et al., 2007). Examples of brain SPECT and PET radiotracers previously developed and correspondent BP_{ND} values are presented in **Table 1** below.

Although the majority of brain radiotracers developed to date are small molecules that interact with transmembrane receptors and transporters, other targets are amenable for *in vivo* imaging using PET and SPECT. Some radiotracers can serve as subtracts for enzymes (a prominent example is 2-deoxy-2-[^{18}F]fluoroglucose) (Van de Bittner et al., 2014) or can bind to protein aggregates, most notably amyloid and tau proteins (Agdeppa and Spiker, 2009; Nordberg, 2014). Furthermore, radiotracers targeting nuclear receptors have also been investigated. These require penetration of the cell nucleus by the radiotracer (Wang et al., 2014). Radiotracers designed to bind to a transmembrane protein, including G-protein coupled receptors, may have to compete with native ligands or allosteric modulation. This means that variations in the endogenous ligand concentrations can impact image quantification of receptor density *in vivo;* setting strict requirements for the candidate radiotracer K_D value. Furthermore, transmembrane receptors have regulatory mechanisms, such as homo- or

TABLE 1 | Examples of brain SPECT and PET radiotracers previously developed and associated BP_{ND} values in healthy humans.

Radiotracer	Target (high to low density)	BP_{ND}	References
^{123}I-Iomazenil	GABA receptors	12.50 ± 0.05 (n = 10)	Abi-Dargham et al., 1994
^{123}I-(R,R)I-QNB	mACh receptors	4.85 (n = 11)	Norbury et al., 2004
^{123}I-5-IA85380	α4β2-nACh receptors	4.43 ± 0.06 (n = 6)	Fujita et al., 2003
^{123}I-β-CIT	Dopamine transporters	6.66 ± 1.54 (n = 5)	Laruelle et al., 1994
^{11}C-Raclopride	D2/3 receptors	2.19 ± 0.18 (n = 40)	Berry et al., 2018
^{123}I-IBZM	D2/3 receptors	0.86 ± 0.11 (n = 10)	Meyer et al., 2008
^{11}C-DASB	Serotonin transporters	2.68 ± 0.68 (n = 5)	Ginovart et al., 2001
^{123}I-ADAM	Serotonin transporters	1.62 ± 0.57 (n = 7)	Yang et al., 2008
^{11}C-PK11195	TSPO	1.60 ± 0.40 (n = 13)	Kropholler et al., 2005
^{11}C-PIB	β-amyloid plaques	0.11 ± 0.15 (n = 13)	Tolboom et al., 2009
^{18}F-FDDNP	β-amyloid plaques	0.05 ± 0.03 (n = 13)	Tolboom et al., 2009

BP_{ND} reduces as a function of target density and radiotracer affinity (e.g., dopamine receptor, serotonin transporter and β-amyloid plaques ligands). The results also depend on method of quantification used, i.e., kinetic modeling with or without input function (details in sections below). Legend: α4β2-nACh receptor = alpha-4 beta-2 nicotinic acetylcholine receptor; mACh receptors = muscarinic acetylcholine receptors; D2 receptors = dopamine type 2 and 3 receptors; TSPO = 18 kDa translocator protein.

heteropolymerization and internalization (Ferré et al., 2014); these can represent unexplored avenues in the development of new therapies (George et al., 2002), but directly impact the radiotracer kinetics and binding affinities *in vivo*. Some radiotracers developed to image the 18-kDa translocator protein (TSPO) are also influenced by a genetic polymorphism that leads to differences in binding affinity within the population (Owen et al., 2012). If a novel target has a known potential for genetic polymorphisms, it is important to consider potential effects of genetic polymorphism on radiotracer binding, and thus imaging. Although, interestingly, the TSPO radiotracer ^{11}C-PK11195 binding does not seem to be affected by the genetic polymorphism (Owen et al., 2010; Owen et al., 2011). This recent observation of genetic polymorphisms impacting radiotracer binding highlights another new feature to consider when selecting the target for radiotracer discovery (**Figure 2**, Case study 1).

Another important consideration while discovering novel radiotracers is to understand the error associated with the imaging technique to be use. Typically for any PET and SPECT radiotracers this is represented by the intra-subject test-retest variability. The majority of brain radiotracers have test-retest results of less than 15% [see for example (Abi-Dargham et al., 1995; Seibyl et al., 1996; Booij et al., 1998; Varrone et al., 2000; Catafau et al., 2005; Laere et al., 2013; Barret et al., 2014b; Tavares A. et al., 2014)], meaning that when investigating longitudinal changes in either target density or receptor occupancy in a single-subject, observed changes must exceed 15% in order to be successfully imaged. Various outcome measures are used to quantify test-rest variability. BP_{ND} is a preferred outcome measure but is not always possible to measure as it requires dynamic imaging data from radiotracers that have reversible binding kinetics and, depending on the target of interest, can also require invasive arterial blood collection for kinetic modeling analysis when a reference region devoid of binding is not available (Innis et al., 2007). BP_{ND} from distribution volume ratio (DVR), calculated from V_T, also requires arterial input function data. The total volume of distribution (V_T) has also been used for quantification of test-retest variability and as an outcome measure in some cases, such as, in the measurement TSPO radiotracers concentration in the CNS (Sandiego et al., 2015; De Picker et al., 2019). V_T also requires dynamic imaging protocols and the use of arterial input function or, even possible, image derived input function. Standard Uptake Value Ratio (SUVr) is also used in some cases such as for amyloid radiotracers (Knešaurek et al., 2018). For estimation of SUVr, static imaging protocols are sufficient.

Despite all the considerations given during target identification, the most practical and commonly used approach in finding potential radiotracers is to identify high-affinity ligands with known structure-activity relationships. These are often discovered through drug development programs; although highly novel targets without known ligands can also be pursued in radiotracer discovery. Highly novel targets without known ligands can, however, be time and cost-intensive, as various compound libraries need to be developed and screened iteratively. Such "risky" targets, therefore, must have a high B_{max} and demonstrate a significant percentage change in density or occupancy relating to the research or clinical question being addressed, in order to be worth the input of radiotracer development.

In summary, it is important to investigate which target(s) play an important role in a given disease and can also be imaged using PET or SPECT (considering, for example, the test-retest variability of the technique). Targets that play important roles in multiple disorders can broaden the range of applications of the novel radiotracer candidate thus make more attractive targets. Suitable target density for high quality *in vivo* imaging should be evaluated and the researcher should also pinpoint the desirable affinity of the novel candidate radiotracer at this stage (**Figure 1**).

Design and Selection of Lead Radiotracer Candidate

It is tempting to start the process of radiotracer discovery by targeting existing therapeutic drugs, however, it is important to

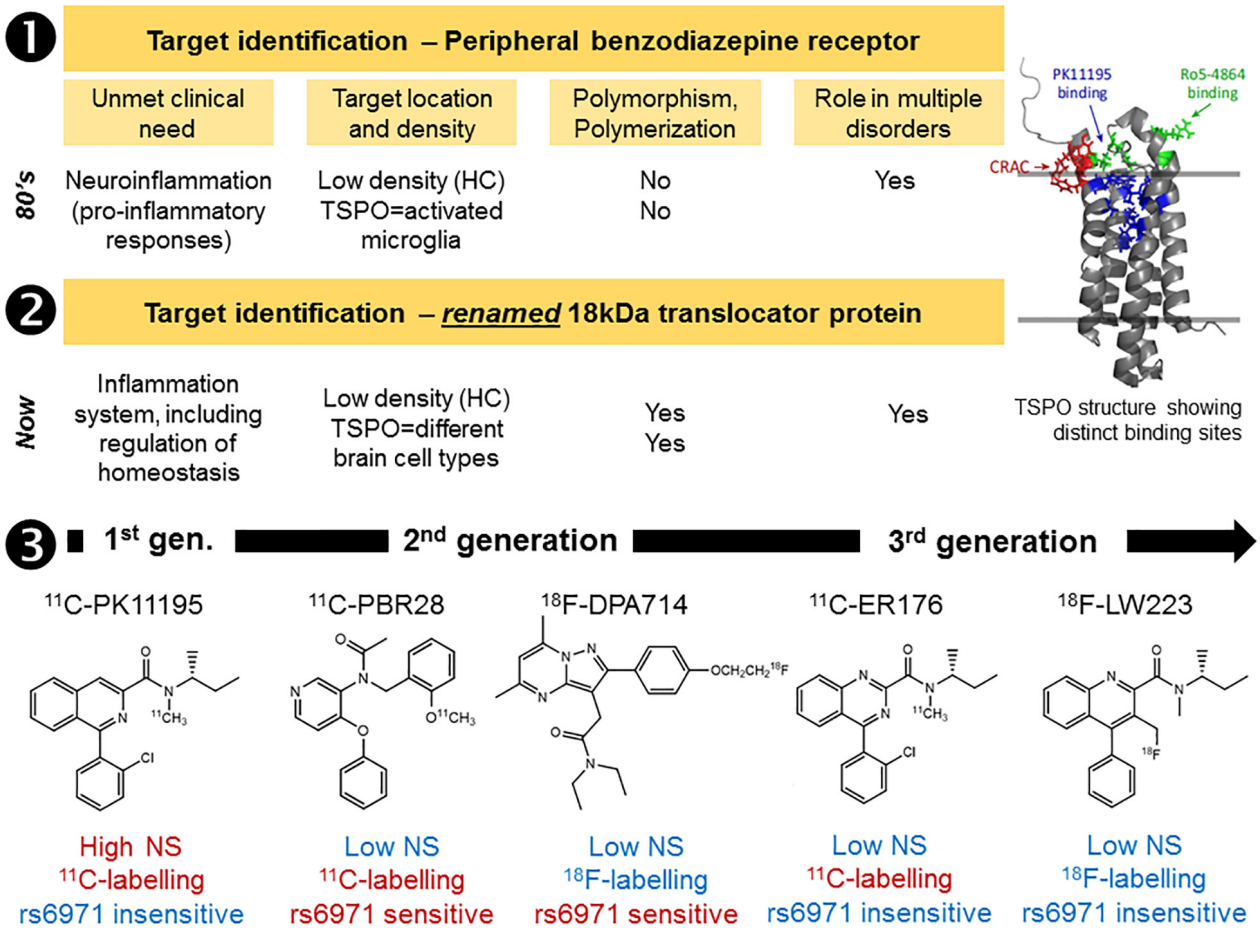

FIGURE 2 | Case study 1: Imaging the 18kDa translocator protein (TSPO), a "moving target" over the past three decades. The development of novel TSPO radiotracers suffered from high degree of attrition over the years (1–3). First there was the renaming of the target, in recognition of the wider functions of this protein. Then the identification of a genetic polymorphism (rs6971) capable of impacting on radiotracer binding in humans (2nd generation, 2nd gen., radiotracers). Alongside these discoveries came the recognition that TSPO has at least three binding sites and can be expressed in a monomer or a polymer configuration depending on the organ or disease process under investigation. Furthermore, limited characterization of the TSPO expression in various cell types decades ago has created a delayed realization that TSPO PET/SPECT imaging was always directed toward understanding TSPO molecular changes rather than cell changes. All these serendipitous findings at the first stage of the radiotracer development pipeline (target identification) have impacted on the development of novel and successful TSPO radiotracers (1 and 2). Despite these difficulties, through a series of compound libraries from 1st generation (1st gen.) radiotracers, like ^{11}C-PK11195, to 3rd generation (3rd gen.) radiotracers like ^{11}C-ER176 and ^{18}F-LW223, it was possible to resolve the target identification issue, while improving radiotracer properties, such as reduction of non-specific binding (NS) and convenient labeling with fluorine-18 (3). Red and blue text indicates limitations and advantages of each example radiotracer displayed in row 3. HC, healthy control brain. TSPO structure taken from Selvaraj and Stocco, Trends in Endocrinology and Metabolism, 2015, 26(7):341.

be aware of the negative aspects associated with this choice. For example, therapeutic drugs aim for a sustained target-engagement after one single administration, but this can be unsuitable for radiotracer imaging; resulting in radiotracers with slow kinetics. ^{18}F-F13714 is an example of a brain radiotracer with slow kinetics. It was developed as a serotonin type 1A (5-HT1A) receptor agonist radiotracer, however, it was found to have such high affinity that its binding resulted in quasi-irreversible kinetics (Tavares et al., 2013; Yokoyama et al., 2016). This sustained binding maybe useful for drugs, however, is sub-optimal for a radiotracer, as it makes quantification difficult using traditional kinetic models that assume reversible Michaelis-Menten kinetics (Innis et al., 2007). Furthermore, it is important to consider the fact that radiotracers require high brain/plasma ratio and should have low non-specific binding, two factors that can at times be less pressing for therapeutic drugs, where it is not infrequent to have a drug able to bind to several targets in the brain. An example of a non-selective radiotracer is the SPECT iodinated analog of Siponimod (a licensed drug for treatment of Multiple Sclerosis), ^{123}I-MS565, which binds to two types of sphingosine-1-phosphate receptors (S1P1 and S1P5) (Tavares A. et al., 2014). It is useful for the use in studying the effects of Siponimod, however, is of limited use when trying to label and track changes in one receptor type in the CNS or to try and establish the role of one of the receptor types in disease development and progression.

De novo radiotracer synthesis is another route for lead candidate selection during radiotracer discovery. This route can

be even more iterative than the approach described in the above paragraph. This is particularly true for novel radiotracers that target complex mechanisms or use non-traditional (non-small) compounds, as *in vitro* screening methods would be more limited in predicting their *in vivo* performance. In these cases, conducting simple animal model studies early could provide information and help to optimize the novel radiotracer candidates' performance *in vivo*. Feedback from preclinical scientists to the chemists can be used to improve the radiotracer's structure before moving into more rigorous preclinical studies, and if successful, clinical studies (Agdeppa and Spiker, 2009). Another approach to improve the likelihood of discovering high-affinity, brain penetrant molecules during *de novo* synthesis of CNS radiotracers includes the concurrent synthesis of compounds with different chemical scaffolds, as well as, scaffolds that offer several sites for easy substitution with various functional groups. Furthermore, when developing compound libraries it is important that the synthesized molecules have relatively minor deviations in chemical structure, as additions of small chemical groups can significantly affect the radiotracer *in vivo* kinetics and binding properties [see for example, Stevenson et al., 2010; Seo et al., 2014 and **Figure 3**, Case Study 2).

Regardless of the approach used to start the novel radiotracer design process, at this stage, it is important to consider the development of compounds with a facile labeling site with the potential to be radiolabeled across multiple derivatives (Van de Bittner et al., 2014). Using the same labeling site across various derivatives would allow for minor changes in the radiolabeling method between molecules, saving time and money while developing novel radiotracers. The radionuclides to be used for radiolabeling should also be considered during radiotracer design. For PET imaging, the use of carbon-11 (^{11}C), nitrogen-13 (^{13}N) and oxygen-15 (^{15}O), which are isotopes of endogenous elements, allows for radiolabeling of target molecules without changing their chemical properties with ^{15}O-Water, ^{15}O-oxygen and ^{15}O-CO as the examples for ^{15}O. Conversely, fluorine is not ubiquitous in endogenous biomolecules, may lead to differences in radiotracer *in vivo* performance from derivative biomolecules. This is exemplified by, ^{11}C-DOPA and *L*-6-fluoro-^{18}F-FOPA having different decarboxylation rates *in vivo* (Torstenson et al., 1999). *L*-6-fluoro-^{18}F-FOPA can be successfully used for PET imaging, however, it is far more heavily metabolized than its carbon-11 counterpart and requires the use of inhibitors (carbidopa with or without entacapone) to reduce this metabolism and to gain reliable PET images (Kumakura et al., 2005; Kyono et al., 2011; Walker et al., 2013). Importantly, the fluorine-19 (^{19}F) commonly present in drug pharmacophores may represent a viable strategy to radiotracer discovery, as in those instances there is only a need for substituting ^{19}F in the drug with ^{18}F in the radiotracer without changing compound kinetic properties. When the drug pharmacophores do not include ^{19}F, one commonly suggested approach involves the use of ^{11}C for early probe development, i.e., proof-of-concept *de novo* radiotracer discovery. Once the hypothesized *in vivo* performance using the ^{11}C-labeled radiotracer is confirmed, ^{18}F-labeled analog or other relatively longer-lived radioisotopes

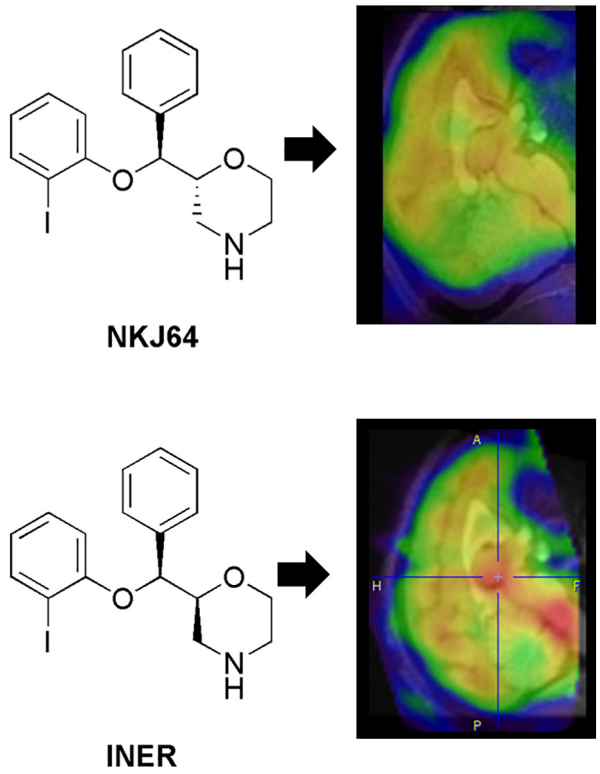

FIGURE 3 | Case study 2: Analog but different. This case study illustrates the impact of small changes in radiotracer structure on binding kinetics *in vivo* and subsequent impact on the translational potential of radiotracers. NKJ64 and INER were both ^{123}I-labeled tracers targeting the noradrenaline transporters (NAT). Both stereoisomers had nanomolar affinity *in vitro*, but different kinetics *in vivo*. The INER compound presented binding in brain consistent with NAT expression (highest in the midbrain, in particular locus coeruleus – in red), while NKJ64 had no specific binding to target in baboon brain. SPECT images co-registered to MRI data for the same baboon. A, anterior; P, posterior; F, feet; H, head.

(e.g., iodine-123 for SPECT or iodine-124 for PET) would be explored for subsequent clinical or commercial use. Although this approach is appealing due to the simplicity of substituting elemental carbon with its isotope counterpart ^{11}C, from a long term development perspective it adds cost in the process of radiotracer development; with potentially no return and/or will substantially limit the market distribution of the ^{11}C-labeled radiotracer, as it is estimated that about 90% of PET scanners are in facilities unable to produce ^{11}C radiotracers with high specific activity (Klunk and Mathis, 2008). Still, when investigating highly novel and unexplored targets, this may be the fastest option. It might also be advantageous to use SPECT radiolabels (e.g., ^{123}I or Technitium-99m, ^{99m}Tc) for biomolecules or drug labeling, as there is a long history of labeling proteins, nucleic acids and small molecules with radioiodine (Agdeppa and Spiker, 2009). Other radionuclides may become more prominent in the future as universal procedures for radiolabeling intact monoclonal antibodies (mAbs) or mAbs fragments become available and increasing interest in using these biomolecules in brain imaging

is raised within the imaging community (Dongen et al., 2012; McLean et al., 2012). These include the long-lived positron emitters iodine-124 (^{124}I, $t_{1/2}$ of 100.3 h) and zirconium-89 (^{89}Zr, $t_{1/2}$ of 78.4 h); and the shorter-lived positron emitters gallium-68 (^{68}Ga, $t_{1/2}$ of 1.13 h), copper-64 (^{64}Cu, $t_{1/2}$ of 12.7 h), yttrium-86 (^{86}Y, $t_{1/2}$ of 14.7 h) and bromine-76 (^{76}Br, $t_{1/2}$ of 16.2 h). The commercially available long life-span ^{68}Ge/^{68}Ga-generator (half-life 271 days) makes ^{68}Ga a particularly interesting radionuclide for clinical use, as it can be continuously available even for centers without a cyclotron and at relatively reasonable costs.

Another aspect to consider during the design of the radiotracer candidate relates with the development of the precursor for radiolabeling. The precursor should allow for a highly reproducible reaction, automation of the radiosynthesis process (labeling, purification, and formulation) and a radiochemical yield of the formulated product high enough to permit human application (Brust et al., 2014). The automation is useful in various ways, in terms of reproducibility, it minimizes human error. Importantly, once the radiosynthesis method is optimized and is fully automated, production of radiotracers can be scaled-up enabling large scale production for local use (multiple patients a day) or distribution to different PET sites (if the radioisotope half-life permits). Several aspects require consideration when designing candidate radiotracers, including type of precursor to be used. For example, tin precursors are sub-optimal for clinical use, because they require additional quality assurance given the highly toxic nature of tin. The type of precursor selected will also impact on the separation method to be used to obtain the final product (e.g., high performance liquid chromatography or solid phase extraction). Two excellent reviews have been recently published detailing PET radiochemistry principles (Brandt et al., 2018; Pichler et al., 2018).

Identifying the lead radiotracer candidate among a library of compounds shares similarities with the process of drug development and includes screening of the affinity for the target, selectivity, metabolism, lipophilicity and molecular weight/size (Agdeppa and Spiker, 2009; Pike, 2009; Van de Bittner et al., 2014) (**Table 2**). Despite the comprehensive list of characteristics that hold promise to yield an ideal radiotracer for brain imaging, the suggested criteria are not a definite recipe for success, but rather some empirical or observation-based guidelines that are continuously being refined. In fact, several physicochemical properties such as Log P, Log D, molecular weight and the acid dissociation constant (pK_a) have been found to correlate with *in vivo* behavior to some extent, but are not necessarily predictive of radiotracer performance *in vivo* (Van de Bittner et al., 2014). Thus, even though a substantial emphasis has been placed in the *in silico* models and computation for assessment of physicochemical properties of potential radiotracers for brain imaging (Clark, 2003; Agdeppa and Spiker, 2009), these methods do not necessarily concur with the *in vivo* performance of a number of radiotracers developed, as has been shown in the literature (Tavares et al., 2012b; Van de Bittner et al., 2014).

Radiotracer metabolism (discussed further in following section) is often a major stumbling point encountered during radiotracer discovery and translational imaging. Although radiotracer metabolism *in vivo* may be hinted during radiotracer design or radiotracer screening *in vitro*, metabolism is highly species-dependent; typically compounds show more extensive metabolism in lower organisms.

TABLE 2 | Criteria for passive diffusion of a radiotracer across the blood-brain-barrier (BBB) and good bioavailability (Lipinski et al., 2001; Clark, 2003; Waterhouse, 2003; Wong and Pomper, 2003; Pike, 2009; Van de Bittner et al., 2014).

Action	Characteristic	Requirement
Crossing BBB	Molecular weight	<450 g/mol
Crossing BBB	Polar surface area	<60–90 Å
Crossing BBB	Number of hydrogen bond donors	<5
Crossing BBB	Sum of nitrogen and oxygen atoms	<10
Crossing BBB	Log P (partition coefficient)	<4 (ideal range of 1–3.5)
Crossing BBB	Affinity for efflux pumps (e.g., P-gp)	Minimal
Crossing BBB	Affinity for enzymes at the BBB	Minimal
Crossing BBB	Brain uptake (%ID)	≥0.5%
	Brain uptake (SUV)	>2.0
Metabolism	Ionization at physiological pH	Low
Metabolism	Presence of radiometabolites in brain	Low
Binding to silent sites	Binding to plasma proteins	Low
Binding to silent sites	Non-specific or non-saturable sites	Low
Binding to target site	Kinetics quantifiable *in vivo*	Reversible or not completely irreversible
Binding to target site	Dissociation or inhibition constants	Nanomolar range
Binding to target site	Selectivity	High
Binding to target site	Specificity	High
Radiological safety	Whole-body and critical organ dosimetry	Low radiation dose

P-gp, P-glycoprotein; %ID, % injected dose; SUV, standard uptake value.

Several methods have been proposed to assist with radiotracer lead candidate selection early in the process of radiotracer discovery. These aim to increase the likelihood of success of a novel brain radiotracer *in vivo*. These methods include *in silico* simulations, *in vitro* testing, high-performance liquid chromatography methods and liquid chromatography–mass spectrometry techniques (Clark, 2003; Agdeppa and Spiker, 2009; Tavares et al., 2012b; Barth and Need, 2014; Van de Bittner et al., 2014). Nonetheless, there is a growing indication from the radiotracer development community that progressing rapidly into *in vivo* imaging following a short high throughput screening exercise targeting key properties (affinity, selectivity and BBB penetration estimation) or even move directly into radiolabeling and *in vivo* imaging studies, with subsequent iterative feedback between preclinical imaging and chemistry, may be the way forward. In this emerging philosophy, the lead candidate selection can be reduced to at most a rapid screening and ranking of molecules prior to radiolabeling, where

the affinity for the target would be assessed in conjunction with the biological target density and the likelihood of BBB penetration would be assessed by a high throughput technique. To maximize efficiency, during radiotracer affinity experiments, it is useful to include a known radiotracer targeting the same process as a control together with the radiotracer library under scrutiny. This has already been applied in the development of novel TSPO ligands based on PK11195 structure (Stevenson et al., 2010) (**Figure 2**, Case Study 1). Although the specific ranking order of the compound's affinity is less central than their clustering based on chemical structure, it can provide a starting point to select which cluster of radiotracer candidates to prioritize for *in vivo* imaging. Similarly, when ranking candidate radiotracers for BBB penetration, it is important to include in the analysis known successful radiotracers. A recently proposed methodology uses high performance liquid chromatography for rapid screening and ranking of candidate radiotracers in terms of permeability, plasma protein binding and compound-membrane interaction (Tavares et al., 2012b) (**Figure 4**) and has been adopted by different research groups working on novel radiotracer development (Blair et al., 2013; Gilfillan et al., 2013; Mark et al., 2013; Philippe et al., 2013a,b; Rami-Mark et al., 2013). This chromatography method uses compound retention time information to derive permeability, plasma protein binding and compound-membrane interaction and vs. a calibration curve. The chromatography outcome measures (permeability, plasma protein binding and compound-membrane interaction) can then be used to predict *in vivo* behavior of the compound using mathematical equations describing the relationships between chromatography outcome measures and *in vivo* measures (%injected dose in brain and BP_{ND}) (Tavares et al., 2012b). Newer mass spectrometry methods have also been proposed for estimation of specific and non-specific binding across brain regions (Barth and Need, 2014). However, the use of unlabeled compounds makes the measurement of metabolites difficult and the proposed approach can be labour intensive. It requires the use of several animals and dissection techniques following administration of the unlabeled compound, as each animal can only provide information for a limited number of time points.

In summary, the design and selection of the lead radiotracer candidate can start by targeting existent therapeutic drugs or initiating a *de novo* radiotracer program. During this stage, the researcher should focus on targeting compounds that would allow for ease radiolabeling, preferably would allow for labeling with different radioisotopes for PET or SPECT imaging (keeping the potential market options open). Once the library of target compounds has been identified or designed, screening of these compounds for key properties (affinity and BBB penetration) must be rapid and simple, with the aim to progress as quickly as possible to *in vivo* imaging. Sometimes it might even be possible to obviate this step all together and move straight into radiolabeling and *in vivo* imaging, depending on the level of information one has on a given molecule (**Figures 1**, **4**).

Preclinical Studies to Evaluate Novel Radiotracer Candidates

For decades, the affinity, selectivity and binding kinetics of novel radiotracers have been studied using autoradiography and binding assay techniques (Udenfriend et al., 1987; Cook, 1996; Schuck, 1997; Qume, 1999; Lazareno, 2001; Frank et al., 2007). However, frequently, these approaches lead to novel radiotracers displaying poor *in vivo* kinetics and high non-specific binding in the first round of *in vivo* imaging, often contributing to the high attrition rate during radiotracer development. Thus, moving the novel radiotracer rapidly into small animal *in vivo* imaging can

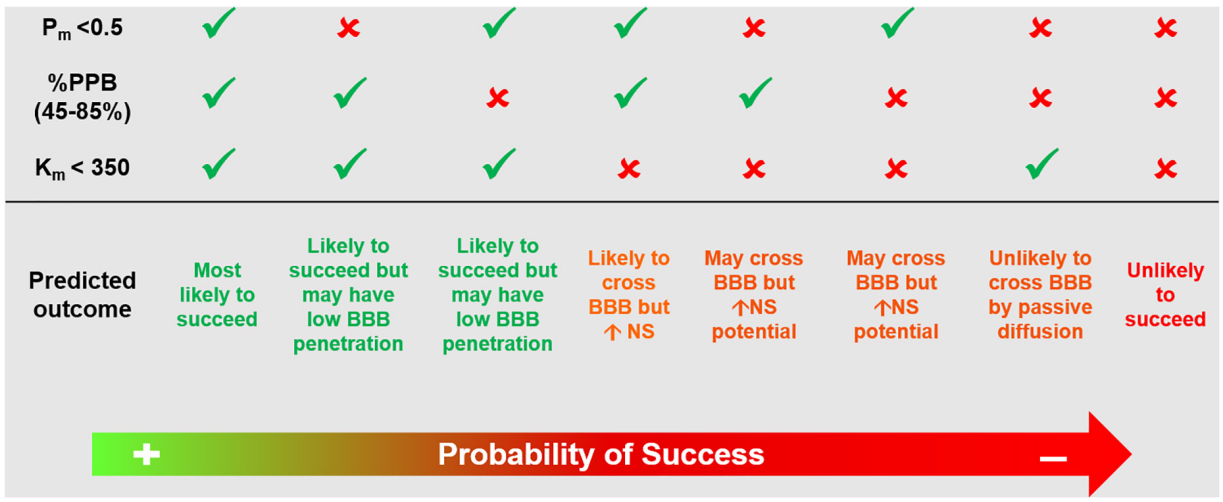

FIGURE 4 | Example of high performance liquid chromatography approach that could be used for screening and ranking of radiotracer candidates. Based on previously published methodology (Tavares et al., 2012b). This chromatography method uses compound retention time information to derive P_m, %PPB and K_m. These chromatography outcome measures can then be used to predict *in vivo* behavior of the compound using mathematical equations describing the relationships between chromatography outcome measures and *in vivo* measures (%injected dose in brain and binding potential BP_{ND}). P_m, permeability; %PPB, %plasma protein binding to human serum albumin; K_m, compound-membrane partition coefficient; BBB, blood brain barrier; NS, non-specific binding.

accelerate the process of radiotracer discovery and development (de Kemp et al., 2010; Koba et al., 2013) by removing redundant steps between compound chemical synthesis and *in vivo* imaging. A successful example that came out of this direct strategy, supported by *in vivo* imaging at early stages, is ^{18}F-MNI444, a novel PET radiotracer targeting adenosine-2A receptors (A2A) in the brain (Barret et al., 2014a; Barret et al., 2015). Preladenant served as target re-purposed structure for development of this radiotracer, then precursors for radiolabeling were designed and synthesized and the new radiotracer immediately tested in non-human primates (Barret et al., 2014a). The promising results in non-human primates rapidly prompted the progression of the compound to humans (Barret et al., 2015). The whole process took only 4 years.

In fact, imaging studies can allow for the determination of major radiotracer attributes traditionally determined using non-imaging methods or *in vitro*/*ex vivo* imaging techniques. For example, *in vivo* imaging can be used to determine binding affinity (BP = B_{max}/K_D, where smaller K_D would corresponds to larger BP for a given target); binding kinetics can be investigated by quantitative analysis and kinetic modeling of the obtained time-activity curves; BBB penetration can be estimated as percentage injected dose in brain; specific binding can be determined using homologous blocking experiments or knockout animals; and selective binding can be determined using heterologous blocking or knockout animals (Kemp et al., 2010; Koba et al., 2013; Van de Bittner et al., 2014). Nowadays, kinetic modeling in rodents much as is done in humans and large animals is becoming more commonplace due to advances in automatic blood sampling instrumentation (Alf et al., 2013; MacAskill et al., 2019). This, however, does have some limitations, namely the fact that it requires expertise in femoral artery cannulation, a procedure that can only typically be performed twice in small animals (Warnock et al., 2014). For those PET/SPECT research sites without access to this blood sampling technology, manual blood collection is possible and would enable the use of population-based curves, or image-derived input functions can be obtained. Although these would result in quantitative bias vs. the continuous arterial sampling per experiment (MacAskill et al., 2019), they can still allow the researcher to quantify PET data and conclude on which radiotracer candidate is the most promising for translation to higher species. Furthermore, moving a novel radiotracer from chemistry directly into *in vivo* preclinical imaging can also reduce the likelihood of researchers to overlook useful radiotracers. For example, the use of autoradiography techniques for assessment of binding kinetics by varying pre-incubation and washing steps would be unsuitable in evaluating whole-body biodidistribution kinetics and metabolism, essential aspects for assuring the success of a novel radiotracer for *in vivo* imaging. Similarly, even the "no wash" autoradiography method proposed for estimation of specific binding (Patel et al., 2003) would be suboptimal at evaluating a novel radiotracer performance *in vivo* (the ultimate targeted environment). Moreover, the resources allocated for these type of *in vitro*/*ex vivo* experiments require radiolabeling of the radiotracer, deeming these approaches inadequate for prospective screening. Consequently, these techniques are slowly, but consistently, being replaced by preclinical imaging techniques, which are becoming key translational tools for proof-of-mechanism and concept studies (Agdeppa and Spiker, 2009; Van de Bittner et al., 2014) (**Figure 1**). That said, the use of *ex vivo* studies to assess radiotracer metabolism is still unavoidable, given the need to sample organ tissue and blood for analysis (as detailed below).

Another important factor that may explain the reasoning behind using *in vivo* preclinical imaging methods vs. *ex vivo* dissection studies for assessment of radiotracer distribution is that imaging devices are seen as technical refinements, in line with the principles of the three Rs (replacement, reduction and refinement). There are several reasons supporting this view, including the fact that: (1) *in vivo* imaging techniques are less invasive that other techniques; (2) by using the animals as their own controls, the number of animals to be sacrificed is reduced and the statistical power is improved, with consequent scientific benefit; and (3) diagnostic and therapeutic agents can be developed on identical platforms, thus providing a unique straightforward translational paradigm. In fact, small animal imaging has been perceived as an approach with potential to provide a natural bridge to the clinical development by the National Institute of Biomedical Imaging and Bioengineering established by the National Institutes of Health (Koba et al., 2013).

Preclinical *in vivo* imaging can be used early in radiotracer discovery to make modifications of the chemical structure based on the novel radiotracer kinetic behavior, allowing for a faster "tailoring" of the most suitable radiotracer candidate. As discussed throughout this review, moving toward this approach could enable rapid and successful translation of novel brain radiotracers to clinical use. Furthermore, preclinical imaging can alternatively be used later (prior to human studies) to obtain the complete kinetics of the radiotracer, as well as, to estimate dosimetry, in order to identify the dose-limiting organ radiation exposure; information that can be used in the translation to humans. In fact, the recently developed MOBY mice phantoms for estimation of radiation exposure using mice models have made it possible to use preclinical imaging for dosimetry estimates, easing translation into humans (Larsson et al., 2007). Although *ex vivo* biodistribution studies can also be used to estimate dosimetry, they require at least 4-6 times more animals, given that each measurement at a given time point requires sacrificing a group of rodents for tissue harvesting, vs. dynamic *in vivo* imaging of multiple points from a single rodent. The use of preclinical dosimetry for estimation of clinical radiological safety has been a regulatory requirement for several years, albeit some recent discussion has questioned its utility given the first in human studies include dosimetry assessments. It is possible that the development of highly sensitive scanners, e.g., the total-body PET (Cherry et al., 2018), would enable even faster translation to humans by minimizing concerns around radiation dose exposure from novel radiotracers.

Given that PET or SPECT radiotracers should not elicit a pharmacologic effect (owing to the radiotracer principle), a pharmacodynamics response is not measurable. This means the burden of proof lies in the ability to correlate the uptake

with modulated target density. This can be easily accomplished using *in vivo* imaging techniques and therapeutics or genetically modified animals (Agdeppa and Spiker, 2009). Assessment of radiotracer brain penetration can be accomplished by inspecting the time-activity curves and expressing the measured signal as a percentage injected dose over time. The cutoff values for accepting a radiotracer as suitable for CNS imaging based on whole-brain uptake are not consensual. Recently, Van de Bittner et al. (2014) reported the values used in their laboratory to be 0.1% injected dose (ID)/cc for rats and 0.01% ID/cc for non-human primates within 5 min of injection. As mentioned previously, values of brain uptake in rodent and non-human primate of $\geq$ 0.5% have also been suggested as a guideline to yield suitable CNS radiotracers. However history has shown that, in humans, BBB-penetrant radiotracers developed for *in vivo* imaging of the CNS have expressed variable%ID in whole-brain. For example, ^{123}I-PK1119, ^{11}C-DASB and ^{123}I-Iomazenil had a peak %ID in whole-brain of around 2.0% (Versijpt et al., 2000), 4.0% (Lu et al., 2004), and 13% (Dey et al., 1994), respectively. This represents a fairly wide range of radiotracer brain uptake, highlighting that definitive cutoff limits might be difficult to implement. This is because %ID values provide little information about radiotracer kinetic properties and are dependent on a number of factors, including radiotracer free fraction in plasma and time of measurement after injection. Still, cutoffs proposed in the literature, as a result of different groups experience while developing radiotracers, can be a useful first line guidance when screening compounds (e.g., by using *in vitro* methodology reported in **Figure 4** and in Tavares et al. (2012b). Another method proposed to evaluate radiotracer penetration is based on the analysis of the standard uptake values (SUVs). This has the advantage of allowing for comparison across different species and tissues, as it is a measure normalize to injected dose and body weight. An SUV value of 1 will correspond to a radiotracer concentration that would result in uniform distribution of the injected dose in the whole-body. Typically, a peak SUV $>$ 2 is generally desirable for brain imaging (Pike, 2009) (**Table 2**).

Subsequent to demonstrating radiotracer brain penetration, it is important to assess the degree and length of radiotracer retention in the brain. For example, evaluating if the radiotracer has been actively effluxed from the brain. This can be accomplished by imaging animals pretreated with inhibitors of active efflux proteins. Active efflux mechanisms show variation across different species and, similarly to metabolism, can be difficult to control or predict when translating a radiotracer from one species to another. In a study comparing three PET radiotracers in different species, it was found pronounced differences in the brain and brain-plasma concentrations of ^{11}C-Verapamil, ^{11}C-GR205171 and ^{18}F-altanserin with lower brain distribution in rats and guinea pigs compared with humans, monkeys and minipigs. One of the conclusions of that study was that compounds found to be P-gp substrates in rodents are also likely to be substrates in higher species, although this is not a linear predictor of BBB permeability and the compound might still be retained in human brain (Syvänen et al., 2009). In general, the majority of the P-gp substrates are transported to a lower extent by human P-gp compared with mouse or rat P-gp (Yamazaki et al., 2001; Ohe et al., 2003; Katoh et al., 2006; Baltes et al., 2007). However, there are exceptions, for example, cyclosporin A (Katoh et al., 2006; Baltes et al., 2007).

When a radiotracer candidate displays good brain penetration and retention, specific binding to the target can be demonstrated by homologous blocking studies. During these measurements it is important to consider potential blockade of the radiotracer binding in peripheral tissues, resulting in increased free radiotracer in plasma with consequent increase of total brain uptake relative to control. This effect can be corrected by normalizing the radiotracer uptake to metabolite-corrected plasma radiotracer levels or by performing kinetic modeling analysis of the acquired data. Furthermore, heterologous blocking studies can be used to evaluate potential off-target binding and knockout animals can be of value for confirming on-target binding.

Analyzing the time-activity curves from *in vivo* preclinical imaging experiments, can infer the suitability of a radiotracer for human imaging. For example, if the measured time-activity curve slope is near zero, this may be indicative of irreversible binding or very slow kinetics, which is not ideal *in vivo*. Conversely, decreases in binding potential during bolus or bolus plus constant infusion experiments with injection of homologous or heterologous blocking agents midscan represent measurable adequate reversible kinetics (Van de Bittner et al., 2014).

Effective radiotracer design can limit potential problems from troublesome radiometabolites, yet radiotracers resistant to extensive metabolism over the duration of the PET or SPECT imaging session are scarce (Pike, 2009). And as mentioned before, the nature and degree of metabolism varies across species. For example, the metabotropic glutamate receptor 5 (mGluR5) radiotracer ^{18}F-SP203 (Siméon et al., 2007) is rapidly defluorinated in the rat brain and blood as well as in monkey blood, however, shows no defluorination in humans (Brown et al., 2008). A similar trend has been observed with the serotonin type 4 receptors (5HT4) radiotracer, ^{11}C-SB207145, that was successfully translated into humans (Gee et al., 2008; Marner et al., 2009), yet displayed pronounced peripheral metabolism in preclinical species. Therefore, it has been argued that the determination of metabolites in rodents or larger animals (pigs or monkeys) provides suitable data to inform clinical PET studies. The argument is that due to the higher surface-to-volume ratio, the influence of metabolism on the PET quantification of human data is usually overestimated when investigated in experimental animals (Brust et al., 2014). Due to the known species differences, it has been argued that efforts should be made to progress to first in human studies as quickly as possible and some have argued that non-human primate preclinical imaging would be more predictable of radiotracer performance in humans (Van de Bittner et al., 2014), although this might not always represent the truth. In fact, for certain complex CNS targets, it might be that small animal models are more suitable to investigate a novel radiotracer, despite the potential for a faster metabolism. Genetically modified rodent models that express human disorder phenotypes are readily available and produce information that may not be so easily obtained from non-human primates. For example, when developing a novel radiotracer targeting

neuroinflammation or beta-amyloid deposition, conditions that are not present in a healthy brain, it can be difficult to judge the novel radiotracer candidate performance without the use of adequate animal models. Weighing the pros and cons of using different animal species for radiotracer development demonstrates why radiotracer metabolism can be considered one of the parameters most difficult to control during radiotracer discovery, and the one potentially causing the most attrition during this process.

Ideally the metabolism of a novel radiotracer would occur outside the brain and produce less lipophilic radiometabolites, than the parent radiotracer, with poor brain penetration. However, this is not always the case. Thus, at times, the rate at which troublesome radiometabolites cross the BBB into the brain parenchyma and their affinity for the target determines the performance of a radiotracer. For example, the presence of non-troublesome radiometabolites in the brain has been reported for several novel radiotracers developed to image phosphodiesterases type 10A (PDE10A) (Celen et al., 2010; Tu et al., 2011; Celen et al., 2013; Van Laere et al., 2013; Barret et al., 2014b). These studies demonstrate a region-dependent metabolite fraction profile, with the highest fraction in the cerebellum and lowest in the caudate/putamen (the target region) (Celen et al., 2010; Celen et al., 2013). This suggests that the radiometabolite entering the brain does not bind to PDE10A and only gives non-specific signal. Furthermore, signal in the brain from the radiometabolite seems consistent, low and negligibly reflected in the *in vivo* time-activity curves of regions with low densities of PDE10A. These observations have allowed for the successful translation of the novel PDE10A radiotracers from preclinical into clinical research, even with the presence of radiometabolites in the brain (Barret et al., 2014b).

As stated throughout this review, a multifactorial and complex issue that causes attrition throughout the radiotracer development pipeline is species differences. Several views on this topic have been largely discussed in the literature. Some defend moving the novel brain radiotracer directly into non-human primate without small animal imaging, to minimize the attrition rate when translating to humans. This view is supported by data demonstrating a close homology between, for example, amino acid content in P-gp in humans compared with non-human primates (93% homology between humans and rhesus monkey, vs. only 85% between human and rat) (Syvänen et al., 2009). Furthermore, target density in brain might be significantly different in rat compared with non-human primate and human. For example, in the non-human primate brain, the density of noradrenaline transporters (NAT) in the locus coeruleus is around 220 fmol/mg, while in rodents the NAT density in the same brain region is around 1500 fmol/mg (Tejani-Butt, 1992; Smith et al., 2006). Thus, rat brain has seven times more NAT binding sites than non-human primate brain. This has been pointed out as one of the potential reasons underlying the different imaging profile measured with ^{123}I-NKJ64 (a SPECT radiotracer candidate for imaging of NAT in brain) in rats compared to baboons (Tavares et al., 2011; Tavares et al., 2012a). It is worth noting that that the density of NATs in human locus coereleus is similar to the one measure in non-human primates (Ordway et al., 1997). Consequently, although rat data demonstrated that ^{123}I-NKJ64 held promise for imaging of NAT in brain, data collected in baboons showed a lack of specific signal in target regions and precluded the translation of this radiotracer into humans (**Figure 3**, Case Study 2). Nonetheless, there might be instances where the use of rodents may be preferred when developing novel radiotracers. The mouse remains the premier animal model for biomedical research because mice have a short reproductive cycle, can be easily genetically modified and are easy to maintain. Furthermore, there is high homology between the human and the mouse genomes, which facilitates the construction of animal models of human disease at a fast rate and with high specificity (Niu and Chen, 2014). There are multiple transgenic animals containing mutations for human disease for with a specific gene has been identified, including for example, Parkinson's disease, Huntington's disease, Alzheimer's disease, epilepsy and multiple sclerosis (Furlan et al., 2009; Casteels et al., 2014). Also, the introduction of the "humanized mouse" models may serve as a preclinical bridge for translating data from animal models into humans (Niu and Chen, 2014). Rodent models may be the best preclinical alternative available when developing novel radiotracer targeting neuroinflammatory human brain disorders, such as multiple sclerosis, or brain disorders that result from abnormal protein accumulation that is not observed in the healthy brain, given that rodent models are reliable and predictive models of human disorders. This does not mean that non-human primate models of brain disorders are not available, however, they are often chemically- or vector-derived models and come at a higher cost, which may add to an already expensive development process. That being said, the use of small animals in psychiatry is limited, especially when investigating pathways without homology in rodents, e.g., the expanded prefrontal cortex of the human brain (Casteels et al., 2014). Furthermore, the metabolism in lower species such as rodents may not directly forecast metabolism in humans, as shown on various publications, because it tends to be faster in rodents compared with humans. Species differences are unavoidable, however, as outline above, preclinical radiometabolism studies can still provide useful information during radiotracer development, because preclinical studies enable organ collection for direct quantification of radiometabolism in tissue – something that is not feasible in humans. Importantly, preclinical rodent studies often present the "worst case scenario" due to rapid metabolism of these species and can enable comparative analysis of analog in a compound library prior to translation to humans.

In addition to the pitfalls and challenges highlighted above, the majority of the preclinical *in vivo* imaging studies are conducted under anesthesia. The list of publications demonstrating the impact of anesthetic agents on radiotracer uptake and kinetics is vast [see for example: (Lee et al., 2005; Fueger et al., 2006; Hildebrandt et al., 2008; Giron, 2009)], so this will not be discussed in detail here, but it is worth to point out the need to be aware of this potential confounder when interpreting *in vivo* preclinical imaging data. Another important aspect that has also been extensively reviewed is the need to accurately control the levels of administered radiotracer mass. If the radiotracer principle is key to PET or SPECT imaging in human subjects,

in preclinical imaging it is imperative that radiotracer levels are controlled owing to the smaller animal body sizes. An example would be the setoronin type 4 receptor (5-HT4) radiotracers, ^{11}C-SB207145 and ^{18}F-MNI698, where microgram per kilogram mass doses were sufficient to induce non-negligible receptor occupancy (Madsen et al., 2011; Tavares A. et al., 2014). These radiotracers were still useful for preclinical and clinical PET imaging of 5-HT4 because the molar activity was sufficiently high, thus respecting the radiotracer principle. However, these cautionary mass-effect studies highlight the importance of quantifying and respecting the molar activity limits to enable high sensitivity PET imaging. With the recent development of total-body PET human systems (Cherry et al., 2018), the molar activity limits might be less restrictive owing to a gain in instrumentation sensitivity, which would in turn require low injected doses of the radiotracer. Notwithstanding, researchers should always be mindful of the radiotracer principle, especially when developing novel PET or SPECT brain radiotracers.

In summary, at this stage of radiotracer development, controversies arise when discussing which animal species to use and good arguments from each side of the fence suggest that a case-by-case analysis is necessary when deciding how to progress in the radiotracer development pipeline. The use of non-human primates can provide the most insightful and "predictive" information prior to human studies, however, there are instances when investigating specific CNS targets where the use of genetically engineering rodent models can be more useful than non-human primates in assessing radiotracer performance. There is, however, a growing consensual view that moving straight to *in vivo* preclinical imaging and skipping *in vitro*/*ex vivo* testing with the radiolabeled compound is the most efficient way to proceed during radiotracer development (**Figures 1**, **5**). Importantly, the process of developing radiotracers is iterative and failure at some stage can lead back to an earlier stage, as illustrated in **Figure 5**.

Proof-of-Concept in Humans

Once a novel radiotracer has passed through preclinical testing and shows promising results, it will enter the final step in radiotracer discovery/development, i.e., proof-of-concept in humans with subsequent clinical trials. To successfully obtain permission to move a radiotracer from preclinical to clinical use it is important to transition from a research-grade radiochemical

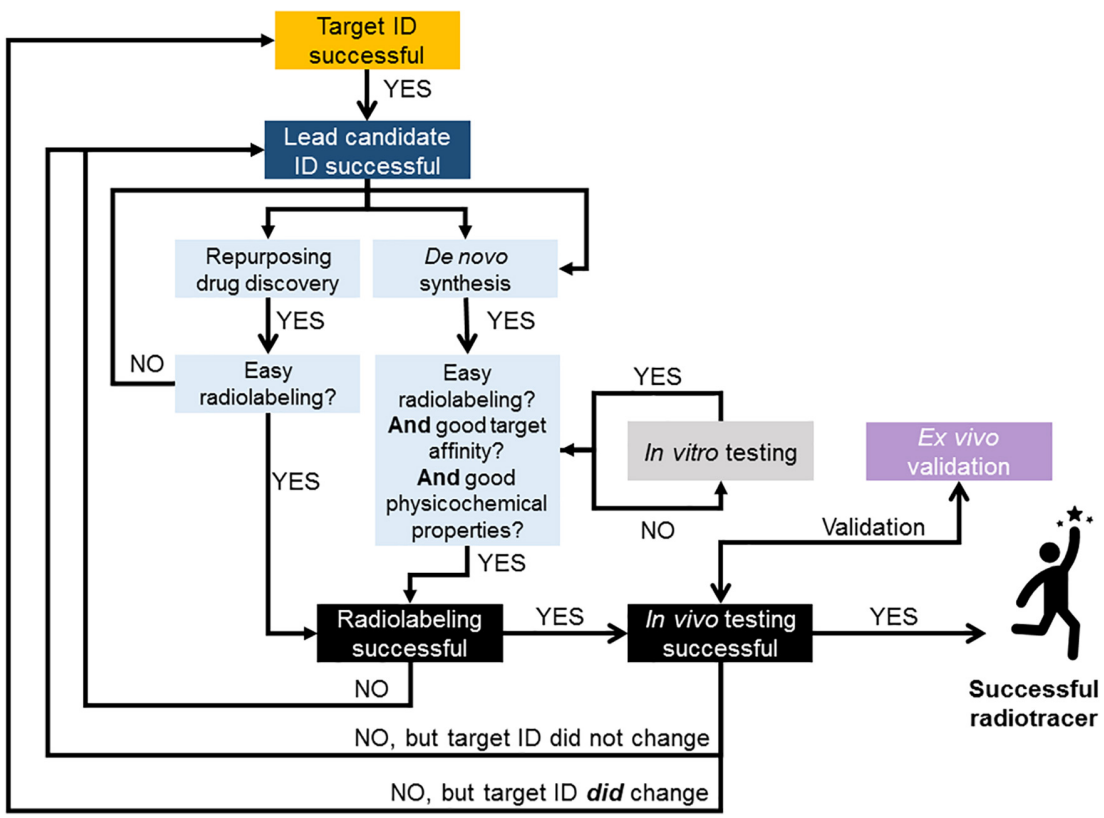

FIGURE 5 | Flow chart illustrating suggested approach to radiotracer discovery and development. Decision points based on literature reviewed in this paper and experience in brain radiotracer development. This illustrates the iterative nature of the process and provides guidance on strategies for successful translation of novel compounds into humans. When possible, repurposing compounds from drug discovery pipelines as potential radiotracer candidates can be advantageous to rapidly and successfully develop new PET and SPECT radiotracers for imaging the human brain. In case of *de novo* chemistry, all *in vitro* testing should be conducted with the non-radioactive library of compounds. This could be done by employing high throughput screening methods for measuring novel compounds' physicochemical properties (e.g., **Figure 4**) and affinity for target. The removal of *in vitro* testing of the radiolabeled compound (as per **Figure 1**) will also further accelerate the process.

to a radiopharmaceutical for which higher standards of product quality must be met (Brust et al., 2014). The list of aspects to consider during this translational process is long and has been extensively reviewed elsewhere (Verbruggen et al., 2008; Agdeppa and Spiker, 2009; Elsinga et al., 2010; VanBrocklin, 2010). Radiation safety, toxicology issues, quality control, licensing and regulatory control are some of the aspects to consider. The regulatory control is often the major bottleneck in the translation process from preclinical to clinical research and has become increasingly restrictive over the last two decades. For example, currently the typical time between the successful radiolabeling of a novel radiotracer and first human use can vary between 5 and 10 years, while at the beginning of neuroreceptor imaging with PET or SPECT this transition was much shorter, in the range of 1–2 years (Brust et al., 2014). Typically the factors contributing to the limited number of approved radiotracers can be classified in three major categories: radiotracer discovery and development, regulatory aspects and clinical development (VanBrocklin, 2010). Another hurdle in transitioning from animal research to human studies relies on the fact that the radiotracer may fail and be deemed unsuitable for *in vivo* imaging of the human brain. However, even if the radiotracer is not further developed into a radiopharmaceutical, it may still find widespread use in preclinical studies to investigate animal models of diseases or new drugs. Thus, one should remain optimistic when discovering and developing novel radiotracers for brain imaging, as with persistence and ever-improving preclinical assessment of radiotracers, the translation gap between animal and human research is rapidly tightening.

Proposed Approach for Rapid Translation of Radiotracers From Animal to Human Research

Developing novel radiotracers for brain imaging is a challenging process, requiring multidisciplinary teams, in order to gather the knowledge from marketing and target identification, disease-related biological mechanisms, chemical synthesis, radiolabeling, and image acquisition and analysis. This process can be lengthy and costly, and circumventing failure is difficult when translating from animal research into clinical use. Several approaches and philosophies have been suggested for improving efficiency of the radiotracer discovery and development pipeline (Nunn, 2007; Salvadori, 2008; Agdeppa and Spiker, 2009; Van de Bittner et al., 2014). An alternative proposed based on the literature reviewed in this paper as well as on current trends and previous experience while developing novel radiotracers is presented as a flow chart in **Figure 5**.

CONCLUDING REMARKS

Biomarkers can be classified into three classes: type 0 biomarkers along the continuum of the natural history of the disorder; type 1 biomarkers for detecting therapeutic drug's mechanisms of action; and type 2 biomarkers that are equivalent to surrogate end points (Frank and Hargreaves, 2003). PET and SPECT imaging target all three types of biomarkers. Hence the potential of these imaging modalities is phenomenal alongside concept of personalized medicine, as well as and the key supportive role they can have in the process of novel therapeutics discovery and development. The development of novel radiotracers and subsequent rapid and successful translation into humans is pivotal to realize the potential of PET and SPECT imaging as useful biomarkers. This translational process can be optimized and efficiently shorten with the aim to move into clinical use as soon as possible. A suggested approach to assist with these goals has been proposed in this manuscript, essential aspects to consider when developing novel radiotracers for brain imaging were highlighted and proposed solutions or alternatives, when available, were described.

AUTHOR CONTRIBUTIONS

RS, GT, and AT made substantial contributions to the manuscript construction, participated in the drafting of the manuscript, approved the final version of the manuscript, and agreed to be accountable for all aspects of this work. All authors contributed to the article and approved the submitted version.

FUNDING

The British Heart Foundation (BHF) was greatly acknowledged for providing funding toward establishment of the preclinical PET/CT laboratory at the University of Edinburgh (RE/13/3/30183) and funding support to AT (FS/19/34/34354). RS was funded by the SPRINT-MND studentship program supported by the Chief Scientist Office (CSO).

REFERENCES

Abi-Dargham, A., Gandelman, M., Zoghbi, S. S., Laruelle, M., Baldwin, R. M., Randall, P., et al. (1995). Reproducibility of SPECT measurement of benzodiazepine receptors in human brain with iodine-123-iomazenil. *J. Nuclear Med.* 36, 167–175.

Abi-Dargham, A., Laruelle, M., Seibyl, J., Rattner, Z., Baldwin, R. M., Zoghbi, S. S., et al. (1994). SPECT measurement of benzodiazepine receptors in human brain with iodine-123-iomazenil: kinetic and equilibrium paradigms. *J. Nuclear Med.* 35, 228–238.

Agdeppa, E. C., and Spiker, M. E. A. (2009). Review of imaging agent development. *J. Am. Assoc. Pharm. Sci.* 11, 286–299. doi: 10.1208/s12248-009-9104-5

Alavi, A., and Basu, S. (2008). Planar and SPECT imaging in the era of PET and PET-CT: can it survive the test of time? *Eur. J. Nuclear Med. Mol. Imag.* 35, 1554–1559. doi: 10.1007/s00259-008-0813-2

Alf, M. F., Martić-Kehl, M. I., Schibli, R., and Krämer, S. D. (2013). FDG kinetic modeling in small rodent brain PET: optimization of data acquisition and analysis. *EJNMMI Res.* 3:61. doi: 10.1186/2191-219X-3-61

Baltes, S., Gastens, A. M., Fedrowitz, M., Potschka, H., Kaever, V., and Löscher, W. (2007). Differences in the transport of the antiepileptic drugs phenytoin, levetiracetam and carbamazepine by human and mouse P-glycoprotein. *Neuropharmacology* 52, 333–346. doi: 10.1016/j.neuropharm.2006.07.038

Barret, O., Hannestad, J., Vala, C., Alagille, D., Tavares, A., Laruelle, M., et al. (2015). Characterization in humans of 18F-MNI-444, a PET radiotracer

for brain adenosine 2A receptors. *J. Nuclear Med.* 56, 586–591. doi: 10.2967/jnumed.114.152546

Barret, O., Hannestad, J., Alagille, D., Vala, C., Tavares, A., Papin, C., et al. (2014a). Adenosine 2A receptor occupancy by tozadenant and preladenant in rhesus monkeys. *J. Nuclear Med.* 55, 1712–1718. doi: 10.2967/jnumed.114.142067

Barret, O., Thomae, D., Tavares, A., Alagille, D., Papin, C., Waterhouse, R., et al. (2014b). *In Vivo* Assessment and dosimetry of 2 novel PDE10A PET radiotracers in humans: ^{18}F-MNI-659 and ^{18}F-MNI-654. *J. Nuclear Med.* 55, 1297–1304. doi: 10.2967/jnumed.113.122895

Barth, V., and Need, A. (2014). Identifying novel radiotracers for pet imaging of the brain: application of LC-MS/MS to tracer identification. *ACS Chem. Neurosci.* 5, 1148–1153. doi: 10.1021/cn500072r

Berry, A. S., Shah, V. D., Furman, D. J., White, R. L., Baker, S. L., O'Neil, J. P., et al. (2018). Dopamine synthesis capacity is associated with D2/3 receptor binding but not dopamine release. *Neuropsychopharmacology* 43, 1201–1211. doi: 10.1038/npp.2017.180

Blair, A., Stevenson, L., Dewar, D., Pimlott, S. L., and Sutherland, A. (2013). Structure-activity relationships of novel iodinated quinoline-2-carboxamides for targeting the translocator protein. *Med. Chem. Commun.* 4, 1461–1466. doi: 10.1039/c3md00249g

Booij, J., Habraken, J. B. A., Bergmans, P., Tissingh, G., Winogrodzka, A. C. H., Wolters, E., et al. (1998). Imaging of dopamine transporters with iodine-123-FP-CIT SPECT in healthy controls and patients with Parkinson's disease. *J. Nuclear Med.* 39, 1879–1884.

Brandt, M., Cardinale, J., Aulsebrook, M. L., Gasser, G., and Mindt, T. L. (2018). An overview of PET radiochemistry, Part 2: radiometals. *J. Nuclear Med.* 59, 1500–1506. doi: 10.2967/jnumed.117.190801

Brooks, D. (2005). Positron emission tomography and single-photon emission computed tomography in central nervous system drug development. *NeuroRx* 2, 226–236. doi: 10.1602/neurorx.2.2.226

Brown, A. K., Kimura, Y., Zoghbi, S. S., Siméon, F. G., Liow, J.-S., Kreisl, W. C., et al. (2008). Metabotropic glutamate subtype 5 receptors are quantified in the human brain with a novel radioligand for PET. *J. Nuclear Med.* 49, 2042–2048. doi: 10.2967/jnumed.108.056291

Brust, P., van den Hoff, J., and Steinbach, J. (2014). Development of ^{18}F-labelled radiotracers for neuroreceptor imaging with positron emission tomography. *Neurosci. Bull.* 30, 777–811. doi: 10.1007/s12264-014-1460-6

Casteels, C., Zaidi, H., and Laere, K. V. (2014). "Applications of small-animal imaging in neurology and psychiatry," in *Molecular Imaging of Small Animals*, ed. H. Zaidi (New York, NY: Springer), 517–546. doi: 10.1007/978-1-4939-0894-3_19

Catafau, A. M., Pérez, V., Penengo, M. M., Bullich, S., Danús, M., Puigdemont, D., et al. (2005). SPECT of serotonin transporters using ^{123}I-ADAM: optimal imaging time after bolus injection and long-term test-retest in healthy volunteers. *J. Nuclear Med.* 48, 1301–1309.

Celen, S., Koole, M., De Angelis, M., Sannen, I., Chitneni, S. K., Alcazar, J., et al. (2010). Preclinical Evaluation of ^{18}F-JNJ41510417 as a radioligand for PET imaging of phosphodiesterase-10A in the Brain. *J. Nuclear Med.* 51, 1584–1591. doi: 10.2967/jnumed.110.077040

Celen, S., Koole, M., Ooms, M., De Angelis, M., Sannen, I., Cornelis, J., et al. (2013). Preclinical evaluation of [^{18}F]JNJ42259152 as a PET tracer for PDE10A. *Neuroimage* 82, 13–22. doi: 10.1016/j.neuroimage.2013.04.123

Cherry, S. R., Jones, T., Karp, J. S., Qi, J., Moses, W. W., and Badawi, R. D. (2018). Total-Body PET: maximizing sensitivity to create new opportunities for clinical research and patient care. *J. Nuclear Med.* 59, 3–12. doi: 10.2967/jnumed.116.184028

Clark, D. E. (2003). *In silico* prediction of blood-brain barrier permeation. *Drug Discov. Today* 8, 927–933. doi: 10.1016/s1359-6446(03)02827-7

Constantinescu, C. C., Tresse, C., Zheng, M., Gouasmat, A., Carroll, V. M., Mistico, L., et al. (2019). Development and in vivo preclinical imaging of fluorine-18-labeled synaptic vesicle protein 2A (SV2A) PET Tracers. *Mol. Imaging Biol.* 21, 509–518. doi: 10.1007/s11307-018-1260-5

Cook, N. (1996). Scintillation proximity assay: a versatile high-throughput screening technology. *Drug Discov. Today* 1, 287–294. doi: 10.1016/1359-6446(96)10026-x

de Kemp, R. A., Epstein, F. H., Catana, C., Tsui, B. M. W., and Ritman, E. L. (2010). Small-animal molecular imaging methods. *J. Nuclear Med.* 51, 18S–32S.

De Picker, L., Ottoy, J., Verhaeghe, J., Deleye, S., Wyffels, L., Fransen, E., et al. (2019). State-associated changes in longitudinal [18F]-PBR111 TSPO PET imaging of psychosis patients: evidence for the accelerated ageing hypothesis? *Brain Behav. Immun.* 77, 46–54. doi: 10.1016/j.bbi.2018.11.318

Dey, H. M., Seibyl, J. P., Stubbs, J. B., Zoghbi, S. S., Baldwin, R. M., Smith, E. O., et al. (1994). Human biodistribution and dosimetry of the SPECT benzodiazepine receptor radioligand Iodine-123-lomazenil. *J. Nuclear Med.* 35, 399–404.

Dongen, G. A. M. S. V., Poot, A. J., and Vugts, D. J. (2012). PET imaging with radiolabeled antibodies and tyrosine kinase inhibitors: immuno-PET and TKI-PET. *Tumour Biol.* 33, 607–615. doi: 10.1007/s13277-012-0316-4

Elsinga, P., Todde, S., Penuelas, I., Meyer, G., Farstad, B., Faivre-Chauvet, A., et al. (2010). Guidance on current good radiopharmacy practice (cGRPP) for the small-scale preparation of radiopharmaceuticals. *Eur. J. Nuclear Med. Mol. Imag.* 37, 1049–1062. doi: 10.1007/s00259-010-1407-3

Ferré, S., Casadó, V., Devi, L. A., Filizola, M., Jockers, R., Lohse, M. J., et al. (2014). G Protein-coupled receptor oligomerization revisited: functional and pharmacological perspectives. *Pharmacol. Rev.* 66, 413–434. doi: 10.1124/pr.113.008052

Frank, R., and Hargreaves, R. (2003). Clinical biomarkers in drug discovery and development. *Nat. Rev. Drug Discov.* 2, 566–580. doi: 10.1038/nrd1130

Frank, R., Langstrom, B., Antoni, G., Montalto, M., Agdeppa, E., Mendizabal, M., et al. (2007). The imaging continuum: bench to biomarkers to diagnostics. *J. Lab. Compounds Radiopharm.* 50, 746–769. doi: 10.1002/jlcr.1444

Fueger, B. J., Czernin, J., Hildebrandt, I., Tran, C., Halpern, B. S., Stout, D., et al. (2006). Impact of animal handling on the results of ^{18}F-FDG PET studies in mice. *J. Nuclear Med.* 47, 999–1006.

Fujita, M., Ichise, M., van Dyck, C. H., Zoghbi, S. S., Tamagnan, G., Mukhin, A. G., et al. (2003). Quantification of nicotinic acetylcholine receptors in human brain using [123I]5-I-A-85380 SPET. *Eur. J. Nucl. Med. Mol. Imag.* 30, 1620–1629. doi: 10.1007/s00259-003-1320-0

Furlan, R., Cuomo, C., and Martino, G. (2009). "Animal models of multiple sclerosis," in *Neural Cell Transplantation: Methods and Protocols*, eds D. Gordon and N. J. Scolding (Totowa, NJ: Humana Press), 157–173.

Gee, A. D., Martarello, L., Passchier, J., Wishart, M., Parker, C., Matthews, J., et al. (2008). Synthesis and evaluation of [^{11}C]SB207145 as the first *in vivo* serotonin 5-HT$_4$ receptor radioligand for PET imaging in man. *Curr. Radiopharm.* 1, 110–114. doi: 10.2174/1874471010801020110

George, S. R., O'Dowd, B. F., and Lee, S. P. G. - (2002). Protein-coupled receptor oligomerization and its potential for drug discovery. *Nat. Rev. Drug Discov.* 1, 808–820. doi: 10.1038/nrd913

Gilfillan, L., Blair, A., Morris, B. J., Pratt, J. A., Schweiger, L., Pimlott, S., et al. (2013). Synthesis and biological evaluation of novel 2,3-dihydro-1H-1,5-benzodiazepin-2-ones; potential imaging agents of the metabotropic glutamate 2 receptor. *Med. Chem. Commun.* 4, 1118–1123. doi: 10.1039/c3md00110e

Ginovart, N., Wilson, A. A., Meyer, J. H., Hussey, D., and Houle, S. (2001). Positron emission tomography quantification of [(11)C]-DASB binding to the human serotonin transporter: modeling strategies. *J. Cereb. Blood Flow Metab.* 21, 1342–1353. doi: 10.1097/00004647-200111000-00010

Giron, M. (2009). Radiopharmaceutical pharmacokinetics in animals: critical considerations. *Q. J. Nuclear Med. Mol. Imag.* 53, 359–364.

Haberkorn, U., and Eisenhurt, M. (2005). Molecular imaging and therapy - a programme based on the development of new biomolecules. *Eur. J. Nuclear Med. Mol. Imag.* 32, 1354–1359. doi: 10.1007/s00259-005-1924-7

Hildebrandt, I. J., Su, H., and Weber, W. A. (2008). Anesthesia and other considerations for in vivo imaging of small animals. *ILAR J.* 49, 17–26. doi: 10.1093/ilar.49.1.17

Innis, R. B., Cunningham, V. J., Delforge, J., Fujita, M., Gjedde, A., Gunn, R. N., et al. (2007). Consensus nomenclature for in vivo imaging of reversibly binding radioligands. *J. Cereb. Blood Flow Metab.* 27, 1533–1539. doi: 10.1038/sj.jcbfm.9600493

Katoh, M., Suzuyama, N., Takeuchi, T., Yoshitomi, S., Asahi, S., and Tokoi, T. (2006). Kinetic analyses for species differences in P-glycoprotein-mediated drug transport. *J. Pharm. Sci.* 95, 2673–2683. doi: 10.1002/jps.20686

Kemp, R., Epstein, F., Catana, C., Tsui, B., and Ritman, E. (2010). Small-animal molecular imaging methods. *J. Nuclear Med.* 51, 18S–32S.

Klunk, W. E., Engler, H., Nordberg, A., Wang, Y., Blomqvist, G., Holt, D. P., et al. (2004). Imaging Brain amyloid in Alzheimer's disease with pittsburgh compound-B. *Ann. Neurol.* 55, 306–319.

Klunk, W. E., and Mathis, C. A. (2008). The future of amyloid-beta imaging: a tale of radionuclides and tracer proliferation. *Curr. Opin. Neurol.* 21, 683–687. doi: 10.1097/wco.0b013e3283168e1a

Knešaurek, K., Warnock, G., Kostakoglu, L., and Burger, C. (2018). Comparison of standardized uptake value ratio calculations in amyloid positron emission tomography brain imaging. *World J. Nuclear Med.* 17, 21–26. doi: 10.4103/wjnm.wjnm_5_17

Koba, W., Jelicks, L. A., and Fine, E. J. (2013). MicroPET/SPECT/CT imaging of small animal models of disease. *Am. J. Pathol.* 182, 320–324.

Kropholler, M. A., Boellaard, R., Schuitemaker, A., van Berckel, B. N., Luurtsema, G., Windhorst, A. D., et al. (2005). Development of a tracer kinetic plasma input model for (R)-[11C]PK11195 brain studies. *J. Cereb. Blood Flow Metab.* 25, 842–851. doi: 10.1038/sj.jcbfm.9600092

Kumakura, Y., Vernaleken, I., Gründer, G., Bartenstein, P., Gjedde, A., and Cumming, P. (2005). PET studies of net blood-brain clearance of FDOPA to human brain: age-dependent decline of [18F]fluorodopamine storage capacity. *J. Cereb. Blood Flow Metab.* 25, 807–819. doi: 10.1038/sj.jcbfm.9600079

Kyono, K., Takashima, T., Katayama, Y., Kawasaki, T., Zochi, R., Gouda, M., et al. (2011). Use of [18F]FDOPA-PET for in vivo evaluation of dopaminergic dysfunction in unilaterally 6-OHDA-lesioned rats. *EJNMMI Res.* 1:25. doi: 10.1186/2191-219X-1-25

Laere, K. V., Ahmad, R. U., Hudyana, H., Dubois, K., Schmidt, M. E., Celen, S., et al. (2013). Quantification of ^{18}F-JNJ-42259152, a novel phosphodiesterase 10A PET tracer: kinetic modeling and test-retest study in human brain. *J. Nuclear Med.* 54, 1285–1293. doi: 10.2967/jnumed.112.118679

Larsson, E., Strand, S., Ljungberg, M., and Jönsson, B. (2007). Mouse S-factors based on Monte Carlo simulations in the anatomical realistic Moby phantom for internal dosimetry. *Cancer Biother. Radiopharm.* 22, 438–442. doi: 10.1089/cbr.2006.320

Laruelle, M., Wallace, E., Seibyl, J. P., Baldwin, R. M., Zea-Ponce, Y., Zoghbi, S. S., et al. (1994). Graphical, kinetic, and equilibrium analyses of in vivo [123I] beta-CIT binding to dopamine transporters in healthy human subjects. *J. Cereb. Blood Flow Metab.* 14, 982–994. doi: 10.1038/jcbfm.1994.131

Lazareno, S. (2001). Quantification of receptor interactions using binding methods. *J. Recept. Signal Transd. Res.* 21, 139–165. doi: 10.1081/rrs-100107426

Lee, K.-H., Ko, B.-H., Paik, J.-Y., Jung, K.-H., Choe, Y. S., Choi, Y., et al. (2005). Effects of anesthetic agents and fasting duration on ^{18}F-fdg biodistribution and insulin levels in tumor-bearing mice. *J. Nuclear Med.* 46, 1531–1536.

Lipinski, C., Lombardo, F., Dominy, B., and Feeney, P. (2001). Experimental and computational approaches to estimate solubility and permeability in drug discovery and development settings. *Adv. Drug Deliv. Rev.* 46, 3–26. doi: 10.1016/s0169-409x(96)00423-1

Lu, J.-Q., Ichise, M., Liow, J.-S., Ghose, S., Vines, D., and Innis, R. B. (2004). Biodistribution and radiation dosimetry of the serotonin transporter ligand^{11}C-DASB determined from human whole-body PET. *J. Nuclear Med.* 45, 1555–1559.

MacAskill, M. G., Walton, T., Williams, L., Morgan, T. E. F., Alcaide-Corral, C. J., Dweck, M. R., et al. (2019). Kinetic modelling and quantification bias in small animal PET studies with [^{18}F]AB5186, a novel 18 kDa translocator protein radiotracer. *PLoS One* 14:e0217515. doi: 10.1371/journal.pone.0217515

Madsen, K., Marner, L., Haahr, M., Gillings, N., and Knudsen, G. M. (2011). Mass dose effects and in vivo affinity in brain PET receptor studies - a study of cerebral 5-HT$_4$ receptor binding with [^{11}C]SB207145. *Nuclear Med. Biol.* 38, 1085–1091.

Mariani, G., Bruselli, L., and Duatti, A. (2008). Is PET always an advantage versus planar and SPECT imaging? *Eur. J. Nuclear Med. Mol. Imag.* 35, 1560–1565. doi: 10.1007/s00259-008-0814-1

Mark, C., Bornatowicz, B., Mitterhauser, M., Hendl, M., Nics, L., Haeusler, D., et al. (2013). Development and automation of a novel NET-PET tracer: [^{11}C]Me@APPI. *Nuclear Med. Biol.* 40, 295–303.

Marner, L., Gillings, N., Comley, R. A., Baaré, W. F. C., Rabiner, E. A., Wilson, A. A., et al. (2009). Kinetic Modeling of ^{11}C-SB207145 binding to 5-HT$_4$ receptors in the human brain in vivo. *J. Nuclear Med.* 50, 900–908. doi: 10.2967/jnumed.108.058552

McLean, D., Cooke, M. J., Wang, Y., Green, D., Fraser, P. E., George-Hyslop, P. S., et al. (2012). Anti-Amyloid-b-mediated positron emission tomography imaging in Alzheimer's disease mouse brains. *PLoS One* 7:e51958. doi: 10.1371/journal.pone.0051958

Mercier, J., Provins, L., and Valade, A. (2017). Discovery and development of SV2A PET tracers: potential for imaging synaptic density and clinical applications. *Drug Discov. Today Technol.* 25, 45–52. doi: 10.1016/j.ddtec.2017.11.003

Meyer, P. T., Sattler, B., Winz, O. H., Fundke, R., Oehlwein, C., Kendziorra, K., et al. (2008). Kinetic analyses of [123I]IBZM SPECT for quantification of striatal dopamine D2 receptor binding: a critical evaluation of the single-scan approach. *Neuroimage* 42, 548–558. doi: 10.1016/j.neuroimage.2008.05.023

Niu, G., and Chen, X. (2014). "Applications of small-animal molecular imaging in drug development," in *Molecular Imaging of Small Animals*, ed. H. Zaidi (New York, NY: Springer), 715–752. doi: 10.1007/978-1-4939-0894-3_24

Norbury, R., Travis, M. J., Erlandsson, K., Waddington, W., Owens, J., Ell, P. J., et al. (2004). SPET imaging of central muscarinic receptors with (R,R)[123I]-I-QNB: methodological considerations. *Nuclear Med. Biol.* 31, 583–590. doi: 10.1016/j.nucmedbio.2004.01.003

Nordberg, A. (2014). "PET tracers for Beta-Amyloid and other proteinpathies," in *PET and SPECT in Neurobiological Systems*, eds R. A. J. O. Dierckx, A. Otte, E. F. Vries, A. V. Waarde, and P. G. M. Luiten (Berlin: Springer), 199–212. doi: 10.1007/978-3-642-42014-6_8

Nunn, A. D. (2006a). From clinical trials to prescriptions. *J. Nuclear Med.* 47, 36N–37N.

Nunn, A. D. (2006b). The cost of developing imaging agents for routine clinical use. *Investig. Radiol.* 41, 206–212. doi: 10.1097/01.rli.0000191370.52737.75

Nunn, A. D. (2007). Molecular imaging and personalized medicine: an uncertain future. *Cancer Biother. Radiopharm.* 22, 722–739. doi: 10.1089/cbr.2007.0417

Ohe, T., Sato, M., Tanaka, S., Fujino, N., Hata, M., Shibata, Y., et al. (2003). Effect of P-glycoprotein-mediated efflux on cerebrospinal fluid/plasma concentration ratio. *Drug Metab. Disposit.* 31, 1251–1254. doi: 10.1124/dmd.31.10.1251

Ordway, G. A., Stockmeier, C. A., Cason, G. W., and Klimek, V. (1997). Pharmacology and distribution of norepinephrine transporters in the human *Locus coeruleus* and Raphe Nuclei. *J. Neurosci.* 17, 1710–1719. doi: 10.1523/jneurosci.17-05-01710.1997

Ottobrini, L., Ciana, P., Biserni, A., Lucignani, G., and Maggi, A. (2006). Molecular imaging: a new way to study molecular processes in vivo. *Mol. Cell. Endocrinol.* 246, 69–75. doi: 10.1016/j.mce.2005.11.013

Owen, D. R., Howell, O. W., Tang, S.-P., Wells, L. A., Bennacef, I., Bergstrom, M., et al. (2010). Two binding sites for [^{3}H]PBR28 in human brain: implications for TSPO PET imaging of neuroinflammation. *J. Cereb. Blood Flow Metab.* 30, 1608–1618. doi: 10.1038/jcbfm.2010.63

Owen, D. R., Yeo, A. J., Gunn, R. N., Song, K., Wadsworth, G., Lewis, A., et al. (2012). An 18-kDa Translocator Protein (TSPO) polymorphism explains differences in binding affinity of the PET radioligand PBR28. *J. Cereb. Blood Flow Metab.* 32, 1–5. doi: 10.1038/jcbfm.2011.147

Owen, D. R. J., Gunn, R. N., Rabiner, E. A., Bennacef, I., Fujita, M., Kreisl, W. C., et al. (2011). Mixed-affinity binding in humans with 18-kDa translocator protein ligands. *Journal of Nuclear Medicine.* 52, 24–32. doi: 10.2967/jnumed.110.079459

Patel, S., and Gibson, R. (2008). In vivo site-directed radiotracers: a mini-review. *Nuclear Med. Biol.* 35, 805–815. doi: 10.1016/j.nucmedbio.2008.10.002

Patel, S., Hamill, T., Hostetler, E., Burns, H. D., and Gibson, R. E. (2003). An *In Vitro* assay for predicting successful imaging radiotracers. *Mol. Imag. Biol.* 5, 65–71. doi: 10.1016/s1536-1632(03)00041-6

Philippe, C., Nics, L., Zeilinger, M., Kuntner, C., Wanek, T., Mairinger, S., et al. (2013a). Preclinical in vitro & in vivo evaluation of [^{11}C]SNAP-7941 - the first PET tracer for the melanin concentrating hormone receptor 1. *Nuclear Med. Biol.* 40, 919–925.

Philippe, C., Nics, L., Zeilinger, M., Schirmer, E., Spreitzer, H., Karanikas, G., et al. (2013b). Preparation and first preclinical evaluation of [^{18}F]FE@SNAP: a potential PET tracer for the melanin-concentrating hormone receptor-1 (MCHR1). *Sci. Pharm.* 81, 625–639. doi: 10.3797/scipharm.1306-02

Pichler, V., Berroterán-infante, N., Philippe, C., Vraka, C., Klebermass, E. M., Balber, T., et al. (2018). An Overview of PET radiochemistry, Part 1: the covalent labels (18)F, (11)C, and (13)N. *J. Nuclear Med.* 59, 1350–1354. doi: 10.2967/jnumed.117.190793

Pike, V. W. (2009). PET radiotracers: crossing the blood-brain barrier and surviving metabolism. *Trends Pharmacol. Sci.* 30, 431–440. doi: 10.1016/j.tips.2009.05.005

Pritchard, J., Jurima-Romet, M., Reimer, M., Mortimer, E., Rolfe, B., and Cayen, M. (2003). Making better drugs: decision gates in non-clinical drug development. *Nat. Rev. Drug Discov.* 2, 542–553. doi: 10.1038/nrd1131

Qume, M. (1999). "Overview of ligand-receptor binding techniques," in *Receptor Binding Techniques. 106*, ed. M. Keen (Totowa, NJ: Humana Press).

Rami-Mark, C., Bornatowicz, B., Fink, C., Otter, P., Ungersboeck, J., Vraka, C., et al. (2013). Synthesis, radiosynthesis and first in vitro evaluation of novel PET-tracers for the dopamine transporter: [^{11}C]IPCIT and [^{18}F]FE@IPCIT. *Bioorgan. Med. Chem.* 21, 7562–7569. doi: 10.1016/j.bmc.2013.10.046

Ruth, T. (2009). The uses of radiotracers in the life sciences. *Rep. Prog. Phys.* 72, 1–23.

Salvadori, P. (2008). Radiopharmaceuticals, drugs development and pharmaceutical regulations in Europe. *Curr. Radiopharm.* 1, 7–11. doi: 10.2174/1874471010801010007

Sandiego, C. M., Gallezot, J. D., Pittman, B., Nabulsi, N., Lim, K., Lin, S. F., et al. (2015). Imaging robust microglial activation after lipopolysaccharide administration in humans with PET. *Proc. Natl. Acad. Sci. U.S.A.* 112, 12468–12473. doi: 10.1073/pnas.1511003112

Schuck, P. (1997). Reliable determination of binding affinity and kinetics using surface plasmon resonace biosensors. *Curr. Opin. Biotechnol.* 8, 498–502. doi: 10.1016/s0958-1669(97)80074-2

Seibyl, J. P., Laruelle, M., Dyck, C. H. V., Wallace, E., Baldwin, R. M., Zoghbi, S., et al. (1996). Reproducibility of Iodine-123-β-CIT SPECT brain measurement of dopamine transporters. *J. Nuclear Med.* 37, 222–228.

Seo, Y., Aparici, C. M., and Hasegawa, B. H. (2008). Technological development and advances in SPECT/CT. *Semin. Nuclear Med.* 38, 177–198.

Seo, Y. J., Kang, Y., Muench, L., Reid, A., Caesar, S., Jean, L., et al. (2014). Image-guided synthesis reveals potent blood-brain barrier permeable histone deacetylase inhibitors. *ACS Chem. Neurosci.* 5, 588–596. doi: 10.1021/cn500021p

Siméon, F., Brown, A., Zoghbi, S., Patterson, V., Innis, R., and Pike, V. (2007). Synthesis and simple ^{18}F-labeling of 3-fluoro-5-(2-(2-(fluoromethyl)thiazol-4-yl)ethynyl)benzonitrile as a high affinity radioligand for imaging monkey brain metabotropic glutamate subtype-5 receptors with positron emission tomography. *J. Med. Chem.* 50, 3256–3266. doi: 10.1021/jm0701268

Smith, H. R., Beveridge, T. J. R., and Porrino, L. J. (2006). Distribution of norepinephrine transporters in the non-human primate brain. *Neuroscience* 138, 703–714. doi: 10.1016/j.neuroscience.2005.11.033

Stevenson, L., Tavares, A. A. S., Brunet, A., McGonagle, F. I., Dewar, D., Pimlott, S. L., et al. (2010). New iodinated quinoline-2-carboxamides for SPECT imaging of the translocator protein. *Bioorgan. Med. Chem. Lett.* 20, 954–957. doi: 10.1016/j.bmcl.2009.12.061

Syvänen, S., Lindhe, Ö, Palner, M., Kornum, B. R., Rahman, O., Långström, B., et al. (2009). Species differences in blood-brain barrier transport of three positron emission tomography radioligands with emphasis on P-glycoprotein transport. *Drug Metab. Disposit.* 37, 635–643. doi: 10.1124/dmd.108.024745

Takebe, T., Imai, R., and Ono, S. (2018). The current status of drug discovery and development as originated in united states academia: the influence of industrial and academic collaboration on drug discovery and development. *Clin. Transl. Sci.* 11, 597–606. doi: 10.1111/cts.12577

Tavares, A., Becker, G., Barret, O., Morley, T., Alagille, D., Vacher, B., et al. (2013). Initial evaluation of [18F]F13714, a novel 5-HT1A receptor agonist in non-human primates. *Eur. J. Nuclear Med. Mol. Imag.* 40:56. doi: 10.1007/s00259-013-2535-3

Tavares, A. A. S., Caillé, F., Barret, O., Papin, C., Lee, H., Morley, T. J., et al. (2014). *In Vivo* evaluation of ^{18}F-MNI698: an ^{18}F-labeled radiotracer for imaging of serotonin 4 receptors in Brain. *J. Nuclear Med.* 55, 858–864. doi: 10.2967/jnumed.113.132712

Tavares, A., Barret, O., Alagille, D., Morley, T., Papin, C., Maguire, R., et al. (2014). Brain Distribution of MS565, an imaging analogue of siponimod (BAF312), in non-human primates (P1.168). *Neurology* 82(10 Suppl.):P1.168.

Tavares, A. A. S., Jobson, N. K., Dewar, D., Sutherland, A., and Pimlott, S. L. (2011). ^{123}I-NKJ64: a novel single photon emission computed tomography radiotracer for imaging the noradrenaline transporter in brain. *Synapse* 65, 658–667. doi: 10.1002/syn.20895

Tavares, A. A. S., Jobson, N. K., Dewar, D., Sutherland, A., Pimlott, S. L., Batis, J., et al. (2012a). Iodine-123 labeled reboxetine analogues for imaging of noradrenaline transporter in brain using single photon emission computed tomography. *Synapse* 66, 923–930. doi: 10.1002/syn.21585

Tavares, A. A. S., Lewsey, J., Dewar, D., and Pimlott, S. L. (2012b). Radiotracer properties determined by high performance liquid chromatography: a potential tool for brain radiotracer discovery. *Nuclear Med. Biol.* 39, 127–135. doi: 10.1016/j.nucmedbio.2011.06.011

Tejani-Butt, S. M. (1992). [^{3}H]Nisoxetine: a radioligand for quantitation of norepinephrine uptake sites by autoradiography or by homogenate binding. *J. Pharmacol. Exper. Therapeut.* 260, 427–436.

Tolboom, N., Yaqub, M., van der Flier, W. M., Boellaard, R., Luurtsema, G., Windhorst, A. D., et al. (2009). Detection of Alzheimer pathology in vivo using both 11C-PIB and 18F-FDDNP PET. *J. Nuclear Med.* 50, 191–197. doi: 10.2967/jnumed.108.056499

Torstenson, R., Tedroff, J., Hartvig, P., Fasth, K.-J., and Umgstrom, B. A. (1999). Comparison of ^{11}C-Labeled L-DOPA and L-fluorodopa as positron emission tomography tracers for the presynaptic dopaminergic system. *J. Cereb. Blood Flow Metab.* 19, 1142–1149. doi: 10.1097/00004647-199910000-00011

Tu, Z., Fan, J., Li, S., Jones, L. A., Cui, J., Padakanti, P. K., et al. (2011). Radiosynthesis and in vivo evaluation of [^{11}C]MP-10 as a PET probe for imaging PDE10A in rodent and nonhuman primate brain. *Bioorgan. Med. Chem.* 19, 1666–1673. doi: 10.1016/j.bmc.2011.01.032

Udenfriend, S., Gerber, L., and Nelson, N. (1987). Scintillation proximity assay: a sensitive and continuous isotopic method for monitoring Ligand/Receptor and antigen/antibody interactions. *Analyt. Biochem.* 161, 494–500. doi: 10.1016/0003-2697(87)90479-9

Van de Bittner, G. C., Ricq, E. L., and Hooker, J. M. A. (2014). Philosophy for CNS radiotracer design. *Acc. Chem. Res.* 47, 3127–3134. doi: 10.1021/ar500233s

Van Laere, K., Ahmad, R., Hudyana, H., Dubois, K., Schmidt, M., Celen, S., et al. (2013). Quantification of ^{18}F-JNJ-42259152, a novel phosphodiesterase 10A PET tracer: kinetic modeling and test-retest study in human brain. *J. Nuclear Med.* 54, 1285–1293. doi: 10.2967/jnumed.112.118679

VanBrocklin, H. F. (2010). The radiotracer approcal bottleneck: improving the flow through the pipeline. *Pathways SNM Clin. Trials Netw. Newslett.* 1:7.

Varrone, A., Fujita, M., Verhoeff, N. P. L. G., Zoghbi, S. S., Baldwin, R. M., Rajeevan, N., et al. (2000). Test-retest reproducibility of extrastriatal dopamine D2 receptor imaging with [^{123}I]Epidepride SPECT in Humans. *J. Nuclear Med.* 41, 1343–1351.

Verbruggen, A., Coenen, H. H., Deverre, J.-R., Guilloteau, D., Langstrom, B., Salvadori, P. A., et al. (2008). Guideline to regulations for radiopharmaceuticals in early phase clinical trials in the EU. *Eur. J. Nuclear Med. Mol. Imag.* 35, 2144–2151. doi: 10.1007/s00259-008-0853-7

Versijpt, J., Dumont, F., Thierens, H., Jansen, H., Vos, F. D., Slegers, G., et al. (2000). Biodistribution and dosimetry of [^{123}I]iodo-PK 11195: a potential agent for SPET imaging of the peripheral benzodiazepine receptor. *Eur. J. Nuclear Med. Mol. Imag.* 27, 1326–1333. doi: 10.1007/s002590000295

von Schulthess, G., and Burger, C. (2010). Integrating imaging modalities: what makes sense from a workflow perspective? *Eur. J. Nuclear Med. Mol. Imag.* 35, 980–990. doi: 10.1007/s00259-009-1378-4

Walker, M. D., Dinelle, K., Kornelsen, R., McCormick, S., Mah, C., Holden, J. E., et al. (2013). In-vivo measurement of LDOPA uptake, dopamine reserve and turnover in the rat brain using [18F]FDOPA PET. *J. Cereb. Blood Flow Metab.* 33, 59–66. doi: 10.1038/jcbfm.2012.120

Wang, C., Schroeder, F. A., and Hooker, J. M. (2014). Visualizing epigenetics: current advances and advantages in HDAC PET imaging techniques. *Neuroscience* 264, 186–197. doi: 10.1016/j.neuroscience.2013.09.018

Warnock, G. I., Aerts, J., Bahri, M. A., Bretin, F., Lemaire, C., Giacomelli, F., et al. (2014). Evaluation of 18F-UCB-H as a novel PET tracer for synaptic vesicle protein 2A in the brain. *J. Nuclear Med.* 55, 1336–1341. doi: 10.2967/jnumed.113.136143

Waterhouse, R. N. (2003). Determination of lipophilicity and its use as a predictor of blood-brain barrier penetration of molecular imaging agents. *Mol. Imag. Biol.* 5, 376–389. doi: 10.1016/j.mibio.2003.09.014

Willmann, J. K., Bruggen, N. V., Dinkelborg, L. M., and Gambhir, S. S. (2008). Molecular imaging in drug development. *Nat. Rev. Drug Discov.* 7, 591–607.

Wong, D. F., and Pomper, M. G. (2003). Predicting the success of a radiopharmaceutical for *in vivo* imaging of central nervous system neuroreceptor systems. *Mol. Imag. Biol.* 5, 350–362. doi: 10.1016/j.mibio.2003.09.011

Wouters, O. J., McKee, M., and Luyten, J. (2020). Estimated research and development investment needed to bring a new medicine to market, 2009–2018. *JAMA* 323, 844–853. doi: 10.1001/jama.2020.1166

Yamazaki, M., Neway, W. E., Ohe, T., Chen, I.-W., Rowe, J. F., Hochman, J. H., et al. (2001). In Vitro substrate identification studies for P-glycoprotein-mediated transport: species difference and predictability of in vivo results. *J. Pharmacol. Exper. Therapeut.* 296, 723–735.

Yang, B. H., Wang, S. J., Chou, Y. H., Su, T. P., Chen, S. P., Lee, J. S., et al. (2008). Evaluation of reference tissue model and tissue ratio method for 5-HTT using [(123)I] ADAM tracer. *Comput. Methods Prog. Biomed.* 92, 294–298. doi: 10.1016/j.cmpb.2008.02.011

Yokoyama, C., Mawatari, A., Kawasaki, A., Takeda, C., Onoe, K., Doi, H., et al. (2016). Marmoset Serotonin 5-HT1A receptor mapping with a biased agonist PET probe 18F-F13714: comparison with an antagonist tracer 18F-mppf in awake and anesthetized states. *Intern. J. Neuropsychopharmacol.* 19:yw079.

Zimmermann, R. G. (2013). Why are investors not interested in my radiotracer? The industrial and regulatory constraints in the development of radiopharmaceuticals. *Nuclear Med. Biol.* 40, 155–166. doi: 10.1016/j.nucmedbio.2012.10.012

Conflict of Interest: GT is the CEO of XingImaging, LLC, United States.

The remaining authors declare that the research was conducted in the absence of any commercial or financial relationships that could be construed as a potential conflict of interest.

Copyright © 2020 Shaw, Tamagnan and Tavares. This is an open-access article distributed under the terms of the Creative Commons Attribution License (CC BY). The use, distribution or reproduction in other forums is permitted, provided the original author(s) and the copyright owner(s) are credited and that the original publication in this journal is cited, in accordance with accepted academic practice. No use, distribution or reproduction is permitted which does not comply with these terms.

frontiers in Neuroscience

REVIEW
published: 02 October 2020
doi: 10.3389/fnins.2020.569361

Cell Calcium Imaging as a Reliable Method to Study Neuron–Glial Circuits

Ricardo Augusto de Melo Reis[1], Hércules Rezende Freitas[2] and Fernando Garcia de Mello[1]*

[1] *Laboratório de Neuroquímica, Instituto de Biofísica Carlos Chagas Filho, CCS, Universidade Federal do Rio de Janeiro, Rio de Janeiro, Brazil,* [2] *Department of Pathology and Laboratory Medicine, MIND Institute, University of California, Davis, Sacramento, CA, United States*

Complex dynamic cellular networks have been studied in physiological and pathological processes under the light of single-cell calcium imaging (SCCI), a method that correlates functional data based on calcium shifts operated by different intracellular and extracellular mechanisms integrated with their cell phenotypes. From the classic synaptic structure to tripartite astrocytic model or the recent quadripartite microglia added ensemble, as well as other physiological tissues, it is possible to follow how cells signal spatiotemporally to cellular patterns. This methodology has been used broadly due to the universal properties of calcium as a second messenger. In general, at least two types of receptor operate through calcium permeation: a fast-acting ionotropic receptor channel and a slow-activating metabotropic receptor, added to exchangers/transporters/pumps and intracellular Ca^{2+} release activated by messengers. These prototypes have gained an enormous amount of information in dynamic signaling circuits. SCCI has also been used as a method to associate phenotypic markers during development and stage transitions in progenitors, stem, vascular cells, neuro- and glioblasts, neurons, astrocytes, oligodendrocytes, and microglia that operate through ion channels, transporters, and receptors. Also, cancer cells or inducible cell lines from human organoids characterized by transition stages are currently being used to model diseases or reconfigure healthy cells in terms of the expression of calcium-binding/permeable molecules and shed light on therapy.

Keywords: calcium imaging, neuron–glia, ATP, glioblastoma, fluorescent indicator

OPEN ACCESS

Edited by:
João O. Malva, University of Coimbra, Portugal

Reviewed by:
Xin Yu, Max Planck Institute for Biological Cybernetics, Germany
Fahmeed Hyder, Yale University, United States

****Correspondence:***
Ricardo Augusto de Melo Reis
ramreis@biof.ufrj.br

Specialty section:
This article was submitted to Brain Imaging Methods, a section of the journal Frontiers in Neuroscience

Received: *03 June 2020*
Accepted: *24 August 2020*
Published: *02 October 2020*

Citation:
de Melo Reis RA, Freitas HR and de Mello FG (2020) Cell Calcium Imaging as a Reliable Method to Study Neuron–Glial Circuits. Front. Neurosci. 14:569361. doi: 10.3389/fnins.2020.569361

INTRODUCTION

Since the revolutionary work of Camilo Golgi, Santiago Ramon y Cajal, and Charles Sherrington at the turn of the twentieth century, scientists have attempted to correlate structure and function to understand the nervous system. At that time, cells were labeled with the technique of silver impregnation, discovered by Golgi in 1873 and later applied by Cajal to almost every part of the brain, from 1887 until the rest of his life. At the same time (1882–1883), Sydney Ringer described the properties of a physiological solution acknowledging the role of Ca^{2+}

(in addition to Na^+ and K^+) (Ringer and Buxton, 1887), essential to contraction and the observed variations of ventricular volume of excised frog heart (Miller, 2004). Around 1910, Sherrington conceptualized the synapse, only deeply comprehended in terms of active zones around the 1950s, with the development of the electronic microscope. Electron-dense pre-synaptic sites were characterized and shown to host multifunctional proteins, including calcium channels. In parallel, the work of brilliant electrophysiologists such as John Eccles, a defendant of the concept of electrical synapse, and the pillars of bioelectrogenesis and action potential, Alan Hodgkin, Andrew Huxley, Bernard Katz, Ricardo Miledi, among others, added another level of signaling in modern neurophysiology.

Cellular neuroscience emerged in the last half-century as a merge of anatomy, histology, physiology, neurochemistry, cell biology, and behavioral sciences to gain information on the rules of neural ensembles and behavior. Lately, questions evolved with data revealed from *in vitro* fluorescence and/or confocal microscope and/or *in vivo* non-invasive high-resolution imaging techniques as the two-photon and/or lightweight miniaturized microscopy that permit optical recordings in freely moving animals for weeks.

Cellular networks can now be visualized with powerful imaging methods using advanced statistics to allow dynamic molecular messages that drive structure and function with fluorescent shuffled reporters (Lichtman et al., 2008). Pharmacological approaches based on functional proteomics add several layers of complexity, evaluated through optogenetics (Kim et al., 2017) or in combination with electrical or optical recordings, providing powerful strategies to alter the neural function and gain behavioral data (Frackowiak and Markram, 2015). This will soon lead to further details on the plasticity and the adaptation of the brain to understand still intangible fields such as cognition and consciousness (Cook, 2008). Here, we will focus on the properties of Ca^{2+} signaling dynamics related to membrane proteins found virtually on every single neural cell, but due to limitation, it will be restricted to selective models.

Single-cell calcium imaging (SCCI) is a versatile methodology used to visualize calcium shifts, from extracellular or intracellular stores, associated with a profile of molecules selectively expressed on living individual cells. Calcium has a central role on almost every cellular task, as a messenger ion and/or interacting with a multitude of binding proteins, adjusting several activities, e.g., gene transcription, cell birth, proliferation, migration, signaling/excitation/contraction, cell growth, metabolism, cytoskeletal dynamics, differentiation, synaptic transmission and plasticity, survival, and death (Carafoli and Krebs, 2016; Islam, 2020). Calcium concentration in the extracellular space is $\sim$1.8–2.5 $\times$ 10^{-3} M, at least 2 $\times$ 10^4 higher than in the cytosolic compartment (typical resting levels $\sim$1–2 $\times$ 10^{-7} M). The expression of calcium-permeable channels, transporters, receptors, and effector molecules is essential to understand spatiotemporal signaling in living cell compartments. Calcium imaging evaluates intracellular Ca^{2+} dynamics that originated with the development of calcium dyes such as 1,2-bis(o-aminophenoxy)ethane-N,N,N',N'-tetraacetic acid from the laboratory of Roger Y. Tsien, with high selectivity against magnesium and protons (Tsien, 1980) and later improved as selective Ca^{2+} indicator, "quin2", studied inside intact lymphocytes (Tsien et al., 1982). Lipophilic groups added [acetoxymethyl or acetate ester (AM) groups] to the charged indicators gave a membrane-permeant property and hidden charges, allowing cleavage by constitutively expressed intracellular esterases. These sensors show stronger fluorescence (intensity increases up to 30-fold) and better affinity for Ca^{2+} and selectivity against Mg^{2+} in the presence of Ca^{2+} shifts (Grynkiewicz et al., 1985). The first six dyes generated [from which fura-2 (**Figure 1A**) and indo-1 are the ratiometric] [measure free Ca^{2+} concentration with Ca^{2+}-free and Ca^{2+}-bound forms having two distinct peaks (**Figure 1B**)] prototypes, based on the fluorescence intensity detected on two wavelengths (Rudolf et al., 2003; Bruton et al., 2020), and are widely recognized to track calcium shifts within cells (**Figures 1C–F**), from intracellular or extracellular sources. The development of better fluorescent microscopes and computation methods yielded high-resolution optical data with a high degree of spatial and temporal resolution to image calcium signaling on living cells and organisms.

The use of genetically coded calcium indicators (GECI) allowed the study of cellular structure/function to match behavior responses. GECIs have been developed as fused proteins to monitor the spatiotemporal patterns of intracellular Ca^{2+} dynamics in functional compartments of living organisms. This strategy has been used from *Drosophila* to the intact brain of transgenic rodents and not only in the cytoplasmic environment but also in organelles such as the mitochondria or the endoplasmic reticulum. Excellent recent reviews are available, so we will not extend on this matter (Inoue, 2020). Briefly, to overcome obstacles in dye loading faced by organic indicators and other variabilities on the lack of cell-type selectivity, chimeric protein has been engineered and named "chameleons" (Miyawaki et al., 1997) based on the color change of fluorescent proteins fused to a Ca^{2+} binding protein (usually calmodulin or troponin C) and M13 [a peptide with a primary sequence based on the skeletal muscle myosin light chain kinase (residues 577–602). This peptide acts as a spacer and binds to Ca^{2+}, modifying the conformation from a weak to strong fluorescence complex. Fluorescence resonance energy transfer is based on Ca^{2+} binding and conformation change of calmodulin around the M13 domain. As an example, GCaMP acts a high-affinity Ca^{2+} probe prototype composed of a single green fluorescent protein (Nakai et al., 2001). Variations (GCaMP3, GCaMP5, and GCaMP6) have been prepared, which are converted from green to red following exposure to blue-green light at 450–500 nm (Ai et al., 2015).

A current challenge faced with GECI live imaging is related to the identification of specific subsets of active neurons within a larger cell population. Accomplishing this task is important to understand ensemble responses and to improve the visualization of signal integration across multiple brain regions. Although several efforts were able to ensure a somewhat automated processing of these imaging results through classic machine learning techniques (Mukamel et al., 2009; Kaifosh et al., 2014;

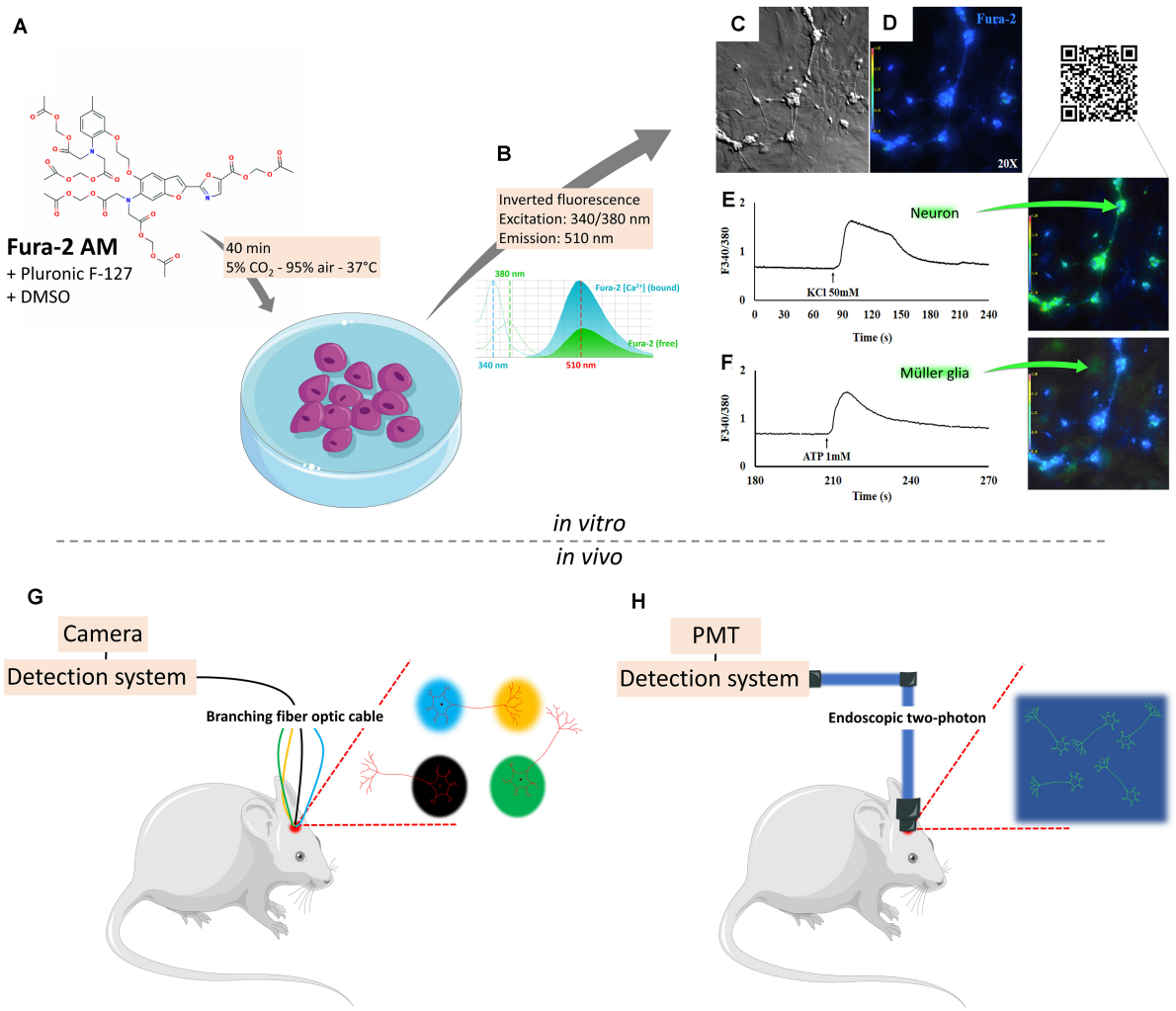

FIGURE 1 | Detecting intracellular calcium changes through single-cell calcium imaging. Single-cell calcium imaging evaluates intracellular Ca^{2+} dynamics through calcium probes as Fura-2 AM **(A)**, a lipophilic acetate ester (AM) that permeates the cell membrane in an apolar environment (DMSO + pluronic F-127), allowing cleavage by intracellular esterases. These sensors show stronger fluorescence and better affinity for Ca^{2+} and selectivity against Mg^{2+} in the presence of Ca^{2+} shifts **(B)**. Neurons and glia in bright field **(C)** or under fluorescence **(D)** when activated by KCl 50 mM **(E)** or ATP 1 mM **(F)** show selective responses. In parallel, the use of inducible genetically encoded calcium indicators and a variety of detection systems made probing neural cell behavior in live animals a possibility. Through a photoreceiver, it is possible to detect changes in cell fluorescence as the animal is awake and freely behaving. An optimized version of this technique can be obtained through multi-site photometry **(G)**, which allows for the detection of spatiotemporal changes as the animal responds to varying environmental patterns. In this method, signals are detected by a complementary metal oxide semiconductor (CMOS) camera. Direct bidimensional fluorescence can be detected with the use of one-photon microendoscopes, capable of imaging a region of interest (ROI) inside the living brain, which in turn is detected by a CMOS camera. Two-photon endoscopes can be used to generate a high-fidelity view of a given ROI. In this case, images are generated after detection by photomultiplier tubes **(H)**.

Guan et al., 2018), current approaches are now entering the realm of convolutional neural networks, which can be used in a 3D architecture to segment active neurons on different layers of the same imaging target (Soltanian-Zadeh et al., 2019). Also, accessible algorithms for imaging motion correction have been recently developed and can be used to improve the output quality of automated segmentation networks (Pnevmatikakis and Giovannucci, 2017).

It is interesting to notice that, while the analysis of live Ca^{2+} imaging data is becoming increasingly accessible and automated through a large array of online resources, the *in vivo* experiments demand progressively more sophisticated tools, either to improve field-of-view resolution or to increase the number of simultaneous detections from different brain regions. The use of confocal and multiphoton laser scanning microscopy helped to extend to the larger scale, obtaining data on organ systems, from small GECI-expressing transparent alive invertebrates to awake transgenic mammals (Russell, 2011). Through a photoreceiver, it is now possible to detect changes in cell fluorescence in different *in vivo* models, as imaging for somatosensorial or visual inputs inducing synaptic plasticity on the dendritic spine patterns on cortical neurons or calcium

imaging in awake and freely behaving animals (Grienberger and Konnerth, 2012). One exciting possibility would be the integration of multiple neuroimaging methods, combining low spatiotemporal fidelity from functional magnetic resonance imaging (fMRI) with multiple-site photometry (**Figure 1G**). Several groups have reported simultaneous acquisition of blood oxygen level-dependent (BOLD) fMRI, regularly used for non-invasive functional neuroimaging, combined with chronically implanted optical fiber, which allow data acquisition of identified cells from transgenic models or through viral electroporation delivered with GCaMP6 (Schlegel et al., 2018), and understand the relationship of neural and vascular signals (Albers et al., 2018). The advantage of animals placed in an MRI scanner coupled to a fiber photometry through a silicon photo multimeter is the prevention of electromagnetic interference seen in electrophysiological recordings during MRI scanning (Logothetis et al., 2001). The increased popularity of this technique came with the development of the multi-channel fiber photometry system to simultaneously monitor neural activities in several brain areas of an animal or in different animals (Guo et al., 2015). It was initially prepared to explore this correlation in rat somatosensory cortex, where forepaw stimulation evoked fast calcium signals of neuronal origin (Schulz et al., 2012) or, as reported, slower calcium signals derived from astrocyte networks. Coupling of GCaMP6-based calcium signal to neural activity produces a novel opportunity with a reproducible temporal relationship, validated, for example, with a visual stimulation experiment, during which robust increases of both calcium and BOLD signals were observed in the superior colliculus of rats (Liang et al., 2017). A following investigation demonstrated that these signals emerge in a region-specific pattern from the SC and the lateral geniculate nucleus (Tong et al., 2019). This strategy has also permitted the mapping of neuronal circuits in the whole mouse cortex, yielding a connective map spanning several cortical subregions (Lake et al., 2018; Schlegel et al., 2018). Today it is possible to study anesthetized or freely behaving animals and probe calcium signals in a variety of brain regions during development, aging, or disease (Wright et al., 2017; Schlegel et al., 2018). An optimized version allows multi-fiber photometry and optogenetic perturbations across many regions in the mammalian brain (the authors managed to detect GCaMP6m-generated Ca^{2+} fluorescence from striatal, thalamic, hippocampal, and cortical areas). In this sense, the spatiotemporal changes of neuronal activity are registered as a go/no-go texture discrimination task runs on awake mice responding to varying environmental patterns (Sych et al., 2019). Alternatively, *in vivo* astrocytic microdomains show spatially restricted synchronized calcium transients that last a few seconds upon activation of transmitter receptors, observed in both anesthetized and awake animals [reviewed in Nimmerjahn and Bergles (2015)]. In this method, signals are detected by a complementary metal oxide semiconductor (CMOS) camera. Direct bidimensional fluorescence can be detected with the use of a one-photon microendoscope, capable of imaging a region of interest (ROI) inside the living brain, which in turn is detected by a CMOS camera. Two-photon endoscopes can be used to generate a high-fidelity view of a given ROI. In this case, images are generated after detection by photomultiplier tubes (**Figure 1H**). In relation to the astrocytic compartment, data on GCaMP-mediated Ca^{2+} optical fiber recordings described a brain-state dependency of both astrocytic Ca^{2+} and BOLD fMRI signals (Wang M. et al., 2018). Distinct Ca^{2+} signals combined with positive BOLD signals and intrinsic astrocytic Ca^{2+} signals coupled with negative BOLD signals were reported. Indeed recent data from anesthetized transgenic mice expressing G-CaMP7 in astrocytes allowed the extraction of patterns and the reconstruction of cortical areas inserted within spontaneous activity as the functional connectivity maps for the individual mice (O'Hashi et al., 2019). Confined, asynchronous, and spontaneous Ca^{2+} signals are commonly seen in fine astrocyte processes. As astrocytes are key elements regulating brain energy metabolism (Oheim et al., 2018), the way molecules signal and exchange metabolites in the neuron–glia–vascular circuitry and the concept of Ca^{2+} waves on microdomains will be greatly improved under the combination of powerful methodologies of calcium recording with fMRI.

One could also apply diffusion tensor imaging measurements, especially fractional anisotropy, with fMRI–BOLD responses to obtain coupled microstructural and functional imaging data (Warbrick et al., 2017). Data could be correlated, *a posteriori*, with chronic multi-site live calcium fluorescence for spatiotemporal measurements of neural activity. The knowledge acquired from such efforts would certainly be useful to corroborate molecular and histological results, strengthening the mechanistic inferences extracted from data.

Different mechanisms approaching external (channels, receptors, transporters, and exchangers) or internal (endoplasmic reticulum, calciosomes, vesicles) sources, using multiple steps and messengers/signaling molecules/binding proteins, virtually in every *in vitro* or *in vivo* cell, can be studied, and due to the scope and the space limitations of this review, we can only exemplify a few. Data shown are on the central and peripheral nervous system (retina and dorsal root ganglia and connections), neurons and glia population, glioblastoma, and cell lineages derived from human organoids.

RETINA, A CENTRAL MODEL

The retina is frequently chosen as a model to study interactions between neural cells due to its unique disposition in layers, from the embryonic to the final mature structure; as the retina develops, the environment changes, so extrinsic factors (transmitters, growth factors, extracellular matrix, and other mediators) interact with the genetic program modifying intrinsic transcription factors, so each cell leaves the cycle chronologically defined (Hatakeyama and Kageyama, 2004); retinal progenitors are multipotential, and region cell–cell interactions imply precise differentiation in a way that first retinal ganglion cells (RGCs), cone, and amacrine emerge from early-born progenitors, and then photoreceptors, bipolar, and Müller glia develop from late-born progenitors (Turner and Cepko, 1987). The vertical or radial axis, made by photoreceptors–bipolar–ganglion cells, is excitatory, while the horizontal or lateral axis, composed by horizontal and amacrine cells, is largely

inhibitory (Barnstable, 1993). Photoreceptors release glutamate in the dark, which activates calcium-permeable ionotropic AMPA/NMDA receptors on OFF-type bipolar cells, while the activation of metabotropic glutamatergic type 6 receptor and ionotropic receptors, among others, mediates ON-type bipolar cell activity (Yang, 2004). Ca^{2+} imaging studies have been used to detail network properties in *ex vivo* retinal preparations and revealed a variety of responses on bipolar cells (at least eight different clusters) in terms of Ca^{2+} shifts in the axon terminals. On the other hand, activation of glutamatergic extrasynaptic NMDA receptors present in the rod pathway show increases in Ca^{2+} dendritic levels in both AII and A17 amacrine cells, postsynaptically at rod bipolar dyad synapses (Veruki et al., 2019). The depolarization of ganglion cells by voltage-dependent calcium channels (VDCC) contributes to soma and dendritic Ca^{2+} increases (Sargoy et al., 2014). These are a few examples on how live calcium imaging details the complex retinal signaling network. Based on two-photon calcium imaging, clustering of more than 11,000 mice RGC recordings shows that more than 30 functional channels are channeled (Baden et al., 2016). Recently, chronically stable *in vivo* recordings from RGCs in awake mice were reported using a genuine epiretinal-implanted 16-channel mesh electronic probe (Hong et al., 2018) delivered non-surgical intravitreally using syringe-injectable. Orientation-selective RGCs were stably registered between recording sessions, 7 days apart, implicating that individual cells can be tracked for 2 weeks.

Retinal neural cells (neurons, glia, and progenitors) can be phenotypically identified when matched in terms of calcium imaging (De Melo Reis et al., 2011). Progenitors cells usually express the intermediate filament marker nestin and are activated by muscimol, a $GABA_A$ receptor-channel agonists in immature networks. The electrochemical gradient for Cl^- favors activation due to high intracellular Cl^- levels; in this sense, the expression of K^+-coupled Cl^- transporter KCC2 is correlated with the modification of GABAergic transmission, switching during development from excitation on progenitors to inhibition on mature GABAergic neurons (Ganguly et al., 2001).

The neuron–glia circuits in the developing retina are shaped by light and sensed by intrinsically photon-detecting retinal ganglion cells, which are coupled electrically to other ganglion cells in a network (Sekaran et al., 2003). Beyond phototransduction, cones and rods regulate important physiological activities (circadian cycle, pupillary reflex, light sensing), which are frequently dependent on dopamine signaling (Caval-Holme et al., 2019). The dopaminergic system is one of the first phenotypes to be expressed in the developing retina (Reis et al., 2007), and dopamine is a potent modulator of spontaneous neural activity and gap junction coupling. Markers for young (doublecortin, β_{III}-tubulin, and PSA-NCAM) and mature (MAP-2) retinal neurons are associated with KCl depolarizing cells (due to the expression of VDCC) [reviewed by Catterall (2000)]; retinal neurons are activated by ionotropic glutamatergic receptors, NMDA (Veruki et al., 2019), AMPA, or kainate (Okada et al., 1999; De Melo Reis et al., 2011; Passos et al., 2019). Some of these responses are modulated by cyclic AMP, which is induced by dopamine, adenosine, and PACAP receptors and functions as a differentiating factor for dopaminergic retinal cells in the chick (Guimaraes et al., 2001) or rat retina (Varella et al., 1999). Cannabinoid receptors present on neurons and glia (Kubrusly et al., 2018) on the avian retina also contribute to the regulation of different outputs such as GABA release, calcium entry, and cAMP mobilization.

Müller cells are the main glial element in the retina, which intermingles with most, if not all, neurons in this tissue. These cells are active players (de Melo Reis et al., 2008) that transverse from the inner to the outer limiting membranes, spanning the whole retinal length, and control numerous activities such as osmotic (solute and water composition in the extracellular space), metabolic (glutamate-glutamine cycle), signaling (trophic factors and mediators), synaptic (release of transmitters), regulation of plasticity (Reichenbach and Bringmann, 2013), and response to excitotoxicity (Schitine et al., 2015). Müller cells are categorized by the expression of glutamine synthetase and glial fibrillary acidic protein, among other markers, and are activated by high concentrations of ATP due to the expression of purinergic calcium-permeable P2X7 receptor-channel, among others (De Melo Reis et al., 2011; Faria et al., 2017). ATP has many signaling and metabolic functions in the retina; it induces ionic waves through gap junctions and is involved with neuronal cell death (Metea and Newman, 2006; Reichenbach and Bringmann, 2016), while metabotropic (Keirstead and Miller, 1997) or ionotropic glutamatergic receptors on Müller glia also contribute to waves that depend on the nature of other transmitters involved (Rosa et al., 2015). Recent data have shown that progenitors from the embryonic avian retina unresponsive to ATP (**Figure 2A**) differentiate into neurons (activated by KCl or glutamate) or glia (activated by ATP) in a cannabinoid-rich environment (**Figure 2B**). Calcium shifts induced by ATP in avian Müller glia increased up to 30% in early retinal cells when cannabinoid receptors CB1 and CB2 are activated by the cannabinoid agonist WIN 55,212-2 (**Figure 2C**) (Freitas et al., 2019). Alternatively, a decrease in the number of glutamate-, GABA, and KCl-responsive cells (neurons and progenitors) was reported. Instead of differentiating, some progenitors die (D) due to the activation of death-inducing pathways (**Figure 2D**).

Müller cells control oxidative species as they participate in glutathione (GSH) synthesis as astrocytes do in the cortex. GSH is the main glial antioxidant found at a greater millimolar concentration when compared to neurons, which in turn show a much higher (10:1) ascorbate concentration compared to glia (Rice and Russo-Menna, 1998). GSH has been shown to induce selective Ca^{2+} shifts in Müller glia in a P2X7-dependent manner, a process that induces GABA release (Freitas et al., 2016), possible to strengthen retinal neuroprotection (Freitas and Reis, 2017). Interestingly, in a recent study where the P2X7 receptor was deleted, the basal GSH levels were decreased without altering GSH synthetic enzyme expression in the mouse hippocampus, a process linked to the glutamate–glutamine cycle and neutral amino acid transporters (Park and Kim, 2020).

The Müller glia has been gathering attention due to its proliferative properties after retinal injury and activation of stem/progenitor cell phenotype, allowing a return to the cell cycle and eventually differentiating into functional neurons. This has

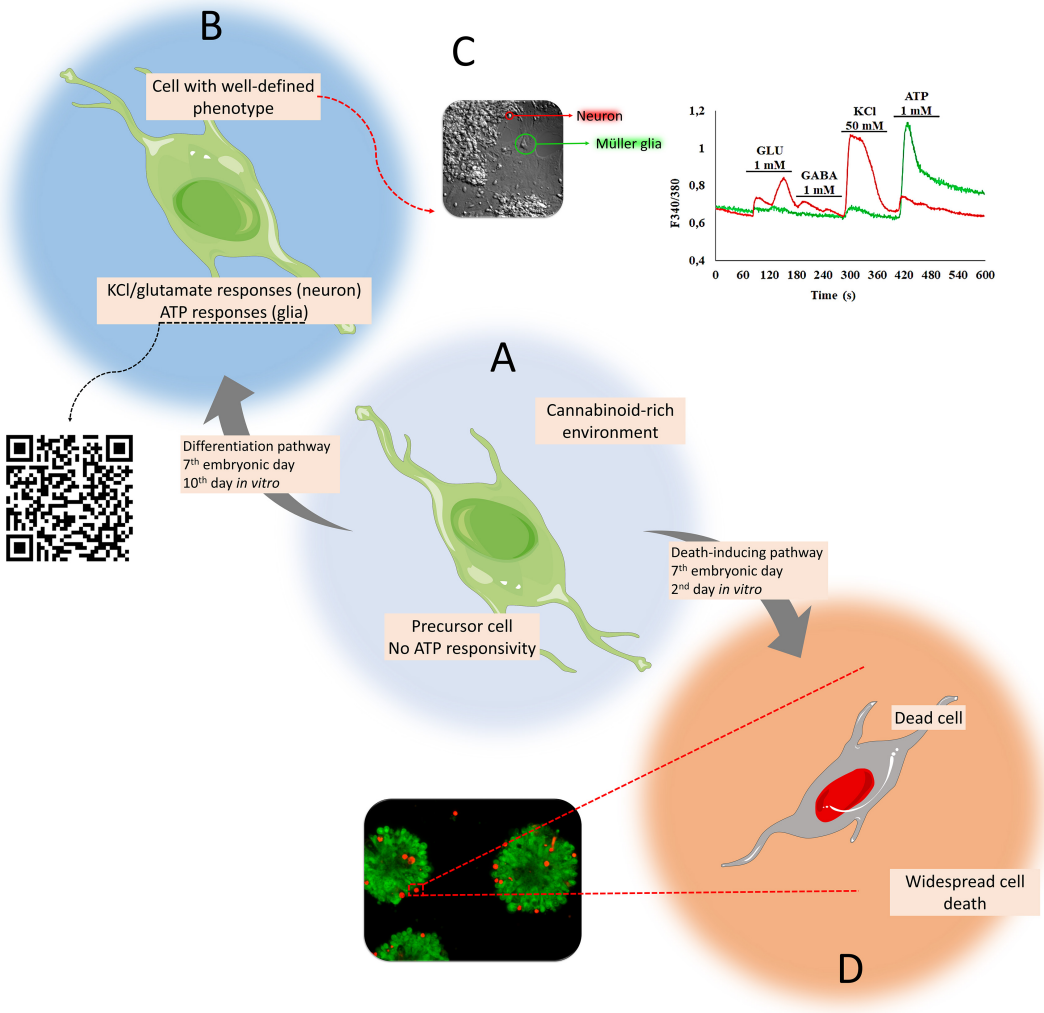

FIGURE 2 | Matching cell phenotypes with calcium signaling activated by P2X7 receptors in retinal cells in culture. Progenitors unresponsive to ATP **(A)** differentiate into neurons (activated by KCl or glutamate) or glia (activated by ATP) in a cannabinoid-rich environment **(B)**. Emerging calcium shifts induced by ATP are exclusive to Müller glia (green trace), primed by the early cannabinoid receptor activation (with WIN 55,212-2). On the other hand, neurons are activated by KCl and glutamate (red trace) (Freitas et al., 2019) **(C)**. Instead of differentiating, some progenitors die **(D)** due to the activation of death-inducing pathways [bottom panel: live (calcein, green) and dead (ethidium homodimer-1, red)].

been shown for neurogenin 2 or ASCL1, transcriptional factors that, when nucleofected onto Müller glia, were reprogrammed into inducible neurons (Guimaraes et al., 2018), functionally monitored in terms of calcium imaging. This strategy has been used by many groups to partially restore vision in different animal models (Hampton, 2018).

Retinal information flows to the thalamus and the primary visual cortex (V1). Pyramidal cells in layers 2/3 were evaluated through two-photon Ca^{2+} imaging in GECI-expressing transgenic mice so excitatory and inhibitory neuron synchronization could be studied during the wakefulness of the animals (Knoblich et al., 2019). Calcium imaging data combined to *in vivo* targeted electrophysiology gave within-type cross-correlation coefficient (CC) profiles, which were used to characterize different populations of interneurons, parvalbumin, and VIP characterized as highly active and homogeneously synchronized; alternatively, somatostatin interneurons were subdivided into two populations, one spontaneously active, but uncorrelated to neighbor cells (Knoblich et al., 2019). These populations were differently modulated by locomotion, adding a functional perspective to neuronal cell typing.

SUBVENTRICULAR ZONE

The subventricular zone (SVZ) is considered as one of the main neurogenic niches in the brain (together with the subgranular zone), where the continuous proliferation of stem cells is actively balanced to generate progenitors, neurons, astrocytes, and oligodendrocytes (Eiriz et al., 2011). Each type of cell can be

phenotypically identified based on selective markers associated with distinct mechanisms of Ca^{2+} entry, i.e., dependent on VDCC fast depolarization induced by KCl on neuroblasts and neurons (Schitine et al., 2012), coupled to metabotropic histamine receptors on progenitors, or modulated by thrombin through the protease-activating receptor on oligodendrocytes (Xapelli et al., 2013, 2014).

SENSORIAL STIMULI, FROM DRG TO CENTRAL PROJECTIONS

Somatosensorial information combine different modalities such as pain, heat, touch, proprioception, and others by stimulation of peripheral receptors in pseudo-unipolar myelinated and unmyelinated first-order dorsal root ganglia (DRG) neurons; upon sensorial transduction, neural codes are generated as action potential patterns to cell bodies and then to synapses onto secondary neurons located in well-organized Rexed laminae of the spinal cord dorsal horn [reviewed in Peirs and Seal (2016)]. Parallel fibers carrying fast (A_{alpha}/A_{beta}, touch, and proprioception) or slow (A_{delta}/C, temperature, and pain) submodalities flow to the thalamus and then to several brain areas.

Locally, the transient receptor potential acts as a non-selective cation channel family, whose vanilloid member (TRPV) depolarizes unmyelinated sensory neurons in the presence of capsaicin to temperature and painful thermal stimuli (Caterina et al., 1997; Peirs and Seal, 2016). Alternatively, ASIC1, acid-sensing ion channel 1, a member of the ASIC family of proteins and part of the degenerin/epithelial sodium channel (DEG/ENaC) superfamily, is expressed in large sensory myelinated neurons (Peirs and Seal, 2016).

Calcium imaging has been employed to DRG and dorsal horn neuron co-cultures to understand the mechanisms behind synaptic transmission coded by A_{delta} (mechanical and thermal nociception) and C-fibers (high-intensity polymodal stimuli). It was shown that Ca^{2+} influx through NMDA receptors induced by glutamate depolarizes dorsal horn neurons (Ohshiro et al., 2007). Schwann and satellite cells interact closely with DRG neurons. At the cellular level, KCl and ATP activate selectively neurons and glia, respectively (Ribeiro-Resende et al., 2014). VDCC are expressed in postnatal primary sensory neurons, while purinergic receptors are broadly expressed in all major classes of glia, including Schwann cells. Indeed purinergic signaling controls many important functions in the neuro-glia compartment in the DRGs such as proliferation, motility, survival, differentiation, and myelination (Fields and Burnstock, 2006). The use of two-photon Ca^{2+} imaging, Ca^{2+} indicators, and/or GECI allow high-resolution measurements with detailed functions of different cell types in DRG, for instance, a particular group of neurons (11 to 33 μm in diameter) is activated by an increase in temperature in the animal hind paw (Anderson et al., 2018). Besides that, freely behaving mice injected with plantar formalin had a DRG neuronal activity (**Figure 3**) associated with phasic pain behavior (Chen et al., 2019). This activity persisted for 5 weeks as a hallmark of neuronal hyperactivity associated with ongoing pain. Classical cannabinoid G protein receptors (CB1 and CB2) have been studied in addition to TRPV1 in DRG neurons to evaluate how endocannabinoids can control pain (Millns et al., 2006). Ca^{2+} influx through purinergic, carbachol-activating muscarinic or TRPV1 receptors increases anandamide synthesis within cells (Ahluwalia et al., 2003) and activates both TRPV1 (van der Stelt et al., 2005) and cannabinoid receptors. CB1 receptors co-localized with purinergic receptors in DRG small-diameter neurons control pain by anandamide and involves the modulation of P2X3 receptor in the primary afferent neuron (Oliveira-Fusaro et al., 2017).

Neurons and glia (visualized as ramified processes and in contact with blood vessels, labeled as SR101+) were also studied in response to heat/cold stimuli in the superficial dorsal horn from anesthetized mice (Johannssen and Helmchen, 2010; Ran et al., 2016). The authors reported different overlapping neurons on dorsal horn ensembles activated by cutaneous stimulation in freely behaving mice, while it was reported that large-scale coordinated calcium responses were generated in astrocytes in response to intense, but not weak, sensory inputs (Sekiguchi et al., 2016). On the other hand, amygdala has also received attention as a hub in the pain matrix, as the basolateral part of the amygdala contributes to the negative affective perception of unpleasant pain (Corder et al., 2019), and P2X7 receptor acts in the modulation of neuropathic pain (Hu et al., 2020). Interestingly, the role of general anesthetics on calcium imaging in awake head-restrained mice was studied, and a combination of ketamine/xylazine, isoflurane, and urethane abolished calcium responses in neocortical astrocytes, modifying synchronized widespread transients related to arousal in awake animals (Thrane et al., 2012). Effects were associated with inositol 1,4,5-triphosphate type 2 receptor but independent of glutamatergic or purinergic signaling.

Microglia, the immune resident cells in the nervous system, and monocyte-derived macrophages derived from the peripheral circulation have significant and distinct roles in neuroinflammation, injured spinal cord (David and Kroner, 2011), or/and progression of neurological and neuropsychiatric diseases (Chen et al., 2018; Tvrdik et al., 2019). Spinal cord lesion is associated with secondary network damage through inflammation, ischemia, edema, generation of reactive oxygen species, and excitotoxicity (Kroner and Rosas Almanza, 2019). Calcium shifts activated by purines, through P2X receptors, particularly P2X7 and P2X4, mediate neuropathic pain. Indeed activation of microglia by ATP contributes to tactile allodynia in the spinal cord (Tsuda et al., 2003), and microglia–neuron interactions are greatly affected in male, but not female, mice, caused by peripheral nerve injury. Inhibition of purinergic P2X4 receptors decreased pain hypersensitivity in male rats only (Mapplebeck et al., 2018). The microglia activated by ATP also releases brain-derived neurotrophic factor (BDNF) on lamina I neurons that change the polarity of currents activated by GABA, a major effect after peripheral nerve injury (Coull et al., 2003). As BDNF is an important player between microglia and neurons, this might represent a therapeutic strategy for treating neuropathic pain (Coull et al., 2005).

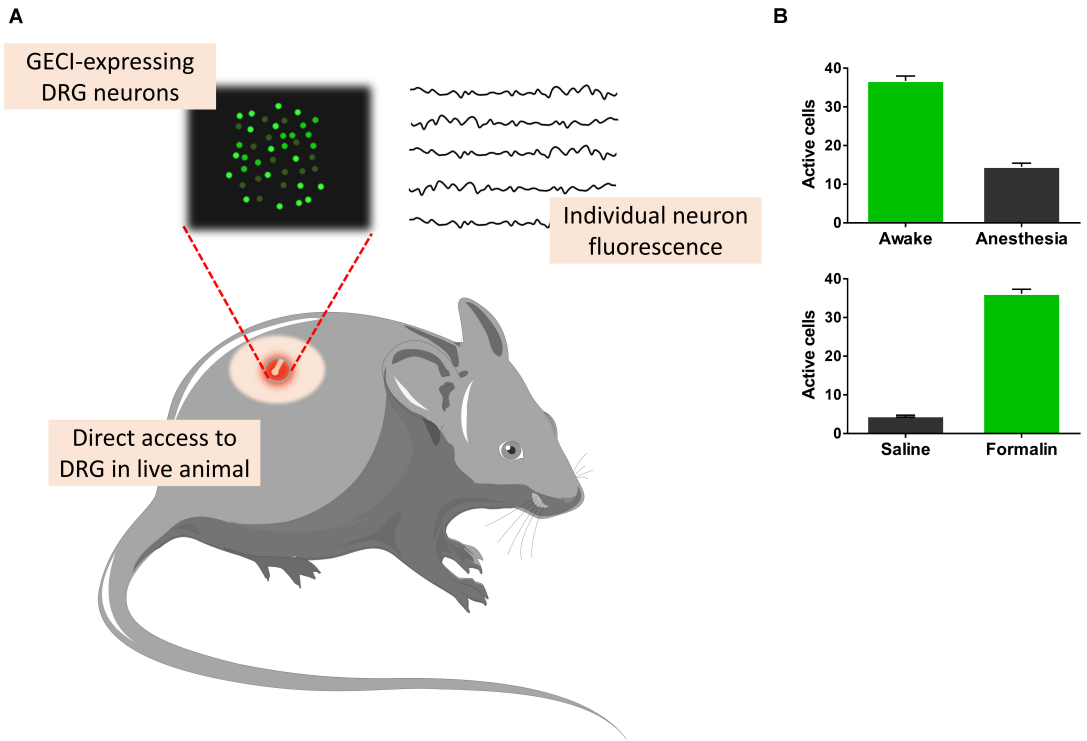

FIGURE 3 | Recording dorsal root ganglia (DRG) cells from awake freely moving animals. Genetically coded calcium indicators (GECIs), which sense the concentration of Ca^{2+}, allow for measurements of different cell types **(A)**. Freely behaving mice injected with plantar formalin showed DRG neuronal activity associated with phasic pain behavior (Chen et al., 2019). This activity persisted for 5 weeks as a hallmark of neuronal hyperactivity associated with ongoing pain (**B**, bottom). Alternatively, GECI-expressing transgenic mice allow the study of excitatory and inhibitory synchronization properties of anesthetized and awake (**B**, top) animals (Knoblich et al., 2019).

Generation of conditional mouse reporter of calcium facilitated the deployment of GECI in microglia, permitting *in vivo* studies of intracellular calcium in large microglial cell populations in cerebral pathologies such as ischemic stroke. The use of reporter mice and recent GECI indicated novel roles in development and plasticity-driven reorganization, as well as a surveillant cell in the homeostatic maintenance of brain tissue (Brawek and Garaschuk, 2013); large cell populations have been imaged in ischemic stroke *in vivo* (Tvrdik et al., 2019).

One of the hottest topics in the last decade related to microglia is the role in neural circuits refinement *via* both promoting synapse formation and by targeting specific synapses for elimination and phagocytosis (Akiyoshi et al., 2018). Ca^{2+} imaging of larger populations of motor cortical layer 2/3 pyramidal neurons show microglia–dendritic spine interactions that increase neuronal activity and consequent neuronal synchronization in healthy brain in awake mice (Akiyoshi et al., 2018).

CANCER

Glioblastoma as a Model

Cancer affects millions worldwide and comprises a multifaceted pathology of different histopathological types. The cancer microenvironment has a unique scenario and shares common strategies for development. Therefore, the use of a methodology to selectively identify, differentiate, and gather information through a functional imaging property is highly desirable.

Glioblastoma multiforme is a grade IV malignant, astrocyte-derived brain tumor, highly heterogeneous, with unfavorable prognosis. Seizures are frequently seen among patients due to an imbalance in the inhibitory interneuron network and excess of glutamate release (Hatcher et al., 2020). In this sense, cell lines have been used to model glioblastoma and other high-grade gliomas, and calcium imaging has been applied as a strategy to evaluate receptors/transporters/exchangers from tumors and healthy cells. GL261 cell line has been used to match pharmacological treatments based on cellular phenotype, cultured under adherent or non-adherent conditions. Both ATP (through P2X7 receptor) and capsaicin (TRPV1 receptor) activate a strong calcium response in GL261 neurospheres, but not on adherent cells (Strong and Daniels, 2017). This cell line secretes glutamate upon ATP activation, which is excitotoxic to healthy tissue and linked to tumorigenicity into adjacent brain regions (Strong et al., 2018). In addition to P2X7 and TPRV receptors, the Na^{+}/Ca^{2+} exchanger (NCX), when activated by SKF 96365 (TRPC channel blocker), increases Ca^{2+} levels in glioblastoma cells (**Figure 4**). NCX controls intracellular Ca^{2+} homeostasis, and silencing of NCX1

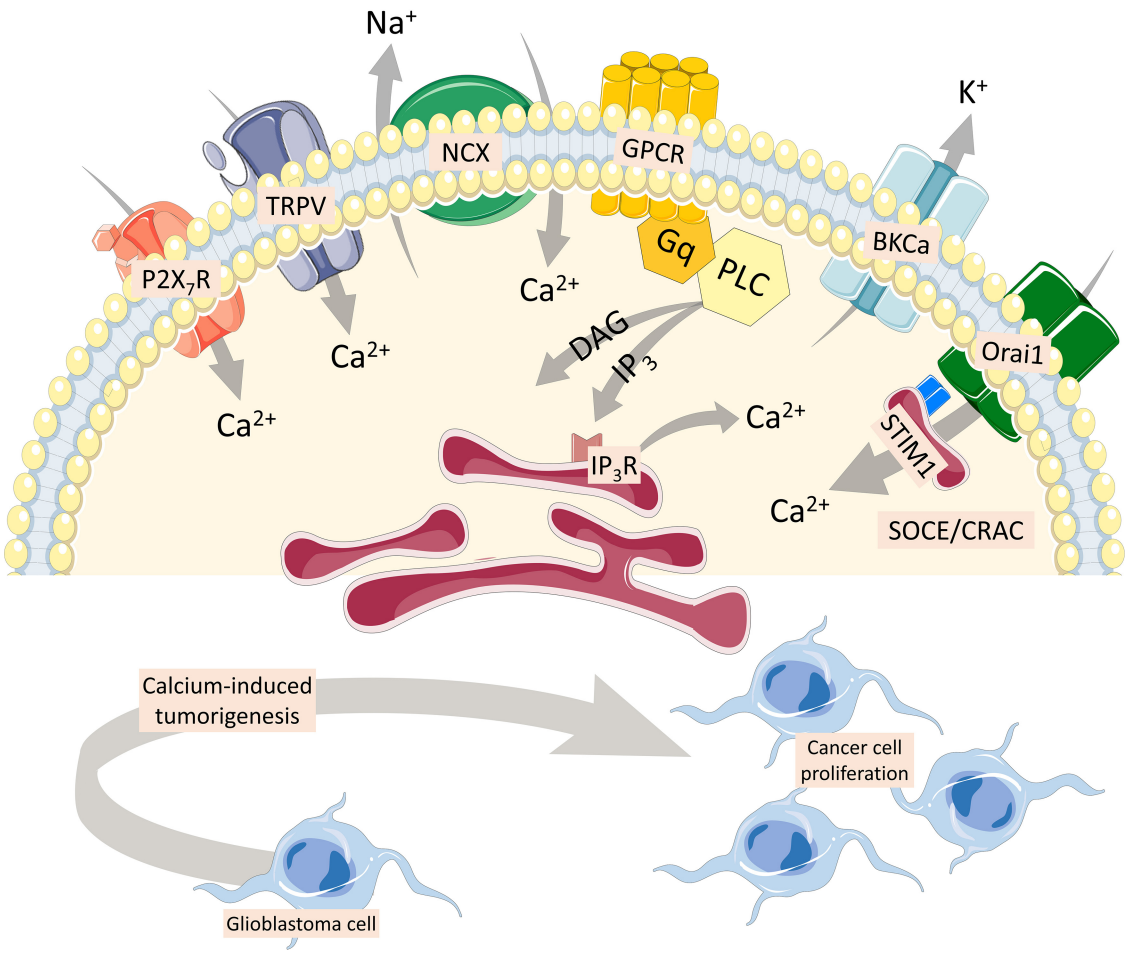

FIGURE 4 | Multiple Ca^{2+} pathways involved in cancer cells. P2X7 and TRPV1 receptors activate a strong calcium response in cancer cells (Strong and Daniels, 2017). Glutamate secretion upon ATP activation is excitotoxic to healthy tissue and linked to tumorigenicity into adjacent brain regions (Strong et al., 2018). The Na^{+}/Ca^{2+} exchanger (NCX), which maintains cytoplasmic calcium homeostatic levels, also increases Ca^{2+} levels in glioblastoma cells (Song et al., 2014). Inhibition of the forward NCX (Ca^{2+} exit mode) induces a Ca^{2+}-mediated injury in glioblastoma cells (Hu et al., 2019). Finally, G protein-coupled metabotropic receptors coupled to activation of phospholipase C result in the generation of the second messenger, inositol 1,4,5 trisphosphate, which increases intracellular Ca^{2+} and diacylglycerol, involved in cancer cell proliferation, with important participation of the large-conductance voltage- and Ca^{2+}-activated K^{+} channel. Store-operated Ca^{2+} entry is mediated through Ca^{2+} release-activated Ca^{2+} current, composed by ORAI1, and stromal interaction molecule 1 (STIM-1), a luminal Ca^{2+} sensor transmembrane protein present in the endoplasmic reticulum membrane (Putney, 2009; De Bock et al., 2013). Both ORAI1 and STIM-1 are upregulated in primary human cell lines obtained from samples of glioblastoma (Motiani et al., 2013).

isoforms diminished the effect of SKF 96365 on glioblastoma cells (Song et al., 2014). In addition, inhibition of the forward NCX (Ca^{2+} exit mode), with bepridil and CB-DMB, induced Ca^{2+}-mediated injury in glioblastoma cells (Hu et al., 2019). NCX maintains cytoplasmic calcium homeostatic levels, in addition to plasma membrane Ca^{2+} transport ATPase (PMCA) and sarco/endoplasmic reticulum (SR/ER) Ca^{2+}-ATPase (SERCA).

The P2X7 receptor is found in several types of tumors, such as neuroblastoma, melanoma, prostate, lung, and breast cancer. P2X7 expression is commonly associated with cancer cell survival, proliferation, and metastatic potential; upon dysregulation, the P2X7 receptor is associated with tumor initiation and development (Gilbert et al., 2019).

ING5, a member of the ING family of epigenetic regulators that alter histone acetylation and, subsequently, gene expression, increased the expression of stem cell markers and, consequently, brain tumor-initiating cells that cause the recurrence of glioblastomas (stemness) affected by epigenetic mechanisms (Wang F. et al., 2018). Proteomics and cell imaging assays demonstrated that ING5-transfected cells had intracellular Ca^{2+} elevation, which was associated with self-renewal, due to an increased expression of several types of Ca^{2+} channels, like L-type and P/Q-type voltage-gated Ca^{2+} channels, and TRPC (Wang F. et al., 2018). Differentiated glioblastoma cells constitute a distinctive niche compared to glioblastoma stem cells, sending cues to the microenvironment, both as juxtacrine (involving direct contact) or paracrine (through secreted factors). One of

these is BDNF, secreted by SOX2-negative tumor cells (Wang X. et al., 2018). Activation of NTRK2, the cognate receptor, activates the PI3K-AKT pathway which is activated in glioblastoma stem cells, leading to tumor growth (Wang X. et al., 2018).

Store-operated Ca^{2+} entry (SOCE) is mediated through Ca^{2+} release-activated Ca^{2+} current (CRAC), non-voltage sensitive channels highly selective for Ca^{2+}. They are composed by ORAI1, a member of the ORAI Ca^{2+} channel family (also known as CRAC modulator 1 or CRACM1), and form a macromolecular complex with the stromal interaction molecule 1 (STIM-1), a luminal Ca^{2+} sensor transmembrane protein present in the ER membrane (Putney, 2009; De Bock et al., 2013). Both ORAI1 and STIM-1 are upregulated in primary human cell lines obtained from surgical samples of glioblastoma multiforme compared to non-tumor human astrocytes (Motiani et al., 2013). CRAC inhibitors SKF-96365, 2-APB, and diethylstilbestrol also blocked GBM cell proliferation, and silencing of ORAI1 and STIM1 proteins using siRNA significantly inhibited C6 cell proliferation and SOCE compared to control cells (Liu et al., 2011).

Mice generated with CRISPR-based *in utero* electroporation of three deleted genes encoding phosphatase and tensin homolog (Pten), neurofibromin 1 (Nf1), and p53 (Trp53), all linked to tumorigenesis in human glioma genes, show a brain tumor with progressive cortical hyperexcitability due to tumor invasion and spontaneous seizures. $Iba1^{+}$ cells (microglia) also increased fivefold in the neighboring tumor area. Intracellular calcium imaging revealed recurrent seizure activity and robust bilateral calcium activity in GCAMP unanesthetized mice (Hatcher et al., 2020).

Metabotropic receptors coupled to the activation of phospholipase C (PLC) results in phosphatidylinositol 4,5 biphosphate cleavage and generation of the second messengers inositol 1,4,5 trisphosphate (IP3), which increases intracellular Ca^{2+}, and diacylglycerol, which activates protein kinase C. Activation of IP3 receptors on intracellular stores (endoplasmic reticulum and calciosomes) permits the release of Ca^{2+} down its electrochemical gradient, reaching cytoplasmic levels up to 10^{-6} M (Berridge et al., 2000). Type 3 IP3 receptor (IP3R3) and voltage- and Ca^{2+} dependent K(+) channels (BKCa) were shown to participate in breast cancer cell proliferation. Cell lines MCF-7 and MCF-10A are activated by 25 μM ATP, which induces a PLC-dependent elevation of intracellular Ca^{2+} and cell proliferation, which is ablated when the expression of both BKCa and/or IP3R3 is inhibited by specific small interfering RNAs, leading to a cell cycle arrest in the G0/G1 phase (Mound et al., 2013). Alternatively, live-cell imaging of intracellular calcium fluxes has been used in human parathyroid tumor sections upon calcium-sensing receptor activation, a metabotropic receptor, and consequently visualize the effects of intratumoral heterogeneity in real time (Koh et al., 2017).

NEURAL CELL LINEAGES DERIVED FROM iPS CELLS

Induced pluripotent stem (iPS) cells have been generated from mouse and human somatic cells by introducing selective transcription factors (Oct3/4, Sox2, Klf4, c-Myc, Nanog, and/or Lin28) using retroviruses or lentiviruses (Okita et al., 2008). Differentiation of iPS on neural cells from self-organized human organoids/spheroids has recently been used to generate multiple classes of cells: progenitors, neurons, and glia to be enriched and considered to be used in healthy and disease models, such as neurological disorders. Indeed astrocyte (Dezonne et al., 2017; Sloan et al., 2017), oligodendrocyte (Marton et al., 2019) and neuron (Nascimento et al., 2019) lineage cells, as well as region-specific cortical neurons and astrocytes, some from both deep and superficial cortical layers that are transcriptionally correlated to *in vivo* fetal development (Paşca et al., 2015), have been generated following multiple strategies, of which functionality data included calcium imaging assays. Derived glia from human cerebral cortical spheroids had similar properties found in primary fetal astrocytes, and upon transition to a more developed state, dozens of astrocytic markers increased as expected, accelerating around birth, while fetal astrocyte markers declined rapidly over this same period. Gene analysis can be hierarchically organized and disposed as three primary clusters of cells: for instance, the expression levels of aquaporin-4, the transcription factor SOX9, and the glial high-affinity glutamate transporter were compatible to astrocyte lineage cells, but not neurons derived from spheroids (Sloan et al., 2017); changes in calcium signaling, phagocytic capacity, and transcriptional regulation approached to those observed in a mature state (Sloan et al., 2017). In general, emerging cortical organoids from iPS replicates most of the characteristics found in the *in vivo* cortex, including temporal corticogenesis and connectivity. The exception seems to be generation of microglia and blood vessels (Varrault et al., 2019). Co-cultures of astrocytes generated from human cerebral cortical spheroids in the presence of early *in vitro*-stage neurons produced an increase in depolarization-induced calcium signaling (Sloan et al., 2017).

Electrophysiology is also a valuable tool to evaluate organoids at the molecular and the cellular levels, comparing gene expression profiles among fetal and adult brains using cerebral organoids (Logan et al., 2020). The activity of cultured neurons from human dissociated embryonic stem cell-derived cerebral organoids was also evaluated through calcium imaging, and the activities were shown to follow synchronized and non-synchronized patterns (Sakaguchi et al., 2019). Part of this activity depends on gamma-aminobutyric acid (GABA) and gap junctions to the development of synchronous activity in hPSC-derived neural networks (Mäkinen et al., 2018). Human organoids are also being developed to model glioblastoma, so invasion can be studied and how tumorigenesis relates to the extracellular matrix can be understood (Silvia and Dai, 2020). Tumor cells within organoids extend a network of long microtubes, recapitulating the *in vivo* behavior of GBM (Krieger et al., 2020). The transcriptional changes implicated in the invasion process are coherent across patient samples, indicating that GBM cells reactively upregulate genes required for their dispersion.

Millions of chronic disease patients with organ insufficiency that cannot be treated with transplant or pharmacotherapy rely on the possibility that 1 day personalized-specific iPS cells might

integrate in target tissues and become a routine in regenerative medicine. In terms of brain function, this type of approach is being used to treat ischemia to replenish neural cells and to approach autism spectral disorder as many proteins involved in the regulation of synaptic plasticity, neuronal excitability, and neuronal connectivity are inappropriately developmentally generated or misplaced, disturbing the neuronal network activity (Culotta and Penzes, 2020). On Alzheimer's disease, early hyperexcitability is linked to widespread synapse loss and cognitive dysfunction, and therefore a culture model derived from human cerebral organoids might shed some light on a synaptic plasticity model comparing aberrant neural networks from controls (Ghatak et al., 2020).

FINAL REMARKS

Calcium imaging has been used in diverse dynamic cellular networks to correlate spatiotemporal calcium shifts to different intracellular and extracellular mechanisms. The transition of progenitors and stem cells to differentiated neurons, astrocytes, oligodendrocytes, and microglia can be followed through ion channels, transporters, and receptors coupled to calcium fluxes. Cancer cells or inducible pluripotent cell lines might help to model diseases and can be differentiated from healthy cells in terms of the expression of calcium-binding/permeable molecules and shed light on therapy.

AUTHOR CONTRIBUTIONS

RM, HF, and FM contributed to the review body text and the conception of the figures. All authors contributed to the article and approved the submitted version.

FUNDING

HF is a post-doctoral fellow at UC Davis. This work was supported by FAPERJ (Fundação Carlos Chagas Filho de Amparo à Pesquisa do Estado do Rio de Janeiro), CNPq (Conselho Nacional de Desenvolvimento Científico e Tecnològico; PQ fellowship 305784/2018-8), and INCT-INNT (National Institute of Translational Neuroscience 465346/2014-6).

REFERENCES

Ahluwalia, J., Urban, L., Bevan, S., and Nagy, I. (2003). Anandamide regulates neuropeptide release from capsaicin-sensitive primary sensory neurons by activating both the cannabinoid 1 receptor and the vanilloid receptor 1 *in vitro*. *Eur. J. Neurosci.* 17, 2611–2618. doi: 10.1046/j.1460-9568.2003.02703.x

Ai, M., Mills, H., Kanai, M., Lai, J., Deng, J., Schreiter, E., et al. (2015). Green-to-Red Photoconversion of GCaMP. *PLoS One* 10:e0138127. doi: 10.1371/journal.pone.0138127

Akiyoshi, R., Wake, H., Kato, D., Horiuchi, H., Ono, R., Ikegami, A., et al. (2018). Microglia enhance synapse activity to promote local network synchronization. *eNeuro* 5:ENEURO.0088-18. doi: 10.1523/eneuro.0088-18.2018

Albers, F., Wachsmuth, L., van Alst, T. M., and Faber, C. (2018). Multimodal functional neuroimaging by simultaneous BOLD fMRI and Fiber-optic calcium recordings and optogenetic control. *Mol. Imaging Biol.* 20, 171–182. doi: 10.1007/s11307-017-1130-6

Anderson, M., Zheng, Q., and Dong, X. (2018). Investigation of pain mechanisms by calcium imaging approaches. *Neurosci. Bull.* 34, 194–199. doi: 10.1007/s12264-017-0139-9

Baden, T., Berens, P., Franke, K., Román Rosón, M., Bethge, M., and Euler, T. (2016). The functional diversity of retinal ganglion cells in the mouse. *Nature* 529, 345–350. doi: 10.1038/nature16468

Barnstable, C. J. (1993). Glutamate and GABA in retinal circuitry. *Curr. Opin. Neurobiol.* 3, 520–525. doi: 10.1016/0959-4388(93)90050-9

Berridge, M. J., Lipp, P., and Bootman, M. D. (2000). The versatility and universality of calcium signalling. *Nat. Rev. Mol. Cell Biol.* 1, 11–21. doi: 10.1038/35036035

Brawek, B., and Garaschuk, O. (2013). Microglial calcium signaling in the adult, aged and diseased brain. *Cell Calcium* 53, 159–169. doi: 10.1016/j.ceca.2012.12.003

Bruton, J., Cheng, A. J., and Westerblad, H. (2020). Measuring Ca(2+) in living cells. *Adv. Exp. Med. Biol.* 1131, 7–26. doi: 10.1007/978-3-030-12457-1_2

Carafoli, E., and Krebs, J. (2016). Why Calcium? How calcium became the best communicator. *J. Biol. Chem.* 291, 20849–20857. doi: 10.1074/jbc.R116.735894

Caterina, M. J., Schumacher, M. A., Tominaga, M., Rosen, T. A., Levine, J. D., and Julius, D. (1997). The capsaicin receptor: a heat-activated ion channel in the pain pathway. *Nature* 389, 816–824. doi: 10.1038/39807

Catterall, W. A. (2000). Structure and regulation of voltage-gated Ca2+ channels. *Annu. Rev. Cell Dev. Biol.* 16, 521–555. doi: 10.1146/annurev.cellbio.16.1.521

Caval-Holme, F., Zhang, Y., and Feller, M. B. (2019). Gap junction coupling shapes the encoding of light in the developing retina. *Curr. Biol.* 29, 4024–4035.e5. doi: 10.1016/j.cub.2019.10.025

Chen, C., Zhang, J., Sun, L., Zhang, Y., Gan, W. B., Tang, P., et al. (2019). Long-term imaging of dorsal root ganglia in awake behaving mice. *Nat. Commun.* 10:3087. doi: 10.1038/s41467-019-11158-0

Chen, G., Zhang, Y. Q., Qadri, Y. J., Serhan, C. N., and Ji, R. R. (2018). Microglia in pain: detrimental and protective roles in pathogenesis and resolution of pain. *Neuron* 100, 1292–1311. doi: 10.1016/j.neuron.2018.11.009

Cook, N. D. (2008). The neuron-level phenomena underlying cognition and consciousness: synaptic activity and the action potential. *Neuroscience* 153, 556–570. doi: 10.1016/j.neuroscience.2008.02.042

Corder, G., Ahanonu, B., Grewe, B. F., Wang, D., Schnitzer, M. J., and Scherrer, G. (2019). An amygdalar neural ensemble that encodes the unpleasantness of pain. *Science* 363, 276–281. doi: 10.1126/science.aap8586

Coull, J. A., Boudreau, D., Bachand, K., Prescott, S. A., Nault, F., Sík, A., et al. (2003). Trans-synaptic shift in anion gradient in spinal lamina I neurons as a mechanism of neuropathic pain. *Nature* 424, 938–942. doi: 10.1038/nature01868

Coull, J. A. M., Beggs, S., Boudreau, D., Boivin, D., Tsuda, M., Inoue, K., et al. (2005). BDNF from microglia causes the shift in neuronal anion gradient underlying neuropathic pain. *Nature* 438, 1017–1021. doi: 10.1038/nature04223

Culotta, L., and Penzes, P. (2020). Exploring the mechanisms underlying excitation/inhibition imbalance in human iPSC-derived models of ASD. *Mol. Autism* 11:32. doi: 10.1186/s13229-020-00339-0

David, S., and Kroner, A. (2011). Repertoire of microglial and macrophage responses after spinal cord injury. *Nat. Rev. Neurosci.* 12, 388–399. doi: 10.1038/nrn3053

De Bock, M., Wang, N., Decrock, E., Bol, M., Gadicherla, A. K., Culot, M., et al. (2013). Endothelial calcium dynamics, connexin channels and blood-brain barrier function. *Prog. Neurobiol.* 108, 1–20. doi: 10.1016/j.pneurobio.2013.06.001

De Melo Reis, R. A., Schitine, C. S., Kofalvi, A., Grade, S., Cortes, L., Gardino, P. F., et al. (2011). Functional identification of cell phenotypes differentiating from mice retinal neurospheres using single cell calcium imaging. *Cell. Mol. Neurobiol.* 31, 835–846. doi: 10.1007/s10571-011-9673-6

de Melo Reis, R. A., Ventura, A. L., Schitine, C. S., de Mello, M. C., and de Mello, F. G. (2008). Muller glia as an active compartment modulating nervous activity

in the vertebrate retina: neurotransmitters and trophic factors. *Neurochem. Res.* 33, 1466–1474. doi: 10.1007/s11064-008-9604-1

Dezonne, R. S., Sartore, R. C., Nascimento, J. M., Saia-Cereda, V. M., Romão, L. F., Alves-Leon, S. V., et al. (2017). Derivation of functional human astrocytes from cerebral organoids. *Sci. Rep.* 7:45091. doi: 10.1038/srep45091

Eiriz, M. F., Grade, S., Rosa, A., Xapelli, S., Bernardino, L., Agasse, F., et al. (2011). Functional evaluation of neural stem cell differentiation by single cell calcium imaging. *Curr. Stem Cell Res. Ther.* 6, 288–296. doi: 10.2174/157488811796575387

Faria, R. X., Freitas, H. R., and Reis, R. A. M. (2017). P2X7 receptor large pore signaling in avian Muller glial cells. *J. Bioenerg. Biomembr.* 49, 215–229. doi: 10.1007/s10863-017-9717-9

Fields, R. D., and Burnstock, G. (2006). Purinergic signalling in neuron-glia interactions. *Nat. Rev. Neurosci.* 7, 423–436. doi: 10.1038/nrn1928

Frackowiak, R., and Markram, H. (2015). The future of human cerebral cartography: a novel approach. *Philos. Trans. R. Soc. Lond. B Biol. Sci.* 370:20140171. doi: 10.1098/rstb.2014.0171

Freitas, H. R., Ferraz, G., Ferreira, G. C., Ribeiro-Resende, V. T., Chiarini, L. B., do Nascimento, J. L., et al. (2016). Glutathione-induced calcium shifts in chick retinal glial cells. *PLoS One* 11:e0153677. doi: 10.1371/journal.pone.0153677

Freitas, H. R., Isaac, A. R., Silva, T. M., Diniz, G. O. F., Dos Santos Dabdab, Y., Bockmann, E. C., et al. (2019). Cannabinoids induce cell death and promote P2X7 receptor signaling in retinal glial progenitors in culture. *Mol. Neurobiol.* 56, 6472–6486. doi: 10.1007/s12035-019-1537-y

Freitas, H. R., and Reis, R. A. (2017). Glutathione induces GABA release through P2X7R activation on Muller glia. *Neurogenesis* 4:e1283188. doi: 10.1080/23262133.2017.1283188

Ganguly, K., Schinder, A. F., Wong, S. T., and Poo, M. (2001). GABA itself promotes the developmental switch of neuronal GABAergic responses from excitation to inhibition. *Cell* 105, 521–532. doi: 10.1016/s0092-8674(01)00341-5

Ghatak, S., Dolatabadi, N., Gao, R., Wu, Y., Scott, H., Trudler, D., et al. (2020). NitroSynapsin ameliorates hypersynchronous neural network activity in Alzheimer hiPSC models. *Mol Psychiatry*. doi: 10.1038/s41380-020-0776-7 [Epub ahead of print].

Gilbert, S. M., Oliphant, C. J., Hassan, S., Peille, A. L., Bronsert, P., Falzoni, S., et al. (2019). ATP in the tumour microenvironment drives expression of nfP2X(7), a key mediator of cancer cell survival. *Oncogene* 38, 194–208. doi: 10.1038/s41388-018-0426-6

Grienberger, C., and Konnerth, A. (2012). Imaging calcium in neurons. *Neuron* 73, 862–885. doi: 10.1016/j.neuron.2012.02.011

Grynkiewicz, G., Poenie, M., and Tsien, R. Y. (1985). A new generation of Ca2+ indicators with greatly improved fluorescence properties. *J. Biol. Chem.* 260, 3440–3450.

Guan, J., Li, J., Liang, S., Li, R., Li, X., Shi, X., et al. (2018). NeuroSeg: automated cell detection and segmentation for *in vivo* two-photon Ca(2+) imaging data. *Brain Struct. Funct.* 223, 519–533. doi: 10.1007/s00429-017-1545-5

Guimaraes, M. Z., Hokoc, J. N., Duvoisin, R., Reis, R. A., and De Mello, F. G. (2001). Dopaminergic retinal cell differentiation in culture: modulation by forskolin and dopamine. *Eur. J. Neurosci.* 13, 1931–1937. doi: 10.1046/j.0953-816x.2001.01575.x

Guimaraes, R. P. M., Landeira, B. S., Coelho, D. M., Golbert, D. C. F., Silveira, M. S., Linden, R., et al. (2018). Evidence of Muller glia conversion into retina ganglion cells using neurogenin2. *Front. Cell. Neurosci.* 12:410. doi: 10.3389/fncel.2018.00410

Guo, Q., Zhou, J., Feng, Q., Lin, R., Gong, H., Luo, Q., et al. (2015). Multi-channel fiber photometry for population neuronal activity recording. *Biomed. Opt. Express* 6, 3919–3931. doi: 10.1364/boe.6.003919

Hampton, T. (2018). Researchers reprogram cells *in vivo* to restore vision in mice. *JAMA* 320, 1745–1745. doi: 10.1001/jama.2017.12866

Hatakeyama, J., and Kageyama, R. (2004). Retinal cell fate determination and bHLH factors. *Semin. Cell Dev. Biol.* 15, 83–89. doi: 10.1016/j.semcdb.2003.09.005

Hatcher, A., Yu, K., Meyer, J., Aiba, I., Deneen, B., and Noebels, J. L. (2020). Pathogenesis of peritumoral hyperexcitability in an immunocompetent CRISPR-based glioblastoma model. *J. Clin. Invest.* 130, 2286–2300. doi: 10.1172/JCI133316

Hong, G., Fu, T.-M., Qiao, M., Viveros, R. D., Yang, X., Zhou, T., et al. (2018). A method for single-neuron chronic recording from the retina in awake mice. *Science* 360, 1447–1451. doi: 10.1126/science.aas9160

Hu, H.-J., Wang, S.-S., Wang, Y.-X., Liu, Y., Feng, X.-M., Shen, Y., et al. (2019). Blockade of the forward Na(+) /Ca(2+) exchanger suppresses the growth of glioblastoma cells through Ca(2+) -mediated cell death. *Br. J. Pharmacol.* 176, 2691–2707. doi: 10.1111/bph.14692

Hu, X., Liu, Y., Wu, J., Liu, Y., Liu, W., Chen, J., et al. (2020). Inhibition of P2X7R in the amygdala ameliorates symptoms of neuropathic pain after spared nerve injury in rats. *Brain Behav. Immun.* 88, 507–514. doi: 10.1016/j.bbi.2020.04.030

Inoue, M. (2020). Genetically encoded calcium indicators to probe complex brain circuit dynamics *in vivo*. *Neurosci. Res.* doi: 10.1016/j.neures.2020.05.013 [Epub ahead of print].

Islam, M. S. (2020). Calcium signaling: from basic to bedside. *Adv. Exp. Med. Biol.* 1131, 1–6. doi: 10.1007/978-3-030-12457-1_1

Johannssen, H. C., and Helmchen, F. (2010). *In vivo* Ca2+ imaging of dorsal horn neuronal populations in mouse spinal cord. *J. Physiol.* 588(Pt 18), 3397–3402. doi: 10.1113/jphysiol.2010.191833

Kaifosh, P., Zaremba, J. D., Danielson, N. B., and Losonczy, A. (2014). SIMA: python software for analysis of dynamic fluorescence imaging data. *Front. Neuroinform.* 8:80. doi: 10.3389/fninf.2014.00080

Keirstead, S. A., and Miller, R. F. (1997). Metabotropic glutamate receptor agonists evoke calcium waves in isolated Müller cells. *Glia* 21, 194–203.

Kim, C. K., Adhikari, A., and Deisseroth, K. (2017). Integration of optogenetics with complementary methodologies in systems neuroscience. *Nat. Rev. Neurosci.* 18, 222–235. doi: 10.1038/nrn.2017.15

Knoblich, U., Huang, L., Zeng, H., and Li, L. (2019). Neuronal cell-subtype specificity of neural synchronization in mouse primary visual cortex. *Nat. Commun.* 10:2533. doi: 10.1038/s41467-019-10498-1

Koh, J., Hogue, J. A., and Sosa, J. A. (2017). Live-cell visualization of calcium flux in vibratome-cut thick sections of viable tumor tissue. *Curr. Protoc. Cell Biol.* 77, 4.34.1–4.34.16. doi: 10.1002/cpcb.37

Krieger, T. G., Tirier, S. M., Park, J., Jechow, K., Eisemann, T., Peterziel, H., et al. (2020). Modeling glioblastoma invasion using human brain organoids and single-cell transcriptomics. *Neuro Oncol.* 22, 1138–1149. doi: 10.1093/neuonc/noaa091

Kroner, A., and Rosas Almanza, J. (2019). Role of microglia in spinal cord injury. *Neurosci. Lett.* 709:134370. doi: 10.1016/j.neulet.2019.134370

Kubrusly, R. C. C., Gunter, A., Sampaio, L., Martins, R. S., Schitine, C. S., Trindade, P., et al. (2018). Neuro-glial cannabinoid receptors modulate signaling in the embryonic avian retina. *Neurochem. Int.* 112, 27–37. doi: 10.1016/j.neuint.2017.10.016

Lake, E. M. R., Ge, X., Shen, X., Herman, P., Hyder, F., Cardin, J., et al. (2018). Simultaneous mesoscopic Ca2+ imaging and fMRI: neuroimaging spanning spatiotemporal scales. *bioRxiv* [Preprint]. doi: 10.1101/464305

Liang, Z., Ma, Y., Watson, G. D. R., and Zhang, N. (2017). Simultaneous GCaMP6-based fiber photometry and fMRI in rats. *J. Neurosci. Methods* 289, 31–38. doi: 10.1016/j.jneumeth.2017.07.002

Lichtman, J. W., Livet, J., and Sanes, J. R. (2008). A technicolour approach to the connectome. *Nat. Rev. Neurosci.* 9, 417–422. doi: 10.1038/nrn2391

Liu, H., Hughes, J. D., Rollins, S., Chen, B., and Perkins, E. (2011). Calcium entry via ORAI1 regulates glioblastoma cell proliferation and apoptosis. *Exp. Mol. Pathol.* 91, 753–760. doi: 10.1016/j.yexmp.2011.09.005

Logan, S., Arzua, T., Yan, Y., Jiang, C., Liu, X., Yu, L. K., et al. (2020). Dynamic characterization of structural, molecular, and electrophysiological phenotypes of human-induced pluripotent stem cell-derived cerebral organoids, and comparison with fetal and adult gene profiles. *Cells* 9:1301. doi: 10.3390/cells9051301

Logothetis, N. K., Pauls, J., Augath, M., Trinath, T., and Oeltermann, A. (2001). Neurophysiological investigation of the basis of the fMRI signal. *Nature* 412, 150–157. doi: 10.1038/35084005

Mäkinen, M. E.-L., Ylä-Outinen, L., and Narkilahti, S. (2018). GABA and Gap junctions in the development of synchronized activity in human pluripotent stem cell-derived neural networks. *Front. Cell. Neurosci.* 12:56. doi: 10.3389/fncel.2018.00056

Mapplebeck, J. C. S., Dalgarno, R., Tu, Y., Moriarty, O., Beggs, S., Kwok, C. H. T., et al. (2018). Microglial P2X4R-evoked pain hypersensitivity is sexually dimorphic in rats. *Pain* 159, 1752–1763.

Marton, R. M., Miura, Y., Sloan, S. A., Li, Q., Revah, O., Levy, R. J., et al. (2019). Differentiation and maturation of oligodendrocytes in human three-dimensional neural cultures. *Nat. Neurosci.* 22, 484–491. doi: 10.1038/s41593-018-0316-9

Metea, M. R., and Newman, E. A. (2006). Calcium signaling in specialized glial cells. *Glia* 54, 650–655. doi: 10.1002/glia.20352

Miller, D. J. (2004). Sydney Ringer; physiological saline, calcium and the contraction of the heart. *J. Physiol.* 555(Pt 3), 585–587. doi: 10.1113/jphysiol.2004.060731

Millns, P. J., Chimenti, M., Ali, N., Ryland, E., De Lago, E., Fernandez-Ruiz, J., et al. (2006). Effects of inhibition of fatty acid amide hydrolase vs. the anandamide membrane transporter on TRPV1-mediated calcium responses in adult DRG neurons; the role of CB1 receptors. *Eur. J. Neurosci.* 24, 3489–3495. doi: 10.1111/j.1460-9568.2006.05236.x

Miyawaki, A., Llopis, J., Heim, R., McCaffery, J. M., Adams, J. A., Ikura, M., et al. (1997). Fluorescent indicators for Ca2+based on green fluorescent proteins and calmodulin. *Nature* 388, 882–887. doi: 10.1038/42264

Motiani, R. K., Hyzinski-Garcia, M. C., Zhang, X., Henkel, M. M., Abdullaev, I. F., Kuo, Y. H., et al. (2013). STIM1 and Orai1 mediate CRAC channel activity and are essential for human glioblastoma invasion. *Pflugers Arch.* 465, 1249–1260. doi: 10.1007/s00424-013-1254-8

Mound, A., Rodat-Despoix, L., Bougarn, S., Ouadid-Ahidouch, H., and Matifat, F. (2013). Molecular interaction and functional coupling between type 3 inositol 1,4,5-trisphosphate receptor and BKCa channel stimulate breast cancer cell proliferation. *Eur. J. Cancer* 49, 3738–3751. doi: 10.1016/j.ejca.2013.07.013

Mukamel, E. A., Nimmerjahn, A., and Schnitzer, M. J. (2009). Automated analysis of cellular signals from large-scale calcium imaging data. *Neuron* 63, 747–760. doi: 10.1016/j.neuron.2009.08.009

Nakai, J., Ohkura, M., and Imoto, K. (2001). A high signal-to-noise Ca(2+) probe composed of a single green fluorescent protein. *Nat. Biotechnol.* 19, 137–141. doi: 10.1038/84397

Nascimento, J. M., Saia-Cereda, V. M., Sartore, R. C., da Costa, R. M., Schitine, C. S., Freitas, H. R., et al. (2019). Human cerebral organoids and fetal brain tissue share proteomic similarities. *Front. Cell Dev. Biol.* 7:303. doi: 10.3389/fcell.2019.00303

Nimmerjahn, A., and Bergles, D. E. (2015). Large-scale recording of astrocyte activity. *Curr. Opin. Neurobiol.* 32, 95–106. doi: 10.1016/j.conb.2015.01.015

O'Hashi, K., Sohya, K., Matsuno, H., Tsuchimine, S., and Kunugi, H. (2019). Construction of the common cortical space by spontaneous activity and its application in the mouse cortex. *Biochem. Biophys. Res. Commun.* 513, 869–874. doi: 10.1016/j.bbrc.2019.04.048

Oheim, M., Schmidt, E., and Hirrlinger, J. (2018). Local energy on demand: are 'spontaneous' astrocytic Ca(2+)-microdomains the regulatory unit for astrocyte-neuron metabolic cooperation? *Brain Res. Bull.* 136, 54–64. doi: 10.1016/j.brainresbull.2017.04.011

Ohshiro, H., Ogawa, S., and Shinjo, K. (2007). Visualizing sensory transmission between dorsal root ganglion and dorsal horn neurons in co-culture with calcium imaging. *J. Neurosci. Methods* 165, 49–54. doi: 10.1016/j.jneumeth.2007.05.018

Okada, T., Schultz, K., Geurtz, W., Hatt, H., and Weiler, R. (1999). AMPA-preferring receptors with high Ca2+ permeability mediate dendritic plasticity of retinal horizontal cells. *Eur. J. Neurosci.* 11, 1085–1095. doi: 10.1046/j.1460-9568.1999.00516.x

Okita, K., Nakagawa, M., Hyenjong, H., Ichisaka, T., and Yamanaka, S. (2008). Generation of mouse induced pluripotent stem cells without viral vectors. *Science* 322, 949–953. doi: 10.1126/science.1164270

Oliveira-Fusaro, M. C. G., Zanoni, C. I. S., Dos Santos, G. G., Manzo, L. P., Araldi, D., Bonet, I. J. M., et al. (2017). Antihyperalgesic effect of CB(1) receptor activation involves the modulation of P2X(3) receptor in the primary afferent neuron. *Eur. J. Pharmacol.* 798, 113–121. doi: 10.1016/j.ejphar.2017.01.030

Park, H., and Kim, J. E. (2020). Deletion of P2X7 receptor decreases basal glutathione level by changing glutamate-glutamine cycle and neutral amino acid transporters. *Cells* 9:995. doi: 10.3390/cells9040995

Paşca, A. M., Sloan, S. A., Clarke, L. E., Tian, Y., Makinson, C. D., Huber, N., et al. (2015). Functional cortical neurons and astrocytes from human pluripotent stem cells in 3D culture. *Nat. Methods* 12, 671–678. doi: 10.1038/nmeth.3415

Passos, A., Herculano, A. M., Oliveira, K., de Lima, S. M. A., Rocha, F. A. F., Freitas, H. R., et al. (2019). Regulation of the serotonergic system by kainate in the avian retina. *Cell. Mol. Neurobiol.* 39, 1039–1049. doi: 10.1007/s10571-019-00701-8

Peirs, C., and Seal, R. P. (2016). Neural circuits for pain: recent advances and current views. *Science* 354, 578–584. doi: 10.1126/science.aaf8933

Pnevmatikakis, E. A., and Giovannucci, A. (2017). NoRMCorre: an online algorithm for piecewise rigid motion correction of calcium imaging data. *J. Neurosci. Methods* 291, 83–94. doi: 10.1016/j.jneumeth.2017.07.031

Putney, J. W. (2009). Capacitative calcium entry: from concept to molecules. *Immunol. Rev.* 231, 10–22. doi: 10.1111/j.1600-065X.2009.00810.x

Ran, C., Hoon, M. A., and Chen, X. (2016). The coding of cutaneous temperature in the spinal cord. *Nat. Neurosci.* 19, 1201–1209. doi: 10.1038/nn.4350

Reichenbach, A., and Bringmann, A. (2013). New functions of Muller cells. *Glia* 61, 651–678. doi: 10.1002/glia.22477

Reichenbach, A., and Bringmann, A. (2016). Role of purines in muller glia. *J. Ocul. Pharmacol. Ther.* 32, 518–533. doi: 10.1089/jop.2016.0131

Reis, R. A., Ventura, A. L., Kubrusly, R. C., de Mello, M. C., and de Mello, F. G. (2007). Dopaminergic signaling in the developing retina. *Brain Res. Rev.* 54, 181–188. doi: 10.1016/j.brainresrev.2007.01.001

Ribeiro-Resende, V. T., Araujo Gomes, T., de Lima, S., Nascimento-Lima, M., Bargas-Rega, M., Santiago, M. F., et al. (2014). Mice lacking GD3 synthase display morphological abnormalities in the sciatic nerve and neuronal disturbances during peripheral nerve regeneration. *PLoS One* 9:e108919. doi: 10.1371/journal.pone.0108919

Rice, M. E., and Russo-Menna, I. (1998). Differential compartmentalization of brain ascorbate and glutathione between neurons and glia. *Neuroscience* 82, 1213–1223. doi: 10.1016/s0306-4522(97)00347-3

Ringer, S., and Buxton, D. W. (1887). Concerning the action of calcium, potassium, and sodium salts upon the eel's heart and upon the skeletal muscles of the frog. *J. Physiol.* 8, 15–19. doi: 10.1113/jphysiol.1887.sp000239

Rosa, J. M., Bos, R., Sack, G. S., Fortuny, C., Agarwal, A., Bergles, D. E., et al. (2015). Neuron-glia signaling in developing retina mediated by neurotransmitter spillover. *eLife* 4:e09590. doi: 10.7554/eLife.09590

Rudolf, R., Mongillo, M., Rizzuto, R., and Pozzan, T. (2003). Looking forward to seeing calcium. *Nat. Rev. Mol. Cell Biol.* 4, 579–586. doi: 10.1038/nrm1153

Russell, J. T. (2011). Imaging calcium signals *in vivo*: a powerful tool in physiology and pharmacology. *Br. J. Pharmacol.* 163, 1605–1625. doi: 10.1111/j.1476-5381.2010.00988.x

Sakaguchi, H., Ozaki, Y., Ashida, T., Matsubara, T., Oishi, N., Kihara, S., et al. (2019). Self-organized synchronous calcium transients in a cultured human neural network derived from cerebral organoids. *Stem Cell Rep.* 13, 458–473. doi: 10.1016/j.stemcr.2019.05.029

Sargoy, A., Barnes, S., Brecha, N. C., and Pérez De Sevilla Müller, L. (2014). Immunohistochemical and calcium imaging methods in wholemount rat retina. *J. Vis. Exp.* 92:e51396. doi: 10.3791/51396

Schitine, C., Xapelli, S., Agasse, F., Sarda-Arroyo, L., Silva, A. P., De Melo Reis, R. A., et al. (2012). Ampakine CX546 increases proliferation and neuronal differentiation in subventricular zone stem/progenitor cell cultures. *Eur. J. Neurosci.* 35, 1672–1683. doi: 10.1111/j.1460-9568.2012.08072.x

Schitine, C. S., Mendez-Flores, O. G., Santos, L. E., Ornelas, I., Calaza, K. C., Perez-Toledo, K., et al. (2015). Functional plasticity of GAT-3 in avian Muller cells is regulated by neurons via a glutamatergic input. *Neurochem. Int.* 82, 42–51. doi: 10.1016/j.neuint.2015.02.004

Schlegel, F., Sych, Y., Schroeter, A., Stobart, J., Weber, B., Helmchen, F., et al. (2018). Fiber-optic implant for simultaneous fluorescence-based calcium recordings and BOLD fMRI in mice. *Nat. Protoc.* 13, 840–855. doi: 10.1038/nprot.2018.003

Schulz, K., Sydekum, E., Krueppel, R., Engelbrecht, C. J., Schlegel, F., Schröter, A., et al. (2012). Simultaneous BOLD fMRI and fiber-optic calcium recording in rat neocortex. *Nat. Methods* 9, 597–602. doi: 10.1038/nmeth.2013

Sekaran, S., Foster, R. G., Lucas, R. J., and Hankins, M. W. (2003). Calcium imaging reveals a network of intrinsically light-sensitive inner-retinal neurons. *Curr. Biol.* 13, 1290–1298. doi: 10.1016/S0960-9822(03)00510-4

Sekiguchi, K. J., Shekhtmeyster, P., Merten, K., Arena, A., Cook, D., Hoffman, E., et al. (2016). Imaging large-scale cellular activity in spinal cord of freely behaving mice. *Nat. Commun.* 7, 11450–11450. doi: 10.1038/ncomms11450

Silvia, N., and Dai, G. (2020). Cerebral organoids as a model for glioblastoma multiforme. *Curr. Opin. Biomed. Eng.* 13, 152–159. doi: 10.1016/j.cobme.2020.03.004

Sloan, S. A., Darmanis, S., Huber, N., Khan, T. A., Birey, F., Caneda, C., et al. (2017). Human astrocyte maturation captured in 3D cerebral cortical spheroids derived from pluripotent stem cells. *Neuron* 95, 779–790.e6. doi: 10.1016/j.neuron.2017.07.035

Soltanian-Zadeh, S., Sahingur, K., Blau, S., Gong, Y., and Farsiu, S. (2019). Fast and robust active neuron segmentation in two-photon calcium imaging using spatiotemporal deep learning. *Proc. Natl. Acad. Sci. U.S.A.* 116, 8554–8563. doi: 10.1073/pnas.1812995116

Song, M., Chen, D., and Yu, S. P. (2014). The TRPC channel blocker SKF 96365 inhibits glioblastoma cell growth by enhancing reverse mode of the Na(+)/Ca(2+) exchanger and increasing intracellular Ca(2+). *Br. J. Pharmacol.* 171, 3432–3447. doi: 10.1111/bph.12691

Strong, A. D., and Daniels, R. L. (2017). Live-cell calcium imaging of adherent and non-adherent GL261 cells reveals phenotype-dependent differences in drug responses. *BMC Cancer* 17:516. doi: 10.1186/s12885-017-3507-y

Strong, A. D., Indart, M. C., Hill, N. R., and Daniels, R. L. (2018). GL261 glioma tumor cells respond to ATP with an intracellular calcium rise and glutamate release. *Mol. Cell. Biochem.* 446, 53–62. doi: 10.1007/s11010-018-3272-5

Sych, Y., Chernysheva, M., Sumanovski, L. T., and Helmchen, F. (2019). High-density multi-fiber photometry for studying large-scale brain circuit dynamics. *Nat. Methods* 16, 553–560. doi: 10.1038/s41592-019-0400-4

Thrane, A. S., Rangroo Thrane, V., Zeppenfeld, D., Lou, N., Xu, Q., Nagelhus, E. A., et al. (2012). General anesthesia selectively disrupts astrocyte calcium signaling in the awake mouse cortex. *Proc. Natl. Acad. Sci. U.S.A.* 109, 18974–18979. doi: 10.1073/pnas.1209448109

Tong, C., Dai, J. K., Chen, Y., Zhang, K., Feng, Y., and Liang, Z. (2019). Differential coupling between subcortical calcium and BOLD signals during evoked and resting state through simultaneous calcium fiber photometry and fMRI. *Neuroimage* 200, 405–413. doi: 10.1016/j.neuroimage.2019.07.006

Tsien, R. Y. (1980). New calcium indicators and buffers with high selectivity against magnesium and protons: design, synthesis, and properties of prototype structures. *Biochemistry* 19, 2396–2404. doi: 10.1021/bi00552a018

Tsien, R. Y., Pozzan, T., and Rink, T. J. (1982). Calcium homeostasis in intact lymphocytes: cytoplasmic free calcium monitored with a new, intracellularly trapped fluorescent indicator. *J. Cell Biol.* 94, 325–334. doi: 10.1083/jcb.94.2.325

Tsuda, M., Shigemoto-Mogami, Y., Koizumi, S., Mizokoshi, A., Kohsaka, S., Salter, M. W., et al. (2003). P2X4 receptors induced in spinal microglia gate tactile allodynia after nerve injury. *Nature* 424, 778–783. doi: 10.1038/nature01786

Turner, D. L., and Cepko, C. L. (1987). A common progenitor for neurons and glia persists in rat retina late in development. *Nature* 328, 131–136. doi: 10.1038/328131a0

Tvrdik, P., Kearns, K. N., Sharifi, K. A., Sluzewski, M. F., Acton, S. T., and Kalani, M. Y. S. (2019). Calcium imaging of microglial network activity in stroke. *Methods Mol. Biol.* 2034, 267–279. doi: 10.1007/978-1-4939-9658-2_19

van der Stelt, M., Trevisani, M., Vellani, V., De Petrocellis, L., Schiano Moriello, A., Campi, B., et al. (2005). Anandamide acts as an intracellular messenger amplifying Ca2+ influx via TRPV1 channels. *EMBO J.* 24, 3026–3037. doi: 10.1038/sj.emboj.7600784

Varella, M. H., de Mello, F. G., and Linden, R. (1999). Evidence for an antiapoptotic role of dopamine in developing retinal tissue. *J. Neurochem.* 73, 485–492. doi: 10.1046/j.1471-4159.1999.0730485.x

Varrault, A., Journot, L., and Bouschet, T. (2019). Cerebral cortex generated from pluripotent stem cells to model corticogenesis and rebuild cortical circuits: *In vitro* veritas? *Stem Cells Dev.* 28, 361–369. doi: 10.1089/scd.2018.0233

Veruki, M. L., Zhou, Y., Castilho, Á, Morgans, C. W., and Hartveit, E. (2019). Extrasynaptic NMDA receptors on rod pathway amacrine cells: molecular composition, activation, and signaling. *J. Neurosci* 39, 627–650. doi: 10.1523/jneurosci.2267-18.2018

Wang, F., Wang, A. Y., Chesnelong, C., Yang, Y., Nabbi, A., Thalappilly, S., et al. (2018). ING5 activity in self-renewal of glioblastoma stem cells via calcium and follicle stimulating hormone pathways. *Oncogene* 37, 286–301. doi: 10.1038/onc.2017.324

Wang, M., He, Y., Sejnowski, T. J., and Yu, X. (2018). Brain-state dependent astrocytic Ca(2+) signals are coupled to both positive and negative BOLD-fMRI signals. *Proc. Natl. Acad. Sci. U.S.A.* 115, E1647–E1656. doi: 10.1073/pnas.1711692115

Wang, X., Prager, B. C., Wu, Q., Kim, L. J. Y., Gimple, R. C., Shi, Y., et al. (2018). Reciprocal signaling between glioblastoma stem cells and differentiated tumor cells promotes malignant progression. *Cell Stem Cell* 22, 514–528.e5. doi: 10.1016/j.stem.2018.03.011

Warbrick, T., Rosenberg, J., and Shah, N. J. (2017). The relationship between BOLD fMRI response and the underlying white matter as measured by fractional anisotropy (FA): a systematic review. *Neuroimage* 153, 369–381. doi: 10.1016/j.neuroimage.2016.12.075

Wright, P. W., Brier, L. M., Bauer, A. Q., Baxter, G. A., Kraft, A. W., Reisman, M. D., et al. (2017). Functional connectivity structure of cortical calcium dynamics in anesthetized and awake mice. *PLoS One* 12:e0185759. doi: 10.1371/journal.pone.0185759

Xapelli, S., Agasse, F., Grade, S., Bernardino, L., Ribeiro, F. F., Schitine, C. S., et al. (2014). Modulation of subventricular zone oligodendrogenesis: A role for hemopressin? *Front. Cell. Neurosci.* 8:59. doi: 10.3389/fncel.2014.00059

Xapelli, S., Agasse, F., Sarda-Arroyo, L., Bernardino, L., Santos, T., Ribeiro, F. F., et al. (2013). Activation of type 1 cannabinoid receptor (CB1R) promotes neurogenesis in murine subventricular zone cell cultures. *PLoS One* 8:e63529. doi: 10.1371/journal.pone.0063529

Yang, X. L. (2004). Characterization of receptors for glutamate and GABA in retinal neurons. *Prog. Neurobiol.* 73, 127–150. doi: 10.1016/j.pneurobio.2004.04.002

Conflict of Interest: The authors declare that the research was conducted in the absence of any commercial or financial relationships that could be construed as a potential conflict of interest.

Copyright © 2020 de Melo Reis, Freitas and de Mello. This is an open-access article distributed under the terms of the Creative Commons Attribution License (CC BY). The use, distribution or reproduction in other forums is permitted, provided the original author(s) and the copyright owner(s) are credited and that the original publication in this journal is cited, in accordance with accepted academic practice. No use, distribution or reproduction is permitted which does not comply with these terms.

frontiers in Neuroscience

MINI REVIEW
published: 05 October 2020
doi: 10.3389/fnins.2020.00914

Tissue Clearing and Expansion Methods for Imaging Brain Pathology in Neurodegeneration: From Circuits to Synapses and Beyond

Arnaldo Parra-Damas[1,2]* *and Carlos A. Saura*[1,2]

[1] *Institut de Neurociències, Departament de Bioquímica i Biologia Molecular, Facultat de Medicina, Universitat Autònoma de Barcelona, Barcelona, Spain,* [2] *Centro de Investigación Biomédica en Red Enfermedades Neurodegenerativas, Instituto de Salud Carlos III, Madrid, Spain*

Studying the structural alterations occurring during diseases of the nervous system requires imaging heterogeneous cell populations at the circuit, cellular and subcellular levels. Recent advancements in brain tissue clearing and expansion methods allow unprecedented detailed imaging of the nervous system through its entire scale, from circuits to synapses, including neurovascular and brain lymphatics elements. Here, we review the state-of-the-art of brain tissue clearing and expansion methods, mentioning their main advantages and limitations, and suggest their parallel implementation for circuits-to-synapses brain imaging using conventional (diffraction-limited) light microscopy -such as confocal, two-photon and light-sheet microscopy- to interrogate the cellular and molecular basis of neurodegenerative diseases. We discuss recent studies in which clearing and expansion methods have been successfully applied to study neuropathological processes in mouse models and postmortem human brain tissue. Volumetric imaging of cleared intact mouse brains and large human brain samples has allowed unbiased assessment of neuropathological hallmarks. In contrast, nanoscale imaging of expanded cells and brain tissue has been used to study the effect of protein aggregates on specific subcellular structures. Therefore, these approaches can be readily applied to study a wide range of brain processes and pathological mechanisms with cellular and subcellular resolution in a time- and cost-efficient manner. We consider that a broader implementation of these technologies is necessary to reveal the full landscape of cellular and molecular mechanisms underlying neurodegenerative diseases.

Keywords: tissue clearing, expansion microscopy, neuropathology, neurodegeneration, super-resolution microscopy

OPEN ACCESS

Edited by:
João O. Malva,
University of Coimbra, Portugal

Reviewed by:
Reinaldo B. Oria,
Federal University of Ceara, Brazil
Fahmeed Hyder,
Yale University, United States

***Correspondence:**
Arnaldo Parra-Damas
arnaldo.parra@e-campus.uab.cat;
arnaldo0283@gmail.com

Specialty section:
This article was submitted to Brain Imaging Methods, a section of the journal Frontiers in Neuroscience

Received: *10 May 2020*
Accepted: *07 August 2020*
Published: *05 October 2020*

Citation:
Parra-Damas A and Saura CA (2020) Tissue Clearing and Expansion Methods for Imaging Brain Pathology in Neurodegeneration: From Circuits to Synapses and Beyond. Front. Neurosci. 14:914. doi: 10.3389/fnins.2020.00914

INTRODUCTION

Neurodegenerative diseases, including Alzheimer's disease (AD), Parkinson's disease (PD), Huntington's disease (HD), amyotrophic lateral sclerosis (ALS), and frontotemporal dementia (FTD), among others, are incurable brain disorders that affect millions of people worldwide, causing enormous social and economic burdens. Despite global intensive research and

development efforts centered on neurodegenerative diseases, there are currently no effective therapies that can revert or prevent their progression. A deeper understanding of the brain structure, function and their pathological alterations is necessary to identify and develop novel therapeutic strategies. This endeavor requires integrating evidence from multiple methodological approaches used in cellular and molecular neuroscience, including structural information at the subcellular and systems biology levels.

The fundamental relationship between the structure and function of biological systems implies that any dysfunction occurring under pathological conditions may be explained in terms of structural alterations. Although this may seem over-simplistic for a highly complex organ such as the brain (whose function is determined by the connectivity and activity patterns of diverse cell populations) indeed structural changes in specific cell types underlie almost every long-term brain function under a wide range of physiological and pathological conditions, including learning, memory, acquisition of motor skills, emotional and stress responses, neurodevelopmental and neuropsychiatric disorders -including addictions-, inflammation, aging, and neurodegeneration. In particular, altered synaptic structures are observed in many neuropsychiatric disorders, whereas early loss of synapses occurs in neurodegenerative dementias such as AD, long before neuronal death occurs (Penzes et al., 2011; Sheng et al., 2012). However, our overall knowledge about the structure-function relationship on the nervous system remains very limited (Lichtman and Denk, 2011). Thus, any progress made on basic and biomedical neuroscience research in this regard will surely impulse therapeutic developments for neurodegenerative brain disorders.

Understanding the cellular and molecular mechanisms underlying neurodegeneration requires unbiased analyses of the neuropathological features and structural alterations affecting heterogeneous cellular populations in specific (often multiple) brain circuits. Ideally, such imaging analyses must be performed throughout the entire volume of the intact brain, spinal cord and peripheral nerves. On the other hand, studying the impact of these pathological features at the individual cellular level also requires imaging small cellular and subcellular structures, such as synapses, organelles and protein complexes, which are often too small to be imaged using standard light microscopy. Therefore, an ideal comprehensive structural assessment should be performed throughout the entire spatial scale of the nervous system, from circuits to synapses. Here, we discuss recent advances on brain tissue clearing and expansion microscopy methods that can facilitate this endeavor in the context of neurodegeneration research, and propose a convenient imaging pipeline (**Figure 1**) that can be implemented using standard light microscopy, consisting on: (1) circuit-level assessment of neuropathological changes using tissue clearing (**Figure 1A**); and (2) nanoscale imaging of pathology-associated alterations in synaptic and subcellular compartments using expansion microscopy (**Figure 1B**).

TISSUE CLEARING METHODS FOR CIRCUIT-LEVEL BRAIN IMAGING

Until recently, it was not possible to image deep brain structures using light microscopy without relying on histological sectioning, because the light transmitted through the sample is absorbed and scattered due to the different refractive indexes (RI) of cellular components, including lipids, proteins, and water. Consequently, the thickness of a brain section that can be efficiently imaged using confocal microscopy is limited to ∼150 μm, whereas two-photon microscopy can reach up to ∼1 mm from the sample surface, which is still not enough for imaging entire brain circuits. Tissue clearing methods homogenize the RI throughout the tissue, resulting in transparent samples that can be imaged from end to end using fluorescence light microscopy. Thus, cleared samples can be imaged using epifluorescence, confocal and two-photon microscopes or, more conveniently, by using light-sheet (selective plane illumination) fluorescence microscopy (LSFM) (Dodt et al., 2007; Hillman et al., 2019), which generates a thin laser sheet to illuminate a single plane in the entire sample, allowing high-speed and high-resolution imaging of large specimens, such as a whole mouse brain and even intact human organs (Zhao et al., 2020). While current light-sheet microscopes allow imaging of intact cleared brains from small animal models (such as mice, rats, pigs, and marmosets), imaging of the entire cleared human brain remains a major challenge.

A wide range of tissue clearing methods has been recently developed (**Table 1**), allowing simultaneous multicolor imaging of several targets in large sample volumes. Besides imaging fluorescent proteins, most of these methods allow labeling of multiple proteins and transcripts using fluorophore-conjugated antibodies, nanobodies, and RNA probes for fluorescent *in situ* hybridization (FISH) (Ueda et al., 2020). A detailed comparison of the fundamentals of tissue clearing methods is beyond the scope of this article since this has been the subject of several recent reviews (Richardson and Lichtman, 2015; Tainaka et al., 2016; Porter and Morton, 2020; Ueda et al., 2020). Nevertheless, before discussing the application of tissue clearing to neuropathological studies, we will first briefly mention the overall basis and the main advantages and limitations of the three major types of clearing methods: hydrophobic-, hydrophilic- and hydrogel-based clearing (**Box 1** and **Table 1**).

Hydrophobic-Based Tissue Clearing

Hydrophobic (organic solvent-based) clearing methods rely on tissue dehydration, delipidation and permeabilization using organic solvents such as ethanol (Dodt et al., 2007), methanol (Renier et al., 2014), tetrahydrofuran (THF) (Ertürk et al., 2012a), and tert-butanol (Pan et al., 2016). Most protocols involve simple tissue immersion (passive clearing) in a graded series of increasing solvent concentration. However, active clearing protocols in which the solvents are perfused through the circulatory system allow clearing entire rodent bodies (Pan et al., 2016) and large organs such as the human brain (Zhao et al., 2020). Further incubation in dichloromethane (DCM) may improve tissue delipidation in large samples, at the expense of

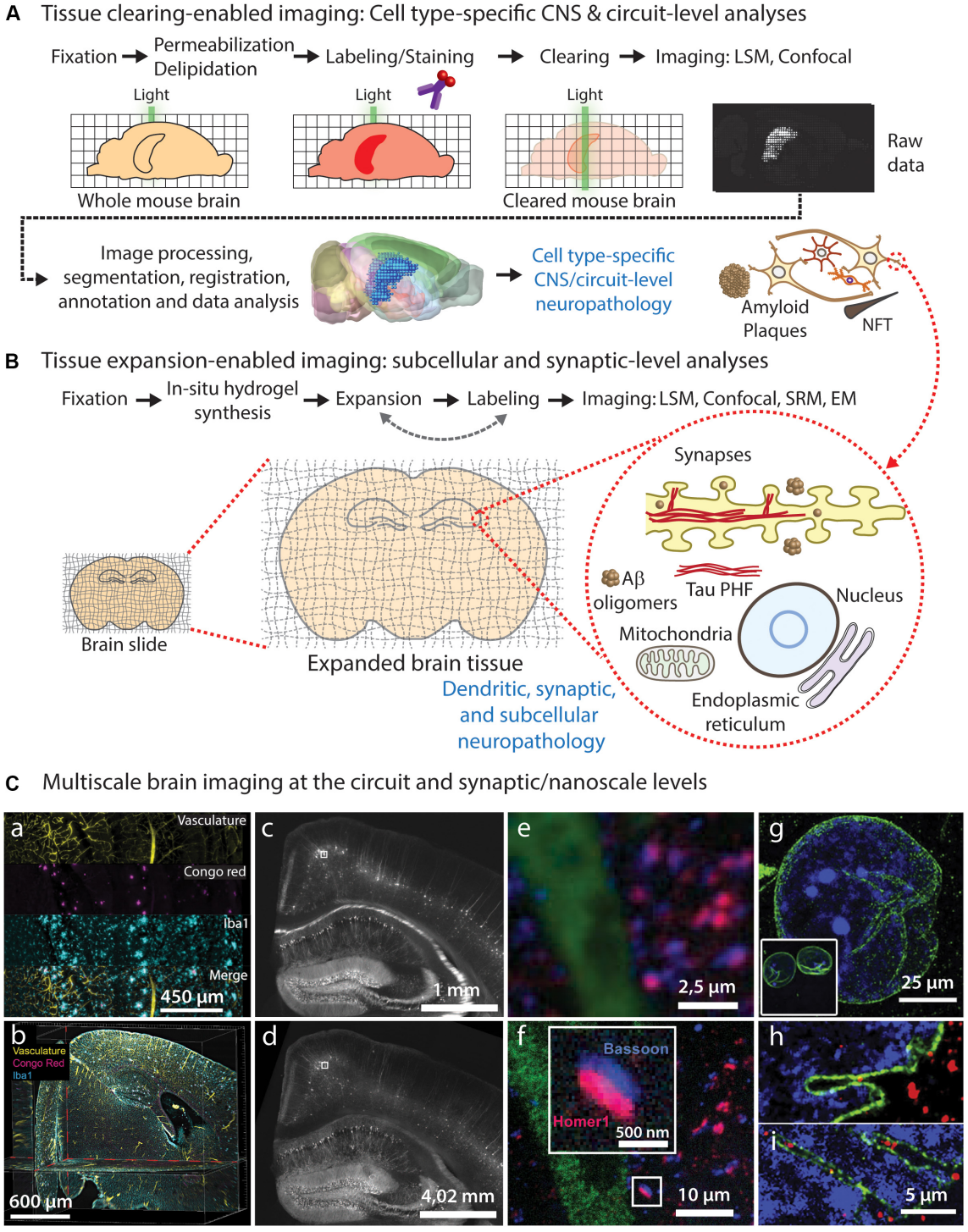

FIGURE 1 | Brain tissue clearing and expansion approaches for neuropathological imaging. **(A)** Common steps required for whole-brain tissue clearing, imaging, and analysis of neuropathological features, allowing CNS-wide identification of vulnerable circuits and cell types. **(B)** Tissue expansion approaches can be used to study early pathological alterations caused by abnormal protein conformation, aggregation, and subsequent ultrastructural changes in specific subcellular compartments and organelles within affected cell types and circuits identified using tissue clearing. **(C)** Diffraction-limited light microscopy of cleared brain tissue allows imaging of large brain circuits at cellular resolution **(a–c)**, including analysis of neuropathological markers **(a,b)**, but it does not reach synaptic nanoscale resolution in non-expanded tissues **(e)**. On the contrary, expansion microscopy of tissues and cells **(d,f-i)** allows nanoscale imaging using diffraction-limited microscopes, enabling detailed visualization of synapses **(e)** and other subcellular structures such as nuclear envelope invaginations **(g–i)** in healthy **(h)** and ALS pathological conditions **(i)**. **(a,b)** LSFM images showing individual channels **(a)** and orthogonal optical planes **(b)** of a cleared transgenic AD mouse brain after

(Continued)

FIGURE 1 | Continued
staining of vasculature (yellow), Aβ plaques (Congo red; magenta) and microglia (Iba1; cyan) using the iDISCO protocol; adapted from Liebmann et al. (2016), with permission from Elsevier. **(c-f)** Epifluorescence images of a Thy1-YFP mouse brain stained with presynaptic (Bassoon, blue) and postsynaptic (Homer1, red) markers, before **(c,e)** and after **(d-f)** expansion microscopy; adapted from Chen et al. (2015), with permission from AAAS. **(g-i)** Confocal microscopy images of expanded human iPSC-derived motor neuron nuclei from healthy control **(h)** and ALS patient **(i)** [**(g)** inset: nuclear size before expansion], immunolabeled for LMNB1 (green) and DNA (blue); adapted from Ortega et al. (2020), with permission from Elsevier.

BOX 1 | Advantages and limitations of the main tissue clearing technologies.

Hydrophobic-based tissue clearing	
Advantages	Very quick and reproducible protocols requiring simple immersion. Higher clearing performance (transparency).
Limitations	Loss of endogenous FP signal. Complete loss of lipids and associated biomolecules. May cause loss of proteins and nuclei acids. May require solvent-resistant materials and optics. Use of volatile and toxic solvents (require fume hoods and ventilated work areas).
Hydrophilic tissue clearing	
Advantages	Endogenous FP signal is preserved. Use of safer reagents. Compatible with standard materials and optics.
Limitations	May require longer incubation times. Protocols using high detergent concentrations may cause loss of lipids and associated biomolecules, proteins and nuclei acids.
Hydrogel-based tissue clearing	
Advantages	Endogenous FP signal is preserved. A higher proportion of biomolecules is retained. The brain anatomy and ultrastructure are better preserved.
Limitations	Longer and more complex protocols (compared with hydrophobic- and hydrophilic- methods) requiring *in situ* hydrogel polymerization. May require active (electrophoretic) labeling and clearing.

decreasing fluorescence from fluorescent proteins (FP) (Ertürk et al., 2012a). After dehydration, samples are immersed in a clearing solution consisting of a mixture of benzyl alcohol and benzyl benzoate (BABB) (Dodt et al., 2007) or dibenzyl ether (DBE) (Ertürk et al., 2012a), to achieve RI homogenization and thus transparency.

Hydrophilic Tissue Clearing

Tissue clearing may also be achieved using hydrophilic reagents, including different detergents (Triton-X100, saponin, sodium dodecyl sulfate -SDS-, etc.) for permeabilization and delipidation, and high-refractive index aqueous solutions containing sugars (fructose, sucrose, sorbitol) (Ke et al., 2013), urea (Hama et al., 2011), aminoalcohols (Susaki et al., 2014), or different combinations of the former (**Table 1**).

Hydrogel-Based Tissue Clearing

Another main approach to clear tissues consists of embedding the samples on a hydrogel matrix to create a cross-linked tissue/gel hybrid containing the fixed proteins and RNA (Gradinaru et al., 2018). Ionic detergents are used for delipidation, which can be enhanced by electrophoresis without causing significant loss of biomolecules.

TISSUE CLEARING APPLIED TO NEUROPATHOLOGY AND NEURODEGENERATION

Despite affecting specific brain circuits, neurodegenerative diseases share several common pathophysiological features, including accumulation of protein aggregates forming characteristic neuropathological lesions. AD neuropathology is characterized by accumulation of extracellular amyloid plaques and intraneuronal neurofibrillary tangles (NFT), formed by aggregated amyloid-β (Aβ) peptides and hyperphosphorylated tau protein, respectively. α-synuclein inclusions, known as Lewy bodies, are found in PD and Lewy body dementias, while mutant huntingtin (mHTT) aggregates are formed in HD, and TAR DNA-binding protein 43 (TDP-43) aggregates are found in ALS and FTD brains (Nguyen et al., 2018). Some of these lesions (like aggregated tau, Lewy bodies and TDP-43 aggregates) are found in more than one disease, suggesting common underlying molecular mechanisms. Furthermore, most of these neuropathologies propagate following a specific anatomical pattern through connected brain circuits (Brettschneider et al., 2015), stressing the necessity of evaluating neuropathology at large spatial scales across multiple brain regions.

Recent studies have applied tissue clearing methods to evaluate some of these neuropathological hallmarks in large human brain samples and entire brains from transgenic mouse models. Huang and colleagues used the fluorescent dye Thioflavin-S for staining Aβ plaques, combined with vasculature labeling using fluorophore-conjugated lectin and BABB clearing of entire mouse brains (Dodt et al., 2007), to show that deletion of the orphan receptor GPR3 reduces the number and volume of amyloid plaques in an AD knock-in mouse model ($App^{NL-F/NL-F}$) (Huang et al., 2015). Hama et al. (2015) applied their Sca*l*eS tissue clearing method to visualize Aβ plaques, microglia and brain ultrastructure in entire mouse brain hemispheres and in 1–2 mm-thick sections from $App^{NL-F/NL-F}$ mice and human AD brains, using dye- (PP-BTA-1) and antibody- (6E10) labeling of plaques, neurons (NeuN) and microgia (Iba1). Compared to other clearing methods such as CUBIC, 3DISCO, and PACT, Sca*l*eS preserved the brain ultrastructure, allowing detection of postsynaptic densities and membranes using electron microscopy. A recent study used a modified Golgi staining combined with Thioflavin-S and CUBIC-based clearing to image detailed neuronal morphology along with Aβ plaques in brain sections and blocks from $App^{NL-F/NL-F}$ mice (Vints et al., 2019).

TABLE 1 | Key features of the main tissue processing methods discussed.

Protocol	Fixation/ Cross-linking	Permeabilization and Delipidation	Decolorization	Preservation of fluorescence from FP	Labeling/ Staining	Clearing performance [RI], Reagent	Effect on tissue size	Max. # Resolution	Clearing time†‡¶	Application to neuropathology **Related computational tools**
Hydrophobic (Organic Solvent) Tissue Clearing										
BABB (Dodt et al., 2007)	Standard PFA perfusion	Strong: EtOH, DCM	-	Low (hours)	Thioflavin-S for Aβ plaques and lectin for vasculature (Huang et al., 2015).	Very high [1.56], BABB	Slight shrinkage	0.5-2 μm	7 days†	Visualization of Aβ plaques and vasculature in entire mouse brains (Huang et al., 2015).
3DISCO (Ertürk et al., 2012a,b)	Standard PFA perfusion	Strong: THF, DCM	-	Low (hours)	-	Highest [1.56], BABB	Shrinkage (∼30% volume)	0.5-2 μm	2 days†	Assessment of axonal degeneration and regeneration in spinal cord injury (Ertürk et al., 2012b).
iDISCO (Renier et al., 2014) iDISCO + (Renier et al., 2016) https://idisco.info/	Standard PFA perfusion	Strong: Methanol, DCM	H_2O_2	Low (hours)	Antibodies, Congo red for Aβ plaques	Highest [1.56], DBE	Minimal	0.5-2 μm	7-14 days†	Evaluation of Aβ pathology in AD transgenic mice and human brains; automated quantification of Aβ plaques with ClearMAP (Liebmann et al., 2016). Imaging of temporal/spatial progression of tau neuropathology in EC-tau mice (Fu et al., 2016).
u/vDISCO (Pan et al., 2016) (Cai et al., 2019) discotechnologies.org	Standard PFA perfusion	Strong: *tert*-Butanol, THF DCM/Triton-X100	Aminoalcohol	Acceptable (hours-days)	Nanobodies (vDISCO; 2-3 d. active or 5-7 d. passive staining)	Highest [1.56], BABB-D	Shrinkage (∼35–55% volume)	1-2 μm	5 days†	Machine learning pipeline for identification and quantification of nanobody-labeled cells (Pan et al., 2019).
SHANEL* (Zhao et al., 2020) discotechnologies.org	PFA perfusion of entire human organs	Strong: CHAPS, DCM	CHAPS/ NMDEA	N/A	Antibodies, Methoxy-X04 for labeling Aβ plaques	Very high [1.56], BABB	Shrinkage (∼30–45% volume)	1-2 μm	1- > 3‡ weeks	Detection of amyloid plaques in human brain tissue (POC); deep learning-based pipeline for 3D reconstruction and data analysis (Zhao et al., 2020).
Hydrophilic Tissue Clearing										
CUBIC 1/2 (Susaki et al., 2014) cubic.riken.jp	Standard PFA perfusion	Strong: ScaleCUBIC-1 (15% Triton-X100 + 25% Aminoalcohol + 25% Urea)	Aminoalcohol	High	Antibodies	High [1.49], ScaleCUBIC-2 (urea + aminoalcohol + sucrose)	Slight expansion	0.5-2 μm	7-14 days†	Visualization of detailed neuronal morphology and Aβ plaques using Golgi and Thioflavin-S staining in AD mice (POC) (Vints et al., 2019).
Updated CUBIC protocols (Tainaka et al., 2018) cubic.riken.jp	Standard PFA perfusion	Strong: CUBIC-L (10% Triton-X100 + 10% Aminoalcohol)	Aminoalcohol	High	Antibodies	High [1.52], CUBIC-R/RA (antipyrine, nicotinamide)	Slight expansion	0.5–2 μm	5–11 days†	–
Sca*l*eS* (Hama et al., 2015).	Standard PFA perfusion	Mild: urea + sorbitol + DMSO	–	High	Antibodies, Lectin	High [1.44] (urea + sorbitol + DMSO)	Minimal	0.5–2 μm	2–5 days for mm-thick slides.	Evaluation of Aβ pathology, microglia and EM ultrastructure in AD transgenic mice and human AD brains (Hama et al., 2015).

(Continued)

TABLE 1 | Continued

Protocol	Fixation/ Cross-linking	Permeabilization and Delipidation	Decolorization	Preservation of fluorescence from FP	Labeling/ Staining	Clearing performance [RI], Reagent	Effect on tissue size	Max. # Resolution	Clearing time†‡¶	Application to neuropathology Related computational tools
Hydrogel-Based Tissue Clearing										
CLARITY (Chung et al., 2013; Tomer et al., 2014) clarityresourcecenter.com	PFA/ acrylamide/ bis-acrylamide	Strong: 4% SDS	–	Temperature-dependent: preserved at 37°C	Antibodies	Good [1.45], FocusClear	Minimal	0.5–2 μm	1 (active)-3 (passive) weeks†	Visualization of Aβ plaques and tangles in human AD brain (POC) (Ando et al., 2014). Identification of fragmented nigrostriatal axons in PD mice (Nordström et al., 2015). Visualization of Lewy pathology in human brain (POC) (Liu et al., 2016).
SWITCH* (Murray et al., 2015) chunglabresources.com	PFA, Glutaraldehyde	200 mM SDS	–	Temperature-dependent: preserved at 37°C requiring longer clearing	Antibodies, Lectin	High, [1.47], diatrizoic acid, *n*-methyl-D-glucamine, iodixanol	Minimal	0.5–2 μm	2–4 weeks†	Assessment of Aβ deposits in 5xFAD mice, revealing early Aβ accumulation in subcortical areas (Gail Canter et al., 2019).
SHIELD* (Park et al., 2019) chunglabresources.com	PFA, Polyepoxide	300 mM SDS	-	Time/temperature-dependent: preserved at 45°C	Antibodies, FISH, Lectin	High, [1.46], Iodixanol- or Iohexol-based Protos media	Minimal	0.5–2 μm	1 (active) -4 (passive) weeks†	Quantitative evaluation of Aβ pathology in 5xFAD mice exposed to gamma sensory stimulation (Martorell et al., 2019).
Tissue Expansion										
ExM/ProExM/iExM (Chen et al., 2015; Chang et al., 2017; Asano et al., 2018) expansionmicroscopy.org	PFA, acrylamide/ bis-acrylamide/ sodium acrylate Acryloyl-X	5% Triton X-100, 1% SDS (for post expansion staining)	–	Partial, only digestion-resistant FP	Antibodies, FISH	High, [~1.33], (water)	20 × (iExM) 4.5 × (ExM) Expansion (3.5 × for FISH)	~25 nm (iExM) or 60 nm (ExM)	1-2 days ¶	Identification of perivascular c43 accumulation on astrocytic endfeet in human brain epilepsy (Deshpande et al., 2017). Identification of eRF1 accumulation within nuclear envelope invaginations in iPSC-derived neurons from ALS patients (Ortega et al., 2020).
ExPath* (Zhao et al., 2017; Bucur et al., 2020)	PFA, formalin or acetone. Acrylamide/ bis-acrylamide/ sodium acrylate	0.1% Triton X-100	–	N/A	Antibodies, DNA-FISH	High, [~1.33], (water)	4.5×	~60 nm	4 h (≤5 μm) – 2 days ¶	–
MAP (Ku et al., 2016) chunglabresources.com	PFA, acrylamide/ bis-acrylamide/ sodium acrylate	200 mM SDS	–	Fluorescence is lost but epitopes are preserved	Antibodies	[1.47] pre-expansion. [~1.33] (water) after expansion.	Fourfold linear expansion	~60-nm	~1 week ¶	–
X10 ExpM (Truckenbrodt et al., 2018, 2019)	Sodium acrylate, *N,N*-dimethyl acrylamide, Acryloyl-X	0.1% Triton X-100	–	Fluorescence is lost but epitopes are preserved	Antibodies	High, [~1.33], (water)	Tenfold expansion	~25 nm	3 days ¶	–
SHIELD-MAP (3x linear expansion) (Park et al., 2019) chunglabresources.com	PFA, Polyepoxide acrylamide/ bis-acrylamide/ sodium acrylate/VA-044	300 mM SDS	–	Time/temperature-dependent. 27-fold signal reduction after expansion.	Antibodies	DI water for expansion.	Threefold linear expansion	?	~2 weeks ¶ (1–3 mm Slices)	–

#*Lateral resolution using standard (diffraction-limited) light microscopy.* **Optimized for human tissue.* †*For an intact mouse brain.* ‡*For ~1 cm³ human brain tissue.* ¶*Expansion of brain slices. DCM, dichloromethane. CHAPS, 3-[(3-cholamidopropyl)dimethylammonio]-1-propanesulfonate. BABB, benzyl alcohol + benzyl benzoate (1:2). BABB-D, BABB + Dibenzyl ether. SDS, sodium dodecyl sulfate. POC, proof-of-concept application.*

The hydrogel-based CLARITY method has also been used to visualize amyloid plaques and NFT in human AD brain samples (Ando et al., 2014), fragmented nigrostriatal axons in a PD mouse model (Nordström et al., 2015), and Lewy pathology in a human PD brain (Liu et al., 2016), relying on antibody labeling for detecting neuropathology and specific cell types, and confocal microscopy for imaging. Imaging of amyloid plaques revealed sparse accumulation and diversity of 3D structures, including dense/focal and diffuse deposits, whereas tau accumulated in discontinuous neuritic processes associated with dense/mature plaques (Ando et al., 2014) which were previously reported using conventional histology and confocal microscopy (Knowles et al., 1999). The immunolabeling and solvent-based clearing method iDISCO has also been used to evaluate tau pathology and Aβ plaques using antibodies and Congo red labeling in APP_{swe}/PSEN1ΔE9 and 3xTg-AD transgenic mice and human AD brains (Liebmann et al., 2016). The authors also developed a computational pipeline based on automated detection of cells and plaques from light-sheet images and further mapping of these features to the Allen Brain Atlas, enabling fast quantification of plaques in different brain regions (Liebmann et al., 2016). iDISCO+ (Renier et al., 2016), an improved version of iDISCO, was successfully applied for whole-brain immunolabeling and 3D imaging of the temporal and spatial progression of tau neuropathology in entorhinal cortex (EC)-tau transgenic mice, revealing age-dependent tau pathology not only in entorhinal and hippocampal regions but also in neocortical areas, which was not previously detected by classical 2D histology in this model (Fu et al., 2016).

More recently, SHIELD-based clearing (Park et al., 2019) of entire mouse brains was used to show that auditory plus visual gamma sensory stimulation reduces the number and volume of amyloid plaques (detected by Aβ immunolabeling) in 6-month-old 5xFAD mice, revealing a greater effect of sensory stimulation on pathology across broad cortical regions than observed with conventional histology (Martorell et al., 2019). Similarly, SWITCH whole-brain immunolabeling and clearing (Murray et al., 2015) were used to monitor the progression of Aβ deposits in 5xFAD mice, revealing early Aβ accumulation in subcortical areas and area-specific aggregation correlating with electrophysiological changes (Gail Canter et al., 2019). Finally, a novel permeabilization and clearing approach, named SHANEL, allowed labeling of cm-thick human brain tissue using conventional antibodies, and was used to detect amyloid plaques in human brains labeled with the Congo red derivative methoxy-X04 (Zhao et al., 2020).

Taken together, these studies have demonstrated the feasibility of using tissue clearing approaches for achieving volumetric imaging and quantitative assessment of neuropathological hallmarks in AD and PD.

NANOSCALE IMAGING USING SUPER-RESOLUTION EXPANSION MICROSCOPY

Studying neuropathology-associated alterations in the molecular composition and ultrastructure of the brain is essential for understanding pathogenic mechanisms underlying neurodegenerative diseases. While electron microscopy achieves the highest spatial resolution for ultrastructural analyses, it still lacks the molecular specificity and throughput provided by multicolor fluorescence microscopy, which is required for simultaneous imaging of multiple targets, including visualizing cell-type-specific nanostructures and/or signaling molecules within a pathological context. However, the minimum size of the structures that can be resolved using conventional fluorescence light microscopy is constrained by the light diffraction limit (about 250 nm, depending on the specific excitation wavelength), which precludes detailed imaging of specific protein complexes, individual synapses and other subcellular structures. Several optical super-resolution microscopy (SRM) methods have been developed to overcome diffraction limitation, including stimulated emission depletion (STED) microscopy, photoactivation localization microscopy (PALM), structured illumination microscopy (SIM), and stochastic optical reconstruction microscopy (STORM), among others (Tønnesen and Nägerl, 2013; Schermelleh et al., 2019). Depending on the specific approach and imaging setup, optical SRM can resolve sub-diffraction size structures ranging from 30 to 100 nm (lateral resolution), enabling detailed visualization of subcellular structures, individual synapses and protein complexes. Interestingly, recent studies have combined the advantage of reduced light scattering (transparency) provided by tissue clearing methods, with SRM to achieve sub-diffraction volumetric brain imaging, revealing novel synaptic structural and functional insights. For instance, Ke et al. (2016) developed a tissue clearing solution (SeeDB2) which, combined with STED SRM, allowed synaptic-resolution imaging through thick brain samples (up to 120 μm). More recently, Hruska et al. (2018) combined CUBIC tissue clearing and STED SRM to demonstrate the occurrence of discrete synaptic nanomodules (∼80 nm in size) in the mouse somatosensory cortex.

However, SR microscopes are not widely available to most biomedical research labs, are expensive, and may require expert personnel to operate. Moreover, multicolor imaging may be challenging for some setups. A clever solution to overcome the light diffraction limit is to increase the size of the specimens to image (Chen et al., 2015). Three main independent approaches have been developed to increase the size of biological tissues: expansion microscopy (ExM) (Chen et al., 2015); magnified analysis of the proteome (MAP) (Ku et al., 2016); and X10 (Truckenbrodt et al., 2018) (**Table 1**). These methods use swellable hydrogels that are cross-linked throughout the tissue to induce isotropic expansion of the samples, allowing super-resolution imaging of the expanded specimens using conventional light microscopes [**Figures 1B,C(c–i)**]. Current tissue expansion methods allow isotropic expansion of tissues up to ∼4.5x (Ku et al., 2016; Tillberg et al., 2016) or 10x (Truckenbrodt et al., 2018) for single-step expansion protocols and up to ∼20x for iterative expansion protocols (Chang et al., 2017), enabling detailed nanoscale imaging of subcellular structures with up to ∼25-nm-resolution using conventional

confocal microscopy (**Table 1**). These methods are easy to implement and optimize (compared with optical SRM), require commercially available reagents, and are compatible with multicolor immunostaining and FISH (Tillberg et al., 2016; Asano et al., 2018).

Moreover, expanded samples can be conveniently imaged using confocal microscopes -which are widely available- and provide enough three-dimensional resolution to enable cost-efficient super-resolution imaging of the brain tissue (Tillberg and Chen, 2019; Wassie et al., 2019). Each tissue expansion approach has its advantages and limitations related to preserving endogenous fluorescence, epitopes, and reduction of fluorescence signal after expansion (**Table 1**). In this regard, performing tissue immunolabeling after expansion may yield higher fluorescence signals, although fewer epitopes can be detected with this strategy (Asano et al., 2018).

INSIGHTS FROM SRM IN NEURODEGENERATION RESEARCH

Besides the evident relevance of assessing synaptic structural and molecular alterations in brain diseases, nanoscale imaging can also provide crucial information on other altered cellular processes. For instance, STORM and STED SRM have been applied to study the aggregation states of Huntingtin exon 1, including the formation of inclusion bodies and other fibrillary species in living and fixed cells (Duim et al., 2014; Sahl et al., 2016), while SIM SRM has been used to study the interaction of mHTT aggregates with transcription factors (Li et al., 2016), which could mediate altered gene expression in HD (Giralt et al., 2012). Different optical SRM approaches have helped to image both Aβ and tau aggregates *in vitro* and in cellular models (Pinotsi et al., 2016; Schierle et al., 2016), while STED SRM was used to image immunolabelled tau filaments in postmortem AD brain sections (50 μm) at ∼80 nm resolution (Benda et al., 2016). A recent study used STED SRM to identify disruption of the lamin nucleoskeleton in a *Drosophila* model of tau pathology and in human postmortem AD brain tissue, suggesting that lamin dysfunction contributes to tau-mediated neurodegeneration (Frost et al., 2016). STORM and STED SRM have also been used to visualize the presenilin-1/γ-secretase complex, which is responsible for the proteolytic cleavage of the amyloid precursor protein (APP) that releases Aβ, in both the pre- and post-synaptic compartments of cultured mouse neurons (Schedin-Weiss et al., 2016). More recently, SIM and PALM were used to study the subunit composition and activity of the γ-secretase complex at the plasma membrane in living cells, revealing complex dynamics involving association with specific substrates (Escamilla-Ayala et al., 2020).

Early after its development, protein-retention ExM (ProExM) (Tillberg et al., 2016) was used to identify "striosome–dendron bouquets" structures formed by intertwined striosomal axons and dopamine-containing dendrites as part of the dopamine-containing nigral system, which may be relevant for motor and neurodegenerative disorders (Crittenden et al., 2016). Deshpande et al. (2017) applied ProExM to human CA1 hippocampal tissue from temporal lobe epilepsy patients to study the subcellular localization of perivascular Connexin-43 (Cx43; GJA1), revealing specific Cx43 accumulation on the parenchymal side of astrocytic endfeet, compared to endothelial or pericytic accumulation. ProExM has also been applied to HeLa cells to study the spatial organization of autophagy-related HSPB1 protein and SQSTM1/p62 bodies in the context of peripheral neuropathy (Haidar et al., 2019). More recently, ProExM was used to show that the protein eRF1 accumulates within the cytosolic side of nuclear envelope invaginations identified in induced pluripotent stem cell (iPSC) neurons derived from ALS patients (Ortega et al., 2020) [**Figures 1C(g–i)**].

Taken together, these studies demonstrate that -similar to optical SRM- expansion-SRM has the potential to deliver relevant structural insights about molecular and cellular mechanisms mediating neuropathology and neurodegeneration. Broader implementation of these methods may be of great value for studying interactions between pathological protein conformations and organelles/membranes, which could mediate aggregation and downstream neurodegenerative processes (Shrivastava et al., 2017).

POTENTIAL APPLICATIONS OF CLEARING AND EXPANSION METHODS IN NEURODEGENERATION RESEARCH

Based on the above considerations, we propose a general straightforward pipeline for structural and molecular analysis of neuropathological and neurodegenerative brain tissues, from circuits to synapses, relying on the capabilities offered by tissue clearing and expansion methods (**Figure 1**). This consists of: (1) Tissue clearing-enabled unbiased imaging of whole brains or specific brain regions; and (2) SR-expansion nanoscale imaging of subcellular compartments from specific cell-types within affected circuits. The first systems/circuit-level approach has several remarkable advantages compared with standard sectioning histology: first, it preserves the full anatomical information, some of which is lost during tissue sectioning. Second, it allows unbiased and automated imaging and data analysis of the whole brain, reducing experimental errors and favoring reproducibility. Third, the time required for tissue processing, labeling, imaging, and data analysis can be significantly reduced, especially when working with large experimental groups if automated imaging and data analysis pipelines are implemented (**Table 1**).

Despite these clear advantages, up to date, most tissue clearing studies have provided limited biological information or only proof-of-concept data on neuropathology and neurodegeneration, particularly in human brain samples (**Table 1**). However, we think that neuropathological studies can leverage tissue clearing methods to deliver insightful systems biology-level information on structural and functional alterations. For instance, tissue clearing approaches may be used

to identify relevant brain circuits showing pathology-induced alterations in the activity and connectivity of specific cell-types, by performing simultaneous analysis of neuropathological hallmarks, cell type-specific and synaptic markers, as well as indicators of neuronal/astrocytic excitability (i.e., immediate early genes such as *c-fos* and *Arc*) or glial reactivity (GFAP, CD45). Indeed, tissue clearing methods have been successfully applied to study brain-wide neuronal activity (Renier et al., 2016; Sylwestrak et al., 2016; Murakami et al., 2018; Park et al., 2019) and -separately- AD neuropathology in mouse models (**Table 1**). These approaches could be combined to study how different neuropathologies affect the activity of specific cell populations in the whole brain, which could shed light into the cellular mechanisms mediating selective/differential vulnerability of different circuits and neuronal/glial subtypes during neurodegenerative diseases (Fu et al., 2018; Forrest et al., 2019). In particular, automated mapping of brain activity based on detection of neuronal activity-induced immediate early genes (Renier et al., 2016) can be combined with assessment of neuropathological features in neurodegeneration or AD mouse models (Liebmann et al., 2016) to obtain physiological functional readouts of circuit- and cell-specific vulnerability to AD neuropathology, and to evaluate potential therapeutic strategies. Different computational methods have been developed to achieve automated identification and quantification of cells and neuropathological hallmarks, which can be of high value in such studies (**Table 1**).

The former circuit-level imaging approaches need to be complemented with SR-expansion nanoscale imaging to further characterize the synaptic and subcellular ultrastructural alterations occurring under neuropathological conditions, and to investigate potential molecular and cellular mechanisms. Thus, cell-type-specific molecular mechanisms mediating alterations in synaptic and subcellular structures (such as altered mRNA and protein localization, local synaptic translation, protein-protein interactions, and pathological protein aggregation, among others) could be approached using expansion SRM (**Figure 1B**). Since SRM methods (including expansion microscopy) have already revealed key molecular mechanisms in physiological and neurodegenerative contexts, it is reasonable to pursue a broader implementation of tissue expansion technologies for studying cellular and molecular mechanisms in neurodegeneration research.

CONCLUDING REMARKS

The astonishing development of tissue clearing and expansion technologies in the last few years suggests that there is still plenty of room for improvement. Future advances in tissue chemistry and optics (Chakraborty et al., 2019; Gwosch et al., 2020) together with recent initiatives to guide the building of open-source light-sheet microscopes (Voigt et al., 2019) will likely facilitate their applicability, while increasing the current resolution and the range of biomolecules (i.e., lipids, sugars), modifications (acetylations, methylations, sumoylation, etc.) and processes (interactions, synthesis, degradation, and aggregation) that can be imaged in fixed samples. On the other hand, recent advances in volumetric imaging of bio-microelectromechanical systems (bioMEMS microdevices) using LSFM opens a promising avenue for achieving 3D and sucellular imaging of *in vitro* model systems under highly controlled experimental conditions (Albert-Smet et al., 2019). Computational developments, including neuropathology-optimized data analysis tools and implementation of standardized pipelines, data formats, and data-sharing platforms can further aid quantitative assessments and systems-biology level interpretation of the vast amount of brain/circuit-wide imaging data that can be generated, as well as integration with functional and cell-specific omics data (Vandenberghe et al., 2018; Hériché et al., 2019). Moreover, incorporation of other structural and functional imaging technologies [such as positron emission tomography (PET), functional magnetic resonance imaging (fMRI), multi-photon microscopy, optical super-resolution imaging, cryo-EM and cryo-electron tomography, among others] is needed to confirm and complement the findings obtained by tissue clearing and expansion methods, as well as to achieve a complete imaging assessment throughout the entire spatial scale of the brain, which remains one of the most challenging tasks of contemporary neuroscience (Lichtman and Denk, 2011; Koning et al., 2018). However, we think that tissue clearing and expansion technologies have already reached enough maturity to be generally embraced by the neurodegeneration research community, and as such, they can be readily implemented to address the underlying biology and pathogenic mechanisms of neurodegeneration, as demonstrated by relevant recent studies (Gail Canter et al., 2019; Martorell et al., 2019). This certainly will enable biological discoveries of great translational impact in the near future.

AUTHOR CONTRIBUTIONS

AP-D conceived the study and designed the figures. AP-D and CS wrote the manuscript. Both authors contributed to the article and approved the submitted version.

FUNDING

This study was supported by research grants from the Ministerio de Ciencia e Innovación of Spain with FEDER funds (SAF2016-80027-R and PID2019-106615RB-100) and Instituto Carlos III (CIBERNED CB06/05/0042).

ACKNOWLEDGMENTS

We thank Dr. Jorge Valero and Dr. Dolores Siedlecki for helpful comments on the manuscript. We also thank Yuruani Audemard for copy editing.

REFERENCES

Albert-Smet, I., Marcos-Vidal, A., Vaquero, J. J., Desco, M., Muñoz-Barrutia, A., and Ripoll, J. (2019). Applications of light-sheet microscopy in microdevices. *Front. Neuroanat.* 13:1 doi: 10.3389/fnana.2019.00001

Ando, K., Laborde, Q., Lazar, A., Godefroy, D., Youssef, I., Amar, M., et al. (2014). Inside Alzheimer brain with CLARITY: senile plaques, neurofibrillary tangles and axons in 3-D. *Acta Neuropathol.* 128, 457–459. doi: 10.1007/s00401-014-1322-y

Asano, S. M., Gao, R., Wassie, A. T., Tillberg, P. W., Chen, F., and Boyden, E. S. (2018). Expansion microscopy: protocols for imaging proteins and RNA in cells and tissues. *Curr. Protoc. Cell Biol.* 80:e56. doi: 10.1002/cpcb.56

Benda, A., Aitken, H., Davies, D. S., Whan, R., and Goldsbury, C. (2016). STED imaging of tau filaments in Alzheimer's disease cortical grey matter. *J. Struct. Biol.* 195, 345–352. doi: 10.1016/j.jsb.2016.07.003

Brettschneider, J., Tredici, K., Del Lee, V. M.-Y., and Trojanowski, J. Q. (2015). Spreading of pathology in neurodegenerative diseases: a focus on human studies. *Nat. Rev. Neurosci.* 16, 109–120. doi: 10.1038/nrn3887

Bucur, O., Fu, F., Calderon, M., Mylvaganam, G. H., Ly, N. L., Day, J., et al. (2020). Nanoscale imaging of clinical specimens using conventional and rapid-expansion pathology. *Nat. Protoc.* 15, 1649–1672. doi: 10.1038/s41596-020-0300-1

Cai, R., Pan, C., Ghasemigharagoz, A., Todorov, M. I., Förstera, B., Zhao, S., et al. (2019). Panoptic imaging of transparent mice reveals whole-body neuronal projections and skull–meninges connections. *Nat. Neurosci.* 22, 317–327. doi: 10.1038/s41593-018-0301-3

Chakraborty, T., Driscoll, M. K., Jeffery, E., Murphy, M. M., Roudot, P., Chang, B.-J., et al. (2019). Light-sheet microscopy of cleared tissues with isotropic, subcellular resolution. *Nat. Methods* 16, 1109–1113. doi: 10.1038/s41592-019-0615-4

Chang, J.-B., Chen, F., Yoon, Y.-G., Jung, E. E., Babcock, H., Kang, J. S., et al. (2017). Iterative expansion microscopy. *Nat. Methods* 14, 593–599. doi: 10.1038/nmeth.4261

Chen, F., Tillberg, P. W., and Boyden, E. S. (2015). Expansion microscopy. *Science* 347, 543–548. doi: 10.1126/science.1260088

Chung, K., Wallace, J., Kim, S.-Y., Kalyanasundaram, S., Andalman, A. S., Davidson, T. J., et al. (2013). Structural and molecular interrogation of intact biological systems. *Nature* 497, 332–337. doi: 10.1038/nature12107

Crittenden, J. R., Tillberg, P. W., Riad, M. H., Shima, Y., Gerfen, C. R., Curry, J., et al. (2016). Striosome–dendron bouquets highlight a unique striatonigral circuit targeting dopamine-containing neurons. *Proc. Natl. Acad. Sci. U.S.A.* 113, 11318–11323. doi: 10.1073/pnas.1613337113

Deshpande, T., Li, T., Herde, M. K., Becker, A., Vatter, H., Schwarz, M. K., et al. (2017). Subcellular reorganization and altered phosphorylation of the astrocytic gap junction protein connexin43 in human and experimental temporal lobe epilepsy. *Glia* 65, 1809–1820. doi: 10.1002/glia.23196

Dodt, H.-U., Leischner, U., Schierloh, A., Jährling, N., Mauch, C. P., Deininger, K., et al. (2007). Ultramicroscopy: three-dimensional visualization of neuronal networks in the whole mouse brain. *Nat. Methods* 4, 331–336. doi: 10.1038/nmeth1036

Duim, W. C., Jiang, Y., Shen, K., Frydman, J., and Moerner, W. E. (2014). Super-resolution fluorescence of huntingtin reveals growth of globular species into short fibers and coexistence of distinct aggregates. *ACS Chem. Biol.* 9, 2767–2778. doi: 10.1021/cb500335w

Ertürk, A., Becker, K., Jährling, N., Mauch, C. P., Hojer, C. D., Egen, J. G., et al. (2012a). Three-dimensional imaging of solvent-cleared organs using 3DISCO. *Nat. Protoc.* 7, 1983–1995. doi: 10.1038/nprot.2012.119

Ertürk, A., Mauch, C. P., Hellal, F., Förstner, F., Keck, T., Becker, K., et al. (2012b). Three-dimensional imaging of the unsectioned adult spinal cord to assess axon regeneration and glial responses after injury. *Nat. Med.* 18, 166–171. doi: 10.1038/nm.2600

Escamilla-Ayala, A. A., Sannerud, R., Mondin, M., Poersch, K., Vermeire, W., Paparelli, L., et al. (2020). Super-resolution microscopy reveals majorly mono- and dimeric presenilin1/γ-secretase at the cell surface. *ELife* 9:e56679. doi: 10.7554/eLife.56679

Forrest, S. L., Kril, J. J., and Halliday, G. M. (2019). Cellular and regional vulnerability in frontotemporal tauopathies. *Acta Neuropathol.* 138, 705–727. doi: 10.1007/s00401-019-02035-7

Frost, B., Bardai, F. H., and Feany, M. B. (2016). Lamin dysfunction mediates neurodegeneration in tauopathies. *Curr. Biol.* 26, 129–136. doi: 10.1016/j.cub.2015.11.039

Fu, H., Hardy, J., and Duff, K. E. (2018). Selective vulnerability in neurodegenerative diseases. *Nat. Neurosci.* 21, 1350–1358. doi: 10.1038/s41593-018-0221-2

Fu, H., Hussaini, S. A., Wegmann, S., Profaci, C., Daniels, J. D., Herman, M., et al. (2016). 3D visualization of the temporal and spatial spread of Tau pathology reveals extensive sites of Tau accumulation associated with neuronal loss and recognition memory deficit in aged Tau transgenic mice. *PLoS One* 11:e0159463. doi: 10.1371/journal.pone.0159463

Gail Canter, R., Huang, W.-C., Choi, H., Wang, J., Ashley Watson, L., Yao, C. G., et al. (2019). 3D mapping reveals network-specific amyloid progression and subcortical susceptibility in mice. *Commun. Biol.* 2:360. doi: 10.1038/s42003-019-0599-8

Giralt, A., Puigdellívol, M., Carretón, O., Paoletti, P., Valero, J., Parra-Damas, A., et al. (2012). Long-term memory deficits in Huntington's disease are associated with reduced CBP histone acetylase activity. *Hum. Mol. Gen.* 21, 1203–1216. doi: 10.1093/hmg/ddr552

Gradinaru, V., Treweek, J., Overton, K., and Deisseroth, K. (2018). Hydrogel-tissue chemistry: principles and applications. *Annu. Rev. Biophys.* 47, 355–376. doi: 10.1146/annurev-biophys-070317-032905

Gwosch, K. C., Pape, J. K., Balzarotti, F., Hoess, P., Ellenberg, J., Ries, J., et al. (2020). MINFLUX nanoscopy delivers 3D multicolor nanometer resolution in cells. *Nat. Methods* 17, 217–224. doi: 10.1038/s41592-019-0688-0

Haidar, M., Asselbergh, B., Adriaenssens, E., De Winter, V., Timmermans, J.-P., Auer-Grumbach, M., et al. (2019). Neuropathy-causing mutations in HSPB1 impair autophagy by disturbing the formation of SQSTM1/p62 bodies. *Autophagy* 15, 1051–1068. doi: 10.1080/15548627.2019.1569930

Hama, H., Hioki, H., Namiki, K., Hoshida, T., Kurokawa, H., Ishidate, F., et al. (2015). ScaleS: an optical clearing palette for biological imaging. *Nat. Neurosci.* 18, 1518–1529. doi: 10.1038/nn.4107

Hama, H., Kurokawa, H., Kawano, H., Ando, R., Shimogori, T., Noda, H., et al. (2011). Scale: a chemical approach for fluorescence imaging and reconstruction of transparent mouse brain. *Nat. Neurosci.* 14, 1481–1488. doi: 10.1038/nn.2928

Hériché, J.-K., Alexander, S., and Ellenberg, J. (2019). Integrating imaging and omics: computational methods and challenges. *Annu. Rev. Biomed. Data Sci.* 2, 175–197. doi: 10.1146/annurev-biodatasci-080917-013328

Hillman, E. M. C., Voleti, V., Li, W., and Yu, H. (2019). Light-sheet microscopy in neuroscience. *Annu. Rev. Neurosci.* 42, 295–313. doi: 10.1146/annurev-neuro-070918-050357

Hruska, M., Henderson, N., Le Marchand, S. J., Jafri, H., and Dalva, M. B. (2018). Synaptic nanomodules underlie the organization and plasticity of spine synapses. *Nat. Neurosci.* 21, 671–682. doi: 10.1038/s41593-018-0138-9

Huang, Y., Skwarek-Maruszewska, A., Horré, K., Vandewyer, E., Wolfs, L., Snellinx, A., et al. (2015). Loss of GPR3 reduces the amyloid plaque burden and improves memory in Alzheimer's disease mouse models. *Sci. Transl. Med.* 7, ra164–ra309. doi: 10.1126/scitranslmed.aab3492

Ke, M.-T., Fujimoto, S., and Imai, T. (2013). SeeDB: a simple and morphology-preserving optical clearing agent for neuronal circuit reconstruction. *Nat. Neurosci.* 16, 1154–1161. doi: 10.1038/nn.3447

Ke, M.-T., Nakai, Y., Fujimoto, S., Takayama, R., Yoshida, S., Kitajima, T. S., et al. (2016). Super-resolution mapping of neuronal circuitry with an index-optimized clearing agent. *Cell Rep.* 14, 2718–2732. doi: 10.1016/j.celrep.2016.02.057

Knowles, R. B., Wyart, C., Buldyrev, S. V., Cruz, L., Urbanc, B., Hasselmo, M. E., et al. (1999). Plaque-induced neurite abnormalities: implications for disruption of neural networks in Alzheimer's disease. *Proc. Natl. Acad. Sci. U.S.A.* 96, 5274–5279. doi: 10.1073/pnas.96.9.5274

Koning, R. I., Koster, A. J., and Sharp, T. H. (2018). Advances in cryo-electron tomography for biology and medicine. *Ann. Anat.* 217, 82–96. doi: 10.1016/j.aanat.2018.02.004

Ku, T., Swaney, J., Park, J.-Y., Albanese, A., Murray, E., Cho, J. H., et al. (2016). Multiplexed and scalable super-resolution imaging of three-dimensional

protein localization in size-adjustable tissues. *Nat. Biotechnol.* 34, 973–981. doi: 10.1038/nbt.3641

Li, L., Liu, H., Dong, P., Li, D., Legant, W. R., Grimm, J. B., et al. (2016). Real-time imaging of huntingtin aggregates diverting target search and gene transcription. *ELife* 5:e17056. doi: 10.7554/eLife.17056

Lichtman, J. W., and Denk, W. (2011). The big and the small: challenges of imaging the brain's circuits. *Science* 334, 618–623. doi: 10.1126/science.1209168

Liebmann, T., Renier, N., Bettayeb, K., Greengard, P., Tessier-Lavigne, M., and Flajolet, M. (2016). Three-dimensional study of alzheimer's disease hallmarks using the iDISCO clearing method. *Cell Rep.* 16, 1138–1152. doi: 10.1016/j.celrep.2016.06.060

Liu, A. K. L., Hurry, M. E. D., Ng, O. T. W., DeFelice, J., Lai, H. M., Pearce, R. K. B., et al. (2016). Bringing CLARITY to the human brain: visualization of Lewy pathology in three dimensions. *Neuropathol. Appl. Neurobiol.* 42, 573–587. doi: 10.1111/nan.12293

Martorell, A. J., Paulson, A. L., Suk, H.-J., Abdurrob, F., Drummond, G. T., Guan, W., et al. (2019). Multi-sensory gamma stimulation ameliorates Alzheimer's-associated pathology and improves cognition. *Cell* 177, 256.e22–271.e22. doi: 10.1016/j.cell.2019.02.014

Murakami, T. C., Mano, T., Saikawa, S., Horiguchi, S. A., Shigeta, D., Baba, K., et al. (2018). A three-dimensional single-cell-resolution whole-brain atlas using CUBIC-X expansion microscopy and tissue clearing. *Nat. Neurosci.* 21, 625–637. doi: 10.1038/s41593-018-0109-1

Murray, E., Cho, J. H., Goodwin, D., Ku, T., Swaney, J., Kim, S.-Y., et al. (2015). Simple, scalable proteomic imaging for high-dimensional profiling of intact systems. *Cell* 163, 1500–1514. doi: 10.1016/j.cell.2015.11.025

Nguyen, H. P., Van Broeckhoven, C., and van der Zee, J. (2018). ALS genes in the genomic era and their implications for FTD. *Trends Gen.* 34, 404–423. doi: 10.1016/j.tig.2018.03.001

Nordström, U., Beauvais, G., Ghosh, A., Pulikkaparambil Sasidharan, B. C., Lundblad, M., Fuchs, J., et al. (2015). Progressive nigrostriatal terminal dysfunction and degeneration in the engrailed1 heterozygous mouse model of Parkinson's disease. *Neurobiol. Dis.* 73, 70–82. doi: 10.1016/j.nbd.2014.09.012

Ortega, J. A., Daley, E. L., Kour, S., Samani, M., Tellez, L., Smith, H. S., et al. (2020). Nucleocytoplasmic proteomic analysis uncovers erf1 and nonsense-mediated decay as modifiers of ALS/FTD C9orf72 toxicity. *Neuron* 106, 90.e13–107.e13. doi: 10.1016/j.neuron.2020.01.020

Pan, C., Cai, R., Quacquarelli, F. P., Ghasemigharagoz, A., Lourbopoulos, A., Matryba, P., et al. (2016). Shrinkage-mediated imaging of entire organs and organisms using uDISCO. *Nat. Methods* 13, 859–867. doi: 10.1038/nmeth.3964

Pan, C., Schoppe, O., Parra-Damas, A., Cai, R., Todorov, M. I., Gondi, G., et al. (2019). Deep learning reveals cancer metastasis and therapeutic antibody targeting in the entire body. *Cell* 179, 1661.e19–1676.e19. doi: 10.1016/j.cell.2019.11.013

Park, Y.-G., Sohn, C. H., Chen, R., McCue, M., Yun, D. H., Drummond, G. T., et al. (2019). Protection of tissue physicochemical properties using polyfunctional crosslinkers. *Nat. Biotechnol.* 37, 73–83. doi: 10.1038/nbt.4281

Penzes, P., Cahill, M. E., Jones, K. A., VanLeeuwen, J.-E., and Woolfrey, K. M. (2011). Dendritic spine pathology in neuropsychiatric disorders. *Nat. Neurosci.* 14, 285–293. doi: 10.1038/nn.2741

Pinotsi, D., Kaminski Schierle, G. S., and Kaminski, C. F. (2016). Optical super-resolution imaging of β-amyloid aggregation in vitro and in vivo: method and techniques. *Methods. Mol. Biol.* 1303, 125–141. doi: 10.1007/978-1-4939-2627-5_6

Porter, D. D. L., and Morton, P. D. (2020). Clearing techniques for visualizing the nervous system in development, injury, and disease. *J. Neurosci. Methods* 334:108594. doi: 10.1016/j.jneumeth.2020.108594

Renier, N., Adams, E. L., Kirst, C., Wu, Z., Azevedo, R., Kohl, J., et al. (2016). Mapping of brain activity by automated volume analysis of immediate early genes. *Cell* 165, 1789–1802. doi: 10.1016/j.cell.2016.05.007

Renier, N., Wu, Z., Simon, D. J., Yang, J., Ariel, P., and Tessier-Lavigne, M. (2014). iDISCO: a simple, rapid method to immunolabel large tissue samples for volume imaging. *Cell* 159, 896–910. doi: 10.1016/j.cell.2014.10.010

Richardson, D. S., and Lichtman, J. W. (2015). Clarifying tissue clearing. *Cell* 162, 246–257. doi: 10.1016/j.cell.2015.06.067

Sahl, S. J., Lau, L., Vonk, W. I. M., Weiss, L. E., Frydman, J., and Moerner, W. E. (2016). Delayed emergence of subdiffraction-sized mutant huntingtin fibrils following inclusion body formation. *Q. Rev. Biophys.* 49, e2. doi: 10.1017/S0033583515000219

Schedin-Weiss, S., Caesar, I., Winblad, B., Blom, H., and Tjernberg, L. O. (2016). Super-resolution microscopy reveals γ-secretase at both sides of the neuronal synapse. *Acta Neuropathol. Commun.* 4:29. doi: 10.1186/s40478-016-0296-5

Schermelleh, L., Ferrand, A., Huser, T., Eggeling, C., Sauer, M., Biehlmaier, O., et al. (2019). Super-resolution microscopy demystified. *Nature Cell Biology* 21, 72–84. doi: 10.1038/s41556-018-0251-8

Schierle, G. S. K., Michel, C. H., and Gasparini, L. (2016). Advanced imaging of tau pathology in Alzheimer disease: new perspectives from super resolution microscopy and label-free nanoscopy. *Microsc. Res. Tech.* 79, 677–683. doi: 10.1002/jemt.22698

Sheng, M., Sabatini, B. L., and Sudhof, T. C. (2012). Synapses and Alzheimer's disease. *Cold Spring Harbor Perspect. Biol.* 4, a005777–a005777. doi: 10.1101/cshperspect.a005777

Shrivastava, A. N., Aperia, A., Melki, R., and Triller, A. (2017). Physico-pathologic mechanisms involved in neurodegeneration: misfolded protein-plasma membrane interactions. *Neuron* 95, 33–50. doi: 10.1016/j.neuron.2017.05.026

Susaki, E. A., Tainaka, K., Perrin, D., Kishino, F., Tawara, T., Watanabe, T. M., et al. (2014). Whole-brain imaging with single-cell resolution using chemical cocktails and computational analysis. *Cell* 157, 726–739. doi: 10.1016/j.cell.2014.03.042

Sylwestrak, E. L., Rajasethupathy, P., Wright, M. A., Jaffe, A., and Deisseroth, K. (2016). multiplexed intact-tissue transcriptional analysis at cellular resolution. *Cell* 164, 792–804. doi: 10.1016/j.cell.2016.01.038

Tainaka, K., Kuno, A., Kubota, S. I., Murakami, T., and Ueda, H. R. (2016). Chemical principles in tissue clearing and staining protocols for whole-body cell profiling. *Annu. Rev. Cell Dev. Biol.* 32, 713–741. doi: 10.1146/annurev-cellbio-111315-125001

Tainaka, K., Murakami, T. C., Susaki, E. A., Shimizu, C., Saito, R., Takahashi, K., et al. (2018). chemical landscape for tissue clearing based on hydrophilic reagents. *Cell Rep.* 24, 2196.e9–2210.e9. doi: 10.1016/j.celrep.2018.07.056

Tillberg, P. W., and Chen, F. (2019). Expansion microscopy: scalable and convenient super-resolution microscopy. *Annu. Rev. Cell Dev. Biol.* 35, 683–701. doi: 10.1146/annurev-cellbio-100818-125320

Tillberg, P. W., Chen, F., Piatkevich, K. D., Zhao, Y., Yu, C.-C., English, B. P., et al. (2016). Protein-retention expansion microscopy of cells and tissues labeled using standard fluorescent proteins and antibodies. *Nat. Biotechnol.* 34, 987–992. doi: 10.1038/nbt.3625

Tomer, R., Ye, L., Hsueh, B., and Deisseroth, K. (2014). Advanced CLARITY for rapid and high-resolution imaging of intact tissues. *Nat. Protoc.* 9, 1682–1697. doi: 10.1038/nprot.2014.123

Tønnesen, J., and Nägerl, U. V. (2013). Superresolution imaging for neuroscience. *Exp. Neurol.* 242, 33–40. doi: 10.1016/j.expneurol.2012.10.004

Truckenbrodt, S., Maidorn, M., Crzan, D., Wildhagen, H., Kabatas, S., and Rizzoli, S. O. (2018). X10 expansion microscopy enables 25-nm resolution on conventional microscopes. *EMBO Rep.* 19, doi: 10.15252/embr.201845836

Truckenbrodt, S., Sommer, C., Rizzoli, S. O., and Danzl, J. G. (2019). A practical guide to optimization in X10 expansion microscopy. *Nat. Protoc.* 14, 832–863. doi: 10.1038/s41596-018-0117-3

Ueda, H. R., Ertürk, A., Chung, K., Gradinaru, V., Chédotal, A., Tomancak, P., et al. (2020). Tissue clearing and its applications in neuroscience. *Nat. Rev. Neurosci.* 21, 61–79. doi: 10.1038/s41583-019-0250-1

Vandenberghe, M. E., Souedet, N., Hérard, A.-S., Ayral, A.-M., Letronne, F., Balbastre, Y., et al. (2018). Voxel-based statistical analysis of 3D immunostained tissue imaging. *Front. Neurosci.* 12:754. doi: 10.3389/fnins.2018.00754

Vints, K., Vandael, D., Baatsen, P., Pavie, B., Vernaillen, F., Corthout, N., et al. (2019). Modernization of Golgi staining techniques for high-resolution, 3-dimensional imaging of individual neurons. *Sci. Rep.* 9:130. doi: 10.1038/s41598-018-37377-x

Voigt, F. F., Kirschenbaum, D., Platonova, E., Pagès, S., Campbell, R. A. A., Kastli, R., et al. (2019). The mesoSPIM initiative: open-source light-sheet microscopes for imaging cleared tissue. *Nat. Methods* 16, 1105–1108. doi: 10.1038/s41592-019-0554-0

Wassie, A. T., Zhao, Y., and Boyden, E. S. (2019). Expansion microscopy: principles and uses in biological research. *Nat. Methods* 16, 33–41. doi: 10.1038/s41592-018-0219-4

Zhao, S., Todorov, M. I., Cai, R., Maskari, R. A., Steinke, H., Kemter, E., et al. (2020). Cellular and molecular probing of intact human organs. *Cell* 180, 796.e19–812.e19. doi: 10.1016/j.cell.2020.01.030

Zhao, Y., Bucur, O., Irshad, H., Chen, F., Weins, A., Stancu, A. L., et al. (2017). Nanoscale imaging of clinical specimens using pathology-optimized expansion microscopy. *Nat. Biotechnol.* 35, 757–764. doi: 10.1038/nbt.3892

Conflict of Interest: The authors declare that the research was conducted in the absence of any commercial or financial relationships that could be construed as a potential conflict of interest.

Copyright © 2020 Parra-Damas and Saura. This is an open-access article distributed under the terms of the Creative Commons Attribution License (CC BY). The use, distribution or reproduction in other forums is permitted, provided the original author(s) and the copyright owner(s) are credited and that the original publication in this journal is cited, in accordance with accepted academic practice. No use, distribution or reproduction is permitted which does not comply with these terms.

frontiers in Neuroscience

REVIEW
published: 14 October 2020
doi: 10.3389/fnins.2020.570750

Current Techniques for Investigating the Brain Extracellular Space

*Federico N. Soria[1,2], Cristina Miguelez[3,4], Olga Peñagarikano[3] and Jan Tønnesen[1,2]**

[1] Achucarro Basque Center for Neuroscience, Leioa, Spain, [2] Department of Neuroscience, Faculty of Medicine and Nursing, University of the Basque Country (UPV/EHU), Leioa, Spain, [3] Department of Pharmacology, Faculty of Medicine and Nursing, University of the Basque Country (UPV/EHU), Leioa, Spain, [4] Autonomic and Movement Disorders Unit, Neurodegenerative Diseases, Biocruces Health Research Institute, Barakaldo, Spain

The brain extracellular space (ECS) is a continuous reticular compartment that lies between the cells of the brain. It is vast in extent relative to its resident cells, yet, at the same time the nano- to micrometer dimensions of its channels and reservoirs are commonly finer than the smallest cellular structures. Our conventional view of this compartment as largely static and of secondary importance for brain function is rapidly changing, and its active dynamic roles in signaling and metabolite clearance have come to the fore. It is further emerging that ECS microarchitecture is highly heterogeneous and dynamic and that ECS geometry and diffusional properties directly modulate local diffusional transport, down to the nanoscale around individual synapses. The ECS can therefore be considered an extremely complex and diverse compartment, where numerous physiological events are unfolding in parallel on spatial and temporal scales that span orders of magnitude, from milliseconds to hours, and from nanometers to centimeters. To further understand the physiological roles of the ECS and identify new ones, researchers can choose from a wide array of experimental techniques, which differ greatly in their applicability to a given sample and the type of data they produce. Here, we aim to provide a basic introduction to the available experimental techniques that have been applied to address the brain ECS, highlighting their main characteristics. We include current gold-standard techniques, as well as emerging cutting-edge modalities based on recent super-resolution microscopy. It is clear that each technique comes with unique strengths and limitations and that no single experimental method can unravel the unknown physiological roles of the brain ECS on its own.

Keywords: single particle tracking, STED microscopy, brain parenchyma, glymphatic system, super-resolution, real-time iontophoresis, electron microscopy, brain extracellular space

OPEN ACCESS

Edited by:
João O. Malva, University of Coimbra, Portugal

Reviewed by:
Karl Helmer, Massachusetts General Hospital, Harvard Medical School, United States
Noam Shemesh, Champalimaud Centre for the Unknown, Champalimaud Foundation, Portugal

****Correspondence:***
Jan Tønnesen
jan.tonnesen@ehu.eus

Specialty section:
This article was submitted to Brain Imaging Methods, a section of the journal Frontiers in Neuroscience

Received: *08 June 2020*
Accepted: *17 September 2020*
Published: *14 October 2020*

Citation:
Soria FN, Miguelez C, Peñagarikano O and Tønnesen J (2020) Current Techniques for Investigating the Brain Extracellular Space. Front. Neurosci. 14:570750. doi: 10.3389/fnins.2020.570750

INTRODUCTION

More than a century ago, Santiago Ramon y Cajal discovered that neurons are separate, individual entities rather than part of a continuum, and thereby laid the foundation for the *Neuron Doctrine* (Ramon and Cajal, 1888). While this doctrine prevails today, the last 20 years have seen a shift from the neuro-centric view of the nervous system toward a more integral scene that increasingly includes non-neuronal glial cells, in recognition of their unique and essential functional properties

[reviewed in (Clarke and Barres, 2013; Araque et al., 2014)], and the fact that they constitute around half the neural cells of the brain (Azevedo et al., 2009). Even more recently, new functional roles of the brain extracellular space (ECS) and its constituent microenvironment have emerged or been hypothesized, with the ECS thereby claiming its place among the intricate ensemble of modulators of neural function. The ECS has recently been referred to as the *final frontier in neuroscience* (Nicholson and Hrabětová, 2017), eluding to its many unknown aspects and potential for new neurobiological discoveries.

The ECS must inevitably resemble a cast of its cellular constituents, a comparatively vast reticulum mirroring their extreme morphological complexity in the form of interwoven sheets, tubes, and bulbs that range over multiple orders of magnitude in size. While it is in one sense an enormous, brain-wide structure, it is in reality more difficult to visualize and study than its individual resident cells, because the substructures of the dense ECS meshwork are commonly only nanometers wide, far smaller than most cellular substructures. This fact is a major obstacle for researchers and a key factor when considering which technique to apply for addressing it.

It contains the diverse glycans and proteins of the extracellular matrix, which constitutes a hygroscopic plastic scaffold for patency and cell attachment. Yet, for the reason mentioned immediately above, the relationship between the structure of the ECS and that of the extracellular matrix is still to be explored. At the same time, all vacant ECS is filled by interstitial fluid (ISF), and as such, the ISF compartment directly corresponds to the ECS in terms of geometric structure. The ISF serves as transport medium for diffusing ions and cellular signaling molecules, and its constituent solutes mirror ongoing signaling and metabolic processes (Holter et al., 2017; Abbott et al., 2018).

Given that cells are separate entities, the ECS is involved in any and all signaling events taking place between cells of the brain, *sauf* that through cellular junctions. Synaptic neurotransmitters traverse the ECS at the synaptic cleft that is only around 25 nm wide (Lučić et al., 2005; Zuber et al., 2005), leaving limited space and time for the ECS compartment to putatively shape the post-synaptic response. However, in addition to such fast synaptic signaling, parallel events occur through *volume transmission* where signaling molecules travel up to several tens of microns through the ECS before reaching their target and exerting an effect (Agnati et al., 1986, 1995). The spread of these molecules will be modulated by ECS geometric shape and viscosity, spanning from the peri-synaptic level (Rusakov and Kullmann, 1998; Zheng et al., 2017), to the brain-wide glymphatic metabolite clearance system (Iliff et al., 2012, 2013a).

One of the most intriguing properties of the ECS is that it is structurally dynamic. It undergoes volumetric changes during hyperexcitatory discharge events (Colbourn et al., 2019) and has a circadian volume-change rhythm that facilitates metabolite clearance during sleep as part of the glymphatic system (Xie et al., 2013). Yet, even this state-of-the-art view represents a largely secondary, uniform role of the ECS with a conspicuous lack of regional specification. This, at least to some extent, reflects the technical limitations for experimentally addressing its structural complexity and dynamics, as we describe in more detail below. Consequently, we commonly describe the ECS in rudimentary terms. The ECS volume fraction (α) of total brain tissue volume is routinely reported as a ubiquitous value around 20% for a given brain area, or even the entire brain, though there must evidently be increasing variation as one zooms in on still smaller areas, with anything between 0 and 100% conceivable, and even inevitable, in submicron volumes. The same is true for the ECS tortuosity (λ), which is a quantification of hindrance to diffusion, and for the intercellular ECS gaps that separate neighboring cells and are currently accepted to be around 40 nm wide with limited variation (Nicholson and Hrabětová, 2017). These seeming generalizations and oversimplifications are rooted in the fact that most data on ECS properties arise from *volume-averaging* techniques, i.e., indirect approaches where the diffusion of extracellular probes is extrapolated and averaged from a relatively large volume of tissue. While indeed ECS parameters have been found to vary with cell type, developmental stage, and disease across studies (compared in Syková and Nicholson, 2008), the considerable differences in methodology and volume-averaging approaches between these studies are a genuine confounder when trying to provide a more comprehensive description of the ECS at any scale. Unfortunately, the requirement for volume-averaging has remained inescapable when investigating live tissue, due to the fact that the geometric structure of the ECS falls beyond what optical microscopy modalities can resolve, including high-resolution confocal and two-photon imaging approaches. We do have knowledge about the ECS meshwork dimensions from electron microscopy (EM), which readily provides nanoscale resolution images. However, EM is incompatible with live tissue imaging and diffusional measurements, and it has been associated with structural artifacts related to fixation procedures (Mishchenko et al., 2010; Korogod et al., 2015).

This highlights a key point: existing experimental techniques for investigating the ECS come with considerable trade-offs between live-cell compatibility, data dimensionality, and spatiotemporal imaging resolution, to mention just a few critical variables. Most notable among conventional techniques, there is a prominent disconnection between methodologies that offer sufficient spatial resolution to resolve ECS structure and the ones that are compatible with time-lapse imaging in live tissue, with limited options to bridge this gap. Only recently have developments in optical microscopy widened this bottleneck considerably and started to reveal the mesmerizing physiological structure and dynamics of the brain ECS in live tissue.

Our aim here is to present an up-to-date overview of the available techniques for experimentally addressing specifically the brain ECS, highlighting their individual strengths and weaknesses, as well as key insights they have brought about. We are not intending to provide a comprehensive review of the physiology and biophysical parameters of the ECS, as others have done so recently (Nicholson and Hrabětová, 2017; Hrabetova et al., 2018). Since the relationship between the distribution and composition of the extracellular matrix and the respective ECS structure and function is still not well understood, we do not here include methods focusing on extracellular matrix molecules. The review is rounded off by identifying open questions that

can now be answered through application of the most recently developed techniques.

POINT-SOURCE DIFFUSION MEASUREMENT TECHNIQUES

Real-Time Iontophoresis Combined With Ion-Selective Electrode Detection

This is the current gold-standard method for experimentally addressing ECS properties and is based on measuring diffusional spread of a molecule from a point-source, commonly in the form of physiologically inert tetra-methyl-ammonium (TMA^+) introduced locally in the tissue *via* a glass capillary by *real-time iontophoresis (RTI)* (Nicholson and Phillips, 1981). Diffusional spread from the iontophoretic microelectrode source is measured by a corresponding TMA^+ ion-selective microelectrode, which can be considered a point-detector, positioned at a chosen recording location, typically 100 μm away (**Figure 1A**). The RTI microelectrode capillary and the respective recording microelectrode can be positioned in the tissue independently or integrated in a single probe. The source/detector pair is calibrated for a given diffusion distance in aqueous agar prior to use, which represents a scenario of unhindered, homogeneous diffusion (Odackal et al., 2017). The technique is readily applied in live tissue, where it yields diffusion curve data (**Figure 1B**; Nicholson and Phillips, 1981). By comparing the measured diffusion curve in tissue to unhindered diffusion, it is possible to extract the ECS volume fraction, α, as well as tissue tortuosity, λ, as:

$$\lambda = \sqrt{(D_{\text{free}}/D_{\text{tissue}})}$$

where D_{free} is the diffusion coefficient in aqueous medium with osmolarity matched to brain ISF, and D_{tissue} is the diffusion coefficient experimentally measured in the tissue (Syková and Nicholson, 2008). The advantage of the RTI method is that it is live tissue compatible and can be performed in brain slices as well as *in vivo*. It allows repeated time-lapse measurements, which have been used to show that hypoosmolar conditions reduce α and increase λ (**Figures 1C,D**), and enhance epileptiform activity in the hippocampus of rodents (Kilb et al., 2006). By combining a single ion-selective recording electrode with two source iontophoresis microelectrodes, the method has further revealed anisotropic diffusion over 100 to 200 μm distances in the corpus callosum and hippocampus (Vorísek and Syková, 1997; Mazel et al., 1998). Through the RTI approach, α has been consistently reported around 20% across different brain areas, though ranging from around 10 up to 43% (Mazel et al., 1998; Syková and Nicholson, 2008), and with λ values around 1.3 to 1.8.

The most notable downside of the point-source/point-detector approach is that it does not visualize ECS structure and has very low spatial resolution relative to ECS structural geometries, defined as the 50 to 150 μm distance between the RTI capillary tip(s) and the recording electrode tip. This necessitates interpolation and averaging of tissue properties across the given probe distance, with physiological variation on smaller scales effectively inaccessible. While for a given probe distance, the exact position of the ion-selective electrode is not critical in homogeneous tissue, in areas with regional ECS variations arising from laminar tissue, such as in the hippocampus (McBain et al., 1990), or from 3D anisotropy, as in the cerebellum (Rice et al., 1993), detector placement becomes of significant importance. In these cases, where inhomogeneity exists on a distance similar to the spatial resolution of the method, the diffusion model needs to take such variation into account to correctly interpret ECS parameters, e.g., through a multilayer analysis (Saghyan et al., 2012).

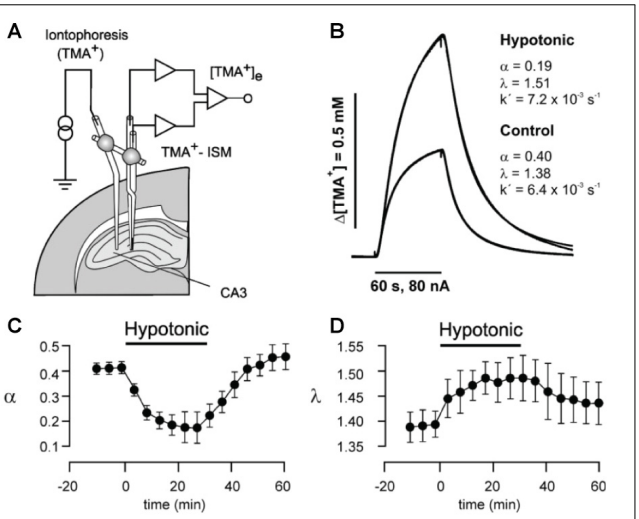

FIGURE 1 | (A) Schematic drawing of setup for *in vivo* or slice real-time iontophoresis measurements of TMA^+ diffusion in hippocampus. TMA^+ is released iontophoretically from a thin capillary from where it spreads diffusionally and is measured by a TMA^+ ion-selective microelectrode (ISM). **(B)** From the measured curves, the ECS volume fraction α and the tortuosity λ that quantifies hindrance to diffusion can be extracted, as here for respective hypotonic and control conditions in brain slices. **(C)** Change in α induced by transient perfusion of brain slice with hypotonic solution, measured by time-lapse RTI measurements. **(D)** Corresponding change in λ during hypotonic perfusion. As expected, hypotonic perfusion causes cells to swell, thereby reducing α and increasing λ. From Kilb et al. (2006), with permission.

Regarding temporal resolution, the electrical current pulses used for iontophoretic application of TMA^+ are typically 1 min duration 100 nA square pulses (Odackal et al., 2017), and subsequent diffusional clearance of TMA^+ from the area following the pulse takes a few minutes, thus enabling repeated sampling with an interval of 5 min. The technique was from the beginning introduced in an *in vivo* setting (Nicholson and Phillips, 1981), though a drawback is that *in vivo* RTI experiments are, to our knowledge, invariably performed in anesthetized animals. The putative effects of anesthesia have not been thoroughly explored, though no effects were reported in one study that did address it (Syková, 1997). Even so, it seems inevitable that anesthesia must have an effect on ECS properties given our current knowledge of brain functional changes in anesthetized animals and over the sleep–wake cycle (Xie et al., 2013; Stowell et al., 2019). The reported lack of anesthesia effects on measured diffusion could reflect limited sensitivity of

the RTI method, which again relates to the required volume-averaging.

Microfiber Optical Measurements

Microfiber imaging is another point-source approach, though it has not gained the popularity of the RTI-TMA method, and the existing publications have emerged from a single lab. In contrast to the RTI-TMA approach, it is optical rather than electrical in nature and measures fluorescence through the tip of an optical fiber inserted in the tissue area of interest. The fiber is used for both delivering excitation light and collecting emitted fluorescence from the illumination volume immediately around the tip, while a fluorophore is delivered iontophoretically or by pressure injection from a nearby capillary. Fluorescence intensity for a given excitation intensity and fluorophore concentration are measured in pure aqueous solution and inside the tissue, where the fluorophore solution distributes in the ECS. Given that the chosen fluorophore does not cross the cell membrane to enter cells, it will distribute exclusively in the ISF. A proportion of ISF is effectively displaced by cellular structures present within the tissue recording volume. Accordingly, the measured fluorescence intensity will scale with the volume fraction of the ISF and, thus, with ECS α. The method can be calibrated for a given experimental setting through cuvette experiments to provide quantitative measurements of α (Magzoub et al., 2009). For a given fluorophore concentration, tissue fluorescence scales roughly linearly with the volume displacement by cellular structures in the illuminated volume and thus with α (Zhang and Verkman, 2010). An extension of the approach is to combine it with transient fluorophore inactivation by photobleaching through high-intensity excitation illumination, followed by measurement of diffusional fluorescence recovery after photobleaching (FRAP). From the FRAP recording the re-equilibrium time constant can be readily obtained to reveal information about tissue diffusional properties, i.e., λ values across mouse brain areas (Zador et al., 2008). The technique resembles the RTI approach in many aspects, though instead of measuring diffusional equilibration electrically between two probes, it does so optically within an illumination volume. Similar to the RTI method, its main drawbacks include the lack of structural geometric ECS data and challenges in measuring from multiple areas, which becomes rather laborious, as it requires repositioning of the optical fiber and/or fluorophore-infusion capillary.

ELECTRON MICROSCOPY

At the opposite end of the spectrum to the point-source approaches, EM offers ECS images with nanoscale resolution and, until recently, has been the sole source of 2D and 3D images of the neuropil and ECS (Kasthuri et al., 2015; Korogod et al., 2015). Based on EM work, α has been estimated at an average 20%, in excellent agreement with the RTI-TMA method, and a predominant width of ECS channels at 40 nm (Nicholson and Hrabětová, 2017; **Figure 2A**). The major drawback of EM is the need for tissue fixation and inescapable incompatibility with live tissue work. The above-referenced data are based on high-pressure cryofixation-EM (cryofixation-EM) followed by freeze-substitution embedding, a technique pioneered more than 50 years ago to preserve water distribution and hence ECS ultrastructure (Vanharreveld et al., 1965). This methodology reduces structural fixation artifacts compared to chemical fixation (**Figures 2A,B**; Ohno et al., 2007; Korogod et al., 2015; Soria et al., 2020), though to some extent this confounder lingers, as it is still impossible to validate against a live tissue ground truth.

Classical chemical glutaraldehyde-based fixation dehydrates the sample and effectively shrinks the ECS, while cryofixation immobilizes molecules in their hydrated state without cross-linking, which has the additional advantage of preserving their antigenicity and therefore enabling concurrent immunolabeling protocols for correlative EM and fluorescence microscopy (van Rijnsoever et al., 2008). In cryofixation-EM, only the outermost tens of microns of a given tissue sample are reportedly artifact-free (Studer et al., 2008), and thicker tissue samples must accordingly be sliced prior to cryofixation. The initial steps of cryofixation-EM are therefore identical to acute brain slice work, such as that for electrophysiological recordings or fluorescence microscopy. In terms of invasiveness and tissue integrity, cryofixation-EM is therefore not superior to acute or cultured

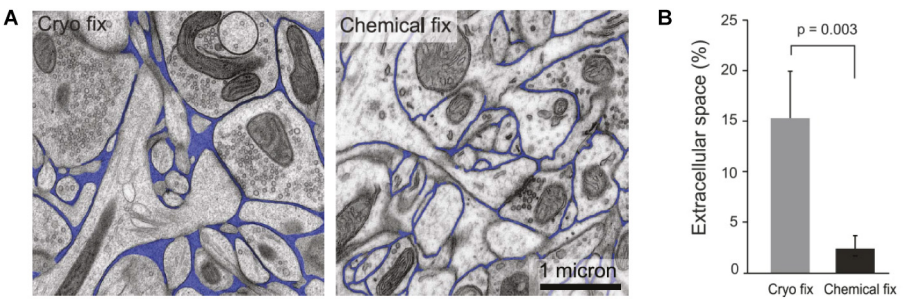

FIGURE 2 | (A) Comparative images of cryo-fixed and chemically fixed brain tissue imaged by electron microscopy, with ECS indicated in blue. It is clear that cryofixation yields better preserved ECS that is more voluminous and heterogeneous in terms of intercellular distances. **(B)** Comparison of α assessed in brain tissue that is cryo-fixed and tissue that is chemically fixed. Cryofixation yields comparable results to RTI measurements, whereas chemical fixation causes cellular swelling and a severe underestimation of α. From Korogod et al. (2015), with permission.

live slices when it comes to investigating cellular morphology in brain tissue. EM is still a superior method to fluorescence microscopy for connectomics studies and for quantifications based on counting, e.g. of synapses or synaptic vesicles, where the confounding effect of nanoscale distortions from fixation and slicing have a more negligible impact on results.

With respect to validation of the various existing and emerging techniques, it is gratifying that the range and distribution of ECS widths measured through cryofixation-EM in the mouse ventral midbrain are comparable to those recently obtained by super-resolution live-imaging methods applied in the same brain area (Soria et al., 2020), although a systematic per-region analysis is needed to further validate such findings.

MAGNETIC RESONANCE IMAGING

Magnetic resonance imaging (MRI) is a non-invasive approach extensively used for diagnostic purposes, as well as for clinical and experimental studies. The technique utilizes strong magnetic fields and radio waves to image protons in tissue, and thereby primarily maps out water and brain fatty tissue. Among the different implementations of this technique [for an overview of MRI subtypes, see (Runge et al., 2015)], diffusion-weighted MRI selectively maps out the random motion of protons and, thus, tissue water contents (Bammer, 2003). It can generate whole-brain 3D images at a spatial resolution up to 100 μm (Stucht et al., 2015), and while this is impressive considering the large field of view, it does not spatially resolve individual cells or individual ECS microstructures. MRI therefore also entails inevitable volume-averaging when analyzing ECS properties. Another notable confounder for studying the ECS is that both extra- and intracellular water will contribute to the MRI signal, and their respective contributions cannot be unambiguously separated (Norris, 2001).

To more specifically address the ECS compartment, some MRI studies rely on introduction of an extracellular contrast agent, e.g., based on hydrophilic gadolinium (Gd), which upon injection distributes by diffusion in the ISF and enhances the MRI signal by increasing the relaxation rate of water protons (Caravan et al., 1999). Comparison between MRI acquisitions before and after the contrast agent is introduced allows extraction of information more specifically related to ECS properties.

Intracerebroventricular infusion of a Gd-based contrast reagent in rats has been used to obtain distinct apparent diffusion coefficients (ADCs) for intra- and extracellular water and to further show that intracellular water is the main determinant of the overall MRI signal in both normal and ischemic rats (Silva et al., 2002). A similar approach, with introduction of the tracer either by intraparenchymal injection (Han et al., 2014) or by systemic injection followed by blood–brain barrier permeabilization *via* focused ultrasound (Mériaux et al., 2018), was used to extract ECS parameters such as λ and D_{tissue} in several regions of the rat brain. These approaches rely on the dynamic mapping of local concentrations of the tracer, followed by computation of ECS parameters using models that assume a constant flow rate of ISF in the whole brain and isotropic diffusion in the large volume scanned. While these assumptions may not hold true at the microscale, the method is very useful in that it maps coarse ECS parameters in 3D throughout the brain. In terms of imaging volume and image dimensionality, it outperforms the RTI-TMA method, though the RTI-TMA comes with superior specificity for the ECS compartment, as contrast-enhanced MRI signals inevitably incorporate confounding contributions from cellular and vascular compartments. A comparison study used MRI to map the movement of TMA and determine its ADC in the ECS (Kroenke et al., 2003). This was then compared to corresponding TMA ADC literature values obtained using the RTI-TMA method. The study revealed that the two techniques do not readily return comparable ADC values and that they are further sensitive to different biophysical parameters, which is not completely unexpected, based on the outlined differences between the techniques.

A free-water imaging (FWI) variant of MRI has been employed to enhance discrimination between extra- and intracellular water of brain tissue, by adding to the signal-processing algorithm a term that represents freely diffusing fluid. However, as this approach is still completely blind to the microscale geometry and absolute volume of the sampled ECS, the signal attributed to extracellular *free water* is not verifiable and is unlikely to represent true ECS values based on the limitations in spatial resolution and signal specificity of MRI in general. This FWI MRI technique, however, has been used in patients to identify an apparent increase in extracellular water associated with episodes of psychosis, which is hypothesized to reflect a neuro-inflammatory response and/or edema (Lyall et al., 2018; Tuozzo et al., 2018). A technique routinely employed in clinical settings, FWI MRI has further been used to demonstrate an increase in extracellular water content specifically in the *substantia nigra* of Parkinson's disease patients (Ofori et al., 2015; Planetta et al., 2016), an area characterized by hallmark dopaminergic cell death in this disease.

MRI has been applied to address molecular transport in cerebrospinal fluid, where the scale of the brain-wide 3D images is particularly suitable for addressing such transport as part of the glymphatic system. However, as we also describe, resolution and specificity instead become bottlenecks. In humans, intrathecal infusion of an MRI tracer revealed a brain-wide drainage of CSF to the cervical nodes, thereby corroborating the existence of a functional glymphatic system also in humans (Eide et al., 2018). The technique was previously employed to identify a reduction of rat brain ECS volume after cortical spreading depression (Hasegawa et al., 1995) and an increase in cortical ECS volume of aged transgenic APP23 Alzheimer's disease model mice that was associated with the presence of cortical plaques and memory impairments (Syková et al., 2005). In the latter study, the authors presented parallel RTI data from the same animals that corroborated the increase in cortical ECS volume compared with controls. MRI has further been used to show an increase in α of the *globus pallidus* in experimental Huntington's disease, consistent with observed cell death in this nucleus (Vorisek et al., 2017; **Figure 3**). The cell death and increased ECS volume were interestingly not associated with changes in

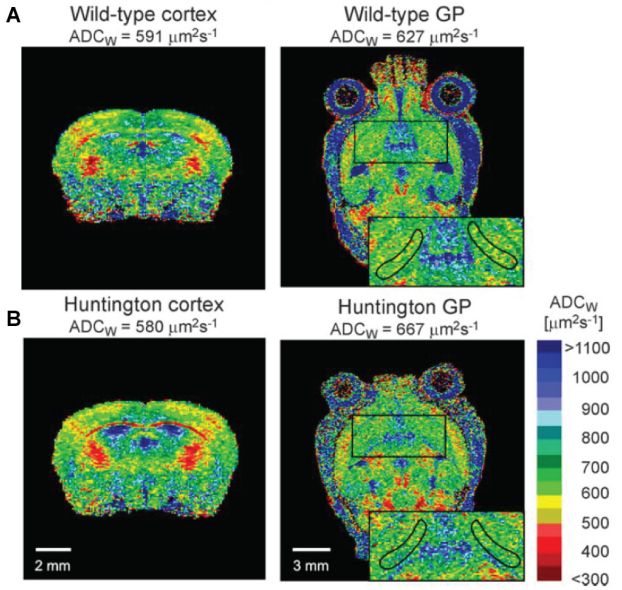

FIGURE 3 | *In vivo* mouse brain MRI images depicted as the *apparent diffusion coefficient of water* (ADC_W), as per the calibration bar. Extracellular water has a higher apparent diffusion coefficient than intracellular water, and the methods can be used to address differences in the extracellular space across conditions. **(A)** Depicts a coronal view and a sagittal view of the brain, including the cortex and the *globus pallidus* (GP; zoomed insert), respectively. **(B)** Depicts corresponding sections from the brain of a Huntington's disease mouse model. It is apparent that water diffusion in the ventricles is much higher than in denser parenchyma, as expected. From Vorisek et al. (2017), with permission.

diffusional properties of the tissue, which the authors attributed to concurrent astrogliosis and presence of reactive astrocytes, which could alter the tissue properties in a more complex way. More recently, MRI was applied to show that the presence of β-amyloid in the APP/PS1 Alzheimer's disease mouse model was associated with reduced perivascular ISF flow and glymphatic system function. Notably, this effect could be effectively reversed through controlled heating of the brain tissue by transcranial illumination with red light over a period of 2 months, and this was further associated with rescue of impaired spatial learning (Yue et al., 2019).

While anesthesia is not a prerequisite for performing MRI, most MRI-based ECS studies to date rely on recordings from anesthetized animals, and this could conceivably influence tissue properties and confound data aiming to explore the normophysiological state. One MRI study in mice found that general anesthesia by ketamine injection or isoflurane inhalation impairs glymphatic system clearance and reduces ECS volume in a dose-dependent manner (Gakuba et al., 2018). This is partially supported by a more recent study in rats, where isoflurane inhalation anesthesia induced a decrease in ECS volume relative to intravenous anesthetics dexmedetomidine and sodium pentobarbital (Zhao et al., 2020). This latter work additionally found that norepinephrine had a negative effect on ECS volume and interstitial fluid drainage, corroborating original studies on the effect of noradrenergic signaling on ECS volume (Xie et al., 2013; Sherpa et al., 2016).

A related and complementary technique performed using the same equipment is *diffusion-weighted magnetic resonance spectroscopy* (DW-MRS), which relies on frequency analysis of the recorded magnetic resonance radio waves. In the detection band, a given frequency peak can be attributed to a given MR-observable molecule, e.g., water, glutamate, or creatine (Tognarelli et al., 2015). Thus, while MRI provides structural images predominantly based on water content of the tissue, DW-MRS provides maps of select biochemical components within a given voxel. The strength of DW-MRS is that it allows detection and discrimination of relatively specific cellular or extracellular species, such as from N-acetylaspartate that is nearly exclusively intracellular (Palombo et al., 2018). However, like MRI, it is ultimately a volume-averaging technique as it lacks the spatial resolution to resolve actual cellular and extracellular structures and is mostly used for qualitative analysis of tissue composition.

To recapitulate, MRI is a highly applicable tool for assessing differences in ECS volume and properties of glymphatic system clearance on a regional or global scale in live animals, where it can be repeatedly applied over periods of time spanning hours to years. The main drawback is the low spatial resolution and the problem in the separation of intracellular and extracellular signals, both of which prevent quantitative analyses of ECS volume fractions at any scale and prevent direct imaging of diffusion or flow of ISF or CSF. It is also not widely available to researchers due to the cost and complexity of the involved equipment.

WIDEFIELD FLUORESCENCE MICROSCOPY

Intrinsic Optical Signal Imaging

Intrinsic optical signal (IOS) imaging is in essence label-free light microscopy that detects changes in the tissue reflectance or transmission of light. As cellular membranes and the interstitial fluid have different refractive indices, light will be reflected and transmitted differently depending on whether photons are traversing cellular membranes, the intracellular or extracellular solute, respectively. The fractional volumes of cellular membranes and the interstitial fluid change with cellular activity, e.g., during cellular swelling, and will be reported as a change in the IOS (Frostig et al., 1995). However, the physics behind the observed signal are still not well understood, and the source of the IOS remains somewhat obscure, so the technique is limited at the level of its specificity to address the ECS (Tao et al., 2002).

The underlying microscopy technique is widefield imaging that can be readily performed at video speed and at a spatial resolution of a few microns. Label-free imaging is inherently associated with low contrast and individual neurons cannot be discerned in the IOS images, though the strength of the technique is exactly the simplicity, independence of

labels, low phototoxicity, and the use of relatively simple widefield microscopes.

Classical IOS imaging detects reflected light and is thereby confined to address the surface of the brain, where it has been used to map out the functional architecture of the cortex, for example by enabling association of activity in specific barrel cortex areas to stimulation of individual whiskers in the rat (Grinvald et al., 1986). While the reliance on reflected light restricts experiments to the first few tens of micrometers of tissue surface, a variant of IOS imaging instead detects changes in transmitted light sent through the tissue of interest. This has been applied to study neuronal activity in unlabeled acute hippocampal slices non-invasively, showing that changing the ionic Cl^- gradient across the cell membrane *via* the loop-diuretic furosemide alters the detected signal (MacVicar and Hochman, 1991). As furosemide inhibits NKCC1 and KCC2 transporters predominantly found on astrocytes, this observation directly implicates astrocytes and their volume changes in the IOS and, thus, ECS volume changes (Andrew et al., 1999). In support of a primary role of glia in the IOS recordings, similar IOS changes in response to loop-diuretics furosemide and bumetanide have been observed in optic nerve preparations, which contain solely glia cells and axons, highlighting that the response is not depending on the presence of neuronal cell bodies (MacVicar et al., 2002). It has accordingly been argued that IOS primarily detects glia cell volume changes and, conversely, also ECS volume changes, which is supported by a positive correlation between ECS volume changes measured through extracellular TMA^+ concentrations and the IOS signal, at least in the initial phase of the response (Holthoff and Witte, 1996). However, given that IOS changes are observed to be also dependent on neuronal activity and that loop-diuretics do not act exclusively on astrocytes, it is inevitable that neurons contribute to the signal too. Indeed, others have pointed out that the IOS changes are likely to involve neuronal components, including changes in mitochondrial membranes and dendritic beading in hyperexcitatory conditions (Aitken et al., 1999; Syková et al., 2003).

The simplicity of the technique, its *ex* and *in vivo* compatibility, and the imaging speed make IOS an attractive method for addressing cellular and ECS volume changes, though the lack of specificity and knowledge about the signal origin prevents quantitative ECS volume change analyses, thereby limiting the usefulness for studying specifically the ECS. The technique further has low spatial resolution, particularly in the *z*-axis when measuring transmitted light, and can only report tissue changes on a population level. It cannot visualize the actual ECS structure or discriminate between neurons and glia cells. Additionally, when applied in acute brain slices, the transmitted light changes report not only changes in the healthy middle layer of the slice, but also incorporate changes of the damaged top and bottom surfaces where the slice has been cut, which will add noise to the signal emerging from the healthy tissue layers.

Integrative Optical Imaging

Integrative optical imaging (IOI) is based on widefield fluorescence microscopy and shares many aspects with IOS imaging described above. Though contrary to IOS imaging, the detected signal is not intrinsic, but instead derives from a designated fluorophore introduced by the experimenter. It is again live cell compatible, allows very fast CCD camera-enabled time-lapse acquisitions, and offers multicolor imaging, though at limited optical resolution and confined to the outermost tens to hundreds of micrometers of tissue. While the technique has low spatial resolution and is unable to resolve the geometric structure of the ECS in live tissue, it holds value for analyzing volume-averaged diffusional properties of larger volumes of tissue, e.g., across the field of view in a widefield microscope. It is based on acute introduction of an inert fluorophore into the tissue by pressure injection from a glass microcapillary tip and evaluation of the diffusional distribution of the fluorophore in the surrounding tissue. This allows diffusional ECS properties to be extracted, based on the static and dynamic fluorophore distribution around the capillary tip point-source. Acquisitions are easily performed using standard widefield microscopy cameras, and experimenters can readily extract data on the effective diffusion coefficient and λ at the resolution of the given microscope.

In the early days of brain ECS exploration, IOI was applied to show that λ increases with the molecular size of the probe (Nicholson and Tao, 1993). This important finding was achieved in rat cortical tissue using fluorescent dextrans of various molecular weights and later confirmed using quantum dots (Thorne and Nicholson, 2006), whose 35 nm diameter and ability to readily diffuse into the parenchyma reported that most ECS channels have at least 40 nm width. A recent development has improved the technique by increasing the temporal resolution from tens of seconds to around 1 s, to capture much faster ECS and tissue dynamics (Hrabe and Hrabetova, 2019). While in IOI the tissue diffusion coefficient (D) is assumed constant over time, in this improved *time-resolved IOI* version, D varies over time, allowing for detection of fast changes in diffusivity. It has been applied to show that diffusion in cortical ECS was greatly reduced during the depolarizing wave spread, consistent with a reduction in ECS volume (Hrabe and Hrabetova, 2019).

Related to IOI, other widefield approaches have made use of fluorophore spreading after pressure injection to demonstrate heterogeneous diffusion across the molecular layer in turtle brain cerebellum (Xiao et al., 2008). Such heterogeneity was also reported across the layers of the hippocampal CA1 area in mice (Arranz et al., 2014), where it was increased after depleting the extracellular matrix protein hyaluronan through genetic knock-out (**Figure 4**). Much earlier, widefield phase contrast microscopy was applied to evaluate the effects altering interstitial fluid osmolarity on ECS volume in hippocampal slices, though here the readout was general histological appearance, not specifically that of the ECS (Newman et al., 1995).

The low cost, simplicity, and applicability of IOI make the approach attractive and readily available to researchers. The technique's strength lies in the relatively high specificity of the fluorescence signal to the ECS compartment, as the fluorophore does not cross cell membranes to enter cells. This particular strength sets it apart from IOS imaging that suffers from low signal specificity. As a widefield microscopy modality, it comes with limited spatial resolution that does not allow ECS structure

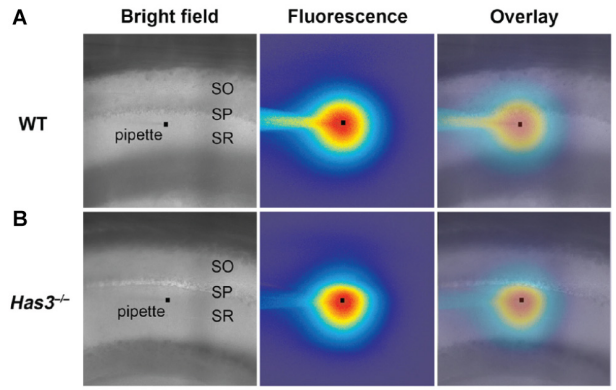

FIGURE 4 | (A) Brightfield microscopy image of the CA1 area in acute brain slice from wild-type (WT) mouse. The *stratum oriens*, *stratum pyramidale*, and *stratum radiatum* layers are indicated as SO, SP, and SR, respectively. The faint outline of a micropipette is visible, with a square marking the tip. The middle panel is the same frame, though in epifluorescent mode 80 s after a brief injection of a fluorophore from the pipette tip. The diffusional spread of the fluorophore will depend on tissue diffusional properties, which can be read out by analyzing potential assymmetries in the fluorophore spreading profile. The right-most frame depicts an overlay of the frame imaged in brightfield and epiflorescence mode, repectively, enabling visual assessment of diffusion with respect to the indicated tissue layers. **(B)** Corresponding image from hyaluronan-deficient hyaluronan synthase-3 (Has3) knock-out mouse, where the fluorophore distribution around the pipete tip appears less symmetric, indicating assymmetric diffusion and changes ECS properties relative to the WT tissue. From Arranz et al. (2014), with permission. Copyright 2014 Society for Neuroscience.

to be addressed, and it relies on extensive volume-averaging within the field of view, not least in the *z*-axis where optical resolution is lowest, commonly several tens of microns.

SCANNING FLUORESCENCE MICROSCOPY

Two-Photon and Confocal Microscopy

Two-photon and confocal microscopy are highly similar optical point-scanning fluorescence microscopy approaches and, therefore, quite different in nature to the widefield modalities described above. Both come with inherently high optical *z*-axis resolution and superior optical sectioning that allows high-resolution imaging inside the tissue. Two-photon and confocal imaging modalities have been used to investigate fluorophore distribution and spread in the ECS, though not often in experiments actually intended to extract ECS physiological parameters. One such implementation was the use of two-photon microscopy to describe the concentration gradient of a membrane-impermeable fluorophore after pressure ejection from a fluorophore-filled microcapillary tip inside a brain slice, though the analysis was not intended to investigate the ECS compartment *per se* (Rusakov et al., 2005). Additional studies have used two-photon microscopy and point-source fluorophore introductions to analyze extracellular diffusivity of molecules, though without attempting to extract ECS geometrical data (Stroh et al., 2003; Savtchenko and Rusakov, 2005).

In (2008), Kitamura et al. performed local injection of fluorophores *in vivo* into the cerebral cortex ECS, as a way to visualize and patch the residing cell somata through two-photon shadow patching. This strategy utilized extracellular application of fluorophores to produce a negative shadow image of unlabeled cells through two-photon microscopy. While this approach directly renders the ECS fluorescent and visible, the diffraction-limited optical resolution of a two-photon microscope blurs most structural details out. This highlights the main drawback of two-photon microscopy for imaging the ECS; the best achievable resolution is around 400 nm laterally (*x*,*y*) and 1 μm axially (*z*), which allows larger dendrites and somata to be resolved faithfully, but not denser neuropil and its ECS geometry (Mishchenko et al., 2010). The optical resolution of confocal microcopy is around twice as good at 200 nm in the lateral plane and 500 nm axially. This resolution advantage over the two-photon modality is mainly due to the shorter wavelength excitation light and is only achievable if the setup is configured perfectly. Even then, this resolution is not sufficient to resolve the entire ECS geometric structure, though indeed many individual ECS channels already become visible and a lot of information is extractable. The shorter wavelengths of confocal microscopy make it less applicable for imaging deeper inside the tissue, and beyond a few tens of micrometers tissue depth, two-photon microscopy is a better choice and can be used to image down to roughly 1 mm depth, though spatial resolution will decrease at deeper layers.

Over recent years, two-photon microscopy has been increasingly used to study the glymphatic system, through its ability to visualize *in vivo* the distribution volume, wash-in rate, and wash-out rate, respectively, of fluorophores introduced into the interstitial fluid of the ECS through the ventricular system (**Figure 5**; Iliff et al., 2012, 2013b; Xie et al., 2013). This approach has been essential for our understanding of the glymphatic system as a metabolite clearance pathway, including the circadian volumetric change it undergoes to facilitate clearance during sleep, and the involved regulation through norepinephrine (Xie et al., 2013). In these studies, the resolution of the two-photon microscopy approach is sufficient to discriminate between perivascular spaces and denser parenchyma, though beyond this it offers no geometric

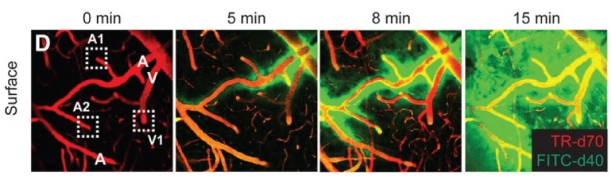

FIGURE 5 | *In vivo* two-photon time-lape microscopy of blood vessels (in red), and a fluorophore spreading first in the perivascular space along arterial vessels (denoted A) and then into the parenchyma and along venules (denoted V), to effectively reveal the glymphatic system in function. From Iliff et al., 2013b, with permission.

information about ECS structure, as it cannot optically resolve this. A precursor work to these studies on the glymphatic system was a paper describing two-photon imaging of fluorescent nanospheres injected locally into cortical tissue, with concurrent imaging of cortical blood vessels in a second color (Foley et al., 2012). This provided the first images of the predominantly perivascular transport of solutes in brain tissue, though the term and concept of the glymphatic system had not yet been proposed. The use of nanospheres was more recently used to perform tracking of spheres along cortical arteries *in vivo*, to show that arterial pulsations drive perivascular cerebrospinal fluid bulk flow (Mestre et al., 2018).

It has further been shown that cortical spreading depression effectively impairs perivascular flow in a reversible way (Schain et al., 2017), consistent with cellular swelling that reduces the ECS volume (Charles and Brennan, 2009), as also reported using both the IOI and MRI methods above. In a mouse model of multiple cerebral microinfarcts by carotid cholesterol crystal injection, a global decrease in fluorophore spreading in the ECS was observed, indicating that focal disruptions of the glymphatic clearance pathway may have a global impact on putative bulk flow of ISF in a negatively age-dependent manner (Wang et al., 2017).

Time-Resolved Fluorescence Anisotropy Imaging

Time-resolved fluorescence anisotropy imaging (TR-FAIM) allows optical assessment of viscosity by measuring the emitted fluorescence light polarization relative to the polarization of the excitation light. Polarized excitation light will preferentially excite fluorophores with a corresponding molecular orientation, and these emit fluorescence with a corresponding certain polarization. However, during the few nanoseconds between excitation and emission, the fluorophore will spontaneously undergo molecular rotation so that the emission polarization diverges from the excitation polarization; i.e., it is anisotropic. The level of anisotropy can be relatively easily quantified using two or more detectors with polarization-sensitive optical filters in front. The observed anisotropy depends on the viscosity of the medium in which the fluorophore resides, by impacting the degree of molecular rotation in a given nanosecond time window. Accordingly, differences in viscosity will give rise to differences in anisotropy, and in parallel to the optical fluorescence image produced by the microscope, a corresponding anisotropy map is produced (Le Grimellec et al., 1982). Fluorescence anisotropy imaging was originally utilized to measure cytosolic viscosity inside living cells (Dix and Verkman, 1990), though it has been adopted to measure viscosity in the extracellular space and even in the synaptic cleft by utilizing two-photon microscopy as the underlying microscopy modality (Zheng et al., 2017).

TR-FAIM has been applied to show that diffusion in the ECS is around 30% slower than in artificial cerebrospinal fluid, while in the synaptic cleft it is 46% slower. As two-photon microscopy is lacking optical resolution to actually resolve the synaptic cleft, this diffusional retardation measurement is incorporating considerable measurement noise and is conceivably substantially larger as well as heterogeneous within the cleft. The technique has been further used to show that viscosity of the interstitial fluid varies only slightly across the respective hippocampal CA1 *strati oriens*, *pyramidale*, and *radiatum* (Zheng et al., 2017). This means that local differences in ECS volume or structural geometry could instead be the main determinants of putative variation in diffusional properties across these same layers, which has been reported, e.g., for the hippocampus (Arranz et al., 2014).

So far, the two-photon TR-FAIM approach has only been used by a single group, though it has a considerable potential for more discoveries, not least incorporated into a super-resolution modality, or in parallel with complementary techniques for addressing the ECS properties.

The technique comes with the advantages and disadvantages of conventional two-photon microscopy, with the additional trade-off that the required polarization-sensitive optical components will lower the photon-detection efficacy of the setup, so that effectively images will be less bright compared to conventional two-photon microscopy. When the involved fluorophore is applied extracellularly through injection or perfusion, this obstacle is quite readily circumventable as fluorophore concentration can simply be increased on the fly during the experiments.

SUPER-RESOLUTION FLUORESCENCE MICROSCOPY

Super-Resolution Shadow Imaging

Super-resolution shadow imaging (SUSHI) is one of two main incarnations of super-resolution microscopy approaches developed specifically to address the geometric structure of the ECS in dense brain parenchyma (Tønnesen et al., 2018). Super-resolution microscopy encompasses several widely different fluorescent microscopy modalities that allow imaging beyond the diffraction barrier of light, which limits optical resolution in conventional microscopy approaches (Tønnesen and Nagerl, 2013). Among these, stimulated emission depletion (STED) microscopy stands out by being a point-scanning technique that optically enhances resolution, in two or three dimensions (3D), to directly produce super-resolved images (Klar et al., 2000). STED is based on either a respective confocal or two-photon microscope, with an additional and spectrally different laser beam co-aligned with the excitation beam to enhance resolution by restricting emission to a subdiffraction volume. In the most common confocal-based incarnation, the achievable optical resolution of 3D-STED inside live tissue is around 50 nm laterally and 150 nm axially, far superior to diffraction-limited microscopy techniques (Tønnesen et al., 2018).

Just like two-photon shadow imaging described above (Kitamura et al., 2008), SUSHI is based on labeling of the interstitial fluid with a freely diffusible hydrophilic fluorophore that renders cellular structures visible as shadows. However, due to the several hundred times higher volume resolution (i.e.,

integrated planar and axial resolution of a microscope) of 3D-STED (Osseforth et al., 2014; Tønnesen et al., 2018), not only somata and dendrites become visible, but also structures of dense parenchyma, such as individual pre- and post-synapses, thereby generating unprecedented images of the entire neuropil (**Figure 6A**). Importantly, because the ISF compartment is literally identical to the ECS in terms of structural geometry, the ECS meshwork becomes directly visible and nearly completely optically resolved, allowing the ECS to be analyzed geometrically (Tønnesen et al., 2018).

As a point-scanning fluorescence microscopy modality, SUSHI is particularly well suited for time-lapse imaging inside live brain tissue, where it has been applied down to at least 50 μm depth in slices. The approach is readily combinable with concurrent imaging of conventionally labeled neural cells to reveal the ECS and neuropil in the context of individual neurons and glia cells (Tønnesen et al., 2018). It has provided the first live tissue quantitative geometric analyses of hippocampal ECS geometry and shown that ECS channel widths represent a continuous distribution spanning from microns down to 50 nm, with some unresolved structures likely even smaller. SUSHI has further revealed activity-dependent microscale ECS dynamics, though the involved cellular structures behind these remain to be identified. From the high-resolution images of the ISF, the ECS volume fraction can be calculated at any area of interest, down to the nanoscale volumes surrounding individual synapses.

Just like the related, but diffraction-limited, point-scanning modalities confocal and two-photon microscopy, the main limitation of the SUSHI approach is the imaging depth. The strict requirement for beam co-alignment and for shaping the STED beam wave front poses restrictions on the achievable imaging depth, though the achieved 50 μm depth of 3D-STED is already sufficient to be applicable in acute slices and *in vivo* in rodents. The effective imaging depth will undoubtedly improve in the near future by adopting emerging technologies from the two-photon and super-resolution microscopy field, including aberration correcting adaptive optics, implantable lenses, and more. In STED imaging, the requirement for an additional and proportionately high-power laser line introduces complexity, especially for multicolor imaging, and increases potential phototoxicity and bleaching effects, which may confound cellular imaging if not performed meticulously (Lenz and Tønnesen, 2019). However, the SUSHI configuration is practically insensitive to photobleaching and phototoxicity because bleached fluorophores simply diffuse away from the field of view and are not trapped inside the cells.

Carbon Nanotube Localization Microscopy

A complementary super-resolution microscopy approach for investigating the ECS is based on imaging and tracking of near-infrared fluorescent nanometer-sized single-walled carbon nanotubes (SWCNTs) inoculated into the brain parenchyma *in vivo* and later observed in acute brain slices (Godin et al., 2017). After injection into the lateral ventricle, nanotubes passively spread through the brain parenchyma, penetrating the structure of the ECS according to their size. Their distribution at given time points after injection will therefore convey information about the diffusional properties of the ECS, as well as describing the involved ECS structure (**Figure 6B**). The diffusing fluorescent nanotubes can be tracked up to 100 μm tissue depth using a widefield microscopy approach at millisecond timescale, opening the possibility for *in vivo* studies of relatively large tissue areas. Analysis of time-lapse images with super-resolution single-particle-tracking algorithms yield real-time data on their dynamics in live tissue, thereby enabling not only nanoscale structure to be determined, but also local relative diffusivity determined from the instantaneous diffusion speed (Godin et al., 2017; Paviolo et al., 2020). This method has provided measurements of the ECS channel widths ranging from near 0 μm to around half a micron, describing a log-norm continuum with the most commonly observed width being just below 100 nm, in excellent agreement with the SUSHI study described above. It is noteworthy that fluorescent SWCNT tracking has suggested the ECS channel widths in organotypic hippocampal slices were slightly wider than in acute brain slices, though this needs to be more specifically addressed, as the organotypic slices were prepared from rat tissue, while the acute brain slices were prepared from mice, and the acute slice data were obtained from diverse regions that could potentially have different properties (Paviolo et al., 2020). This very basic question highlights the technical limitations that have hampered progress in the field, as well as the advantages of these latest methods.

The strength of the SWCNT imaging and tracking technique lies in providing both topological and diffusional information of the ECS simultaneously and enabling direct comparison between these two parameters. In a recent study that delivered the first nanoscopic characterization of pathological brain ECS, SWCNT tracking revealed poor correlation between local ECS width and nanoscale diffusion, suggesting that ECS diffusive inhomogeneities are not only driven by geometrical factors (Soria et al., 2020). In fact, SWCNT data from hyaluronan-depleted mice and mice with parkinsonian-like dopaminergic cell loss, which also induces hyaluronan degradation, showed that while matrix modification has a greater impact on molecular mobility, neurodegeneration affects both ECS channel width and diffusion (Soria et al., 2020). This interestingly suggests that hyaluronan, the main component of the extracellular matrix, is partially responsible for local variations in ECS diffusional properties.

Among the limitations of the technique is that ECS spaces smaller than the tubes will remain inaccessible and thus invisible and that tubes may conceivably get stuck and lose the ability to convey dynamic information, which further limits the potential for repeated experiments over time. A recent variation of the method, developed independently, makes use of fluorescent nanoparticles and multiple particle tracking algorithms to characterize diffusion in the ECS at single-particle resolution (McKenna et al., 2020). This approach confirmed increased nanoparticle diffusivity after matrix removal, although instead of hyaluronan as above, chondroitin-sulfate proteoglycan (CSPG) was modified by enzymatic digestion.

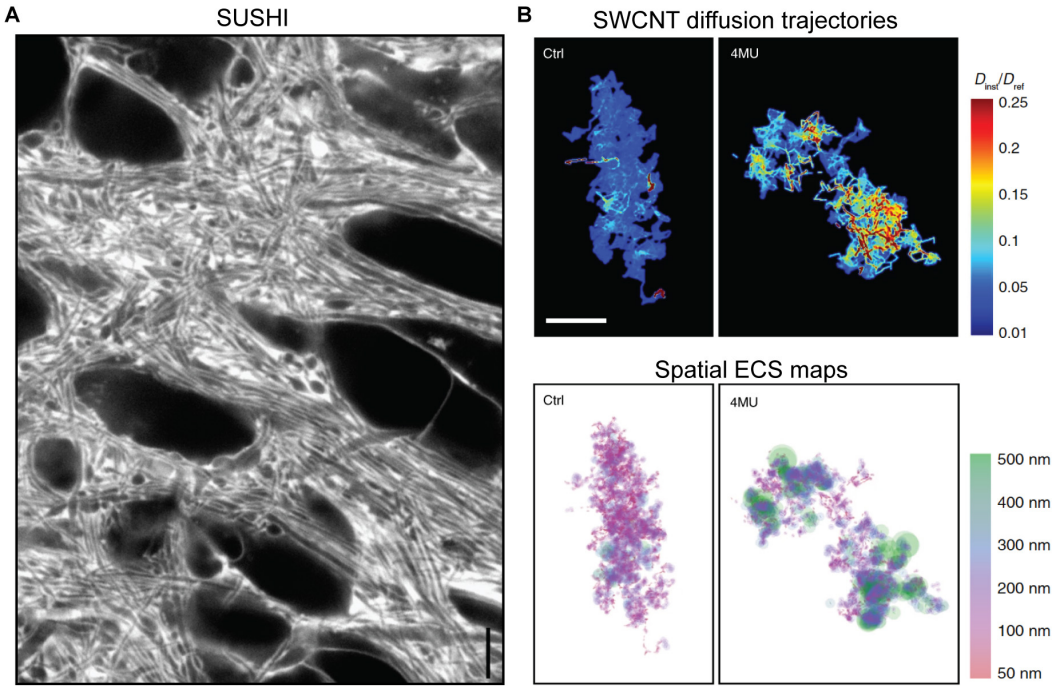

FIGURE 6 | (A) Super-resolution shadow imaging (SUSHI) of the neuropil in cultured hippocampal slice. During perfusion of the slice with a fluorophore in solution, the interstitial fluid becomes brightly fluorescent, while cellular structures appear as dark shadows. As it is based on 3D-STED microscopy as the underlying imaging technique, it offers 50 nm planar resolution, which is sufficient to optically resolve the majority of ECS geometries in the frame. Scale bar is 4 μm. Modified from Figure 1E in Tønnesen et al. (2018), with permission. **(B)** Super-resolved maps of single-walled carbon nanotube diffusion trajectories (top) and corresponding ECS maps (bottom) in acute rat brain slices, with calibration bars indicating diffusional accesibility for SWCNTs in the ECS and derived ECS dimensions. The left panels are from control animals, while the right ones are from hyaluronan-depleted animals that were chronically administered 4-methylumbelliferone (4MU; a hyaluronan synthase inhibitior) prior to the experiment. Scale bar is 2 μm. From Soria et al. (2020), Nature Communications (scale bar inserted from cropped panel in the original figure), with permission (http://creativecommons.org/licenses/by/4.0/).

DISCUSSION

Dog-Eat-Dog or Horses for Courses?

From their individual presentations above, and further by rating and comparing their main characteristics (**Figure 7**), it is clear that the various available techniques for addressing the brain ECS differ fundamentally in nature. They all have restriction in the sample they can be applied on and the type of data they provide, meaning that not all the above-described types of data can be collected from a given sample. In other words, no single technique is capable of extracting structural and biophysical data at high spatiotemporal resolution inside the intact live brain, which would be the ultimate experiment. Instead, each modality comes with particular limitations and particular strengths that limit the choice of techniques suitable for a given scientific question. In designing their experiments, investigators must carefully weigh the necessity for specific parameters, including spatial and temporal resolution, multicolor imaging, size of the field of view, and whether experiments must be live cell and repeated over time. Conversely, the availability of the techniques within an experimenter's research institution or collaborative network may decide how a given scientific question can be addressed, if at all. Due to their widely differing nature, the techniques are not as much in competition with each other (dog-eat-dog scenario) as they are complementary, and each has its merit (horses-for-courses scenario).

If more than one method can be applied to a given sample, this can add synergy, as layers of variability can be peeled off during analyses to enable new insights. For example, knowing the relative diffusivity gradients across the hippocampal CA1 cell layer will allow stronger conclusions on how structure may shape diffusion across this layer and, accordingly, the determinants of tortuosity. Also, TR-FAIM should be readily doable using two-photon excitation STED microscopy in live brain slices or *in vivo* (Bethge et al., 2013; Takasaki et al., 2013), which would provide parallel nanoscale structural and diffusional data in a single acquisition step.

New Discoveries on the Horizon

While a steady flow of publications, particularly from a few dedicated labs, have provided still deeper insights into the brain ECS structure and function, one frontier has remained inaccessible, namely the submicron ECS structure and its dynamics in live brain tissue. No method has existed that would provide credible structural images of the complex channels and reservoirs of the ECS in live brain tissue. The different nuclei and areas of the brain have hallmark organizations of neural cells into distinct layers and patterns, sometimes recognizable

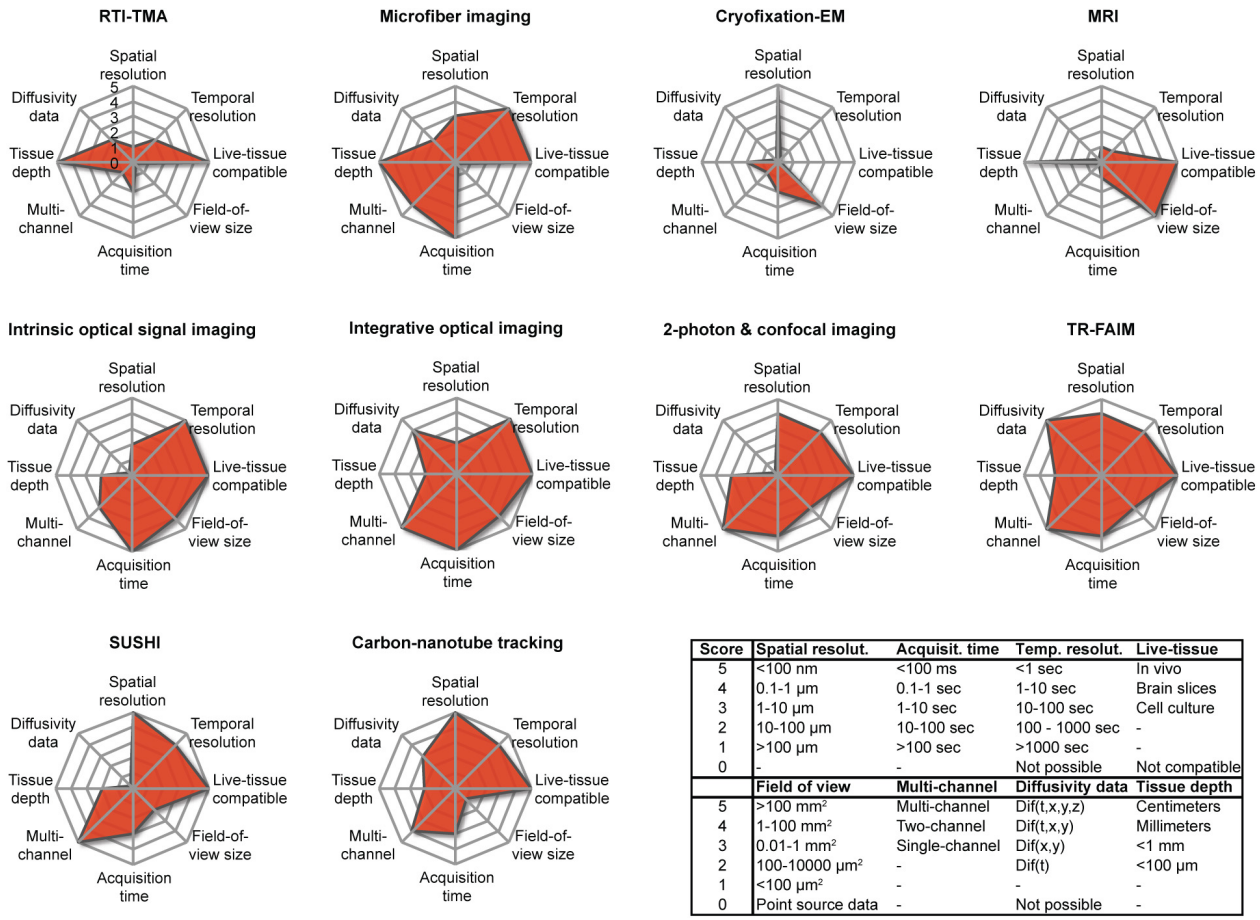

Score	Spatial resolut.	Acquisit. time	Temp. resolut.	Live-tissue
5	<100 nm	<100 ms	<1 sec	In vivo
4	0.1-1 μm	0.1-1 sec	1-10 sec	Brain slices
3	1-10 μm	1-10 sec	10-100 sec	Cell culture
2	10-100 μm	10-100 sec	100 - 1000 sec	-
1	>100 μm	>100 sec	>1000 sec	-
0	-	-	Not possible	Not compatible
	Field of view	**Multi-channel**	**Diffusivity data**	**Tissue depth**
5	>100 mm^2	Multi-channel	Dif(t,x,y,z)	Centimeters
4	1-100 mm^2	Two-channel	Dif(t,x,y)	Millimeters
3	0.01-1 mm^2	Single-channel	Dif(x,y)	<1 mm
2	100-10000 μm^2	-	Dif(t)	<100 μm
1	<100 μm^2	-	-	-
0	Point source data	-	Not possible	-

FIGURE 7 | Overview of the parameters associated with the described modalities for investigating the brain ECS, as scored by us according to the inserted table using an arbitrary scale from 0 to 5. Note that the graphs are representative only of the current situation and that the parameters of a given technique may change and improve as a result of technical developments. The individual scores must be seen as estimates.

even to the naked eye, as for the hippocampus and striatum. This provides a convenient map for researchers, enabling them to quickly navigate the macrostructures of the brain, and even more so if individual cells are made visible through routine fluorescent labeling to bring them out in images. This mapping is still lacking for the ECS, and we have no information about its putative regional patterning across the areas of the brain. In other words, there is no ECS map to complement the existing cellular maps and, similarly, no regional ECS structure–function relationships attributed to specific brain areas.

We have referred frequently to the glymphatic system in this review, and several prominent questions pertaining to this are unanswered. Among the most prominent ones is the extent of ISF or CSF flow in the brain and the importance of this for metabolite clearance. Flow in the perivasculature does not equate flow in dense parenchyma, and indeed, the presence and extent of ISF flow in the ECS is currently being debated. Furthermore, it remains unknown how the overall circadian volume change of the glymphatic system is manifested across brain areas that differ greatly in terms of cell density and composition and across dense neuropil where structural changes may be very different from those of the immediate perivascular spaces. It similarly remains unknown which cell types mediate ECS dynamics at any scale, diurnal and others.

In this context, the appearance of the new super-resolution microscopy modalities, SUSHI and carbon nanotube tracking, can be considered a battering ram being moved into position, one that will inevitably open up access to new knowledge beyond this frontier. These techniques are further well suited for the all-important investigation of ECS structure and dynamics with respect to the organization of extracellular matrix molecules, as well as with respect to the accumulation of aggregating toxic protein species, such as prominent α-synuclein in Parkinson's disease and β-amyloid plaques in Alzheimer's disease, as reviewed in Irvine et al. (2008). Needless to say, these should be applied along the well-proven existing techniques, which will contribute in reciprocal validation, and putatively new unexpected biological insights.

The stage is set for near future breakthroughs in the brain ECS field, which will seed new research lines in fundamental brain physiology, as well as further translational studies in neurodegenerative disorders and beyond.

AUTHOR CONTRIBUTIONS

All authors listed have made a substantial, direct and intellectual contribution to the work, and approved it for publication.

FUNDING

This work was supported by the grants from the Spanish Ministry for Research and Innovation SAF2017-83776-R and RYC-2014-15994 to JT, IJCI-2017-32114 to FS, University of the Basque Country grant GIU18/094 to OP and JT, and a Basque Government grant PIBA 2019-65 to JT.

ACKNOWLEDGMENTS

We would like to thank members of the labs of Dr. Sabina Hrabetova and Prof. Charles Nicholson for the critical appraisal of the manuscript.

REFERENCES

Abbott, N. J., Pizzo, M. E., Preston, J. E., Janigro, D., and Thorne, R. G. (2018). The role of brain barriers in fluid movement in the CNS: is there a 'glymphatic' system? *Acta Neuropathol.* 135, 387–407.

Agnati, L. F., Fuxe, K., Zoli, M., Ozini, I., Toffano, G., and Ferraguti, F. (1986). A correlation analysis of the regional distribution of central enkephalin and beta-endorphin immunoreactive terminals and of opiate receptors in adult and old male rats. Evidence for the existence of two main types of communication in the central nervous system: the volume transmission and the wiring transmission. *Acta Physiol. Scand.* 128, 201–207. doi: 10.1111/j.1748-1716.1986.tb07967.x

Agnati, L. F., Zoli, M., Strömberg, I., and Fuxe, K. (1995). Intercellular communication in the brain: wiring versus volume transmission. *Neuroscience* 69, 711–726.

Aitken, P. G., Fayuk, D., Somjen, G. G., and Turner, D. A. (1999). Use of intrinsic optical signals to monitor physiological changes in brain tissue slices. *Methods* 18, 91–103. doi: 10.1006/meth.1999.0762

Andrew, R. D., Jarvis, C. R., and Obeidat, A. S. (1999). Potential sources of intrinsic optical signals imaged in live brain slices. *Methods* 18, 185–196. doi: 10.1006/meth.1999.0771

Araque, A., Carmignoto, G., Haydon, P. G., Oliet, S. H. R., Robitaille, R., and Volterra, A. (2014). Gliotransmitters travel in time and space. *Neuron* 81, 728–739. doi: 10.1016/j.neuron.2014.02.007

Arranz, A. M., Perkins, K. L., Irie, F., Lewis, D. P., Hrabe, J., Xiao, F., et al. (2014). Hyaluronan deficiency due to Has3 knock-out causes altered neuronal activity and seizures via reduction in brain extracellular space. *J. Neurosci.* 34, 6164–6176. doi: 10.1523/JNEUROSCI.3458-13.2014

Azevedo, F. A. C., Carvalho, L. R. B., Grinberg, L. T., Farfel, J. M., Ferretti, R. E. L., Leite, R. E. P., et al. (2009). Equal numbers of neuronal and nonneuronal cells make the human brain an isometrically scaled-up primate brain. *J. Comp. Neurol.* 513, 532–541. doi: 10.1002/cne.21974

Bammer, R. (2003). Basic principles of diffusion-weighted imaging. *Eur. J. Radiol.* 45, 169–184.

Bethge, P., Chéreau, R., Avignone, E., Marsicano, G., and Nägerl, U. V. (2013). Two-photon excitation STED microscopy in two colors in acute brain slices. *Biophys. J.* 104, 778–785. doi: 10.1016/j.bpj.2012.12.054

Caravan, P., Ellison, J. J., McMurry, T. J., and Lauffer, R. B. (1999). Gadolinium(III) chelates as MRI contrast agents: structure, dynamics, and applications. *Chem. Rev.* 99, 2293–2352. doi: 10.1021/cr980440x

Charles, A., and Brennan, K. (2009). Cortical spreading depression—new insights and persistent questions. *Cephalalgia* 29, 1115–1124. doi: 10.1111/j.1468-2982.2009.01983.x

Clarke, L. E., and Barres, B. A. (2013). Emerging roles of astrocytes in neural circuit development. *Nat. Rev. Neurosci.* 14, 311–321. doi: 10.1038/nrn3484

Colbourn, R., Naik, A., and Hrabetova, S. (2019). ECS dynamism and its influence on neuronal excitability and seizures. *Neurochem. Res.* 44, 1020–1036. doi: 10.1007/s11064-019-02773-w

Dix, J. A., and Verkman, A. S. (1990). Mapping of fluorescence anisotropy in living cells by ratio imaging. Application to cytoplasmic viscosity. *Biophys. J.* 57, 231–240.

Eide, P. K., Vatnehol, S. A. S., Emblem, K. E., and Ringstad, G. (2018). Magnetic resonance imaging provides evidence of glymphatic drainage from human brain to cervical lymph nodes. *Sci. Rep.* 8:7194.

Foley, C. P., Nishimura, N., Neeves, K. B., Schaffer, C. B., and Olbricht, W. L. (2012). Real-time imaging of perivascular transport of nanoparticles during convection-enhanced delivery in the rat cortex. *Ann. Biomed. Eng.* 40, 292–303. doi: 10.1007/s10439-011-0440-0

Frostig, R. D., Masino, S. A., Kwon, M. C., and Chen, C. H. (1995). Using light to probe the brain: intrinsic signal optical imaging. *Int. J. Imaging Syst. Technol.* 6, 216–224. doi: 10.1002/ima.1850060212

Gakuba, C., Gaberel, T., Goursaud, S., Bourges, J., Di Palma, C., Quenault, A., et al. (2018). General anesthesia inhibits the activity of the "glymphatic system." *Theranostics* 8, 710–722. doi: 10.7150/thno.19154

Godin, A. G., Varela, J. A., Gao, Z., Danné, N., Dupuis, J. P., Lounis, B., et al. (2017). Single-nanotube tracking reveals the nanoscale organization of the extracellular space in the live brain. *Nat. Nanotechnol.* 12, 238–243. doi: 10.1038/nnano.2016.248

Grinvald, A., Lieke, E., Frostig, R. D., Gilbert, C. D., and Wiesel, T. N. (1986). Functional architecture of cortex revealed by optical imaging of intrinsic signals. *Nature* 324, 361–364. doi: 10.1038/324361a0

Han, H., Shi, C., Fu, Y., Zuo, L., Lee, K., He, Q., et al. (2014). A novel MRI tracer-based method for measuring water diffusion in the extracellular space of the rat brain. *IEEE J. Biomed. Health Inform.* 18, 978–983. doi: 10.1109/JBHI.2014.2308279

Hasegawa, Y., Latour, L. L., Formato, J. E., Sotak, C. H., and Fisher, M. (1995). Spreading waves of a reduced diffusion coefficient of water in normal and ischemic rat brain. *J. Cereb. Blood Flow Metab.* 15, 179–187. doi: 10.1038/jcbfm.1995.23

Holter, K. E., Kehlet, B., Devor, A., Sejnowski, T. J., Dale, A. M., Omholt, S. W., et al. (2017). Interstitial solute transport in 3D reconstructed neuropil occurs by diffusion rather than bulk flow. *Proc. Natl. Acad. Sci. U.S.A.* 114, 9894–9899. doi: 10.1073/pnas.1706942114

Holthoff, K., and Witte, O. W. (1996). Intrinsic optical signals in rat neocortical slices measured with near-infrared dark-field microscopy reveal changes in extracellular space. *J. Neurosci.* 16, 2740–2749.

Hrabe, J., and Hrabetova, S. (2019). Time-resolved integrative optical imaging of diffusion during spreading depression. *Biophys. J.* 117, 1783–1794. doi: 10.1016/j.bpj.2019.08.031

Hrabetova, S., Cognet, L., Rusakov, D. A., and Nägerl, U. V. (2018). Unveiling the extracellular space of the brain: from super-resolved microstructure to in vivo function. *J. Neurosci.* 38, 9355–9363. doi: 10.1523/JNEUROSCI.1664-18.2018

Iliff, J. J., Lee, H., Yu, M., Feng, T., Logan, J., Nedergaard, M., et al. (2013a). Brain-wide pathway for waste clearance captured by contrast-enhanced MRI. *J. Clin. Invest.* 123, 1299–1309. doi: 10.1172/JCI67677

Iliff, J. J., Wang, M., Zeppenfeld, D. M., Venkataraman, A., Plog, B. A., Liao, Y., et al. (2013b). Cerebral arterial pulsation drives paravascular CSF–interstitial fluid exchange in the murine brain. *J. Neurosci.* 33, 18190–18199. doi: 10.1523/JNEUROSCI.1592-13.2013

Iliff, J. J., Wang, M., Liao, Y., Plogg, B. A., Peng, W., Gundersen, G. A., et al. (2012). A paravascular pathway facilitates CSF flow through the brain parenchyma and the clearance of interstitial solutes, including amyloid β. *Sci. Transl. Med.* 4:147ra111. doi: 10.1126/scitranslmed.3003748

Irvine, G. B., El-Agnaf, O. M., Shankar, G. M., and Walsh, D. M. (2008). Protein aggregation in the brain: the molecular basis for Alzheimer's and Parkinson's diseases. *Mol. Med.* 14, 451–464. doi: 10.2119/2007-00100.Irvine

Kasthuri, N., Hayworth, K. J., Berger, D. R., Schalek, R. L., Conchello, J. A., Knowles-Barley, S., et al. (2015). Saturated reconstruction of a volume of neocortex. *Cell* 162, 648–661. doi: 10.1016/j.cell.2015.06.054

Kilb, W., Dierkes, P. W., Syková, E., Vargová, L., and Luhmann, H. J. (2006). Hypoosmolar conditions reduce extracellular volume fraction and enhance epileptiform activity in the CA3 region of the immature rat hippocampus. *J. Neurosci. Res.* 84, 119–129. doi: 10.1002/jnr.20871

Kitamura, K., Judkewitz, B., Kano, M., Denk, W., and Häusser, M. (2008). Targeted patch-clamp recordings and single-cell electroporation of unlabeled neurons in vivo. *Nat. Methods* 5, 61–67. doi: 10.1038/nmeth1150

Klar, T. A., Jakobs, S., Dyba, M., Egner, A., and Hell, S. W. (2000). Fluorescence microscopy with diffraction resolution barrier broken by stimulated emission. *Proc. Natl. Acad. Sci. U.S.A.* 97, 8206–8210. doi: 10.1073/pnas.97.15.8206

Korogod, N., Petersen, C. C. H., and Knott, G. W. (2015). Ultrastructural analysis of adult mouse neocortex comparing aldehyde perfusion with cryo fixation. *eLife* 4:e05793. doi: 10.7554/eLife.05793

Kroenke, C. D., Ackerman, J. J. H., and Neil, J. J. (2003). Magnetic resonance measurement of tetramethylammonium diffusion in rat brain: comparison of magnetic resonance and ionophoresis in vivo diffusion measurements. *Magn. Reson. Med.* 50, 717–726. doi: 10.1002/mrm.10579

Le Grimellec, C., Giocondi, M. C., Carriere, B., Carriere, S., and Cardinal, J. (1982). Membrane fluidity and enzyme activities in brush border and basolateral membranes of the dog kidney. *Am. J. Physiol.* 242, F246–F253. doi: 10.1152/ajprenal.1982.242.3.F246

Lenz, M. O., and Tønnesen, J. (2019). Considerations for imaging and analyzing neural structures by STED microscopy. *Methods Mol. Biol.* 1941, 29–46. doi: 10.1007/978-1-4939-9077-1_3

Lucić, V., Yang, T., Schweikert, G., Förster, F., and Baumeister, W. (2005). Morphological characterization of molecular complexes present in the synaptic cleft. *Structure* 13, 423–434. doi: 10.1016/j.str.2005.02.005

Lyall, A. E., Pasternak, O., Robinson, D. G., Newell, D., Trampush, J. W., Gallego, J. A., et al. (2018). Greater extracellular free-water in first-episode psychosis predicts better neurocognitive functioning. *Mol. Psychiatry* 23, 701–707. doi: 10.1038/mp.2017.43

MacVicar, B. A., Feighan, D., Brown, A., and Ransom, B. (2002). Intrinsic optical signals in the rat optic nerve: role for K(+) uptake via NKCC1 and swelling of astrocytes. *Glia* 37, 114–123. doi: 10.1002/glia.10023

MacVicar, B. A., and Hochman, D. (1991). Imaging of synaptically evoked intrinsic optical signals in hippocampal slices. *J. Neurosci.* 11, 1458–1469.

Magzoub, M., Zhang, H., Dix, J. A., and Verkman, A. S. (2009). Extracellular space volume measured by two-color pulsed dye infusion with microfiberoptic fluorescence photodetection. *Biophys. J.* 96, 2382–2390. doi: 10.1016/j.bpj.2008.12.3916

Mazel, T., Simonová, Z., and Syková, E. (1998). Diffusion heterogeneity and anisotropy in rat hippocampus. *Neuroreport* 9, 1299–1304.

McBain, C. J., Traynelis, S. F., and Dingledine, R. (1990). Regional variation of extracellular space in the hippocampus. *Science* 249, 674–677. doi: 10.1126/science.2382142

McKenna, M., Shackelford, D., Pontes, H. F., Ball, B., Gao, T., and Nance, E. (2020). Multiple particle tracking detects changes in brain extracellular matrix structure and predicts neurodevelopmental age. *biorxiv [Preprint]* doi: 10.1101/2020.04.20.050112

Mériaux, S., Conti, A., and Larrat, B. (2018). Assessing diffusion in the extracellular space of brain tissue by dynamic MRI mapping of contrast agent concentrations. *Front. Phys.* 6:38. doi: 10.3389/fphy.2018.00038

Mestre, H., Tithof, J., Du, T., Song, W., Peng, W., Sweeney, A. M., et al. (2018). Flow of cerebrospinal fluid is driven by arterial pulsations and is reduced in hypertension. *Nat. Commun.* 9:4878.

Mishchenko, Y., Hu, T., Spacek, J., Mendenhall, J., Harris, K. M., and Chklovskii, D. B. (2010). Ultrastructural analysis of hippocampal neuropil from the connectomics perspective. *Neuron* 67, 1009–1020. doi: 10.1016/j.neuron.2010.08.014

Newman, G. C., Hospod, F. E., Qi, H., and Patel, H. (1995). Effects of dextran on hippocampal brain slice water, extracellular space, calcium kinetics and histology. *J. Neurosci. Methods* 61, 33–46. doi: 10.1016/0165-0270(95)00020-U

Nicholson, C., and Hrabětová, S. (2017). Brain extracellular space: the final frontier of neuroscience. *Biophys. J.* 113, 2133–2142. doi: 10.1016/j.bpj.2017.06.052

Nicholson, C., and Phillips, J. M. (1981). Ion diffusion modified by tortuosity and volume fraction in the extracellular microenvironment of the rat cerebellum. *J. Physiol.* 321, 225–257. doi: 10.1113/jphysiol.1981.sp013981

Nicholson, C., and Tao, L. (1993). Hindered diffusion of high molecular weight compounds in brain extracellular microenvironment measured with integrative optical imaging. *Biophys. J.* 65, 2277–2290.

Norris, D. G. (2001). The effects of microscopic tissue parameters on the diffusion weighted magnetic resonance imaging experiment. *NMR Biomed.* 14, 77–93. doi: 10.1002/nbm.682

Odackal, J., Colbourn, R., Odackal, N. J., Tao, L., Nicholson, C., and Hrabetova, S. (2017). Real-time iontophoresis with tetramethylammonium to quantify volume fraction and tortuosity of brain extracellular space. *J. Vis. Exp.* 125:55755. doi: 10.3791/55755

Ofori, E., Pasternak, O., Planetta, P. J., Burciu, R., Snyder, A., Febo, M., et al. (2015). Increased free water in the substantia nigra of Parkinson's disease: a single-site and multi-site study. *Neurobiol. Aging* 36, 1097–1104. doi: 10.1016/j.neurobiolaging.2014.10.029

Ohno, N., Terada, N., Saitoh, S., and Ohno, S. (2007). Extracellular space in mouse cerebellar cortex revealed by in vivo cryotechnique. *J. Comp. Neurol.* 505, 292–301. doi: 10.1002/cne.21498

Osseforth, C., Moffitt, J. R., Schermelleh, L., and Michaelis, J. (2014). Simultaneous dual-color 3D STED microscopy. *Opt. Express* 22, 7028–7039. doi: 10.1364/OE.22.007028

Palombo, M., Shemesh, N., Ronen, I., and Valette, J. (2018). Insights into brain microstructure from in vivo DW-MRS. *Neuroimage* 182, 97–116. doi: 10.1016/j.neuroimage.2017.11.028

Paviolo, C., Soria, F. N., Ferreira, J. S., Lee, A., Groc, L., Bezard, E., et al. (2020). Nanoscale exploration of the extracellular space in the live brain by combining single carbon nanotube tracking and super-resolution imaging analysis. *Methods* 174, 91–99. doi: 10.1016/j.ymeth.2019.03.005

Planetta, P. J., Ofori, E., Pasternak, O., Burciu, R. G., Shukla, P., DeSimone, J. C., et al. (2016). Free-water imaging in Parkinson's disease and atypical Parkinsonism. *Brain* 139, 495–508. doi: 10.1093/brain/awv361

Ramon, Y., and Cajal, S. (1888). *Estructura de los Centros Nerviosos de las Aves. Revista Trimestral de Histología Normal y Patológica. Patológica Año 1*. Available online at: https://zaguan.unizar.es/record/4583 (accessed October 10, 2018).

Rice, M. E., Okada, Y. C., and Nicholson, C. (1993). Anisotropic and heterogeneous diffusion in the turtle cerebellum: implications for volume transmission. *J. Neurophysiol.* 70, 2035–2044. doi: 10.1152/jn.1993.70.5.2035

Runge, V. M., Aoki, S., Bradley, W. G., Chang, K.-H., Essig, M., Ma, L., et al. (2015). Magnetic resonance imaging and computed tomography of the brain-50 years of innovation, with a focus on the future. *Invest. Radiol.* 50, 551–556. doi: 10.1097/RLI.0000000000000170

Rusakov, D. A., and Kullmann, D. M. (1998). Extrasynaptic glutamate diffusion in the hippocampus: ultrastructural constraints, uptake, and receptor activation. *J. Neurosci.* 18, 3158–3170.

Rusakov, D. A., Saitow, F., Lehre, K. P., and Konishi, S. (2005). Modulation of presynaptic Ca2+ entry by AMPA receptors at individual GABAergic synapses in the cerebellum. *J. Neurosci.* 25, 4930–4940. doi: 10.1523/JNEUROSCI.0338-05.2005

Saghyan, A., Lewis, D. P., Hrabe, J., and Hrabetova, S. (2012). Extracellular diffusion in laminar brain structures exemplified by hippocampus. *J. Neurosci. Methods* 205, 110–118. doi: 10.1016/j.jneumeth.2011.12.008

Savtchenko, L. P., and Rusakov, D. A. (2005). Extracellular diffusivity determines contribution of high-versus low-affinity receptors to neural signaling. *Neuroimage* 25, 101–111. doi: 10.1016/j.neuroimage.2004.11.020

Schain, A. J., Melo-Carrillo, A., Strassman, A. M., and Burstein, R. (2017). Cortical spreading depression closes paravascular space and impairs glymphatic flow: implications for migraine headache. *J. Neurosci.* 37, 2904–2915. doi: 10.1523/JNEUROSCI.3390-16.2017

Sherpa, A. D., Xiao, F., Joseph, N., Aoki, C., and Hrabetova, S. (2016). Activation of β-adrenergic receptors in rat visual cortex expands astrocytic processes and reduces extracellular space volume. *Synapse* 70, 307–316. doi: 10.1002/syn.21908

Silva, M. D., Omae, T., Helmer, K. G., Li, F., Fisher, M., and Sotak, C. H. (2002). Separating changes in the intra- and extracellular water apparent diffusion coefficient following focal cerebral ischemia in the rat brain. *Magn. Reson. Med.* 48, 826–837. doi: 10.1002/mrm.10296

Soria, F. N., Paviolo, C., Doudnikoff, E., Arotcarena, M.-L., Lee, A., Danné, N., et al. (2020). Synucleinopathy alters nanoscale organization and diffusion in the brain extracellular space through hyaluronan remodeling. *Nat. Commun.* 11:3440.

Stowell, R. D., Sipe, G. O., Dawes, R. P., Batchelor, H. N., Lordy, K. A., Whitelaw, B. S., et al. (2019). Noradrenergic signaling in the wakeful state inhibits microglial surveillance and synaptic plasticity in the mouse visual cortex. *Nat. Neurosci.* 22, 1782–1792.

Stroh, M., Zipfel, W. R., Williams, R. M., Webb, W. W., and Saltzman, W. M. (2003). Diffusion of nerve growth factor in rat striatum as determined by multiphoton microscopy. *Biophys. J.* 85, 581–588.

Stucht, D., Danishad, K. A., Schulze, P., Godenschweger, F., Zaitsev, M., and Speck, O. (2015). Highest resolution in vivo human brain MRI using prospective motion correction. *PLoS One* 10:e0133921. doi: 10.1371/journal.pone.0133921

Studer, D., Humbel, B. M., and Chiquet, M. (2008). Electron microscopy of high pressure frozen samples: bridging the gap between cellular ultrastructure and atomic resolution. *Histochem. Cell Biol.* 130, 877–889.

Syková, E. (1997). The extracellular space in the CNS: its regulation, volume and geometry in normal and pathological neuronal function. *Neuroscientist* 3, 28–41. doi: 10.1177/107385849700300113

Syková, E., and Nicholson, C. (2008). Diffusion in brain extracellular space. *Physiol. Rev.* 88, 1277–1340. doi: 10.1152/physrev.00027.2007

Syková, E., Vargová, L., Kubinová, S., Jendelová, P., and Chvátal, A. (2003). The relationship between changes in intrinsic optical signals and cell swelling in rat spinal cord slices. *Neuroimage* 18, 214–230.

Syková, E., Voříšek, I., Antonova, T., Mazel, T., Meyer-Luehmann, M., Jucker, M., et al. (2005). Changes in extracellular space size and geometry in APP23 transgenic mice: a model of Alzheimer's disease. *Proc. Natl. Acad. Sci. U.S.A.* 102, 479–484. doi: 10.1073/pnas.0408235102

Takasaki, K. T., Ding, J. B., and Sabatini, B. L. (2013). Live-cell superresolution imaging by pulsed STED two-photon excitation microscopy. *Biophys. J.* 104, 770–777. doi: 10.1016/j.bpj.2012.12.053

Tao, L., Masri, D., Hrabetová, S., and Nicholson, C. (2002). Light scattering in rat neocortical slices differs during spreading depression and ischemia. *Brain Res.* 952, 290–300.

Thorne, R. G., and Nicholson, C. (2006). In vivo diffusion analysis with quantum dots and dextrans predicts the width of brain extracellular space. *Proc. Natl. Acad. Sci. U.S.A.* 103, 5567–5572. doi: 10.1073/pnas.0509425103

Tognarelli, J. M., Dawood, M., Shariff, M. I. F., Grover, V. P. B., Crossey, M. M. E., Cox, I. J., et al. (2015). Magnetic resonance spectroscopy: principles and techniques: lessons for clinicians. *J. Clin. Exp. Hepatol.* 5, 320–328. doi: 10.1016/j.jceh.2015.10.006

Tønnesen, J., Inavalli, V. V. G. K., and Nägerl, U. V. (2018). Super-resolution imaging of the extracellular space in living brain tissue. *Cell* 172, 1108–1121.e15. doi: 10.1016/j.cell.2018.02.007

Tønnesen, J., and Nagerl, U. V. (2013). Superresolution imaging for neuroscience. *Exp. Neurol.* 242, 33–40. doi: 10.1016/j.expneurol.2012.10.004

Tuozzo, C., Lyall, A. E., Pasternak, O., James, A. C. D., Crow, T. J., and Kubicki, M. (2018). Patients with chronic bipolar disorder exhibit widespread increases in extracellular free water. *Bipolar Disord.* 20, 523–530. doi: 10.1111/bdi.12588

van Rijnsoever, C., Oorschot, V., and Klumperman, J. (2008). Correlative light-electron microscopy (CLEM) combining live-cell imaging and immunolabeling of ultrathin cryosections. *Nat. Methods* 5, 973–980. doi: 10.1038/nmeth.1263

Vanharreveld, A., Crowell, J., and Malhotra, S. K. (1965). A study of extracellular space in central nervous tissue by freeze-substitution. *J. Cell Biol.* 25, 117–137. doi: 10.1083/jcb.25.1.117

Vorisek, I., Syka, M., and Vargova, L. (2017). Brain diffusivity and structural changes in the R6/2 mouse model of Huntington disease. *J. Neurosci. Res.* 95, 1474–1484. doi: 10.1002/jnr.23965

Vorísek, I., and Syková, E. (1997). Evolution of anisotropic diffusion in the developing rat corpus callosum. *J. Neurophysiol.* 78, 912–919. doi: 10.1152/jn.1997.78.2.912

Wang, M., Ding, F., Deng, S., Guo, X., Wang, W., Iliff, J. J., et al. (2017). Focal solute trapping and global glymphatic pathway impairment in a murine model of multiple microinfarcts. *J. Neurosci.* 37, 2870–2877. doi: 10.1523/JNEUROSCI.2112-16.2017

Xiao, F., Nicholson, C., Hrabe, J., and Hrabětová, S. (2008). Diffusion of flexible random-coil dextran polymers measured in anisotropic brain extracellular space by integrative optical imaging. *Biophys. J.* 95, 1382–1392. doi: 10.1529/biophysj.107.124743

Xie, L., Kang, H., Xu, Q., Chen, M. J., Liao, Y., Thiyagarajan, M., et al. (2013). Sleep drives metabolite clearance from the adult brain. *Science* 342, 373–377. doi: 10.1126/science.1241224

Yue, X., Mei, Y., Zhang, Y., Tong, Z., Cui, D., Yang, J., et al. (2019). New insight into Alzheimer's disease: light reverses Aβ-obstructed interstitial fluid flow and ameliorates memory decline in APP/PS1 mice. *Alzheimers Dement. Transl. Res. Clin. Interv.* 5, 671–684. doi: 10.1016/j.trci.2019.09.007

Zador, Z., Magzoub, M., Jin, S., Manley, G. T., Papadopoulos, M. C., and Verkman, A. S. (2008). Microfiberoptic fluorescence photobleaching reveals size-dependent macromolecule diffusion in extracellular space deep in brain. *FASEB J.* 22, 870–879. doi: 10.1096/fj.07-9468com

Zhang, H., and Verkman, A. S. (2010). Microfiberoptic measurement of extracellular space volume in brain and tumor slices based on fluorescent dye partitioning. *Biophys. J.* 99, 1284–1291. doi: 10.1016/j.bpj.2010.06.023

Zhao, G., Han, H., Yang, J., Sun, M., Cui, D., Li, Y., et al. (2020). Brain interstitial fluid drainage and extracellular space affected by inhalational isoflurane: in comparison with intravenous sedative dexmedetomidine and pentobarbital sodium. *Sci. China Life Sci.* 63, 1–17.

Zheng, K., Jensen, T. P., Savtchenko, L. P., Levitt, J. A., Suhling, K., and Rusakov, D. A. (2017). Nanoscale diffusion in the synaptic cleft and beyond measured with time-resolved fluorescence anisotropy imaging. *Sci. Rep.* 7:42022. doi: 10.1038/srep42022

Zuber, B., Nikonenko, I., Klauser, P., Muller, D., and Dubochet, J. (2005). The mammalian central nervous synaptic cleft contains a high density of periodically organized complexes. *Proc. Natl. Acad. Sci. U.S.A.* 102, 19192–19197. doi: 10.1073/pnas.0509527102

Conflict of Interest: The authors declare that the research was conducted in the absence of any commercial or financial relationships that could be construed as a potential conflict of interest.

Copyright © 2020 Soria, Miguelez, Peñagarikano and Tønnesen. This is an open-access article distributed under the terms of the Creative Commons Attribution License (CC BY). The use, distribution or reproduction in other forums is permitted, provided the original author(s) and the copyright owner(s) are credited and that the original publication in this journal is cited, in accordance with accepted academic practice. No use, distribution or reproduction is permitted which does not comply with these terms.

frontiers in Neuroscience

CASE REPORT
published: 21 October 2020
doi: 10.3389/fnins.2020.544802

The Application of MR Spectroscopy and MR Perfusion in Cerebral Syphilitic Gumma: A Case Report

*Linyang Cui, Jie Liu, Wenjun Zhang, Zushan Xu and Hongjun Hou**

Department of Radiology, Weihai Central Hospital, Weihai, China

Cerebral syphilitic gumma is a rare disease and can be misdiagnosed as a common brain tumor when only conventional imaging results are adopted. Differentiating between syphilitic gumma and tumors may be achieved by applying advanced magnetic resonance (MR) techniques, such as MR spectroscopy and MR perfusion. However, the MR perfusion characteristics of cerebral syphilitic gumma have not been reported yet. Here, we report a case of cerebral syphilitic gumma in a 52-year-old woman and discuss the imaging features of conventional MR, MR spectroscopy, and MR perfusion. The results suggest that the application of MR spectroscopy and MR perfusion could provide additional information that contributes to the diagnosis of cerebral syphilitic gumma.

Keywords: cerebral syphilitic gumma, brain tumor, magnetic resonance imaging, MR perfusion, MR spectroscopy cerebral syphilitic gumma

OPEN ACCESS

Edited by:
Alard Roebroeck,
Maastricht University, Netherlands

Reviewed by:
Salem Hannoun,
American University of Beirut, Lebanon
Dong-Hoon Lee,
Yonsei University, South Korea

***Correspondence:**
Hongjun Hou
houhj9899@163.com

Specialty section:
This article was submitted to Brain Imaging Methods, a section of the journal Frontiers in Neuroscience

Received: *26 March 2020*
Accepted: *22 September 2020*
Published: *21 October 2020*

Citation:
Cui L, Liu J, Zhang W, Xu Z and Hou H (2020) The Application of MR Spectroscopy and MR Perfusion in Cerebral Syphilitic Gumma: A Case Report. Front. Neurosci. 14:544802. doi: 10.3389/fnins.2020.544802

INTRODUCTION

Neurosyphilis is a chronic infection in the central nervous system caused by *Treponema pallidum*. Cerebral syphilitic gumma is a rare subtype of neurosyphilis disease and was first reported by Botalli in 1563 (Oblu, 1975). This disease is usually occult in onset, with headache, nausea, and vomiting as the most common clinical manifestations. The typical magnetic resonance (MR) imaging features of cerebral syphilitic gumma either are isolated or consist of multiple intracranial lesions growing from the meninges, with irregular enhancement and surrounding edema, which may closely resemble those of some brain tumors. Because of its rarity in the clinic and non-specific manifestations and findings on neuroimaging, cerebral syphilitic gumma is often misdiagnosed as brain neoplasm, which requires surgical treatment. Therefore, it is necessary to find ways to correctly diagnose syphilitic gumma before starting therapy, since patients with syphilis respond well to penicillin. In recent years, functional MRI techniques, such as MR spectroscopy and perfusion MRI have brought additional value to the differential diagnosis between tumors and non-tumor lesions. Previously, MR spectroscopy findings of cerebral gumma have been reported (Ventura et al., 2012) and seem to be helpful in generating a differential diagnosis. However, to date, there have been no studies that demonstrate the diagnostic utility of perfusion MRI in cerebral syphilitic gumma. In the current study, we are the first to report on the perfusion MRI features of cerebral syphilitic gumma. More importantly, we found that MR spectroscopy and perfusion MRI can help improve the specificity and capability of diagnosing cerebral syphilitic gumma under appropriate clinical circumstances.

CASE REPORT

A 52-year-old woman was admitted with intermittent headache lasting for 5 months. The patient's headache gradually worsened 1 week before admission, and vomiting occurred 2 days before hospitalization. Physical examination revealed normal findings. The patient had a history of hypertension and hyperlipidemia. No abnormality was found in the laboratory test results, which included blood routine examination, C-reactive protein, and erythrocyte sedimentation rate measurement. The serum tuberculosis antibody, toxoplasma antibody, and tumor markers were all negative. Serologic tests revealed positive results of the *T. pallidum* particle agglutination (TPPA) and toluidine red unheated serum test (TRUST), with a TRUST titer of 1:64. The human immunodeficiency virus (HIV) test was negative. Cerebrospinal fluid (CSF) examination was not performed. The patient denied any history related to venereal diseases, and the skin mucous membrane was free of rash and erythema. Conventional MR, proton MR spectroscopy, and perfusion MRI were carried out in the patient. All MR images were obtained using a 3.0 T clinical MR scanner (Discovery MR750, General Electric Healthcare, Milwaukee, WI, United States) with an eight-channel head coil. The conventional MRI sequences and parameters were as follows: axial T2-weighted imaging [repetition time (TR)/echo time (TE) = 5,200/90 ms, matrix = 512 × 512, field of view (FOV) = 24 cm, thickness = 5 mm, gap = 1.5 mm], axial T1-weighted imaging (TR/TE 1,750/25 ms, matrix = 320 × 256, FOV = 24 cm, thickness = 5 mm, gap = 1.5 mm), and diffusion-weighted imaging (TR/TE = 3,000/10 ms, matrix = 160 × 160, FOV = 24 cm, thickness = 5 mm, gap = 1.5 mm, b-value = 0, 1,000). Axial, sagittal, and coronal T1-weighted images after injection of gadolinium contrast agent (0.1 mmol/kg) were acquired. Perfusion imaging was performed by using a three-dimensional pseudo-continuous arterial spin labeling (ASL) technique with the specific imaging parameters: TR/TE = 4,600/10 ms, PLD = 1,525 ms, matrix = 128 × 128, FOV = 24 cm, thickness = 4 mm. ASL images were transferred to the workstation (ADW4.6, General Electric Healthcare) for post-processing and analyzed using FuncTool software (General Electric Healthcare) with the quantitative perfusion cerebral blood flow (CBF) map. Proton MR spectroscopy was obtained using a single-voxel point-resolved spectroscopy sequence (TR = 1,500 ms, TE = 35 ms). A volume of interest of 2 × 2 × 2 cm^3 was selected from the lesion identified on the T2-weighted imaging sequence, and saturation bands were placed around the voxel. The process of shimming and water suppression was completed by the automatic pre-scanning program, making the bandwidth <7 and water suppression >97%. The MR machine's individual configuration software was applied to complete the correction of the baseline, identification of each compound, and analysis of peak value and ratio of each compound. MRI (**Figures 1A–C**) revealed multiple nodules with evident perilesional edema in the right temporal lobe, which was characterized by hypointensity on T1-weighted images, mostly hyperintensity on T2-weighted images, and slight hyperintensity on diffusion-weighted imaging. Contrast-enhanced T1-weighted images (**Figures 1D–F**) showed significant enhancement of the nodules and adjacent meninges ("dural tail"). In addition, the right ventricle was compressed and the middle line structure was skewed to the left. Single-voxel MR spectroscopy with an echo time of 35 ms (**Figures 2A,B**) revealed a slightly increased choline (Cho) peak and a slight decrease in the peaks of creatine (Cr) and N-acetylaspartate (NAA). The Cho/Cr and Cho/NAA ratio over the lesion was 1.24 and 0.932, respectively. A peak rising between 0.9 and 1.3 ppm represented the lipid/lactate. Perfusion MRI (**Figure 2C**) suggested that regional CBF in the nodule area was lower than that of the contralateral normal regions, with the highest relative CBF value of 0.84 in the lesion area, while the edema area around the lesion presented less perfusion. Merely based on the clinical manifestations, laboratory results, and conventional MR images, the diagnosis of inflammatory granuloma should be first suspected, while a differential diagnosis including neoplastic lesions such as meningiomas and brain metastasis should also be considered. However, the findings of advanced techniques such as MR spectroscopy and MR perfusion provide more clues in diagnosing inflammatory granuloma and have effectively ruled out meningioma and brain metastasis. Considering the evident mass effect of the lesion, the patient underwent surgical resection of the nodules. During the surgery, multiple solid nodules were seen protruding from the dura of the temporal lobe into the adjacent cerebral cortex and had an unclear boundary, hard and brittle texture, and general blood supply. Severe edema in the brain tissue of the right temporal lobe was also observed. Post-operative pathology (**Figure 3**) revealed granulation tissue with ischemic necrosis surrounded by multinucleated giant cells, plasmacytes, and lymphocytes. Based on the above findings, the clinical diagnosis of cerebral syphilitic gumma was made. Penicillin treatment (18 million U/day) was given for 2 weeks after the operation, and the patient's symptoms were relieved gradually. On the seventh day post-op, the patient was examined with non-contrast computed tomography (CT). The post-op CT (**Figure 1G**) showed no nodules, and a certain amount of hypodense edematous zone could be found on the right temporal lobe. After 6 months, the patient's headache disappeared completely.

DISCUSSION

Since 2013, due to the AIDS epidemic and increase of the homosexual population and high-risk sexual behaviors, syphilis has made a comeback, affecting people of all ages and races (Puccio et al., 2019). Neurosyphilis accounts for 3.5% of syphilis cases with clinical or ophthalmologic manifestations (Ropper, 2019) and occurs mostly in untreated or undertreated patients. Neurosyphilis can occur during all stages of syphilis infection. According to the clinical manifestations, it can be divided into various forms, including asymptomatic, meningeal, meningovascular, parenchymal, and gummatous neurosyphilis. In 2016, Drago et al. (2016) reviewed 286 reported cases of neurosyphilis and found that the incidence of gumma was the lowest (3.5%) among all the subtypes. Cerebral

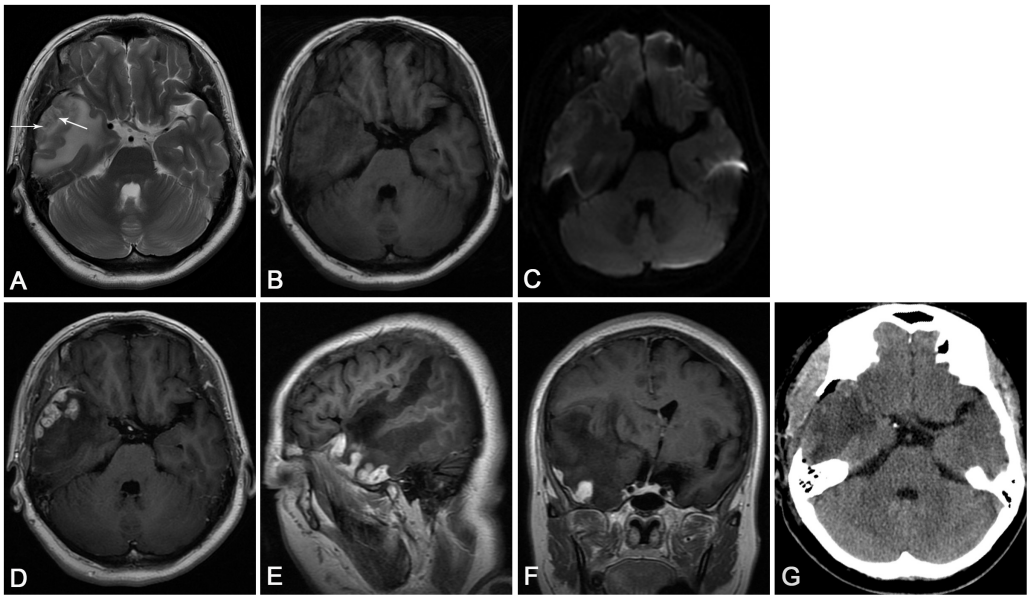

FIGURE 1 | (A) Axial T2-weighted imaging showed multiple heterogeneous hypersignal nodules with central spots of hyposignal (arrows) in the right temporal lobe and significant edema around the lesion. **(B)** Axial T1-weighted imaging revealed the heterogeneous hyposignal nodules. **(C)** Diffusion-weighted imaging revealed slight hyperintense nodules. **(D)** Axial and **(E)** sagittal T1-weighted images with contrast demonstrated the enhancing nodules arising from the meninges, with significant perilesional edema. **(F)** Coronal T1-weighted images with contrast showed the mass effect of the nodules, which led to the compression of the right lateral ventricle and evident midline shift. **(G)** Post-operative CT showed that no nodules with a certain amount of hypodense edematous zone could be found on the right temporal lobe.

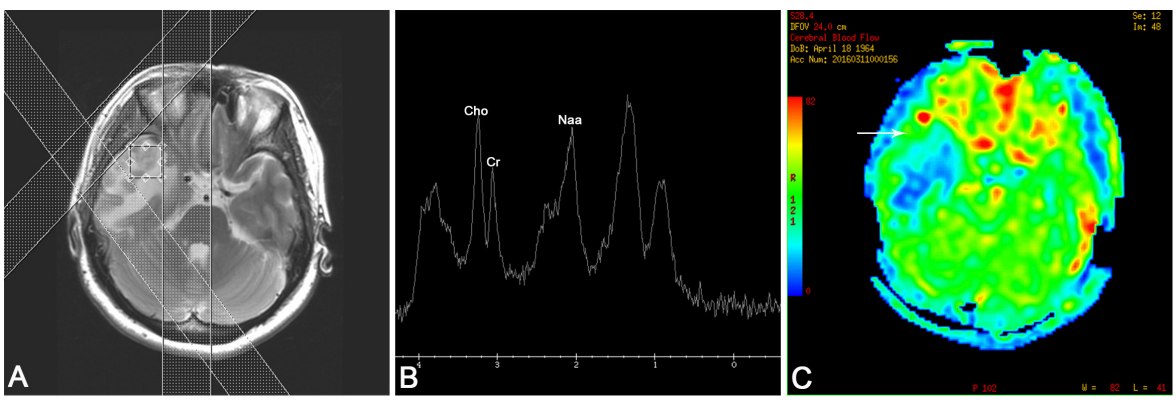

FIGURE 2 | (A) Positioning image of single-voxel magnetic resonance (MR) spectroscopy. **(B)** MR spectroscopy [echo time (TE) 35 ms] revealed a slightly increased choline (Cho) peak and a moderate decrease in the peaks of creatine (Cre) and N-acetylaspartate (NAA). A lipid/lactate peak was observed at 0.9 and 1.3 ppm. **(C)** MR perfusion reflected that the cerebral blood flow of the nodules (arrow) was lower than that of the contralateral hemisphere, and significant low perfusion was observed in the edema area.

syphilitic gumma is a benign proliferative lesion caused by the local meningovascular inflammatory response induced by *T. pallidum*, which generates a cell-mediated overreaction of the immune system. The pathological manifestation of syphilitic gumma is similar to that of tuberculosis, which includes inflammatory infiltration of a large number of lymphocytes and plasma cells and central caseous necrosis surrounded by epithelioid cells, multinucleated giant cells, and lymphocytes. Other major features include intimal hyperplasia and peripheral arterial inflammation.

Conventional MRI commonly reveals a single or multiple round mass located in the convex part of the hemisphere with varying degrees of edema. On T2-weighted images, the lesions were mostly displayed as hyperintense with the center having a low signal, while on T1-weighted images, the lesions were generally presented as a low signal, which showed annular enhancement under contrast conditions. The low signal on T2-weighted images indicates the caseous necrosis. In diffusion-weighted imaging, the non-caseating portion of the lesion presented a mildly elevated signal, which was probably due to the

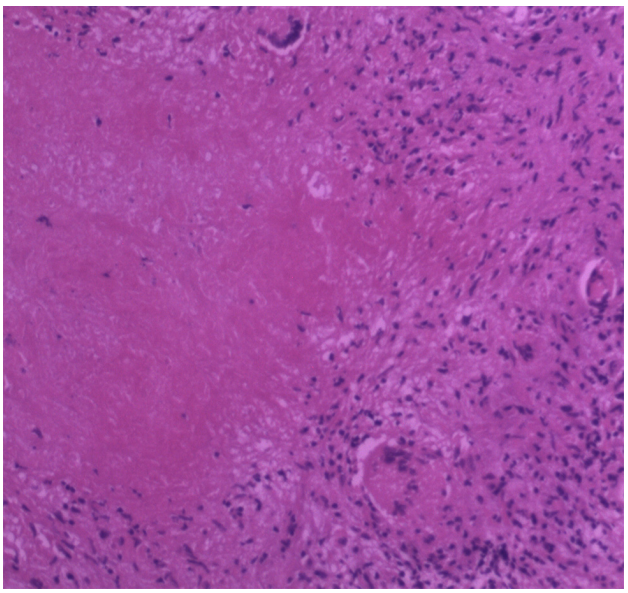

FIGURE 3 | Histopathology showed granulation tissue with ischemic necrosis surrounded by multinucleated giant cells, plasmacytes, and lymphocytes (HE staining, original magnification ×100).

cytotoxic edema of inflammatory cells (Soares-Fernandes et al., 2007). Perilesional meningeal enhancement and thickening or a dural tail can be found in 35% of the cerebral syphilitic gumma cases (Fargen et al., 2009), while calcification or hemorrhage may occur in only a few cases. In our case, several typical imaging characteristics of syphilitic gumma were found in the multiple nodules in the right temporal cortex. The nodules showed a low signal on T1-weighted images, heterogeneous high signal on T2-weighted images, and mild hyperintensity on diffusion-weighted imaging, with enhanced presentation and enormous edema in the surrounding area under the contrast condition. Low signal foci on T2-weighted images and the characteristic "dural tail" were also seen. However, it was still difficult to differentiate between the diagnosis of cerebral syphilitic gumma and intracranial neoplasias due to the lack of specific MR characteristics. In clinical practice, cerebral syphilitic gumma is most commonly misdiagnosed as high-grade gliomas, metastatic tumors, or meningiomas, which leads to subsequent surgeries in the patients (Noel et al., 2011; Xia et al., 2017; Zhang et al., 2017; Li et al., 2019; Weng et al., 2019).

Advanced MRI techniques, such as MR spectroscopy and perfusion MRI, can greatly contribute to the differential diagnosis of neoplastic and non-neoplastic lesions by providing functional information. MR spectroscopy can reflect the change in cerebral metabolism and biochemistry from an objective perspective, including neuronal injury, membrane phospholipid metabolism, lipid storage, and energy and oxidative metabolism. High-grade glioma, metastatic tumor, and meningioma often exhibit prominent elevation of Cho and significantly decreased levels or even lack of Cr and NAA, while non-neoplastic lesions generally present slightly decreased levels of Cho, Cr, and NAA (Möller-Hartmann et al., 2002). The most frequently used chemical ratios to differentiate tumors from non-neoplastic diseases with MR spectroscopy are Cho/Cr and Cho/NAA (Callot et al., 2008), though there is little consensus in the literature regarding the actual integral value of Cho/Cr and Cho/NAA ratios. In general, a Cho/NAA ratio greater than 1 is considered to indicate a neoplasm (Callot et al., 2008). However, in a previous report, a Cho/Cr ratio of 1.97 or greater could indicate high sensitivity and specificity in differentiating between inflammatory lesions and tumors (Ferraz-Filho et al., 2009). Furthermore, the Cho/Cr and Cho/NAA ratios are higher in neoplastic diseases such as high-grade glioma, metastatic tumor, and meningioma. Perfusion MRI is an emerging technique that provides tissue hemodynamic results. ASL is a non-invasive perfusion imaging technique that has rapidly developed in clinical practice and can quantitatively detect the CBF by labeling the arterial blood as an inner tracer, thus obviating exogenous contrast. Previous research that explored the application of ASL in the evaluation of the flow perfusion of cerebral tumors indicated a high CBF value in high-grade gliomas, metastatic tumors, and meningiomas, which was speculated to be due to tumor angiogenesis (Soni et al., 2018; Huang et al., 2019). However, a few reports that focused on the perfusion MRI characteristics among infection cases indicated that, except for herpes simplex virus infection, the vast majority presented low perfusion due to lack of angiogenesis (Noguchi et al., 2016). In imaging with addition of contrast agents, the infection showed significant enhancement because of the destruction of the blood–brain barrier rather than an increase in blood supply. The MR spectroscopic findings in our case showed a mild increase in Cho as well as slight decreased Cr and NAA (Cho/Cr = 1.24; Cho/NAA = 0.932), which was similar to the observation in a previously published case report of intracranial syphilitic gumma (Ventura et al., 2012). In addition, the focal MR perfusion of the lesion in our case had a lower CBF compared to the contralateral normal brain tissue. The above functional MR results may contribute to the exclusion of common intracranial neoplasia, such as high-grade glioma, metastatic tumors, and meningioma in the differential diagnosis, thus further confirming the diagnosis of syphilitic gumma based on serologic tests and conventional MR findings. To our knowledge, this is the first report evaluating the perfusion MRI characteristics of cerebral syphilitic gumma.

Surgery should not be performed in cerebral syphilitic gumma patients without significant intracranial hypertension or progressive exacerbation of symptoms, while the intravenous administration of penicillin G for 2 weeks (18–24 million U/day) is recommended as treatment according to international guidelines.

It is generally accepted that the diagnosis of cerebral syphilitic gumma should be made based on the patient history, clinical manifestations, laboratory tests, and MRI results. However, non-specific symptoms and the inability of the patient to provide a medical history or concealing it may hamper diagnostic accuracy. Syphilis serology and CSF tests (e.g., TPPA, TRUST) are critical

to the diagnosis. Although conventional MRI can provide clues for the diagnosis of cerebral syphilitic gumma based on certain characteristics, it is often misdiagnosed as high-grade glioma, metastatic tumors, and meningioma due to the lack of specific imaging features, which can be complemented by advanced MRI techniques. Combined application of conventional and advanced MRI and laboratory tests could increase the accuracy of the preoperative diagnosis of cerebral syphilitic gumma, thus avoiding unnecessary surgeries.

ETHICS STATEMENT

Written informed consent was obtained from the individual for the publication of this case report, including any potentially identifiable images or data included in this article.

AUTHOR CONTRIBUTIONS

LC wrote the manuscript. WZ and ZX collected the patient's materials. HH and JL guided the completion of this article. All authors contributed to the article and approved the submitted version.

ACKNOWLEDGMENTS

We thank the patient and her family for their collaboration.

REFERENCES

Callot, V., Galanaud, D., Le Fur, Y., Confort-Gouny, S., Ranjeva, J. P., and Cozzone, P. J. (2008). (1)H MR spectroscopy of human brain tumours: a practical approach. *Eur. J. Radiol.* 67, 268–274. doi: 10.1016/j.ejrad.2008.02.036

Drago, F., Merlo, G., Ciccarese, G., Agnoletti, A. F., Cozzani, E., Rebora, A., et al. (2016). Changes in neurosyphilis presentation: a survey on 286 patients. *J. Eur. Acad. Dermatol. Venereol.* 30, 1886–1900. doi: 10.1111/jdv.13753

Fargen, K. M., Alvernia, J. E., Lin, C. S., and Melgar, M. (2009). Cerebral syphilitic gummata: a case presentation and analysis of 156 reported cases. *Neurosurgery* 64, 568–576. doi: 10.1227/01.NEU.0000337079.12137.89

Ferraz-Filho, J. R., Santana-Netto, P. V., Rocha-Filho, J. A., Sgnolf, A., Mauad, F., and Sanches, R. A. (2009). Application of magnetic resonance spectroscopy in the differentiation of high-grade brain neoplasm and inflammatory brain lesions. *Arq. Neuropsiquiatr.* 67, 250–253. doi: 10.1590/s0004-282x2009000200014

Huang, R. Y., Bi, W. L., Griffith, B., Kaufmann, T. J., Fougère, C., Schmidt, N., et al. (2019). Imaging and diagnostic advances for intracranial meningiomas. *Neuro Oncol.* 21(Suppl._1), i44–i61. doi: 10.1093/neuonc/noy143

Li, C., Wang, S. J., Tang, G. C., Liu, L. T., and Chen, G. X. (2019). Neuroimaging findings of cerebral syphilitic gumma. *Exp. Ther. Med.* 18, 4185–4192. doi: 10.3892/etm.2019.8089

Möller-Hartmann, W., Herminghaus, S., Krings, T., Marquardt, G., Lanfermann, H., Pilatus, U., et al. (2002). Clinical application of proton magnetic resonance spectroscopy in the diagnosis of intracranial mass lesions. *Neuroradiology* 44, 371–381. doi: 10.1007/s00234-001-0760-0

Noel, C. B., Moeketsi, K., and Kies, B. (2011). Cavernous sinus syndrome, an atypical presentation of tertiary syphilis: case report and review of the literature. *Clin. Neurol. Neurosurg.* 113, 65–67. doi: 10.1016/j.clineuro.2010.08.007

Noguchi, T., Yakushiji, Y., Nishihara, M., Togao, O., Yamashita, K., Kikuchi, K., et al. (2016). Arterial spin-labeling in central nervous system infection. *Magn. Reson. Med. Sci.* 15, 386–394. doi: 10.2463/mrms.mp.2015-0140

Oblu, N. (1975). "Gumma of the brain," in *Handbook of Clinical Neurology [M]*, eds P. J. Vinken and G. W. Bruyn (New York, NY: Elsevier), 427–434.

Puccio, J. A., Cannon, A., Derasari, K., and Friend, R. (2019). Resurgence of syphilis. *Adv. Pediatr.* 66, 231–244. doi: 10.1016/j.yapd.2019.03.006

Ropper, A. H. (2019). Neurosyphilis. *N. Engl. J. Med.* 381, 1358–1363. doi: 10.1056/NEJMra1906228

Soares-Fernandes, J. P., Ribeiro, M., Maré, R., Magalhães, Z., Lourenço, E., and Rocha, J. F. (2007). Diffusion-weighted magnetic resonance imaging findings in a patient with cerebral syphilitic gumma. *J. Comput. Assist. Tomogr.* 31, 592–594. doi: 10.1097/01.rct.0000284391.91320.89

Soni, N., Srindharan, K., Kumar, S., Mishra, P., Bathla, G., Kalita, J., et al. (2018). Arterial spin labeling perfusion: prospective MR imaging in differentiating neoplastic from non-neoplastic intra-axial brain lesions. *Neuroradiol. J.* 31, 544–553. doi: 10.1177/1971400918783058

Ventura, N., Cannelas, R., Bizzo, B., and Gasparetto, E. L. (2012). Intracranial syphilitic gumma mimicking a brain stem glioma. *AJNR Am. J. Neuroradiol.* 33, E110–E111. doi: 10.3174/ajnr.A3236

Weng, C., Huang, K., Jiang, T., Zhou, G., and Wu, T. (2019). Cerebral syphilitic gumma masquerading as cerebral metastatic tumors: case report. *Neurosurg. Focus* 47:E15. doi: 10.3171/2019.5.FOCUS1953

Xia, D. Y., Zhu, M. F., Liu, C. G., Dai, Y., Li, Z. B., Jiang, X. C., et al. (2017). Cerebral syphilitic gumma misdiagnosed as a malignant brain tumor. *J. Craniofac. Surg.* 28, e170–e172. doi: 10.1097/SCS.0000000000003191

Zhang, L. L., Zhou, Y. L., Chen, J., Yan, W. L., Kong, Q. T., Chen, P., et al. (2017). A case of a cerebral syphilitic gumma developed in a few months mimicking a brain tumor in a human immunodeficiency virus-negative patient. *Br. J. Neurosurg.* 31, 481–483. doi: 10.3109/02688697.2016.1173190

Conflict of Interest: The authors declare that the research was conducted in the absence of any commercial or financial relationships that could be construed as a potential conflict of interest.

Copyright © 2020 Cui, Liu, Zhang, Xu and Hou. This is an open-access article distributed under the terms of the Creative Commons Attribution License (CC BY). The use, distribution or reproduction in other forums is permitted, provided the original author(s) and the copyright owner(s) are credited and that the original publication in this journal is cited, in accordance with accepted academic practice. No use, distribution or reproduction is permitted which does not comply with these terms.

frontiers in Neuroscience

REVIEW
published: 23 October 2020
doi: 10.3389/fnins.2020.569517

Dissecting Neuronal Activation on a Brain-Wide Scale With Immediate Early Genes

*Alessandra Franceschini[1], Irene Costantini[1,2], Francesco S. Pavone[1,2,3] and Ludovico Silvestri[1,2,3]**

[1] European Laboratory for Non-linear Spectroscopy (LENS), Sesto Fiorentino, Italy, [2] National Institute of Optics, National Research Council (INO-CNR), Sesto Fiorentino, Italy, [3] Department of Physics and Astronomy, University of Florence, Florence, Italy

Visualizing neuronal activation on a brain-wide scale yet with cellular resolution is a fundamental technical challenge for neuroscience. This would enable analyzing how different neuronal circuits are disrupted in pathology and how they could be rescued by pharmacological treatments. Although this goal would have appeared visionary a decade ago, recent technological advances make it eventually feasible. Here, we review the latest developments in the fields of genetics, sample preparation, imaging, and image analysis that could be combined to afford whole-brain cell-resolution activation mapping. We show how the different biochemical and optical methods have been coupled to study neuronal circuits at different spatial and temporal scales, and with cell-type specificity. The inventory of techniques presented here could be useful to find the tools best suited for a specific experiment. We envision that in the next years, mapping of neuronal activation could become routine in many laboratories, allowing dissecting the neuronal counterpart of behavior.

Keywords: immediate early genes, tissue clearing, light-sheet microscopy, high-throughput microscopy, image analysis, whole-brain mapping

OPEN ACCESS

Edited by:
Alard Roebroeck, Maastricht University, Netherlands

Reviewed by:
Matthew ManHin Cheung, CUHK Medical Centre, Hong Kong
Lana Vasung, Harvard Medical School, United States

****Correspondence:***
Ludovico Silvestri
silvestri@lens.unifi.it

Specialty section:
This article was submitted to Brain Imaging Methods, a section of the journal Frontiers in Neuroscience

Received: *04 June 2020*
Accepted: *28 September 2020*
Published: *23 October 2020*

Citation:
Franceschini A, Costantini I, Pavone FS and Silvestri L (2020) Dissecting Neuronal Activation on a Brain-Wide Scale With Immediate Early Genes. Front. Neurosci. 14:569517. doi: 10.3389/fnins.2020.569517

INTRODUCTION

The most direct readout of brain activity is behavior. Although there is a consensus about the fact that our actions are a result of the coordinated activity of our neurons, the causal links between these two phenomena are still largely unknown. Understanding how neuronal networks in the brain drive specific behaviors, and how these networks change with experience is thus a fundamental challenge of neuroscience. In addition, a deeper insight into the connection between brain activity and behavior would also shed light on the mechanisms that disrupt this link in pathology, laying the basis for better treatment of mental diseases.

From a methodological point of view, understanding this connection requires techniques for whole-brain mapping. Indeed, neuronal activation patterns should be studied on the same scale of the structural organization of neuronal networks, i.e., brain-wide. One would ideally need some methods to record *electrical activity simultaneously* from *all* the neurons in the brain of a *freely behaving subject*, with *single-cell resolution*. It is immediately apparent that no technique with such capabilities exists, and even if we relax, some of the requirements in italics, whole-brain mapping still sounds like a formidable task for state-of-the-art technologies. Traditional functional

imaging methods used to reveal large-scale neuronal activity, like functional magnetic resonance imaging (fMRI) or electroencephalography (EEG), lack the proper spatial resolution to record single-cell activity (Logothetis, 2008; Michel and Brunet, 2019). On the other hand, single-cell electrophysiology cannot scale to more than a handful of neurons (Perin and Markram, 2013).

Over the last decade, *in vivo* optical methods have demonstrated the ability to work across different scales (Carrillo-Reid et al., 2017; Yang and Yuste, 2017; Sancataldo et al., 2019), allowing registration of membrane potential or of intracellular calcium in hundreds or even thousands of neurons simultaneously (Ahrens et al., 2013; Prevedel et al., 2014; Nöbauer et al., 2017). However, these techniques still suffer several limitations:

1. There is a practical trade-off between spatial resolution and field of view (FOV). For instance, calcium imaging of the entire mouse cortex can be achieved only at coarse resolution (Vanni et al., 2017), while single-cell recordings are limited to a smaller spatial area (Prevedel et al., 2014).
2. Light scattering by nervous tissue limits imaging penetration to less than an mm (Helmchen and Denk, 2005). Thus, in rodents, *in vivo* optical imaging is limited to the cortex [unless endoscopic approaches are used (Dombeck et al., 2010)]. Whole-brain imaging has been achieved hitherto only in small organisms like the nematode *Caenorhabditis elegans* or the larva of *Danio Rerio* (zebrafish) (Ahrens et al., 2013; Prevedel et al., 2014).
3. Optical microscopes are usually quite sophisticated and heavy, and thus hardly compatible with freely behaving animals. Simpler systems—with poor resolution—can be used on mice moving freely in their cage (Aharoni et al., 2019). However, when single-cell resolution is sought, the only acceptable compromise is to place a head-fixed animal in a virtual reality environment (Dombeck et al., 2010).

To circumvent these constraints, a radical solution is to tag activated neurons *in vivo* and image them subsequently *ex vivo* (**Figures 1A,B**). Fixed murine brains can be cleared and labeled using many different protocols (**Figure 1C**). Afterward, a comprehensive yet high-resolution reconstruction of these samples can be obtained using the latest developments in *ex vivo* microscopy (**Figure 1D**). Finally, quantitative data can be extracted from raw images using state-of-the-art algorithms (**Figure 1E**). These inherent advantages have been exploited to quantify brain-wide neuronal activation by targeting neurons expressing immediate early genes (IEGs). These genes are expressed by neurons under sustained activation (Bartel et al., 1989) and are considered a reliable proxy for activity. Indeed, IEG quantification is a classical method to study neuronal activation in selected brain areas (Morgan et al., 1987; Sagar et al., 1988).

Ex vivo whole-brain mapping of IEGs eventually allows to *map activated neurons* across *the entire brain* of a *freely behaving subject*, with *single-cell resolution*. In the end, this is not too far from the original challenge we issued a few lines before.

In the following, we review the latest technological developments concurring to map and manipulate activated neurons across the entire mouse brain. This ambitious goal is today possible by combining advancements from multiple fields, including genetics, tissue preparation, optical imaging, and image analysis. The purpose of our review is to guide the reader into this multidisciplinary research, offering the tools to choose the techniques that are best suited for a specific application. For detailed recapitulation of the single topics, we refer to excellent reviews that have been published in the last years (Mayford and Reijmers, 2016; Peng et al., 2016; Sbalzarini, 2016; Tainaka et al., 2016; DeNardo and Luo, 2017; Power and Huisken, 2017; He et al., 2019; Ueda et al., 2020).

TAGGING NEURON ACTIVATION FOLLOWING SENSORY AND BEHAVIORAL STIMULI

The first step to map activated neurons across the whole brain is to tag them with a label allowing visualization through an optical microscope. Different methods have been proposed during the years, ranging from classical immunohistochemistry to sophisticated transgenic or viral approaches. All these different techniques share a common principle: the use of immediate early genes (IEGs). In this section, we first recall the basic features of IEGs and then describe in detail the various methods that could be used to tag neurons according to the expression of one of these genes.

IEG-Based Approaches as Useful Tools to Access Activated Neurons

Nowadays, the discovery of IEGs has enabled us to reconstruct functional maps with single-cell resolution. IEGs, such as *c-fos*, *Arc*, and *Egr1* (also known as *ZiF268),* are a class of genes that is activated transiently and rapidly in response to a wide variety of cellular stimuli (Hunt et al., 1988; Sagar et al., 1988; Kaczmarek and Nikolajew, 1990; Hughes et al., 1992; Pinaud, 2004; Terleph and Tremere, 2006; Bahrami and Drabløs, 2016). At the brain level, the expression of all IEGs is induced by neuronal activity through depolarization (Greenberg et al., 1986; Morgan et al., 1987; Bartel et al., 1989; Sheng and Greenberg, 1990; Smeyne et al., 1992). In this way, the rise of intracellular Ca^{2+} levels activates second messenger pathways that, in turn, stimulate transcriptional factors. Within few minutes, these factors trigger the expression of the relative genes. For that reason, for a long time, they have been used as an indirect marker to measure neuronal activity. In addition to their rapid induction, IEG proteins have a relatively short life due to their fast transcription that is interrupted with the end of external stimulation. Thus, in a few hours, the expression levels of these proteins return to their baseline (Sheng and Greenberg, 1990).

These genes respond to a wide variety of intrinsic and extrinsic stimuli, including growth factors, high intracellular levels of Ca^{2+}, and cAMP, strong depolarization, receptors activating, and neurotransmitters, indicating a very general response mechanism

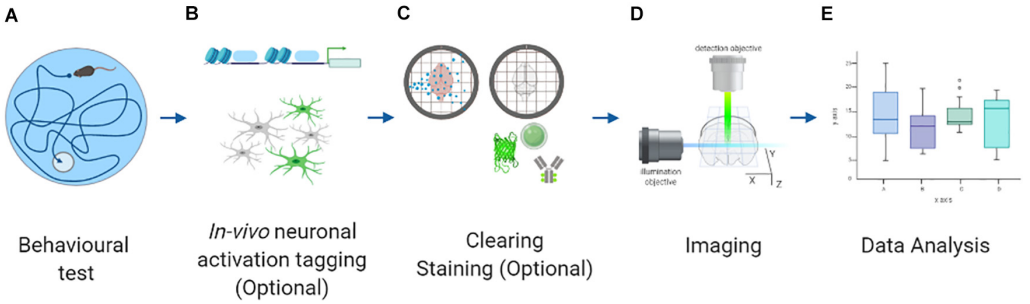

FIGURE 1 | Scheme representing the different steps to perform whole-brain neuronal activation mapping. **(A)** Behavioral testing. **(B)** *In vivo* neuronal activation tagging with endogenous fluorescence proteins. **(C)** Sample preparation protocol: clearing and staining (optional, when the tagging is not performed). **(D)** Imaging with advanced fluorescence microscopy. **(E)** Data analysis with different algorithms. Created with BioRender.com.

(Bartel et al., 1989; Sheng and Greenberg, 1990; Ghosh et al., 1994; Fowler et al., 2011). Regulation of gene transcription varies according to the type of gene and brain region (Sheng and Greenberg, 1990; Mayford and Reijmers, 2016). For example, growth factors and membrane depolarization activate distinct programs of early response gene expression (Bartel et al., 1989). Cole et al. (1989) found that a rapid increase in IEGs due to neuronal stimulation has a critical role in long-term change in synaptic efficiency. They proved that *in vivo* stimulation of DG hippocampal cells with electrodes was sufficient to produce long-term potentiation (LTP), causing the induction only of Egr1, while c-fos needed more prolonged stimulation (Cole et al., 1989; Sheng and Greenberg, 1990). In both cases, the IEG activation was correlated to the elevated presence of NMDA receptors (Morgan et al., 1987; Sheng and Greenberg, 1990).

Starting from these characteristic features of IEGs, a series of IEG-based tools have been developed either in the form of transgenic mice or viral vectors (Reijmers et al., 2007; Guenthner et al., 2013; Kawashima et al., 2013; Sakurai et al., 2016; Sørensen et al., 2016; DeNardo et al., 2019; Hasan et al., 2019). These genetic approaches have been developed to translate neuronal activity into gene expression by making possible the visualization of behavioral-relevant cells and also the access to the same neurons in living animals or *ex vivo* tissue slices. Most of these strategies pave the way to cell manipulation with chemogenetic or optogenetic tools, giving to researchers the possibility to activate, inactivate, and record neuronal activity using electrophysiology or genetically encoded calcium indicators (Barth et al., 2004; Wang et al., 2006).

Before describing in detail the mechanisms, advantages, and disadvantages of each genetic approach, it is worth adding a few general considerations. IEG transcripts or proteins are present in neurons for a limited time after the stimulus that elicited the activity of a specific brain circuit. Therefore, any protocol aimed at mapping the presence of IEGs must be performed within a limited time window after the behavioral test. If proteins or transcripts have to be mapped directly, e.g., with immunohistochemistry (IHC), this means that the animal must be sacrificed after the stimulus, preventing further behavioral tests. The limitation of IHC is related to IEG kinetics because its peak expression and the return to baseline are very rapid (Morgan et al., 1987). Genetic approaches, driving recombination in the presence of IEGs, have been developed to overcome this limitation allowing access to activated cells for a period much longer than the IEG timescale, even 1 month later (DeNardo et al., 2019).

The time window of IEG expression also defines the maximum temporal resolution of the method, i.e., the capability to distinguish neurons activated by the stimulus of interest from those activated by subsequent or previous stimuli. When using transgenic or viral strategies in combination with some drug, the pharmacokinetics of the drug itself must also be taken into account, as it will often extend the time window beyond the natural half-life of IEG proteins (Sheng and Greenberg, 1990; Reijmers et al., 2007; Guenthner et al., 2013). For instance, Cre-based recombination systems isolates activated cells with a time resolution similar to that of endogenous IEG expression (few hours) (DeNardo et al., 2019), while in some approaches based on Tet-tag, the half-life of the drug determines a time window of few days (Reijmers et al., 2007). This loss of temporal resolution leads to the labeling of more neurons than those activated in the behavior of interest. These "false positives," usually referred to as "background," effectively reduce the capability of the method to find statistically significant variations in the number of activated neurons between different areas or subjects.

On the contrary, "false negatives" can appear when the method fails either to tag-activated cells or to maintain labeling after the recombination event (as in the case of genetic methods). In both cases, a fraction of IEG-positive neurons is missing, again reducing statistical power. The main reasons for the insufficient labeling of activated cells are limited efficiency of the recombination mechanisms in selected cell types or also the limited penetration of exogenous dyes (e.g., in IHC).

Here below, we describe in detail the existing methods able to tag activated neurons, providing useful information for researchers. **Figure 2** summarizes them with schematic illustrations, while **Table 1** recapitulates the main features of each method.

Immunohistochemistry

The immunohistochemical staining has been considered the "gold standard" for the reconstruction of whole-brain activity

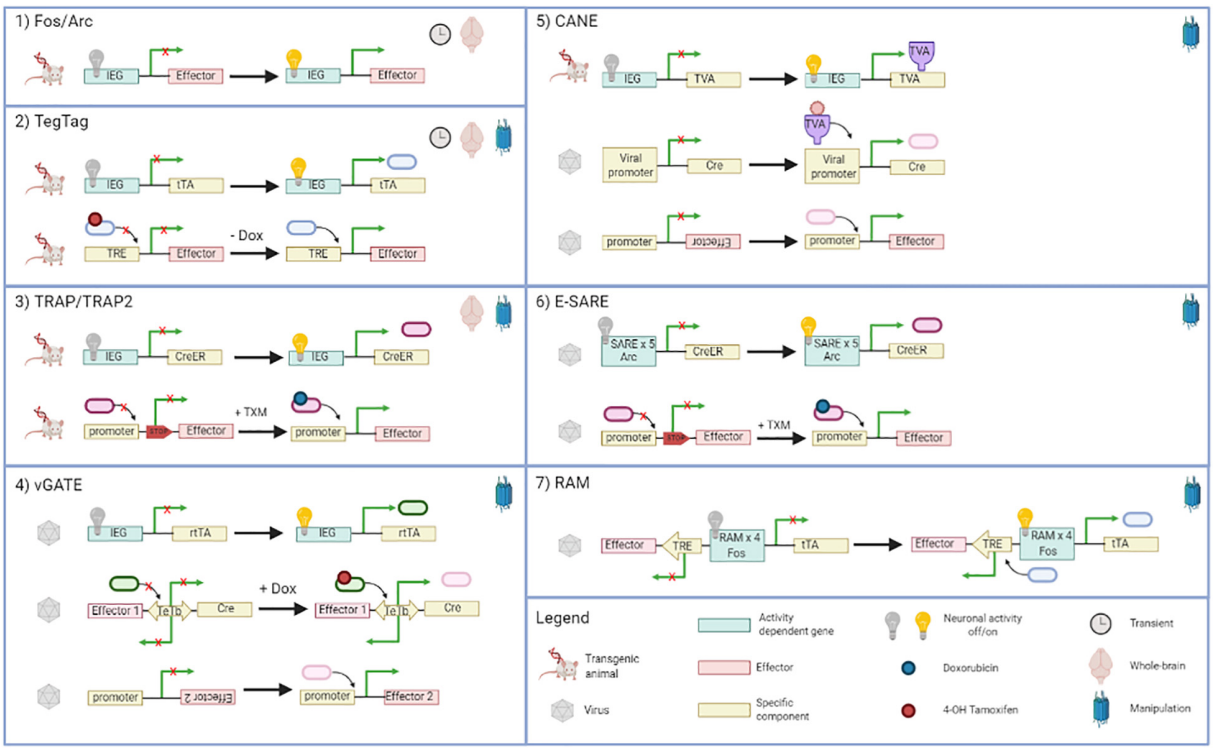

FIGURE 2 | Diagram of immediate early gene (IEG)-based approaches for neuron tagging. For each method, information about the characteristic of the final effect is described. In particular: the duration time (transient or not), the location (whole-brain or not), and if the method can be coupled with optogenetic and chemogenetic tools (manipulation). TRE, tetracycline responsive element; Dox, doxycycline; tTA, artificial transcription factor; TXM, 4-hydroxytamoxifen; CreER, tamoxifen-inducible recombinase; rtTA, reverse tetracycline transactivator; TeTb, bidirectional Tet promoter. Created with BioRender.com.

TABLE 1 | Summary of the main features of each immediate early gene (IEG) tagging method.

	IHC	Fos-GFP Arc-dVenus	TetTag	TRAP	TRAP2	CANE	vGATE	E-SARE	RAM
Whole-brain cell counts	X	X	X	X	X				
Projection mapping of activated cells				X	X	X	X	X	X
Tran-synaptic tagging				X	X	X			
Optogenetic or chemogenetic manipulation of activated cells			X	X	X	X	X	X	X
Subsequent behavioral test				X	X	X	X	X	X
Cell-type specificity							X		

X, Means that this IEG tools has that feature.

maps at the cellular scale. Leveraging the fact that IEG synthesis is induced by neuronal activity, the first way to visualize the activity at the brain level was obtained by the immunostaining of *c-fos* (Morgan et al., 1987; Sagar et al., 1988). Despite the large number of genetic approaches developed in the last years, IHC still remains the reference method to map IEG-expressing cells. It has been coupled with many clearing techniques, such as iDISCO, CLARITY, CUBIC, for the 3D reconstruction of brain-wide activated circuits (Susaki et al., 2014; Tomer et al., 2014; Renier et al., 2016). However, there are some limitations concerning this method. After the stimulus, when IEGs arrive at the transcription peak, animals have to be sacrificed, so it is not possible to carry out other studies on the same animal.

Moreover, it is often interesting to understand whether a neuronal ensemble, activated with a stimulus, could be reactivated with a distinct one, and the traditional immunohistochemistry does not allow this type of investigation. In order to solve this latter problem, *cellular compartment analysis of temporal activity by fluorescent in situ hybridization* (catFISH) has been developed. This technique exploits different compartmentalization of mRNA into the nucleus and the cytoplasmic region (Guzowski and Worley, 2001). However, starting from the previous method, a new double-labeling technique is applied in order to study two sequential stimuli separated by an appropriate interval. Thus, the *tyramide-amplified ICH-FISH* (TAI-FISH) exploits different

compartmentalization of IEG protein and the relative mRNA, in this way the first stimulus is visualized by IEG cytoplasmic protein while the second with the mRNA in the nucleus (Xiu et al., 2014).

Fos-GFP and Arc-dVenus

As mentioned above, IEGs offer genetic access to neurons activated in response to specific stimuli; therefore, strains of transgenic or knock-in mice have been developed to directly link IEG transcription to some type of reporter. Genes coding for fluorescent proteins, LacZ markers or luciferase, are inserted under the control of the IEG-promoters (Smeyne et al., 1992; Barth et al., 2004; Wang et al., 2006; Xie et al., 2014; Kim Y. et al., 2015; Vousden et al., 2015). This approach has been first proven in transgenic mice in which *Fos* promoter drove transcription of the β-galactosidase; neurons activated in response to light pulse stimulation during the dark cycle were then identified as Fos-LacZ positive through a blue pigment (Smeyne et al., 1992). More recently, several transgenic models have used fluorescent proteins as reporters in an activity-dependent manner (Barth et al., 2004; Wang et al., 2006; Xie et al., 2014; Kim Y. et al., 2015; Vousden et al., 2015). For example, *Fos-GFP* mice have been used to map the neurons stimulated during social or parenting behaviors (Kim Y. et al., 2015), while different activation patterns involved in recalling contextual and tone fear memories at whole-brain level were explored with the *Arc-dVenus* strain (Vousden et al., 2015). The half-life of the fluorescent proteins is similar to endogenous IEGs ones, leading to fluorescent peaks in a short time, about 1–2 h, and lasts approximately 6–8 h. This temporary access to neurons prevents manipulation of the same activated cells later in time. Still, GFP-expressing cells may be targeted *in vivo* for electrophysiological recording right after the behavioral experiment (Barth et al., 2004). *Fos-GFP* and *Arc-dVenus* have been included inside a pipeline that demonstrated, for the first time, the possibility to detect neural activity on a brain-wide scale, using automated whole brain imaging (Kim Y. et al., 2015; Vousden et al., 2015).

TetTag

More complex strategies limit the expression of an IEG-linked effector to some kind of pharmacological treatment. One of the first approaches demonstrated in this sense is *TetTag*, which uses *Fos* promoter to drive the expression of a doxycycline-repressible tetracycline transactivator (tTA) (Reijmers et al., 2007). This strategy has been developed to understand whether neurons activated during fear learning are reactivated during fear memory recall (Reijmers et al., 2007). This inducible expression system, called *Tet-Off*, exploits the "switch-off" mode in the presence of the doxycycline antibiotic (DOX). The *TetTag* strategy needs two transgenes: the first requires the tTA, an artificial transcription factor while the second, a tetracycline-responsive element (TRE) that is a synthetic promoter. TRE needs to bind to tTA for the expression of any genes. During the resting state, tTA is usually bound to DOX and consequently unable to link to the TRE sequence. Therefore, in the presence of a stimulus and of a diet lacking in DOX at the same time, the *Fos* promoter stimulates the synthesis of tTA, which now is able to bind TRE for the effector expression, achieving neuronal labeling. Due to the slow metabolism of DOX, the time window becomes very wide and leads to high levels of neuronal background (Shockett and Schatz, 1996; Reijmers et al., 2007). Moreover, this method does not allow to permanently access to activate neurons because TRE-conditional effectors last only few days (Reijmers et al., 2007).

Finally, for the manipulation of behavioral-responsive ensembles in many paradigms, this technique can be coupled with optogenetic and chemogenetic tools, using some rhodopsins and excitatory human M3 muscarinic (hM3Dq) receptors directly as effectors (Koya et al., 2009; Garner et al., 2012; Liu et al., 2012; Ramirez et al., 2013, 2015; Cowansage et al., 2014; Redondo et al., 2014).

TRAP

Targeted recombination in active populations (TRAP) is another drug-dependent approach, such as *TetTag*. However, compared to the latter, TRAP shows a better temporal resolution and permanent genetic access to neurons, making activated cells permanently fluorescent (Guenthner et al., 2013). Like the previous one, also this strategy needs two transgenes: the first expressing a tamoxifen-inducible recombinase CreER^{T2} in an activity-dependent way, i.e., under the control of *Arc* and *Fos* promoter (ArcTRAP and FosTRAP) (Feil et al., 1997). The second exploits the Cre-Lox recombination under a ubiquitous promoter for the reporter expression.

CreER^{T2} is expressed in active cells but is not effective unless in the presence of tamoxifen (TMX). When present inside cells, TMX binds the ER site allowing CreER^{T2} to move from the cytoplasm to the nucleus, driving the expression of a reporter *(i.e., fluorescent protein*) by the removal of loxP-stop-loxP sequence (Guenthner et al., 2013). The time window for "*cell TRAPing*" is provided by the lifetime of TMX and, therefore, by its metabolism and excretion. Due to the long lifetime of TMX, Guenthner et al. (2013) have decided to use its metabolic form, 4-hydroxytamoxifen (4-TMX), limiting the time window to a period <12 h. As a result, only neurons that are activated around drug administration can be TRAPed.

This genetic tool has facilitated previously impossible experiments, enabling the manipulation of neural ensembles activated during a specific task later in time, even days after (Ye et al., 2016; Ishii et al., 2017; Kim and Cho, 2017; Girasole et al., 2018). Moreover, this method has allowed whole-brain reconstructions and it is often coupled with clearing approaches. Besides the many progresses made in this field, TRAP has some limitations: the first is caused by the *Arc* and *Fos* haploinsufficiency that provokes the disruption of their endogenous expression; the second is about stochastic labeling mainly due to random reporter expression.

TRAP2

Recently, *TRAP* has been improved with a new version, called *TRAP2* (DeNardo et al., 2019). The mechanism is the same as *TRAP* with few but essential developments. *TRAP2* is further optimized with an improved Cre (iCre) to enhance the effector expression (Shimshek et al., 2002). It preserves the Fos endogenous expression, allowing keeping transgenic animals

in homozygosis. Therefore, this capability of maintaining Fos endogenous expression also improves the penetration in many brain regions. Using the *TRAP2* tool, *Luo's group* has studied fear memory retrieval in the prelimbic cortex.

CANE

Sakurai et al. (2016) have developed a "lock-and-key strategy" for *capturing activated neuronal ensembles with engineered mice and viruses (CANE)*. In the *CANE* system, a destabilized targeting avian leukosis (dsTVA) receptor, not present in mice, is knocked-in to endogenous Fos locus. In the presence of external stimuli, Fos and dsTVA are co-translated in the same neuron so that all Fos^+ cells have on their membrane the avian receptors. Before any external stimulation, rabi/lentiviruses coated with a surface glycoprotein (EnvA), a typical ligand of TVA, are delivered into the brain and infect Fos^+ neurons in the injection area. After transfection, the virus genome is inserted into the neuron and allows the effector expression (Sakurai et al., 2016).

CANE leads to a more precise temporal and spatial resolution compared to previous techniques. Its short time window depends a) on the brief half-life of dsTVA, which mimics the kinetics of the endogenous *Fos*, and b) on tightened limitations of viral vectors transduction. For those reasons, it enables low background and it has been used to study "mild behavior" (*i.e., brief behavioral encounters or brief behavioral events*). Moreover, this double-control mechanism appears to permanently tag the majority of activated cells, leading to high efficiency. The use of lenti and rabiviruses allows the labeling of two or more ensembles in the same brain region and also *trans*-synaptic tracing of activated cells (Sakurai et al., 2016; Rodriguez et al., 2017; Jiang-Xie et al., 2019; Tschida et al., 2019). CANE is an excellent technology, able to reconstruct efferent and afferent connections, but it cannot be used for whole-brain labeling because viral infection is limited to the injection site. Moreover, virus delivery requires stereotaxic surgery and anesthesia, which could alter behavior and neuronal response.

vGATE

The most recent genetic approach, which uses a mixture of three viruses, is called *virus-delivered genetic activity-induced tagging of cell ensembles* (vGATE). This multilevel strategy has been used to investigate fear memory engrams and especially to manipulate hypothalamic oxytocin neurons with the aim of understanding the role of this subpopulation in fear response (Hasan et al., 2019). The authors used a system composed of three adeno-associated viruses (AAV). The first one drives the expression of a reverse tetracycline transactivator (rtTA) under the *Fos* promoter. In order to have a permanent tagging of Fos^+ neurons, a Tet operator sequence has been integrated upstream of *Fos* promoter, able to sustain an extensive induction of rtTA in the presence of DOX through an autoregulatory expression loop. The second virus contains a bidirectional Tet promoter that, in the presence of the DOX, stimulates the expression of a fluorescent protein and simultaneously activates the Cre recombinase. The last virus uses a cell-type-specific promoter that, under a Cre recombinase, expresses Channelrhodopsin-2 (ChR2) to optically manipulate neuronal activity (Hasan et al., 2019).

Contrary to *TetTag*, this IEG-based method exploits a Tet-On system, i.e., DOX "switch-on" mode. By the intraperitoneal DOX injection, the transcriptional activator is expressed, providing a better-controlled time window, which depends only on the drug metabolism and viral transduction, avoiding the integration of the DOX in the feed.

The great advantage of the vGATE is the lack of use of transgenic mice; in this case, there is the possibility to switch to other species. For instance, Hasan et al. (2019) have applied this tool to rats for their study. Moreover, the last virus contains a cell-type-specific promoter, and consequently, a specific neuron subpopulation may be manipulated and visualized. The use of viruses has its own limitations, yet it cannot be used for systemic tagging due to the local nature of viral injection; furthermore, as always in a complex stereotaxic surgery, the potential effects of any brain injury on animal behavior could not be overlooked.

E-SARE

Recently, many researchers focused on endogenous promoters, modifying their genomic sequences to have better control of the transcription of IEGs induced by neuronal activity. Therefore, viral strategies using engineered promoters have expanded the horizon of IEG-based methods to improve the specificity and efficiency of activated neurons, increasing reporter expression level more than 20-fold. Kawashima et al. have introduced the *synaptic activity-responsive elements* (SAREs), which regulate *Arc* expression throughout the cooperation of three activity-dependent transcription factors (CREB, MEF2, and SRF) to induce a strong transcription (Kawashima et al., 2009). Exploiting their study based on the SARE enhancer element of the Arc promoter, the same authors have constructed a new synthetic promoter called "E-SARE" that is composed of five tandem repeats of SARE sequence fused into an *Arc* minimal promoter (Kawashima et al., 2013). This genetic tool has been used to tag neurons activated by different visual orientation stimuli. In order to obtain a reliable circuitry map and to manipulate permanently tagged neuronal ensembles, E-SARE has been coupled to an inducible Cre sequence. The combination of the E-SARE upstream of the $CreER^{T2}$ allows to have a tightly controlled time resolution (Kawashima et al., 2013). This system can be packed into AAV vectors or lentivirus without the use of transgenic animals; consequently, the great advantage is the potential "switching" to larger mammalian species.

RAM

Robust activity marking (RAM) system is another method, such as E-SARE, that exploits a synthetic promoter to investigate activity-dependent cells. This strategy has been used to label and manipulate neuronal ensembles in the hippocampus of animals subjected to contextual fear conditions (CFC) and in the amygdala following tone-fear conditioning (TCF) (Sørensen et al., 2016). The RAM promoter (P_{RAM}) is composed of four repeats of an enhancer module, which is composed by the AP-1 site and the neuronal-specific activity-dependent gene Npas4-binding motif, upstream of *Fos* minimal promoter (Sørensen et al., 2016). Related to existing IEG-genetic tools that do not take advantage of synthetic promoters, RAM has been developed

to reduce background levels, meaning that it only responds to neuronal activity with a robust signal and to precisely control the time of its activation. P_{RAM} has been combined with an improved version of a Tet-Off system with a destabilized version of tTA (d2tTA) for many reasons: best activation time and tight time-window that leads to lower basal expression. Moreover, the P_{RAM} small dimension allows to pack the entire DNA sequence into a single virus, bypassing transgenic animals and using it in other species like rats or flies, thanks to high conservation of the sequence used (Sørensen et al., 2016). Finally, to show the versatility of this method, a Cre-dependent RAM has been developed to study cell type-specific ensembles activated by a specific stimulus (Sørensen et al., 2016).

Different Approaches, Not Based on IEG, to Tag Activated Neurons

IEG-based approaches have been generally used to tag neurons activated during behavioral experiences. Still, these methods cannot be used to study "mild" behaviors or behaviors that produce neuronal activity less sustained in time. The reason lies in the fact that these IEGs share some limitations, which are mainly caused by the long time-window, ranging from hours to days, and high-level background. For that reason, photoactivatable approaches have been developed to overcome the problems related to IEG's nature, using calcium as indicator for neuronal activity and light instead of drugs, as tool for a more rapid temporal resolution and better control of non-specific reporter expression, significantly lowering the background. FLARE (Wang et al., 2017) and Cal-Light (Lee et al., 2017) are the first Ca^{2+}-and-light-gated tools that exploit a transcriptional readout, while CaMPARI (Fosque et al., 2015) is another Ca^{2+}-and-light-gated tool that uses fluorescent protein photoconversion.

TISSUE-CLEARING PROTOCOLS AS FITTING TOOLS TO IMAGE THREE-DIMENSIONAL (3D) BRAIN VOLUME

Once neurons are activated and labeled in response to behavioral stimuli, brain samples can be analyzed with optical microscopy. However, given the opaque nature of biological specimens, the full volume of the brain cannot be directly reconstructed in 3D. From standard histology to more recent techniques, methods based on serial sectioning are able to reconstruct the 3D volume (for more details, see section "Quantifying Neuronal Activation Across the Entire Murine Brain"). These methods are based on mechanical operations that lead to sample disruption. Indeed, the brain cutting could cause compression, stretching, or accidental incision, which often make the volumetric reconstruction hard. Although these approaches are widely used, the most straightforward way to preserve the 3D structure is to make specimens transparent through tissue clearing methods. The transparency provides direct optical access to bulky specimens, allowing to overcome sample sectioning. In general, keeping brains intact rather than exploring smaller parts is important to achieve a better comprehension of neuronal mechanisms. It is evident that virus injections, generally used to tag neuronal projections of neuronal subgroups activated by a particular stimulus, or used to select specific subpopulations, could be scarcely evaluated by two-dimensional (2D) sections. Neuronal projections are extended in every possible direction; therefore, brain cutting can result in loss of information about connections between regions or about the virus pathway.

As mentioned above, a relevant problem to rapidly image large volumes of tissue is associated with the milky aspect of the brain due to its heterogeneous composition. This heterogeneity leads to light scattering, with light rays diffused in random directions by the microscopic components of the sample. This diffusion of light hinders brain imaging. Indeed, light is scattered as a result of the mismatch between the refractive indices (RIs) of different tissue components (see **Figure 3**). Possible solutions to overcome this problem consist of limiting the scattering effects by reducing optical inhomogeneities within the sample (Tuchin, 1997; Richardson and Lichtman, 2015). Thus, the clearing protocols work by minimizing the mismatch between macromolecules and the surrounding medium. Generally, the "dry" part of biological tissue (proteins and lipids) has a high RI (ranging from 1.4 to 1.6), while the surrounding medium is mainly composed of water, which has an RI of 1.33 (Jacques, 2013). The first approach to achieve the transparency of the brain is related to the removal of lipids that are the primary source of scattering in the fixed sample. By eliminating lipids from the sample, "dry" RI is reduced, and the surrounding medium is replaced with a solution that has the same RI of the delipidated tissue. The other approach consists of directly acting on the surrounding medium, immerging the brain in solutions able to increase the RI of the medium to homogenize it with the components of our tissue. In conclusion, the clearing approaches operate in two ways: on the brain components or on the surrounding medium. Depending on the clearing approach researchers use, the final RI for cleared brain or other tissues ranges from 1.33 (water RI) to 1.6 (lipid RI).

In this section, we review all of the existing clearing methods. Different classifications have been proposed (Richardson and Lichtman, 2015; Silvestri et al., 2016; Tainaka et al., 2016). Still, we try to gather them into three groups: (1) hydrophobic-reagent or organic solvent-based clearing methods, (2) hydrophilic-reagent or water-based clearing methods, and finally (3) hydrogel-based clearing methods.

It is worth emphasizing that in this review, we are focused on the brain, but clearing methods can be applied to many other organs.

Hydrophobic-Reagent or Organic Solvent-Based Clearing Methods

More than a century ago, Spalteholz described, for the first time, a clearing approach for fixed tissue using organic solvents (Spalteholz, 1914). He replaced water with a high-RI mixture, composed of benzyl benzoate and methyl salicylate, and observed that biological tissue became almost entirely transparent. In

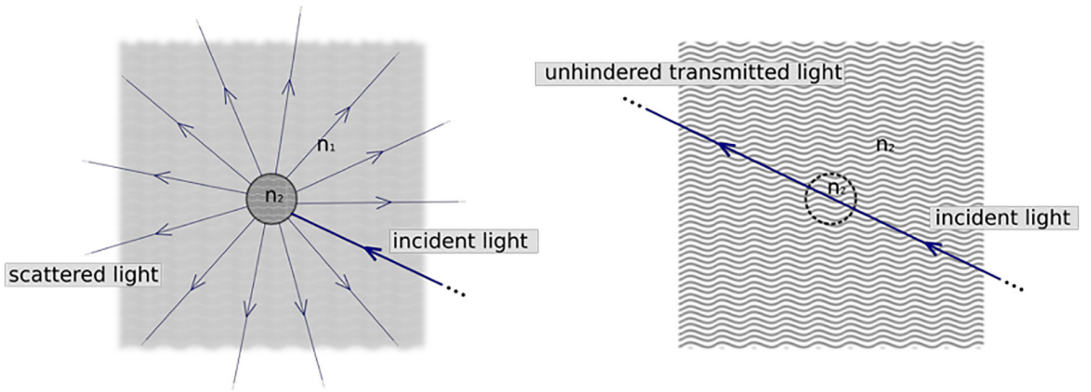

FIGURE 3 | Physical principle underlying tissue clearing. In normal tissue **(left)** cellular components have a refractive index n_2 significantly larger than that of the surrounding medium (water, n_1). This inhomogeneity results in scattering of light and thus opaqueness of the sample. Clearing methods try to match refractive indices **(right)**, so that tissue appears as a homogeneous optical medium where light can travel unhindered. Created with BioRender.com.

general, hydrophobic-reagent methods involve organic solvents with high-RI and provide remarkable transparency of large samples (i.e., brain) in a quick time (1–2 days), perfect for a whole-brain pipeline. Due to their rapid "brain-transparentizing" capability, this class is the most used among clearing techniques (Costantini et al., 2019). Since tissues are mainly composed of water, the main principle of this method is based on dehydration and RI matching. The first step consists of water removal by organic solvent as alcohols or ethers, which are also able to solvate a small fraction of lipids. Dehydration usually leads to sample shrinkage and hardening whereas agents used in the second step, have the function to match the high-RI of water-free tissues and also to remove the remaining lipids.

This general scheme, composed of dehydration and RI matching, has been later used by Dodt, replacing methyl salicylate with benzyl alcohol. BABB (the acronym of agents used) has been created from this change (Dodt et al., 2007). A relevant limitation of organic solvent-based clearing methods is related to the dehydration step, which often leads to fluorescent protein quenching. For that reason, this method is not suitable for the endogenous reporters as GFP or tdTomato. Thus, using this type of clearing on transgenic or transfected mice is discouraged. The introduction of tetrahydrofuran (THF) and dibenzyl ether (DBE), respectively, as dehydrated and RI matching agent has developed 3DISCO techniques and has improved fluorescence preservation that lasts for a few days (Becker et al., 2012; Ertürk et al., 2012). This has been possible by the elimination of peroxides generating from THF and DBE before usage of these solvents. Other improvements have allowed the development of many variants of DISCO-based techniques. Renier et al. (2014) using iDISCO, overcame the problem related to fluorescence quenching, combining clearing with whole-mount immunohistochemistry, with the aim to direct an antibody against the different fluorescent proteins. Anyway, they have also used a combination of phosphate-buffer saline (PBS) and dimethyl sulfoxide (DMSO) also to preserve GFP expression for a few days. These techniques make tissue highly transparent, and they allow permanent preservation of specimens, owing to their hardening. Moreover, organic solvent-based techniques are extremely rapid. To understand their speed, just think that an entire brain is cleared in only a few days. However, the use of many toxic and dangerous agents, the scarce availability of appropriate immersion lenses for imaging, the fluorescent protein quenching, have induced researchers to develop alternative approaches.

Hydrophilic-Reagent or Water-Based Clearing Methods

The extensive use of endogenous fluorescent reporters, as GFP or tdTomato protein, has driven the development of new clearing protocols replacing organic solvents with water-soluble reagents. These hydrophilic clearing methods exploit two different approaches: passive immersion in high-RI aqueous solution, and delipidation with hyperhydrating reagents. The former approach is based on a direct immersion of the sample in a high-RI solution to clear the sample gradually. In detail, saturated sugar solutions that are prepared with elevated concentration of sucrose or fructose are used in SeeDB and FRUIT techniques, respectively (Ke et al., 2013; Hou et al., 2015). The practical drawbacks of using high-sugar concentration are the high viscosity that limits sample manipulation and could introduce air bubbles, the potential precipitation at room temperature, and browning coloration at more elevated temperatures. The sugar viscosity causes slow penetration inside the sample, thereby extending clearing time up to months. This problem can be overcome using different water-based reagents with low viscosity as 2,2′-thiodiethanol (TDE) and FocusClear (Chiang et al., 2002; Staudt et al., 2007; Aoyagi et al., 2015; Costantini et al., 2015). The use of this latter is limited by its expensive cost.

On the other side, hyperhydrating reagents operate increasing osmotic pressure and water flux inside the cell. The water entrance tries to maintain an aqueous environment for fluorescence preservation, while the simultaneous use of detergents for lipid removal lowers the tissue RI. Hyperhydrating reagents are also used to hydrate and often partially denature

proteins, the other major tissue component, further reducing the overall RI closer to that of water. The Miyawaki group has discovered the clearing ability of urea, thereby developing *Scale* approach (Hama et al., 2011). Urea is able to simultaneously penetrate and to break protein folded regions, requiring water to adjust RI. *Scale*, which involves urea, glycerol, and a detergent (Triton-X), was the first technique taking advantage of hyperhydrating reagents. In general, these protocols produce abundant hydration that leads to an optimal "specimen-transparentizing" but causes sample swelling. Therefore, in the *ScaleS* method, the substitution of glycerol with sorbitol was used to avoid the deformation and expansion of the sample (Hama et al., 2015). Although hydrophilic methods have overcome fluorescence preservation problems relative to the use of organic reagents, they require lengthy incubation times (from days to months) to clear only small portions of tissue. Starting from the ingredients of *Scale* solution, the Ueda group has developed an alternative approach called CUBIC. The aim was to clear entire organs and to accelerate clearing process without losing safety and preservation of protein function, typical of this clearing class (Susaki et al., 2014; Tainaka et al., 2014). They have screened many chemical agents and find that a series of amino alcohols have both decolorization and delipidation functions. Therefore, a mixture of selected amino alcohols, together with Triton-X and urea, has been included in the CUBIC protocol. High concentrations of Triton-X maximize lipid removal but also damage some protein epitopes. To allow whole-mount immunostaining, CUBIC protocols found an optimal concentration of detergent that permeabilizes membranes while preserving epitopes useful for antibody labeling. New CUBIC versions are extended even in the expansion microscopy (ExM) field (CUBIC-X) (Murakami et al., 2018). ExM is a method able to improve the resolution of light microscopy by physically expanding biological samples (Chen et al., 2015). This approach allows to reconstruct full details of small structures (i.e., synaptic connections). In conclusion, another strategy that exploits hyperhydrating reagents is *Clear*^{T} that uses a solution composed of water and formamide. Starting from *Clear*^{T}, various methods were proposed as *Clear*^{T2} and RTF (Kuwajima et al., 2013; Yu et al., 2018).

Tissue Transformation-Based Clearing Methods

In the last years, new clearing approaches based on tissue transformation have been developed to combine the advantages of the abovementioned techniques. In 2013, the Deisseroth group was the first to introduce a hydrogel-based clearing method, called CLARITY (Chung et al., 2013). The basic idea behind CLARITY is to transform a biological tissue, in our case brain, into a hydrogel–tissue hybrid. The hydrogel, which is mainly composed of acrylamide monomers, has the function of stabilizing dispersed proteins and nucleic acid by covalent bonds. Moreover, this hybrid construct has to support and preserve tissue architecture after lipid removal. In general, for every tissue, lipids have a structural function, but as we have explained before, they are the primary source of scattering. Thus, their elimination facilitates achieving brain transparency. The removal of all lipids from the tissue using a high concentration of detergent [in this case, sodium dodecyl sulfate (SDS)] is a process that takes a long time, typically many weeks for an entire murine brain. To reduce the incubation time of the sample, an electrophoretic field could be applied to accelerate the diffusion of the ionic detergent.

Furthermore, the large gel meshes allow macromolecule penetration, like antibodies or fluorescent dyes, and the hydrogel itself increases the preservation of epitopes. For this reason, CLARITY can often be coupled with immunostaining techniques for the imaging of large tissue. Passive diffusion of probes requires longer incubation times, and the application of stochastic electric field has thereby sped up their diffusion (Kim S.Y. et al., 2015). During the years, many variants of CLARITY have been implemented. Researchers have looked for alternative methods in which passive diffusion of detergent has been preferred to electrophoretic transport. Also, the index-matching solution Focus Clear has been replaced with cheaper ones. Thus, PACT, PARS, CLARITY/TDE, CLARITY/glycerol are developed (Tomer et al., 2014; Yang et al., 2014; Costantini et al., 2015). Harsh conditions applied in the clearing process could cause troubles for protein antigenicity, fluorescence reporters, and tissue architecture. Chung lab has addressed these limitations by promoting two different techniques. SWITCH protects protein antigenicity for a rapid tissue clearing and unlimited rounds of antibody labeling (Murray et al., 2015), while SHIELD uses epoxides as chemical compounds able to create *intra e* intermolecular crosslinking in order to preserve fluorescence and probe-binding capability (Park et al., 2019). Moreover, these hydrogel-based clearing approaches have demonstrated useful for super resolution imaging, reconstructing details of neuronal projections, or even synaptic contacts (Ku et al., 2016). MAP technique exploits the idea of brain expansion, using a hydrogel that is isotropically expanded. However, in contrast to classic ExM, this approach avoids protein digestion, then the entire proteome is preserved. Although the elevated cost and long process, these hydrogel-based methods are commonly applied over the whole brain or other organs with much more safety than organic solvent ones.

QUANTIFYING NEURONAL ACTIVATION ACROSS THE ENTIRE MURINE BRAIN

After tagging activated neurons and preparing samples for imaging, murine brains have to be reconstructed in 3D with some high-throughput optical microscope. In this section, we review imaging methods used for whole-brain activation mapping, together with the software tools necessary to extract quantitative information from raw data.

Imaging

Three-dimensional optical imaging of biological tissue is traditionally achieved using confocal (Conchello and Lichtman, 2005) or two-photon microscopy (Zipfel et al., 2003). These methods afford three-dimensional resolution (which is also known as "optical sectioning") either by removing out of

focus fluorescence with a spatial filter (confocal microscopy) or by restricting fluorescence excitation to the focus of the objective lens (two-photon microscopy). However, standard implementations of both techniques are not suitable for whole-brain reconstruction for two reasons. First, they are point-scanning methods, meaning that the image is reconstructed point-by-point. This approach is inherently slow, with typical volumetric imaging rates in the order of $10^{-4} \div 10^{-3}$ mm^3/s. Considering that a mouse brain is about 1 cm^3, this means that 10 to 100 days are needed to fully reconstruct one full murine encephalon. Second, optical sectioning in two-photon or confocal microscopy is proportional to the numerical aperture (NA) of the imaging objective, i.e., the angle of emitted light that is collected by the lens. Typically, NA is inversely proportional to the objective working distance, i.e., the distance between the first lens and the focal plane. Thus, high-NA objectives, which are needed to achieve proper 3D resolution in confocal or two-photon microscopy, usually have limited working distances that cannot encompass the entire murine brain.

To overcome these limitations several approaches have been developed during the years. Serial two-photon tomography (STP) incorporates a vibratome inside a standard two-photon microscope, reconstructing the volume by a continuous sequence of cutting and imaging operations (**Figure 4A**; Ragan et al., 2012). In this way, only the sample layers closer to the vibratome cut are imaged, allowing the use of standard high-NA objectives with limited working distance. To reduce reconstruction times, a sampling strategy is usually adopted, acquiring one optical section (1 to 2-μm thick) every 50 or 100 μm. STP has been exploited to study neuronal activation in Fos-GFP and Arc-dVenus transgenic mice (Kim Y. et al., 2015; Vousden et al., 2015).

Speed up of confocal microscopy can be obtained by parallel scanning. Spinning-disk approaches exploit multiple pinholes arranged on a rotating disk to image multiple spots simultaneously, increasing the volumetric imaging rate to 10^{-1} mm^3/s (Wilson, 2010). Seiriki et al. (2017) developed block-face serial microscopy tomography (FAST), a spinning-disk confocal system coupled with a vibratome (**Figure 4A**) that can image entire mouse brains with micron resolution in 2.5 h. The authors reported the use of FAST to map fluorescent neurons in Arc-dVenus mice during acute vs. chronic restraint stress (Seiriki et al., 2017).

Sectioning methods, like FAST and STP, are, in general, used without any tissue clearing since the microscope does not need to penetrate deep inside the sample. In addition, the specimen needs to be sufficiently stiff to be adequately cut by the vibratome, a requirement incompatible with most clearing protocols. On the one hand, avoiding tissue clearing simplifies and speeds up experimental procedures. On the other hand, this prevents exogenous staining of samples, limiting the application of these methods to animal models providing intrinsic fluorescence.

The technique of choice in combination with whole-brain clearing is light-sheet microscopy (LSM) (Dodt et al., 2007; Keller and Dodt, 2012; Ueda et al., 2020). In this method, the sample is illuminated from the side with a thin sheet of light, and fluorescence is collected along an axis perpendicular to the illumination plane (**Figure 4A**). In this way, optical sectioning is achieved in a plane-scanning rather than a point-scanning approach. LSM is thus considerably faster than confocal or two-photon microscopy: a whole mouse brain can be reconstructed in a time ranging from hours to minutes, depending on the resolution. Indeed, a key advantage of LSM is its flexibility: the resolution of the system can be modulated from tens of microns—sufficient to discriminate cell bodies when neuronal processes are not labeled—to less than 1 μm—allowing distinguishing axons and dendrites. Low-resolution LSM has the merits of a simple optical layout and the reasonable size of the generated datasets; for these reasons, several groups were able to use it to study neuronal activation in large behavioral cohorts (Susaki et al., 2014; Renier et al., 2016; Tatsuki et al., 2016; Ye et al., 2016). However, when labeling of active neurons includes small processes, a subcellular resolution is needed to distinguish cell bodies from bundles of axons or dendrites. For instance, Ye et al. (2016) used low-resolution LSM on TRAP mice and were forced to exclude several brain regions from their analysis. High-resolution LSM can instead produce a quantitative mapping of neuronal activation independently of the labeling strategy used. The challenges, in this case, are represented by the size of the datasets produced (usually exceeding one TeraByte per brain) and the need for more complex optical systems. Indeed, high-resolution imaging through several millimeters of tissue introduces optical artifacts even with the best possible clearing. For instance, specimen-induced defocus needs to be corrected automatically to produce sharp images (Tomer et al., 2014; Silvestri et al., 2017; Matsumoto et al., 2019). Another issue that has to be addressed is the presence of shadowing artifacts introduced by adsorbing or scattering objects in the sample. Different methods have been proposed in this respect, including the use of non-Gaussian laser beams (Fahrbach and Rohrbach, 2012; Müllenbroich et al., 2018a,b) and axial sweeping of the excitation light sheet (Chakraborty et al., 2019; Voigt et al., 2019). Anyhow, whatever optical improvement must rely on a good optical clearing, which is an essential prerequisite for the use of high-resolution LSM. The group of Hiroki Ueda has pioneered IEG mapping at subcellular resolution, demonstrating the potential of this approach to quantify neuronal activation across the entire murine brains without excluding any areas (Murakami et al., 2018; Matsumoto et al., 2019; Susaki et al., 2020).

Whatever the microscopy method used to image brain samples, the next step is to transform the raw images—which are just a matrix of gray values—into semantically relevant information. This process involves two different phases that could be performed in parallel: cell detection (**Figure 4B**) and atlas registration (**Figure 4C**).

Cell Detection

Automatic detection or segmentation of labeled cells is a well-known problem in biomedical image analysis, and many different methods have been developed during the years (Acciai et al., 2016; Magliaro et al., 2019). However, whole-brain images present some peculiar challenges that need to be faced. First, datasets are usually extensive, ranging from tens of gigabytes

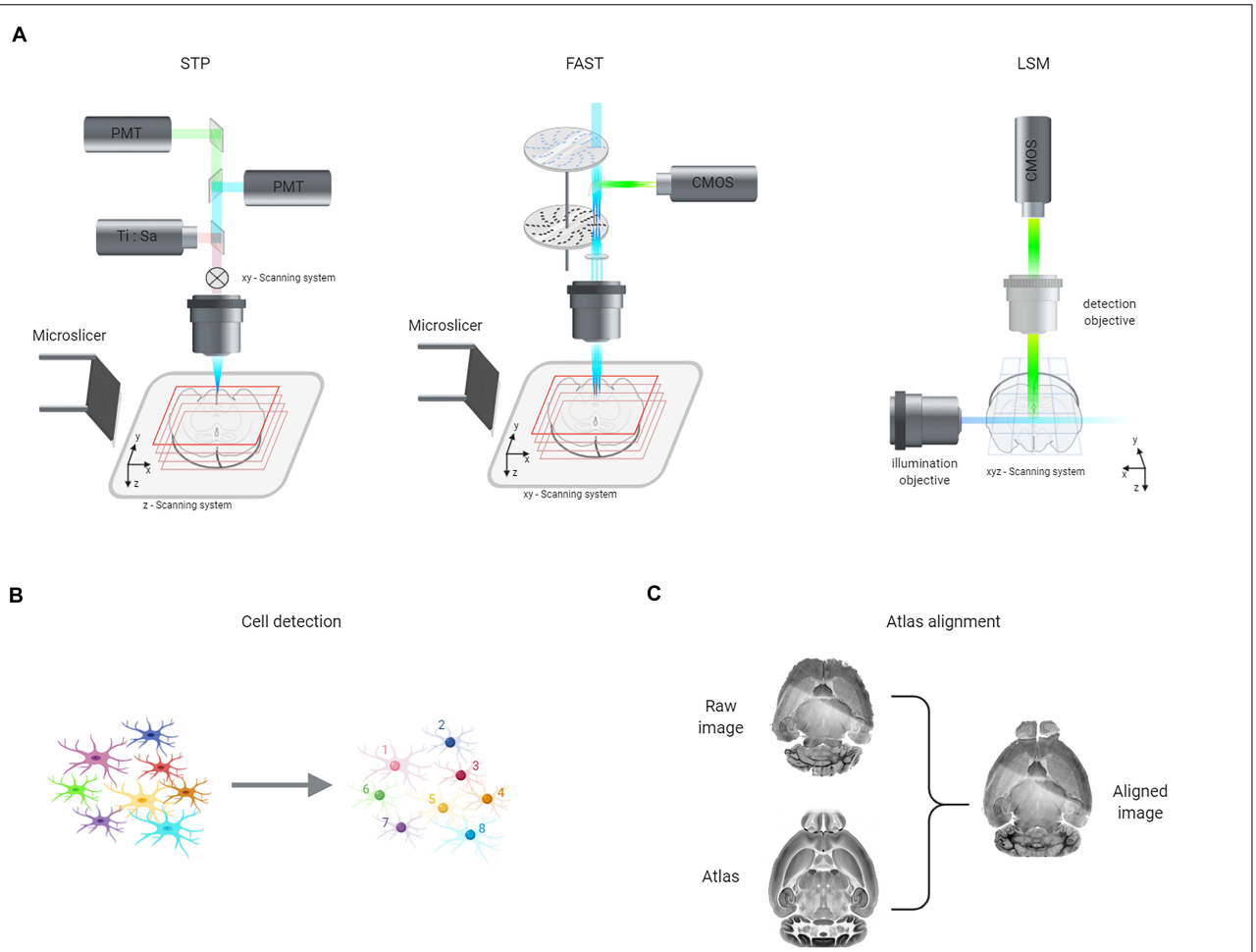

FIGURE 4 | Representation of the three steps necessary to obtain neuronal quantification across the entire murine brain. **(A)** Scheme of advanced imaging approaches for whole-brain reconstruction: serial two-photon tomography (STP), block-face serial microscopy tomography (FAST), and light-sheet microscopy (LSM). **(B)** The spatial position of individual cells **(left)** can be automatically detected **(right)** using various algorithms, including machine learning ones (see text). **(C)** Finally, brain volumes can be spatially aligned to reference atlas using different computational approaches (see text).

to tens of terabytes for a single sample. Thus, algorithms must be fast and scalable. Second, in LSM images, the contrast is very heterogeneous between deep and superficial brain regions since excitation and fluorescence cross variable thicknesses of biological tissue. Third, when the entire neuron is filled with the fluorescent label (e.g., when using transgenic strategies), an additional problem is represented by the presence of bright axons or dendrites, which may confound the detection algorithm.

Standard pipelines for cell detection use a combination of filters to homogenize contrast and highlight spherical objects, followed by adaptive thresholding of the images and then some operations/filters on binary data to refine segmentation. Such pipelines are highly parametrical: estimation of parameters is usually done on a small training set of manually annotated images. Sometimes, different sets of parameters are estimated for different brain areas to improve accuracy (Seiriki et al., 2017). Standard image processing pipelines are effective when labeling is confined to cell bodies, as in anti-c-fos immunohistochemistry (Renier et al., 2016), or when imaging quality is highly homogeneous, as in STP (Ragan et al., 2012) or FAST (Seiriki et al., 2017). Their use in LSM images of transgenic animals has been sometimes reported, but on a subset of brain regions (Ye et al., 2016), or on the whole brain but without a clear evaluation of the accuracy of the results (Menegas et al., 2015; DeNardo et al., 2019).

Machine learning approaches can be used to cope with complex or inhomogeneous images. In these methods, a model for classification of pixels or image transformation is trained using example data ("ground truth") provided by the user. As a general principle, the performances of the model increase with its complexity (the number of hidden parameters). However, more complex models require more ground truth for successful training. Thus, in practice, a trade-off between performances and manual annotation has to be found.

Ilastik (Berg et al., 2019) is a popular image-processing tool implementing simpler models—a random forest classifier based on a set of user-defined image features. This software allows real-time training and testing, together with a user-friendly

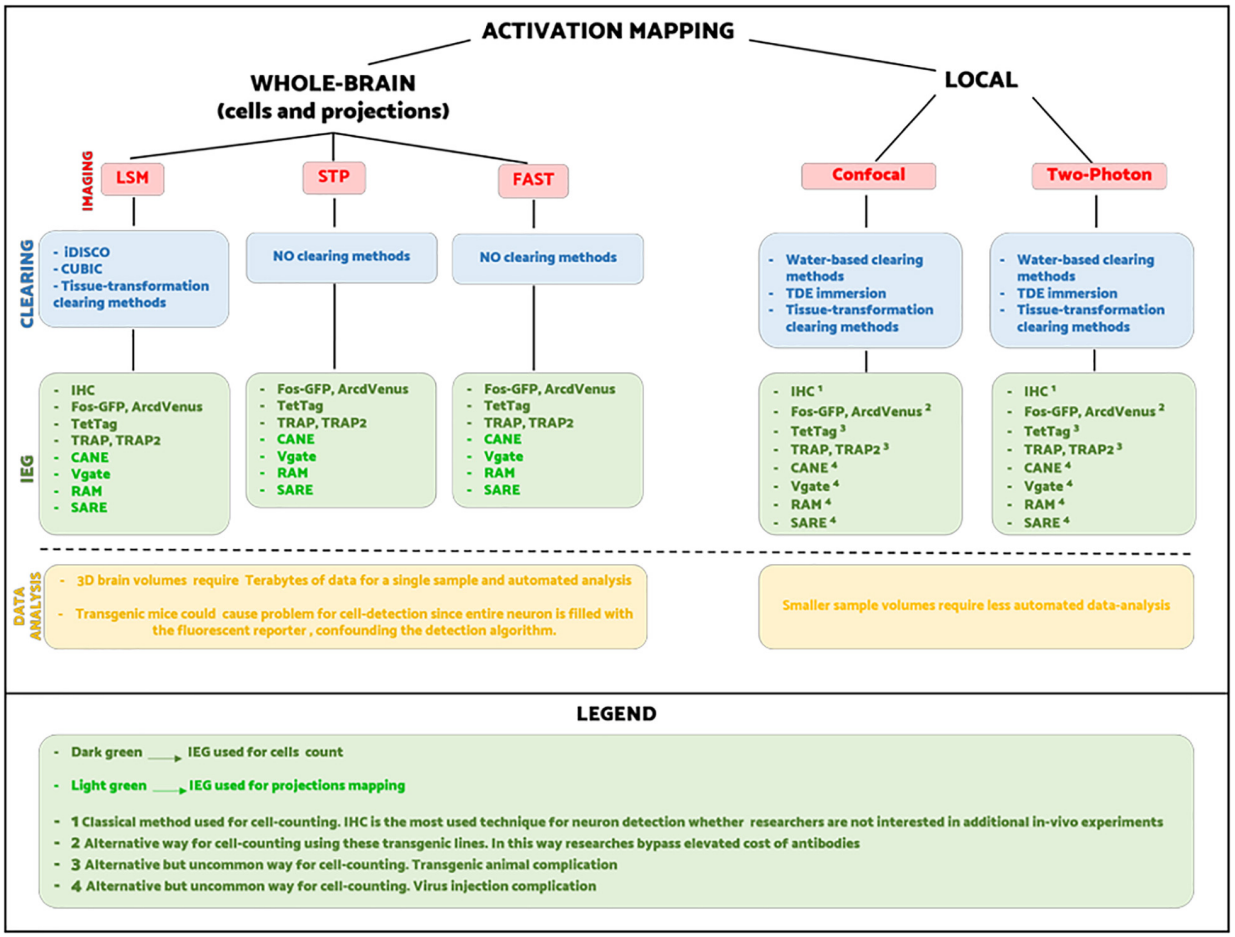

FIGURE 5 | Schematic of experimental pipelines that could be used for activation mapping.

environment suitable also for researchers with limited background in computer science. Menegas and coworkers reported its use in whole-brain LSM images, although not for an application related to IEG mapping (Menegas et al., 2015).

More sophisticated models, like the multilayered neural network used in the emerging field of deep learning (Gupta et al., 2019), have the potential to process images with human-level (or even super-human) performances. They are an established standard in the analysis of natural images, and their application to whole-brain image analysis has been reported (Kim Y. et al., 2015; Kirst et al., 2020; Todorov et al., 2020). Even if they are extremely powerful, their use is still quite limited in the field, probably because they need large human-annotated training datasets. In this respect, strategies to speed up labeling, e.g., by pinpointing the position of the neuronal soma rather than segmenting the neuronal volume, are promising to generate annotations much faster (Frasconi et al., 2014; Silvestri et al., 2015).

Spatial Registration to Reference Atlas

Detected cells must then be assigned to a specific brain region to allow precise quantification of which areas are elicited during a specific behavior. Although anatomy experts can directly draw major regions on the collected images (Seiriki et al., 2017), the standard choice is to refer to standard atlases, like the classic Franklin and Paxinos (Paxinos and Franklin, 2004) or the more recent one from the Allen Institute for Brain Science (Jones et al., 2009). This latter is the average of more than 1,000 whole-brain images obtained with STP and is associated with a 3D parcelation operated by a group of expert neuroanatomist. By registering, i.e., aligning, a sample image to the atlas template (or vice versa), detected cells can be directly assigned to a specific brain region.

Image registration is performed by finding the best transformation mapping one image into the other and is thus defined by the transformation itself, a quality metric, and an optimization strategy. Intersample differences are usually quite significant because of both biological variability (Scholz et al., 2016) and the deformation introduced by chemical clearing (Kutten et al., 2016). Global affine transformations, which are composed of translation, rotation, global (anisotropic) scaling, and shear, are usually not enough to match samples and reference. Conversely, non-linear local transformations, like B-spline (Klein et al., 2010; Fürth et al., 2018) or symmetric diffeomorphisms (Avants et al., 2011; Kutten et al., 2016), can recover sample deformations and provide reliable mapping onto the atlas.

The parameters of any transformation are obtained by maximizing some measures of registration quality. The most commonly used are cross-correlation—which works nicely for images sharing the same type of labeling—and mutual information—which performs well when the datasets are based on different stains. By coupling the quality metrics of choice with a suitable optimization algorithm, it is then possible to find the best transformation, mapping the sample to the atlas or vice versa. The most common 3D registration tools used in the field are probably Elastix (Klein et al., 2010) and ANTs (Advanced Normalization Tools) (Avants et al., 2011), and they have also been incorporated in larger projects like ClearMap (Renier et al., 2016) or CUBIC-X (Murakami et al., 2018).

In practice, registration is performed on images at coarse resolution, typically 25-μm-pixel size or worse. To facilitate the process, a reference channel containing either tissue autofluorescence (Kim Y. et al., 2015; Menegas et al., 2015; Renier et al., 2016; Ye et al., 2016) or some kind of nuclear staining [e.g., propidium iodide (Murakami et al., 2018)] is used rather than the channel related to labeled cells. Several authors also suggested to first perform a mutual registration of all the samples into an "average brain," followed by semi-manual registration of this latter to the reference atlas (Vousden et al., 2015; Ye et al., 2016; Murakami et al., 2018). Finally, it is worth noting that direct 3D registration is often quite challenging, especially for cleared samples that underwent severe deformations. Some groups proposed hybrid strategies, where a first 3D coarse alignment is followed by 2D accurate registration slice-by-slice (Tainaka et al., 2014; Fürth et al., 2018; Murakami et al., 2018).

CONCLUSION AND OUTLOOK

It is not yet clear how neuronal activity is correlated to specific behaviors. Stimuli from the world outside activate different neuronal pathways inside the brain. In turn, this activation triggers a cascade of events that eventually result in a precise behavior. Whole-brain mapping is an emerging technique to understand how the brain drives specific behaviors, even though it is still rarely used because of its multidisciplinary nature. Indeed, this sector of neuroscience ranges from genetics, sample preparation to imaging, and image analysis. This paper reviews the latest developments of each field with the general aim to combine every area of interest into a single pipeline for a routine and large-scale use.

Nowadays, there is not a unique way for visualizing neuronal activation on a brain-wide scale. Hence, it is up to researchers to choose the combination of methods best suited to their experimental purpose. In **Figure 5**, we try to summarize all the different experimental pipelines for whole-brain activity mapping. As the scheme shows, the number of possible combinations between labeling, clearing, imaging, and image processing is very high, and thus the choice falls on practical aspects. For instance, regarding short-term experiments where animals are sacrificed immediately after the behavioral task, it is preferable to use classic techniques as IHC rather than viruses or transgenes. On the other hand, transgenic mice are more appropriate for experiments that need to last over time, allowing multiple behavioral tests.

Whole-brain activation mapping naturally complements anatomical mapping, both in terms of cellular architecture (Kim et al., 2017) and of long-range axonal projections (Oh et al., 2014; Economo et al., 2016; Winnubst et al., 2019). Indeed, the knowledge of structural wiring of neuronal networks helps the interpretation of activity data. For example, co-activation of two brain areas could occur either because they are directly connected or via the involvement of a third brain region. This kind of information cannot be inferred from activation data only, but needs anatomical investigation and targeted stimulation with opto- or chemogenetics (Ye et al., 2016; Franklin et al., 2017; Vetere et al., 2017).

The majority of the techniques discussed in this review have been hitherto applied only to rodents, mainly mice. An important step for future research would be to map behavior-related neuronal activation in larger mammalian species. While transgenic strategies are currently not applicable to non-human primates (NHP), viral approaches like RAM could be, in principle, switched to map-activated neurons in different animals (Sørensen et al., 2016). Indeed, large-scale clearing and imaging methods have been demonstrated in small NHP like the marmoset (Seiriki et al., 2017; Susaki et al., 2020). When coupled with standard neuroimaging like functional magnetic resonance imaging (fMRI) or positron-emission tomography (PET), single-cell activation mapping in NHP could provide a unique framework to better understand the relationship between neuronal activity and imaging data. In turn, this would improve the interpretation of fMRI and PET in humans, with relevant implications for clinical practices.

In conclusion, this review confirms that the brain mapping is a constantly evolving field of neuroscience, and we are convinced that these approaches could not only be used in a routine way but also and overall, on a larger scale, in the near future.

AUTHOR CONTRIBUTIONS

All authors listed have made a substantial, direct and intellectual contribution to the work, and approved it for publication.

FUNDING

Authors received funding from the European Union's Horizon 2020 Research and Innovation Program under grant agreements No. 785907 (Human Brain Project) and 654148 (Laserlab-Europe), from the EU Program H2020 EXCELLENT SCIENCE—European Research Council (ERC) under grant agreement ID No. 692943 (BrainBIT), and from Fondazione CR Firenze (Private Foundation).

REFERENCES

Acciai, L., Soda, P., and Iannello, G. (2016). Automated neuron tracing methods: an updated account. *Neuroinformatics* 14, 353–367. doi: 10.1007/s12021-016-9310-0

Aharoni, D., Khakh, B. S., Silva, A. J., and Golshani, P. (2019). All the light that we can see: a new era in miniaturized microscopy. *Nat. Methods* 16, 11–13. doi: 10.1038/s41592-018-0266-x

Ahrens, M. B., Orger, M. B., Robson, D. N., Li, J. M., and Keller, P. J. (2013). Whole-brain functional imaging at cellular resolution using light-sheet microscopy. *Nat. Methods* 10, 413–420. doi: 10.1038/nmeth.2434

Aoyagi, Y., Kawakami, R., Osanai, H., Hibi, T., and Nemoto, T. (2015). A rapid optical clearing protocol using 2,2'-thiodiethanol for microscopic observation of fixed mouse brain. *PLoS One* 10:e0116280. doi: 10.1371/journal.pone.0116280

Avants, B. B., Tustison, N. J., Song, G., Cook, P. A., Klein, A., and Gee, J. C. (2011). A reproducible evaluation of ANTs similarity metric performance in brain image registration. *NeuroImage* 54, 2033–2044. doi: 10.1016/j.neuroimage.2010.09.025

Bahrami, S., and Drabløs, F. (2016). Gene regulation in the immediate-early response process. *Adv. Biol. Regul.* 62, 37–49. doi: 10.1016/j.jbior.2016.05.001

Bartel, D. P., Sheng, M., Lau, L. F., and Greenberg, M. E. (1989). Growth factors and membrane depolarization activate distinct programs of early response gene expression: dissociation of fos and jun induction. *Genes Dev.* 3, 304–313. doi: 10.1101/gad.3.3.304

Barth, A. L., Gerkin, R. C., and Dean, K. L. (2004). Alteration of neuronal firing properties after in vivo experience in a FosGFP transgenic mouse. *J. Neurosci.* 24, 6466–6475. doi: 10.1523/JNEUROSCI.4737-03.2004

Becker, K., Jährling, N., Saghafi, S., Weiler, R., and Dodt, H. U. (2012). Chemical clearing and dehydration of GFP expressing mouse brains. *PLoS One* 7:e33916. doi: 10.1371/journal.pone.0033916

Berg, S., Kutra, D., Kroeger, T., Straehle, C. N., Kausler, B. X., Haubold, C., et al. (2019). ilastik: interactive machine learning for (bio)image analysis. *Nat. Methods* 16, 1226–1232. doi: 10.1038/s41592-019-0582-9

Carrillo-Reid, L., Yang, W., Kang Miller, J., Peterka, D. S., and Yuste, R. (2017). Imaging and optically manipulating neuronal ensembles. *Annu. Rev. Biophys.* 46, 271–293. doi: 10.1146/annurev-biophys-070816-033647

Chakraborty, T., Driscoll, M. K., Jeffery, E., Murphy, M. M., Roudot, P., Chang, B. J., et al. (2019). Light-sheet microscopy of cleared tissues with isotropic, subcellular resolution. *Nat. Methods* 16, 1109–1113. doi: 10.1038/s41592-019-0615-4

Chen, F., Tillberg, P. W., and Boyden, E. S. (2015). Expansion microscopy. *Science* 347, 543–548. doi: 10.1126/science.1260088

Chiang, A. S., Lin, W. Y., Liu, H. P., Pszczolkowski, M. A., Fu, T. F., Chiu, S. L., et al. (2002). Insect NMDA receptors mediate juvenile hormone biosynthesis. *Proc. Natl. Acad. Sci. U.S.A.* 99, 37–42. doi: 10.1073/pnas.012318899

Chung, K., Wallace, J., Kim, S. Y., Kalyanasundaram, S., Andalman, A. S., Davidson, T. J., et al. (2013). Structural and molecular interrogation of intact biological systems. *Nature* 497, 332–337. doi: 10.1038/nature12107

Cole, A. J., Saffen, D. W., Baraban, J. M., and Worley, P. F. (1989). Rapid increase of an immediate early gene messenger RNA in hippocampal neurons by synaptic NMDA receptor activation. *Nature* 340, 474–476. doi: 10.1038/340474a0

Conchello, J. A., and Lichtman, J. W. (2005). Optical sectioning microscopy. *Nat. Methods* 2, 920–931. doi: 10.1038/nmeth815

Costantini, I., Cicchi, R., Silvestri, L., Vanzi, F., and Pavone, F. S. (2019). In-vivo and ex-vivo optical clearing methods for biological tissues: review. *Biomed. Opt. Express* 10, 5251–5267. doi: 10.1364/boe.10.005251

Costantini, I., Ghobril, J. P., di Giovanna, A. P., Allegra Mascaro, A. L., Silvestri, L., Müllenbroich, M. C., et al. (2015). A versatile clearing agent for multi-modal brain imaging. *Sci. Rep.* 5, 1–9. doi: 10.1038/srep09808

Cowansage, K. K., Shuman, T., Dillingham, B. C., Chang, A., Golshani, P., and Mayford, M. (2014). Direct reactivation of a coherent neocortical memory of context. *Neuron* 84, 432–441. doi: 10.1016/j.neuron.2014.09.022

DeNardo, L., and Luo, L. (2017). Genetic strategies to access activated neurons. *Curr. Opin. Neurobiol.* 45, 121–129. doi: 10.1016/j.conb.2017.05.014

DeNardo, L. A., Liu, C. D., Allen, W. E., Adams, E. L., Friedmann, D., Fu, L., et al. (2019). Temporal evolution of cortical ensembles promoting remote memory retrieval. *Nat. Neurosci.* 22, 460–469. doi: 10.1038/s41593-018-0318-7

Dodt, H. U., Leischner, U., Schierloh, A., Jährling, N., Mauch, C. P., Deininger, K., et al. (2007). Ultramicroscopy: three-dimensional visualization of neuronal networks in the whole mouse brain. *Nat. Methods* 4, 331–336. doi: 10.1038/nmeth1036

Dombeck, D. A., Harvey, C. D., Tian, L., Looger, L. L., and Tank, D. W. (2010). Functional imaging of hippocampal place cells at cellular resolution during virtual navigation. *Nat. Neurosci.* 13, 1433–1440. doi: 10.1038/nn.2648

Economo, M. N., Clack, N. G., Lavis, L. D., Gerfen, C. R., Svoboda, K., Myers, E. W., et al. (2016). A platform for brain-wide imaging and reconstruction of individual neurons. *eLife* 5:e10566. doi: 10.7554/eLife.10566

Ertürk, A., Becker, K., Jährling, N., Mauch, C. P., Hojer, C. D., Egen, J. G., et al. (2012). Three-dimensional imaging of solvent-cleared organs using 3DISCO. *Nat. Protoc.* 7, 1983–1995. doi: 10.1038/nprot.2012.119

Fahrbach, F. O., and Rohrbach, A. (2012). Propagation stability of self-reconstructing Bessel beams enables contrast-enhanced imaging in thick media. *Nat. Commun.* 3:632. doi: 10.1038/ncomms1646

Feil, R., Wagner, J., Metzger, D., and Chambon, P. (1997). Regulation of Cre recombinase activity by mutated estrogen receptor ligand-binding domains. *Biochem. Biophys. Res. Commun.* 237, 752–757. doi: 10.1006/bbrc.1997.7124

Fosque, B. F., Sun, Y., Dana, H., Yang, C. T., Ohyama, T., Tadross, M. R., et al. (2015). Labeling of active neural circuits in vivo with designed calcium integrators. *Science* 347, 755–760. doi: 10.1126/science.1260922

Fowler, T., Sen, R., and Roy, A. L. (2011). Regulation of primary response genes. *Mol. Cell* 44, 348–360. doi: 10.1016/j.molcel.2011.09.014

Franklin, T. B., Silva, B. A., Perova, Z., Marrone, L., Masferrer, M. E., Zhan, Y., et al. (2017). Prefrontal cortical control of a brainstem social behavior circuit. *Nat. Neurosci.* 20, 260–270. doi: 10.1038/nn.4470

Frasconi, P., Silvestri, L., Soda, P., Cortini, R., Pavone, F. S., and Iannello, G. (2014). Large-scale automated identification of mouse brain cells in confocal light sheet microscopy images. *Bioinformatics* 30, i587–i593. doi: 10.1093/bioinformatics/btu469

Fürth, D., Vaissière, T., Tzortzi, O., Xuan, Y., Märtin, A., Lazaridis, I., et al. (2018). An interactive framework for whole-brain maps at cellular resolution. *Nat. Neurosci.* 21, 139–153. doi: 10.1038/s41593-017-0027-7

Garner, A. R., Rowland, D. C., Hwang, S. Y., Baumgaertel, K., Roth, B. L., Kentros, C., et al. (2012). Generation of a synthetic memory trace. *Science* 335, 1513–1516. doi: 10.1126/science.1214985

Ghosh, A., Ginty, D. D., Bading, H., and Greenberg, M. E. (1994). Calcium regulation of gene expression in neuronal cells. *J. Neurobiol.* 25, 294–303. doi: 10.1002/neu.480250309

Girasole, A. E., Lum, M. Y., Nathaniel, D., Bair-Marshall, C. J., Guenthner, C. J., Luo, L., et al. (2018). A subpopulation of striatal neurons mediates levodopa-induced dyskinesia. *Neuron* 97, 787–795.e6. doi: 10.1016/j.neuron.2018.01.017

Greenberg, M. E., Ziff, E. B., and Greene, L. A. (1986). Stimulation of neuronal acetylcholine receptors induces rapid gene transcription. *Science* 234, 80–83. doi: 10.1126/science.3749894

Guenthner, C. J., Miyamichi, K., Yang, H. H., Heller, H. C., and Luo, L. (2013). Permanent genetic access to transiently active neurons via TRAP: targeted recombination in active populations. *Neuron* 78, 773–784. doi: 10.1016/j.neuron.2013.03.025

Gupta, A., Harrison, P. J., Wieslander, H., Pielawski, N., Kartasalo, K., Partel, G., et al. (2019). Deep learning in image cytometry: a review. *Cytometry Part A* 95, 366–380. doi: 10.1002/cyto.a.23701

Guzowski, J. F., and Worley, P. F. (2001). Cellular compartment analysis of temporal activity by fluorescence in situ hybridization (catFISH). *Curr. Protoc. Neurosci.* 15, 1.8.1–1.8.16. doi: 10.1002/0471142301.ns0108s15

Hama, H., Hioki, H., Namiki, K., Hoshida, T., Kurokawa, H., Ishidate, F., et al. (2015). ScaleS: an optical clearing palette for biological imaging. *Nat. Neurosci.* 18, 1518–1529. doi: 10.1038/nn.4107

Hama, H., Kurokawa, H., Kawano, H., Ando, R., Shimogori, T., Noda, H., et al. (2011). Scale: a chemical approach for fluorescence imaging and reconstruction of transparent mouse brain. *Nat. Neurosci.* 14, 1481–1488. doi: 10.1038/nn.2928

Hasan, M. T., Althammer, F., Silva da Gouveia, M., Goyon, S., Eliava, M., Lefevre, A., et al. (2019). A fear memory engram and its plasticity in the hypothalamic oxytocin system. *Neuron* 103, 133–146.e8. doi: 10.1016/j.neuron.2019.04.029

He, Q., Wang, J., and Hu, H. (2019). Illuminating the activated brain: emerging activity-dependent tools to capture and control functional neural circuits. *Neurosci. Bull.* 35, 369–377. doi: 10.1007/s12264-018-0291-x

Helmchen, F., and Denk, W. (2005). Deep tissue two-photon microscopy. *Nat. Methods* 2, 932–940. doi: 10.1038/nmeth818

Hou, B., Zhang, D., Zhao, S., Wei, M., Yang, Z., Wang, S., et al. (2015). Scalable and DiI-compatible optical clearance of the mammalian brain. *Front. Neuroanat.* 9:19. doi: 10.3389/fnana.2015.00019

Hughes, P., Lawlor, P., and Dragunow, M. (1992). Basal expression of Fos, Fos-related, Jun, and Krox 24 proteins in rat hippocampus. *Mol. Brain Res.* 13, 355–357. doi: 10.1016/0169-328X(92)90219-2

Hunt, S. P., Pini, A., and Evan, G. (1988). Induction of c-fos-like protein in spinal cord neurons following sensory stimulation. *Nature* 328, 632–634. doi: 10.1038/328632a0

Ishii, K. K., Osakada, T., Mori, H., Miyasaka, N., Yoshihara, Y., Miyamichi, K., et al. (2017). A labeled-line neural circuit for pheromone-mediated sexual behaviors in mice. *Neuron* 95, 123–137.e8. doi: 10.1016/j.neuron.2017.05.038

Jacques, S. L. (2013). Optical properties of biological tissues: a review. *Phys. Med. Biol.* 58, R37–R61. doi: 10.1088/0031-9155/58/11/R37

Jiang-Xie, L. F., Yin, L., Zhao, S., Prevosto, V., Han, B. X., Dzirasa, K., et al. (2019). A common neuroendocrine substrate for diverse general anesthetics and sleep. *Neuron* 102, 1053–1065.e4. doi: 10.1016/j.neuron.2019.03.033

Jones, A. R., Overly, C. C., and Sunkin, S. M. (2009). The allen brain atlas: 5 years and beyond. *Nat. Rev. Neurosci.* 10, 821–828. doi: 10.1038/nrn2722

Kaczmarek, L., and Nikolajew, E. (1990). C-fos protooncogene expression and neuronal plasticity. *Acta Neurobiol. Exp.* 50, 173–179.

Kawashima, T., Kitamura, K., Suzuki, K., Nonaka, M., Kamijo, S., Takemoto-Kimura, S., et al. (2013). Functional labeling of neurons and their projections using the synthetic activity-dependent promoter E-SARE. *Nat. Methods* 10, 889–895. doi: 10.1038/nmeth.2559

Kawashima, T., Okuno, H., Nonaka, M., Adachi-Morishima, A., Kyo, N., Okamura, M., et al. (2009). Synaptic activity-responsive element in the Arc/Arg3.1 promoter essential for synapse-to-nucleus signaling in activated neurons. *Proc. Natl. Acad. Sci. U.S.A.* 106, 316–321. doi: 10.1073/pnas.0806518106

Ke, M. T., Fujimoto, S., and Imai, T. (2013). SeeDB: a simple and morphology-preserving optical clearing agent for neuronal circuit reconstruction. *Nat. Neurosci.* 16, 1154–1161. doi: 10.1038/nn.3447

Keller, P. J., and Dodt, H. U. (2012). Light sheet microscopy of living or cleared specimens. *Curr. Opin. Neurobiol.* 22, 138–143. doi: 10.1016/j.conb.2011.08.003

Kim, S. Y., Cho, J. H., Murray, E., Bakh, N., Choi, H., Ohn, K., et al. (2015). Stochastic electrotransport selectively enhances the transport of highly electromobile molecules. *Proc. Natl. Acad. Sci. U.S.A.* 112, E6274–E6283. doi: 10.1073/pnas.1510133112

Kim, W. B., and Cho, J. H. (2017). Encoding of discriminative fear memory by input-specific LTP in the amygdala. *Neuron* 95, 1129–1146.e5. doi: 10.1016/j.neuron.2017.08.004

Kim, Y., Venkataraju, K. U., Pradhan, K., Mende, C., Taranda, J., Turaga, S. C., et al. (2015). Mapping social behavior-induced brain activation at cellular resolution in the mouse. *Cell Rep.* 10, 292–305. doi: 10.1016/j.celrep.2014.12.014

Kim, Y., Yang, G. R., Pradhan, K., Venkataraju, K. U., Bota, M., García del Molino, L. C., et al. (2017). Brain-wide maps reveal stereotyped cell-type-based cortical architecture and subcortical sexual dimorphism. *Cell* 171, 456–469.e22. doi: 10.1016/j.cell.2017.09.020

Kirst, C., Skriabine, S., Vieites-Prado, A., Topilko, T., Bertin, P., Gerschenfeld, G., et al. (2020). Mapping the fine-scale organization and plasticity of the brain vasculature. *Cell* 180, 780–795.e25. doi: 10.1016/j.cell.2020.01.028

Klein, S., Staring, M., Murphy, K., Viergever, M. A., and Pluim, J. P. W. (2010). elastix: a toolbox for intensity-based medical image registration. *IEEE Trans. Med. Imaging* 29, 196–205. doi: 10.1109/TMI.2009.2035616

Koya, E., Golden, S. A., Harvey, B. K., Guez-Barber, D. H., Berkow, A., Simmons, D. E., et al. (2009). Targeted disruption of cocaine-activated nucleus accumbens neurons prevents context-specific sensitization. *Nat. Neurosci.* 12, 1069–1073. doi: 10.1038/nn.2364

Ku, T., Swaney, J., Park, J. Y., Albanese, A., Murray, E., Hun Cho, J., et al. (2016). Multiplexed and scalable super-resolution imaging of three-dimensional protein localization in size-adjustable tissues. *Nat. Biotechnol.* 34, 973–981. doi: 10.1038/nbt.3641

Kutten, K. S., Charon, N., Miller, M. I., Ratnanather, J. T., Matelsky, J., Baden, A. D., et al. (2017). "A large deformation diffeomorphic approach to registration of CLARITY images via mutual information," in *International Conference on Medical Image Computing and Computer-Assisted Intervention* (Berlin: Springer), 275–282. Available online at: https://link.springer.com/chapter/10.1007%2F978-3-319-66182-7_32

Kuwajima, T., Sitko, A. A., Bhansali, P., Jurgens, C., Guido, W., and Mason, C. (2013). ClearT: a detergent- and solvent-free clearing method for neuronal and non-neuronal tissue. *Development* 140, 1364–1368. doi: 10.1242/dev.091844

Lee, D., Hyun, J. H., Jung, K., Hannan, P., and Kwon, H. B. (2017). A calcium-A nd light-gated switch to induce gene expression in activated neurons. *Nat. Biotechnol.* 35, 858–863. doi: 10.1038/nbt.3902

Liu, X., Ramirez, S., Pang, P. T., Puryear, C. B., Govindarajan, A., Deisseroth, K., et al. (2012). Optogenetic stimulation of a hippocampal engram activates fear memory recall. *Nature* 484, 381–385. doi: 10.1038/nature11028

Logothetis, N. K. (2008). What we can do and what we cannot do with fMRI. *Nature* 453, 869–878. doi: 10.1038/nature06976

Magliaro, C., Callara, A. L., Vanello, N., and Ahluwalia, A. (2019). Gotta Trace 'em All: a mini-review on tools and procedures for segmenting single neurons toward deciphering the structural connectome. *Front. Bioeng. Biotechnol.* 7:202. doi: 10.3389/fbioe.2019.00202

Matsumoto, K., Mitani, T. T., Horiguchi, S. A., Kaneshiro, J., Murakami, T. C., Mano, T., et al. (2019). Advanced CUBIC tissue clearing for whole-organ cell profiling. *Nat. Protoc.* 14, 3506–3537. doi: 10.1038/s41596-019-0240-9

Mayford, M., and Reijmers, L. (2016). Exploring memory representations with activity-based genetics. *Cold Spring Harb. Perspect. Biol.* 8:a021832. doi: 10.1101/cshperspect.a021832

Menegas, W., Bergan, J. F., Ogawa, S. K., Isogai, Y., Umadevi Venkataraju, K., Osten, P., et al. (2015). Dopamine neurons projecting to the posterior striatum form an anatomically distinct subclass. *eLife* 4:e10032. doi: 10.7554/eLife.10032.001

Michel, C. M., and Brunet, D. (2019). EEG source imaging: a practical review of the analysis steps. *Front. Neurol.* 10:325. doi: 10.3389/fneur.2019.00325

Morgan, J. I., Cohen, D. R., Hempstead, J. L., and Curran, T. (1987). Mapping patterns of c-fos expression in the central nervous system after seizure. *Science* 237, 192–197. doi: 10.1126/science.3037702

Müllenbroich, M. C., Silvestri, L., di Giovanna, A. P., Mazzamuto, G., Costantini, I., Sacconi, L., et al. (2018a). High-fidelity imaging in brain-wide structural studies using light-sheet microscopy. *eNeuro* 5, 1–13. doi: 10.1523/ENEURO.0124-18.2018

Müllenbroich, M. C., Turrini, L., Silvestri, L., Alterini, T., Gheisari, A., Vanzi, F., et al. (2018b). Bessel beam illumination reduces random and systematic errors in quantitative functional studies using light-sheet microscopy. *Front. Cell. Neurosci.* 12:315. doi: 10.3389/fncel.2018.00315

Murakami, T. C., Mano, T., Saikawa, S., Horiguchi, S. A., Shigeta, D., Baba, K., et al. (2018). A three-dimensional single-cell-resolution whole-brain atlas using CUBIC-X expansion microscopy and tissue clearing. *Nat. Neurosci.* 21, 625–637. doi: 10.1038/s41593-018-0109-1

Murray, E., Cho, J. H., Goodwin, D., Ku, T., Swaney, J., Kim, S. Y., et al. (2015). Simple, scalable proteomic imaging for high-dimensional profiling of intact systems. *Cell* 163, 1500–1514. doi: 10.1016/j.cell.2015.11.025

Nöbauer, T., Skocek, O., Pernía-Andrade, A. J., Weilguny, L., Martínez Traub, F., Molodtsov, M. I., et al. (2017). Video rate volumetric Ca2+ imaging across cortex using seeded iterative demixing (SID) microscopy. *Nat. Methods* 14, 811–818. doi: 10.1038/nmeth.4341

Oh, S. W., Harris, J. a, Ng, L., Winslow, B., Cain, N., Mihalas, S., et al. (2014). A mesoscale connectome of the mouse brain. *Nature* 508, 207–214. doi: 10.1038/nature13186

Park, Y. G., Sohn, C. H., Chen, R., McCue, M., Yun, D. H., Drummond, G. T., et al. (2019). Protection of tissue physicochemical properties using polyfunctional crosslinkers. *Nat. Biotechnol.* 37:73. doi: 10.1038/nbt.4281

Paxinos, G., and Franklin, K. (2004). *The Mouse Brain in Stereotaxic Coordinates*. Available online at: https://books.google.com/books?hl=it&lr=&id=EHy1QN1xv0gC&oi=fnd&pg=PR9&ots=80XUsTGL_o&sig=LH9tOACXe-6e_bS9RGg87Ka688g (accessed June 1, 2020).

Peng, H., Zhou, J., Zhou, Z., Bria, A., Li, Y., Kleissas, D. M., et al. (2016). Bioimage informatics for big data. *Adv. Anat. Embryol. Cell Biol.* 219, 263–272. doi: 10.1007/978-3-319-28549-8_10

Perin, R., and Markram, H. (2013). A computer-assisted multi-electrode patch-clamp system. *J. Vis. Exp.* 80:e50630. doi: 10.3791/50630

Pinaud, R. (2004). Experience-dependent immediate early gene expression in the adult central nervous system: evidence from enriched-environment studies. *Int. J. Neurosci.* 114, 321–333. doi: 10.1080/00207450490264142

Power, R. M., and Huisken, J. (2017). A guide to light-sheet fluorescence microscopy for multiscale imaging. *Nat. Methods* 14, 360–373. doi: 10.1038/nmeth.4224

Prevedel, R., Yoon, Y. G., Hoffmann, M., Pak, N., Wetzstein, G., Kato, S., et al. (2014). Simultaneous whole-animal 3D imaging of neuronal activity using light-field microscopy. *Nat. Methods* 11, 727–730. doi: 10.1038/nmeth.2964

Ragan, T., Kadiri, L. R., Venkataraju, K. U., Bahlmann, K., Sutin, J., Taranda, J., et al. (2012). Serial two-photon tomography for automated ex vivo mouse brain imaging. *Nat. Methods* 9, 255–258. doi: 10.1038/nmeth.1854

Ramirez, S., Liu, X., Lin, P. A., Suh, J., Pignatelli, M., Redondo, R. L., et al. (2013). Creating a false memory in the hippocampus. *Science* 341, 387–391. doi: 10.1126/science.1239073

Ramirez, S., Liu, X., MacDonald, C. J., Moffa, A., Zhou, J., Redondo, R. L., et al. (2015). Activating positive memory engrams suppresses depression-like behaviour. *Nature* 522, 335–339. doi: 10.1038/nature14514

Redondo, R. L., Kim, J., Arons, A. L., Ramirez, S., Liu, X., and Tonegawa, S. (2014). Bidirectional switch of the valence associated with a hippocampal contextual memory engram. *Nature* 513, 426–430. doi: 10.1038/nature13725

Reijmers, L. G., Perkins, B. L., Matsuo, N., and Mayford, M. (2007). Localization of a stable neural correlate of associative memory. *Science* 317, 1230–1233. doi: 10.1126/science.1143839

Renier, N., Adams, E. L., Kirst, C., Wu, Z., Azevedo, R., Kohl, J., et al. (2016). Mapping of brain activity by automated volume analysis of immediate early genes. *Cell* 165, 1789–1802. doi: 10.1016/j.cell.2016.05.007

Renier, N., Wu, Z., Simon, D. J., Yang, J., Ariel, P., and Tessier-Lavigne, M. (2014). IDISCO: a simple, rapid method to immunolabel large tissue samples for volume imaging. *Cell* 159, 896–910. doi: 10.1016/j.cell.2014.10.010

Richardson, D. S., and Lichtman, J. W. (2015). Clarifying tissue clearing. *Cell* 162, 246–257. doi: 10.1016/j.cell.2015.06.067

Rodriguez, E., Sakurai, K., Xu, J., Chen, Y., Toda, K., Zhao, S., et al. (2017). A craniofacial-specific monosynaptic circuit enables heightened affective pain. *Nat. Neurosci.* 20, 1734–1743. doi: 10.1038/s41593-017-0012-1

Sagar, S. M., Sharp, F. R., and Curran, T. (1988). Expression of c-fos protein in brain: metabolic mapping at the cellular level. *Science* 240, 1328–1331. doi: 10.1126/science.3131879

Sakurai, K., Zhao, S., Takatoh, J., Rodriguez, E., Lu, J., Leavitt, A. D., et al. (2016). Capturing and manipulating activated neuronal ensembles with CANE delineates a hypothalamic social-fear circuit. *Neuron* 92, 739–753. doi: 10.1016/j.neuron.2016.10.015

Sancataldo, G., Silvestri, L., Mascaro, A. L. A., Sacconi, L., and Pavone, A. F. S. (2019). Advanced fluorescence microscopy for in vivo imaging of neuronal activity. *Optica* 6:758. doi: 10.1364/OPTICA.6.000758

Sbalzarini, I. F. (2016). Seeing is believing: quantifying is convincing: computational image analysis in biology. *Adv. Anat. Embryol. Cell Biol.* 219, 1–39. doi: 10.1007/978-3-319-28549-8_1

Scholz, J., LaLiberté, C., van Eede, M., Lerch, J. P., and Henkelman, M. (2016). Variability of brain anatomy for three common mouse strains. *NeuroImage* 142, 656–662. doi: 10.1016/j.neuroimage.2016.03.069

Seiriki, K., Kasai, A., Hashimoto, T., Schulze, W., Niu, M., Yamaguchi, S., et al. (2017). High-speed and scalable whole-brain imaging in rodents and primates. *Neuron* 94, 1085–1100.e6. doi: 10.1016/j.neuron.2017.05.017

Sheng, M., and Greenberg, M. E. (1990). The regulation and function of c-fos and other immediate early genes in the nervous system. *Neuron* 4, 477–485. doi: 10.1016/0896-6273(90)90106-P

Shimshek, D. R., Kim, J., Hübner, M. R., Spergel, D. J., Buchholz, F., Casanova, E., et al. (2002). Codon-improved Cre recombinase (iCre) expression in the mouse. *Genesis* 32, 19–26. doi: 10.1002/gene.10023

Shockett, P. E., and Schatz, D. G. (1996). Diverse strategies for tetracycline-regulated inducible gene expression. *Proc. Natl. Acad. Sci. U.S.A.* 93, 5173–5176. doi: 10.1073/pnas.93.11.5173

Silvestri, L., Costantini, I., Sacconi, L., and Pavone, F. S. (2016). Clearing of fixed tissue: a review from a microscopist's perspective. *J. Biomed. Opt.* 21:081205. doi: 10.1117/1.JBO.21.8.081205

Silvestri, L., Muellenbroich, M. C., Costantini, I., Di Giovanna, A. P., Sacconi, L., and Pavone, F. S. (2017). RAPID: real-time image-based autofocus for all wide-field optical microscopy systems. *bioRxiv* [Preprint]. doi: 10.1101/170555 bioRxiv170555,

Silvestri, L., Paciscopi, M., Soda, P., Biamonte, F., Iannello, G., Frasconi, P., et al. (2015). Quantitative neuroanatomy of all Purkinje cells with light sheet microscopy and high-throughput image analysis. *Front. Neuroanat.* 9:68. doi: 10.3389/fnana.2015.00068

Smeyne, R. J., Schilling, K., Robertson, L., Luk, D., Oberdick, J., Curran, T., et al. (1992). Fos-IacZ transgenic mice: mapping sites of gene induction in the central nervous system. *Neuron* 8, 13–23. doi: 10.1016/0896-6273(92)90105-M

Sørensen, A. T., Cooper, Y. A., Baratta, M. v, Weng, F. J., Zhang, Y., Ramamoorthi, K., et al. (2016). A robust activity marking system for exploring active neuronal ensembles. *eLife* 5:e13918. doi: 10.7554/eLife.13918

Spalteholz, W. (1914). *Über das Durchsichtigmachen von Menschlichen und Tierischen Präparaten und Seine Theoretischen Bedingungen, Nebst Anhang: Über Knochenfärbung*. North Andover, MA: S. Hirzel.

Staudt, T., Lang, M. C., Medda, R., Engelhardt, J., and Hell, S. W. (2007). 2,2'-thiodiethanol: a new water soluble mounting medium for high resolution optical microscopy. *Microsc. Res. Tech.* 70, 1–9. doi: 10.1002/jemt.20396

Susaki, E. A., Shimizu, C., Kuno, A., Tainaka, K., Li, X., Nishi, K., et al. (2020). Versatile whole-organ/body staining and imaging based on electrolyte-gel properties of biological tissues. *Nat. Commun.* 11:1982. doi: 10.1038/s41467-020-15906-5

Susaki, E. A., Tainaka, K., Perrin, D., Kishino, F., Tawara, T., Watanabe, T. M., et al. (2014). Whole-brain imaging with single-cell resolution using chemical cocktails and computational analysis. *Cell* 157, 726–739. doi: 10.1016/j.cell.2014.03.042

Tainaka, K., Kubota, S. I., Suyama, T. Q., Susaki, E. A., Perrin, D., Ukai-Tadenuma, M., et al. (2014). Whole-body imaging with single-cell resolution by tissue decolorization. *Cell* 159, 911–924. doi: 10.1016/j.cell.2014.10.034

Tainaka, K., Kuno, A., Kubota, S. I., Murakami, T., and Ueda, H. R. (2016). Chemical principles in tissue clearing and staining protocols for whole-body cell profiling. *Annu. Rev. Cell Dev. Biol.* 32, 713–741. doi: 10.1146/annurev-cellbio-111315-125001

Tatsuki, F., Sunagawa, G. A. A., Shi, S., Susaki, E. A. A., Yukinaga, H., Perrin, D., et al. (2016). Involvement of Ca2+-dependent hyperpolarization in sleep duration in mammals. *Neuron* 90, 70–85. doi: 10.1016/j.neuron.2016.02.032

Terleph, T. A., and Tremere, L. A. (2006). "The use of immediate early genes as mapping tools for neuronal activation: concepts and methods," in *Immediate Early Genes in Sensory Processing, Cognitive Performance and Neurological Disorders*, eds R. Pinaud and L. A. Tremere (Boston, MA: Springer). doi: 10.1007/978-0-387-33604-6_1

Todorov, M. I., Paetzold, J. C., Schoppe, O., Tetteh, G., Shit, S., Efremov, V., et al. (2020). Machine learning analysis of whole mouse brain vasculature. *Nat. Methods* 17, 442–449. doi: 10.1038/s41592-020-0792-1

Tomer, R., Ye, L., Hsueh, B., and Deisseroth, K. (2014). Advanced CLARITY for rapid and high-resolution imaging of intact tissues. *Nat. Protoc.* 9, 1682–1697. doi: 10.1038/nprot.2014.123

Tschida, K., Michael, V., Takatoh, J., Han, B. X., Zhao, S., Sakurai, K., et al. (2019). A specialized neural circuit gates social vocalizations in the mouse. *Neuron* 103, 459–472.e4. doi: 10.1016/j.neuron.2019.05.025

Tuchin, V. v (1997). Light propagation in tissues with controlled optical properties. *J. Biomed. Opt.* 2:401. doi: 10.1117/12.281502

Ueda, H. R., Dodt, H. U., Osten, P., Economo, M. N., Chandrashekar, J., and Keller, P. J. (2020). Whole-brain profiling of cells and circuits in mammals by tissue clearing and light-sheet microscopy. *Neuron* 106, 369–387. doi: 10.1016/j.neuron.2020.03.004

Vanni, M. P., Chan, A. W., Balbi, M., Silasi, G., and Murphy, T. H. (2017). Mesoscale mapping of mouse cortex reveals frequency-dependent cycling between distinct macroscale functional modules. *J. Neurosci.* 37, 7513–7533. doi: 10.1523/JNEUROSCI.3560-16.2017

Vetere, G., Kenney, J. W., Tran, L. M., Xia, F., Steadman, P. E., Parkinson, J., et al. (2017). Chemogenetic interrogation of a brain-wide fear memory network in mice. *Neuron* 94, 363–374.e4. doi: 10.1016/j.neuron.2017.03.037

Voigt, F. F., Kirschenbaum, D., Platonova, E., Pagès, S., Campbell, R. A. A., Kastli, R., et al. (2019). The mesoSPIM initiative: open-source light-sheet microscopes

for imaging cleared tissue. *Nat. Methods* 16, 1105–1108. doi: 10.1038/s41592-019-0554-0

Vousden, D. A., Epp, J., Okuno, H., Nieman, B. J., van Eede, M., Dazai, J., et al. (2015). Whole-brain mapping of behaviourally induced neural activation in mice. *Brain Struct. Funct.* 220, 2043–2057. doi: 10.1007/s00429-014-0774-0

Wang, K. H., Majewska, A., Schummers, J., Farley, B., Hu, C., Sur, M., et al. (2006). In vivo two-photon imaging reveals a role of Arc in enhancing orientation specificity in visual cortex. *Cell* 126, 389–402. doi: 10.1016/j.cell.2006.06.038

Wang, W., Wildes, C. P., Pattarabanjird, T., Sanchez, M. I., Glober, G. F., Matthews, G. A., et al. (2017). A light- A nd calcium-gated transcription factor for imaging and manipulating activated neurons. *Nat. Biotechnol.* 35, 864–871. doi: 10.1038/nbt.3909

Wilson, T. (2010). Spinning-disk microscopy systems. *Cold Spring Harb. Protoc.* 5:db.to88. doi: 10.1101/pdb.top88

Winnubst, J., Bas, E., Ferreira, T. A., Wu, Z., Economo, M. N., Edson, P., et al. (2019). Reconstruction of 1,000 projection neurons reveals new cell types and organization of long-range connectivity in the mouse brain. *Cell* 179, 268–281.e13. doi: 10.1016/j.cell.2019.07.042

Xie, H., Liu, Y., Zhu, Y., Ding, X., Yang, Y., and Guan, J. S. (2014). In vivo imaging of immediate early gene expression reveals layer-specific memory traces in the mammalian brain. *Proc. Natl. Acad. Sci. U.S.A.* 111, 2788–2793. doi: 10.1073/pnas.1316808111

Xiu, J., Zhang, Q., Zhou, T., Zhou, T. T., Chen, Y., and Hu, H. (2014). Visualizing an emotional valence map in the limbic forebrain by TAI-FISH. *Nat. Neurosci.* 17, 1552–1559. doi: 10.1038/nn.3813

Yang, B., Treweek, J. B., Kulkarni, R. P., Deverman, B. E., Chen, C. K., Lubeck, E., et al. (2014). Single-cell phenotyping within transparent intact tissue through whole-body clearing. *Cell* 158, 945–958. doi: 10.1016/j.cell.2014.07.017

Yang, W., and Yuste, R. (2017). In vivo imaging of neural activity. *Nat. Methods* 14, 349–359. doi: 10.1038/nmeth.4230

Ye, L., Allen, W. E., Thompson, K. R., Tian, Q., Hsueh, B., Ramakrishnan, C., et al. (2016). Wiring and molecular features of prefrontal ensembles representing distinct experiences. *Cell* 165, 1776–1788. doi: 10.1016/j.cell.2016.05.010

Yu, T., Zhu, J., Li, Y., Ma, Y., Wang, J., Cheng, X., et al. (2018). RTF: a rapid and versatile tissue optical clearing method. *Sci. Rep.* 8, 1–9. doi: 10.1038/s41598-018-20306-3

Zipfel, W. R., Williams, R. M., and Webb, W. W. (2003). Nonlinear magic: multiphoton microscopy in the biosciences. *Nat. Biotechnol.* 21, 1369–1377. doi: 10.1038/nbt899

Conflict of Interest: The authors declare that the research was conducted in the absence of any commercial or financial relationships that could be construed as a potential conflict of interest.

Copyright © 2020 Franceschini, Costantini, Pavone and Silvestri. This is an open-access article distributed under the terms of the Creative Commons Attribution License (CC BY). The use, distribution or reproduction in other forums is permitted, provided the original author(s) and the copyright owner(s) are credited and that the original publication in this journal is cited, in accordance with accepted academic practice. No use, distribution or reproduction is permitted which does not comply with these terms.

frontiers in Neuroscience

ORIGINAL RESEARCH
published: 25 November 2020
doi: 10.3389/fnins.2020.570019

Alterations in Sub-Axonal Architecture Between Normal Aging and Parkinson's Diseased Human Brains Using Label-Free Cryogenic X-ray Nanotomography

Hung Tri Tran[1], Esther H. R. Tsai[1†], Amanda J. Lewis[2], Tim Moors[3], J. G. J. M. Bol[3], Iman Rostami[1], Ana Diaz[1], Allert J. Jonker[3], Manuel Guizar-Sicairos[1], Joerg Raabe[1], Henning Stahlberg[2], Wilma D. J. van de Berg[3], Mirko Holler[1] and Sarah H. Shahmoradian[1]*

[1] Paul Scherrer Institut, Villigen, Switzerland, [2] Center for Cellular Imaging and NanoAnalytics (C-CINA), Biozentrum, University of Basel, Basel, Switzerland, [3] Department of Anatomy and Neurosciences, Section Clinical Neuroanatomy, Amsterdam Neuroscience, Amsterdam UMC, Vrije Universiteit Amsterdam, Amsterdam, Netherlands

OPEN ACCESS

Edited by:
Alard Roebroeck, Maastricht University, Netherlands

Reviewed by:
Amit Sethi, Indian Institute of Technology Bombay, India
Matthew ManHin Cheung, CUHK Medical Centre, Hong Kong

***Correspondence:**
Sarah H. Shahmoradian
sarah.shahmoradian@psi.ch;
sarah.shahmoradian@unibas.ch

†Present address:
Esther H. R. Tsai
Center for Functional Nanomaterials, Brookhaven National Laboratory, Upton, NY, United States

Specialty section:
This article was submitted to Brain Imaging Methods, a section of the journal Frontiers in Neuroscience

Received: *05 June 2020*
Accepted: *14 October 2020*
Published: *25 November 2020*

Citation:
Tran HT, Tsai EHR, Lewis AJ, Moors T, Bol JGJM, Rostami I, Diaz A, Jonker AJ, Guizar-Sicairos M, Raabe J, Stahlberg H, van de Berg WDJ, Holler M and Shahmoradian SH (2020) Alterations in Sub-Axonal Architecture Between Normal Aging and Parkinson's Diseased Human Brains Using Label-Free Cryogenic X-ray Nanotomography. Front. Neurosci. 14:570019. doi: 10.3389/fnins.2020.570019

Gaining insight to pathologically relevant processes in continuous volumes of unstained brain tissue is important for a better understanding of neurological diseases. Many pathological processes in neurodegenerative disorders affect myelinated axons, which are a critical part of the neuronal circuitry. Cryo ptychographic X-ray computed tomography in the multi-keV energy range is an emerging technology providing phase contrast at high sensitivity, allowing label-free and non-destructive three dimensional imaging of large continuous volumes of tissue, currently spanning up to 400,000 μm^3. This aspect makes the technique especially attractive for imaging complex biological material, especially neuronal tissues, in combination with downstream optical or electron microscopy techniques. A further advantage is that dehydration, additional contrast staining, and destructive sectioning/milling are not required for imaging. We have developed a pipeline for cryo ptychographic X-ray tomography of relatively large, hydrated and unstained biological tissue volumes beyond what is typical for the X-ray imaging, using human brain tissue and combining the technique with complementary methods. We present four imaged volumes of a Parkinson's diseased human brain and five volumes from a non-diseased control human brain using cryo ptychographic X-ray tomography. In both cases, we distinguish neuromelanin-containing neurons, lipid and melanic pigment, blood vessels and red blood cells, and nuclei of other brain cells. In the diseased sample, we observed several swellings containing dense granular material resembling clustered vesicles between the myelin sheaths arising from the cytoplasm of the parent oligodendrocyte, rather than the axoplasm. We further investigated the pathological relevance of such swollen axons in adjacent tissue sections by immunofluorescence microscopy for phosphorylated alpha-synuclein combined with multispectral imaging. Since cryo ptychographic X-ray tomography is non-destructive, the large dataset volumes were used to guide further investigation of such swollen

axons by correlative electron microscopy and immunogold labeling post X-ray imaging, a possibility demonstrated for the first time. Interestingly, we find that protein antigenicity and ultrastructure of the tissue are preserved after the X-ray measurement. As many pathological processes in neurodegeneration affect myelinated axons, our work sets an unprecedented foundation for studies addressing axonal integrity and disease-related changes in unstained brain tissues.

Keywords: human brain, neurodegeneration, Tomography – X-ray computed, Parkinson's and related diseases, label-free, electron microscograpy, ptychography, axons

INTRODUCTION

Multi-scale visualization of the hierarchical organization of human brain is critical to neuroscience. Micro- and nanomorphology of the neuronal network is tightly linked with the brain's functionality, from the macroscopic level, i.e., specialized populations of neurons, to the nanoscopic level, i.e., synaptic connections between individual neurons. Large-scale, label-free 3D imaging at nanoscale resolution of near-native state tissues can reveal new insights to such hierarchically organized neuronal structures.

The neuronal network of the human brain is complex. Neurons communicate via their extensions known as dendrites or axons. Axons are often wrapped in segments of lipid membrane sheaths known as myelin, which provide it with insulating and stabilizing properties. Myelin sheaths are essentially flattened portions of extensions of the cell membrane of oligodendrocytes. The high lipid content of myelin sheaths encasing the axon serves to enhance conduction velocity (Nave and Werner, 2014). Myelinated axons are a critical part of the neuronal circuitry and constitute approximately 40% of the human brain (Morell and Norton, 1980).

Neurites, especially myelinated axons, are a critical functional component of brain cells, serving as highways of cross-communication. They relay physical cargo and electrical signals from one neuron to another. Pathologically related aggregation processes within the axon can cause a localized swelling that interferes with normal trafficking (Chevalier-Larsen and Holzbaur, 2006). Alzheimer's disease, Parkinson's disease, and multiple sclerosis are a few examples of such diseases (Su et al., 1993; Adalbert et al., 2009; Inglese and Petracca, 2013; Lee et al., 2014; Friese, 2016) in which axonal integrity is affected. The ability to image several axons and their inner contents at once is particularly advantageous when applied to diseased and degenerative brain conditions in which neurites are pathologically involved or affected. Capturing a wide and inclusive view of features in normal and dystrophic axons within the tissue can permit new insights to the axonal component of pathology in neurodegenerative diseases, which is not well understood.

Synchrotron X-ray micro-tomography is an imaging technique that can be used to map neural circuits in brain tissue with reported resolutions of down to 1 μm, using heavy-metal staining such as silver nitrate for contrast enhancement and oftentimes plastic- or paraffin-embedding for rigid preservation (Mizutani et al., 2009; de Castro Fonseca et al., 2018). Phase contrast has also been used in propagation-based X-ray imaging to obtain high-quality 3D images of myelinated axons (Dyer et al., 2017). However, the resolution in these techniques is insufficient for a detailed morphological characterization of axons. Lens-based X-ray microscopy makes use of X-ray optics for magnification, as in holo-tomography, for example (Khimchenko et al., 2018). At the water window, i.e., at photon energies between 281 and 533 eV, carbon-rich structures in biological tissue exhibit a high contrast compared to water. In this way, biological matter can be imaged in 3D at a resolution of about 30 nm, albeit with a depth limited to a couple of micrometers (Le Gros et al., 2016; Pérez-Berná et al., 2016).

However, for imaging myelinated axons, volumes of several tens of micrometers are required while preserving a high spatial resolution, for which harder X-rays with photon energies above about 2 keV are necessary. Despite the difficulty to fabricate optimally efficient lenses for hard X-rays, lens-based microscopy of neural tissue has been demonstrated (Wu et al., 2012). Additionally, propagation-based hard X-ray microscopy can be achieved by using a divergent beam to produce magnified images (Mokso et al., 2007; Bartels et al., 2015), which allowed resolving myelinated axons within resin-embedded nerves specimens (Bartels et al., 2015; Kuan et al., 2020).

In contrast, ptychographic X-ray computed tomography (PXCT) is a lens-less technique in which spatial resolution is not limited by imaging optics. It currently allows reaching a resolution down to about 15 nm in 3D (Holler et al., 2014, 2017a) on specimens that exhibit small features with sufficient density contrast. As density contrast is small in biological samples for hard X-rays, resolution has been typically limited to the 100 nm range in both stained, resin-embedded and frozen-hydrated specimens (Diaz et al., 2015; Pfister et al., 2016; Shahmoradian et al., 2017b). However, the sensitivity of PXCT is high enough to visualize ultrastructural features in fully hydrated samples without requiring heavy metal staining for contrast purposes, or destruction of material (ion beam milling, sectioning) for accessing tissue depths (Shahmoradian et al., 2017b). These are important factors for enabling multi-scale downstream processing in a relatively minimally perturbed state. The OMNY instrument (Holler et al., 2018) allows cryogenic PXCT (cryo-PXCT) measurements of biological samples in cryo conditions and under vacuum, forming a powerful label-free microscopy technique.

All of the resulting ultrastructural information from cryo-PXCT data can be correlated to electron density, directly interpretable from the grayscale values of the tomographic data,

which can be, in turn, related to its local mass density using reasonable assumptions about the stoichiometric composition (Diaz et al., 2015). This is useful for attributing an identity to each ultrastructural feature within the complex and crowded tissue landscape. Cryo-PXCT at photon energies between about 6 and 8 keV has the ability to provide information across relatively large volumes of unstained tissue, enabling the imaging of multiple cell bodies and the tracking of morphological intracellular changes along the lengths of radiating structures such as cellular extensions; in the case of brain tissue, along the length of neuronal processes.

Using cryo-PXCT, the visualization of tissue contents including myelinated axons at a resolution in the 100 nm range is independent of pre-marking selected features using pigment-based or fluorescent labels (Kremers et al., 2011; Shu et al., 2011; Manning et al., 2012; Lam et al., 2015). This enables a wide and inclusive view of numerous features existing in the tissue, including normal and dystrophic axons, which are otherwise easily missed or unintentionally excluded.

Parkinson's disease is a complex neurodegenerative disease, the second most common after Alzheimer's disease, in which the axonal component of pathology is not well understood. While axonal pathology, including swollen (dystrophic) axons and alterations in axonal transport, have been extensively noted in Parkinson's disease patients, animal and cell culture-based models, little is known beyond the facts that they can appear physically swollen, have slower vesicular transport and contain aggregated material including alpha-synuclein (aSyn), beta-synuclein, and gamma-synuclein (Galvin et al., 1999; Kotzbauer et al., 2004; Saha et al., 2004; Chung et al., 2009; Burke and O'Malley, 2013; Koch et al., 2015; Sekigawa et al., 2015; Tagliaferro and Burke, 2016; Kouroupi et al., 2017). Correlative light and electron microscopy of Parkinson's diseased human brain tissue sections has recently shown such dystrophic axons, specifically Lewy neurites, to contain vesicular structures, dysmorphic mitochondria and disrupted cytoskeletal elements (Shahmoradian et al., 2017a). However, imaging several dystrophic axons and their contained ultrastructures simultaneously is not efficient by electron microscopy alone. Cryo-PXCT enables the simultaneous visualization of several axons and the subtleties within and throughout each axon that are easily missed unless visualizing a continuous length, i.e., across tens of microns, up to $(100\ \mu m)^3$. Such subtleties include, but are not limited to, disruptions or abnormalities within the myelin sheath wrappings at specific points along the length of the axon, or abnormalities within the axon itself.

Beyond generating a 3D picture of multiple axons and brain cells to recognize pathologically relevant features, cryo-PXCT allows for the tissue to remain intact at the nanoscale after imaging. This aspect opens up the unique possibility of downstream processing of selected features of interest by higher resolution techniques such as electron microscopy, as also shown herein, or gaining biochemical information by different spectroscopic-based imaging approaches, such as Fourier-transform infrared spectroscopy (FTIR), coherent anti-Stokes Raman spectroscopy (CARS), and matrix-assisted laser desorption/ionization mass spectroscopy imaging (MALDI-IMS).

Starting with several chemically fixed, hydrated tissue blocks from a postmortem Parkinson's diseased human brain and from a control/non-demented human brain, we processed and imaged these by cryo-PXCT, followed by cryo-ultramicrotomy and cryo-immunogold labeling and electron microscopy. We thus demonstrate a multi-scale imaging pipeline using cryo-PXCT followed by immuno-electron microscopy, with a cross investigation of pathological features of interest using fluorescence microscopy combined with multispectral imaging.

RESULTS

Cryo-PXCT Imaging, Feature Segmentation and Quantification

Cryo-PXCT using the OMNY (tOMography Nano crYo) instrument (Holler et al., 2018) at the cSAXS beamline of the Swiss Light Source was utilized to visualize five and four brain tissue samples, respectively (**Table 1**) from a control, non-demented donor and a Parkinson's diseased donor (**Table 2**, Donors B and D). Cryo-PXCT was used to identify pathological-related abnormalities in postmortem brain tissue from Parkinson's diseased (PD) human patients, within roughly cubic volumes spanning $\sim(100\ \mu m)^3$ at a resolution ranging from 145 to 390 nm. The *substantia nigra pars compacta* (SNpc) brain region was selected for dissection and imaging since this region typically contains the most Lewy pathology in the context of dopaminergic degeneration (Fearnley and Lees, 1991). Samples were prepared according to a pre-established protocol optimal for cryo-PXCT imaging of mouse brain tissue (Shahmoradian et al., 2017b), with an improved trimming procedure (**Figure 1**) for more efficient imaging.

Four cryo-PXCT tomographic datasets were generated from four separate blocks of human postmortem brain tissue from a PD brain donor (**Table 1**, Movies 5–8). As a control, five cryo-PXCT tomographic datasets were generated from five separate blocks of human postmortem brain tissue from a non-demented, age-matched control human brain donor (**Table 1**, Movies 1–4), three of which are shown as virtual slices in **Figure 1**.

The tomograms showed neuromelanin-containing cells typical of the *substantia nigra* region (**Figure 1**, white dotted lines), as well as the cross-sections of myelinated axons (high contrast ellipsoid and circular structures). Nuclei (**Figure 1**, yellow dotted lines) of these neuromelanin-containing cells, and a smaller dense nucleolus (**Figure 1a**, white arrowhead), were also visible. Nuclei likely corresponding to microglial cells were observed as an elongated, irregular nucleus with characteristic peripheral heterochromatin and heterochromatin net made of multiple fused granules (García-Cabezas et al., 2016) (**Figure 1**, orange double-arrowhead), and dense, round nuclei were also visible (**Figure 1**, orange single-arrowheads). Following 3D color segmentation of the tomograms, the identity of several other features became more apparent. One tomogram from each group (control and PD) was selected for subsequent 3D color segmentation (**Figures 2**, **3**, Movies 1 and 5, respectively).

TABLE 1 | Imaging parameters and characteristics of biological samples imaged by cryo-PXCT using OMNY.

	Control brain donors					Parkinson's diseased brain donors			
	Tomo 1	Tomo 2	Tomo 3	Tomo 4	Tomo 5	Tomo 1	Tomo 2	Tomo 3	Tomo 4
Data collection	33 h	28 h	19 h	35 h	34 h	37 h	31 h	62 h	42 h
Volume imaged	230,000 μm^3	123,000 μm^3	55,000 μm^3	260,000 μm^3	204,000 μm^3	400,000 μm^3	258,000 μm^3	426,000 μm^3	220,000 μm^3
Dimensions (X,Y)	150 μm	120 μm	110 μm	110 μm	140 μm	160 μm	112 μm	150 μm	120 μm
Depth (Z)	30 μm	25 μm	20 μm	50 μm	30 μm	35 μm	50 μm	50 μm	40 μm
Projections	750	850	850	700	600	800	640	1100	700
Estimated dose	9 MGy	9 MGy	9 MGy	7 MGy	4 MGy	15 MGy	11 MGy	19 MGy	12 MGy
3D resolution estimation	255 nm	215 nm	145 nm	240 nm	245 nm	280 nm	270 nm	250 nm	190 nm
						(2D) 380 nm	(2D) 390 nm		

Table represents the volume imaged per tomogram, data collection time, dimensions in X-Y-Z of the imaged region of the tissue block, projections used for tomographic reconstruction, estimated dose (MGy), and estimated 3D resolution, for each of the samples. Tomo 5 (control human brain, Movie 1) and Tomo 4 (Parkinson's diseased human brain, Movie 5), shown in black-outlined rectangles, were selected for 3D color segmentation. Control: Tomo 1 = Movie 2; Tomo 2 = Movie 3; Tomo 3 = movie not shown; Tomo 4 = Movie 4; Tomo 5 = Movie 1. Parkinson's diseased: Tomo 1 = Movie 6; Tomo 2 = Movie 7; Tomo 3 = Movie 8.

TABLE 2 | Clinical and pathological characteristics of brain donors.

Donor	Diagnosis	Age at onset (years)	Age at death (years)	Sex	PMD (hrs:min)	Braak aSyn stage
A	PDD	59	77	M	5:15	6
B	PDD	75	90	F	4:45	6
C	NDC	–	85	F	6:25	0
D	NDC	–	92	M	7:45	0
E	NDC	–	89	F	13:00	0

PDD, Parkinson's disease with dementia; age-at-onset, age at clinical diagnosis of PD; n.a., not applicable; NDC, non-demented control; aSyn, α-synuclein; PMD, postmortem delay. Age at onset, age at clinical diagnosis of PD. Donors B and D were used for cryo-PXCT and cryo immuno-electron microscopy. All donors were used for optical microscopy studies.

While features such as neuromelanin-containing cells, blood vessels, glial nuclei, and myelinated axons could all similarly be segmented from both control and PD cryo-PXCT human brain tomograms (**Figures 2**, **3**), one feature that was uniquely observed in all four PD brain datasets as compared to all five control brain datasets was the presence of swellings within the myelinated axons (**Figures 3b,d**, purple segments within the aqua axons; **Figure 4** and **Supplementary Figures 1, 2**, yellow crosses) as compared to the rest of the axons (**Figures 3b,d**, aqua axons). These swellings were in close proximity to the neuromelanin-containing cells, which are majorly affected in PD. Different views of approximately ten of these swellings, or dystrophic myelinated axons (DMAs) are shown at greater detail within one of the PD brain tomograms (**Figure 4** and **Supplementary Figures 1, 2**; yellow crosses). The variability of the type of swelling is more apparent when the DMAs are visualized in 3D color segmentations, four of which are shown in **Figure 5**. For example, the inner part of the axon, or axoplasm, can appear relatively "normal" and consistent in diameter along the length of the axon (**Figures 5a–c**) with the swelling rather occurring in the layers comprising the myelin sheath of the axon, or the axoplasm itself can also become swollen (**Figure 5d**).

Two types of DMAs were identified and characterized by cryo-PXCT: one population we refer to as SWiA (swollen in axoplasm) and another as SWiM (swollen in myelin). "In axoplasm" refers to cytoskeletal part of the axon that is in direct continuation from the neuron (**Figure 6b**), whereas "in myelin cytoplasm" refers to the cytoplasm within the myelin sheaths (**Figure 6c**) corresponding to that of the parent oligodendrocyte rather than the neuron (Fields, 2014). Since the resolution of these reconstructed tomograms enables distinguishing the axoplasm from the myelin sheath, especially when the myelin sheath appears to have partially separated, we could detect dense granular cytoplasmic material comprising these DMAs that appeared surprisingly often within the wrappings of the myelin sheath (**Figures 4a–c** and **Supplementary Figure 1** all excluding A–C, 2) of the parent oligodendrocyte, hence the SWiM type, rather than simply within the axonal passage itself (the SWiA type). This was counter-intuitive considering that the clogging of the axon was not mainly occurring in the axonal passage itself, but rather in the exterior myelin sheaths compromising the axon.

Typically, axonal traffic jams associated with neurodegenerative disease are generally attributed to material accumulating within the axonal passage itself (Kuusisto et al., 2003; Chevalier-Larsen and Holzbaur, 2006; Doorn et al., 2014) thereby resulting in a local swelling of the SWiA type, which we did observe albeit to a lesser extent (**Figure 4** "DMA2" A–C and **Supplementary Figures 1A–C**). Overall, 74% (40) of DMAs were found to be the SWiM type (**Figure 6c**), corresponding to a swelling within the cytoplasm of the actual myelin sheath, while 26% (14) of DMAs were found to correspond to the SWiA type (**Figure 6b**), corresponding to the more intuitive case of a swelling within the neuronal cytoplasm inside the axon itself (**Supplementary Figure 4A**). Quantification performed

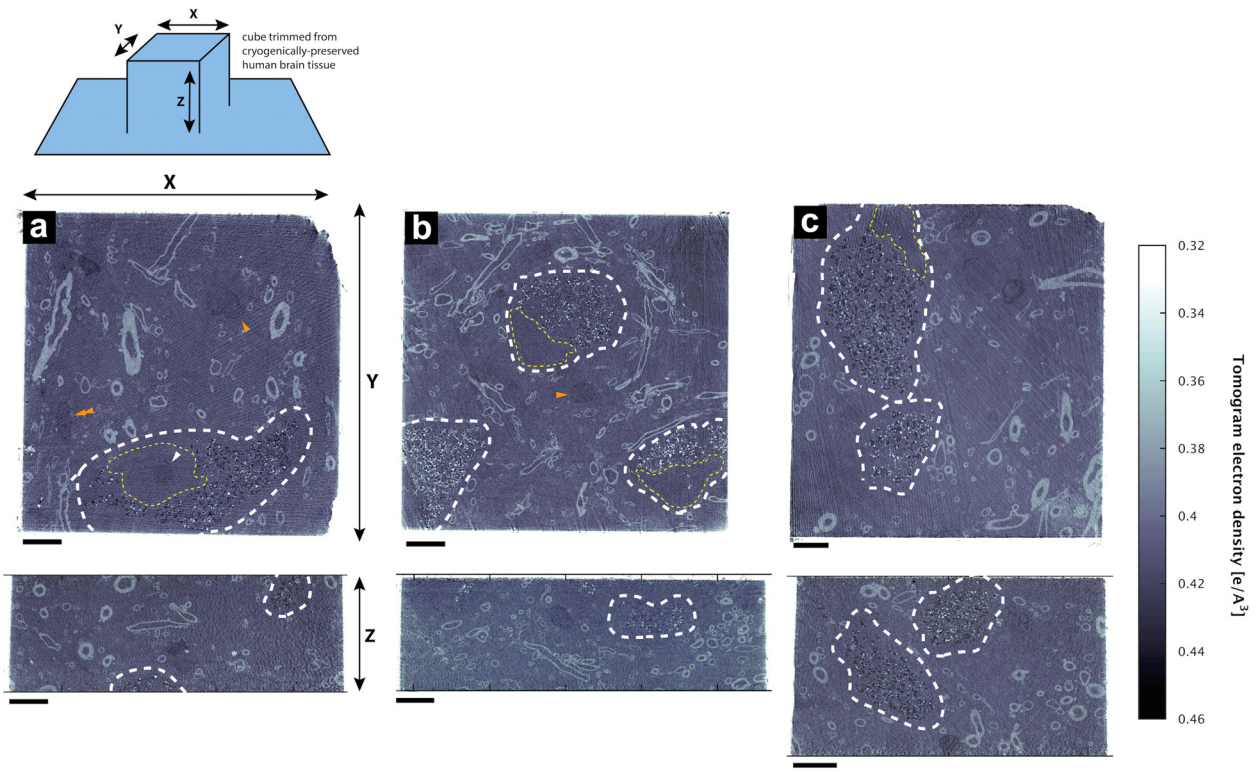

FIGURE 1 | Hydrated, unstained non-demented human brain as imaged by cryo-PXCT using OMNY (Holler et al., 2018). Trimmed tissue volume schematic corresponding to orthoslice views is shown above. Representative orthoslices are shown from an X-Y plane (top panels) and X-Z plane (bottom panels) from three of the nine total human brain samples measured. Grayscale intensity values directly correspond to electron density. Data shown corresponds to orthoslices from **(a)** Tomo 5, **(b)** Tomo 1, **(c)** Tomo 4 (**Table 1**). Scale bars: 10 μm.

for each of the four PD brain tomograms independently (**Supplementary Figures 4B–E**) also showed a similar theme with the majority of DMAs corresponding to the SWiM rather than the SWiA type. To assess the degree of swelling in each DMA, three groups of measurements were taken for each DMA before, within, and after the swelling: (1) the axon diameter, averaged across three positions on the axon preceding the swelling, (2) of the maximum diameter of the axonal swelling, and (3) the axon diameter, averaged across three positions on the axon following the swelling. A great variability was observed for each swelling, ranging from ∼3 to 11 μm (**Supplementary Figure 4**).

Optical Imaging: Alpha Synuclein Immunofluorescence With Bielschowsky Silver Staining

The DMAs were only observed in the PD human brain cryo-PXCT tomograms and were not present in the control human brain tomograms. To further investigate the pathological relevance of DMAs, we applied immunohistochemistry using a phosphorylated alpha-synuclein antibody (p-aSyn, Ser129-P aSyn, 11A5, gift from Prothena), together with a Bielschowsky silver staining protocol (Uchihara, 2007) on adjacent sections from same tissues as used for the X-ray/EM studies, in order to co-visualize nerve fibers as well as p-aSyn-immunopositive Lewy neurites in adjacent tissue blocks to those collected for cryo-PXCT. Stainings were analyzed by fluorescent microscopy – in combination with multispectral imaging – and confocal microscopy. The Bielschowsky staining showed the thickness and direction of axons originating from and directed to the SNpc. In a subset of p-aSyn immunopositive Lewy neurites, immunoreactivity overlapped partially or completely with swollen axons revealed by Bielschowsky stain, demonstrating the presence of p-aSyn inclusions in these dysmorphic processes (**Figure 7**).

Correlative Electron Microscopy

For imaging downstream target structures at higher resolution, one PD and one control tissue block after cryo-PXCT imaging were selected for subsequent cryo ultramicrotomy at −100°C (Tokuyasu, 1980). The blocks were transferred and thawed at room temperature as routine for cryo-immunogold electron microscopy (Peters et al., 2006). Structures of interest were labeled by primary antibody followed by secondary immunogolds and contrast-stained by uranyl acetate (Peters and Pierson, 2008), then imaged by transmission electron microscopy (TEM) at ambient temperature. This workflow is shown in **Supplementary Figure 5**. For imaging downstream

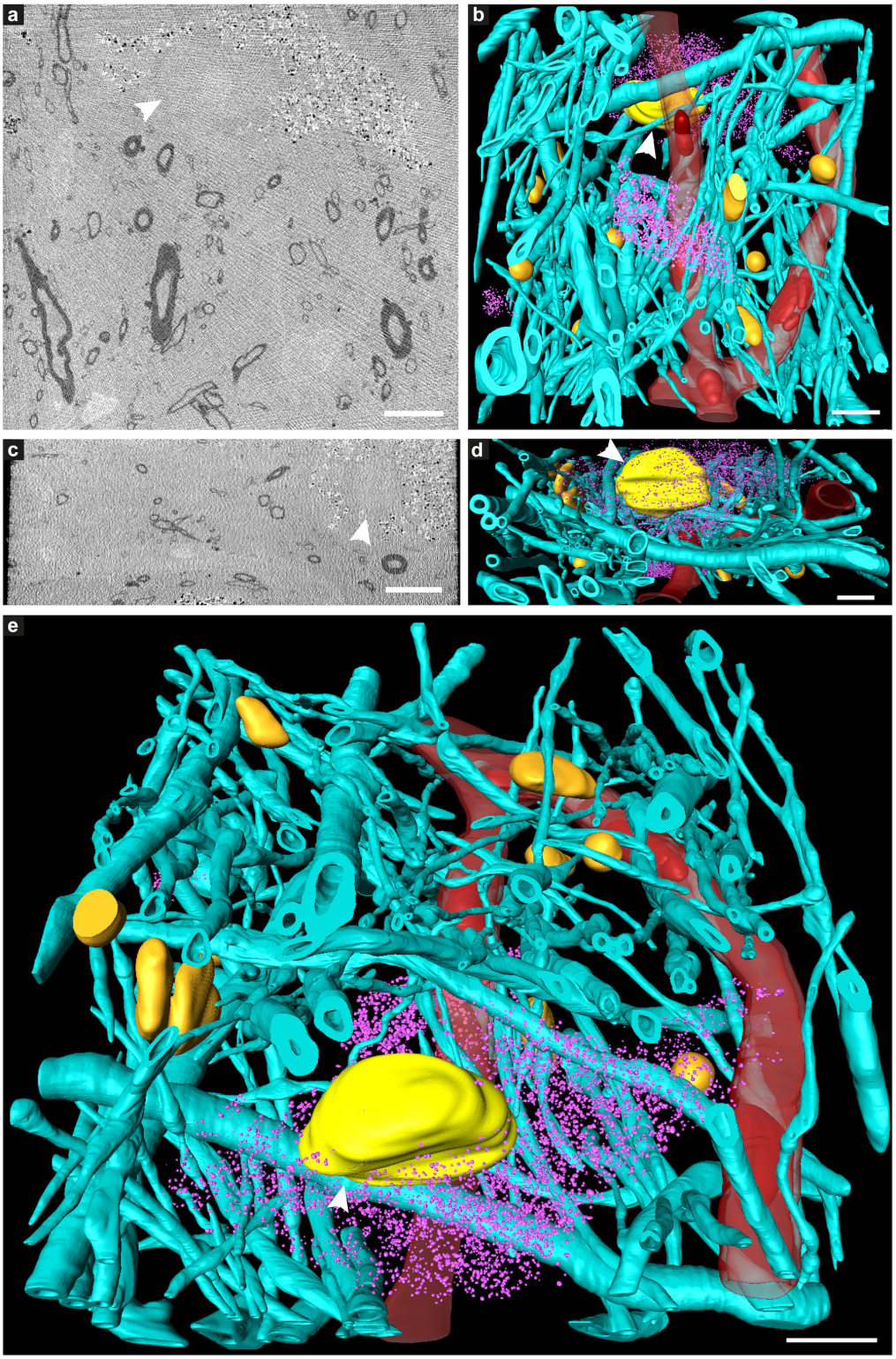

FIGURE 2 | Tissue components in 3D color-segmented cryo-PXCT datasets of non-demented control human brain. Single 2D orthoslices with inverted grayscale in the **(a)** X-Y plane and **(c)** X-Z plane, shown from the 3D volume used for the corresponding color segmentation, displayed in the **(b)** X-Y plane, **(d)** X-Z plane, and **(e)** tilted larger-scale view. Aqua = myelinated axons; Yellow (white arrowhead) = nucleus of neuromelanin-containing cell; Orange = nuclei of non-neuromelanin-containing cells; Pink = neuromelanin-containing organelles; Red = blood vessels; Dark red = blood cells within the blood vessels. Corresponds to "Control human brain," Tomo 5 (**Table 1**). Scale bars: 10 μm.

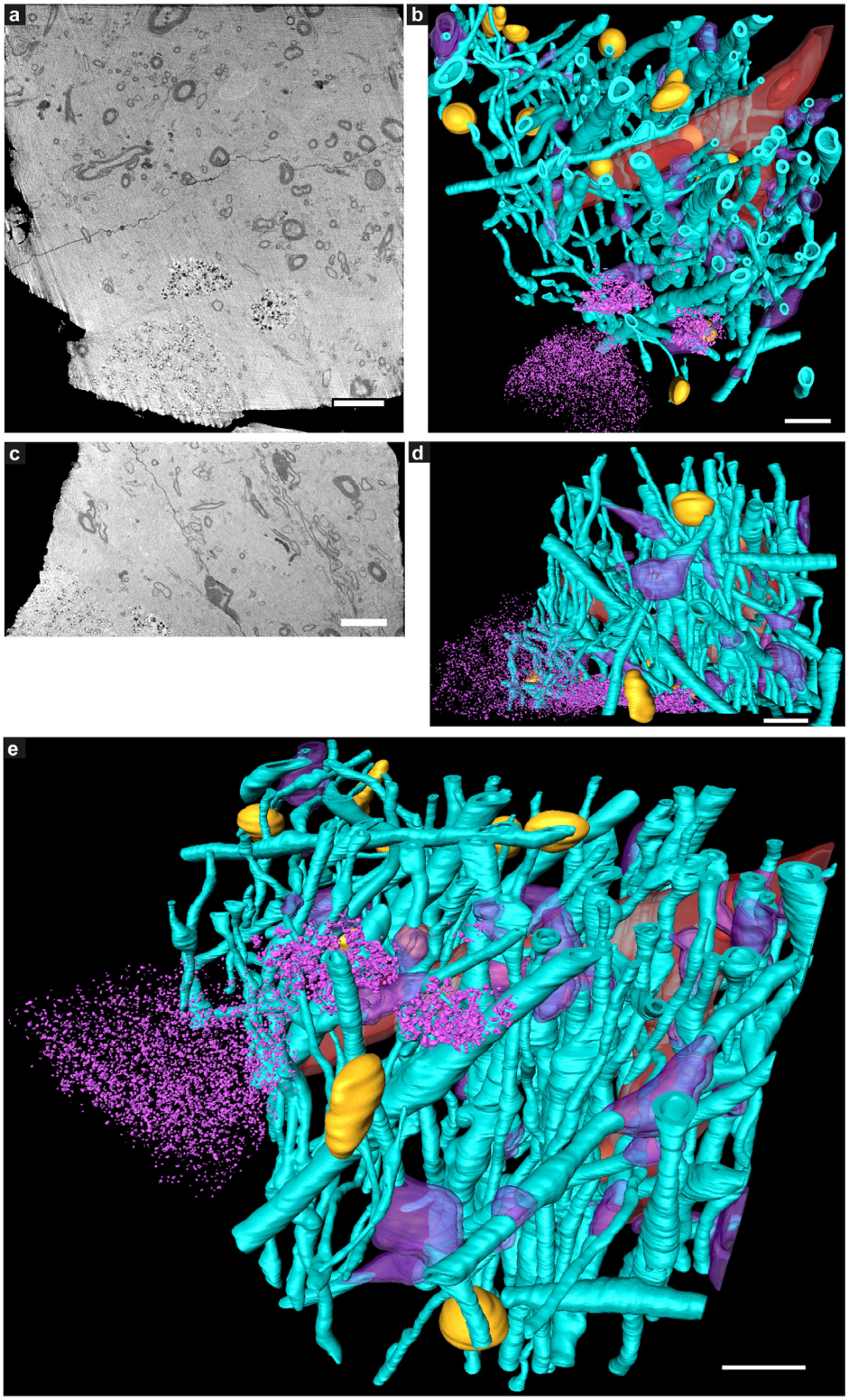

FIGURE 3 | Tissue components in 3D color-segmented cryo-PXCT tomograms of Parkinson's diseased human brain. Single 2D orthoslices with inverted grayscale in the **(a)** X-Y plane and **(c)** X-Z plane, shown from the 3D volume used for the corresponding color segmentation, displayed in the **(b)** X-Y plane, **(d)** X-Z plane, and **(e)** tilted larger-scale view. Aqua = myelinated axons; Purple = swellings along the axons (DMAs); Orange = nuclei of non-neuromelanin-containing cells; Pink = neuromelanin-containing organelles; Red = blood vessels; Dark red = blood cells within the blood vessels. Corresponds to "Parkinson's diseased human brain," Tomo 4 (**Table 1**). Grayscale shown herein does not correspond directly to mass density as opposed to **Figure 1**. Scale bars: 10 μm.

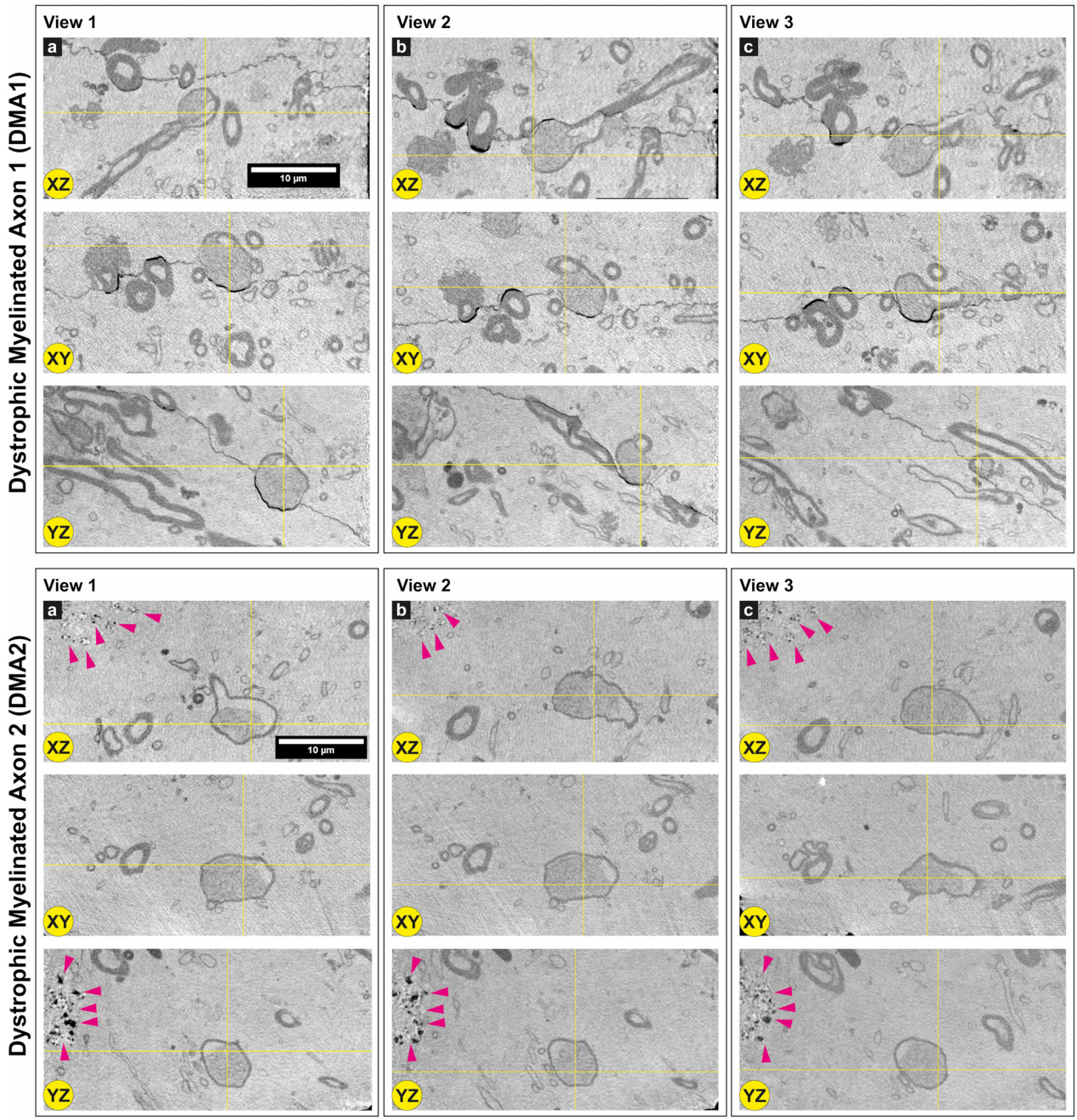

FIGURE 4 | Dystrophic myelinated axons (DMAs) by cryo-PXCT in Parkinson's diseased human brain. Single 2D orthoslices with inverted grayscale showing the appearance of two DMAs in different planes (X-Z, X-Y, Y-Z) and different positions (Views 1, 2, 3) in the 3D tomogram. Yellow crosses indicate the position of the DMA in the different views and planes. Several other DMAs are shown in **Supplementary Figures 1, 2**. Grayscale of all 2D cutaways shown herein correspond to electron density. Pink arrowheads = neuromelanin-containing organelles of adjacent cell. Scale bars: 10 µm. a, b, c refer to the different columns corresponding to View 1, View 2, and View 3, for clarity sake.

target structures at higher resolution, one PD and one control tissue block after cryo-PXCT imaging were selected for subsequent cryo ultramicrotomy at −100°C (Tokuyasu, 1980), transferred and thawed at room temperature as routine for cryo-immunogold electron microscopy (Peters et al., 2006), labeled by primary antibody followed by secondary immunogolds and contrast-stained by uranyl acetate (Peters and Pierson, 2008), then imaged by transmission electron microscopy (TEM) at ambient temperature. This workflow is shown in **Supplementary Figure 5**.

Each tissue block was schematically divided into three zones, and ultra-microtomed sections (70 nm thin) were

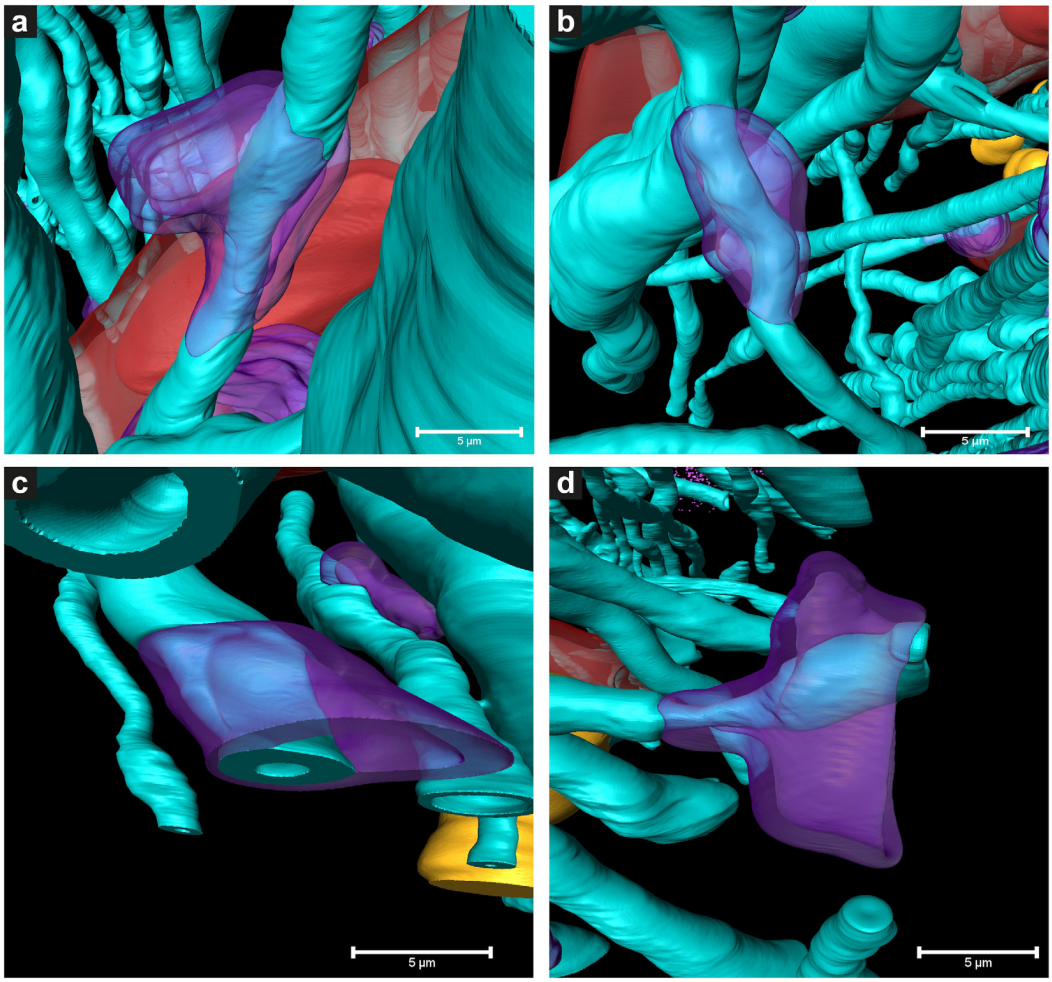

FIGURE 5 | 3D color representations of DMAs in Parkinson's diseased human brain by cryo-PXCT. **(a–c)** DMAs in which the oligodendrocyte cytoplasm within the myelin sheaths is swollen (purple) at a region along the length of the myelinated axon (aqua), **(d)** DMA in which swelling is visible in both the oligodendrocyte cytoplasm (purple) and underlying axoplasm (aqua swelling beneath the purple). Red = blood vessel; Dark red = blood cell; Orange = nuclei of non-neuromelanin containing cells. Scale bars = 5 μm.

cut and collected onto TEM grids sequentially from top of the block to bottom of the block, and immunolabeled accordingly. EM grids at low magnification showed the general shape and position of the resulting ultrathin sections from control human brain (**Figures 8a**, **9a**) and PD human brain (**Figures 10a,g**). The integrity of the tissue was as expected for cryo immunogold labeling (Tokuyasu, 1986; Peters et al., 2006), with the gaps and holes typical of the methodology when applied to non-densely packed tissues with high water content like brain.

Neuromelanin-containing cells, of high clinical relevance in PD, were the most prominent and easily identifiable features within the tissue sections (**Figures 8–10**), after using the cryo-PXCT tomographic maps to navigate to the appropriate region in which these cells were originally found. By scrolling up and down through the corresponding cryo-PXCT reconstructed tomogram, we could determine the appropriate region (top, middle, bottom; edge, center) of the imaged cube in which the cells where located, which allowed to define the immunogold-stained tissue section(s) that would be most relevant to subsequently image. One neuromelanin-containing cell (**Figures 8b,c**) from a non-immunogold stained tissue section (**Figure 8a**) from a non-demented control human brain donor is shown to display clear neuromelanin-containing organelles in which the lipid vesicle component is clearly preserved amongst the typically dark, dense globules representing neuromelanin-containing organelles (Zucca et al., 2018) (**Figures 8d,e**, blue arrowheads). The dark appearance of the globules by electron microscopy (**Figures 8c–e**) is attributable to the naturally high metal content of such structures, while the dark appearance typically observed by brightfield light microscopy is attributable to the fact that these are pigmented akin to melanin in skin tissue. Furthermore, mitochondria with clear cristae were also visible within the tissue sections, one of which is shown enclosed within a clear axonal cross section (**Figure 8F**, white asterisk). The individual lipid layers of myelin sheath that compose the axon are also clearly

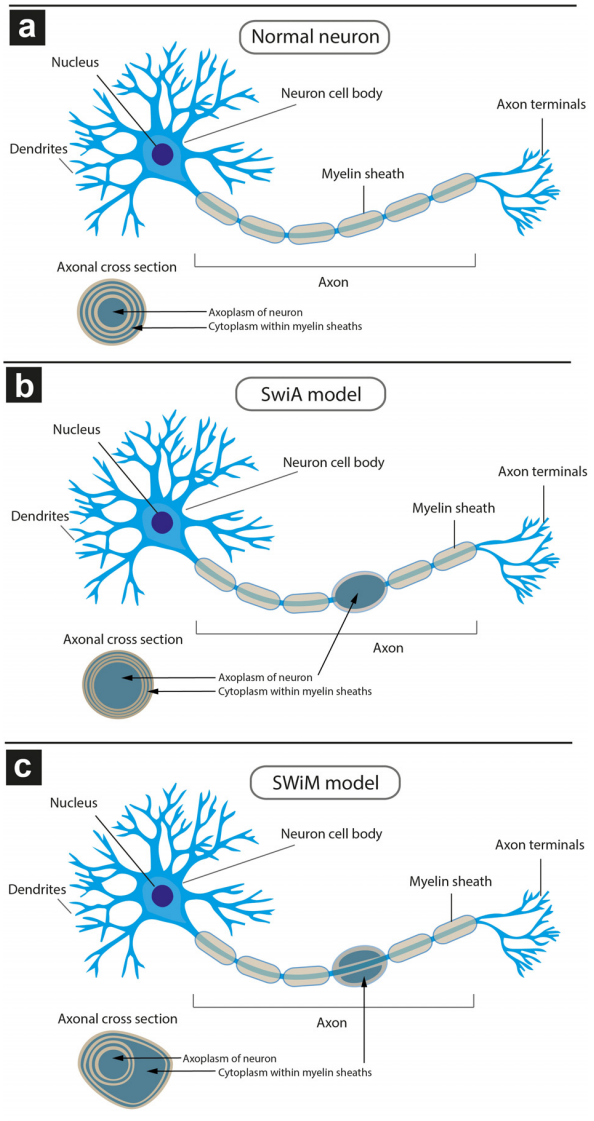

FIGURE 6 | Schematic model of different types of dystrophic myelinated axons (DMAs) as observed by cryo-PXCT in Parkinson's diseased human brain. Overall appearance of the myelinated axon protruding from a neuron, and zoomed-in cross-section of the myelinated axon (inset), is shown for each type: **(a)** neuron with a normal appearance of myelinated axon, in which the cytoplasm of the oligodendroglial cell is barely visible due to the typical tight compaction of the myelin sheaths (beige); **(b)** neuron with swelling in the axon, in which the neuronal cytoplasm within the axon is enlarged, referred to as "swelling in axoplasm" or SWiA; **(c)** neuron in which cytoplasm within myelin sheath is expanded, referred to as "swelling in myelin sheath" or SWiM. Oligodendroglial cells are not shown. Their extensions flatten out and wrap around the axon multiple times, forming the myelinations that appear as "sausage"-like pieces (beige) from the overview. The layers of myelin are apparent from the cross-sectional inset views.

visible, as well as the membranous profiles of vesicles (**Figure 8f**, orange arrowheads).

In another neuromelanin-containing cell (**Figure 9b**) shown in a control human brain tissue section (**Figure 9a**) that was immunogold-stained for a prominent mitochondrial porin antibody (VDAC1, Abcam ab14734), the nucleus and nucleolus are clearly visible (**Figures 9c,d**); furthermore, the nuclear membrane is also visible at higher magnification (**Figure 9d**, aqua arrowheads). Below the neuromelanin-containing cell (**Figure 9e**), several mitochondria were visualized, some of which are shown in **Figures 9f–j** (white asterix). Immunogolds (**Figures 9f–j**, yellow arrowheads) are visible at the edges of the mitochondria, where the VDAC1 porin protein is expected to be localized, being an outer mitochondrial membrane protein. Specificity is demonstrated by the lack of labeling in the tissue surrounding the mitochondria. This suggests that some protein antigenicity is retained even after cryo-PXCT imaging. Interestingly, a pool of synaptic vesicles (**Figure 9j**, orange arrowheads), synaptic cleft (aqua arrowheads), and a mitochondrion (white asterix) visible in the postsynaptic zone, were also clearly visible.

Several neuromelanin-containing cells (**Figures 10a,b,g,h**) could be localized in the appropriate EM tissue sections from the PD brain tissue samples, using the corresponding cryo-PXCT tomograms as a guide. In one tissue section (**Figure 10a**) immunogold-stained for LB509 (Abcam ab27766), an antibody that is routinely used to identify Lewy pathology as aSyn-immunopositive structures in PD, we observed that immunogolds localized to lamellar membranous structures (**Figures 10e,f**, yellow dotted lines) within the neuromelanin-containing organelles. These immunogolds were not visible in the background, suggesting a specificity to these structures. Similar to the control human brain tissue section, the quality of the tissue post cryo-PXCT imaging was sufficient to clearly resolve both the neuromelanin-containing organelles (**Figures 10b–f,i–l**, black, dark-contrast features) and their typical corresponding lipidic vesicle component known as lipid bodies (Zucca et al., 2018) (**Figures 10d,e,j**, blue arrowheads). In another tissue section (**Figure 10g**) immunogold-stained for p-aSyn (phospho S129, Abcam ab59264), we found immunogolds (yellow arrowheads) localized to the edge of the lipid bodies. Our results are in line with similar immunogold electron microscopy-based studies that show aSyn is localized in the neuromelanin (Zucca et al., 2018), similar to our result. Those researchers suggest that the process of neuromelanin synthesis that starts in the cytosol, may involve accumulation of aggregated and β-structured proteins, including aSyn (Zucca et al., 2018).

DISCUSSION

Our results using cryo-PXCT on unstained human brain tissue samples have revealed that several key cellular components can be resolved at the nanoscale, including myelinated axons, neuromelanin-containing cells and their nuclei, the nuclei of other brain cells such as glia, red blood cells and blood vessels within the brain. We have demonstrated that resolution is sufficient to visualize fine details including changes between the myelin sheaths of axons, particularly clarifying the ultrastructural nature of swellings within axons in this case. Not only can such structures be clearly visualized, but also with sufficient resolution

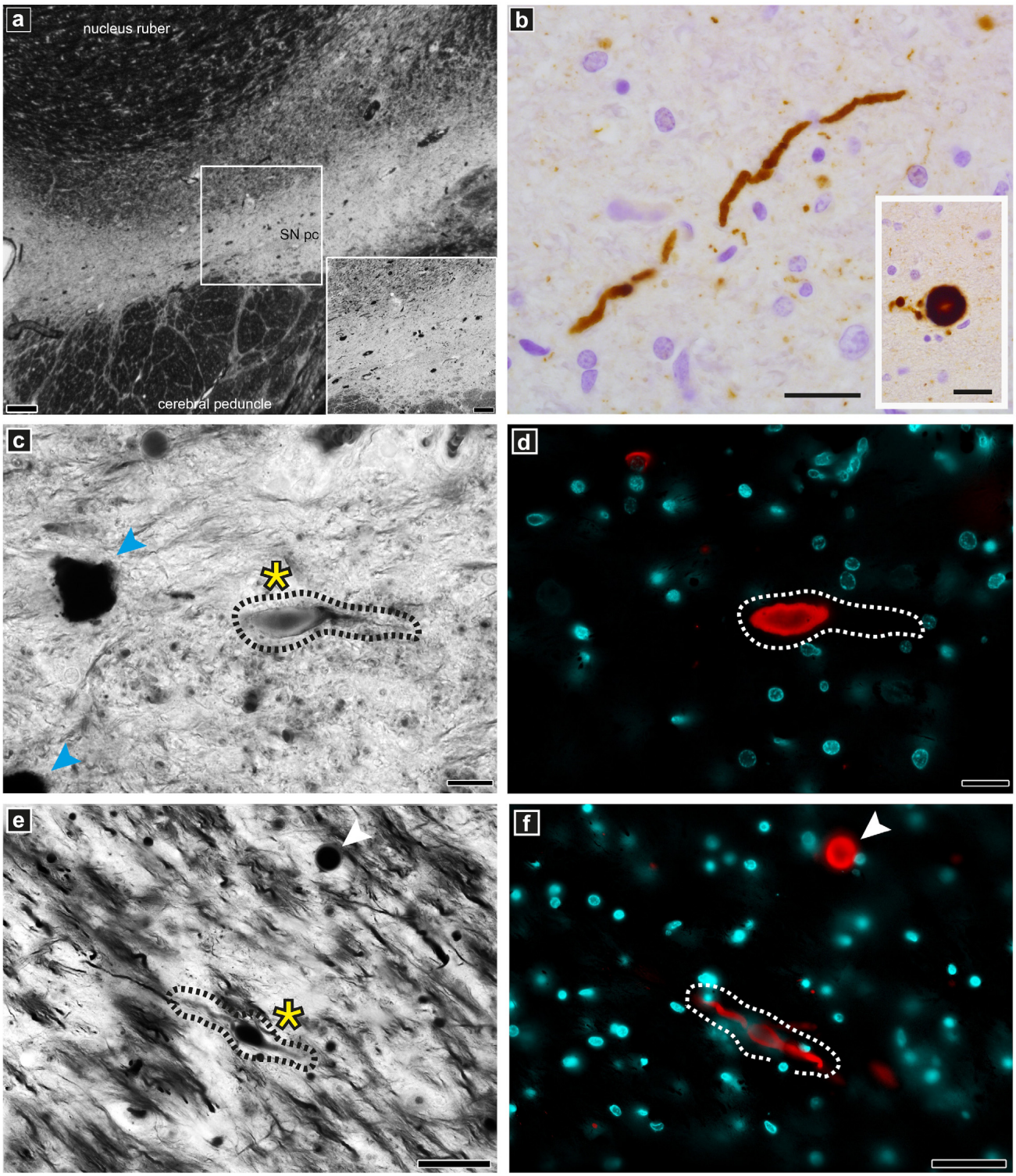

FIGURE 7 | Optical microscopy and immunofluorescence of pathologically relevant structures in PD brain donor tissue. Staining and imaging was performed on adjacent tissue sections from the same PD brain donor SNpc region as used for the cryo-PXCT and EM studies. **(a)** overview of Bielschowsky silver staining of the SNpc. **(b)** Lewy neurite and Lewy body (insert) as revealed by p-aSyn immunohistochemistry. **(c,e)** Representative example of a dystrophic axon (black dotted lines, yellow asterix) visible by silver staining corresponding to be **(d,f)** Lewy neurite (white dotted lines) by fluorescence microscopy with spectral imaging. Lewy body is visible (white arrowhead) in both panels **(e)** and **(f)**. Neuromelanin-containing cells (blue arrowheads) are visible in panel **(c)**. Scale bars: **(a)** = 200 μm, inset 100 μm; **(b)** = 25 μm; **(c,d)** = 20 μm; **(e,f)** = 50 μm.

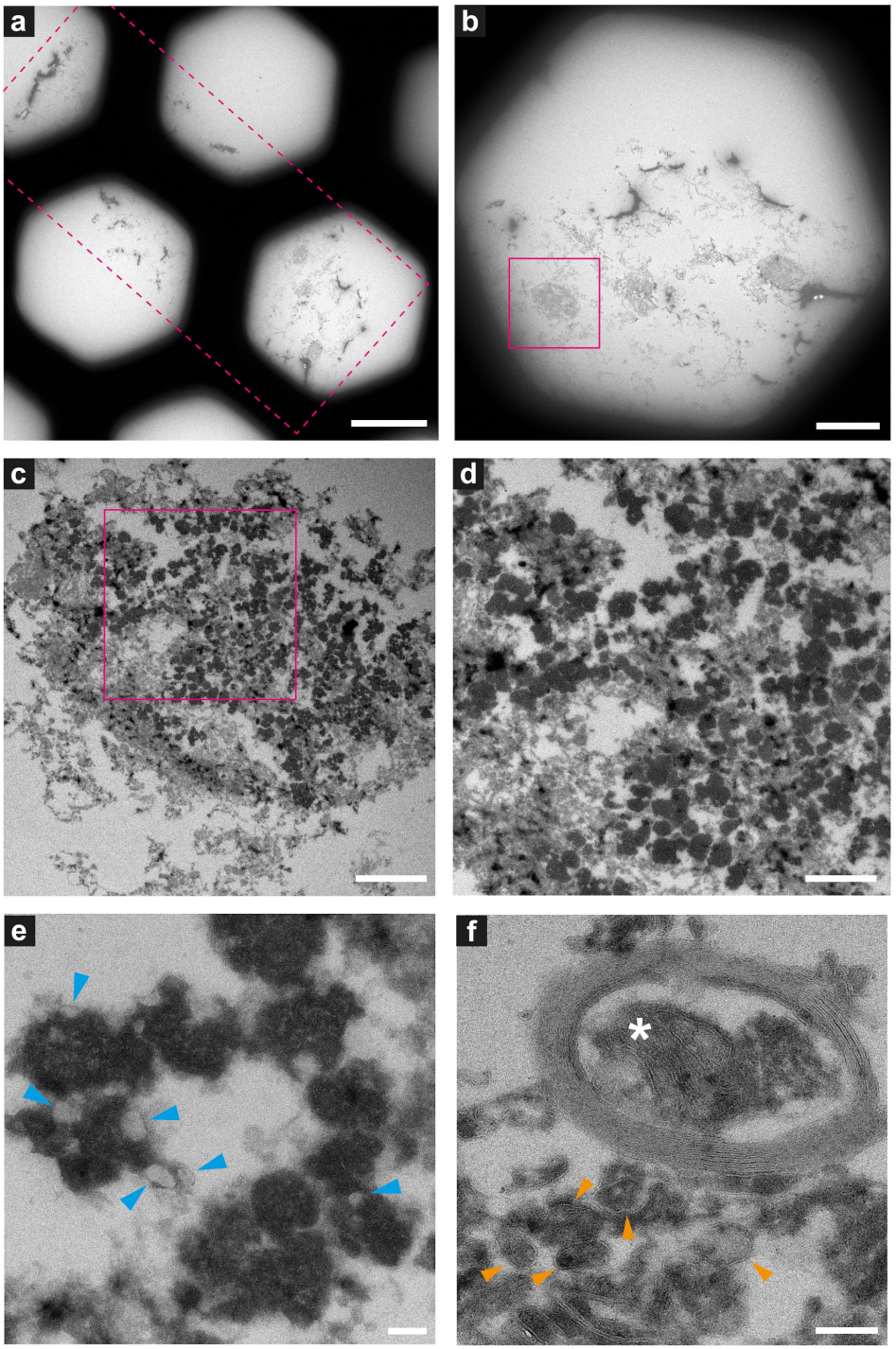

FIGURE 8 | Electron microscopy of ultrathin tissue sections post cryo-PXCT imaging of non-demented control human brain. Sections were generated by cryo-ultramicrotomy of the tissue block of non-demented control human brain (Tomo 5, **Table 1**) and contrast-enhanced using uranyl acetate, following cryo-PXCT imaging. Images show progressively zoomed-in views of a neuromelanin containing cell and other higher-resolution cellular features. **(a)** Overview of the ultrathin tissue sections (pink dotted box) on the formvar-carbon support film of a hexagonal EM grid. **(b)** One neuromelanin-containing cell (pink box) visible in a section zoomed-in from panel **(a)**. **(c)** Zoomed-in view of the same neuromelanin-containing cell as shown in panel **(b)**, **(d)** Zoomed-in view of the neuromelanin as shown in the pink box in panel **(c)**, **(e)** Neuromelanin granules (dark dense blobs) and typically associated lipid globules (blue arrowheads) are visible at higher magnification and resolution, **(f)** A mitochondrion (white asterix) is visible within the cross-section of a myelinated axon in which the individual membranes of the myelin are clearly visible, as well as individual membranes of other vesicles and features within the tissue (orange arrowheads). Scale bars: **(a)** = 80 μm; **(b)** = 30 μm; **(c)** = 3 μm; **(d)** = 2 μm; **(e,f)** = 200 nm.

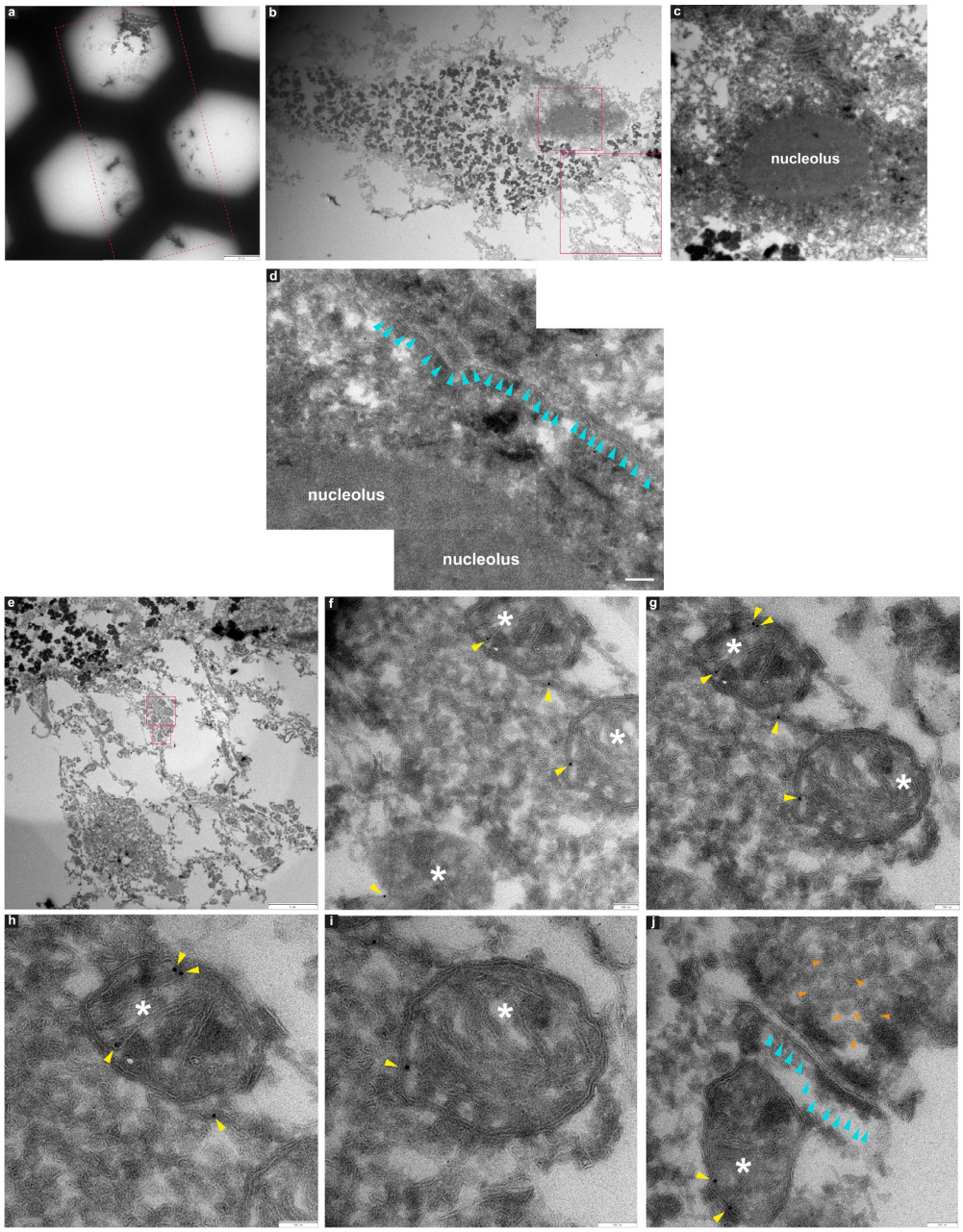

FIGURE 9 | Immuno-electron microscopy of ultrathin tissue sections post cryo-PXCT imaging of non-demented control human brain. After cryo-PXCT imaging, sections were generated by cryo-ultramicrotomy of the tissue block of non-demented control human brain (Tomo 5, **Table 1**) followed by immunogold labeling using anti-VDAC1 (mitochondrial membrane marker), standard uranyl acetate contrast enhancement, and electron microscopy. Images **(a–c)** show progressively zoomed-in views of a neuromelanin containing cell. **(a)** Overview of the ultrathin tissue sections (pink dotted box) on the formvar-carbon support film of a hexagonal EM grid. **(b)** One neuromelanin-containing cell visible in a section zoomed-in from panel **(a)**. Neuromelanin granules are the dark dense globules. **(c)** Zoomed-in view of the nucleus [top pink box in panel **(b)**] including the clearly visible nucleolus of the same neuromelanin-containing cell, **(d)** Zoomed-in view of a part of the same nucleolus within the nucleus of the neuromelanin-containing cell, in which the nuclear membrane (aqua arrowheads) is preserved and clearly visible. **(e)** Zoomed-in view of the region as shown in the bottom pink box depicted in panel **(b)**, directly underneath the neuromelanin-containing cell, **(f)** three mitochondria (white asterix) zoomed-in from the top pink box as shown in panel **(e)**, with anti-VDAC1 (outer mitochondrial membrane marker) immunogolds (yellow arrowheads) visible as expected on their periphery. **(g)** View of two of the same mitochondria as shown in panel **(f)** in which more immunogolds (yellow arrowheads) can be visible at the top of the top-most mitochondrion. **(h)** Zoomed-in view of the top-most mitochondrion (white asterix) as shown in panel **(g)** where four immunogolds (yellow arrowheads) are visible. **(i)** Zoomed-in view of the bottom mitochondrion (white asterix) shown in panel **(g)** where one immunogold is visible. **(j)** Zoomed-in view of the synaptic cleft as shown in the bottom-most pink box shown in panel **(e)**, in which the membranes of the synaptic cleft (aqua arrowheads) are visible, a mitochondrion (white asterix) with two immunogolds (yellow arrowheads) visible on the post-synaptic side, and clusters of synaptic vesicles (orange arrowheads) visible on the presynaptic side. Scale bars: **(a)** = 60 μm; **(b)** = 4 μm; **(c)** = 1 μm; **(d)** = 4 μm; **(e)** = 3 μm; **(f–j)** = 100 nm.

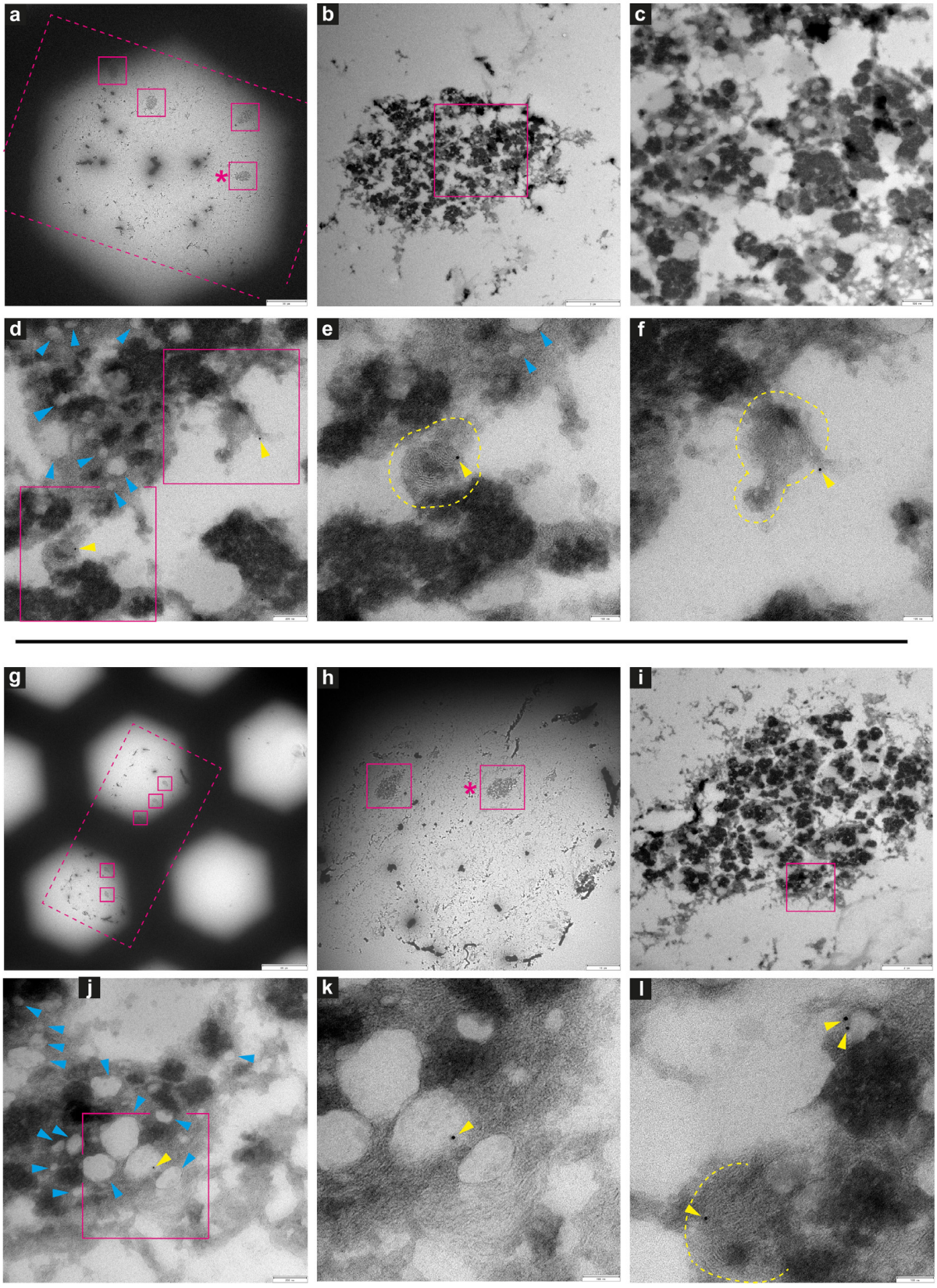

FIGURE 10 | Continued

FIGURE 10 | Immuno-electron microscopy of ultrathin tissue sections post cryo-PXCT imaging of Parkinson's diseased human brain. After cryo-PXCT imaging, sections were generated by cryo-ultramicrotomy of the tissue block of Parkinson's diseased human brain (Tomo 2, **Table 1**) followed by immunogold labeling, standard uranyl acetate contrast enhancement, and electron microscopy. Images in panels **(a–f)** and **(g–l)** correspond to different tissue sections: **(a–f)** immunogold-labeled using LB509 (anti-alpha synuclein), and **(g–l)** immunogold-labeled for p-aSyn (anti- phosphorylated alpha synuclein at S129). Images show progressively zoomed-in views of a neuromelanin containing cell from each tissue section. **(a)** Overview of the ultrathin tissue sections (pink dotted box) on the formvar-carbon support film of a hexagonal EM grid, with neuromelanin-containing cells visible (pink solid boxes). **(b)** Zoomed-in view of neuromelanin-containing cell shown in pink box (asterix) in panel **(a)**, and progressively zoomed-in view in panel **(c)** where lipid globules (pale gray globules) are clustered with neuromelanin granules (darker globules) as typically expected. **(d)** Zoomed-in view within the neuromelanin-containing cell where lipid globules are more clearly visible (blue arrowheads) and immunogolds (yellow arrowheads) for LB509 (anti alpha-synuclein) are visible. **(e)** Zoomed-in view of the bottom-most pink box shown in panel **(d)**, and the **(f)** top-most pink box shown in panel **(d)**, in which immunogolds for LB509 (anti alpha-synuclein) are visible, both on lamellar multi-membranous structures. **(g)** Overview of the ultrathin tissue sections (pink dotted box) on the formvar-carbon support film of a hexagonal EM grid, with neuromelanin-containing cells visible (pink solid boxes). **(h)** Zoomed-in view of neuromelanin-containing cell shown in pink box (asterix) in panel **(g)**, and progressively zoomed-in view in panel **(i)** where lipid globules (pale gray globules) are clustered with neuromelanin granules (darker globules) as typically expected. **(j)** Zoomed-in view within the neuromelanin-containing cell where membrane-enclosed structures are visible (blue arrowheads) and immunogold (yellow arrowhead) is visible, **(k)** zoomed-in view of the region in pink box shown in panel **(j)**, where immunogold is visible at the edge of a vesicle. **(l)** Another zoomed-in view of the neuromelanin-containing cell in which an immunogold is visible on another lamellar multi-membranous structure (delimited by yellow dotted lines) and two immunogolds are visible at the edge of a vesicle. Scale bars: **(a)** = 30 μm; **(b)** = 3 μm; **(c)** = 500 nm; **(d)** = 200 nm; **(e,f)** = 100 nm; **(g)** = 80 μm; **(h)** = 10 μm; **(i)** = 2 μm; **(j)** = 200 nm; **(k,l)** = 100 nm.

(145–390 nm) providing a level of detail that allows us to clarify whether these swellings are occurring within the actual axon or within the myelin sheath composing the axon, suggestive of different biological mechanisms. We have found that such swellings, or dystrophic myelinated axons (DMAs), appear only within the PD human brain tissue samples as compared to the control brain samples that we have imaged; in this case, in the SNpc brain region that is highly clinically relevant to this disease.

As the phosphorylation of serine 129 of alpha synuclein (p-aSyn) is considered the dominant pathological modification in both familial and sporadic Lewy body diseases including PD, we have investigated the pathological relevance of the DMAs in this PD case using a phosphorylated alpha-synuclein antibody (p-aSyn, Ser129-P aSyn, 11A5, gift from Prothena) for fluorescent confocal microscopy, together with a Bielschowsky silver staining protocol (Uchihara, 2007) followed by multispectral imaging, on adjacent sections from same tissues as used for the X-ray/EM studies. By co-visualizing the nerve fibers with the Bielschowsky stain as well as p-aSyn-immunopositive Lewy neurites in adjacent tissue blocks to those collected for cryo-PXCT, we found that immunoreactivity overlapped partially or completely with swollen axons, demonstrating the presence of such pathologically relevant p-aSyn inclusions in these DMAs of the PD brain samples (**Figure 7**).

We have also shown that the majority of these DMAs occur within the myelin sheaths (**Supplementary Figure 3** and **Figure 6**) corresponding to the cytoplasm of the parent oligodendrocyte, in contrast to the expectation that they would occur within the main passage of the axon corresponding to the neuronal cell itself. This suggests that processes in which the oligodendrocytes, or cells that produce the myelin sheath, are involved in the pathology of PD. The number of reports on the role of oligodendroglial cells in neurodegeneration has increased substantially over recent years (Ettle et al., 2016). In addition to their well-known role of producing myelin that mediates action potential conduction and communication between neurons, oligodendrocytes also provide trophic support for axonal and neuronal maintenance. Typically, oligodendrocytes are implicated in diseases such as multiple systems atrophy (MSA), amyotrophic lateral sclerosis (ALS), and more recently, Alzheimer's disease (AD) (Chevalier-Larsen and Holzbaur, 2006). The aggregated cellular material that we observe in the oligodendrocyte cytoplasm composing the myelin sheaths (**Figures 3b,d**, **4**, **6** and **Supplementary Figures 1, 2**), may indeed correspond to a pathological accumulation, one likely involving aSyn according to our in-parallel confocal microscopy datasets that reveal aSyn-immunopositive aggregates co-localizing with swollen axons (**Figure 7**).

This pathological accumulation within these swellings appeared very granular (**Figure 4** and **Supplementary Figures 1, 2**), which we attribute to the presence of clustered vesicles. Indeed, correlative light and electron microscopy and tomography, and parallel studies using multi-labeling super resolution light microscopy, have recently shown a high lipid content and a crowding of vesicular structures including lysosomes and autophagosomes within both Lewy bodies and dystrophic axons corresponding to be Lewy neurites based on immunohistochemical staining (Shahmoradian et al., 2017a). Multiple studies have shown a potential link between disturbances in myelin integrity, myelin breakdown and axonal damage as an early event in the onset of neurodegenerative diseases including PD, AD, and Huntington's disease (HD), using magnetic resonance imaging (MRI) (Bartzokis, 2004; Rosas et al., 2006). Furthermore, the occurrence of heightened tissue iron levels complexed with ferritin (produced in the brain mainly by oligodendrocytes) in PD, AD, and HD (Bartzokis et al., 2004, 2007; Todorich et al., 2009) is known to increase the concentration of reactive oxygen species (Puntarulo, 2005) that can initiate changes in the proteins' tertiary structure, leading to aggregation that is associated with neurodegeneration. High tissue iron is considered as a risk factor in developing neurodegenerative disease, with oligodendrocytes playing a key role (Grune et al., 2004; Doorn et al., 2014; Ward et al., 2014).

Considering that myelin represents a vital factor for human brain connectivity, is profoundly evolved in humans compared to non-human primates and other mammals, and progressively declines in the aging human brain, oligodendrocyte dysfunction would logically contribute to the vulnerability of the human brain in regard to neurodegenerative diseases. We have demonstrated

that cryo-PXCT is a useful tool to simultaneously visualize several axons in a continuous volume, currently limited to $\sim(100\ \mu m)^3$, without the addition of any stain, allowing the detection of subtle changes in axonal ultrastructure and enabling us to distinguish between types of swellings and furthermore the extent to which the axon is myelinated: thin myelin sheaths which are more frequently associated with neurodegeneration, as compared to thicker myelin sheaths which are more frequently associated with a healthier state (Braak et al., 2006b; Braak and Del Tredici, 2016). While cryo-PXCT would hence be useful to investigate diseases in which neuronal, oligodendrocytes and axonal degeneration are majorly implicated, our unexpected finding of axonal swellings directly arising within the myelin sheaths originating from the parent oligodendrocyte rather than within the axoplasm of the associated neuron from the human postmortem PD brain, brings forth the question of whether other neurodegenerative diseases displaying axonal swellings may also involve oligodendrocytes in a similar manner. Such an observation would have implications for disease pathogenesis and warrant closer investigation using complementary techniques.

Recognizing and differentiating abnormal features within the axon as opposed to those within the myelin sheath that encase the axon, is a crucial step toward pinpointing the underlying physiological and pathological processes. For example, abnormalities within the axon rather than the myelin sheath would implicate a cellular process that is specific to the parent neuron from which the axon extends. Abnormalities within the myelin sheath itself would correspond to pathologically relevant processes that are occurring within the parent oligodendrocyte cell from which the myelin sheath is produced. More specifically, each individual wrapping of myelin sheath around an axon protruding from a neuron, also contains its own cytoplasm that belongs to the oligodendrocyte cell producing that myelin sheath (Simons and Nave, 2015). Since oligodendrocyte cells are different in both composition and function as compared to neurons, abnormalities arising in their cytoplasm are important to distinguish from abnormalities in the neuronal cytoplasm, and would refer to a pathological process attributable to a different – either separate or concerted – cellular mechanism (Bradl and Lassmann, 2010).

Furthermore, we have demonstrated for the first time that after cryo-PXCT imaging, protein antigenicity is preserved, as demonstrated here by subsequent ultramicrotomy, immunogold labeling, and correlative electron microscopy (**Figures 8–10**), revealing the ultrastructure of cellular features including mitochondria, myelinated axons, synaptic clefts and the typical associated protein densities, synaptic vesicles, neuromelanin-containing organelles, nuclear membrane, nucleus and nucleolus, and various lipid vesicles. This demonstration has important implications for investigations which would greatly benefit from first generating a large map of complex, hierarchical multi-component features – typical to the crowded environment of biological tissues – by using cryo-PXCT, and subsequently imaging at higher resolution using correlative electron microscopy of target structures localized in the cryo-PXCT tomograms.

In general, X-ray ptychography has been shown to provide resolutions as high as 20 nm in 2D projections of single biological cryo-preserved cells (Deng et al., 2017). There is potential for increasing the resolution in large tissue volumes such as the ones investigated here, as there are studies supporting that biological tissue could withstand doses up to 1e9 Grays, which is about 2 orders of magnitude more than the dose deposited by PXCT in our work, while preserving features at length scales well below 100 nm (Howells et al., 2009). The development of diffraction-limited storage rings (Eriksson et al., 2014) and other improvements in instrumentation will allow to increase the coherent flux required for these experiments and thereby the spatial resolution could be increased up to the limit imposed by radiation damage within practical measurement times.

We have shown that cryo-PXCT is a useful tool for visualizing several features in both control and diseased postmortem human brain tissue samples, and for facilitating detection of subtle ultrastructural differences amongst structures that continuously span the examined tissue volumes, especially axons in this case. Evidence suggests that changes to axonal ultrastructure are considered as one of the early events in neurodegeneration, thereby justifying closer nanoscale-based investigations. For example, the appearance of neurite swellings marks an early event in neuritic degeneration in Parkinson's diseased patient-derived neurons (Kouroupi et al., 2017), and dystrophic axons and alterations in axonal transport induced by overexpression of mutant alpha synuclein (p.A53T) in rats are known to precede neuronal loss (Chung et al., 2009).

Although our cryo-PXCT study generated five datasets from a single control aged human brain and four datasets restricted to a single age-matched PD brain donor, the unexpected finding of expansions and aggregations in myelin sheaths corresponding to the cytoplasm of the parent oligodendrocytes in the PD brain suggests a closer investigation of such processes in PD and other neurodegenerative conditions. Our results also prove cryo-PXCT as an appropriate tool for imaging such phenomena and related ultrastructural changes at the nanoscale. More remains to be clarified on samples taken from more patients, how such dense cytoplasmic aggregations arise within the parent oligodendrocytes, their specific relation with the dominant pathological form of alpha synuclein (phosphorylated Ser-129) (Anderson et al., 2006), and why they occur at specific points along the axon. Investigating across PD brains of different disease stages (Braak stages) and quantifying both the incidence and heterogeneity at the nanoscale of such DMAs may also prove to be useful in uncovering new aspects of the disease progression. Furthermore, our results warrant further investigations in other neurodegenerative diseases in which oligodendrocytes and axonal abnormalities are primarily involved, to yield a better understanding of subtle nanoscale changes that occur in different disease states and stages.

Here we have shown for the first time that nanoscale label-free imaging of diseased human brain tissues using hard X-rays can visualize several ultrastructural features and provide insight to pathologically relevant processes spanning continuous volumes. Our successful demonstration of downstream electron microscopy, and immunogold labeling for electron microscopy,

post cryo-PXCT imaging on human brain tissue is anticipated to finally open the doors for clarifying the identity and ultrastructure of nanoscale biological features in large volume X-ray tomographic data. While the imaging rate of cryo-PXCT is currently comparable to destructive methods, with synchrotron upgrades occurring worldwide according to the multi-bend achromat and additional beamline improvements we expect an increase in coherent photon flux by up to four orders of magnitude, and thus a dramatic increase in imaging rate and/or resolution (Holler et al., 2017a). This will allow increasing the number of samples studied for a wider investigation.

METHODS

Human Postmortem Brain Tissue Samples

Post-mortem brain tissue samples from *Donors A* and *B* (**Table 2**) with clinical diagnosis PD with dementia (PDD) and brain tissue samples from non-demented patients as controls (*Donors C-E,* **Table 2**) were obtained from the Netherlands Brain Bank (NBB[1]; **Table 2**) and the Normal Aging Brain Collection (Dept. Anatomy and Neurosciences, VUmc), respectively. Tissues were collected using a rapid autopsy protocol (NBB). Brain tissues from *Donors B* and *D* (**Table 2**) were used for cryo-PXCT and electron microscopy studies, while tissues from all donors were used for optical microscopy studies.

All protocols of the Netherlands Brain Bank (NBB), Netherlands Institute for Neuroscience, Amsterdam (open access; see text footnote 1), and of the Normal Aging Brain Collection (NABC), VU University Medical Center, Amsterdam, were approved by the Medical Ethical Committee (METC), VU University Medical Center, Amsterdam, the Netherlands. For brain samples and/or bio samples obtained from the NBB, all material has been collected from donors for or from whom a written informed consent for a brain autopsy and the use of the material and clinical information for research purposes was obtained by the NBB. For brain samples obtained from NABC, all material has been collected from donors for or from whom a written informed consent for a autopsy and the use of the material and clinical information for teaching and research purposes was obtained by the department of Anatomy and Neurosciences, VUmc, the Netherlands. For samples from both brain banks, detailed neuropathological and clinical information was made available, in compliance with local ethical and legal guidelines, and all protocols were approved by the local institutional review board.

At autopsy, 0.5 cm-thick adjacent brain slices of the SNpc were collected. Cubes of ∼1–2 mm^3 of the ventral part of the SNpc were dissected and fixed for 6 h in a mixture of 2% paraformaldehyde/2.5% glutaraldehyde in 0.15 M cacodylate buffer with 2 mM calcium chloride, pH 7.4 and then washed with PBS. The PD brain donor fulfilled the United Kingdom Parkinson's Disease Society Brain Bank (UK-PDSBB) clinical diagnostic criteria for PD (Emre et al., 2007). Neuropathological evaluation was performed on 7 μm formalin-fixed paraffin-embedded sections collected from multiple brain regions according to the guidelines of BrainNet Europe.

As is routine for such brain donors, staging of Alzheimer's disease was evaluated according to the Braak criteria for NFTs (Braak et al., 2006a), CERAD criteria adjusted for age and Thal criteria (Thal et al., 2006). The presence and topographical distribution of aSyn (monoclonal mouse anti-human-α-synuclein, clone KM51, Monosan; **Supplementary Figure 1**) was rated according to Braak's staging scheme for aSyn (Braak et al., 2004) and a modified version of McKeith's staging system for aSyn (i.e., brainstem, limbic system, amygdala-predominant or neocortical (McKeith et al., 2005).

Safety Considerations for Tissue Handling

All tools/surfaces coming in contact with the chemically fixed, postmortem human brain tissues were sterilized with a mixture of 2% sodium dodecyl sulfate (SDS) and 1% acetic acid, for sterilization against potential pathogenic agents (Rutala and Weber, 2010). For delicate parts such as the fine diamond tips of the Diatome™ knives, 50% ethanol – as recommended – was used.

Tissue Preparation for Cryo-PXCT Imaging

Tissues were prepared as previously described for mouse brain (Shahmoradian et al., 2017b) with some alterations regarding the final trimmed sample shape and more details provided herein, also shown in a workflow (**Supplementary Figure 6**). The fixed tissue was sectioned using a Vibratome into 60 μm-thick slices, kept at 4°C in glass scintillator vials with tight rubber seals in 0.15M cacodylate buffer. PBS (without calcium or magnesium) can be substituted. Circular regions were biopsy-punched out from the tissue in the neuromelanin-rich areas using a Harris Uni-Core biopsy punch tool (diameter 1.20 mm) on a Harris Cutting Mat. Punched-out pieces were placed in cryoprotectant (1.2M sucrose with 15% polyvinylpyrrolidone) in small plastic vials, rotating at 4°C for 2–3 weeks. Prior to cryo-ultramicrotomy, tissue pieces were checked to ensure that all sunk to the bottom of the tubes, indicating full penetration of cryoprotectant to the tissue. Tissue pieces were kept in the tubes on ice while preparing the OMNY pins (Holler et al., 2017b) in a method as previously described (Shahmoradian et al., 2017b).

On the day of cryo-trimming, cryo-knives (Diatome™ 45° diamond trim knife and 90° diamond trim knife) were loaded and the cryo chamber was cooled to −90°C. OMNY pins were slightly shaved down to an appropriate height as previously described. For dissection, pieces of biopsy-punched tissue were placed in droplets of cryo-protectant on a black plastic block on ice; a black piece of paper glued to the other side of a petri dish, on ice, could also be used. This black plastic block (Leica) is typically used for mounting of pins for cryo ultramicrotomy Tokuyasu technique. A Microfeather 30° ophthalmological scalpel was used to cut the pieces (in cryoprotectant) into four quadrants, further

[1]www.brainbank.nl

cut into 8 "pie pieces" in total. The sample was held in place using fine electronic-grade tweezers during this cutting.

The leg of one of the tweezers was used to position one "pie-piece" of tissue onto the tip of a shaved OMNY pin (Shahmoradian et al., 2017b) positioned in a small aluminum cube adaptor. Ethanol (70%) was used to continuously clean the tweezers to prevent hardening/sticking due to the cryoprotectant. A clean 200 μl pipette tip was used to gently position the piece of tissue straight and centered onto the OMNY pin. The pipette tip did not stick as much to the tissue as the metal tweezers. The OMNY pin and adaptor was then placed into the cryo chamber at −90°C and kept therein for 1 h. This is a "slow-freezing" technique typical for cryo-immunogold electron microscopy (Tokuyasu, 1986; Peters et al., 2006). This procedure was repeated for mounting all "pie pieces" of tissue from two biopsy-punched pieces of tissue, onto multiple OMNY pins. The small aluminum cube adaptors, holding the OMNY pin on which each tissue piece was previously "glued" using the extra cryoprotectant (liquid at room temperature, then hardened while transferred and left in the cryo ultramicrotome chamber at −90°C), were then firmly clamped into the standard clamping chuck of the Leica cryo ultramicrotome for subsequent trimming into a skyscraper-type shape of approximately 100 μm in X-Y-Z dimensions using a Trim90 (Diatome^{TM}) diamond knife with a 90° cutting angle. Samples were stored in liquid nitrogen until imaging by cryo-PXCT. Safety considerations were performed according to section "Safety Considerations for Tissue Handling."

Cryo-PXCT Data Collection and Tomogram Reconstruction

Cryo-PXCT measurements were carried out at the cSAXS beamline at the Swiss Light Source, Paul Scherrer Institut (PSI), Switzerland. Nine tomograms (four of Parkinson's diseased human brain and five of non-demented control human brain) were obtained under cryogenic conditions (−180°C) using OMNY (Holler et al., 2018). A general description of the experimental setup is provided as follows. Samples were mounted on customized sample pins (Holler et al., 2017b) and imaged at a photon energy of 6.2 keV, defined by a double crystal Si (111) monochromator. The illumination on the sample was defined by the combination of a 50 μm-diameter central stop, a coherently illuminated 220 μm-diameter Fresnel zone plate (FZP) with an outer-most zone width of 60 nm, and a 30 μm-diameter order sorting aperture. The FZP was fabricated by the Laboratory for Micro and Nanotechnology, Paul Scherrer Institut. The focal distance was 66 mm while the sample was placed 2.4 mm downstream the focus to give an illumination of around 8 um in diameter on the sample. For each ptychographic projection, the scanning followed a Fermat spiral pattern (Huang et al., 2014) with an average step size of 2.6 micron. For each scanning position, a diffraction pattern was collected 7.3 m downstream of the sample with an EIGER (Guizar-Sicairos et al., 2014) detector and exposure time of 0.1 s. Projections were taken from 0 to 180 degrees. The field of view and the number of projections for each tomogram are detailed in **Table 1**.

Ptychographic reconstructions were obtained through the difference map algorithm (Thibault et al., 2008) followed by maximum likelihood algorithm (Thibault and Guizar-Sicairos, 2012) using software PtychoShelves (Wakonig et al., 2020). For each diffraction pattern an area of 500 by 500 pixels was used for the reconstruction, giving an image pixel size of approximately 40 nm. 2D projections were aligned (Guizar-Sicairos et al., 2011, 2015) to generate 3D tomograms based on modified filtered back projection (Guizar-Sicairos et al., 2011). The grayscale in the tomograms correspond to absolute electron density (Diaz et al., 2012). Image resolution was estimated by FSC (Van Heel and Schatz, 2005). The number of photons incident on the sample for one projection fell in the range of 2.5×10^6 to 4.5×10^6 photons/μm^2. X-ray doses exposed to the frozen brain samples were estimated using absorption coefficients of water with attenuation length of 451 μm and density 1,000 kg/m^3. Estimated resolutions and X-ray doses can be found for each measurement in **Table 1**. Safety considerations were performed according to section "Safety Considerations for Tissue Handling."

Immuno-Electron Microscopy After Cryo-PXCT Imaging

Tissue blocks corresponding to Tomo 5 (Control human brain) and Tomo 2 (Parkinson's diseased human brain) were selected for downstream cryo-ultramicrotomy and immunogold labeling followed by imaging by electron microscopy (**Supplementary Figure 5**). Tissue blocks were mounted into the cryo ultramicrotome chamber and sectioned at −100°C, typical for cryo-immunogold labeling for electron microscopy (Tokuyasu, 1986; Peters et al., 2006). Sections of 70 nm thickness were created using a sectioning speed of 0.2 mm/s with a Diatome^{TM} "Cryo35" knife, without use of the static ionizer. Sections were picked up from surface of the knife using a Diatome^{TM} "Perfect Loop" with a droplet of solution prepared by adding 2.3 M sucrose in phosphate buffer to 2% methylcellulose in distilled water with a ratio 3:1, and transferred to the surface of a hexagonal 200-mesh gold EM grid using a technique as previously described (Peters et al., 2006).

Calcium-/magnesium-free PBS were used to wash sections from both control human brain and Parkinson's diseased human brain tissue blocks to remove pick-up solution (three times for 2 min each). After washing, those sections were inactivated free aldehyde group by incubating with 50 mM glycine in calcium-/magnesium-free PBS for 15 min and were then blocked hydrophobic areas using AURION^{TM} Blocking Solution for Goat antibody Gold Conjugated (product code 905.002) for 30 min. After washing by calcium-/magnesium-free PBS buffer containing 0.1% AURION^{TM} BSA-c (product code 900.099), they were immunolabeled using the following primary antibodies: 1 μg/ml of anti-VDAC1 (mitochondrial porin antibody, Abcam ab14734), 2 μg/ml of anti-LAMP1 antibody (lysosomal marker, Abcam ab24170), 5 μg/ml of anti-alpha-synuclein (LB509, Abcam ab27766), or 10 μg/ml of anti- phosphorylated alpha-synuclein (S129, Abcam ab59264). Sections on each EM grid were subject to only 1 kind of antibody each (no multiple labeling). Antibodies were diluted in a calcium-/magnesium-free

PBS buffer containing 0.1% AURION^{TM} BSA-c. Sections on the EM grids were incubated for 1 h at room temperature with the primary antibodies.

After primary antibody incubation, they were washed 6 times, 5 min each with calcium-/magnesium-free PBS solution containing 0.1% AURION^{TM} BSA-c. Secondary immunogolds (10 nm diameter, AURION^{TM} ImmunoGold reagents) were incubated for 90 min at room temperature, then washed with calcium-/magnesium-free PBS containing 0.1% AURION^{TM} BSA-c, followed by additional wash by calcium-/magnesium-free PBS. Afterward, sections on grids were postfixed by 2% glutaraldehyde in calcium-/magnesium-free PBS for 5 min. To remove glutaraldehyde, grids were washed extensively with calcium-/magnesium-free PBS, then deionized/distilled water. Subsequently, grids were additionally contrast-enhanced using 4% neutral uranyl acetate, which was prepared by mixing 4% uranyl acetate and 0.3M oxalic acid and was adjusted to pH 7 by 25% ammonium hydroxide. A solution of 0.4% uranyl acetate in 2% methylcellulose was then used for further contrast-enhancement (on ice). EM grids were then imaged at room temperature using an FEI T12 (Thermo Fisher Scientific, United States) operated at 120 kV. Electron micrographs were recorded on a 4096 × 4096 pixel F416 CMOS camera (TVIPS GmbH, Germany). Safety considerations were performed according to section "Safety Considerations for Tissue Handling."

3D Color Segmentation and Statistical Analysis of Dystrophic Myelinated Axons (DMAs)

Three-dimensional visualization and color segmentation was performed using commercial software Avizo 9.2.0 (Thermo Scientific). The images were imported into Avizo software and the threshold of the colormap was adjusted appropriately. The features of interest including blood vessels, nuclei, red blood cells and myelinated axons were segmented semi-automatically with the use of the "Brush" and "Interpolate" tools. The neuromelanin-containing organelles that appear as dark, dense globules could be segmented by "Threshold" tool. The masking value was adjusted until all neuromelanin-containing organelles were masked and identified precisely, then were selected and assigned by "Select Masked Material" tool for all slices. Unexpected selected regions not corresponding to neuromelanin were deselected semi-automatically afterward by using "Brush" and "Interpolate" tools.

After all structures were segmented and registered to their appropriate materials (blood vessel, myelinated axon, etc.), they were smoothed independently by locking other materials. Afterward, smoothed materials were exported into individual data objects from the Labels dataset by the "Arithmetic" function and surfaces were then generated for visualization. Myelinated axons, neuromelanin, nuclei, red blood cells were visualized by the "Shaded" draw style while blood vessels and the swollen part of the myelinated axons were visualized by "Transparent" draw style to reveal their inside contents. This label separation process allowed us to visualize the surface of single material without disturbing others. Afterward, snapshots of 3D color-rendered surfaces and movies were created for presentation.

Optical Microscopy Data Collection

Experiments were performed on 10 and 20 μm-thick formalin-fixed paraffin-embedded sections of the midbrain containing the SNpc, from 2 PD patients and 2 non-neurological control subjects, including adjacent tissue sections from the same PD brain donor as used for the cryo-PXCT and EM studies (**Table 2**). First, an immunofluorescent staining was performed using a primary antibody directed specifically against Ser-129 p-aSyn (11A5, Prothena, 0.3 μg/ml, incubation overnight at 4°C), a secondary antibody coupled to an Alexa 594 fluophore (Molecular Probes; art. no. A21203; 1/400 diluted; incubation 2 h at RT), and DAPI (1 μg/ml). Afterward, a Bielschowsky silver staining protocol was performed, according to the protocol previously described (Litchfield and Nagy, 2001).

Sections were analyzed by brightfield and fluorescent microscopy, which was performed using a Leica DM5000B automated microscope (Leica Microsystems), equipped with a Nuance camera (Nuance 3.02, Perkin Elmer Inc) for multispectral imaging. Images were captured at wavelengths ranging from 440 to 540 nm (for DAPI), and ranging from 580 to 720 nm (for p-aSyn) with HC PL APO 40 × 1.30 NA and HC PL APO 63 × 1.40 NA – 0.60 oil objectives. The spectrum of autofluorescent signal was determined and removed from the images. Brightfield images were subsequently made at the same locations using the Nuance camera. In addition, additional brightfield images were captured using a Leica DFC450 camera with PL FLUOTAR 2.5 X/0.07 and HC PL APO 10 × 0.40 NA objectives.

DATA AVAILABILITY STATEMENT

The raw data supporting the conclusions of this article will be made available by the authors, without undue reservation.

ETHICS STATEMENT

The studies involving human participants were reviewed and approved by the medical ethical committee of VU University Medical Center Amsterdam. The patients/participants of next of kin provided written informed consent for the use of clinical data and brain tissue for research purposes.

AUTHOR CONTRIBUTIONS

HT performed all color segmentations of the tomograms, completed quantification and measurements for all dystrophic axons in all of the diseased datasets, made all movies, helped to make the schematic model, and performed ultramicrotomy and immunogold labeling. IR assisted with ultramicrotomy and immunogold labeling. ET, AD, MG-S, and MH collected

the cryo-PXCT data. ET primarily completed all of the tomographic reconstructions and made the descriptive table. MH, JR, AD, and MG-S developed the OMNY instrument and associated software. WB dissected postmortem human brain tissue and provided all tissue samples from NBB and NABCA to SS. WB supervised the stainings and analysis with optical microscopy. HS provided resources and contributed to electron microscopy. SS interpreted biological results. AL collected electron microscopy data with SS and JB. TM performed the combined Bielchowsky and immunofluorescence experiment. Analysis of optical microscopy was done by TM, AJ, and JB. WB and TM wrote text of optical microscopy section. SS planned the experiments, trained and supervised HT, prepared and cryo-trimmed all tissues for subsequent cryo-PXCT imaging, made the figures, and wrote the manuscript, with input from all authors.

FUNDING

HT was supported by a CROSS fellowship through the Paul Scherrer Institute's Directorate, Division of Biology and Chemistry, and Photon Science Division. ET was supported by SNSF grant number 200021_152554 and 200020_169623. IR was supported by the NEW PSI-FELLOW-III-3i – International Fellowship Program through SS (PI). OMNY setup was supported by the Swiss National Science Foundation SNF (Funding scheme R'EQUIP, Project number 145056, "OMNY") and by the Competence Centre for Materials Science and Technology (CCMX, Project number 77) of the ETH-Board, Switzerland. WB was supported by ZONMW 40-43500-98-4151.

ACKNOWLEDGMENTS

We thank Helmut Gnaegi (Diatome Ltd., Nidau, Switzerland) for his expert help and guidance with cryo-ultramicrotomy of the post-imaged cryo-PXCT tissue blocks. We thank Peter van de Plas (Aurion Immuno Gold company, Wageningen, Netherlands) for expert support and advice with immunogold labeling. We thank the NBB (www.brainbank.nl) and Normal Aging Brain Collection (www.nabca.eu) team for assistance in collection of postmortem human brain tissue samples. We thank B. Sarafimov and X. Donath for technical assistance with OMNY. We also thank the Swiss Light Source, Paul Scherrer Institut for providing the beamtime required to conduct the PXCT measurements.

SUPPLEMENTARY MATERIAL

The Supplementary Material for this article can be found online at: https://www.frontiersin.org/articles/10.3389/fnins.2020.570019/full#supplementary-material

REFERENCES

Adalbert, R., Nogradi, A., Babetto, E., Janeckova, L., Walker, S. A., Kerschensteiner, M., et al. (2009). Severely dystrophic axons at amyloid plaques remain continuous and connected to viable cell bodies. *Brain* 132, 402–416. doi: 10.1093/brain/awn312

Anderson, J. P., Walker, D. E., Goldstein, J. M., de Laat, R., Banducci, K., Caccavello, R. J., et al. (2006). Phosphorylation of Ser-129 is the dominant pathological modification of alpha-synuclein in familial and sporadic Lewy body disease. *J. Biol. Chem.* 281, 29739–29752. doi: 10.1074/jbc.M600933200

Bartels, M., Krenkel, M., Cloetens, P., Möbius, W., and Salditt, T. (2015). Myelinated mouse nerves studied by X-ray phase contrast zoom tomography. *J. Struct. Biol.* 192, 561–568. doi: 10.1016/j.jsb.2015.11.001

Bartzokis, G. (2004). Age-related myelin breakdown: a developmental model of cognitive decline and Alzheimer's disease. *Neurobiol. Aging* 25, 5–18. doi: 10.1016/j.neurobiolaging.2003.03.001

Bartzokis, G., Lu, P. H., Tishler, T. A., Fong, S. M., Oluwadara, B., Finn, J. P., et al. (2007). Myelin breakdown and iron changes in Huntington's disease: pathogenesis and treatment implications. *Neurochem. Res.* 32, 1655–1664. doi: 10.1007/s11064-007-9352-7

Bartzokis, G., Tishler, T. A., Shin, I. S., Lu, P. H., and Cummings, J. L. (2004). Brain ferritin iron as a risk factor for age at onset in neurodegenerative diseases. *Ann. N. Y. Acad. Sci.* 1012, 224–236. doi: 10.1196/annals.1306.019

Braak, H., Alafuzoff, I., Arzberger, T., Kretzschmar, H., and Del Tredici, K. (2006a). Staging of Alzheimer disease-associated neurofibrillary pathology using paraffin sections and immunocytochemistry. *Acta Neuropathol.* 112, 389–404. doi: 10.1007/s00401-006-0127-z

Braak, H., and Del Tredici, K. (2016). Potential pathways of abnormal tau and alpha-synuclein dissemination in sporadic alzheimer's and parkinson's diseases. *Cold Spring Harb. Perspect. Biol.* 8:a023630. doi: 10.1101/cshperspect.a023630

Braak, H., Ghebremedhin, E., Rub, U., Bratzke, H., and Del Tredici, K. (2004). Stages in the development of Parkinson's disease-related pathology. *Cell Tissue Res.* 318, 121–134. doi: 10.1007/s00441-004-0956-9

Braak, H., Rub, U., Schultz, C., and Del Tredici, K. (2006b). Vulnerability of cortical neurons to Alzheimer's and Parkinson's diseases. *J. Alzheimers Dis.* 9, 35–44. doi: 10.3233/JAD-2006-9S305

Bradl, M., and Lassmann, H. (2010). Oligodendrocytes: biology and pathology. *Acta Neuropathol.* 119, 37–53. doi: 10.1007/s00401-009-0601-5

Burke, R. E., and O'Malley, K. (2013). Axon degeneration in Parkinson's disease. *Exp. Neurol.* 246, 72–83. doi: 10.1016/j.expneurol.2012.01.011

Chevalier-Larsen, E., and Holzbaur, E. L. (2006). Axonal transport and neurodegenerative disease. *Biochim. Biophys. Acta (BBA) Mol. Basis Dis.* 1762, 1094–1108. doi: 10.1016/j.bbadis.2006.04.002

Chung, C. Y., Koprich, J. B., Siddiqi, H., and Isacson, O. (2009). Dynamic changes in presynaptic and axonal transport proteins combined with striatal neuroinflammation precede dopaminergic neuronal loss in a rat model of AAV alpha-synucleinopathy. *J. Neurosci.* 29, 3365–3373. doi: 10.1523/JNEUROSCI.5427-08.2009

de Castro Fonseca, M., Araujo, B. H. S., Dias, C. S. B., Archilha, N. L., Neto, D. P. A., Cavalheiro, E., et al. (2018). High-resolution synchrotron-based X-ray microtomography as a tool to unveil the three-dimensional neuronal architecture of the brain. *Sci. Rep.* 8, 1–13. doi: 10.1038/s41598-018-30501-x

Deng, J., Vine, D. J., Chen, S., Jin, Q., Nashed, Y. S., Peterka, T., et al. (2017). X-ray ptychographic and fluorescence microscopy of frozen-hydrated cells using continuous scanning. *Sci. Rep.* 7:445. doi: 10.1038/s41598-017-00569-y

Diaz, A., Malkova, B., Holler, M., Guizar-Sicairos, M., Lima, E., Panneels, V., et al. (2015). Three-dimensional mass density mapping of cellular ultrastructure by ptychographic X-ray nanotomography. *J. Struct. Biol.* 192, 461–469. doi: 10.1016/j.jsb.2015.10.008

Diaz, A., Trtik, P., Guizar-Sicairos, M., Menzel, A., Thibault, P., and Bunk, O. (2012). Quantitative x-ray phase nanotomography. *Phys. Rev.B* 85:020104. doi: 10.1103/PhysRevB.85.020104

Doorn, K. J., Goudriaan, A., Blits-Huizinga, C., Bol, J. G., Rozemuller, A. J., Hoogland, P. V., et al. (2014). Increased amoeboid microglial density in the

olfactory bulb of Parkinson's and Alzheimer's patients. *Brain Pathol.* 24, 152–165. doi: 10.1111/bpa.12088

Dyer, E. L., Gray Roncal, W., Prasad, J. A., Fernandes, H. L., Gürsoy, D., Andrade, V. De, et al. (2017). Quantifying mesoscale neuroanatomy using X-ray microtomography. *eNeuro* 4:ENEURO.0195-17.2017. doi: 10.1523/ENEURO.0195-17.2017

Emre, M., Aarsland, D., Brown, R., Burn, D. J., Duyckaerts, C., Mizuno, Y., et al. (2007). Clinical diagnostic criteria for dementia associated with Parkinson's disease. *Mov. Disord.* 22, 1689–1707. doi: 10.1002/mds.21507

Eriksson, M., van der Veen, J. F., and Quitmann, C. (2014). Diffraction-limited storage rings – a window to the science of tomorrow. *J. Synchrotron. Radiat.* 21, 837–842. doi: 10.1107/S1600577514019286

Ettle, B., Schlachetzki, J. C. M., and Winkler, J. (2016). Oligodendroglia and myelin in neurodegenerative diseases: more than just bystanders? *Mol. Neurobiol.* 53, 3046–3062. doi: 10.1007/s12035-015-9205-3

Fearnley, J. M., and Lees, A. J. (1991). Ageing and Parkinson's disease: substantia nigra regional selectivity. *Brain* 114, 2283–2301. doi: 10.1093/brain/114.5.2283

Fields, R. D. (2014). Myelin formation and remodeling. *Cell* 156, 15–17. doi: 10.1016/j.cell.2013.12.038

Friese, M. A. (2016). Widespread synaptic loss in multiple sclerosis. *Brain* 139, 2–4. doi: 10.1093/brain/awv349

Galvin, J. E., Uryu, K., Lee, V. M., and Trojanowski, J. Q. (1999). Axon pathology in Parkinson's disease and Lewy body dementia hippocampus contains alpha-, beta-, and gamma-synuclein. *Proc. Natl. Acad. Sci. U.S.A.* 96, 13450–13455. doi: 10.1073/pnas.96.23.13450

García-Cabezas, M. Á, John, Y. J., Barbas, H., and Zikopoulos, B. (2016). Distinction of neurons, glia and endothelial cells in the cerebral cortex: an algorithm based on cytological features. *Front. Neuroanat.* 10:107. doi: 10.3389/fnana.2016.00107

Grune, T., Jung, T., Merker, K., and Davies, K. J. (2004). Decreased proteolysis caused by protein aggregates, inclusion bodies, plaques, lipofuscin, ceroid, and 'aggresomes' during oxidative stress, aging, and disease. *Int. J. Biochem. Cell Biol.* 36, 2519–2530. doi: 10.1016/j.biocel.2004.04.020

Guizar-Sicairos, M., Diaz, A., Holler, M., Lucas, M. S., Menzel, A., Wepf, R. A., et al. (2011). Phase tomography from x-ray coherent diffractive imaging projections. *Optics express* 19, 21345–21357. doi: 10.1364/OE.19.021345

Guizar-Sicairos, M., Boon, J. J., Mader, K., Diaz, A., Menzel, A., and Bunk, O. (2015). Quantitative interior x-ray nanotomography by a hybrid imaging technique. *Optica* 2, 259–266. doi: 10.1364/OPTICA.2.000259

Guizar-Sicairos, M., Johnson, I., Diaz, A., Holler, M., Karvinen, P., Stadler, H.-C., et al. (2014). High-throughput ptychography using Eiger: scanning X-ray nano-imaging of extended regions. *Optics Express* 22, 14859–14870. doi: 10.1364/OE.22.014859

Holler, M., Diaz, A., Guizar-Sicairos, M., Karvinen, P., Farm, E., Harkonen, E., et al. (2014). X-ray ptychographic computed tomography at 16 nm isotropic 3D resolution. *Sci. Rep.* 4:3857. doi: 10.1038/srep03857

Holler, M., Guizar-Sicairos, M., Tsai, E. H. R., Dinapoli, R., Muller, E., Bunk, O., et al. (2017a). High-resolution non-destructive three-dimensional imaging of integrated circuits. *Nature* 543, 402–406. doi: 10.1038/nature21698

Holler, M., Raabe, J., Diaz, A., Guizar-Sicairos, M., Wepf, R., Odstrcil, M., et al. (2018). OMNY—A tOMography Nano crYo stage. *Rev. Sci. Instrum.* 89:043706. doi: 10.1063/1.5020247

Holler, M., Raabe, J., Wepf, R., Shahmoradian, S. H., Diaz, A., Sarafimov, B., et al. (2017b). OMNY PIN-A versatile sample holder for tomographic measurements at room and cryogenic temperatures. *Rev. Sci. Instrum.* 88:113701. doi: 10.1063/1.4996092

Howells, M. R., Beetz, T., Chapman, H. N., Cui, C., Holton, J. M., Jacobsen, C. J., et al. (2009). An assessment of the resolution limitation due to radiation-damage in x-ray diffraction microscopy. *J. Electron Spectros Relat. Phenomena* 170, 4–12. doi: 10.1016/j.elspec.2008.10.008

Huang, X., Yan, H., Harder, R., Hwu, Y., Robinson, I. K., and Chu, Y. S. (2014). Optimization of overlap uniformness for ptychography. *Optics Express* 22, 12634–12644. doi: 10.1364/OE.22.012634

Inglese, M., and Petracca, M. (2013). Imaging multiple sclerosis and other neurodegenerative diseases. *Prion* 7, 47–54. doi: 10.4161/pri.22650

Khimchenko, A., Bikis, C., Pacureanu, A., Hieber, S. E., Thalmann, P., Deyhle, H., et al. (2018). Hard X−ray nanoholotomography: large−scale, label−free, 3D neuroimaging beyond optical limit. *Adv. Sci.* 5:1700694. doi: 10.1002/advs.201700694

Koch, J. C., Bitow, F., Haack, J., d'Hedouville, Z., Zhang, J. N., Tonges, L., et al. (2015). Alpha-Synuclein affects neurite morphology, autophagy, vesicle transport and axonal degeneration in CNS neurons. *Cell Death Dis.* 6:e1811. doi: 10.1038/cddis.2015.169

Kotzbauer, P. T., Giasson, B. I., Kravitz, A. V., Golbe, L. I., Mark, M. H., Trojanowski, J. Q., et al. (2004). Fibrillization of alpha-synuclein and tau in familial Parkinson's disease caused by the A53T alpha-synuclein mutation. *Exp. Neurol.* 187, 279–288. doi: 10.1016/j.expneurol.2004.01.007

Kouroupi, G., Taoufik, E., Vlachos, I. S., Tsioras, K., Antoniou, N., Papastefanaki, F., et al. (2017). Defective synaptic connectivity and axonal neuropathology in a human iPSC-based model of familial Parkinson's disease. *Proc. Natl. Acad. Sci. U.S.A.* 114, E3679–E3688. doi: 10.1073/pnas.1617259114

Kremers, G. J., Gilbert, S. G., Cranfill, P. J., Davidson, M. W., and Piston, D. W. (2011). Fluorescent proteins at a glance. *J. Cell Sci.* 124, 157–160. doi: 10.1242/jcs.072744

Kuan, A. T., Phelps, J. S., Thomas, L. A., Nguyen, T. M., Han, J., Chen, C.-L., et al. (2020). Dense neuronal reconstruction through X-ray holographic nano-tomography. *Nat. Neurosci.* doi: 10.1038/s41593-020-0704-9 [Epub ahead of print].

Kuusisto, E., Parkkinen, L., and Alafuzoff, I. (2003). Morphogenesis of Lewy bodies: dissimilar incorporation of alpha-synuclein, ubiquitin, and p62. *J. Neuropathol. Exp. Neurol.* 62, 1241–1253. doi: 10.1093/jnen/62.12.1241

Lam, S. S., Martell, J. D., Kamer, K. J., Deerinck, T. J., Ellisman, M. H., Mootha, V. K., et al. (2015). Directed evolution of APEX2 for electron microscopy and proximity labeling. *Nat. Methods* 12, 51–54. doi: 10.1038/nmeth.3179

Le Gros, M. A., Clowney, E. J., Magklara, A., Yen, A., Markenscoff-Papadimitriou, E., Colquitt, B., et al. (2016). Soft X-ray tomography reveals gradual chromatin compaction and reorganization during neurogenesis in vivo. *Cell Reports* 17, 2125–2136. doi: 10.1016/j.celrep.2016.10.060

Lee, J. Y., Taghian, K., and Petratos, S. (2014). Axonal degeneration in multiple sclerosis: can we predict and prevent permanent disability? *Acta Neuropathol. Commun.* 2:97. doi: 10.1186/s40478-014-0097-7

Litchfield, S., and Nagy, Z. (2001). New temperature modification makes the Bielschowsky silver stain reproducible. *Acta Neuropathol.* 101, 17–21. doi: 10.1007/s004010000248

Manning, C. F., Bundros, A. M., and Trimmer, J. S. (2012). Benefits and pitfalls of secondary antibodies: why choosing the right secondary is of primary importance. *PLoS One* 7:e38313. doi: 10.1371/journal.pone.0038313

McKeith, I. G., Dickson, D. W., Lowe, J., Emre, M., O'Brien, J. T., Feldman, H., et al. (2005). Consortium on, diagnosis and management of dementia with Lewy bodies: third report of the DLB Consortium. *Neurology* 65, 1863–1872. doi: 10.1212/01.wnl.0000187889.17253.b1

Mizutani, R., Takeuchi, A., Uesugi, K., Suzuki, Y., Osamura, R. Y., and Takekoshi, S. (2009). Microtomographic analysis of neuronal circuits of human brain. *Cereb. Cortex* 20, 1739–1748. doi: 10.1093/cercor/bhp237

Mokso, R., Cloetens, P., Maire, E., Ludwig, W., and Buffière, J. Y. (2007). Nanoscale zoom tomography with hard x rays using Kirkpatrick-Baez optics. *Appl. Phys. Lett.* 90:144104. doi: 10.1063/1.2719653

Morell, P., and Norton, W. T. (1980). Myelin. *Sci. Am.* 242, 88–119. doi: 10.1038/scientificamerican0580-88

Nave, K. A., and Werner, H. B. (2014). Myelination of the nervous system: mechanisms and functions. *Annu. Rev. Cell Dev. Biol.* 30, 503–533. doi: 10.1146/annurev-cellbio-100913-013101

Pérez-Berná, A. J., Rodríguez, M. J., Chichón, F. J., Friesland, M. F., Sorrentino, A., Carrascosa, J. L., et al. (2016). Structural changes in cells imaged by soft X-ray cryo-tomography during hepatitis C virus infection. *ACS Nano* 10, 6597–6611. doi: 10.1021/acsnano.6b01374

Peters, P. J., Bos, E., and Griekspoor, A. (2006). Cryo−immunogold electron microscopy. *Curr. Protocols Cell Biol.* 30, 4.7.1–4.7.19. doi: 10.1002/0471143030.cb0407s30

Peters, P. J., and Pierson, J. (2008). Immunogold labeling of thawed cryosections. *Methods Cell Biol.* 88, 131–149. doi: 10.1016/S0091-679X(08)00408-1

Pfister, B., Sanchez-Ferrer, A., Diaz, A., Lu, K. J., Otto, C., Holler, M., et al. (2016). Recreating the synthesis of starch granules in yeast. *eLife* 5:29. doi: 10.7554/eLife.15552.024

Puntarulo, S. (2005). Iron, oxidative stress and human health. *Mol. Aspects Med.* 26, 299–312. doi: 10.1016/j.mam.2005.07.001

Rosas, H. D., Tuch, D. S., Hevelone, N. D., Zaleta, A. K., Vangel, M., Hersch, S. M., et al. (2006). Diffusion tensor imaging in presymptomatic and early Huntington's disease: selective white matter pathology and its relationship to clinical measures. *Mov. Disord.* 21, 1317–1325. doi: 10.1002/mds.20979

Rutala, W. A., and Weber, D. J. (2010). A society for healthcare epidemiology of, guideline for disinfection and sterilization of prion-contaminated medical instruments. *Infect Control Hosp. Epidemiol.* 31, 107–117. doi: 10.1086/650197

Saha, A. R., Hill, J., Utton, M. A., Asuni, A. A., Ackerley, S., Grierson, A. J., et al. (2004). Parkinson's disease alpha-synuclein mutations exhibit defective axonal transport in cultured neurons. *J. Cell Sci.* 117, 1017–1024. doi: 10.1242/jcs.00967

Sekigawa, A., Takamatsu, Y., Sekiyama, K., and Hashimoto, M. (2015). Role of alpha- and beta-synucleins in the axonal pathology of parkinson's disease and related synucleinopathies. *Biomolecules* 5, 1000–1011. doi: 10.3390/biom5021000

Shahmoradian, S. H., Genoud, C., Graff-Meyer, A., Hench, J., Moors, T., Schweighauser, G., et al. (2017a). Lewy pathology in Parkinson's disease consists of a crowded organellar membranous medley. *bioRxiv* [Preprint]. 137976. doi: 10.1101/137976

Shahmoradian, S. H., Tsai, E. H. R., Diaz, A., Guizar-Sicairos, M., Raabe, J., Spycher, L., et al. (2017b). Three-dimensional imaging of biological tissue by cryo X-ray ptychography. *Sci. Rep.* 7:6291. doi: 10.1038/s41598-017-05587-4

Shu, X., Lev-Ram, V., Deerinck, T. J., Qi, Y., Ramko, E. B., Davidson, M. W., et al. (2011). A genetically encoded tag for correlated light and electron microscopy of intact cells, tissues, and organisms. *PLoS Biol.* 9:e1001041. doi: 10.1371/journal.pbio.1001041

Simons, M., and Nave, K. A. (2015). Oligodendrocytes: myelination and axonal support. *Cold Spring Harb. Perspect. Biol.* 8:a020479. doi: 10.1101/cshperspect.a020479

Su, J. H., Cummings, B. J., and Cotman, C. W. (1993). Identification and distribution of axonal dystrophic neurites in Alzheimer's disease. *Brain Res.* 625, 228–237. doi: 10.1016/0006-8993(93)91063-X

Tagliaferro, P., and Burke, R. E. (2016). Retrograde axonal degeneration in parkinson disease. *J. Parkinsons Dis.* 6, 1–15. doi: 10.3233/JPD-150769

Thal, D. R., Capetillo-Zarate, E., Del Tredici, K., and Braak, H. (2006). The development of amyloid beta protein deposits in the aged brain. *Sci. Aging Knowledge Environ.* 2006:re1. doi: 10.1126/sageke.2006.6.re1

Thibault, P., Dierolf, M., Menzel, A., Bunk, O., David, C., and Pfeiffer, F. (2008). High-resolution scanning x-ray diffraction microscopy. *Science* 321, 379–382. doi: 10.1126/science.1158573

Thibault, P., and Guizar-Sicairos, M. (2012). Maximum-likelihood refinement for coherent diffractive imaging. *New J. Physics* 14:063004. doi: 10.1088/1367-2630/14/6/063004

Todorich, B., Pasquini, J. M., Garcia, C. I., Paez, P. M., and Connor, J. R. (2009). Oligodendrocytes and myelination: the role of iron. *Glia* 57, 467–478. doi: 10.1002/glia.20784

Tokuyasu, K. (1986). Application of cryoultramicrotomy to immunocytochemistry. *J. Microscopy* 143, 139–149. doi: 10.1111/j.1365-2818.1986.tb02772.x

Tokuyasu, K. T. (1980). Immunochemistry on ultrathin frozen sections. *Histochem. J.* 12, 381–403. doi: 10.1007/BF01011956

Uchihara, T. (2007). Silver diagnosis in neuropathology: principles, practice and revised interpretation. *Acta Neuropathol.* 113, 483–499. doi: 10.1007/s00401-007-0200-2

Van Heel, M., and Schatz, M. (2005). Fourier shell correlation threshold criteria. *J. Struct. Biol.* 151, 250–262. doi: 10.1016/j.jsb.2005.05.009

Wakonig, K., Stadler, H. C., Odstrcil, M., Tsai, E. H. R., Diaz, A., Holler, M., et al. (2020). PtychoShelves, a high-level, versatile framework for high-performance analysis of ptychographic data. *J. Appl. Crystallogr.* doi: 10.1107/S1600576720001776

Ward, R. J., Zucca, F. A., Duyn, J. H., Crichton, R. R., and Zecca, L. (2014). The role of iron in brain ageing and neurodegenerative disorders. *Lancet Neurol.* 13, 1045–1060. doi: 10.1016/S1474-4422(14)70117-6

Wu, H. R., Chen, S. T., Chu, Y. S., Conley, R., Bouet, N., Chien, C. C., et al. (2012). Nanoresolution radiology of neurons. *J. Phys. D Appl. Phys.* 45:242001. doi: 10.1088/0022-3727/45/24/242001

Zucca, F. A., Vanna, R., Cupaioli, F. A., Bellei, C., De Palma, A., Di Silvestre, D., et al. (2018). Neuromelanin organelles are specialized autolysosomes that accumulate undegraded proteins and lipids in aging human brain and are likely involved in Parkinson's disease. *NPJ Parkinsons Dis.* 4:17.

Conflict of Interest: The authors declare that the research was conducted in the absence of any commercial or financial relationships that could be construed as a potential conflict of interest.

Copyright © 2020 Tran, Tsai, Lewis, Moors, Bol, Rostami, Diaz, Jonker, Guizar-Sicairos, Raabe, Stahlberg, van de Berg, Holler and Shahmoradian. This is an open-access article distributed under the terms of the Creative Commons Attribution License (CC BY). The use, distribution or reproduction in other forums is permitted, provided the original author(s) and the copyright owner(s) are credited and that the original publication in this journal is cited, in accordance with accepted academic practice. No use, distribution or reproduction is permitted which does not comply with these terms.

frontiers in Neuroscience

ORIGINAL RESEARCH
published: 26 November 2020
doi: 10.3389/fnins.2020.569706

Zero Echo Time MRAC on FDG-PET/MR Maintains Diagnostic Accuracy for Alzheimer's Disease; A Simulation Study Combining ADNI-Data

Takahiro Ando[1], Bradley Kemp[2], Geoffrey Warnock[3,4], Tetsuro Sekine[1,5,6], Sandeep Kaushik[7], Florian Wiesinger[7] and Gaspar Delso[7] for the Alzheimer's Disease Neuroimaging Initiative[†]*

[1] Department of Radiology, Nippon Medical School, Tokyo, Japan, [2] Department of Radiology, Mayo Clinic, Rochester, MN, United States, [3] Institute of Pharmacology and Toxicology, University of Zurich, Zurich, Switzerland, [4] PMOD Technologies Ltd., Zurich, Switzerland, [5] Department of Radiology, Nippon Medical School Musashi-Kosugi Hospital, Kawasaki, Japan, [6] Department of Nuclear Medicine, University Hospital Zurich, Zurich, Switzerland, [7] GE Healthcare, Waukesha, WI, United States

Aim: Attenuation correction using zero-echo time (ZTE) – magnetic resonance imaging (MRI) (ZTE-MRAC) has become one of the standard methods for brain-positron emission tomography (PET) on commercial PET/MR scanners. Although the accuracy of the net tracer-uptake quantification based on ZTE-MRAC has been validated, that of the diagnosis for dementia has not yet been clarified, especially in terms of automated statistical analysis. The aim of this study was to clarify the impact of ZTE-MRAC on the diagnosis of Alzheimer's disease (AD) by performing simulation study.

Methods: We recruited 27 subjects, who underwent both PET/computed tomography (CT) and PET/MR (GE SIGNA) examinations. Additionally, we extracted 107 subjects from the Alzheimer Disease Neuroimaging Initiative (ADNI) dataset. From the PET raw data acquired on PET/MR, three FDG-PET series were generated, using two vendor-provided MRAC methods (ZTE and Atlas) and CT-based AC. Following spatial normalization to Montreal Neurological Institute (MNI) space, we calculated each patient's specific error maps, which correspond to the difference between the PET image corrected using the CTAC method and the PET images corrected using the MRAC methods. To simulate PET maps as if ADNI data had been corrected using MRAC methods, we multiplied each of these 27 error maps with each of the 107 ADNI cases in MNI space. To evaluate the probability of AD in each resulting image, we calculated a cumulative *t*-value using a fully automated method which had been validated not only in the original ADNI dataset but several multi-center studies. In the method, PET score = 1 is the 95% prediction limit of AD. PET score and diagnostic accuracy for the discrimination of AD were evaluated in simulated images using the original ADNI dataset as reference.

Results: Positron emission tomography score was slightly underestimated both in ZTE and Atlas group compared with reference CTAC (-0.0796 ± 0.0938 vs. -0.0784 ± 0.1724). The absolute error of PET score was lower in ZTE than Atlas group

OPEN ACCESS

Edited by:
Miguel Castelo-Branco, Coimbra Institute for Biomedical Imaging and Translational Research (CIBIT), Portugal

Reviewed by:
Ninon Burgos, Centre National de la Recherche Scientifique (CNRS), France
Luca Presotto, San Raffaele Hospital (IRCCS), Italy

***Correspondence:**
Tetsuro Sekine
tetsuro.sekine@gmail.com

[†] Data used in preparation of this article were obtained from the Alzheimer's Disease Neuroimaging Initiative (ADNI) database (adni.loni.usc.edu). As such, the investigators within the ADNI contributed to the design and implementation of ADNI and/or provided data but did not participate in analysis or writing of this report. A complete listing of ADNI investigators can be found at: http://adni.loni.usc.edu/wp-content/uploads/how_to_apply/ADNI_Acknowledgement_List.pdf. The primary investigator is Michael W. Weiner, MD. His contact email address is Michael.Weiner@ucsf.edu

Specialty section:
This article was submitted to Brain Imaging Methods, a section of the journal Frontiers in Neuroscience

Received: 04 June 2020
Accepted: 03 November 2020
Published: 26 November 2020

Citation:
Ando T, Kemp B, Warnock G, Sekine T, Kaushik S, Wiesinger F and Delso G (2020) Zero Echo Time MRAC on FDG-PET/MR Maintains Diagnostic Accuracy for Alzheimer's Disease; A Simulation Study Combining ADNI-Data. Front. Neurosci. 14:569706. doi: 10.3389/fnins.2020.569706

(0.098 ± 0.075 vs. 0.145 ± 0.122, $p < 0.001$). A higher correlation to the original PET score was observed in ZTE vs. Atlas group (R^2: 0.982 vs. 0.961). The accuracy for the discrimination of AD patients from normal control was maintained in ZTE and Atlas compared to CTAC (ZTE vs. Atlas. vs. original; 82.5% vs. 82.1% vs. 83.2% (CI 81.8–84.5%), respectively).

Conclusion: For FDG-PET images on PET/MR, attenuation correction using ZTE-MRI had superior accuracy to an atlas-based method in classification for dementia. ZTE maintains the diagnostic accuracy for AD.

Keywords: PET/MR, attenuation correction, dementia, Alzheimer's disease, ADNI database, ZTE MRI, atlas-based MRAC, statistical analysis

INTRODUCTION

Positron emission tomography (PET)/magnetic resonance (MR) has been distributed worldwide and started to be used for the evaluation of dementia both in the clinical and research setting (Drzezga et al., 2014; Barthel et al., 2015; Fendler et al., 2016; Henriksen et al., 2016; Mainta et al., 2017; Zhang et al., 2017; Hope et al., 2019; Prato et al., 2019; Yan et al., 2020). The multi-modal evaluation combining functional images such as PET and morphological images such as MR imaging (MRI) is optimal because each of them provides complementary information (Teipel et al., 2015; Kaltoft et al., 2019). In addition, the motion artifact or partial volume effect on PET images can be minimized by utilizing simultaneous acquisition of MRI (Chen et al., 2018; Yan et al., 2020).

One of the fundamental limitations of PET/MR systems is attenuation correction (AC) derived from MRI (MRAC). With conventional MRI sequences, bone has subtle or no signal intensity because of fast T2* decay. This results in a difficulty to discriminate bone from other components. This is particularly relevant in brain parenchyma which is covered entirely by the skull. Neglecting attenuation correction from bone causes large and spatially varying error (Andersen et al., 2014).

In this decade, there has already been a vast number of published papers proposing and validating novel MRAC methods. Several novel MRAC methods has been identified that can effectively estimate skull bone (Mehranian et al., 2016; Ladefoged et al., 2017; Teuho et al., 2020). However, the implementation of these methods into commercial PET/MR scanners is still lacking. In addition, the question about how the impact of subtle residual errors on the diagnostic accuracy in dementia is still unanswered, because well-controlled clinical trials using PET/MR scanners have not been conducted so far (Catana et al., 2018; Hope et al., 2019; Teuho et al., 2020). For the evaluation of Alzheimer's disease (AD), spatial normalization, intensity normalization and statistical analysis such as *t*-value calculation are generally performed (Herholz et al., 2002; Haense et al., 2009). Spatial normalization is performed by non-rigidly transforming the original images to PET template. Intensity normalization consists in dividing the 2-Deoxy-2-[18F] fluoroglucose (FDG) uptake by the average uptake in a reference region (e.g., cerebellum, non-AD-related voxels or whole brain). Following it, *t*-value is statistically calculated as the difference between the patient's uptake and the average uptake of healthy controls. These steps compensate the variability of brain shape and tracer uptake among subjects. In this setting, not only the net error of tracer uptake, but the distribution of error may impact the result. For example, the underestimation of the reference regions leads to an overestimation of the tracer uptake in AD-related regions, or vice versa. From this point of view, one can argue whether the normal FDG-PET database acquired on PET/computed tomography (CT) scanners could be directly applied to that on PET/MR.

In our previous simulation study, the diagnostic accuracy of FDG-PET on PET/MR was tested by using normal database of FDG-PET on PET/CT (Sekine et al., 2020). That study combined real patients' FDG-PET images from PET/MR and well-controlled large cohort FDG-PET data from PET/CT in the same space (spatially normalized to the same brain template with the same voxel size). In the study, FDG-PET from PET/MR was generated based on atlas-based MRAC (Atlas) which is one of the commercially available MRAC methods installed in the GE SIGNA PET/MR (Sekine et al., 2016a; Yang et al., 2017a). The results showed that Atlas had similar diagnostic accuracy to the gold-standard, CT-based attenuation correction (CTAC), for the diagnosis of AD, although it slightly impaired sensitivity (Sekine et al., 2020). Currently, Atlas is rarely used for brain PET/MR because the vendor already developed a more accurate MRAC by using zero-echo time MRI (ZTE) which estimates head skull bone by capturing subtle proton density (Delso et al., 2015; Wiesinger et al., 2016). Although several previous studies have clarified that ZTE has substantial accuracy in the net quantification of tracer uptake (i.e., the error is below 10 % generally), the effect of residual error from ZTE was not validated in terms of diagnostic accuracy of AD (Sekine et al., 2016c; Yang et al., 2017b; Sousa et al., 2018; Schramm et al., 2019; Sgard et al., 2019). Before the implementation of ZTE into the clinical FDG-PET/MR evaluation of AD, the diagnostic performance should be validated.

The purpose of this study was to test the diagnostic accuracy of FDG-PET/MR applying vendor-provided ZTE-MRAC to discriminate AD from healthy controls. We performed a simulation study combining real patient' data and an Alzheimer Disease Neuroimaging Initiative (ADNI) dataset, a well-established large cohort. The whole process was done in

an objective and standardized manner, using semi-automatic statistical processing without user interaction.

MATERIALS AND METHODS

Alzheimer Disease Neuroimaging Initiative (ADNI) Data

Data used in the preparation of this article were obtained from the ADNI database[1]. ADNI was launched in 2003 as a public-private partnership, led by Principal Investigator Michael W. Weiner, MD. The primary goal of ADNI has been to test whether serial MRI, PET, other biological markers, and clinical and neuropsychological assessment can be combined to measure the progression of mild cognitive impairment (MCI) and early AD. For up-to-date information[2].

From ADNI-1 data, we extracted 107 participants (48 healthy and 59 AD participants). The inclusion criteria were completeness of date of birth and diagnosis (healthy or AD) who visit 24 months after 1st PET scan, which inclusion criteria was the same as our previous simulation study focusing on Atlas-based MRAC (Sekine et al., 2020). All raw PET images were of sufficient quality for visual scoring and for software-based analysis using PALZ (PMOD Alzheimer's Discrimination tool, Zurich, Switzerland). The reported FDG-PET imaging parameters were: injected dose, 185 MBq (5 mCi), dynamic 3D acquisition, six 5-min frames 30–60 min post injection.

Patients

We recruited 27 patients who underwent both PET/CT and PET/MR for oncologic staging from our previous study (Delso et al., 2018; Sekine et al., 2020). The 27 patients (15 males and 12 females, 60.0 ± 13.0 years) with lymphoma, pheochromocytoma, myeloma, melanoma, Merkel-cell cancer, lung cancer, pancreatic cancer, breast cancer and dementia were collected from another previous study, after excluding 3 patients. Two of these three excluded patients had infarction and one had multiple brain metastases. A neuroradiologist (TS) reviewed and confirmed that all included patients were free of brain abnormalities.

PET/CT and PET/MR Acquisition

The averaged injected dose of FDG was 534 ± 42 MBq [range, 434–566 MBq]. The PET/CT acquisition followed the standard protocol for a clinical oncology study using a Discovery RX/MI/690/710 PET/CT (GE Healthcare). A helical whole-body CT scan (120 - 140 kV, slice thickness 3.75–5.00 mm, pixel size 1.37 mm× 1.37 mm) was acquired for AC of PET data and diagnostic purposes. Subsequently, a whole-body PET dataset including the head was acquired. Immediately before or after the PET/CT scan, patients were transferred to the integrated PET/MR scanner (SIGNA PET/MR, GE Healthcare), and a brain PET/MR scan was performed as part of the study examination. A 10 min acquisition with a standard head coil (8-channel HD Brain; GE Healthcare) was performed. The duration between tracer injection and PET acquisition was 112 ± 15 min [range, 66–138 min].

During the PET acquisition on the PET/MR, liver acquisition with volume acceleration flex (LAVA-Flex) T1w images (axial acquisition, TR ∼ 4 ms, TE 2.23 ms, flip angle 5°, slice thickness 5.2 mm with 2.6 mm overlap, 120 slices, pixel size 1.95 mm × 1.95 mm, number of excitations (NEX) 0.9, acquisition time: 18 s) were acquired for vendor-provided atlas-based AC.

Additionally, proton-density ZTE MR images (sagittal acquisition; non-selective hard pulse excitation; 3-dimensional center-out radial acquisition; repetition time, 410 ms; nominal echo time, 0 ms; transmit-receive switching times, 20 μs; flip angle, 1°; slice thickness, 2.78 mm; 118 slices; pixel size, 1.17 mm × 1.17 mm; bandwidth ± 62.5 kHz; number of excitations, 4; acquisition time, 48 s; spokes per segment, 512) were acquired.

Attenuation Map Generation

For each patient, 3 AC maps were generated, Atlas-AC, ZTE-AC and CT-AC. The brief overview of the algorithm was described below.

Attenuation MAP Based on Atlas Methods (Sekine et al., 2016a; Yang et al., 2017a)

An atlas-based method was used to derive a pseudo-CT that included continuous attenuation information for the head, using a single-head atlas, which was provided by the vendor and is based on CT images from 50 subjects. The pseudo-CT was generated as follows. First, 3-mm Hessian-bone enhancement from LAVA in-phase images was performed. Second, pseudo-CT was generated by rigid and non-rigid B-spine-based elastic registration between bone-enhanced MR image and the head atlas. Third, the attenuation map is generated from the pseudo-CT using the standard energy conversion and resampling. Finally, the MR hardware, coil, and bed are added to the attenuation map.

Attenuation MAP Based on ZTE Imaging (Sekine et al., 2016c; Wiesinger et al., 2016; Yang et al., 2017b)

The processing steps detailed below were performed using custom Matlab scripts (version 7.11.0; The MathWorks) but whole steps are the same as the commercial version. Attenuation Map based on ZTE imaging includes three steps. First, bias correction was applied. Second, tissue classification was performed by thresholding for soft tissue/bone and bone/air, based on the values of the tissue and air histogram peaks. Third, continuous attenuation values were assigned to the bone, based on the linear correlation between CT values and ZTE MR values (offset, 300; slope, 2,400; maximum bone value, 2,000 Hounsfield units). To the soft tissue, a fixed attenuation value of 42 Hounsfield units was assigned. The formulas to generate the thresholds and attenuation value were defined empirically before the study and remained constant for all patients.

[1] adni.loni.usc.edu

[2] www.adni-info.org

Co-registered Attenuation Map Based on CT Method

The processing steps detailed below were performed using custom Matlab scripts and PMOD (version 4.0; PMOD Inc., Zurich, Switzerland). The co-registered CT-AC map was generated as follows. First, the original head CT was exported from the PET/CT scanner and converted into AC-map using a Matlab version of the same bilinear mapping implemented in the SIGNA PET/MRI. Second, from this map, the CT table was removed manually. Third, a threshold was set to extract the outside air component from the CT-AC map. None of the images used in this study contained artifacts likely to affect air thresholding. Fourth, a normalized mutual information matching algorithm (PMOD) was used to derive the registration parameters necessary to match CT to LAVA-Flex T1w, and the final matching was performed using custom Matlab routines. Finally, the CT-AC map was superimposed on the atlas-AC map, thereby replacing it.

Reconstruction of PET Images

Only the raw PET data from the TOF PET/MR examination were used. PET images were reconstructed with AC based on each of the 3 attenuation maps and the following parameters: fully 3-dimensional ordered-subset expectation maximization iterative reconstruction; subsets, 28; iterations, 8; pixel size, 1.17 mm × 1.17 mm; point spread function modeling; transaxial post reconstruction gaussian filter cutoff, 3 mm; axial filter, 1:4:1; scatter; normalization; dead-time and decay corrections; TOF reconstruction.

Automated Software for AD Probability Assessment

Automated AD probability assessment was performed in a commercially available tool which was established in the ADNI study and validated in several multi-center study, such as NEST-DD and SEADS-JAPAN (PMOD Alzheimer's Discrimination, PALZ) (Haense et al., 2009; Herholz et al., 2011; Ito et al., 2015). The software ran the following procedure, in a fully automated workflow based on the previous study (Herholz et al., 2002). First, spatial normalization is performed by transforming the original images to the SPM 99 PET template, followed by smoothing with Gaussian filter of 12 × 12 × 12 mm. In these images, voxel values are normalized by dividing each image voxel value by the mean voxel value, averaged within a mask representing voxels in which FDG uptake is typically preserved even in AD patients. The expected value in each voxel is calculated from a pre-stored, age-matched, reference PET database of healthy controls using voxel-wise age regression parameters. By comparing the voxel-wise differences between expected value and the patient-specific value, a Student's *t*-value is calculated. The AD t-sum is calculated by summing the *t*-value in predefined AD-related voxels. Finally, the PET Score was calculated as log2 (AD t-sum/11089 +1), for which the 95% prediction limit (11089) of AD t-sum was established in the ADNI or NEST-DD multi-center trial. This analysis was initially performed in all 107 ADNI-PET data (e.g., $PETscore^{original}$) before multiplication with the 27 error maps.

Creation of Simulated Data: ADNI-Data With Atlas-AC or ZTE-AC

The whole steps were done according to the previous report (Sekine et al., 2020). All simulation steps were performed in MNI space with same spatial resolution (2 mm isotropic voxels). First, we divided the locally acquired PET images based on atlas AC or ZTE by those based on CTAC (27 patients) (e.g., ${}_{Error}PET^{pt-i}$). Second, the resulting images were spatially normalized to the SPM99 PET template using the transformation calculated for PET images based on CTAC to the template, then a Gaussian filter of 12 × 12 × 12 mm full-width half-maximum was applied (${}^{Norm}_{Error}PET^{pt-i}$). A brain mask was applied to avoid distortion at the edges of the measured data. These steps were designed to replicate the preprocessing steps used in the PMOD Alzheimer's Discrimination tool, as used to calculate PET score. Therefore, the resulting images were the error maps (between MRAC and CTAC) in the same image space as the spatially normalized ADNI PET data (${}_{Norm}PET_{ADNI-j}$). It minimized the error derived from the difference of scan condition (e.g., imaging protocol of PET scanner) between ADNI data and patients' data. Third, we multiplied each of the 107 normalized ADNI data with each of the 27 normalized error maps, resulting in 107 × 27 = 2889 normalized PET images (e.g., ${}^{Norm}_{Error}PET^{pt-i}_{ADNI-j}$) for each MRAC method. Thus, the value-error was simply imposed in a voxel-wise manner and further PET score calculation was performed without additional need for spatial deformation or filtering. Therefore, we expected any bias due to impaired spatial normalization or differences in PET acquisition protocol to be minimized. For each of these 5778 images (2889 × 2), PALZ analysis was performed to calculate the PET score based on MRAC ($PETscore^{MRAC}$).

Evaluation of Diagnostic Accuracy for Alzheimer's Disease

We calculated the absolute PET score difference between $PETscore^{MRAC}$ and $PETscore^{original}$. This PET score difference was compared between Atlas-AC and ZTE-AC by using paired *t*-test. We also drew performed regression and Bland-Altman analysis between $PETscore^{MRAC}$ and $PETscore^{original}$.

We evaluated the diagnostic accuracy of discrimination of AD from normal patients. Setting cut-off value to PET score = 1 based on a previous study, we calculated the accuracy, sensitivity, and specificity of each MRAC series (Haense et al., 2009; Herholz et al., 2011). Additionally, we performed a receiver-operating-curve analysis to define the modified cut-off values for each MRAC series according to the maximum value of the Youden index (Youden, 1950; Schisterman et al., 2005).

RESULTS

$PETscore^{Atlas}$ and $PETscore^{ZTE}$ were underestimated compared to $PETscore^{original}$ ($PETscore^{Atlas}$ minus $PETscore^{original}$: −0.0784 ± 0.1724; $PETscore^{ZTE}$ minus $PETscore^{original}$: −0.0796 ± 0.0938) (**Tables 1A,B** and **Figure 1**). The absolute PETscore difference between $PETscore^{ZTE}$ and

TABLE 1-A | *PETscore* in each 2889 simulated dataset.

PETscore	Ave	SD	Max	Min
$PETscore^{Atlas}$	1.0792	0.7614	3.6136	0.0956
$PETscore^{ZTE}$	1.0755	0.7852	3.6193	0.1118
$PETscore^{original}$	1.1443	0.7972	3.6488	0.1669

Ave, average; SD, standard deviation; Max, maximum; Min, minimum.

TABLE 1-B | Positron emission tomography score difference ($PETscore^{MRAC}$-$PETscore^{original}$) in each 2889 simulated dataset.

PET score difference	Ave	SD	Max	Min
Atlas	−0.0651	0.1669	0.3840	−0.8404
ZTE	−0.0689	0.0918	0.2070	−0.4873

Ave, average; SD, standard deviation; Max, maximum; Min, minimum.

TABLE 1-C | Absolute PET score difference ($|PETscore^{MRAC}$-$PETscore^{original}|$) in each 2889 simulated dataset.

Absolute PET score difference	Ave	SD	Max	Min	*P*-value
Atlas	0.1392	0.1128	0.8404	0.0000	< 0.0001
ZTE	0.0885	0.0731	0.4873	0.0000	

Paired samples t-test was performed between $|PETscore^{Atlas}$-$PETscore^{original}|$ and $|PETscore^{ZTE}$-$PETscore^{original}|$. Ave, average; SD, standard deviation; Max, maximum; Min, minimum.

$PETscore^{original}$ was slightly lower than that between $PETscore^{Atlas}$ and $PETscore^{original}$ (0.098 ± 0.075 vs. 0.145 ± 0.122, $p < 0.0001$) (**Table 1C**).

Regression and Bland-Altman analysis between $PETscore^{original}$ and either $PETscore^{Atlas}$ or $PETscore^{ZTE}$ are shown in **Figures 2**, **3**. The slope of the regression lines between $PETscore^{original}$ and $PETscore^{Atlas}$ were 0.9342 and between $PETscore^{original}$ and $PETscore^{ZTE}$ 0.9882. The coefficient of determination (R^2) was higher for $PETscore^{ZTE}$ and limits of agreement (LOA) of $PETscore^{ZTE}$ was lower than $PETscore^{Atlas}$ (R^2: 0.982 vs. 0.961, LOA: −0.211 to 0.073 vs. −0.323 to 0.194).

Accuracy, sensitivity, and specificity of each attenuation method with cut-off values of PET score = 1 are shown in **Table 2**. The accuracy for the discrimination of AD patients from normal control derived from Atlas or ZTE was maintained [Atlas vs. ZTE vs. original; 82.5% (CI 81.0–83.8%) vs. 82.1% (CI 80.7–83.5%) vs. 83.2% (CI 81.8–84.5%)] but sensitivity was slightly impaired compared with those derived from CTAC [Atlas vs. ZTE vs. original; 77.2% (CI 74.9–79.5%) vs. 78.6% (76.3–80.8%), 83.3% (CI 81.2–85.3%)].

The receiver-operating-curve analysis to determine modified cut-off values of PET score is shown in **Figure 3**. The modified cut off values are $PETscore^{Atlas}$ = 0.924, $PETscore^{ZTE}$ = 1.143, respectively. Setting cut-off values to these modified scores, the accuracy and specificity of ZTE was slightly improved [83.7% (CI 82.3–85.1%) and 91.0% (CI 89.5–92.4%)]. The values of area under the curve (AUC) of ROC curve were not impaired in Atlas {0.859 [CI: 0.844–0.875]) or ZTE (0.870 [CI: 0.855–0.884]), compared with CTAC (0.876 [CI: 0.862–0.890])}.

DISCUSSION

In the current study, we validated the diagnostic performance of two types of MRAC methods in the classification of AD with FDG-PET. We generated simulated images by multiplying well-controlled cohort, ADNI-dataset and real patients' error

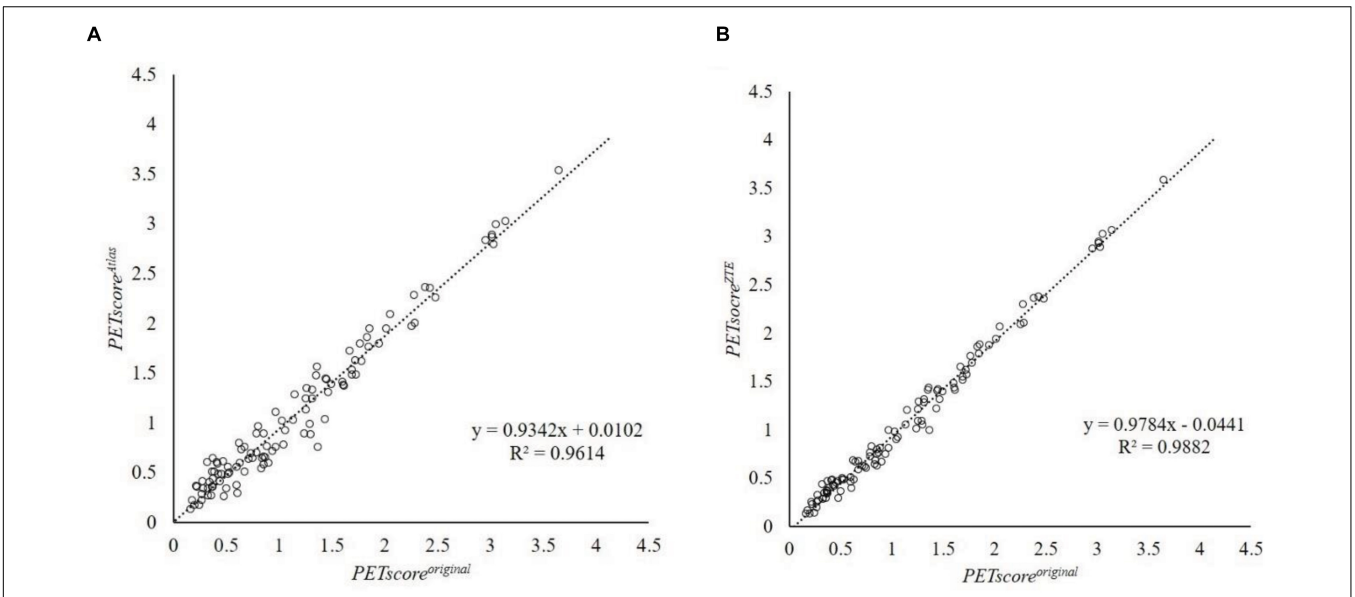

FIGURE 1 | Regression line analysis between $PETscore^{MRAC}$ and $PETscore^{original}$. This plot shows 107 data which are averaged from 27 error maps. The horizontal axis shows $PETscore^{original}$ and the vertical axis shows $PETscore^{Atlas}$ **(A)** or $PETscore^{ZTE}$ **(B)**. Regression equation were $y = 0.9342x + 0.0102$ **(A)** and $y = 0.9784x + 0.0441$ **(B)**, respectively. R^2 were 0.9614 **(A)** and 0.9882 **(B)**, respectively. R^2, coefficient of determination.

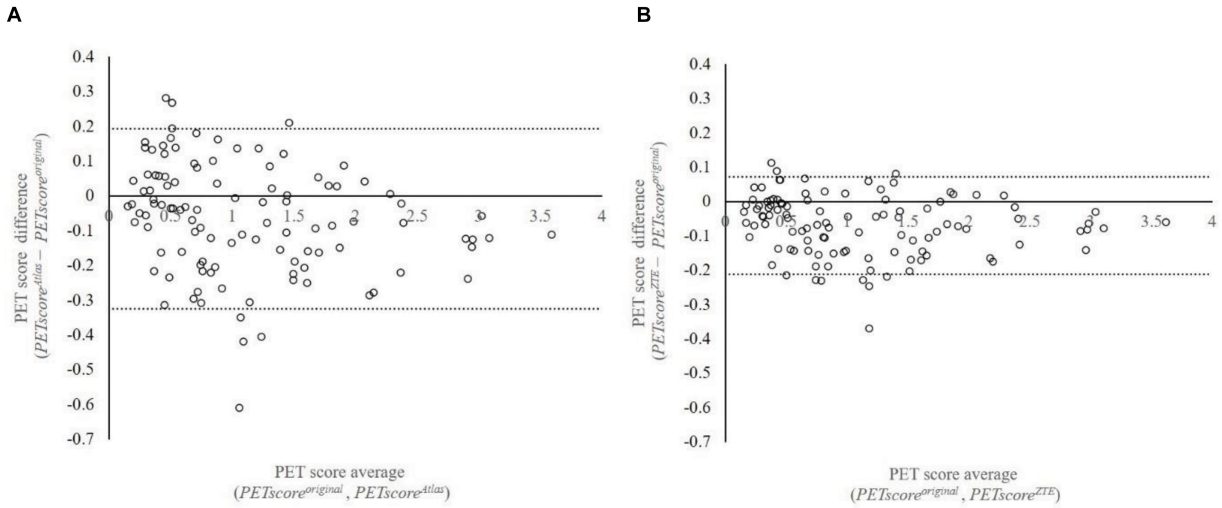

FIGURE 2 | Bland-Altman plot between $PETscore^{MRAC}$ and $PETscore^{original}$. This plot shows 107 data which are averaged based on 27 error maps. The vertical axis shows difference of $PETscore^{original}$ and $PETscore^{Atlas}$ **(A)** or $PETscore^{ZTE}$ **(B)**. The horizontal axis shows average of $PETscore^{original}$ and $PETscore^{Atlas}$ **(A)** or $PETscore^{ZTE}$ **(B)**. LOA were –0.323 to 0.194 **(A)** and –0.211 to 0.073 **(B)**, respectively. LOA, limits of agreement.

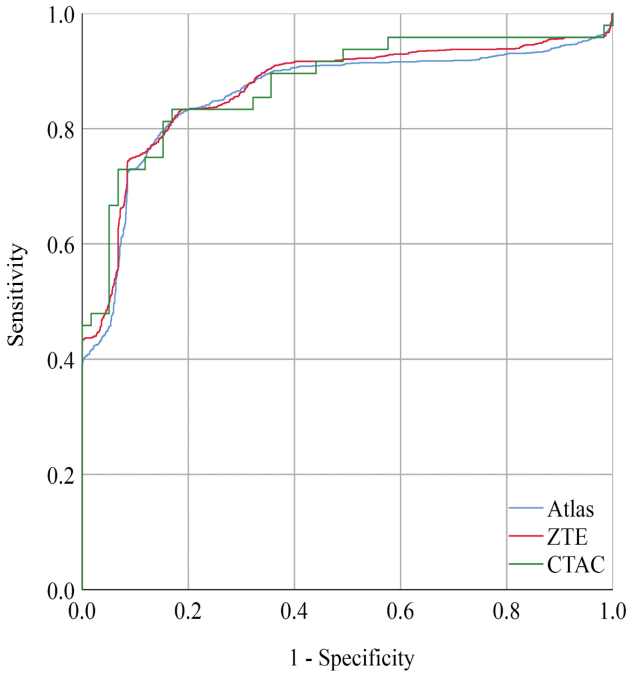

FIGURE 3 | When setting the cut-off value to $PETscore^{ZTE}$ = 1.143, the sensitivity and specificity were 75 and 91% with AUC = 0.870 (CI: 0.855–0.884). When setting the cut-off value to $PETscore^{Atlas}$ = 0.924, the sensitivity and specificity were 81 and 84% with AUC = 0.859 (CI: 0.844–0.875). The AUC of CTAC was 0.876 (CI: 0.862–0.890). AUC, area under curve.

maps derived from each MRAC method. The results show the PETscore based on both Atlas and ZTE were underestimated compared with the original PETscore based on CTAC. ZTE had smaller variability of the error than Atlas MRAC. The accuracy was not impaired by either MRAC, though the sensitivity was slightly impaired due to the underestimation of PETscore. By determining and setting modified cut off values, slightly better accuracy and specificity of Atlas and ZTE were obtained.

There are several studies which compared the accuracy of Atlas and ZTE MRAC (Sekine et al., 2016c; Yang et al., 2017b; Sousa et al., 2018; Sgard et al., 2019). These studies revealed that both the averaged error and the variability (standard deviation) of the error among subjects were minimized by ZTE compared to Atlas. Our results are in agreement with these previous studies: both averaged and standard deviation of absolute PET score difference were lower in ZTE than in Atlas. In addition, there were two interesting results observed. First, the averaged PET score difference of ZTE was not superior to Atlas. This may indicate that the minimization of the net regional error doesn't directly lead to an improvement of the diagnosis accuracy of dementia after the value normalization and t-score calculation. Second, the PETscore error was not systematically under- or over-estimated in each of the original 107 datasets. The t-score calculation is based on the difference from averages and the magnitude of the standard deviation in each region derived from a normal database. It resulted in heterogeneous effect on each 107 dataset by identical MRAC error.

In one sole previous study, statistical analysis using SPM procedure was performed for FDG-PET generated based on ZTE. Sgard et al. (2019) recruited 50 patients who underwent FDG-PET/MR as part of an investigation of suspected dementia. The study revealed that ZTE was more accurate than Atlas for the quantification of FDG uptake especially in the parietotemporal junction, one of the earliest regions involved in AD. In that study, the relative difference both of net SUV value and of t-score calculated by using SPM was evaluated. Interestingly, the distribution is similar but not the same between the two. For

TABLE 2 | Diagnostic accuracy of original PET data and simulated MRAC PET data with various PET score values in each of the 2889 simulated datasets.

	Cut-off value	Accuracy	Sensitivity	Specificity
CTAC	1	83.2% (CI 81.8–84.5%)	83.3% (CI 81.2–85.3%)	83.1% (CI 81.1–84.9%)
Atlas-AC	1	82.5% (CI 81.0–83.8%)	77.2% (CI 74.9–79.5%)	86.7% (CI 84.9–88.3%)
Atlas-AC	0.924	82.5% (CI 81.0–83.8%)	80.8% (CI 78.5–82.9%)	83.8% (CI 81.9–85.6%)
ZTE-AC	1	82.1% (CI 80.7–83.5%)	78.6% (CI 76.3–80.8%)	85.0% (CI 83.1–86.7%)
ZTE-AC	1.143	83.7% (CI 82.3–85.1%)	74.8% (CI 72.3–77.1%)	91.0% (CI 89.5–92.4%)

example, supratentorial regions were generally underestimated by ZTE MRAC but this underestimation was not observed after the SPM procedure because the procedure includes intensity normalization. Underestimation in the reference regions leads to overestimation, which compensates the underestimation in the target regions. In addition, they evaluated voxel-wise differences between normal and abnormal brain FDG-PET. Although ZTE-MRAC was more accurate than Atlas-AC, there were still clear differences between CT-AC and ZTE-AC. One can expect that even if the regional accuracy in AD-related voxels is achieved by any MRAC, the result after value-normalization and *t*-value calculation should be validated separately.

In terms of the validation of MRAC, one of the largest studies is the two-institutional study conducted by Ladefoged et al. (2017). They performed cross-comparison of 11 MRAC methods to 337 subjects undergoing brain PET/MR and CT. They clarified all of the novel methods provided by each research group had an acceptable error (e.g., the MRAC error to silver standard CTAC is less than 5 %). Though one of these methods is freely accessible via web-based process[3], MRAC which is not supported by vendors is difficult to implement into clinical workflow (Burgos et al., 2015; Sekine et al., 2016b). Apart from these atlas/template-based or segmentation-based MRAC methods, deep learning-based MRAC have been proposed in research field. In published data, the method seems to be more accurate than clinically available methods such as Atlas-AC or ZTE-AC (Liu et al., 2018; Arabi et al., 2019; Shiri et al., 2019). However, there is some variability of the methodology in each published paper. Thus, the clinical implementation of this MRAC method is not achieved yet.

The diagnostic accuracy was evaluated by using a single software tool, and not done by other statistical approaches or visual assessment. It was one of main limitations of the current study. However, the diagnostic concept was similar to that used in other software and in visual inspection. These evaluations generally apply value-normalization and *t*-/*z*-score calculation. We chose this software because of four reasons. First, the whole steps were done in semi-automatic manner without any interruption. It was practical and assured objective results. Second, the model had validated in several large cohort study. As a result, the method is used widely in clinical setting as commercial software. Third, the statistical model is the simplest to minimize the secondary effect by the statistical model. The novel classification method has additional steps such as partial volume effect and the normalization combining T1WI (Samper-González et al., 2018). However, in the complicated statistical mode, it becomes difficult to separate the primary effect of MRAC error to value-normalization from whole effect of MRAC error as the summing of each analysis steps.

The limitations of this study were as below. First, the conclusions of the current study were based on a simulation study rather than on "real" PET images of AD subjects reconstructed with both MR and CT AC. To confirm the result in the current study, well-controlled clinical trials using PET/MR scanners should be performed in the future. Second, some of the error maps were generated from patients imaged for the evaluation of malignancy. The error derived from MRAC was mainly derived from the incorrect estimation of skull thickness/density which does not differ between oncology and dementia patients. Third, we only recruited a limited number of patients, $n = 27$ for the generation of MRAC. The simulation model multiplying 27 error maps for each ADNI data might cause statistical ambiguousness. However, a significant improvement of absolute PETscore based on ZTE was observed. The validation of MRAC on large cohorts is difficult to perform because additional CT is required to acquire the gold-standard AC map.

CONCLUSION

In conclusion, statistical analysis utilizing a normal database scanned by PET/CT can be applied to FDG-PET images scanned by PET/MR implementing ZTE-MRAC. ZTE-MRAC had superior accuracy to Atlas-MRAC even after statistical analysis such as value-normalization and *t*-value calculation. It is expected that the diagnostic accuracy for the discrimination of AD from healthy control would be maintained by using FDG-PET scanned by commercial PET/MR system.

DATA AVAILABILITY STATEMENT

The raw data supporting the conclusions of this article will be made available by the authors, without undue reservation.

ETHICS STATEMENT

The studies involving human participants were reviewed and approved by the Local Institutional Review Board of Mayo Clinic. The patients/participants provided their written informed consent to participate in this study.

[3]http://niftyweb.cs.ucl.ac.uk/program.php?p=PCT

AUTHOR CONTRIBUTIONS

TA, TS, and GD designed the study and contributed to the data analysis. BK, SK, FW, and GD contributed to the data acquisition. SK, FW, and GD generated PET images. GW advised the data analysis. TA, GW, TS, and GD contributed to drafting of the manuscript together. All authors contributed to the article and approved the submitted version.

REFERENCES

Andersen, F. L., Ladefoged, C. N., Beyer, T., Keller, S. H., Hansen, A. E., Hojgaard, L., et al. (2014). Combined PET/MR imaging in neurology: MR-based attenuation correction implies a strong spatial bias when ignoring bone. *Neuroimage* 84, 206–216. doi: 10.1016/j.neuroimage.2013.08.042

Arabi, H., Zeng, G., Zheng, G., and Zaidi, H. (2019). Novel adversarial semantic structure deep learning for MRI-guided attenuation correction in brain PET/MRI. *Eur. J. Nucl. Med. Mol. Imaging* 46, 2746–2759. doi: 10.1007/s00259-019-04380-x

Barthel, H., Schroeter, M. L., Hoffmann, K.-T., and Sabri, O. (2015). PET/MR in dementia and other neurodegenerative diseases. *Semin. Nucl. Med.* 45, 224–233. doi: 10.1053/j.semnuclmed.2014.12.003

Burgos, N., Cardoso, M. J., Thielemans, K., Modat, M., Dickson, J., Schott, J. M., et al. (2015). Multi-contrast attenuation map synthesis for PET/MR scanners: assessment on FDG and Florbetapir PET tracers. *Eur. J. Nucl. Med. Mol. Imaging* 42, 1447–1458. doi: 10.1007/s00259-015-3082-x

Catana, C., Quick, H. H., and Zaidi, H. (2018). Current commercial techniques for MRI-guided attenuation correction are insufficient and will limit the wider acceptance of PET/MRI technology in the clinic. *Med. Phys.* doi: 10.1002/mp.12963 [Epub ahead of print].

Chen, K. T., Salcedo, S., Chonde, D. B., Izquierdo-Garcia, D., Levine, M. A., Price, J. C., et al. (2018). MR-assisted PET motion correction in simultaneous PET/MRI studies of dementia subjects. *J. Magn. Reson. Imaging* 48, 1288–1296. doi: 10.1002/jmri.26000

Delso, G., Kemp, B., Kaushik, S., Wiesinger, F., and Sekine, T. (2018). Improving PET/MR brain quantitation with template-enhanced ZTE. *Neuroimage* 181, 403–413. doi: 10.1016/j.neuroimage.2018.07.029

Delso, G., Wiesinger, F., Sacolick, L. I., Kaushik, S. S., Shanbhag, D. D., Hullner, M., et al. (2015). Clinical evaluation of zero-echo-time MR imaging for the segmentation of the skull. *J. Nucl. Med.* 56, 417–422. doi: 10.2967/jnumed.114.149997

Drzezga, A., Barthel, H., Minoshima, S., and Sabri, O. (2014). Potential clinical applications of PET/MR imaging in neurodegenerative diseases. *J. Nucl. Med.* 55, 47S–55S. doi: 10.2967/jnumed.113.129254

Fendler, W. P., Czernin, J., Herrmann, K., and Beyer, T. (2016). Variations in PET/MRI operations: results from an international survey among 39 active sites. *J. Nucl. Med.* 57, 2016–2021. doi: 10.2967/jnumed.116.174169

Haense, C., Herholz, K., Jagust, W. J., and Heiss, W. D. (2009). Performance of FDG PET for detection of Alzheimer's disease in two independent multicentre samples (NEST-DD and ADNI). *Dement. Geriatr. Cogn. Disord.* 28, 259–266. doi: 10.1159/000241879

Henriksen, O. M., Marner, L., and Law, I. (2016). Clinical PET/MR imaging in dementia and neuro-oncology. *PET Clinics* 11, 441–452. doi: 10.1016/j.cpet.2016.05.003

Herholz, K., Salmon, E., Perani, D., Baron, J. C., Holthoff, V., Frolich, L., et al. (2002). Discrimination between Alzheimer dementia and controls by automated analysis of multicenter FDG PET. *Neuroimage* 17, 302–316. doi: 10.1006/nimg.2002.1208

Herholz, K., Westwood, S., Haense, C., and Dunn, G. (2011). Evaluation of a calibrated (18)F-FDG PET score as a biomarker for progression in Alzheimer disease and mild cognitive impairment. *J. Nucl. Med.* 52, 1218–1226. doi: 10.2967/jnumed.111.090902

Hope, T. A., Fayad, Z. A., Fowler, K. J., Holley, D., Iagaru, A., McMillan, A. B., et al. (2019). Summary of the First ISMRM–SNMMI Workshop on PET/MRI: applications and limitations. *J. Nucl. Med.* 60, 1340–1346. doi: 10.2967/jnumed.119.227231

Ito, K., Fukuyama, H., Senda, M., Ishii, K., Maeda, K., Yamamoto, Y., et al. (2015). Prediction of outcomes in mild cognitive impairment by using 18F-FDG-PET: a multicenter study. *J. Alzheimers Dis.* 45, 543–552. doi: 10.3233/jad-141338

Kaltoft, N. S., Marner, L., Larsen, V. A., Hasselbalch, S. G., Law, I., and Henriksen, O. M. (2019). Hybrid FDG PET/MRI vs. FDG PET and CT in patients with suspected dementia – A comparison of diagnostic yield and propagated influence on clinical diagnosis and patient management. *PLoS One* 14:e0216409. doi: 10.1371/journal.pone.0216409

Ladefoged, C. N., Law, I., Anazodo, U., St Lawrence, K., Izquierdo-Garcia, D., Catana, C., et al. (2017). A multi-centre evaluation of eleven clinically feasible brain PET/MRI attenuation correction techniques using a large cohort of patients. *Neuroimage* 147, 346–359. doi: 10.1016/j.neuroimage.2016.12.010

Liu, F., Jang, H., Kijowski, R., Bradshaw, T., and McMillan, A. B. (2018). Deep Learning MR Imaging-based Attenuation Correction for PET/MR Imaging. *Radiology* 286, 676–684. doi: 10.1148/radiol.2017170700

Mainta, I. C., Perani, D., Delattre, B. M., Assal, F., Haller, S., Vargas, M. I., et al. (2017). FDG PET/MR Imaging in Major Neurocognitive Disorders. *Curr. Alzheimer Res.* 14, 186–197. doi: 10.2174/1567205013666160620115130

Mehranian, A., Arabi, H., and Zaidi, H. (2016). Vision 20/20: magnetic resonance imaging-guided attenuation correction in PET/MRI: challenges, solutions, and opportunities. *Med. Phys.* 43, 1130–1155. doi: 10.1118/1.4941014

Prato, F. S., Pavlosky, W. F., Foster, S. C., Thiessen, J. D., and Beaujot, R. P. (2019). Screening for dementia caused by modifiable lifestyle choices using hybrid PET/MRI. *J. Alzheimers Dis. Rep.* 3, 31–45. doi: 10.3233/ADR-180098

Samper-González, J., Burgos, N., Bottani, S., Fontanella, S., Lu, P., Marcoux, A., et al. (2018). Reproducible evaluation of classification methods in Alzheimer's disease: framework and application to MRI and PET data. *Neuroimage* 183, 504–521. doi: 10.1016/j.neuroimage.2018.08.042

Schisterman, E. F., Perkins, N. J., Liu, A., and Bondell, H. (2005). Optimal cut-point and its corresponding Youden Index to discriminate individuals using pooled blood samples. *Epidemiology* 16, 73–81. doi: 10.1097/01.ede.0000147512.81966.ba

Schramm, G., Koole, M., Willekens, S. M. A., Rezaei, A., Van Weehaeghe, D., Delso, G., et al. (2019). Regional accuracy of ZTE-based attenuation correction in static [18F]FDG and dynamic [18F]PE2I Brain PET/MR. *Front. Phys.* 7:211. doi: 10.3389/fphy.2019.00211

Sekine, T., Buck, A., Delso, G., Kemp, B., ter Voert, E. E. G. W., Huellner, M., et al. (2020). The impact of atlas-based MR attenuation correction on the diagnosis of FDG-PET/MR for Alzheimer's diseases— A simulation study combining multi-center data, and ADNI-data. *PLoS One* 15:e0233886. doi: 10.1371/journal.pone.0233886

Sekine, T., Buck, A., Delso, G., Ter Voert, E. E., Huellner, M., Veit-Haibach, P., et al. (2016a). Evaluation of atlas-based attenuation correction for integrated PET/MR in human brain: application of a head atlas and comparison to true CT-Based Attenuation Correction. *J. Nucl. Med.* 57, 215–220. doi: 10.2967/jnumed.115.159228

Sekine, T., Burgos, N., Warnock, G., Huellner, M., Buck, A., Ter Voert, E. E., et al. (2016b). Multi-atlas-based attenuation correction for brain 18F-FDG PET imaging using a time-of-flight PET/MR scanner: comparison with clinical single-atlas- and ct-based attenuation correction. *J. Nucl. Med.* 57, 1258–1264. doi: 10.2967/jnumed.115.169045

Sekine, T., Ter Voert, E. E., Warnock, G., Buck, A., Huellner, M., Veit-Haibach, P., et al. (2016c). Clinical evaluation of zero-echo-time attenuation correction for brain 18F-FDG PET/MRI: comparison with atlas attenuation correction. *J. Nucl. Med.* 57, 1927–1932. doi: 10.2967/jnumed.116.175398

Sgard, B., Khalifé, M., Bouchut, A., Fernandez, B., Soret, M., Giron, A., et al. (2019). ZTE MR-based attenuation correction in brain FDG-PET/MR: performance in patients with cognitive impairment. *Eur. Radiol.* 30, 1770–1779. doi: 10.1007/s00330-019-06514-z

Shiri, I., Ghafarian, P., Geramifar, P., Leung, K. H., Ghelichoghli, M., Oveisi, M., et al. (2019). Direct attenuation correction of brain PET images using only emission data via a deep convolutional encoder-decoder (Deep-DAC). *Eur. Radiol.* 29, 6867–6879. doi: 10.1007/s00330-019-06229-1

Sousa, J. M., Appel, L., Engström, M., Papadimitriou, S., Nyholm, D., Larsson, E.-M., et al. (2018). Evaluation of zero-echo-time attenuation correction for integrated PET/MR brain imaging—comparison to head atlas and 68Ge-transmission-based attenuation correction. *EJNMMI Phys.* 5:20. doi: 10.1186/s40658-018-0220-0

Teipel, S., Drzezga, A., Grothe, M. J., Barthel, H., Chetelat, G., Schuff, N., et al. (2015). Multimodal imaging in Alzheimer's disease: validity and usefulness for early detection. *Lancet Neurol.* 14, 1037–1053. doi: 10.1016/s1474-4422(15)00093-9

Teuho, J., Torrado-Carvajal, A., Herzog, H., Anazodo, U., Klén, R., Iida, H., et al. (2020). Magnetic resonance-based attenuation correction and scatter correction in neurological positron emission tomography/magnetic resonance imaging—current status with emerging applications. *Front. Phys.* 7:243. doi: 10.3389/fphy.2019.00243

Wiesinger, F., Sacolick, L. I., Menini, A., Kaushik, S. S., Ahn, S., Veit-Haibach, P., et al. (2016). Zero TE MR bone imaging in the head. *Magn. Reson. Med.* 75, 107–114. doi: 10.1002/mrm.25545

Yan, S., Zheng, C., Cui, B., Qi, Z., Zhao, Z., An, Y., et al. (2020). Multiparametric imaging hippocampal neurodegeneration and functional connectivity with simultaneous PET/MRI in Alzheimer's disease. *Eur. J. Nucl. Med. Mol. Imaging* 47, 2440–2452. doi: 10.1007/s00259-020-04752-8

Yang, J., Jian, Y., Jenkins, N., Behr, S. C., Hope, T. A., Larson, P. E. Z., et al. (2017a). Quantitative evaluation of atlas-based attenuation correction for brain pet in an integrated time-of-flight PET/MR imaging system. *Radiology* 284, 169–179. doi: 10.1148/radiol.2017161603

Yang, J., Wiesinger, F., Kaushik, S., Shanbhag, D., Hope, T. A., Larson, P. E. Z., et al. (2017b). Evaluation of sinus/edge-corrected zero-echo-time-based attenuation correction in brain PET/MRI. *J. Nucl. Med.* 58, 1873–1879. doi: 10.2967/jnumed.116.188268

Youden, W. J. (1950). Index for rating diagnostic tests. *Cancer* 3, 32–35. doi: 10.1002/1097-0142(1950)3:1<32::aid-cncr2820030106>3.0.co;2-3

Zhang, X. Y., Yang, Z. L., Lu, G. M., Yang, G. F., and Zhang, L. J. (2017). PET/MR imaging: new frontier in Alzheimer's disease and other dementias. *Front. Mol. Neurosci.* 10:343. doi: 10.3389/fnmol.2017.00343

Conflict of Interest: GD, SK, and FW are employees of GE Healthcare. Only non-GE employees had control of inclusion of data and information that might present a conflict of interest for authors who are employees of GE Healthcare. GW is an employee of PMOD Technologies LLC.

The remaining authors declare that the research was conducted in the absence of any commercial or financial relationships that could be construed as a potential conflict of interest.

Copyright © 2020 Ando, Kemp, Warnock, Sekine, Kaushik, Wiesinger and Delso. This is an open-access article distributed under the terms of the Creative Commons Attribution License (CC BY). The use, distribution or reproduction in other forums is permitted, provided the original author(s) and the copyright owner(s) are credited and that the original publication in this journal is cited, in accordance with accepted academic practice. No use, distribution or reproduction is permitted which does not comply with these terms.

frontiers in Neuroscience

ORIGINAL RESEARCH
published: 08 December 2020
doi: 10.3389/fnins.2020.561594

Functional Segregation of Human Brain Networks Across the Lifespan: An Exploratory Analysis of Static and Dynamic Resting-State Functional Connectivity

Benjamin M. Rosenberg[1], Eva Mennigen[1,2], Martin M. Monti[1] and Roselinde H. Kaiser[3]*

[1] Department of Psychology, University of California, Los Angeles, Los Angeles, CA, United States, [2] Department of Psychiatry and Psychotherapy, University Hospital Carl Gustav Carus, Technische Universität Dresden, Dresden, Germany, [3] Department of Psychology and Neuroscience, University of Colorado Boulder, Boulder, CO, United States

OPEN ACCESS

Edited by:
Miguel Castelo-Branco, Coimbra Institute for Biomedical Imaging and Translational Research (CIBIT), Portugal

Reviewed by:
Nicola Filippini, University of Oxford, United Kingdom
Martin J. McKeown, University of British Columbia, Canada

****Correspondence:***
Benjamin M. Rosenberg
benrosenberg@g.ucla.edu

Specialty section:
This article was submitted to Brain Imaging Methods, a section of the journal Frontiers in Neuroscience

Received: *13 May 2020*
Accepted: *16 November 2020*
Published: *08 December 2020*

Citation:
Rosenberg BM, Mennigen E, Monti MM and Kaiser RH (2020) Functional Segregation of Human Brain Networks Across the Lifespan: An Exploratory Analysis of Static and Dynamic Resting-State Functional Connectivity. Front. Neurosci. 14:561594. doi: 10.3389/fnins.2020.561594

Prior research has shown that during development, there is increased segregation between, and increased integration within, prototypical resting-state functional brain networks. Functional networks are typically defined by static functional connectivity over extended periods of rest. However, little is known about how time-varying properties of functional networks change with age. Likewise, a comparison of standard approaches to functional connectivity may provide a nuanced view of how network integration and segregation are reflected across the lifespan. Therefore, this exploratory study evaluated common approaches to static and dynamic functional network connectivity in a publicly available dataset of subjects ranging from 8 to 75 years of age. Analyses evaluated relationships between age and static resting-state functional connectivity, variability (standard deviation) of connectivity, and mean dwell time of functional network states defined by recurring patterns of whole-brain connectivity. Results showed that older age was associated with decreased static connectivity between nodes of different canonical networks, particularly between the visual system and nodes in other networks. Age was not significantly related to variability of connectivity. Mean dwell time of a network state reflecting high connectivity between visual regions decreased with age, but older age was also associated with increased mean dwell time of a network state reflecting high connectivity within and between canonical sensorimotor and visual networks. Results support a model of increased network segregation over the lifespan and also highlight potential pathways of top-down regulation among networks.

Keywords: development, resting state networks, functional connectivity, brain dynamics, brain imaging

INTRODUCTION

The organization of the human brain includes distinct functional brain networks that are implicated in different cognitive functions (Fox et al., 2005). Prior work has demonstrated that resting-state functional connectivity (rsFC) can be used to identify several canonical brain networks that are reliably observed within and between individual subjects (Damoiseaux et al., 2006). Studies

of functional neurodevelopment have since examined how the brain's functional connections change over the course of aging, as these changes may be especially relevant to psychopathology, neurodegeneration, or normative cognitive decline.

Two dimensions of rsFC may contain complementary information about intrinsic properties of network functioning: static rsFC and dynamic rsFC. The most basic distinction between these terms is that static rsFC refers to properties that do not vary over time, whereas dynamic rsFC refers to properties that vary over time or capture variance in static rsFC over time (although other definitions of dynamic rsFC reserve this term only for properties that capture the temporal sequence of data-points; see Liégeois et al., 2017). Although there is considerable debate regarding how best to disentangle meaningful dynamic signal from measurement noise (Hindriks et al., 2016), dynamic properties may represent the processes by which network form, dissolve, and interact with one another over time (Hutchison et al., 2013; Kaiser et al., 2016).

Within the static rsFC literature, prior research has suggested a pattern of neurodevelopment characterized by network "segregation," wherein short-range connections between separable canonical resting-state networks (RSNs) become less coordinated, as well as network "integration," wherein long-range connections within canonical RSNs tend to become more coordinated, particularly along the anterior-posterior axis (Dosenbach et al., 2010; Grayson and Fair, 2017). While adolescence has been identified as a crucial period concerning the development of functional integration and segregation (Stevens, 2016), functional segregation appears to decrease later in adulthood (Betzel et al., 2014; Chan et al., 2014).

In addition to the general patterns of RSN development described above, changes in particular RSNs have been highlighted in prior research on neurodevelopment, particularly among nodes of the prototypical default-mode (DN), frontoparietal (FN), salience (SN), and sensory networks. Broadly, static connectivity between nodes of different RSNs appears to decrease with aging, with some of the most pronounced changes involve sensorimotor regions and the precuneus (a structure spanning the FN and DN) (Allen et al., 2011). However, many changes in static connectivity have been highlighted within specific developmental periods. For instance, while segregation of sensorimotor regions appears to occur in childhood, segregation of task-positive networks such as the FN and SN continues throughout the transition from childhood into adulthood (Gu et al., 2015). Convergent findings further indicate that static connectivity specifically within the DN decreases over the course of advanced aging (Andrews-Hanna et al., 2007; Damoiseaux et al., 2007; Koch et al., 2010), whereas connectivity among regions of the DN, FN, and SN appears to strengthen from childhood into adulthood (Uddin et al., 2011; Gu et al., 2015), and then decrease in strength from early to late adulthood (He et al., 2013).

The extant literature relating development to dynamic rsFC within and between prototypical RSNs is far more limited, but early studies have provided insight into emerging directions in the field. For instance, while functional networks are generally preserved across the lifespan, young adults compared with children tend to show higher variability in rsFC, but lower variability in task-related functional connectivity during cognitive tasks (Hutchison and Morton, 2015). One interpretation is that these developmental changes in rsFC variability reflect either continued exploration of various brain states during early development (Deco et al., 2013), or the capacity for adult brains to suppress dynamic fluctuations when engaging in a cognitive task (Cohen, 2018). Interestingly, prior evidence also indicates that older adults tend to exhibit weaker connections throughout the brain, but this difference is primarily attributable to decreases in absolute rsFC rather than increases in rsFC variability (Tian et al., 2018). As these studies demonstrate, dynamic measures of functional connectivity can provide unique information about neurodevelopment over and above static connectivity measures.

Although research into neurodevelopment of functional networks has revealed promising insights, a number of important gaps remain. First, few prior studies have considered rsFC across the lifespan, instead tending to focus on specific periods of development. By leveraging data across a range of ages from childhood through late adulthood, it may be possible to detect age-related differences that occur on a longer timescale. Likewise, using such an approach may also highlight specific developmental periods most strongly associated with these changes. Second, the majority of rsFC studies focus on static or dynamic connectivity, rather than integrating multiple analytical methods into a common framework. As a result, the overlapping and distinct contributions of static and dynamic rsFC strategies remain largely understudied.

This exploratory project aimed to evaluate the relationships between age and static and dynamic rsFC in healthy individuals from the publicly available Human Connectome Project (HCP) Lifespan dataset (Van Essen et al., 2013). Strengths of this dataset include the broad age range, the high quality of data acquisition (functional neuroimaging data were collected at high temporal resolution, supporting dynamic analytic methods), and public availability of data (supporting open science goals and replication). Because data were drawn from an existing dataset, there are also some limitations (addressed further in the Discussion). Therefore, we emphasize the exploratory nature of these analyses. Analyses used complementary methods for interrogating rsFC: static rsFC, which we define as average connectivity across the scans, as well as dynamic rsFC, which we define as metrics of connectivity stability over time (e.g., variability in connectivity, persistence of network connectivity "states"). This study specifically aimed to compare the effects of age on functional network properties across these validated approaches. In light of the above discussion, we predicted that (1) older age would be related to higher static rsFC among regions within canonical RSNs and (2) older age would be related to lower static rsFC among regions in different canonical RSNs, particularly along the anterior-posterior axis. In addition, we hypothesized that (3) older age would be related to differences in rsFC variability and functional network dwell time. The latter dynamic hypotheses do not predict the direction of effects, because these methods are relatively new and there is mixed evidence regarding the direction of age-related

effects on network dynamics. Because sex (Biswal et al., 2010; Allen et al., 2011; Zhang et al., 2018) and working memory task performance (Damoiseaux et al., 2007; Sala-Llonch et al., 2012) have been previously implicated in studies of rsFC, we included these variables as covariates in all analyses. Additional analyses evaluated the extent to which sex and working memory task performance moderate observed differences in static and dynamic rsFC across the lifespan.

MATERIALS AND METHODS

Participants

Original data collection was approved by the Washington University Institutional Review Board. The HCP Lifespan Pilot (Van Essen et al., 2013) includes eight functional magnetic resonance imaging (fMRI) scans during eyes-open rest for 27 healthy individuals (15 female, 12 male) ranging from 8 to 75 years of age, organized into one of five age bins (8–9; 14–15; 25–35; 45–55; 65–75).

Data Acquisition Parameters

Data were acquired on a 3-Tesla Siemens Connectome MRI scanner at Washington University in St. Louis, MO. Functional runs were acquired with a voxel resolution of 2 mm × 2 mm × 2 mm, 72 slices, using an 810 mm × 936 mm field of view. Each run was comprised of 420 frames using a repetition time (TR) of 0.72 s and an echo time (TE) of 33.2 ms. For each individual subject, the runs alternated phase encoding directions, such that the odd runs were in the left-to-right direction, whereas the even runs were in the right-to-left direction.

Data Pre-processing

Unprocessed functional and structural MRI data corrected for gradient distortion were downloaded directly from the HCP website (Marcus et al., 2011). Our pre-processing pipeline was implemented in SPM12. Images were realigned using the default least squares approach in SPM12. Due to the rapid acquisition parameters (TR = 0.72 s, multi-band factor = 8) of these data, slice-timing correction was not applied (Glasser et al., 2013). Data were then spatially normalized into the standard Montreal Neurological Institute (MNI) space (Friston et al., 1994), resliced to 2 mm × 2 mm × 2 mm voxels, and smoothed using a Gaussian kernel with a full-width at half-maximum (FWHM) of 6mm. At the first-level of analysis, outlier volumes were censored and motion regressors were included as first-level covariates. To further reduce spurious correlations in rsFC due to subject head motion (Power et al., 2013), the Artifact Detection Tools (ART)[1] software was used to identify and statistically censor volumes of significant movement or signal spikes from individual fMRI runs, also on the first level of analysis.

The total number of outlier motion volumes was also calculated in ART to identify if individual subjects lost an excessive amount of data due to censoring, thereby warranting exclusion from statistical analysis. Using a threshold of ≥15% volumes censored across the four fMRI runs, no subjects were identified as motion outliers. To account for the effects of frame-by-frame head displacement on rsFC (Power et al., 2012), estimates of total framewise displacement from ART were averaged across the four runs and included as a covariate in the group level of analysis. As gray matter volume is known to change across the lifespan (Ge et al., 2002), it is possible that changes in gray matter could influence the results of the present study. Unfortunately, it was not possible to disentangle effects of age from effects of gray matter volume, given high collinearity between these variables in prior studies (Walhovd et al., 2011) and in the present sample (r = 0.9497, $p < 0.0001$) (see **Supplement 1**). However, this is an intriguing question for future research.

Independent Components Analysis (ICA)

In preparation for our analyses investigating persistence of whole-brain functional connectivity states, we first performed independent components analysis (ICA) implemented in the Group ICA of fMRI Toolbox v3.0b (GIFT[2]; Calhoun, 2004) to create spatial maps of nodes that would be used in subsequent analysis. Concatenating across the four runs of rsfMRI for each participant, we used ICA to detect voxels that are temporally correlated with one another (compared with chance likelihood). Correlated voxels were then blindly separated using Infomax (Calhoun et al., 2001), an algorithm that was repeated 10 times in ICASSO (Himberg and Hyvarinen, 2003) on 200 subject-specific principal components in order to compile the data into statistically independent components. We implemented group information guided independent component analysis (Calhoun et al., 2001) to perform back-reconstruction, yielding subject-specific spatial maps and time-courses. Based on prior work (Allen et al., 2011), we selected 100 components as the final model order for the present analysis, thresholding each component at $Z > 3.5$ to enhance spatial specificity.

We were specifically interested in functional networks that included spatial components overlapping with the AN, DN, FN, Somatomotor (SM), SN, and Visual (VIS) networks. Based on visual inspection of the components in MNI space by two independent raters (Kelly et al., 2010), we identified 38 components for analysis. The other 62 components were omitted because they either belonged to other RSNs (e.g., auditory) or they were deemed to reflect motion- or noise-related artifacts. Of the 38 components included for analysis, we sorted them into one of the six canonical networks-of-interest. For a visual representation of how these components compare to a functional atlas of canonical resting brain networks (Yeo et al., 2011), see **Supplement 2**.

Primary and Exploratory Analyses

The HCP protocol includes resting-state fMRI scans following both structural and task-fMRI paradigms. In order to avoid contamination effects of task-related activation on subsequent rsfMRI scans, we included only the resting scans collected prior to task scanning (i.e., we included four of the eight rsfMRI scans

[1] http://www.nitrc.org/projects/artifact_detect

[2] https://trendscenter.org/trends/software/gift/

for each subject) in the primary neuroimaging analyses. Our group-level variables were mean-centered Age (binned by: 8–9; 14–15; 25–35; 45–55; 65–75), contrast-coded Sex (male; female), mean-centered WM performance (% accuracy during the neutral N-Back Task), and Framewise Displacement (average framewise displacement across the four runs).

Exploratory analyses were conducted to evaluate replication of findings in the second series of resting data collected from the same subjects, after completing task neuroimaging. Although we focus our main analyses on pre-task resting scans (due to the potential confounding effect of prior task engagement), replication could support reliability of methods and age differences. As one subject only completed six of the eight fMRI runs, this subject was omitted from replication analyses. Statistically significant results from the primary analyses were examined for replicability at uncorrected $p < 0.05$.

Moderating Variables: Sex and Working Memory (WM) Task Performance

All subjects completed an N-Back task using neutral images (places, tools, faces, and body parts). Averaging across 2-back and 0-back trials, mean-centered performance (% accuracy) on the N-Back task was included as a behavioral regressor in group-level general linear models investigating static and dynamic rsFC metrics. Of the 27 subjects included in the analyses, all but one subject performed at greater than 50% accuracy in the WM task, so that subject was omitted from analyses. Therefore, the final dataset included 26 subjects (14 female, 12 male).

Sex, working memory task performance, and framewise displacement were included as covariates in all models. Unless noted (see **Supplement 6**), there were no significant effects of these covariates on rsFC measures.

Analytical Approaches

Static rsFC Analyses

Static, time-invariant analyses were implemented in the CONN functional connectivity toolbox (Whitfield-Gabrieli and Nieto-Castanon, 2012)[3]. Physiological noise was controlled with CompCor, an algorithm in which the timeseries of activation is extracted from subject-specific tissue masks (white matter, cerebrospinal fluid), and principal components analysis is applied to estimate physiological noise reflected in these timeseries, after which the resulting components are included as covariates in a denoising regression (for additional details on this approach, see Behzadi et al., 2007; Chai et al., 2012; Whitfield-Gabrieli and Nieto-Castanon, 2012). Finally, we applied a band-pass filter of 0.008–0.09 Hz to further remove high-frequency activity associated with physiological functioning (oscillations at a frequency higher than expected for functional brain data, e.g., respiratory and cardiac noise, see Cordes et al., 2001) and low-frequency activity associated with scanner drift.

One of the 38 components, centered on bilateral anterior insula, underwent additional editing in the MarsBaR Toolbox (Brett et al., 2002) to enhance anatomical specificity by removing midline structures. To test for lateralized effects among regions of interest (ROIs), 14 of the 38 components were split in MarsBaR, yielding separate left and right ROIs for these components. Therefore, a total of 52 ROIs were used in this analysis.

We then performed a general linear model to investigate main effects of Age, and effects of Age moderated by Sex, or WM performance, on static rsFC among the ROIs derived from ICA. Across all static rsFC models, significance testing in CONN was thresholded at a false-discovery rate (FDR) $p < 0.05$ to correct for multiple comparisons at the analysis-level (Benjamini and Hochberg, 1995).

Dynamic rsFC Analyses: Variability in rsFC (vFC)

For analysis of dynamic variability in functional connectivity between individual ROIs, we utilized a sliding-window approach to measure the variability in ROI-ROI connectivity (vFC) (for examples, see Kaiser et al., 2016; Pelletier-Baldelli et al., 2018). To complete vFC, we entered the same 52 ROIs in the CONN toolbox. Initial denoising (for motion and physiological noise) was identical to that above, for static rsFC, but the band-pass filter was set at 0.0224–0.09 Hz to remove high-frequency activity characteristic of physiological noise and remove low-frequency activity with a period that is greater than the duration of each sliding window (Leonardi and Van De Ville, 2015). Sliding windows were calculated using a window length of 44.64 s and sliding the onset of each window by 3.6 s for a total of 72 windows (see **Supplement 3** for details on how these parameters were selected; of note, the same sliding window size was used for GIFT analyses, below). Within each sliding window, we computed a Pearson's correlation between individual seeds and all other seeds, yielding a single 52 × 52 correlation matrix of Fisher-transformed correlation coefficients (beta values) for each window and for each participant. To capture dynamic variability in rsFC over time, we computed the standard deviation of the beta values (SD_b) across matrices for each ROI-to-ROI correlation coefficient, for each participant. This calculation yielded a matrix of ROI-to-ROI SD_b values for each participant. We then performed a general linear model to investigate main effects of Age, and effects of Age moderated by Sex or WM performance, on these SD_b values for each ROI with every other ROI. Across all dynamic rsFC models, significance testing was thresholded at a false-discovery rate (FDR) $p < 0.05$ to correct for multiple comparisons at the analysis-level (Benjamini and Hochberg, 1995). These corrections were performed in MATLAB 2015b using the fdr_bh function (written by David Groppe).

Dynamic rsFC Analyses: Intrinsic Functional Connectivity States

For analysis of dynamic network functioning as operationalized by functional connectivity states, we implemented the time-varying approach developed by Allen et al. (2014) and Rashid et al. (2014, 2016). First, to remove low-frequency noise, such as scanner drift, motion artifacts, and other sources of variance that may not be captured during ICA, component time-courses underwent post-processing using a fifth-order Butterworth low-pass filter with a high frequency cutoff of 0.15Hz. Outliers were removed based on the median absolute deviation using

[3]http://www.nitrc.org/projects/conn

3dDespike in AFNI (Cox, 1996) and were replaced using a third-order spline fit to the clean time-courses.

After ICA post-processing, the subject-specific spatial maps were then analyzed using a sliding-window procedure identical to the steps described in vFC, with a window length of 44.64 s and sliding the onset of each window by 3.6 s. Next, within each sliding window, pair-wise Pearson's correlations were performed between each spatial component and all other spatial components from the ICA, yielding a 38 × 38 correlation matrix for each sliding window.

These correlation matrices (across windows and participants) were partitioned via *k*-means clustering, a data-driven method to cluster the average correlations over time into a discrete number of categories. Our approach adhered to the standard settings for *k*-means clustering within the GIFT Toolbox (Allen et al., 2014; additional information about the implementation of *k*-means clustering can be found in the GIFT Toolbox manual[4]). At a given time-point, each correlation matrix was categorized into one discrete "intrinsic connectivity network state" (ICN state), which represents a pattern of brain functional connectivity across ROIs. The present analysis yielded four ICN states (with the number of clusters (*k*) determined using the elbow criterion of the cluster validity index). The categorization of a correlation matrix into one discrete ICN state was assigned based on the likelihood that it resembled one ICN state compared to other ICN states (for details, see Allen et al., 2014; Rashid et al., 2014). For ease of interpretability, the matrices displaying each network state have been organized so that spatial components are grouped in adjacent rows/columns according to prior canonical RSNs.

Next, brain activity was classified into one of the four states at a given time-point. Then, we calculated the average time spent in each state before switching to another state (mean dwell time; MDT). We then performed a general linear model to investigate main effects of Age, and effects of Age as moderated by Sex and WM performance, on MDT in a particular ICN state.

Supplementary Analyses

Based on current standards, the three analytical approaches described above employed slightly different pre-processing methods to investigate static and dynamic rsFC (specifically with regard to temporal filtering). Therefore, we repeated the static and MDT analyses to match the temporal filtering used in the vFC approach (see **Supplements 7, 8** for additional information).

RESULTS

Age was not significantly correlated with Framewise Displacement (R^2 = 0.044, p = 0.295). However, the youngest (ages 8–9) and oldest (ages 65–75) subjects tended to exhibit greater movement than did subject from other age bins (see **Table 1** and **Figure 1**).

TABLE 1 | Sex, age, and average framewise displacement values for each subject in the HCP Lifespan dataset.

HCP ID	Sex	Age bin	Estimate of average framewise displacement (mm)
LS2001	F	8–9	0.227275
LS2003	M	8–9	0.292575
LS2008	M	8–9	0.45585
LS2009	F	8–9	0.214069
LS2037	M	8–9	0.241275
LS2043	F	8–9	0.143725
LS3017	F	14–15	0.060225
LS3019	M	14–15	0.1583
LS3026	F	14–15	0.129525
LS3029	F	14–15	0.06995
LS3040	F	14–15	0.10705
LS3046	F	14–15	0.0994
LS4025	M	25–35	0.148225
LS4036	M	25–35	0.097575
LS4041	F	25–35	0.08575
LS4043	F	25–35	0.1028
LS4047	F	25–35	0.1752
LS5007	F	45–55	0.1444
LS5038	M	45–55	0.1506
LS5040	M	45–55	0.109475
LS5041	F	45–55	0.13035
LS5049	M	45–55	0.075475
LS6003	M	65–75	0.33965
LS6006	M	65–75	0.118725
LS6009	F	65–75	0.13815
LS6046	M	65–75	0.140525

Static rsFC Analyses

General linear models first investigated main effects of Age (controlling for Sex, WM Performance, and Framewise Displacement) and the moderating effects of Sex and WM Performance in predicting static rsFC among pairs of the 52 ICA-derived components.

A total of 26 ROI-to-ROI pairs exhibited a significant main effect of Age. All of these effects were negative, including decreasing connectivity of AN ROIs with the SN as well as decreasing connectivity of VIS ROIs with ROIs in the AN, FN, SM, and SN (see **Figure 2** and **Table 2** for list of effects, see **Supplementary Table S4a** for average connectivity values within each age bin). Further inspecting these effects, positive rsFC between these ROIs tended to exhibit a positive-to-negative change in connectivity over the course of aging, particularly involving the right inferior occipital gyrus ROIs (see **Figure 3A**). However, four ROI-ROI pairs became less positive across the lifespan (see **Figure 3B**): the left putamen (of the AN) with the right anterior insula (of the SN), the right putamen (of the AN) with the right anterior insula (of the SN), and the right putamen (of the AN) with the left anterior insula (of the SN, two separate ROIs). There were no main or interactive effects regarding Sex and WM Performance.

Dynamic rsFC Analyses: Variability in rsFC (vFC)

General linear models investigated main effects of Age (controlling for Sex, WM Performance, and

[4]https://trendscenter.org/trends/software/gift/docs/v4.0b_gica_manual.pdf

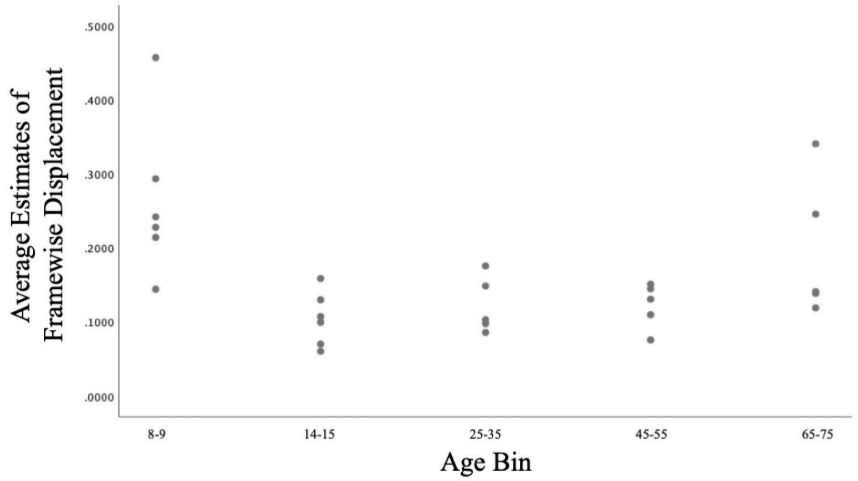

FIGURE 1 | Scatterplot of the relationship between Age and Framewise Displacement in the current sample.

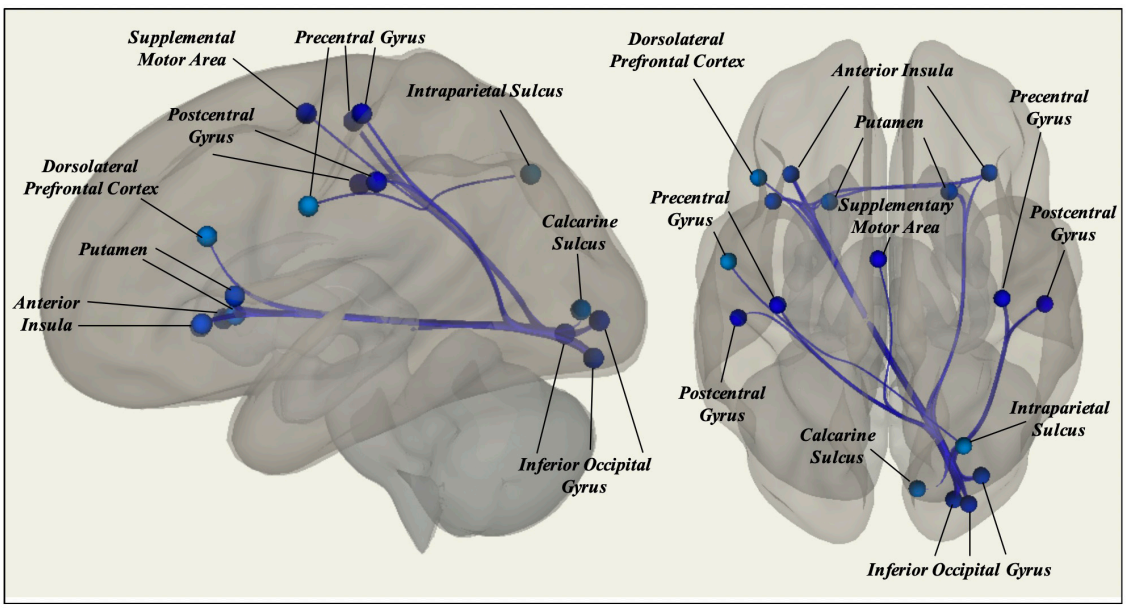

FIGURE 2 | Significant effects of Age on static rsFC controlling for Gender, WM Performance, and Framewise Displacement, with resting-state functional connectivity tending to decrease among ROIs in different canonical functional networks.

Framewise Displacement) and the moderating effects of Sex and WM Performance in predicting the SD_b for each ROI-to-ROI pair. Significance testing was thresholded at a false-discovery rate $p < 0.05$ for each set of linear models.

No ROI-to-ROI pairs exhibited a significant main effect of Age in predicting SD_b of rsFC across sliding-windows. Several ROI-to-ROI pairs exhibited non-significant main effects of Age on SD_b that failed to survive FDR correction (see **Supplement 5** for details). There were no significant main or interactive effects of Sex or WM Performance, controlling for other covariates.

Dynamic rsFC Analyses: Intrinsic Functional Connectivity States

General linear models first investigated the main effects of Age (controlling for Sex, WM Performance, and Framewise Displacement) in predicting MDT of the four GIFT-derived network states. Although Sex and WM performance were also included as moderators, no moderated effects emerged across any group-level analyses (see **Supplement 6** for main effects of these variables). Significance testing was thresholded at a false-discovery rate $p < 0.05$ to correct for four

TABLE 2 | Significant effects of Age in predicting static rsFC between ROIs, grouped by network.

Effects of age on static rsFC of AN ROIs with SN ROIs		**Resting-state series 1 (Pre-task scans)**		**Resting-state series 2 (Post-task scans)**	
AN component	**SN component**	**T-statistic**	***p*-value**	**T-statistic**	***p*-value**
Left putamen	Right anterior insula	$t(21) = -3.94$	0.00075	$t(20) = -3.92$	0.0009
Right putamen	Left anterior insula (a)	$t(21) = -5.29$	0.00003	$t(20) = -2.86$	0.0097
Right putamen	Left anterior insula (b)	$t(21) = -5.46$	0.00001	$t(20) = -3.26$	0.0039
Right putamen	Right anterior insula	$t(21) = -5.12$	0.00005	$t(20) = -3.06$	0.0062
Effects of age on static rsFC of AN ROIs with VIS ROIs		**Pre-task scans**		**Post-task scans**	
AN component	**VIS component**	**T-statistic**	***p*-value**	**T-statistic**	***p*-value**
Left putamen	Right calcarine sulcus	$t(21) = -4.00$	0.00065	$t(20) = -2.69$	0.0140
Left putamen	Right inferior occipital gyrus (a)	$t(21) = -4.53$	0.00018	$t(20) = -3.75$	0.0013
Left putamen	Right inferior occipital gyrus (c)	$t(21) = -4.93$	0.00007	$t(20) = -5.27$	0.00002
Right putamen	Right inferior occipital gyrus (a)	$t(21) = -5.04$	0.00003	$t(20) = -2.80$	0.0111
Right putamen	Right inferior occipital gyrus (c)	$t(21) = -4.37$	0.00027	$t(20) = -3.42$	0.0027
Effects of age on static rsFC of FN ROIs with VIS ROIs		**Pre-task scans**		**Post-task scans**	
FN component	**VIS component**	**T-statistic**	***p*-value**	**T-statistic**	***p*-value**
Left dorsolateral prefrontal cortex	Right inferior occipital gyrus (c)	$t(21) = -4.01$	0.00063	$t(20) = -0.98$	0.3372
Effects of age on static rsFC of SM ROIs with VIS ROIs		**Pre-task scans**		**Post-task scans**	
SM component	**VIS component**	**T-statistic**	***p*-value**	**T-statistic**	***p*-value**
Left postcentral gyrus	Right inferior occipital gyrus (c)	$t(21) = -4.48$	0.00021	$t(20) = -1.52$	0.1436
Left precentral gyrus (a)	Right inferior occipital gyrus (b)	$t(21) = -4.78$	0.00010	$t(20) = -3.34$	0.0033
Left precentral gyrus (a)	Right inferior occipital gyrus (c)	$t(21) = -5.82$	0.00001	$t(20) = -2.78$	0.0177
Left precentral gyrus (b)	Right intraparietal sulcus	$t(21) = -4.75$	0.00011	$t(20) = 0.89$	0.3857
Right postcentral gyrus	Right inferior occipital Gyrus (a)	$t(21) = -3.97$	0.00070	$t(20) = -1.68$	0.1094
Right postcentral gyrus	Right inferior occipital gyrus (c)	$t(21) = -4.62$	0.00015	$t(20) = -2.02$	0.0567
Right precentral gyrus	Right inferior occipital gyrus (a)	$t(21) = -4.03$	0.00060	$t(20) = -2.27$	0.0347
Right precentral gyrus	Right inferior occipital gyrus (b)	$t(21) = -5.29$	0.00003	$t(20) = -2.48$	0.0223
Right precentral gyrus	Right inferior occipital gyrus (c)	$t(21) = -4.25$	0.00036	$t(20) = -1.98$	0.0620
Supplementary motor area	Right inferior occipital gyrus (c)	$t(21) = -4.27$	0.00034	$t(20) = -1.81$	0.0858
Effects of age on static rsFC of SN ROIs with VIS ROIs		**Pre-task scans**		**Post-task scans**	
SN component	**VIS component**	**T-statistic**	***p*-value**	**T-statistic**	***p*-value**
Left anterior insula (a)	Right inferior occipital gyrus (a)	$t(21) = -4.16$	0.00044	$t(20) = -1.86$	0.0780
Left anterior insula (a)	Right inferior occipital gyrus (c)	$t(21) = -5.16$	0.00004	$t(20) = -2.98$	0.0074
Left anterior insula (b)	Right inferior occipital gyrus (a)	$t(21) = -4.81$	0.00009	$t(20) = -2.84$	0.0102
Left anterior insula (b)	Right inferior occipital gyrus (b)	$t(21) = -4.89$	0.00008	$t(20) = -2.00$	0.0587
Left anterior insula (b)	Right inferior occipital gyrus (c)	$t(21) = -6.06$	0.00001	$t(20) = -3.84$	0.0010
Right anterior insula	Right inferior occipital gyrus (a)	$t(21) = -3.87$	0.00089	$t(20) = -3.04$	0.0064

AN, Affective Network; DN, Default Network; FN, Frontoparietal Network; SM, Sensorimotor; SN, Salience Network, VIS, Visual. The letters (a), (b), and (c) denote regions for which multiple ROIs were used. Primary analyses focusing on the pre-task scans were corrected for multiple comparisons at an analysis-level FDR of $p < 0.05$. For significant connectivity pathways that survived FDR correction, exploratory analyses examined these pathways in the post-task scans at uncorrected $p < 0.05$.

comparisons using the same procedure described above (p-crit = $r \times 0.05/n$).

State 1

Intrinsic connectivity network (ICN) State 1 was characterized by pronounced coordination among regions of the VIS (see **Figure 4**). This ICN state also included positive rsFC between the dorsomedial prefrontal cortex (of the DN) and the rostral anterior cingulate cortex (of the FN), the bilateral hippocampus (of the AN) and the rostral anterior cingulate cortex (of the FN), and between the superior parietal lobule (of the FN) and the intraparietal sulcus (of the VIS), as well as negative rsFC (anticorrelations) between the ventral striatum (of the AN) and the dorsal anterior cingulate cortex (of the SN) and between

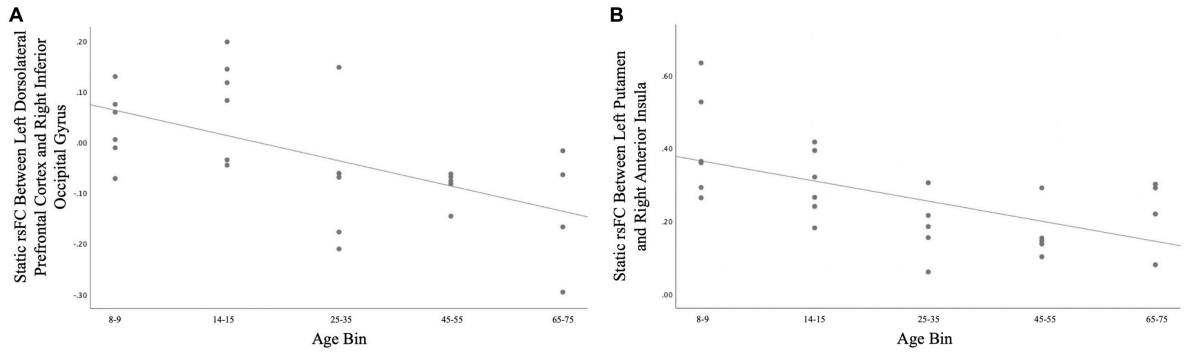

FIGURE 3 | (A) Age differences in static rsFC between right inferior occipital gyrus and left dorsolateral prefrontal cortex [$t(21) = -4.01$, $p = 0.00063$]. Of note, similar patterns were observed for the effect of age on static rsFC between other ROIs in visual systems and ROIs in other canonical networks. **(B)** Age differences in static rsFC between left putamen and right anterior insula [$t(21) = -3.92$, $p = 0.00075$]. Similar age effects were detected between other ROIs in the canonical affective network and ROIs in the canonical salience network.

the bilateral inferior frontal gyrus (of the FN) and the superior parietal lobule (of the FN).

FDR-corrected regression analyses revealed a significant main effect of Age predicting MDT of State 1 [$t(20) = -3.494$, $p = 0.002$], such that younger subjects tended to exhibit greater MDT in this ICN state (see **Supplementary Table S4b** for average MDT values within each age bin).

State 2

State 2 was defined by positive rsFC within and between regions of the Sensorimotor and VIS networks, except for negative rsFC (anticorrelations) between the bilateral inferior occipital gyrus (in the VIS) with SM regions (see **Figure 4**). This functional network state was also defined by positive rsFC between regions of the SM and VIS networks with the superior parietal lobule (of the FN) and by negative rsFC between the ventral striatum (of the AN) with the bilateral anterior insula (of the SN).

FDR-corrected regression analyses revealed a significant main effect of Age predicting MDT of State 2 [$t(20) = 3.780$, $p = 0.001$] such that older subjects tended to exhibit greater MDT of this ICN state (see **Supplementary Table S4b** for average MDT values within each age bin).

State 3

ICN State 3 was defined by positive rsFC within the SM and within the VIS, as well as a mixture of positive and negative rsFC among regions of the DN, FN, and SN (see **Figure 4**).

FDR-corrected regression analyses did not reveal a significant main effect of Age predicting MDT of State 3 [$t(21) = -1.072$, $p = 0.296$].

State 4

ICN State 4 was defined by positive rsFC within the SM and within the VIS, as well as a mixture of positive and negative rsFC among regions of the DN, FN, and SN (see **Figure 4**).

One subject was omitted from regression analysis because their MDT for State 4 was a significant outlier (>3 standard deviations above the mean). FDR-corrected regression analyses did not reveal a significant main effect of Age predicting MDT of State 4 [$t(20) = -0.700$, $p = 0.492$]. Inclusion or removal of the outlier subject did not alter the significance of these results [$t(21) = -0.616$, $p = 0.545$].

Exploratory Analyses

As noted above, exploratory analyses were performed to test replication of age effects in the second series of (post-task) resting-state scans. Only effects that were significant in the main experimental analyses (i.e., the first series of pre-task resting-state scans) were eligible for testing in these exploratory analyses.

Static rsFC Analyses

General linear models investigated main effects of Age (controlling for Sex, WM Performance, and Framewise Displacement) in predicting static rsFC among the 26 ROI-ROI pairs implicated by the primary analysis, in the second series of resting-state scans.

A total of 18 ROI-ROI pairs exhibited a significant main effect of Age in the replication dataset (included in **Table 2**). All of these effects were negative, as in the primary analysis. An additional four ROI-ROI pairs exhibited a non-significant trending main effect of Age, and four ROI-ROI pairs did not exhibit a replication of effects presented in the primary analysis.

Dynamic rsFC Analyses: Intrinsic Functional Connectivity States

The replication analysis in the second resting-state series yielded three ICN states, which showed connectivity profiles that were highly similar to those in the primary analysis (see **Figure 4**). General linear models investigated the main effects of Age (controlling for Sex, WM Performance, and Framewise Displacement) in predicting MDT of the three GIFT-derived network states.

In this exploratory replication analysis a significant main effect of Age was detected for State 3 [$t(19) = 3.326$, $p = 0.003$], an intrinsic connectivity network that was similar to State 2 from the primary analysis. As in the primary analysis, older subjects tended to exhibit greater MDT in this functional network state.

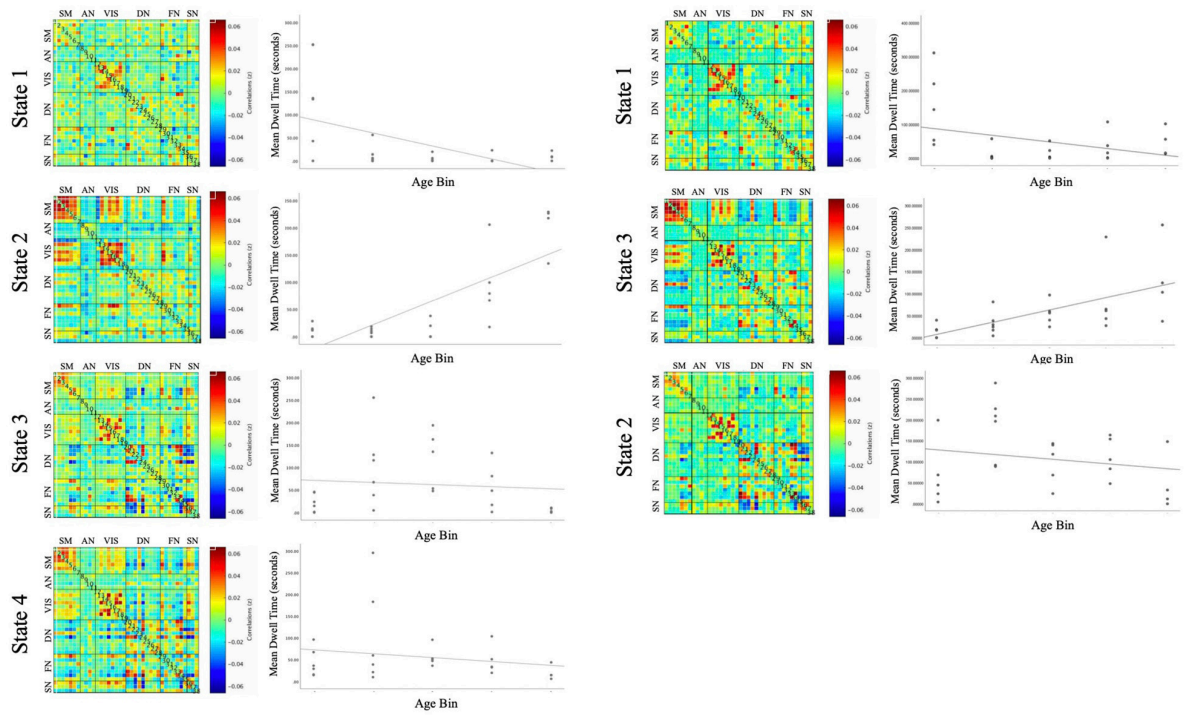

FIGURE 4 | Each of the intrinsic functional connectivity states are organized into a correlation matrix, with ROIs grouped by functional domain for pre-task **(left)** and post-task **(right)** functional runs. Scatterplots depict the association between Age and Mean Dwell Time for each of the ICN states. State 2 **(left)** and State 3 **(right)** exhibited similar profiles of connectivity, with Mean Dwell Time tending to increase across the lifespan [$t(20) = 3.780$, $p = 0.001$; $t(19) = 3.326$, $p = 0.003$].

DISCUSSION

The present study leveraged a publicly available dataset to explore how several different aspects of brain network functioning may differ across age groups, ranging from childhood to older adulthood. We first conducted a static rsFC analysis to evaluate overarching patterns of functional connectivity over time between ROIs. We then analyzed the standard deviation of these correlations as a method for evaluating the variability in functional connectivity patterns over time. Finally, we evaluated average dwell time in particular functional connectivity "states" of coordinated brain activity before neural systems switch to another state. These approaches each provided a different measure of how brain networks function, which we then linked to age-related differences across the lifespan.

Considering static rsFC, associations between anterior and posterior ROIs in different canonical networks tended to exhibit a positive-to-negative shift across the lifespan. These effects notably involved correlations between ROIs in the VIS (especially the right inferior occipital gyrus) and ROIs in the FN, SN, and SM. Associations between posterior and subcortical ROIs in different canonical networks exhibited a similar positive-to-negative shift, notably involving correlations between the right inferior occipital gyrus and right calcarine sulcus (of the VIS) with the left and right putamen (of the AN). In contrast to anterior-posterior and posterior-subcortical findings, associations between anterior and subcortical ROIs tended to involve positive correlations that become less positive across the lifespan, rather than shifting from positive to negative associations. These effects notably involved correlations between the left and right putamen (of the AN) with the left and right anterior insula (of the SN).

Several of the static rsFC findings replicated in exploratory analyses that aimed to reproduce main effects (from resting-state scan series 1, pre-task) in a second dataset (resting-state scan series 2, post-task). Of the 26 ROI-ROI pairs that were significantly associated with Age in the primary analysis, 18 of these effects replicated and an additional four of these effects exhibited a (non-significant) trend in the same direction. Effects that did not replicate included age effects on connectivity between the right inferior occipital gyrus (of the VIS) the right and left postcentral gyrus (of the SM), the right intraparietal sulcus (of the VIS) and the left precentral gyrus (of the SM), and the right inferior occipital gyrus (of the VIS) with the right inferior frontal gyrus (of the FN).

There were no significant associations between Age and vFC, although non-significant associations suggested potential decreases in variability between anterior and posterior ROIs in different canonical networks (see **Supplement 5**). This contrasts with prior findings of increased rsFC variability in young adults compared with children and youth (Hutchison and Morton, 2015). However, as the present study assessed vFC differences across the lifespan, this study is better positioned to evaluate

overarching lifespan changes in vFC and less suited to detect subtle changes that emerge during the transitions from childhood to adolescence and early adulthood. Furthermore, the small sample size employed in the present study may further limit its ability to detect such changes. Research aimed at understanding the precise association between vFC and Age within specific developmental periods, such as during adolescence, can address these limitations.

Converging with static rsFC patterns, the findings related to persistence of functional connectivity brain states (evaluated here with MDT) revealed that older subjects tended to spend more time dwelling in a state characterized by integration within and between VIS and SM ROIs (State 2). Of note, exploratory analyses provided evidence of replication in the second dataset collected from the same subjects (following task administration). In contrast, younger subjects tended to spend more time in a state characterized by less substantial integration among specifically VIS ROIs (State 1). However, these age effects were not replicated and should be interpreted with caution.

Interestingly, the tendency for older adults to dwell in a state defined by positive rsFC between SM and VIS ROIs may appear inconsistent with the results of static rsFC analyses, which showed decreasing overall rsFC between VIS and SM ROIs. However, this discrepancy also highlights the differences in age effects on standard static rsFC (which is based on overarching patterns of coordination) compared with dynamic measures of dwell time in transient rsFC networks (which are based on time spent in a particular state of rsFC, although patterns of rsFC may be quite different at other times in the scan). For example, these findings suggest that at older ages, SM and VIS ROIs tend to become less coordinated on average across an extended period of scanning; however, older brains also tend to persist longer in a brain state defined by increased integration among these systems once that brain state has been entered. These effects highlight the value of investigating and comparing age differences in static vs. dynamic properties of rsFC. A next step for this work may build on this comparative approach by developing methods that integrate static and dynamic properties in the same measurement or analyses.

Overall, the present findings support the theory that network boundaries become sharper across development (Fair et al., 2007; Grayson and Fair, 2017), evidenced by decreasing static rsFC among regions of distinct prototypical networks (Tian et al., 2018). The positive-to-negative shift in static rsFC among many of these ROIs suggests that network segregation may result in a qualitative shift in the relationship between regions, such that correlated regions not only disassociate from one another but may become anticorrelated later in life. Based on the present results, this phenomenon may especially emerge between regions of the visual system and other canonical networks, whereas regions of the affective and salience systems may simply become less correlated across the lifespan. Furthermore, age-related differences in MDT tended to show increased time spent in states of integration within and between the SM and VIS networks. Many of these same pathways were implicated in the static rsFC analysis, suggesting that the combined use of static and dynamic approaches may reveal subtle features of functional brain connectivity across the lifespan.

Limitations and Future Directions

We chose to test hypotheses in the HCP Lifespan dataset because of several notable strengths: e.g., the sample featured a broad age range, and data were collected at high temporal resolution (important for dynamic analytic methods). However, there are also some limitations which restrict the scope and generalizability of the present study.

First, although the present analyses were conducted to be as similar as possible in processing steps, it is important to note that we chose to accept some differences in processing in order to follow standard conventions for each method (see CONN[5] and GIFT[4] manuals). Specifically, this included some differences in low- and high-pass temporal filtering, differences in the number of ROIs included (i.e., splitting of bilateral components in the static and vFC analyses), and differences in artifact detection and removal (i.e., use of CompCor and ART in CONN, use of 3dDespike in GIFT). Future research should explore how differences in standard approaches to physiological denoising and temporal filtering (such as those implemented in CONN and GIFT, as well as other toolboxes) may affect estimates of static and dynamic functional connectivity.

Second, the sample size for this publicly available dataset is modest, limiting statistical power. As the present study constitutes an initial step in characterizing patterns of functional connectivity across the human lifespan, it will be necessary to replicate and extend these exploratory findings in larger studies with a lifespan age range. In larger samples, replication of linear effects may be tested, in addition to exploring non-linear effects of age that may highlight specific developmental periods as crucial windows of dynamic network development. Likewise, a critical next step will be to focus on patterns of functional connectivity within specific age ranges, utilizing large datasets from studies such as the HCP Development (ages 5–21), HCP Aging (ages 36+), and Adolescent Brain Cognitive Development (a longitudinal study from age 9–20) initiatives.

Third, in cases where individuals tend to dwell longer in rare ICN states, it would be especially interesting to understand the cognitive significance of such a pattern. As the present study included only one metric of cognitive functioning, future research should evaluate a wider range of cognitive tasks to better characterize the psychological correlates of ICN state persistence, and how these correlates differ across the lifespan.

Fourth, future research should further clarify the relationship between static rsFC and MDT approaches, especially considering findings that diverge across the modalities. Given the rapidly changing suite of methods for investigating resting-state functional connectivity (Calhoun et al., 2014), methods comparison is an important step for evaluating the unique vs. overlapping information that can be gained with these different techniques.

Finally, the risk of onset of specific psychiatric disorders varies over development (Paus et al., 2008), and may correspond with key changes in functional brain

[5]https://web.conn-toolbox.org/resources/manual

networks. Future clinical research may employ a similar combination of approaches to identify how disruptions in network integration and segregation relate to the emergence of psychopathology during development. In sum, we emphasize the exploratory nature of the present analyses, and the potential value of future replication and new directions for this work.

CONCLUSION

In conclusion, the present study supports a framework of both network segregation and integration across the lifespan, wherein sensory networks tend to become more integrated with one another and more segregated from other canonical brain networks. Likewise, the present study supports the use of multiple analytical approaches to evaluate static and dynamic trends in functional connectivity during the resting-state.

DATA AVAILABILITY STATEMENT

All datasets generated for this study are included in the article/**Supplementary Material**. Further inquiries can be directed to the corresponding author.

ETHICS STATEMENT

The studies involving human participants were reviewed and approved by Washington University Institutional Review Board. Written informed consent to participate in this study was provided by the participants or their legal guardian/next of kin.

AUTHOR CONTRIBUTIONS

BR: conceptualization, formal analysis, and writing. EM: methodology and software. MM: methodology and supervision. RK: conceptualization, methodology, supervision, and writing. All authors contributed to the article and approved the submitted version.

FUNDING

BR was supported by the National Science Foundation Graduate Research Fellowship (DGE-1650604) during the completion of this work.

ACKNOWLEDGMENTS

Data were provided by the Human Connectome Project, WU-Minn Consortium (Principal Investigators: David Van Essen and Kamil Ugurbil; 1U54MH091657) funded by the 16 NIH Institutes and Centers that support the NIH Blueprint for Neuroscience Research; and by the McDonnell Center for Systems Neuroscience at Washington University.

SUPPLEMENTARY MATERIAL

The Supplementary Material for this article can be found online at: https://www.frontiersin.org/articles/10.3389/fnins.2020.561594/full#supplementary-material

REFERENCES

Allen, E. A., Damaraju, E., Plis, S. M., Erhardt, E. B., Eichele, T., and Calhoun, V. D. (2014). Tracking whole-brain connectivity dynamics in the resting state. *Cereb. Cortex* 24, 663–676. doi: 10.1093/cercor/bhs352

Allen, E. A., Erhardt, E. B., Damaraju, E., Gruner, W., Segall, J. M., Silva, R. F., et al. (2011). A baseline for the multivariate comparison of resting-state networks. *Front. Syst. Neurosci.* 5:2. doi: 10.3389/fnsys.2011.00002

Andrews-Hanna, J. R., Snyder, A. Z., Vincent, J. L., Lustig, C., Head, D., Raichle, M. E., et al. (2007). Disruption of large-scale brain systems in advanced aging. *Neuron* 56, 924–935. doi: 10.1016/j.neuron.2007.10.038

Behzadi, Y., Restom, K., Liau, J., and Liu, T. T. (2007). A component based noise correction method (CompCor) for BOLD and perfusion based fMRI. *Neuroimage* 37, 90–101. doi: 10.1016/j.neuroimage.2007.04.042

Benjamini, Y., and Hochberg, Y. (1995). Controlling the false discovery rate: a practical and powerful approach to multiple testing. *J. R. Stat. Soc. Ser. B* 57, 289–300. doi: 10.1111/j.2517-6161.1995.tb02031.x

Betzel, R. F., Byrge, L., He, Y., Goñi, J., Zuo, X. N., and Sporns, O. (2014). Changes in structural and functional connectivity among resting-state networks across the human lifespan. *NeuroImage* 102, 345–357. doi: 10.1016/j.neuroimage.2014.07.067

Biswal, B. B., Mennes, M., Zuo, X. N., Gohel, S., Kelly, C., Smith, S. M., et al. (2010). Toward discovery science of human brain function. *Proc. Natl. Acad. Sci. U.S.A.* 107, 4734–4739. doi: 10.1073/pnas.0911855107

Brett, M., Anton, J. L., Valabregue, R., and Poline, J. B. (2002). "Region of interest analysis using an SPM toolbox," in *Proceedings of the 8th International Conference on Functional Mapping of the Human Brain* Sendai.

Calhoun, V. D. (2004). *Group ICA of fMRI Toolbox (GIFT)*. Available online at: http://icatb.sourceforge.net (accessed November 14, 2017).

Calhoun, V. D., Adali, T., Pearlson, G. D., and Pekar, J. J. (2001). A method for making group inferences from functional MRI data using independent component analysis. *Hum. Brain Mapp.* 14, 140–151. doi: 10.1002/hbm.1048

Calhoun, V. D., Miller, R., Pearlson, G., and Adalı, T. (2014). The chronnectome: time-varying connectivity networks as the next frontier in fMRI data discovery. *Neuron* 84, 262–274. doi: 10.1016/j.neuron.2014.10.015

Chai, X. J., Castañón, A. N., Öngür, D., and Whitfield-Gabrieli, S. (2012). Anticorrelations in resting state networks without global signal regression. *NeuroImage* 59, 1420–1428. doi: 10.1016/j.neuroimage.2011.08.048

Chan, M. Y., Park, D. C., Savalia, N. K., Petersen, S. E., and Wig, G. S. (2014). Decreased segregation of brain systems across the healthy adult lifespan. *Proc. Natl. Acad. Sci. U.S.A.* 111, E4997–E5006. doi: 10.1073/pnas.1415122111

Cohen, J. R. (2018). The behavioral and cognitive relevance of time-varying, dynamic changes in functional connectivity. *NeuroImage* 180(Pt B), 515–525. doi: 10.1016/j.neuroimage.2017.09.036

Cordes, D., Haughton, V. M., Arfanakis, K., Carew, J. D., Turski, P. A., Moritz, C. H., et al. (2001). Frequencies contributing to functional connectivity in the cerebral cortex in "resting-state" data. *Am. J. Neuroradiol.* 22, 1326–1333.

Cox, R. W. (1996). AFNI: software for analysis and visualization of functional magnetic resonance neuroimages. *Comput. Biomed. Res.* 29, 162–173. doi: 10.1006/cbmr.1996.0014

Damoiseaux, J. S., Beckmann, C. F., Arigita, E. S., Barkhof, F., Scheltens, P., Stam, C. J., et al. (2007). Reduced resting-state brain activity in the "default network" in normal aging. *Cerebr. Cortex* 18, 1856–1864. doi: 10.1093/cercor/bhm207

Damoiseaux, J. S., Rombouts, S. A., Barkhof, F., Scheltens, P., Stam, C. J., Smith, S. M., et al. (2006). Consistent resting-state networks across healthy subjects. *Proc. Natl. Acad. Sci. U.S.A.* 103, 13848–13853. doi: 10.1073/pnas.0601417103

Deco, G., Jirsa, V. K., and McIntosh, A. R. (2013). Resting brains never rest: computational insights into potential cognitive architectures. *Trends Neurosci.* 36, 268–274. doi: 10.1016/j.tins.2013.03.001

Dosenbach, N. U., Nardos, B., Cohen, A. L., Fair, D. A., Power, J. D., Church, J. A., et al. (2010). Prediction of individual brain maturity using fMRI. *Science* 329, 1358–1361. doi: 10.1126/science.1194144

Fair, D. A., Dosenbach, N. U., Church, J. A., Cohen, A. L., Brahmbhatt, S., Miezin, F. M., et al. (2007). Development of distinct control networks through segregation and integration. *Proc. Natl. Acad. Sci. U.S.A.* 104, 13507–13512. doi: 10.1073/pnas.0705843104

Fox, M. D., Snyder, A. Z., Vincent, J. L., Corbetta, M., Van Essen, D. C., and Raichle, M. E. (2005). The human brain is intrinsically organized into dynamic, anticorrelated functional networks. *Proc. Natl. Acad. Sci. U.S.A.* 102, 9673–9678. doi: 10.1073/pnas.0504136102

Friston, K. J., Holmes, A. P., Worsley, K. J., Poline, J. P., Frith, C. D., and Frackowiak, R. S. (1994). Statistical parametric maps in functional imaging: a general linear approach. *Hum. Brain Mapp.* 2, 189–210. doi: 10.1002/hbm.460020402

Ge, Y., Grossman, R. I., Babb, J. S., Rabin, M. L., Mannon, L. J., and Kolson, D. L. (2002). Age-related total gray matter and white matter changes in normal adult brain. Part I: volumetric MR imaging analysis. *Am. J. Neuroradiol.* 23, 1327–1333.

Glasser, M. F., Sotiropoulos, S. N., Wilson, J. A., Coalson, T. S., Fischl, B., Andersson, J. L., et al. (2013). The minimal preprocessing pipelines for the human connectome Project. *NeuroImage* 80, 105–124. doi: 10.1016/j.neuroimage.2013.04.127

Grayson, D. S., and Fair, D. A. (2017). Development of large-scale functional networks from birth to adulthood: a guide to the neuroimaging literature. *NeuroImage* 160, 15–31. doi: 10.1016/j.neuroimage.2017.01.079

Gu, S., Satterthwaite, T. D., Medaglia, J. D., Yang, M., Gur, R. E., Gur, R. C., et al. (2015). Emergence of system roles in normative neurodevelopment. *Proc. Natl. Acad. Sci. U.S.A.* 112, 13681–13686. doi: 10.1073/pnas.1502829112

He, X., Qin, W., Liu, Y., Zhang, X., Duan, Y., Song, J., et al. (2013). Age-related decrease in functional connectivity of the right fronto-insular cortex with the central executive and default-mode networks in adults from young to middle age. *Neurosci. Lett.* 544, 74–79. doi: 10.1016/j.neulet.2013.03.044

Himberg, J., and Hyvarinen, A. (2003). "Icasso: software for investigating the reliability of ICA estimates by clustering and visualization," in *Proceedings of the 2003 IEEE XIII Workshop on Neural Networks for Signal Processing (IEEE Cat. No. 03TH8718)* (Piscataway, NJ: IEEE), 259–268.

Hindriks, R., Adhikari, M. H., Murayama, Y., Ganzetti, M., Mantini, D., Logothetis, N. K., et al. (2016). Can sliding-window correlations reveal dynamic functional connectivity in resting-state fMRI? *NeuroImage* 127, 242–256. doi: 10.1016/j.neuroimage.2015.11.055

Hutchison, R. M., and Morton, J. B. (2015). Tracking the brain's functional coupling dynamics over development. *J. Neurosci.* 35, 6849–6859. doi: 10.1523/jneurosci.4638-14.2015

Hutchison, R. M., Womelsdorf, T., Allen, E. A., Bandettini, P. A., Calhoun, V. D., Corbetta, M., et al. (2013). Dynamic functional connectivity: promise, issues, and interpretations. *NeuroImage* 80, 360–378. doi: 10.1016/j.neuroimage.2013.05.079

Kaiser, R. H., Whitfield-Gabrieli, S., Dillon, D. G., Goer, F., Beltzer, M., Minkel, J., et al. (2016). Dynamic resting-state functional connectivity in major depression. *Neuropsychopharmacology* 41, 1822–1830. doi: 10.1038/npp.2015.352

Kelly, R. E. Jr., Alexopoulos, G. S., Wang, Z., Gunning, F. M., Murphy, C. F., Morimoto, S. S., et al. (2010). Visual inspection of independent components: defining a procedure for artifact removal from fMRI data. *J. Neurosci. Methods* 189, 233–245. doi: 10.1016/j.jneumeth.2010.03.028

Koch, W., Teipel, S., Mueller, S., Buerger, K., Bokde, A. L., Hampel, H., et al. (2010). Effects of aging on default mode network activity in resting state fMRI: does the method of analysis matter? *NeuroImage* 51, 280–287. doi: 10.1016/j.neuroimage.2009.12.008

Leonardi, N., and Van De Ville, D. (2015). On spurious and real fluctuations of dynamic functional connectivity during rest. *NeuroImage* 104, 430–436. doi: 10.1016/j.neuroimage.2014.09.007

Liégeois, R., Laumann, T. O., Snyder, A. Z., Zhou, J., and Yeo, B. T. (2017). Interpreting temporal fluctuations in resting-state functional connectivity MRI. *Neuroimage* 163, 437–455. doi: 10.1016/j.neuroimage.2017.09.012

Marcus, D. S., Harwell, J., Olsen, T., Hodge, M., Glasser, M. F., Prior, F., et al. (2011). Informatics and data mining tools and strategies for the human connectome project. *Front. Neuroinform.* 5:4. doi: 10.3389/fninf.2011.00004

Paus, T., Keshavan, M., and Giedd, J. N. (2008). Why do many psychiatric disorders emerge during adolescence? *Nat. Rev. Neurosci.* 9, 947–957. doi: 10.1038/nrn2513

Pelletier-Baldelli, A., Andrews-Hanna, J. R., and Mittal, V. A. (2018). Resting state connectivity dynamics in individuals at risk for psychosis. *J. Abnorm. Psychol.* 127, 314–325. doi: 10.1037/abn0000330

Power, J. D., Barnes, K. A., Snyder, A. Z., Schlaggar, B. L., and Petersen, S. E. (2012). Spurious but systematic correlations in functional connectivity MRI networks arise from subject motion. *NeuroImage* 59, 2142–2154. doi: 10.1016/j.neuroimage.2011.10.018

Power, J. D., Barnes, K. A., Snyder, A. Z., Schlaggar, B. L., and Petersen, S. E. (2013). Steps toward optimizing motion artifact removal in functional connectivity MRI; a reply to Carp. *NeuroImage* 76, 439–441. doi: 10.1016/j.neuroimage.2012.03.017

Rashid, B., Arbabshirani, M. R., Damaraju, E., Cetin, M. S., Miller, R., Pearlson, G. D., et al. (2016). Classification of schizophrenia and bipolar patients using static and dynamic resting-state fMRI brain connectivity. *NeuroImage* 134, 645–657. doi: 10.1016/j.neuroimage.2016.04.051

Rashid, B., Damaraju, E., Pearlson, G. D., and Calhoun, V. D. (2014). Dynamic connectivity states estimated from resting fMRI identify differences among schizophrenia, bipolar disorder, and healthy control subjects. *Front. Hum. Neurosci.* 8:897. doi: 10.3389/fnhum.2014.00897

Sala-Llonch, R., Arenaza-Urquijo, E. M., Valls-Pedret, C., Vidal-Piñeiro, D., Bargalló, N., Junqué, C., et al. (2012). Dynamic functional reorganizations and relationship with working memory performance in healthy aging. *Front. Hum. Neurosci.* 6:152. doi: 10.3389/fnhum.2012.00152

Stevens, M. C. (2016). The contributions of resting state and task-based functional connectivity studies to our understanding of adolescent brain network maturation. *Neurosci. Biobehav. Rev.* 70, 13–32. doi: 10.1016/j.neubiorev.2016.07.027

Tian, L., Li, Q., Wang, C., and Yu, J. (2018). Changes in dynamic functional connections with aging. *NeuroImage* 172, 31–39. doi: 10.1016/j.neuroimage.2018.01.040

Uddin, L. Q., Supekar, K. S., Ryali, S., and Menon, V. (2011). Dynamic reconfiguration of structural and functional connectivity across core neurocognitive brain networks with development. *J. Neurosci.* 31, 18578–18589. doi: 10.1523/jneurosci.4465-11.2011

Van Essen, D. C., Smith, S. M., Barch, D. M., Behrens, T. E., Yacoub, E., Ugurbil, K., et al. (2013). The WU-Minn human connectome project: an overview. *NeuroImage* 80, 62–79. doi: 10.1016/j.neuroimage.2013.05.041

Walhovd, K. B., Westlye, L. T., Amlien, I., Espeseth, T., Reinvang, I., Raz, N., et al. (2011). Consistent neuroanatomical age-related volume differences across multiple samples. *Neurobiol. Aging* 32, 916–932. doi: 10.1016/j.neurobiolaging.2009.05.013

Whitfield-Gabrieli, S., and Nieto-Castanon, A. (2012). Conn: a functional connectivity toolbox for correlated and anticorrelated brain networks. *Brain Connect.* 2, 125–141. doi: 10.1089/brain.2012.0073

Yeo, B. T., Krienen, F. M., Sepulcre, J., Sabuncu, M. R., Lashkari, D., Hollinshead, M., et al. (2011). The organization of the human cerebral cortex estimated by intrinsic functional connectivity. *J. Neurophysiol.* 106, 1125–1165. doi: 10.1152/jn.00338.2011

Zhang, C., Dougherty, C. C., Baum, S. A., White, T., and Michael, A. M. (2018). Functional connectivity predicts gender: evidence for gender differences in resting brain connectivity. *Hum. Brain Mapp.* 39, 1765–1776. doi: 10.1002/hbm.23950

Conflict of Interest: The authors declare that the research was conducted in the absence of any commercial or financial relationships that could be construed as a potential conflict of interest.

Copyright © 2020 Rosenberg, Mennigen, Monti and Kaiser. This is an open-access article distributed under the terms of the Creative Commons Attribution License (CC BY). The use, distribution or reproduction in other forums is permitted, provided the original author(s) and the copyright owner(s) are credited and that the original publication in this journal is cited, in accordance with accepted academic practice. No use, distribution or reproduction is permitted which does not comply with these terms.

frontiers in Neuroscience

ORIGINAL RESEARCH
published: 15 December 2020
doi: 10.3389/fnins.2020.562830

Preliminary Study of Subclinical Brain Alterations in Patients With Asymptomatic Carotid Vulnerable Plaques Using Intravoxel Incoherent Motion Imaging by Voxelwise Comparison: A Study of Whole-Brain Imaging Measures

Jiuqing Guo[1†], Lirong OuYang[1†], Xiaoyi Wang[1], Weihua Liao[1], Qing Huang[2], Wei He[2], Gaofeng Zhou[1] and Shuai Yang[1]*

[1] Department of Radiology, Xiangya Hospital, Central South University, Changsha, China, [2] Department of Neurology, Xiangya Hospital, Central South University, Changsha, China

Objective: To preliminarily explore subclinical brain alterations in an asymptomatic carotid vulnerable plaque group based on intravoxel incoherent motion (IVIM) imaging through voxelwise comparison in the whole brain.

Materials and Methods: Forty-nine elderly participants underwent multi-*b*-value DWI, of whom 24 participants with asymptomatic carotid vulnerable plaques and <50% stenosis served as the test group, while the rest served as the healthy control group. After fitting the double-exponential model, slow ADC (Ds) and the fraction of fast ADC (*f*) values of the whole brain were obtained, which then were compared in a voxelwise manner by two-sample *t*-test. Multiple comparisons were corrected by the family-wise error (FWE) method with a corrected threshold of $P < 0.05$. Pearson correlations between IVIM parameters in altered brain regions and blood pressure, glucose, lipid, and homocysteine were calculated.

Results: For the test group, the *Z*-normalized Ds values were significantly higher in the left median cingulate and paracingulate gyrus (DCG.L), posterior cingulate gyrus (PCG. L), and left precuneus gyrus (PCUN.L) (cluster size = 156) and in the left middle frontal gyrus (MFG.L), orbital middle frontal gyrus (ORBmid.L), and superior frontal gyrus (SFG.L) (cluster size = 165); the *Z*-normalized Ds values were significantly lower in the right middle temporal gyrus (MTG.R) and inferior temporal gyrus (ITG.R) (cluster size = 116); and the *Z*-normalized *f*-values were significantly lower in the MTG.R and ITG.R (cluster size = 85) ($p < 0.05$, FWE correction). LDL-C was negatively correlated with the *Z*-normalized Ds values in the DCG.L, PCG.L, and PCUN.L ($r = 0.601$, $p = 0.002$). LDL-C was positively correlated with the *Z*-normalized *f*-value in the MTG.R and ITG.R ($r = 0.405$, $p = 0.05$). Systolic blood pressure was positively correlated with the *Z*-normalized Ds values in the MFG.L, ORBmid.L, and SFG.L ($r = 0.433$, $p = 0.035$).

OPEN ACCESS

Edited by:
Miguel Castelo-Branco, Coimbra Institute for Biomedical Imaging and Translational Research (CIBIT), Portugal

Reviewed by:
Muge Karaman, University of Illinois at Chicago, United States
Zhigang Qi, Capital Medical University, China
Qi Yang, Capital Medical University, China

****Correspondence:***
Shuai Yang
148101032@csu.edu.cn

† These authors have contributed equally to this work and share first authorship

Specialty section:
This article was submitted to Brain Imaging Methods, a section of the journal Frontiers in Neuroscience

Received: *16 May 2020*
Accepted: *16 November 2020*
Published: *15 December 2020*

Citation:
Guo JQ, OuYang LR, Wang XY, Liao WH, Huang Q, He W, Zhou GF and Yang S (2020) Preliminary Study of Subclinical Brain Alterations in Patients With Asymptomatic Carotid Vulnerable Plaques Using Intravoxel Incoherent Motion Imaging by Voxelwise Comparison: A Study of Whole-Brain Imaging Measures. Front. Neurosci. 14:562830. doi: 10.3389/fnins.2020.562830

Conclusion: This study was the first to detect subclinical brain alterations in asymptomatic carotid vulnerable plaque group through IVIM using whole-brain voxelwise comparisons, which were partially correlated with blood pressure and lipids. Thus, IVIM might be utilized as a noninvasive biomarker of microvascular and microstructural brain changes in the asymptomatic carotid vulnerable plaque group.

Keywords: multi-*b*-value DWI, double-exponential model, carotid artery, vulnerable plaque, intravoxel incoherent motion imaging

INTRODUCTION

Asymptomatic carotid artery stenosis is common in the general population; its prevalence is 6% in elderly male people and 4.4% in elderly female people (de Weerd et al., 2010). Patients with asymptomatic carotid artery stenosis without recent neurological symptoms have an increased risk of ischemic stroke, especially in the ipsilateral carotid artery region (Halliday et al., 2010). Carotid endarterectomy has a much lower efficiency in reducing the risk of stroke in asymptomatic patients than in symptomatic patients (Halliday et al., 2004). This difference in absolute risk reduction after carotid endarterectomy suggests the importance of plaque vulnerability, except for plaque size and lumen occlusion. Several clinical studies showed that in addition to the degree of carotid artery stenosis, the thickness of the carotid intima-media and the size of the hypoechoic area in plaques reflect the vulnerability of carotid plaques, which is closely associated with the occurrence of cerebral infarction (Moroni et al., 2016). Carotid plaques are associated with white matter lesions and resting infarction. Although no causal correlation has been identified from his association, the existence of carotid plaques may be regarded as an important risk factor for subclinical brain injury (Moroni et al., 2016).

Although some studies have shown that carotid plaques are related to changes in cerebral diffusion or perfusion (Gao et al., 2009; Rowe Bijanki et al., 2013; Moroni et al., 2016; Liu et al., 2020), few studies have combined diffusion and perfusion in the same patient. Diffusion-weighted imaging (DWI) is a functional magnetic resonance imaging (MRI) technique that can assess the microscopic motion of water protons in tissues. The apparent diffusion coefficient (ADC) can quantitatively reflect the diffusivity. The monoexponential model is widely used in DWI. Some researchers have found that with an increase in the *b*-value, the signal of DWI is no longer linear but shows double exponential characteristics (Kwee et al., 2010). To obtain information on perfusion, another functional MRI technique, called intravoxel incoherent motion (IVIM), can supply information about both tissue diffusion and perfusion components. IVIM uses multiple *b*-values and a biexponential signal model to enable quantitative parameters that can separately reflect tissue microcapillary perfusion and tissue microstructure and could potentially provide a noninvasive tool for monitoring tissue microvascular growth and degeneration (Finkenstaedt et al., 2017). The IVIM model ascribes the signal attenuation in diffusion-weighted images to two main components: a slow component that is due to water self-diffusion, i.e., the transport of water molecules within tissue as a result of random molecular movements, and a fast component that is due to the flow of water molecules in segments of the capillary network (Le Bihan et al., 1986, 1988). In the brain, the IVIM model has been used to quantify changes in perfusion or diffusion in the presence of disease, such as tumors and acute stroke (Iima and Bihan, 2016; Keil et al., 2017). However, there is a lack of study on diffusion functional MRI based on IVIM compared to classic functional MRI, such as resting-state fMRI, diffusion tensor imaging (DTI), and artery spin labeling (ASL).

Carotid vulnerable plaques may be considered a marker of higher ischemic or cognitive vulnerability of the brain, which may allow clinicians to identify subjects at risk of stroke and cognitive impairments and prompt an aggressive correction of cardiovascular risk factors, eventually including the initiation of treatment. This study aimed to investigate subclinical brain alterations in patients with asymptomatic carotid vulnerable plaques using biexponential model parameters [slow ADC (Ds) and fraction of fast ADC (f)] through voxelwise comparison in the whole brain and to determine whether IVIM reflects subclinical brain alterations at an early stage in patients with asymptomatic carotid vulnerable plaques.

MATERIALS AND METHODS

This prospective observational study was approved by the ethical standards committee on human experimentation at Central South University (CSU), and all patients signed written informed consent. This study was a part of the National Health Commission's stroke screening and prevention program.

Study Participants

The study recruited 1,054 volunteers from the Wujialing community in Changsha city, Hunan Province, China, from December 2015 to June 2018. Demographic information and stroke risk factors (including age, sex, race, education, alcohol intake, smoking, obesity, family history, past history, blood pressure, and lifestyle) were recorded using questionnaires. The inclusion criteria were as follows: (1) between 40 and 75 years old; (2) Chinese Han population; (3) right-handed; (4) no cardiac or neurological diseases; (5) no history of psychiatric disease or severe emotional trauma; (6) no evidence of cardiac emboli; (7) no alcohol or drug dependence; and (8) no history of carotid endarterectomy or carotid stunting. Volunteers with

atrial fibrillation, cardiovascular disease, neurologic disease, psychosis, psychological trauma, cardiogenic embolism, or alcohol or drug dependence were excluded. Then,753 volunteers underwent carotid ultrasound. Volunteers with >50% carotid stenosis, subclavian artery plaques or vertebral artery plaques, calcific plaques with hyperecho, and mixed plaques with both calcific plaques and soft plaques were excluded. Volunteers without contraindications for MRI, without severe liver and kidney diseases, who were not pregnant, and who provided consent to join the study underwent brain MRI, including routine MRI and multi-*b*-value DWI. Three patients with arachnoid cysts and seven patients with motion artifacts were excluded. Abnormalities were absent or the Fazekas scale was less than two based on routine MRIs of the remaining volunteers. After screening based on the inclusion and exclusion criteria, a total of 49 participants were ultimately recruited and entered the final analysis. The flowchart is shown in **Figure 1**.

Blood Collection

Fasting venous blood was collected from an elbow vein. Blood glucose, total cholesterol, triglycerides, high-density lipoprotein cholesterol (HDL-C), low-density lipoprotein cholesterol (LDL-C), and homocysteine (Hcy) were measured by the Department of Laboratory Medicine, Xiangya Hospital, Center South University. Blood pressure (systolic and diastolic blood pressure) was recorded.

Carotid Ultrasound Acquisition and Analysis

The presence of plaques in the same region of the left and right sides of the common carotid artery [common carotid arteries (CCAs)] and bifurcation was detected by ultrasound. Carotid ultrasound was performed by a sonographer using a Philips 5-MHz Sector Array transducer (IU22, Philips Ultrasound, Bothell, WA, United States). All measurements were obtained using the grayscale median (GSM) (Elatrozy et al., 1998). The plaques were divided into three types: hypoechoic, isoechoic, or hyperechoic. The plaques were hypoechoic or isoechoic, the plaque echo was mixed, and the plaque surface was irregular or ulcerated, which is the standard for the definition of vulnerable plaques identified by color Doppler ultrasound of the carotid artery (Gray-Weale et al., 1988; Elatrozy et al., 1998). Among the 49 participants, 24 with asymptomatic carotid vulnerable plaques but <50% carotid artery stenosis were included in the test group; among these patients, 11 had left carotid vulnerable plaques, 10 had right carotid vulnerable plaques, and three had bilateral carotid vulnerable plaques. Twenty-five participants without carotid vulnerable plaques were used as the control group (see flowchart, **Figure 1**).

IVIM-MRI Imaging Acquisition

Images were acquired on a 3-T MRI scanner (Signa HDx; General Electric Healthcare, Milwaukee, WI, United States) with an eight-channel head coil. The MRI sequences included 3D T1-weighted imaging, T2-weighted imaging, T2-weighted fluid attenuated inversion recovery imaging (T2/FLAIR), and multi-*b*-value DWI. Structural images were acquired using an axial 3D brain volume imaging (3D-BRAVO) sequence. The parameters were as follows: voxel size = 1 × 1 × 1 mm^3; section thickness = 1 mm; repetition time (TR) = 8 ms, echo time (TE) = 3 ms; inversion time (TI) = 800 ms; flip angle = 7°; and field of view (FOV) = 256 × 256 mm^2. The IVIM DWI was performed with a single-shot diffusion-weighted spin-echo echo-planar sequence using 20 different *b*-values: *b* = 0, 10, 30, 50, 80, 100, 120, 150, 200, 300, 500, 800, 1000, 1300, 1500, 1800, 2400, 3000, 3600, and 4500 s/mm^2. The following MR imaging parameters were used: TR = 5600 ms; TE = 105 ms; imaging matrices = 256 × 256; slice thickness = 4 mm; axial slices = 28; gap = 5 mm; and two excitations.

Image Analysis

All data for processing were transferred to a workstation (Advantage Windows Workstation 4.4; GE Healthcare) to produce the IVIM parameters (Ds, f with a two-segment mono-exponential fitting with a *b*-value threshold of 200 s/mm^2 separating the diffusion and perfusion effects, using all *b*-values in the following equation: $s(b)/s0 = fe^{-b*Df} + (1 - f)e^{-b*Ds}$). Maps of the Ds, *f*, and Df values were obtained (**Figure 2**); however, based on the study of Wen-Chau Wu et al. (2015), who stated that D*-Df in this study-has limited robustness and should be interpreted with caution, Df analysis was not conducted in this study. Five circular regions of interest (ROIs) in five locations of the ipsilateral cerebral hemisphere of carotid vulnerable plaques-ACA territory, MCA territory, PCA territory, anterior limb of internal capsule, and posterior limb of internal capsule-were delineated by an experienced radiologist (with 5 years of experience in neuroimaging), and the same was performed in the opposite hemisphere to obtain the Ds values and *f*-values. The ROIs were values less than the analyzed anatomical structure size and were limited to 20–40 pixels, avoiding blood vessels and cerebrospinal fluid. The ROIs were delineated again with approximately the same size after 30 days by the same radiologist.

Data preprocessing was performed using SPM12 (Statistical Parametric Mapping, Wellcome Trust Center for Neuroimaging,[1]) in MATLAB 2013b (MathWorks, Natick, MA, United States). First, we coregistered the 3D T1 images and the parametric maps (Ds maps and *f* maps) to the first b0-volume. Second, for each subject, the transformation matrix was calculated by nonlinear registration of the coregistered 3D T1 images to the tissue probability maps in the Montreal Neurological Institute (MNI) space and then applied to normalize the parametric maps into the MNI space. Third, the normalized parametric maps were standardized using the *z*-standardization method (De Luca et al., 2019). The method was as follows: (1) calculate the global mean and standard deviation across voxels for the parametric map; (2) subtract the global mean from the value in each voxel and

[1]http://www.fil.ion.ucl.ac.uk/spm/software/spm12/

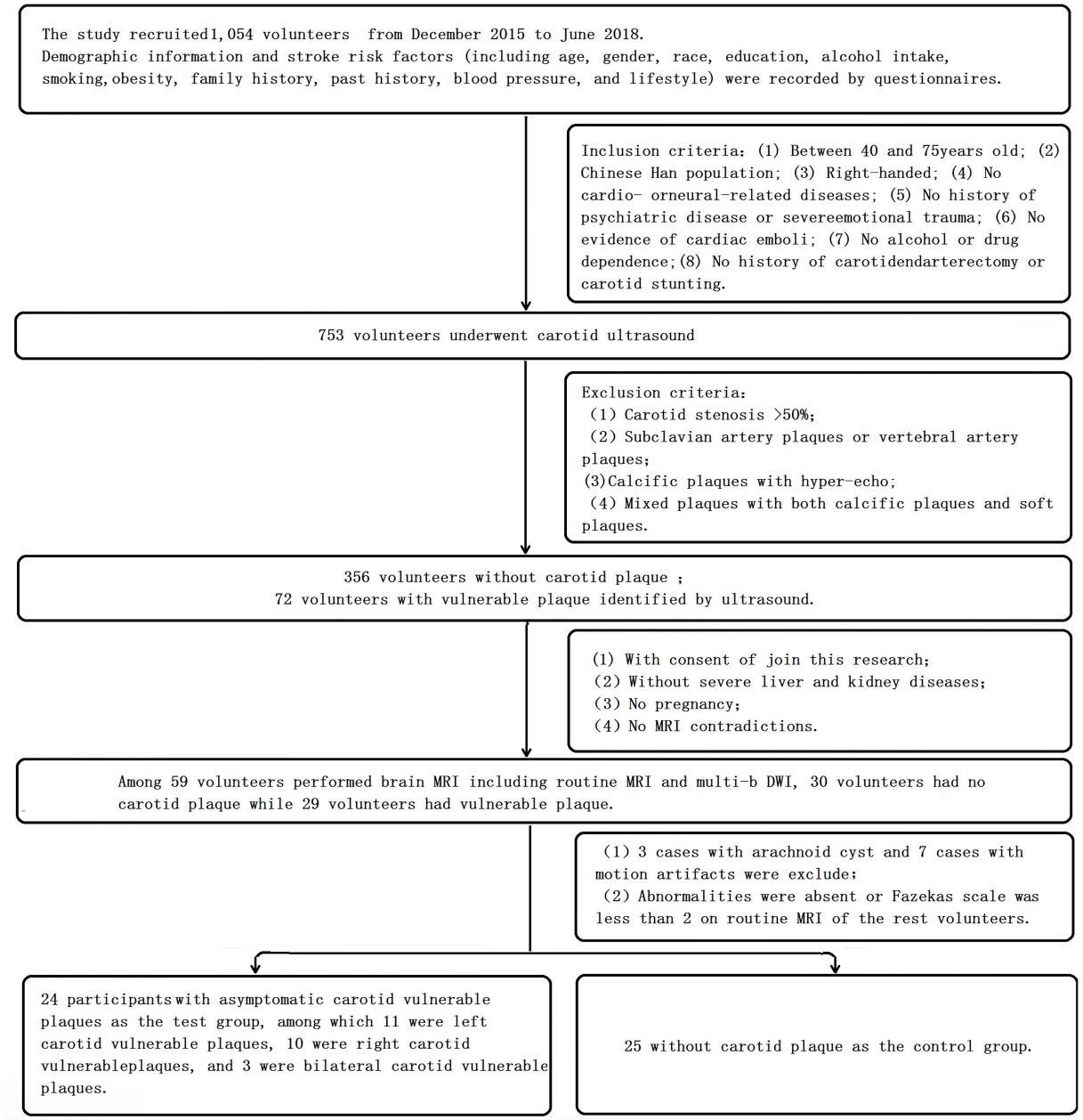

FIGURE 1 | Flowchart.

divide the value in each voxel by the standard deviation. Finally, the standardized parametric maps were spatially smoothed with a Gaussian kernel of 8 mm × 8 mm × 8 mm FWHM. The main data preprocessing workflow is shown in **Figure 3**.

Statistical Analysis

Statistical analysis was performed using the SPSS 23.0 statistical package (SPSS Version 23.0; IBM, Armonk, NY, United States). The measurement data are presented as the mean ± standard deviation (SD), and the enumeration data are presented as a proportion (%). The independent sample *t*-test or Wilcoxon rank sum test was used for comparison of measurement data between groups, and the chi-square test or Fisher's test was used for comparison of enumeration data between groups. The ROI was measured twice at different times by the same radiologist. Interobserver agreement was assessed using the interclass correlation coefficient (ICC). A paired, two-tailed *t*-test was used to assess the Ds values and *f*-values of the cerebral region between the ipsilateral hemisphere of unilateral carotid vulnerable plaques and the contralateral hemisphere. Two-sample *t*-tests were used to assess whole-brain

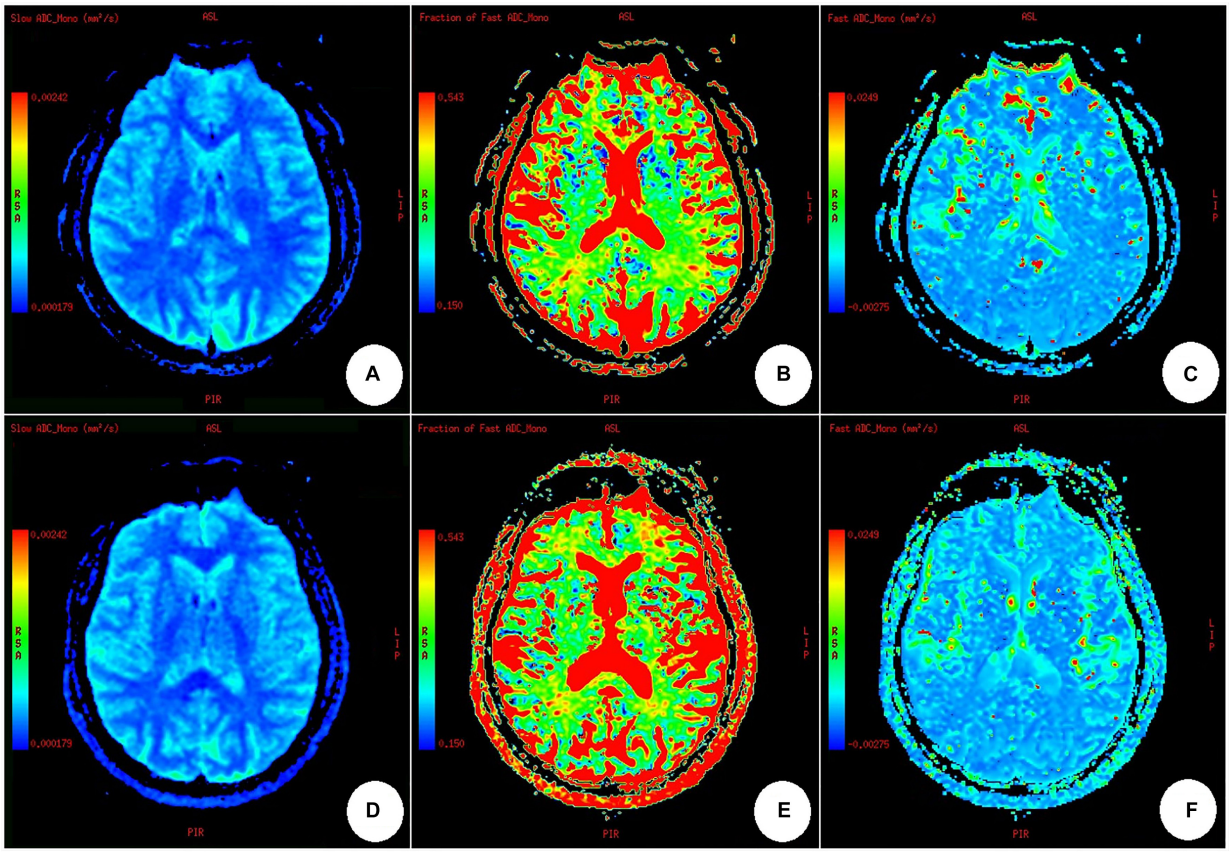

FIGURE 2 | Maps of slow ADC (Ds), fraction of fast ADC (f), and fast ADC (Df) through IVIM fitting. **(A–C)** A healthy participant; **(D–F)** a participant with carotid vulnerable plaques. There was no difference among the IVIM parameters obtained from a healthy subject **(A–C)** and a participant with carotid artery plaques **(D–F)**, nor was there any difference between the bilateral cerebral hemispheres in **(A–F)**, by naked eye observation.

parameters using SPM12 software (cluster level $P < 0.05$, FWE correction) based on MATLAB 2013b, with age and sex as covariates. Pearson correlation was used to evaluate the relationship between the Ds values and f-values of the altered cerebral regions and systolic blood pressure, diastolic blood pressure, blood glucose, total cholesterol, triglycerides, HDL-C, LDL-c, and Hcy. $P < 0.05$ was considered to indicate statistical significance.

RESULTS

A total of 49 participants underwent MRI scans, 24 participants with asymptomatic carotid vulnerable plaques and 25 participants without carotid vulnerable plaques. The baseline characteristics of the patients with asymptomatic carotid vulnerable plaques and the controls are summarized in **Table 1**. The asymptomatic carotid vulnerable plaque and control groups did not significantly differ with respect to age, sex, hypertension, hyperlipidemia, diabetes mellitus, smoking, lack of exercise, body mass index (BMI), family history of stroke, systolic blood pressure, diastolic blood pressure, blood glucose, total cholesterol, triglycerides, HDL-C, LDL-C, or Hcy.

For 11 participants with left carotid vulnerable plaques and 10 participants with right carotid vulnerable plaques, the reproducibility of the size of ROIs and the first and second measurement of similar locations of ACA territory, MCA territory, PCA territory, anterior limb of internal capsule, and posterior limb of internal capsule were excellent, with ICC >0.8.

The Ds value and f-values of five locations of the brain (ACA territory, MCA territory, PCA territory, anterior limb of internal capsule, and posterior limb of internal capsule) between the ipsilateral hemisphere of unilateral carotid vulnerable plaques and the contralateral hemisphere were not significantly different ($P > 0.05$) (**Table 2**).

Based on whole-brain voxelwise comparison, for patients with carotid vulnerable plaques but <50% stenosis, the Z-normalized Ds values were significantly higher than those of the control subjects in the left median cingulate and paracingulate gyrus (DCG.L), posterior cingulate gyrus (PCG.L) and left precuneus gyrus (PCUN.L) (cluster size = 156), and in the left middle frontal gyrus (MFG.L), orbital middle frontal gyrus (ORBmid.L), and superior frontal gyrus (SFG.L) (cluster size = 165). The Z-normalized Ds values were significantly lower in the right middle temporal gyrus (MTG.R) and inferior temporal gyrus (ITG.R) (cluster size = 116), and the Z-normalized f-values were

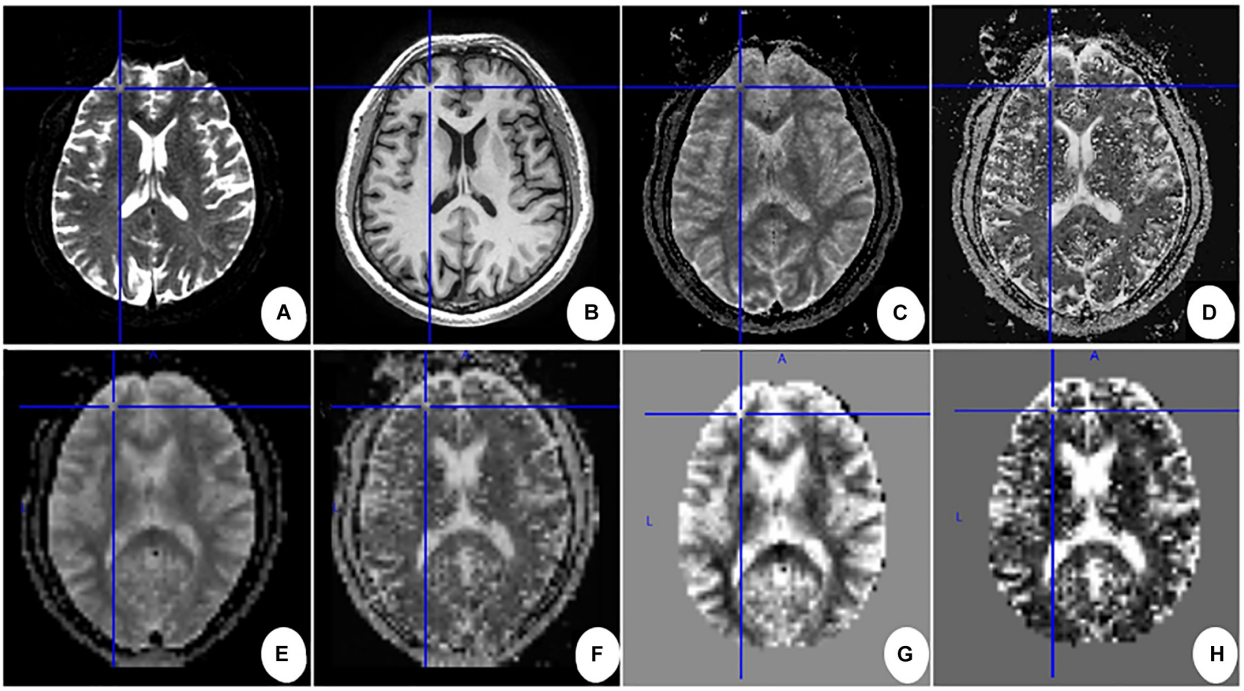

FIGURE 3 | Main data pre-processing work flow for one subject. **(A)** First b0-volume; **(B–D)** 3D T1 images, Ds maps, and *f* maps after being coregistered to the first b0-volume. **(E,F)** Ds maps and *f* maps in the MNI space after normalizing. **(G,H)** The *Z*-normalized Ds maps and *f* maps after removing the skull. Cross lines are shown to help comparison between images.

TABLE 1 | Baseline characteristics of patients with asymptomatic carotid vulnerable plaques and controls.

	Asymptomatic carotid vulnerable plaque group (*n* = 24)	Control group (*n* = 25)	*p*-value
Mean age (years)	62 ± 7	59 ± 7	0.263
Sex (male), *n* (%)	11 (45.8%)	11 (44.0%)	0.897
Hypertension, *n* (%)	12 (50.0%)	11 (44.0%)	0.674
Hyperlipemia, *n* (%)	8 (33.3%)	7 (28.0%)	0.686
Diabetes, *n* (%)	1 (4.2%)	3 (12.0%)	0.317
Smoking, *n* (%)	7 (29.2%)	8 (32.0%)	0.83
Lack of exercises, *n* (%)	7 (29.2%)	8 (32.0%)	0.83
BMI	26.23 ± 3.92	27.41 ± 3.52	0.57
Family history of stroke, *n* (%)	14 (58.3%)	15 (60.0%)	0.906
Systolic blood pressure (mmHg)	61.75 ± 7.37	59.48 ± 6.65	0.263
Diastolic blood pressure (mmHg)	140.42 ± 18.88	135.32 ± 14.22	0.29
Blood glucose (HbA1c)	86.75 ± 10.60	84.36 ± 11.17	0.446
Triglycerides	5.67 ± 1.06	5.82 ± 1.04	0.616
Total cholesterol	2.14 ± 1.18	2.02 ± 0.85	0.678
HDL-C	5.17 ± 1.19	5.76 ± 0.78	0.053
LDL-C	1.38 ± 0.52	1.41 ± 0.44	0.833
Hcy	3.54 ± 0.98	3.58 ± 0.68	0.876

Data are presented as the mean ± standard deviation. Body mass index (BMI), high-density lipoprotein cholesterol (HDL-C), low density lipoprotein cholesterol (LDL-c), homocysteine (Hcy).

significantly lower in the MTG.R and ITG.R (cluster size = 85) ($p < 0.05$, FWE correction) (**Figures 4–6**).

In the brain regions with altered *Z*-normalized Ds values or *Z*-normalized *f*-values, LDL-C was negatively correlated with the Ds values in the DCG.DCGL, PCG.L, and PCUN.L ($r = 0.601$, $p = 0.002$). LDL-C was positively correlated with the *f*-values in the MTG.R and ITG.R ($r = 0.405$, $p = 0.05$). Systolic blood pressure was positively correlated with the Ds values in the MFG.L, ORBmid.L, and SFG.L ($r = 0.433$, $p = 0.035$) (**Figures 7–9**).

TABLE 2 | Comparison between the corresponding side of the hemisphere and the contralateral hemisphere of 21 patients with unilateral carotid vulnerable plaques.

	Ipsilateral cerebral hemisphere of carotid vulnerable plaques	Contralateral cerebral hemisphere of carotid vulnerable plaques	*p*-value
Ds (mm^2/s)			
ACA territory	0.000465 ± 0.000063	0.000460 ± 0.000055	0.808
MCA territory	0.000511 ± 0.000047	0.000521 ± 0.000065	0.490
PCA territory	0.000441 ± 0.000053	0.000442 ± 0.000052	0.94
Anterior limb of internal capsule	0.000461 ± 0.000035	0.000451 ± 0.000031	0.289
Posterior limb of internal capsule	0.000338 ± 0.000043	0.000343 ± 0.000044	0.627
f			
ACA territory	0.432 ± 0.074	0.442 ± 0.080	0.634
MCA territory	0.449 ± 0.055	0.443 ± 0.079	0.809
PCA territory	0.372 ± 0.070	0.371 ± 0.058	0.947
Anterior limb of internal capsule	0.417 ± 0.063	0.441 ± 0.119	0.479
Posterior limb of internal capsule	0.428 ± 0.103	0.423 ± 0.075	0.821

Data are presented as the mean ± standard deviation. Anterior cerebral artery (ACA), middle cerebral artery (MCA), and posterior cerebral artery (PCA).

DISCUSSION

To the best of our knowledge, this is the first study to use IVIM combined with voxelwise comparisons based on a whole-brain spatial registration method to observe microcapillary perfusion and the brain microstructure in patients with carotid vulnerable plaques. We found that the cerebral regions with altered Ds values and *f* values in the carotid vulnerable plaque group were mostly related to cognition and emotion (e.g., the superior frontal gyrus, middle frontal gyrus, median cingulate and paracingulate gyrus, and posterior cingulate gyrus) and anoxia-sensitive regions (e.g., precuneus, middle temporal gyrus, and inferior temporal gyrus). Changes in microcapillary perfusion and the brain structure in patients with carotid vulnerable plaques showed no lateralization. Analysis of the blood and brain regions with altered Ds and *f* values showed that these parameters were partially related to LDL-C and systolic blood pressure, indicating the potential relationship between microvascular and microstructure alterations of the brain and vascular risk factors.

Previous studies have reported brain lateralization in whole-brain voxel-based morphometry (Gainotti, 2015). In the present study, first, the possible effect of the side with vulnerable plaques of carotid arteries was initially excluded because the stenosis of the carotid artery with unilateral plaques was less than 50%, which does not cause hemodynamic changes, and the circle of Willis could maintain cerebral hemodynamic stability (Liebeskind, 2003). Additionally, alterations in the *Z*-normalized Ds and *f* maps suggested that there was no lateralization in the changes in microcapillary perfusion and brain structure in patients with carotid vulnerable plaques.

Our study showed that the *Z*-normalized Ds values of the asymptomatic vulnerable carotid plaque group were significantly higher in the DCG.L, PCG.L, PCUN.L, MFG.L, ORBmid.L, and SFG.L at the cluster level. Ds is a diffusion coefficient, which represents the simple diffusion of water molecules. Possible reasons for an increase in Ds include decreased intracellular water content, increased cell membrane permeability, damage to the structural barrier, increased extracellular water ratio, widening of the extracellular space, and decreased limitation of water molecular activity, which represents damage to the microstructure of tissue.

Both the *Z*-normalized Ds and *Z*-normalized *f* values in the MTG.R and ITG.R of the asymptomatic vulnerable carotid plaque group were significantly lower than those of the control group at the cluster level. The decreased Ds values suggested that injury resulted in a decrease in extracellular water content, a decrease in cell membrane permeability, damage to the structural barrier, a decrease in the extracellular water ratio, a reduction in the extracellular space, and an increase in the water molecular activity, which reflected damage to tissue microstructures. The value of *f* represents the perfusion fraction, which indicates the proportion of related diffusion of microcirculatory perfusion in total diffusion of voxels and is related to blood volume. The decrease in the *f*-values suggested disorder of microperfusion in this region.

Alterations in the Ds values and *f*-values in the carotid vulnerable plaque group were mostly located in the regions related to cognition and emotion (e.g., SFG, MFG, DCG, and PCG) and anoxia-sensitive regions (e.g., PCUN, MTG, and ITG). Patients with carotid atherosclerosis with or without symptoms or increased carotid intima-media thickness often experience cognitive impairment and emotional symptoms (ESs) (Everts et al., 2014; Belem da Silva et al., 2019; Zhang et al., 2020). The SFG is thought to be involved in cognitive functions and emotion regulation-related processes, such as working memory and depression (Niendam et al., 2012), and low-frequency oscillation stimulation of the left SFG enhances working memory (Frank et al., 2014; Alagapan et al., 2019). It has been reported that perceived stress was positively correlated with fALFF in the left SFG and MFG, which play a partial mediating role in the relationship between perceived stress and depression (Wang et al., 2019). The DCG, PCG, and the precuneus are critical parts of the default mode network (DMN), which is related to cognition and emotion (Cavanna and Trimble, 2006; Leech and Sharp, 2014; Caruana et al., 2018). The ITG and MTG are associated

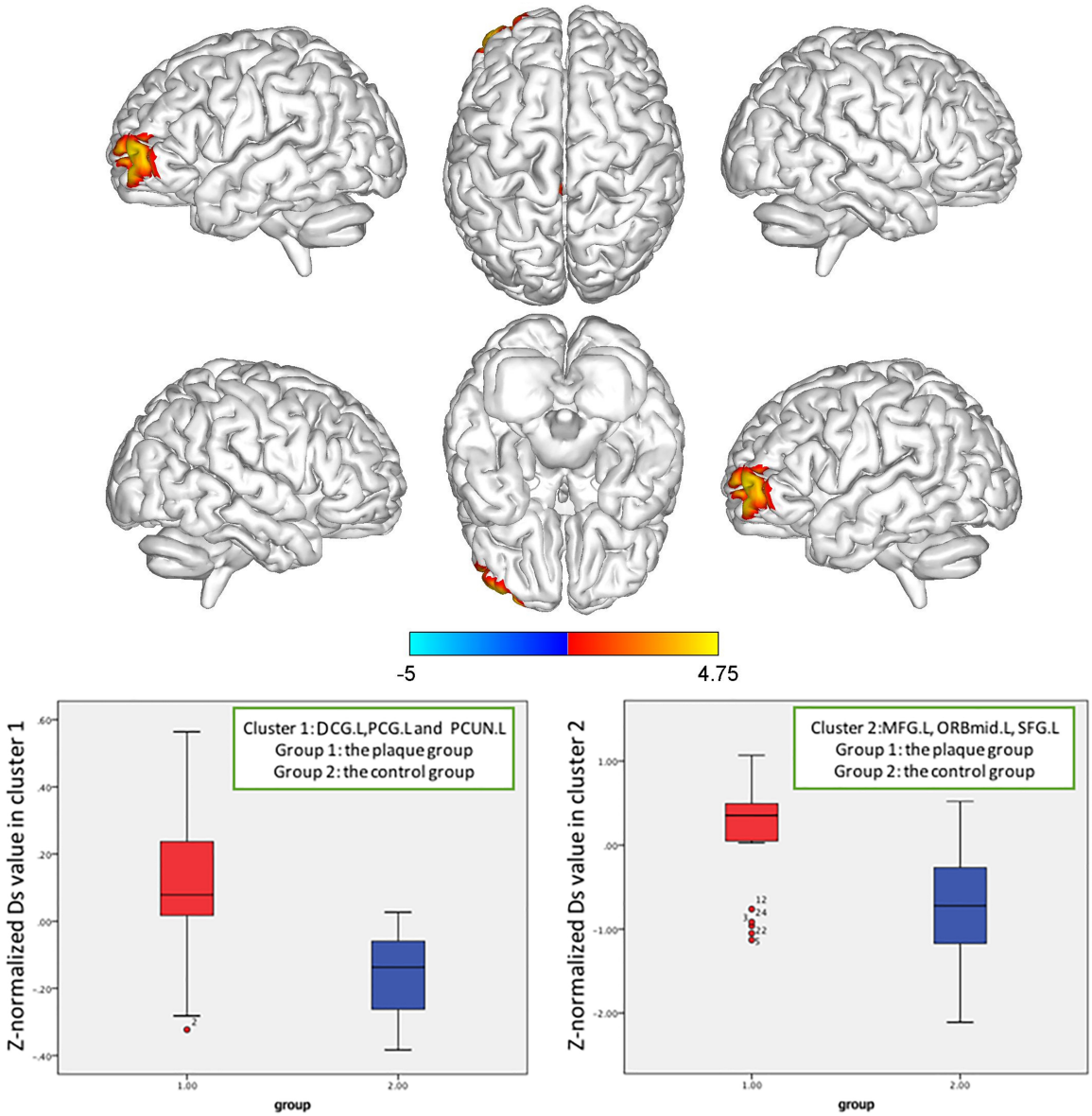

FIGURE 4 | *Z*-normalized Ds value alterations in the asymptomatic carotid vulnerable plaque group. Significantly increased Ds values in the left median cingulate and paracingulate gyrus (DCG.L), posterior cingulate gyrus (PCG.L) and left precuneus gyrus (PCUN.L) (cluster size = 156), left middle frontal gyrus (MFG.L), orbital middle frontal gyrus (ORBmid.L), and superior frontal gyrus (SFG.L) (cluster size = 165) ($p < 0.05$, FWE correction) compared to the control group.

with word comprehension-a cognitive process-in chronic post-stroke aphasia patients (Bonilha et al., 2017). A resting-state fMRI study showed synchronal abnormalities in the ITG and MTG of depressive patients who also have anxiety (Li et al., 2018). The ITG and MTG are also anoxia-sensitive regions, and hypoperfusion in the ITG and MTG was observed in amnestic mild cognitive impairment (aMCI), indicating impaired blood oxygen (Wang et al., 2020).

The Ds and f values in the altered brain areas were related to the LDL-C levels and systolic blood pressure. Smit et al. found that changes in the LDL-C levels were associated with lower cognitive impairment, reduced cerebral blood flow, and higher white matter hyperintensity in older people at different visits (Smit et al., 2016). LDL-C level and hypertension were associated with regional gray matter volume (GMV), and there was an interactive effect between low circulatory LDL-C level and hypertension (Chung et al., 2018). The explanation might be damage to the neurovascular unit (NVU), which causes neuronal degeneration and cognitive impairment (Zlokovic, 2011).

In the current study, alterations in the Ds and *f*-values were mainly distributed in the core brain areas of the combined cortex (e.g., the anterior cuneiform lobe, the superior frontal gyrus, and the middle frontal gyrus). This finding suggests that although there are no clinical symptoms in

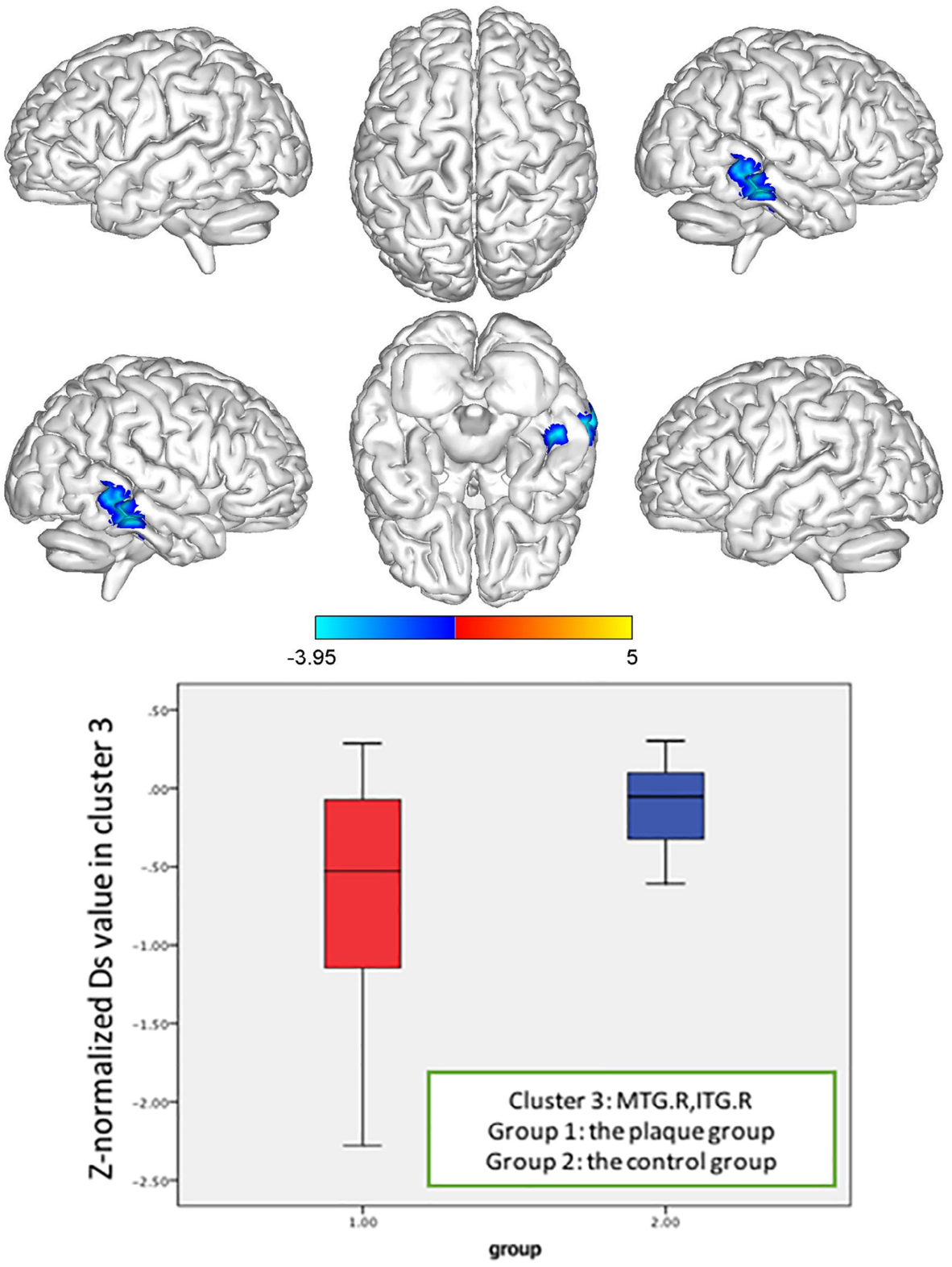

FIGURE 5 | *Z*-normalized Ds value alterations in the asymptomatic carotid vulnerable plaque group. Significantly decreased Ds values in the right middle temporal gyrus (MTG.R) and inferior temporal gyrus (ITG.R) (cluster size = 116) ($p < 0.05$, FWE correction) compared to the control group.

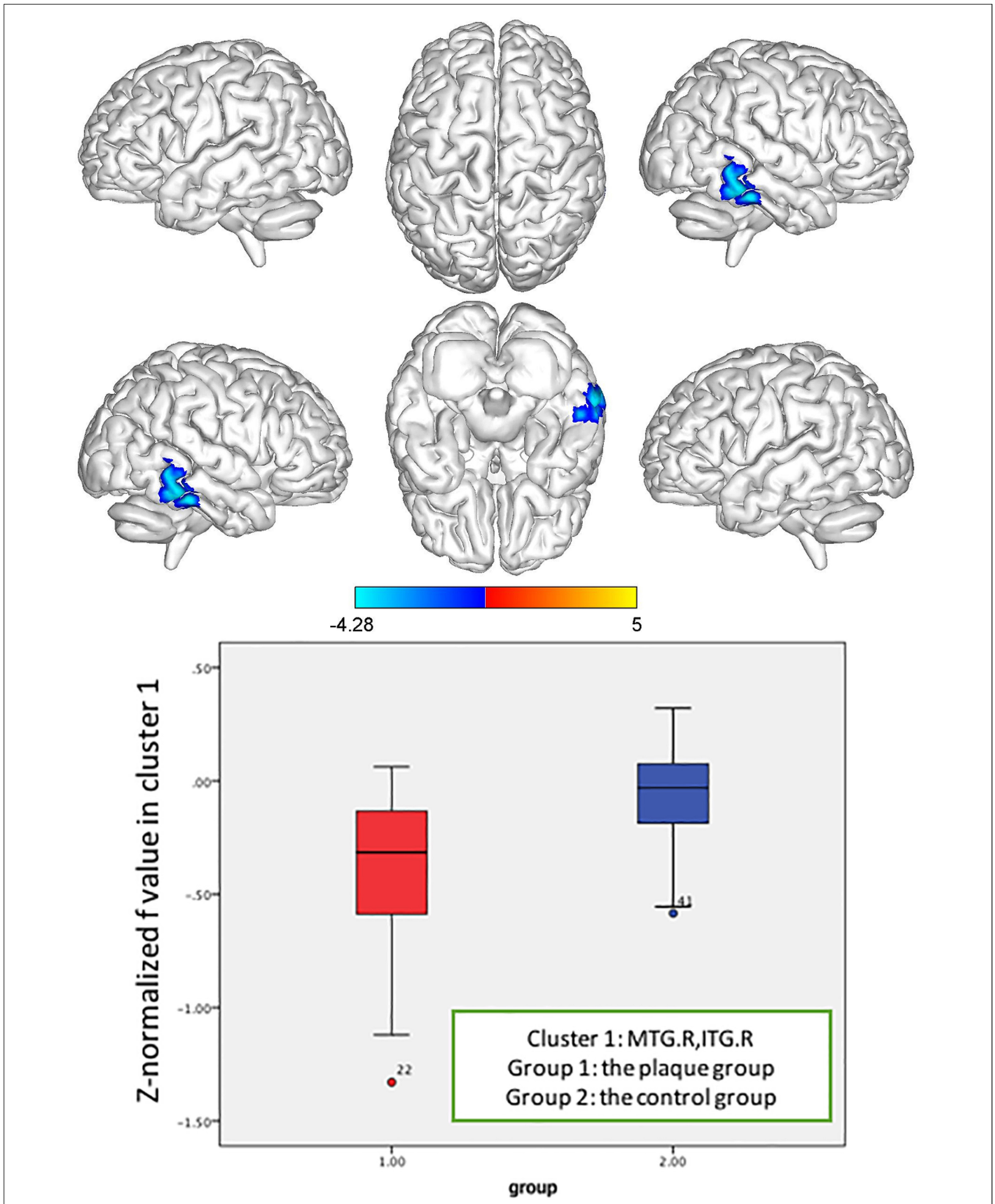

FIGURE 6 | *Z*-normalized *f* value alterations in the asymptomatic carotid vulnerable plaque group. Significantly decreased *f* values in the right middle temporal gyrus (MTG.R) and inferior temporal gyrus (ITG.R) (cluster size = 85) ($p < 0.05$, FWE correction) compared to the control group.

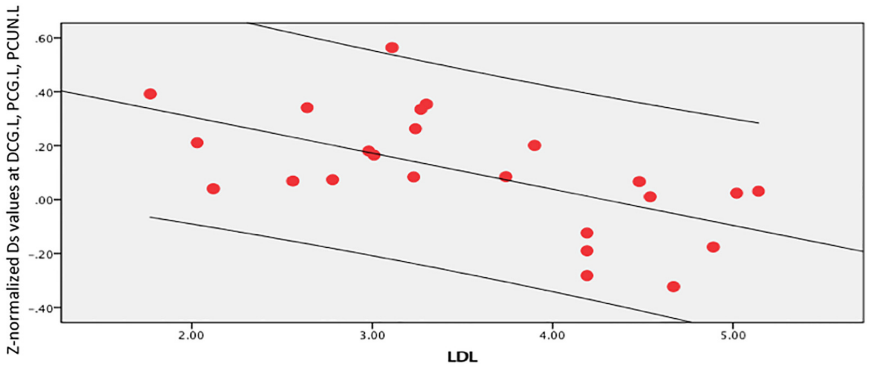

FIGURE 7 | LDL-C was negatively correlated with Ds values in the left median cingulate and paracingulate (DCG.L), posterior cingulate gyrus (PCG.L), and left precuneus gyrus (PCUN.L) (r = 0.601, p = 0.002).

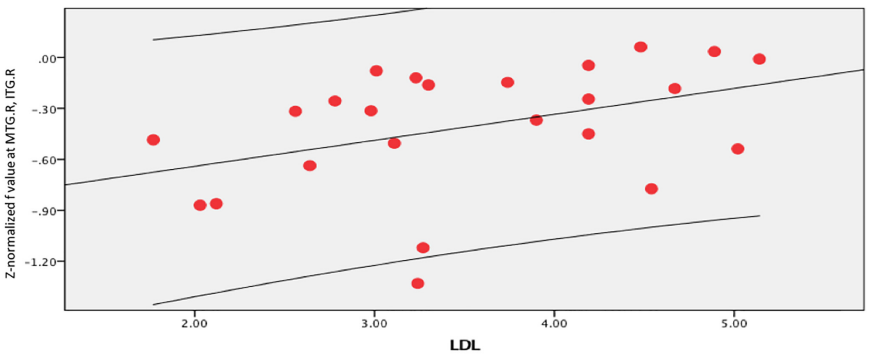

FIGURE 8 | LDL-C was positively correlated with f value in the right middle temporal gyrus (MTG.R) and inferior temporal gyrus (ITG.R) (r = 0.405, p = 0.05).

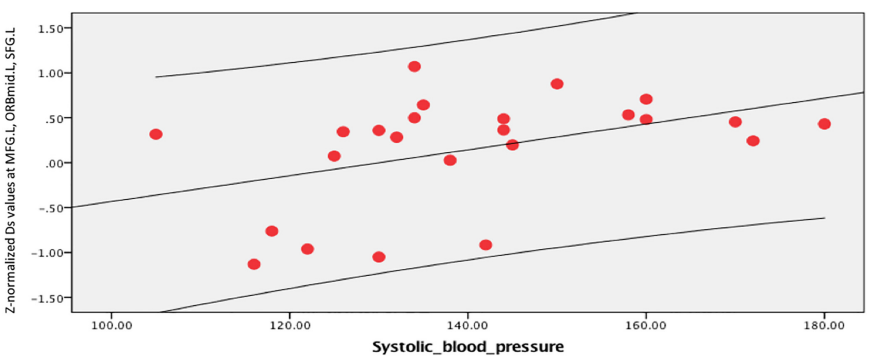

FIGURE 9 | Systolic blood pressure was positively correlated with Ds values in the left middle frontal gyrus (MFG.L), orbital middle frontal gyrus (ORBmid.L), and superior frontal gyrus (SFG.L) (r = 0.433, p = 0.035).

patients with asymptomatic carotid vulnerable plaques, the brain microstructure and microvessels changed at an early stage, and changes in the brain are complex and diffusive. Carotid atherosclerosis in asymptomatic populations was associated with brain structural changes and resting cerebral infarction (Romero et al., 2009; Cardenas et al., 2012). Increased carotid artery IMT and carotid stenosis ≥25% are related to a decrease in global brain volume, as well as white matter hyperintensity (Romero et al., 2009). These previous studies, together with this study, indicated that there was a relationship between asymptomatic carotid vulnerable plaques and subclinical brain injury, although the mechanism of this process is still unclear but may be explained by the following aspects. First, atherosclerosis is a systematic and complex pathological change that can occur simultaneously in multiple vessel beds, such as the carotid artery and cerebral artery (including microvessels) (Task Force Members et al., 2013;

Wong et al., 2017). Second, vulnerable carotid plaques are a source of brain microemboli (Halliday et al., 2010) and are among the most important causes of sudden onset cerebral infarction (Ueda et al., 2010). Finally, inflammation might play a mediating role (Drakopoulou et al., 2011). Inflammatory cells are thought to play important roles in the occurrence and development of atherosclerosis, which is a type of inflammatory disease caused by multiple factors. Inflammation is the physiological basis of cognitive impairment. IVIM parameters can reflect subclinical brain alterations in patients with asymptomatic carotid vulnerable plaques and provide an imaging basis for the early diagnosis of asymptomatic carotid vulnerable plaques. Whether these altered diffusion and perfusion indices can be used as biomarkers for early warning of fatal or disabling diseases (e.g., stroke or cerebral vascular dementia) and their sensitivity and specificity will be the focus of our next study.

This study does have limitations. First, our sample size was small, which may obscure some subtle neuroimaging findings. Nevertheless, our study may allow hypothesis generation for future large-scale multicenter studies to identify the specific changes in the brains of people with asymptomatic carotid vulnerable plaques. Second, this was a single-center study, which may limit its generalization to asymptomatic carotid vulnerable plaque patients outside our institution. Third, we were limited by the cross-sectional design of this study, which could not determine the causes underlying the findings. We were also limited by lack of longitudinal follow-up data for these patients; however, as we said above, this will be included in our subsequent work.

CONCLUSION

We suggest that IVIM should reflect subclinical brain alterations at an early stage in patients with asymptomatic carotid vulnerable plaques to a certain extent. Cerebral regions with altered IVIM parameters in the carotid vulnerable plaque group were mostly related to cognition and emotion, which could provide further insights into the potential association between carotid vulnerable plaques and cognition or emotion. IVIM might be utilized as a noninvasive biomarker of microvascular and microstructural changes in the brains of patients with asymptomatic carotid vulnerable plaques.

DATA AVAILABILITY STATEMENT

The raw data supporting the conclusions of this article will be made available by the authors, without undue reservation.

ETHICS STATEMENT

The studies involving human participants were reviewed and approved by the ethical standards committee on human experimentation at Central South University (CSU). The patients/participants provided their written informed consent to participate in this study.

AUTHOR CONTRIBUTIONS

SY conceived the study and was in charge of overall direction and planning. LO analyzed the data. JG drafted the manuscript in consultation with SY. XW, WL, QH, WH, and GZ discussed the results and commented on the manuscript. All authors contributed to the article and approved the submitted version.

FUNDING

This research is a part of the National Health Commission's stroke screening and prevention program.

ACKNOWLEDGMENTS

The authors would like to thank Jinbiao Chen (Department of Medical Record Management and Statistical Information Center, Xiangya Hospital) for his most helpful statistical support. The authors would like to thank Weiyin Vivian Liu (MR Rearch, GE Healthcare, Beijing, China) for her most helpful comments on technical support of this manuscript.

REFERENCES

Alagapan, S., Lustenberger, C., Hadar, E., Shin, H. W., and Frhlich, F. (2019). Low-frequency direct cortical stimulation of left superior frontal gyrus enhances working memory performance. *Neuroimage* 184, 697–706. doi: 10.1016/j.neuroimage.2018.09.064

Belem da Silva, C. T., Hoffmann, M. S., Sant Anna, R. T., Wehrmeister, F. C., Goncalves, H., Oliveira, I. O., et al. (2019). Early emotional symptoms predicting carotid atherosclerosis in youth: results from a birth cohort in Latin America. *J. Am. Heart Assoc.* 8:e011011. doi: 10.1161/JAHA.118.011011

Bonilha, L., Hillis, A. E., Hickok, G., den Ouden, D. B., Rorden, C., and Fridriksson, J. (2017). Temporal lobe networks supporting the comprehension of spoken words. *Brain* 140, 2370–2380. doi: 10.1093/brain/awx169

Cardenas, V. A., Reed, B., Chao, L. L., Chui, H., Sanossian, N., DeCarli, C. C., et al. (2012). Associations among vascular risk factors, carotid atherosclerosis, and cortical volume and thickness in older adults. *Stroke* 43, 2865–2870. doi: 10.1161/STROKEAHA.112.659722

Caruana, F., Gerbella, M., Avanzini, P., Gozzo, F., Pelliccia, V., Mai, R., et al. (2018). Motor and emotional behaviours elicited by electrical stimulation of the human cingulate cortex. *Brain* 141, 3035–3051. doi: 10.1093/brain/awy219

Cavanna, A. E., and Trimble, M. R. (2006). The precuneus: a review of its functional anatomy and behavioural correlates. *Brain* 129(Pt 3), 564–583. doi: 10.1093/brain/awl004

Chung, C. P., Chou, K. H., Peng, L. N., Liu, L. K., Lee, W. J., Chen, L. K., et al. (2018). Associations between low circulatory low-density lipoprotein cholesterol level and brain health in non-stroke non-demented subjects. *Neuroimage* 181, 627–634. doi: 10.1016/j.neuroimage.2018.07.049

De Luca, A., Schlaffke, L., Siero, J. C. W., Froeling, M., and Leemans, A. (2019). On the sensitivity of the diffusion MRI signal to brain activity in response to a motor cortex paradigm. *Hum. Brain Mapp.* 40, 5069–5082. doi: 10.1002/hbm.24758

de Weerd, M., Greving, J. P., Hedblad, B., Lorenz, M. W., Mathiesen, E. B., O'Leary, D. H., et al. (2010). Prevalence of Asymptomatic Carotid Artery Stenosis in the General Population: an individual participant data meta-analysis. *Stroke* 41, 1294–1297. doi: 10.1161/strokeaha.110.581058

Drakopoulou, M., Toutouzas, K., Michelongona, A., Tousoulis, D., and Stefanadis, C. (2011). Vulnerable plaque and inflammation:potential clinical strategies. *Curr. Pharm. Des.* 17, 4190–4209. doi: 10.2174/138161211798764816

Elatrozy, T., Nicolaides, A., Tegos, T., Zarka, A. Z., Griffin, M., and Sabetai, M. (1998). The effect of B-mode ultrasonic image standardisation on the echodensity of symptomatic and asymptomatic carotid bifurcation plaques. *Int. Angiol.* 17, 179–186.

Everts, R., Wapp, M., Burren, Y., Kellner-Weldon, F., El-Koussy, M., Jann, K., et al. (2014). Cognitive and emotional effects of carotid stenosis. *Swiss Med. Wkly.* 144:w13970. doi: 10.4414/smw.2014.13970

Finkenstaedt, T., Klarhoefer, M., Eberhardt, C., Becker, A. S., Andreisek, G., Boss, A., et al. (2017). The IVIM signal in the healthy cerebral gray matter: a play of spherical and non-spherical components. *NeuroImage* 152, 340–347. doi: 10.1016/j.neuroimage.2017.03.004

Frank, D. W., Dewitt, M., Hudgens-Haney, M., Schaeffer, D. J., Ball, B. H., Schwarz, N. F., et al. (2014). Emotion regulation: quantitative meta-analysis of functional activation and deactivation. *Neurosci. Biobehav. Rev.* 45, 202–211. doi: 10.1016/j.neubiorev.2014.06.010

Gainotti, G. (2015). The influence of handedness on hemispheric representation of tools: a survey. *Brain Cogn.* 94, 10–16. doi: 10.1016/j.bandc.2014.12.005

Gao, D. Y., Varcoe, R. L., Niesche, J. W., Lennox, A. R., Haindl, W., and Frawley, J. E. (2009). Association of carotid artery atheromatous plaque types with cerebral perfusion. *ANZ J. Surg.* 79, 824–828. doi: 10.1111/j.1445-2197.2009.05110.x

Gray-Weale, A. C., Graham, J. C., Burnett, J. R., Byrne, K., and Lusby, R. J. (1988). Carotid artery atheroma: comparison of preoperative B-mode ultrasound appearance with carotid endarterectomy specimen pathology. *J. Cardiovasc. Surg.* 29, 676–681.

Halliday, A., Harrison, M., Hayter, E., Kong, X., Mansfield, A., Marro, J., et al. (2010). 10-year stroke prevention after successful carotid endarterectomy for asymptomatic stenosis (ACST-1): a multicentre randomised trial. *Lancet* 376, 1074–1084. doi: 10.1016/S0140-6736(10)61197-X

Halliday, A., Mansfield, A., Marro, J., Peto, C., Potter, J., Thomas, D., et al. (2004). Prevention of disabling and fatal strokes by successful carotid endarterectomy in patients without recent neurological symptoms: randomised controlled trial. *Lancet* 363, 1491–1502. doi: 10.1016/s0140-6736(04)16146-1

Iima, M., and Bihan, D. L. (2016). Clinical intravoxel incoherent motion and diffusion MR imaging: past, present, and future. *Radiology* 278, 13–32. doi: 10.1148/radiol.2015150244

Keil, V. C., Mädler, B., Gielen, G. H., Pintea, B., Hiththetiya, K., Gaspranova, A. R., et al. (2017). Intravoxel incoherent motion MRI in the brain: impact of the fitting model on perfusion fraction and lesion differentiability. *J. Magn. Reson. Imaging* 46, 1187–1199. doi: 10.1002/jmri.25615

Kwee, T. C., Galbán, C. J., Tsien, C., Junck, L., Sundgren, P. C., Ivancevic, M. K., et al. (2010). Comparison of apparent diffusion coefficients and distributed diffusion coefficients in high-grade gliomas. *J. Magn. Reson. Imaging* 31, 531–537. doi: 10.1002/jmri.22070

Le Bihan, D., Breton, E., Lallemand, D., Aubin, M. L., Vignaud, J., and Laval-Jeantet, M. (1988). Separation of diffusion and perfusion in intravoxel incoherent motion MR imaging. *Radiology* 168, 497–505.

Le Bihan, D., Breton, E., Lallemand, D., Grenier, P., Cabanis, E., and Laval-Jeantet, M. (1986). MR imaging of intravoxel incoherent motions: application to diffusion and perfusion in neurologic disorders. *Radiology* 161, 401–407. doi: 10.1148/radiology.161.2.3763909

Leech, R., and Sharp, D. J. (2014). The role of the posterior cingulate cortex in cognition and disease. *Brain* 137(Pt 1), 12–32. doi: 10.1093/brain/awt162

Li, M., Xu, H., and Lu, S. (2018). Neural basis of depression related to a dominant right hemisphere a resting-state fMRI study. *Behav. Neurol.* 2018:5024520. doi: 10.1155/2018/5024520

Liebeskind, D. S. (2003). Collateral circulation. *Stroke* 34, 2279–2284. doi: 10.1161/01.STR.0000086465.41263.06

Liu, L., Huang, Q., Yang, S., Wen, Y., He, W., Liu, H., et al. (2020). Micro-structural white matter abnormalities and cognitive impairment in asymptomatic carotid plaque patients: a DTI study using TBSS analysis. *Clin. Neurol. Neurosurg.* 197:106096. doi: 10.1016/j.clineuro.2020.106096

Moroni, F., Ammirati, E., Magnoni, M., D'Ascenzo, F., Anselmino, M., Anzalone, N., et al. (2016). Carotid atherosclerosis, silent ischemic brain damage and brain atrophy: a systematic review and meta-analysis. *Int. J. Cardiol.* 223, 681–687. doi: 10.1016/j.ijcard.2016.08.234

Niendam, T. A., Laird, A. R., Ray, K. L., Dean, Y. M., Glahn, D. C., and Carter, C. S. (2012). Meta-analytic evidence for a superordinate cognitive control network subserving diverse executive functions. *Cogn. Affect. Behav. Neurosci.* 12, 241–268. doi: 10.3758/s13415-011-0083-5

Romero, J. R., Beiser, A., Seshadri, S., Benjamin, E. J., Polak, J. F., Vasan, R. S., et al. (2009). Carotid artery atherosclerosis, MRI indices of brain ischemia, aging, and cognitive impairment: the Framingham study. *Stroke* 40, 1590–1596. doi: 10.1161/STROKEAHA.108.535245

Rowe Bijanki, K., Arndt, S., Magnotta, V. A., Nopoulos, P., Paradiso, S., Matsui, J. T., et al. (2013). Characterizing white matter health and organization in atherosclerotic vascular disease: a diffusion tensor imaging study. *Psychiatry Res.* 214, 389–394. doi: 10.1016/j.pscychresns.2013.07.011

Smit, R. A., Trompet, S., Sabayan, B., le Cessie, S., van der Grond, J., van Buchem, M. A., et al. (2016). Higher visit-to-visit low-density lipoprotein cholesterol variability is associated with lower cognitive performance, lower cerebral blood flow, and greater white matter hyperintensity load in older subjects. *Circulation* 134, 212–221. doi: 10.1161/CIRCULATIONAHA.115.020627

Task Force Members, Montalescot, G., Sechtem, U., Achenbach, S., Andreotti, F., Arden, C., et al. (2013). 2013 ESC guidelines on the management of stable coronary artery disease: the task force on the management of stable coronary artery disease of the European society of cardiology. *Eur. Heart J.* 34, 2949–3003. doi: 10.1093/eurheartj/eht296

Ueda, Y., Miyati, T., Ohno, N., Motono, Y., Hara, M., Shibamoto, Y., et al. (2010). Apparent diffusion coefficient and fractional anisotropy in the vertebral bone marrow. *J. Magn. Reson. Imaging* 31, 632–635.

Wang, S., Zhao, Y., Zhang, L., Wang, X., Wang, X., Cheng, B., et al. (2019). Stress and the brain: perceived stress mediates the impact of the superior frontal gyrus spontaneous activity on depressive symptoms in late adolescence. *Hum. Brain Mapp.* 40, 4982–4993. doi: 10.1002/hbm.24752

Wang, X., Ding, D., Zhao, Q., Liang, X., Peng, L., Zhao, X., et al. (2020). Brain hemodynamic changes in amnestic mild cognitive impairment measured by pulsed arterial spin labeling. *Aging (Albany N. Y.)* 12, 4348–4356. doi: 10.18632/aging.102888

Wong, S. M., Zhang, C. E., Bussel, F. C. G. v, Staals, J., Jeukens, C. R. L. P. N., Hofman, P. A. M., et al. (2017). Simultaneous investigation of microvasculature and parenchyma in cerebral small vessel disease using intravoxel incoherent motion imaging. *Neuroimage Clin.* 14, 216–221. doi: 10.1016/j.nicl.2017.01.017

Wu, W.-C., Chen, Y.-F., Tseng, H.-M., Yang, S.-C., and My, P.-C. (2015). Caveat of measuring perfusion indexes using intravoxel incoherent motion magnetic resonance imaging in the human brain. *Eur. Radiol.* 25, 2485–2492. doi: 10.1007/s00330-015-3655-x

Zhang, J., Wang, Z., Zhou, M., Jia, J., Liu, Y., Wang, A., et al. (2020). Association between asymptomatic vulnerable carotid plaques and cognitive impairment in rural adults. *Front. Neurol.* 11:662. doi: 10.3389/fneur.2020.00662

Zlokovic, B. V. (2011). Neurovascular pathways to neurodegeneration in Alzheimer's disease and other disorders. *Nat. Rev. Neurosci.* 12, 723–738. doi: 10.1038/nrn3114

Conflict of Interest: The authors declare that the research was conducted in the absence of any commercial or financial relationships that could be construed as a potential conflict of interest.

Copyright © 2020 Guo, OuYang, Wang, Liao, Huang, He, Zhou and Yang. This is an open-access article distributed under the terms of the Creative Commons Attribution License (CC BY). The use, distribution or reproduction in other forums is permitted, provided the original author(s) and the copyright owner(s) are credited and that the original publication in this journal is cited, in accordance with accepted academic practice. No use, distribution or reproduction is permitted which does not comply with these terms.

frontiers in Neuroscience

REVIEW
published: 08 January 2021
doi: 10.3389/fnins.2020.578409

Unraveling the Nanoscopic Organization and Function of Central Mammalian Presynapses With Super-Resolution Microscopy

Lia G. Carvalhais[1,2,3†], Vera C. Martinho[1,2,3†], Elisabete Ferreiro[1,2,3] and Paulo S. Pinheiro[1,2,3]*

[1] Center for Neuroscience and Cell Biology, University of Coimbra, Coimbra, Portugal, [2] Center for Innovative Biomedicine and Biotechnology, University of Coimbra, Coimbra, Portugal, [3] Institute for Interdisciplinary Research, University of Coimbra, Coimbra, Portugal

OPEN ACCESS

Edited by:
Dong Song, University of Southern California, Los Angeles, United States

Reviewed by:
Daniel Choquet, Université Bordeaux Segalen, France
Arnav Bhavsar, Indian Institute of Technology Mandi, India

***Correspondence:**
Paulo S. Pinheiro
pinheiro@cnc.uc.pt

† These authors have contributed equally to this work

Specialty section:
This article was submitted to Brain Imaging Methods, a section of the journal Frontiers in Neuroscience

Received: *30 June 2020*
Accepted: *03 December 2020*
Published: *08 January 2021*

Citation:
Carvalhais LG, Martinho VC, Ferreiro E and Pinheiro PS (2021) Unraveling the Nanoscopic Organization and Function of Central Mammalian Presynapses With Super-Resolution Microscopy. Front. Neurosci. 14:578409. doi: 10.3389/fnins.2020.578409

The complex, nanoscopic scale of neuronal function, taking place at dendritic spines, axon terminals, and other minuscule structures, cannot be adequately resolved using standard, diffraction-limited imaging techniques. The last couple of decades saw a rapid evolution of imaging methods that overcome the diffraction limit imposed by Abbe's principle. These techniques, including structured illumination microscopy (SIM), stimulated emission depletion (STED), photo-activated localization microscopy (PALM), and stochastic optical reconstruction microscopy (STORM), among others, have revolutionized our understanding of synapse biology. By exploiting the stochastic nature of fluorophore light/dark states or non-linearities in the interaction of fluorophores with light, by using modified illumination strategies that limit the excitation area, these methods can achieve spatial resolutions down to just a few tens of nm or less. Here, we review how these advanced imaging techniques have contributed to unprecedented insight into the nanoscopic organization and function of mammalian neuronal presynapses, revealing new organizational principles or lending support to existing views, while raising many important new questions. We further discuss recent technical refinements and newly developed tools that will continue to expand our ability to delve deeper into how synaptic function is orchestrated at the nanoscopic level.

Keywords: super-resolution microscopy, presynaptic structure, active zone, vesicle exocytosis, neurotransmitter release

INTRODUCTION

Imaging in neurosciences has come a long way since 19th-century neuroanatomist Ramon y Cajal made detailed drawings of silver-stained neurons and postulated that they were not continuous, but instead connected through gaps. These would be known as synapses. Synapses were first visualized in detail in the 1950s (e.g., Palay, 1956) and are believed to be the sites where learning and memory are molecularly encoded (Mayford et al., 2012). Classical optical microscopy techniques have been paramount for our understanding of the structural and molecular organization of neurons. However, the more we learn about their intricate features, the more

the limitations of these techniques become apparent. While electron microscopy has provided exquisite structural details of membrane-limited or electron-dense synaptic structures, it cannot adequately resolve their crowded molecular composition or be used in live specimens and is technically demanding. Fluorescence microscopy, on the other hand, is a less demanding technique that can be used in live tissues and provides the ability to determine the abundance, cellular localization, interactions, and dynamics of specific molecules, by resorting to direct or antibody-mediated multi-color target labeling and simultaneous imaging (Lichtman and Conchello, 2005). However, as powerful as conventional fluorescence microscopy techniques have become, they are generally limited to a resolution of roughly half the excitation wavelength (a couple hundred nanometers) and are, therefore, unable to properly resolve the subcellular neuronal structures that most interest neurobiologists, notably synapses, subsynaptic compartments, and their underlying molecular complexes and nanodomains. Unraveling their detailed molecular composition and functional dynamics (for example, the trafficking of receptors or channels at the membrane or the changes in protein cluster number or size with synaptic activity) requires imaging at the nanoscale, using so-called super-resolution microscopy (SRM) techniques, that were developed to surpass the diffraction-limited resolution of conventional light microscopy while attempting to retain its versatility. Owing to the evolution of fluorophores and both hardware and software, many SRM techniques have been successfully and routinely used in biology for live-cell imaging (e.g., Godin et al., 2014) and applied to neurons.

Neurons are arguably the most compartmentalized cells in nature. At chemical synapses, neurotransmitters are released from presynaptic terminals in an extremely fast and precisely timed manner to activate neurotransmitter receptors on the postsynaptic neuron (Südhof, 2013). The entire process requires complex, spatially restricted, and often stoichiometrically defined interactions between specific sets of proteins (Patrizio and Specht, 2016) whose structural organization, dynamics, and expression levels are critical for the function of neuronal circuits (Emes and Grant, 2012). Electrophysiology techniques have been paramount to our understanding of synaptic function, since they provide unsurpassed temporal resolution for detecting the electrical changes produced by the activation of neurotransmitter receptors or ion channels, and have even allowed direct recordings from small presynaptic terminals (Novak et al., 2013). However, they don't provide any spatial or dynamic information regarding the molecular players involved in synaptic activity and plasticity, creating the need for correlative structural data. This is where SRM techniques provide unique advantages for studying synaptic function over diffraction-limited microscopy or fixed-sample-only electron microscopy. In the following sections, we begin with a brief description of the most common SRM techniques. We then review how SRM has shed light on the molecular complexity and structural features of presynaptic neuronal compartments of central mammalian synapses, and how protein distribution, nanoclustering, and dynamics shape neuronal signaling. We finish by presenting recent developments in SRM that will, undoubtedly, continue to revolutionize synapse biology. We apologize in advance for any omissions that may have been made due to space constraints or to our focus on central mammalian synapses.

BRIEF OVERVIEW OF SUPER-RESOLUTION IMAGING METHODS

Super-resolution fluorescence microscopy techniques can be broadly divided into two main categories: deterministic and stochastic. Deterministic SRM techniques are based on exploiting non-linear interactions of fluorophores with light, using patterned illumination, to limit the focal spot size. Among these techniques, we find structured illumination microscopy (SIM) and its variations, stimulated emission depletion (STED) and reversible saturable optical fluorescence transition (RESOLFT) microscopy. STED pioneered these techniques by combining an excitation laser beam with a second, donut-shaped, laser beam with a red-shifted emission wavelength (depletion or STED beam) with ideally zero intensity at the center ring. This second beam suppresses peripheral excitation by quenching excited fluorophores, thereby limiting fluorescence emission to its centermost part and allowing resolutions well below the diffraction limit (Klar and Hell, 1999; Klar et al., 2000). STED is versatile for imaging fast cellular events but can be costly to implement, and there is limited fluorophore choice due to the high laser intensities that are required. RESOLFT is based on a similar illumination principle but employing photoswitchable emitters (Hofmann et al., 2005), namely photostable reversibly photoswitchable fluorescent proteins. In SIM, the samples are illuminated with a grating pattern that shifts phase over several frames to produce a *moiré* pattern. The results of this pattern are processed and reconstructed into images with an approximately two-fold improvement in resolution (Gustafsson, 2000). SIM can be used with conventional dyes in multi-color imaging and yield high-speed acquisition frame rates for monitoring live cell dynamics (Kner et al., 2009; Lefman et al., 2011), but requires a dedicated microscope and substantial computation for image reconstruction. SIM is best suited to thin samples and the gain in resolution is smaller than with other techniques. However, non-linear SIM (NL-SIM), which uses a photoswitchable protein and low irradiation intensities, allows a resolution of 50 nm in biologically compatible imaging conditions (Rego et al., 2012). The higher resolutions achievable with STED and RESOLFT, which are based on laser scanning (as in confocal microscopy), come at the tradeoff of speed. However, parallelized acquisition strategies have allowed for much faster imaging rates (Chmyrov et al., 2013; Yang et al., 2014). STED also uses much higher laser intensities than RESOLFT (Hofmann et al., 2005; Willig et al., 2007), which can be a concern in long studies in living preparations and cause significant photobleaching and phototoxicity. To overcome these limitations, a new variation of 3D-STED, termed super-resolution shadow imaging (SUSHI), was recently developed (Tønnesen et al., 2018). SUSHI is based on imaging the extracellular space with diffusible dyes, thereby producing super-resolved negative images of all cellular

structures that can reveal the micro-anatomy of living brain tissue, including dendritic spines and the synaptic cleft. This technique holds great promise for the future study of the dynamic processes associated with development and with synaptic activity and plasticity. It is also insensitive to photobleaching and poses less phototoxicity concerns due to the extracellular labeling, allowing for prolonged imaging sessions on large fields of view.

Stochastic methods, on the other hand, are based on the precise localization of the emitting fluorophores by temporally separating the activation of individual molecules in successive rounds of frame acquisitions (hence, they are also referred to as single-molecule localization methods). These methods include photoactivatable localization microscopy (PALM), stochastic optical reconstruction microscopy (STORM), and universal point accumulation for imaging in nanoscale topography (uPAINT) and can achieve resolutions well below the diffraction limit. PALM and STORM use a somewhat similar principle to achieve their high resolution but, whereas the first was developed using photoactivatable, genetically encoded fluorescent proteins fused to the protein of interest (Betzig et al., 2006; Hess et al., 2006), the later used pairs of organic fluorophores linked to antibodies (Rust et al., 2006). In PALM, specific illumination wavelengths are used to stochastically activate only a small subset of molecules, which are imaged and returned to a dark state, and the process repeated over many photoswitching iterations. In STORM, fluorophores are driven into a dark state in the absence of oxygen, from which a small number stochastically recovers and is imaged, and the process is also repeated over many iterations. Though these images are still diffraction-limited, mathematically localizing the center of the sparse fluorescent spots generates coordinates for each molecule, with a pointing accuracy of detection dependent on the square root of the intensity of the collected signal. Over-accumulation of all the detections is then used to obtain a pointillistic representation of all individual positions across all acquired frames (Betzig et al., 2006; Hess et al., 2006; Rust et al., 2006). This yields a merged image that contains the high-resolution information from the processed frames. One of the main advantages of PALM lies in the simplicity of its implementation, requiring basic molecular manipulations for expression of photoactivatable proteins fused to the targets of interest, simple imaging systems with suitable lasers, and analysis software that can be found for free. However, both PALM and STORM usually require very large numbers of iterations to reconstruct a single image, making them rather slow (minutes to tens of minutes per complete acquisition). Additionally, fluorophore photostability is a concern and the methods are prone to artifacts due to the complex post-acquisition processing for image reconstruction. Conceptually similar to STORM, direct STORM (*d*STORM) was developed using conventional cyanine dyes that can efficiently and reversibly photoswitch between dark and fluorescent states. This provides a simpler method that does not require the presence of activator fluorophores and does not rely on specific ratios and distances between two fluorophores attached to antibodies (Heilemann et al., 2008). Many organic fluorophores can be made to photoswitch in the presence of reducing buffers and are suitable to use in *d*STORM (Endesfelder and Heilemann, 2014). Finally, uPAINT, developed as a variation of PAINT (Sharonov and Hochstrasser, 2006), is based on imaging the real-time stochastic interaction of a specific fluorophore-coupled ligand with its target molecule (Sharonov and Hochstrasser, 2006; Giannone et al., 2010, 2013) by continuously and stochastically labeling while imaging. When such interaction occurs, the diffusion of the fluorophore is reduced, making it more likely to be detected than unbound fluorophores under specific illumination and imaging conditions. uPAINT allows following the trajectories of many single molecules simultaneously and for extended periods of time, but is limited to membrane-localized molecules. More recent variations employ fluorophore-labeled DNA oligos that bind to their unlabeled complementary sequences (DNA-PAINT; Jungmann et al., 2014). The different SRM methods have been thoroughly reviewed elsewhere (e.g., Godin et al., 2014; Sydor et al., 2015; Wu and Shroff, 2018; Dietz and Heilemann, 2019; Huszka and Gijs, 2019; Schermelleh et al., 2019) and a detailed breakdown of the features, advantages, and disadvantages of each has been published while this manuscript was under writing (Jacquemet et al., 2020).

SUPER-RESOLUTION IMAGING OF THE PRESYNAPSE

Presynaptic active zones—the sites where neurotransmitters are released—are dynamic structures where molecular and functional changes are responsible for the regulation of neurotransmitter release and trigger several forms of short- and long-term synaptic plasticity (Choquet and Triller, 2013). Neurotransmitter release occurs with nanoscale and sub-millisecond precision and is orchestrated by the molecular interactions between a defined set of proteins forming the so-called SNARE complex, composed of Synaptosomal-Associated Protein, 25 KDa (SNAP25), synaptobrevin and syntaxin-1, and requires additional players such as Munc13, Munc18, complexins, and synaptotagmins acting as calcium sensors (Südhof, 2012). Exocytosis is then followed by the retrieval of proteins and membrane through endocytosis. At vertebrate central synapses, active zones are disk-like structures with a diameter of 200–500 nm; synaptic vesicles are only ∼40 nm in diameter and the protein complexes driving their fusion are smaller still. An elegant study, combining quantitative proteomics, STED microscopy at ∼40 nm resolution and 3D modeling, reconstructed the "average" presynaptic bouton as a structure of 0.37 μm^3 containing approximately 380 vesicles and an astonishing 300,000 densely packed proteins that were modeled in atomic detail according to their known structures (with copy numbers ranging from a few tens to over 20,000), and distributed according to SRM imaging data (**Figure 1**) (Wilhelm et al., 2014). Even though only 60 proteins were included in the 3D model, this clearly illustrates how the precise localization, spatiotemporal interaction, and dynamics of active zone components remain far beyond the reach of conventional microscopy techniques in such a small and crowded environment. By complementing the detailed ultrastructural data provided by electron microscopy, studies resorting to

SRM—though still relatively few—have contributed important insights into the molecular composition, organization, and dynamics of the presynaptic active zone.

Nanoarchitecture of Active Zones

At fast inhibitory and excitatory mammalian central synapses, several active zone scaffolding and tethering proteins have been identified, including Piccolo, Bassoon, Rab3-interacting molecule (RIM) and RIM-binding proteins (BPs), ELKS and Munc13, which are believed to connect vesicles to the plasma membrane and define the sites of exocytosis (Südhof, 2012). A first SRM study to look at the distribution of presynaptic proteins used multi-color 3D-STORM in mouse brain tissue sections to achieve a localization precision of 14 nm in the lateral plane and 35 nm in the axial plane (Dani et al., 2010). Both Piccolo and Bassoon, two active zone proteins that may have evolved to perform specific functions in vertebrate synapses, were found to have a similar axial distribution and to be organized in a highly oriented and extended manner, perpendicular to the active zone, with their C-termini pointing toward the presynaptic membrane and at distances close to 50 nm from it. Similar axial distributions were observed in subsequent studies using STED (Wong et al., 2018) or 3D-STORM (Trotter et al., 2019). The seemingly ubiquitous presence and precise arrangement of Bassoon at presynaptic active zones have made it a bona fide marker for the localization of other proteins with respect to active zones in many subsequent SRM studies. However, Bassoon itself may be implicated in synaptic modulation, since differences in its density in individual Bassoon clusters seem to explain the differences in the strength of presynaptic Cannabinoid receptor type 1 (CB1R) modulation between perisomatic and dendritic GABAergic terminals in the hippocampus (Dudok et al., 2015). Additionally, using dual-color dSTORM, Bassoon was shown to segregate from $Ca_v2.1$ and RIM clusters and to suffer an activity-dependent unclustering at hippocampal synapses, with a concomitant increase in Bassoon nanodomains, which allow the recruitment of multiple active zone components (Glebov et al., 2017). This demonstrates that the macromolecular crowding of the active zone limits presynaptic function and that dynamic unclustering can be used to change presynaptic strength. A similar localization and organization of Bassoon at active zones was demonstrated using X10 expansion microscopy (Truckenbrodt et al., 2018), a technique that achieves its high resolution by physical sample expansion through embedding into swellable gels, instead of using advanced microscopy methods (see below).

In a more recent study using 3D-STORM, RIM1/2 was found to be more clustered than Munc13 or Bassoon and to preferentially localize at the center of synapses (Tang et al., 2016). RIM cluster numbers and size paralleled those of postsynaptic density protein 95 (PSD95) clusters, whereas Munc13 clusters were more abundant and widely distributed, and Bassoon clusters less abundant and more uniformly distributed. Using PALM, the distribution of RIM nanoclusters was found to closely match vesicle fusion sites and to align trans-synaptically with nanoclusters of PSD95 and glutamate receptors while extending even deeper into the postsynaptic structure (Tang et al., 2016). These results support the notion of a trans-synaptic nano-column aligning presynaptic regions of high vesicle fusion probability to postsynaptic regions of high receptor density at excitatory synapses. A subsequent study using multi-color STED at excitatory synapses, both *in vitro* and *in vivo*, showed a correlation between dendritic spine size and the number of aligned *trans*-synaptic modules, further supporting the notion of a precise trans-synaptic alignment. Though the number (but not the size) and dynamics of these modules changes rapidly with synaptic plasticity, they remain aligned (Hruska et al., 2018). These results also suggest that structural plasticity linked to synaptic potentiation could be mediated by addition of building blocks made of unitary synaptic nanomodules. It would be interesting to investigate if a reverse mechanism operates in synaptic depression. Using multi-color 3D-SIM, a similar trans-synaptic organization was also found at inhibitory synapses. Here, presynaptic RIM subsynaptic domains align opposite to postsynaptic γ-aminobutyric acid $(GABA)_A$ receptor and gephyrin subsynaptic domains (Crosby et al., 2019). The number and volume of RIM clusters correlates with the number and volume of $GABA_A$ receptor and gephyrin clusters at individual synapses, with a significant pairing between the pre- and postsynaptic structures, independently of synapse size. However, presynaptic structures positive for the vesicular GABA transporter do not show such correlation and are thus not representative of the active zone (Crosby et al., 2019). Therefore, similarly to glutamatergic synapses, $GABA_A$ receptors and RIM at inhibitory synapses display a spatial segregation that strongly suggests a trans-synaptic coupling between them, likely reflecting the functional similarities between both synapse types, that is, optimized for fast ionotropic synaptic transmission. Identifying the molecular players involved in this *trans*-synaptic alignment will be important to better understand the coupling between pre- and postsynaptic function, and synaptic adhesion molecules, such as neurexins and neuroligins, are likely candidates. Indeed, using 3D-STORM, the adhesion molecule neurexin-1 was found to concentrate at presynaptic membranes within the synaptic cleft and to form discrete nanoclusters at a subset of excitatory synapses in both cultured neurons and hippocampal sections, which increased in size with development (Trotter et al., 2019). Typically, however, only one neurexin-1 cluster is found per synapse and only at a subset of synapses, which is incompatible with the widespread presence of trans-synaptic nanocolumns proposed to align sites of presynaptic vesicle fusion to postsynaptic receptor nanoclusters (Tang et al., 2016). Notwithstanding, expression of a C-terminal truncated neuroligin-1—the postsynaptic partner of neurexin—in neurons delocalizes it from α-amino-3-hydroxy-5-methyl-4-isoxazolepropionic acid (AMPA) receptor nanodomains and perturbs the trans-synaptic neurexin-neuroligin adhesion complex. This decreases the apposition of presynaptic RIM and postsynaptic AMPA receptors, as shown by dual-color *d*STORM, thus leading to impaired synaptic transmission (Haas et al., 2018). Other molecular adhesion complexes, such as those formed between Caspr2-Contactin-2, ephrin–ephrin receptors, and cadherins are also likely to play a role in trans-synaptic organization but remain to be studied in detail by SRM at central mammalian synapses.

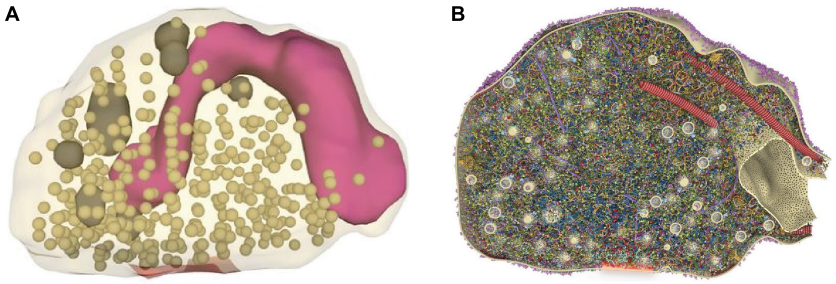

FIGURE 1 | Reconstruction of an average presynaptic terminal from purified synaptosomes. **(A)** Following a synaptosome purification procedure, serial electron micrographs were used to determine organelle numbers, sizes, and positions and reconstruct entire synapses. Shown is a single synaptosome representing the average physical parameters, with vesicles illustrated in dark beige, the active zone in red, larger organelles in dark gray, and mitochondria in purple **(B)** Section through the synaptic bouton showing the localization and abundance of 60 distinct proteins. Using information on protein copy numbers and their positions obtained by STED microscopy and other sources, they were placed in this synaptic structure in atomic detail. The reconstructed image reveals a densely crowded synaptic space, particularly around the active zone and vesicle cluster. Adapted, with permission from Wilhelm et al. (2014).

3D-STORM and STED also revealed that RIM1, Munc13-1, ELKS, and RIM-BP2 are placed as close to the presynaptic membrane as Piccolo and Bassoon and essentially localized at the active zone of murine synapses, where they form a large protein complex beneath the membrane (Dani et al., 2010; Grauel et al., 2016; Tang et al., 2016; Wong et al., 2018). At hippocampal synapses, using multi-color time-gated STED (gSTED) with a lateral resolution of ∼50 nm, RIM-BP2 was found to be part of the active zone scaffold and to form a complex with the priming factors RIM and Munc13 (Grauel et al., 2016). Deletion of RIM-BP2 causes mild changes in the localization of $Ca_V2.1$ calcium channels relative to Bassoon. This results in a moderate reduction in release efficiency but leads to pronounced alterations in short-term plasticity. Therefore, by contributing to the proper localization of $Ca_V2.1$ at active zones, RIM-BP2 fine-tunes the calcium-secretion coupling, with important consequences for synaptic output. RIM was shown to bind to the membrane phospholipid phosphatidylinositol 4,5 biphosphate (PIP2) via its C2B domain in a calcium-independent manner (de Jong et al., 2018). The deletion of RIM significantly reduces Munc13 and primed vesicles at actives zones, as assessed by STED. A C2B deletion mutant still localizes to active zones and can revert both Munc13 levels and primed vesicles. However, it fails to rescue exocytosis, probably by mistargeting the PIP2-dependent release machinery away from PIP2 in the membrane (de Jong et al., 2018). The localization of RIM-BP2 clusters relative to Munc13-1 clusters displays synapse specificity in the hippocampus, with the average distance to the nearest cluster being over 50% larger at mossy fiber synapses than at CA3-CA1 synapses, as shown by multi-color gSTED with a lateral resolution of 50 nm (Hofmann et al., 2005). A greater distance between RIM1 and $Ca_V2.1$ clusters was also observed in mossy fiber synapses, where RIM-BP2 deletion alters Munc13-1 cluster number and distribution, but not at CA3-CA1 synapses. These results reveal that, beyond the striking structural differences, distinct active zone nano-architectures may explain functional differences between the two synapse types. Yet, the determinants of these nano-architectural differences remain unexplained. In yet another study, 3D-STORM was used to show that Munc13-1 forms discrete supramolecular nano-assemblies at active zones of glutamatergic synapses in hippocampal neurons, whose number closely matches the number of release sites. These supramolecular complexes recruit syntaxin-1 and define the physical entities that constitute functional quantal release sites where vesicles can dock, prime, and fuse (Sakamoto et al., 2018). Their multiplicity at single active zones provides a purely presynaptic mechanism for setting synaptic weight across synapses.

Unlike the sub-millisecond neurotransmission operating at glutamatergic and GABAergic synapses, where specialized sites support a tight coupling between pre- and postsynaptic compartments, some neurotransmitters have a more widespread action through diffusion over large areas. Dopamine is an important neuromodulator that controls brain functions essential for reward, motivation, and the control of movement, and generally acts as a volume transmitter at much slower time scales than glutamate or GABA. However, fast and spatially localized dopamine signaling has also been observed (e.g., Howe and Dombeck, 2016), prompting the search for specialized dopamine secretion sites supporting fast signaling. Using 3D-SIM, several typical active zone scaffold proteins, including Bassoon, RIM, and ELKS, were identified in striatal dopamine axons. These proteins were also shown to be co-clustered in tyrosine hydroxylase (TH)-positive synaptosomes using multi-color STED, which also revealed that Bassoon colocalized with synaptobrevin-2-positive vesicles (Liu et al., 2018). However, the participation of RIM and ELKs in dopamine release were distinct from fast synapses, with RIM being essential and ELKS dispensable. This study also demonstrates that ∼30% of dopamine varicosities contain active zone-like release sites that could execute fast signaling, though most receptors seem to be localized outside synapses, meaning that dopamine would still typically act as a volume neuromodulator. Regardless, the existence of active zone-like dopamine release sites containing molecular players that are common to other synapse types could implicate dopaminergic dysfunction in diseases linked to mutations in release machinery components and typically associated with glutamatergic or GABAergic dysfunction.

Synaptic Vesicle Ultrastructure and Dynamics

The fusion of synaptic vesicles with the plasma membrane to release neurotransmitters is the last step in a long chain of complex—and not yet fully understood—molecular events involving a large number of presynaptic players (Südhof, 2013). Vesicles fuse at the active zone, are endocytosed in a compensatory, coupled exo-endocytic process, and are subsequently refilled with neurotransmitter for reuse (Maritzen and Haucke, 2018). These processes imply vesicle movement within the presynaptic bouton, but their small size precludes imaging of single vesicles with conventional microscopy techniques. Therefore, the movement of vesicles toward the plasma membrane, of vesicle material at the membrane, and of the endocytosed vesicles back to the vesicle pool had not been investigated in detail prior to the advent of SRM. The first study to address these questions used STED microscopy at low-intensity excitation to achieve live imaging of fluorescently labeled synaptic vesicles inside the axons of cultured neurons, at speeds of 28 frames per second and a focal spot size of 62 nm (Westphal et al., 2008). Within presynaptic boutons, vesicles were mostly in a low mobility and constrained state with average speeds of ∼2 nm/ms, characterized by both diffusive and motor-driven non-directional movement; however, rapid movement along axons was also recorded. Vesicle "hot spots" were also observed, where vesicles remain temporarily trapped. Subsequent research, also using STED, showed that the relatively high level of vesicle mobility initially reported—which contradicted the accepted dogma of low vesicle mobility—was due to imaging of recently endocytosed vesicles, since resting vesicles imaged after a prolonged incubation were largely stationary (Kamin et al., 2010). Quite surprisingly, and contrary to hypothetical assumptions, vesicle mobility was not altered by electrical or high KCl stimulation (Westphal et al., 2008; Kamin et al., 2010), two manipulations that greatly accelerate vesicle fusion rates. The explanation for these behaviors could be rather simple; vesicles undergoing fusion are already docked to the membrane and part of an immobile pool, whereas moving vesicles have enough motility to reach active zones to replenish the releasable pool. Therefore, changes in vesicle mobility may not be a prerequisite to sustain synaptic transmission, but it should be noted that technical issues related with the time at which imaging was possible after stimulation may have hampered detecting very immediate changes in mobility (Kamin et al., 2010). After fusion, the vesicle material was also found to have a limited motion at the membrane, contradicting the notion of its free diffusion out of synapses. Inhibition of synaptic activity, however, results in decreased mobility of recently endocytosed vesicles (Kamin et al., 2010). These results also question the physiological significance of the resting vesicle pool, since their immobility precludes any participation in the release process, except maybe under non-physiological stimulation conditions. A bi-directional shuttling between the membrane and an inner vesicle pool was also observed at hippocampal synapses by single-molecule localization microscopy using a vesicular Glutamate transporter 1 (vGlut1)-pHluorin fusion protein, with a localization precision of ∼27 nm. The retention of vesicles at the plasma membrane was shown to depend on myosin V acting as a tether instead of a motor, that also plays a role in refilling the release sites during repetitive stimulation, and in regulating the spatial distribution of release at more central sites in the synapse (Maschi et al., 2018). These results pave the way toward understanding the mechanisms involved in making vesicles available for release and in refilling release sites.

The existence of multiple release sites per active zone has long been put forward based on indirect estimates from electrophysiology experiments and on electron microscopy data showing the presence of docked vesicles at multiple active zone locations. Indeed, multivesicular release has been demonstrated at many excitatory and inhibitory brain synapses (reviewed in Rudolph et al., 2015), and occasionally observed by electron microscopy at snap-frozen hippocampal synapses (Abenavoli et al., 2002). SRM techniques have enabled the direct visualization of vesicle fusion events at central mammalian synapses and estimation of the number of functional release sites at individual active zones. By combining PALM and single-molecule localization, it was shown that vesicle fusion sites were coincident with RIM nanoclusters (Tang et al., 2016). However, vesicle fusion sites were found widely distributed throughout the active zones (Maschi and Klyachko, 2017; Maschi et al., 2018) and to undergo repeated reuse, though there is an activity-dependent reduction in reuse and relocation to the active zone periphery (Maschi and Klyachko, 2017). This reduction in reuse may reflect rate-limiting steps such as the availability of docking/priming sites for new vesicles (Neher, 2010) while relocation of release sites could represent a mechanism for minimizing postsynaptic receptor saturation to maintain transmission fidelity. Additionally, action potential-evoked release is more restricted to central, RIM-rich areas of active zones, compared to spontaneous release (Tang et al., 2016; but see Kusick et al., 2018). This raises the hypothesis of different fusion mechanisms operating across the presynaptic active zone, which may become permissive with repeated use, for example, resulting from sustained calcium elevation. Therefore, it would be interesting to investigate if more peripheral spontaneous fusion events colocalize preferentially with scaffold clusters other than RIM. A more recent study using 3D-STORM also demonstrated the existence of multiple quantal release sites at excitatory synapses, that are defined by the presence of Munc13-1 nano-assemblies. Though variable between synapses, these were stable at individual synapses (Sakamoto et al., 2018). Collectively, these results have shown a variable number of active release sites, averaging around 10 per active zone, a number that agrees rather well with the number of docked vesicles found at hippocampal synapses and shown to be the morphological correlate of fusion-competent vesicles (Schikorski and Stevens, 2001). However, there seems to be an unexplained discrepancy between the restricted localization of scaffold nanoclusters at the center of the active zones and the more widespread distribution of release sites throughout the active zone. Explanations could lie in differences in thresholding for cluster detection, and labeling and detection methods across studies. It also remains to be determined if the sites of morphological vesicle docking and vesicle fusion are one

and the same, and further refinements are needed to provide a clearer picture of the vesicle fusion process at active zones.

In order to maintain efficient, sustained, synaptic activity vesicles must recycle fast enough, and clearance of release sites for subsequent fusion is rate-limiting (Neher, 2010). Secretory carrier membrane proteins (SCAMPs) are a family of conserved membrane proteins involved in membrane trafficking events and found, among others, in secretory granules, transporter vesicles, and synaptic vesicles. SCAMP5 is highly enriched in synaptic vesicles and a candidate gene for autism (Castermans et al., 2010), though its synaptic function has remained elusive. In cultured neurons, dual-color STORM revealed that SCAMP5 plays an important role in endocytosis and release site clearance, since newly exocytosed synaptotagmin does not relocate to perisynaptic areas when SCAMP5 is knocked down (Park et al., 2018). This leads to slower recovery of releasable synaptic vesicles and to synaptic depression, which could underlie synaptic dysfunction in the context of at least some forms of autism.

The ultrastructure of synaptic vesicles themselves in brain synapses has also been resolved by SRM at a resolution comparable to that obtained by immunogold electron microscopy, but with vastly improved label density, using multi-color caged *d*STORM (a variation of *d*STORM that employs spectral demixing and reductive dye caging; Lampe et al., 2012). By superimposing many ring-like structures labeled for either VGlut1 or clathrin, it was possible to reconstruct rings of 41 and 56 nm, consistent with the sizes of synaptic vesicles and endocytic intermediates seen by transmission electron microscopy, respectively (Lehmann et al., 2015). The drawback of this approach is that individual vesicles at synapses cannot be detected in sufficient detail, as with electron microscopy. In addition to small synaptic vesicles used to release neurotransmitters, neurons also secrete neurotrophins and neuropeptides in a regulated manner from dense-core vesicles (DCVs) from both axons and dendrites. *d*STORM and STED were used to estimate the number of DCVs in cultured neurons and their axonal density *in vivo*, respectively (Persoon et al., 2018). DCVs were found to fuse in dendrites and, preferentially, in axons, but the nanoscopic organization of the release sites was not investigated. This would be very interesting, though, to see if the nanoscopic organization of such sites in neurons resembles the active zones where small synaptic vesicles fuse. Finally, using dual-color *d*STORM with a resolution of ∼20 nm, it was shown that the endogenous neurotrophin, brain-derived neurotrophic factor (BDNF) was contained in small granule-like clusters of ∼60 nm, mostly within the presynapse of glutamatergic—but not GABAergic—terminals in long-term cultured hippocampal neurons (Andreska et al., 2014). Retrograde BDNF signaling has been shown to exert important roles in the brain (e.g., Choo et al., 2017). This SRM study demonstrates that most BDNF is, in fact, available for anterograde release at the synaptic sites where it is known to exert a strong neuromodulatory effect.

Vesicle Fusion Machinery and Calcium Channels

The tethering and docking of synaptic vesicles are followed by vesicle fusion, orchestrated by the SNARE complex together with auxiliary proteins such as Munc18 and complexins, and triggered by a calcium sensor of the synaptotagmin family (Jahn and Scheller, 2006). A large body of evidence on the nanoscopic organization of the exocytotic machinery has been obtained from neuroendocrine cells or at the Drosophila neuromuscular junction using SRM techniques. Surprisingly, though, given the large interest in understanding the nanoscale organization of the release machinery at central mammalian synapses, SRM studies in these structures are quite scarce. The distribution of SNAP-25, syntaxin-1, and Munc18 were resolved in cultured neurons using a dual-color stochastic method with a resolution of 13 nm, showing that they colocalize at axonal membranes in clusters of 100 nm or less (Pertsinidis et al., 2013), though it is unclear if these correspond to active zones. However, STED showed that SNAP-25 and syntaxin are, as expected from their functions, enriched at synapses (Wilhelm et al., 2014). Ablation of syntaxin expression causes complete loss of the Munc18-1/SNAP-25 association and loss of Munc18-1 into the cytoplasm. This shows that Munc18-1 associates with SNAP-25 through syntaxin-1 (Pertsinidis et al., 2013), the only t-SNARE to possess a transmembrane domain. In cortical neurons, *d*STORM and PALM revealed the localization and dynamics of syntaxin-1a and Munc18-1 at synapses, as identified by co-labeling for synapsin (Kavanagh et al., 2014). Munc18-1 is mobile along axons, displaying directed movement and traveling long distances between synapses, while exhibiting a restricted movement in puncta. Consistent with its binding to syntaxin, the speed of Munc18-1 increases upon disruption of its interaction with syntaxin-1a, as shown by single-particle tracking PALM. Also in cultured neurons, multi-color gSTED showed that the distance between the synaptic vesicle-anchored, SNARE complex protein synaptobrevin 2, and the scaffold protein intersectin 1, present at active zones, is reduced during synaptic activity, indicating that the latter directly associates with the SNARE complex during exocytosis (Jäpel et al., 2020). This association is key for the clearance of release sites, thereby providing a mechanism for exo-endocytic coupling that allows synapses to sustain high-frequency neurotransmission. One potential issue in detecting the proper localization and interactions of SNARE proteins (or others) at the nanoscale is not only the large size of the antibodies used for labeling but also their potential to form aggregates, which can cause localization/distribution errors in SRM. Using the much smaller camelid single domain antibodies (or nanobodies) combined with dual-color STED, SNAP-25 and syntaxin-1a were shown to cluster at synapses of cultured neurons, with syntaxin-1a presenting more homogeneous cluster sizes. Considerable extrasynaptic localization was also detected, implying that, while essential for vesicle fusion, these proteins are not likely to play major roles in defining the sites of exocytosis (Maidorn et al., 2019). However, their recruitment to synapses upon stimulation suggests an active functional role, and it would be interesting to investigate whether a substantial extrasynaptic localization of SNARE proteins is also observed in intact brain tissue.

Calcium channels are crucial players in neurotransmitter release, since they provide the trigger for the exocytotic machinery to execute vesicle fusion. Their localization in respect to both fusion sites and the release machinery is considered essential for a tight coupling between action potential-driven

calcium influx and neurotransmitter release (Eggermann et al., 2012), which, in turn, is required for high-fidelity synaptic transmission. However, a loose coupling has been reported at hippocampal synapses (Vyleta and Jonas, 2014) and, indeed, SRM has shown that calcium channel distribution can be quite variable at mammalian synapses. At cerebellar parallel fiber synapses, dual-color *d*STORM with a localization precision of ∼13 nm showed an enrichment of $Ca_V2.1$ channels at active zones, close to Bassoon and metabotropic glutamate 4 receptors (mGluR4), but also outside the active zones (Siddig et al., 2020). The proximity of $Ca_V2.1$ to mGluR4 is also closer than expected for a random distribution, suggesting a functional interaction (see discussion below). At excitatory hippocampal synapses, multi-color gSTED showed that $Ca_V2.1$ clusters significantly segregate from Bassoon clusters (Grauel et al., 2016). Similar observations were made using *d*STORM, that additionally showed no overlap of $Ca_V2.1$ with RIM clusters (Glebov et al., 2017), with spatial segregations as large as 50 nm. These results are surprising since RIM was shown to tether calcium channels through a direct interaction with their PDZ domain (Kaeser et al., 2011), which is likely incompatible with the range of segregation distances observed. Again, labeling densities and detection thresholds could account for smaller measured protein cluster sizes, or to failure in detecting calcium channels in close proximity to RIM clusters, if they are too few, leading to apparent spatial segregation. However, indirect interactions of RIM with calcium channels, mediated by RIM-BPs (Hibino et al., 2002; Grauel et al., 2016), could also help explain this spatial segregation, if an intermediary link is present that would increase the distance between the two proteins. Interesting insight into how these proteins can organize at active zones came from the demonstration that RIM and RIM-BP can autonomously assemble into condensed complexes by liquid-liquid phase separation and cluster calcium channels into microdomains (Wu et al., 2019). It would be most interesting to demonstrate if additional active zone components also spontaneously tether around these assemblies to form active zone-like structures. One outstanding question has been whether calcium channels—or their activity—promote synapse assembly or, conversely, whether active zone proteins organize these channels at release sites. Using 3D-STORM, the nanoscale organization of RIM clusters relative to PSD-95 was shown to be unchanged in the absence of all three Ca_V2 calcium channel subunits in cultured hippocampal neurons. Furthermore, STED showed that the presence and localization of the active zone proteins RIM, RIM-BP2, Liprin-α3, ELKS2, Bassoon, and Munc13-1 are unchanged by the absence of calcium channels, though some are even mildly upregulated (Held et al., 2020). Therefore, neither the organization of presynaptic active zone scaffold nano-domains, nor their trans-synaptic alignment with postsynaptic nano-domains, require the presence of calcium channels. Notwithstanding, the nano clustered organization of presynaptic calcium channels remains consistent with the concept of calcium microdomains, shaped by the distance of calcium channels to vesicle docking sites together with the diffusion and buffering of calcium (Neher, 1998), though how the calcium channel nanodomains and release sites are coupled still remains unclear. Rather surprisingly, calcium channels also present considerable mobility at the presynaptic membrane of hippocampal synapses (Schneider et al., 2015). Indeed, in cultured hippocampal neurons, single particle tracking PALM with a localization accuracy of ∼27 nm revealed that a large proportion (∼60%) of exogenously expressed $Ca_V2.1$ channels are mobile in the presynaptic membrane, though their movement is confined. Calcium channel movement was shown to be reduced by buffering basal calcium but unchanged by its rise during synaptic activity. Importantly, STED showed that RIM and Bassoon clusters scale with Ca_V channel number in a way that allows active zones to maintain channel density and mobility (Schneider et al., 2015). These mechanisms may allow the cooperation between calcium domains and equalize the probability of release among docked vesicles. It would be interesting to see if similar observations are made at other types of synapses and, quite importantly, at synapses in intact tissue.

Presynaptic Neurotransmitter Receptors

Several classes of neurotransmitter receptors, including glutamate, GABA, and cannabinoid receptors, have been known for many decades to have a prominent presynaptic localization where they play important regulatory functions as auto- or heteroreceptors (e.g., Draguhn et al., 2007; Pinheiro and Mulle, 2008; Banerjee et al., 2016). However, detailed information on their specific subunits/assemblies, density, trafficking, and precise localization at presynaptic sites is scarce, and their very existence is, in some cases, still debated. One of the earliest SRM studies in brain tissue identified the presence of $GABA_BR1$ receptors at active zones of glutamatergic synapses by STORM, with an axial localization overlapping that of the presynaptic membrane (Dani et al., 2010). Retrograde endocannabinoid signaling through presynaptic CB1Rs is a widespread mechanism of modulation of synaptic transmission and plasticity (Ohno-Shosaku and Kano, 2014) that displays marked synapse-specific differences (Miles et al., 1996). Using multi-color 3D-STORM with a lateral localization precision of 6 nm and 41 nm axially, presynaptic CB1Rs were found to have a uniform distribution on GABAergic terminals in acute hippocampal slices, though they were more abundant on perisomatic than on dendritic interneuron terminals (Dudok et al., 2015). A higher CB1/Bassoon ratio was observed at perisomatic synapses, which may allow the more efficient coupling to the modulation of the release machinery, thereby explaining their higher sensitivity to endocannabinoid signaling. Chronic treatment with Δ^9-tetrahydrocannabinol (THC) causes internalization and loss of CB1 receptors at these terminals, as assessed by 3D-STORM (Dudok et al., 2015), thereby explaining the reduced efficacy of cannabinoids on GABA release following THC administration (Hoffman et al., 2007). Quite interestingly, at these same CB1-positive terminals in the hippocampus, dual-color 3D-*d*STORM identified the presence of ribosomes within 25–400 nm of the presynaptic membrane (Younts et al., 2016). Here, they integrate CB1R signaling to mediate the protein synthesis-dependent long-term depression (LTD) of GABAergic transmission through cap-dependent local presynaptic translation (Younts et al., 2016). The presence of ribosomes in the presynaptic compartment was also identified in most glutamatergic and GABAergic synapses

of both cultured hippocampal neurons and brain slices using expansion microscopy (Hafner et al., 2019), indicating that local protein synthesis is ubiquitously present at synapses. Another type of neurotransmitter receptor frequently found at presynaptic sites are $G_{i/o}$-coupled metabotropic glutamate receptors (mGluRs) that exert a critical inhibitory function as auto- or heteroreceptors (Huang and Thathiah, 2015). Using dual-color *d*STORM with a localization precision of 13 nm, a recent study obtained a detailed characterization of presynaptic mGuR4R number, stoichiometry, and spatial arrangement at parallel fiber synapses in the cerebellum (Siddig et al., 2020). At these synapses, mGluR4 was found concentrated within the active zones, which contained an average of 35 mGluR4 subunits mostly arranged in small nanoclusters of 1–2 subunits (average, 25 nanoclusters of 1.4 subunits), though high variability was observed. mGluR4 nanodomains were found close to Munc18-1 (30 nm) and $Ca_v2.1$ (65 nm), suggesting that these proteins might co-exist in functional macromolecular complexes that influence neurotransmission by direct regulation of the exocytotic machinery and calcium channel function. While scarce, given the wealth of reports on their existence and functions, overall, these studies highlight the diversity of localization and nanoscopic organization of presynaptic neurotransmitter receptors relative to the active zones, which will have important consequences for presynaptic modulation. Further studies are needed to understand where other presynaptic neurotransmitter receptor types localize to function in the modulation of neurotransmission.

Other Presynaptic Elements

Besides the obvious interest in studying the nanoscale localization, abundance, and dynamics of active zone proteins, various other presynaptic elements have been researched using SRM imaging at mammalian presynapses. The first application of STED to investigate synaptic organization achieved a lateral resolution of 40 nm at the calyx of Held synapse, a giant glutamatergic terminal located in the auditory brainstem that contains hundreds of individual active zones. Here, VGlut1, synaptophysin, Rab3A, and synapsin signals were shown to be consistent with a vesicular distribution, although synapsin was absent from a subpopulation of vGlut1-positve vesicles (Kempf et al., 2013). Using N-SIM, the presence of c-Jun NH2-terminal protein kinase (JNK)—mainly recognized as being postsynaptic—was found colocalized with synaptophysin in mouse purified cortical synaptosomes, where it was coupled to the activity of presynaptic NMDA receptors (Biggi et al., 2017). Presynaptic NMDARs, once considered an exception, are now believed to be quite widespread in the brain and to play important roles in modulating synaptic transmission and plasticity (Bouvier et al., 2015). However, anatomical data for their localization comes mainly from immunogold EM, which fails to report accurate receptor densities and colocalization with other synaptic components. It is, therefore, unfortunate that the presence and precise localization of the NMDARs in question were not investigated by SRM in the study by Biggi et al. (2017), which could also lend support to their functional presynaptic interaction with JNK. Using a combination of multi-color STORM and multi-color STED, gamma secretase, the enzyme responsible for the last processing step of the amyloid precursor protein, was found to localize in close proximity (down to <10 nm) of presynaptic synaptophysin-positive vesicles in hippocampal neurons (Schedin-Weiss et al., 2016), but to be absent from docked synaptic vesicles. This suggests that gamma secretase localizes to intracellular membranes/vesicular structures other than synaptic vesicles. Its presence is also very variable, with some synapses containing almost no labeling. Finally, despite being predominantly nuclear, the small ubiquitin-like modifier (SUMO) 2/3 protein was found to colocalize with the presynaptic protein synaptophysin using N-SIM (Colnaghi et al., 2019), although no attempt was made to further resolve its nanoscopic organization relative to active zones. The functions of RIM1α, synaptotagmin1, syntaxin1A, synapsyn1a, and possibly other proteins are modulated by SUMOylation (Henley et al., 2018), and demonstrating the presence of SUMO proteins at presynapses was a missing piece of the puzzle, though it requires further investigation.

Outlook

Almost 500 proteins, from a wide variety of functional categories, were identified in biochemically purified presynaptic fractions of central synapses (Boyken et al., 2013; Weingarten et al., 2014); about half of these are from the active zone. However, only a small amount has ever been studied in detail by SRM, and the vast amount of information that can still be gathered using these techniques will be crucial for a better understanding of presynaptic function. For example, different synaptotagmin isoforms contribute to the full capacity of release at central synapses (e.g., Bacaj et al., 2013, 2015), but it remains debated if they are co-localized in vesicles, sorted to distinct vesicle populations, or even whether some may act from the plasma membrane side. Another C2 domain protein akin to synaptotagmins is Doc2b, whose precise role at central synapses is still controversial. Doc2b has been postulated as a high-affinity calcium sensor for spontaneous neurotransmitter release (Groffen et al., 2010) and traffics to the plasma membrane in a calcium-dependent manner in chromaffin cells (Groffen et al., 2004, 2006), where it plays important roles in DCV priming (Pinheiro et al., 2013; Houy et al., 2017). However, its precise localization at mammalian presynapses, and whether it displays calcium-dependent membrane translocation in this nano-environment—important to understand its synaptic function—have not been determined. Additionally, despite the plethora of functional and biochemical evidence for the existence of presynaptic GABA, NMDA, kainate, and, to a lesser extent, AMPA receptors, their study at presynaptic structures using SRM has attracted surprisingly little interest. However, this would be highly relevant to complement existing functional studies, since their localization relative to active zone components, molecular composition, surface trafficking, and whether they are concentrated in highly organized nanodomains—like their postsynaptic counterparts—are likely to influence how they modulate presynaptic activity. The results obtained from studying vesicle fusion by SRM also raised interesting questions regarding the local segregation of release sites and the tethering

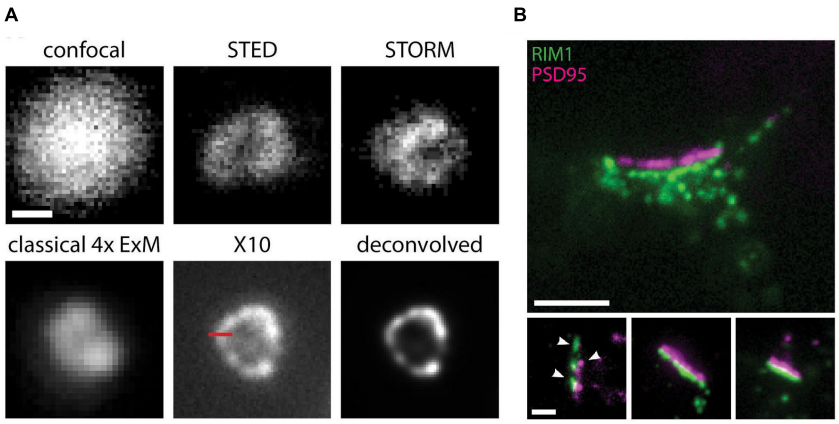

FIGURE 2 | X10 expansion microscopy can achieve super resolved images on a conventional microscope. **(A)** Immunostaining for the peroxisome membrane protein Pmp70 in neurons, imaged before expansion by confocal, STED, or STORM microscopy, and by standard epifluorescence microscopy after classical 4x sample expansion or X10 sample expansion. The last panel shows the X10 image after deconvolution. Scale bar, 100 nm. **(B)** Representative immunostaining images for postsynaptic PSD95 (magenta) and presynaptic RIM1/2 (green) proteins in cultured neurons at an expansion factor of 10.4x. Nanocolumns of aligned pre- and postsynaptic proteins are indicated by arrowheads. Scale bars: 500 nm (upper panel) and 200 nm (lower panels). Adapted, with permission from Truckenbrodt et al. (2018).

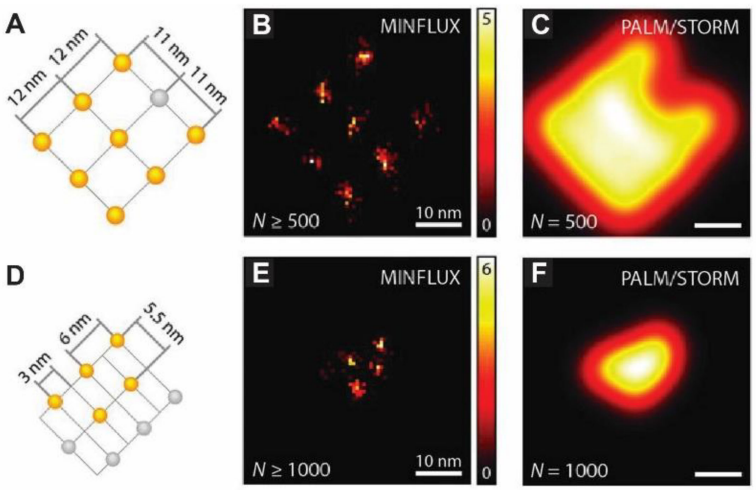

FIGURE 3 | MINFLUX nanoscopy of labeled DNA origamis allows resolving molecules only 6 nm apart. **(A)** Arrangement of up to nine on-off switchable Alexa Fluor 647 fluorophores on the DNA origami with an 11 nm spacing (in gray are depicted those that remained in the off state throughout the measurement). **(B)** Spatial binning (bin size, 0.75 nm) of direct MINFLUX localizations renders a nanoscopic image of the origami from events yielding > 500 photons. **(C)** Simulated ideal PALM/STORM image of the origami using detections of 500 photons. **(D–F)** Similar representations as in **(A–C)** but for the smaller DNA origami depicted in **(D)**. Events with under 100 detected photos were discarded. Adapted, with permission from Balzarotti et al. (2017).

of the active zone scaffold proteins to the membrane, since none possesses a transmembrane domain. One key element could be the membrane phospholipid PIP2. PIP2 is required for the function of many components of the vesicle fusion machinery including syntaxin, Munc13, calcium channels, and synaptotagmin (Bai et al., 2004; Chun et al., 2010; Suh et al., 2010; Van Den Bogaart et al., 2011). RIM1, whose nanodomains at the active zone define vesicle release sites, binds to PIP2 via its C2B domain (de Jong et al., 2018), thereby targeting the release machinery to sites where this lipid is present and necessary for fusion efficiency. Visualizing the nanoscale co-distribution of PIP2 and RIM (or RIM-ΔC2B) at active zones and acutely manipulating PIP2 levels (for example, using the recently developed caged PIP2; Walter et al., 2017) could help to clarify if this phospholipid is the orchestrator of active release sites at the membrane. Several other scaffold proteins, including Bassoon and Munc13, also contain C2 or other lipid-binding domains; whether their interaction with PIP2 also contributes to active zone organization remains to be determined. These, and many other outstanding questions, could probably find an answer by imaging in the nanoscale domain using SRM techniques.

PERSPECTIVES FOR SRM OF THE PRESYNAPTIC COMPARTMENT

Despite the large accomplishments of "classical" SRM techniques, each has its weaknesses or limitations, and continued research into ways of further improving their resolving power, speed, or imaged area has led, in recent years, to the development of both entirely new concepts and variations of existing ones. Combining different SRM methods, or SRM with other imaging or experimental approaches, has proven effective at harnessing the advantages of each. For example, STED microscopy has been combined with expansion microscopy (ExSTED; Gao et al., 2018; Kim et al., 2019), allowing further resolution gains to under 10 nm. This approach could be particularly relevant in the extremely crowded space of synaptic compartments, particularly if using probes that are smaller than antibodies. By enabling significant molecular decrowding and fluorophore separation due to sample volume expansions of up to 1000 fold (Truckenbrodt et al., 2018), the recently developed X10 expansion microscopy alone can produce super resolution images on standard epifluorescence microscopes that rival those obtained in commercial implementations of STED or STORM (**Figure 2**). If combined with these physics-based SRM techniques, X10 microscopy may allow resolution gains down to the size of single fluorophores and the generation of extremely accurate maps of protein distribution and density. Expansion microscopy is also enormously advantageous since it's cheap to implement and allows significant resolution gains without the need for specialized equipment, technical knowledge, or complex analysis software, making it accessible to virtually any lab with an epifluorescence microscope. It is also compatible with thick samples and standard fluorophores, but cannot be used for live imaging. Also noteworthy is the combined use of PALM and uPAINT with 3D-STED or SUSHI imaging methods onto a single microscope platform (Inavalli et al., 2019). By combining the strengths of deterministic and stochastic SRM methods, this system allows the simultaneous investigation of both the nanoscale morphology of synapses and the localization and dynamics of synaptic proteins in living samples and opens the possibility of applying a similar approach using other SRM techniques. Finally, approaches using correlative SRM and electron microscopy have succeeded in combining the superior resolution of the electron microscope with the molecular specificity and ability to provide quantitative data on the number, distribution, and size of protein complexes afforded by SRM techniques (Nanguneri et al., 2012; Kim et al., 2015; Johnson and Kaufmann, 2017; Ando et al., 2018; Dietz and Heilemann, 2019; Franke et al., 2019). However, SRM or other imaging techniques cannot decipher the complexity of synapses and neuronal and brain function on their own, since images alone will not tell the whole story. The combination of SRM with electrophysiology (Chéreau et al., 2017; Yadav and Lu, 2018; Schmidl et al., 2019), digital holography (Lauterbach et al., 2016), and optogenetics (Dani et al., 2010; Glebov et al., 2017) holds great promise toward correlating functional and structural/molecular aspects of synapse function.

Although some SRM techniques have reached a high level of maturity and are now offered as commercial solutions, emerging new concepts are again pushing the boundaries of resolution and/or speed. MINFLUX nanoscopy, for example, can probe single-molecule emitters with a donut-shaped illumination pattern and resolve molecules distanced by as little as 6 nm with a precision of 1 nm, while requiring a much lower photon budget than common centroid-based methods (Balzarotti et al., 2017) (**Figure 3**). However, unlike STED, where the donut-shaped illumination pattern is used both to generate the fluorophore state transitions and for their localization, in MINFLUX it is used only for localization. The concept is compatible with 3D multi-color labeling applications (Gwosch et al., 2020), has been extended to the use of sinusoidal illumination patterns (Reymond et al., 2019; Cnossen et al., 2020), and could replace the now common SRM methods, eventually allowing molecular resolution in lensless designs (Balzarotti et al., 2017). Applied to neurons and synapses, these methods could push our understanding of their intricate nano-organization and dynamics down to molecular resolution while limiting phototoxicity concerns, particularly if they can be made compatible with *in vivo* deep-tissue imaging.

CONCLUSION

By harnessing the resolving power of super-resolution optical microscopy, our understanding of synapse structure and function has taken big leaps in recent years. With the incessant quest for further refinements in terms of better hardware, increasingly powerful processing algorithms (e.g., Xu et al., 2017), or deep learning strategies (Ouyang et al., 2018; Wang et al., 2019; Jin et al., 2020), fluorophores with improved or tailored photophysical properties (e.g., Minoshima and Kikuchi, 2017; Thiel and Rivera-Fuentes, 2018; Halabi et al., 2019; Kozma and Kele, 2019; Velde et al., 2019; Xu et al., 2020), and, quite likely, yet new and revolutionary technical approaches altogether, the limits of what can be resolved today are bound to keep shrinking. In parallel, the evolution of strategies for high-throughput SRM are allowing faster imaging of increasing numbers of simultaneous targets over larger sample areas (Guo et al., 2019; Mahecic et al., 2019). We look forward to seeing—in super-resolution—what synapses and other neuronal structures will resemble in the future.

AUTHOR CONTRIBUTIONS

All authors listed have made a substantial, direct and intellectual contribution to the work, and approved it for publication.

FUNDING

This work was financed by the European Regional Development Fund (ERDF), through the Centro 2020 Regional Operational

Programme under project CENTRO-01-0145-FEDER-000008: BrainHealth 2020 (scholarship to VM), and through the COMPETE 2020 – Operational Programme for Competitiveness and Internationalization and Portuguese national funds via FCT – Fundação para a Ciência e a Tecnologia, I.P., under project UIDB/04539/2020, and grants PTDC/BIA-CEL/29451/2017, CEECIND/00003/2018 (to PP) and CEECIND/00322/2017 (to EF). LC was supported in part by a "Summer with Science" research fellowship from FCT.

ACKNOWLEDGMENTS

The authors are grateful to Dr. Eric Hosy, IINS Bordeaux, for critical reading of the manuscript and for helpful suggestions.

REFERENCES

Abenavoli, A., Forti, L., Bossi, M., Bergamaschi, A., Villa, A., and Malgaroli, A. (2002). Multimodal quantal release at individual hippocampal synapses: evidence for no lateral inhibition. *J. Neurosci.* 22, 6336–6346. doi: 10.1523/jneurosci.22-15-06336.2002

Ando, T., Bhamidimarri, S. P., Brending, N., Colin-York, H., Collinson, L., De Jonge, N., et al. (2018). The 2018 correlative microscopy techniques roadmap. *J. Phys. D. Appl. Phys.* 51:443001. doi: 10.1088/1361-6463/aad055

Andreska, T., Aufmkolk, S., Sauer, M., and Blum, R. (2014). High abundance of BDNF within glutamatergic presynapses of cultured hippocampal neurons. *Front. Cell. Neurosci.* 8:107. doi: 10.3389/fncel.2014.00107

Bacaj, T., Wu, D., Burré, J., Malenka, R. C., Liu, X., and Südhof, T. C. (2015). Synaptotagmin-1 and -7 are redundantly essential for maintaining the capacity of the readily-releasable pool of synaptic vesicles. *PLoS Biol.* 13:e002267. doi: 10.1371/journal.pbio.1002267

Bacaj, T., Wu, D., Yang, X., Morishita, W., Zhou, P., Xu, W., et al. (2013). Synaptotagmin-1 and synaptotagmin-7 trigger synchronous and asynchronous phases of neurotransmitter release. *Neuron* 80, 947–959. doi: 10.1016/j.neuron.2013.10.026

Bai, J., Tucker, W. C., and Chapman, E. R. (2004). PIP2 increases the speed of response of synaptotagmin and steers its membrane-penetration activity toward the plasma membrane. *Nat. Struct. Mol. Biol.* 11, 36–44. doi: 10.1038/nsmb709

Balzarotti, F., Eilers, Y., Gwosch, K. C., Gynnå, A. H., Westphal, V., Stefani, F. D., et al. (2017). Nanometer resolution imaging and tracking of fluorescent molecules with minimal photon fluxes. *Science* 355, 606–612. doi: 10.1126/science.aak9913

Banerjee, A., Larsen, R. S., Philpot, B. D., and Paulsen, O. (2016). Roles of presynaptic NMDA receptors in neurotransmission and plasticity. *Trends Neurosci.* 39, 26–39. doi: 10.1016/j.tins.2015.11.001

Betzig, E., Patterson, G. H., Sougrat, R., Lindwasser, O. W., Olenych, S., Bonifacino, J. S., et al. (2006). Imaging intracellular fluorescent proteins at nanometer resolution. *Science* 313, 1642–1645. doi: 10.1126/science.1127344

Biggi, S., Buccarello, L., Sclip, A., Lippiello, P., Tonna, N., Rumio, C., et al. (2017). Evidence of presynaptic localization and function of the c-Jun N-terminal kinase. *Neural Plast.* 2017:6468356. doi: 10.1155/2017/6468356

Bouvier, G., Bidoret, C., Casado, M., and Paoletti, P. (2015). Presynaptic NMDA receptors: roles and rules. *Neuroscience* 311, 322–340. doi: 10.1016/j.neuroscience.2015.10.033

Boyken, J., Grønborg, M., Riedel, D., Urlaub, H., Jahn, R., and Chua, J. J. E. (2013). Molecular profiling of synaptic vesicle docking sites reveals novel proteins but few differences between glutamatergic and GABAergic synapses. *Neuron* 78, 285–297. doi: 10.1016/j.neuron.2013.02.027

Castermans, D., Volders, K., Crepel, A., Backx, L., de Vos, R., Freson, K., et al. (2010). SCAMP5, NBEA and AMISYN: three candidate genes for autism involved in secretion of large dense-core vesicles. *Hum. Mol. Genet.* 19, 1368–1378. doi: 10.1093/hmg/ddq013

Chéreau, R., Saraceno, G. E., Angibaud, J., Cattaert, D., and Nägerl, U. V. (2017). Superresolution imaging reveals activity-dependent plasticity of axon morphology linked to changes in action potential conduction velocity. *Proc. Natl. Acad. Sci. U.S.A.* 114, 1401–1406. doi: 10.1073/pnas.1607541114

Chmyrov, A., Keller, J., Grotjohann, T., Ratz, M., D'Este, E., Jakobs, S., et al. (2013). Nanoscopy with more than 100,000 "doughnuts". *Nat. Methods* 10, 737–740. doi: 10.1038/nmeth.2556

Choo, M., Miyazaki, T., Yamazaki, M., Kawamura, M., Nakazawa, T., Zhang, J., et al. (2017). Retrograde BDNF to TrkB signaling promotes synapse elimination in the developing cerebellum. *Nat. Commun.* 8, 1–13. doi: 10.1038/s41467-017-00260-w

Choquet, D., and Triller, A. (2013). The dynamic synapse. *Neuron* 80, 691–703. doi: 10.1016/j.neuron.2013.10.013

Chun, Y. S., Shin, S., Kim, Y., Cho, H., Park, M. K., Kim, T.-W., et al. (2010). Cholesterol modulates ion channels via down-regulation of phosphatidylinositol 4,5-bisphosphate. *J. Neurochem.* 112, 1286–1294. doi: 10.1111/j.1471-4159.2009.06545.x

Cnossen, J., Hinsdale, T., Thorsen, R., Siemons, M., Schueder, F., Jungmann, R., et al. (2020). Localization microscopy at doubled precision with patterned illumination. *Nat. Methods* 17, 59–63. doi: 10.1038/s41592-019-0657-7

Colnaghi, L., Russo, L., Natale, C., Restelli, E., Cagnotto, A., Salmona, M., et al. (2019). Super resolution microscopy of SUMO proteins in neurons. *Front. Cell. Neurosci.* 13:486. doi: 10.3389/fncel.2019.00486

Crosby, K. C., Gookin, S. E., Garcia, J. D., Hahm, K. M., Dell'Acqua, M. L., and Smith, K. R. (2019). Nanoscale subsynaptic domains underlie the organization of the inhibitory synapse. *Cell Rep.* 26, 3284–3297.e3. doi: 10.1016/j.celrep.2019.02.070

Dani, A., Huang, B., Bergan, J., Dulac, C., and Zhuang, X. (2010). Superresolution imaging of chemical synapses in the brain. *Neuron* 68, 843–856. doi: 10.1016/j.neuron.2010.11.021

de Jong, A. P. H., Roggero, C. M., Ho, M. R., Wong, M. Y., Brautigam, C. A., Rizo, J., et al. (2018). RIM C 2 b domains target presynaptic active zone functions to PIP 2 -containing membranes. *Neuron* 98, 335–349.e7. doi: 10.1016/j.neuron.2018.03.011

Dietz, M. S., and Heilemann, M. (2019). Optical super-resolution microscopy unravels the molecular composition of functional protein complexes. *Nanoscale* 11, 17981–17991. doi: 10.1039/c9nr06364a

Draguhn, A., Axmacher, N., and Kolbaev, S. (2007). Presynaptic ionotropic GABA receptors. *Results Probl. Cell Differ.* 44, 69–85. doi: 10.1007/400_2007_040

Dudok, B., Barna, L., Ledri, M., Szabó, S. I., Szabadits, E., Pintér, B., et al. (2015). Cell-specific STORM super-resolution imaging reveals nanoscale organization of cannabinoid signaling. *Nat. Neurosci.* 18, 75–86. doi: 10.1038/nn.3892

Eggermann, E., Bucurenciu, I., Goswami, S. P., and Jonas, P. (2012). Nanodomain coupling between Ca 2+ channels and sensors of exocytosis at fast mammalian synapses. *Nat. Rev. Neurosci.* 13, 7–21. doi: 10.1038/nrn3125

Emes, R. D., and Grant, S. G. N. (2012). Evolution of synapse complexity and diversity. *Annu. Rev. Neurosci.* 35, 111–131. doi: 10.1146/annurev-neuro-062111-150433

Endesfelder, U., and Heilemann, M. (2014). Direct stochastic optical reconstruction microscopy (Dstorm). *Methods Mol. Biol.* 1251, 263–276. doi: 10.1007/978-1-4939-2080-8_14

Franke, C., Repnik, U., Segeletz, S., Brouilly, N., Kalaidzidis, Y., Verbavatz, J. M., et al. (2019). Correlative single-molecule localization microscopy and electron tomography reveals endosome nanoscale domains. *Traffic* 20, 601–617. doi: 10.1111/tra.12671

Gao, M., Maraspini, R., Beutel, O., Zehtabian, A., Eickholt, B., Honigmann, A., et al. (2018). Expansion stimulated emission depletion microscopy (ExSTED). *ACS Nano* 12, 4178–4185. doi: 10.1021/acsnano.8b00776

Giannone, G., Hosy, E., Levet, F., Constals, A., Schulze, K., Sobolevsky, A. I., et al. (2010). Dynamic superresolution imaging of endogenous proteins on living cells at ultra-high density. *Biophys. J.* 99, 1303–1310. doi: 10.1016/j.bpj.2010.06.005

Giannone, G., Hosy, E., Sibarita, J. B., Choquet, D., and Cognet, L. (2013). High-content super-resolution imaging of live cell by uPAINT. *Methods Mol. Biol.* 950, 95–110. doi: 10.1007/978-1-62703-137-0_7

Glebov, O. O., Jackson, R. E., Winterflood, C. M., Owen, D. M., Barker, E. A., Doherty, P., et al. (2017). Nanoscale structural plasticity of the active zone matrix modulates presynaptic function. *Cell Rep.* 18, 2715–2728. doi: 10.1016/j.celrep.2017.02.064

Godin, A. G., Lounis, B., and Cognet, L. (2014). Biophysical review super-resolution microscopy approaches for live cell imaging. *Biophysj* 107, 1777–1784. doi: 10.1016/j.bpj.2014.08.028

Grauel, M. K., Maglione, M., Reddy-Alla, S., Willmes, C. G., Brockmann, M. M., Trimbuch, T., et al. (2016). Rim-binding protein 2 regulates release probability by fine-tuning calcium channel localization at murine hippocampal synapses. *Proc. Natl. Acad. Sci. U.S.A.* 113, 11615–11620. doi: 10.1073/pnas.1605256113

Groffen, A. J., Martens, S., Arazola, R. D., Cornelisse, L. N., Lozovaya, N., De Jong, A. P. H., et al. (2010). Doc2b is a high-affinity Ca2+sensor for spontaneous neurotransmitter release. *Science* 327, 1614–1618. doi: 10.1126/science.1183765

Groffen, A. J. A., Brian, E. C., Dudok, J. J., Kampmeijer, J., Toonen, R. F., and Verhage, M. (2004). Ca2+-induced recruitment of the secretory vesicle protein DOC2B to the target membrane. *J. Biol. Chem.* 279, 23740–23747. doi: 10.1074/jbc.M400731200

Groffen, A. J. A., Friedrich, R., Brian, E. C., Ashery, U., and Verhage, M. (2006). DOC2A and DOC2B are sensors for neuronal activity with unique calcium-dependent and kinetic properties. *J. Neurochem.* 97, 818–833. doi: 10.1111/j.1471-4159.2006.03755.x

Guo, S. M., Veneziano, R., Gordonov, S., Li, L., Danielson, E., Perez de Arce, K., et al. (2019). Multiplexed and high-throughput neuronal fluorescence imaging with diffusible probes. *Nat. Commun.* 10:4377. doi: 10.1038/s41467-019-12372-6

Gustafsson, M. G. L. (2000). Surpassing the lateral resolution limit by a factor of two using structured illumination microscopy. *J. Microsc.* 198, 82–87. doi: 10.1046/j.1365-2818.2000.00710.x

Gwosch, K. C., Pape, J. K., Balzarotti, F., Hoess, P., Ellenberg, J., Ries, J., et al. (2020). MINFLUX nanoscopy delivers 3D multicolor nanometer resolution in cells. *Nat. Methods* 17, 217–224. doi: 10.1038/s41592-019-0688-0

Haas, K. T., Compans, B., Letellier, M., Bartol, T. M., Grillo-Bosch, D., Sejnowski, T. J., et al. (2018). Pre-post synaptic alignment through neuroligin-1 tunes synaptic transmission efficiency. *eLife* 7:e031755. doi: 10.7554/eLife.31755

Hafner, A. S., Donlin-Asp, P. G., Leitch, B., Herzog, E., and Schuman, E. M. (2019). Local protein synthesis is a ubiquitous feature of neuronal pre-And postsynaptic compartments. *Science* 364:eaau3644. doi: 10.1126/science.aau3644

Halabi, E. A., Pinotsi, D., and Rivera-Fuentes, P. (2019). Photoregulated fluxional fluorophores for live-cell super-resolution microscopy with no apparent photobleaching. *Nat. Commun.* 10:1232. doi: 10.1038/s41467-019-09217-7

Heilemann, M., Van De Linde, S., Schüttpelz, M., Kasper, R., Seefeldt, B., Mukherjee, A., et al. (2008). Subdiffraction-resolution fluorescence imaging with conventional fluorescent probes. *Angew. Chem. Int. Edn.* 47, 6172–6176. doi: 10.1002/anie.200802376

Held, R. G., Liu, C., Ma, K., Sun, J., Blanpied, T. A., Kaeser, P. S., et al. (2020). Synapse and active zone assembly in the absence of presynaptic Ca 2+ channels and Ca 2+ entry. *Neuron* 107, 1–17. doi: 10.1016/j.neuron.2020.05.032

Henley, J. M., Carmichael, R. E., and Wilkinson, K. A. (2018). Extranuclear SUMOylation in Neurons. *Trends Neurosci.* 41, 198–210. doi: 10.1016/j.tins.2018.02.004

Hess, S. T., Girirajan, T. P. K., and Mason, M. D. (2006). Ultra-high resolution imaging by fluorescence photoactivation localization microscopy. *Biophys. J.* 91, 4258–4272. doi: 10.1529/biophysj.106.091116

Hibino, H., Pironkova, R., Onwumere, O., Vologodskaia, M., Hudspeth, A. J., and Lesage, F. (2002). RIM binding proteins (RBPs) couple Rab3-interacting molecules (RIMs) to voltage-gated Ca2+ channels. *Neuron* 34, 411–423. doi: 10.1016/S0896-6273(02)00667-0

Hoffman, A. F., Oz, M., Yang, R., Lichtman, A. H., and Lupica, C. R. (2007). Opposing actions of chronic Δ9-tetrahydrocannabinol and cannabinoid antagonists on hippocampal long-term potentiation. *Learn. Mem.* 14, 63–74. doi: 10.1101/lm.439007

Hofmann, M., Eggeling, C., Jakobs, S., and Hell, S. W. (2005). Breaking the diffraction barrier in fluorescence microscopy at low light intensities by using reversibly photoswitchable proteins. *Proc. Natl. Acad. Sci. U.S.A.* 102, 17565–17569. doi: 10.1073/pnas.0506010102

Houy, S., Groffen, A. J., Ziomkiewicz, I., Verhage, M., Pinheiro, P. S., and Sørensen, J. B. (2017). Doc2B acts as a calcium sensor for vesicle priming requiring synaptotagmin-1, Munc13-2 and SNAREs. *eLife* 6:e27000. doi: 10.7554/eLife.27000

Howe, M. W., and Dombeck, D. A. (2016). Rapid signalling in distinct dopaminergic axons during locomotion and reward. *Nature* 535, 505–510. doi: 10.1038/nature18942

Hruska, M., Henderson, N., Le Marchand, S. J., Jafri, H., and Dalva, M. B. (2018). Synaptic nanomodules underlie the organization and plasticity of spine synapses. *Nat. Neurosci.* 21, 671–682. doi: 10.1038/s41593-018-0138-9

Huang, Y., and Thathiah, A. (2015). Regulation of neuronal communication by G protein-coupled receptors. *FEBS Lett.* 589, 1607–1619. doi: 10.1016/j.febslet.2015.05.007

Huszka, G., and Gijs, M. A. M. (2019). Super-resolution optical imaging : a comparison. *Micro Nano Eng.* 2, 7–28. doi: 10.1016/j.mne.2018.11.005

Inavalli, V. V. G. K., Lenz, M. O., Butler, C., Angibaud, J., Compans, B., Levet, F., et al. (2019). A super-resolution platform for correlative live single-molecule imaging and STED microscopy. *Nat. Methods* 16, 1263–1268. doi: 10.1038/s41592-019-0611-8

Jacquemet, G., Carisey, A. F., Hamidi, H., Henriques, R., and Leterrier, C. (2020). The cell biologist's guide to super-resolution microscopy. *J. Cell Sci.* 133:jcs240713. doi: 10.1242/jcs.240713

Jahn, R., and Scheller, R. H. (2006). SNAREs–engines for membrane fusion. *Nat. Rev. Mol. Cell Biol.* 7, 631–643. doi: 10.1038/nrm2002

Jäpel, M., Gerth, F., Sakaba, T., Bacetic, J., Yao, L., Koo, S. J., et al. (2020). Intersectin-mediated clearance of SNARE complexes is required for fast neurotransmission. *Cell Rep.* 30, 409–420.e6. doi: 10.1016/j.celrep.2019.12.035

Jin, L., Liu, B., Zhao, F., Hahn, S., Dong, B., Song, R., et al. (2020). Deep learning enables structured illumination microscopy with low light levels and enhanced speed. *Nat. Commun.* 11:1934. doi: 10.1038/s41467-020-15784-x

Johnson, E., and Kaufmann, R. (2017). Correlative in-resin super-resolution fluorescence and electron microscopy of cultured cells. *Methods Mol. Biol.* 1663, 163–177. doi: 10.1007/978-1-4939-7265-4_14

Jungmann, R., Avendaño, M. S., Woehrstein, J. B., Dai, M., Shih, W. M., and Yin, P. (2014). Multiplexed 3D cellular super-resolution imaging with DNA-PAINT and Exchange-PAINT. *Nat. Methods* 11, 313–318. doi: 10.1038/nmeth.2835

Kaeser, P. S., Deng, L., Wang, Y., Dulubova, I., Liu, X., Rizo, J., et al. (2011). RIM proteins tether Ca2+ channels to presynaptic active zones via a direct PDZ-domain interaction. *Cell* 144, 282–295. doi: 10.1016/j.cell.2010.12.029

Kamin, D., Lauterbach, M. A., Westphal, V., Keller, J., Schönle, A., Hell, S. W., et al. (2010). High- and low-mobility stages in the synaptic vesicle cycle. *Biophys. J.* 99, 675–684. doi: 10.1016/j.bpj.2010.04.054

Kavanagh, D. M., Smyth, A. M., Martin, K. J., Dun, A., Brown, E. R., Gordon, S., et al. (2014). A molecular toggle after exocytosis sequesters the presynaptic syntaxin1a molecules involved in prior vesicle fusion. *Nat. Commun.* 5, 1–14. doi: 10.1038/ncomms6774

Kempf, C., Staudt, T., Bingen, P., Horstmann, H., Engelhardt, J., Hell, S. W., et al. (2013). Tissue Multicolor STED nanoscopy of presynaptic proteins in the calyx of held. *PLoS One* 8:e062893. doi: 10.1371/journal.pone.0062893

Kim, D., Deerinck, T. J., Sigal, Y. M., Babcock, H. P., Ellisman, M. H., and Zhuang, X. (2015). Correlative stochastic optical reconstruction microscopy and electron microscopy. *PLoS One* 10:e0124581. doi: 10.1371/journal.pone.0124581

Kim, D., Kim, T., Lee, J., and Shim, S. H. (2019). Amplified expansion stimulated emission depletion microscopy. *Chembiochem* 20, 1260–1265. doi: 10.1002/cbic.201800775

Klar, T. A., and Hell, S. W. (1999). Subdiffraction resolution in far-field fluorescence microscopy. *Opt. Lett.* 24:954. doi: 10.1364/ol.24.000954

Klar, T. A., Jakobs, S., Dyba, M., Egner, A., and Hell, S. W. (2000). Fluorescence microscopy with diffraction resolution barrier broken by stimulated emission. *Proc. Natl. Acad. Sci. U.S.A.* 97, 8206–8210. doi: 10.1073/pnas.97.15.8206

Kner, P., Chhun, B. B., Griffis, E. R., Winoto, L., and Gustafsson, M. G. L. (2009). Super-resolution video microscopy of live cells by structured illumination. *Nat. Methods* 6, 339–342. doi: 10.1038/nmeth.1324

Kozma, E., and Kele, P. (2019). Fluorogenic probes for super-resolution microscopy. *Org. Biomol. Chem.* 17, 215–233. doi: 10.1039/c8ob02711k

Kusick, G. F., Chin, M., Lippmann, K., Adula, K. P., Davis, M. W., Jorgensen, E. M., et al. (2018). Synaptic vesicles undock and then transiently dock after an action potential. *bioRxiv* [Preprint], doi: 10.1101/509216

Lampe, A., Haucke, V., Sigrist, S. J., Heilemann, M., and Schmoranzer, J. (2012). Multi-colour direct STORM with red emitting carbocyanines. *Biol. Cell* 104, 229–237. doi: 10.1111/boc.201100011

Lauterbach, M. A., Guillon, M., Desnos, C., Khamsing, D., Jaffal, Z., Darchen, F., et al. (2016). Superresolving dendritic spine morphology with STED microscopy under holographic photostimulation. *Neurophotonics* 3:041806. doi: 10.1117/1.nph.3.4.041806

Lefman, J., Scott, K., and Stranick, S. (2011). Live, video-rate super-resolution microscopy using structured illumination and rapid GPU-based parallel processing. *Microsc. Microanal.* 17, 191–196. doi: 10.1017/S1431927611000158

Lehmann, M., Gottschalk, B., Puchkov, D., Schmieder, P., Schwagerus, S., Hackenberger, C. P. R., et al. (2015). Multicolor caged dSTORM resolves the ultrastructure of synaptic vesicles in the brain. *Angew. Chem. Int. Edn.* 54, 13230–13235. doi: 10.1002/anie.201505138

Lichtman, J. W., and Conchello, J. A. (2005). Fluorescence microscopy. *Nat. Methods* 2, 910–919. doi: 10.1038/nmeth817

Liu, C., Kershberg, L., Wang, J., Schneeberger, S., and Kaeser, P. S. (2018). Dopamine secretion is mediated by sparse active zone-like release sites. *Cell* 172, 706–718.e15. doi: 10.1016/j.cell.2018.01.008

Mahecic, D., Testa, I., Griffié, J., and Manley, S. (2019). Strategies for increasing the throughput of super-resolution microscopies. *Curr. Opin. Chem. Biol.* 51, 84–91. doi: 10.1016/j.cbpa.2019.05.012

Maidorn, M., Olichon, A., Rizzoli, S. O., and Opazo, F. (2019). Nanobodies reveal an extra-synaptic population of SNAP-25 and Syntaxin 1A in hippocampal neurons. *MABS* 11, 305–321. doi: 10.1080/19420862.2018.1551675

Maritzen, T., and Haucke, V. (2018). Coupling of exocytosis and endocytosis at the presynaptic active zone. *Neurosci. Res.* 127, 45–52. doi: 10.1016/j.neures.2017.09.013

Maschi, D., Gramlich, M. W., and Klyachko, V. A. (2018). Myosin V functions as a vesicle tether at the plasma membrane to control neurotransmitter release in central synapses. *eLife* 7:e039440. doi: 10.7554/eLife.39440

Maschi, D., and Klyachko, V. A. (2017). Spatiotemporal regulation of synaptic vesicle fusion sites in central synapses. *Neuron* 94, 65–73.e3. doi: 10.1016/j.neuron.2017.03.006

Mayford, M., Siegelbaum, S. A., and Kandel, E. R. (2012). Synapses and memory storage. *Cold Spring Harb. Perspect. Biol.* 4, 1–18. doi: 10.1101/cshperspect.a005751

Miles, R., Tóth, K., Gulyás, A. I., Hájos, N., and Freund, T. F. (1996). Differences between somatic and dendritic inhibition in the hippocampus. *Neuron* 16, 815–823. doi: 10.1016/S0896-6273(00)80101-4

Minoshima, M., and Kikuchi, K. (2017). Photostable and photoswitching fluorescent dyes for super-resolution imaging. *J. Biol. Inorg. Chem.* 22, 639–652. doi: 10.1007/s00775-016-1435-y

Nanguneri, S., Flottmann, B., Horstmann, H., Heilemann, M., and Kuner, T. (2012). Three-dimensional, tomographic super-resolution fluorescence imaging of serially sectioned thick samples. *PLoS One* 7:e038098. doi: 10.1371/journal.pone.0038098

Neher, E. (1998). Vesicle pools and Ca2+ microdomains: new tools for understanding their roles in neurotransmitter release. *Neuron* 20, 389–399. doi: 10.1016/S0896-6273(00)80983-6

Neher, E. (2010). What is rate-limiting during sustained synaptic activity: vesicle supply or the availability of release sites. *Front. Synapt. Neurosci.* 2:144. doi: 10.3389/fnsyn.2010.00144

Novak, P., Gorelik, J., Vivekananda, U., Shevchuk, A. I., Ermolyuk, Y. S., Bailey, R. J., et al. (2013). Nanoscale-targeted patch-clamp recordings of functional presynaptic ion channels. *Neuron* 79, 1067–1077. doi: 10.1016/j.neuron.2013.07.012

Ohno-Shosaku, T., and Kano, M. (2014). Endocannabinoid-mediated retrograde modulation of synaptic transmission. *Curr. Opin. Neurobiol.* 29, 1–8. doi: 10.1016/j.conb.2014.03.017

Ouyang, W., Aristov, A., Lelek, M., Hao, X., and Zimmer, C. (2018). Deep learning massively accelerates super-resolution localization microscopy. *Nat. Biotechnol.* 36, 460–468. doi: 10.1038/nbt.4106

Palay, S. L. (1956). Synapses in the central nervous system. *J. Biophys. Biochem. Cytol.* 2, 193–202. doi: 10.1083/jcb.2.4.193

Park, D., Lee, U., Cho, E., Zhao, H., Kim, J. A., Lee, B. J., et al. (2018). Impairment of release site clearance within the active zone by reduced SCAMP5 expression causes short-term depression of synaptic release. *Cell Rep.* 22, 3339–3350. doi: 10.1016/j.celrep.2018.02.088

Patrizio, A., and Specht, C. G. (2016). Counting numbers of synaptic proteins: absolute quantification and single molecule imaging techniques. *Neurophotonics* 3:041805. doi: 10.1117/1.nph.3.4.041805

Persoon, C. M., Moro, A., Nassal, J. P., Farina, M., Broeke, J. H., Arora, S., et al. (2018). Pool size estimations for dense-core vesicles in mammalian CNS neurons. *EMBO J.* 37, 1–18. doi: 10.15252/embj.201899672

Pertsinidis, A., Mukherjee, K., Sharma, M., Pang, Z. P., Park, S. R., Zhang, Y., et al. (2013). Ultrahigh-resolution imaging reveals formation of neuronal SNARE/Munc18 complexes in situ. *Proc. Natl. Acad. Sci. U.S.A.* 110, E2812–E2820. doi: 10.1073/pnas.1310654110

Pinheiro, P. S., de Wit, H., Walter, A. M., Groffen, A. J., Verhage, M., and Sorensen, J. B. (2013). Doc2b synchronizes secretion from chromaffin cells by stimulating fast and inhibiting sustained release. *J. Neurosci.* 33, 16459–16470. doi: 10.1523/jneurosci.2656-13.2013

Pinheiro, P. S., and Mulle, C. (2008). Presynaptic glutamate receptors: physiological functions and mechanisms of action. *Nat. Rev. Neurosci.* 9, 423–436. doi: 10.1038/nrn2379

Rego, E. H., Shao, L., Macklin, J. J., Winoto, L., Johansson, G. A., Kamps-Hughes, N., et al. (2012). Nonlinear structured-illumination microscopy with a photoswitchable protein reveals cellular structures at 50-nm resolution. *Proc. Natl. Acad. Sci. U.S.A.* 109, E135–E143. doi: 10.1073/pnas.1107547108

Reymond, L., Ziegler, J., Knapp, C., Wang, F.-C., Huser, T., Ruprecht, V., et al. (2019). SIMPLE: structured illumination based point localization estimator with enhanced precision. *Opt. Express* 27:24578. doi: 10.1364/oe.27.024578

Rudolph, S., Tsai, M. C., von Gersdorff, H., and Wadiche, J. I. (2015). The ubiquitous nature of multivesicular release. *Trends Neurosci.* 38, 428–438. doi: 10.1016/j.tins.2015.05.008

Rust, M. J., Bates, M., and Zhuang, X. (2006). Sub-diffraction-limit imaging by stochastic optical reconstruction microscopy (STORM). *Nat. Methods* 3, 793–795. doi: 10.1038/nmeth929

Sakamoto, H., Ariyoshi, T., Kimpara, N., Sugao, K., Taiko, I., Takikawa, K., et al. (2018). Synaptic weight set by Munc13-1 supramolecular assemblies. *Nat. Neurosci.* 21, 41–55. doi: 10.1038/s41593-017-0041-9

Schedin-Weiss, S., Caesar, I., Winblad, B., Blom, H., and Tjernberg, L. O. (2016). Super-resolution microscopy reveals γ-secretase at both sides of the neuronal synapse. *Acta Neuropathol. Commun.* 4:29. doi: 10.1186/s40478-016-0296-5

Schermelleh, L., Ferrand, A., Huser, T., Eggeling, C., Sauer, M., Biehlmaier, O., et al. (2019). Super-resolution microscopy demystified. *Nat. Cell Biol.* 21, 72–84. doi: 10.1038/s41556-018-0251-8

Schikorski, T., and Stevens, C. F. (2001). Morphological correlates of functionally defined synaptic vesicle populations. *Nat. Neurosci.* 4, 391–395. doi: 10.1038/86042

Schmidl, L., Schmidl, G., Gawlik, A., Dellith, J., Hübner, U., Tympel, V., et al. (2019). Combining super-resolution microscopy with neuronal network recording using magnesium fluoride thin films as cover layer for multi-electrode array technology. *Sci. Rep.* 9, 1–9. doi: 10.1038/s41598-019-52397-x

Schneider, R., Hosy, E., Kohl, J., Klueva, J., Choquet, D., Thomas, U., et al. (2015). Mobility of calcium channels in the presynaptic membrane. *Neuron* 86, 672–679. doi: 10.1016/j.neuron.2015.03.050

Sharonov, A., and Hochstrasser, R. M. (2006). Wide-field subdiffraction imaging by accumulated binding of diffusing probes. *Proc. Natl. Acad. Sci. U.S.A.* 103, 18911–18916. doi: 10.1073/pnas.0609643104

Siddig, S., Aufmkolk, S., Doose, S., Jobin, M. L., Werner, C., Sauer, M., et al. (2020). Super-resolution imaging reveals the nanoscale organization of metabotropic glutamate receptors at presynaptic active zones. *Sci. Adv.* 6:eaay7193. doi: 10.1126/sciadv.aay7193

Südhof, T. C. (2012). The presynaptic active zone. *Neuron* 75, 11–25. doi: 10.1016/j.neuron.2012.06.012

Südhof, T. C. (2013). Neurotransmitter release: the last millisecond in the life of a synaptic vesicle. *Neuron* 80, 675–690. doi: 10.1016/j.neuron.2013.10.022

Suh, B.-C., Leal, K., and Hille, B. (2010). Modulation of high-voltage activated Ca(2+) channels by membrane phosphatidylinositol 4,5-bisphosphate. *Neuron* 67, 224–238. doi: 10.1016/j.neuron.2010.07.001

Sydor, A. M., Czymmek, K. J., Puchner, E. M., and Mennella, V. (2015). Super-resolution microscopy: from single molecules to supramolecular assemblies. *Trends Cell Biol.* 25, 730–748. doi: 10.1016/j.tcb.2015.10.004

Tang, A. H., Chen, H., Li, T. P., Metzbower, S. R., MacGillavry, H. D., and Blanpied, T. A. (2016). A trans-synaptic nanocolumn aligns neurotransmitter release to receptors. *Nature* 536, 210–214. doi: 10.1038/nature19058

Thiel, Z., and Rivera-Fuentes, P. (2018). Photochemically active dyes for super-resolution microscopy. *Chimia* 72, 764–770. doi: 10.2533/chimia.2018.764

Tønnesen, J., Inavalli, V. V. G. K., and Nägerl, U. V. (2018). Super-resolution imaging of the extracellular space in living brain tissue. *Cell* 172, 1108–1121.e15. doi: 10.1016/j.cell.2018.02.007

Trotter, J. H., Hao, J., Maxeiner, S., Tsetsenis, T., Liu, Z., Zhuang, X., et al. (2019). Synaptic neurexin-1 assembles into dynamically regulated active zone nanoclusters. *J. Cell Biol.* 218, 2677–2698. doi: 10.1083/JCB.201812076

Truckenbrodt, S., Maidorn, M., Crzan, D., Wildhagen, H., Kabatas, S., and Rizzoli, S. O. (2018). X10 expansion microscopy enables 25-nm resolution on conventional microscopes. *EMBO Rep.* 19:e45836. doi: 10.15252/embr.201845836

Van Den Bogaart, G., Meyenberg, K., Risselada, H. J., Amin, H., Willig, K. I., Hubrich, B. E., et al. (2011). Membrane protein sequestering by ionic protein-lipid interactions. *Nature* 479, 552–555. doi: 10.1038/nature10545

Velde, J. H. M., van der Smit, J. H., Hebisch, E., Punter, M., and Cordes, T. (2019). Self-healing dyes for super-resolution fluorescence microscopy. *J. Phys. D Appl. Phys.* 52:34001. doi: 10.1088/1361-6463/AAE752

Vyleta, N. P., and Jonas, P. (2014). Loose coupling between Ca2+ channels and release sensors at a plastic hippocampal synapse. *Science* 343, 665–670. doi: 10.1126/science.1244811

Walter, A. M., Müller, R., Tawfik, B., Wierda, K. D., Pinheiro, P. S., Nadler, A., et al. (2017). Phosphatidylinositol 4,5-bisphosphate optical uncaging potentiates exocytosis. *eLife* 6:e30203. doi: 10.7554/eLife.30203

Wang, H., Rivenson, Y., Jin, Y., Wei, Z., Gao, R., Günaydın, H., et al. (2019). Deep learning enables cross-modality super-resolution in fluorescence microscopy. *Nat. Methods* 16, 103–110. doi: 10.1038/s41592-018-0239-0

Weingarten, J., Laßek, M., Mueller, B. F., Rohmer, M., Lunger, I., Baeumlisberger, D., et al. (2014). The proteome of the presynaptic active zone from mouse brain. *Mol. Cell. Neurosci.* 59, 106–118. doi: 10.1016/j.mcn.2014.02.003

Westphal, V., Rizzoli, S. O., Lauterbach, M. A., Kamin, D., Jahn, R., and Hell, S. W. (2008). Video-rate far-field optical nanoscopy dissects synaptic vesicle movement. *Science* 320, 246–249. doi: 10.1126/science.1154228

Wilhelm, B. G., Mandad, S., Truckenbrodt, S., Kröhnert, K., Schäfer, C., Rammner, B., et al. (2014). Composition of isolated synaptic boutons reveals the amounts of vesicle trafficking proteins. *Science* 344, 1023–1028. doi: 10.1126/science.1252884

Willig, K. I., Harke, B., Medda, R., and Hell, S. W. (2007). STED microscopy with continuous wave beams. *Nat. Methods* 4, 915–918. doi: 10.1038/nmeth1108

Wong, M. Y., Liu, C., Wang, S. S. H., Roquas, A. C. F., Fowler, S. C., and Kaeser, P. S. (2018). Liprin-α3 controls vesicle docking and exocytosis at the active zone of hippocampal synapses. *Proc. Natl. Acad. Sci. U.S.A.* 115, 2234–2239. doi: 10.1073/pnas.1719012115

Wu, X., Cai, Q., Shen, Z., Chen, X., Zeng, M., Du, S., et al. (2019). RIM and RIM-BP Form presynaptic active-zone-like condensates via phase separation. *Mol. Cell* 73, 971–984.e5. doi: 10.1016/j.molcel.2018.12.007

Wu, Y., and Shroff, H. (2018). Faster, sharper, and deeper: structured illumination microscopy for biological imaging. *Nat. Methods* 15, 1011–1019. doi: 10.1038/s41592-018-0211-z

Xu, F., Zhang, M., He, W., Han, R., Xue, F., Liu, Z., et al. (2017). Live cell single molecule-guided Bayesian localization super resolution microscopy. *Cell Res.* 27, 713–716. doi: 10.1038/cr.2016.160

Xu, Y., Zhang, H., Zhang, N., Wang, X., Dang, D., Jing, X., et al. (2020). Deep-red fluorescent organic nanoparticles with high brightness and photostability for super-resolution in vitro and in vivo imaging using STED nanoscopy. *ACS Appl. Mater. Interf.* 12, 6814–6826. doi: 10.1021/acsami.9b18336

Yadav, R., and Lu, H. P. (2018). Revealing dynamically-organized receptor ion channel clusters in live cells by a correlated electric recording and super-resolution single-molecule imaging approach. *Phys. Chem. Chem. Phys.* 20, 8088–8098. doi: 10.1039/c7cp08030a

Yang, B., Przybilla, F., Mestre, M., Trebbia, J.-B., and Lounis, B. (2014). Large parallelization of STED nanoscopy using optical lattices. *Opt. Express* 22:5581. doi: 10.1364/oe.22.005581

Younts, T. J., Monday, H. R., Dudok, B., Klein, M. E., Jordan, B. A., Katona, I., et al. (2016). Presynaptic protein synthesis is required for long-term plasticity of GABA release. *Neuron* 92, 479–492. doi: 10.1016/j.neuron.2016.09.040

Conflict of Interest: The authors declare that the research was conducted in the absence of any commercial or financial relationships that could be construed as a potential conflict of interest.

Copyright © 2021 Carvalhais, Martinho, Ferreiro and Pinheiro. This is an open-access article distributed under the terms of the Creative Commons Attribution License (CC BY). The use, distribution or reproduction in other forums is permitted, provided the original author(s) and the copyright owner(s) are credited and that the original publication in this journal is cited, in accordance with accepted academic practice. No use, distribution or reproduction is permitted which does not comply with these terms.

frontiers in Neuroscience

ORIGINAL RESEARCH
published: 11 February 2021
doi: 10.3389/fnins.2021.546312

Clear and Consistent Imaging of Hippocampal Internal Architecture With High Resolution Multiple Image Co-registration and Averaging (HR-MICRA)

Lawrence Ver Hoef[1,2,3], Hrishikesh Deshpande[4], Joel Cure[4], Goutham Selladurai[1], Julia Beattie[5], Richard E. Kennedy[6], Robert C. Knowlton[7] and Jerzy P. Szaflarski[1]*

[1] Department of Neurology, The University of Alabama at Birmingham, Birmingham, AL, United States, [2] Department of Biomedical Engineering, The University of Alabama at Birmingham, Birmingham, AL, United States, [3] Neurology Service, Birmingham VA Medical Center, Birmingham, AL, United States, [4] Department of Radiology, The University of Alabama at Birmingham, Birmingham, AL, United States, [5] Division of Behavioral Medicine and Clinical Psychology, Cincinnati Children's Hospital Medical Center, Cincinnati, OH, United States, [6] Division of Gerontology, Geriatrics, and Palliative Care, Department of Medicine, The University of Alabama at Birmingham, Birmingham, AL, United States, [7] Department of Neurology, University of California, San Francisco, San Francisco, CA, United States

OPEN ACCESS

Edited by:
Alard Roebroeck, Maastricht University, Netherlands

Reviewed by:
Tae Kim, University of Pittsburgh, United States
Steffen Bollmann, The University of Queensland, Australia

***Correspondence:**
Lawrence Ver Hoef
lverhoef@uabmc.edu

Specialty section:
This article was submitted to Brain Imaging Methods, a section of the journal Frontiers in Neuroscience

Received: *27 March 2020*
Accepted: *20 January 2021*
Published: *11 February 2021*

Citation:
Ver Hoef L, Deshpande H, Cure J, Selladurai G, Beattie J, Kennedy RE, Knowlton RC and Szaflarski JP (2021) Clear and Consistent Imaging of Hippocampal Internal Architecture With High Resolution Multiple Image Co-registration and Averaging (HR-MICRA). Front. Neurosci. 15:546312. doi: 10.3389/fnins.2021.546312

Magnetic resonance imaging of hippocampal internal architecture (HIA) at 3T is challenging. HIA is defined by layers of gray and white matter that are less than 1 mm thick in the coronal plane. To visualize HIA, conventional MRI approaches have relied on sequences with high in-plane resolution (≤0.5 mm) but comparatively thick slices (2–5 mm). However, thicker slices are prone to volume averaging effects that result in loss of HIA clarity and blurring of the borders of the hippocampal subfields in up to 61% of slices as has been reported. In this work we describe an approach to hippocampal imaging that provides consistently high HIA clarity using a commonly available sequence and post-processing techniques that is flexible and may be applicable to any MRI platform. We refer to this approach as High Resolution Multiple Image Co-registration and Averaging (HR-MICRA). This approach uses a variable flip angle turbo spin echo sequence to repeatedly acquire a whole brain T2w image volume with high resolution in three dimensions in a relatively short amount of time, and then co-register the volumes to correct for movement and average the repeated scans to improve SNR. We compared the averages of 4, 9, and 16 individual scans in 20 healthy controls using a published HIA clarity rating scale. In the body of the hippocampus, the proportion of slices with good or excellent HIA clarity was 90%, 83%, and 67% for the 16x, 9x, and 4x HR-MICRA images, respectively. Using the 4x HR-MICRA images as a baseline, the 9x HR-MICRA images were 2.6 times and 16x HR-MICRA images were 3.2 times more likely to have high HIA ratings ($p < 0.001$) across all hippocampal segments (head, body, and tail). The thin slices of the HR-MICRA images allow reformatting in any plane with clear visualization of hippocampal dentation in the sagittal plane. Clear and consistent visualization of HIA will allow application of this technique to future hippocampal structure research, as well as more precise manual or automated segmentation.

Keywords: hippocampus, subfields, high-resolution MRI, internal architecture, dentation

INTRODUCTION

The hippocampus is one of the most studied subcortical structures in the brain. It has been linked to the pathobiology of epilepsy (Sloviter, 1987; De Lanerolle et al., 1989; Wieser, 2004), Alzheimer's disease (Jack et al., 1992), schizophrenia (Lahti et al., 2006; Kraguljac et al., 2013, 2016), PTSD (Smith, 2005; Shin et al., 2006; Wang et al., 2010), and TBI (Ariza et al., 2006). For many years, hippocampal imaging research focused largely on volumetric measurements and surface morphometry, but in recent years there has been increasing interest in studying specific hippocampal subfields (Mueller et al., 2007; Van Leemput et al., 2009; Yushkevich et al., 2010, 2015a; Pluta et al., 2012; Wisse et al., 2012, 2016). A number of protocols for manual subfield segmentation have been proposed and widely discussed (Zeineh et al., 2001; Mueller et al., 2007; La Joie et al., 2010; Malykhin et al., 2010; Wisse et al., 2012; Winterburn et al., 2013; Yushkevich et al., 2015a; Steve et al., 2017), and several automated subfield segmentation software tools are available (Van Leemput et al., 2009; Pipitone et al., 2014; Iglesias et al., 2015; Yushkevich et al., 2015b). Precise subfield segmentation requires direct visualization of the hippocampal internal architecture, defined by apposing layers of gray and white matter that create the characteristic spiral appearance of Ammon's horn in coronal section. Specifically, the strata radiatum, lacunosum, and moleculare (SRLM) together have a hypointense (dark) appearance on T2w scans, while the pyramidal cell layer (CA1-4) is more hyperintense and is isointense with cortical gray matter (**Figure 1**). However, the dark band of the SRLM is often not clearly or consistently seen in images acquired with conventional MRI sequences. We have previously demonstrated that hippocampal internal architecture (HIA) is seen clearly in only 39% of slices through the body of the hippocampus using common high-resolution T2-weighted coronal images (Ver Hoef et al., 2013b), and in fact even adjacent slices from a good-quality scan may show internal architecture with drastically different clarity. As a consequence, manual subfield segmentation in some slices must rely on *inferring* the boundaries of Ammon's horn based on "fuzzy" image features or expected boundary location as opposed to direct, clear visualization of the SRLM in each slice. Likewise, many of the automated methods must rely heavily on atlas/template-based approaches and somewhat less on the boundary information contained in the image itself (Wisse et al., 2014). Consequently the resulting automated segmentation may reflect the template to a greater or lesser degree than the target image.

Standard high-resolution sequences with adequate in-plane resolution (<0.5 mm) typically require a slice thickness of 2–3 mm or greater to have adequate signal-to-noise ratio (SNR). These relatively thick slices result in volume averaging of any features that vary through the thickness of a single slice. In some cases, the gray and white matter layers may be very consistent across the slice thickness resulting in clear visualization of internal architecture, while in others slices the layers may vary or undulate through the thickness of the slice resulting in blurring of these features (i.e., volume averaging effects). Sequences with relatively thinner slices, like common T1-weighted volumetric sequences with ∼1 mm isotropic resolution, lack the resolution in the coronal plane to fully depict the contours of the SRLM and Ammon's horn, which may be less than 1 mm thick. If we simply modify a typical 2D T2w TSE sequence to have thinner slices, the time of acquisition (TA) doubles for each reduction of slice thickness by half. So a 6-min scan with 3 mm thick slices would become a 12-min scan with 1.5 mm thick slices, which dramatically increases sensitivity to movement. Indeed experience teaches us that even highly motivated control subjects have a hard time remaining still enough for a 10-min scan, so simple extension of a 2D TSE sequence cannot work in this case. Further, the SNR, which is directly related to the quality of the image, drops in half when slice thickness is cut in half, resulting in a noisy image that precludes confident delineation of subtle image features such as the margins of the SRLM and hippocampal subfields. Poor SNR can be improved by acquiring multiple samples and averaging them (Bronen et al., 2002), but SNR only improves with the square root of the increase in the number of samples averaged, so to double the SNR requires increasing the number of samples by a factor of 4 and tripling the SNR requires increasing the samples by a factor of 9. The dramatically increased time this takes would absolutely necessitate compensating for the inevitable movement associated with long scanning sessions. From these considerations we can conclude that any sequence that will show hippocampal internal architecture clearly must have the following characteristics: sufficient resolution in the coronal plane to show the SRLM and boundaries of Ammon's horn clearly; sufficiently thin slices (i.e., resolution in the A-P direction) to minimize volume averaging; and the TA of a single acquisition must be reasonable so as to keep movement artifacts to a minimum in most subjects.

In this work, as proof-of-principle, we describe a flexible approach to clearly and consistently image HIA. Unlike some advanced approaches that require ultra-high field strength (e.g., 7T), special research pulse sequences, or complicated post-processing pipelines, we use a first generation clinical 3T platform with a basic 8-channel parallel coil with a commonly available sequence. The approach uses at variable flip-angle turbo spin echo sequence (BrainView, Phillips Healthcare) to acquire a 3D volumetric T2-weighted image with parameters adjusted for the

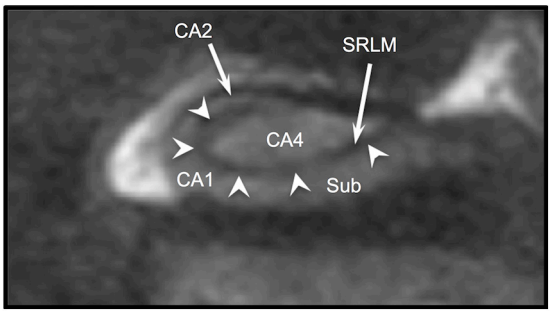

FIGURE 1 | T2w coronal section through body of hippocampus. Arrowheads indicate the "dark band" of the SRLM. Sub (subiculum), CA1, CA2, and CA4 indicate regions of Ammon's horn.

shortest possible TA while preserving gray-white contrast, but with relative disregard for SNR. By acquiring an image volume in as short TA as possible, we minimize movement artifact in the individual scan, then we repeat the scan many times and co-register each scan to the first scan in post-processing using freely available software. The co-registered scans are then averaged to improve SNR. We refer to this approach as HR-MICRA (High Resolution Multiple Image Co-registration and Averaging). While the concept of co-registering and averaging multiple scans to improve SNR is nothing new (Bronen et al., 2002), the innovation of this work lies in the combination of the specific application to HIA visualization, the counter-intuitive use of low SNR base images, and the absence of necessity of sophisticated hardware or proprietary software. We report the performance of the HR-MICRA approach in regard to depicting HIA clarity at three different levels of averaging (4x, 9x, and 16x), using a single acquisition of a common high-resolution 2D T2-weighted scan as a baseline reference. The purpose of this work is to demonstrate that it is possible to show HIA with good to excellent clarity in a high proportion of slices using relatively basic equipment and methods with this approach.

MATERIALS AND METHODS

Subject Demographics

After obtaining approval from our Institutional Review Board, 20 healthy control subjects were recruited, consented, and enrolled. Among study subjects, 11 were female, and ages ranged from 21 to 57 with a mean of 28.25 years. Four participants self-identified as African-American, 15 as white, and one as "other." Years of formal education ranged from 12 to 22 years with a mean of 16.

Imaging Sequences

All scans were performed on a Philips Achieva 3T platform with an 8-channel head coil. The HR-MICRA scans were based on a variable flip angle turbo spin echo sequence [BrainView on the Phillips platform, similar to SPACE (Sampling Perfection with Application optimized Contrasts using different flip angle Evolution) on Siemens platforms or CUBE on GE platforms]. By using a prescribed evolution of refocusing pulses with variable flip angles, this sequence preserves nearly constant T2 contrast between gray and white matter over a prolonged echo train duration allowing for over 100 echoes in a single TR (Busse et al., 2006). Since almost all of these refocusing pulses are less than 180°, long echo trains can be used without exceeding SAR limits (Busse et al., 2006) allowing for efficient acquisition of 3D T2-weighted data. While most structural imaging sequences are designed to balance TA, resolution, and SNR, this sequence was designed specifically to minimize TA for a specific target resolution while preserving *contrast* as opposed to SNR. A typical T2 sequence uses a moderately long TE (100–140 ms) and a very long TR (3000–4000 ms) to maximize longitudinal relaxation prior to the next excitation pulse. One can easily obtain high resolution within a long TR by extending the echo train length further into the TR, but this has the consequence of prolonging the effective TE, which ultimately decreases the T2 contrast between gray and white matter. This results in an image in which tissue is dark and CSF is bright, which works very well for high-resolution imaging of CSF filled structures like the semi-lunar canals and cochlea of the inner ear, but gray-white borders become indistinct. Variable flip angle sequences help with this effect dramatically by maintaining a shorter equivalent TE for a given effective TE, Busse et al. (2006) but there is a limit to this ability. In light of this, we designed our sequence with an equivalent TE that provides good gray-white contrast (143 ms), but shortened the TR dramatically from a typical TR of 3200 to 1750 ms. This results in decreased SNR due to the fact that the transverse magnetization has not fully relaxed into the longitudinal axis, but it also shortens the scan time to a reasonable amount that most subjects can remain still for. Conversely, using a more typical TR (e.g., 3200 ms), each scan would be over 11 min, but few subjects can remain still for that long.

The time-optimized sequence has an in-plane resolution of 0.5 mm in the coronal plane and a slice thickness of 0.75 mm (A-P) with a scan time of 6:02 min. The resolution of 0.5 mm in the coronal plane was chosen to ensure that HIA was visible throughout the length of the SRLM given that the thickness of this band may be slightly less than 1 mm. The slice thickness of 0.75 mm was secondarily derived as the minimum resolution that could be acquired with a target time of acquisition of approximately 6 min to minimize the likelihood of intra-scan movement. We chose to use this non-isotropic resolution with lower resolution in the A-P direction instead of a larger isotropic voxel size because curvature of the SRLM in A-P direction is generally less than in the coronal plane, and we wanted to maintain high resolution in the plane in which HIA is visualized. This is a whole-brain sequence with parameters as follows: FOV (mm) = FH 200/RL 178/AP 219, TR (ms) = 1750, TE_{eff}/TE_{equiv} (ms) = 348/143, TSE factor = 100, Echo spacing (ms) = 6.0, and Echo train duration (ms) = 643. This sequence was repeated 16 times over one long session for most subjects. For two subjects, the scan was broken into two shorter sessions due to subject and scanner availability. There was no perceptible difference in the scan-to-scan variation between individual scans acquired across two sessions as compared to those acquired within a single session. The total scan time for all 16 iterations of the sequence is 96.5 min, not including brief pauses between scans to check on patient comfort. In post-processing, the scans were co-registered using FSL-FLIRT (Jenkinson et al., 2002) and averaged. A shell script to perform co-registration and averaging along with detailed instructions are included in the **Supplementary Material**. To assess the effect of the number of scans averaged on image quality, mean images were generated from a subset of 4 and 9 scans as well as the total 16 scans (HR-MICRA 4x, HR-MICRA 9x, and HR-MICRA 16x), which reflect a theoretical improvement in SNR by a factor of 2, 3, and 4, respectively, over a single base scan. In a few subjects, one to four scans were discarded due to obvious, marked intra-scan movement artifact such that inclusion in the average would degrade image quality. Scans with minor movement artifact were not excluded. One subject had one scan removed, two subjects had two scans removed, one subject had three scans removed, and three subjects had four scans removed. The removed scans tended to be at

the end of the scanning session, presumably due to the fact that some subjects were becoming restless due to the long scanning session. In cases where scans were removed due to movement, the remaining scans were averaged and used in place of the full set of 16 scans in reporting the proportions of slices with each HIA score because to remove them could artificially inflate the proportion of good or excellent slices, which would be a misrepresentation of what was available with the investment of time to acquire all 16 scans. However, the statistical model used the exact number of scans used to estimate the relationship between HIA clarity and number of scans averaged. The presence of a shortened dataset due to movement was included in our multivariate logistic regression model and did not significantly affect the results when correcting for the number of scans used.

Image Scoring

After generating separate mean images (HR-MICRA 4x, HR-MICRA 9x, and HR-MICRA 16x), each slice through the hippocampi was scored on each side for HIA clarity according to a previously published and validated rating scale (Ver Hoef et al., 2013a). This rating scale is based on clarity of visualization of the hypointense band of the SRLM allowing delineation of hippocampal subfields and is described in brief in **Figure 2** (Ver Hoef et al., 2013a). Scoring was performed by one of two experienced raters (LWV, JC), both of whom were involved in a previous study describing the rating system and reporting its inter-rater reliability. Because inter-rater reliability was already established and published including these two raters (Ver Hoef et al., 2013a), it was not deemed necessary to repeat it within this dataset.

The anatomic differences of the head, body, and tail make imaging HIA more or less challenging in different segments, particularly the digitations of the head. Therefore each segment (head, body, and tail) was scored separately. Similar to other published hippocampal segmentation schemes (Boccardi et al., 2015), the landmark for the boundary between head and body was the first slice in which the hippocampus shows the characteristic c-shaped appearance and is not a double-layered structure, and boundary between body and tail was the first coronal slice showing in which the quadrigeminal cistern can be seen in the midline (i.e., the plane of the superior and inferior colliculi). In the most anterior slices through the head, the SRLM appears as a single horizontal line without distinct subfields, so scoring in the head started six slices posterior to the first slice in which the SRLM is visible. In the tail, scoring continued until the hippocampal gray matter abuts the splenium of the corpus callosum. Scores in the head, body, and tail are reported separately and together.

Statistical Analysis

We used generalized estimating equations (GEE) for ordinal data (Heagerty and Zeger, 1996) to examine the association between

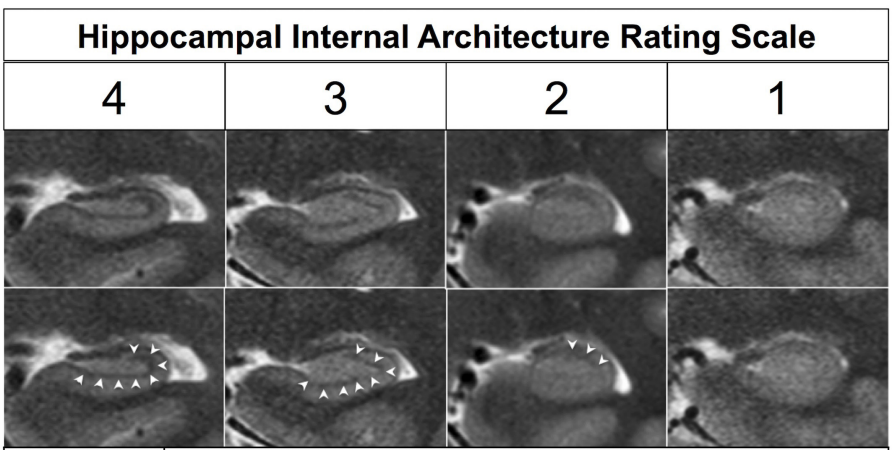

Score	Description
4	**Excellent HIA clarity** – All subfields are clearly defined with excellent contrast between SRLM and gray matter of Ammon's horn.
3	**Good HIA clarity** – Subfields are readily discernable with moderate contrast between SRLM and gray matter of Ammon's horn or only a short discontinuity in the hypointense band that does not preclude inferring the boundaries of the gray matter layers.
2	**Poor HIA clarity** – Only a portion of the hypointense band is clearly visible leaving a significant portion of the boundaries of Ammon's horn ambiguous.
1	**No discernable HIA** – The hypointense band of the SRLM cannot be confidently identified leaving the boundaries of all subfields undefined.

FIGURE 2 | Description of the previously published HIA rating system. The images show examples of each of the four scoring levels. The both rows of images are identical except for the addition of arrowheads in the bottom row to indicate the dark band of the SRLM.

HIA ratings of hippocampal architecture clarity and image type (4x HR-MICRA, 9x HR-MICRA, and 16x HR-MICRA) and side (left, right) for each slice. GEE was employed as it utilizes data from all participants and provides more robust estimates in the presence of missing data (Schafer and Graham, 2002). All analyses modeled the odds of higher ratings (better clarity) with the 4x HR-MICRA images used as the reference category. Since SNR increases with the square root of the number of averages, we modeled the relationship between number of averages and improvement in HIA clarity using the *square root* of the number of averages instead of as a direct linear relationship between the raw number of averages. An exchangeable correlation structure was used to model the correlation of scores among images obtained from the same participant. Analyses were performed using the *geepack* package (Halekoh et al., 2006), version 1.2-1, in the R statistical environment, version 3.5.0 (R Core Team, 2017).

RESULTS

As expected, an obvious reduction in noise is visible with the increased number of samples averaged using the HR-MICRA approach. **Figure 3** illustrates how image quality and HIA clarity improves from a single scan to HR-MICRA 4x, HR-MICRA 9x, and HR-MICRA 16x. Examples of HIA clarity in representative slices of each hippocampal segment are shown in **Figure 4** depicting their markedly different cross sectional appearances. The distribution of HIA scores for the head, body, tail, and total hippocampus are shown in **Figure 5**. An HIA score of 3 or 4 indicates that all subfields can be directly visualized; therefore for purposes of doing accurate subfield segmentation, the proportion of slices rated as a 3 or greater is the best metric of performance. In the body of the hippocampus, the proportion of slices scoring 3 or greater is 90%, 83%, and 67% for the 16x, 9x, and 4x HR-MICRA images, respectively. Using the 4x HR-MICRA images

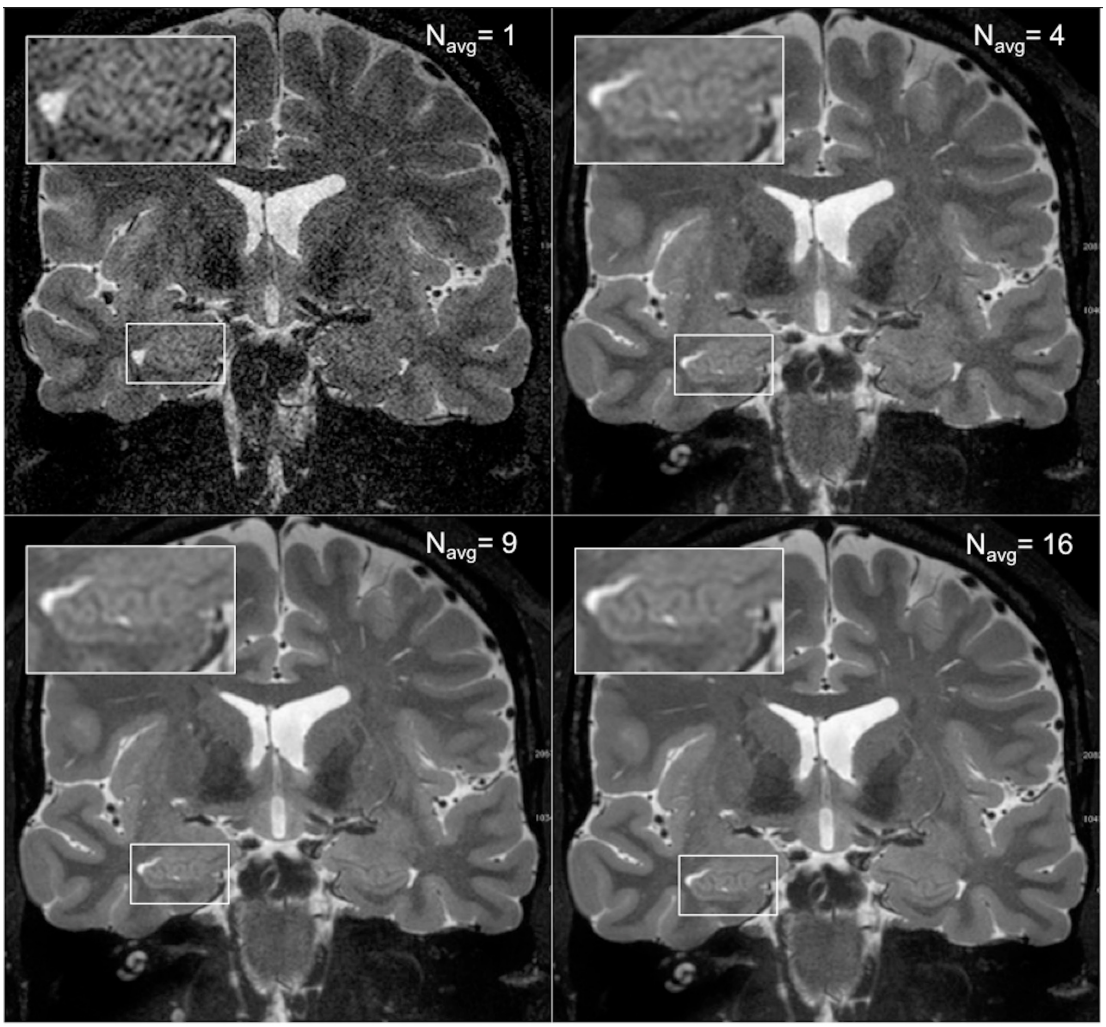

FIGURE 3 | The four panels show how image quality improves with increasing the number of scans averaged. The **upper right panel** shows a single scan and the inset box shows that essentially no internal structure can be distinguished from background noise. The subsequent panels show the result of averages of 4, 9, and 16 samples, which corresponds to a boost of SNR by a factor of 2, 3, and 4, respectively, and increased clarity of the digitations of the hippocampal head.

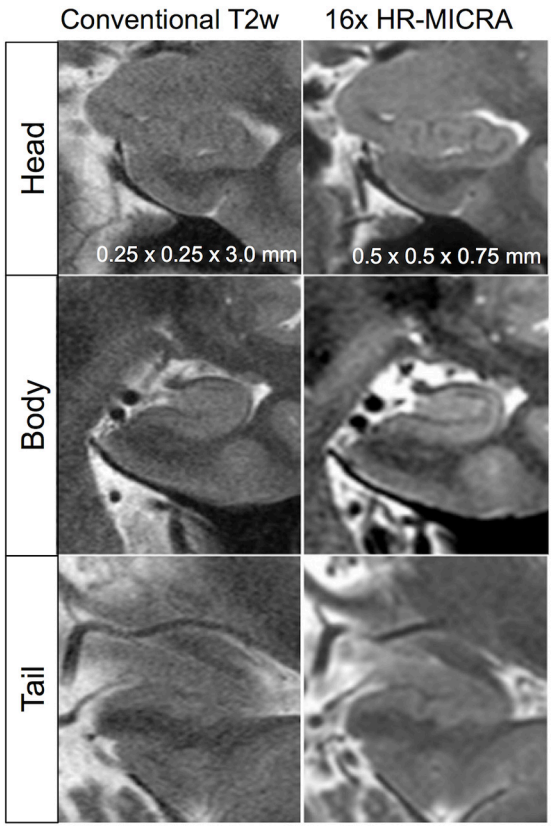

FIGURE 4 | Illustration of differences in internal architecture clarity between standard T2w images and 16x HR-MICRA images across hippocampal segments in a single subject.

as a baseline, the 9x HR-MICRA images were 2.6 times, and 16x HR-MICRA images were 3.2 times more likely to have high HIA ratings ($p < 0.001$). As expected, due to differences in the complexity of anatomy across the three segments of the hippocampus the data shows the head has 58% more low ratings (2 or less) than the body ($p < 0.001$) across all HR-MICRA images. The ratings for the tail segment were also lower, but this was not statistically significant ($p = 0.06$). No significant differences in HIA scores were seen between left and right sides ($p = 0.627$) across all image types.

Key to demonstrating HIA clearly is obtaining slices that are thin enough to minimize volume averaging effect. A common 2D coronal T2w sequence used at our institution has an in-plane resolution of ∼0.25 mm and slices that are 3 mm thick versus the HR-MICRA images that are 0.75 mm thick, thus four HR-MICRA slices cover the same 3 mm thick slab of tissue represented by a single conventional T2 slice. As such, any feature of the image that is consistent across all four HR-MICRA slices will be represented well in a single conventional T2w slice, but any features that vary across those four slices will be blurred in the conventional T2w slice due to volume averaging. This is illustrated in **Figure 6**. Specifically, note that the lateral inferior portion of the SRLM in the conventional T2 slice is blurred, but the four HR-MICRA images that correspond to the same slab show that the contour of the SRLM is changing markedly in this area from slice to slice, even with a slice thickness of only 0.75 mm. By contrast, on the right side the SRLM has a more consistent appearance across three of the four HR-MICRA slices in the CA1 region, which translates to good HIA clarity in the corresponding conventional T2w image. It is also important to note that the HR-MICRA images in **Figure 6** show the SRLM more clearly despite the fact that the *in-plane* resolution of the HR-MICRA images (0.5 mm) is significantly less than that of the conventional T2w images (0.25 mm).

Because the HR-MICRA approach is a 3D acquisition with a sub-millimeter slice thickness, the 3D volumes can be reformatted in any plane with good image clarity. This allows for clear visualization of hippocampal dentation, a morphologic feature of the human hippocampus that varies dramatically across healthy individuals and correlates with measures of memory (Beattie et al., 2017). While some individuals have rather "smooth" contours on the inferior aspect of the hippocampus, other individuals show a prominently dentated (tooth-like) appearance of the inferior aspect of the hippocampus as shown in **Figure 7**. Note that both of the individuals in this figure are healthy controls, so the variation in the degree of complexity of the hippocampal contours is not due to pathology. In contrast, all information about dentation is lost when conventional 2D approaches with thicker slices are used as shown in **Figure 7**.

While diagrams of the hippocampus and exemplary MRI images almost universally show SRLM to have a perfect C-shape (**Figure 1**), thin-sliced images can show a great deal of variation in the appearance of the SRLM, particularly in subjects with prominently dentated hippocampi. **Figure 8** demonstrates how the SRLM can vary from being a thin band to a very thick band or even thin discontinuous segments in adjacent slices depending how it cuts through the folds in CA1 that create hippocampal dentation.

DISCUSSION

Many reports have been written about subfield segmentation but rarely is it stated how clearly the imaging sequence used showed HIA, or if it is mentioned, the ability of a particular sequence to show HIA is not examined rigorously. Instead it is generally merely presumed that HIA is shown well enough to outline subfields or at least to infer their location from surrounding landmarks. Similarly, automated subfield segmentation algorithms tend to rely heavily on atlas templates to apply probabilistic estimates of subfield boundaries to fill in gaps when the source image is not clear and may even segment a subfield that is not visible in the source image. In this work we evaluate HR-MICRA, an approach that allows direct visualization of the hippocampal internal architecture and hippocampal subfields and we rigorously examine its performance. We show HR-MICRA's ability to delineate all subfields clearly in the hippocampal body in up to 90% of individual slices. Furthermore, the location of subfields in most of the other suboptimal slices may be reasonably estimated from adjacent slices because they are

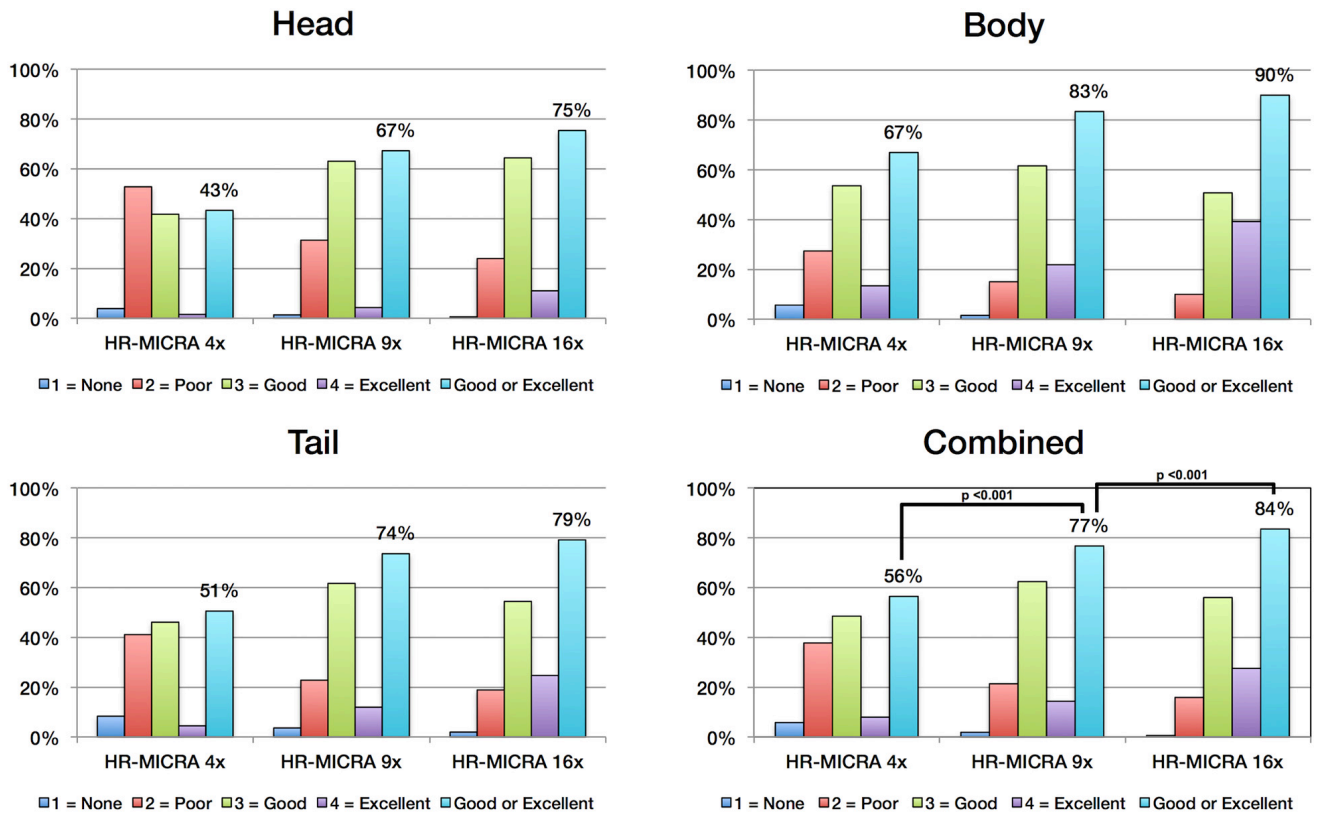

FIGURE 5 | Charts show the distribution of HIA scores for each hippocampal segment and for all segments combined. Each bar represents the percent of slices across all subjects receiving the designated HIA score. The light blue colored bar indicates the percentage of slices scored as a 3 or 4, which is sufficient for direct visualization of all subfields. Statistically significant comparisons are marked with bars between pairs.

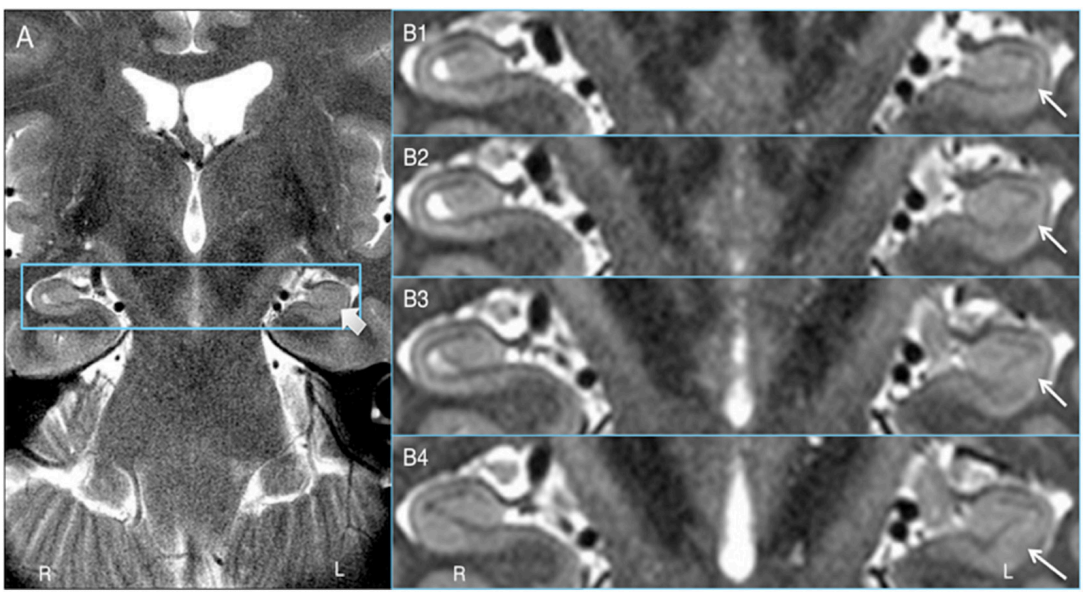

FIGURE 6 | Volume averaging effects. **(A)** shows a 3 mm thick standard T2 slice and the thick arrow showing blurring of the SRLM. **(B1–4)** shows four contiguous 0.75 mm thick HR-MICRA slices that together cover the same 3.0 mm thick coronal slab as **(A)**. The thin arrows show that the contour of the SRLM on the left varies significantly from slice to slice in the inferolateral aspect of the hippocampus, which results in blurring in that portion of the SRLM in **(A)** due to volume averaging. The SRLM of the right hippocampus is generally consistent across slices in **(B1–4)** and is not blurred in **(A)**.

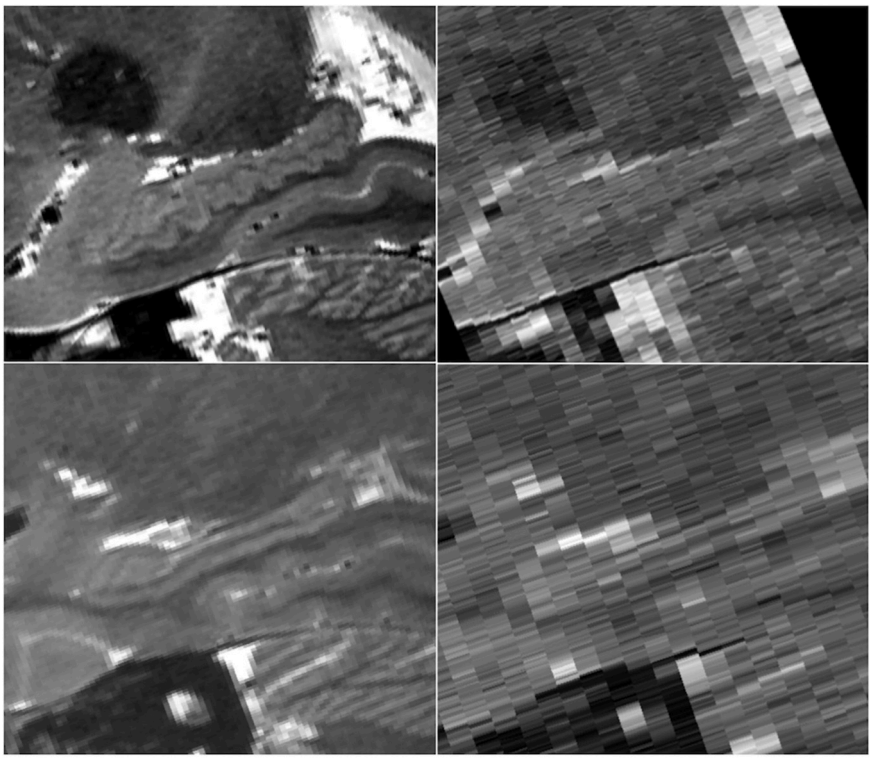

FIGURE 7 | Sagittal views of a prominently dentated hippocampus **(top)** and minimally dentation hippocampus **(bottom)** using HR-MICRA 16x **(left)** and conventional T2 **(right)**. The difference in dentation between the upper and lower images is obvious in the HR-MICRA images, but the thick slices of the conventional T2 image do not allow differentiation between the two. Images are not interpolated.

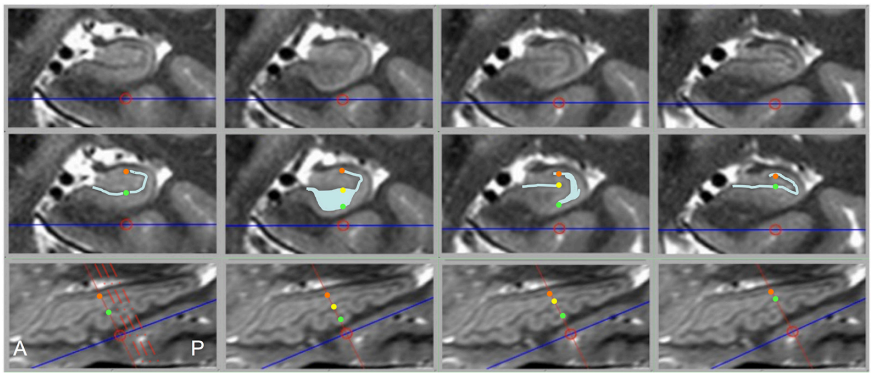

FIGURE 8 | Dramatic changes in SRLM shape can be seen in consecutive slices in prominently dentated hippocampi. The **top row** shows coronal slices through a left hippocampus and **middle row** shows identical slices with the SRLM highlighted in light blue and index points marked with colored dots. The **bottom row** shows a sagittal slice through the same hippocampus. Solid red lines indicate the slice location of the images above, the dashed red lines in the bottom left image indicate the relative location of the other three slices, and the colored dots indicate the location of the corresponding dots in the **middle row**. In the first and last column, the SRLM has a simple curvilinear shape, but in the second column the SRLM is cut *en face* as it dips down into a dente (fold in CA1) and widens in appearance. In the third column, the SRLM is split into two parts as it weaves in and out of the plane of section.

likely to have good clarity and with minimal interpolation error due to the small slice thickness.

Not only does this approach provide greater clarity of each slice, it provides many more slices and correspondingly much more data. Because the coronal slice thickness of HR-MICRA images is less than 1 mm, the image volumes are amenable to reformatting in any plane. This is best illustrated in visualizing the complex contours of hippocampal dentation in the sagittal plane, which would be impossible to visualize with common 2D approaches (**Figure 7**). Angulation of the plane of section such that it is orthogonal to the long axis of the hippocampus is important to optimize HIA clarity when slices

are relatively thick, but for many subjects, particularly those with prominent dentation, slice thicknesses in the range of 2–4 mm are insufficient to avoid volume averaging effects, as seen in **Figure 6**. Ideally, the slice thickness should be relatively small compared to the contour of the structure to be visualized for volume averaging effects to be ameliorated, and contour information of features that vary significantly across a thick slice cannot be seen even with many averages. Dentation can be visualized to a limited degree in other 3D volumetric sequences, such as a T1w MPRAGE, but only when HIA is seen with sufficient contrast in the coronal plane can distinct gray and white matter layers be visualized in the sagittal plane. So, while dentation may be appreciated as bumps on the inferior surface in common T1w images, HR-MICRA images allow visualization of all the layers and the full extent of in-folding of CA1.

Thinner slices will also allow for more precise measurements of subfield volumes and surface contours, particularly in cases with prominent dentation where the subfield pattern varies significantly from slice to slice. Consistent and clear visualization of HIA should also allow automated or semi-automated subfield segmentation algorithms to more accurately define these small, but distinct, and important regions of interest by relying more on the features of the image and less on an atlas template. In this study, averaged images were created in the same resolution as the source images using linear registration methods for simplicity sake. However, image quality potentially could be further improved by upsampling images to an even higher resolution and/or employing non-linear registration techniques as has been demonstrated elsewhere (Shaw et al., 2019). While the ability to show HIA clearly with this approach is very good, it is not perfect. In fact, one in 10 of slices through the body show suboptimal HIA clarity, as well as one in four in the head and approximately one in five in the tail. However, these limitations should be considered in context. First, even with relatively thin slices of 0.75 mm, volume averaging effects are still at play for layers that dramatically undulate through the plane of section as seen in the second column of **Figure 8**. This phenomenon, particularly frequent in subjects with prominent dentation, is a common cause of blurring of HIA in the body and tail. This will always be a factor for visualizing HIA until slices become extremely thin (e.g., much less than 0.5 mm), which will be very challenging at 3T. Second, using a sub-millimeter slice thickness provides many more slices, which minimizes error that comes from inferring the location of an ambiguous subfield boundary. For example, if only one in ten or one in five slices shows suboptimal HIA out of 60 slices through a typical 4.5 cm long hippocampus, the contours of the subfield boundaries can be reasonably estimated from surround slices with minimal error. Furthermore, most of the suboptimal slices still show some degree of internal architecture [HIA rating of 2 (**Figure 2**)], and no slices in the body (for HR-MICRA 16x) and very small percent in the head and tail show no internal architecture at all. This means that using adjacent slices to infer the location of the SRLM, which defines HIA, is only necessary for *part* of the SRLM in almost all cases, which further minimizes error. With HR-MICRA, subfield definition in the body is excellent, which is the area focused on the most in the subfield segmentation literature. While HIA clarity is not as consistent in the head and tail as it is in the body, which is a nearly always the case in *in vivo* hippocampal imaging, our finding of good HIA clarity in 75%+ of slices in the head or tail is remarkable compared to standard T2 sequences with thick slices that virtually never show HIA clearly in the head and tail.

The obvious limitation of this approach is the amount of time it takes to acquire a full dataset. The 16x HR-MICRA scans take well over 1 h. However, several factors are important to consider. First, The approach is flexible and can be adapted to, however, much time is available. Even the 4x HR-MICRA images showed HIA significantly better than conventional T2 images. The repetition of the sequence up to 16 times here was not intended to be the most common implementation of this approach, but rather to demonstrate how good the performance can be if enough time is committed. The improvement in percentage of scans showing HIA clearly is roughly linear from 4 to 9 to 16 averages, which is consistent with the theoretical linear relationship between SNR and the square of the number of images averaged. As such, if the scan time did not allow acquiring four scans, one could extrapolate the SNR of averaging less scans, which would be proportional to the ratio of the square root of the number of scans averaged [e.g., SNR_3/SNR_4 = sqrt(3)/sqrt(4) = 0.87]. This yields an estimated 13% decrement in clarity using a three-scan average and 29% decrement using a two-scan average compared to a four-scan average. Likewise, the clarity for any higher number of scans could be estimated in a similar fashion. Second, the current experiments were performed on a first-generation clinical 3T scanner (installed 2004) with only an 8-channel parallel coil to demonstrate that high-resolution 3D data sets can be generated without the necessity of ultra high field scanners (7T+) or state-of-the-art high performance 3T scanners, which makes access to such high quality images far more widespread. Given enough time and repetitions, virtually any scanner worldwide could generate very high quality images with this approach, even with field strengths lower than 3T. We have, however, implemented a similar sequence on a Siemens Prisma platform (Siemens Healthcare, Erlangen, Germany) with a high performance gradient set and 64-channel head coil and are able to generate a 6x average image that is similar to the 16x HR-MICRA images in this study, for a time savings of almost two-thirds (data not shown). Higher channel-count coils (e.g., 32, 48, and 64) that are commonly available now allow both higher SNR and better parallel acceleration. Third, at this point this approach is not intended to be used as part of a routine clinical study, but rather as a research tool for investigating the hippocampus or other brain structures requiring high resolution in all three dimensions. Though, combining this approach with other highly accelerated MRI acquisition techniques, such as CAIPI imaging (Breuer et al., 2006; Bilgic et al., 2015) (Controlled Aliasing in Parallel Imaging Results in Higher Acceleration), other forms of simultaneous multi-slice imaging (Barth et al., 2016), or compressed sensing (Lustig et al., 2007; Toledano-Massiah et al., 2018) for example, may further compress the total study time to something reasonable for a research protocol. In any case, we want to be very clear that this approach is best suited for applications that place a premium on hippocampal internal

architecture clarity and can justify investing significant scanner time to obtain high resolution hippocampal images and is not intended to be used in routine clinical scans.

Numerous factors affect SNR including TE, TR, acceleration factor, acquisition scheme (2D vs. 3D, constant refocusing flip angle vs. variable flip angle), and many others. And as described in the "Materials and Methods" section, we deliberately chose a short TR in order to get more TRs in limited time to scan the whole volume, but the short TR limits the relaxation between excitations and consequently decreases the SNR because there is less longitudinal magnetization to be excited at the beginning of the next TR. However, this short TR allows scanning of a large, high-resolution volume in a reasonable period of time (which minimizes movement) with good gray-white contrast, at the expense of SNR. SNR can be compensated for with co-registration and averaging of additional acquisitions, but intra-scan movement and poor gray-white contrast that come with longer sequences with better SNR cannot.

There is a slight smoothing effect that comes from interpolation in resampling a co-registered image volume. This effect is more prominent when the source image and target image have different resolutions. Since our images were all of identical resolution, we did not consider this to be a significant factor and any smoothing that may be present was not apparent in visual comparison of the original reference image to the co-registered images. A nearest neighbor interpolation scheme would avoid any smoothing, but is not commonly used. Moreover, since the approach relies heavily on averaging anyway the effect of smoothing from interpolation is expected to be comparatively small.

CONCLUSION

High Resolution Multiple Image Co-registration and Averaging is a flexible approach that provides consistently clear visualization of HIA that is notably inconsistent in common 2D TSE scans. Using thin coronal slices not only minimizes volume averaging effects but also allows reformatting in any plane of section, which allows for study of hippocampal morphologic features such as dentation. The improved clarity of HIA visualization allows more precise and accurate segmentation of hippocampal subfields as well as more sensitive detection of pathologic alterations of HIA. This approach was demonstrated using a basic 3T imaging platform without advanced head coils, advanced pulse sequences, or proprietary processing software, making it widely accessible to any imaging laboratory. Furthermore, the approach is generally applicable to and will further benefit from advanced imaging techniques like ultra high field imaging, high channel head coils, and accelerated pulse sequences and reconstruction schemes.

DATA AVAILABILITY STATEMENT

Data used in the study will be made available to investigators upon request after receipt of an IRB approved protocol and a signed data use agreement from the receiving institution.

ETHICS STATEMENT

The studies involving human participants were reviewed and approved by the Institutional Review Board, The University of Alabama at Birmingham, Birmingham, AL, United States. The patients/participants provided their written informed consent to participate in this study.

AUTHOR CONTRIBUTIONS

LV: conceptualization, formal analysis, funding acquisition, investigation, methodology, project administration, supervision, roles/writing – original draft, and writing – review and editing. HD: data curation and investigation. JC: formal analysis. GS: data curation and writing – review and editing. JB: data curation, investigation, and writing – review and editing. REK: formal analysis, methodology, software, and writing – review and editing. RCK: conceptualization, methodology, and writing – review and editing. JS: conceptualization and writing – review and editing. All authors contributed to the article and approved the submitted version.

FUNDING

This work was supported by the National Institutes of Health (K23EB008452 and R01NS094743).

SUPPLEMENTARY MATERIAL

The Supplementary Material for this article can be found online at: https://www.frontiersin.org/articles/10.3389/fnins.2021.546312/full#supplementary-material

REFERENCES

Ariza, M., Serra-Grabulosa, J. M., Junqué, C., Ramírez, B., Mataró, M., Poca, A., et al. (2006). Hippocampal head atrophy after traumatic brain injury. *Neuropsychologia* 44, 1956–1961. doi: 10.1016/j.neuropsychologia.2005.11.007

Barth, M., Breuer, F., Koopmans, P. J., Norris, D. G., and Poser, B. A. (2016). Simultaneous multislice (SMS) imaging techniques. *Magn. Reson. Med.* 75, 63–81. doi: 10.1002/mrm.25897

Beattie, J. F., Martin, R. C., Kana, R. K., Deshpande, H., Lee, S., Curé, J., et al. (2017). Hippocampal dentation: structural variation and its association with episodic memory in healthy adults. *Neuropsychologia* 101, 65–75. doi: 10.1016/j.neuropsychologia.2017.04.036

Bilgic, B., Gagoski, B. A., Cauley, S. F., Fan, A. P., Polimeni, J. R., Grant, P. E., et al. (2015). Wave-CAIPI for highly accelerated 3D imaging. *Magn. Reson. Med.* 73, 2152–2162. doi: 10.1002/mrm.25347

Boccardi, M., Bocchetta, M., Apostolova, L. G., Barnes, J., Bartzokis, G., Corbetta, G., et al. (2015). Delphi definition of the EADC-ADNI harmonized protocol for hippocampal segmentation on magnetic resonance. *Alzheimers Dement.* 11, 126–138. doi: 10.1016/j.jalz.2014.02.009

Breuer, F. A., Blaimer, M., Mueller, M. F., Seiberlich, N., Heidemann, R. M., Griswold, M. A., et al. (2006). Controlled aliasing in volumetric parallel imaging (2D CAIPIRINHA). *Magn. Reson. Med.* 55, 549–556. doi: 10.1002/mrm.20787

Bronen, R. A., Knowlton, R., Garwood, M., Maravilla, K. R., and Jack, CR. Jr. (2002). High-resolution imaging in epilepsy. *Epilepsia* 43, 11–18.

Busse, R. F., Hariharan, H., Vu, A., and Brittain, J. H. (2006). Fast spin echo sequences with very long echo trains: design of variable refocusing flip angle schedules and generation of clinical T2 contrast. *Magn. Reson. Med.* 55, 1030–1037. doi: 10.1002/mrm.20863

De Lanerolle, N. C., Kim, J. H., Robbins, R. J., and Spencer, D. D. (1989). Hippocampal interneuron loss and plasticity in human temporal lobe epilepsy. *Brain Res.* 495, 387–395. doi: 10.1016/0006-8993(89)90234-5

Halekoh, U., Højsgaard, S., and Yan, J. (2006). The R package geepack for generalized estimating equations. *J. Stat. Softw.* 15, 1–11. doi: 10.1201/9781420035285.ch1

Heagerty, P. J., and Zeger, S. L. (1996). Marginal regression models for clustered ordinal measurements. *J. Am. Stat. Assoc.* 91, 1024–1036. doi: 10.1080/01621459.1996.10476973

Iglesias, J. E., Augustinack, J. C., Nguyen, K., Player, C. M., Player, A., Wright, M., et al. (2015). A computational atlas of the hippocampal formation using ex vivo, ultra-high resolution MRI: application to adaptive segmentation of in vivo MRI. *NeuroImage* 115, 117–137. doi: 10.1016/j.neuroimage.2015.04.042

Jack, C. R., Petersen, R. C., O'Brien, P. C., and Tangalos, E. G. (1992). MR—based hippocampal volumetry in the diagnosis of Alzheimer's disease. *Neurology* 42:183. doi: 10.1212/wnl.42.1.183

Jenkinson, M., Bannister, P., Brady, M., and Smith, S. (2002). Improved optimization for the robust and accurate linear registration and motion correction of brain images. *NeuroImage* 17, 825–841. doi: 10.1006/nimg.2002.1132

Kraguljac, N. V., White, D. M., Hadley, N., Hadley, N., Hadley, J. A., Ver Hoef, L., et al. (2016). Aberrant hippocampal connectivity in unmedicated patients with schizophrenia and effects of antipsychotic medication: a longitudinal resting state functional MRI study. *Schizophr. Bull.* 42:1046. doi: 10.1093/schbul/sbv228

Kraguljac, N. V., White, D. M., Reid, M. A., and Lahti, A. C. (2013). Increased hippocampal glutamate and volumetric deficits in unmedicated patients with schizophrenia. *JAMA Psychiatry* 70, 1294–1302. doi: 10.1001/jamapsychiatry.2013.2437

La Joie, R., Fouquet, M., Mézenge, F., Landeau, B., Villain, N., Mevel, K., et al. (2010). Differential effect of age on hippocampal subfields assessed using a new high-resolution 3T MR sequence. *NeuroImage* 53, 506–514. doi: 10.1016/j.neuroimage.2010.06.024

Lahti, A. C., Weiler, M. A., Holcomb, H. H., Tamminga, C. A., Carpenter, W. T. Jr., and McMahon, R. (2006). Correlations between rCBF and symptoms in two independent cohorts of drug-free patients with schizophrenia. *Neuropsychopharmacology* 31:221. doi: 10.1038/sj.npp.1300837

Lustig, M., Donoho, D., and Pauly, J. M. (2007). Sparse MRI: the application of compressed sensing for rapid MR imaging. *Magn. Reson. Med.* 58, 1182–1195. doi: 10.1002/mrm.21391

Malykhin, N. V., Lebel, R. M., Coupland, N. J., Wilman, A. H., and Carter, R. (2010). In vivo quantification of hippocampal subfields using 4.7 T fast spin echo imaging. *NeuroImage* 49, 1224–1230. doi: 10.1016/j.neuroimage.2009.09.042

Mueller, S. G., Stables, L., Du, A. T., Schuff, N., Truran, D., Cashdollar, N., et al. (2007). Measurement of hippocampal subfields and age-related changes with high resolution MRI at 4 T. *Neurobiol. Aging* 28, 719–726. doi: 10.1016/j.neurobiolaging.2006.03.007

Pipitone, J., Park, M. T. M., Winterburn, J., Lett, T. A., Lerch, J. P., Pruessner, J. C., et al. (2014). Multi-atlas segmentation of the whole hippocampus and subfields using multiple automatically generated templates. *NeuroImage* 101, 494–512. doi: 10.1016/j.neuroimage.2014.04.054

Pluta, J., Yushkevich, P., Das, S., and Wolk, D. (2012). In vivo analysis of hippocampal subfield atrophy in mild cognitive impairment via semi-automatic segmentation of T2-weighted MRI. *J. Alzheimers Dis.* 31, 85–99. doi: 10.3233/jad-2012-111931

R Core Team (2017). *R: A Language and Environment for Statistical Computing*. Vienna: R Foundation for Statistical Computing.

Schafer, J. L., and Graham, J. W. (2002). Missing data: our view of the state of the art. *Psychol. Methods* 7:147. doi: 10.1037/1082-989x.7.2.147

Shaw, T. B., Bollmann, S., Atcheson, N. T., Strike, L. T., Guo, C., McMahon, K. L., et al. (2019). Non-linear realignment improves hippocampus subfield segmentation reliability. *NeuroImage* 203:116206. doi: 10.1016/j.neuroimage.2019.116206

Shin, L. M., Rauch, S. L., and Pitman, R. K. (2006). Amygdala, medial prefrontal cortex, and hippocampal function in PTSD. *Ann. N. Y. Acad. Sci.* 1071, 67–79. doi: 10.1196/annals.1364.007

Sloviter, R. S. (1987). Decreased hippocampal inhibition and a selective loss of interneurons in experimental epilepsy. *Science* 235, 73–76. doi: 10.1126/science.2879352

Smith, M. E. (2005). Bilateral hippocampal volume reduction in adults with post—traumatic stress disorder: a meta—analysis of structural MRI studies. *Hippocampus* 15, 798–807. doi: 10.1002/hipo.20102

Steve, T. A., Yasuda, C. L., Coras, R., Lail, M., Blumcke, I., Livy, D. J., et al. (2017). Development of a histologically validated segmentation protocol for the hippocampal body. *NeuroImage* 157, 219–232. doi: 10.1016/j.neuroimage.2017.06.008

Toledano-Massiah, S., Sayadi, A., De Boer, R., Gelderblom, J., Mahdjoub, R., Gerber, S., et al. (2018). Accuracy of the compressed sensing accelerated 3D-FLAIR sequence for the detection of MS plaques at 3T. *Am. J. Neuroradiol.* 39, 454–458. doi: 10.3174/ajnr.a5517

Van Leemput, K., Bakkour, A., Benner, T., Wiggins, G., Wald, L. L., Augustinack, J., et al. (2009). Automated segmentation of hippocampal subfields from ultra—high resolution in vivo MRI. *Hippocampus* 19, 549–557. doi: 10.1002/hipo.20615

Ver Hoef, L. W., Paige, A. L., Riley, K. O., Cure, J., Soltani, M., Williams, F. B., et al. (2013a). Evaluating hippocampal internal architecture on MRI: inter-rater reliability of a proposed scoring system. *Epilepsy Res.* 106, 146–154. doi: 10.1016/j.eplepsyres.2013.05.009

Ver Hoef, L. W., Williams, F. B., Kennedy, R. E., Szaflarski, J. P., and Knowlton, R. C. (2013b). Predictive value of hippocampal internal architecture asymmetry in temporal lobe epilepsy. *Epilepsy Res.* 106, 155–163. doi: 10.1016/j.eplepsyres.2013.05.008

Wang, Z., Neylan, T. C., Mueller, S. G., Lenoci, M., Truran, D., Marmar, C. R., et al. (2010). Magnetic resonance imaging of hippocampal subfields in posttraumatic stress disorder. *Arch. Gen. Psychiatry* 67, 296–303. doi: 10.1001/archgenpsychiatry.2009.205

Wieser, H.-G. (2004). ILAE commission report. mesial temporal lobe epilepsy with hippocampal sclerosis. *Epilepsia* 45, 695–714. doi: 10.1111/j.0013-9580.2004.09004.x

Winterburn, J. L., Pruessner, J. C., Chavez, S., Schira, M. M., Lobaugh, N. J., Voineskos, A. N., et al. (2013). A novel in vivo atlas of human hippocampal subfields using high-resolution 3 T magnetic resonance imaging. *NeuroImage* 74, 254–265. doi: 10.1016/j.neuroimage.2013.02.003

Wisse, L. E. M., Biessels, G. J., and Geerlings, M. I. (2014). A critical appraisal of the hippocampal subfield segmentation package in FreeSurfer. *Front. Aging Neurosci.* 6:261. doi: 10.3389/fnagi.2014.00261

Wisse, L. E. M., Gerritsen, L., Zwanenburg, J. J. M., Kuijf, H. J., Luijten, P. R., Biessels, G. J., et al. (2012). Subfields of the hippocampal formation at 7 T MRI: in vivo volumetric assessment. *NeuroImage* 61, 1043–1049. doi: 10.1016/j.neuroimage.2012.03.023

Wisse, L. E. M., Kuijf, H. J., Honingh, A. M., Wang, H., Pluta, J. B., Das, S. R., et al. (2016). Automated hippocampal subfield segmentation at 7T MRI. *Am. J. Neuroradiol.* 37, 1050–1057. doi: 10.3174/ajnr.a4659

Yushkevich, P. A., Amaral, R. S. C., Augustinack, J. C., Bender, A. R., Bernstein, J. D., Boccardi, M., et al. (2015a). Quantitative comparison of 21 protocols for labeling hippocampal subfields and parahippocampal subregions in in vivo MRI: towards a harmonized segmentation protocol. *NeuroImage* 111, 526–541. doi: 10.1016/j.neuroimage.2015.01.004

Yushkevich, P. A., Pluta, J. B., Wang, H., Xie, L., Ding, S. L., Gertje, E. C., et al. (2015b). Automated volumetry and regional thickness analysis of

hippocampal subfields and medial temporal cortical structures in mild cognitive impairment. *Hum. Brain Mapp.* 36, 258–287. doi: 10.1002/hbm.22627

Yushkevich, P. A., Wang, H., Pluta, J., Das, S. R., Craige, C., Avants, B. B., et al. (2010). Nearly automatic segmentation of hippocampal subfields in in vivo focal T2-weighted MRI. *NeuroImage* 53, 1208–1224. doi: 10.1016/j.neuroimage.2010.06.040

Zeineh, M. M., Engel, S. A., Thompson, P. M., and Bookheimer, S. Y. (2001). Unfolding the human hippocampus with high resolution structural and functional MRI. *Anat. Rec.* 265, 111–120. doi: 10.1002/ar.1061

Conflict of Interest: The authors declare that the research was conducted in the absence of any commercial or financial relationships that could be construed as a potential conflict of interest.

Copyright © 2021 Ver Hoef, Deshpande, Cure, Selladurai, Beattie, Kennedy, Knowlton and Szaflarski. This is an open-access article distributed under the terms of the Creative Commons Attribution License (CC BY). The use, distribution or reproduction in other forums is permitted, provided the original author(s) and the copyright owner(s) are credited and that the original publication in this journal is cited, in accordance with accepted academic practice. No use, distribution or reproduction is permitted which does not comply with these terms.

frontiers in Neuroscience

METHODS
published: 24 February 2021
doi: 10.3389/fnins.2021.574979

Correcting for Non-stationarity in BOLD-fMRI Connectivity Analyses

Catherine E. Davey[1,2]*, *David B. Grayden*[1] *and Leigh A. Johnston*[1,2]

[1] *Department of Biomedical Engineering, University of Melbourne, Melbourne, VIC, Australia,* [2] *Melbourne Brain Centre Imaging Unit, University of Melbourne, Melbourne, VIC, Australia*

In this work fMRI BOLD datasets are shown to contain slice-dependent non-stationarities. A model containing slice-dependent, non-stationary signal power is proposed to address time-varying signal power during BOLD data acquisition. The impact of non-stationary power on functional MRI connectivity is analytically derived, establishing that pairwise connectivity estimates are scaled by a function of the time-varying signal power, with magnitude upper bound by 1, and that the variance of sample correlation is increased, thereby inducing spurious connectivity. Consequently, we make the observation that time-varying power during acquisition of BOLD timeseries has the propensity to diminish connectivity estimates. To ameliorate the impact of non-stationary signal power, a simple correction for slice-dependent non-stationarity is proposed. Our correction is analytically shown to restore both signal stationarity and, subsequently, the integrity of connectivity estimates. Theoretical results are corroborated with empirical evidence demonstrating the utility of our correction. In addition, slice-dependent non-stationary variance is experimentally determined to be optimally characterized by an inverse Gamma distribution. The resulting distribution of a voxel's signal intensity is analytically derived to be a generalized Student's-*t* distribution, providing support for the Gaussianity assumption typically imposed by fMRI connectivity methods.

Keywords: fMRI, non-stationarity, correlation, connectivity, resting-state, power

OPEN ACCESS

Edited by:
Alard Roebroeck, Maastricht University, Netherlands

Reviewed by:
Benito de Celis Alonso, Meritorious Autonomous University of Puebla, Mexico
Miguel Castelo-Branco, Coimbra Institute for Biomedical Imaging and Translational Research, Portugal

***Correspondence:**
Catherine E. Davey
catherine.davey@unimelb.edu.au

Specialty section:
This article was submitted to Brain Imaging Methods, a section of the journal Frontiers in Neuroscience

Received: *22 June 2020*
Accepted: *02 February 2021*
Published: *24 February 2021*

Citation:
Davey CE, Grayden DB and Johnston LA (2021) Correcting for Non-stationarity in BOLD-fMRI Connectivity Analyses. Front. Neurosci. 15:574979. doi: 10.3389/fnins.2021.574979

1. INTRODUCTION

Functional MRI (fMRI) connectivity analysis utilizes blood oxygen level dependent (BOLD) data to determine how spatially remote brain regions cooperate when a subject is completing a task or is simply at rest. BOLD data is noisy, being impacted by both equipment-related noise, such as coil interference (Bandettini et al., 1998) and scanner drift (Bianciardi et al., 2009), and subject noise, such as physiological interference (Biswal et al., 1995) and subject movement (Barry et al., 2010). Both equipment and subject noise can be irregular and, therefore, non-stationary. Scanners can generate non-stationary signal variance from inhomogeneous radio-frequency (RF) amplification (Tanase et al., 2011), coil resistance (Gudbjartsson and Patz, 1995), disparities in scanner performance over time (Weisskoff, 1996), and signal attenuation from diffusion and dissemination amongst surrounding voxels (Ojemann et al., 1997). B_0 fluctuations exhibit slice dependence due to factors such as respiration effects and cardiac effects (de Moortele et al., 2002), and the slice-dependence of susceptibility-induced signal loss has been recognized and attempts made at compensation (Rick et al., 2010; Anderson et al., 2014). Delay between slice acquisitions can render the introduced non-stationarity slice dependent, which is significant for connectivity in

which comparison between voxels is key, in contrast to an activation analysis in which voxels are typically analyzed independently (Kimberg, 2008).

Connectivity analyses in fMRI frequently employ a linear Gaussian model (LGM) to estimate dependence between a seed timeseries and brain voxels (Goebel et al., 2003; Marrelec et al., 2005; Wang and Xia, 2007; Tana et al., 2008). A core assumption of the LGM class is weak stationarity of the constituent timeseries, requiring the mean and variance of the timeseries to be constant over time. Violation of this assumption has implications for the integrity of connectivity results since the distribution of the test statistic is altered (Granger and Newbold, 1974). Linear dependence estimates may also be affected as time-varying variance is analogous to applying a (non-constant) weight to each sample; samples associated with higher variance receive a greater weighting and are consequently more significant in the correlation estimate (Cohen et al., 2003). Random noise occurring at samples accompanied by large variance can alter results and even induce spurious connectivity (Granger and Newbold, 1974). Therefore, if the non-stationarity remains uncorrected, connectivity results may not be reflective of the underlying linear dependence between voxels.

Non-stationarity of BOLD timeseries has been modeled in an effort to resolve the loss of integrity associated with a stationarity assumption imposed on non-stationary data. Lund et al. (2006) modeled non-stationarity of noise via nuisance variable regression in an fMRI activation analysis. They incorporated cosine regressors for low-frequency drift resulting from hardware instabilities, first order Volterra expansion regressors to model rigid subject movement, and harmonic regressors to model aliased physiological noise. This approach restricts removal of non-stationary effects to noise processes explicitly modeled in the regressors. Diedrichsen and Shadmehr (2005) addressed time-varying volume variance in a fMRI activation study by employing a linear model with Gaussian noise characterized by time dependent variance. The non-stationary variance process was empirically determined to apply globally, so that sample variance was estimated for each image volume, and employed as a weight in a least squares estimate of regression coefficients. Luo and Puthusserypady (2007) consider the noise model proposed by Diedrichsen and Shadmehr (2005), addressing robustness concerns regarding estimation of the noise covariance matrix by employing a Bayesian framework to estimate the time-varying weights. Oikonomou et al. (2010) introduced a model of non-stationary noise for BOLD activation analyses that assumed that image slices contained unique stationary variance, applied as weights to the non-stationary noise variance of each voxel; the spatial extent of the non-stationary noise was not explored.

The necessity for modeling non-stationarity of BOLD timeseries has often been argued with visual evidence (Calhoun et al., 1999; Diedrichsen and Shadmehr, 2005; Lund et al., 2006) or otherwise assumed (Long et al., 2005; Oikonomou et al., 2009, 2010), so that there has been a notable absence of statistical evidence demonstrating non-stationarity (Park et al., 2010). Turner and Twieg (2005) established the temporal non-stationarity of independent component analysis (ICA) components derived from fMRI noise and found evidence for the persistence of the spatial components, although what these components represented is not stated. Furthermore, modeling of non-stationary processes has historically been limited to fMRI activation data; until recently there had been few investigations into non-stationarity in resting state fMRI and existent studies focussed on addressing the non-stationarity of noise processes (Calhoun et al., 1999; Diedrichsen and Shadmehr, 2005; Lund et al., 2006).

More recently, there has been increased interest in examining the non-stationarity of functional connectivity in resting state fMRI, such as Hindriks et al. (2016), Long et al. (2005), Chang and Glover (2010), Niazy et al. (2011), and Park et al. (2010), with a corresponding attempt to discern if the evident time variance is of neural or physiological origin. Handwerker et al. (2012) examined the non-stationarity of brain correlations, demonstrating the existence of periodic fluctuations in correlation at distinct frequencies, noting that the origin of the fluctuations remains unclear, which limits the basis for neural interpretation. Lindquist et al. (2014) examine the use of sliding window correlation as a means to reveal non-stationarity in underlying BOLD connectivity. Cribben et al. (2014) present a method for identifying distinct periods with respect to changing connectivity patterns. Allen et al. (2012) employ both sliding window correlation and spatial ICA to identify time-varying correlation, and a k-means clustering technique to isolate reoccurring connectivity patterns, though spatial stationarity is assumed. Hutchison et al. (2013) review recent the literature discussing non-stationarity of functional connectivity in resting-state fMRI, specifically examining sliding-window correlation and the non-stationarity of spatial ICA components. Despite the recent interest in time-varying connectivity, there has been an absence of discussion regarding the potential impacts of time-varying signal power.

Abbreviations: ACF, autocorrelation function; AIC, Akaike's information criterion; AR, autoregressive; ARX, autoregressive exogenous input; BIC, Bayesian information criterion; BOLD, blood oxygen level dependent; CDGC, conditional directed Granger causality; CGGC, conditional Geweke's Granger causality; CIGC, conditional instantaneous Granger causality; CSF, cerebrospinal fluid; DCM, dynamic causal modeling; DGC, directed Granger causality; EEG, electroencephalography; EPI, echo-planar imaging; FIR, finite impulse response; fMRI, Functional MRI; FDR, false discovery rate; FPE, final prediction error; FWER, family-wise error rate; GC, Granger causality; GGC, Geweke's Granger causality; GLM, general linear model; GOF, goodness of fit; HQC, Hannan and Quinn's information criterion; HRF, hemodynamic response function; iid, independent and identically distributed; ICA, independent component analysis; IGC, instantaneous Granger causality; IIR, infinite impulse response; LFP, local field potential; LGM, linear Gaussian model; LISREL, linear structural relations; LMC, left hemisphere primary motor cortex; LSE, least squares estimation; MATLAB, matrix laboratory; MC, multiple correlation; MDL, minimum description length; MEG, magnetoencephalography; MLE, maximum likelihood estimation; MRI, magnetic resonance imaging; OSC, order selection criteria; PACF, partial autocorrelation function; PC, partial correlation; PCA, principal component analysis; PET, positron emission tomography; pdf, probability density function; PDGC, partial directed Granger causality; PET, positron emission tomography; RF, radio-frequency; RMC, right hemisphere primary motor cortex; ROC, receiver operating characteristic; ROI, region of interest; RSS, residual sum of squares; SEM, structural equation modeling; sICA, spatial ICA; sMRI, structural MRI; SNR, signal to noise ratio; SVD, singular value decomposition; tICA, temporal ICA; TR, repetition time; tSNR, temporal SNR; VAR, vector autoregressive; WGN, white Gaussian noise.

In this paper, we correct fMRI connectivity estimates for non-stationarity induced by time-varying signal power during BOLD data acquisition. Experimental fMRI data is empirically shown to contain time-varying slice variance that is optimally characterized by an inverse gamma distribution. The resulting distribution of voxel intensity values is analytically determined to be a generalization of Student's-t distribution. On the basis of these empirical results, a model of slice-dependent non-stationarity is introduced, and an analytic derivation of sample correlation between non-stationary timeseries is presented. It should be noted that the proposed model captures non-stationarity induced by slice-dependent, time-varying signal power, and is not intended to be a universal model of all sources of non-stationarity in the data. We demonstrate the capacity for time-varying weights to alter both the magnitude and, in specific cases, the sign of correlation estimates. A straightforward correction to voxel timeseries affected by time-varying signal power is proposed, and is analytically shown to both restore signal stationarity, and to ameliorate the impact of non-stationary signal power on subsequent linear dependence estimates. Theoretical results are corroborated with empirical evidence that demonstrates the utility of our correction in restoring stationarity and the integrity of connectivity results.

This paper is organized as follows. Theoretical results are detailed in section 3.1, incorporating a description of the non-stationary signal model, with a derivation for the distribution of voxel intensity for signals with time-varying variance (subsection 3.1.1), and the consequent expression for correlation between non-stationary timeseries with proposed correction (subsection 3.1.2). Empirical and experimental methods are described in section 2, followed by a description of results in section 3 and discussion in section 4.

2. METHODS

We examine the impact of non-stationary signal power multiplicatively applied to underlying stationary signals during acquisition. In order to avoid confusion, we introduce a nomenclature to describe the multiple sources of signal variance. Underlying stationary timeseries are associated with a constant variance, which will be referred to as stationary signal variance. Time-varying signal power, modeled as a slice-dependent, non-stationary variance, will be referred to as slice dependent non-stationary variance or, equivalently, as time-varying signal power. Sample variance of voxel intensities within a slice will be referred to as sample slice variance and, similarly, sample variance of voxels within a specific tissue type will be referred to as sample tissue variance. Finally, variance of sample correlation will be explicitly identified as such.

2.1. Simulated Data

MATLAB was used to generate simulation datasets of 2,000 timeseries pairs. Denote the constituent timeseries in each pair by $x_{m,t}^{(st)}$ and $y_{n,t}^{(st)}$, where m and n index slice number. Each pair was generated from a bivariate normal distribution characterized by: timeseries length, $T = 500$; underlying correlation, $\rho = 0.3$; mean values of $x_{m,t}^{(st)}$ and $y_{n,t}^{(st)}$, denoted μ_x and μ_y, respectively, and drawn from the range $[-100, 100]$; and stationary signal variance of $x_{m,t}^{(st)}$ and $y_{n,t}^{(st)}$, denoted σ_x and σ_y, respectively, both randomly selected from the range $(0, 10]$. For each dataset, a slice dependent non-stationary variance was randomly generated for timeseries in slice m, i.e., $x_{m,t}^{(st)}$, and another for timeseries in slice n, $y_{n,t}^{(st)}$, to emulate the time-varying signal power associated with acquisition of voxels within a slice, and denoted $\sigma_{m,t}^2$ and $\sigma_{n,t}^2$, respectively. Samples for each time point of the time-varying power processes were randomly drawn from an inverse gamma distribution, which was characterized by two parameters randomly drawn from the range $[1, 10]$. Each timeseries in the dataset slice was then weighted by the square root of the appropriate time-varying signal power according to whether it was designated $x_{m,t}^{(st)}$ or $y_{n,t}^{(st)}$, within the pair, to generate the non-stationary signals $x_{m,t}$, and $y_{n,t}$, respectively.

Slice dependent non-stationary variance was estimated for each slice by calculating sample variance spatially, across the 2,000 $x_{m,t}^{(st)}$ signals, and separately for the 2,000 $y_{n,t}^{(st)}$ signals, to emulate the number of voxels that would typically be available in a fMRI dataset. The precision correction, Equation (12), was applied to generate timeseries corrected for non-stationarity of the form proposed in Equation (2). Correlation was calculated between each timeseries pair before being weighted by time-varying signal power, after being weighted, and after the precision correction was applied.

In order to determine the impact of both time-varying signal power, and our subsequent correction, on autocorrelated signals, we followed the same technique as for the white signals above, but generated the signals using a vector autoregression (VAR) model. In this case,

$$\begin{bmatrix} x_{m,t}^{(st)} \\ y_{n,t}^{(st)} \end{bmatrix} = \begin{bmatrix} \nu_x \\ \nu_y \end{bmatrix} + \mathbf{A_1} \begin{bmatrix} x_{m,t-1}^{(st)} \\ y_{n,t-1}^{(st)} \end{bmatrix} + \cdots + \mathbf{A_p} \begin{bmatrix} x_{m,t-p}^{(st)} \\ y_{n,t-p}^{(st)} \end{bmatrix} + \epsilon,$$
$$\epsilon \sim \mathcal{N}\left(\mathbf{0}, \begin{bmatrix} \sigma_x^2 & \rho\sigma_x\sigma_y \\ \rho\sigma_x\sigma_y & \sigma_x^2 \end{bmatrix},\right) \quad (1)$$

where ν_x and ν_y allow for timeseries with non-zero mean, $\mathbf{A_p}$ are the 2×2 matrices of coefficients at the designated lag, p, $x_{m,t-p}^{(st)}$ is the value of the stationary timeseries at lag p and ϵ is a noise vector with Gaussian distribution as specified.

We generated random VAR models using randomly selected model order, $p \in [1, 3]$, and all other values the same as for the white signals above, including σ_x^2 and σ_y^2 randomly drawn from the range $(0, 10]$, and both ν_x and ν_y randomly set so that μ_x and μ_y are in the range $[-100, 100]$, where $\mu = \left(\mathbf{I} - \mathbf{A_1} - \cdots - \mathbf{A_p}\right)^{-1} \begin{bmatrix} \nu_x \\ \nu_y \end{bmatrix}$, for $\mu = [\mu_x, \mu_y]'$. The $\mathbf{A}_p$ matrices were specified via random generation of the poles of each VAR(p) model with magnitude <1, and each model tested for stability.

We followed the same precision correction as for the white signals, in weighting the timeseries with time-varying variance according to whether the signal was allocated to slice m or n, and applying the precision correction to generate timeseries corrected for non-stationarity in signal power.

2.2. Experimental Data

Two distinct datasets were collected. For the first dataset, two healthy subjects were scanned on a 3T Siemens Tim TRIO MRI scanner using two different procedures: (1) resting state BOLD echo planar imaging, and (2) a motor task performance BOLD EPI. For both procedures, we collected 219 volumes for each participant (repetition time = 1, 600 ms; echo time = 20 ms; flip angle = 90°; 24 trans-axial slices, each 5.5mm thick, matrix = 64×64, field of view [FOV] = 200×200 mm^2; acquisition voxel size=$3.125 \times 3.125 \times 5.5$ mm^3). The motor task was a block design containing alternating periods of 30s each. During the active period, the subjects were instructed to press either the left or right button, according to an arrow displayed on the screen that changed randomly every second. During the baseline period, subjects were instructed to focus on a crosshair at the screen's center point. This dataset will be referred to as dataset 1.

For the second dataset three additional subjects were scanned on a 3T Siemens Tim TRIO MRI scanner using resting state BOLD echo planar imaging. We collected 240 volumes for each subject (repetition time = 2, 000 ms; echo time = 20 ms; flip angle = 90°; 91 trans-axial slices, each 5 mm thick, matrix = 91×109, field of view [FOV] = 200×200 mm^2; acquisition voxel size=$3.125 \times 3.125 \times 5.5$ mm^3). This dataset will be referred to as dataset 2.

All images were motion corrected and smoothed using a 2D isotropic Gaussian 6mm kernel, applied using MATLAB. A conventional general linear model (GLM) activation analysis (Friston et al., 1994) was applied to the motor task data; the maximum t-statistic in the right hemisphere primary motor cortex (RMC) region was used to identify the RMC. An average hemodynamic timeseries was created for the RMC of each subject by averaging across voxels in the region of interest (ROI).

For each subject, slice dependent non-stationary variance was estimated by calculating the sample slice variance of voxel intensities in each slice at each time point. The best-fit distribution for the sample slice variance of each slice was determined by calculating the maximum likelihood estimates (MLEs) for distribution parameters and identifying the distribution that attained the minimum negative log-likelihood amongst the set of Weibull, Gaussian, Gamma, Inverse Gamma, Student's-t, Exponential, Log-normal, Laplace, and Rayleigh distributions. The Wilcoxon signed-rank test was used to determine if sample slice variances of different slices were drawn from distributions with equal mean (Wilcoxon, 1945). This choice was motivated by the non-normal distribution of slice variance. The test was applied pairwise between all slices. The null hypothesis was that the median difference when comparing sample slice variances between two slices, is zero, while the alternative hypothesis was that the median difference is non zero. If the null hypothesis was rejected, the samples for the two slice variances being examined could be considered to be drawn from different distributions. Sample slice variance was also tested for stationarity, for which the augmented Dickey Fuller test was employed (Said and Dickey, 1984). In both cases, the results were significance tested with $\alpha = 0.01$.

To establish whether tissue type is a significant determinant of slice dependent variance, tissue masks were generated for each subject using the FSL software suite. For each image volume, the sample tissue variance across all voxels associated with a specific tissue type was calculated, yielding a timeseries of volume dependent variance for each tissue, including gray matter, white matter, and cerebrospinal fluid (CSF). Given that sample tissue variance and sample slice variance were necessarily generated from a common set of voxels, to establish whether tissue type is a significant determinant of slice-dependent variance, whole-volume variance was calculated at each time point and regressed out from both the tissue variance timeseries and the slice variance timeseries. The resulting tissue variance timeseries were correlated with slice variance timeseries, and tested for significance using a Student's t-test. Additionally, to establish whether the ratios of tissue types within each slice impacted the sample slice variance, the optimal inverse gamma parameters for each slice variance process were correlated with the proportion of each specific tissue type in each slice, and tested for significant using a Fisher's-z transform.

Corrected voxel timeseries were formed by weighting voxel samples using the slice dependent variance, as an estimate of time-varying signal power. Seed-voxel correlation maps were generated with a RMC seed for datasets with and without applying the correction for time-varying signal power. Correlation estimates were significance tested using Fisher's z-transformation (Fisher, 1915), with degrees of freedom corrected for dependent samples (Davey et al., 2013), and the resulting maps thresholded ($\alpha = 0.01$, Bonferroni corrected).

3. RESULTS

3.1. Theoretical Results

In the acquisition of EPI BOLD data, two-dimensional slices are usually obtained serially, on a millisecond time scale. This can result in changes in the equipment and subject environment, ultimately modifying signal characteristics between slices, resulting in non-stationarity of voxel timeseries (Calhoun et al., 1999). The slice dependence of the non-stationary processes impacting fMRI data is verified experimentally in section 2.2. Voxels within the same slice are acquired simultaneously and hence signal power within a slice is constant.

fMRI analyses typically assume stationarity of voxel timeseries and therefore it is desirable to determine a correction to restore stationarity. We propose a model of non-stationarity for resting state BOLD data in which each two-dimensional slice variance is characterized by a distinct time-varying signal power. The distribution of voxel intensity is analytically derived for this model and the impact of the non-stationarity on correlation is determined. Crucially, a simple correction is proposed that is analytically shown to restore stationarity and correct correlation values so that they reflect the underlying linear dependence between voxel timeseries.

3.1.1. A Non-stationary Model of Resting State Timeseries

We begin by proposing a model for the measured, non-stationary signal in a voxel x situated in slice n. The form of the model was motivated by the need to account for slice-dependent signal

power in conjunction with the experimental results detailed in section 3. The signal model decomposes the voxel intensity into stationary and non-stationary components,

$$x_{m,t} = x^{(st)}_{m,t}\sigma_{m,t}, \quad t = 1, \ldots, T, \tag{2}$$

where $x^{(st)}_{m,t}$ denotes the stationary signal component at time t, and $\sigma_{m,t}$ is a time-varying multiplicative variance process associated with slice m, and distributed across time according to an inverse gamma distribution,

$$\sigma^2_{m,t} \sim IG\left(\alpha_m, \frac{1}{\beta_m}\right). \tag{3}$$

Here α_m and β_m are slice specific shape and scale parameters, respectively. Consequently, slice dependent non-stationary variance has a mean of $\frac{1}{\beta_m(\alpha_m-1)}$, for $\beta_m > 0, \alpha_m > 2$.

We now determine the distribution of non-stationary voxel intensity, $x_{m,t}$, when $\sigma_{m,t}$ is unknown (Equation 2). The resting state stationary component, $x^{(st)}_{m,t}$, is assumed to be Gaussian distributed (Wink and Roerdink, 2006),

$$x^{(st)}_{m,t} \sim \mathcal{N}\left(0, \sigma^2_x\right). \tag{4}$$

As $x^{(st)}_{m,t}$ and $\sigma_{m,t}$ are independent random variables, at each time point a voxel in slice m has distribution

$$x_{m,t} \sim \mathcal{N}\left(0, \sigma^2_x\sigma^2_{m,t}\right). \tag{5}$$

The distribution of voxel intensity as derived in **Appendix A** is given by

$$p\left(x_{m,t}\right) = \frac{\Gamma\left(\alpha+\frac{1}{2}\right)}{\Gamma(\alpha)}\left(\frac{1}{2\pi\beta\sigma^2_x}\right)^{\frac{1}{2}}\left(1+\frac{{x_{m,t}}^2}{2\sigma^2_x\beta}\right)^{-(\alpha+\frac{1}{2})}. \tag{6}$$

The voxel intensity distribution (Equation 6), is an instance of the generalized Student's-t distribution (Härdle and Simar, 2007, p.129) with parameterization $\mu_t = 0$, $\nu_t = 2\alpha$, and $\sigma^2_t = \frac{\beta}{\alpha}\sigma^2_x$, where subscript t denotes a Student's-t distribution parameter. Consequently, the voxel intensity of sampled non-stationary resting state BOLD data described by the proposed model in Equations (2)–(3) is characterized by a generalized Student's-t distribution.

3.1.2. Impact of Non-stationary Signal Power on fMRI Connectivity

Correlation-based measures assume stationarity of timeseries and are known to be susceptible to spurious significance if the stationarity assumption is violated (Granger and Newbold, 1974). We derive expressions for both correlation between non-stationary timeseries to determine the impact of time-varying noise on estimates of connectivity. In **Appendix B** sample correlation was derived as

$$\text{corr}\left(x_{m,t}, y_{n,t}\right) = \kappa\ \text{corr}\left(x^{(st)}_{m,t}, y^{(st)}_{n,t}\right), \tag{7}$$

where

$$\kappa = \frac{\mu_{\sigma_{m,t}\sigma_{n,t}}}{\sqrt{\mu_{\sigma^2_{m,t}}\mu_{\sigma^2_{n,t}}}}, \tag{8}$$

and by the Cauchy-Schwarz inequality (Cauchy, 1921),

$$|\kappa| \leq 1. \tag{9}$$

Consequently, time-varying signal weights necessarily reduce the magnitude of correlation between non-stationary signals, where the extent of the reduction depends on the similarity of the time-varying weight processes. It is important to note that it is feasible for the time-varying processes to modify the sign of the correlation in the event that the weights are drawn from the set of real numbers. In such a case, correlation may appear as anti-correlation and vice-versa.

The variance of sample correlation was found in **Appendix B** to be

$$\text{var}\left(\text{corr}\left(x_{m,t}, y_{n,t}\right)\right) \approx \frac{1-\kappa^2\text{corr}\left(x^{(st)}_{m,t}, y^{(st)}_{n,t}\right)^2}{T-2}. \tag{10}$$

Since $\kappa \leq 1$, the variance of sample correlation between non-stationary timeseries will be larger than that of stationary signals. Consequently, estimates of correlation will be more prone to spurious significance.

3.1.3. Correcting fMRI Connectivity for Non-stationary Signal Power

Several fMRI connectivity methods, such as correlation-based measures (Friston et al., 1994; Wang and Xia, 2007), Granger causality methods (Goebel et al., 2003; Chen et al., 2006; Guo et al., 2008), and structural equation modeling (McIntosh and Gonzalez-Lima, 1994), assume stationarity of voxel timeseries. If BOLD data is acquired with non-stationary signal power, this assumption is violated. We now propose a correction to apply to voxel timeseries generated from time-varying signal power of the form proposed in our model (Equation 2). The correction is analytically shown to restore stationarity in the event of such time-varying power during image acquisition.

Let $x^{(c)}_{m,t}$ denote a corrected voxel timeseries given by

$$x^{(c)}_{m,t} = \frac{x_{m,t}}{\hat{\sigma}_{n,t}}, \tag{11}$$

where $\hat{\sigma}^2_{n,t}$ is the sample slice variance of voxel intensities within slice m at time t. It is assumed that this sample slice variance will include both the time-varying signal power of interest, $\sigma^2_{m,t}$, and a stationary signal variance component, or scale factor, σ_m, such that

$$\begin{aligned} x^{(c)}_{m,t} &= \frac{x^{(st)}_{m,t}\sigma_{m,t}}{\sigma_{m,t}\sigma_m} \\ &= \frac{x^{(st)}_{m,t}}{\sigma_m}. \end{aligned} \tag{12}$$

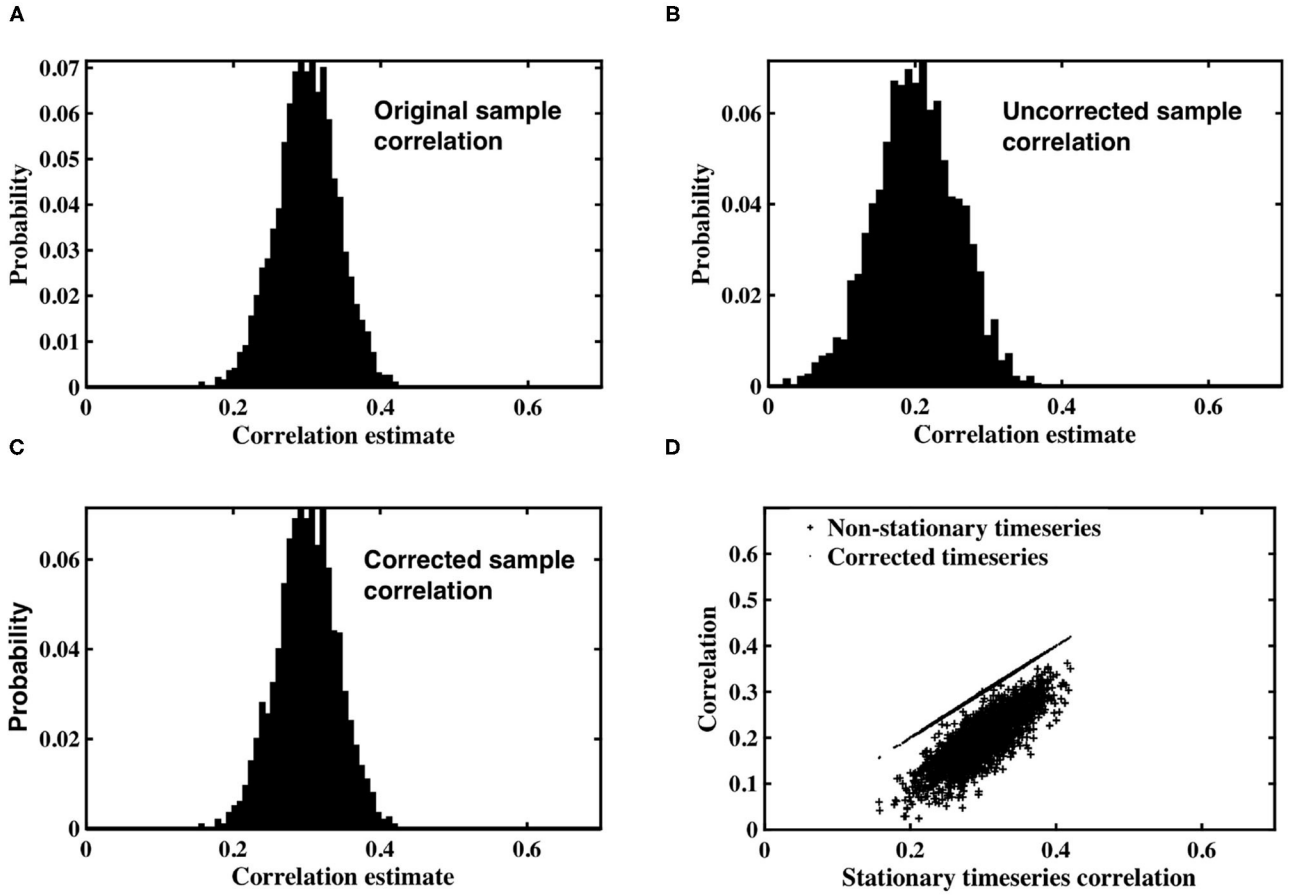

FIGURE 1 | (A) Histogram of correlation estimates between stationary timeseries pairs with underlying correlation, $\rho = 0.3$. **(B)** Histogram of correlation estimates acquired from non-stationary timeseries pairs, with time-varying signal power for each timeseries within a pair randomly derived from *IG*(2, 2) or *IG*(3, 2). **(C)** Histogram of correlation between timeseries pairs corrected for non-stationarity. **(D)** Scatter plots between original correlation estimates drawn from stationary timeseries against correlation estimates of weighted, non-stationary timeseries (crosses) and correlation estimates derived from timeseries corrected to restore stationarity (dots).

Observe that the corrected voxel timeseries is now stationary, but with a variance that differs by a constant factor from that of the underlying stationary signal variance component, $x_{m,t}^{(st)}$ (Equation 4). Consequently,

$$x_{m,t}^{(c)} \sim \mathcal{N}\left(0, \frac{\sigma_x^2}{\sigma_m^2}\right). \tag{13}$$

Correlation between corrected timeseries is given by

$$\begin{aligned} \text{corr}\left(x_{m,t}^{(c)}, y_{n,t}^{(c)}\right) &= \frac{1}{T}\sum_{t=1}^{T}\left(\frac{x_{m,t}^{(st)}}{\frac{\sigma_x}{\sigma_m}}\right)\left(\frac{y_{n,t}^{(st)}}{\frac{\sigma_y}{\sigma_n}}\right) \\ &= \text{corr}\left(x_m^{(st)}, y_n^{(st)}\right), \end{aligned} \tag{14}$$

where the first line is a direct result of the definition of corrected timeseries in Equation (12). This demonstrates that correlation between timeseries with time-varying signal power, corrected for this source of non-stationarity, is equivalent to correlation between the underlying stationary voxel timeseries. The impact of the non-stationary signal weighting has been removed and the intrinsic linear dependence has been recovered, as required.

3.2. Simulation Results

Simulated datasets were used to examine the impact of spatially dependent non-stationary variance on sample correlation, as well as the utility of the timeseries correction proposed in Equation (12). Pairs of correlated, stationary timeseries were generated using the methods described in section 2.1, and sample correlation calculated between each pair. A histogram of the correlation estimates is shown in **Figure 1A**, in which the expected value of sample correlation matches the underlying true correlation value of 0.3. Each stationary timeseries in a pair was weighted by one of two time-varying inverse Gamma variance processes, simulating time-varying signal power, depending on whether the timeseries was designated as coming from slice *m*, or slice *n*. A histogram of correlation estimates acquired for the non-stationary pairs is shown in **Figure 1B**. The expected value of sample correlation between the non-stationary timeseries is clearly diminished, having a value of 0.48, in precise

agreement with the analytic expression derived in Equation (7). Furthermore, the variance of the correlation estimates for the weighted, non-stationary timeseries is increased, thereby reducing confidence in the estimates. Consequently, if left uncorrected, the non-stationarity has the propensity to induce spurious correlation.

The non-stationary timeseries were corrected by an estimate of slice variance at each time point, according to the simple correction proposed in Equation (12). Sample correlation was calculated between corrected timeseries pairs (**Figure 1C**). The results clearly demonstrate the efficacy of our correction in restoring stationarity to the timeseries, and re-establishing the expected value of correlation estimates to the true, underlying correlation of 0.3.

Figure 1D contains a scatterplot between sample correlation values calculated between the stationary timeseries, against both sample correlation estimates between the non-stationary timeseries, and those between the corrected timeseries. While the histograms are indicative of changes in the distribution of sample correlation, the scatterplots depict changes in individual correlation estimates as a consequence of the time-varying weighting and subsequent correction. Correlation estimates of weighted timeseries differ by up to 0.25 from the correlation contained in the original, stationary timeseries. Conversely, the scatterplot between correlation estimates from the stationary timeseries, and those derived from timeseries corrected by estimates of the time-varying weights, are almost indistinguishable.

The impact of the autocorrelation of fMRI timeseries on our proposed correction was examined. Pairs of stationary VAR timeseries were generated according to Equation (1), and one timeseries within each pair allocated to slice m or n. Each VAR timeseries within a slice was weighted with a time-varying signal power, generated according to an inverse gamma distribution. The non-stationary variance was estimated for each slice, the VAR timeseries precision corrected, and sample correlation recalculated for each VAR timeseries pair.

As shown in **Figure 2**, the distribution of sample correlation for the stationary VAR timeseries is larger than that of the white timeseries (**Figure 1A**), as expected due to the impact of the autocorrelation. The coefficients determining autocorrelation in the VAR timeseries were randomly generated, and hence had a variable impact on instantaneous correlation. Sample correlation between the non-stationary VAR timeseries (**Figure 2B**) is shown to be significantly impacted by the weighting of time-varying signal power. The mean correlation is reduced, showing that the slice dependent non-stationary variance has a destructive effect on correlation. After applying the precision correction the distribution of sample correlation is restored to that of the original stationary VAR timeseries (**Figure 2C**).

Figure 2D depicts a scatterplot of the correlation between the underlying stationary timeseries, and that estimated between the non-stationary VAR timeseries pairs, and the VAR timeseries pairs corrected using our proposed precision correction. The scatterplot shows that correlation between the non-stationary VAR timeseries almost always has magnitude less than that from which the stationary timeseries were generated. There are also many cases in which the sign of correlation between the non-stationary VAR timeseries has changed, from positive to negative or vice-versa. Importantly, sample correlation between the corrected timeseries has recovered to agree with the underlying correlation between the stationary VAR timeseries.

3.3. Experimental Results

3.3.1. Non-stationarity of Resting State Data

For each subject, and for all slices within each subject's experimental dataset, the inverse gamma distribution best characterized the distribution of sample slice variance estimates of voxel intensities within the slice, as shown in **Figure 3**. For all slices, **Figure 4** displays the distribution of sample slice variance, in addition to the MLE fit of the inverse gamma distribution to this experimental data. Despite significant variation in slice mean and variance, in each case the distribution of the sample slice variance is accurately characterized by an inverse gamma distribution.

The probability distribution of Gaussian intensity values with an inverse gamma, non-stationary variance was analytically derived to be a generalization of a Student's-t distribution (Equation 6). Experimental intensity values corroborate this theoretical result; for each subject, the temporal distribution of voxel intensity values within a slice, as well as the distribution of individual voxel intensities, were optimally characterized by a three parameter Student's-t distribution. The resulting distributions for the slice and voxel are similar, although the voxel distribution has significantly reduced degrees of freedom (**Figure 5**). Since a Student's-t distribution is asymptotically Gaussian with degrees of freedom, our empirical results support the Gaussianity assumption inherent in a linear Gaussian model (LGM).

Our theoretical results in section 3.1.1 were derived using a model of slice dependent, time-varying variance. This model differs to that of Diedrichsen and Shadmehr (2005), in which a global time-varying variance was assumed so that all voxels within a 3D image were associated with a single non-stationary weighting. We verify the applicability of our model of slice dependent, non-stationary signal power using an experimental fMRI dataset. **Figures 6A,C** depicts the sample slice variance for two exemplar slices, demonstrating both the non-stationarity and the dissimilarity of the time-varying processes, and **Figures 6B,D** displays the mean slice variance for each slice across two different subjects.

A more formal examination of dissimilarity was performed using the Wilcoxin rank-sum test to assess the equality of sample slice variance distributions. The test was applied to each slice pair; **Figure 7** shows the result in matrix form. Black indicates that the null hypothesis of identical means was supported while white designates a rejection of the null hypothesis, indicating that sample slice variances for the pair were drawn from different distributions. The result clearly shows that slice variance distributions are dissimilar in most cases (93%), supporting our model of slice dependent non-stationary variance.

To determine if the slice dependence of the non-stationary weights was induced by differing ratios of tissue types in each slice, the linear association between slice time-varying weights,

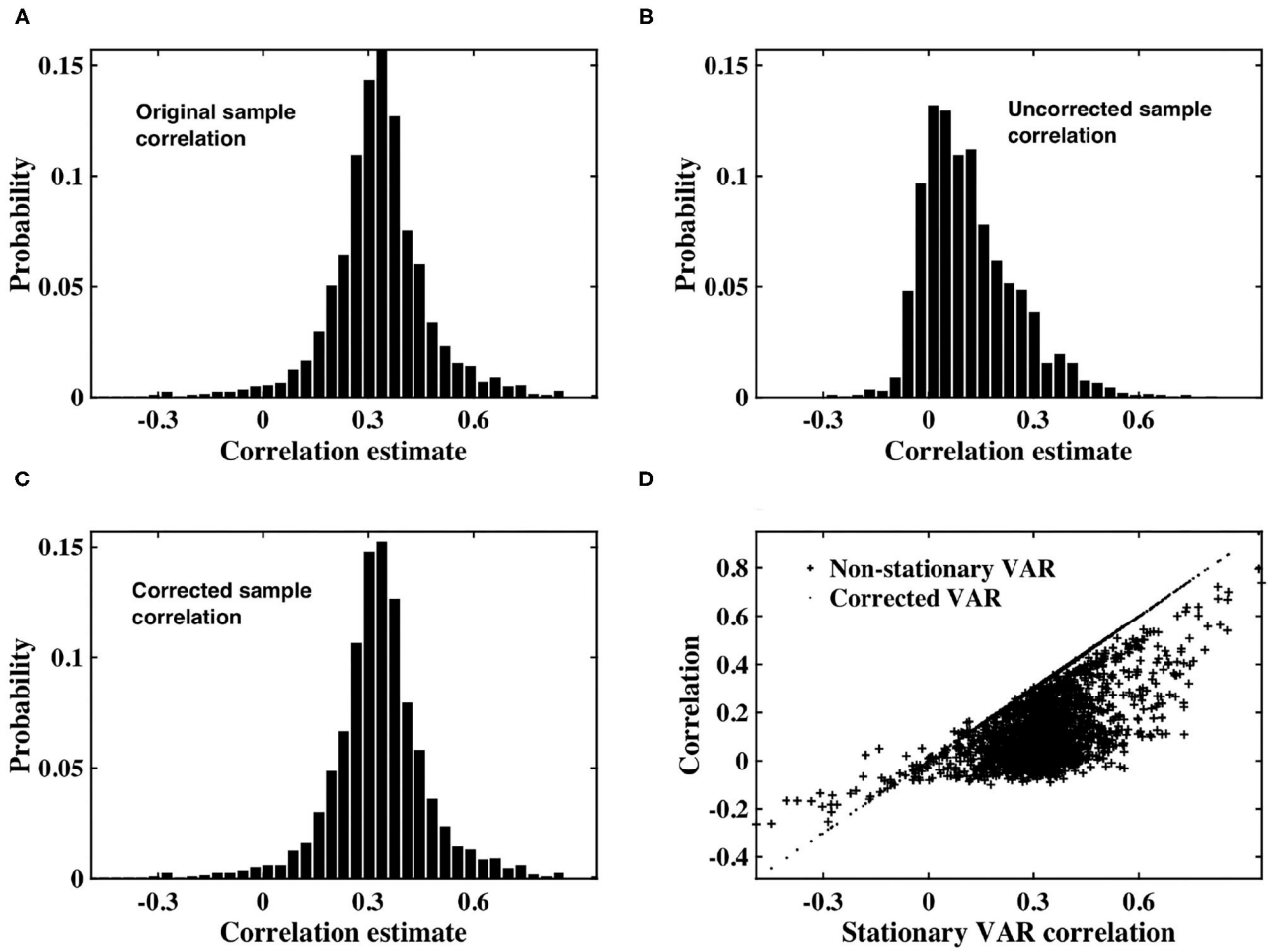

FIGURE 2 | (A) Histogram of correlation estimates between stationary VAR timeseries pairs with underlying noise correlation, $\rho = 0.3$, according to Equation (1). **(B)** Histogram of correlation estimates acquired from non-stationary VAR timeseries pairs, with time-varying signal power for each timeseries within a pair randomly derived from $IG(2, 5)$ or $IG(3, 7)$. **(C)** Histogram of correlation between VAR timeseries pairs corrected for non-stationarity. **(D)** Scatter plots between original correlation estimates drawn from stationary VAR timeseries against correlation estimates of weighted, non-stationary VAR timeseries (crosses) and correlation estimates derived from timeseries corrected to restore stationarity (dots).

and each sample tissue variance timeseries, was examined. For all subjects, <10% of slices showed significant correlation with the sample tissue variance timeseries, and none of the inverse gamma parameters were significantly associated with the proportion of tissue type within each slice.

Stationarity of slices was evaluated by applying the augmented Dickey-Fuller (ADF) stationarity test to each slice. For all subjects, more than 70% of the sample slice variance timeseries were found to be non-stationary. None of the inverse gamma parameters were significantly associated with the proportion of tissue type within each slice.

3.3.2. Impact on Connectivity

Non-stationary slice variance is problematic when methods that assume stationarity are employed to estimate brain connectivity. The theoretical results detailed in section 3.1.1 model non-stationarity derived from temporal changes in signal power. The impact of non-stationarity on correlation was analytically established in section 3.1.2, in which it was shown that a non-stationary weighting alters the expected value of sample correlation, which is a critical result for fMRI connectivity research. In this section, the theoretical results are corroborated with empirical evidence from both simulated and experimental data.

The simple timeseries correction (Equation 12), was applied to the experimental resting state dataset introduced in section 2.2 to examine its ability to restore stationarity of fMRI data. The weighting of correlation anticipated by the theory as a consequence of the non-stationary signal power (Equation 8), was found to be in close agreement with those found experimentally. For example, for voxels co-located with the RMC, the weighting anticipated by the sample slice variance was 0.8 for subject 1, while experimentally the change was 0.81. Furthermore, the scatterplot between experimental correlation

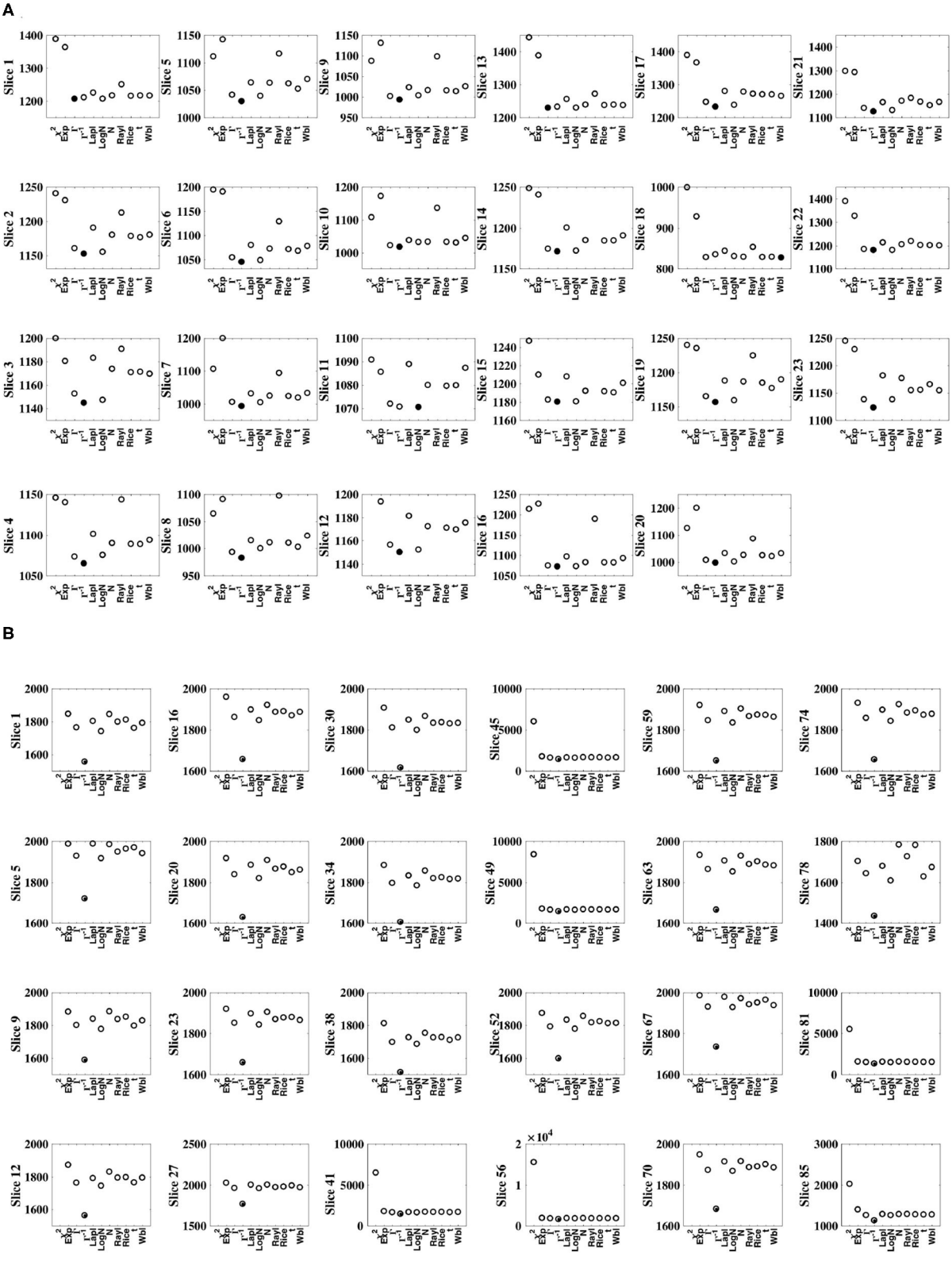

FIGURE 3 | Comparison of MLE distribution fits to sample slice variance. Goodness of fit was evaluated using negative log likehood. The optimal fit is identified by a solid circle. **(A)** Shows results for dataset 1, while **(B)** shows results for dataset 2. In all cases, for both datasets, the inverse gamma distribution fits the data optimally.

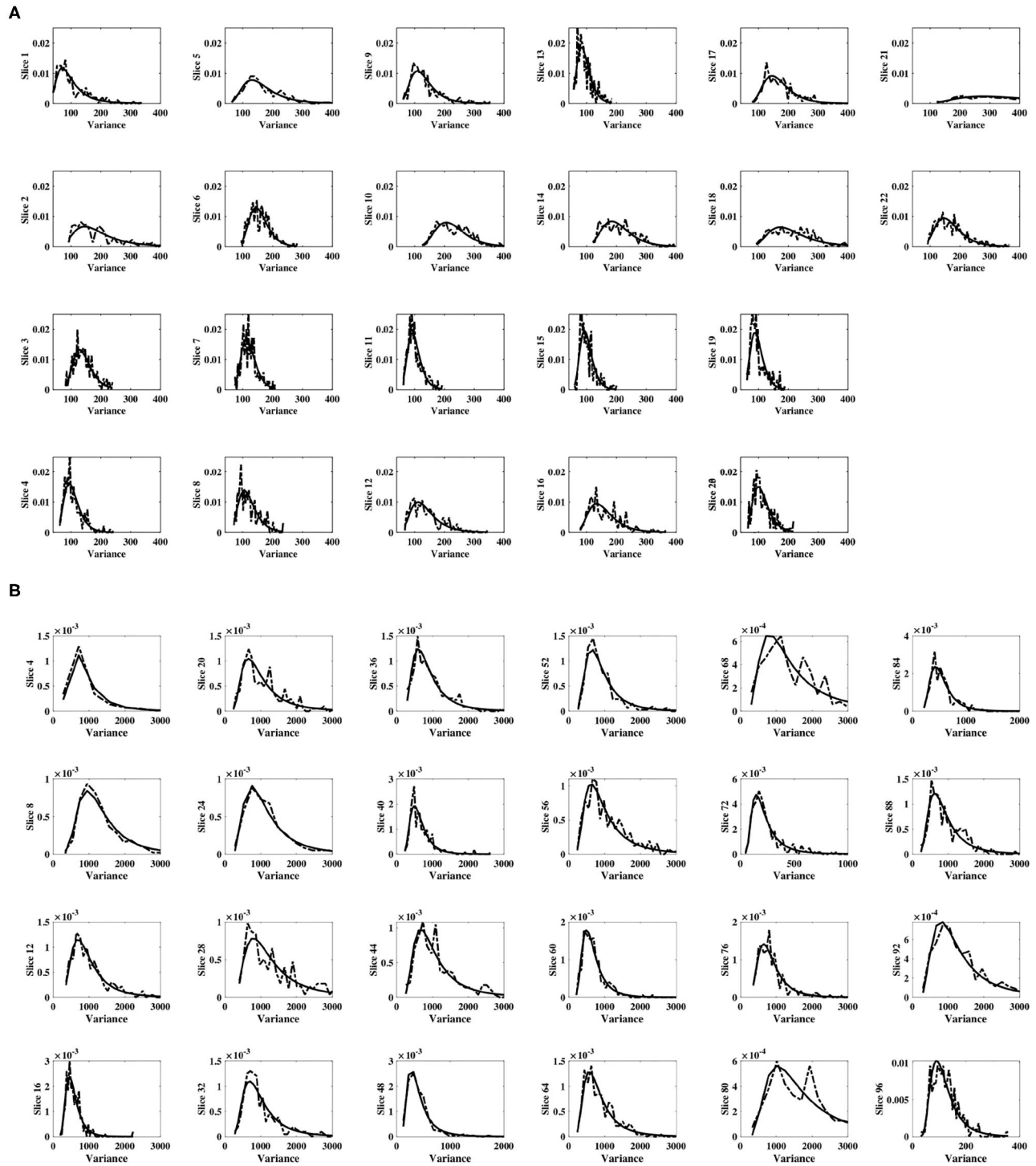

FIGURE 4 | Distribution of sample slice variance of voxel intensities within each slice. Distribution of sample slice variance values within each slice (dashed) and MLE inverse gamma distribution fit to slice variance (solid), across slices. **(A)** Shows results for dataset 1, while **(B)** shows results for dataset 2.

estimates before and after correction, **Figure 8** is reminiscent of the scatterplot generated using simulated data, **Figure 1D**. Although the spread of correlation in **Figure 8** is greater, reflecting a more diverse range in underlying true correlation values, the principal eigenvector in the transformation of correlation between uncorrected timeseries, to correlation

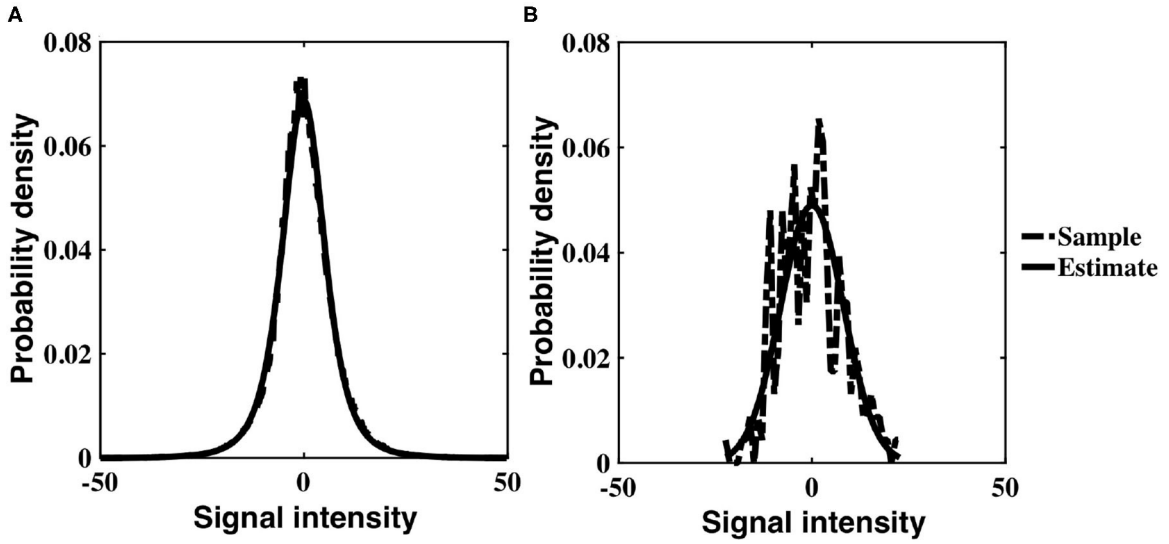

FIGURE 5 | Three parameter Student's-*t* distribution (solid) fit to experimental data values (dashed) for a single subject, drawn from **(A)** all voxels within a slice, z = 16, and across time, **(B)** a single voxel timeseries within a slice (z = 16, x = 32, y = 32).

between corrected timeseries, clearly shows a size dependent amplification of correlation. This is highlighted by inclusion of the identity line in **Figure 8**, which designates where the eigenvector would lie if there was no change in the expected value of sample correlation between corrected timeseries. Note that the gradient of the eigenvector depends on the time-varying weights.

The utility of our correction is demonstrated in **Figure 9**, in which seed-voxel correlation maps with a RMC seed are shown prior, and subsequent, to applying the correction for time-varying signal power (Equation 12), for two different subjects. The z-maps for both subjects show a visible difference in connectivity to the RMC as a result of applying the correction. Uncorrected z-maps contain a higher number of outliers than z-maps acquired using corrected timeseries, suggesting that uncorrected maps contain some connectivity artificially induced by the time-varying nature of voxel variance. This result agrees with the increased variance of sample correlation between non-stationary timeseries. If the significance tests of sample correlation are not altered to allow for this increased variance, spurious correlation will be erroneously identified as significant. Note that removal of non-stationarity changes both the mean and variance of sample correlation, as demonstrated in **Figure 1**, and thus the correction may appear as a change in threshold when applied to experimental data.

4. DISCUSSION

Connectivity analyses of resting state fMRI data typically require stationarity of timeseries. However, this assumption is violated by non-stationarity derived from noise sources such as head movement, or by variable signal power originating from sources such as inhomogeneous RF amplification (Tanase et al., 2011) and signal attenuation (Stejskal, 1965). Violation of the stationarity assumption impacts connectivity results by implicitly applying a time-varying weight to timeseries elements. Random noise occurring at a sample associated with high variance may contribute more to a correlation estimate than a sample containing signal of interest but located in a region of low signal variance. Consequently, correcting for such time-varying signal power is not only desirable but necessary (Cohen et al., 2003).

We propose a model of non-stationarity motivated by time-varying signal power during acquisition. Since voxels within a slice are acquired simultaneously in 2D EPI acquisitions, we examined sample slice variance, describing temporal changes in the variance of voxel intensities within a slice. We established empirically that sample slice variance is non-stationary and can be well modeled by an inverse gamma distribution, in agreement with Hansen et al. (2003). Importantly, each sample slice variance process was found to be particular to that slice, contrary to the global assumption made by Diedrichsen and Shadmehr (2005). Incorrectly assuming an identical non-stationary process for all slices adversely affects connectivity results because signal of interest may be ignored based on an increase in noise variance in the overall image volume.

While signal non-stationarity can come from many potential sources, each impacting a different spatial extent, we chose to focus on slice specific variance due to striking observations of this in experimental results. Conversely, a voxelwise model of non-stationarity is difficult to substantiate and implement due to the need for sample variance to be calculated from multiple samples over space or time. Further, there is an infinite number of ways to separate the voxel's signal variance into spatial and temporal origins, that in the absence of prior or secondary information renders the approach intractable.

Our slice-specific method does not preclude the removal of regionally specific non-stationarity as a subsequent pre-processing step. The combination of the two would be

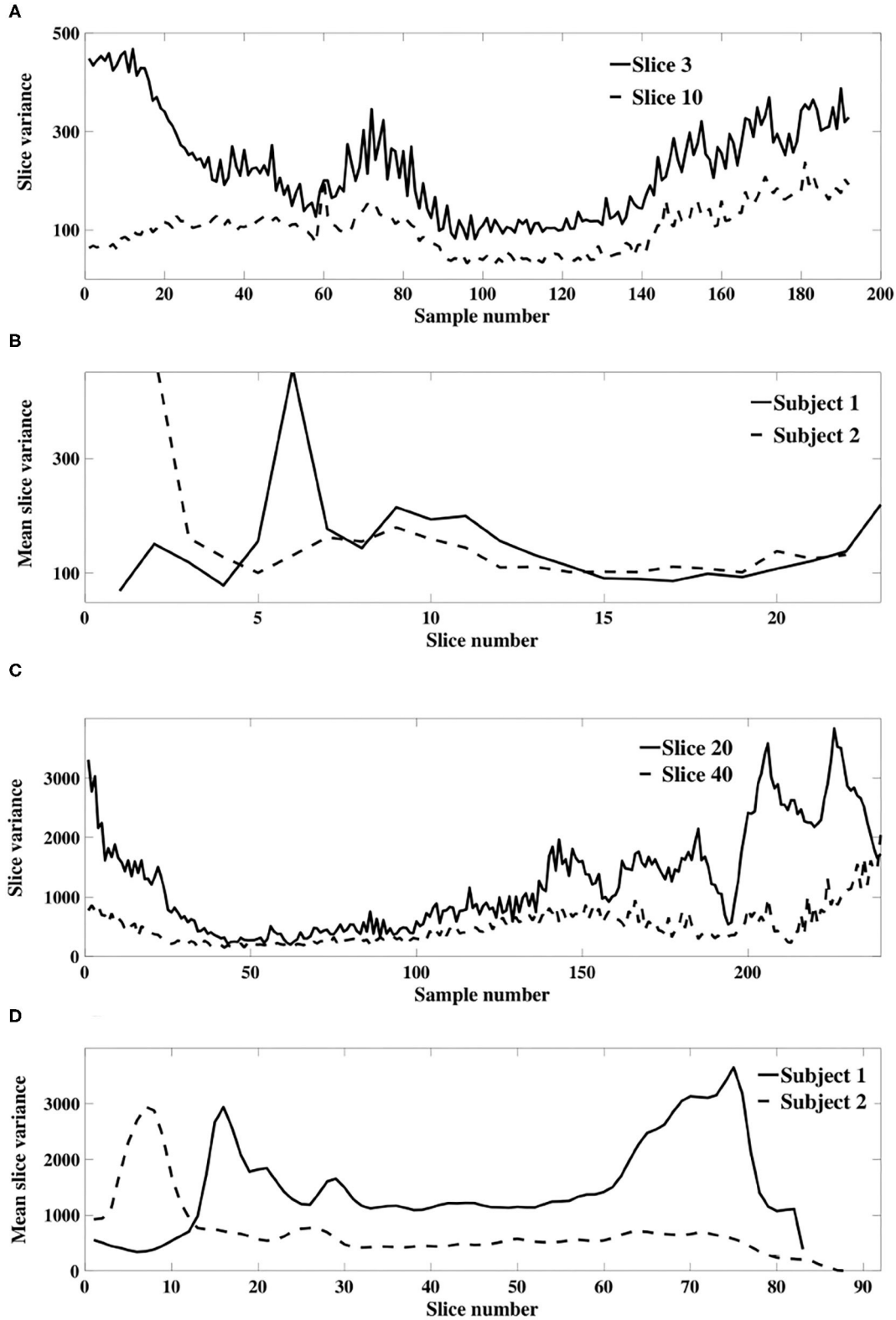

FIGURE 6 | (A) Example sample slice variance from each resting state dataset. **(A)** (Dataset 1) and **(C)** (dataset 2) show calculated slice variance for exemplar slices from subject 1 of each dataset. **(B)** (Dataset 1) and **(D)** (dataset 2) show the mean sample slice variance across all slices of subject 1 and 2 in each dataset.

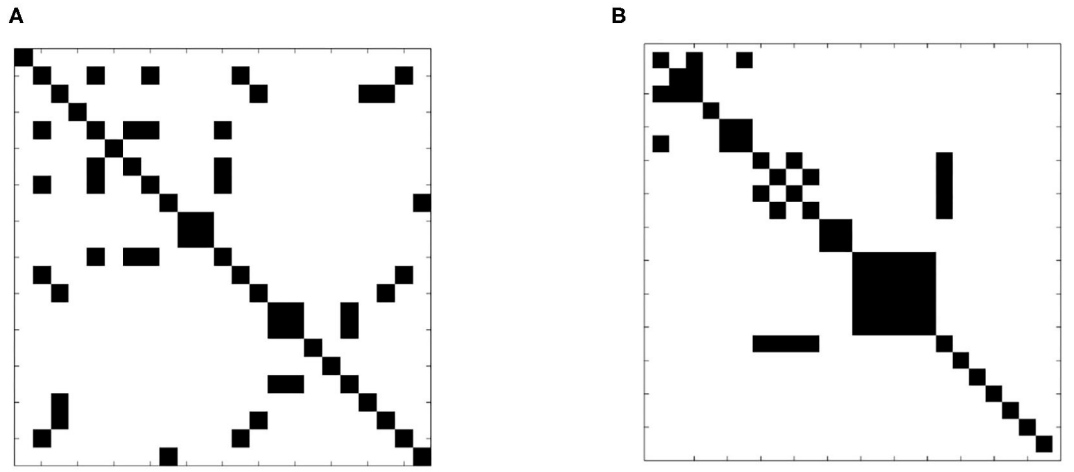

FIGURE 7 | Test of distribution dependence between sample slice variance processes. The Wilcoxon signed-rank test was applied to each slice pair for each subject to identify dependence between sample slice variance distributions. **(A)** (Subject 1 from dataset 1) and **(B)** (subject 1 from dataset 2) show the results of each pairwise assessment. Black indicates that the null hypothesis of equivalence was supported whilst white indicates rejection of the null hypothesis ($\alpha = 0.01$).

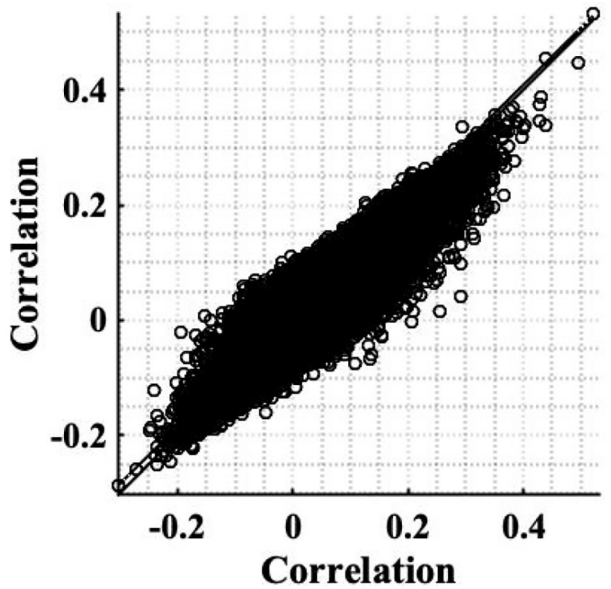

FIGURE 8 | Scatterplot of correlation estimates between the RMC and brain voxels (slice 19), before correcting for non-stationarity, against correlation estimates acquired after applying the correction to restore stationarity. A line of best fit of pre-correction correlation, to post-correction correlation, values is shown (dashed), as well as the identity line denoting no change, to aid comparison (solid).

confounded, as a given brain region may cross multiple slices, and would then contain voxels acquired with varying levels of signal power that should be removed first. The secondary analysis and removal of regional non-stationarity is beyond the scope of this paper, and research we intend to pursue in the future.

In establishing that the non-stationarity of voxel timeseries has a spatial dependence, it was shown that the time-varying weights for each slice are drawn from statistically significant distributions. We further established that there does not appear to be evidence for tissue specificity. Given that the slice dependence is dispersed across all tissue types, scaling timeseries by sample slice variance will not destroy dynamic connectivity. Consequently, additional methods can be employed to model time-varying connectivity.

Non-stationary signal power applied to voxel signals during acquisition has the propensity to change the distribution of the intensity values (Granger and Newbold, 1974). We have derived an analytic expression for the distribution of normally distributed voxel intensity, with non-stationary variance described by an inverse gamma distribution. The resulting distribution of voxel intensity was shown to be a generalization of a Student's-*t* distribution, which was further validated using an experimental resting state dataset. This result extends support to the normality assumption typically imposed by linear fMRI connectivity measures.

Having modeled the non-stationary distribution of fMRI voxel intensities, we subsequently considered the impact of non-stationary slice variance in the context of connectivity analyses, obtaining an analytic expression for correlation between non-stationary signals. Sample correlation between non-stationary timeseries was shown to derive from correlation between the underlying stationary signals, scaled by a function of the time-varying processes. Importantly, the scale factor was shown to have an absolute value less than unity. Consequently, slice dependent non-stationary variance processes diminish the strength of linear association between voxels. Furthermore, in the case where time-varying weights are drawn from the set of real numbers, the non-stationary process has the propensity to change the sign of association so that a positive correlation can become negative and vice-versa.

We derived the variance of sample correlation estimates between non-stationary timeseries. We demonstrated that

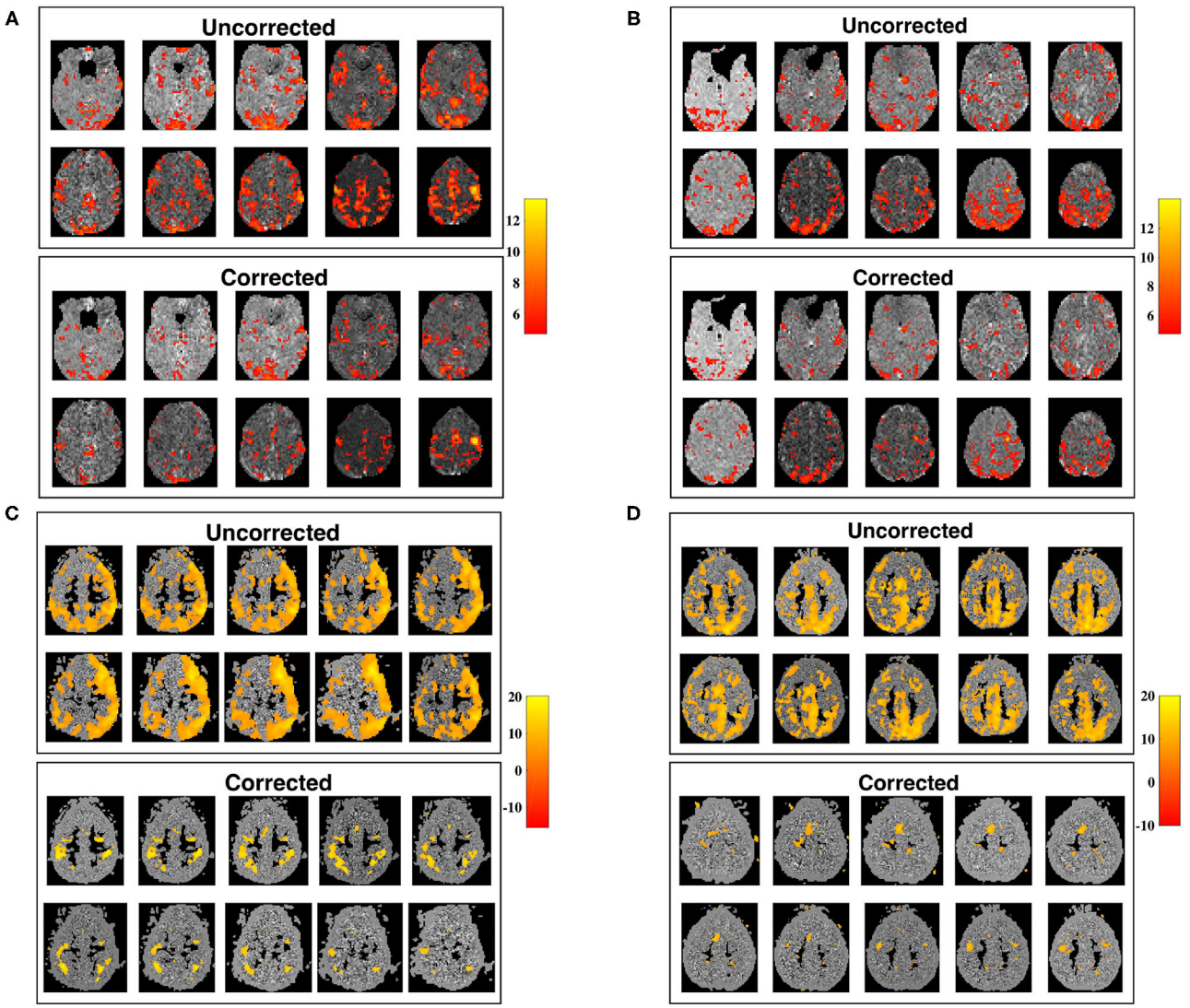

FIGURE 9 | Slice maps of significant RMC-seed voxel correlation for uncorrected timeseries, and timeseries corrected for non-stationary signal power, tested using Fisher's z-transformation. **(A,B)** Show subjects 1 and 2 from dataset 1 while **(C,D)** show subjects 1 and 2 from dataset 2, before (above) and after (below) correcting for non-stationary signal power. For each subject, the number of outliers for corrected datasets is reduced. Spatial smoothing can cause clusters of outliers, which are visibly reduced after correction, creating significance maps in closer conformance with expected results.

time-varying power increases the variance. The theoretical results were corroborated with empirical results, which demonstrated a discernible change in the variance of sample correlation between non-stationary timeseries. This is significant as, if not accounted for, it will result in an increase in the incidence of spurious correlation. This may explain the large amount of correlation found in some fMRI datasets before correction, and the reduced amount of activation following correcting for time-varying signal power.

While this paper considers non-stationary signal power in resting state data, the result can equally be applied to activation data. The correction procedure has the propensity to change the signal means, however relative differences between signal means both spatially, in different brain regions, and temporally, will be preserved, and the linear relationship between the signal and the task will be preserved as the signal mean is an offset factor. This is the subject of our current work, and our preliminary testing confirms this supposition.

To address the impact of non-stationarity signal power on fMRI connectivity, a simple precision correction was proposed, which was analytically demonstrated to restore signal stationarity. The correction generated stationary signals that differ in value from the underlying stationary signals by a constant scale factor, which is inconsequential for correlation since it is insensitive to scale. The efficacy of our correction was validated using simulation data; after applying our proposed

correction the mean value of sample correlation coincided with the underlying correlation between the stationary signals. Experimental data showed reduced outlier connectivity and the number of significant connections reduced in accordance with the smaller variance of stationary signals. Furthermore, the change in mean correlation agreed with that anticipated by the analytically derived expression for correlation between non-stationary signals. Note that removal of time-varying signal power will increase estimates of underlying linear connectivity since the time-varying weights diminish sample correlation estimates between timeseries.

The scope of current work has been to identify slice dependent non-stationary variance and propose a statistical correction for its presence in fMRI connectivity analyses. The 2D EPI datasets examined were both acquired in the standard axial slice direction. In order to probe the physical origins of non-stationarity, it will be of interest in future work to alter the slice direction to coronal, sagittal, or oblique slices. With B0 inhomogeneities more concentrated at the base of the frontal lobe, this is expected to change the signal power distributions when distributed across slices rather than confined within certain slices. Investigation into slice ordering, contiguous vs interleaved, and a comparison with 3D acquisitions are all potential ways in which the origins of the non-stationarity can be scrutinized. Further, it is of interest to explore Simultaneous Multi-Slice fMRI approaches that are increasingly popular for the increased temporal resolution they offer. The concurrent acquisition of multiple slices and un-aliasing of the slices via the receive array coils will likely render this a challenging statistical inference problem, but as with the current work, this is vital for the statistical integrity of the resultant brain connectivity maps.

5. CONCLUSION

Linear fMRI connectivity methods typically require stationarity of timeseries. We have demonstrated that resting state fMRI data do not meet this requirement but rather have time-varying, slice-dependent, variance that is well-modeled by an inverse gamma distribution. The resulting voxel intensity distribution under this model is a generalization of a Student's-*t* distribution. The impact of non-stationary signal power on connectivity was established by analytically deriving an expression for correlation between timeseries with time-varying variance. Subsequently, a correction was proposed and validated using both simulated and experimental datasets.

DATA AVAILABILITY STATEMENT

Requests to access these datasets should be directed to cedavey@unimelb.edu.au.

ETHICS STATEMENT

All human imaging was conducted with the approval of the University of Melbourne Human Research Ethics Committee, and volunteers gave an informed consent prior to the experiment. The patients/participants provided their written informed consent to participate in this study.

AUTHOR CONTRIBUTIONS

LJ made the initial proposal to model variance using a time-varying inverse Gamma distribution. LJ and DG provided supervision and guidance on maths and data processing techniques. CD did the maths derivations and primarily implemented the Matlab coding and fMRI data processing. All authors contributed to the article and approved the submitted version.

ACKNOWLEDGMENTS

The content of this manuscript has been published as part of the thesis of Davey (2011).

SUPPLEMENTARY MATERIAL

The Supplementary Material for this article can be found online at: https://www.frontiersin.org/articles/10.3389/fnins.2021.574979/full#supplementary-material

REFERENCES

Allen, E., Damaraju, E., Plis, S., Erhardt, E., Eichele, T., and Calhoun, V. D. (2012). Tracking whole-brain connectivity dynamics in the resting state. *Cereb. Cortex* 24, 663–676. doi: 10.1093/cercor/bhs352

Anderson, R., Poser, B., and Stenger, V. (2014). Simultaneous multislice spectral-spatial excitations for reduced signal loss susceptibility artifact in BOLD functional MRI. *Magn. Reson. Med.* 72, 1342–1352. doi: 10.1002/mrm.25050

Bandettini, P., Jesmanowicz, A., Kylen, J., Birn, R., and Hyde, J. (1998). Functional MRI of brain activation induced by scanner acoustic noise. *Magn. Reson. Med.* 39, 410–416. doi: 10.1002/mrm.1910390311

Barry, R., Williams, J., Klassen, L., Gallivan, J., Culham, J., and Menon, R. (2010). Evaluation of preprocessing steps to compensate for magnetic field distortions due to body movements in bold fMRI. *Magn. Reson. Imaging* 28, 235–244. doi: 10.1016/j.mri.2009.07.005

Bianciardi, M., Fukunaga, M., van Gelderen, P., Horovitz, S., de Zwart, J., Shmueli, K., et al. (2009). Sources of functional magnetic resonance imaging signal fluctuations in the human brain at rest: a 7 T study. *Magn. Reson. Imaging* 27, 1019–1029. doi: 10.1016/j.mri.2009.02.004

Biswal, B., Yetkin, F., Haughton, V., and Hyde, J. (1995). Functional connectivity in the motor cortex of resting human brain using echo-planar MRI. *Magn. Reson. Med.* 34, 537–541. doi: 10.1002/mrm.1910340409

Calhoun, V., Adah, T., and Pearlson, G. (1999). "(Non)stationarity of temporal dynamics in fMRI," in *Annual Fall Meeting of the Biomedical Engineering Society* (Atlanta, GA), 1079. doi: 10.1109/IEMBS.1999.804239

Cauchy, A. (1921). Cours d'analyse de l'École royale polytechnique, 1ére partie: analyse algébrique. *Oeuvres* 2:373.

Chang, C., and Glover, G. (2010). Time-frequency characteristic of resting state brain connectivity measured with fMRI. *NeuroImage* 50, 81–98. doi: 10.1016/j.neuroimage.2009.12.011

Chen, Y., Bressler, S., and Ding, M. (2006). Frequency decomposition of conditional Granger causality and application to multivariate neural field potential data. *J. Neurosci. Methods* 150, 228–237. doi: 10.1016/j.jneumeth.2005.06.011

Cohen, J., Cohen, P., West, S., and Aiken, L. (2003). *Applied Multiple Regression/Correlation Analysis for the Behavioral Sciences, Vol. 1, 3rd Edn*. New York, NY: Lawrence Erlbaum Associates, Inc., Publishers.

Cribben, I., Haraldsdottir, R., Atlas, L. Y., Wager, T. D., and Lindquist, M. A. (2014). Dynamic connectivity regression: determining state-related changes in brain connectivity. *NeuroImage* 61, 907–920. doi: 10.1016/j.neuroimage.2012.03.070

Davey, C. E. (2011). *Critique of linear connectivity methods in functional magnetic resonance imaging* (Ph.D. thesis). University of Melbourne, Melbourne, VIC, Australia.

Davey, C. E., Grayden, D. B., Egan, G. F., and Johnston, L. A. (2013). Filtering induces correlation in fMRI resting state data. *NeuroImage* 64, 728–740. doi: 10.1016/j.neuroimage.2012.08.022

de Moortele, P. F. V., Pfeuffer, J., Glover, G. H., Ugurbil, K., and Hu, X. (2002). Respiration-induced B0 fluctuations and their spatial distribution in the human brain at 7 Tesla. *Magn. Reson. Med*. 47, 888–895. doi: 10.1002/mrm.10145

Diedrichsen, J., and Shadmehr, R. (2005). Detecting and adjusting for artifacts in fMRI time series data. *NeuroImage* 27, 624–634. doi: 10.1016/j.neuroimage.2005.04.039

Fisher, R. (1915). Frequency distribution of the values of the correlation coefficient in samples from an indefinitely large population. *Biometrika* 10, 507–521. doi: 10.1093/biomet/10.4.507

Friston, K., Jezzard, P., and Turner, R. (1994). Analysis of functional MRI time-series. *Hum. Brain Mapp*. 1, 153–171. doi: 10.1002/hbm.460010207

Goebel, R., Roebroeck, A., Kim, D., and Formisano, E. (2003). Investigating directed cortical interactions in time-resolved fMRI data using vector autoregressive modelling and Granger causality mapping. *Magn. Reson. Imaging* 21, 1251–1261. doi: 10.1016/j.mri.2003.08.026

Granger, C., and Newbold, P. (1974). Spurious regressions in econometrics. *J. Econ*. 2, 111–112. doi: 10.1016/0304-4076(74)90034-7

Gudbjartsson, H., and Patz, S. (1995). The Rician distribution of noisy MRI data. *Magn. Reson. Med*. 34, 910–914. doi: 10.1002/mrm.1910340618

Guo, S., Seth, A., Kendrick, K., Zhou, C., and Feng, J. (2008). Partial Granger causality - eliminating exogenous inputs and latent variables. *J. Neurosci. Methods* 172, 79–93. doi: 10.1016/j.jneumeth.2008.04.011

Handwerker, D. A., Roopchansing, V., Gonzalez-Castillo, J., and Bandettini, P. A. (2012). Periodic changes in fMRI connectivity. *NeuroImage* 63, 1712–1719. doi: 10.1016/j.neuroimage.2012.06.078

Hansen, L., Purushotham, A., and Kim, S. (2003). "Chapter 3: Testing competing hypothesis about single trial fMRI," *Exploratory Methods in Neuroimaging*, 49–62.

Härdle, W., and Simar, L. (2007). *Applied Multivariate Statistical Analysis, 2nd Edn*. Berlin: Springer.

Hindriks, R., Adhikari, M. H., Murayama, Y., Ganzetti, M., Mantini, D., Logothetis, N. K., et al. (2016). Can sliding-window correlations reveal dynamic functional connectivity in resting-state fMRI. *NeuroImage* 242–256. doi: 10.1016/j.neuroimage.2015.11.055

Hutchison, R. M., Womelsdorf, T., Allen, E. A., Bandettini, P. A., Calhoun, V. D., Corbetta, M., et al. (2013). Dynamic functional connectivity: promise, issues, and interpretations. *NeuroImage* 80, 1–32. doi: 10.1016/j.neuroimage.2013.05.079

Kimberg, D. (2008). *A Functional Connectivity Primer*. Center for Functional Neuroimaging University of Pennsylvania.

Lindquist, M., Xu, Y., Nebel, M. B., and Caffo, B. S. (2014). Evaluating dynamic bivariate correlations in resting-state fMRI: a comparison study and a new approach. *NeuroImage* 101, 531–546. doi: 10.1016/j.neuroimage.2014.06.052

Long, C., Brown, E., Triantafyllou, C., Aharon, I., Wald, L., and Solo, V. (2005). Nonstationary noise estimation in functional MRI. *NeuroImage* 28, 890–903. doi: 10.1016/j.neuroimage.2005.06.043

Lund, T., Madsen, K., Sidaros, K., Luo, W., and Nichols, T. (2006). Non-white noise in fMRI: Does modelling have an impact. *NeuroImage* 29, 54–66. doi: 10.1016/j.neuroimage.2005.07.005

Luo, H., and Puthusserypady, S. (2007). fMRI data anaysis with nonstationary noise models: a Bayesian approach. *IEEE Trans. Biomed. Eng*. 54, 1621–1630. doi: 10.1109/TBME.2007.902591

Marrelec, G., Daunizeau, J., Pelegrini-Issac, M., Doyon, J., and Benali, H. (2005). Conditional correlation as a measure of mediated interactivity in fMRI and MEG/EEG. *IEEE Trans. Signal Process*. 53, 3503–3516. doi: 10.1109/TSP.2005.853211

McIntosh, A., and Gonzalez-Lima, F. (1994). Structural equation modeling and its application to network analysis in functional brain imaging. *Hum. Brain Mapp*. 2, 2–22. doi: 10.1002/hbm.460020104

Niazy, R., Xie, J., Miller, K., Beckmann, C., and Smith, S. (2011). Spectral characteristics of resting state networks. *Prog. Brain Res*. 193, 259–276. doi: 10.1016/B978-0-444-53839-0.00017-X

Oikonomou, V., Tripoliti, E., and Fotiadis, D. (2009). "A sparse linear model for the analysis of fMRI data with non stationary noise," in *4th International IEEE EMBS Conference on Neural Engineering* (Antalya), 253–257. doi: 10.1109/NER.2009.5109281

Oikonomou, V. P., Tripoliti, E. E., and Fotiadis, D. I. (2010). Bayesian methods for fMRI time-series analysis using a non-stationary model for the noise. *IEEE Trans. Inform. Technol. Biomed*. 14, 664–674. doi: 10.1109/TITB.2009.2039712

Ojemann, J., Akbudak, E., Snyder, A., McKinstry, R., Raichle, M., and Conturo, T. (1997). Anatomic localization and quantitative analysis of gradient refocused echo-planar fMRI susceptibility artifacts. *NeuroImage* 6, 156–167. doi: 10.1006/nimg.1997.0289

Park, C., Lazar, N., Ahn, J., and Sornborger, A. (2010). A multiscale analysis of the temporal characteristics of resting-state fMRI data. *J. Neurosci. Methods* 193, 334–342. doi: 10.1016/j.jneumeth.2010.08.021

Rick, J., Speck, O., Maier, S., Tüscher, O., Dossel, O., Hennig, J., et al. (2010). Optimized EPI for fMRI using a slice-dependent template-based gradient compensation method to recover local susceptibility-induced signal loss. *Magn. Reson. Mater. Phys*. 23, 165–176. doi: 10.1007/s10334-010-0215-x

Said, E., and Dickey, D. (1984). Testing for unit roots in autoregressive moving average models of unknown order. *Biometrika* 71, 599–607. doi: 10.1093/biomet/71.3.599

Stejskal, E. (1965). Use of spinechoes in a pulsed magnetic-field gradient to study anisotropic restricted diffusion and flow. *J. Chem. Phys*. 43:3597. doi: 10.1063/1.1696526

Tana, M., Bianchi, A., Vitali, P., Villani, F., and Cerutti, S. (2008). "Exploring interregional brain interactivity in temporal lobe epilepsy using partial correlation analysis of fMRI data," in *30th Annual International IEEE EMBS Conference* (Vancouver, BC: IEEE), 4423–4426. doi: 10.1109/IEMBS.2008.4650192

Tanase, C., O'Hara, J., Davis, D., Boada, F., Buonocore, M. H., and Carter, C. S. (2011). "Identifying and separating the RF fluctuations from the measurement noise," in *Proceedings of the International Society of Magnetic Resonance in Medicine, Vol. 19* (Quebec, QC), 3629.

Turner, G., and Twieg, D. (2005). Study of temporal stationarity and spatial consistency of fMRI noise using independent component analysis. *IEEE Trans. Med. Imaging* 24, 712–718. doi: 10.1109/TMI.2005.846852

Wang, Y., and Xia, J. (2007). "Functional interactivity in fMRI using multiple seeds correlation analyses - novel methods and comparisons," in *Information Processing in Medical Imaging, 20th International Conference* (Kerkrade), 147–159. doi: 10.1007/978-3-540-73273-0_13

Weisskoff, R. (1996). Simple measurement of scanner stability for functional NMR imaging of activation in the brain. *Magn. Reson. Med*. 36, 643–645. doi: 10.1002/mrm.1910360422

Wilcoxon, F. (1945). Individual comparisons by ranking methods. *Biometr. Bull*. 1, 80–83. doi: 10.2307/3001968

Wink, A., and Roerdink, J. (2006). BOLD noise assumptions in fMRI. *Int. J. Biomed. Imaging* 2006:12014. doi: 10.1155/IJBI/2006/12014

Conflict of Interest: The authors declare that the research was conducted in the absence of any commercial or financial relationships that could be construed as a potential conflict of interest.

Copyright © 2021 Davey, Grayden and Johnston. This is an open-access article distributed under the terms of the Creative Commons Attribution License (CC BY). The use, distribution or reproduction in other forums is permitted, provided the original author(s) and the copyright owner(s) are credited and that the original publication in this journal is cited, in accordance with accepted academic practice. No use, distribution or reproduction is permitted which does not comply with these terms.

frontiers in Neuroscience

ORIGINAL RESEARCH
published: 09 March 2021
doi: 10.3389/fnins.2021.552666

Contextual MEG and EEG Source Estimates Using Spatiotemporal LSTM Networks

Christoph Dinh[1,2,3†], John G. Samuelsson[1,4,5†], Alexander Hunold[6], Matti S. Hämäläinen[1,2,4] and Sheraz Khan[1,2,4]*

[1] Athinoula A. Martinos Center for Biomedical Imaging, Massachusetts General Hospital, Charlestown, MA, United States, [2] Department of Radiology, Massachusetts General Hospital (MGH), Charlestown, MA, United States, [3] Institute for Medical Engineering, Research Campus STIMULATE, Otto-von-Guericke University, Magdeburg, Germany, [4] Harvard Medical School, Boston, MA, United States, [5] Harvard-MIT Division of Health Sciences and Technology (HST), Massachusetts Institute of Technology, Cambridge, MA, United States, [6] Institute of Biomedical Engineering and Informatics, Technische Universität Ilmenau, Ilmenau, Germany

OPEN ACCESS

Edited by:
Miguel Castelo-Branco, Coimbra Institute for Biomedical Imaging and Translational Research (CIBIT), Portugal

Reviewed by:
Alberto Sorrentino, University of Genoa, Italy
Théodore Papadopoulo, Research Centre Inria Sophia Antipolis Méditerranée, France
Annalisa Pascarella, Istituto per le Applicazioni del Calcolo "Mauro Picone" (IAC), Italy
Arpan Banerjee, National Brain Research Centre (NBRC), India

***Correspondence:**
Christoph Dinh
christoph.dinh@mne-cpp.org

† These authors have contributed equally to this work

Specialty section:
This article was submitted to Brain Imaging Methods, a section of the journal Frontiers in Neuroscience

Received: 16 April 2020
Accepted: 25 January 2021
Published: 09 March 2021

Citation:
Dinh C, Samuelsson JG, Hunold A, Hämäläinen MS and Khan S (2021) Contextual MEG and EEG Source Estimates Using Spatiotemporal LSTM Networks. Front. Neurosci. 15:552666. doi: 10.3389/fnins.2021.552666

Most magneto- and electroencephalography (M/EEG) based source estimation techniques derive their estimates sample wise, independently across time. However, neuronal assemblies are intricately interconnected, constraining the temporal evolution of neural activity that is detected by MEG and EEG; the observed neural currents must thus be highly context dependent. Here, we use a network of Long Short-Term Memory (LSTM) cells where the input is a sequence of past source estimates and the output is a prediction of the following estimate. This prediction is then used to correct the estimate. In this study, we applied this technique on noise-normalized minimum norm estimates (MNE). Because the correction is found by using past activity (context), we call this implementation Contextual MNE (CMNE), although this technique can be used in conjunction with any source estimation method. We test CMNE on simulated epileptiform activity and recorded auditory steady state response (ASSR) data, showing that the CMNE estimates exhibit a higher degree of spatial fidelity than the unfiltered estimates in the tested cases.

Keywords: MEG, EEG, source estimation, spatiotemporal source estimation, spatial filtering, grid-based Markov localization, LSTM, deep learning

INTRODUCTION

Magneto- and electroencephalography (M/EEG) have excellent sub-millisecond temporal resolution but limited spatial resolution. The most commonly used M/EEG distributed source estimation methods, e.g., MNE, dSPM, and sLORETA, are linear and source estimates are derived time-sample by time-sample, without considering the temporal sequence (Hamalainen and Ilmoniemi, 1994; Dale et al., 2000; Pascual-Marqui, 2002). In other words, these methods fit their source estimates directly to the sensor data without assuming any relationship between the neuronal current distributions across time. This inverse problem is ill-posed because different current distributions can produce the same or similar electric potentials and magnetic fields around the head as detected by the limited amount of M/EEG sensors (Helmholtz, 1853; Hämäläinen et al., 1993). The ill-posedness of the inverse problem along with the low SNR in M/EEG recordings cause the limited spatial resolution of the MEG and EEG technologies (Samuelsson et al., 2020).

A few different approaches have been developed to deal with this ill-posedness. The most common approach involves penalty terms on the source amplitude (regularization) or constraints limiting the solution space of the inverse problem. Constraining the solution space can be achieved by, e.g., assuming spatial smoothness (Pascual-Marqui et al., 1994; Dinh et al., 2015, 2018) or imposing focal estimates (Gorodnitsky et al., 1995). Bayesian methods that employ an estimated source covariance matrix as a prior have also been employed to restrict the solution space to sparse source reconstructions (Phillips et al., 2005; Mattout et al., 2006) or by computing posterior distributions based on hierarchical priors (Sato et al., 2004; Nummenmaa et al., 2007; Costa et al., 2017). These methods, however, commonly assume that the prior probability distribution of the sources is independent of time. This assumption ignores the temporal structure of the underlying neural activity that could be used to help reduce the ill-posedness of the inverse problem by constraining the solution space.

It is well-known that the human brain is intricately interconnected and several studies have shown that dynamic spatiotemporal interactions are central features of brain activity (Khan et al., 2015). For example, intracranial cortical recordings show strong local spatial correlations within 10 mm along the cortex (Bullock et al., 1995; Destexhe et al., 1999; Leopold et al., 2003) and physiologically motivated spatiotemporal models of neuronal networks have had success in explaining EEG and MEG data (Gross et al., 2001; Jirsa et al., 2002; Wright et al., 2003; Izhikevich and Edelman, 2008). These observations indicate that neural activity has a distinct spatiotemporal dynamics meaning that the brain state at any given time is a function of past brain activity, i.e., its context (Kozhemiako et al., 2020).

There have been efforts to include spatiotemporal dynamics in M/EEG source estimation but these methods have assumed certain constrained spatiotemporal interactions. One such example is the use of Bayesian source estimation methods that incorporate temporal smoothness constraints, which specify various prior distributions for the sources in space and time (Baillet and Garnero, 1997; Greensite, 2003; Somersalo et al., 2003; Friston et al., 2008; Limpiti et al., 2008; Trujillo-Barreto et al., 2008; Zumer et al., 2008; Bolstad et al., 2009; Ou et al., 2009; Sorrentino et al., 2009; Lucka et al., 2012; Vivaldi and Sorrentino, 2016; Calvetti et al., 2019). Mixed-Norm estimates have been introduced that impose spatial stationarity of the source estimates within a given time window and quasinorm penalties to promote spatial sparsity (Gramfort et al., 2012; Gramfort et al., 2013b; Strohmeier et al., 2014). Linear state-space models have also been employed that either apply temporally independent approximations (Galka et al., 2004) or a parametric approach (Long et al., 2011) to reduce their computational burden. Recent studies have introduced more realistic spatiotemporal dynamic models using Kalman filters, which take local cortical interactions into account (Lamus et al., 2012; Pirondini et al., 2018) by assuming a linear relationship between subsequent samples. This approach implicitly includes the estimation history but with the limiting assumption that past activity is linearly related to the subsequent activation and directly manifests in the source estimate. Although these models have shown promise, the potential of incorporating non-linear long range dynamic interactions without strict *a priori* assumptions to improve inverse solutions has remained largely unexplored.

Meanwhile, recent advances in machine learning have focused on sequential data sets, e.g., recurrent neural networks (RNN), enabling contextual data recognition (LeCun et al., 2015; Schmidhuber, 2015). These new contextual capabilities have been demonstrated to significantly improve classification accuracy in natural language processing (NLP) and have been successfully applied in, e.g., text and speech recognition (Graves et al., 2013; Chorowski et al., 2015). Although some studies have used machine learning techniques to classify various brain states or seizures based on MEG and particularly EEG data, most studies have done so in sensor space and the use of machine learning techniques in the M/EEG inverse problem has yet to be fully explored (Hofmann et al., 2018; Ali et al., 2019; Yu et al., 2019).

Here we investigate whether contextual machine learning techniques can be applied to reduce the ill-posedness of the M/EEG inverse problem, thus utilizing the superior temporal resolution of M/EEG to increase the spatial fidelity of source estimates. This approach thus constitutes a spatiotemporal inverse method that is based on deep learning without too strong explicit *a priori* modeling assumptions, except for those intrinsic to MNE, which has been the main focus of previous spatiotemporal inverse methods. In our approach, source estimates are spatially filtered, or "corrected," by a prediction that has been generated by a network of long short-term memory (LSTM) cells (Hochreiter and Schmidhuber, 1997) from a sequence of previous source estimates. LSTM cells constitute a special type of RNN which has consistently shown success when applied to data with a temporal structure, e.g., in natural language processing and grid-based markov localization problems, and is thus a suitable candidate for a spatiotemporal inverse operator.

In this study we implemented the technique together with noise-normalized minimum norm estimates (MNE), and therefore call this implementation Contextual Minimum Norm Estimates (CMNE). Importantly, this method can also be described in the framework of linear algebra, where the weighing vector is being updated in a time-dependent manner using the prior context. Conceptually, the main advantage of the CMNE approach over recursive Bayesian filters like the Kalman filter is that its model is not explicitly defined and can instead be learned from the data; RNNs are thus more general than Kalman filter approaches. We tested our CMNE implementation on simulated epileptiform and recorded M/EEG data from auditory steady state response (ASSR) experiments. An earlier preprint version of this work was posted at arXiv (Dinh et al., 2019).

MATERIALS AND METHODS

Contextual Estimates

We begin by describing our method and the specific implementation used in this study. The implementation of the presented method can be found at https://github.com/chdinh/cmne. We then describe the data analysis and training of

the LSTM network. We denote vectors and scalars by lowercase and matrices by uppercase characters.

M/EEG signals are linked to their neural sources by a time-invariant gain matrix G, which incorporates the forward model:

$$y_t = Gx_t + n_t, \tag{1}$$

where the vector y_t represents the sensor data at time t, the vector x_t represents the true source distribution, and n_t is the noise. In the following, we will be using the whitened measured signals $\tilde{y}_t$ and whitened gain matrix $\tilde{G}$,

$$\tilde{y}_t = C_n^{-1/2} y_t \tag{2}$$

and

$$\tilde{G} = C_n^{-1/2} G, \tag{3}$$

where C_n is the noise covariance matrix. Most source estimates $\hat{x}_t$ are found by minimizing a cost function,

$$\hat{x}_t = \arg\min_{x_t} \left(\left|\left| \tilde{y}_t - \tilde{G}x_t \right|\right|_2^2 + f(x_t) \right) \tag{4}$$

where the first term is the Euclidean norm of the difference between the measured data $\tilde{y}_t$ and the predicted signal $\tilde{G}x_t$ based on the model $\tilde{G}$ and source distribution x_t, while $f(x_t)$ incorporates *a priori* assumptions or regularization. In MNE, $f(x_t) = \lambda^2 x_t^T C_R^{-1} x_t$, where C_R is the source covariance matrix and λ^2 is the Tikhonov regularization parameter, which was set to $\lambda^2 = 1/\mathrm{SNR}^2 = 1/9$, assuming an SNR of 3. The solution to this minimization problem can be written as a product of the measured data $\tilde{y}_t$ and an inverse kernel K,

$$\hat{x}_t = K\tilde{y}_t, \tag{5}$$

$$K = C_R \tilde{G}^T \left(\tilde{G} C_R \tilde{G}^T + \lambda^2 I \right)^{-1}, \tag{6}$$

which is thus time-invariant and is applied sample-wise to compute the source estimate $\hat{x}_t$ from each measurement $\tilde{y}_t$. In dynamic statistical parametric mapping (dSPM) (Dale et al., 2000), the inverse kernel K is normalized with respect to the noise energy mapped to each source;

$$K_{\mathrm{dSPM}} = W_{\mathrm{dSPM}} K, \tag{7}$$

where W_{dSPM} is a diagonal matrix;

$$W_{\mathrm{dSPM}_{i,i}} = \frac{1}{\sqrt{\mathrm{diag}_i \left(K C_n K^T \right)}}. \tag{8}$$

In this study, the dSPM estimates were rectified and then normalized by z-scoring;

$$\hat{q}_{t_i} = (|\hat{x}_{t_i}| - \mu\left(|\hat{x}_{t_i}|\right))/\sigma(|\hat{x}_{t_i}|). \tag{9}$$

In CMNE, the estimates are then reweighted with a time-dependent diagonal weighting matrix whose diagonal elements are the output of the LSTM network;

$$b_t = W_t^{CMNE} \hat{q}_t, \tag{10}$$

$$\mathrm{diag}(W_t^{CMNE}) = \left| \mathrm{LSTM}\left(\{b_i\}_{i=t-k,\ ...,\ t-1} \right) \right| / \max\left(\left| \mathrm{LSTM}\left(\{b_i\}_{i=t-k,\ ...,\ t-1} \right) \right| \right) |_{t \geq k}, \tag{11}$$

$$W_t^{CMNE} = I\ |_{t=0..k-1} \tag{12}$$

where b_t is the final contextual estimate, LSTM is our network of LSTM cells, k is the number of LSTM cells in our network, which is a hyperparameter, and W_t^{CMNE} is a diagonal matrix whose diagonal entries is the prediction output of the LSTM network after the first k time steps, when the LSTM network has sufficient history to make a prediction, and the identity matrix before then. After the first k timesteps, the CMNE estimate itself is used as input to the LSTM network, forming a Markov chain;

$$b_t = W_t^{CMNE}(b_{i=t-1,\ldots,t-k})\hat{q}_t. \tag{13}$$

In this approach, we thus use two spatial filters, first the filter found by the inverse of the noise covariance matrix (dSPM) and secondly the spatial filter given by the LSTM prediction which contains the contextual information. These two filters serve different functionalities; dSPM gives statistical scores with respect to the baseline while keeping the weights static. In contrast, the CMNE weights are updated in a recursive fashion. This algorithm is illustrated in **Figure 1**.

The employed LSTM network consists of an LSTM cell sequence, shown in **Figure 2**, where each cell i has a source estimate of the corresponding past time step $b(\hat{q}_{t-i})$ as its input, which was standardized by z-scoring. For the first k time steps, before we have enough previous estimates to generate a prediction, the non-contextual dSPM estimates $\hat{q}_i$ are used (**Figure 1**). Each LSTM cell consists of four fully connected neural networks (NN); the "forget gate layer," "input gate layer," "candidate cell state layer," and "output gate layer." All of those networks have sigmoidal activation functions except for the candidate cell state layer which has tanh activation functions. The actual output h_t of the LSTM cell is a filtered subset of the cell state S_t. The number of neurons in each neural network layer d is another hyperparameter, in addition to the number of LSTM cells k. There are thus two hyperparameters in this network; k and d. The LSTM network is followed by a densely connected neural network layer with linear activation functions, i.e., a linear transformation with adaptable entries, mapping the output of the last LSTM cell h_t to the prediction $\overline{b_t}$ (**Figure 2**). The processing steps of each LSTM cell can thus be summarized in the following equations (Hochreiter and Schmidhuber, 1997);

$$f_t = \sigma(b_{t-1}^T W_f + h_{t-1}^T V_f + B_f) \tag{14}$$

$$i_t = \sigma(b_{t-1}^T W_i + h_{t-1}^T V_i + B_i) \tag{15}$$

$$\widetilde{S_t} = \tanh(b_{t-1}^T W_s + h_{t-1}^T V_s + B_s) \tag{16}$$

$$o_t = \sigma(b_{t-1}^T W_o + h_{t-1}^T V_o + B_o) \tag{17}$$

$$S_t = \sigma(f_t * S_{t-1} + i_t * \widetilde{S_t}) \tag{18}$$

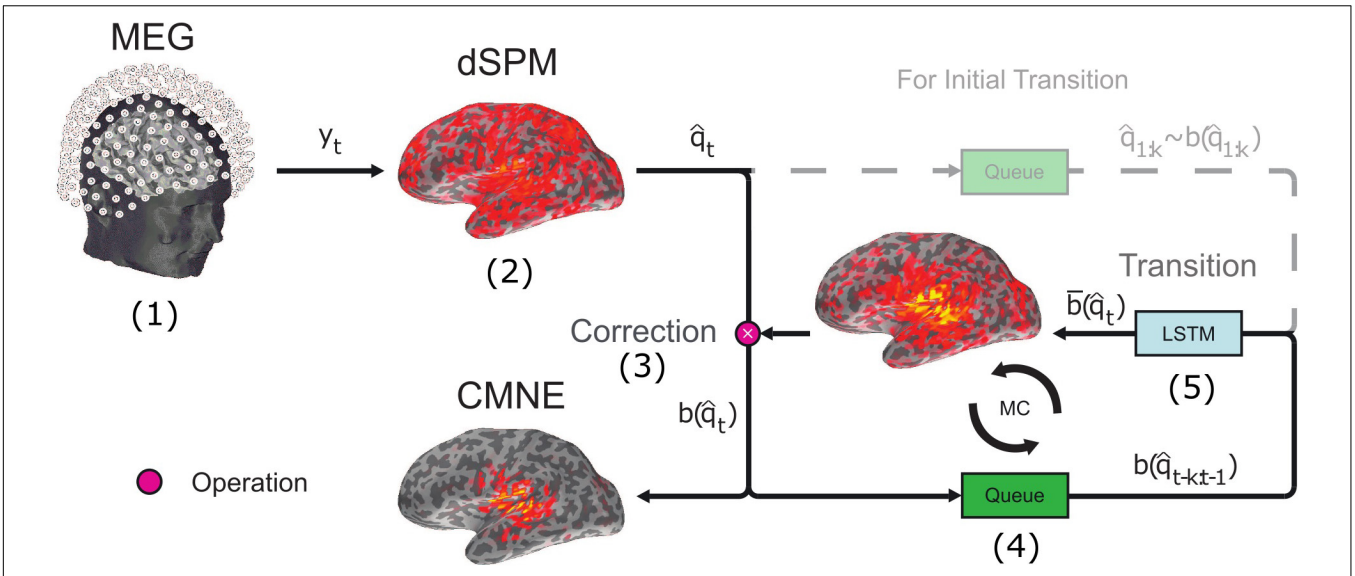

FIGURE 1 | Schematic illustration of CMNE outlining the major steps. (1) M/EEG data are measured, saved and processed as per standard protocol. (2) Based on the measurement data y_t, a source estimate $\hat{q}_t$ is found by dSPM. (3) The dSPM source estimate $\hat{q}_t$ is corrected by a prediction $\bar{b}\,(\hat{q}_t)$ of what the estimate is expected to be based upon previous activations. This prediction $\bar{b}\,(\hat{q}_t)$ is found by an LSTM network (explained in step 5). The correction is an elementwise product $*$ of the source estimate $\hat{q}_t$ and the prediction $\bar{b}\,(\hat{q}_t)$, and the resulting product $b\,(\hat{q}_t)$ is the CMNE estimate: $b\,(\hat{q}_t) = \hat{q}_t * \bar{b}\,(\hat{q}_t)$. (4) The CMNE estimate $b\,(\hat{q}_t)$ is put into a stack together with the k previous activations $b\,(\hat{q}_{t-k:t})$. (5) This stack of previous CMNE estimates is given to the LSTM network to predict the next activation $\bar{b}\,(\hat{q}_{t+1})$. This forms an iterative circle, i.e., a Markov chain (MC) (Dinh, 2015). In the first k time steps there is not enough prior history to make a prediction and the dSPM estimates are therefore not corrected and used as input to the LSTM network instead of the CMNE estimates.

$$h_t = o_t * tanh(S_t) \tag{19}$$

$$\bar{b}_t = h_t^T W_d + B_d \tag{20}$$

where $*$ denotes elementwise multiplication (Hadamard product), + elementwise addition, W is the adaptable weights kernel multiplied with b_{t-1}, V is the adaptable weights kernel multiplied with h_{t-1} and B is the adaptable bias. $W_{\{f,i,s,o\}}$ are all $n_s \times d$ dimensional real matrices, $V_{\{f,i,s,o\}}$ are all $d \times d$ dimensional real matrices and $B_{\{f,i,s,o\}}$ are all d dimensional real vectors, where $n_s = 5124$ is the number of sources. W_d is the adaptable weights kernel matrix of the last densely connected neural network of dimensions $d \times n_s$ and B_d is the n_s dimensional bias vector. f_t, i_t, $\tilde{S}_t$, o_t, S_t, h_t are d-dimensional and b_t is n_s-dimensional. The weight matrices and bias vectors W, V, B were trained using supervised learning and is described in section "LSTM Network".

Data Analysis

Data Acquisition

MEG and MRI data were collected after informed consent from a healthy 27 years old male under a protocol approved by the Massachusetts General Hospital Institutional Review Board. The subject had no medical history of hearing loss.

T1-weighted, high resolution MPRAGE (Magnetization Prepared Rapid Gradient Echo) structural images were acquired on a 1.5 T Siemens whole-body MRI (magnetic resonance) scanner (Siemens Medical Systems) using a 32 channel head coil at MGH.

Auditory steady state response (ASSR) data were recorded from the subject in the MGH Martinos center MEG core in Charlestown, MA, using MEG and EEG. It is the same ASSR data that were used in Samuelsson et al. (2019). The MEG system was an Elekta-Neuromag (Helsinki, Finland) VectorView 306 channel MEG with 102 triplets consisting of one magnetometer and two orthogonal planar gradiometers for a total of 204 planar gradiometers and 102 magnetometers. The EEG was recorded with a 58 channel EasyCap system (EasyCap GmbH, Germany). The experiment was performed in a quiet, magnetically shielded room (Imedco, Switzerland). The recording was bandpass filtered between 0.1 and 1,650 Hz and sampled at 5,000 samples/s. The data were then digitally lowpass filtered at a cutoff frequency of 270 Hz and downsampled to 810 Hz. The ASSRs were elicited by an amplitude modulated (AM) sound which lasted 1 s. The AM sound was followed by an inter-stimulus interval of 500 ms plus jitter that was uniformly distributed between 0 and 750 ms, U(0, 0.75). The sound was thus played to the subject with an inter-trial pause uniformly distributed between 0.5 and 1.25 s duration. The carrier signal was a $f_0 = 1$ kHz sinusoid and was amplitude modulated to a depth of 90% by a superposition of a $f_1 = 40$ Hz and $f_2 = 223$ Hz sinusoid;

$$y(t) = \left(0.1 + 0.9[\sin\left(2\pi f_1 t\right) + \sin\left(2\pi f_2 t\right)]/2\right) \sin\left(2\pi f_0\, t\right). \tag{21}$$

Data Processing

The structural data were preprocessed using FreeSurfer (Dale et al., 1999; Fischl et al., 1999). After correcting for topological

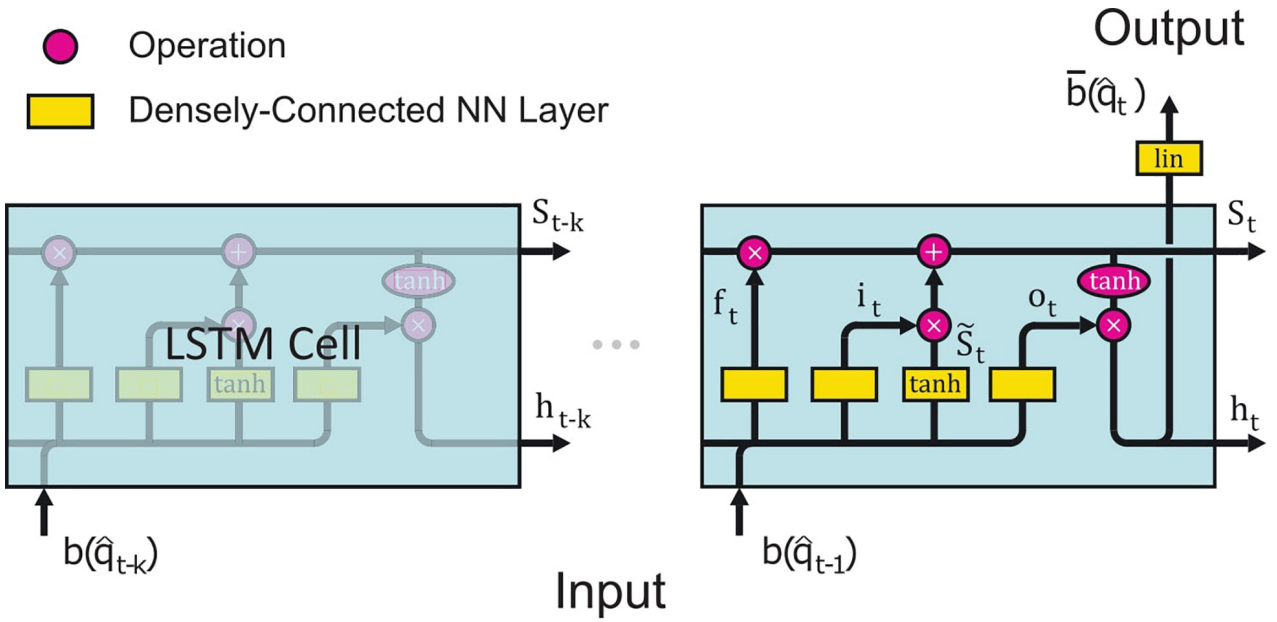

FIGURE 2 | Schematic illustration of the LSTM network architecture. The basic structure encompasses k LSTM cells connected in series, where the cell i receives input from the previous cell in the form of the cell state S_{i-1} (Eq. 18) and hidden cell state h_{i-1} (Eq. 19), and then ends with a fully connected NN layer, which outputs the prediction of the LSTM network $\bar{b}$. Apart from the input from the previous cell, each LSTM cell also receives input from the stack of previous estimates b_i. Each LSTM cell consists of four fully connected NN layers (yellow boxes) which all have the same complexity d = 1,280: (i) f_t (Eq. 14), the "forget gate layer," is an NN with a sigmoid activation function. This layer gates the previous cell states $0 \leq S_{t-1} \leq 1$ (Eq. 18) depending on h_{t-1} (Eq. 19) and the previous estimate b $(\hat{q}_{t-1})$ (Eq. 20). (ii) i_t (Eq. 15), the "input gate layer," is also a sigmoid layer with the same inputs as f_t. It determines which cell state values to update. (iii) $\tilde{S}_t$ (Eq. 16) is the subsequent fully connected NN layer with a *tanh* activation function, which creates candidate cell state values gated by i_t. The state S_t of the current cell is formed by "forgetting" outdated information of the previous cell state S_{t-1} through a multiplication with f_t followed by an update with the gated new cell state candidates $i_t * \tilde{S}_t$. (iv) o_t is a fully connected NN layer activated by a sigmoid function. This layer decides which cell states to output. It gates the *tanh* scaled cell state S_t. Because all NN layers have the same number of neurons d except for the final output layer, S_t and h_t are both d-dimensional vectors, see section "Contextual Estimates" for more details. The illustration is adapted from Olah (2015).

defects, cortical surfaces were tessellated using triangular meshes with ∼130,000 vertices in each hemisphere. To expose the sulci in the visualization of cortical data, we used the inflated surfaces computed by FreeSurfer. 49 bad epochs were dropped using autoreject (Jas et al., 2017), resulting in 1,653 clean, i.e., artifact free, epochs.

Forward Model and Inverse Operator

The dense triangulation of the folded cortical surface provided by FreeSurfer was decimated to a grid of 2,562 dipoles per hemisphere, corresponding to a spacing of approximately 6.2 mm between adjacent source locations. A piecewise-homogenous head conductor model with three compartments bounded by the inner skull, outer skull and outer skin was assumed, and the boundary element method (BEM) was used to compute the gain matrix (Hamalainen and Sarvas, 1989). The conductivities were 0.3, 0.006, 0.3 for the brain, skull and scalp, respectively. The watershed algorithm in FreeSurfer was used to generate the tessellations based on the MRI scan of the participant.

The initial current distribution estimate $\widehat{q_t}$ was obtained using dSPM with loose current dipole orientation constraints set at 0.2, where 0.0 corresponds to fixed and 1.0 to free orientations. The regularized ($\lambda = 0.1$) noise covariance matrix used to calculate the inverse operator was calculated over the pre-stimulus period. All forward and inverse calculations were done using MNE-C and MNE-python software (Gramfort et al., 2013a; Esch et al., 2019).

Simulation Study

A simulation study was conducted to test the performance of CMNE in comparison to dSPM, pure LSTM prediction, a control estimate, mixed-norm estimate (MxNE) and the spatiotemporal Kalman approach estimate as presented in Lamus et al. (2012). In the control estimate, 80 sequential dSPM distributions were averaged and multiplied with the dSPM of the following sample, thus mimicking our contextual estimate but without the LSTM network, which used a lookback of k = 80 samples. The gain of using LSTM networks can thus be examined by comparing this control estimate to CMNE. The simulations were designed to mimic the propagation of an epileptiform discharge in the left supratemporal cortex. The source configuration consisted of 5,124 current dipoles placed over the cortex with free orientations. Source space noise was added as stationary Gaussian noise with spectral characteristics taken from EEG readings, as described in Hunold et al. (2016). The activation wave form that modeled the epileptiform discharge was a

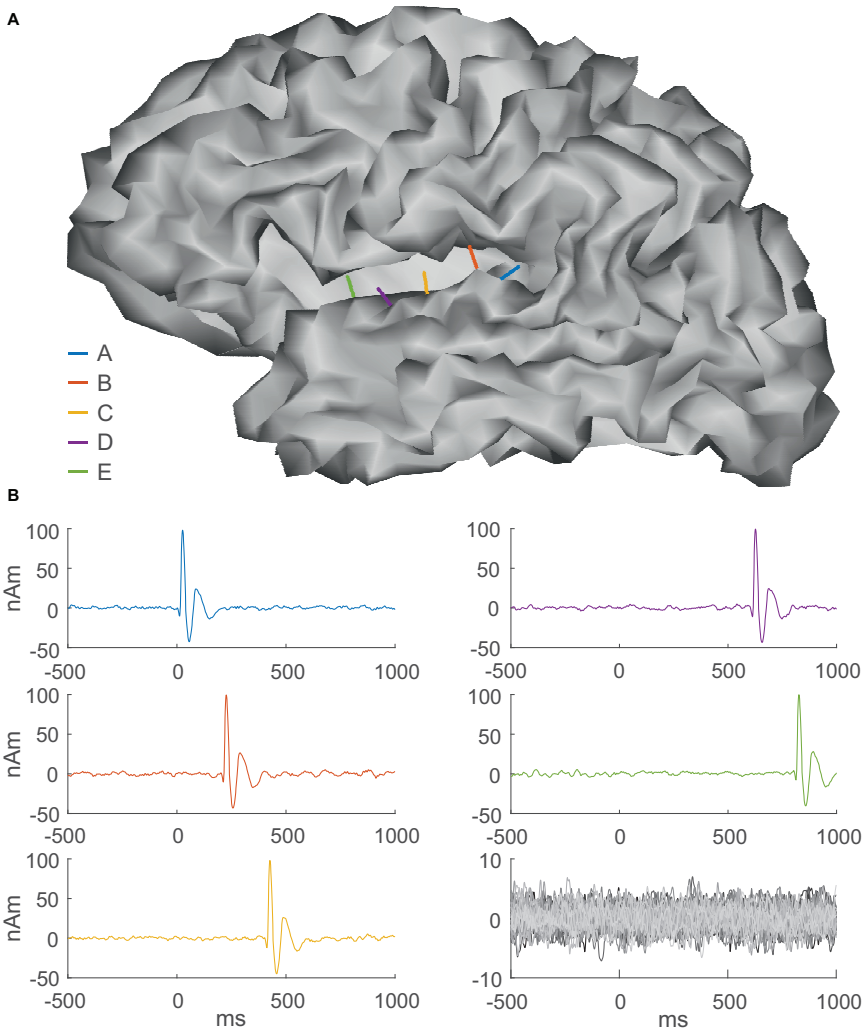

FIGURE 3 | Simulation setup. **(A)** Gray matter surface with five current dipoles in the superior temporal gyrus modeling epileptic foci, color-coded according to their sequential activation pattern as shown in **(B)**. **(B)** Time courses of sequentially activated dipoles (A–E) (color-coded graphs) modeling epileptiform discharges and background activity (lower right). One epoch comprises background activity lasting for 500 ms followed by a propagating epileptiform discharge lasting for 1 s.

spike-wave complex lasting 200 ms, starting sequentially in the posterior-anterior direction and making one simulated epileptiform discharge lasting for a total duration of 1,000 ms (**Figure 3**) and was superimposed on the noise. The spike-wave complex had an amplitude 5 times larger than that of the background activity (10 nAm). The propagating epileptic foci were represented by five current dipoles that were sequentially activated from posterior to anterior locations on the supratemporal cortex with a mutual distance of 9 mm. A total of 250 epileptiform discharges were simulated with a 500 ms interictal period. **Figure 3** shows an outline of the dipole activations.

Performance Metrics

To evaluate the performance of CMNE and compare it to other related source estimation methods we used the spatial fidelity evaluation metrics presented in Samuelsson et al. (2020); we calculated the peak localization error PE and spatial dispersion SD,

$$\mathrm{PE} = ||r_i - r_j||_2, \tag{22}$$

$$j = \underset{i}{\operatorname{argmax}} \left(\{ |\hat{x}_i| \}_i \right), \tag{23}$$

$$\mathrm{SD} = \frac{\sum_{k=1}^{N_s} d_{jk} |\hat{x}_k|}{\sum_{k=1}^{N_s} |\hat{x}_k|}, \tag{24}$$

$$d_{jk} = ||r_j - r_k||_2, \tag{25}$$

where r_i is the location of the active source, r_j is the location of the peak reconstruction amplitude, d_jk is the distance between r_j and source k and $\hat{x}_\mathrm{i}$ is, as before, the estimate at source i. To evaluate temporal fidelity, we calculated Pearson's correlation coefficient r in the simulation study between the true source activations (**Figure 3**) and the time courses of the estimated reconstructions

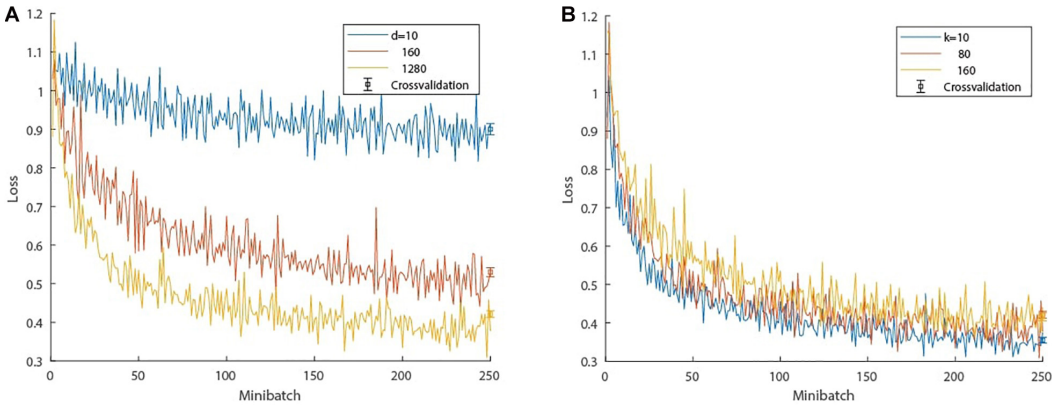

FIGURE 4 | Cross-validation of hyperparameter evaluation. **(A)** Loss progression: influence of the number of hidden units d in the LSTM network on the performance with a constant look back of $k = 80$ samples. **(B)** Loss progression: influence of the look back, i.e., number of past samples k used in the LSTM network with a fixed number of hidden units $d = 1280$. The bar plots depict the cross-validation testing loss after training. The whiskers denote one standard error and the center refers to the mean loss.

that peaked at the time of the spikes $\hat{x}(t)_{\mathrm{j}}$. We also quantified SNR in source space as

$$\mathrm{SNR} = \frac{\sigma\left(\left\{\left|\hat{x}_{t,i}\right|\right\}_{i\in A,\ t\in S}\right)^2}{\sigma\left(\left\{\left|\hat{x}_{t,i}\right|\right\}_{i\in A,\ t\notin S}\right)^2}, \tag{26}$$

where σ is the standard deviation, A is the primary auditory cortex A1 in the ASSR data and the entirety of the auditory cortex in the simulations and S is the signal segment defined as the ictal period in the simulations and as the N1 and P2 responses in the ASSR data, i.e., the SNR is defined as the standard deviation of the activation in the auditory cortex during the activation period divided by standard deviation of the activation in the auditory cortex outside of the activation period (Shahin et al., 2007).

LSTM Network

The LSTM networks were trained on dSPM source estimates. The available epochs were randomly divided up in one training data set (85%) and one validation data set (15%). The training and validation data sets were thus disjoint. The training data were generated using overlapping sliding windows in time over the epochs, each window containing k time steps, one for each LSTM cell. The LSTM network predicts the subsequent dSPM activation based on these k past time steps and the ground truth is the actual dSPM estimate that it is trying to predict. Prior to the training, the input (past k dSPM estimates) and ground truth (current dSPM estimate) were standardized by z-scoring.

We employed the mean-square error (MSE) as the loss function and stochastic gradient descent (Adam algorithm) as the optimization method (Kingma and Ba, 2014). The training was organized in a minibatch setting which split the training process into small batches comprising a small set of gradient evaluations, the LSTM weights being updated using the anti-gradient of the error with respect to the LSTM weights over each minibatch. The LSTM setup, training and evaluation was realized in CNTK/TensorFlow in combination with Keras as the frontend API (Abadi et al., 2015; Seide and Agarwal, 2016; Chollet, 2018).

Hyperparameter evaluation (the number of hidden units d in the LSTM network and the number of past time steps k used as inputs to the LSTM prediction) was done by cross-validation on the ASSR data. In the cross-validation, the training data sets amounted to 85% of all data points and the remaining 15% were used for testing; cross-validation was performed 10 times. The training data were grouped into 30 minibatches. Each minibatch consisted of 30 feature representations, each feature representation being a randomly selected window of 81 consecutive samples, 80 being used as inputs to the LSTM network to predict the 81st sample, which is compared to the ground truth. First, the influence of the LSTM units on the performance was tested by varying d with a constant look back of $k = 80$ samples. The training and testing results are shown in a loss graph in **Figure 4A**. Second, the optimal number of past time steps k was determined with a fixed number of hidden units $d = 1280$, which is an appropriate trade-of between prediction accuracy and training time. The results are depicted in **Figure 4B**, which also offers insight into the genericity of the length of the time window used as input to the LSTM prediction; generally a longer time window results in more accurate predictions but comes at a higher computational cost in the case of the ASSR data. It is conceivable that other brain states elicited by other stimuli could affect these results.

Based on this evaluation, we chose a final LSTM network topology of $d = 1280$ units and a window size comprising the past $k = 80$ samples. The selection of the number of hidden units was a compromise between training time and prediction accuracy. We anticipate that a larger number of units would further improve the network performance. The choice of k was also a trade-off; shorter windows have fewer LSTM cells and thus fewer weights to adjust, leading to faster convergence, while wider time windows are more robust

to fluctuations. $k = 80$ was found to be a suitable trade-off between the two.

RESULTS

Simulation Study

In the simulation study, we trained the LSTM network with the topology ($d = 1280$, $k = 80$) using only 100 minibatch iterations. Each minibatch comprised 30 evaluations of 25 windows per evaluation. The windows contained 81 consecutive source estimation samples (80 used as input and 1 as the label), corresponding to a time window of 0.1 s, whose starting points were randomly selected from the 212 raw training epochs.

Figure 5 shows a comparison between CMNE, dSPM, MxNE, LSTM prediction and a control estimate applied to an average of 20 epochs as well as the Kalman source estimation. CMNE has the highest SNR (Eq. 26) as seen in the third column of **Figure 5**. However, the LSTM prediction is not able to capture the temporal dynamics of the neural activation patterns adequately; the waveforms get distorted as seen in the second column of **Figure 5**. The correction step that utilizes the current dSPM estimation compensates for this; the peak of the CMNE estimate is on time but the ripples following the spikes are suppressed. The control estimate has a reduced SNR, significantly lower than the SNR of CMNE, and distorts the waveforms as well as exhibiting a high degree of spatial dispersion. The Kalman source estimate and particularly MxNE result in focal estimates with a low degree of spatial dispersion (column 4), although with lower noise suppression than the CMNE estimate as evident in the lower source space SNR.

Figure 6 shows the source reconstruction by dSPM, CMNE, MxNE, and the Kalman approach at the time of maximal activation along with the ground truth. The localization error PE was lower with CMNE as compared to dSPM for all dipole activations. While MxNE had zero localization error for dipoles B and D, and the Kalman approach resulted in marginally lower localization error than CMNE for dipole activations A and B, CMNE showed a consistent small localization error, being no larger than 4.5 mm for any activation, whereas the other spatiotemporal methods showed a highly variant result, particularly MxNE that resulted in localization errors varying between 0 and 25 mm. We also notice that while dSPM and the Kalman approach do not manage to reconstruct the amplitudes of dipoles C, D, and E, CMNE maintains an adequate amplitude reconstruction for all active vertices. Furthermore, CMNE does not result in spurious activations during interstimulus periods. However, while the activation signals are relatively well reconstructed with dSPM as measured by the relative amplitude of the damped oscillations to the peak value, CMNE concentrates most of the signal energy around the peak activation timepoint, resulting in a less authentic temporal reconstruction, quantified in the Pearson's correlation coefficient which is higher for dSPM than CMNE for all activations except one. This is, however, a drawback that CMNE shares with the other spatiotemporal methods; while MxNE and the Kalman approach adequately reconstruct the activation in some cases, the reconstruction is completely off in other activations resulting in a very low correlation coefficient.

Auditory Steady State Response

The same LSTM network topology was used for processing of the ASSR data ($d = 1280$, $k = 80$) and the results were compared with dSPM, MxNE, the Kalman approach and the LSTM prediction alone as well as the control estimate, as was done in the simulation study. The training was performed with 250 minibatch iterations each comprising 30 evaluations containing 20 windows per evaluation. The windows contained 81 subsequent source estimation samples, which were randomly selected from the 1,405 artifact-free epochs used for training. Validation was made based on the remaining 248 epochs that were not used in the training.

Figure 7 shows the results where the estimates have been found from 20 averaged ASSR epochs. The label A1 marks the primary auditory cortex. The spatial dispersion of CMNE is lower than that with dSPM and results in higher SNR (Eq. 26). The MxNE does not reconstruct any activation in the primary auditory cortex, likely because the input SNR was too low. The Kalman estimate shows higher spatial dispersion than CMNE and does not seem to be able to capture the N1 and P2 responses well. The control estimate resulted in a very inadequate reconstruction, showcasing the added benefit of the LSTM prediction.

DISCUSSION

The contextual nature of brain activity as evidenced by intracranial electrophysiology and functional connectivity studies (Bullock et al., 1995; Destexhe et al., 1999; Leopold et al., 2003) in addition to the recent advances in employing RNN for processing data with a temporal structure, e.g., natural language processing, inspired the use of LSTM networks in the M/EEG inverse problem for predicting and correcting M/EEG source estimates based on their context. In this study, we developed this technique and applied it to dSPM estimates, naming the implementation CMNE. The approach presented here thus constitutes a novel spatiotemporal inverse method where M/EEG estimates are filtered based on their context without too strong and explicit *a priori* assumptions of their spatiotemporal dynamics.

We tested CMNE on simulated epileptiform and recorded ASSR data, showing that in the cases tested here, the CMNE estimates exhibited a higher SNR in source space (**Figures 5**, **7**), less spatial dispersion (**Figure 7**) and smaller localization error (**Figure 6**), thus implying a higher degree of spatial fidelity, than the unfiltered dSPM estimates. The other spatiotemporal methods tested in this study was the Kalman approach proposed by Lamus et al. (2012) and MxNE. While MxNE and the Kalman approach showed a high degree of spatial fidelity in some cases, manifested in very low localization error for some activations and low spatial dispersion in the simulation study, the simulation also showed that their performance was highly variant, e.g., the reconstruction error with MxNE varied between 0 and 25 mm. In comparison to the other spatiotemoral methods,

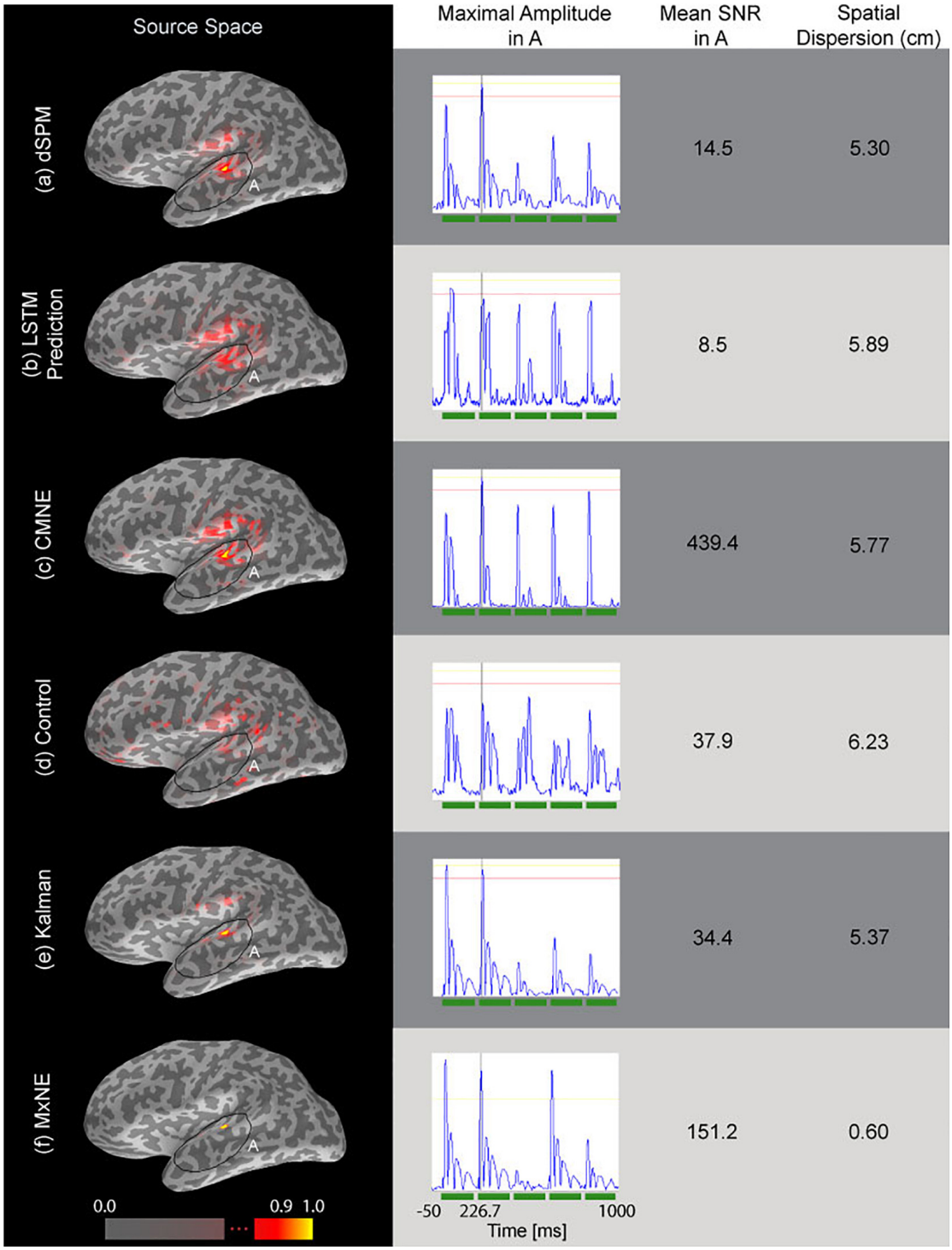

FIGURE 5 | Source estimations based on simulated data (20 averaged epochs) are shown in the source space column. The second column from the left shows the time traces of the estimated dipole with maximal amplitude within the marked area A as depicted in the first column. The third column shows the estimated SNR of the respective source reconstruction method (Eq. 26) and the fourth column shows the spatial dispersion of the estimates (Eq. 24). The tested source estimation methods are divided into rows: **(a)** dSPM estimate $\hat{q}_t$, **(b)** LSTM network prediction $\bar{b}\left(\hat{q}_t\right)$, **(c)** CMNE estimate $b\left(\hat{q}_t\right)$, **(d)** control estimate, which averages the 80 previous estimates and uses that average to correct the current dSPM estimate based on the average of 20 epochs, **(e)** Kalman estimate, **(f)** MxNE estimate. All estimates were rectified and normalized to their peak value.

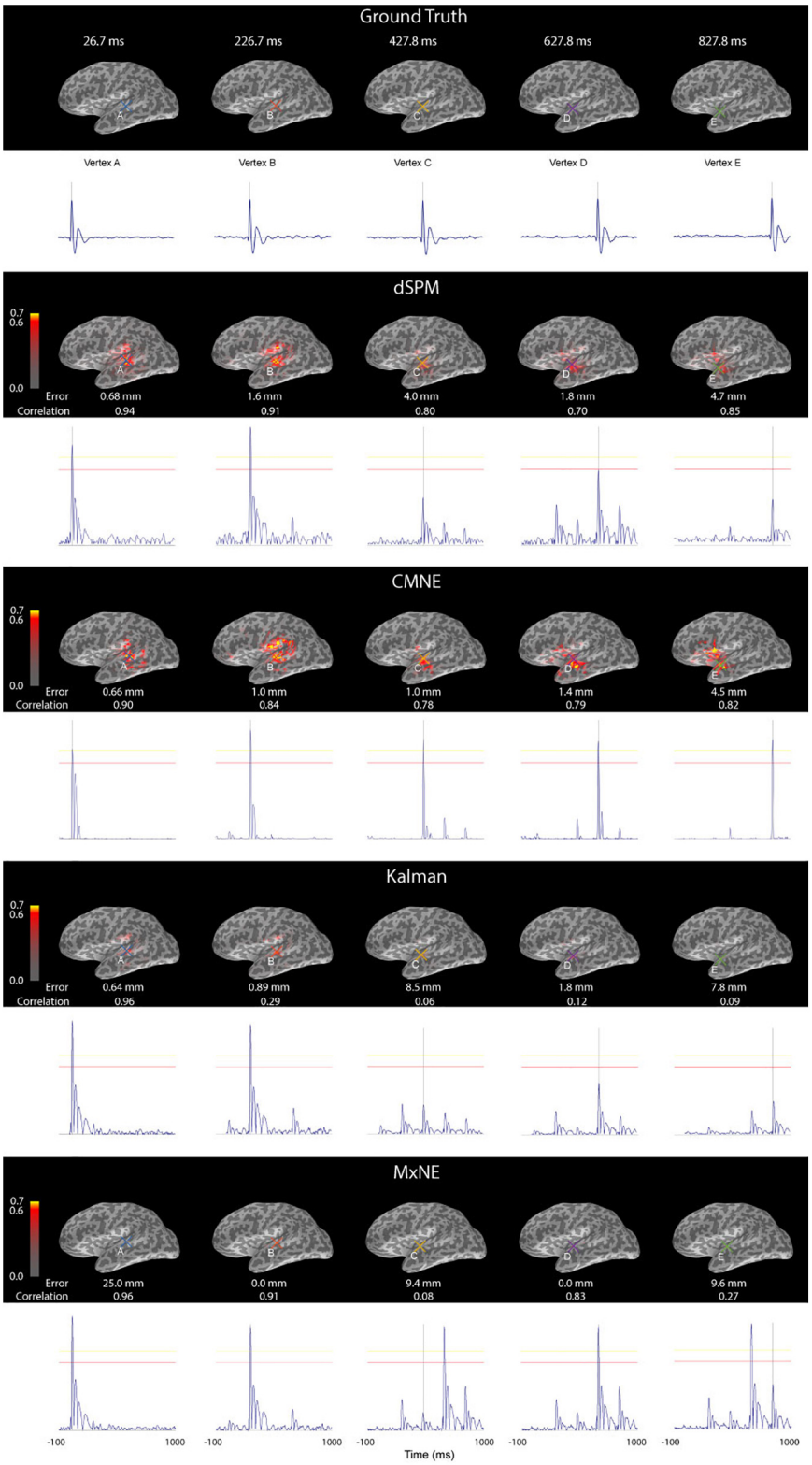

FIGURE 6 | Source activation (first row), dSPM estimate (second row), CMNE estimate (third row), Kalman estimate (fourth row) and MxNE (fifth row) of simulated data displayed over an inflated cortex at the time of peak activations of dipoles (A-E) along with the time traces of the reconstructured dipoles that had the largest amplitudes at the time of peak activations (marked A-E). The results are based on an average of 20 epochs. All estimates were rectified and normalized to their peak value.

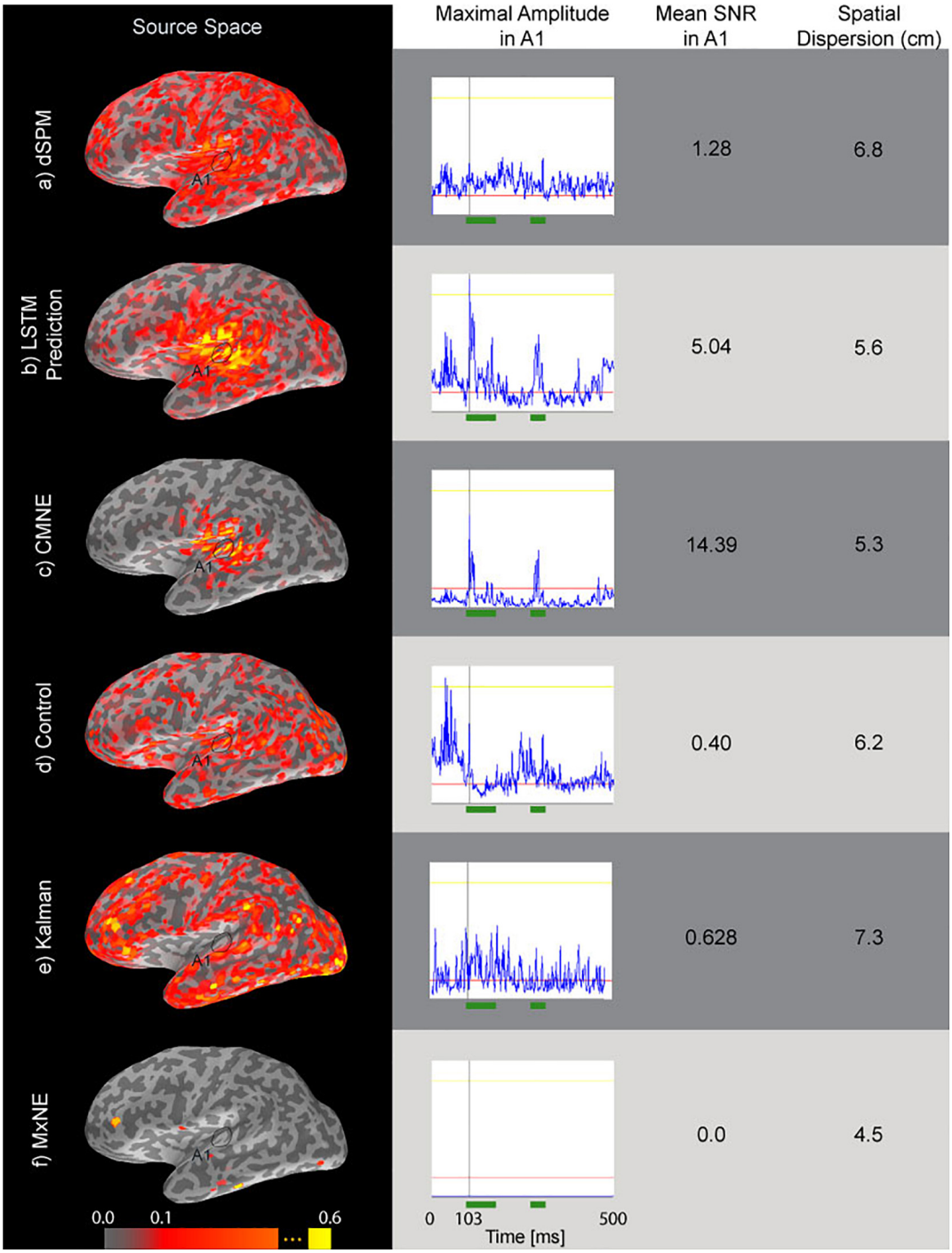

FIGURE 7 | Source estimates (first column) of ASSR data based on averages of 20 epochs, time courses (second column) of the source dipole in A1 with the greatest amplitude over the evoked response, SNR (Eq. 26, third column) and spatial dispersion (Eq. 24, fourth column) of the estimates. The green segments in the time courses mark the N1 and P2 responses that were used in the calculation of SNR (Eq. 26). The rows correspond to dSPM **(a)**, LSTM prediction **(b)**, CMNE **(c)**, control estimate **(d)**, Kalman estimate **(e),** and MxNE **(f)**. All estimates were rectified and normalized to their peak value.

CMNE thus showed a more consistent performance. That was also observed in the temporal fidelity comparison which showed that CMNE had a Pearson's correlation coefficient consistently above 0.78 with the true activation signal while the Kalman and mixed norm approaches resulted in a correlation varying between 0.06 and 0.96. Furthermore, the assessed source space SNR was significantly higher with CMNE than in any of the other approaches tested here because of the temporal sparsity. This

ability of CMNE to extract the signal from noisy data could be the reason for the superior performance on the ASSR data, where the Kalman and MxNE approaches performed substantially worse than CMNE in spite of the steady local activity in the auditory cortex that occurs during ASSR where one might think the Kalman and MxNE approaches would do better.

However, the reconstructed time courses of the sources as predicted by the LSTM network were not always able to follow steep ascends, which relates to a lowpass characteristic (**Figures 5**, **6**). Correcting the prediction with the dSPM estimate based on the sensor data resulted in a higher degree of temporal fidelity than the LSTM prediction. Even after the correction, however, the damped oscillations following the spikes in the simulation study were not faithfully reconstructed. The CMNE filtering thus resulted in a distortion of the waveform following the spike, which does not take place to the same extent with dSPM. This highlights a drawback of CMNE; although we can achieve enhanced spatial fidelity, the fact that we have a spatial filter that changes over time can introduce a temporal phase shift which could distort the waveform reconstruction. This is, however, a characteristic that CMNE shares with other spatiotemporal methods and they must therefore be used with caution when doing temporal analysis, e.g., examining frequency bands or performing phase synchrony analysis. How to introduce a zero-phase shift spatial filter based upon spatiotemporal information without explicit *a priori* assumptions, such as the technique presented here, should be the topic of a future study.

In the simulation study, the activation pattern was in the form of dipoles at different locations activated subsequently. This activation pattern should be predictable and the CMNE estimation should therefore give better results over time as progressively more information on past activity is gathered since the internal cell state of each LSTM cell is passed forward to the next cell in the chain. This is indeed the case, as it can be seen from **Figure 6** that while the dSPM estimate exhibited an increasingly higher degree of spatial dispersion, the CMNE estimate maintained an adequate amplitude reconstruction. It should also be noted that we here used the same source mesh and field computation method in the forward modeling as in the inverse modeling, which resulted in low localization errors for some of the inverse methods.

There is no definite rule how to select the number of neurons in each neural network layer d and the number of LSTM cells k; cross-validation is normally employed to select these hyperparameters. Due to limitations in computational resources and the difficulties in presenting results for many different hyperparameter values, we resorted here to the conventional approach of evaluating hyperparameters by cross-validation first and then employing these hyperparameters throughout the study. Further evaluation of how the choice of network topology could influence the result should be explored in future studies. How well these hyperparameters will generalize to unseen data, such as a new subject or measurement system or evoked response, will depend upon the spatiotemporal distribution of the new data.

The distributed source estimates found with dSPM that we use as inputs to the network makes the input data somewhat more invariant across subjects and measurement systems than if we had used sensor space data, which would likely not have generalized well across measurement systems. However, different subjects, evoked responses and measurement systems might still require new training of a subset of the weights. It is also possible that this spatial and temporal variability could be addressed by using a larger k and d to account for temporal and spatial variability, respectively. Larger LSTM networks with a high dropout rate (>0.7) might thus improve the generalization of CMNE by increasing the complexity of the model and letting a high dropout rate mitigate overfitting. This would, however, also increase the computational complexity of the training which is already quite high ($\sim$8–12 h on a conventional workstation with dual XEON E5-2687W, 64 GB RAM, and NVIDIA Quadro 4000). Efficient transfer learning schemes with automatic hyperparameter search could potentially be employed as an alternative (Yogatama and Mann, 2014). It would also be of great interest to see how the weights in the LSTM network differs in different evoked responses. It is conceivable that the internal cell states that are modulated by the weights carry information about the active brain state. How these are modulated in different tasks that activate different functional networks is an interesting aspect of this technique that needs further investigation.

Another aspect that warrants further investigation is combining the CMNE approach used here with other spatiotemporal source estimates. For instance, this approach could be combined with Kalman filtering, e.g., where a Kalman or extended Kalman filter could be used to update the weights in the LSTM network, instead of backpropagation.

Finally, there is a wide variety of neural networks and it is hard to predict, without empirical testing, which implementation and combination of networks that would yield the optimal performance given a measure of goodness. It is conceivable that, for instance, bi-directional LSTM networks using both past and future estimates would capture the temporal dynamics better than the unidirectional LSTM network implemented in this study, or that convolutional neural networks (CNN), commonly used in computer vision, could be used to increase the spatial fidelity even further. A fundamental issue with implementing machine learning methods in M/EEG source estimation is the lack of ground truth data. It also remains unclear to what degree the networks can be trained on a variety of subjects and tasks or if they should be trained separately as was done here. Addressing these questions will be critical for the future of machine learning in M/EEG source estimation.

CONCLUSION

A novel technique was introduced where a spatiotemporal LSTM network is used to predict the source estimate following a sequence of past estimates. The prediction is then used as a spatial filter to correct the estimate, which is context dependent since it is a function of past estimates. Because this technique can be used in conjunction with any source estimation method that has a temporal sequence and does not rest on strong and explicit *a priori* modeling assumptions, any source estimation method can be turned into a spatiotemporal method using the technique

presented here. We tested an implementation of this technique on dSPM estimates, naming it CMNE, and benchmarked it on simulations of ictal events and recorded M/EEG data from an ASSR experiment, showing that it can result in a higher degree of spatial fidelity as compared to the unfiltered, non-contextual estimates. We conclude that the results shown here indicate promise for the emerging field of the application of machine learning in M/EEG source estimation and warrant more studies on different network configurations and training procedures.

DATA AVAILABILITY STATEMENT

The raw data supporting the conclusions of this article will be made available by the authors, without undue reservation, to any qualified researcher.

ETHICS STATEMENT

The studies involving human participants were reviewed and approved by Massachusetts General Hospital Institutional Review Board. The patients/participants provided their written informed consent to participate in this study.

AUTHOR CONTRIBUTIONS

CD conceptualized and designed the study and performed the data visualization. JS and SK collected the ASSR data. AH performed the epileptiform simulations. CD and JS performed the analysis. CD, JS, and MH wrote the first draft of the manuscript. MH contributed funding. All authors contributed to manuscript revision, read, and approved the submitted version.

FUNDING

This work was supported by the National Institutes of Health (NIH, grants 1U01EB023820, 1P41EB030006, 1R01NS104585, and 5P41EB015896), Microsoft Azure Research Award and the Sweden-America foundation.

REFERENCES

Abadi, M., Agarwal, A., Barham, P., Brevdo, E., Chen, Z., Citro, C., et al. (2015). *TensorFlow: Large-Scale Machine Learning on Heterogeneous Systems*. Available online at: https://arxiv.org/abs/1603.04467 (accessed December 1, 2017).

Ali, H., Karim, F., Qureshi, J. J., Abuassba, A. O., and Bulbul, M. F. (2019). Seizure prediction using bidirectional LSTM. in *Proceedings of the International Conference Cyberspace Data and Intelligence, and Cyber-Living, Syndrome, and Health*. Berlin: Springer, 349–356. doi: 10.1007/978-981-15-1922-2_25

Baillet, S., and Garnero, L. (1997). A bayesian approach to introducing anatomo-functional priors in the EEG/MEG inverse problem. *IEEE Trans. Biomed. Eng.* 44, 374–385. doi: 10.1109/10.568913

Bolstad, A., Van Veen, B., and Nowak, R. (2009). Space–time event sparse penalization for magneto-/electroencephalography. *Neuroimage* 46, 1066–1081. doi: 10.1016/j.neuroimage.2009.01.056

Bullock, T., McClune, M., Achimowicz, J., Iragui-Madoz, V., Duckrow, R., and Spencer, S. (1995). Temporal fluctuations in coherence of brain waves. *Proc. Natl. Acad. Sci. U.S.A.* 92, 11568–11572. doi: 10.1073/pnas.92.25.11568

Calvetti, D., Somersalo, E., and Strang, A. (2019). Hierachical bayesian models and sparsity: l 2-magic. *Inverse Probl.* 35:035003.

Chollet, F. (2018). *Keras: The Python Deep Learning Library.* Astrophysics Source Code Library. Available online at: https://ui.adsabs.harvard.edu/abs/2018ascl.soft06022C/abstract (accessed June, 2018).

Chorowski, J. K., Bahdanau, D., Serdyuk, D., Cho, K., and Bengio, Y. (2015). "Attention-based models for speech recognition," in *Advances in Neural Information Processing Systems*, eds M. I. Jordan, Y. LeCun, and S. A. Solla (Cambridge, MA: MIT Press).

Costa, F., Batatia, H., Oberlin, T., d'Giano, C., and Tourneret, J.-Y. (2017). Bayesian EEG source localization using a structured sparsity prior. *Neuroimage* 144, 142–152. doi: 10.1016/j.neuroimage.2016.08.064

Dale, A. M., Fischl, B., and Sereno, M. I. (1999). Cortical surface-based analysis. i. segmentation and surface reconstruction. *Neuroimage* 9, 179–194.

Dale, A. M., Liu, A. K., Fischl, B. R., Buckner, R. L., Belliveau, J. W., Lewine, J. D., et al. (2000). Dynamic statistical parametric mapping: combining fMRI and MEG for high-resolution imaging of cortical activity. *Neuron* 26, 55–67.

Destexhe, A., Contreras, D., and Steriade, M. (1999). Spatiotemporal analysis of local field potentials and unit discharges in cat cerebral cortex during natural wake and sleep states. *J. Neurosci.* 19, 4595–4608. doi: 10.1523/jneurosci.19-11-04595.1999

Dinh, C. (2015). *Brain monitoring: Real-time Localization of Neuronal Activity. 1st edn*. Aachen: Shaker. doi: 10.2370/9783844038378

Dinh, C., Esch, L., Rühle, J., Bollmann, S., Güllmar, D., Baumgarten, D., et al. (2018). Real-time clustered multiple signal classification (RTC-MUSIC). *Brain Topogr.* 31, 125–128. doi: 10.1007/s10548-017-0586-7

Dinh, C., Samuelsson, J. G., Hunold, A., Hämäläinen, M. S., and Khan, S. (2019). Contextual minimum-norm estimates (CMNE): a deep learning method for source estimation in neuronal networks. *arXiv [preprint]* doi: arXiv:1909.02636.

Dinh, C., Strohmeier, D., Luessi, M., Gullmar, D., Baumgarten, D., Haueisen, J., et al. (2015). Real-time MEG source localization using regional clustering. *Brain Topogr.* 28, 771–784. doi: 10.1007/s10548-015-0431-9

Esch, L., Dinh, C., Larson, E., Engemann, D., Jas, M., Khan, S., et al. (2019). "MNE: software for acquiring, processing, and visualizing MEG/EEG data," in *Magnetoencephalography: From Signals to Dynamic Cortical Networks*, eds S. Supek and C. J. Aine (Berlin: Springer), 355–371. doi: 10.1007/978-3-030-00087-5_59

Fischl, B., Sereno, M. I., and Dale, A. M. (1999). Cortical surface-based analysis. II: inflation, flattening, and a surface-based coordinate system. *Neuroimage* 9, 195–207. doi: 10.1006/nimg.1998.0396

Friston, K., Harrison, L., Daunizeau, J., Kiebel, S., Phillips, C., Trujillo-Barreto, N., et al. (2008). Multiple sparse priors for the M/EEG inverse problem. *Neuroimage* 39, 1104–1120. doi: 10.1016/j.neuroimage.2007.09.048

Galka, A., Yamashita, O., Ozaki, T., Biscay, R., and Valdés-Sosa, P. (2004). A solution to the dynamical inverse problem of EEG generation using spatiotemporal kalman filtering. *Neuroimage* 23, 435–453. doi: 10.1016/j.neuroimage.2004.02.022

Gorodnitsky, I. F., George, J. S., and Rao, B. D. (1995). Neuromagnetic source imaging with FOCUSS: a recursive weighted minimum norm algorithm. *Electroencephalogr. Clin. Neurophysiol.* 95, 231–251. doi: 10.1016/0013-4694(95)00107-a

Gramfort, A., Kowalski, M., and Hamalainen, M. (2012). Mixed-norm estimates for the M/EEG inverse problem using accelerated gradient methods. *Phys. Med. Biol.* 57, 1937–1961. doi: 10.1088/0031-9155/57/7/1937

Gramfort, A., Luessi, M., Larson, E., Engemann, D. A., Strohmeier, D., Brodbeck, C., et al. (2013a). MEG and EEG data analysis with MNE-Python. *Front. Neurosci.* 7:267.

Gramfort, A., Strohmeier, D., Haueisen, J., Hamalainen, M. S., and Kowalski, M. (2013b). Time-frequency mixed-norm estimates: sparse M/EEG imaging with non-stationary source activations. *Neuroimage* 70, 410–422. doi: 10.1016/j.neuroimage.2012.12.051

Graves, A., Mohamed, A.-R., and Hinton, G. (2013). "Speech recognition with deep recurrent neural networks," in *Proceedings of the 2013 IEEE International Conference on Acoustics, Speech and Signal Processing*, (Pisacataway, NJ: IEEE), 6645–6649.

Greensite, F. (2003). The temporal prior in bioelectromagnetic source imaging problems. *IEEE Trans. Biomed. Eng.* 50, 1152–1159. doi: 10.1109/tbme.2003.817632

Gross, J., Kujala, J., Hämäläinen, M., Timmermann, L., Schnitzler, A., and Salmelin, R. (2001). Dynamic imaging of coherent sources: studying neural interactions in the human brain. *Proc. Natl. Acad. Sci. U.S.A.* 98, 694–699. doi: 10.1073/pnas.98.2.694

Hamalainen, M. S., and Ilmoniemi, R. J. (1994). Interpreting magnetic-fields of the brain - minimum norm estimates. *Med. Biol. Eng. Comput.* 32, 35–42. doi: 10.1007/bf02512476

Hamalainen, M. S., and Sarvas, J. (1989). Realistic conductivity geometry model of the human head for interpretation of neuromagnetic data. *IEEE Trans. Biomed. Eng.* 36, 165–171. doi: 10.1109/10.16463

Hämäläinen, M., Hari, R., Ilmoniemi, R. J., Knuutila, J., and Lounasmaa, O. V. (1993). Magnetoencephalography - theory, instrumentation, and applications to noninvasive studies of the working human brain. *Rev. Mod. Phys.* 65:413. doi: 10.1103/revmodphys.65.413

Helmholtz, H. V. (1853). Ueber einige gesetze der vertheilung elektrischer ströme in körperlichen leitern, mit anwendung auf die thierisch-elektrischen versuche (schluss.). *Annalen der Physik* 165, 353–377. doi: 10.1002/andp.18531650702

Hochreiter, S., and Schmidhuber, J. (1997). Long short-term memory. *Neural Comput.* 9, 1735–1780.

Hofmann, S. M., Klotzsche, F., Mariola, A., Nikulin, V. V., Villringer, A., and Gaebler, M. (2018). "Decoding subjective emotional arousal during a naturalistic VR experience from EEG using LSTMs," in *Proceedings of the 2018 IEEE International Conference on Artificial Intelligence (AIVR)*, (Piscataway, NJ: IEEE), 128–131.

Hunold, A., Funke, M. E., Eichardt, R., Stenroos, M., and Haueisen, J. (2016). EEG and MEG: sensitivity to epileptic spike activity as function of source orientation and depth. *Physiol. Meas.* 37, 1146–1162. doi: 10.1088/0967-3334/37/7/1146

Izhikevich, E. M., and Edelman, G. M. (2008). Large-scale model of mammalian thalamocortical systems. *Proc. Natl. Acad. Sci. U.S.A.* 105, 3593–3598. doi: 10.1073/pnas.0712231105

Jas, M., Engemann, D. A., Bekhti, Y., Raimondo, F., and Gramfort, A. (2017). Autoreject: automated artifact rejection for MEG and EEG data. *Neuroimage* 159, 417–429. doi: 10.1016/j.neuroimage.2017.06.030

Jirsa, V. K., Jantzen, K. J., Fuchs, A., and Kelso, J. S. (2002). Spatiotemporal forward solution of the EEG and MEG using network modeling. *IEEE Trans. Med. Imaging* 21, 493–504. doi: 10.1109/tmi.2002.1009385

Khan, S., Michmizos, K., Tommerdahl, M., Ganesan, S., Kitzbichler, M., Zetino, M., et al. (2015). Somatosensory cortex functional connectivity abnormalities in autism show opposite trends, depending on direction and spatial scale. *Brain* 138(Pt 5), 1394–1409. doi: 10.1093/brain/awv043

Kingma, D. P., and Ba, J. (2014). Adam: a method for stochastic optimization. *Comput. Sci. Mach. Learn.* 1–15. Available online at: http://arxiv.org/abs/1412.6980 (accessed May 5, 2018).

Kozhemiako, N., Nunes, A., Samal, A., Rana, K., Calabro, F., Hämäläinen, M., et al. (2020). Neural activity underlying the detection of an object movement by an observer during forward self-motion: dynamic decoding and temporal evolution of directional cortical connectivity. *Prog. Neurobiol.* 195:101824. doi: 10.1016/j.pneurobio.2020.101824

Lamus, C., Hamalainen, M. S., Temereanca, S., Brown, E. N., and Purdon, P. L. (2012). A spatiotemporal dynamic distributed solution to the MEG inverse problem. *Neuroimage* 63, 894–909. doi: 10.1016/j.neuroimage.2011.11.020

LeCun, Y., Bengio, Y., and Hinton, G. (2015). Deep learning. *Nature* 521, 436–444.

Leopold, D. A., Murayama, Y., and Logothetis, N. K. (2003). Very slow activity fluctuations in monkey visual cortex: implications for functional brain imaging. *Cereb. Cortex* 13, 422–433. doi: 10.1093/cercor/13.4.422

Limpiti, T., Van Veen, B. D., Attias, H. T., and Nagarajan, S. S. (2008). A spatiotemporal framework for estimating trial-to-trial amplitude variation in event-related MEG/EEG. *IEEE Trans. Biomed. Eng.* 56, 633–645. doi: 10.1109/tbme.2008.2008423

Long, C. J., Purdon, P. L., Temereanca, S., Desai, N. U., Hamalainen, M. S., and Brown, E. N. (2011). State-space solutions to the dynamic magnetoencephalography inverse problem using high performance computing. *Ann. Appl. Stat.* 5, 1207–1228. doi: 10.1214/11-aoas483

Lucka, F., Pursiainen, S., Burger, M., and Wolters, C. H. (2012). Hierarchical Bayesian inference for the EEG inverse problem using realistic FE head models: depth localization and source separation for focal primary currents. *Neuroimage* 61, 1364–1382. doi: 10.1016/j.neuroimage.2012.04.017

Mattout, J., Phillips, C., Penny, W. D., Rugg, M. D., and Friston, K. J. (2006). MEG source localization under multiple constraints: an extended Bayesian framework. *Neuroimage* 30, 753–767. doi: 10.1016/j.neuroimage.2005.10.037

Nummenmaa, A., Auranen, T., Hamalainen, M. S., Jaaskelainen, I. P., Lampinen, J., Sams, M., et al. (2007). Hierarchical Bayesian estimates of distributed MEG sources: theoretical aspects and comparison of variational and MCMC methods. *Neuroimage* 35, 669–685. doi: 10.1016/j.neuroimage.2006.05.001

Olah, C. (2015). *Understanding Lstm Networks*. Available online at: http://colah.github.io/posts/2015-08-Understanding-LSTMs/ (accessed March 17, 2018).

Ou, W., Hamalainen, M. S., and Golland, P. (2009). A distributed spatio-temporal EEG/MEG inverse solver. *Neuroimage* 44, 932–946. doi: 10.1016/j.neuroimage.2008.05.063

Pascual-Marqui, R. D. (2002). Standardized low-resolution brain electromagnetic tomography (sLORETA): technical details. *Methods Find. Exp. Clin. Pharmacol.* 24, 5–12.

Pascual-Marqui, R. D., Michel, C. M., and Lehmann, D. (1994). Low resolution electromagnetic tomography: a new method for localizing electrical activity in the brain. *Int. J. Psychophysiol.* 18, 49–65. doi: 10.1016/0167-8760(84)90014-x

Phillips, C., Mattout, J., Rugg, M. D., Maquet, P., and Friston, K. J. (2005). An empirical Bayesian solution to the source reconstruction problem in EEG. *Neuroimage* 24, 997–1011. doi: 10.1016/j.neuroimage.2004.10.030

Pirondini, E., Babadi, B., Obregon-Henao, G., Lamus, C., Malik, W. Q., Hamalainen, M. S., et al. (2018). Computationally efficient algorithms for sparse, dynamic solutions to the Eeg source localization problem. *IEEE Trans. Biomed. Eng.* 65, 1359–1372. doi: 10.1109/tbme.2017.2739824

Samuelsson, J. G., Khan, S., Sundaram, P., Peled, N., and Hämäläinen, M. S. (2019). Cortical Signal suppression (CSS) for detection of subcortical activity using MEG and EEG. *Brain Topogr.* 32, 215–228. doi: 10.1007/s10548-018-00694-5

Samuelsson, J. G., Peled, N., Mamashli, F., Ahveninen, J., and Hämäläinen, M. S. (2020). Spatial fidelity of MEG/EEG source estimates: a general evaluation approach. *Neuroimage* 224:117430. doi: 10.1016/j.neuroimage.2020.117430

Sato, M.-A., Yoshioka, T., Kajihara, S., Toyama, K., Goda, N., Doya, K., et al. (2004). Hierarchical Bayesian estimation for MEG inverse problem. *Neuroimage* 23, 806–826. doi: 10.1016/j.neuroimage.2004.06.037

Schmidhuber, J. (2015). Deep learning in neural networks: an overview. *Neural Netw.* 61, 85–117. doi: 10.1016/j.neunet.2014.09.003

Seide, F., and Agarwal, A. (2016). "CNTK: Microsoft's open-source deep-learning toolkit," in *Proceedings of the 22nd ACM SIGKDD International Conference on Knowledge Discovery and Data Mining*, (New York, NY: Association for Computing Machinery).

Shahin, A. J., Roberts, L. E., Miller, L. M., McDonald, K. L., and Alain, C. (2007). Sensitivity of EEG and MEG to the N1 and P2 auditory evoked responses modulated by spectral complexity of sounds. *Brain Topogr.* 20, 55–61. doi: 10.1007/s10548-007-0031-4

Somersalo, E., Voutilainen, A., and Kaipio, J. (2003). Non-stationary magnetoencephalography by Bayesian filtering of dipole models. *Inverse Probl.* 19:1047. doi: 10.1088/0266-5611/19/5/304

Sorrentino, A., Parkkonen, L., Pascarella, A., Campi, C., and Piana, M. (2009). Dynamical MEG source modeling with multi-target Bayesian filtering. *Hum. Brain Mapp.* 30, 1911–1921. doi: 10.1002/hbm.20786

Strohmeier, D., Haueisen, J., and Gramfort, A. (2014). "Improved MEG/EEG source localization with reweighted mixed-norms," in *Proceedings of the 2014 International Workshop on Pattern Recognition in Neuroimaging*, (Piscataway, NJ: IEEE), 1–4.

Trujillo-Barreto, N. J., Aubert-Vázquez, E., and Penny, W. D. (2008). Bayesian M/EEG source reconstruction with spatio-temporal priors. *Neuroimage* 39, 318–335. doi: 10.1016/j.neuroimage.2007.07.062

Vivaldi, V., and Sorrentino, A. (2016). Bayesian smoothing of dipoles in magneto-/electroencephalography. *Inverse Probl.* 32:045007. doi: 10.1088/0266-5611/32/4/045007

Wright, J., Rennie, C., Lees, G., Robinson, P., Bourke, P., Chapman, C., et al. (2003). Simulated electrocortical activity at microscopic, mesoscopic, and global scales. *Neuropsychopharmacology* 28, S80–S93.

Yogatama, D., and Mann, G. (2014). "Efficient transfer learning method for automatic hyperparameter tuning," *Proceedings of the Seventeenth International Conference on Artificial Intelligence and Statistics*, 33, 1077–1085.
Proceedings of the Seventeenth International Conference on Artificial Intelligence and Statistics, PMLR 33:1077-1085, 2014.

Yu, B.-W., Jeong, J.-H., Lee, D.-H., and Lee, S.-W. (2019). "Detection of pilot's drowsiness based on multimodal convolutional bidirectional LSTM network," in *Proceedings of the Asian Conference on Pattern Recognition*, (Berlin: Springer).

Zumer, J. M., Attias, H. T., Sekihara, K., and Nagarajan, S. S. (2008). Probabilistic algorithms for MEG/EEG source reconstruction using temporal basis functions learned from data. *Neuroimage* 41, 924–940. doi: 10.1016/j.neuroimage.2008.02.006

Conflict of Interest: The authors declare that the research was conducted in the absence of any commercial or financial relationships that could be construed as a potential conflict of interest.

Copyright © 2021 Dinh, Samuelsson, Hunold, Hämäläinen and Khan. This is an open-access article distributed under the terms of the Creative Commons Attribution License (CC BY). The use, distribution or reproduction in other forums is permitted, provided the original author(s) and the copyright owner(s) are credited and that the original publication in this journal is cited, in accordance with accepted academic practice. No use, distribution or reproduction is permitted which does not comply with these terms.

frontiers in Neuroscience

METHODS
published: 09 June 2021
doi: 10.3389/fnins.2021.569918

ConvDip: A Convolutional Neural Network for Better EEG Source Imaging

Lukas Hecker[1,2,3,4]*, *Rebekka Rupprecht*[5], *Ludger Tebartz Van Elst*[1,2] and *Jürgen Kornmeier*[1,2,3]

[1] Department of Psychiatry and Psychotherapy, University of Freiburg Medical Center, Freiburg, Germany, [2] Faculty of Medicine, University of Freiburg, Freiburg, Germany, [3] Institute for Frontier Areas of Psychology and Mental Health (IGPP), Freiburg, Germany, [4] Faculty of Biology, University of Freiburg, Freiburg, Germany, [5] Machine Learning Lab, University of Freiburg, Freiburg, Germany

The electroencephalography (EEG) is a well-established non-invasive method in neuroscientific research and clinical diagnostics. It provides a high temporal but low spatial resolution of brain activity. To gain insight about the spatial dynamics of the EEG, one has to solve the inverse problem, i.e., finding the neural sources that give rise to the recorded EEG activity. The inverse problem is ill-posed, which means that more than one configuration of neural sources can evoke one and the same distribution of EEG activity on the scalp. Artificial neural networks have been previously used successfully to find either one or two dipole sources. These approaches, however, have never solved the inverse problem in a distributed dipole model with more than two dipole sources. We present ConvDip, a novel convolutional neural network (CNN) architecture, that solves the EEG inverse problem in a distributed dipole model based on simulated EEG data. We show that (1) ConvDip learned to produce inverse solutions from a single time point of EEG data and (2) outperforms state-of-the-art methods on all focused performance measures. (3) It is more flexible when dealing with varying number of sources, produces less ghost sources and misses less real sources than the comparison methods. It produces plausible inverse solutions for real EEG recordings from human participants. (4) The trained network needs <40 ms for a single prediction. Our results qualify ConvDip as an efficient and easy-to-apply novel method for source localization in EEG data, with high relevance for clinical applications, e.g., in epileptology and real-time applications.

Keywords: EEG-electroencephalogram, artificial neural networks, convolutional neural networks (CNN), inverse problem, machine learning, electrical source imaging

OPEN ACCESS

Edited by:
Alard Roebroeck,
Maastricht University, Netherlands

Reviewed by:
Annalisa Pascarella,
Istituto per le Applicazioni del Calcolo "Mauro Picone" (IAC), Italy
Miguel Castelo-Branco,
Coimbra Institute for Biomedical Imaging and Translational Research (CIBIT), Portugal

***Correspondence:**
Lukas Hecker
lukas_hecker@web.de

Specialty section:
This article was submitted to Brain Imaging Methods, a section of the journal Frontiers in Neuroscience

Received: *05 June 2020*
Accepted: *14 April 2021*
Published: *09 June 2021*

Citation:
Hecker L, Rupprecht R, Tebartz Van Elst L and Kornmeier J (2021) ConvDip: A Convolutional Neural Network for Better EEG Source Imaging. Front. Neurosci. 15:569918. doi: 10.3389/fnins.2021.569918

1. INTRODUCTION

1.1. The EEG and the Inverse Problem

Electroencephalography (EEG) is among the most used imaging techniques for noninvasive measurements of electromagnetic brain activity. Its main advantage over other methods (e.g., functional magnetic resonance imaging [fMRI]) is the high temporal resolution, which comes at the cost of a considerably low spatial resolution (Luck, 2014). As a consequence, EEG was mainly used to study temporal brain dynamics at fine time scales. In the past decades, however, there has been a steady growth of interest in the neural sources underlying the EEG signal (Koles, 1998; Pascual-Marqui, 1999; Grech et al., 2008; He et al., 2018; Michel and Brunet, 2019). The

non-invasive estimations of neural generators, based on their projections to the scalp electrodes/sensors, constitutes an inverse problem. Without further constraints, it is ill posed because it lacks an unique solution, since multiple configurations of neural sources can produce identical topographies of electrical activity at the scalp (see e.g., Nunez and Srinivasan, 2006).

Invasive multimodal methods (e.g., using combined EEG and electrocorticography) help to bridge the gap between scalp recordings and neural generators, and thus in handling the inverse problem in this constellation. However, access to these methods is limited and the conclusions that can be drawn are constrained by various factors such as placement of the cortical electrodes or coverage of brain areas that project to the scalp electrodes. Combined EEG-fMRI has also been shown as a useful tool in providing insight into the spatiotemporal dynamics of the EEG (Ritter and Villringer, 2006). However, the costs of this technique are considerably high and the relation between electromagnetic and metabolic dynamics is yet not fully understood.

1.2. Classical Approaches to the EEG Inverse Problem

Introducing some constraints on the solution, one can solve the inverse problem or at least reduce the number of possible solutions. One approach is the equivalent current dipole model, which is based on the assumption that the source of a signal, measured with the EEG, can be modeled by a single (or sometimes few) dipole(s) (Kavanagk et al., 1978; Scherg, 1990; Delorme et al., 2012). Although single-dipole sized sources are too small to generate detectable scalp potentials (Nunez and Srinivasan, 2006), they can produce reasonable results (Ebersole, 1994; Lantz et al., 1996; Willemse et al., 2016; Sharma et al., 2018).

A more physiologically realistic approach is the distributed dipole model in which activity is expected to extend over larger areas of the brain (as opposed to tiny dipoles). Distributed dipole models aim to find the 3D distribution of neural activity underlying the EEG measurement (Hämäläinen and Ilmoniemi, 1994; Pascual-Marqui et al., 1994). A distributed dipole model proposes that sources of the EEG are better modeled using hundreds to many thousand dipoles and therefore aim to find a distributed activity that can explain the EEG data. This model can be viewed opposed to single- to few-dipole models, which assume that EEG data can be sufficiently modeled using point sources.

A popular family of distributed dipole solutions is the *Minimum Norm Estimates* (MNE; Ioannides et al., 1990; Hämäläinen and Ilmoniemi, 1994), which aim to find the source configuration that minimizes the required power to generate a given potential at the scalp electrodes. Low Resolution Electromagnetic Tomography (LORETA) is a famous proponent of the MNE-family that assumes sources to be smoothly distributed (Pascual-Marqui et al., 1994). In the most sophisticated version, exact LORETA (eLORETA, Pascual-Marqui, 2007) showed zero localization error when localizing single sources in simulated data (Pascual-Marqui, 2007).

Another popular family of inverse solutions is the beamforming approach. The linear constrained minimum variance (LCMV) beamforming approach is a spatial filter that assumes that neural sources are uncorrelated and in which portions of the data that do not belong to the signal are suppressed (Van Veen et al., 1997). Drawbacks of the LCMV approach are the susceptibility to imprecisions in the forward model and that correlated sources are often not found.

Growing interest toward a Bayesian notation of the inverse problem could be observed in the past two decades (Friston et al., 2008; Wipf and Nagarajan, 2009; Chowdhury et al., 2013). One prominent Bayesian approach is the maximum entropy on the mean (MEM) method, which aims to make the least assumptions on the current distribution by maximizing entropy (Amblard et al., 2004; Grova et al., 2006; Chowdhury et al., 2013).

1.3. Artificial Neural Networks and Inverse Solutions

Artificial neural networks (ANN)-based inverse solutions follow a data-driven approach and were of increasing interest in the past years (Awan et al., 2019). A large number of simulated EEG data samples is used to train an ANN to correctly map electrode-space signals to source-space locations (Jin et al., 2017). Long training periods are usually required for an ANN to generalize beyond the training set. After successful training, it is capable of predicting the coordinates and orientations of a dipole correctly, given only the measurements at the scalp electrodes without further priors (Zhang et al., 1998; Abeyratne et al., 2001).

Robert et al. (2002) reviewed the literature on ANN-based methods to solve the inverse problem of single dipoles and found that all reports achieved localization errors of <5%. The low computational time (once trained) and robustness to measurement noise was highlighted when compared to classical approaches. However, the classical approaches were capable of achieving zero localization error in single-dipole simulations under zero-noise conditions (Hoey et al., 2000).

In an effort to predict source locations of two dipoles, Yuasa et al. (1998) presented a feed-forward network with two hidden layers and achieved localization errors in a range between 3 and 9%. They found that if multiple simulated dipoles have a sufficient distance among each other the localization success of ANNs even for multiple simulated sources is equal to classical approaches, making a strong case for the feasibility of ANNs for the EEG inverse problem, already in 1998. Although ANNs as such gained popularity in the past decade on other areas (e.g., image classification or natural language processing), the idea of ANN-based solutions to the EEG inverse problem received little further attention.

Only very recently several studies about ANN-based solutions to the inverse problem have been published. Cui et al. (2019) showed that a neural network can be trained to reconstruct the position and time course of a single source using a long-short term memory (LSTM) recurrent neural network architecture (Hochreiter and Schmidhuber, 1997). LSTMs allow to not only use single time instances of (e.g., EEG) data but instead learn from temporally lagged information.

In a recent work, Razorenova et al. (2020) showed that the inverse problem for cortical potential imaging could be solved

using a deep U-Net architecture, once more providing a strong case for the feasibility of ANNs to solve the EEG inverse problem (Fedorov et al., 2020).

Tankelevich (2019) showed that a deep feed-forward network can find the correct set of source clusters that produced a given scalp signal. To our knowledge, this was the first ANN approach to calculate distributed dipole solutions.

In the very recent years, convolutional neural networks (CNNs) have proven to be a useful tool in a steadily increasing number of domains, like image classification (Krizhevsky et al., 2012), natural language processing (Kim, 2014), and decoding of single trial EEG (Schirrmeister et al., 2017). CNNs are capable of learning patterns in data with a preserved temporal (e.g., time sequences) or spatial (e.g., images) structure by optimizing filter kernels that are convolved with a given input. Two famous CNNs are AlexNet (Krizhevsky et al., 2012) and VGG16 (Simonyan and Zisserman, 2014) that won the ImageNet classification competition in 2012 and 2014, respectively.

In the current study, we explored the feasibility of CNNs to solve the EEG inverse problem. Specifically, we constructed a CNN, named *ConvDip*, that is capable of detecting multiple sources using training data with biologically plausible constraints. ConvDip solves the EEG inverse problem using a distributed dipole solution in a data-driven approach. ConvDip was trained to work on single time instances of EEG data and predicts the position of sources from potentials measured with scalp electrodes.

2. METHODS

A Python package to create a forward model, simulate data, train an ANN, and perform predictions is available at https://github.com/LukeTheHecker/ESINet.

2.1. Forward Model

To simulate EEG data realistically, one has to solve the forward problem and construct a generative model (GM). An anatomical template was used as provided by the Freesurfer image analysis suite (http://surfer.nmr.mgh.harvard.edu/) called *fsaverage* (Fischl et al., 1999).

We calculated the three shell boundary element method (BEM, Fuchs et al., 2002) head model with 5120 vertices per shell using the python package MNE (v 19, Gramfort et al., 2013) and the functions *make_bem_model* and *make_bem_solution* therein. The conductivity, measured by Siemens per square meter, was set to 0.3 S/m^2 for brain and scalp tissue and 0.06 S/m^2 for the skull.

The source model was created with $p = 5124$ dipoles along the cortical surface provided by Freesurfer with icosahedral spacing. We chose $q = 31$ electrodes based on the 10–20 system (Fp1, F3, F7, FT9, FC5, FC1, C3, T7, TP9, CP5, CP1, Pz, P3, P7, O1, Oz, O2, P4, P8, TP10, CP6, CP2, Cz, C4, T8, FT10, FC6, FC2, F4, F8, and Fp2). The leadfield $\mathbf{K} \in \mathbb{R}^{q \times p}$ was then calculated using the head model with dipole orientations fixed orthogonal to the cortical surface (see e.g., Michel and Brunet, 2019 for explanation).

Additionally, we created a second forward model that we refer to as the alternative generative model (AGM). The AGM will be used to simulate data for the model evaluation and serves the purpose to avoid the *inverse crime*. The inverse crime is committed when the same GM is used to both simulate data *and* calculate inverse solutions, leading to overoptimistic results (Wirgin, 2004). First, electrode positions were changed by adding random normal distributed noise $\mathcal{N}(0, 2\ mm)$ to the X, Y, and Z coordinate of each electrode. This resulted in an average displacement per electrode of$\approx$ 3.7 mm. Furthermore, we changed the tissue conductivity in the BEM solution to 0.332 S/m^2 for brain and scalp tissue and 0.0113 S/m^2 for skull tissue (values were adapted from Wolters et al., 2010). This step was done in order to introduce some alterations in the volume conduction of the brain-electric signals, which are never known precisely *a priori*. Importantly, this changes the skull-to-brain conductivity ratio from 1:50 to 1:25. Last, we changed the spacing of the dipoles along the cortical sheet from icosahedral to octahedral with a higher resolution. This resulted in 8,196 dipoles in the source model of the AGM, all of which were placed at slightly different locations on the cortex compared to the source model of the GM. The idea of increasing the resolution of the source model to avoid the inverse crime was adapted from Kaipio and Somersalo (2006). All simulations in the evaluation section were carried out using this AGM, whereas the calculation of the inverse solutions of cMEM, eLORETA, and LCMV beamformer was based on the GM. Likewise, data used for training ConvDip was simulated using only the GM.

2.2. Simulations

Training data for ConvDip were created using the GM, whereas the data for the evaluation of the model were created using the AGM. Since AGM and GM have different source models, we implemented a function which transforms a source vector $\mathbf{j}_{AGM}$ to a source vector $\mathbf{j}_{GM}$. This was achieved by K nearest-neighbor interpolation, i.e., each value in the target space was assigned the average value of the K nearest neighbors in the initial space. K was set to 5 neighbors. Since the source model of AGM contained almost twice as many dipoles as that of the GM, a source vector translated from AGM to GM will effectively loose total source power. We therefore normalized the resulting source vector $\mathbf{j}_{GM}$ to have equal energy (sum of all dipole moments) as $\mathbf{j}_{AGM}$.

In summary, different sets of simulated EEG samples were generated to (1) create training data for ConvDip and (2) for evaluation of ConvDip and other inverse solutions.

Each simulation contained at least one dipole cluster, which can be considered as a smooth region of brain activity. A dipole cluster was generated by selecting a random dipole in the cortical source model and then adapting a region growing approach as described in Chowdhury et al. (2013). In brief, we recursively included all surrounding neighbors starting from a single seeding location, thereby creating a larger source extent with each iteration. The number of iterations define the neighborhood order s, where the first order s_1 entails only the single selected dipole. Each seed location was assigned a dipole moment between 5 and 10 Nano-Ampere Meter (nAm). The neighboring dipoles were assigned attenuated moments based on the distance to seeding location. The attenuation followed a Gaussian distribution with a mean of the seeding dipole moment

and a standard deviation of half the radius of the dipole cluster, yielding smooth source patches.

After generating this spatial pattern, we added a temporal dimension to the data as follows. We considered an epoch length of 1 s at a sampling frequency of 100 Hz (i.e., $t = 100$ time points). The time course was modeled by a central peak of 100 ms temporal extension using half a period of a 5 *Hz* sinusoidal, surrounded by zeros. Each dipole moment was then multiplied by this time course. The simulated source $\mathbf{J} \in \mathbb{R}^{p \times t}$ of $p = 5{,}124$ dipoles was then projected to $q = 31$ EEG electrodes $\mathbf{M} \in \mathbb{R}^{q \times t}$ by solving the forward problem using the leadfield $\mathbf{K} \in \mathbb{R}^{q \times p}$:

$$\mathbf{M} = \mathbf{KJ} \tag{1}$$

To generate realistic training data, we added real noise from pre-existing EEG recordings, conducted with the same set of electrodes as described above. Therefore, from a set of different raw EEG recordings, we extracted 200 random segments. These EEG segments were filtered beforehand using a band-pass between 0.1 and 30 Hz. Each segment contained 1 s of EEG data. The sampling frequency was reduced from 1,000 to 100 Hz. Baseline correction was applied based on the first 100 ms, and the resulting data were re-referenced to common average. For each sample, we then created 20 EEG trials by adding a randomly selected noise segment to the simulated EEG. Prior to this, the noise was scaled to yield a signal-to-noise ratio (SNR) of 1 within single trials. The average of these 20 trials, i.e., the event-related potential, should therefore exhibit a theoretical SNR of 4.5 ($1 \times \sqrt{(20)}$) at the ERP peak.

The extent of the sources was defined between two (s_2) and five (s_5) neighborhood orders, which corresponds to diameters between $\approx$ 21 and $\approx$ 58 mm (or 19–91 dipoles).

2.2.1. Training Data

For training ConvDip, we simulated in total 100,000 samples using the GM as described above. Each sample contained between 1 and 5 source clusters of extent between 2 and 5 neighborhood orders. Since ConvDip operates on single time instances of EEG or ERP data, we only used the EEG at the signal peak as input.

2.2.2. Evaluation Data

Two separate sets of simulations of 1,000 samples each were created for the evaluation. The first set contained samples of single source clusters with varying extents from two to seven neighborhood orders, which we will refer to as single-source set. The second set contained samples with varying numbers of source clusters from 1 to 10 and with varying extents from 2 to 7 neighborhood orders or diameters from $\approx$ 21 to $\approx$ 58 *mm* (or 16–113 dipoles in the AGM). We will refer to this as the multi-source set. Source extents have different diameters for different source models, especially in our case where the source model of GM has roughly half the number of dipoles compared to AGM. This explains why s_7 for the AGM has approximately as many dipoles as s_6 in the GM. Note that both sets were created using simulations of brain-electric activity based on an AGM that differs from that used in the inversion/training process. This was done in order to avoid the *inverse crime* (for details, see Methods section 2.1).

2.3. ConvDip

In this section, the architecture of ConvDip, a CNN which solves the inverse problem, is described and a mathematical description in the classical notation of inverse solutions is given.

2.3.1. I/O of ConvDip

Since ConvDip was designed to operate on single time instances of EEG data, we extracted from each simulated data sample only the time point of the peak source activity. The EEG data at this time frame was then interpolated on a 2D image of size 7×11. This is necessary, given that the architecture of ConvDip (**Figure 1**) requires a 2D matrix input to perform spatial convolutions on. Note that this interpolation procedure does not add information to the EEG data. The output of ConvDip is a vector of size 5,124 corresponding to the dipoles in the source model (see **Figure 1**).

2.3.2. ConvDip Architecture

The design and training of the neural network was accomplished using the Tensorflow (Abadi et al., 2016) and Keras (Chollet, 2015) libraries, which are based on Python 3. Training was partially accomplished on a Nvidia Titan V graphical processing unit (GPU) and an Nvidia RTX 2070.

The architecture of ConvDip (**Figure 1**) is inspired by CNNs for image classification, in which the input layer is forwarded to a series of convolutional layers followed by a series of fully connected layers followed by the output layer (e.g., AlexNet; Krizhevsky et al., 2012). In typical CNNs, the convolution layers are followed by pooling layers to reduce dimensionality and to promote invariance to an object's position Deru and Ndiaye (2019). Notice that in ConvDip no pooling layers were used since spatial information would get lost or at least blurred. While invariance to the position of an object is desirable in image classification tasks (what-task), it would be detrimental in the case of source localization problems (where-task). Finally, we decided for a moderately shallow architecture with a single convolution layer followed by a fully connected layer and an output layer.

We decided to use Rectified Linear Units (ReLUs) as activation functions after each layer (Nair and Hinton, 2010; Glorot et al., 2011). ReLUs have shown to exhibit the best performance in our preliminary tests compared to alternatives (e.g., sigmoid function). After each of the inner layers, we added a batch normalization layer (Ioffe and Szegedy, 2015) in order to speed up training and to reduce internal covariance shifts. In the current version of ConvDip, the output layer consists of 5,124 neurons, which equals the number of voxels in the modeled brain. ReLU activation functions were used in the output layer. Typical CNNs for regression use linear activation functions, however, since predictions are by definition non-negative in our application, ReLUs appeared to us as an appropriate alternative.

ConvDip can be described as a function $\phi : \mathbf{M} \mapsto \hat{\mathbf{j}}, \mathbf{M} \in \mathbb{R}^{7 \times 11}, \hat{\mathbf{j}} \in \mathbb{R}^{p}$, with $p = 5124$ that maps a single time instance

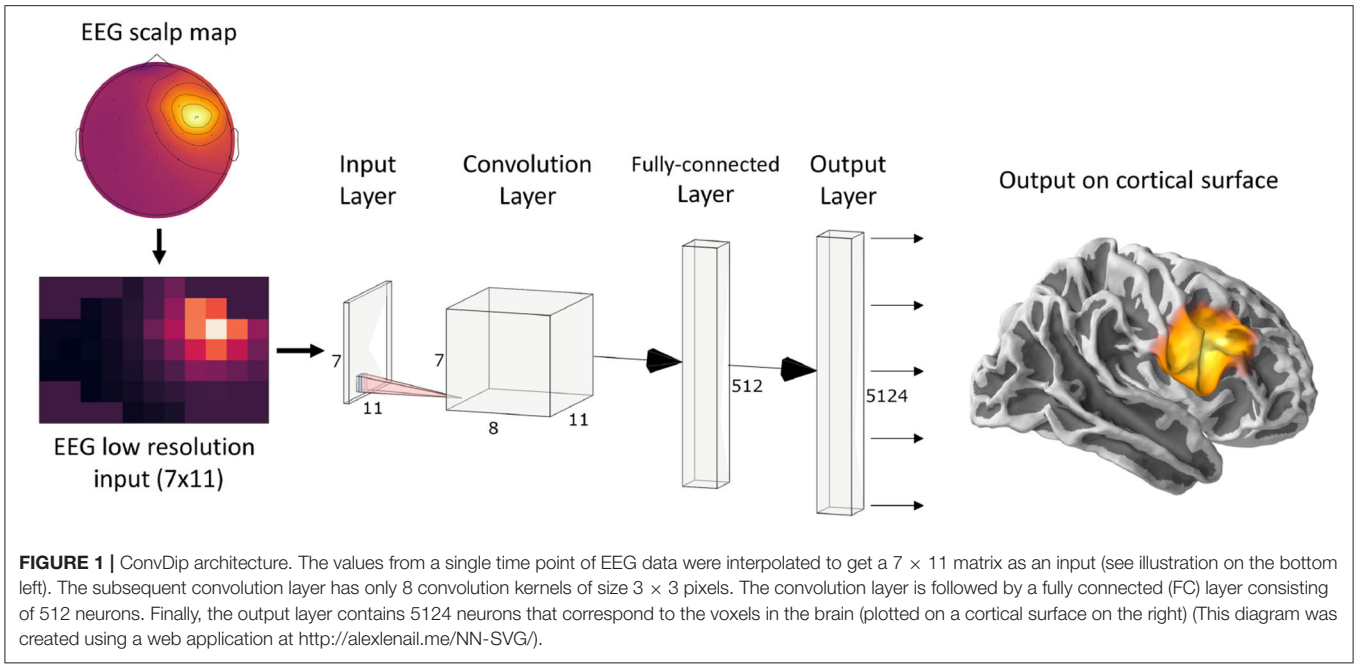

FIGURE 1 | ConvDip architecture. The values from a single time point of EEG data were interpolated to get a 7 × 11 matrix as an input (see illustration on the bottom left). The subsequent convolution layer has only 8 convolution kernels of size 3 × 3 pixels. The convolution layer is followed by a fully connected (FC) layer consisting of 512 neurons. Finally, the output layer contains 5124 neurons that correspond to the voxels in the brain (plotted on a cortical surface on the right) (This diagram was created using a web application at http://alexlenail.me/NN-SVG/).

of 2D-interpolated EEG data $\mathbf{M}$ to a source vector $\hat{\mathbf{j}}$:

$$\hat{\mathbf{j}} = \phi(\mathbf{M}) \tag{2}$$

The architecture of ConvDip starts with a convolution layer with only 8 filters $\mathbf{F}_i, i = \{1, \ldots 8\}$ of size 3 × 3. The weights of these filters are determined during the training period. In the forward pass, the padded input EEG data $\mathbf{M}$ are convolved with each filter $\mathbf{F}_i$, resulting in one feature map $\mathbf{G}_i \in \mathbb{R}^{7\times11}$.

$$\mathbf{G}_i = \mathbf{M} * \mathbf{F}_i \tag{3}$$

The feature maps $\mathbf{G}_i, i \in \{1, \ldots, 8\}$ are stacked to a tensor $\mathbf{G} \in \mathbb{R}^{7\times11\times8}$ and reshaped to a vector $\tilde{\mathbf{g}} \in \mathbb{R}^{616}$ (also called *flattening*) to enable a connection to the next FC Layer. The flattened vector $\tilde{\mathbf{g}}$ consists of 616 output nodes. Each node is connected to every neuron of the following FC Layer.

For each of the 512 neurons in the hidden fully connected layer, we transform its input $\tilde{\mathbf{g}}$ using the weight vector $\mathbf{w}$, bias b, and the activation function h:

$$z = h(\mathbf{w}^T\tilde{\mathbf{g}} + b) \tag{4}$$

The hidden layer is finally connected to the output layer of 5,124 neurons.

2.3.3. Optimization and Loss Function

Convolution filters, weights, and biases were optimized using adaptive momentum estimation (ADAM, Kingma and Ba, 2014) with default settings as suggested by the authors (*learning_rate* = 0.001, $\beta_1 = 0.9, \beta_2 = 0.999, \epsilon = 10^8$).

We tried out various loss functions for the training of ConvDip. The *mean squared error* loss is a classical loss for regression tasks. For EEG inverse solutions, however, it is not appropriate since it operates pixel-wise, i.e., the error does not provide information on how close a wrong prediction is to the true source. This is especially problematic when ConvDip is designed to find focal sources. Various approaches exist to tackle this issue, e.g., by solving an *optimal transport problem* (e.g., using Wasserstein metric) or by calculating the distance between two sets of coordinates (e.g., Hausdorff distance). We decided for the weighted Hausdorff distance (WHD) as described by Ribera et al. (2019)[1].

The WHD has shown to perform well on image segmentation tasks and allowed for a fast convergence of ConvDip compared to MSE. Note that WHD requires a normalization of the prediction and target to ensure all values are between 0 and 1. Therefore, only positional information is regarded in this loss. The rationale for this is to disentangle the problem of estimating absolute dipole moments and that of estimating dipole positions.

As mentioned above, ConvDip predicts source locations without correct global scaling (see also Equation 2). To obtain the true amplitude of the sources, we used Brent's method (Brent, 1971) to find a scalar $\hat{s}$ that minimizes the mean squared error between the forward solution ($\hat{\mathbf{x}}$) of the predicted sources ($\hat{\mathbf{j}}$) and the unscaled EEG vector $\mathbf{x}$:

$$\hat{s} = \arg\min_s \frac{1}{m}\sum_{j=1}^{m}(\hat{\mathbf{x}}_j \cdot s) - \mathbf{x}_j \tag{5}$$

The scalar $\hat{s}$ can then be used to scale the prediction.

[1]Implementation was adapted from https://github.com/N0vel/weighted-hausdorff-distance-tensorflow-keras-loss/.

2.4. Implementation of cMEM, eLORETA, and LCMV

To evaluate ConvDip, we calculated inverse solutions on the same set of simulations using eLORETA, LCMV beamformer, and cMEM, and compared the different methods with each other.

eLORETA and LCMV were carried out by the implementations in the Python library MNE. Using the same head model as described in section 2.1, each inverse algorithm was subjected to each sample of the evaluation set as described in section 2.2. The first 400 ms of each trial were used to estimate the noise covariance matrices. Regularization of the noise covariance was established using the standard MNE procedure as described in Gramfort et al. (2014). We choose the regularization parameter for eLORETA inverse solutions at $\lambda_2 = \frac{1}{9}$ and for LCMV beamforming we set the data covariance regularization to $\lambda = 0.05$, which both correspond to MNE's default parameters. Dipole orientations were restricted to be fixed orthogonal to the cortical surface.

cMEM inverse solutions were calculated with Brainstorm (Tadel et al., 2011), which is documented and freely available for download online under the GNU general public license (http://neuroimage.usc.edu/brainstorm). The same template brain (fsaverage) was used to calculate a forward model in Brainstorm. Furthermore, the BEM solution was calculated using the same parameters as in MNE. cMEM inverse solutions were calculated using a neighborhood order of 4 with temporally stable clusters. Precomputed noise covariance matrices were imported from MNE Python to ensure that inverse solutions were calculated under the same conditions in Brainstorm and MNE. After calculating all inverse solutions, the files were exported again for further evaluation in Python.

2.5. Evaluation Metrics

We calculated a number of performance metrics to assess the quality of an inverse solution. Note that for each sample in the evaluation sets, we only analyzed the central peak activity.

1) **Area under the ROC curve**: We calculated the area under the receiver operator curve (ROC) to assess the ability to estimate the correct spatial extent of sources. We adapted a similar procedure as described in Grova et al. (2006) and Chowdhury et al. (2013) with minor changes to the procedure. The dipole clusters in the target source vector $\mathbf{j}$ have a Gaussian distribution of dipole moments in our simulations. Therefore, we had to normalize all members of all dipole clusters (i.e. the target source vector) to unit amplitude (i.e. values between 0 and 1). The estimated source vector $\hat{\mathbf{j}}$ was normalized between 0 and 1 by division of the maximum. The AUC metric requires equal as many positives as there are negatives in the data. However, in our simulations only few dipoles were active (positives) compared to those not being active (negatives). Therefore, we adapted the procedure as described by Grova et al. (2006) and Chowdhury et al. (2013) by calculating two types of AUC: Both AUCs included all positives and only differ in the selection of negatives. AUC_{close} contained negative examples that closely surrounded the positive voxels by sampling randomly from the closest 20% voxels. This metric therefore captures how well the source extent is captured. AUC_{far} on the other hand sampled the negatives from voxels far away from true sources, therefore capturing possible false positives in the estimated source vector $\hat{\mathbf{j}}$. Far negatives were sampled from the 50% of the farthest negatives to the next active dipole. The overall AUC was then calculated by taking the average of AUC_{close} and AUC_{far}.
2) **Mean localization error (MLE)**: The Euclidean distance between the locations of the predicted source maximum and the target source maximum is a common measure of inverse solution accuracy as it captures the ability to localize the source center accurately. MLE was calculated between the positions of the maxima of $\hat{\mathbf{j}}$ and $\mathbf{j}$. This metric is only suitable for calculating MLE when a single source patch is present.

   For multiple sources, we adapted the following procedure. First, we identified local maxima in both the true source vector $\mathbf{j}$ and the estimated source vector $\hat{\mathbf{j}}$. First, local maxima were identified where a voxel value is larger than all of its neighboring voxels. This then yields many local maxima, which had to be filtered in order to achieve reasonable results. First, we removed all maxima whose neighbors were not sufficiently active ($<$ 20% of the maximum). This takes care of false positive maxima that do not constitute an active cluster of voxels. Then, we removed those maxima that had a larger maximum voxel in close neighborhood within a radius of 30 mm. These procedures result in a list of coordinates of maxima for both $\mathbf{j}$ and $\hat{\mathbf{j}}$. We then calculated the pairwise Euclidean distances and between the two lists of coordinates of maxima. For each true source, we identified the closest estimated source and calculated the MLE by averaging of these minimum distances. We further labeled those estimated sources that were $\geq$ 30*mm* away from the next true maximum as *ghost sources*. True maxima that did have an estimated source within a radius of 30*mm* were labeled as *found sources*, whereas those true maxima that did not have an estimated maximum within a radius of 30*mm* were labeled as missed sources. Finally, we calculated the *percentage of found sources*, i.e., the ratio of the number of correctly identified sources and the number of all true sources.
3) **Mean squared error (MSE)**: The MSE is calculated voxel-wise between the true source vector $\mathbf{j}$ and the predicted source vector $\hat{\mathbf{j}}$:

$$MSE = \frac{1}{p}\sum_{i=1}^{p}(\mathbf{j}_i - \hat{\mathbf{j}}_i)^2 \tag{6}$$

4) **Normalized mean squared error (nMSE)**: The nMSE is calculated by first normalizing both $\hat{\mathbf{j}}$ and $\mathbf{j}$ to values between 0 and 1. Then, the voxel-wise MSE is calculated as described above.

2.6. Statistics

Statistical comparison between the outcomes of different inverse solutions was done using an unpaired permutation test with 10^6 permutations. The rationale behind this choice is that most

TABLE 1 | Comparison of inverse algorithm performance for samples containing a single source cluster.

Inverse solution	AUC [%] (SD)	MSE (SD)	nMSE (SD)	MLE [mm] (SD)
ConvDip	**98.31** (3.41)	$\mathbf{3.9 \cdot 10^{-19}}$ ($2.9 * 10^{-19}$)	**0.0033** (0.0015)	**11.05** (4.96)
cMEM	90.99 (7.88)	$4.3 \cdot 10^{-13}$ ($3.2 \cdot 10^{-12}$)	0.0087 (0.0045)	18.80 (7.37)
eLORETA	85.06 (6.22)	$6.4 \cdot 10^{-08}$ ($1.1 \cdot 10^{-07}$)	0.0436 (0.0122)	13.26 (6.22)
LCMV	94.96 (4.04)	0.4 (0.1)	0.1274 (0.0356)	20.52 (6.83)

Source clusters were of varying spatial extents from two to seven neighborhood orders. AUC: Area under the receiver operator curve. MSE: Mean squared error, nMSE: normalized mean squared error, MLE: mean localization error. Best performances are highlighted in bold font.

distributions did not meet the criteria for parametric and rank-based tests. Additionally, Cohens d is given for each statistical test (Cohen, 1992).

2.7. Evaluation With Real Data

To evaluate the performance of ConvDip and the other inverse algorithms in a more realistic set-up, we used data of a real EEG recording. The data were recorded while a single participant (first author of this article) viewed fast presentations of faces and scrambled faces. The participant had to indicate whether a face was presented by button press. The duration of a stimulus presentation was 600 ms, followed by 200 ms of black screen. Note that 300 trials of both faces and scrambled faces were presented, which corresponds to a total of 4 min.

The EEG was recorded with 31 electrodes of the 10–20 system using the ActiCap electrode cap and the Brain Vision amplifier ActiCHamp. Data was sampled at $1,000Hz$ and filtered online using a band-pass of 0.01–120 Hz. The EEG data were imported to MNE Python and filtered using a band-pass filter between 0.1 and 30 Hz. Data were re-referenced to common average. The trials in which faces were presented were then selected and baseline corrected by subtracting the average amplitude in the interval −0.06 to 0.04 s relative to stimulus onset.

3. RESULTS

In this section, we evaluate the performance of ConvDip and compare it to state-of-the-art inverse algorithms, namely eLORETA, LCMV beamformer, and cMEM. Note that the evaluation set was not part of the training set of ConvDip, hence it is unknown to the model. Furthermore, all samples in the evaluation set were created using the AGM in order to avoid the inverse crime. Exemplary and representative samples are shown in **Appendices A**, **B**.

3.1. Evaluation With Single Source Set

3.1.1. Evaluation of Source Extents

We will now evaluate the ability of ConvDip to estimate the correct size of sources and to correctly localize sources with varying depth. For this purpose, we used the data samples from the single-source set. An exemplary and representative sample is shown in **Appendix–A**.

One of the advantages of inverse algorithms such as cMEM over minimum norm solutions is their capability to estimate not only the position of a source cluster but also its spatial extent. This can be tested using the AUC metric. Chowdhury et al. (2013) suggested that an AUC of 80% and above can be considered acceptable.

This criterion is met by all inverse algorithms in the present evaluation (**Table 1**). ConvDip achieves the best scores in this comparison with an overall AUC of 98%, closely followed by LCMV (95%) and cMEM (91%). Furthermore, ConvDip inverse solutions show the highest global similarity with nMSE at 0.0033, which is less than half of the error yielded by cMEM. Moreover, the other two methods are far behind (**Table 1**). MLE of ConvDip is lowest with 11.05 mm, which is remarkably small considering the variance introduced by the AGM. eLORETA yields significantly larger MLE than ConvDip ($diff_{median} = 2.21mm, p = 10^{-6}, d = 0.34$).

3.1.1.1. AUC

In **Figure 2** (left graph), the AUC for each inverse algorithm is depicted per simulated source extent. ConvDip is able to reach best performance for extents of s_3 and s_4 ($AUC_{convdip,s_3,s_4} = 99\%$) with attenuated AUC especially for larger sizes ($AUC_{convdip,s_7} = 94\%$). The AUC drops by $\approx 5.2\%$ from s_3 to s_7. cMEM, an inverse algorithm aiming at estimating both location and size of source clusters, shows similar properties. cMEM shows it is best AUC at s_2 ($AUC_{cMEM,s_2} = 93\%$). The AUC decreases by $\approx 5.5\%$ from the smallest to the largest source extent, which is comparable to ConvDip. We conclude that while ConvDip yields significantly higher AUC overall ($p \leq 10^{-6}, d > 0.40$), its behavior to varying source sizes is similar to that of cMEM. The other inverse algorithms perform significantly worse (**Figure 2**).

3.1.1.2. MLE

MLE of ConvDip is affected by source extent, as $MLE_{convdip,s_2}$ is 39% higher compared to $MLE_{convdip,s_7}$. This observation does not apply to the MLE yielded by inverse solutions of cMEM, which is fairly stable (7% variation). Overall, MLE was smaller for ConvDip inverse solutions compared to the other three inverse algorithms. One particular exception is the case of small source clusters (s_2), for which eLORETA yields the most accurate estimates ($MLE_{eLORETA,s_2} = 10.34mm$, see **Figure 2**).

3.1.2. Evaluation of Source Eccentricity

Next, we evaluated the ability of ConvDip to correctly localize source clusters of different eccentricity (i.e., distance from all electrodes). The further away a source is from the electrodes, the harder it is to localize due to volume conduction.

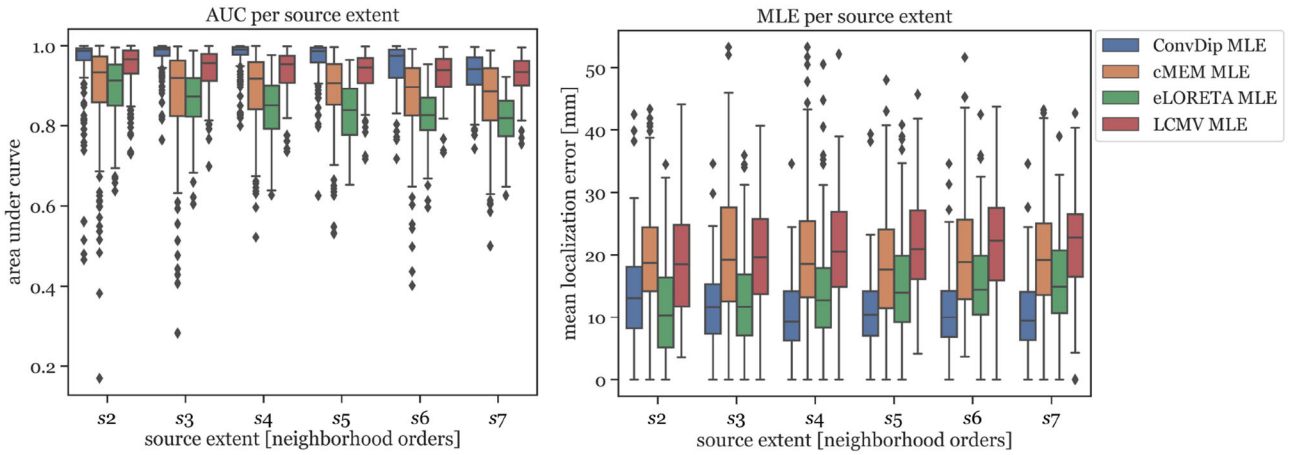

FIGURE 2 | Area under the curve and mean localization error for each inverse solution algorithm grouped by the source extent. AUC reflects capability of finding source at correct location, estimating its size and reducing false positives. MLE reflects the capability to correctly localize the center of the source cluster. Simulations used for this analysis contained only a single source cluster per sample with varying size from two to seven neighborhood orders.

3.1.2.1. AUC

In **Figure 3 left**, the AUC metric is shown for each inverse algorithm grouped by bins of eccentricity. Bins were defined from 20 mm (deep source clusters) to 80 mm (superficial source clusters). Since deeper sources are harder to localize accurately, AUC is expected to be correlated with eccentricity. However, this could be verified only for ConvDip ($r = 0.27, p < 10^{-16}$) and cMEM ($r = 0.31, p < 10^{-23}$). For LCMV beamformer, depth is barely associated with AUC ($r = 0.07, p < 0.05$) and for eLORETA no such association could be found ($r = 0, p > 0.9$). Despite these interesting dynamics, ConvDip shows for all eccentricities higher AUC compared to almost all other inverse algorithms. Only the LCMV beamformer shows a non-significant tendency ($p < 0.1, d = 0.2$) for a higher AUC for low eccentricity of 20mm ($median = 93.39\% \pm 3.19$) than ConvDip ($median = 93.44\% \pm 5.35$).

3.1.2.2. MLE

MLE is also affected by source depth as can be seen in **Figure 3 right**. We calculated the ratio between the MLE of the deepest source clusters ($eccentricity = 20\ mm$) to the MLE of superficial source clusters ($eccentricity = 80\ mm$) in order to calculate depth sensitivity of each inverse algorithm, henceforth called *drop-off*. cMEM shows a drop-off of 64%, eLORETA has a drop-off of 23%, and LCMV beamformer has a drop-off of 18%. ConvDip shows the lowest MLEs across eccentricities, compared to the other inverse methods. Moreover, ConvDip shows an inverted U-shaped behavior, with lowest MLE for the deepest and most superficial source clusters. MLE of ConvDip decreases slightly with depth of the source cluster and are not correlated with eccentricity ($r = -0.02, p > 0.5$), whereas this relation was found for all other inverse algorithms: cMEM ($r = -0.30, p < 10^{-21}$), eLORETA ($r = -0.15, p < 10^{-5}$), and LCMV beamformer ($r = -0.09, p < 0.01$).

Concluding, we find no drop-off in localization accuracy with depth of source clusters when using ConvDip, highlighting a systematically more robust behavior of ConvDip compared to all other inverse algorithms. With depth, however, the ability to estimate the extent of a source cluster is reduced.

3.1.3. Evaluation of Dipole Moments

Finally, we utilized the single-source set to evaluate how well the moments of the dipoles was reconstructed by ConvDip and the other inverse algorithms. We calculated the MSE between each true and predicted source vector (as described in section 2.5). We find that the scaled predictions of ConvDip yielded the lowest MSE ($3.93 \cdot 10^{-19} \pm 2.91 \cdot 10^{-19}$), followed by cMEM ($4.32 \cdot 10^{-13} \pm 3.24 \cdot 10^{-12}$) and eLORETA ($6.40 \cdot 10^{-8} \pm 1.05 \cdot 10^{-7}$). We excluded LCMV beamformer since the approach does not yield dipole moments that can be interpreted in this way. This result is less surprising in the light of the aforementioned results since ConvDip is able to estimate the extent of sources well, which facilitates the estimation of correct dipole moments through the scaling process (refer to section 2.3.3 for an explanation of our scaling approach).

3.2. Evaluation With Multiple Sources

In a realistic situation, the EEG may pick up signals originating from many regions in the brain simultaneously, aggravating the inversion process. Due to the low spatial resolution of the EEG, not all sources can be identified reliably. To evaluate the performance of the inverse algorithms in reconstructing more challenging samples of the multi-source set, we calculated the aforementioned metrics that are summarized in **Table 2**.

3.2.1. AUC

Overall, the AUC for the multi-source set is low since the desirable 80% AUC is undercut by each inverse algorithm. ConvDip achieved the highest AUC of 78%, thereby surpassing the next best competitor LCMV by $\approx 7.2\%$.

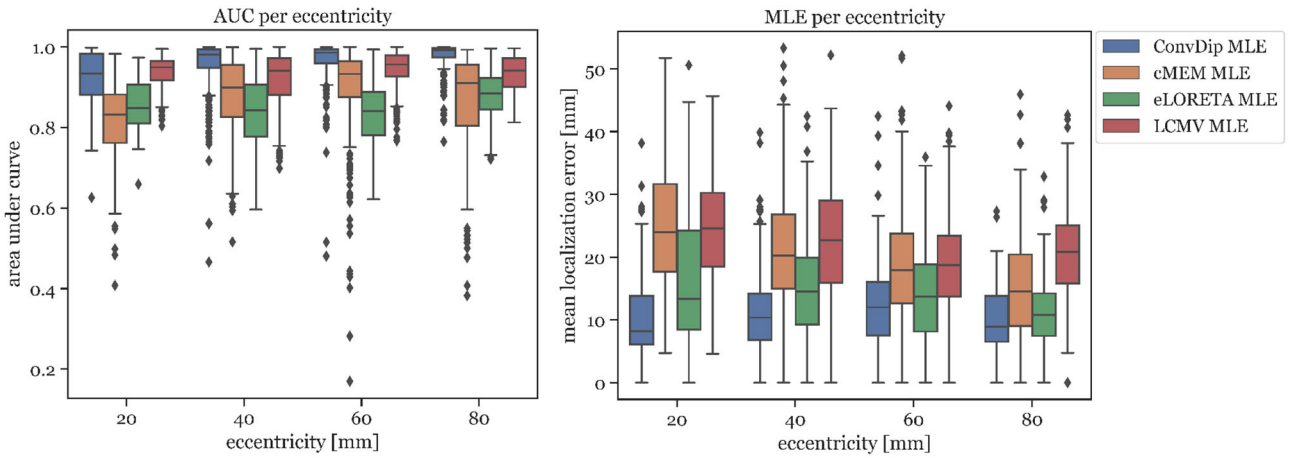

FIGURE 3 | Area under the curve and mean localization error for each inverse algorithm grouped by the source eccentricity. Simulations used for this analysis contained only a single source cluster per sample of varying size from two to seven neighborhood orders.

TABLE 2 | Comparison of inverse algorithm performance for samples containing multiple source clusters.

Inverse solution	AUC [%] (SD)	MSE (SD)	nMSE (SD)	MLE (SD)	% of sources found (SD)
ConvDip	**78.29** (9.39)	$\mathbf{1.6 \cdot 10^{-18}}$ ($4.4 \cdot 10^{-19}$)	**0.0087** (0.0042)	28.18 (12.10)	**62.71** (22.38)
cMEM	70.76 (8.95)	$1.2 \cdot 10^{-12}$ ($3.9 \cdot 10^{-12}$)	0.0139 (0.0057)	38.61 (16.11)	50.12 (24.02)
eLORETA	69.94 (7.54)	$1.9 \cdot 10^{-07}$ ($1.6 \cdot 10^{-07}$)	0.0559 (0.0152)	29.51 (8.98)	60.71 (22.60)
LCMV	71.13 (10.30)	0.4 (0.1)	0.1592 (0.0415)	**28.09** (5.50)	62.36 (23.67)

Samples contained between one and ten source clusters of varying spatial extent. Each cell contains the median and mean absolute deviation of the medians over all samples in the multi-source set. For the "percentage of sources found" metric, the mean was calculated instead of median. AUC: Area under the receiver operator curve; nMSE: normalized mean squared error, MLE: mean localization error, Percentage of sources found: The percentage of sources whose maxima was correctly localized. Best performances are highlighted in bold font.

3.2.2. nMSE

nMSE is substantially smaller for ConvDip inverse solutions compared to all other inverse algorithms with 60% lower nMSE compared to the next best performing algorithm cMEM.

3.2.3. MLE

LCMV beamforming is the only inverse solution (of the tested ones) with lower MLE than ConvDip (**Table 2**), albeit the absolute difference of the median MLEs is small ($\text{diff_}MLE \approx 0.1mm, p = 10^{-6}, d = 0.22$).

3.2.4. Percentage of Found Sources

The percentage of sources found was fairly similar for ConvDip, eLORETA, and LCMV and 10% lower for cMEM (**Table 2**). **Figure 4** shows the results for the metrics AUC and nMSE grouped by the number of sources present in the samples. It is apparent that the accuracy of all inverse solutions depends strongly on the total number of sources that contribute to the EEG signal on the scalp since for each inverse algorithm, the results worsen with increasing numbers of source clusters present in the sample. Pearson correlation between AUC and the number of present source clusters was strong and statistically significant for each inverse algorithm: ConvDip ($r = 0.70, p < 10^{-147}$), cMEM ($r = 0.60, p < 10^{-97}$), eLORETA ($r = 0.73, p < 10^{-163}$), and LCMV ($r = 0.73, p < 10^{-167}$).

This relationship was also found to exists between MLE and the number of source clusters. For large numbers of source clusters ($\geq$ 5), LCMV shows the lowest MLE ($29.41mm$) or $4.24mm$ less than ConvDip ($p = 10^{-6}, d = 0.60$, **Figure 5**). This may be a result of the inherent noise-suppressing properties of the LCMV beamformer.

A core result of this analysis is that although ConvDip was trained with samples containing between 1 and 5 source clusters, it is capable of inverting more challenging samples as well (**Figure 4**).

Furthermore, we showed that discrepancies between the assumed GM and the true bio-physical properties underlying an EEG measurement (e.g., tissue conductivity, precise electrode locations, spacing of the discrete dipole model) can be handled by ConvDip.

ConvDip provides inverse solutions that are valid for samples generated with the AGM and different configurations (namely, different numbers of source clusters). This shows that ConvDip is able to generalize well beyond samples within the training set. This in turn confirms the validity of this purely data-driven approach to solve the EEG inverse problem.

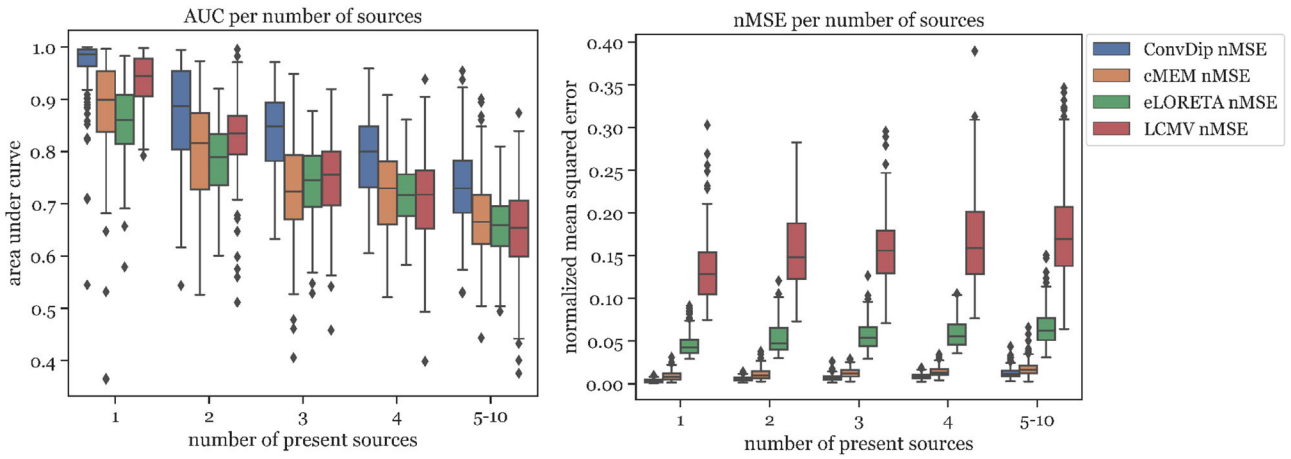

FIGURE 4 | Area under the curve and normalized mean squared error for each inverse algorithm grouped by the number of present source clusters. The right-most columns in each of the graphs display the results for samples containing between 5 and 10 source clusters.

4. DISCUSSION

4.1. Overview

We have presented ConvDip, a CNN that aims to find extended sources of EEG signals. The approach of using a neural network to solve the inverse problem is distinct from classical methods, mainly because it works purely data driven. All constraints on the solution of ConvDip are given implicitly. The performance of ConvDip was evaluated and tested against commonly used inverse algorithms cMEM, eLORETA, and LCMV beamforming. In the following, we discuss the significance of these results.

4.2. Using ANNs to Solve the Inverse Problem

One major result of this work is that the CNN ConvDip was capable to reliably find the locations of neural sources that give rise to the EEG. ConvDip transforms a 7×11 image to a large vector of 5,124 voxels. In image classification, CNNs are utilized to do the opposite: To extract hidden information from a large input matrix and output, a single value that indicates some property, e.g., the presence of a cat or a dog. Our work verifies that CNNs are capable to solve an underdetermined problem. This issue was already addressed by Lucas et al. (2018), who demonstrated the advantages of ANNs over analytical approaches to solve the inverse problem.

We trained ConvDip on data generated by GM and subsequently evaluated ConvDip on simulated samples that were generated by the AGM in order to avoid committing the inverse crime. Overall, the performance of ConvDip was sometimes comparable but in most cases better than the classical inverse solutions cMEM, eLORETA, and LCMV beamformer. This provides evidence that ConvDip learned to generalize beyond samples in the training data and remains robust to deviations from the training data. This holds for small deviations in the position of the electrodes (± 3.7 *mm*), tissue conductivities, but also in the configuration of sources (number and size of clusters, deviations from the GM source model grid), and provides another remarkable advantage of these data-driven approach.

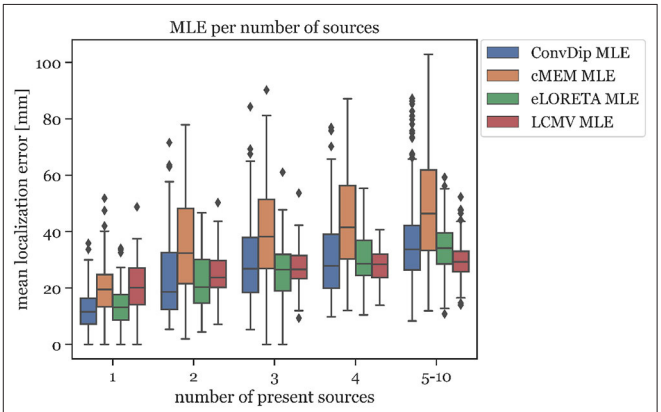

FIGURE 5 | Mean localization error for each inverse algorithm grouped by the number of present source clusters. The rightmost column displays the results for samples containing between 5 and 10 source clusters.

We evaluated the performance of ConvDip and the alternative inverse algorithms concerning multiple objectives, the results of which we will discuss in the following.

4.3. Estimating Source Extent

The ability to estimate not only the location of a neural source but also its extent was tested for all inverse algorithms on the single-source set using the AUC and nMSE performance. We find that ConvDip reaches a nearly perfect AUC of $\approx$ 98%, which is not met by any other inverse algorithm. nMSE, a measure of global similarity between the true and estimated source, was smallest using ConvDip, with less than half the error compared to the next best inverse solutions yielded from cMEM (**Table 1**). ConvDip furthermore estimated different source sizes appropriately (**Figure 2**) with higher AUC than all other inverse algorithms. Although these findings are remarkable

we have to regard that the shape and size of the sources was rather predictable for ConvDip. All sources in the training and evaluation set had a more or less circular shape due the region growing approach we chose. It may be presumably a large challenge for ConvDip to estimate ellipitical shapes or shapes that are even more deviant to a circle. Despite this caveat, it is remarkable how well ConvDip performs in this comparison considering the variability introduced by the AGM.

4.4. Localizing Deep Sources

A further surprising result for us during the evaluation was that for ConvDip the MLE did not depend on the depth of the source cluster, i.e., ConvDip is capable to correctly localize even deep sources with nearly no drop-off (see **Figure 3**). This finding was a strong contrast to the findings from other inverse algorithms, which all tend to mislocate deeper sources more than superficial ones. Although source depth did not influence the MLE of ConvDip, we find that the AUC is indeed compromised by depth. This holds also true for cMEM but not for eLORETA and barely for LCMV beamformer. Overall, ConvDip achieved comparable AUCs and MLEs for various depth of source clusters, compared to other inverse solutions, rendering it a viable option for localizing deep sources.

4.5. Performance With Multiple Active Source Clusters

In section 3.2, we evaluated how ConvDip performs when many source clusters are simultaneously active. We observed a drop-off in AUC with increasing numbers of active source clusters from $\approx$ 99% with single sources to $\approx$ 73% when 5 or more sources were active simultaneously. Similar behavior was observed for all inverse algorithms tested (see **Figure 4**). But, ConvDip achieved the highest AUC compared to all alternatives tested, surpassing the best competitor LCMV by $\approx$ 7.2%. Furthermore, ConvDip also outperformed all other inverse algorithms concerning nMSE (**Table 2**). Only when five or more source clusters are present, we find slightly lower MLE using LCMV beamformer compared to ConvDip. This increased localization ability of LCMV beamformer could be due to the active suppression of noise signals in the beamforming process. Another reason could be that ConvDip was never trained with samples that contained more than five active source clusters, therefore struggling to accurately localize at least a subset of the source clusters.

4.6. Computation Speed

As already pointed out by Sclabassi et al. (2001), ANNs naturally yield faster inverse solutions than classical methods. On our workstation (CPU: Intel i5 6400, GPU: Nvidia RTX 2070, 16 Gb RAM), one forward pass of ConvDip took on average $\approx$ 31 *ms* on the GPU. When all necessary preprocessing steps (such as re-referencing, scaling, and interpolation to 2-D scalp maps) are taken into account, we reached $\approx$ 32 *ms* of computation time on average. In comparison, it takes $\approx$ 129 *ms* ($\approx$factor 4) to calculate the eLORETA inverse solution using MNE, $\approx$ 98 *ms* ms ($\approx$factor 3) for LCMV beamforming and astonishing 11.55 *s* ($\approx$factor 360) to calculate the iterative cMEM inverse solution using brainstorm. Additionally, one has to provide the noise covariance matrix, which takes on average $\approx$ 45 *ms* to compute using the empirical estimation of MNE. In practical terms, ConvDip is capable to compute 31.25 inverse solutions per second (ips) on a GPU, whereas eLORETA reaches 7.75 *ips* LCMV beamformer 10.20 *ips* on a CPU. Possibly, implementations of eLORETA and LCMV beamforming that can be run on a GPU achieve lower computation times compared to CPU. The short computation times of ConvDip are at a distinct advantage over other inverse solutions, e.g., in real-time applications as in neurofeedback experiments or in the development of brain–computer interfaces. When comparing our approach to the existing literature on ANN-based inverse solutions, we can now confirm that an ANN not only provides competitively accurate single dipole locations but also a distributed dipole model of the brain-electric activity, taking into account more than one dipole. This can be attributed mostly to the rapid developments in the machine learning domain such as the introduction of convolutional layers (LeCun and Bengio, 1995) and the improvements of GPUs that render the training of large ANNs possible in acceptable time.

4.7. Realistic Simulations

The simulation of EEG data in this study was based on different assumptions on the number, distribution, and shape of electromagnetic fields, which is inspired by Nunez and Srinivasan (2006). The validity of predictions of any inverse solution is only granted if the assumptions on the origin of the EEG signal are correct. This is indeed one of the critical challenges toward realistic inverse solutions in general, both for data-driven inverse solutions (such as ConvDip) as well as classical inverse solutions with physiological constraints (e.g., eLORETA). Therefore, when interpreting the applicability of ConvDip to real data, it is important to specify and justify these assumptions. We show that the knowledge about brain-electric activity underlying EEG signals is emulated by ConvDip after it was trained. However, it is evident from the present work, how critical the particular choice of parameters is with respect to the performance, as ConvDip produces solutions that closely resemble the training samples (see **Appendices A**, **B**). A more sophisticated approach to this problem would be to diversify the training data, e.g., by changing the region-growing procedure to produce sources with higher variety of shapes beyond simple spheric source clusters. Nonetheless, ConvDip finds reasonable source clusters when presented with real data (see **Appendix–C** for an example).

An important observation in real EEG data is the inter-individual variability, which is in part a direct result of individual brain anatomies. For ConvDip application to real EEG data, particularly with group data, it is thus advised to collect anatomical MRI brain scans of each individual subject. Individual neural networks then need to be trained based on each subjects' individual anatomy provided by the MRI data. This may help to achieve accurate group-study source estimations. This, however, raises the problem of computation time, since training individual CNNs is time consuming. A solution to this is an inter-individual

transfer learning approach, where ConvDip is trained on one subjects' anatomy and fine-tuned for each additional subject with new training data of the individual anatomies. Fine tuning could be achieved by replacing the output-layer, lowering the learning rate and retraining for only few epochs. Training time *per se* is another important topic, when considering CNNs to handle the inverse problem.

4.8. Training Time

Although the availability of high-performing hardware resources (e.g., high performing graphic cards) is growing rapidly, the training of the presented neural network architecture requires a considerable amount of processing power and processing time. The version of ConvDip shown in this work required $\approx$ 10.5 h of training for 500 epochs and 100,000 samples of data using a NVIDIA RTX 2070 GPU. Improving the architecture of ConvDip to shorten training time is an important task for future research, especially when individualized models are required. Limiting the solution space to fewer voxels may be one way to decrease the computation time since most trainable parameters are located at the final fully connected layers. The easiest way would be to reduce the number of parameters of the neural network, e.g., by targeting a CNN with volumetric output of the ANN corresponding to a volumetric source model of the brain. This could spare the computationally expensive fully connected layers and reduce the number of weights in the network. Another possibility is to segment the cortical surface into parcels, i.e., clusters of neighboring dipole positions. This would reduce the size of the output layer by one to two orders of magnitude and thereby reduce the number of trainable parameters dramatically. The feasibility of such a dimension reduction is to be investigated in future developments.

Another computationally expensive processing step is the generation of realistic artificial training data. In this study, we projected neural activity using a three-layer BEM head model. Generating 100,000 simulations of neural activity took 12 min using a PC with CPU @ 4 $\times$ 4.3 GHz and 16 GB of RAM. Software that enables EEG researchers to perform physiologically realistic simulations of neural activity for their own ConvDip application is available from different resources, e.g., from the MNE library in Python (Gramfort et al., 2014).

4.9. Further Perspectives for Improvement

The present version of ConvDip is trained on single time instances of EEG data. From a single EEG data point, it is, however, not possible to estimate a noise baseline. As a consequence, such a baseline has not yet been taken into account in ConvDip, which leaves room for improvements toward more regularized and adaptive solutions that are computed flexibly depending on noise conditions. In contrast, LCMV, eLORETA, and cMEM explicitly make use of a noise covariance matrix, which is used to regularize the inverse solution. ConvDip could be improved by extending the data input to an EEG time series, allowing the neural network to learn spatiotemporal patterns.

Possible further advances could be made by preserving the 3D structure of the output space by, instead of a flattened output layer. This can be realized using a deconvolutional neural network for 2D-3D projections (Lin et al., 2018) or by using spatiotemporal information with a LSTM network (Cui et al., 2019). One obvious further way to improve the performance of ConvDip may be to increase the capacity of the neural network, e.g., by adding more layers. In our initial testing phase, we tried different neural architectures without observing significant improvements by adding more layers that justify the increase in training time. Neural architecture search should be used to find a compact, well-performing architecture to solve the EEG inverse problem (Liu et al., 2018).

Finally, the development of a both meaningful and computationally inexpensive loss function, which makes training faster and allows for faster convergence, is key for ANN-based approaches to the inverse problem that can run on ordinary PC within a reasonable amount of time.

4.10. Outlook

We showed that ConvDip, a shallow CNN, is capable of solving the inverse problem using a distributed dipole solution. The association between single time points of EEG measurements and underlying source distributions can be learned and used to predict plausible inverse solutions. These inverse solutions were, furthermore, shown to globally reflect the topology of the brain-electric activity given by the training data.

Predictions yielded from ConvDip are in rare cases comparable to but in the majority of cases better than the here tested existing inverse algorithms in the measures we focused on. Furthermore, the application of ConvDip to real EEG data yields reasonable results. The fully trained ConvDip requires only little computational costs of 32 ms, which makes it a promising tool for real-time applications where only single time points of EEG data are available.

We want to emphasize the importance of realistic simulations of *real* neural activity that can be measured by EEG. Although a lot of knowledge about the generation of scalp potentials was implemented in our EEG simulations, including more physiological constraints can further reduce the complexity of the inverse problem. One example is the estimation of cortical column orientation (Bonaiuto et al., 2019) or the incorporation of empirical knowledge about region-specific activity from *in-vivo* (e.g., electrocorticogram) studies. Taking into account these additional aspects may further improve ConvDip's performance.

The current ConvDip version was based on single time points of artificial EEG data. Exploiting temporal aspects of brain dynamics (neighboring time points) may provide additional valuable information and increase the predictive power that may further refine future ConvDip versions.

DATA AVAILABILITY STATEMENT

The simulations and the ConvDip model can be reproduced using the python package located at: https://www.github.com/LukeTheHecker/ESINet.

ETHICS STATEMENT

Ethical review and approval was not required for the study on human participants in accordance with the local legislation and institutional requirements. The patients/participants provided their written informed consent to participate in this study.

AUTHOR CONTRIBUTIONS

LH conceptualisation, initial idea, implementation, testing, evaluation, and writing the manuscript. RR technical supervision for mathematics, implementation, and artificial neural networks. LT conceptualisation, remarks on results, manuscript, and remarks on future perspectives. JK conceptualization, writing and revising the manuscript, development of evaluation procedure, and discussion. All authors participated in discussing the methodology and evaluating the results and revising the manuscript.

FUNDING

The project was funded by the European Campus (Eucor) seeding money.

ACKNOWLEDGMENTS

The authors want to thank NVIDIA Corporation for supplying us with a Titan V GPU as part of the academic seeding program. We thank Roman Tankelevich for his remarks in the early stage of the project.

REFERENCES

Abadi, M., Agarwal, A., Barham, P., Brevdo, E., Chen, Z., Citro, C., Corrado, G. S., et al. (2016). Tensorflow: large-scale machine learning on heterogeneous distributed systems. *arXiv preprint arXiv:1603.04467*.

Abeyratne, U. R., Zhang, G., and Saratchandran, P. (2001). EEG source localization: a comparative study of classical and neural network methods. *Int. J. Neural Syst.* 11, 349–359. doi: 10.1142/S0129065701000813

Amblard, C., Lapalme, E., and Lina, J.-M. (2004). Biomagnetic source detection by maximum entropy and graphical models. *IEEE Trans. Biomed. Eng.* 51, 427–442. doi: 10.1109/TBME.2003.820999

Awan, F. G., Saleem, O., and Kiran, A. (2019). Recent trends and advances in solving the inverse problem for EEG source localization. *Inverse Prob. Sci. Eng.* 27, 1521–1536. doi: 10.1080/17415977.2018.1490279

Bonaiuto, J. J., Afdideh, F., Ferez, M., Wagstyl, K., Mattout, J., Bonnefond, M., et al. (2019). Estimates of cortical column orientation improve MEG source inversion. *bioRxiv* 810267. doi: 10.1101/810267

Brent, R. P. (1971). An algorithm with guaranteed convergence for finding a zero of a function. *Comput. J.* 14, 422–425. doi: 10.1093/comjnl/14.4.422

Chollet, F. (2015). *Keras.* Available online at: https://keras.io

Chowdhury, R. A., Lina, J. M., Kobayashi, E., and Grova, C. (2013). MEG source localization of spatially extended generators of epileptic activity: comparing entropic and hierarchical bayesian approaches. *PLoS ONE* 8:e55969. doi: 10.1371/journal.pone.0055969

Cohen, J. (1992). Statistical power analysis. *Curr. Direct. Psychol. Sci.* 1, 98–101. doi: 10.1111/1467-8721.ep10768783

Cui, S., Duan, L., Gong, B., Qiao, Y., Xu, F., Chen, J., et al. (2019). EEG source localization using spatio-temporal neural network. *China Commun.* 16, 131–143. doi: 10.23919/JCC.2019.07.011

Delorme, A., Palmer, J., Onton, J., Oostenveld, R., and Makeig, S. (2012). Independent EEG sources are dipolar. *PLoS ONE* 7:e30135. doi: 10.1371/journal.pone.0030135

Deru, M., and Ndiaye, A. (2019). Deep learning with tensorFlow, keras and tensorFlow. js. *Rheinwerk Comput.* 1, 15–55.

Ebersole, J. S. (1994). Non-invasive localization of the epileptogenic focus by EEG dipole modeling. *Acta Neurol. Scand.* 89, 20–28. doi: 10.1111/j.1600-0404.1994.tb05179.x

Fedorov, M., Koshev, N., and Dylov, D. V. (2020). "Deep learning for Non-invasive cortical potential imaging," in *Machine Learning in Clinical Neuroimaging and Radiogenomics in Neuro-Oncology: Third International Workshop, MLCN 2020, and Second International Workshop, RNO-AI 2020, Held in Conjunction with MICCAI 2020, Lima, Peru, October 4–8, 2020, Proceedings*, Vol. 12449, (Springer Nature), 45.

Fischl, B., Sereno, M. I., Tootell, R. B., and Dale, A. M. (1999). High-resolution intersubject averaging and a coordinate system for the cortical surface. *Hum. Brain Mapp.* 8, 272–284. doi: 10.1002/(SICI)1097-0193(1999)8:4<272::AID-HBM10>3.0.CO;2-4

Friston, K., Harrison, L., Daunizeau, J., Kiebel, S., Phillips, C., Trujillo-Barreto, N., et al. (2008). Multiple sparse priors for the M/EEG inverse problem. *NeuroImage* 39, 1104–1120. doi: 10.1016/j.neuroimage.2007.09.048

Fuchs, M., Kastner, J., Wagner, M., Hawes, S., and Ebersole, J. S. (2002). A standardized boundary element method volume conductor model. *Clin. Neurophysiol.* 113, 702–712. doi: 10.1016/S1388-2457(02)00030-5

Glorot, X., Bordes, A., and Bengio, Y. (2011). "Deep sparse rectifier neural networks," in *Proceedings of the Fourteenth International Conference on Artificial Intelligence and Statistics* (Fort Lauderdale, FL), 315–323.

Gramfort, A., Luessi, M., Larson, E., Engemann, D. A., Strohmeier, D., Brodbeck, C., et al. (2013). MEG and EEG data analysis with MNE-Python. *Front. Neurosci.* 7:267. doi: 10.3389/fnins.2013.00267

Gramfort, A., Luessi, M., Larson, E., Engemann, D. A., Strohmeier, D., Brodbeck, C., et al. (2014). MNE software for processing MEG and EEG data. *Neuroimage* 86, 446–460. doi: 10.1016/j.neuroimage.2013.10.027

Grech, R., Cassar, T., Muscat, J., Camilleri, K. P., Fabri, S. G., Zervakis, M., et al. (2008). Review on solving the inverse problem in EEG source analysis. *J. Neuroeng. Rehabil.* 5:25. doi: 10.1186/1743-0003-5-25

Grova, C., Daunizeau, J., Lina, J.-M., Bénar, C. G., Benali, H., and Gotman, J. (2006). Evaluation of EEG localization methods using realistic simulations of interictal spikes. *Neuroimage* 29, 734–753. doi: 10.1016/j.neuroimage.2005.08.053

Hämäläinen, M. S., and Ilmoniemi, R. J. (1994). Interpreting magnetic fields of the brain: minimum norm estimates. *Med. Biol. Eng. Comput.* 32, 35–42. doi: 10.1007/BF02512476

He, B., Sohrabpour, A., Brown, E., and Liu, Z. (2018). Electrophysiological source imaging: a noninvasive window to brain dynamics. *Ann. Rev. Biomed. Eng.* 20, 171–196. doi: 10.1146/annurev-bioeng-062117-120853

Hochreiter, S., and Schmidhuber, J. (1997). Long short-term memory. *Neural Comput.* 9, 1735–1780. doi: 10.1162/neco.1997.9.8.1735

Hoey, G. V., Clercq, J. D., Vanrumste, B., de Walle, R. V., Lemahieu, I., D'Havé, M., et al. (2000). EEG dipole source localization using artificial neural networks. *Phys. Med. Biol.* 45, 997–1011. doi: 10.1088/0031-9155/45/4/314

Ioannides, A. A., Bolton, J. P. R., and Clarke, C. J. S. (1990). Continuous probabilistic solutions to the biomagnetic inverse problem. *Inverse Probl.* 6:523. doi: 10.1088/0266-5611/6/4/005

Ioffe, S., and Szegedy, C. (2015). Batch normalization: accelerating deep network training by reducing internal covariate shift. *arXiv preprint arXiv:1502.03167*.

Jin, K. H., McCann, M. T., Froustey, E., and Unser, M. (2017). Deep convolutional neural network for inverse problems in imaging. *IEEE Trans. Image Proc.* 26, 4509–4522. doi: 10.1109/TIP.2017.2713099

Joos, E., Giersch, A., Hecker, L., Schipp, J., Heinrich, S. P., Tebartz van Elst, L., et al. (2020). Large EEG amplitude effects are highly similar

across Necker cube, smiley, and abstract stimuli. *PLoS ONE* 15:e0232928. doi: 10.1371/journal.pone.0232928

Kaipio, J., and Somersalo, E. (2006). *Statistical and Computational Inverse Problems*. Luxemburg: Springer Science & Business Media.

Kanwisher, N., and Yovel, G. (2006). The fusiform face area: a cortical region specialized for the perception of faces. *Philos. Trans. R. Soc. B Biol. Sci.* 361, 2109–2128. doi: 10.1098/rstb.2006.1934

Kavanagk, R. N., Darcey, T. M., Lehmann, D., and Fender, D. H. (1978). Evaluation of methods for three-dimensional localization of electrical sources in the human brain. *IEEE Trans. Biomed. Eng.* 25, 421–429. doi: 10.1109/TBME.1978.326339

Kim, Y. (2014). Convolutional neural networks for sentence classification. *arXiv preprint arXiv:1408.5882*. doi: 10.3115/v1/D14-1181

Kingma, D. P., and Ba, J. (2014). Adam: a method for stochastic optimization. *arXiv preprint arXiv:1412.6980*.

Koles, Z. J. (1998). Trends in EEG source localization. *Electroencephalogr. Clin. Neurophysiol.* 106, 127–137. doi: 10.1016/S0013-4694(97)00115-6

Krizhevsky, A., Sutskever, I., and Hinton, G. E. (2012). "Imagenet classification with deep convolutional neural networks," in *Advances in Neural Information Processing Systems* (Lake Tahoe, NV), 1097–1105.

Lantz, G., Holub, M., Ryding, E., and Rosén, I. (1996). Simultaneous intracranial and extracranial recording of interictal epileptiform activity in patients with drug resistant partial epilepsy: Patterns of conduction and results from dipole reconstructions. *Electroencephalogr. Clin. Neurophysiol.* 99, 69–78. doi: 10.1016/0921-884X(96)95686-6

LeCun, Y., and Bengio, Y. (1995). Convolutional networks for images, speech, and time series. *Handbook Brain Theory Neural Netw.* 3361:1995.

Lin, C.-H., Kong, C., and Lucey, S. (2018). "Learning efficient point cloud generation for dense 3d object reconstruction," in *Thirty-Second AAAI Conference on Artificial Intelligence* (New Orleans, LA).

Liu, C., Zoph, B., Neumann, M., Shlens, J., Hua, W., Li, L.-J., et al. (2018). "Progressive neural architecture search," in *Proceedings of the European Conference on Computer Vision (ECCV)* (Munich), 19–34.

Lucas, A., Iliadis, M., Molina, R., and Katsaggelos, A. K. (2018). Using deep neural networks for inverse problems in imaging: beyond analytical methods. *IEEE Signal Proc. Mag.* 35, 20–36. doi: 10.1109/MSP.2017.2760358

Luck, S. J. (2014). *An Introduction to the Event-Related Potential Technique*. Cambridge: MIT press.

Michel, C. M., and Brunet, D. (2019). EEG source imaging: a practical review of the analysis steps. *Front. Neurol.* 10:325. doi: 10.3389/fneur.2019.00325

Nair, V., and Hinton, G. E. (2010). "Rectified linear units improve restricted boltzmann machines," in *Proceedings of the 27th International Conference on Machine Learning (ICML-10)* (Madison, WI), 807–814.

Nunez, P. L., and Srinivasan, R. (2006). *Electric Fields of the Brain: The Neurophysics of EEG*. Oxford: Oxford University Press, USA.

Pascual-Marqui, R., Michel, C. M., and Lehmann, D. (1994). Low-resolution electromagnetic tomography–a new method for localizing electrical activity in the brain. *Int. J. Psychophysiol.* 18, 49–65. doi: 10.1016/0167-8760(84)90014-X

Pascual-Marqui, R. D. (1999). Review of methods for solving the EEG inverse problem. *Int. J. Bioelectromagn.* 1, 75–86.

Pascual-Marqui, R. D. (2007). Discrete, 3D distributed, linear imaging methods of electric neuronal activity. Part 1: Exact, zero error localization. *arXiv preprint arXiv:0710.3341*.

Razorenova, A., Yavich, N., Malovichko, M., Fedorov, M., Koshev, N., and Dylov, D. V. (2020). "Deep Learning for Non-Invasive Cortical Potential Imaging," in *Machine Learning in Clinical Neuroimaging and Radiogenomics in Neuro-Oncology* (Lima: Springer), 45–55.

Ribera, J., Guera, D., Chen, Y., and Delp, E. J. (2019). "Locating objects without bounding boxes," in *Proceedings of the IEEE Conference on Computer Vision and Pattern Recognition* (San Juan), 6479–6489.

Ritter, P., and Villringer, A. (2006). Simultaneous EEG–fMRI. *Neurosci. Biobehav. Rev.* 30, 823–838. doi: 10.1016/j.neubiorev.2006.06.008

Robert, C., Gaudy, J.-F., and Limoge, A. (2002). Electroencephalogram processing using neural networks. *Clin. Neurophysiol.* 113, 694–701. doi: 10.1016/S1388-2457(02)00033-0

Scherg, M. (1990). Fundamentals of dipole source potential analysis. *Auditory Evoked Magn. Fields Electr. Potent. Adv. Audiol.* 6, 40–69.

Schirrmeister, R. T., Springenberg, J. T., Fiederer, L. D. J., Glasstetter, M., Eggensperger, K., Tangermann, M., et al. (2017). Deep learning with convolutional neural networks for EEG decoding and visualization. *Hum. Brain Mapp.* 38, 5391–5420. doi: 10.1002/hbm.23730

Sclabassi, R. J., Sonmez, M., and Sun, M. (2001). EEG source localization: a neural network approach. *Neurol. Res.* 23, 457–464. doi: 10.1179/016164101101198848

Sharma, P., Scherg, M., Pinborg, L. H., Fabricius, M., Rubboli, G., Pedersen, B., et al. (2018). Ictal and interictal electric source imaging in pre-surgical evaluation: a prospective study. *Eur. J. Neurol.* 25, 1154–1160. doi: 10.1111/ene.13676

Simonyan, K., and Zisserman, A. (2014). Very deep convolutional networks for large-scale image recognition. *arXiv preprint arXiv:1409.1556*.

Tadel, F., Baillet, S., Mosher, J. C., Pantazis, D., and Leahy, R. M. (2011). Brainstorm: a user-friendly application for MEG/EEG analysis. *Comput. Intell. Neurosci.* 2011:879716. doi: 10.1155/2011/879716

Tankelevich, R. (2019). Inverse problem's solution using deep learning: An EEG-based study of brain activity. Part 1. Available online at: https://www.researchgate.net/publication/331153114_Inverse_Problem's_Solution_Using_Deep_Learning_An_EEG-based_Study_of_Brain_Activity_Part_1_-_rel_10

Van Veen, B. D., van Drongelen, W., Yuchtman, M., and Suzuki, A. (1997). Localization of brain electrical activity via linearly constrained minimum variance spatial filtering. *IEEE Trans. Biomed. Eng.* 44, 867–880. doi: 10.1109/10.623056

Willemse, R. B., Hillebrand, A., Ronner, H. E., Peter Vandertop, W., and Stam, C. J. (2016). Magnetoencephalographic study of hand and foot sensorimotor organization in 325 consecutive patients evaluated for tumor or epilepsy surgery. *Neuroimage Clin.* 10, 46–53. doi: 10.1016/j.nicl.2015.11.002

Wipf, D. and Nagarajan, S. (2009). A unified Bayesian framework for MEG/EEG source imaging. *Neuroimage* 44, 947–966. doi: 10.1016/j.neuroimage.2008.02.059

Wirgin, A. (2004). The inverse crime. *arXiv:math-ph/0401050*.

Wolters, C. H., Lew, S., MacLeod, R. S., and Hämäläinen, M. (2010). Combined EEG/MEG source analysis using calibrated finite element head models. *Biomed. Technik Biomed. Eng. Rostock Germany* 55(Suppl. 1), 64–68.

Yuasa, M., Zhang, Q., Nagashino, H., and Kinouchi, Y. (1998). "EEG source localization for two dipoles by neural networks," in *Proceedings of the 20th Annual International Conference of the IEEE Engineering in Medicine and Biology Society. Vol. 20 Biomedical Engineering Towards the Year 2000 and Beyond (Cat. No. 98CH36286)*, Vol. 4 (Hong Kong: IEEE), 2190–2192.

Zhang, Q., Yuasa, M., Nagashino, H., and Kinouchi, Y. (1998). "Single dipole source localization from conventional EEG using BP neural networks," in *Proceedings of the 20th Annual International Conference of the IEEE Engineering in Medicine and Biology Society. Vol. 20 Biomedical Engineering Towards the Year 2000 and Beyond (Cat. No. 98CH36286)*, Vol. 4 (IEEE), 2163–2166.

Conflict of Interest: The authors declare that the research was conducted in the absence of any commercial or financial relationships that could be construed as a potential conflict of interest.

Copyright © 2021 Hecker, Rupprecht, Tebartz Van Elst and Kornmeier. This is an open-access article distributed under the terms of the Creative Commons Attribution License (CC BY). The use, distribution or reproduction in other forums is permitted, provided the original author(s) and the copyright owner(s) are credited and that the original publication in this journal is cited, in accordance with accepted academic practice. No use, distribution or reproduction is permitted which does not comply with these terms.

A. APPENDIX

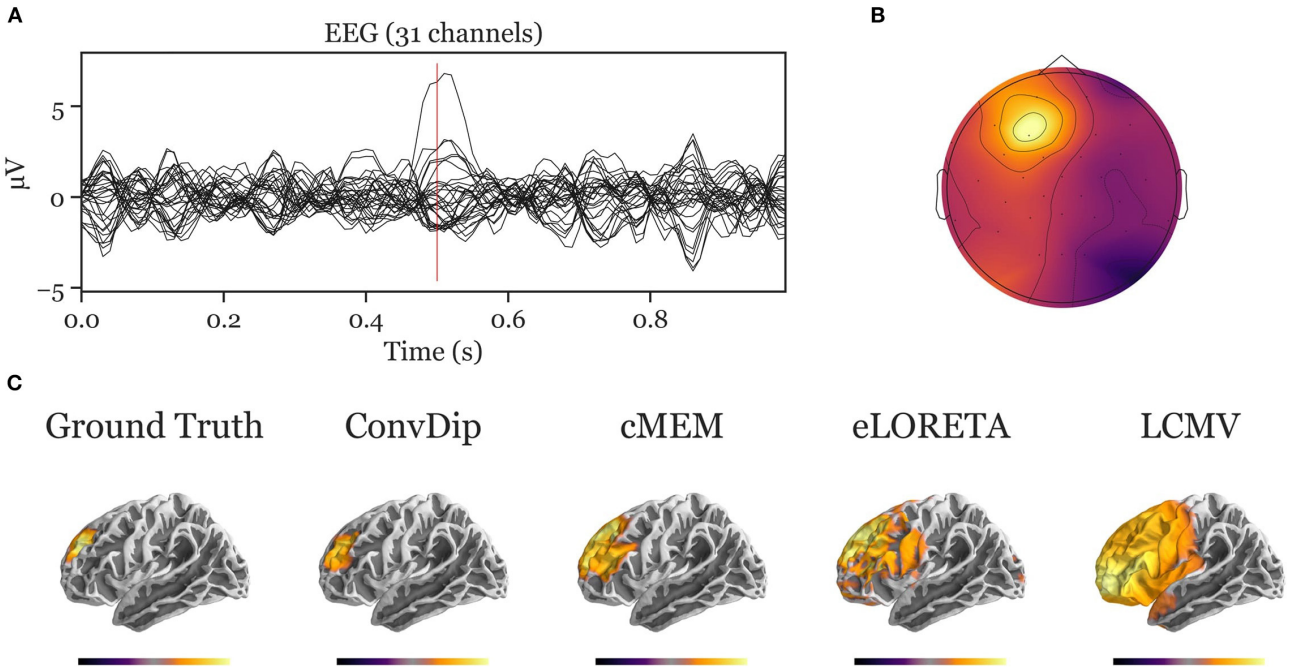

FIGURE A1 | Inverse solution of a simulation containing a single source cluster. An exemplary, representative sample of inverse solutions for a single source cluster. **(A)** The ERP at each of the 31 channels containing both signal (central peak) and realistic noise from real recordings. **(B)** The scalp map at the central ERP peak (as indicated by the vertical red line in **A**). **(C)** The dipole moments plotted on the white matter surface of the template brain in lateral view of the left hemisphere. On the *left*, the ground truth source pattern is depicted with a source cluster in the frontal cortex of the left hemisphere. Various inverse solutions that aim to recover this pattern are depicted next to it. Voxels below 25% of the respective maximum are omitted for a clearer representation of the current distribution.

B. APPENDIX

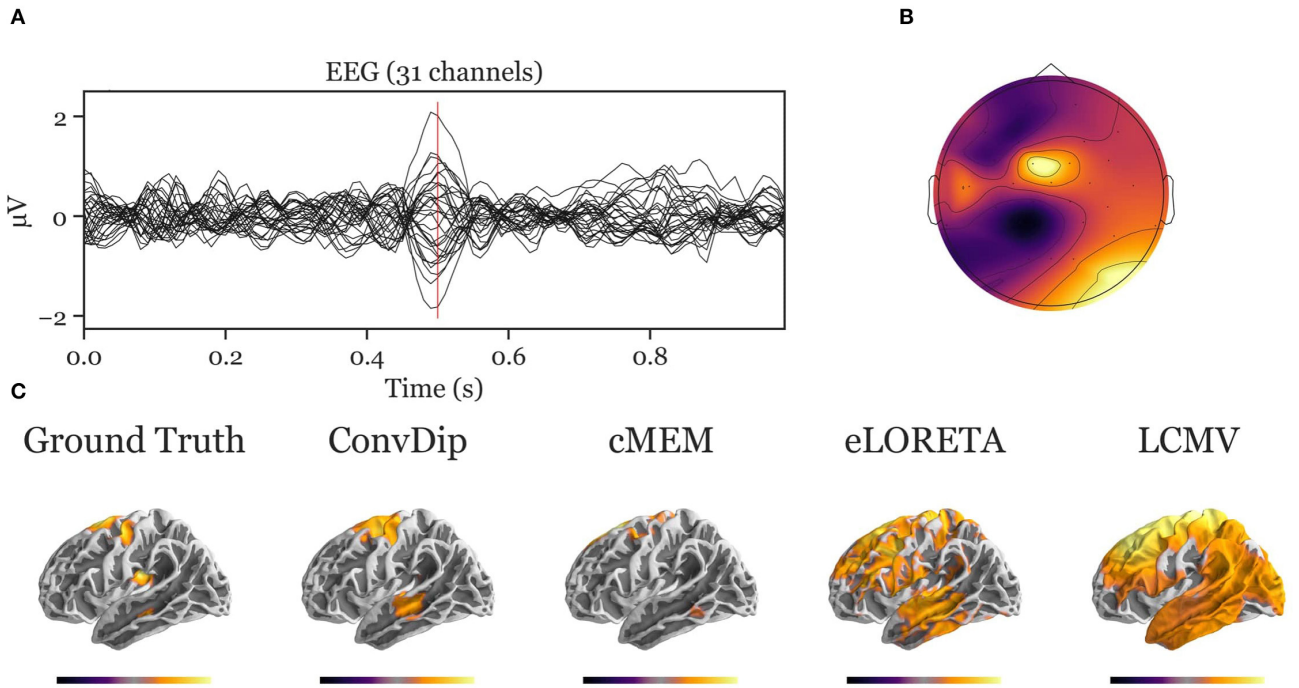

FIGURE A2 | Inverse solution of a simulation containing four source clusters. An exemplary, representative sample of inverse solutions for four source clusters. **(A)** The ERP at each of the 31 channels containing both signal (central peak) and realistic noise from real recordings. **(B)** The scalp map at the central ERP peak (vertical red line in **A**). **(C)** The dipole moments plotted on the white matter surface of the template brain in lateral view of the left hemisphere. On the *left*, the ground truth source pattern is depicted with a source cluster in the motor cortex, supplementary motor area, insula and the middle temporal lobe of the left hemisphere. Various inverse solutions that aim to recover this pattern are depicted next to it. Voxels below 25% of the respective maximum are omitted for a clearer representation of the current distribution.

C. APPENDIX

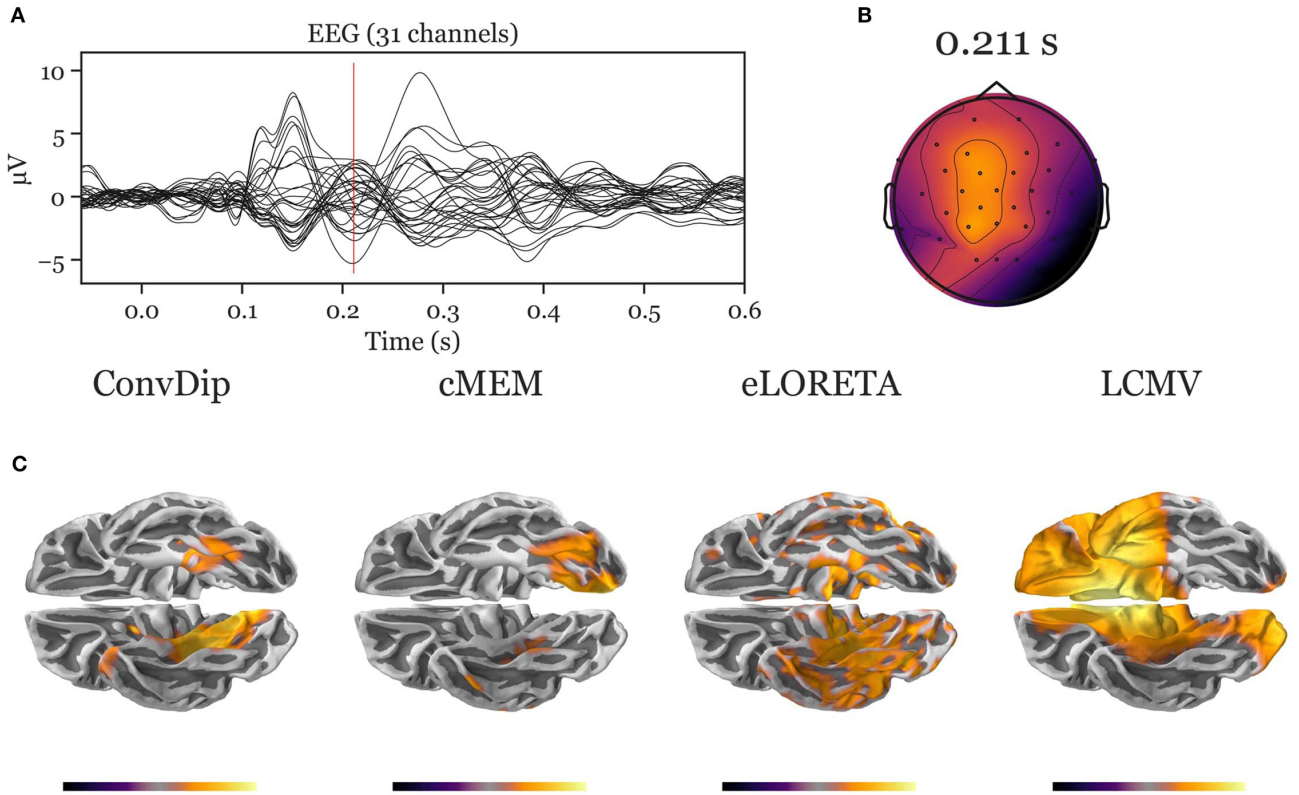

FIGURE A3 | Inverse solution of real face-evoked data. All inverse algorithms were subjected to real EEG data recorded from a single participant containing 150 trials of face-evoked potentials. **(A)** The ERP at each of the 31 channels. **(B)** The scalp map at a N170-like component (vertical red line in A, 211 ms after stimulus onset). **(C)** The dipole moments plotted on the white matter surface of the template brain in ventral view of the right hemisphere to reveal the inferior temporal cortex (ITC). Various inverse solutions show activity in the ITC. Notably, ConvDip and cMEM recover a focal source cluster close or within the fusiform face area, a region known to be involved in face processing (e.g., Kanwisher and Yovel, 2006; Joos et al., 2020). Voxels below 25% of the respective maximum are omitted for a clearer representation of the current distribution.

Advantages of publishing in Frontiers

OPEN ACCESS
Articles are free to read for greatest visibility and readership

FAST PUBLICATION
Around 90 days from submission to decision

HIGH QUALITY PEER-REVIEW
Rigorous, collaborative, and constructive peer-review

TRANSPARENT PEER-REVIEW
Editors and reviewers acknowledged by name on published articles

Frontiers
Avenue du Tribunal-Fédéral 34
1005 Lausanne | Switzerland

Visit us: www.frontiersin.org
Contact us: frontiersin.org/about/contact

REPRODUCIBILITY OF RESEARCH
Support open data and methods to enhance research reproducibility

DIGITAL PUBLISHING
Articles designed for optimal readership across devices

FOLLOW US
@frontiersin

IMPACT METRICS
Advanced article metrics track visibility across digital media

EXTENSIVE PROMOTION
Marketing and promotion of impactful research

LOOP RESEARCH NETWORK
Our network increases your article's readership